Advances in Engineering 2

Handbook of Vehicle-Road Interaction

David Cebon

Taylor & Francis
Taylor & Francis Group

Library of Congress Cataloging-in-Publication Data

Handbook of vehicle-road interaction : vehicle dynamics, suspension design, and road damage / edited by David Cebon.
p. cm. -- (Advances in engineering)
Includes bibliographical references and index.
ISBN 9026515545
1. Motor vehicles--Dynamics. 2. Pavements--Live loads.
I. Cebon, David. II. Series: Advances in engineering (Lisse, Netherlands)
TL243.H37 1999
629.2'31--dc21 99-16701
CIP

First published 1999
Reprinted August 2000

Cover design: Ivar Hamelink
Printed in the Netherlands by Krips, Meppel

Copyright © 1999 Swets & Zeitlinger B.V., Lisse, the Netherlands

All rights reserved. No part of this publication may be reproduced, stored in a retrieval system, or transmitted in any form or by any means, electronic, mechanical, photocopying, recording, or otherwise, without the prior written permission of the publisher.

ISBN 90 265 1554 5

CONTENTS

Preface x

Acknowledgements xii

Part 1 - Introduction 1

Chapter 1 A Brief History 3
1.1 Road Construction 3
1.2 Vehicle–Road Interaction 7
1.3 Load Equivalence Factors 8

Chapter 2 Background 12
2.1 Some Terminology 12
2.2 Background to Road Surface Wear 15

Part 2 - Vehicle Dynamics 19

Chapter 3 Road Surface Topography 21
3.1 Summary 21
3.2 Introduction 21
3.3 Spectral Descriptions of Road Roughness 22
3.4 Artificial Generation of Road Surface Topography 24
3.5 Conclusions 28

Chapter 4 Suspension Components 29
4.1 Summary 29
4.2 Introduction 29
4.3 Leaf Springs 32
4.4 Hydraulic Dampers 41
4.5 Controllable Dampers 55
4.6 Conclusions 65

Chapter 5 Simulating Dynamic Tyre Forces 67
5.1 Summary 67
5.2 Introduction 67
5.3 Two Simple Vehicle Models 67
5.4 Simulation Methods 70
5.5 An Alternative Matrix Formulation of the Vehicle Vibration Equations 76
5.6 Conclusions 82

Chapter 6 Case Studies in Vehicle Simulation 83
6.1 Summary 83
6.2 Introduction 83
6.3 A Rigid Off-Road Vehicle 84
6.4 A Tractor-Semi Trailer Model 91
6.5 Conclusions 106
6.6 Summary of Vehicle Modelling Guide-Lines 107

Chapter 7 Dynamic Tyre Forces 108
7.1 Summary 108
7.2 Introduction 108
7.3 Measuring Dynamic Tyre Forces 108
7.4 Principal Features of Dynamic Tyre Forces 115
7.5 Influence of Tyres and Suspensions 122

Chapter 8 Introduction to Weigh-in-Motion 125
8.1 Summary 125
8.2 Introduction 125
8.3 Errors and calibration 126
8.4 Theory of Multiple-Sensor Weigh-In-Motion 132
8.5 Validation of MS-WIM Theory 140
8.6 High-Accuracy MS-WIM Systems 147
8.7 Conclusions 153

Part 3 - Guideway Response 155

Chapter 9 Background to Guideway Response 157
9.1 Summary 157
9.2 Principal Features of Road Surface Response 157
9.3 Modelling Pavement Response 159
9.4 Modelling Bridges 162

Chapter 10 Response of Continuous Pavements 165
10.1 Summary 165
10.2 Introduction 165
10.3 Theoretical Response of a Road Surface to Moving Dynamic Loads 167
10.4 Experimental Investigation 173
10.5 Responses to Idealised loads 181
10.6 The Influence Function 187
10.7 Comparison of Convolution and Influence Function 190
10.8 Conclusions 195

Chapter 11 Response of Jointed Rigid Pavements 196
11.1 Summary 196
11.2 Introduction 196
11.3 The Rigid Pavement Model 196
11.4 Combination of Loads with Influence Functions 199
11.5 Field Experiments 200
11.6 Model Validation 201
11.7 Conclusions 207

Chapter 12 Dynamic Response of Bridges 208
12.1 Summary 208
12.2 Introduction 208
12.3 Calculating Bridge Response to Vehicle Loads 209
12.4 Examples 214
12.5 Instrumentation and Experimental Procedure 219
12.6 Modal Analysis 223
12.7 Validation of Theory 228
12.8 Conclusions 233

Part 4 - Damage Mechanisms: Flexible Pavements 235

Chapter 13 Background to Road Damage Prediction 237
13.1 Methodology 237
13.2 Primary Response 238
13.3 Material Damage Relationships 239
13.4 Success of the Mechanistic Approach 239

Chapter 14 Permanent Deformation of Flexible Pavements 241
14.1 Summary 241
14.2 Introduction 241
14.3 Theoretical Rutting Model 242
14.4 Asphalt Mixture Viscosity 244
14.5 Viscosity of Soils and Unbound Granular Materials 254
14.6 Experimental Validation 254
14.7 Conclusions 259

Chapter 15 Fatigue Cracking of Flexible Pavements 260
15.1 Summary 260
15.2 Introduction 260
15.3 Primary Responses 261
15.4 Primary Responses due to Periodic Thermal Loading 268
15.5 Cracking Damage 272
15.6 Conclusions 282

Chapter 16 Stiffness Loss in Flexible Pavements due to Cumulative Loading 283
16.1 Summary 283
16.2 Introduction 283
16.3 Methods of Surface Deflection Measurement 284
16.4 Review of Back Calculation Models 285
16.5 VESYSBACK Back Calculation Model 286
16.6 Accelerated Loading Facility 286
16.7 Asphalt Modulus Degradation 288
16.8 Continuum Damage Mechanics Model 292
16.9 Conclusions 294

Part 5 - Vehicle-Guideway Interaction 295

Chapter 17 Background to Vehicle Road Interaction 297
17.1 Summary 297
17.2 Introduction 297
17.3 Static Loading 297
17.4 Dynamic Loading 309
17.5 Conclusions: Comparison of Vehicle Features 320

Chapter 18 Spatial Repeatability 322
18.1 Summary 322
18.2 Introduction 322
18.3 Theoretical Study 323
18.4 Experimental Study 332
18.5 Conclusions 348

Chapter 19 Road Damaging Potential of Measured Dynamic Tyre Forces 349
19.1 Summary 349
19.2 Introduction 349
19.3 Phase I Tests 350
19.4 Phase II Tests 357
19.5 Conclusions 365

Chapter 20 Modelling Whole-Life Flexible Pavement Performance 367
20.1 Summary 367
20.2 Introduction 367
20.3 Description of the Whole-Life Pavement Performance Model 369
20.4 Simplified Case Studies 379
20.5 Parametric Study of Factors Affecting Flexible Pavement Performance 390
20.6 Conclusions 401

Chapter 21 Effects of Spatial Repeatability and Suspension Type 402
21.1 Summary 402
21.2 Introduction 402
21.3 Modelling Assumptions 403
21.4 Effects of Spatial Repeatability 404
21.5 Effects of Suspension Type 414
21.6 Conclusions 424

Chapter 22 Effects of Vehicle Suspensions on the Response of Highway Bridges 427
22.1 Summary 427
22.2 Introduction 427
22.3 Parametric Study of Dynamic Bridge Displacements 428
22.4 Discussion 434
22.5 Conclusions 434

Part 6 - Suspension Design to Minimise Road Damage 435

Chapter 23 Background to Suspension Design 437
23.1 Introduction 437
23.2 Passive Suspensions 438
23.3 Advanced Suspensions 438

Chapter 24 Leaf Springs and Tyres 439
24.1 Summary 439
24.2 Introduction 439
24.3 Test Vehicle And Simulation Validation 440
24.4 Tandem Suspension Measurements 441
24.5 Suspension Parameter Study 443
24.6 Tests On The Modified Vehicle 449
24.7 Dynamic Tyre Forces due to Single and Dual Tyres 453
24.8 Influence of Tyres 454
24.9 Conclusions 458

Chapter 25 Optimising Passive Suspensions 459
25.1 Summary 459
25.2 Introduction 459
25.3 Calculation of Tyre Forces and Road Damage 459
25.4 Bounce Model 461
25.5 Roll-Plane Model 465
25.6 Pitch Plane Model 467
25.7 Optimisation of an Air Suspended Articulated Vehicle 471
25.8 Conclusions 474

Chapter 26 Semi-Active Suspensions 476
26.1 Summary 476
26.2 Introduction 476
26.3 Experimental Details 478
26.4 Passive Damping 479
26.5 Semi-Active damping 481
26.6 More Sophisticated Control Strategies 500
26.7 Conclusions 503

Part 7 - Assessing Road-Damaging Potential **505**

Chapter 27 Background to Suspension Assessment 507
27.1 Summary 507
27.2 Introduction 507
27.3 The European Suspension Test 511
27.4 Vehicle Response Issues 515
27.5 Conclusions 521

Chapter 28 Tractor-Trailer Interaction 523
28.1 Summary 523
28.2 Introduction 523
28.3 Mathematical Model 525
28.4 Correlation Analysis 528
28.5 Discussion of Results 532
28.6 Conclusions 533

Chapter 29 Indirect Vehicle Testing 534
29.1 Summary 534
29.2 Introduction 534
29.3 Test rig 535
29.4 The Convolution Method 539
29.5 Parameter Estimation Method 543
29.6 Conclusions 549

Chapter 30 Implementation Issues and Recommendations 550
30.1 Summary 550
30.2 Implementation Issues 550
30.3 Recommendations 554

Part 8 - Main Conclusions and Recommendations **555**

Chapter 31 Summary of Main Conclusions 557
31.1 Vehicle Dynamics 557
31.2 Guideway Response 557
31.3 Road Damage Mechanisms 558
31.4 Vehicle–Guideway Interaction 558
31.5 Suspension Design 560
31.6 Suspension assessment 561

Chapter 32 Recommendations and Future Research 562
32.1 Recommendations 562
32.2 Future Research 563
32.3 Closing Comments 564

Appendices **565**

Abbreviations 567

References 569

Index 589

Chapter 21 Effects of Spatial Repeatability and Suspension Type 402
21.1 Summary 402
21.2 Introduction 402
21.3 Modelling Assumptions 403
21.4 Effects of Spatial Repeatability 404
21.5 Effects of Suspension Type 414
21.6 Conclusions 424

Chapter 22 Effects of Vehicle Suspensions on the Response of Highway Bridges 427
22.1 Summary 427
22.2 Introduction 427
22.3 Parametric Study of Dynamic Bridge Displacements 428
22.4 Discussion 434
22.5 Conclusions 434

Part 6 - Suspension Design to Minimise Road Damage 435

Chapter 23 Background to Suspension Design 437
23.1 Introduction 437
23.2 Passive Suspensions 438
23.3 Advanced Suspensions 438

Chapter 24 Leaf Springs and Tyres 439
24.1 Summary 439
24.2 Introduction 439
24.3 Test Vehicle And Simulation Validation 440
24.4 Tandem Suspension Measurements 441
24.5 Suspension Parameter Study 443
24.6 Tests On The Modified Vehicle 449
24.7 Dynamic Tyre Forces due to Single and Dual Tyres 453
24.8 Influence of Tyres 454
24.9 Conclusions 458

Chapter 25 Optimising Passive Suspensions 459
25.1 Summary 459
25.2 Introduction 459
25.3 Calculation of Tyre Forces and Road Damage 459
25.4 Bounce Model 461
25.5 Roll-Plane Model 465
25.6 Pitch Plane Model 467
25.7 Optimisation of an Air Suspended Articulated Vehicle 471
25.8 Conclusions 474

Chapter 26 Semi-Active Suspensions 476
26.1 Summary 476
26.2 Introduction 476
26.3 Experimental Details 478
26.4 Passive Damping 479
26.5 Semi-Active damping 481
26.6 More Sophisticated Control Strategies 500
26.7 Conclusions 503

Part 7 - Assessing Road-Damaging Potential **505**

Chapter 27 Background to Suspension Assessment 507
27.1 Summary 507
27.2 Introduction 507
27.3 The European Suspension Test 511
27.4 Vehicle Response Issues 515
27.5 Conclusions 521

Chapter 28 Tractor-Trailer Interaction 523
28.1 Summary 523
28.2 Introduction 523
28.3 Mathematical Model 525
28.4 Correlation Analysis 528
28.5 Discussion of Results 532
28.6 Conclusions 533

Chapter 29 Indirect Vehicle Testing 534
29.1 Summary 534
29.2 Introduction 534
29.3 Test rig 535
29.4 The Convolution Method 539
29.5 Parameter Estimation Method 543
29.6 Conclusions 549

Chapter 30 Implementation Issues and Recommendations 550
30.1 Summary 550
30.2 Implementation Issues 550
30.3 Recommendations 554

Part 8 - Main Conclusions and Recommendations **555**

Chapter 31 Summary of Main Conclusions 557
31.1 Vehicle Dynamics 557
31.2 Guideway Response 557
31.3 Road Damage Mechanisms 558
31.4 Vehicle–Guideway Interaction 558
31.5 Suspension Design 560
31.6 Suspension assessment 561

Chapter 32 Recommendations and Future Research 562
32.1 Recommendations 562
32.2 Future Research 563
32.3 Closing Comments 564

Appendices **565**

Abbreviations 567

References 569

Index 589

PREFACE

This handbook discusses tyre-road contact forces generated by heavy vehicles, their influence on road surface and bridge response and damage, as well as ways of assessing and improving vehicles so as to minimise road damage.

The vertical force applied to the road surface by each tyre of a heavy vehicle can be separated into two components: the static load, due to weight, and a fluctuating component known as the dynamic tyre force or dynamic wheel (axle) load. The static load depends on the geometry and mass distribution of the vehicle and the static load sharing characteristics of the suspension system. Uneven load sharing can result in unnecessarily high average tyre forces with consequently high stresses and strains in the road surface and additional road damage. Dynamic tyre forces are caused by vibration of the vehicle when it is excited by roughness of the road surface. They normally occur at frequencies below 20 Hz. Dynamic tyre forces generate additional dynamic stresses and strains in pavements which are thought to accelerate road surface deterioration, although the mechanisms by which this occurs are not well understood.

There is considerable civil engineering literature concerned with experimental and theoretical studies of road damage caused by heavy vehicles, however it is mostly based on the notion that vehicles apply constant (static) tyre forces to the road surface. These studies have achieved mixed success due to the extremely complex nature of the road damage problem. Comparatively few researchers have investigated the influence of vehicle suspension design features on static and dynamic tyre forces and the consequent effects on pavement damage. This is the main theme of the book.

The primary incentive for understanding these problems is the possibility of reducing the road damage caused by heavy vehicles and the very large associated costs. This may be achieved by highway authorities, through improved design and construction of roads; or by government agencies, through regulations intended to encourage the use of more 'road-friendly' vehicles (for example, the European regulation that provides a payload incentive for vehicles with air suspensions, or suspensions with 'equivalent' performance.) A third possibility is for vehicle engineers to design improved suspensions which minimise road damage. Such suspensions could be based on conventional passive suspension components, or possibly computer-controlled 'active' or 'semi-active' suspension technology.

In order to improve heavy vehicles to minimise road damage and react to suspension performance regulations, it is desirable for vehicle designers to have some understanding of the mechanisms of road damage, and the vehicle factors that have the strongest influence. It is equally important for highway engineers to understand the importance of vehicle features which affect their roads. The main purpose of this book is to provide some of this information and to highlight the important issues in the road damage debate.

This handbook is divided into eight parts. The first four parts provide background information and mathematical models of vehicles and roads. This material underpins the next three parts, which are concerned with combining the models to understand various aspects of vehicle-road interaction.

Part 1 contains general background material about road wear, expenditure on roads and some historical perspectives.

Part 2 is concerned with vehicle dynamics, and includes chapters on road surface roughness, suspension components, measuring and simulating dynamic tyre forces and a brief introduction to the subject of 'weigh-in-motion'.

Part 3 is concerned with the response of the guideway to heavy vehicle loads. It includes chapters on response of continuous flexible pavements, jointed rigid pavements and short-span highway bridges to dynamic vehicle loads.

Part 4 concentrates on the mechanisms of damage of flexible pavements: particularly permanent deformation and fatigue cracking.

Part 5 discusses vehicle-guideway interaction. It presents simple models for predicting the road damage done by dynamic tyre forces of vehicles; 'spatial repeatability' of dynamic tyre forces generated by a vehicle 'fleet'; models of the long-term performance of roads subject to vehicle and environmental loads; and the effects of spatial repeatability and suspension design on road life.

Part 6 is concerned with the design of suspensions to minimise road damage. It investigates improvement and optimisation of conventional 'passive' suspensions, as well as the use of controllable 'semi-active' suspensions.

Part 7 is concerned with the problem of assessing the road-damaging potential of heavy vehicles for regulatory puposes. It discusses the fundamental issues of vehicle dynamics which must be addressed by any testing programme, such as wheel-base filtering, statistical issues associated with vehicle testing, the dynamic interaction between tractor and semi-trailer, and non-linearities of the suspension components.

Part 8 presents conclusions and suggests areas needing further research.

The Appendices contain lists of abbreviations, references and the index.

Much of the work contained in this book has been published in the form of technical papers by the author working in collaboration with others.

ACKNOWLEDGEMENTS

This book could not have been written without the assistance of many colleagues. I would like to express my sincere appreciation to a number of my former research students, who made key contributions to the research described here:

Frank H Besinger
David J Cole
Andrew C Collop
Mark F Green
Michael S A Hardy
Kevin J Kitching
Theo EC Potter

I would particularly like to single-out David Cole, with whom I have collaborated closely since 1986, and who deserves much of the credit for the success of our research into vehicle dynamics.

I am also particularly grateful for the support and advice of a number of members of academic, research and technical staff of Cambridge University Engineering Department: David Newland, Ken Johnson, Mike Ashby, Derek Smith, Hugh Hunt, Michael Sutcliffe, Jim Woodhouse, Ken Wallace, Malcolm Macleod, the late Arthur Timbs, Phil Atkin, Raymond Cheung, Vikram Deshpande, Lampros Stergioulas, Richard Dorling, John Walden, David Miller, Frank Dolman, Gareth Rider, and Chris Wyatt. Thanks also to Atanas Popov, Judith Harvey, David Sampson, Richard Roebuck and Ben Jeppesen for their help with proof reading the final manuscript.

Over the years, many individuals and organisations have been involved in our research programme. I am indebted to them all. They include the following:

• Industrial members of the Cambridge Vehicle Dynamics Consortium, who provided funding and support, including: David Owens and Phil Coddington of Tinsley Bridge Ltd; Les Price, Paul Griffiths and Martin Peaker of Meritor HVS; Robert Harris of Shell Oil; Roger Williams and his staff at Dunlop Tyres; John Aurell and Stefan Edlund of Volvo Trucks; Brian Manton and Peter Allan of Crane Fruehauf; Peter Bakkeren, Roland Vrenken and Ard de Ruiter of Koni Dampers; Alan Arnott, Phil Dandy and his staff at DERA. • Staff of the University of Michigan Transportation Research Institute including: Chris Winkler, Tom Gillespie, Mike Sayers, John Koch, Steve Karimihas, Mike Campbell and MA Nasim. • Staff of the Transport Research Laboratory including: Kit Mitchell, Laszlo Gyenes, Ian Simmons, David Jacklin, Bill Newton, Rod Addis and John Page. • Brian Bevan and Peter Randall of the Motor Industry Research Association. • Robin Sharp of Cranfield University; • Graham Bowskill and Stephen Phillips of the Highways Agency; • Michael Dalgleish and his staff at Golden River Traffic; • Peter Sweatman of Road User Research.

I am also very grateful to the following organisations for funding various parts of the research: The UK Engineering and Physical Sciences Research Council; The Isaac Newton Trust; The Royal Society; The US Strategic Highway Research Program and the European Commission. Thanks also to the many publishers who gave permission to re-print their copyright figures.

I would particularly like to thank Roxy Saadatnejad for her help with the preparation and checking of the final manuscript; and Alyssa Jacobs and John Chambal for providing food and shelter during my periods of escape from Cambridge to work on this project. Finally, I can only partially acknowledge the encouragement and patience of my wife, Ericka, and daughter, Noa, who put up with an absent husband and father during the writing process, and helped to make this book possible.

David Cebon.
1 June 1999

PART 1 - INTRODUCTION

1
A BRIEF HISTORY

The history of roads is much longer than the history of motor vehicles. In the first chapter of this book, the histories of road construction and vehicle–road interaction are reviewed briefly. A detailed history of heavy goods vehicles is not presented: this can be found elsewhere (see, for example, [21, 62, 254, 289, 320, 507][1]). An excellent book on the history of roads and vehicles is 'Ways of the World' by Max Lay [298].

1.1 ROAD CONSTRUCTION

The first pathways were made by animals. By 10,000 BC, these pathways were used by human travellers in temperate areas. Humans began settling in villages around 4,000 BC, and street paving has been found in the remains of settlements dating from around this time [298]. The Egyptian king Cheops was said to have constructed a stone paved road to facilitate building of the Great Pyramid in about 3000 BC [131]. The Incas built fine highways through the Andes, and the Mayans built an extensive network of paved roads in Mexico before the discovery of the New World [79]. The ancient Chinese constructed an extensive system of roads, some of which were paved, from about 1,100 BC onwards. By 20 AD, the Chinese road network extended over some 40,000 km [298].

From about 300 BC, the Caesars of the Roman Empire built strong stone highways throughout Europe, necessitated by their military campaigns [131]. Some of these roads were up to three feet thick, but their surfaces were still worn by the un-suspended steel wheels of chariots (figure 1.1).



Fig. 1.1 A street in Pompeii showing stepping stones and grooves worn by chariot wheels. From [251]

[1] Numbers in parenthesis [ ] refer to reference listed in Appendix B.

Many of the Roman routes are still in use today. By early in the fifth century AD the Romans had built approximately 80,000 km of first class paved roads around the Mediterranean, through Asia Minor and Europe. Of these approximately 12,000 to 15,000 km of paved roads were in Britain alone. After the departure of the Roman legions (around 406 AD), most roads in Europe fell into disrepair and the art of road-making was forgotten.

For many centuries, road construction and maintenance was done on a local basis. Around 1706, the first of the 'Turnpike Trusts' was formed in Britain to build roads and collect tolls from passing vehicles. Eventually there were approximately 1,100 Trusts administering some 38,000 km of roads. They were corrupt organisations, and despite their considerable income, the roads remained in a deplorable state [131].

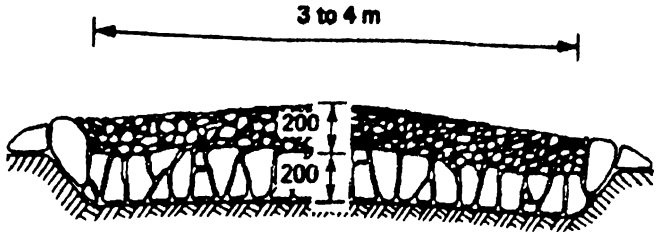
'Modern' road construction began in the late Eighteenth Century, and is usually credited to Trésaguet in France about 1764 [79]. Trésaguet's method is shown in figure 1.2a. It used large paving stones, placed on the ground, with broken stones that were hammered into the interstices and placed on top of the large stones to provide the running surface [297].

Around 1820, Thomas Telford, (the first President of the Institution of Civil Engineers), developed a method based on the French practice, but using carefully placed cubical stones of equal size as a base [297], as shown in figure 1.2b. Telford also paid particular attention to drainage of the subgrade and provided a crowned impermeable surface to aid run-off [79].

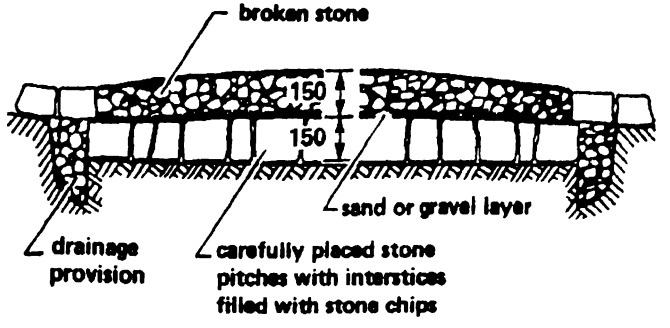
John L. McAdam (1756–1836) published a treatise on road building in 1822 [330]. It was circulated so widely that it effectively became an international standard [148]. McAdam's method was the forebear of modern flexible pavement construction. It did not use a base of large placed stones, but instead relied on interlock between randomly located, angular stone pieces about 25–35 mm (1–1.5 inches) in size. The stones were hand-broken, laid on the natural formation to a depth of approximately 200–250 mm (8–10 inches), and crowned slightly to drain water (figure 1.2c). The surface was originally compacted by hand tools and later by rollers. McAdam insisted that *"nothing is to be laid on the clean stone on pretence of binding; broken stone will combine by its own angles into a smooth solid surface that cannot be affected by vicissitudes of weather, or displaced by the actions of wheels"* [330]. He forbade the addition of earth, clay, or chalk to the broken stone, because such materials absorbed water and were affected by frost. McAdam's method spread the load more widely and uniformly, than those of Trésaguet or Telford, and usually provided a more durable surface [297]. The road was often placed above the natural ground, thereby improving drainage. The foundation material of broken, compacted stones became known as *macadam*.

Although macadam made a vast difference to road making, the surfaces were difficult to clean and required constant sweeping and watering to reduce dust in urban areas. In 1848 the Lincoln road near Nottingham, England was constructed of macadam coated with coal tar residue from a gasworks [131]. This new material became known as tar-macadam and was the predecessor of modern asphalt paving materials. Tar-macadam was only considered suitable for light traffic [131]. The first Portland cement bound macadam pavement was built in Edinburgh, Scotland in 1872 and a road of similar construction was built in Lynn, Massachusetts in 1906 [79].

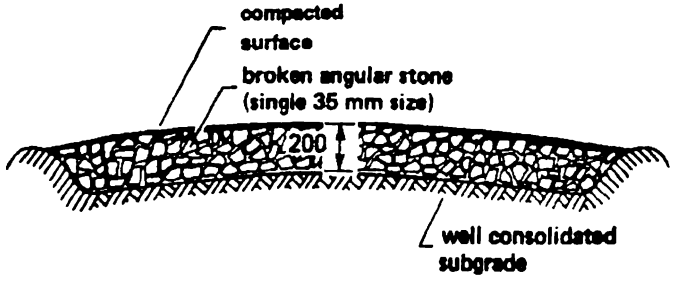
The rise of the railways in the 1830s and 1840s removed the need for road travel, and the construction and improvement of roads essentially stopped: road systems were again neglected [131]. In Britain, travel by rail became considerably faster and cheaper than travel by stage coach [62]. In the US, the railways became the most powerful sector of the economy. American roads were in very poor state by the end of the nineteenth century [418].



(a) Trésaguet's method (1764)



(b) Telford's method (1820)



(c) McAdam's method (1822)

Fig. 1.2 Forms of early road construction after [297]. Note that the vertical scale is exaggerated.

The invention of the 'safety bicycle' in 1887 and use of the pneumatic tyre in the following year, led to a bicycle craze in 1890–5. This was one of the most powerful factors in re-awakening the need for investment in roads.

In Britain in 1896, the bicycle lobby forced the repeal of the 'Red Flag Act' of 1864[1]. Removal of this Act gave considerable impetus to the use and development of mechanical road transport [131][2]. In the US, the League of American Wheelmen, (a bicycle riders group formed in 1880) led the first campaign for state funds for local road construction in 1888 [418], and organised the National League for Good Roads (NLGR) in 1892. As a result of the NLGR's campaign, Congress established the Office of Road Inquiry (ORI)[3] and earmarked $10,000 of the Department of Agriculture's 1894 budget for investigations of road construction and management [418]. This was the beginning of widespread improvement of roads in the USA.

The various asphalt paving techniques did not come into widespread use until the turn of the twentieth century. At this time, the appearance of automobiles with pneumatic tyres rapidly increased the demand for smooth road surfaces [297]. Furthermore a plentiful supply of bitumen, which could be used for making asphalt, was obtained from the distillation of oil for petroleum (gasoline) [131].

Asphalt paving technology developed throughout the twentieth century and by the 1950s, asphalt ('flexible') pavements were constructed in two main ways [323].

(i) Penetration and layer systems (including the seal–coated macadam roads, developed in Australia and New Zealand [297]) were generally used for light construction. They consisted of layers of thoroughly rolled clean aggregate and sprayed bitumen.

(ii) Plant mix systems were used for heavier constructions. Graded aggregate was mixed together with bitumen at approximately 150 °C (300 °F) in a central mixing plant. The hot mix was transported to site, spread, smoothed and rolled into a thick asphalt layer.

These general construction methods are still used today, although there are many classes of asphalts, depending on the size distribution of the aggregate and the grade and proportion of bituminous binder [402].

Other paving methods, including stone, brick and wooden blocks were used successfully in towns up to the turn of the twentieth century. Wooden block pavements were used widely in Australia until the second world war, but they were considerably more expensive than the alternative of tar–macadam [297].

The first *rigid* pavement (Portland cement concrete) in the USA was a rural road, constructed in Wayne County, Michigan in 1909 [131]. A variety of construction types have been employed subsequently for rigid pavements: with and without reinforcing steel and expansion joints (see Bruce, [79] for a description of the early rigid pavement construction methods used in the US).

---

[1] An Act of Parliament in 1861 limited the size and weight of mechanically–propelled road vehicles, and fixed maximum speeds of 10 mph in the country and 5 mph in cities and towns. An amending Act in 1864 reduced the maximum speed of mechanical vehicles to 4 mph in the country and 2 mph in towns, and also stipulated that such vehicles should be attended by three persons, one of whom had to walk sixty yards ahead of the engine carrying a red flag by day, and a red lantern by night.

[2] With the increased popularity of mechanically–propelled vehicles came the dissolution of the last of the Turnpike Trusts in Britain, and the roads previously managed by them became public highways. The British Road Board was formed in 1909 and was given powers to increase taxation on cars and ensure that the new users of roads paid their fair share towards the greatly increased cost of maintenance [131]. It also conducted valuable research on road surfacing methods. In 1919, the Ministry of Transport was formed to supersede the Road Board.

[3] In 1899, the US ORI was renamed the Office of Public Road Inquiry (OPRI), which built a laboratory for testing road construction materials and methods in 1900. It also constructed many demonstration highway sections around the country. The OPRI was renamed the Office of Public Roads (OPR) in 1905 and became the foremost road research establishment in the US under the direction of I.W Page [418]. In 1916, the OPR was enlarged and renamed the Bureau of Public Roads (BPR). The BPR held a conference in 1916 to promote highway engineering and cooperative research between the states. It was attended by representatives of 21 states and led directly to the formation of the American Association of State Highway Officials (AASHO) in 1917 [147]. (AASHO was renamed AASHTO in 1973.)

Typical modern 'high' type pavements have asphalt or Portland cement concrete surfaces 150–450 mm (6–18 inches) thick, built on granular sub-bases, 150–300 mm (6–12 in.) thick [20, 162, 259, 378]. In the USA in 1990, 48% of interstate highway pavements were of flexible construction; 10% were composite; and 42% were rigid [30].

1.2 VEHICLE–ROAD INTERACTION

Horse-drawn heavy goods vehicles were used by the ancient Romans, particularly for military purposes. For many centuries after the withdrawal of the Romans from Europe, horseback was the main mode of personal transportation, with pack-horses used to carry goods [298]. However, in the mid sixteenth century, coach travel began to gain popularity. Steel spring suspensions came into general use on passenger coaches late in the seventeenth century and coach travel expanded rapidly as a result [131]. Before the improved roads of McAdam and Telford, the effect of heavy wagons on un-metalled roads was to generate ruts that were often axle deep. This made travelling dangerous and often impossible in winter months. In 1622, James I of England prohibited loads greater than one tonne on any vehicle operating during the winter [298]. An Act of 1751 attempted to eliminate the rutting effect of narrow wheels by prohibiting the use of wagons with wheel rims less than 9 inches wide on turnpike roads [131].

The first full-size vehicle to run on the road under its own power was a three-wheeled, front wheel drive steam carriage, built by the Frenchman Nicholas Cugnot in 1770 [131]. Many steam-powered road vehicles were built in the nineteenth century, beginning with Trevithick's passenger-carrying steam carriage of 1801, but restrictive legislation prevented their wide-spread use in Britain [131]. In 1840, Worsley, a steam carriage inventor, said that *"the only real difficulty to the general use of steam vehicles on roads instead of horse-power, arises from the great irregularities of surface resistance on common roads"* [131]. Diplock [156] observed that road-adhesion, road-resistance and damage to roads were closely allied, and that the tractive ability of steam traction engines was limited by the small area of contact between wheel and road. In 1893 he patented a traction engine with four-wheel steering and permanent four-wheel drive (including a third differential between the axles)[1]. After the repeal of the 'Red Flag Act' in 1896, steam-powered road vehicles were developed rapidly, despite significant restrictions on weights and speeds. By 1900, Thornycroft and Co. had introduced a six-wheeled, articulated steam truck capable of carrying 5 tons [62]. Steam-powered trucks continued to be developed in Britain until the 1930s, but they never gained significant popularity in the US. However, electric trucks were used in the US around the turn of the century.

Carl Benz patented the first gasoline-powered automobile in 1886 [21], and the Winton Company started manufacturing trucks with internal combustion engines in the US in 1898 [13]. Fuel cost was a *minor* item in the early years of automobiles, however, failure of the solid rubber tyres was frequent (up to one tyre every 700 miles), difficult and expensive to repair [62]. Before 1900, the cost of running commercial petrol-driven vehicles in Britain was more than horse traction, and steam engines were popular [62].

Road deformation remained a problem, and in Britain in 1904, the minimum widths of steel tyres for vehicles over 2 tons unladen weight were fixed in relation to axle loads [131]. The Road Traffic Act of 1930 introduced similar regulations that favoured pneumatic tyres and penalised vehicles with

---

[1] In his book, Diplock [156] also described a device he called a 'Pedrail' (a cross between the walking action of a horse and the low rolling resistance of a railway wheel), which was intended to maximise wheel/road contact area and tractive force. The Pedrail could be considered to be a predecessor of the modern agricultural tractor tyre. Diplock also proposed the use of road trains that could be *"split into smaller units for collection and distribution through branch routes and terminals"*, and he recognised the problem of 'off-tracking' of multiple unit vehicles.

solid tyres that damaged road surfaces [131]. The same sort of legislation is still being enacted today, for example, with restrictions on the use of wide-single tyres on so called 'road-friendly' suspensions in the European Community [32].

Damage to the early asphalt roads became a problem, partly because of higher vehicle speeds. Colonel R.E.B. Crompton, The Engineer of the (British) Road Board, discussed vehicle-road interaction in a paper to the Institution of Mechanical Engineers in 1913 [146]. He believed that road deformation (particularly corrugation) was due to *"the repeated action of vehicles closely resembling one another in their harmonious action, passing over the road at a speed sufficient to transform the smooth rolling of the wheels into bouncing or pulsating motion"*. This was probably the first reference to the topic of 'spatial repeatability' which is currently an important research issue (see Chapter 18).

In 1905, 750 trucks were produced annually in the US. By 1914, this had increased to 25,000 [507]. Great strides were made in the development of heavy commercial vehicles during the first world war, including development of the first pneumatic truck tyre by Goodyear in 1917 [227]. After the war, many military trucks were pressed into civilian peacetime duty. By 1918, US truck production had increased to 230,000 per year [507] and there were approximately 600,000 trucks in the country [13]. According to Cron, [147]: *"this tremendous additional burden (on US highways) reached its peak at the worst possible time: during the spring thaw of 1918. The results were catastrophic. In Delaware, the Philadelphia Pike was reduced from a good bituminous macadam road to a quagmire by the passage of a single 100-truck convoy. In the Mid West, supposedly high-type roads of brick on concrete bases or bituminous concrete on macadam bases also warped and crumbled. By the end of the war, thousands of miles of roads were barely passable despite skyrocketing maintenance expenditures."*

In 1919 Congress provided $200 million of aid for State highways. However, at the annual AASHO meeting in December of that year, Anson Marston pointed out that: *"The country is about to spend untold billions of dollars in the construction of paved roads. Yet there is a serious lack of the fundamental scientific data which are absolutely essential to the correct design and construction of paved roads"* [147]. It could be argued that the same statement still holds true today! In the intervening years, however, very large research efforts have taken place to improve the design and construction of roads.

1.3 LOAD EQUIVALENCE FACTORS

As early as 1822, McAdam proposed that heavy vehicles should pay road tolls according to the amount of road damage they caused [330]. The subsequent history of vehicle-road interaction has been influenced strongly by the attempts of road engineers to find a common unit for defining the road damaging-potential of various classes of vehicles.

In the 1870's, the French Corps of Bridges and Roads began taking traffic censuses as a means of estimating surface wear on paved roads [147]. To translate animals and vehicles into surface wear, they designated the *collar* as a standard unit for measuring traffic. One collar was defined as a single animal harnessed to a loaded vehicle. A pair of cattle harnessed to a heavy load counted as two collars. Subsequent to the French census in 1904, motorcycles were assigned 0.3 collars; vehicles licensed to travel less than 30 km/h (20 mph) were assigned one collar; and vehicles licensed to travel more than 30 km/h were assigned three collars [147].

The French method was adopted in Great Britain, but the English ton was used instead of the collar as the standard unit of traffic. Sheep and pigs were assigned 0.1 ton each; motorcycles were assigned 0.13 tons; omnibuses drawn by two or more horses were assigned 3 tons; steel-tyred trucks were assigned 10 tons and steam-powered traction engines were assigned 12 tons [147]. In the USA, the Office of Public Roads studied traffic on the Rockville Pike experimental road, near Washington DC in 1915. The results were reduced to tonnage by assigning average weights to

several classes: 0.28 tons for a rubber–tyred, horse–drawn vehicle; 2 tons for an automobile and 2.4 tons for a loaded 'motor dray' [147].

Despite these censuses, road engineers did not have reliable methods for incorporating traffic data into their pavement designs during the first half of the twentieth century. Therefore, pavements were essentially designed like conventional civil engineering structures, to withstand a limiting maximum load, rather than to wear out gradually in a specified service life.

The early design procedure for rigid pavements was relatively straightforward, because concrete had well known strength characteristics, and simple beam equations could be used to estimate stresses for the worst case condition of a wheel load applied to the unsupported end or corner of a slab (see, for example [79]). In 1926, Westergaard modelled a rigid pavement as an elastic plate supported by a Winkler foundation [489], and his more accurate formulae for slab stresses were subsequently incorporated into rigid pavement design methods.

The load–carrying characteristics of flexible pavements were not understood nearly as well as for rigid pavements. Until the late 1950s, civil engineers mainly used the principle that the vertical stress under a load in a flexible pavement *"diminishes in geometrical proportion as it is transmitted downward from the surface, by virtue of spreading over a larger area"* [323]. The dispersion angle was generally taken as 45 degrees [131]. The main design methods therefore involved first measuring the bearing capacity of the natural soil (often specified by the 'California Bearing Ratio'); and second choosing the thickness of the various layers, using a simple formula or design chart, to ensure that the vertical stress in the subgrade and other layers did not exceed their bearing capacities [131, 323].

In the 1940s and 1950s, more sophisticated pavement design methods were developed, some of which used empirical corrections to modify pavement thickness design charts according to the expected daily traffic of heavy vehicles (*eg* light/medium/heavy traffic). An advanced design procedure called the 'Hveem–Carmany method' was used in California by 1958. It involved converting the expected traffic in the design life into a number of equivalent 5,000 lb wheel loads, using a logarithmic equivalence formula. A design chart enabled the thickness of asphalt to be determined from the equivalent number of standard axle loads [323]. The idea of *equivalent standard axle loads* was subsequently adopted widely, and is still used today in most pavement design methods.

In 1958–60, the American Association of State Highway Officials (AASHO) performed a very large, full–scale road test in Ottawa, Illinois [7, 8]. Six test tracks were built with various constructions, including flexible and jointed rigid pavements. Only one set of materials and one road–bed soil was used for each pavement type [20]. The US Army Transportation Corps drove 200 vehicles around the tracks at 35 mph, for up to 1.1 million axle applications on the sections that survived the test: a total of some 17 million vehicle–miles in two years.

Probably the most important result of the AASHO road test was the 'fourth power law' which has had a profound influence on pavement design and operating practice throughout the world ever since. A regression analysis on the results of the test indicated that the decrease in 'pavement serviceability' caused by a heavy vehicle axle could be related to the fourth power of its static load [367]. Pavement serviceability was assessed by a panel of experts. It was rated on a scale known as the 'Present Serviceability Index' (PSI), with values ranging from 0 to 5: a value of 5 representing a 'perfect' road[1]. It was found that the PSI could be expressed in a regression equation relating 'cracking and patching', rut depth and surface roughness [367].

---

[1] Roads are generally re-surfaced or re-constructed when the PSI reaches 2.0 to 2.5 [20]. In 1990, approximately 59% of Interstate highways in the USA had PSI values of 3.5–5.0; 32% had PSIs of 2.6–3.4; and 8.7% had PSIs of 2.5 or less [30]

The loads applied to a road by mixed traffic can be converted into a number of Equivalent Standard Axle Loads (ESALs) [413], by applying the fourth power law to each axle [20, 367]. The number of ESALs N attributed to static load P is

$$N = (P/P_0)^n, \text{ with } n = 4. \tag{1.1}$$

P_0 is generally taken to be 80 kN.

The AASHO road test therefore yielded the 'Holy Grail' that road engineers had been seeking for nearly a century: the ESAL. It provided enormous simplification for pavement design, since the road-damaging characteristics of any traffic stream could be characterised by a single number - the number of ESALs. ESALs were immediately incorporated into manual pavement design procedures (*eg* [20]), and later were used in computer-aided 'mechanistic' pavement design packages, to characterise the traffic. The ESAL also provided a simple tool for evaluating the road damaging potential of vehicles. It is used universally throughout the world, for assigning road user charges for heavy goods vehicles – and it will continue to be used for the foreseeable future.

Table 1.1 presents ESAL data collected on Weigh-in-Motion scales in the UK. The data is averaged by vehicle class. It shows that the number of ESALs per axle generally diminishes with increasing number of axles on a vehicle.

Vehicle Class	*Number of ESALs*
Buses and coaches	1.3
2-axle rigid	0.34
3-axle rigid	1.7
3-axle articulated	0.65
4-axle rigid	3.0
4-axle articulated	3.6
5-axles or more	3.5

Table 1.1 Approximate national average ESAL values in the UK. From [135].

The validity of the 'fourth power law' is, however, questionable [4], particularly for current axle loads and axle group configurations; tyre sizes and pressures; road construction; and traffic volumes: all of which are significantly different from the conditions of the AASHO road test [8, 281]. More recent research has indicated that the damage exponent n in equation 1.1 may take a wide range of values. For flexible pavements, values of 2–6 [4] and 1.3–4.1 [457] have been cited in the literature. For composite and rigid pavements, values are thought to be as high as 8–12 [16, 109] and 11–33 [26]. An extensive discussion of the fourth power law is provided in [281]. The fourth power law is essentially a 'rule of thumb' that is used in the absence of a convenient alternative.

The importance of the fourth power assumption should not be underestimated – it has a great influence on political decisions concerning the axle loads of trucks, and hence the economics of freight transport. For example, using the fourth power law, one application of an 80 kN axle load is equivalent to 65,500 applications of a 5 kN axle of a car. Consequently road charging agencies attribute virtually all road damage to trucks.

Furthermore, conclusions about road damage are extremely sensitive to the power used in the equivalence relation. (The power is not known accurately as explained above.) Figure 1.3 shows the equivalence factors, calculated using equation 1.1, for a range of loads, with exponents n between 1 and 6. Consider, for example, an axle load P = 100 kN compared with a standard axle load P_0 = 80 kN. The value of P/P_0 is 1.25. A *second* power indicates that it is 1.56 times more damaging to roads, whereas a *fourth* power indicates that it is 2.44 times more damaging (2.44 ESALs). If the correct equivalence relationship had a *sixth* power, then a 100 kN axle would be 3.81 times more damaging than an 80 kN axle.

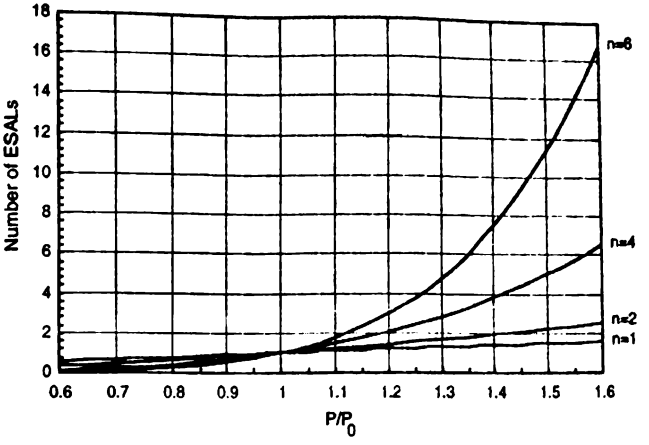


Fig. 1.3 Equivalence factors for various values of the exponent n in the power law equation 1.1.

It should be a matter of concern to the heavy vehicle industry, that the basis on which vehicle operating charges are calculated is so *numerically sensitive*, and yet open to considerable doubt.

Much research into road–vehicle interaction has been conducted since the AASHO road test. Some of it is discussed in the remainder of this book.

2
BACKGROUND

2.1 SOME TERMINOLOGY

Some of the more important terms used to describe tyre forces and pavement response are defined in the following sections. A list of abbreviations can be found in Appendix A.

2.1.1 Vehicle Dynamics

The instantaneous tyre force *P(t)* at time *t* comprises the average *static* value plus an oscillating dynamic component: the *dynamic tyre force* (also known as the dynamic wheel load or dynamic axle load).

Frequency refers to the spectral content of *P(t)* as measured by an observer moving with the vehicle, and *speed* refers to the speed of the moving vehicle, measured relative to a stationary observer (the pavement). These are the usual definitions used in vehicle ride dynamics.

Random tyre forces have a relatively broad-band frequency content. They are not 'stochastic' in the strict sense, because they are essentially predictable (deterministic) and repeatable on subsequent runs of a particular vehicle over a given stretch of road.

The Root Mean Square *(RMS)* value of a random process is equal to its standard deviation, providing the mean value has been removed.

Spectral Density: Random signals, like tyre force time histories or road surface profiles, can be decomposed into a series of sine waves of different frequencies and amplitudes, by Fourier analysis. The spectral density is the square of the amplitude of the sine waves, divided by the frequency bandwidth. When the spectral density is plotted against frequency on linear scales, the area under the curve is equal to the mean-square value of the signal (square of the standard deviation). The spectral density is sometimes known as the 'power spectral density' (PSD), the 'mean square spectral density', or simply the 'spectrum'. See Newland [355] for an introduction to the subject.

The main types of suspensions discussed to in the book are defined in figure 2.1.

(i) *Tandem suspensions* are suspension groups (sometimes known as 'bogies') with two axles (figures 2.1 a-d, e, g). *Triaxle suspensions* have three axles (figures 2.1 f, h).

(ii) In *steel leaf spring* suspensions (figures 2.1 a, c, e, f), the spring element consists of one or more steel beams (leaves) which bend elastically under load. Energy dissipation (damping) is provided by dry ('Coulomb') friction between the leaves at a number of contact points. The leaves can be of uniform thickness or have a tapered or parabolic thickness distribution.

(iii) In *air* suspensions (figures 2.1 g, h), the spring element consists of a sealed rubber bag, filled with pressurised air. Adiabatic compression of the air provides a nonlinear spring stiffness. Hydraulic dampers (not shown) usually provide the main source of energy dissipation. The airbags are normally connected to an automatic levelling system which increases or decreases the volume of air in response to quasi-static changes in the height of the vehicle body. The airbags are often inter-connected to facilitate static load sharing.

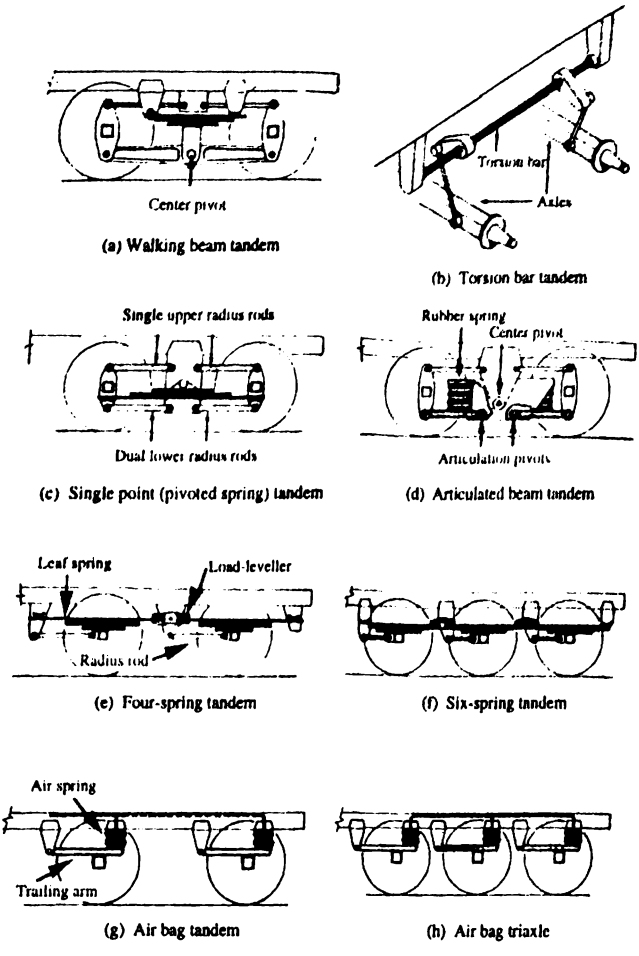


Fig. 2.1 Schematic diagrams of typical heavy vehicle suspensions from [443]

(iv) In *walking-beam* suspensions (figure 2.1a) two axles are linked by a rigid beam. Torque rods may provide additional axle location. The centre of the beam is connected by a pin joint to a steel leaf spring or rubber spring, which is in-turn connected to the frame of the vehicle. This allows free articulation of the axles in pitch. Damping of vertical vibration is provided by inter-leaf friction. Pitch articulation is essentially undamped, unless hydraulic dampers are fitted between the axles and the chassis. Walking beam suspensions are typically used for tandem drive axles, particularly for off-road applications, since the distance between the axles remains essentially fixed, even for large inter-axle articulation angles.

(v) *Torsion bar* suspensions (figure 2.1b), utilise a torque rod with offset cranks attached to the axles. The rod twists elastically under load to provide a restoring force which reacts vertical movements of the axles. Damping is normally provided by hydraulic dampers (not shown).

(vi) In *Single-point* suspensions (figure 2.1c), two axles are connected by a leaf spring, which is connected to the chassis by a pin joint at its centre. These suspensions are sometimes known as *pivoted-spring* suspensions. They are used in similar applications to walking-beam suspensions.

(vii) *Articulated beam* suspensions (figure 2.1d) are a variation on the single-point suspension concept. They use two rubber springs instead of a single leaf spring. The rubber provides vibration damping due to internal hysteresis.

2.1.2 Pavement Engineering

Modern road surfaces (or pavements) may be classified as flexible, composite or rigid. A *flexible* pavement consists of one or more layers of asphalt supported by a granular subbase. *Composite* pavements consist of a flexible surface layer supported by a stiff Portland Cement Concrete (PCC) base; and *rigid* pavements consist of a layer of PCC on a granular foundation. Rigid pavements can be classified further according to their arrangement of steel reinforcement and joints.

Seal-coated pavements, (sometimes known as 'spray-seal' or 'chip-seal') consist of layers of compacted unbound aggregate with a thin bituminous surface layer to prevent water ingress. Stone chips coated with bitumen are normally rolled into the surface layer to provide skid resistance.

Asphalt consists of a mixture of crushed rock aggregate (with a graded size distribution), and bitumen binder. *Bitumen* is essentially the residue remaining after distillation of oil. Its properties can be enhanced by addition of filler and polymer modifying agents.

The *subgrade* is the natural soil on which a pavement is constructed.

The *subbase* is a foundation of compacted unbound granular material upon which the bound layers of the road are built.

In a flexible pavement, the *road base* is the lower layer of asphaltic material, which is often made of Dense Bituminous Macadam - DBM. It can be quite thick, typically up to 300mm, on heavily trafficked European roads. The *wearing course* is the relatively thin (typically 50mm) top layer of asphalt. It is often made of Hot Rolled Asphalt - HRA, and is normally designed to have a surface texture with good skid resistance and high resistance to permanent deformation.

High type pavements are used for heavily trafficked principal roads and truck routes. They usually have a strong surface layer of asphalt or Portland cement concrete, of thickness 150 mm or more, built on one or more layers of compacted granular material. *Intermediate* and *Low type* pavements are used for moderately trafficked local routes and unsealed rural roads respectively.

The *primary response* of a pavement is the stress, strain, or displacement (or time derivatives thereof) at a particular point in the pavement when it is loaded by a vehicle.

Contact tractions refer to distributed vertical or horizontal forces applied to the surface of the pavement by tyres. They are often called contact stresses or contact pressures.

Road *damage* refers to degradation of the structural integrity or surface profile of a road when it is trafficked by vehicles. Since roads are designed for a finite service life and are expected to deteriorate with time, it may alternatively be called *wear*. The most important types of road damage due to heavy vehicles are *fatigue cracking* and *permanent deformation* (or rutting – formation of longitudinal ruts).

Throughout the book it is assumed that vehicles are travelling in a straight line at constant speed, so that the tyre forces are primarily vertical with no appreciable lateral or longitudinal components. The book does not include discussion of the forms of road damage which are essentially caused by environmental factors alone.

2.2 BACKGROUND TO ROAD SURFACE WEAR

According to Rauhut, Roberts and Kennedy [279, 384] and Jackson [259], the most important road damage mechanisms, (which are defined by Kennedy *et al* [279]) are:

(i) Fatigue cracking for all types of pavements;

(ii) Permanent deformation (longitudinal rutting) for flexible and composite pavements;

(iii) Reduced skid resistance for flexible and composite pavements;

(iv) Low temperature cracking for flexible pavements;

(v) Reflection cracking for composite pavements;

(vi) Faulting, spalling, low temperature and shrinkage cracking, blow-ups, punch–outs and steel rupture for rigid pavements, depending on their structural category (see [279] for definitions).

Each failure mechanism is affected by many factors including the roadway design and construction methods, the material properties of each constituent layer, the traffic loading and the environmental conditions throughout the service life [279]. A useful comparison of the influences of vehicle loading and the environment can be found in [20].

Vehicles most directly affect fatigue cracking and permanent deformation, and examples of these failures are shown in figures 2.2 – 2.4.

There are various advantages and disadvantages of rigid versus flexible pavement construction. Appendix B–3 of the AASHTO pavement design guide [20] lists the factors that affect the choice of pavement type, but it does not make any specific recommendations.



Fig. 2.2 Fatigue cracking in an asphalt pavement. From [259].

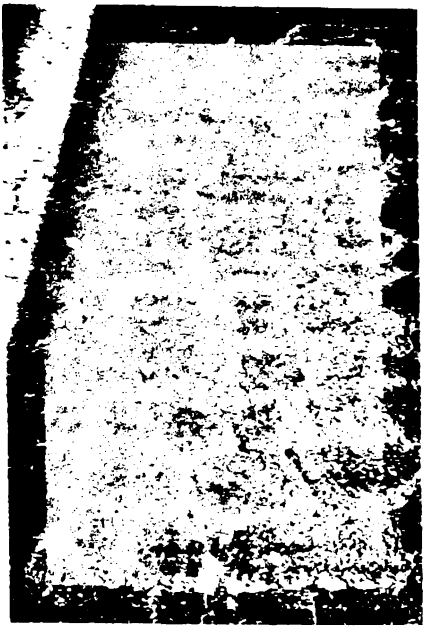


Fig. 2.3 Fatigue cracking, final stage. From [259].



Fig. 2.4 Rutting in an asphalt pavement. From [259].

The main structural difference is that rigid pavements have considerably higher bending stiffnesses than flexible pavements, and therefore they can be used on relatively weak natural soils without thick

base courses [10]. Bituminous materials are very sensitive to temperature: some mixes can rut easily at high temperatures [42, 162], and they become brittle at low temperatures [42, 482]. Both flexible and rigid pavements can crack at low temperatures due to thermal contraction, but rigid pavements are usually reinforced or provided with expansion joints that are intended to minimise this problem. An example of low temperature cracking in an asphalt pavement is shown in figure 2.5. Note that traffic loading has caused secondary cracking, around the primary transverse thermal crack. Rigid pavements have several other failure modes (vi, above), which can lead to a poor running surface.

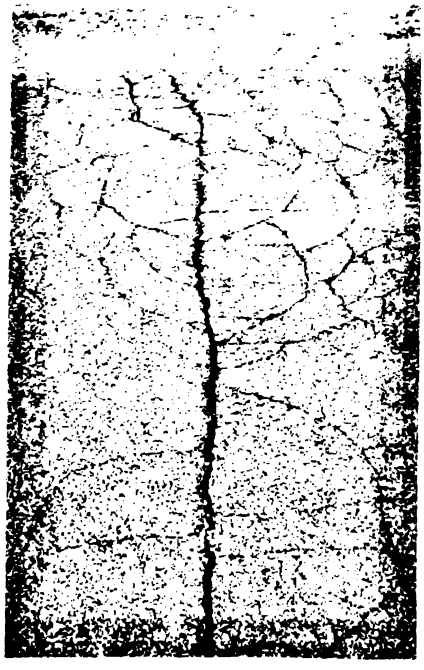


Fig. 2.5 A transverse crack in an asphalt pavement due to thermal contraction, with secondary cracks due to traffic loading.

According to [10], the working life of rigid pavements can be increased significantly by a modest increase in concrete thickness, and they are therefore usually designed to last 40 years. Conversely, flexible pavements are more economical for shorter working lives, and they can be overlaid easily to extend their lives. Therefore they are usually designed to last 20 years. It is also important to note that new concrete takes up to 28 days to cure, whereas asphalt can be trafficked almost immediately after construction or maintenance. This can be an important consideration in minimising traffic disruption.

Undoubtedly the most important factor in the choice of pavement type is the cost of initial construction and subsequent maintenance. Whole-life costs are comparable because of competition between the asphalt and PCC industries [20], so both materials are likely to be used in the future.

PART 2 - VEHICLE DYNAMICS



3
ROAD SURFACE TOPOGRAPHY

3.1 SUMMARY

Spectral descriptions of road surface roughness, suitable for simulating vehicle ride dynamics, are presented. Methods for generating pseudo-random samples of single tracks and pairs of correlated tracks, with desired spectral characteristics are discussed.

3.2 INTRODUCTION

In order to simulate vehicle vibration behaviour for the purposes of calculating dynamic tyre forces or ride performance, it is necessary to assume a road roughness input.

Extensive road roughness surveys have been performed in various countries, for example [293, 407]. Road surfaces can normally be considered as random with a Gaussian (normal) probability distribution, providing occasional large local irregularities, such as potholes, are isolated and treated separately [159]. It is generally found that the amplitude/wavelength characteristics of roads can be characterised in terms of the spectral density of the profile height.

Linearised frequency domain simulations of vehicle response can use the spectral densities of road profiles directly to calculate vehicle response spectral densities and RMS values. In order to perform time domain simulations it is necessary to generate samples of the road surface profile. Single pseudo-random profiles can be generated artificially given a target spectral density. These are suitable for two-dimensional 'pitch-plane' simulations. Pairs of pseudo-random profiles with appropriate correlation can be generated providing the cross spectral density between the profiles is known or can be approximated by a simple model.

Section 3.3 presents the most common spectral descriptions of road surface roughness that are used for vehicle response calculations. Section 3.4 discusses the artificial generation of road surface topography, given known direct and cross spectral densities.

3.3 SPECTRAL DESCRIPTIONS OF ROAD ROUGHNESS

Two general models have been proposed for the spectral densities of the profiles of single tracks along typical roads.

3.3.1 The Draft ISO Formulation

Based on extensive measurements of the profiles of European roads from [293], a proposal for an ISO standard for road roughness was prepared in 1972 [12]. The spectral density $S_u(\kappa)$ of road height u was classified as follows:

$$S_u(\kappa) = \begin{cases} S_u(\kappa_0)\left(\dfrac{\kappa}{\kappa_0}\right)^{-n_1} & \dfrac{\kappa}{\kappa_0} \le 1 \\ S_u(\kappa_0)\left(\dfrac{\kappa}{\kappa_0}\right)^{-n_2} & \dfrac{\kappa}{\kappa_0} > 1, \end{cases} \tag{3.1}$$

where

κ = wavenumber[1]
κ_0 = datum wavenumber, cycles/m
$S_u(\kappa)$ = displacement spectral density, m^3/cycle
$S_u(\kappa_0)$ = spectral density at κ_0, m^3/cycle.

The values of the constants recommended in [12] (but later corrected in [393]) were $n_1 = 3$, $n_2 = 2.25$, $\kappa_0 = 1/(2\pi)$ cycles/m and $S(\kappa_0)$, defined as in Table 3.1.

Road Class	$S(\kappa_0) / 10^{-6}$ m^3/cycle
Very Good	2 – 8
Good	8 – 32
Average	32 – 128
Poor	128 – 512
Very Poor	512 – 2048

Table 3.1 Values of the constant $S(\kappa_0)$ in the corrected ISO standard for road roughness.

These corrected values were used for plotting the classifications shown in figure 3.1[2]. Also shown on the figure are the spectral densities of the left and right wheel paths of a section of the TRL test track in the UK. The two wheel tracks have similar roughness. The test lane does not fit the ISO classifications exactly, but corresponds approximately to the 'good' classification (poor motorway or

---

[1] Wavenumber κ (cycles/m) expresses rate of change with respect to distance in the same way as frequency f (cycles/s) expresses rate of change with respect to time. Just as the period T (in seconds) of a time–varying sine wave is related to frequency f by $T = 1/f$, so the wavelength λ (in metres) of a sinusoidal roughness component is related to the wavenumber κ by $\lambda = 1/\kappa$.

[2] In 1995, the ISO finally published the results of the 25 years of deliberations by its technical committee ISO/TC 108 on road roughness. The result was ISO Standard ISO 8608: 1995 [38] (and the corresponding identical British Standard BS 7853: 1996). Unlike the draft proposals [12], ISO 8608: 1995 does not include any classifications of profile spectra (eg see Table 3.1 and figure 3.1). Nor does it discuss how road profiles should be measured. Instead it specifies how road profile measurements (and the corresponding information about the measuring methods) should be reported. The conclusion is that the road profile data should be reported as a spectral density of the vertical displacement against wavenumber. When data for two parallel tracks is reported, the coherence function between the two tracks should also be specified.

average principal road). The measured profiles shown in this figure were used in the vehicle simulation study which is described in the second half of Chapter 6.

Robson [393] also suggested that an adequate description of road profile spectra can often be given by an equation of the form

$$S_u(\kappa) = S_0|\kappa|^{-n} \tag{3.2}$$

where $n = 2.5$, and S_0 takes values as follows:

Road Class	S_0 /$10^{-8}m^{0.5}cycle^{1.5}$
Motorway	3-50
Principal road	3-800
Minor road	50-3000

Table 3.2 Values of the constant S_0 in Robson's proposal for road roughness, equation 3.2 [393].

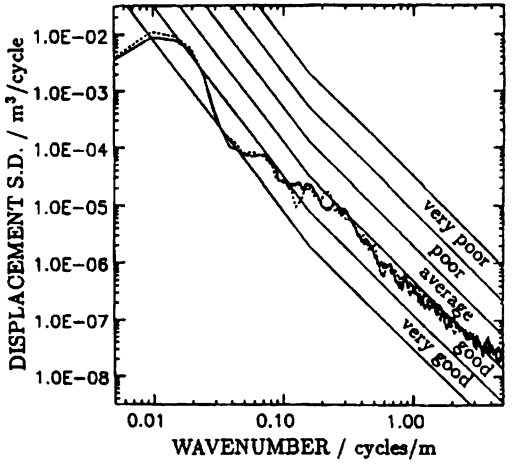


Fig. 3.1 Draft ISO classification for road roughness spectral densities. Also shown are spectral densities of a section of the TRL test track in the UK. From [120].
_____ nearside wheel path - - - - - - offside wheel path

3.3.2 An Alternative Formulation

Sayers [407] proposed a more general road roughness model, which can be fitted to a wide range of measured road profile spectral densities. It takes the form:

$$S_u(\kappa) = \frac{G_a}{(2\pi\kappa)^4} + \frac{G_s}{(2\pi\kappa)^2} + G_e \tag{3.3}$$

where G_a G_s and G_e are fitted constants. See Appendix E of [192] for a summary of the approach.

3.3.3 Tyre Envelopment of Short-Wavelength Features

Experimental measurements have shown that truck tyres 'envelop' short wavelength road roughness components of the order of the tyre contact length, (for example grooves in PCC pavements) [304]. This envelopment has the effect of filtering the short wavelength (large wavenumber) components from the roughness spectral density $S_u(\kappa)$. This phenomenon is not usually very important for normal highway speeds, because the short wavelength components correspond to frequencies that are too high to excite suspension resonances.

For low speed travel on rough roads, however, tyre envelopment can be a significant factor and needs to be included in vehicle simulations (see Section 6.3). Various tyre envelopment models have been proposed, (see [86, 87]). A simple and reasonably accurate approach is to apply a moving average filter to the road profile before using it in the vehicle simulation. The filter should have a length equal to the tyre contact length [87, 192, 356].

3.4 ARTIFICIAL GENERATION OF ROAD SURFACE TOPOGRAPHY

3.4.1 A Single Road Profile

Time-domain vehicle vibration simulations require road surface input profiles which are described by the heights of equally spaced points along the road. Such descriptions may come directly from measurements of the surface roughness used to test the vehicle. However, when such measurements are not available, pseudo-random profiles can be generated to have spectral densities given by equations 3.1 – 3.3, or some other similar description.

A one-dimensional random profile may be generated by applying a set of random phase angles, uniformly distributed between 0 and 2π, to a series of coefficients derived from the desired direct spectral density. The corresponding series of spot heights $\{z_r^{(1)}\}$ at regular intervals along the track is obtained by taking the inverse discrete Fourier transform (DFT) [355] of the spectral coefficients[1].

$$z_r^{(1)} = \sum_{k=0}^{N-1} \sqrt{S_k}\, e^{i\left(\theta_k^{(1)} + \frac{2\pi kr}{N}\right)}, \qquad r = 0,1,2,....(N-1), \tag{3.4}$$

where

S_k = $(2\pi/N\Delta)\, S_{11}(\gamma_k)$
$S_{11}(\gamma_k)$ = the target spectral density
γ_k = $2\pi k/N\Delta$ = the wavenumber[2] in rad/m
Δ = the distance interval between successive ordinates of the surface profile and
$\{\theta_k^{(1)}\}$ = a set of independent random phase angles uniformly distributed between 0 and 2π.

By the central limit theorem, the amplitude distribution of the $\{z_r^{(1)}\}$ series is asymptotically Gaussian as $N \to \infty$ [423, 510].

The process is essentially the reverse of conventional spectral analysis... In spectral analysis, the direct spectral density is determined by squaring the spectral coefficients (outputs of the discrete Fourier transform), thereby discarding their phase information. In the inverse process, (equation 3.4) this information is replaced by random phases, thereby creating a 'random' profile with the exact target amplitude spectral density.

---

[1] Note that the parentheses { } are used to denote a series of values.

[2] The two different wavenumbers γ (rad/m) and κ (cycles/m) have a similar relationship to the angular frequency ω (rad/s) and the temporal frequency f (cycles/s), namely: $\gamma = 2\pi\kappa$. The relationship between the corresponding spectral densities is $S(\gamma) = (1/2\pi)S(\kappa)$, (see [356]).

3.4.2 *A Pair of Correlated Road Profiles*

If two tracks are needed across a surface - *eg* for simulating three-dimensional vehicle models, a second correlated random profile may be generated in a similar way to the first. If the second track has direct spectral density $S_{22}(\gamma)$ and the cross spectral density between the two tracks is $S_{12}(\gamma)$, then the second track is generated by summing two independent series $\{y_r^{(2)}\}$ and $\{w_r^{(2)}\}$. The $\{y_r^{(2)}\}$ series uses phase angles given by

$$\theta_k^{(2)} = \theta_k^{(1)} + \psi_{12_k} \tag{3.5}$$

where $\{\psi_{12_k}\}$ are the phase angles of the cross spectral density. The series $\{y_r^{(2)}\}$ is therefore correlated with the first track. The $\{w_r^{(2)}\}$ series uses a new set of random phase angles $\{\phi_k^{(2)}\}$, also uniformly distributed between 0 and 2π, and so it is not correlated with track 1.

The series for the correlated component is given by

$$y_r^{(2)} = \sum_{k=0}^{N-1} \eta_{12_k} \sqrt{S_{22_k}}\, e^{i\left(\theta_k^{(1)} + \psi_{12_k} + \frac{2\pi kr}{N}\right)}, \qquad r = 0,1,2,....(N-1). \tag{3.6}$$

and the series for the uncorrelated component is given by

$$w_r^{(2)} = \sum_{k=0}^{N-1} \sqrt{1-\eta_{12_k}^2}\, \sqrt{S_{22_k}}\, e^{i\left(\phi_k^{(2)} + \frac{2\pi kr}{N}\right)}, \qquad r = 0,1,2,....(N-1), \tag{3.7}$$

where

$$\eta_{12_k}^2 = \frac{\left|S_{12_k}\right|^2}{S_{11_k} S_{22_k}} \tag{3.8}$$

is the ordinary coherence function between the tracks, and $S_k = (2\pi/N\Delta)S(\gamma_k)$, as before. The second track is then given by

$$z_r^{(2)} = y_r^{(2)} + w_r^{(2)}, \qquad r = 0,1,2,....(N-1). \tag{3.9}$$

When the ensemble averages are calculated, $\{z_r^{(1)}\}$ and $\{z_r^{(2)}\}$ are found to have direct spectral densities $S_{11}(\gamma)$ and $S_{22}(\gamma)$ and cross spectral density $S_{12}(\gamma)$, as required [88].

The use of equations 3.4 to 3.9 to synthesise a pair of correlated random profiles requires complete knowledge of the direct and cross spectral densities. Although the direct spectral densities of single tracks along typical road surfaces are readily available from descriptions like equation 3.1 – 3.3, reliable cross spectral data for road profile pairs is difficult to obtain, either from the literature or by measurement.

Various approaches are possible:

(i) $S_{11}(\gamma) = S_{22}(\gamma)$, and $S_{12}(\gamma) = 0$ for all wavenumbers: the two profiles have the same direct spectral densities but are completely uncorrelated [111, 477, 478].

(ii) $S_{11}(\gamma) = S_{22}(\gamma) = S_{12}(\gamma)$ for all wavenumbers: the two profiles are perfectly correlated ($\eta_{12} = 1$), with the same roughness, *ie* identical. This is the assumption implicit in 'pitch-plane' vehicle simulations, which neglect roll excitation.

(iii) Dodds and Robson [159] assumed a simple analytical form for the coherence $\eta_{12}^2(\gamma)$, with $S_{11}(\gamma) = S_{22}(\gamma)$ and $\psi_{12}(\gamma) = 0$. No physical reason was provided for their choice of function, although it has been suggested [157, 158, 270] that $S_{12}(\gamma)$ is often real valued ($\psi_{12}(\gamma) = 0$) for road surfaces.

(iv) $\eta_{12}(\gamma)$ can be obtained from measurements of two tracks along a road. In this case the two artificial profiles will have the same statistics (direct and cross spectral densities) as the measured surface, but different details - as if the real profiles and the measurements were different samples of the same random processes.

(v) $\eta_{12}(\gamma)$ can be obtained from a model of the correlation between the tracks (*eg* those used by Rill [388] and by Ruf [398]). Of those available, the 'isotropic' surface model is the most popular.

The concept of a homogeneous, isotropic and Gaussian surface, whose statistical properties are the same everywhere and have no directional bias, has been discussed in the theoretical literature [158, 230, 269, 270]. Such a surface has a real-valued cross-spectral density between the profiles of parallel tracks, and this may be calculated from the autocorrelation function (or direct spectral density) of a single track across the surface. This property allows the profiles of two correlated parallel tracks to be generated using equations 3.4 to 3.9. Note that in order for the direct spectral density of the surface to be admissible, it must decrease monotonically with increasing wavenumber [230, 269].

The cross-correlation function between two parallel tracks spaced distance b apart on an isotropic surface may is given by

$$R_{12}(x) = R_{21}(x) = R_{11}\left(\sqrt{x^2 + b^2}\right), \tag{3.10}$$

where $R_{11}(x)$ is the autocorrelation function along a single track on the surface [158, 270].

The cross spectral density[1] is obtained from the usual Fourier transform relationship:

$$S_{12}(\gamma) = S_{21}(\gamma) = \frac{1}{2\pi}\int_{-\infty}^{\infty} R_{11}\left(\sqrt{x^2 + b^2}\right) e^{-i\gamma x} dx. \tag{3.11}$$

Equation (3.11) can be evaluated using a method involving Bessel functions, derived by Heath [230], or using the discrete Fourier transform according to

$$S_{12_k} = \frac{1}{N}\sum_{r=0}^{N-1} R_{11}\left(\sqrt{(r\Delta)^2 + b^2}\right) e^{-i\frac{2\pi kr}{N}}, \qquad k = 0,1,2,...(N-1) \tag{3.12}$$

where the cross correlation coefficients $R_{11}\left(\sqrt{(r\Delta)^2 + b^2}\right)$ are calculated from the linear autocorrelation function $R_{11}(x)$ by interpolation. Care must be taken to ensure that the correct linear autocorrelation function is obtained, rather than the so-called circular correlation function, that is usually generated by the DFT [355].

Figure 3.2 shows the coherence function (generated using equations 3.8, 3.10 and 3.11) for two parallel tracks on an isotropic surface at various different spacings b. The direct spectral density of the tracks corresponds to a 'good' road (equation 3.1), smoothed to improve its cross spectral characteristics[2]:

$$S(\kappa) = \frac{S_u(\kappa_0)}{\left(\frac{\kappa}{\kappa_0} + \frac{\kappa_{co}}{\kappa_0}\right)^{n_1}\left(\frac{\kappa}{\kappa_0} + 1\right)^{(n_2 - n_1)}}, \tag{3.13}$$

---

[1] As $S_{12} = S_{21}$ and $S_{12} = S_{21}^*$ for an isotropic surface, they must be real valued (ψ_{12}=0).

[2] Heath [230] showed that the cross spectral density (and hence the coherence function) depends on $dS(\gamma)/d\gamma$ - the derivative of the direct spectral density.

where κ_{c0} is a low wavenumber cut-off, which was set to $0.1/2\pi$ cycles/m, and the other parameters correspond to those in equation 3.1.

Figure 3.3 shows sections of two tracks along the isotropic surface, spaced 2m apart, generated using equations 3.4 to 3.9. The RMS profile roughness is approximately 12mm. At small wavenumbers (long wavelengths) the tracks are well correlated and the coherence approaches unity[1]. This is an intuitive result, since it is expected that for long wavelengths (*ie* travelling over 'mountains') two parallel tracks on a surface will essentially follow the same undulations. Conversely at large wavenumbers, the coherence goes to zero, since the profiles are uncorrelated at short wavelengths - *eg* travelling over 'pebbles'.

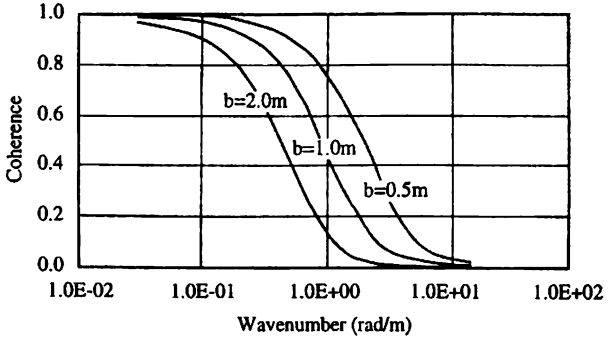


Fig. 3.2 Coherence between two parallel tracks across an isotropic surface with a 'good' ISO spectral density.

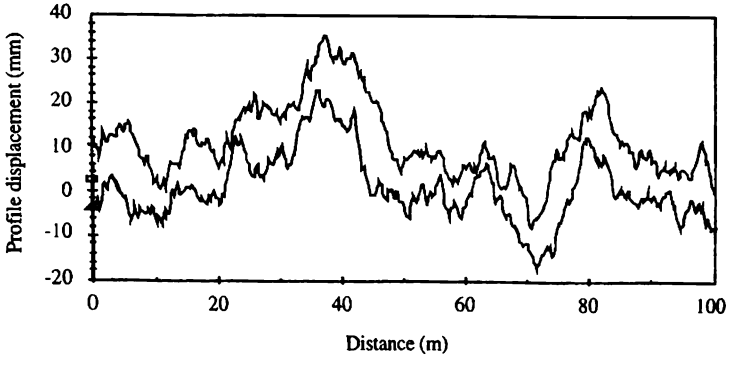


Fig. 3.3 Two parallel tracks across a 'good' isotropic surface at a spacing of 2m. The second track has been shifted up by 10mm for clarity.

[1] Note that the coherence function does not necessarily always approach unity at small wavenumbers: the limiting value depends on the low frequency behaviour of the direct spectral density. See Heath [2.30] for details.

3.4.3 More than Two Random Profiles - an Entire Isotropic Surface

To generate the profiles of more than two parallel tracks across a fully isotropic surface, a two-dimensional inverse DFT must be used. Assuming isotropy, a complete two-dimensional surface can be generated from a one-dimensional spectral density. The method is discussed in detail in [100, 355]. An example is given in [100], in which a sample surface is generated from the measured one-dimensional spectral density of a rough 'pavé' test track. Some one-dimensional statistics of this surface are computed. This topic will not be pursued further here.

3.5 CONCLUSIONS

(i) Spectral descriptions of road roughness profiles are well established and can be used directly in frequency-domain simulations of vehicle response to road roughness.

(ii) Methods for generating artificial road profiles from spectral densities of the roughness of single tracks are well understood and straightforward. Such artificial profiles can be used in time-domain simulations of the response of 'pitch-plane' vehicle models.

(iii) Pairs of pseudo-random road surface profiles can be generated for parallel tracks across a surface, providing the direct spectral densities of the two tracks and the cross spectral density between them are known. The assumption that the surface is isotropic can be used to generate suitable cross-spectral densities. Such pairs of artificial profiles can be used in time-domain simulations of the response of three-dimensional vehicle models.

(iv) If the profiles of more than two parallel tracks are needed, it is possible to use a method involving the two-dimensional DFT to generate a complete pseudo-random isotropic surface.

4
SUSPENSION COMPONENTS

4.1 SUMMARY

An examination is made of the force developing characteristics of road vehicle leaf springs under realistic broad band random loading conditions. A program of laboratory measurements on two vehicle springs is described. The measured responses are compared with digital computer simulations of the springs which use empirical descriptions of their low frequency (quasi-static) behaviour. It is concluded that two different empirical descriptions can be used for predicting accurately the forces developed by typical road vehicle leaf springs to at least three times the highest frequency of major excitation. Both require a detailed knowledge of the small amplitude, low frequency behaviour of the springs at the static load of interest. The popular Coulomb friction model of leaf spring behaviour is shown to be inaccurate throughout the entire frequency range.

A laboratory rig for testing hydraulic dampers using the 'hardware-in-the-loop' method is described. A mathematical model of a hydraulic shock absorber is then developed. The model is suitable for vehicle simulations and has seven parameters which can be determined by simple dynamic measurements on a test damper. The shock absorber model is validated under realistic operating conditions using the test rig, and the relative importance of various features of the model on the accuracy of vehicle simulations is investigated.

Two strategies are investigated for controlling a semi-active damper to track a prescribed force demand signal: (i) 'open loop' control, using a model of the damping force versus velocity characteristics; and (ii) force feedback (closed loop) control. The damping characteristics and switching transients of a prototype damper were measured, and used to develop a mathematical model of the dynamics of the damper. The two control strategies were investigated using an idealised (constant velocity) test. Their performance was also simulated and measured under realistic operating conditions using the Hardware-in-the-Loop testing method. Open loop damper control was generally found to give superior performance to force feedback control, due to its smaller phase lag at high frequencies.

This chapter is based on work that was previously published in [89] and [55, 56].

4.2 INTRODUCTION

In order to simulate accurately the vibration of heavy vehicles subjected to road surface roughness, it is necessary to model the nonlinear characteristics of their suspension elements. This is the subject of this chapter.

4.2.1 Leaf Springs

Leaf springs are the most common suspension elements in modern commercial road vehicles. They are nonlinear devices which dissipate energy through interleaf friction and which have force developing characteristics that are dependent on the static load and the amplitude of imposed

displacements. Detailed knowledge of these characteristics is necessary for accurate computer simulation of the vibration of many commercial vehicles.

Traditional calculations of the behaviour of leaf springs were based on simple beam theory. Various authors have extended the calculations to include large deflections [253], dual rate springs [333, 397], stiffness modification due to shackles [11], initial camber [201] and constant cross section (single leaf) design [201] (applicable to composite springs). These calculations neglect interleaf friction but provide designers with estimates of spring rates for large deflections.

Fancher *et al* [175] performed a series of sinusoidal tests on heavy vehicle springs and concluded that providing a correction is made for the effective inertia of the spring, the shape of small amplitude hysteresis loops is independent of stroking frequency. They therefore recommended the use of equations representing low frequency (quasi-static) hysteresis characteristics for the description of high frequency response in vehicle simulations.

A common description of leaf spring hysteresis characteristics used in early vehicle simulations is the combined (parallel) linear spring and Coulomb friction element (see for example [161, 252, 478, 509]). The accuracy of this model can be unsatisfactory. Some workers have attempted to describe measured low frequency force-deflection characteristics. Potts and Walker [377] tabulated the large deflection behaviour of motor cycle coil springs used in their 1/8 scale model articulated vehicle study. The tables were interrogated directly in a computer simulation. Kunjamboo *et al* [292] used a fitted force-deflection characteristic with divergent loading and unloading curves linked by parabolic transition curves. Fancher *et al* [175] devised an empirical equation in which the spring force decayed exponentially (with displacement) towards arbitrary 'envelope' curves.

The high sensitivity of simulated vehicle responses (and particularly dynamic axle load calculations) to spring model assumptions was shown by Sayers and Gillespie [405]. As a result of this sensitivity, it is important to establish the expected accuracy and limitations of the leaf spring models used in commercial vehicle vibration simulations.

Section 4.3 describes an experimental investigation into the behaviour of some typical automotive leaf springs for realistic operating conditions, and examines the accuracy of three alternative spring models, suitable for use in vehicle vibration simulations.

4.2.2 Hydraulic Shock Absorbers

Hydraulic shock absorbers (dampers) are common suspension elements in modern commercial road vehicles. Their nonlinear force generating characteristics depend on the amplitude and frequency of the imposed motion. Accurate mathematical models of the ride dynamics of commercial vehicles require detailed knowledge of these characteristics.

Published work on the behaviour of automotive shock absorbers has focused on devices for passenger cars. This work has utilised three approaches, of varying complexity:

(i) Segel and Lang [419] presented a detailed mechanistic model of a shock absorber, based on the internal pressure/flow processes. The model had 82 parameters, was computationally complex and not suitable for comprehensive vehicle simulation studies. Hall *et al* [217] used this model in a quarter car vehicle simulation and established that typical linear and bi-linear models of dampers are inaccurate and lead to over optimistic estimates of ride performance.

(ii) A nonlinear shock absorber model suitable for vehicle simulation was described by Karadayi [272]. This model was based on an experimental study of two passenger car shock absorbers. The model included hysteresis due to fluid compressibility and backlash, in addition to asymmetric damping and dry friction. Good agreement between experimental measurements and theoretical predictions was found for tests at 0.2Hz, but no experimental results were presented for higher frequencies.

(iii) The application of harmonic and stochastic linearisation procedures to shock absorber dynamics was discussed by Wallaschek [485]. A linearisation procedure using experimental data was introduced, leading to a comparison of some simple dynamic models of a particular shock absorber, with experimental results. Wallaschek's analysis showed that simple models with a small number of parameters did not describe the behaviour of shock absorbers adequately.

The objective of the research described in Section 4.4 was to develop an accurate semi-empirical damper model with the fewest possible parameters, and to investigate the sensitivity of simulated vehicle responses to various simplifications of the damper model.

4.2.3 Controllable (Semi-Active) Dampers

A semi-active damper is a suspension damper which is able to dissipate energy at a continuously-variable, controllable rate. The damper is switched off when the control action requires the damper to feed power into the suspension. Very little work has been published on the use of semi-active dampers in the suspensions of heavy goods vehicles, largely because suitable hardware is not readily available. Some previous work is reviewed briefly in Chapter 26. (See also [53]).

Most theoretical studies of semi-active suspension systems have assumed that controlled dampers can track a prescribed force demand perfectly (when they dissipate energy). This assumption is not accurate for many *real* controllable dampers because of time delays, valve dynamics, friction, and limits on the range of possible damping coefficients. To quantify the errors caused by implementing continuous control strategies using a real semi-active damper, and the potential performance improvements of semi-active compared with optimised passive systems, it is necessary to investigate the force tracking ability of such a damper.

In Section 4.5 a prototype continuously variable semi-active damper, provided by a European manufacturer, is studied. The damper is designed for use in passenger cars (a suitable truck damper could not be found at the time of the research). Control strategies for vehicles incorporating semi-active dampers are discussed in Chapter 26.

4.2.4 Other Suspension Elements

Heavy vehicle suspension systems can contain combinations of suspension elements with linkages, sliding ends, bump stops, flexible bushes and so on. These systems will not be discussed in detail here, other than to say that their behaviour can often be modelled by combining the leaf spring and damper models described here with other simple mechanical elements. Some examples can be found elsewhere in this book:

Suspension	Description	Section of book
Single-point tandem suspension (figure 2.1e)	Centrally pivoted leaf spring with an axle connected to each end, and a complex frictional torque restricting pitch motion of the assembly.	6.3
Four-spring tandem suspension (figure 2.1e)	Two leaf springs with sliding ends, connected by a pivoted link.	6.4 and 24.4
Walking-beam tandem suspension (figure 2.1a)	Centrally pivoted rigid beam with an axle connected to each end, and a steel leaf spring or rubber spring connecting the centre of the beam to the frame.	5.3
Air suspensions (figure 2.1g,h)	Rubber air bags with associated linkages. The air bag can often be considered as a linear spring.	22.3 and 25.7
Independent air suspension	Two separate trailing arms – one at each end of the axle.	24.8 and 25.5

4.3 LEAF SPRINGS

4.3.1 Leaf Spring Testing Apparatus

A testing machine consisting of a stiff frame, spring mounting and loading assembly and a preloading arrangement using air springs, was fabricated. An electrodynamic vibrator with 20mm (peak to peak) maximum stroke, dynamic force limit of 1.5kN p-p (up to 5kHz) and maximum power of 1 kW was used to excite the centres of the springs.

The instrumentation consisted of a strain-gauged load link, which measured the applied force, a linear resistive displacement transducer and an accelerometer which monitored spring centre deflections and accelerations respectively. This arrangement was similar to that described by Fancher *et al* [175] and is discussed in more detail in [88].

A series of steady state harmonic tests and random input tests were performed on two different lightweight leaf springs from an off road utility vehicle (gross vehicle mass approx 1.2 tonnes). Practical limitations prevented the testing of heavy truck springs, however the results are expected to be broadly similar to those shown here.

4.3.2 Experimental Results

Sinusoidal Load Cycling

In order to verify the conclusion of Fancher *et al* [175] that the force-deflection characteristics of leaf springs are independent of load cycling frequency, a series of steady state harmonic tests was performed. Each spring was loaded to typical in-service static loads (corresponding to laden and unladen vehicles) and cycled over various displacement amplitudes for frequencies up to 18Hz. The magnitude of the inertia correction was established experimentally, and found to be 70%-90% of the total mass of the spring and clamp assembly, depending on the distribution of mass along the spring.

Figure 4.1 shows typical results. The effect of the inertia correction can be seen in the last frame of the figure. Considerable high frequency noise (at approximately 200Hz) is observed at high cycling rates. This can be attributed to beaming vibration of the test specimen [334] and structural vibration of the apparatus [88] and is well above the frequency range of interest. These results verify the conclusions of Fancher *et al.*

A series of low frequency sinusoidal tests (2.7Hz) were performed at static loads corresponding to vehicles in the laden and unladen conditions (1.47kN and 2.94kN). The displacement amplitude was varied within the available stroke of the vibrator (20mm p-p) and empirical equations were fitted to the resulting force-deflection characteristics. The average force and displacement levels were removed as they were found to prevent accurate fitting of the empirical equations. These fitted equations were used for predicting forces in the random-input tests described later.

The equation presented by Fancher *et al* [175] formed the basis of the fitting procedure:

$$\frac{\partial F}{\partial \delta} = \frac{F_{env} - F}{\beta}, \tag{4.1}$$

where

F = Spring force (N)
F_{env} = Force on the envelope at the δ of interest (N) (upper boundary for increasing deflection and lower boundary for decreasing deflection)
δ = Spring deflection (m)
β = Decay constant (m).

For sufficiently small time steps, a valid digital solution to (4.1) is

$$F_i = F_{env_i} + \left(F_{i-1} - F_{env_i}\right)e^{-|\delta_i - \delta_{i-1}|/\beta}, \tag{4.2}$$

where subscript 'i' indicates the current simulation time step and 'i-1' the previous time step. In this study, linear envelopes of the form

$$F_{env_u} = k_u\delta + F_u \quad \text{and} \quad F_{env_l} = k_l\delta + F_l \tag{4.3}$$

were found to be adequate. Subscript 'u' indicates the upper envelope and '*l*' the lower envelope.

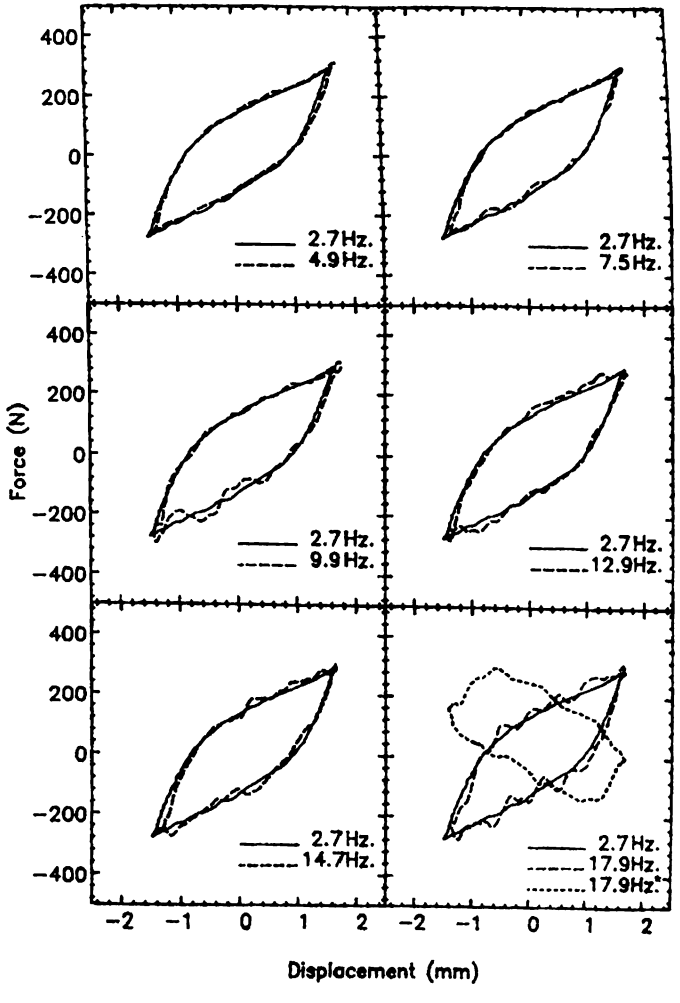


Fig. 4.1 The effect of cycling frequency on hysteresis loops. * = no correction for effective inertia. From [89].

It was found that equation 4.2 could be fitted quite accurately to a particular measured hysteresis loop. In some cases it was found to be desirable to use different decay constants β_u and β_l for the loading and unloading curves. It was also found that the parameter values (k_u, k_l, F_u, F_l, β_u and β_l) for the closest fit were strongly sensitive to the displacement amplitude. As a result it was not possible to fit equation 4.2 to all hysteresis loops developed by a spring at a given preload, using a single set of fitted parameters.

Three fitting procedures were therefore employed:

(i) Equation 4.2 was fitted to a hysteresis loop with displacement amplitude near to the anticipated RMS of the road surface input. This procedure will be known as the 'direct' method. Typical results are shown in figure 4.2.

(ii) It was assumed that small force variations would follow curves defined by the projection of a 'base' loop of large amplitude generated from equation 4.2 (see figure 4.3). This procedure (known as the 'projection' method) requires the additional knowledge of the base loop amplitude (δ_0) and the displacement at the last turning point (points A and B on figure 4.3). Figure 4.4 shows typical results of this procedure.

(iii) To compare procedures (i) and (ii) with the popular simple Coulomb friction model of leaf spring behaviour, equation 4.2 was used with $\beta_u = \beta_l = 0.1$mm, giving sharp vertical transitions between the upper and lower envelopes (figure 4.5).

Once the empirical parameters were established, each of these fitting procedures was used to simulate the response of leaf springs to random inputs as described in the following section.

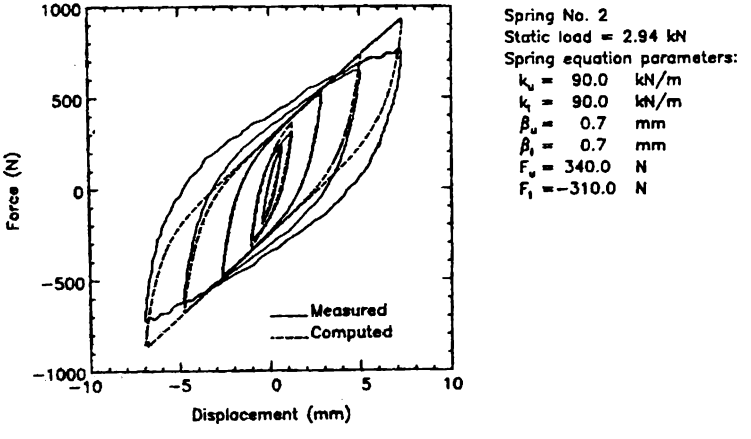


Fig. 4.2 Comparison of measured hysteresis loops and responses computed by the 'direct' method. Equation 4.2 was fitted to the loop of amplitude (approximately) 3 mm. From [89].

Response To Random Excitation

In order to provide a realistic environment for the test specimen a simple nonlinear 'quarter-car' vehicle simulation (with two degrees of freedom) was excited by a random road profile signal. The quarter-car model does not contain the detailed suspension nonlinearities and complexities of sprung mass motion that are typical of heavy vehicles [118, 121], however the suspension deflection has

appropriate amplitude and frequency content for testing of suspension components under relatively realistic operating conditions. (See Chapter 5 for further discussion of this model.)

The relative displacement of the sprung and unsprung masses provided the input for the electrodynamic vibrator (figure 4.6). Displacement feedback reduced errors between the target and measured spring displacements. The measured spring displacement and inertia-corrected force signals were digitised and theoretical force time histories were computed from the displacements, using the three simulation methods. The vehicle model parameters can be found in [89].

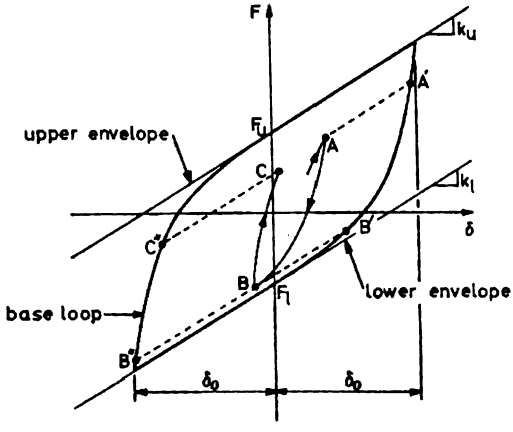
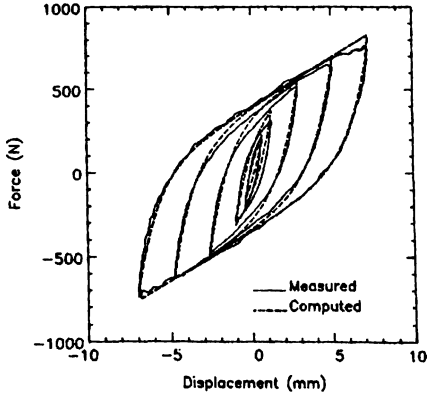


Fig. 4.3 The 'projection' fitting procedure line AB is the projection of A'B' on the base loop. Similarly BC is the projection of B"C". From [89].



Spring No. 2
Static load = 2.94 kN
Spring equation parameters:

k_u =	60.0	kN/m
k_l =	60.0	kN/m
β_u =	1.2	mm
β_l =	1.2	mm
F_u =	460.0	N
F_l =	−410.0	N
δ_0 =	7.3	mm

Fig. 4.4 'Projection' fit to measured hysteresis loops. From [89].

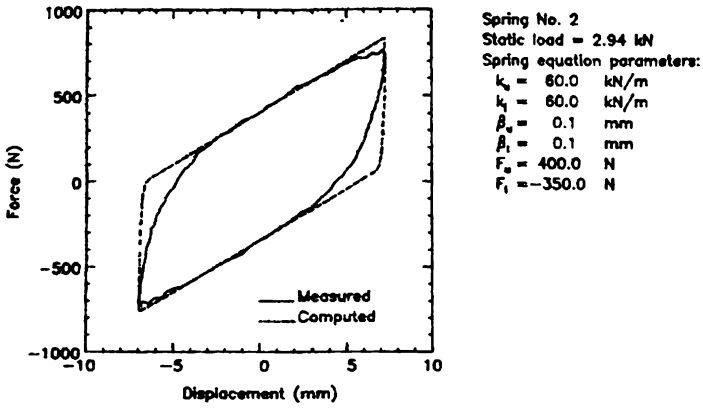


Fig. 4.5 Simple Coulomb model of leaf spring behaviour (equation 4.2 with $\beta_u = \beta_l = 0.1$ mm). From [89].

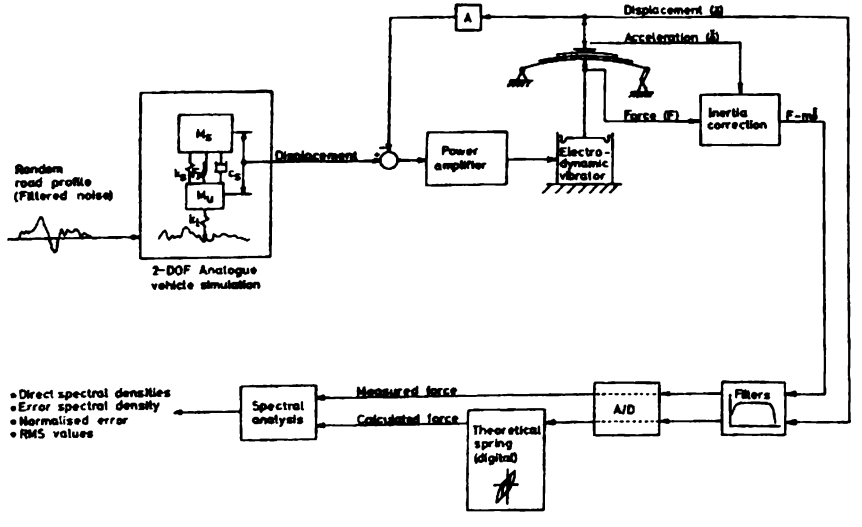


Fig. 4.6 Block diagram of apparatus and analysis for random excitation tests. From [92].

The vehicle simulation parameters were chosen to represent 1/4 of a lightweight utility vehicle. The suspension spring was modelled by a linear spring and an optional parallel Coulomb friction element, designed to dissipate the same amount of energy as the test specimen over a 10mm (p-p) displacement cycle.

The road profile input had a 'one-sided' displacement spectral density of the form

$$S_{uu}(\gamma) = \frac{S_0}{(1+\gamma/\gamma_0)^2} \quad (m^3/rad) \tag{4.4}$$

where

γ = wavenumber in rad/m
γ_0 = 0.15 m/rad
S_0 2.6 x 10^{-5} m^3/rad.

This approximated the roughness of a good highway (see Section 3.3). It was converted to temporal inputs at 40 and 60 km/h by filtering an analogue white noise with a first order low-pass filter. The stroke limit of the vibrator (20mm p-p) prevented the use of rougher road profiles or higher speeds. Tests on the two springs were performed using identical vehicle simulation parameters.

Cross-spectral analysis was used to determine:

(i) $S_{mm}(f)$ = Direct spectral density of the measured force $F_m(t)$.

(ii) $S_{cc}(f)$ = Direct spectral density of the computed force $F_c(t)$.

(iii) $S_{ee}(f)$ = Direct spectral density of the force error $[F_e(t) = F_m(t)-F_c(t)]$,
$=S_{mm}(f)+S_{cc}(f)-2Re\{S_{cm}(f)\}$

(iv) $\eta(f)$ = $S_{ee}(f)/S_{mm}(f)$= Normalised Error.

The Normalised Error should be small but may exceed unity if, at some frequency, the spectral component of the computed force is significantly larger than the spectral component of the measured (target) force.

A total of 10 tests were performed on the lightweight springs from the full matrix of 16 parameter combinations (2 springs, 2 static preloads, 2 simulated vehicle speeds, optional simulated suspension spring friction). All three theoretical spring models were examined for each test. Both springs yielded similar results for all parameter combinations, hence discussion will be restricted to one of the springs in the laden condition (static load = 2.94kN), with no Coulomb friction in the input vehicle simulation. An equivalent set of results for the case with Coulomb friction in the input vehicle simulation can be found in [89]. The results are broadly similar, (except there is only one main excitation frequency instead of two) and the general conclusions are the same.

Typical measured and simulated forces and the associated input displacements are presented in figures 4.7-4.9. Figure 4.7 shows the force response time histories for the three spring models as well as the spring displacement. Figure 4.8 shows the corresponding spectral densities, while 4.9 shows the normalised error η for each simulation method.

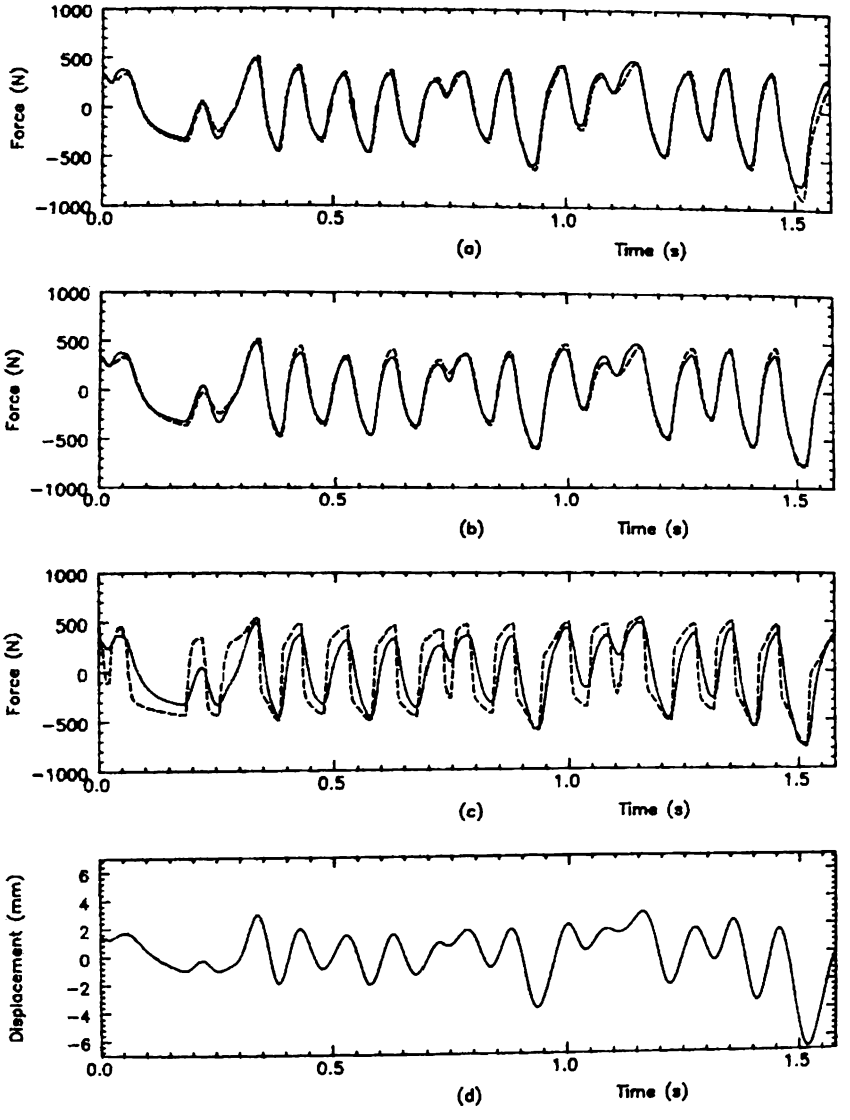


Fig. 4.7 Random spring force predictions. ———— = measured; - - - - - - = computed. From [92].
(a) Spring force: Direct method (see figure 4.2)
(b) Spring force: Projection method (see figure 4.4)
(c) Spring force: Simple Coulomb model (see figure 4.5)
(d) Spring displacement.

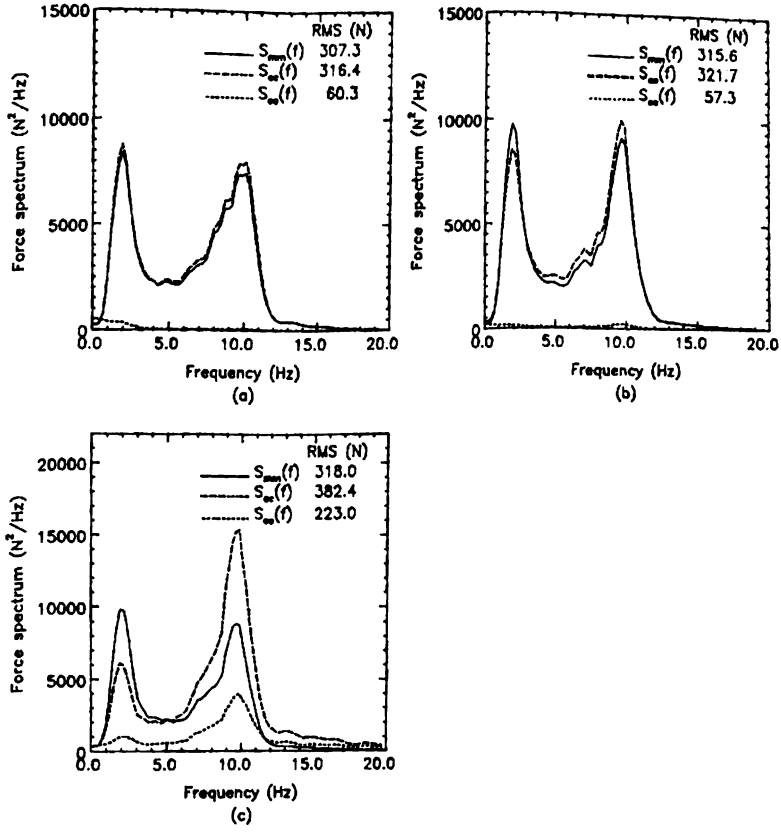


Fig. 4.8 Comparison between spectral densities of the measured forces (S_{mm}), computed forces (S_{cc}) and the force error (S_{ee}) for the three calculation methods. From [92].

(a) Direct method (see figure 4.2 and figure 4.7a)

(b) Projection method (see figure 4.4 and figure 4.7b)

(c) Simple Coulomb model (see figure 4.5 and figure 4.7c)

Given the frequency independence of leaf spring response, verified above, simulation errors must be attributed to:

(i) Lack of fit of the simulation equation

(ii) Noise and extraneous vibration of the apparatus and test specimen.

The 'simple Coulomb' model considerably overestimates the forces throughout the frequency range (figures 4.8c and 4.9) due to its poor fit (figure 4.7c). When the input simulation includes suspension friction, the simulated force may oscillate between its limiting friction levels during periods of inactivity (not shown - see [89]). This leads to large errors.

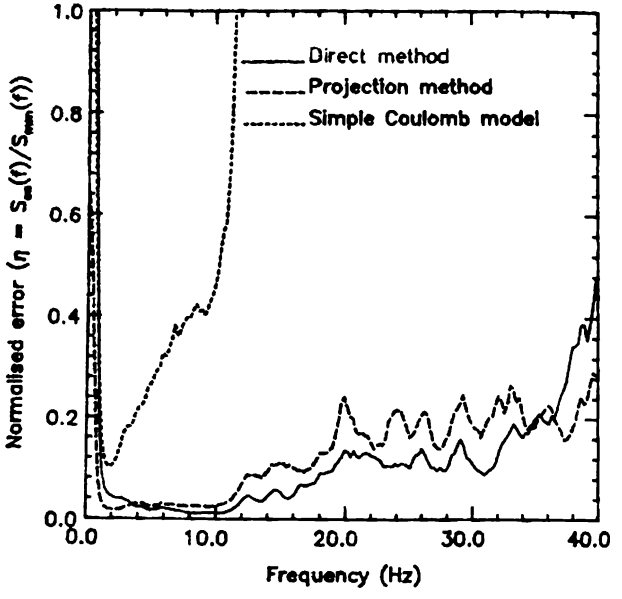


Fig. 4.9 Normalised error of each simulation method (corresponding to figure 4.10). From [92].

The 'direct' and 'projection' simulation methods are seen to predict force levels quite accurately (figure 4.7a,b) particularly between 2Hz and 12Hz (figure 4.8a,b). Poor estimation of forces for large displacements (figure 4.2) results in low frequency errors for the direct method (figure 4.9). Above 12Hz the equations must simulate higher harmonics of the responses at the major excitation frequencies. The direct method appears to perform slightly better than the projection method (figure 4.9) due to its better fit for small amplitudes. The low signal/noise ratio and structural vibration of the testing machine increase the errors at high frequencies.

Acceptable accuracy ($\eta < 0.25$) was obtained for both methods up to approximately 36Hz for the linear analogue model (figure 4.9). When the analogue model contained friction the maximum frequency was approximately 24Hz (See [89]). Similar results were observed in all other tests. This indicates that either method could be used confidently to approximately three times the highest frequency of major excitation, providing the empirical equation is fitted accurately to the low frequency force-deflection characteristics.

It is probable that empirical relationships can be found which describe more accurately the measured hysteresis loops of these springs. The relationship that is used in a vehicle simulation should be the most accurate one available, however it is clear that reasonable amount of error in the empirical equations can be tolerated. For the springs examined in this study, the accuracy of the fits seen in figures 4.2 and 4.4 would be adequate throughout the frequency range of interest in whole vehicle vibration studies.

4.4 HYDRAULIC DAMPERS

4.4.1 Experimental Method

The characteristics of hydraulic shock absorbers can be measured under realistic operating conditions using: (i) an instrumented damper fitted to a test vehicle, driven over a particular road surface [160, 234, 287, 308], or tested on a 'road simulator' [153, 244]; (ii) using a model vehicle test rig; or (iii) using the 'Hardware–in–the–Loop' (HiL) measurement method [54, 410].

The HiL method was chosen for this study because it can provide a realistic and repeatable testing environment with low hydraulic power consumption and relatively low cost. It is straightforward to change the vehicle model parameters, and so a wide range of operating conditions can be investigated in the laboratory. The method can also be used for investigating the performance and control of semi–active dampers, as discussed in Section 4.5 (see [54]).

Hardware in the Loop Method

HiL measurements of suspension damper performance utilise a real time computer simulation of a vehicle, interfaced to a test rig containing the damper of interest, as shown schematically in figure 4.10. The computer model includes the sprung and unsprung masses, the tyre and suspension spring stiffnesses and the road excitation, but not the suspension damper. On each integration time step, the computer provides a displacement demand signal to the test rig, through a digital/analogue interface. The test damper is driven by a hydraulic actuator which tracks the demanded displacement. The force generated by the damper is measured by a load cell, and fed back into the simulation via an analogue/digital interface. Thus the simulation behaves as if it contains an 'exact' model of the real damper, and the damper is tested in the realistic (but idealised) operating conditions of the simulation.

In the following sections, the HiL hardware is described briefly. The design of the HiL simulation software, the hardware/software interface, details of the numerical integration routines and errors associated with HiL testing are discussed in [55].

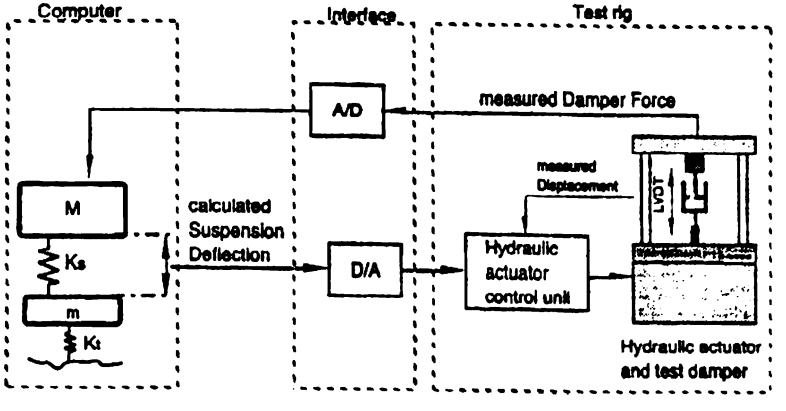


Fig. 4.10 Schematic diagram of Hardware–in–the–loop testing apparatus. From [55].

Apparatus

The test rig frame consisted of a stiff solid steel foundation block (1.51m x 0.68m x 0.18m) clamped between two steel U sections, securely bolted to the thick concrete slab floor of the laboratory The hydraulic actuator was mounted vertically onto the foundation block using a welded steel angle

bracket fabricated from 30 mm thick steel plate. A similar bracket was made to hold either a damper end or a strain gauged load cell. The load cell, the damper mounting pieces and the top angle bracket had interchangeable connections in order to provide a versatile system for mounting most common sizes and types of hydraulic shock absorbers.

The instrumentation system consisted of:

(i) A strain gauged load cell, connected to a conditioning module in the actuator controller;

(ii) A LVDT displacement transducer built into the actuator;

(iii) A piezoelectric accelerometer and charge amplifier with a low frequency cut-off of 0.3 Hz, used to measure vertical acceleration of the actuator;

(iv) A personal computer, fitted with an analogue/digital interface card with eight channels of 12-bit analogue-to-digital converters, two channels of 12-bit digital-to-analogue converters, and maximum data acquisition rate of 91 kHz.

To minimise phase lags, all signals were digitised and read into the computer without any analogue filtering or processing. Anti-aliasing filters were not necessary because the dynamics of the actuator and damper system eliminated high frequency components.

The test rig was fitted with a hydraulic actuator with a 250 mm nominal stroke, capable of generating a force of 25 kN. It included a servo valve with a rated oil flow of 38 l/min and was driven by a hydraulic power supply with 40 l/min maximum flow and 280 bar operating pressure. The nominal bandwidth of the hydraulic actuator system was 40 Hz.

Two shock absorbers were investigated:

(i) A standard twin-tube shock absorber for the drive axle of a Ford/Iveco tractor;

(ii) A semi-active damper used in 'passive' mode, provided by the Lord Corporation.

This chapter discusses the results for shock absorber (i) only. Results for (ii) can be found in [55].

Vehicle Simulation

The HiL computer model was a two-degree-of-freedom 'quarter car' model, which represents one wheel station of a heavy vehicle, as shown in the left hand block in figure 4.10. Three different sets of parameters were used in the quarter-car model to simulate three different heavy commercial vehicles. Vehicle model 1 had parameters representative of a lorry with a typical leaf spring suspension, while model 2 had parameters representative of an air spring suspension. Model 3 had considerably reduced masses and stiffness to enable HiL damper tests with large damping ratios. Scaling down the vehicle model parameters was found to give more stable operation of the HiL apparatus than scaling up the damping force by an equivalent amount. The parameters of the three vehicle models are provided Table 4.1.

Model Parameter		*Vehicle Model*					
		1		*2*		*3*	
Sprung mass	M	4450	kg	4450	kg	1112	kg
Unsprung mass	m	420	kg	420	kg	105	kg
Suspension stiffness	K_s	1000	kN/m	500	kN/m	125	kN/m
Tyre stiffness	K_t	1950	kN/m	1950	kN/m	487	kN/m
Suspension damping*	C_s	15	kNs/m	20	kNs/m	20	kNs/m

Table 4.1 Parameters values for the three quarter-car vehicle models used in the HiL tests.
* Optional suspension damping

The performance of the suspension was assessed using three response parameters [422]: RMS tyre force (TF), RMS body acceleration (BA) and RMS suspension deflection (SD). The RMS tyre force influences the road damage caused by the vehicle and also its road holding. RMS body acceleration is a useful criterion for driver ride comfort and payload vibration. RMS suspension deflection is a measure of the working space required by the suspension.

The vehicle models in the HiL apparatus were excited by artificially generated random road profiles with spectral densities given by equation 3.2 using n = 2.5. Three road profiles, representative of a motorway, a principal road and a minor road were used. The simulated vehicle speeds were different on each profile, to represent typical operating conditions, as shown in Table 4.2 below. Road surface profiles were generated from the prescribed spectral densities using the inverse FFT method described in Chapter 3.

Profile	S_0 $(m^{1/2}/cycle^{3/2})$	*Speed (km/h)*
Motorway	7×10^{-8}	110
Principal road	44×10^{-8}	80
Minor road	135×10^{-8}	50

Table 4.2 Road profile parameters used in the HiL tests. n = 2.5 for all profiles. (See equation 3.2).

HiL Measurement Errors

The errors resulting from the imperfect dynamics of the HiL apparatus (hydraulic actuator, servo-valves, *etc*) are discussed in [55].

Virtually no difference was found between the spectral densities of the HiL system and the theoretical responses at frequencies less than 8Hz. At higher frequencies the magnitudes of the spectra differed slightly and the frequency of the wheel hop mode of vibration of the HiL vehicle model increased, due to the phase lag in the HiL apparatus. The resulting RMS errors, for principal road input conditions were found to be relatively small at 0.26%, 0.63% and 0.62% for RMS tyre force, RMS body acceleration and RMS suspension deflection respectively.

4.4.2 A Simple Damper Model for Vehicle Simulations

In this section, a simple mathematical model of a hydraulic shock absorber is developed and used to verify the accuracy of the HiL procedure described in the previous section. The performance of the shock absorber model is then tested under realistic operating conditions and the relative importance of various features of the model are investigated.

The Damper Model

The shock absorber was subjected to sinusoidal displacement inputs at various frequencies. From these tests the main features of the response could be identified:

(i) Asymmetric damping, (different rates in compression and extension);

(ii) Hysteresis;

(iii) Saturation at high force levels.

Hysteresis in the force-velocity curves is caused by the compliance of the rubber bushings and the damping fluid (mainly due to entrapped gas). The saturation force level is set by a relief valve in the damper, and prevents it from producing excessive force levels.

The shock absorber model is shown schematically in figure 4.11. It includes a nonlinear viscous damping element connected in series with a nonlinear spring. The viscous damping element is modelled using three damping rates: a low damping rate C_c for compression and a high rate C_e for

extension, levelling off to a lower rate C_b above a saturation velocity v_{lim}. When a periodic input is applied to the damper, there is a phase lag in the increase of chamber pressures at the start of the compression and extension cycles [272]. This build up of pressure is included in the model by a smooth hyperbolic transition of the damping coefficient between compression and extension values. This gives a velocity dependent damping coefficient C(v) for damper velocities v below the saturation velocity:

$$C(v) = \frac{c_1(v - \alpha)}{\alpha\sqrt{1 + \left(\frac{v - \alpha}{\alpha}\right)^2}} + c_2, \qquad \text{for } v < v_{lim} \tag{4.5}$$

where
- v = velocity across viscous damping element = $\dot{x}_0 - \dot{x}$;
- α = damping transition parameter;
- c_1 = $(C_e - C_c)/2$;
- c_2 = $(C_e + C_c)/2$.

Figure 4.12 shows transition of the damping coefficient C(v) between the compression and extension rates for various values of α.

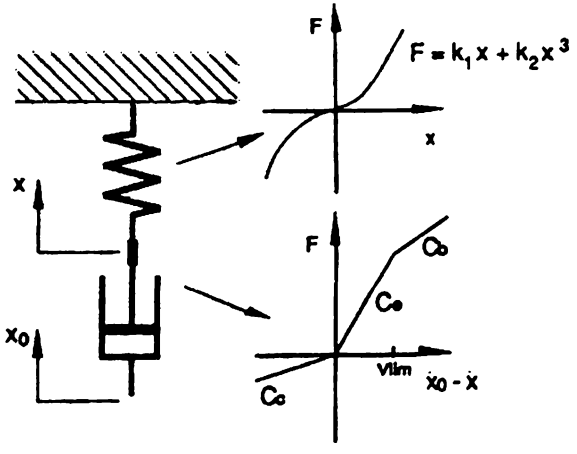


Fig. 4.11 Hydraulic shock absorber model From [55].

Using C(v) from equation 4.5, the viscous damping force F_v can be written as

$$F_v = \begin{cases} C(v)\, v, & \text{for } v < v_{lim} \\ C_e\, v_{lim} + C_b (v - v_{lim}), & \text{for } v \geq v_{lim}. \end{cases} \tag{4.6}$$

The compliance of the shock absorber is modelled by a cubic spring,

$$F_c = k_1 x + k_2 x^3, \tag{4.7}$$

where k_1 and k_2 are coefficients describing the force deflection characteristic of the spring and x is the relative deflection of the spring. Equating the spring and damping forces of equations 4.6 and 4.7 gives a first order non–linear differential equation for the shock absorber model:

$$\dot{x} = \begin{cases} \dfrac{k_1 x + k_2 x^3}{C(v)} + \dot{x}_0, & \text{for } v < v_{lim} \\ \dfrac{k_1 x + k_2 x^3}{C_b} + \dfrac{C_e - C_b}{C_b} v_{lim} + \dot{x}_0 & \text{for } v \geq v_{lim}. \end{cases} \tag{4.8}$$

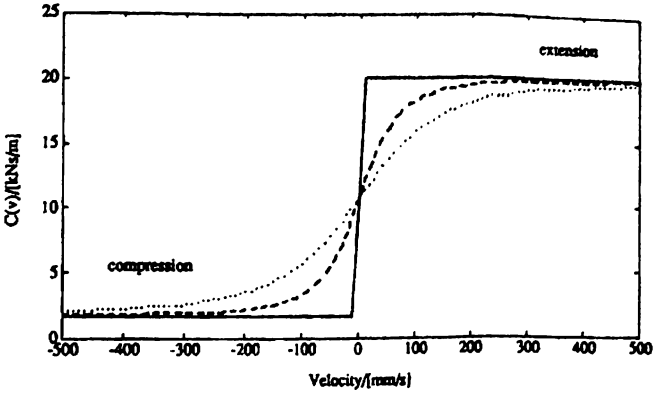


Fig. 4.12 Transition of damping coefficient between the compression rate C_c and the extension rate C_e, for various values of the transition parameter α. From [55].
———— $\alpha = 0$, – – – – – – $\alpha = 0.07$, · · · · · · $\alpha = 0.15$.

It is usually not possible to measure the internal velocity $v = \dot{x}_0 - \dot{x}$ on a test shock absorber, however, the velocity $\dot{x}_0$ applied across the entire shock absorber can be used instead of v to evaluate the damping coefficient $C(v) \approx C(\dot{x}_0)$ and to evaluate the saturation condition $\dot{x}_0 <> v_{lim}$, without significant loss of accuracy in the frequency range of interest.

Parameter Identification

The parameters for the shock absorber model were obtained from measured damping force–velocity characteristics. The shock absorber was excited by a constant sinusoidal displacement input, and the damper velocity was determined by differentiating the measured displacement signal. Typical force-velocity characteristics are shown for various damper body temperatures in figure 4.13a. The results of figure 4.13a are summarised in figure 4.13b, where the maximum damping force is plotted against temperature. The strong temperature dependence of damping characteristics made it necessary to conduct all further tests at a constant damper body temperature. A testing temperature of 25°C was chosen.

Evaluation of equation 4.8 requires values for seven parameters: C_b, C_c, C_e, k_1, k_2, α and v_{lim}. The model parameters were chosen to give good agreement with the measured force-velocity characteristics and are provided in Table 4.3.

Parameter	*Value*	
C_c	1.7	kNs/m
C_e	21	kNs/m
C_b	6.5	kNs/m
v_{lim}	0.175	m/s
α	0.07	m/s
k_1	2	kN/mm
k_2	0.16	kN/mm^3

Table 4.3 Parameter values used in the damper model.

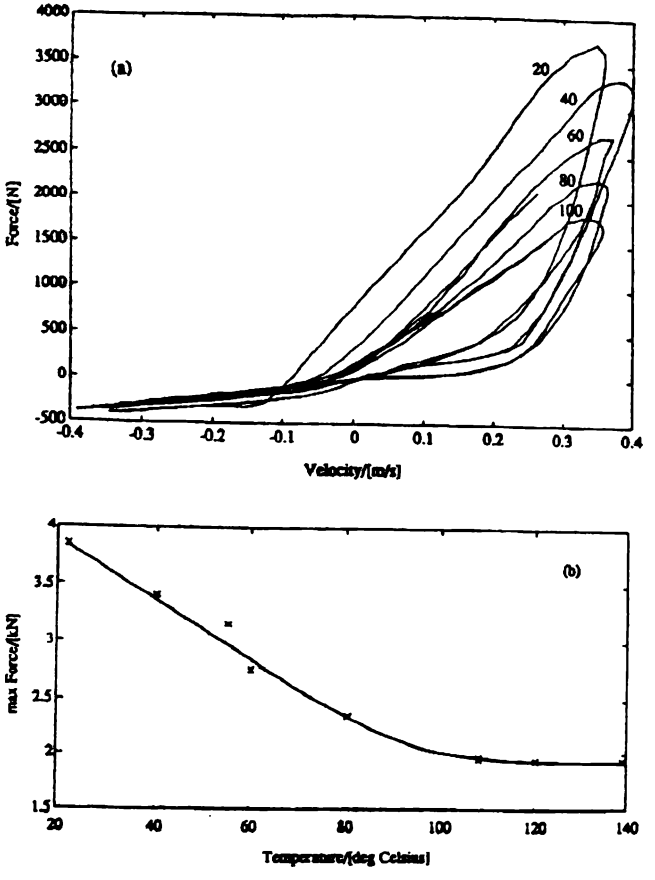


Fig. 4.13 Damping characteristics of the Ford/Iveco shock absorber obtained from sinusoidal velocity inputs at frequencies of 3 Hz, for various temperatures. From [55].
(a) Force–velocity characteristics
(b) Maximum damping force as a function of temperature

The saturation damping rate C_b, the threshold velocity v_{lim} and the first estimate of C_e and C_c were taken directly from the measured low frequency force–velocity characteristic. The parameters k_1, k_2 and α were obtained by fitting the model to the measured damping characteristics at high frequencies. For shock absorbers with soft rubber bushings it is possible to measure k_1 and k_2 directly by deflecting the rubber bushings.

Comparison of Sinusoidal Responses

The damping characteristics of the Ford/Iveco shock absorber are shown in figures 4.14a-f. The hysteresis loops are caused by flexibility of the damper. It can be seen that there is good agreement between measurement and the fitted model for small amplitudes (figures 4.14a,c,e) and high frequencies (figures 4.14e,f). At high frequencies and amplitudes large enough to drive the shock absorber into saturation (figures 4.14b,d,f) the measured hysteresis loops are larger than the fitted ones. This suggests an increase in shock absorber flexibility with frequency, which may be due to foaming of the damper fluid. Figure 4.14a shows high frequency fluctuations in the measured

damping force characteristic which can not be found in the model. These 'ripples' are thought to be caused by the dynamics of internal valves in the damper.

Overall the shock absorber model can easily be fitted to the measured characteristics over the range of frequencies and amplitudes typically encountered during vehicle operation, and it is therefore well suited to use in heavy vehicle ride simulations. Similar agreement to that shown in figure 4.14 was obtained for the Lord damper [55] . More recent work on various different dampers has shown that the model can be fitted to a wide range of other damper types.

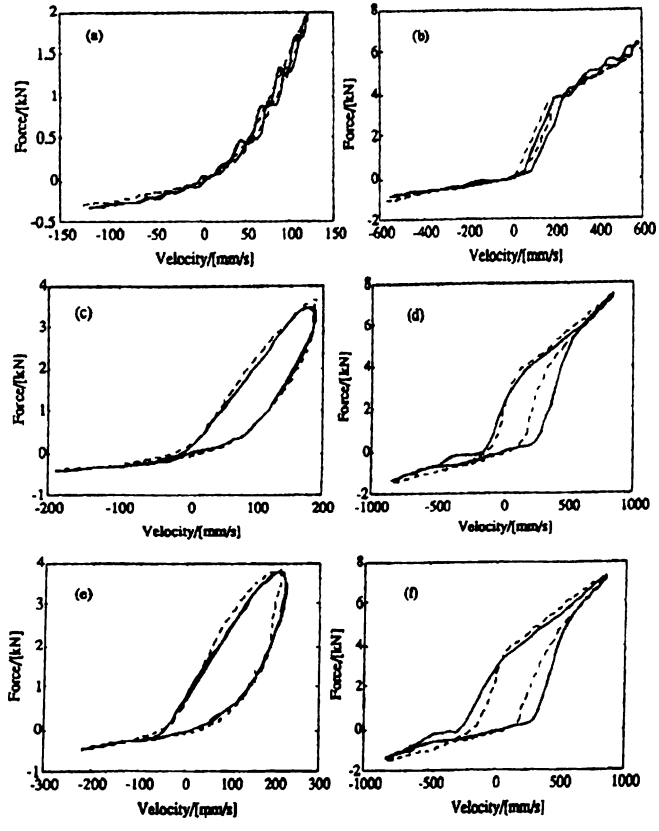


Fig. 4.14 Force–velocity characteristics of the Ford/Iveco shock absorber obtained from sinusoidal velocity inputs at frequencies of: From [55]. ——— Measurement - - - - - - Fitted model
(a), (b) 1 Hz (c), (d) 6 Hz (e), (f) 10 Hz

Comparison of Random Responses with the HiL System

The accuracy of the HiL system was verified by comparing the response of:

(i) the HiL rig incorporating the Ford/Iveco shock absorber with vehicle model 2, and

(ii) a computer simulation of vehicle model 2, using the theoretical damper model and parameter values described above.

The time responses of body acceleration, tyre force, suspension deflection and damping force are shown in figures 4.15a-d for the minor road input condition (see Table 4.2). The corresponding spectral densities are shown in figures 4.16a-d. All of the figures show that the responses of the HiL apparatus and computer simulation agree closely. The largest discrepancy can be seen in the damping force spectral density at high frequencies (figure 4.16d).

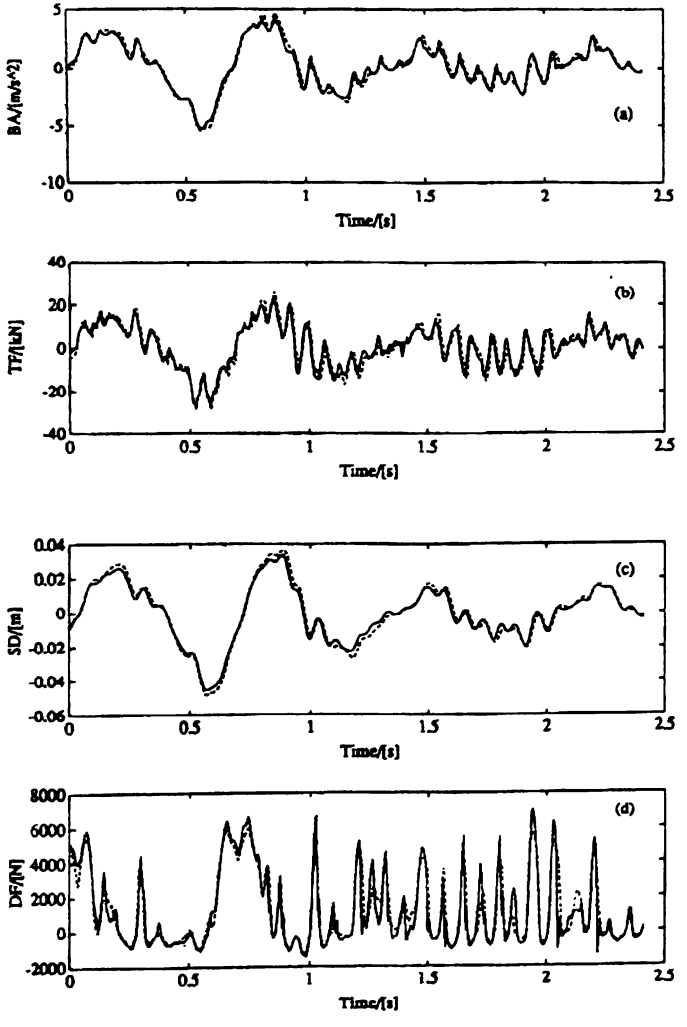


Fig. 4.15 Time histories of (a) Body Acceleration, (b) Tyre Force, (c) Suspension Deflection, and (d) Damping Force, for vehicle model 2, with the minor road input condition. From [55].
———— = HiL measurement - - - - - - = Digital simulation

The combined error of the HiL apparatus and the shock absorber model can be evaluated by calculating the normalised RMS difference between time histories x(t) obtained from HiL measurements, and y(t) obtained from the computer simulation. This error measurement is denoted the 'Normalised RMS Error' (NRE):

$$NRE = 100\left[\frac{\int_0^T (x(t)-y(t))^2 dt}{\int_0^T x(t)^2 dt}\right] \quad (\%). \qquad (4.9)$$

The Normalised RMS Error of the body acceleration, tyre force, suspension deflection and damping force for case shown in figures 4.15 and 4.16 were 13.1%, 20.4%, 9.4% and 44.8% respectively. The NRE can be seen to be a sensitive measure of the combined error.

The same comparison was made for a matrix of tests performed with all three vehicle models (1, 2, 3) and all three road input conditions (motorway, principal road and minor road). The results are presented in [53], and are summarised in the following.

It was found that the damper model was accurate for vehicle models 1 and 2, giving Normalised RMS Errors for body acceleration, tyre force and suspension deflection less than 25% for all roads. Larger errors occurred for vehicle model 3, mainly due to discrepancies at frequencies higher than 20 Hz. In this frequency range, the dynamics of the hydraulic actuator also contributes significantly to the Normalised RMS Error.

In general, the Normalised RMS Error between the measured and simulated *damping force* time histories was found to be larger than for the body acceleration, tyre force and suspension deflection time histories. This is because the dynamics of the vehicle system attenuates the inaccuracies in the damping model. For higher damping ratios, damping forces increasingly influence the system dynamics and inaccuracies in the shock absorber model lead to larger Normalised RMS Errors.

The generally good agreement between computer simulation and HiL measurements for the shock absorber model indicates that the HiL apparatus operates satisfactorily.

4.4.3 Damping Model Assumptions

This section examines the influence of various features of the shock absorber model on the accuracy of vehicle simulations incorporating the model. Five different damper model variants were derived by modifying the 'full' (validated) shock absorber model described by equation 4.8, as follows:

(i) *No saturation:* The full model, but excluding the force saturation above $v = v_{lim}$;

(ii) *No linear spring:* The full model, but with no linear stiffness ($k_1 = \infty$);

(iii) *No spring:* The full model, excluding all series compliance ($k_1 = k_2 = \infty$);

(iv) *No damping transition:* The full model excluding the damping coefficient transition;

(v) *Linear viscous damping:* The damper model replaced by a linear viscous damper with rate $C = (C_e + C_c)/2$.

These five damper model variants were used in the three vehicle simulations, and excited by the three road input conditions (Table 4.2). Equation 4.10 was used to calculate Normalised RMS Errors for between the time responses of: (i) a vehicle model incorporating the full validated damper model, and (ii) the same vehicle model incorporating each of the damper model variants. The results are presented in detail in [53], and are summarised for vehicle model 2 in figure 4.17.

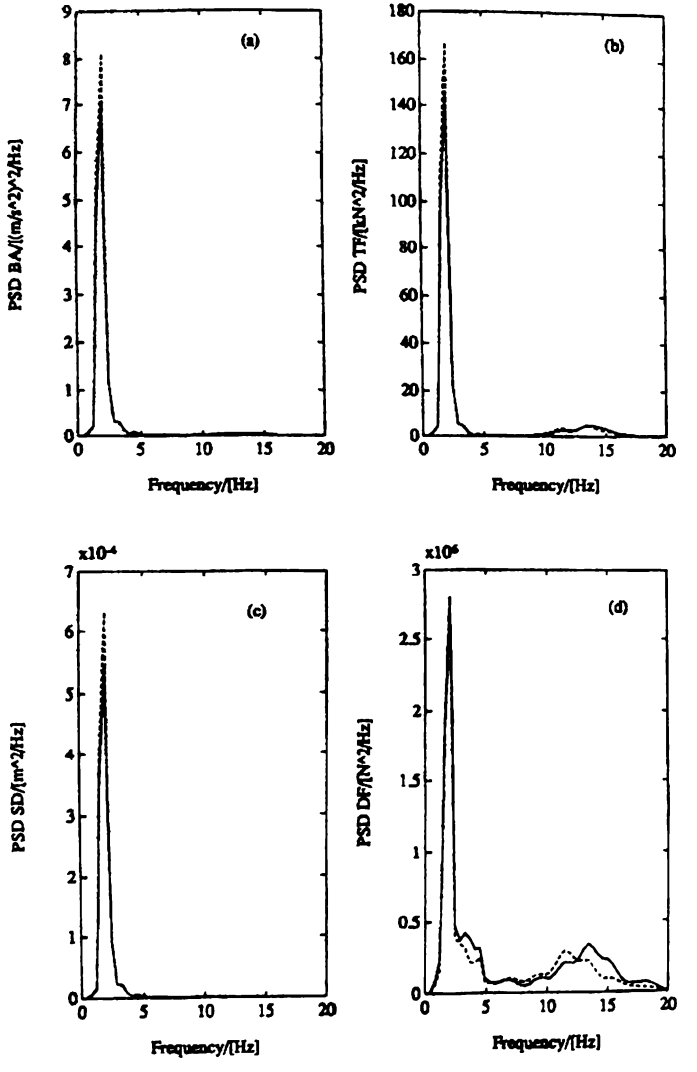


Fig. 4.16 Spectral densities of (a) Body Acceleration, (b) Tyre Force, (c) Suspension Deflection, and (d) Damping Force, for vehicle model 2, with the minor road input condition. From [55].
———— HiL measurement - - - - - - Digital simulation.

No Saturation

Figures 4.18a,b compare the damping force and tyre force time histories for the full damper model and the modified damper model without saturation, for minor road input conditions. It can be seen that saturation limits the maximum damping forces, effectively reducing damping at large velocities. The difference in maximum damping force primarily affects the body mode of vibration as evident from the power spectral densities in figure 4.19a. For smoother roads, the saturation effects are less important, because the suspension velocities are generally lower, and the damper does not reach the

saturation threshold as often. Saturation was also found to be less important for vehicle model 3, which had a larger damping ratio and hence reduced suspension velocities (see [53]).

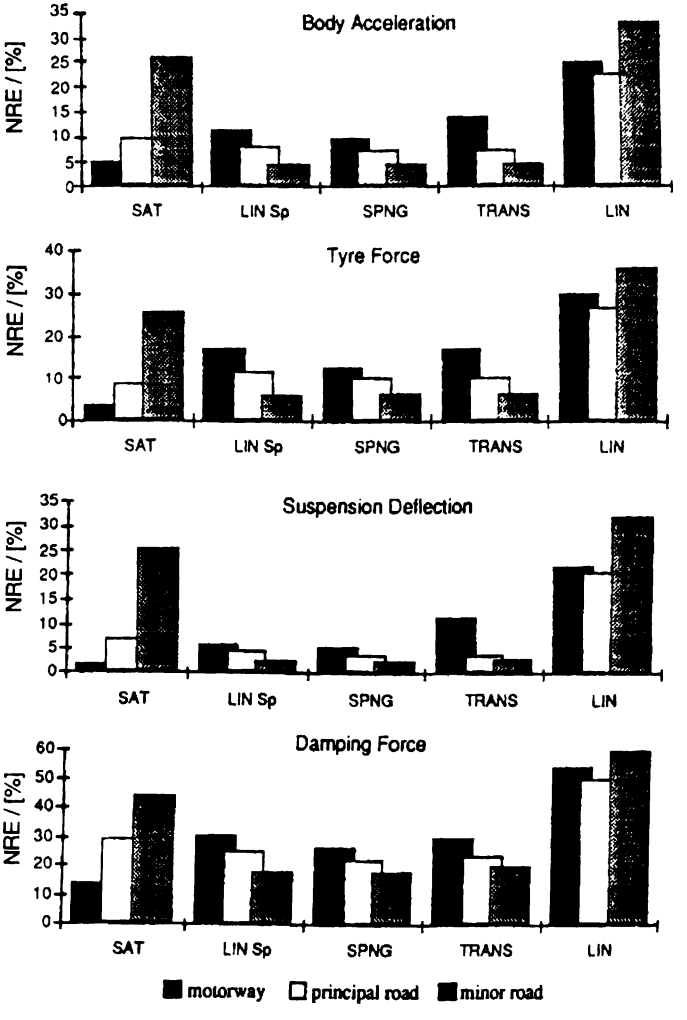


Fig. 4.17 Normalised RMS Errors between the responses of vehicle model 2 incorporating the full Ford/Iveco damper model and its variants. From [55].
SAT = No saturation, LIN Sp = No linear spring SPNG = No spring
TRANS = No damping transition LIN = Linear viscous damper

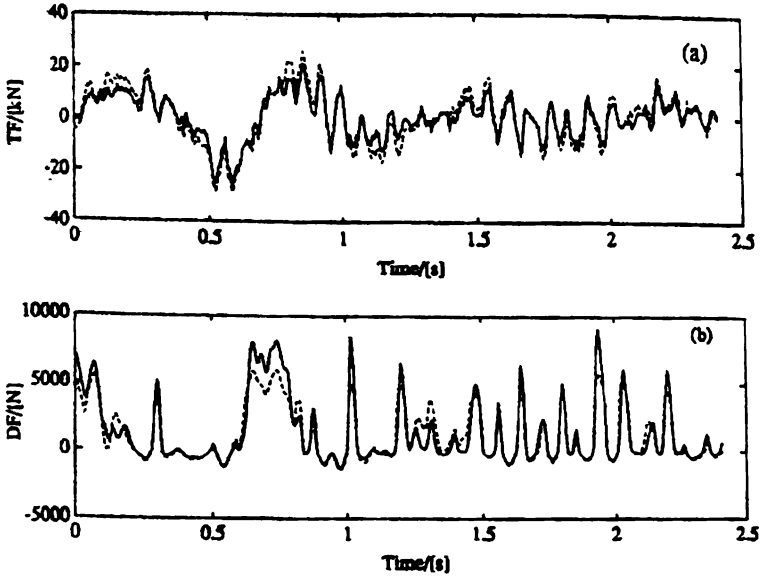


Fig. 4.18 Time histories of response of vehicle model 2 with a 'minor' road input. From [55].
(a) Tyre Force (b) Damping Force
_____ Damper model without saturation - - - - - - 'Full' damper model

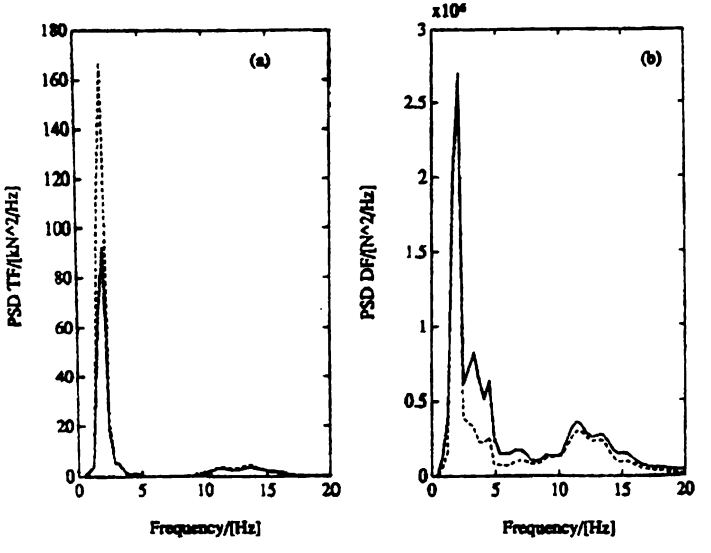


Fig. 4.19 Spectral densities of response of vehicle model 2 with a 'minor' road input. From [55]. (a) Tyre Force (b) Damping Force
_____ Damper model without saturation - - - - - - 'Full' damper model

No Linear Spring

A damper with no linear component in the spring stiffness produces almost no force output for small deflections, but a rapidly increasing force at larger deflections. This effect is similar to backlash, but without discontinuity of displacement.

On rough roads (*eg* minor road) and for vehicles with relatively less damping (*eg* vehicle model 1), damper velocities and displacements are generally large and the compliance of the damper is dominated by the cubic term k_2x^3. The linear stiffness component k_1x is therefore relatively unimportant for these conditions. As the roughness input decreases (*eg* motorway), and/or the relative damping increases (*eg* vehicle 3), the damper velocities and displacements decrease, and the linear stiffness term becomes more important. This can be seen in figure 4.17, where the errors in all of the vehicle response components for 'no linear spring' are seen to increase with decreasing road roughness.

The amplitude of suspension deflection generally decreases with frequency (because of the nature of the road input), thus absence of a linear stiffness term mainly affects damper response at higher frequencies, and the errors are concentrated at the wheel hop peak (see [53] for further details).

No Spring

For the Ford/Iveco damper, the linear spring stiffness term k_1 is relatively large and the cubic stiffness term k_2 is relatively small (see Table 4.3). Thus eliminating all compliance has a similar effect to eliminating just the linear term (as in the previous paragraph). For the motorway input, removing all compliance causes smaller errors than just removing the linear component. This result is not fully understood, but is thought to be related to the relative magnitudes of k_1 and k_2 for this damper.

No Damping Transition

Damping coefficient transition reduces damping rates at low velocities, and therefore affects the response of the vehicle in the low frequency (body bounce) region. The significance of damping coefficient transition is largest for smooth road inputs (motorway) and higher damping ratios, when the damper velocities are generally low. Its significance diminishes with worsening road quality (see [53] for further details).

Linear Viscous Damping

The linear damping model is the least accurate of the five damping model variants, irrespective of the road input, as seen by the large Normalised RMS Errors in figure 4.17. The reasons are evident from the time histories in figures 4.20a,b. Note particularly the zero mean level of the force generated by the linear damper compared with the non–zero mean of the full damper model caused by its different rates in extension and compression (figure 4.20b). Despite the large differences in the damping force time histories there is still reasonable agreement between the tyre force time response (figure 4.20a), and the damper force and tyre force spectral densities (figures 4.21a,b).

The NREs for the linear damper model do not follow a simple trend with road input conditions (figure 4.17), because some of the nonlinearities are important for small damper velocities, hence smooth roads (*eg* damping coefficient transition), whereas other nonlinearities are important for larger velocities and rougher roads (*eg* saturation).

In general, the more the damping force is dominated by nonlinearities, the larger the errors caused by using a linearised damper model. This particularly affects the damping forces at large amplitudes (see [53]).

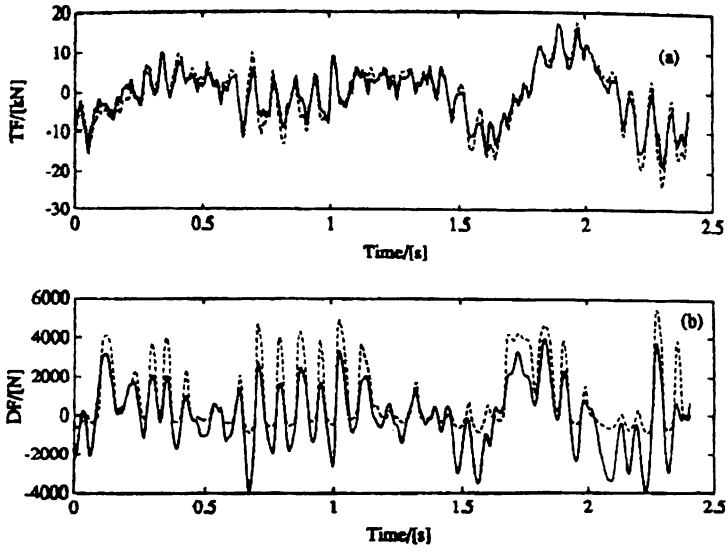


Fig. 4.20 Time histories of response of vehicle model 2 with a 'principal' road input. From [55]. (a) Tyre Force (b) Damping Force
_____ Linear viscous damper - - - - - - 'Full' damper model

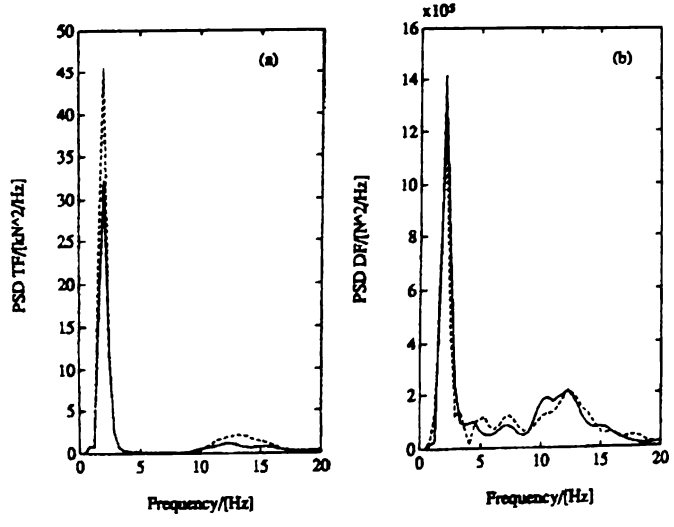


Fig. 4.21 Spectral densities of response of vehicle model 2 with a 'principal' road input. From [55]. (a) Tyre Force (b) Damping Force
_____ Linear viscous damper - - - - - - 'Full' damper model

Summary

In summary, it is important to include saturation in the damper model for rougher road inputs. When saturation is neglected, the Normalised RMS Error for dynamic tyre forces was found to be 26% for vehicle model 2 incorporating the Ford/Iveco damper (minor road). As the damping ratio increases, or road roughness decreases, saturation becomes less important.

Neglecting damping coefficient transition and the series compliance are most significant for smooth road inputs. Eliminating damping coefficient transition increases the response at the body mode of vibration while eliminating the series compliance increases the response mainly at the wheel resonance. The two effects were found to be of approximately equal importance causing NREs for tyre forces of approximately 16% (motorway). If damping is increased both effects become more significant.

The NREs for tyre forces using linear viscous damping were found to be large, in the range of 27% to 36%. This indicates that care should be exercised in the choice of linearised damper model for accurate simulations of heavy vehicle dynamics.

4.5 CONTROLLABLE DAMPERS

This section discusses the modelling of a semi-active damper and strategies for controlling its force output in response to an input demand signal.

4.5.1 Experimental Set-up

The semi-active damper investigated is shown in figure 4.22. This damper produces a force which is the sum of a static force, due to internal gas pressure (essentially constant), and a dynamic viscous damping force. The damping rate is continuously variable and set by an internal valve. The valve is controlled by a voltage signal U between –10V (low damping) and 0V (high damping), taken directly from an analogue output channel of the digital/analogue interface board of a personal computer. The supply current for the damper valve (5A) was taken from a 12V car battery. The drive electronics for the valve were supplied by the damper manufacturer.

4.5.2 Semi-Active Damper Model

Damping–Voltage Model

The damping force versus velocity characteristics of the semi-active damper were obtained from sinusoidal velocity tests with various input amplitudes, for several constant values of the control voltage U. The tests were performed at a constant damper body temperature, and subject to a maximum allowable damping force of 4 kN. Typical output is shown in figure 4.23. A linear viscous damping characteristic (straight line) was fitted to the measured data for each control voltage. This was a reasonable approximation because the damper did not saturate, had equal damping rates in compression and extension, and very little associated compliance (hysteresis on the force–velocity plot). The fitted damping coefficients provided an average damping coefficient $\overline{C}$ for each value of U. The resulting graph of $\overline{C}$ as a function of the control voltage U is shown in figure 4.24.

A quadratic polynomial of the form

$$\overline{C} = a_1 U^2 + a_2 U + a_3 \qquad (4.10)$$

was fitted to the data for several temperature and velocity combinations and the results are shown as a solid lines in figure 4.24. In the following discussion, this equation is known as the 'damping–voltage model'. The coefficients of equation 4.10 were obtained from the least square fit. For a damper body temperature of 56°C and input velocity amplitude of 0.28 m/s: a_1=106.9 $Nsm^{-1}V^{-2}$, a_2=1756.3 $Nsm^{-1}V^{-2}$ and a_3=7505.5 Nsm^{-1}.

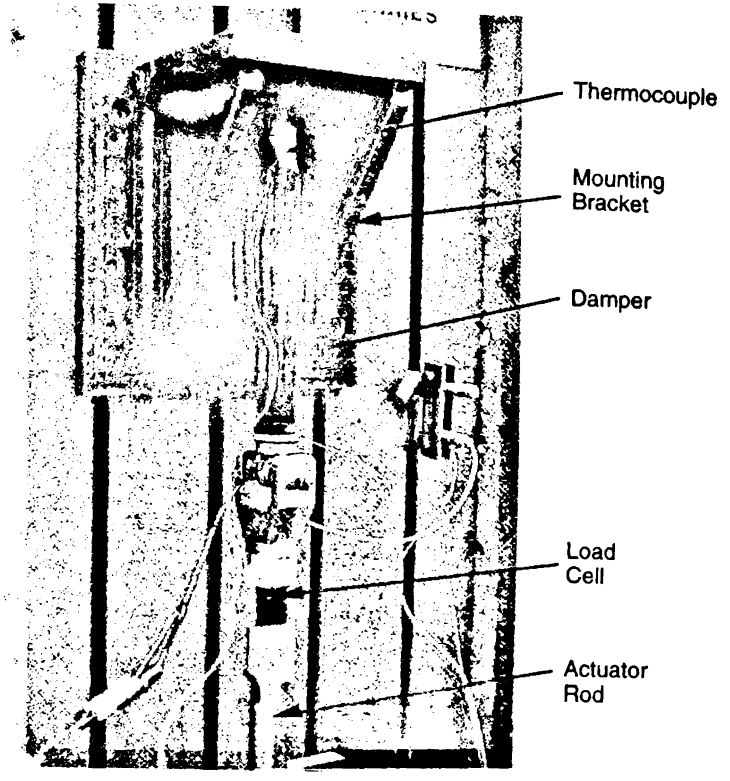


Fig. 4.22 Semi-active damper in test rig. From [56]

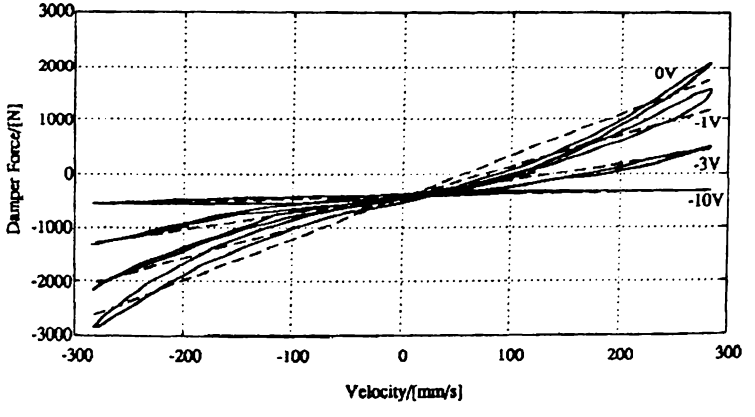


Fig. 4. 23 Force–velocity characteristics of the test damper for various control voltages. From [56].
———— measurement - - - - - - - straight-line least squares fit.

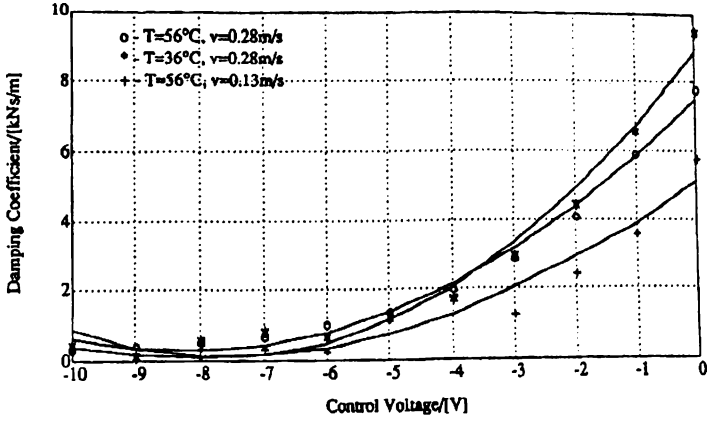


Fig. 4. 24 Effect of temperature and applied velocity on damping–voltage characteristics. From [56].
———— = quadratic polynomial least squares fit.

Fitting a cubic polynomial to the data gave a slightly better fit in the low damping region, U = –8V to –10V, however, small inaccuracies in the damping–voltage model for low values of damping have negligible effect on the overall dynamics of the vehicle system. The quadratic relationship has the advantage that it can be inverted easily and therefore it was used in the 'open loop' control algorithm described later.

For the tests at 36°C, the damping coefficients increase slightly due to higher fluid viscosity. This difference is largest at high control voltages.[1] For the test carried out with reduced (halved) velocity input of 0.13 m/s, the damping coefficients decrease, with approximately 25% reduction at 0V. This is mainly caused by the nonlinear variation of damping with velocity shown in figure 4.23. In the operating range of interest, the damping coefficients are more sensitive to velocity input level than to temperature.

Damping Force Transients

A constant extensional velocity input was applied to the semi–active damper, and the damping rate was switched rapidly. The transient response for switching from minimum to maximum damping rate is shown in figure 4.25a for various constant velocities across the damper. Figure 4.25b shows the damping force transients (also during extension) when damping is switched from maximum to minimum.

Both figures show a delay of approximately 3 ms between the applied control voltage and the damper force response. It can also be seen that the time taken for the damping force to reach its steady state is essentially independent of the velocity across the damper. This indicates that a stiff linear compliance largely governs the damping force transients. (This can also be deduced from the small hysteresis loops in the measured damping force characteristics of figure 4.23.)

For the *off-on* transition (figure 4.25a) the damper force rises gradually, reaching its steady state after approximately 15 ms. The low frequency vibration in the damping force response is due to transient motion of the hydraulic actuator excited by the abrupt reversal of direction associated with

[1] In the laboratory investigation the errors caused by temperature variation were eliminated by conducting all tests at the same temperature. It would alternatively be possible to measure the damper body temperature and incorporate the variation of damping with temperature in equation 4.10.

the start of its stroke. The *on-off* transient response of the damper (figure 4.25b) settles after 6 ms and steady state is reached. The vibration with a frequency of approximately 200 Hz in the damping force response is thought to be caused by a resonance in the damping valve control system.

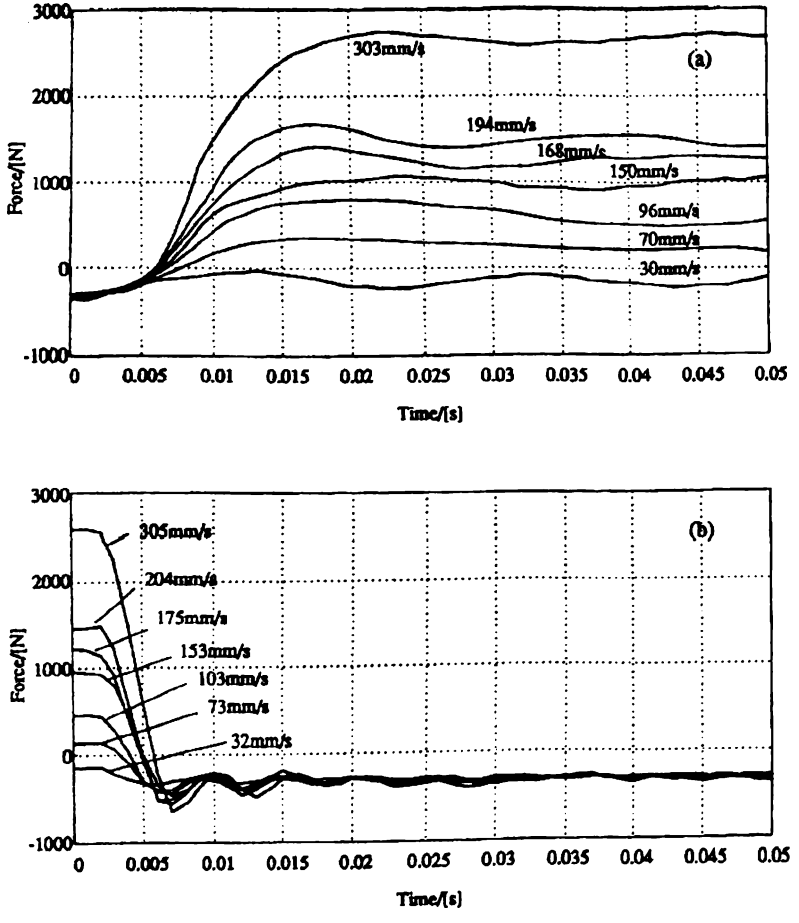


Fig. 4. 25 Damping force transition during extension for various damper velocities. From [56].
(a) Off–on transition (b) On–off transition

The damper responds much more quickly when switching the damping setting from *on* to *off*. This indicates that this process is assisted by flow forces. The 200 Hz vibration can not be seen in the *off-on* damping force transients (figure 4.25a) and this may be due to the increased damping rate not allowing this mode of vibration to develop.

Similar damping force transients were measured during the compression phase of the damper [53].

Damper Dynamics

The damper model is shown schematically in figure 4.26. The dynamics of the damping valve were modelled as a second order system with the transfer function:

$$G_v(s) = \frac{\omega_0^2}{s^2 + 2\zeta\omega_0 s + \omega_0^2} \tag{4.11}$$

where the natural frequency $\omega_0 = 1257$ rad/s (200 Hz) and damping ratio $\zeta = 0.3$ were estimated from the transients in figure 4.25b.

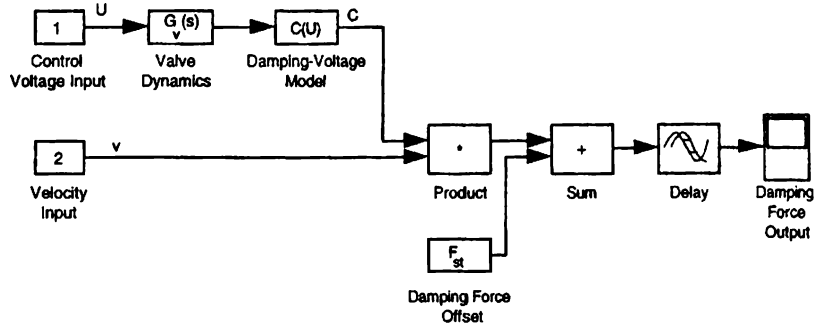


Fig. 4.26 Schematic diagram of the semi-active damper model. From [56].

The damping coefficient is set by the control voltage input using the damping-voltage model (equation 4.10). The viscous component of the damping force is then the product of the input velocity and damping coefficient.

The total damping force is the sum of a static force of 400 N, shown as 'Damping Force Offset' (F_{st}) in figure 4.26 and the viscous force component. The total force is delayed in the model by 3 ms, as found in the previous section.

This damper model is compared with experimental measurements later in the chapter.

4.5.3 Damper Force Control: Open Loop

Two input signals are required for open loop damper control, the instantaneous velocity across the damper v and the demanded force F_d. The difference between demanded force and static damper force F_{st} has to be provided by viscous damping. The required damping coefficient C_d to produce that force is:

$$C_d = \frac{F_d - F_{st}}{v} \tag{4.12}$$

and is limited within the achievable range of the damper:

$$C_d = C_{min} \qquad \text{for } C_d < C_{min}$$
$$C_d = C_{max} \qquad \text{for } C_d > C_{max}.$$

Once the demanded damping coefficient has been calculated the damping-voltage model (equation 4.10) can be solved for the desired control voltage. This strategy automatically implements a control action that can only dissipate power, by ensuring that damping is set to minimum if the velocity and demand force have opposite signs.

4.5.4 Damper Force Control: Force Feedback

Semi-Active Pre-processor

The force feedback control loop is shown in figure 4.27. The 'semi-active pre-processor' calculates the error e between demanded force F_d and measured force F_m:

$$e = |F_d - F_{st}| - |F_m - F_{st}| \tag{4.13}$$

where F_{st} is the static force due to the internal gas pressure. (It is necessary to calculate the error from the absolute values of the forces to obtain the correct control action for the damper during extension as well as compression.)

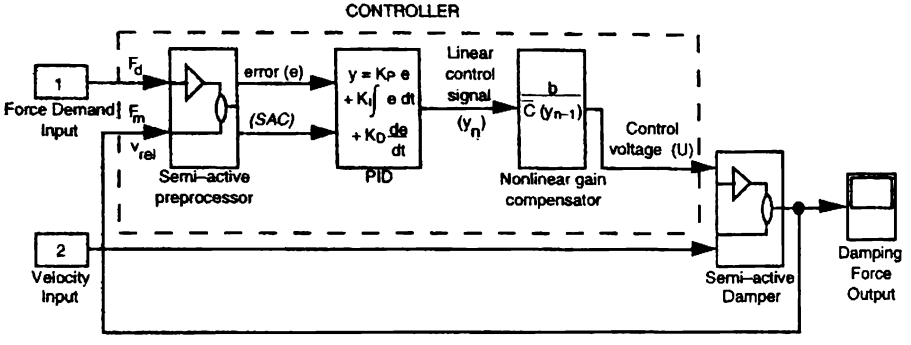


Fig. 4.27 Force feedback control loop for semi-active damper. From [56]

The semi-active pre-processor also generates an output for the 'semi-active constraint' (*SAC*). This output indicates whether the control action dissipates energy, *ie* whether the damper can track the demanded force, or whether the damper has to be switched off. If the semi-active constraint output is positive the damping force is controlled by the feedback loop. If the semi-active constraint output is negative the damping rate is set to minimum.

Two alternative methods exist for calculating the semi-active constraint, and this leads to two possible force feedback control strategies, both of which were investigated in this study:

(i) 'Force feedback (velocity)', using the relative velocity between vehicle body and axle v_{rel} to determine the SAC. This requires measurement of this velocity or differentiation of a damper displacement signal. In this case the semi-active constraint is given by:

$$SAC_v = \text{sign}\{v_{rel}(F_d - F_{st})\} \tag{4.14a}$$

(ii) 'Force feedback (force)', using the measured damping force to estimate the sign of the relative velocity. (The sign of the dynamic component of the damping force (F_m–F_{st}) and of the relative velocity v_{rel} should be the same.) In this case the SAC is given by:

$$SAC_f = \text{sign}\{(F_m - F_{st})(F_d - F_{st})\} \tag{4.14b}$$

Linear PID Controller

The Proportional–Integral–Derivative (PID) controller takes the form:

$$y = K_P e + K_I \int e\,dt + K_D \frac{de}{dt}, \tag{4.15}$$

where y is the controller output voltage, e is the error signal and K_P, K_I and K_D are the proportional, integral and derivative gains.

The discrete implementation of this PID controller is given by:

$$y_n = y_{n-1} + k_1 e_n + k_2 e_{n-1} + k_3 e_{n-2} \tag{4.16}$$

where subscript 'n' denotes the n^{th} sample.

The discrete gains k_1, k_2 and k_3 were calculated from the continuous controller gains according to:

$$\begin{aligned} k_1 &= K_P + K_I \tau + K_D/\tau \\ k_2 &= -(K_P + 2K_D/\tau) \\ k_3 &= K_D/\tau, \end{aligned} \tag{4.17}$$

with τ denoting the sampling time interval.

To prevent the integrator from saturating the output of the controller was limited to the minimum (y_{min}) and maximum (y_{max}) control voltages of the damper:

$$\begin{aligned} y_n &= y_{min} \quad \text{if } y_n < y_{min} \\ y_n &= y_{max} \quad \text{if } y_n > y_{max}. \end{aligned}$$

Nonlinear Gain Compensation

The damping valve is nonlinear, as seen in figure 4.24. At low control voltages (around –8V), a change in the input voltage causes a relatively small change in the output force (*ie* low gain). At higher input voltages (around 0V), a relatively small change is needed to obtain the same change in output force (*ie* high gain). Unless this nonlinearity is corrected in controller, the force tracking response will be slow at low control voltages and faster at higher control voltages (see [53]). Stability considerations limit the maximum possible controller gain, and the nonlinearity will therefore cause unnecessarily slow overall force tracking performance.

The nonlinear behaviour of the damping valve is known from the damping–voltage model $\bar{C}(U)$ (equation 4.10). This can be used (approximately) to implement a gain compensator, using the value of the control signal from the previous time step y_{n-1}.

The nonlinear gain compensation function $K_A(y_n)$ was given by:

$$K_{A_n}(y_n) = \begin{cases} 1 & \text{for } y_n \le -8 \text{ V} \\ \dfrac{b}{\bar{C}(y_{n-1})} & \text{for } y_n > -8 \text{ V}. \end{cases} \tag{4.18}$$

The gain compensation function was calculated only in the control voltage range between –8V to 0V, using equation 4.10 to evaluate $\bar{C}(y_{n-1})$. The constant b was chosen to be 300 Ns/m in order to set the nonlinear gain function to unity at U = –8V. For voltages less than -8V, K_{A_n} was set to unity because the damping-voltage-model is essentially flat in this region (figure 4.24).

The gain–compensated output of the force feedback controller (voltage input to the damper) U was then (figure 4.27)

$$U = y_n K_{A_n}. \tag{4.19}$$

A computer simulation of the damper model was used to determine controller gains giving good dynamic response of the damper. Simulation results and measurements are compared in the following sections.

4.5.5 Force Tracking Tests

A force tracking test was devised to investigate the ability of the semi-active damper to follow a prescribed force demand signal. The damper stroke was driven by a saw–tooth displacement input, producing a square wave velocity, with amplitude 0.28m/s and frequency 2Hz. The damper was made to track a sinusoidal force demand signal of constant amplitude and frequency.

Open Loop Damper Control

Figure 4.28a shows the measured damping force response of the open loop controller at 3 Hz (around the frequency of vehicle body bounce vibration), for a force demand signal of amplitude 2 kN. The periodic spikes in the damping force responses (at 0.4 s, 1.4 s, 2.4 s) are caused by the discontinuities in the square wave velocity input. The damper switches on and off according to the sign of the demanded force and velocity, so as always to dissipate energy. During the dissipative periods, the measured force tracks the *phase* of the demand signal accurately, but the measured *amplitude* is approximately 25% greater than the demanded force. This is caused by inaccuracies in the damping–voltage model (equation 4.10).

Figure 4.28b shows the force tracking of the open loop controller at 11 Hz (approximately the wheel hop frequency) for a demand force amplitude of 3kN. Some phase lag can be observed in the measured response. The amplitude tracking is better for the higher force demand, because the overshoot is limited by the maximum force that the damper can develop at the given input velocity.

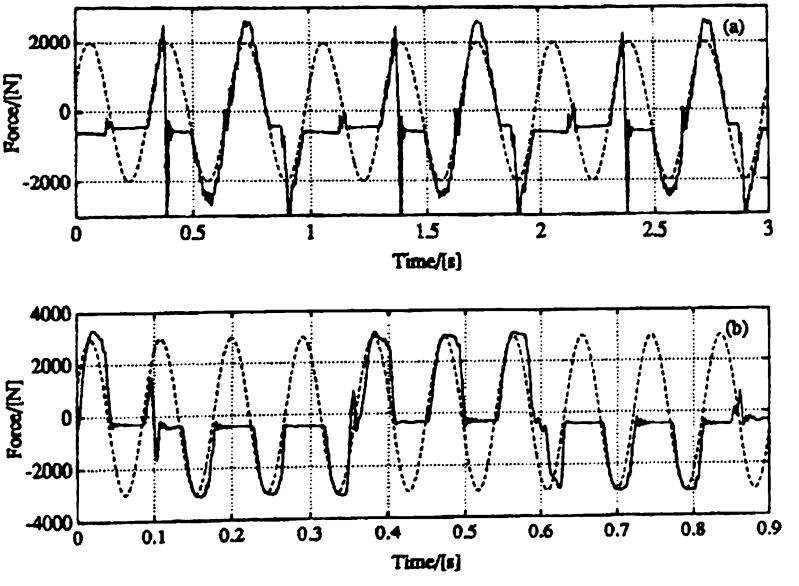


Fig. 4.28 Open–loop force tracking test (damper velocity amplitude = 0.28 m/s) with a demanded damping force of: (a) 2 kN at 3 Hz (b) 3 kN at 11 Hz. From [56]
——— damper force - - - - - - - demand force

The performance of the open loop controller is expected to be least accurate for high frequencies and relatively low force levels. The measured performance in this region (1 kN, 23 Hz) is shown in figure 4.29, and can be compared with the *simulated* performance shown in figure 4.30. Figures 4.29a and 4.30a show the force response, whereas, figures 4.29b and 4.30b show the damper control voltage. Measurement and simulation can be seen to be very similar, indicating that the open loop characteristics of the damper are modelled accurately enough for use in controller design. The small discrepancy between measured and demand force *amplitude* is again mainly due to the inaccuracy of the damping–voltage model. Noise on the measured damper voltage signal (figure 4.29b) is mainly caused by the differentiation process used to obtain the velocity across the damper from the measured displacement.

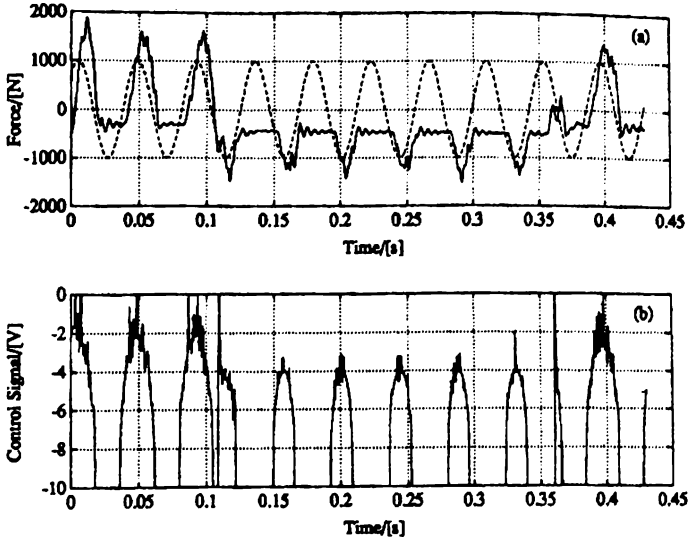


Fig. 4.29 Measured force tracking of the open loop damper controller, for a demand force of 1 kN at 23 Hz (damper velocity amplitude = 0.28 m/s). From [56]. (a) damper force and demand (b) damper control voltage.

The disturbances at 0.12s and at 0.37s in figure 4.29, and at 0.01s and 0.25s in figure 4.30, are due to discontinuities in the damper velocity input. A time delay (phase lag) of approximately 10 ms can be seen on both the measured and simulated responses. Despite the overshoot and time delay, the tracking performance is considered to be satisfactory.

Force Feedback Control

The measured force tracking and control voltage responses of the damper using the force feedback controller are shown in figure 4.31. The sampling frequency of the controller was set to 1 kHz and the gains used in experiment were: $K_P = 10mV/N$, $K_I \tau = 5mV/N$ and $K_D/\tau = 0mV/N$. The semi-active constraint (SAC) was calculated using the measured damping force to estimate the sign of the relative velocity, according to equation 4.10b.

The amplitude of the damper force in figure 4.31a can be seen to track the demanded force more accurately than the open loop controller (figure 4.29a), but the phase lag is noticeably larger (approx 12 ms for the force feedback controller, compared with 10 ms for the open loop controller). This is because the open loop controller has a faster dynamic response than the force feedback controller. Oscillations of the measured force around the static level cause the SAC to switch on and off, and generate the spikes in the control voltage signal in figure 4.31b.

It was necessary to use a large integral control gain in order to avoid force oscillations at large control voltages. The de-stabilising effects of the damping valve dynamics and the time delay limited the bandwidth of the controller and therefore limited the proportional gain. Derivative control was not found to improve the force tracking response, because large derivative gains made the controller respond to noise in the measured force, and increasing K_D de-stabilised the force feedback control loop (see analysis in [53]).

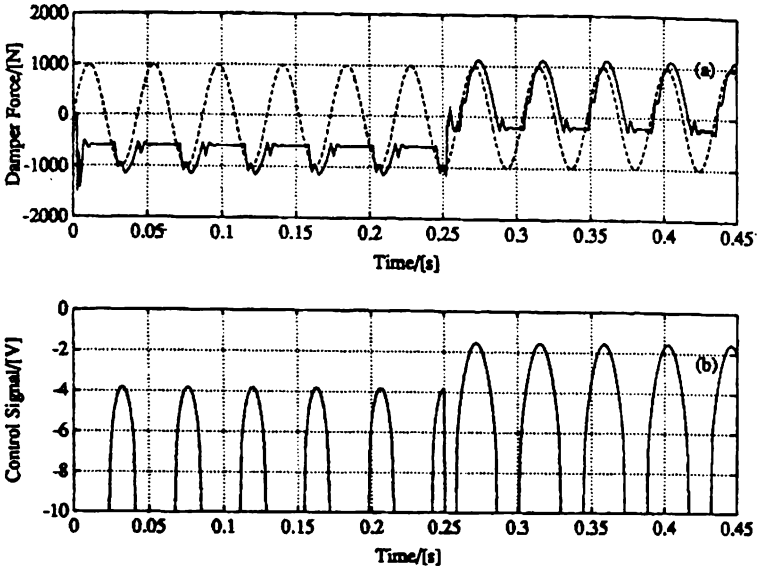


Fig. 4.30 Simulated force tracking of the open loop damper controller, for a demand force of 1 kN at 23 Hz (velocity amplitude = 0.28 m/s). From [56]. (a) damper force and demand (b) damper control voltage.

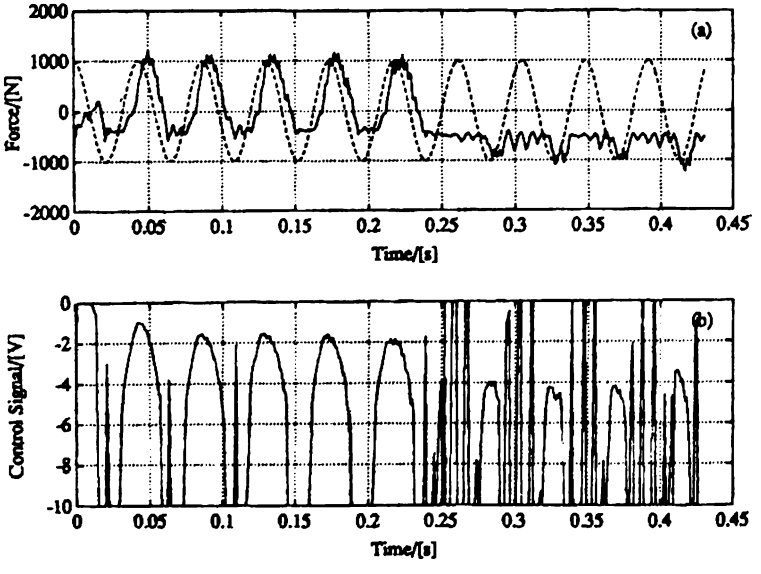


Fig. 4.31 Measured force tracking of the force feedback damper controller, for a demand force of 1 kN at 23 Hz (damper velocity amplitude = 0.28 m/s). From [56].
(a) damper force and demand (b) damper control voltage.

The force tracking response was also measured at a lower sampling rate of 600 Hz [53]. This increased the phase lag slightly, but the amplitude performance was essentially unchanged from figure 4.31.

Vehicle dampers are subject to a wide range of input velocities and operating conditions. It is therefore difficult to draw definitive conclusions about control of real dampers from the simplified constant velocity tests described above. In particular, the performance of force feedback controllers depends on the gains chosen. For low input velocities larger gains are permissible than for higher input velocities. The gains which yield the best operation of the damper therefore depend on the vehicle speed and roughness of the road.

In Chapter 26, the semi-active damper, with both the open-loop and force-feedback controllers, is tested in the HiL rig. The effectiveness of various different vehicle control strategies is investigated.

4.6 CONCLUSIONS

4.6.1 Leaf Springs

(i) The small amplitude force-deflection characteristics of 3 typical leaf springs were found to be independent of the load cycling frequency to 18Hz providing a correction (70-90% of the total mass) was made for the effective inertia of the spring and mounting assembly.

(ii) Two different techniques can be used for predicting accurately the forces developed by a typical leaf spring under realistic operating conditions to at least three times the highest frequency of major excitation. They require a detailed knowledge of the small amplitude, low frequency behaviour of the spring at the static load of interest.

(iii) The popular Coulomb friction model of leaf spring behaviour was found to be significantly less accurate than the other models investigated, throughout the frequency range of interest.

4.6.2 Hydraulic Dampers

(i) A seven–parameter non–linear damper model suitable for vehicle ride simulations was developed and validated in the HiL apparatus. The parameters can be determined using simple measurements on a test damper.

(ii) The RMS errors in simulated vehicle response variables, caused by neglecting damping coefficient saturation, are of the order of 25% RMS for rough roads, but less for smoother roads.

(iii) Neglecting damping coefficient transition or the series compliance introduces simulation errors in the range of 6%-17% RMS for motorway road inputs.

(iv) If damping is assumed to be linear and viscous, the simulation errors are typically up to 30% RMS for a reasonably linear damper, but can be much larger if the damper is nonlinear.

(v) With increasing damping, or decreasing input roughness, errors caused by neglecting saturation decrease, whereas errors due to neglecting compliance, damping coefficient transition or using linear viscous damping all increase.

4.6.3 Controllable Dampers

(i) A model of a semi–active automobile damper was identified from sinusoidal and transient tests, and validated with simple force tracking experiments.

(ii) Two damping force control methods were investigated: (a) open loop control, in which the damper was controlled by a 'lookup table' of damping rate versus input voltage; and (b) force feedback control, with a proportional–integral controller and nonlinear gain compensation. Both controllers were found to track the demanded damping force well, but the open loop controller responded faster, with less phase delay than the force feedback controller.

(iii) Open loop control has the advantage of relatively simple instrumentation (velocity transducer and possibly a temperature transducer) and the benefits of faster response. Force feedback control requires a force transducer and has a slower dynamic response. It can be implemented by estimating damper switching times from the measured damping force, and this eliminates the need to measure the velocity across the damper. Force feedback control has the advantages of more accurate force tracking and insensitivity to variations in damper temperature and wear.

5
SIMULATING DYNAMIC TYRE FORCES

5.1 SUMMARY

Two simple vehicle models are presented. These models represent the general vibration characteristics of the majority of heavy vehicle suspensions. Methods for simulating the responses of simple vehicles in the time and frequency domains are discussed with examples.

A method is presented for computer simulation of more complex two– and three–dimensional vehicle models with non linear tyre and suspension elements. These are represented as general lumped parameter vibrating systems, with arbitrary constitutive elements, moving in an inertial frame of reference. The geometry of the system is treated independently of the constitutive elements. As a result, nonlinear (time domain) or linearised (frequency domain) calculations can be performed using a single input description of the system.

5.2 INTRODUCTION

The mathematical models used for simulating dynamic tyre forces are similar to the models used for simulating vehicle ride. The fundamentals of this subject are covered in detail by Gillespie [190], and will not be repeated here. The following is a brief introduction to vehicle simulations for calculating dynamic tyre forces. The reader is referred to [190], [87] and [121] for further background.

For most heavy vehicle ride models, vibrational motions are small, so that the geometry can be assumed to be linear. Nonlinearities arise from the characteristics of the suspension and tyre elements. These elements can be linearised for simplified analyses of vehicle behaviour. Alternatively they can be modelled in detail, using methods like those described in Chapter 4, for more realistic simulations. Both linear and nonlinear models have value for particular applications, and both are used in this book.

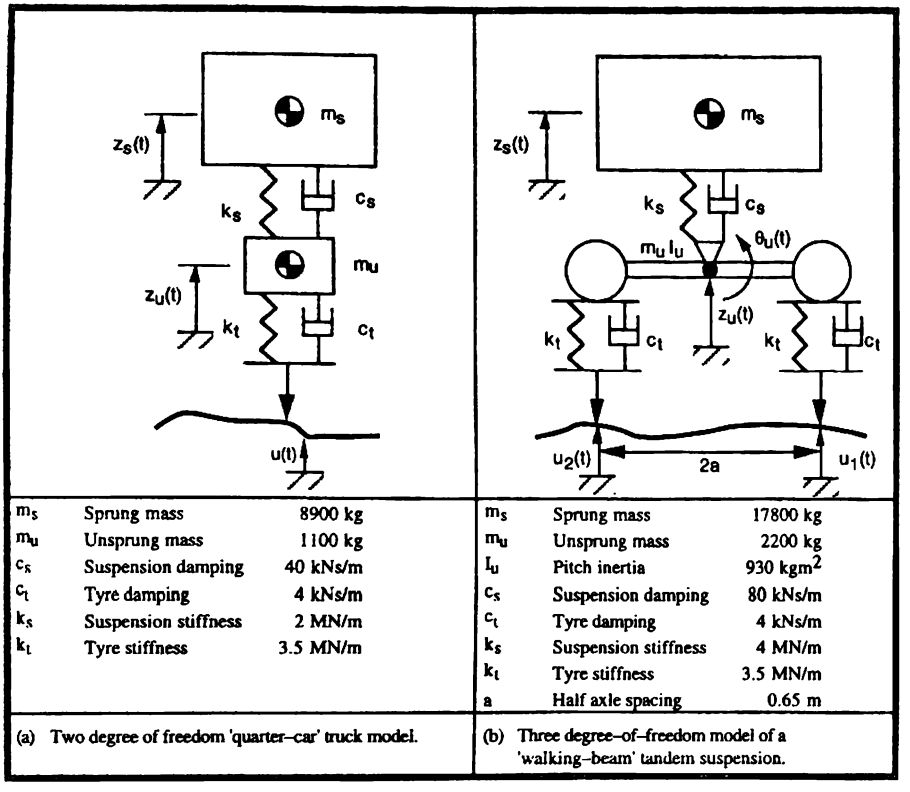
5.3 TWO SIMPLE VEHICLE MODELS

5.3.1 The Models

Figures 5.1 a,b show simplified models of two truck suspensions. The 'quarter-car' model[1] in figure 5.1a has two masses, a sprung mass m_s and an unsprung mass m_u, both of which are constrained to move vertically. It therefore has two degree–of–freedom, the vertical displacements z_s and z_u. The road profile displacement input to the tyre is u. This model generates its main dynamic tyre force components due to sprung mass motion in the frequency range 1.5–4 Hz, which

[1] This model is known as a 'quarter car' because it is traditionally used for analysis of the ride dynamics of passenger cars. In this application, the parameters are chosen so as to model the dynamics of a single wheel station (one of four).

makes it broadly representative of the majority of single axle truck suspensions in current highway use [96]. The parameter values are representative of a single axle air suspension.



m_s	Sprung mass	8900 kg
m_u	Unsprung mass	1100 kg
c_s	Suspension damping	40 kNs/m
c_t	Tyre damping	4 kNs/m
k_s	Suspension stiffness	2 MN/m
k_t	Tyre stiffness	3.5 MN/m

(a) Two degree of freedom 'quarter-car' truck model.

m_s	Sprung mass	17800 kg
m_u	Unsprung mass	2200 kg
I_u	Pitch inertia	930 kgm^2
c_s	Suspension damping	80 kNs/m
c_t	Tyre damping	4 kNs/m
k_s	Suspension stiffness	4 MN/m
k_t	Tyre stiffness	3.5 MN/m
a	Half axle spacing	0.65 m

(b) Three degree-of-freedom model of a 'walking-beam' tandem suspension.

Fig. 5.1 Simple vehicle models

The three degree-of-freedom 'walking-beam' model in figure 5.1b (see also figure 2.1a) consists of a sprung mass m_s which is constrained to move vertically with displacement z_s. A rigid beam joins the two axles, and is connected to the suspension spring by a pin joint at its centre. The combined beam and axle assembly has mass m_u and pitch moment of inertia I_u. It moves with vertical displacement z_u and pitch rotation θ_u. This arrangement generally provides very good static load sharing, and is intended particularly for off-road use. It also allows lightly damped pitching vibration of the beam/axle assembly in the frequency range 8–15 Hz, unless hydraulic dampers are fitted between the axles and frame. The road profile displacement inputs to the two tyres are u_1 and u_2. This model represents the minority of suspensions which generate large dynamic tyre forces due to unsprung mass pitching motion as well as low frequency sprung mass motion [96].

These simple vehicle models do not contain the detailed suspension nonlinearities and complexities of sprung mass motion that are typical of heavy vehicles, however their responses illustrate many of the more important characteristics of dynamic tyre forces. More realistic vehicle models are described in the next chapter.

5.3.2 *Equations of Motion*

The equations of motion of vibration of a linear vehicle model (with linear geometry and linear springs and dampers representing tyre and suspension elements) can be written in matrix form as follows:

$$[M]\ddot{\mathbf{q}} + [C]\dot{\mathbf{q}} + [K]\mathbf{q} = \mathbf{Q} \tag{5.1}$$

where $\mathbf{q}$ is a vector of generalised coordinates,
$\mathbf{Q}$ is a vector of generalised forces,
[M] is the mass matrix,
[C] is the damping matrix and
[K] is the stiffness matrix.

Applying Newton's second law to the two simple vehicle models shown in figures 5.1(a, b), gives the following matrices (all terms are defined on the figures).

Quarter Car Model (2 degrees of freedom)

$$\mathbf{q} = \begin{Bmatrix} z_s \\ z_u \end{Bmatrix}, \qquad \mathbf{Q} = \begin{Bmatrix} 0 \\ c_t\dot{u} + k_t u \end{Bmatrix}$$

$$[\mathrm{M}] = \begin{bmatrix} m_s & 0 \\ 0 & m_u \end{bmatrix},$$

$$[\mathrm{C}] = \begin{bmatrix} c_s & -c_s \\ -c_s & c_s + c_t \end{bmatrix}, \tag{5.2}$$

$$[\mathrm{K}] = \begin{bmatrix} k_s & -k_s \\ -k_s & k_s + k_t \end{bmatrix}.$$

Walking Beam Model (3 degrees of freedom)

$$\mathbf{q} = \begin{Bmatrix} z_s \\ z_u \\ \theta_u \end{Bmatrix}, \qquad \mathbf{Q} = \begin{Bmatrix} 0 \\ c_t(\dot{u}_1 + \dot{u}_2) + k_t(u_1 + u_2) \\ ac_t(\dot{u}_2 - \dot{u}_1) + ak_t(u_2 - u_1) \end{Bmatrix},$$

$$[\mathrm{M}] = \begin{bmatrix} m_s & 0 & 0 \\ 0 & m_u & 0 \\ 0 & 0 & I_u \end{bmatrix},$$

$$[C] = \begin{bmatrix} c_s & -c_s & 0 \\ -c_s & c_s + 2c_t & 0 \\ 0 & 0 & 2a^2c_t \end{bmatrix}, \tag{5.3}$$

$$[K] = \begin{bmatrix} k_s & -k_s & 0 \\ -k_s & k_s + 2k_t & 0 \\ 0 & 0 & 2a^2k_t \end{bmatrix}.$$

5.4 SIMULATION METHODS

Simulations of vehicle response to road roughness can be performed in the time domain or the frequency domain.

5.4.1 Time Domain Simulations

Solution Method

In time domain simulations, the equations of motion are solved by numerical integration with respect to time, and the outputs are time histories of the vehicle response variables. Time domain simulations are used when the vehicle model is non-linear and/or when the response to a deterministic (transient) input is required.

Time domain simulations require the road roughness to be specified as a function of distance. For random road profiles this requires the generation of a random function with the correct spectral density. Methods for achieving this are described in Chapter 3.

Numerical integration routines generally require the equations of motion to be written in first order form. This can be achieved by introducing a new 'state' vector $\mathbf{z}$ which contains the generalised coordinate velocities and displacements:

$$\mathbf{z} = \begin{Bmatrix} \dot{\mathbf{q}} \\ \mathbf{q} \end{Bmatrix} \quad \text{and} \quad \dot{\mathbf{z}} = \begin{Bmatrix} \ddot{\mathbf{q}} \\ \dot{\mathbf{q}} \end{Bmatrix}. \tag{5.4}$$

If there are N degrees of freedom (and hence N elements in $\mathbf{q}$), then $\mathbf{z}$ and $\dot{\mathbf{z}}$ each have 2N elements. Combining equations 5.1 and 5.4, gives

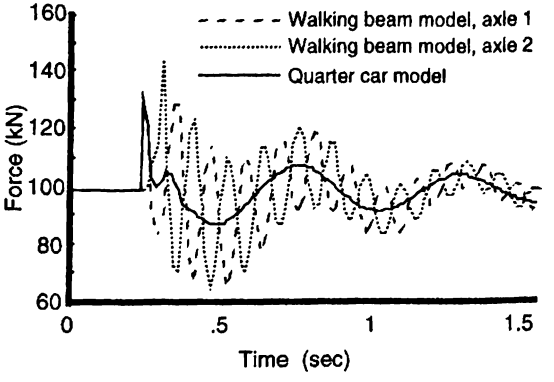
$$\dot{\mathbf{z}} = \begin{Bmatrix} [M]^{-1}(\mathbf{Q} - [C]\dot{\mathbf{q}} - [K]\mathbf{q}) \\ \dot{\mathbf{q}} \end{Bmatrix}. \tag{5.5}$$

In a time domain simulation, vector $\dot{\mathbf{z}}$ is calculated on each time step by evaluating equation 5.5. $\dot{\mathbf{z}}$ is then supplied to the numerical integration routine, which returns the value of $\mathbf{z}$ on the next time step, and so on.

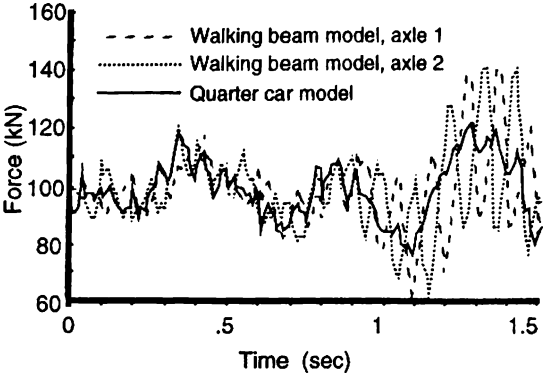
Sample Results

Figure 5.2a shows time histories of the dynamic tyre forces generated by the two simple vehicle models travelling at 80 km/h, in response to a 10 mm step up in the road profile (as might be observed at a bridge abutment or a faulted joint between two PCC pavement slabs). Figure 5.2b shows the response of the models to a 'good' random road (as per equation 3.1) at 80 km/h. (Note that the tyre and suspension parameters in figure 5.1 were chosen so that both models would have similar body bounce motion).

The quarter car model shows an initial spike when the wheel first encounters the step in figure 5.2a, followed by a damped high frequency transient due to axle hop at approximately 12 Hz. The low frequency, lightly damped body bounce motion at 2 Hz continues for several seconds after the step.



(a) Response to a 10mm step



(b) Response to a sample of 'good' random road

Fig. 5.2 Dynamic tyre force time histories generated by the simple vehicle models at 80km/h. From [96].

Both tyres of the walking beam model generate large forces when they first encounter the step in figure 5.2a. (The peak generated by the first axle coincides almost exactly with the peak generated by the quarter-car model). Lightly damped pitching of the walking beam at approximately 9 Hz (with the axles bouncing out of phase) continues for many cycles after the step, and this is superimposed upon the 2 Hz body bounce motion. This behaviour is typical of walking beam suspensions with low bogie pitch damping.

On the random road profile (figure 5.2b), both models generate similar tyre force components at the body bounce natural frequency (2 Hz), but the walking beam model generates much larger peak forces because of its bogie pitching mode at 9 Hz.

A parameter used frequently to characterise the magnitude of dynamic tyre forces is the 'Dynamic Load Coefficient' (DLC), which is defined as:

$$\text{DLC} = \frac{\text{RMS dynamic tyre force}}{\text{Static tyre force}}, \tag{5.6}$$

The RMS tyre force σ can be calculated using:

$$\sigma^2 = \frac{1}{T}\int_0^T f(t)^2 dt = \frac{1}{N}\sum_{k=1}^{N} f_k^2 \tag{5.7}$$

where

f_k = the dynamic tyre force f(t) at time $t = k\,\Delta t$
Δt = the simulation output time step
T = $N\Delta t$ is the total simulation time.

5.4.2 Frequency Domain Simulations

Linear vehicle simulations can be performed efficiently in the frequency domain, for random inputs. In this approach, spectral densities of the output variables (tyre forces, accelerations, *etc*) are calculated directly from a vehicle response transfer function and the road roughness spectral densities. Three dimensional vehicle models require direct spectral densities of the left and right hand wheel paths and the cross spectral densities between them [393].

For a linearised vehicle model, a matrix of dynamic tyre force spectral densities $[S_F(\omega)]$ can be found from a matrix of road profile displacement spectral densities $[S_u(\omega)]$ and a matrix of vehicle transfer function $[H(\omega)]$, according to [355, 393]:

$$[S_F(\omega)] = [H(\omega)]^*[S_u(\omega)][H(\omega)]^T, \tag{5.8}$$

where, for a two-wheeled vehicle model

$$[S_F(\omega)] = \begin{bmatrix} S_{F_1F_1}(\omega) & S_{F_1F_2}(\omega) \\ S_{F_2F_1}(\omega) & S_{F_2F_2}(\omega) \end{bmatrix},$$

$$[S_u(\omega)] = \begin{bmatrix} S_{u_1u_1}(\omega) & S_{u_1u_2}(\omega) \\ S_{u_2u_1}(\omega) & S_{u_2u_2}(\omega) \end{bmatrix},$$

$$[H(\omega)] = \begin{bmatrix} H_{u_1F_1}(\omega) & H_{u_1F_2}(\omega) \\ H_{u_2F_1}(\omega) & H_{u_2F_2}(\omega) \end{bmatrix}.$$

Here '*' denotes the complex conjugate, ^{T} denotes the matrix transpose.

Note that element (i, j) of the transfer function matrix $[H(\omega)]$ is the dynamic force generated by tyre i due to a unit harmonic displacement input at tyre j. Clearly, these matrices can be expanded for vehicle models with more inputs (wheels) and outputs (dynamic tyre forces).

Input Spectral Matrix $[S_u(\omega)]$

The diagonal terms of $[S_u(\omega)]$ are the direct spectral densities of the road profile inputs to the tyres. The off-diagonal terms of $[S_u(\omega)]$ are the cross spectral densities between the inputs to pairs of tyres. These are related to the direct spectral densities:

(i) If one tyre follows another in the same wheel path, then the input to the second is a delayed version of the input to the first. The cross spectral density between them contains information about the time lag.

(ii) If the two tyres are at the same longitudinal position on the vehicle, but are running in different wheel paths, then the cross spectral densities contain information about the coherence between the two profiles (see Section 3.4.2).

The direct and cross spectral densities of the wheel paths can be obtained from measurements or from a model of the road surface roughness (see Chapter 3).

It is necessary to convert the spectral densities and coherence functions from wavenumber to frequency. If the direct spectral density of wheel track j at wavenumber κ is $S_{jj}(\kappa)$, and the coherence function between two tracks is $\eta(\kappa)$, then at angular frequency ω, S_{jj} and η are given by:

$$S_{jj}(\omega) = \frac{1}{2\pi V} S_{jj}(\kappa = \omega / 2\pi V)$$
$$\eta(\omega) = \eta(\kappa = \omega / 2\pi V). \tag{5.9}$$

where V is the speed in m/s.

For *pitch-plane vehicle models*, the off-diagonal (cross-spectral) elements of $[S_u(\omega)]$ are given by [393]:

$$S_{jk}(\omega) = S_{jj}(\omega) e^{-i\omega T_{jk}} \tag{5.10}$$

where $T_{jk} = \ell_{jk} / V$ is the time lag between axles j and k, which are spaced apart by distance ℓ_{jk}. Since $T_{kj} = -T_{jk}$, it follows that $S_{kj}(\omega) = S^*_{jk}(\omega)$.

For *roll-plane models*, with wheel paths 1 and 2, the off-diagonal elements of $[S_u(\omega)]$ are the cross spectral densities $S_{12}(\omega)$ and $S_{21}(\omega)$. If the road surface is assumed to be isotropic (see Section 3.4.2), the direct spectral densities of the two wheel paths are equal and the cross spectral densities are related by:

$$S_{12}(\omega) = S_{11}(\omega)\, \eta(\omega)$$
$$S_{21}(\omega) = S^*_{12}(\omega). \tag{5.11}$$

where $\eta(\omega)$ is the ordinary coherence function relating the two profiles (equation 3.8).

If the model is *three-dimensional*, the input spectral matrix contains both *time lag* and *coherence* terms. Consider, for example, the four-wheeled vehicle shown in plan, in figure 5.3. It has wheelbase ℓ and moves with speed V. Wheels 1 and 3 are in wheel path 1, while wheels 2 and 4 are in wheel path 2. The direct spectral densities of wheel paths 1 and 2 are $S_{11}(\kappa)$ and $S_{22}(\kappa)$ respectively, and the cross spectral densities are $S_{12}(\kappa)$ and $S_{21}(\kappa)$. These can be converted to functions of frequency using equation 5.9.

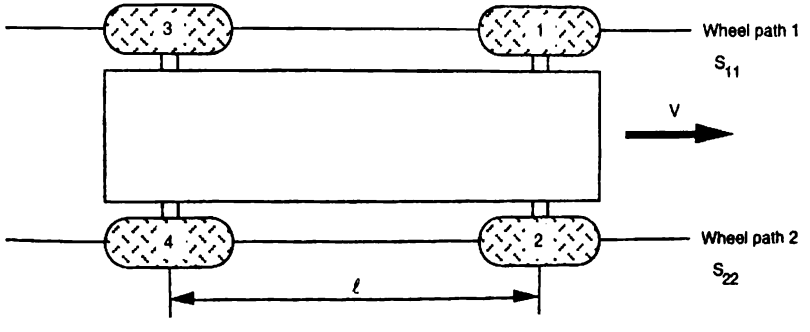


Fig. 5.3 Plan view of a four-wheeled vehicle model.

The input spectral matrix is given by

$$[S_u(\omega)] = \begin{bmatrix} S_{11}(\omega) & S_{12}(\omega) & S_{11}(\omega)e^{-i\omega T_{13}} & S_{12}(\omega)e^{-i\omega T_{14}} \\ S_{21}(\omega) & S_{22}(\omega) & S_{21}(\omega)e^{-i\omega T_{23}} & S_{22}(\omega)e^{-i\omega T_{24}} \\ S_{11}(\omega)e^{-i\omega T_{31}} & S_{12}(\omega)e^{-i\omega T_{32}} & S_{11}(\omega) & S_{12}(\omega) \\ S_{21}(\omega)e^{-i\omega T_{41}} & S_{22}(\omega)e^{-i\omega T_{42}} & S_{12}(\omega) & S_{22}(\omega) \end{bmatrix}.$$

If the road surface is assumed to be isotropic, with direct spectral density $S_{11}(\omega)$ and coherence function $\eta(\omega)$, this reduces to:

$$[S_u(\omega)] = S_{11}(\omega)\begin{bmatrix} 1 & \eta(\omega) & e^{-i\omega\ell/V} & \eta e^{-i\omega\ell/V} \\ \eta(\omega) & 1 & \eta e^{-i\omega\ell/V} & e^{-i\omega\ell/V} \\ e^{i\omega\ell/V} & \eta e^{i\omega\ell/V} & 1 & \eta(\omega) \\ \eta e^{i\omega\ell/V} & e^{i\omega\ell/V} & \eta(\omega) & 1 \end{bmatrix}. \tag{5.12}$$

Transfer Function Matrix [H(ω)]

Assuming a sinusoidal displacement input of the form $\mathbf{u}(t) = \bar{\mathbf{u}}e^{i\omega t}$, it can be shown that the vector of generalised force $\mathbf{Q}(t) = \bar{\mathbf{Q}}e^{i\omega t}$ is given by

$$\bar{\mathbf{Q}} = [D][R]\bar{\mathbf{u}}, \tag{5.13}$$

where

$[R] = \left[\text{diag}(k_t + i\omega c_t)\right]$, and

$[D]$ = linear transformation matrix

$= \begin{bmatrix} 0 \\ 1 \end{bmatrix}$ for the quarter car model and

$= \begin{bmatrix} 0 & 0 \\ 1 & 1 \\ -a & a \end{bmatrix}$ for the walking beam model.

Assuming the response to be sinusoidal with the form $\mathbf{q}(t) = \bar{\mathbf{q}}e^{i\omega t}$, equations 5.1 and 5.13 can be combined to give:

$$[B]\bar{\mathbf{q}} = [D][R]\bar{\mathbf{u}} \tag{5.14a}$$

where

$$[B] = -\omega^2[M] + i\omega[C] + [K]. \tag{5.14b}$$

It can also be shown that the vector of complex dynamic tyre force amplitudes $\bar{\mathbf{F}}_t$ is given by

$$\bar{\mathbf{F}}_t = [R]\left([D]^T\bar{\mathbf{q}} - \bar{\mathbf{u}}\right). \tag{5.15}$$

Substituting for $\bar{\mathbf{q}}$ from equation 5.14 into equation 5.15 gives the required expression for the dynamic tyre forces, in terms of the road profile input:

$$\bar{\mathbf{F}}_t = [H(\omega)]\bar{\mathbf{u}}, \tag{5.16a}$$

where

$$[H(\omega)] = [R]\left([D]^T[B]^{-1}[D][R] - [I]\right), \tag{5.16b}$$

and [I] is the identity matrix.

Solution Procedure

At each frequency of interest ω, the dynamic tyre force spectral matrix $[S_f(\omega)]$ is calculated as follows:

(i) Generate the complex [B] matrix using equation 5.14b with the mass, stiffness and damping matrices of the vehicle model (*eg* equations 5.2 or 5.3);

(ii) Calculate $[B]^{-1}$ using a complex matrix inversion routine;

(iii) Multiply out equation 5.16b to obtain the transfer function matrix $[H(\omega)]$;

(iv) Generate the input spectral matrix $[S_u(\omega)]$ using equations 5.9 to 5.12;

(v) Finally determine $[S_F(\omega)]$ using equation 5.8.

If the Dynamic Load Coefficient is required, the RMS dynamic load σ_j (for tyre j) can be calculated by calculating the area under tyre force spectral density graph by numerical integration as follows:

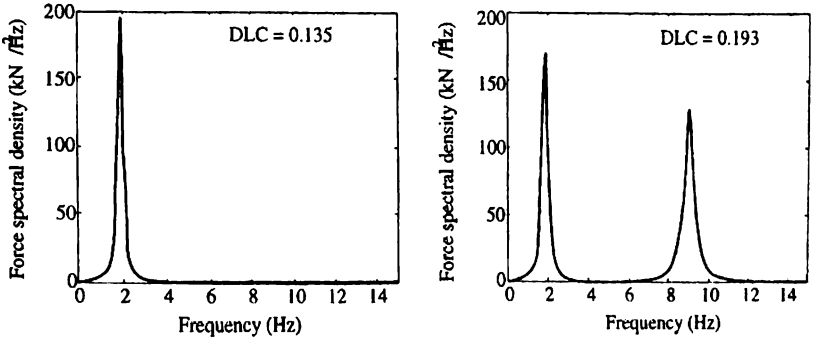
$$\sigma_j^2 = \int_0^\infty S_{F_jF_j}(\omega)\, d\omega. \tag{5.17}$$

This general procedure can be used for any linear vehicle model.

Sample Results

Figure 5.4a shows the tyre force spectral density generated by the quarter–car model travelling at 80 km/h over a 'good' road, as defined by equation 3.1. There is one main spectral peak at a frequency of approximately 2 Hz, which corresponds to the main body bounce mode of vibration, as seen in figure 5.2a. The wheel hop mode of vibration at approximately 12 Hz, hardly contributes to the wheel forces (it is too small to be seen on the linear scales), because it is reasonably well damped, and the level of excitation from the random road roughness is relatively small at this frequency. The DLC, calculated from figure 5.4a is 0.135.

Figure 5.4b shows the corresponding tyre force spectral density for the walking–beam tandem suspension model. In addition to the low frequency body bounce peak, this model displays a significant peak at approximately 9 Hz, due to the lightly–damped pitching motion of the walking beam, as seen in figures 5.2a,b. This motion increases the DLC to 0.193.



(a) Quarter–car model (b) Walking–beam model

Fig. 5.4 Tyre force spectral densities for the two linearised vehicle models travelling at 80 km/h on a 'good' road. From [96].

The dynamic load coefficients generated by both vehicle models are plotted as a function of speed in figure 5.5. It can be seen that the wheel forces generated by the quarter–car model increase smoothly with speed, whereas the walking–beam model has small peaks at speeds of approximately 12 km/h, 17 km/h and 28 km/h. These are caused by the phenomenon known as 'wheel–base filtering' that is discussed briefly in Section 7.4.5. (See [190] for a good explanation.)

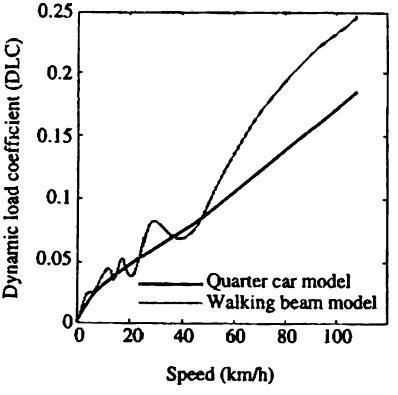


Fig. 5.5 Variation of DLC with speed for the two simple vehicle models. From [96].

5.4.3 Note on Natural Motions (Eigenvalues and Eigenvectors)

Given the mass, damping and stiffness matrices of a linearised vehicle model, it is relatively straightforward to calculate the eigenvalues and eigenvectors (natural frequencies and natural mode shapes). It is generally not sufficiently accurate to assume that the damping is light. This means that the conventional techniques of modal analysis of undamped vibrating systems cannot be used. It is necessary to cast the equations of motion into first order form (similar to equation 5.4) and then calculate the eigenvalues and eigenvectors of the corresponding 2Nx2N characteristic matrix equation. The method is detailed in [354], and will not be discussed further here.

5.5 AN ALTERNATIVE MATRIX FORMULATION OF THE VEHICLE VIBRATION EQUATIONS

Vehicle simulation models which agree well with field measurements can be developed by careful attention to the roughness of the road surface, the overall vehicle configuration and the major sources of suspension system nonlinearity. The next chapter presents examples of two such simulation studies. Although it is desirable to develop these realistic simulations it is often useful to perform eigenvalue and/or frequency domain calculations for linearised versions of the equations of motion. Therefore, it is important to be able to generate linearised equations of motion from the same mathematical model.

Conventional matrix formulation of the equations of motion of vibration of multiple degrees-of-freedom, lumped parameter systems (as described in Section 5.3.2), precludes the use of nonlinear constitutive elements. Sophisticated multibody software systems are available for complex vehicle simulation problems, however it is not necessary to resort to such levels of sophistication when the system can be treated in an inertial frame of reference with the assumption of small deflections. In this case, advantage can be taken of the fact that the geometry of the system is unaffected by assumptions regarding the elements that connect rigid bodies.

An alternative matrix formulation of the vibration equations is presented here. The method treats the geometry of the system independently of the constitutive elements and as a result allows nonlinear (time domain) or linearised (frequency domain) calculations from a single input description.

5.5.1 Equations of Motion for Rigid Bodies Experiencing Small Deflections

Consider a rigid body moving in an inertial reference frame, with generalised coordinates q_i subjected to a number of external but not necessarily conservative forces $F_j^{(k)}$ as shown in figure 5.6[1].

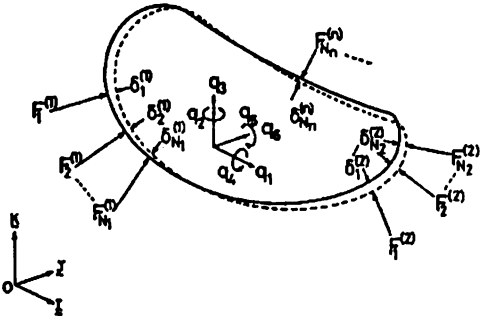


Fig. 5.6 Virtual displacements $\delta_i^{(k)}$ of a rigid body under the action of external forces $F_i^{(k)}$.

Assuming small vibrations, Lagrange's equations may be used to write the equation of motion :

$$\frac{d}{dt}\left\{\frac{\partial T}{\partial \dot{q}}\right\} = [M]\ddot{q} = P, \tag{5.18}$$

where T is the kinetic energy and [M] is the inertia matrix.

To obtain the generalised forces **P** it is usual to apply the method of virtual work. The total virtual work done by the generalised forces is:

$$\sum \delta W = P^T \delta q. \tag{5.19}$$

If a compatible set of virtual displacements $\delta^{(k)}$ is introduced such that $\delta_i^{(k)}$ is the displacement at the point of application of external force $F_i^{(k)}$ (figure 5.6), then the total virtual work done by these forces is:

$$\sum \delta W = \sum_{i=1}^{N_1} F_i^{(1)} \delta_i^{(1)} + \sum_{i=1}^{N_2} F_i^{(2)} \delta_i^{(2)} + ... + \sum_{i=1}^{N_n} F_i^{(n)} \delta_i^{(n)}. \tag{5.20}$$

Combining equations 5.19 and 5.20:

$$P^T \delta q = F^{(1)T} \delta^{(1)} + F^{(2)T} \delta^{(2)} + ... + F^{(n)T} \delta^{(n)}. \tag{5.21}$$

Providing small deflections are assumed, simple linear transformations can be written, relating the original generalised coordinates to the virtual displacements $\delta_i^{(k)}$:

---

[1] A distinction is made between the different types of forces which may act on the body, (eg forces arising from input excitation or from the interaction with other rigid bodies) by the superscript (k).

$$\delta^{(1)} = \left[Z^{(1)}\right]\delta q, \qquad \delta^{(2)} = \left[Z^{(1)}\right]\delta q \quad \ldots\delta^{(n)} = \left[Z^{(n)}\right]\delta q, \tag{5.22}$$

where $[Z^{(k)}]$ is the transformation matrix for forces of type (k). Equation 5.21 now becomes

$$\mathbf{P}^{T}\delta\mathbf{q} = \mathbf{F}^{(1)T}\left[Z^{(1)}\right]\delta\mathbf{q}^{(1)} + \mathbf{F}^{(2)T}\left[Z^{(2)}\right]\delta\mathbf{q}^{(2)} + \ldots + \mathbf{F}^{(n)T}\left[Z^{(n)}\right]\delta\mathbf{q}^{(n)}.$$

Hence the generalised forces are given by

$$\mathbf{P} = \left[Z^{(1)}\right]^{T}\mathbf{F}^{(1)} + \left[Z^{(2)}\right]^{T}\mathbf{F}^{(2)} + \ldots + \left[Z^{(n)}\right]^{T}\mathbf{F}^{(n)}. \tag{5.23}$$

Thus for each rigid body the equation of motion (equation 5.18) may be written

$$[M]\ddot{\mathbf{q}} = \left[Z^{(1)}\right]^{T}\mathbf{F}^{(1)} + \left[Z^{(2)}\right]^{T}\mathbf{F}^{(2)} + \ldots + \left[Z^{(n)}\right]^{T}\mathbf{F}^{(n)}. \tag{5.24}$$

Figure 5.7 shows a generalised vehicle model consisting of several unsprung masses subjected to a set of generalised input ('tyre') forces $\mathbf{F_t}$ and joined to the sprung masses by a set of connection ('suspension') forces $\mathbf{F_s}$. Constant gravitational forces $\mathbf{F_g}$ act at the centre of gravity of each mass.

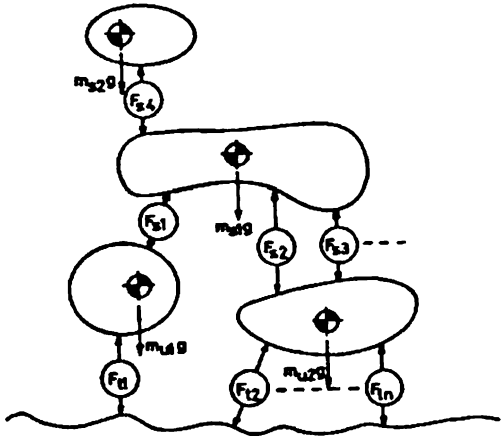


Fig. 5.7 Generalised multibody vehicle model: suspension forces $\mathbf{F_s}$, tyre forces $\mathbf{F_t}$ and gravitational forces $\mathbf{F_g}$.

In this case equation 5.24 may be written

$$[M]\,\ddot{\mathbf{q}} = [S]\,\mathbf{F_s} + [T]\,\mathbf{F_t} + \mathbf{F_g}, \tag{5.25}$$

where the terms $[Z^{(j)}]^{T}\mathbf{F}^{(j)}$ in equation 5.24 have been replaced by $[S]\,\mathbf{F_s}$, $[T]\,\mathbf{F_t}$ and $\mathbf{F_g}$ and all of the rigid bodies have been included in [M]. The constraints on the geometry introduced by the (connections between masses) are implicit in [S], [T], and $\mathbf{F_g}$.

5.5.2 Time Domain Vehicle Modelling

In order to calculate the forces $\mathbf{F_s}$ and $\mathbf{F_t}$, it is necessary to know the relative deflections and velocities experienced by the tyre and suspension elements. To this end the following linear coordinate transformations are introduced

$$\eta_{ss} = [Z_{ss}]\mathbf{q}, \qquad \eta_{us} = [Z_{us}]\mathbf{q}, \qquad \eta_{ut} = [Z_{ut}]\mathbf{q}, \tag{5.26}$$

where

η_{ss} = Displacements of the suspension attachment points on sprung masses,
η_{us} = Displacements of the suspension attachment points on the unsprung masses,
η_{ut} = Displacements of the tyre attachment points on the unsprung masses.

and the [Z] matrices produce the desired transformations from the generalised coordinates **q**.

Examination of equations 5.22, 5.25 and 5.26 reveals a close relationship between the force transformation matrices ($[Z^{(i)}]$, $[S]^T$ and $[T]^T$) and the coordinate transformation matrices ($[Z_{ss}]$, $[Z_{us}]$, $[Z_{ut}]$). In fact with a little manipulation it can be shown that

$$[T] = [Z_{ut}]^T \tag{5.27}$$

$$[S] = ([Z_{ss}] - [Z_{us}])^T. \tag{5.28}$$

The tyre force vector $\mathbf{F_t}$ is a function of the displacements and velocities imposed on each tyre element. If the vector of input road displacements by are denoted by **u** then

$$\mathbf{F}_t = g_1(\mathbf{u} - \eta_{ut}) + g_2(\dot{\mathbf{u}} - \dot{\eta}_{ut}). \tag{5.29a}$$

where $g_i(\eta)$ are appropriate functions which depend on the characteristics of the tyres.

Similarly the suspension force vector is given by

$$\mathbf{F}_s = g_3(\eta_{us} - \eta_{ss}) + g_4(\dot{\eta}_{us} - \dot{\eta}_{ss}). \tag{5.29b}$$

A simple computation procedure may be used to evaluate the necessary derivatives for a numerical integration routine using subroutines to evaluate the suspension and tyre forces (figure 5.8).

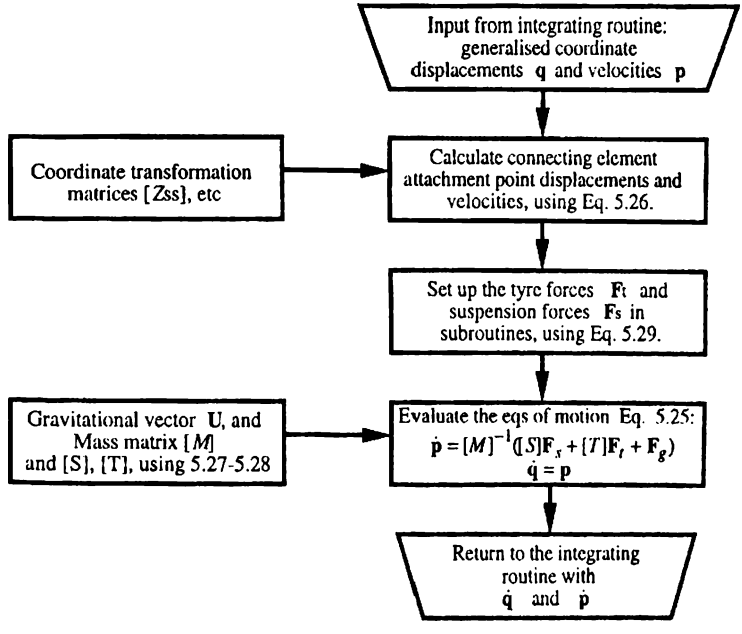


Fig. 5.8 Flow diagram of the procedure for evaluating the equations of motion for a time domain simulation of a lumped-parameter vehicle model, subject to small displacements.

5.5.3 *Linearised Vehicle Modelling*

For a linear vehicle model, the functions g_1 to g_4 are simple linear combinations of the various displacements and velocities, and the constitutive equations (equation 5.29) can be written

$$\begin{aligned}\mathbf{F}_t &= [\text{diag}(K_t)](\mathbf{u} - \boldsymbol{\eta}_{ut}) + [\text{diag}(C_t)](\dot{\mathbf{u}} - \dot{\boldsymbol{\eta}}_{ut}) \\ \mathbf{F}_s &= [\text{diag}(K_s)](\boldsymbol{\eta}_{us} - \boldsymbol{\eta}_{ss}) + [\text{diag}(C_s)](\dot{\boldsymbol{\eta}}_{us} - \dot{\boldsymbol{\eta}}_{ss}).\end{aligned} \tag{5.30}$$

where $[\text{diag}(X_y)]$ = diagonal matrix of linearised parameter values, and

X = K denotes spring stiffness
= C denotes damping constants
y = s denotes suspension elements
= t denotes tyres.

Combining equation 5.25 and equation 5.1:

$$\mathbf{Q} - [C]\dot{\mathbf{q}} - [K]\mathbf{q} = [S]\mathbf{F}_s + [T]\mathbf{F}_t + \mathbf{F}_g. \tag{5.31}$$

Now substitute for $\mathbf{F}_s$ and $\mathbf{F}_t$ from equation 5.30 and for $\boldsymbol{\eta}_{ss}$, $\boldsymbol{\eta}_{us}$ and $\boldsymbol{\eta}_{ut}$ from equation 5.26 into the right hand side of equation 5.31. Then equating the coefficients of $\mathbf{q}$ and $\dot{\mathbf{q}}$, and using 5.27 and 5.28, the following simple expressions are obtained for the conventional damping and stiffness matrices and the generalised forces:

$$\begin{aligned}[C] &= [S][\text{diag}(C_s)][S]^T + [T][\text{diag}(C_t)][T]^T \\ [K] &= [S][\text{diag}(K_s)][S]^T + [T][\text{diag}(K_t)][T]^T \\ \mathbf{Q} &= [T]\left([\text{diag}(K_t)]\mathbf{h} + [\text{diag}(C_t)]\dot{\mathbf{h}} + \mathbf{F}_g\right).\end{aligned} \tag{5.32}$$

[C] and [K] are clearly symmetric, which is expected from stiffness and damping matrices derived using Lagrange's equation.

Finally we note four advantages of writing the equations of motion in the form of equation 5.25:

(i) The models of the suspension and tyre elements are separated from the geometry. They can therefore be evaluated in separate subroutines (equations 5.29) and can be represented by any linear or nonlinear functions or by lookup tables. This contrasts with the normal linear form of the equations of motion (equation 5.1), where the constitutive parameters (k_s, c_t, *etc*) are 'buried' in the stiffness and damping matrices (*eg* equations 5.2 and 5.3).

(ii) It is possible to use identical input formats for linear (frequency domain) or nonlinear (time domain) simulations, providing a facility is included in the connecting element subroutines to return linearised parameter values for the $[\text{diag}(X_y)]$ matrices needed in equation 5.30.

(iii) For models of heavy vehicle vibration, derivation of the $[Z_{ss}]$, $[Z_{us}]$ and $[Z_{ut}]$ transformation matrices is very straightforward compared with deriving the conventional damping and stiffness matrices [*C*] and [*K*] by the methods of Lagrange or Newton II. The calculation of [*C*] and [*K*] (equation 5.32) is easily automated. It is still necessary to calculate the inertia matrix [*M*] and the gravitational vector $\mathbf{F}_g$, but these are usually straightforward for simple small vibration problems of the nature considered here.

(iv) It is possible to generate all of the necessary matrices *automatically* by computer, from a simple geometric description of the vehicle model and information about the mass and moments of inertia of each body. This requires some sophistication in order to handle various types of constraints and the possibility of kinematic 'closed loops'. The method will not be discussed further here.

5.5.4 Example – Walking-Beam Model

Consider, for example, the linear 'walking beam' vehicle model shown in figure 5.1b.

There is only one 'suspension' element, the central damped spring, the top of which moves with displacement z_s. Thus $\boldsymbol{\eta}_{ss}$ (the vector of displacements of the suspension attachment points on sprung masses) has only one element which is given by:

$$\boldsymbol{\eta}_{ss} = \{\eta_{ss1}\} = z_s = \begin{bmatrix}1 & 0 & 0\end{bmatrix}\begin{Bmatrix}z_s\\ z_u\\ \theta_u\end{Bmatrix} \Rightarrow [Z_{ss}] = \begin{bmatrix}1 & 0 & 0\end{bmatrix}. \tag{5.33}$$

Similarly, the displacements of the suspension attachment points on the unsprung masses are:

$$\boldsymbol{\eta}_{us} = \{\eta_{us1}\} = z_u = \begin{bmatrix}0 & 1 & 0\end{bmatrix}\begin{Bmatrix}z_s\\ z_u\\ \theta_u\end{Bmatrix} \Rightarrow [Z_{us}] = \begin{bmatrix}0 & 1 & 0\end{bmatrix}. \tag{5.34}$$

The displacements of the two tyre attachment points on the unsprung masses (*ie* the displacement of the centre of each wheel) are:

$$\boldsymbol{\eta}_{ut} = \begin{Bmatrix}\eta_{ut1}\\ \eta_{ut2}\end{Bmatrix} = \begin{Bmatrix}z_u + a\theta_u\\ z_u - a\theta_u\end{Bmatrix} = \begin{bmatrix}0 & 1 & a\\ 0 & 1 & -a\end{bmatrix}\begin{Bmatrix}z_s\\ z_u\\ \theta_u\end{Bmatrix} \Rightarrow [Z_{ut}] = \begin{bmatrix}0 & 1 & a\\ 0 & 1 & -a\end{bmatrix} \tag{5.35}$$

These simple transformation matrices $[Z_{ss}]$, $[Z_{us}]$ and $[Z_{ut}]$, along with descriptions of the suspension and tyre elements, $\mathbf{F_s}$, and $\mathbf{F_t}$, the inertia matrix [M], and the gravitational vector $\mathbf{F_g}$ are sufficient to perform (non-linear) time-domain simulations of the vehicle. It is necessary to calculate [S] and [T], using equations 5.27 and 5.28:

$$[S] = \begin{bmatrix}1\\ -1\\ 0\end{bmatrix}, \text{ and } [T] = \begin{bmatrix}0 & 0\\ 1 & 1\\ a & -a\end{bmatrix}. \tag{5.36}$$

[S] and [T] can easily be checked by application of virtual work to each mass, using equation 5.20.

The tyre and suspension elements $\mathbf{F_s}$, and $\mathbf{F_t}$ can be represented by functions of arbitrary complexity. For example, they could include the nonlinear leaf spring and damper models described in Chapter 4. If instead, they are linearised to comprise simple springs and dashpots, the linearised stiffness and damping matrices [K] and [C], can be calculated using equation 5.32.

Since there is only one suspension element, the diagonal matrix of suspension stiffnesses is simply

$$[\text{diag}(K_s)] = k_s. \tag{5.37}$$

There are two tyre elements (assumed here to have the same stiffness k_t), so the diagonal matrix of tyre stiffnesses is simply

$$[\text{diag}(K_t)] = \begin{bmatrix}k_t & 0\\ 0 & k_t\end{bmatrix}. \tag{5.38}$$

Thus substituting equations 5.36-5.38 into equation 5.32 gives:

$$[K] = \begin{bmatrix} 1 \\ -1 \\ 0 \end{bmatrix} k_s \begin{bmatrix} 1 & -1 & 0 \end{bmatrix} + \begin{bmatrix} 0 & 0 \\ 1 & 1 \\ a & -a \end{bmatrix} \begin{bmatrix} k_t & 0 \\ 0 & k_t \end{bmatrix} \begin{bmatrix} 0 & 1 & a \\ 0 & 1 & -a \end{bmatrix}$$

$$= \begin{bmatrix} k_s & -k_s & 0 \\ -k_s & k_s + 2k_t & 0 \\ 0 & 0 & 2a^2 k_t \end{bmatrix},$$

as per equation 5.3. The damping matrix [C] can be calculated using the same approach.

5.6 CONCLUSIONS

(i) Two simple generic vehicle models have been derived. They can be used to predict the general form of the dynamic tyre forces generated by most heavy vehicle suspensions. The computational requirements are small, particularly for linearised frequency domain calculations.

(ii) A method has been developed for computer simulation of multiple degrees of freedom, nonlinear, lumped parameter vibrating systems. The assumption of small motions is used, however no restriction is placed on the nonlinear elements that connect rigid bodies in the system. Derivation of the equations is simple compared with conventional methods, and the equations may be solved by numerical integration in the time domain or linearised automatically and solved in the frequency domain. The method is particularly suited to predicting the response of realistic heavy vehicle models to road surface roughness.

The method derived in Section 5.5 will be used in the next chapter in two case studies of heavy vehicle vibration.

6
CASE STUDIES IN VEHICLE SIMULATION

6.1 SUMMARY

This chapter presents two case studies of heavy vehicle vibration simulation.

Tests were performed on a 3-axle rigid truck operating under harsh vibrating conditions, and a four-axle leaf-sprung articulated vehicle operating under highway conditions. Dynamic tyre forces and sprung mass accelerations and unsprung mass accelerations were measured in both cases. The measured road profile data and vehicle response data are used to determine some of the important characteristics of heavy vehicle vibration behaviour; in particular the effects of roll motion and frame bending on dynamic tyre forces.

The measured data are used to validate two and three-dimensional computer models of the vehicles, which were developed using the methods described in the previous chapter. Attention is given to modelling the tyres and suspensions. Agreement between the response of the three-dimensional vehicles models and the measurements is generally good. The conditions under which two-dimensional models can accurately simulate vehicle behaviour are examined.

This chapter is based on work previously published in [87] and [121].

6.2 INTRODUCTION

The simulation of vehicle vibration is valuable for understanding the ways in which dynamic tyre forces are generated, and for predicting the effect of vehicle design changes on road damage.

There is a considerable amount of literature concerned with modelling the ride dynamics of heavy vehicles and hence simulating dynamic wheel loads. This field was reviewed by El Madany *et al* in 1979 [169] and Cebon in 1985 [88]. Further information can be found in [121, 190, 362, 422].

A number of detailed two- and three-dimensional computer simulations of heavy vehicles have been developed and validated by comparison with full-scale tests [86, 87, 121, 192, 229, 243, 400, 406, 478]. Most have solved the equations of motion in the time domain by numerical integration. However, relatively few of these studies have made a detailed comparison of the theoretical results with vehicle test data.

This chapter presents the results of two separate vehicle model validation studies. The first is concerned with a 3-axle rigid vehicle, and the second with an articulated vehicle. Both vehicles were instrumented extensively to measure dynamic tyre forces and accelerations. The rigid vehicle was tested on a rough pavé test track at the Motor Industry Research Association in the UK, and the articulated vehicle was tested on a relatively smooth section of the TRRL test track. The road profile input was known in both cases, as were many of the suspension characteristics and inertial parameters. The validation exercises shows the likely levels of simulation accuracy that can be expected when most of the necessary information is available.

6.3 A RIGID OFF-ROAD VEHICLE

6.3.1 Vehicle Testing Program

A program of measurements was performed on a 3-axle, 23 tonne, rigid 6 x 4 fuel tanker with a 'single point' tandem bogie suspension (see figure 2.1), on a rough pavé test track in the UK [98]. A number of accelerometers were mounted on the vehicle to measure sprung mass bounce, pitch and roll accelerations, frame bending and twisting as well as bounce and roll of the two drive axles. A linear displacement transducer monitored axle travel and bump stop contact. The casing of the leading drive axle was strain gauged at each end, outboard of the spring hangers, to measure bending strains due to vertical loads. Tyre forces were obtained by appropriate calibration and the assumption that the distances between the strain gauge installations and the tyre contact centres of pressure were constant. It was necessary to make corrections for the inertia (linear and angular) of the axle and wheel components outboard of the strain gauges [491]. This method of measuring dynamic tyre forces is discussed further in Section 7.3. The vehicle was tested in the laden and unladen conditions (gross vehicle weights of 22 970 kg and 12 250 kg) at nominal speeds of 5,10 and 15 km/h.

6.3.2 Measurement and Modelling of Road Surface Roughness

Topographical data for the test track, measured on a 0.25 m grid was available [18]. In order to obtain information regarding the short wavelength roughness[1], 10 local height surveys were performed along a number of 1m lengths of the test track. The average displacement spectral densities of the two sets of topographical data are shown in figure 6.1. Harmonics of the 140 mm paving interval can be seen clearly at wavenumbers of approximately 45, 90, 135 ... rad/m.

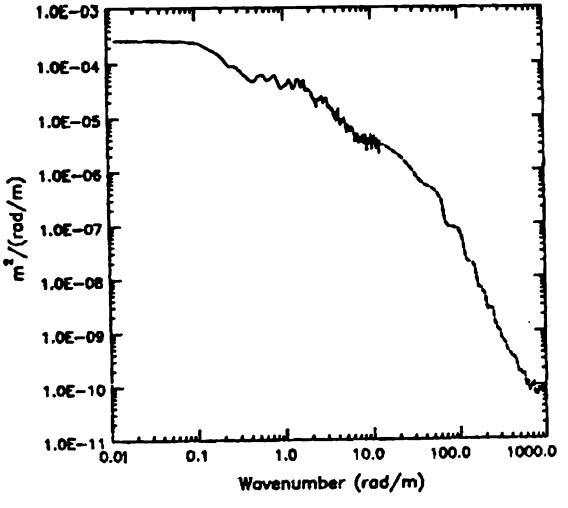


Fig. 6.1 Height spectral densities along the centre line of the pavé test track. From [87].
- - - - - - - Average of 10 local height surveys (1m sample lengths)
——— Original topographical survey, grid spacing = 0.25m

[1] At the highest testing speed (15 km/h) the relatively large grid spacing of the original data limited the maximum simulation frequency to 8.3 Hz.

Assuming that the coherence between the left and right hand wheel paths (track spacing = 2.0m) was zero for wavenumbers greater than 0.25 rad/m, and using the one dimensional inverse discrete Fourier transform techniques described in Chapter 3, the measured direct and cross spectral densities of the test track were converted into correlated pairs of Gaussian, random profiles with an ordinate spacing of 25 mm. These profiles were used for time domain simulations of the vehicle.

6.3.3 Mathematical Vehicle Models

Two lumped parameter, nonlinear mathematical models of the fuel tanker were developed using the matrix formulation described in Section 5.5. (See [88] for the derivation of these matrices for the vehicle models used in this study.) The simpler was a two-dimensional, 4 degrees-of-freedom (4 DOF) model of the 'single point' tandem bogie suspension (figure 6.2a). Sprung mass effects were modelled by a single mass free to move vertically. The more complex model is shown in figure 6.2b. It was three dimensional, with 14 degrees of freedom. These were:

(i) 3 rigid axles, each with freedom to bounce and roll;

(ii) two centrally pivoted, rigid beams with pitch freedom, modelling bogie suspension pitch;

(iii) a rigid sprung mass with 6 degrees of freedom.

Important features of the models are:

(i) The chassis is assumed to be rigid.

(ii) Tyres (see legend figure 6.2):
(a) Nonlinear force-deflection characteristics including wheel lift-off.
(b) Envelopment of short wavelength irregularities.

(iii) Suspension Systems (see legend figure 6.2):
(a) The bogie suspension is idealised by a rigid beam with a 'Fancher-model' leaf spring element at each end (see Chapter 4). Bogie pitch is restricted by a friction torque which depends on the instantaneous value of the normal load.
(b) Stiff rubber bump stops are fitted on all axles.

Details of the parameter selection can be found in [88].

6.3.4 Simulation Results

Envelopment of Short Wavelength Road Roughness

For low speeds, the forces developed by the tyres of a vehicle are strongly influenced by the mechanisms of filtering of short wavelength road roughness [193]. A number of mathematical models have been developed by previous workers (see Captain *et al* [86]).

Three tyre models were investigated in this study. All consisted of a linear spring and parallel viscous damper and included a facility for departure from the road surface (force = 0 for negative displacements). The models differed in their mechanisms of short wavelength filtering. These were:

(i) Point contact

(ii) Fixed footprint ('boxcar' weighting contact length = 0.3m)

(iii) Variable contact length .

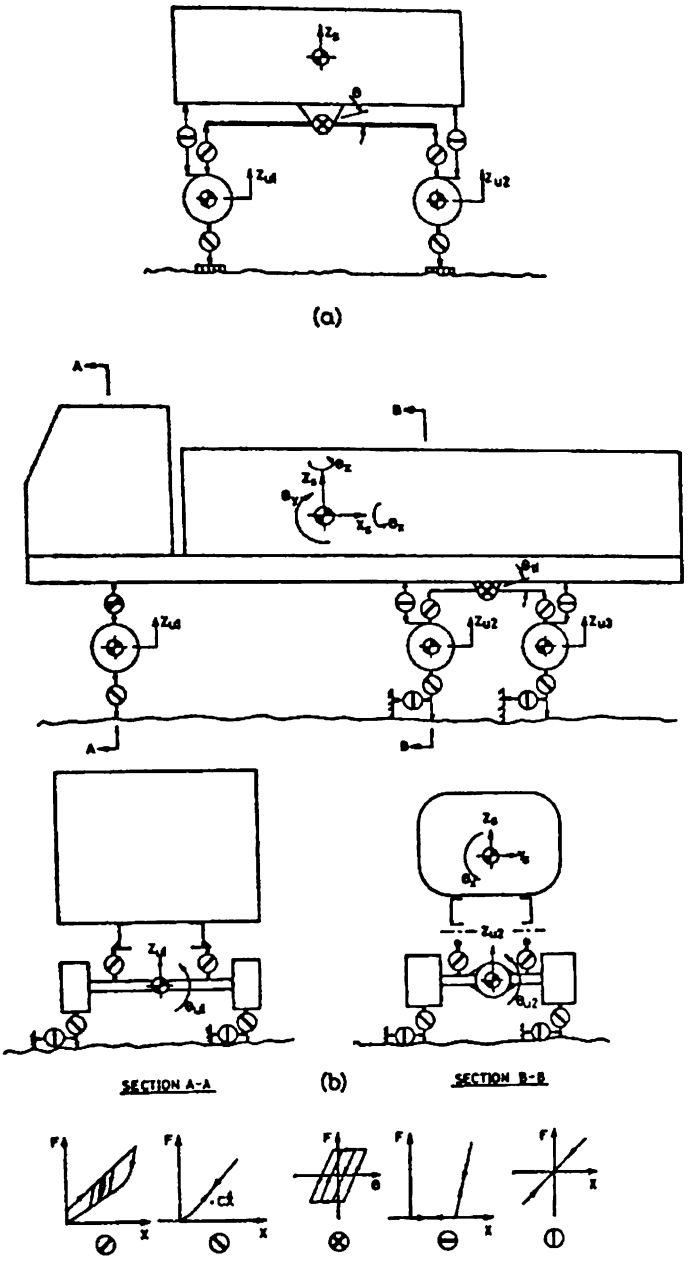


Fig. 6.2 Nonlinear vehicle models. From [87].
(a) 4 degrees of freedom bogie model
(b) 14 degrees of freedom, three–dimensional, whole vehicle model.

The variable contact length model was developed from the fixed footprint model, for the purpose of this study, to eliminate the zeros resulting from the Fourier transform of the boxcar function [193]. It was assumed that the contact length of the tyre is proportional to its deflection (see [428]). A simple iterative calculation was performed at each time step to determine the average profile height and hence the current contact length and vertical tyre force. Details of the calculation are presented in [88].

The 4 DOF tandem bogie model (figure 6.2a) was used to compare the three tyre models. Spectral densities of the tyre forces generated by this vehicle model travelling at 4.2m/s (15 km/h) on the pavé track are shown in figure 6.3. Two important observations may be made:

(i) Relative to the variable contact length model, the point contact follower results in considerable overestimation of the tyre forces at high frequencies (see also [86]).

(ii) The fixed footprint model produces the expected zero tyre forces at 14Hz and 28Hz[1].

The variable contact length tyre model was used for all other time domain simulation runs in this study.

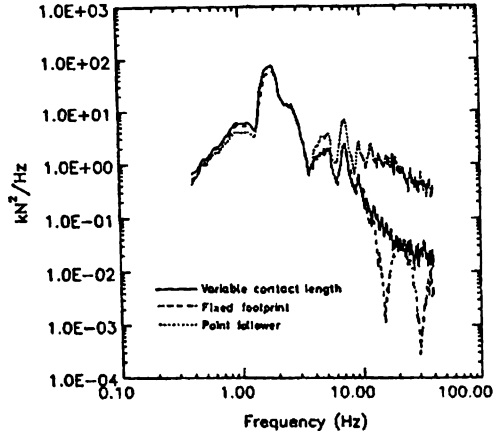


Fig. 6.3 Spectral densities of the tyre forces generated by the 4 DOF bogie model using the three tyre envelopment models: laden, 15 km/h (4.2 m/s), pavé. From [87].

Linearised Vehicle Model

The 4 DOF bogie suspension model was linearised by replacing the nonlinear suspension and tyre elements with linear springs and dashpots. Equations described by Sayers and Gillespie [405] were used to determine the small displacement stiffnesses of the leaf springs at their static loads. Linear viscous damping coefficients were estimated by equating the energy dissipated per cycle by the leaf springs and pivot friction element with the energy dissipated per cycle by the equivalent dashpots at a frequency of 7Hz and displacement amplitude equal to the expected RMS (this involved some

[1] The Fourier transform of a boxcar weighting of length 2ℓ is $[\sin(\gamma\ell)/\gamma\ell]$, γ=wavenumber. For a vehicle travelling at speed V (m/s), this will result in zero excitation at frequencies of $nV/2\ell$ Hz, where n = 1, 2, 3...

iteration). The fixed footprint tyre model was used in this calculation. The theoretical tyre force spectral density shown in figure 6.4 was calculated using the formula

$$S_{ff}(\omega) = \left[k_t^2 + \omega^2 c_t^2\right]\left[S_{uu}(\omega) + S_{zz}(\omega) - 2\,\mathrm{Re}\{S_{uz}(\omega)\}\right], \tag{6.1}$$

where k_t and c_t are the linearised stiffness and damping coefficient of the tyre of interest and $S_{uu}(\omega)$, $S_{zz}(\omega)$ and $S_{uz}(\omega)$ are the direct spectral densities of the road profile displacement u(t), axle displacement z(t), and the cross spectral density between them. Re{•} denotes the real part. $S_{zz}(\omega)$ and $S_{uz}(\omega)$ were calculated by linear frequency domain methods (see Chapter 5 and [88, 393]).

Qualitative agreement between the theoretical and experimental curves is satisfactory however the linearised models of suspension pivot friction (see 7 Hz bogie pitch resonance) and tyre filtering (frequencies above 7 Hz) are clearly inadequate.

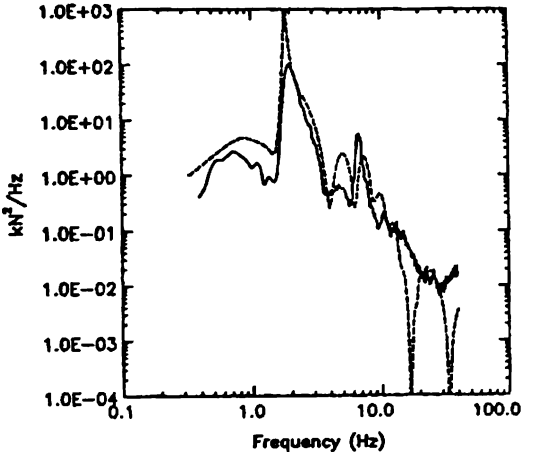


Fig. 6.4 Tyre force spectral densities (15 km/h, laden, pavé track). From [87].
———— Experiment - - - - - - - - Linearised 4 DOF simulation.

Whole Vehicle Simulations

The 14 DOF whole vehicle model was used to simulate the tanker operating on the pavé test track at 15km/h in the laden condition[1]. Figure 6.5 shows the spectral densities of: the force generated by the nearside tyre of the leading drive axle, the bounce and roll angle accelerations of the leading drive axle, and the sprung mass pitch angle, roll angle and vertical accelerations. The corresponding acceleration spectral densities for the trailing drive axle and force spectral densities for the offside tyre of the leading drive axle were quite similar to those shown in figure 6.5. These will not be presented here.

[1] Responses were also calculated for a number of other operating conditions [88] and general agreement was similar to that in figure 6.5. Space constraints prevents the presentation of these results.

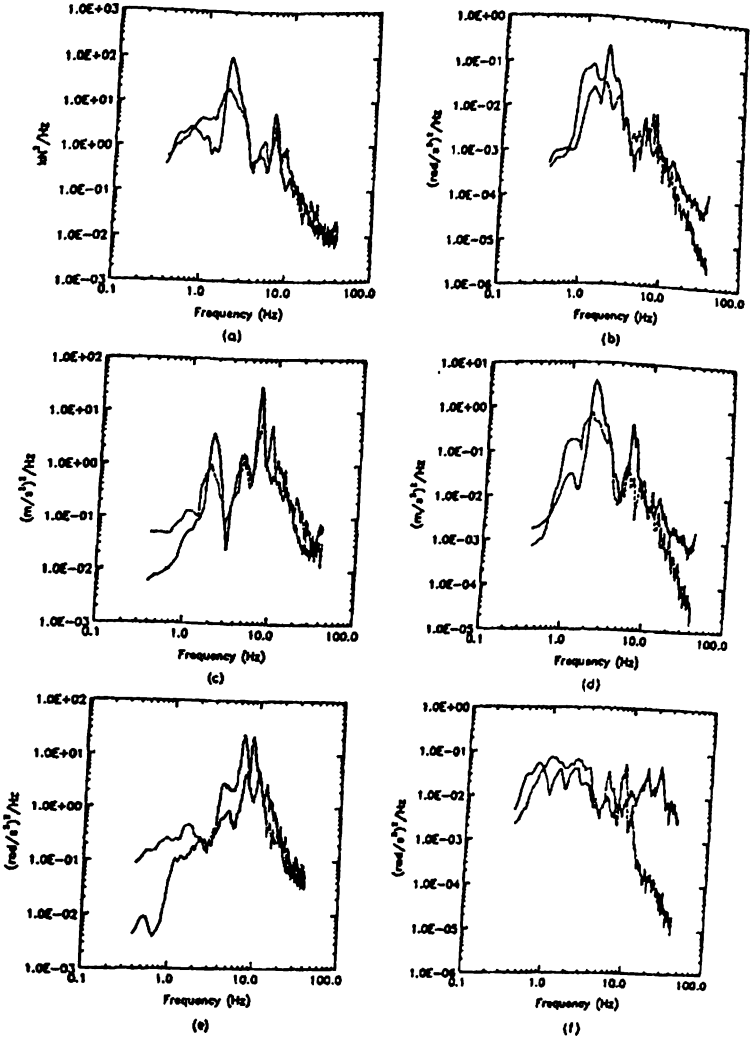


Fig. 6.5 Comparison between measured and simulated spectral densities (14 DOF model) of the tanker traversing the pavé test track at 15km/h in the laden condition. From [87].
———— = Experiment - - - - - - - - = Simulation

(a) Leading drive axle, nearside tyre force
(b) Sprung mass pitch angle acceleration
(c) Leading drive axle CG vertical acceleration
(d) Sprung mass CG vertical acceleration
(e) Leading drive axle roll angle acceleration
(f) Sprung mass roll angle acceleration

General agreement between measured and simulated responses is satisfactory throughout the frequency range, however several discrepancies are apparent:

(i) Inaccurate bogie pitch modelling produces errors in the tyre forces and the unsprung mass vertical and roll accelerations in the vicinity of the 7Hz bogie pitch frequency [88].

(ii) The most significant area of inaccuracy in the simulation is in the range of sprung mass rigid body modes (below 3Hz). The errors are thought to be caused by inadequate modelling of the bogie suspension spring characteristics (for which no measured force-deflection data was available).

(iii) Another large discrepancy between measured and simulated responses if for high frequency sprung mass roll accelerations (figure 6.5f). This is due to twisting of front portion of the chassis of the vehicle. The twist angle was registered as roll angle by the instrumentation and data reduction procedures (see [88]).

(iv) A similar effect to (iii) above causes the simulation to underestimate the sprung mass pitch accelerations (figure 6.5b) and sprung mass CG vertical accelerations (figure 6.5d) at high frequencies. In this case, however, bending of the front portion of the frame (about a horizontal-lateral axis) results in increased measured bounce and pitch accelerations.

(v) Figure 6.6 compares the measured chassis bending acceleration (acceleration of the frame centre relative to a straight line between its ends) with the measured sprung mass CG vertical acceleration. The main flexural peak at 6Hz is visible on both curves. This indicates that the simulation inaccuracy observed at 6Hz on figure 6.5d is due to measurement errors caused by frame flexure.

(vi) Errors in unsprung mass roll predictions (figure 6.5e) are thought to be caused by failure to account for the auxiliary roll stiffness of the bogie springs.

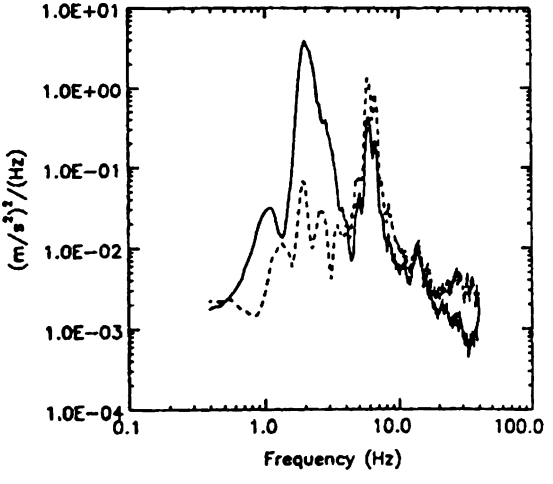


Fig. 6.6 Measured spectral densities of frame bending acceleration and sprung mass CG vertical acceleration (laden, 15km/h, pavé). The major flexural vibration peak at 6Hz is visible on both curves. From [87].
———— = Sprung mass CG vertical acceleration - - - - - - - - = Frame bending acceleration

Returning to the tyre force spectral densities (figure 6.5a) it is apparent that the 6Hz frame flexural mode does not contribute significantly to the dynamic wheel loads. This is thought to be because the suspension systems are located near to the nodes of the lowest bending mode of the frame. Thus displacements and accelerations imposed on the axles by frame bending are small relative to motion caused by the major sprung and unsprung mass resonances.

A number other areas of inaccuracy exist between the simulated and measured vehicle responses. They cannot all be explained simply. However, considering the harsh vibrating conditions and the highly nonlinear suspension components on this vehicle (bump stop contact and tyre departure from the road surface were observed frequently in the simulations), the results are thought to be satisfactory.

6.4 A TRACTOR-SEMI TRAILER MODEL

6.4.1 Experiments

Vehicle Tests

A typical UK articulated lorry, with four axles and a maximum allowable gross mass of 32.5 tonnes (figure 6.7) was provided by the Transport and Road Research Laboratory (TRRL). The tractor had two axles, each fitted with multi-leaf springs, hydraulic dampers, and anti-roll bars. The trailer was fitted with a wide-spread tandem axle group having mono-leaf springs and a load equalising mechanism (figure 6.8). The steering axle was fitted with single radial-ply tyres and all other axles were fitted with dual radial-ply tyres.



Fig. 6.7 The instrumented test vehicle, shown in the half laden condition. From [121].

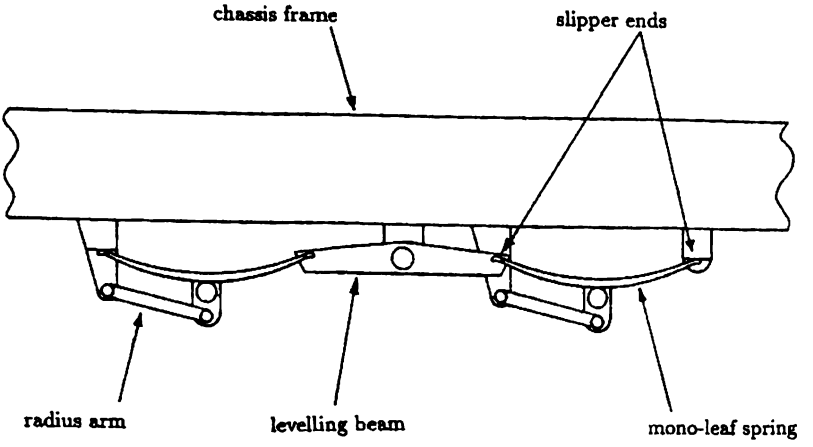


Fig. 6.8 Schematic view of the trailer suspension. From [121].

The vehicle was instrumented by TRRL to measure dynamic tyre forces, by means of strain gauges bonded to each axle between the spring mounting and brake back plate. Accelerometers were fitted near to the ends of each axle so that a correction could be made for the inertia of the mass outboard of each strain gauge [88, 491] (see Section 7.3). Static force components were measured with the vehicle stationary using portable weighpads. The static forces were added to the dynamic components to give the total tyre forces. This method for measuring dynamic tyre force is thought by Sweatman to be the best compromise between accuracy and complexity [445], but it assumes that the distance between the strain gauge and the line of action of tyre force remains constant. Tractor and trailer frame vertical accelerations were measured by eight piezoelectric accelerometers, three on the tractor and five on the trailer.

The vehicle was tested at speeds of 13, 18 and 22m/s (30, 40, 50 mph) and three payloads (unladen, half laden, fully laden). The payload consisted of concrete blocks (each 500 kg) placed at the front and rear of the trailer load bed.

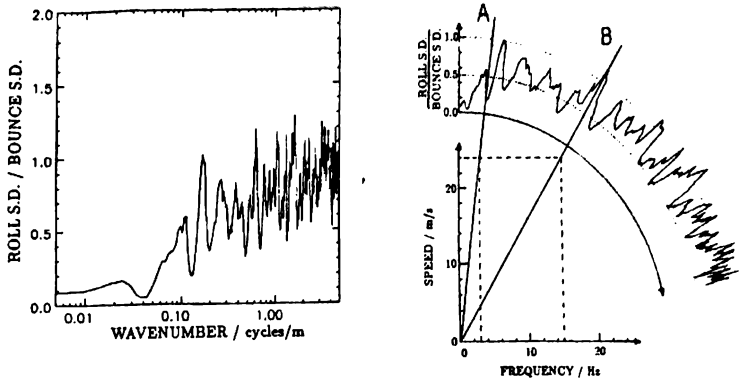
Road Profile

The vehicle was tested on a 530m long straight section of the TRRL test track which had a jointed concrete surface with joints at 30m intervals. The profiles of left and right hand wheel tracks were measured by TRRL using their high-speed profilometer [439], which provides measurements at 0.107m intervals along the road. The measured height is the average height over the preceding 0.107m distance along the road. This averaging process and the effects of aliasing result in a lower wavelength limit of about 0.5m [439]. The upper limit is several hundred metres. For the slowest of the three testing speeds (13m/s), the minimum wavelength (0.5m) corresponds to a frequency of 26Hz. For the highest speed (22m/s), the maximum wavelength (200m) corresponds to about 0.1Hz. These frequencies are outside the main frequencies of interest in this study.

The displacement spectral densities of the measured vertical profiles of the nearside and offside wheel tracks are given in figure 3.1, which shows that the two wheel tracks have similar roughness, corresponding approximately to 'good' classification (poor motorway or average principal road).

The nearside and offside profiles (u_1 and u_2) were transformed into a vertical 'bounce' displacement $(u_1 + u_2)/2$ and a 'roll' displacement $(u_1 - u_2)/2$. The ratio of roll spectral density to bounce spectral density for the test lane is shown in figure 6.9a. The ratio is close to zero at small

wavenumbers, and increases to about one at higher wavenumbers. This is typical of many road surfaces [190, 404]. The ratio is generally less than 0.5 at wavenumbers below 0.2 cycles/m.



(a) Roll/bounce ratio against wavenumber.

(b) Roll/bounce ratio on a radial plot. A radial line drawn through the desired speed and frequency determines the corresponding roll/bounce ratio.

Fig. 6.9 Ratio of roll displacement spectral density to bounce displacement spectral density of the test lane. From [121].

Figure 6.9b contains the same data as figure 6.9a, but the wavenumber axis is plotted on a circular arc. At the centre of the arc is the origin of a set of rectangular axes, with speed on the vertical axis and frequency along the horizontal axis. A straight line drawn between the origin of the rectangular axes and a point on the roll/bounce ratio curve defines the combinations of speed and frequency that correspond to this point.

The line labelled A on figure 6.9b corresponds to a typical sprung mass mode frequency of 3Hz and a typical vehicle speed of 24m/s. The corresponding value of roll/bounce ratio is below 0.5, and so there is comparatively little roll excitation of vehicles at (or below) this frequency. Therefore, the sprung mass roll modes, which generally have frequencies below 3Hz, are unlikely to contribute significantly to the dynamic tyre forces [190]. (However, this may not be the case for poorer roads where the nearside wheel track is sometimes rougher than the offside wheel track [231]). The line labelled B corresponds to a typical unsprung mass mode frequency of 15Hz and a speed of 24m/s. The corresponding roll/bounce ratio is above 0.5, and therefore unsprung mass roll modes will have significant excitation at this speed.

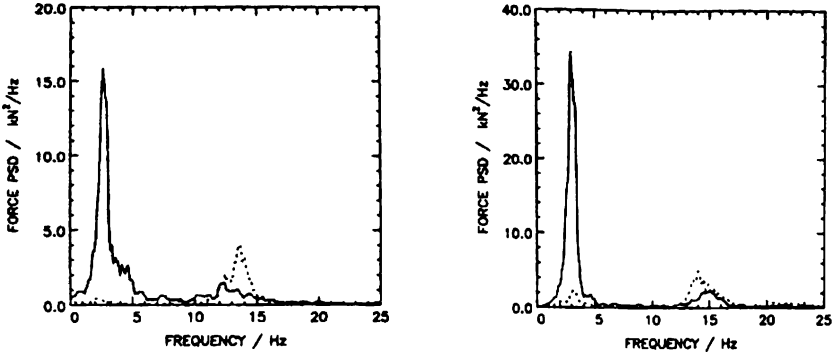
If the vehicle speed is decreased from 24m/s, the frequency corresponding to a given point on the roll/bounce ratio graph will decrease, and the excitation of the sprung mass roll modes will become comparable to the excitation of the bounce modes. The unsprung mass modes (above 10Hz) will normally always be excited at wavenumbers where the ratio of roll to bounce excitation is close to one. These results were derived for one particular road surface but it is likely that the general trends will hold for most highway surfaces [190, 404].

The measured vehicle responses are used in the next section to examine the relationship between road profile and vehicle roll motions.

Vehicle Response

Roll Motion.

The nearside and offside tyre forces ($F_1(t)$ and $F_2(t)$) measured on the tractor drive axle and the leading trailer axle were transformed into 'bounce ($F_1(t)+F_2(t)$)/2 and 'roll' ($F_1(t)$ - $F_2(t)$)/2 components. Figure 6.10 shows the spectral densities of these components for the fully laden vehicle travelling at 22m/s.



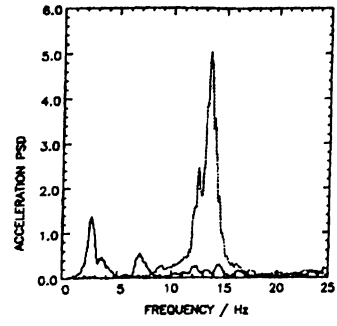
(a) Drive axle. (b) Leading trailer axle.

Fig. 6.10 Bounce and roll components of tyre forces - fully laden, 22m/s. From [121].
——— bounce - - - - - - roll

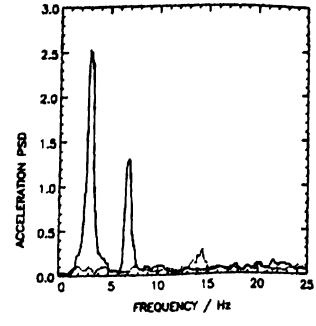
In the frequency range of the sprung mass modes (1-4Hz), the roll components of the drive axle force (figure 6.10a) and trailer axle force (figure 6.10b) are negligible compared to the bounce components. In the frequency range of the unsprung mass modes (10-15Hz) the bounce and roll components have similar magnitudes. These results are generally consistent with the measured roll/bounce characteristics of the road profile described above.

Figure 6.11 shows spectral densities of measured bounce and roll accelerations (units $(m/s^2)^2$/Hz and $(rad/s^2)^2$/Hz respectively) for the fully laden vehicle at 22m/s. Both spectral densities are plotted on the same axes. This is equivalent to comparing the average $(\ddot{z}_1+\ddot{z}_2)/2$ and difference $(\ddot{z}_1-\ddot{z}_2)/2$ of vertical accelerations $\ddot{z}_1$ and $\ddot{z}_2$ at points 1m each side of the longitudinal vehicle centreline.

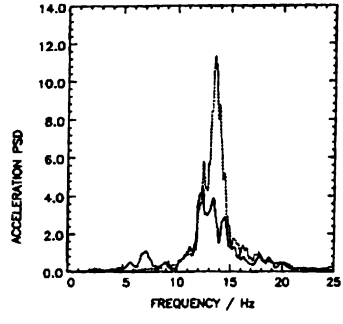
Figures 6.11a,b show that in the range 1-4Hz the sprung mass roll accelerations measured at the rear of the tractor and the rear of the trailer are small compared to the bounce accelerations. (The peak at 7Hz in these graphs is due to trailer bending, described later). This confirms that low frequency sprung mass roll motions are small. However, figure 6.11a shows that in the range 12-15Hz the roll acceleration at the rear of the tractor frame is very large, particularly when compared to the roll acceleration of the trailer, figure 6.11b. This is likely to be because the rear portion of the tractor frame has low mass and is torsionally flexible. The rear of the tractor frame appears to follow the roll motion of the drive axle closely, figure 6.11c.



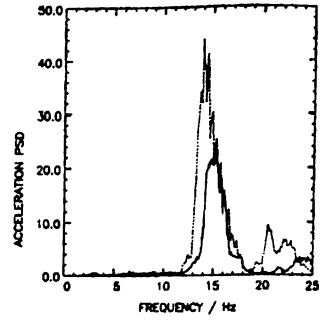
(a) Rear of tractor frame.



(b) Rear of trailer frame.



(c) Drive axle.



(d) Leading trailer axle.

Fig. 6.11 Bounce and roll acceleration spectral densities - fully laden, 22m/s. From [121].
———— bounce (units: $(m/s^2)^2/Hz$) - - - - - - roll (units: $rad/s^2)^2/Hz$)

The bounce and roll acceleration spectral densities of the leading trailer axle are shown in figure 6.11d. The peak at 14Hz corresponds to the tandem axles rolling in antiphase with respect to each other, and the peak at 15Hz corresponds to the axles bouncing in phase with respect to each other. In these two modes there is significant motion of the levelling beams. The peak at 22Hz corresponds to the axles rolling in phase with respect to each other, and the peak at 24Hz corresponds to the axles bouncing in phase with respect to each other, but in each of these modes there is little motion of the levelling beams.

These results suggest that for simulating the sprung mass modes (1-4Hz) of heavy lorries travelling under typical operating conditions, it is satisfactory to model the vehicle in only two dimensions. The simulation of the unsprung mass modes (10-15Hz) in two dimensions may or may not be satisfactory, depending on the characteristics of the suspension and the roll behaviour of the sprung masses.

For this particular vehicle the contribution of the unsprung mass modes to the dynamic tyre forces is generally small compared to that of the sprung mass modes. This is typical of many heavy vehicles [172, 229, 337, 443]. For these vehicles, two-dimensional models are likely to be adequate for simulating dynamic tyre forces.

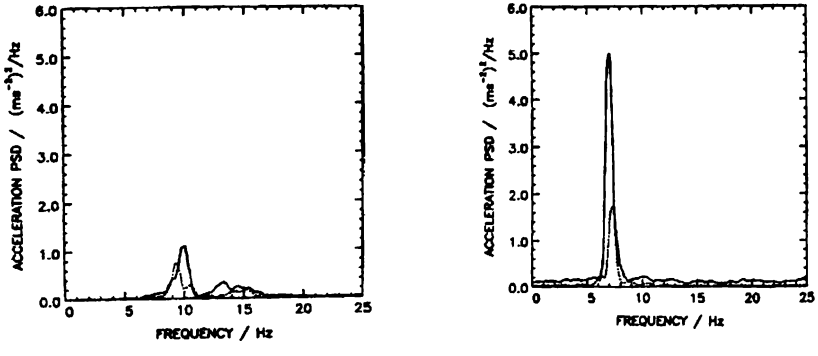
Some types of suspension do generate large tyre forces at high frequencies. The worst cases are tandem suspensions with lightly damped pitch modes (for example, walking beam suspensions [443]). Other suspensions, such as those with air springs, can generate low dynamic tyre forces with contributions of similar magnitudes from sprung and unsprung mass modes [337]. In these cases a three-dimensional model may be necessary for accurate simulation of dynamic tyre forces.

Wheel Non-uniformities

Several experimental studies have noted a contribution to dynamic tyre forces from wheel out of balance, radial run-out, or circumferential stiffness variations [94, 190, 229, 406, 443, 491]. The effects of wheel non-uniformities on dynamic tyre forces are usually only detected when the excitation from the road roughness is small [94, 190]. The wheel rotation frequency for the test speed of 22m/s is 7.1Hz. The tyre force spectral densities shown in figures 6.5a,b do not show any significant peaks at this frequency.

Trailer Bending.

Figure 6.12a shows the measured 'bending acceleration'[1] response of the half laden trailer at 13m/s and 22m/s. The graph indicates a lightly damped peak at 9 to 10Hz, with slightly greater response at the higher test speed. Figure 6.12b shows the corresponding responses for the fully laden trailer. The resonant frequency has decreased to 7Hz, as would be expected from the increase in trailer mass. The response at the higher test speed is significantly greater than at the lower speed. This is likely to be because wheel rotation frequency at a vehicle speed of 22m/s coincides with the 7Hz resonant frequency. In all four cases of speed and payload, examination of the corresponding tyre force spectral densities revealed very little response at the trailer bending resonant frequency. (see also Section 6.3.4).



(a) Half laden.

(b) Fully laden.

Fig. 6.12 Trailer bending acceleration. From [121]. ——— 22m/s, - - - - - - - - - 13m/s

[1] The 'bending' acceleration is the difference between the accelerations of the centre and the ends of the trailer.

The implication of these results is that it is satisfactory not to include frame bending modes when simulating dynamic tyre forces. This is in contrast to simulating ride accelerations, when frame bending can be very important [168, 169, 170, 188, 190, 243, 400][1]. These results may depend on the distribution of payload on the vehicle. During the vehicle tests the payload was concentrated at the two ends of the trailer (figure 6.7). Greater influence of frame bending modes on tyre forces may have been observed if the payload was distributed nearer the middle of the load bed.

6.4.2 Vehicle Model:

Vehicle Models

The non-linear vehicle vibration simulation method described in Section 5.5 was used to create three models of the test vehicle:

(i) A 6 degrees of freedom (DOF), two-dimensional trailer suspension model.

(ii) An 11 DOF, two-dimensional tractor and trailer model.

(iii) A 21 DOF, three-dimensional whole vehicle model, shown in figure 6.13.

Features of these models are:

(i) Non-linear leaf spring elements, the hysteresis characteristic being modelled according to the equation devised by Fancher *et al* [175], described in Section 4.3.

(ii) Anti-roll bars on the tractor axles (21 DOF model).

(iii) Viscous dampers on the tractor axles, with different rates in bump and rebound.

(iv) Tyres modelled as linear springs in parallel with light viscous dampers. The tyres can lose contact with the road [86, 87].

(v) Simple tyre contact patch averaging for the envelopment of short wavelength irregularities [86, 87].

(vi) Rigid tractor and trailer sprung masses.

Inertia properties of the sprung and unsprung masses were estimated using the measured static tyre forces and dimensions of the test vehicle. Tyre stiffness values were derived from manufacturer's force-deflection data. Parameter values for the three-dimensional model are given in [113].

Tractor Suspension Model

Tractor suspension properties were provided by the manufacturer. The leaf spring data consisted only of values for linear (large deflection) stiffness. The hysteresis characteristics were estimated from results of tests on springs of similar type [89, 175, 498, 500].

Four-Spring Trailer Suspension Model

The four-spring trailer suspension consisted of two mono-leaf springs attached to each axle. The springs had slipper mounts at each end, and longitudinal location of each axle was provided by two radius arms (figure 6.8).

The force-deflection characteristic of a single trailer leaf spring tested on a laboratory rig (with slipper end mounts, but without radius arms), was provided by the suspension manufacturer and used to determine suitable values for the parameters of the leaf spring model. The manufacturer's data and the fitted characteristic are shown in figure 6.14.

---

[1] Frame bending vibration is often an important consideration in heavy vehicle ride vibration, particularly if the frame bending frequency coincides with the wheel rotation frequency. Accurate analysis of this problem requires vehicle models with flexible frames and excitation due to tyre non-uniformities [243].

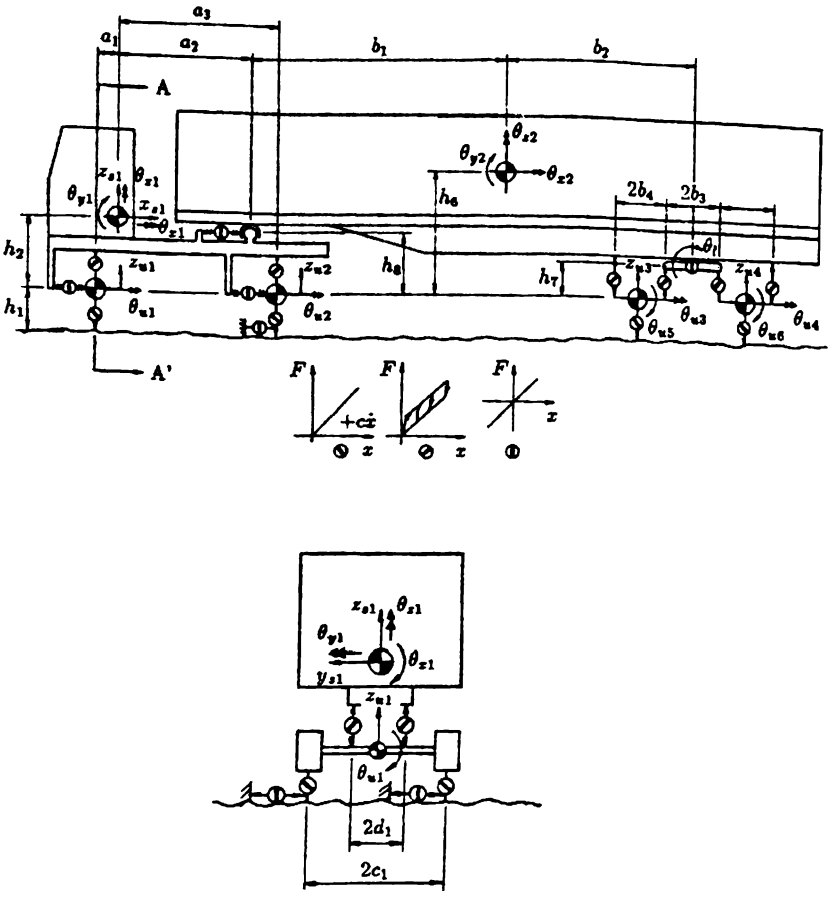


Fig. 6.13 21 DOF three-dimensional whole vehicle model. For clarity, the force elements necessary for simulating the trailer suspension radius arms are not shown. Double-headed arrows indicate angular motion or torque. From [121].

The effects of the forces in the radius arms on the behaviour of the suspension were modelled using the following assumptions:

(i) small displacements about the equilibrium position;

(ii) friction forces at the slipper ends are horizontal and normal forces are vertical.

(iii) pitch moments applied by the axle tubes and by rotational inertia of the axles are zero;

(iv) longitudinal acceleration of the unsprung masses is zero;

(v) the leaf springs are treated kinematically as a rigid beams.

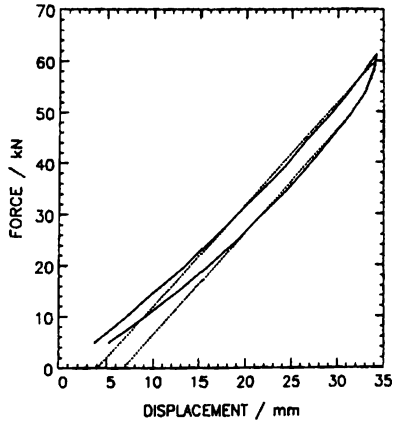


Fig. 6.14 Measured and simulated behaviour of a single trailer leaf spring. From [88].
_____ manufacturer's data - - - - - - fitted characteristic

The idealised geometry used for this analysis is shown in figure 6.15a. Each leaf spring is considered to consist of a non-linear vertical stiffness and a linear pitch ('wind-up') stiffness τ_y (at the point RQ in figure 6.15a). The vertical displacement of the axle is z and the pitch angle is θ_y.

The pitch angle across the two ends of the leaf spring is θ'_y, and is directly related to the pitch angle of the levelling beam θ_l by

$$\theta_l b = -2a\theta'_y. \tag{6.2}$$

The angular deflection across the pitch stiffness τ_y is therefore

$$\theta_w = \theta_y - \theta'_y, \tag{6.3}$$

where θ_w is the 'wind-up' angle. When there is no force in the radius arm θ_w is zero. The radius arm provides a kinematic constraint such that

$$\theta_y = -\frac{z\tan\beta}{c}. \tag{6.4}$$

Thus from (6.2) to (6.4)

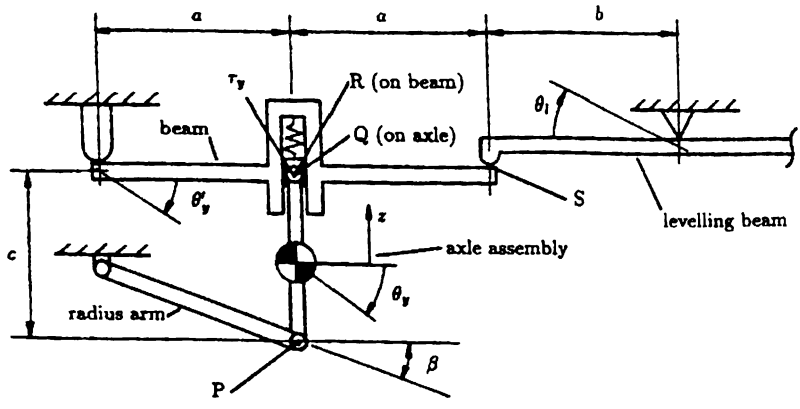
$$\theta_w = -\frac{z\tan\beta}{c} + \frac{\theta_l b}{2a}. \tag{6.5}$$

This equation gives the angular deflection θ_w across the pitch stiffness of the spring in terms of the displacement of the axle z and the pitch angle of the levelling beam θ_l, assuming that there is no horizontal movement of the spring due to sliding at the slipper ends of the spring.

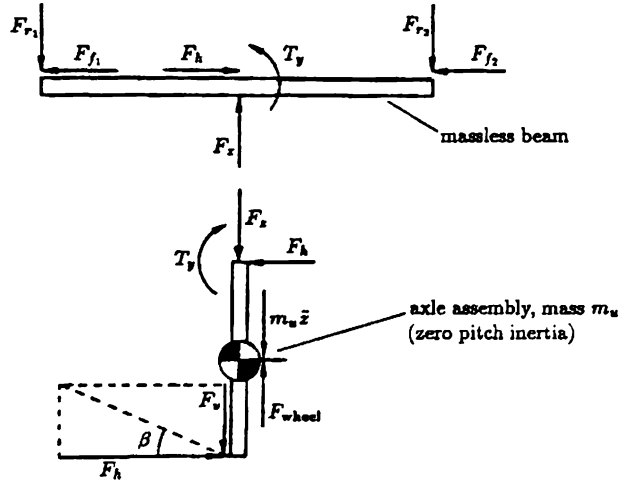
Now consider the forces acting on the spring and axle assembly (figure 6.15b). The torque T_y necessary to cause the wind-up θ_w, and the corresponding horizontal force F_h applied by the radius arm are given by

$$T_y = \theta_w \tau_y, \tag{6.6}$$

$$F_h = \frac{T_y}{c}. \tag{6.7}$$



(a) Trailer suspension geometry. (All displacements are relative to the trailer sprung mass).



(b) Forces acting on the idealised spring and axle.

Fig. 6.15 Trailer suspension model. From [121].

The horizontal component of force in the radius arm F_h is reacted by the horizontal friction forces F_{f1} and F_{f2} at the spring ends. There is therefore a limit to the force F_h that can be generated, determined by the coefficient of friction μ and normal forces F_{r1} and F_{r2} at the spring ends,

$$|F_h|_{\max} = (F_{r1} + F_{r2})\mu. \tag{6.8}$$

If the horizontal force F_h calculated from (6.8) is greater in magnitude than $|F_h|_{\max}$ then sliding at the slipper ends is assumed to occur, and F_h is limited to $|F_h|_{\max}$.

When sliding occurs, the vertical component of the arm force F_v and the torque T_y acting on the spring are given by

$$F_v = \frac{F_h}{\tan\beta}, \tag{6.9}$$

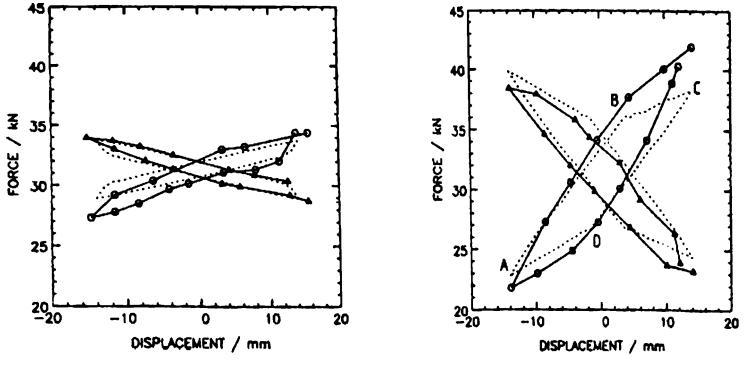
$$T_y = cF_h, \tag{6.10}$$

where F_h is limited according to (6.8).

The tandem suspension is modelled by treating each spring as a rigid massless beam with a non-linear leaf spring element at each end. The vertical component of the arm force F_v (from equation 6.9) is applied between the axle and chassis, along the vertical centreline of the axle. Horizontal suspension forces are not calculated in the vehicle simulations, therefore the two slipper friction forces and the equal and opposite horizontal component of radius arm force are applied as the pitch moment T_y (from equation 6.10), between the axle and chassis. The levelling beam pivots on a bush with linear pitch stiffness τ_l.

Published measurements from tests performed by TRRL on the test trailer [425] were used to determine values for the parameters of the tandem suspension model. In the TRRL tests, the laden trailer was supported at the fifth wheel by a crane, and weighpads were placed under each wheel to measure the tyre forces. The fifth wheel was raised and lowered through several cycles to give a trailer pitch angle amplitude of 0.8°. The force amplitude at the tyres was measured to be 10.3kN for the leading axle and 7.6kN for the trailing axle. The maximum tyre force occurred on each axle when the corresponding axle to trailer frame distance was a minimum. The measurements were repeated with PTFE inserts in the slipper end mountings, and the measured force amplitudes were 3.5kN and 2.8kN. The static inclination of the radius arms β was measured to be 12°.

The 6 DOF trailer suspension model was used to simulate the TRRL tests, by running the model slowly over a sinusoidal road profile with displacement amplitude 14mm and wavelength equal to twice the axle spacing. The values of the tandem suspension model parameters were chosen to give best agreement with the TRRL measurements [113]. Figure 6.16 compares the TRRL measurements with the results of the simulation.



(a) Test with low friction PTFE inserts in the slipper end mountings.

(b) Test with standard slipper ends (metal to metal sliding).

Fig. 6.16 Measured and simulated trailer tilt tests. The measurements are from tests performed by TRRL. The horizontal axis is the road profile displacement seen by the leading axle in the simulation. From [121]. —— o —— = measured leading axle tyre force; —— ▲ —— = measured trailing axle tyre force - - - - - - - - - simulated tyre forces.

The difference in force amplitudes for the leading and trailing axles measured in the tests could not be simulated. Use of unequal friction coefficients μ, unequal wind-up stiffnesses τ_y, and unequal radius arm inclinations β between the two axles in the simulation all gave equal force amplitudes.

The main features of the simulated tyre force response shown in figure 6.16b will now be described. Starting at the point of minimum tyre force on the leading axle (point A), the tyre force increases at a rate controlled mainly by the wind-up stiffnesses of both leading axle and trailing axle springs. At point B, sliding begins at the slipper ends of the now lesser-laden trailing axle spring. The leading axle tyre force then increases at a lower rate, because the trailing axle radius arm cannot exert any further force. On reversing the tyre displacements at point C, sliding at the ends of the trailing axle spring stops, and the tyre forces again change at a rate controlled by the wind-up stiffnesses of both springs. At point D, sliding begins at the ends of the leading axle spring.

The corresponding measured characteristic in figure 6.16b does not show the distinct changes in stiffness predicted by the simulation; this is likely to be because in practice the transition from sticking to sliding occurs gradually. Non-linearity in the wind-up stiffness τ_y, may also cause discrepancy between measurement and simulation.

Displacement of both axles in phase with each other was simulated, and the force-deflection behaviour was very similar to that of the single spring without radius arm (figure 6.14). This is because the high vertical stiffness allows only a relatively small vertical displacement to occur, which is insufficient to generate large forces in the radius arms. However, it is clear that the radius arms strongly affect the pitch behaviour of the suspension.

6.4.3 Vehicle Simulation Results

Three-Dimensional Model

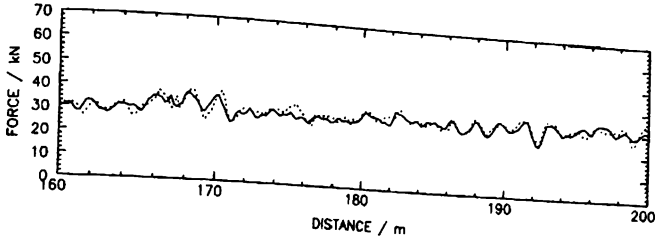
Response time histories for the 21 DOF three-dimensional model were calculated by numerical integration, using the measured test lane profile as the input.

Figure 6.17 shows measured and simulated tyre force histories for the nearside wheels of the fully laden vehicle travelling at 22m/s. In this figure, the horizontal axes show the position of each axle along the test section. Slight variations in test vehicle speed mean that the measured and simulated force histories are not always exactly synchronised: the maximum discrepancy in longitudinal position apparent from these graphs is about ±0.5m.

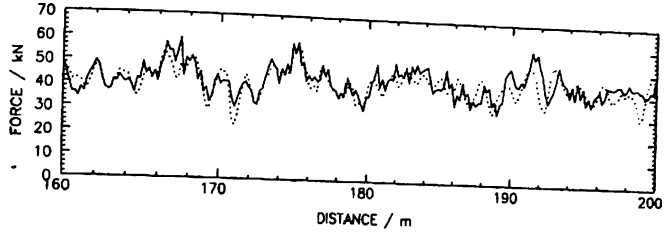
Figures 6.18 compares measured and simulated response spectral densities for the fully laden vehicle at 22m/s. Figures 6.18a-d correspond to the tyre forces in figure 6.17. Figure 6.18e is the vertical acceleration of the leading trailer axle, and figure 6.18f is the pitch acceleration of the tractor sprung mass. Overall the agreement between measurement and simulation is very good.

The tyre force spectral densities show some small discrepancies in the region of the sprung mass modes (1-4Hz), although the frequencies agree quite closely (figures 6.18a-d). In the region of the unsprung mass modes (10-15Hz) the steer and drive axle tyre forces and the leading trailer axle bounce acceleration agree quite closely (figures 6.18a,b,e), but the agreement is not so good for the trailer axle tyre forces (figures 6.18c,d). These results suggest that further refinement of the trailer suspension model is needed to simulate its complex behaviour accurately. Comparison of measured and simulated responses for other conditions of speed and payload showed similar agreement [113].

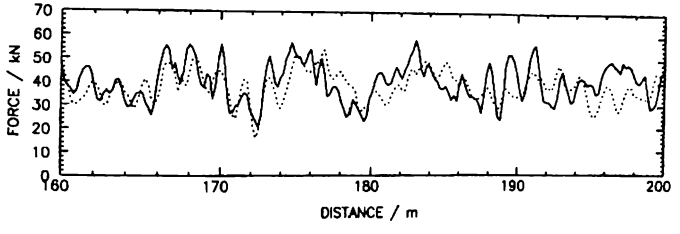
Some of the low frequency discrepancies may be partly due to the assumption of rigid sprung masses. For example, in figure 6.18f the measured tractor pitch response shows a small contribution from trailer bending at 7Hz (see also figure 6.12). The measured sprung mass 'whole body' motions (roll, bounce, pitch) may be inaccurate because the accelerometer data reduction cannot distinguish exactly between 'whole body' motion and flexible frame motion, as described in [87, 88]. The tractor sprung mass was treated as one rigid mass. In practice the cab and engine are flexibly mounted to the chassis, and have modes of vibration in the frequency range of interest.



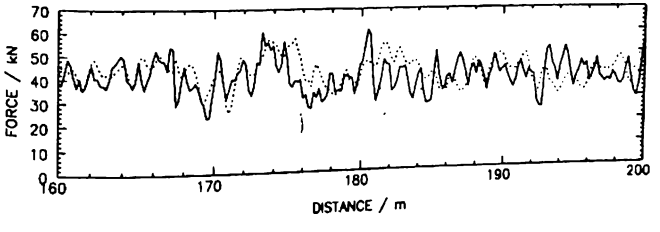
(a) Steer axle.



(b) Drive axle.

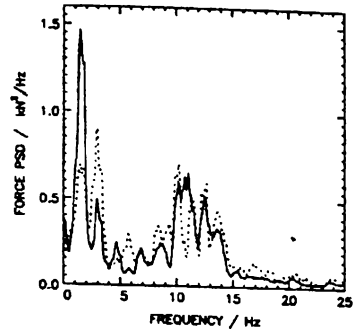


(c) Leading trailer axle.

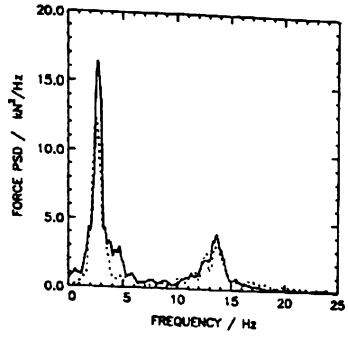


(d) Trailing trailer axle.

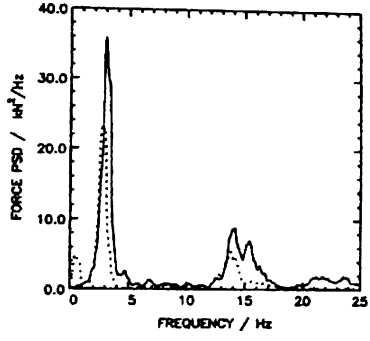
Fig. 6.17 Measured and simulated nearside (ns) tyre force histories - fully laden, 22m/s. From [121].
———— = measured; - - - - - - - = simulated



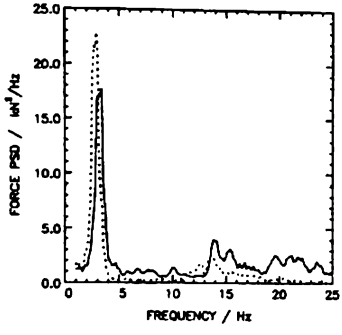
(a) Steer axle ns tyre force.



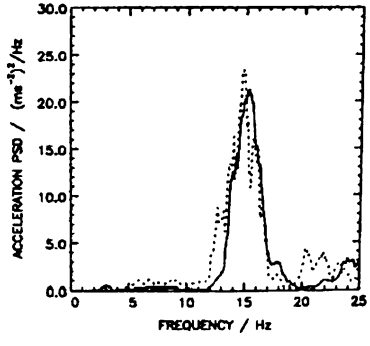
(b) Drive axle ns tyre force.



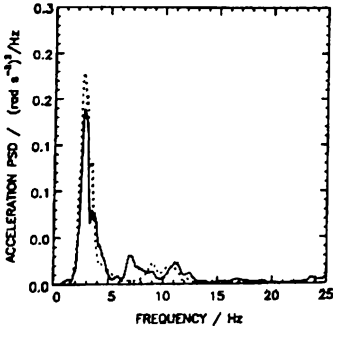
(c) Leading trailer axle ns tyre force.



(d) Trailing trailer axle ns tyre force.

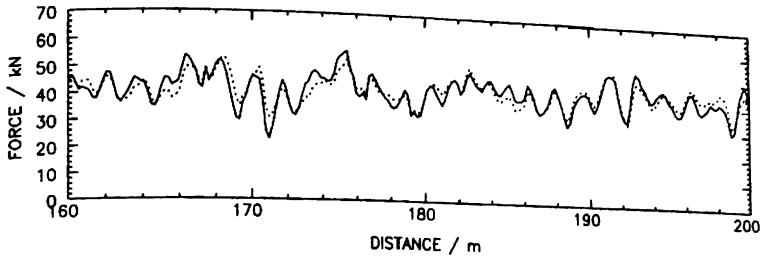


(e) Leading trailer axle bounce acceleration.

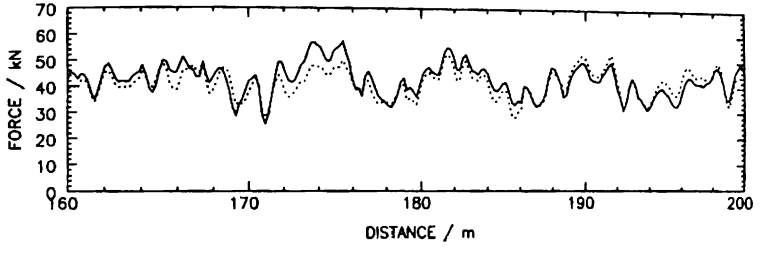


(f) Tractor sprung mass pitch acceleration.

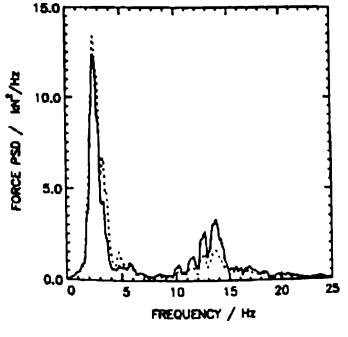
Fig. 6.18 Measured and simulated spectral densities - fully laden, 22m/s. From [121].
———— measured - - - - - - simulated



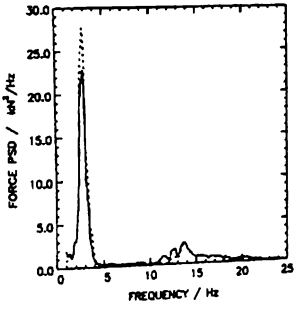
(a) Drive axle ns tyre force history.



(b) Trailing trailer axle ns tyre force history.



(c) Drive axle ns tyre force spectral density.



(d) Trailing trailer axle ns tyre force spectral density.

Fig. 6.19 Tyre force responses from 21 DOF and 11 DOF models - fully laden, 22m/s. From [121].

——— 21 DOF three-dimensional model.

- - - - - - 11 DOF two-dimensional model.

An additional source of error may be the tractor suspension parameters, which were derived entirely from the manufacturer's data and published measurements on similar components. Ideally the suspension properties would be determined from 'in-situ' tests [498, 500]. The simple bilinear characteristic used for the damper simulation is also likely to be inaccurate (see Section 4.4).

Experimental error and data processing may contribute to some of the discrepancy between measurement and simulation. It is estimated that the vehicle speed varied by up to ±5% during each test run. The error in the tyre forces measured by the lorry instrumentation was estimated to be 1.5% RMS [113].

It is difficult to determine how each of the possible sources of error contributes to the overall discrepancy. However, none of the experimental or numerical errors are thought to be excessive, and therefore the results of this study indicate the likely agreement that can be obtained when using a non-linear, rigid body vehicle model with accurate road profile input and good estimates of the vehicle properties. Overall, the agreement is considerably better than that achieved in previous heavy vehicle simulation validation studies [86, 88, 229, 243, 400, 406, 478, 491].

Comparison of Two and Three-Dimensional Models

Response time histories for the 11 DOF model were calculated using the nearside wheel track of the measured lane profile as input. Figure 6.19 compares nearside tyre force histories and spectral densities of the 21DOF and 11 DOF models (fully laden, 22m/s). Similar results were obtained for the offside wheel track.

Agreement between the two models is good in the region of the sprung mass modes. At this speed, sprung mass roll modes are not excited significantly (Section 6.4.1), and therefore the two models are expected to give similar results. (The two models give identical results when the 21 DOF model has a symmetrical road profile input).

There is significant difference between the tyre force responses of the two models in the region of the unsprung mass modes (above 10Hz). This is because the unsprung mass bounce and roll modes are excited by the road profile and they do not have similar frequencies and damping.

In summary, a two-dimensional model may be satisfactory for predicting the tyre forces of a heavy vehicle if:

(i) the vehicle speed is high enough to prevent excitation of sprung mass roll modes, and

(ii) the unsprung mass modes have similar frequencies and damping in bounce and roll, or the contribution of unsprung mass modes to the tyre forces is small.

The benefits of using a two-dimensional model are significantly simpler model creation and lower computation time. The three-dimensional model described here required approximately three times more CPU time, than the two-dimensional model.

6.5 CONCLUSIONS

(i) A three–dimensional simulation of a rigid commercial vehicle operating in a harsh vibrating environment was performed. It was necessary to consider carefully the short wavelength road roughness and the filtering of this roughness by the vehicle tyres. Also important were the major sources of vehicle nonlinearity including the departure of wheels from the road surface, bump stop contact, bogie pitch friction and leaf spring hysteresis. The agreement between experiment and simulation was good.

(ii) Tests were performed on a leaf-sprung articulated vehicle. Analysis of the measured tyre forces and road profile indicated that under normal operating conditions sprung mass roll motions do not contribute significantly to tyre forces. The contributions of unsprung mass modes and wheel non-uniformities to the tyre forces were also small.

(iii) A trailer frame bending mode at 7-10Hz did not significantly influence the dynamic tyre forces. Torsional frame resonance was not apparent, but torsional flexibility of the tractor frame and fifth wheel was thought to influence the roll response of the rear of the tractor frame and the drive axle.

(iv) The main sources of error in the simulation were thought to be the trailer suspension model properties and the assumption of rigid sprung masses.

(v) The tyre force responses of an 11 DOF two-dimensional model were compared with those of the three-dimensional model. The results suggest that the resonant frequencies and damping of the unsprung mass roll modes could be significantly different from those of the bounce modes. It may therefore be necessary to use a three-dimensional model when the unsprung mass roll modes contribute significantly to dynamic tyre forces.

(vi) A two-dimensional model (pitch–plane) should be satisfactory for predicting the tyre forces of typical leaf-sprung articulated vehicles with well damped suspension modes, operating under typical conditions of speed and road roughness.

6.6 SUMMARY OF VEHICLE MODELLING GUIDE-LINES

As a consequence of the case studies presented in this chapter, it can be seen that dynamic tyre forces can be predicted quite accurately for highway conditions using relatively simple vehicle models, by observing the following modelling guide–lines:

(i) The road profile input must be known accurately. For validation purposes it should preferably be obtained from measurements on the test section.

(ii) The nonlinear characteristics of the suspensions must be modelled accurately.

(iii) The payload distribution must be modelled accurately.

(iv) The models should have the correct arrangement and longitudinal spacing of wheels along the vehicle, so that wheel–base filtering effects are included correctly.

(v) The sprung masses can be assumed rigid, and frame flexibility ignored.

(vi) Pitch–plane models are usually sufficiently accurate, and roll freedom can often be ignored.

(vii) The effects of tyre non–uniformities can generally be neglected.

(viii) The effects of tyre envelopment of short wavelength road surface roughness can be neglected for normal highway speeds. For simulations of low speed travel over rough roads, tyre envelopment can be approximated by smoothing the profile with a 'moving average' equivalent to the tyre contact length.

7
DYNAMIC TYRE FORCES

7.1 SUMMARY

Methods for measuring dynamic tyre forces are presented. The most important features of dynamic tyre forces are then reviewed. These include their amplitude statistics; frequency content; and the effects of nonlinearities, wheelbase filtering, cross-coupling between suspensions, payload distribution, structural vibration, roll motion, tyre non-uniformities and 'spatial repeatability'. Finally the effects of tyres and suspensions on dynamic tyre forces are discussed.

7.2 INTRODUCTION

Dynamic tyre forces are thought to be a cause of increased damage to roads caused by heavy vehicles. For many years, research into 'vehicle-highway interaction' involved measuring or simulating the dynamic tyre forces generated by heavy vehicles, without reference to the response of the road (or bridge) surface. As a consequence, there is considerable literature concerning dynamic tyre forces generated by trucks.

In more recent times, the response of road and bridge surfaces to dynamic vehicle loads have been investigated. In order to understand the interactions between the vehicle and its guideway, and hence to devise improvements or assessment procedures for either system, it is useful to have a basic understanding of the principal features of dynamic tyre forces.

This chapter reviews some of the important literature concerned with measuring and simulating dynamic tyre forces, and attempts to draw-out some general conclusions about their features and the influence of suspension design.

7.3 MEASURING DYNAMIC TYRE FORCES

A variety of techniques can used for measuring the dynamic tyre forces generated by heavy vehicles. For testing programs involving a limited number of vehicles, it is convenient and practical to mount instrumentation on each vehicle. In some applications, however, it is desirable to measure dynamic tyre forces *without* instrumenting vehicles. For example, in studies of road damage, it may be necessary to test many vehicles – on a public highway, or in a 'road–friendliness' test for regulatory purposes. In these cases, road–based instrumentation can be used. Both vehicle–based and road–based instrumentation systems are discussed below.

7.3.1 Vehicle–Based Instrumentation Systems

Strain-gauged axles

Perhaps the simplest method for measuring dynamic wheel forces is to strain gauge the axle housing between the spring mounting and brake back plate, to measure bending moments due to vertical tyre forces [87, 115, 215, 295, 336, 337, 491, 505]. The bending strain is proportional to the shear

force carried by the axle, providing the lateral movement of the tyre contact centre of pressure is small compared with the distance between the static centre of pressure and the strain gauge installation. It is necessary to correct the measured shear force for the inertia (linear and angular) of all wheel and axle components 'outboard' of the load cells (axle housing, brakes, wheel and tyre) [88]. Mitchell and Gyenes [337] claimed measurement errors of 3-5% with their system.

Le Blanc *et al* [299] noted that this method becomes inaccurate in the presence of side forces or roll motion and they recommended that strain gauges be used to measure the *shear force* carried by the axle rather than the *bending moment*.

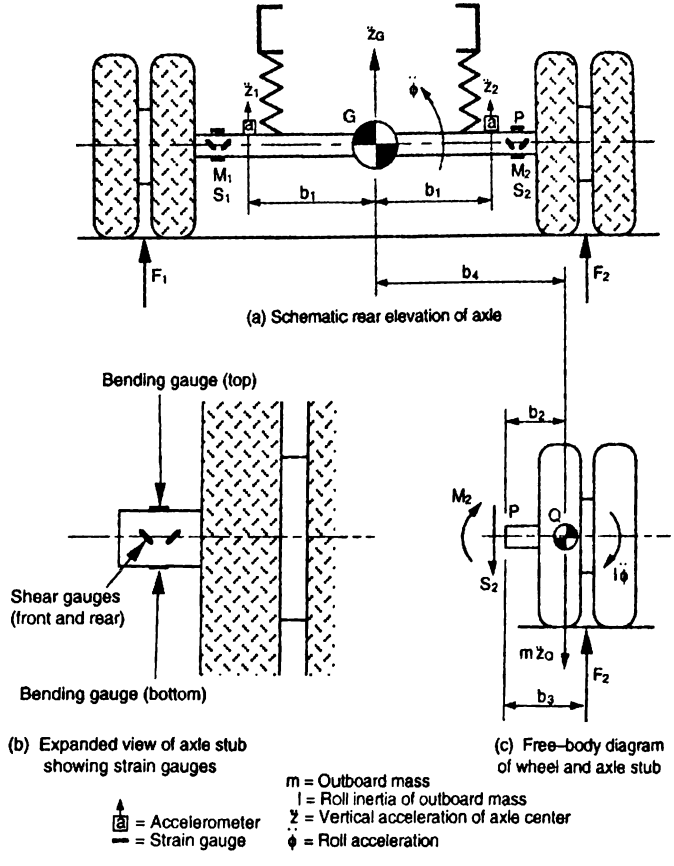


Fig. 7.1 Instrumentation layout for measuring dynamic tyre forces using strain-gauged axles.

The instrumentation system consists of two accelerometers that measure the vertical accelerations $\ddot{z}_1$ and $\ddot{z}_2$, of the axle as shown in figure 7.1a, and either of two different strain gauge arrangements (figure 7.1b):

(i) two strain gauges mounted on the *upper and lower surfaces* of the axle that measure bending strains and hence the bending moments M_1 and M_2, (two additional dummy gauges would normally be used for temperature compensation),

(ii) two pairs of strain gauges mounted on the *front and rear faces* of the axle, oriented at 45° to the vertical, that measure strains due to axle shear and hence shear forces S_1 and S_2.

The accelerations are used to correct the measured bending moments or shear forces for the 'inertia force' and couple generated by acceleration of the 'outboard mass' (the mass of wheel components outboard of the strain gauges).

In the frequency range of interest, the vertical acceleration of the centre of the axle $\ddot{z}_G$ and the roll acceleration of the axle $\ddot{\phi}$ can be determined from the calibrated outputs of the accelerometers, according to:

$$\ddot{z}_G = \frac{\ddot{z}_1 + \ddot{z}_2}{2} \tag{7.1}$$

$$\ddot{\phi} = \frac{\ddot{z}_2 - \ddot{z}_1}{2\,b_1}, \tag{7.2}$$

where $2b_1$ is the spacing of the accelerometers.

Assuming the roll angle ϕ is small, and using equations 7.1 and 7.2, the vertical acceleration of point Q (the centre of gravity of axle components outboard of P) is given by:

$$\begin{aligned} \ddot{z}_Q &= \ddot{z}_G + b_4\ddot{\phi} \\ &= \frac{1}{2}\left[\ddot{z}_2\left(1 + \frac{b_4}{b_1}\right) + \ddot{z}_1\left(1 - \frac{b_4}{b_1}\right)\right]. \end{aligned} \tag{7.3}$$

The vertical acceleration $\ddot{z}_Q$ of the outboard mass m results in an inertia force $-m\ddot{z}_Q$ and the rotational acceleration $\ddot{\phi}$ of the outboard components results in an inertia couple $-I\ddot{\phi}$, where I is the roll inertia about Q of the components outboard of P. These are shown on the free body diagram of the right hand wheel in figure 7.1c.

Consider dynamic vertical equilibrium of the forces, plus the inertia force and couple, acting on the right hand wheel and axle. Using Newton's second law (or d'Alembert's principle), it can be seen that the tyre force F_2 is related to the shear force S_2 (measured by the shear strain gauges) and acceleration by:

$$F_2 = S_2 + m\,\ddot{z}_Q, \tag{7.4}$$

where the acceleration $\ddot{z}_Q$ can be obtained from equation 7.3. A similar equation applies for the other dynamic tyre force F_1.

Alternatively, considering dynamic moment equilibrium about point P for the outboard mass, it can be seen that the tyre force F_2 is given by:

$$F_2 = \frac{1}{b_3}\left[M_2 + I\ddot{\phi} + b_2\,m\,\ddot{z}_Q\right], \tag{7.5}$$

where the acceleration terms can be obtained from equations 7.2 and 7.3, and M_2 is measured by the bending strain gauges.

The strain gauge bridges can be calibrated by driving the wheel onto a static weighing pad and then gradually jacking–up the vehicle to reduce the load on the wheel, while recording the outputs of the weighing pad and strain gauge bridge simultaneously.

The main advantage of measuring the bending moments M_1 and M_2 instead of the shear forces S_1 and S_2 is that the bending strains are larger than the shear strains (by a factor of approximately 2.5 [299]) and therefore the measurements are less prone to noise. The main disadvantage of using bending gauges is that roll or side–slip motion can cause errors due to side forces or variation of the moment arm b_3. Furthermore, the outboard mass m can be measured or estimated quite easily, but the roll moment of inertia I cannot. For these reasons, Le Blanc et al [299] recommended the shear force method defined by equation 7.4.

Tyre Pressure Measurements

Attempts to measure dynamic forces by monitoring tyre pressure variations [215, 380, 491] have not been successful due to the nonlinear, frequency-dependent relationship between tyre force and pressure change[1].

Several systems based on the measurement of tyre deflections have been developed. These include (i) measurement of vertical deflections using an optical sensor mounted on the axle [3, 83, 155], or a potentiometer mounted in the wheel rim of a tubeless tyre, joined to the inner liner of the tyre by a cable [479][2] and (ii) measurement of the lateral deflections of the side wall by a mechanical or electrical pick up [479]. These methods can give erroneous results when the tyre is rolling with side-slip. Both methods use the assumption that the vertical stiffness of the tyre is independent of rolling velocity. This assumption is not correct [479], and in practice, this means that the measurement system must be calibrated in the laboratory with the tyre on a 'rolling road', for a range of speeds.

Vehicle Body Accelerations

Hahn [213, 215] determined the wheel forces generated by a 2-axle bus, by measuring the accelerations of the sprung and unsprung masses and multiplying these by appropriate inertias. This method is suitable only for simple vehicles (with one or two axles). Furthermore, flexural vibration of the vehicle frame introduces significant errors [213][3].

Instrumented Hubs

A number of workers [172, 213, 214, 215, 229, 406, 442, 443, 491] have used strain gauged hubs (first developed by General Motors), described in detail by Whittemore *et al*, [491], and shown in figure 7.2. The transducers measure forces acting in the plane of the wheel, between the rim and hub, by monitoring two orthogonal force components whose axes rotate with the wheel. Vector addition of these components yields the resultant force in the wheel plane. A correction for the inertia of the wheel rim and tyre may be included [172, 229, 406, 491]. A number of significant technical difficulties exist in the calibration and data processing. These are described in detail in [172, 229, 491].

Comparison

A comparison of the accuracy of various tyre force measurement methods, as a function of frequency, is presented in figure 7.3, from [215]. It can be seen that the instrumented hub is considerably more accurate than the other methods, throughout the frequency range.

Sweatman [445] presented a brief review of the methods described above and concluded that instrumented hubs are most accurate, but also the most complex, and that strain gauging the axles is the only practical way to measure the tyre forces generated by all axles simultaneously.

---

[1] This method was first used in the AASHO road test [7, 181] when it was reported that a linear correlation was obtained between dynamic axle load measured on an electronic weigh scale, and tyre pressure change. Subsequent research has shown this to be incorrect.

[2] Hu [244] deduced the tyre forces developed by a vehicle on a road simulator (electro-hydraulic shaker rig) by measuring tyre deflection with a linear displacement transducer.

[3] Woodrooffe et al [506] proposed a suspension testing procedure using this method to measure the forces generated by suspensions mounted on a purpose-built trailer.

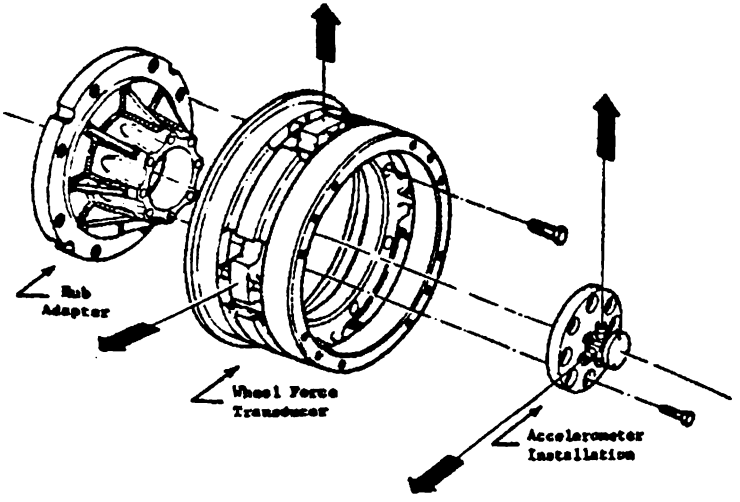


Fig. 7.2 GM wheel force transducer, from [491].

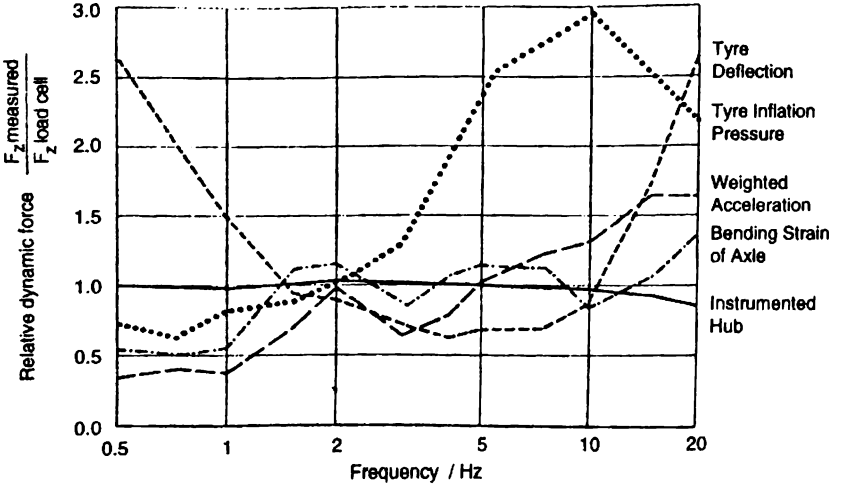


Fig. 7.3 The accuracy of various wheel force measurement systems as a function of frequency. From Hahn [215].

7.3.2 Road-Based Instrumentation Systems

Dynamic wheel loads have been measured at particular points on a road with weigh plates imbedded in the road surface [71, 302, 491], or with piezoelectric cables [178]. Such systems are generally of limited use because they only measure dynamic loads over very short lengths of road.

To collect statistically representative dynamic tyre force data, it is necessary, to use an array of sensors, spaced regularly along the road. The equipment must satisfy three main requirements:

(i) *Accuracy:* The individual sensors must measure the instantaneous dynamic tyre force accurately. This requires sensors with low noise, good resolution, high frequency response, linearity, repeatability and uniform sensitivity across each sensor. Low temperature sensitivity and low cost are also desirable.

(ii) *High frequency tyre forces:* The sensors must be spaced sufficiently closely to measure dynamic tyre forces at the highest frequency of interest. In order to avoid 'aliasing'[1], at least two sensors are needed per dynamic tyre force cycle. The limiting condition occurs at the 'wheel–hop' frequency, for vehicles travelling at low speeds. Assuming that the minimum speed of interest is 16 m/s (60 km/h), and that the maximum frequency of interest is 20 Hz, one dynamic tyre force cycle corresponds to a wavelength along the road of 16/20 = 0.8 m, and the sensor spacing should therefore be approximately 0.4 m.

(iii) *Low frequency tyre forces:* The instrumented length of road must be sufficiently long to measure a statistically representative number of dynamic tyre force cycles. Therefore the second limiting condition corresponds to high vehicle speeds and low frequency tyre forces. If the lowest frequency of the tyre forces is 2.0 Hz and the maximum vehicle speed is 25 m/s, then one dynamic force cycle corresponds to a wavelength of 12.5 m. In order to measure 8 complete dynamic force cycles, an instrumented length of 8 x 12.5 = 100 m would be needed[2].

Therefore the 'ideal' sensor array would have perhaps 250 sensors spaced at 0.4 m intervals, along at least 100m of road. The concept is shown schematically in figure 7.4.

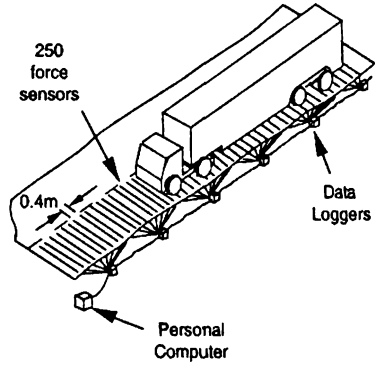


Fig. 7.4 The 'ideal' arrangement of road–mounted sensors for measuring dynamic tyre forces without on–vehicle instrumentation.

A novel 'wheel load measuring mat' was developed by Cole and Cebon for measuring dynamic tyre forces [116, 119]. The mat's configuration corresponds approximately to the 'ideal' arrangement of sensors described above. It consists of 1.5 m square polymer 'tiles', each 13 mm thick. Each tile

[1] Aliasing occurs when an analogue signal is 'digitised' (sampled) at a frequency that is too low: less than two samples per cycle. If aliasing occurs, it is not possible to resolve the frequency content correctly from the sampled data. See any book on digital signal processing for details, eg. [355].

[2] A statistical analysis of this problem is presented in Section 27.4, where it is shown that the length of road needed to predict the statistics of the dynamic tyre load accurately is in fact nearer 250 m.

contains three narrow, capacitative strip transducers, of length 1.5 m, and thickness 9 mm, mounted perpendicular to the wheel path at 0.4 m intervals. Any number of tiles can be laid end-to-end, and attached to the road.

A schematic cross section of an encapsulated capacitative strip sensor is shown in figure 7.5[1]. Tyre contact pressure applied to the top surface of the mat causes the top 'plate' of the aluminium extrusion to deflect and hence the air gap between the top plate and the inner copper electrode is reduced. This results in an increase in the capacitance of the device, which, with appropriate processing, can be related directly to the contact pressure change. In order to determine the instantaneous wheel load it is necessary to integrate the transducer output with respect to time for the duration of the tyre contact. Details of the sensor design theory and some sources of error are discussed in [119].

The mat is portable so that it can be used on different road surfaces to establish the influence of road roughness on dynamic tyre forces. For permanent weigh-in-motion sites, the bare sensors can be glued into slots cut across the surface of the road.

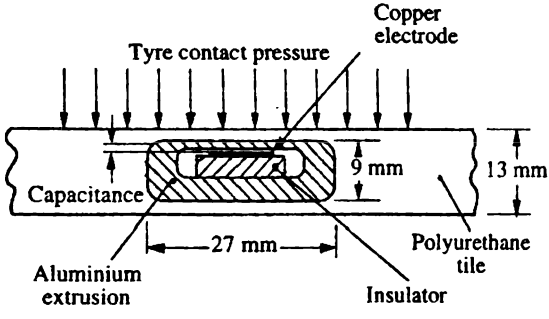


Fig. 7.5 Cross-section of a capacitative strip sensor cast into a polyurethane tile. From [116].

A load–measuring mat has been used in two major research projects. The first was performed during 1989 in collaboration with the University of Michigan, on the Navistar test track in Fort Wayne, Indiana, as part of a SHRP/IDEA project [101, 102]. This installation contained 32 tiles, with a total of 96 sensors. Six articulated vehicles were tested at speeds up to 80 km/h. The second study utilised a mat with 48 tiles and 144 sensors that was tested on the Transport Research Laboratory (TRL) test track in the UK, with 15 articulated vehicle combinations, and on the A34 trunk road near Oxford [129, 144]. In the latter tests, the dynamic wheel loads generated by approximately 2000 heavy vehicles travelling at speeds of 65–80 km/h were recorded during 13 hours of testing on the highway (see figure 7.6). Some results of the first project are presented in Chapter 8 and results of the second are presented in Chapter 19.

In the SHRP study [101, 102], the individual sensors were found to be accurate in measuring dynamic tyre forces to approximately 4% RMS; and the calibration factors were found to be independent of: (a) vehicle speed in the range 8–80 km/h, (b) mat surface temperature in the range 15-40 °C, (c) tyre contact width. (See also Chapter 8.)

[1] The sensors are manufactured by Golden River Traffic, Ltd. in Bicester, Oxfordshire, UK.

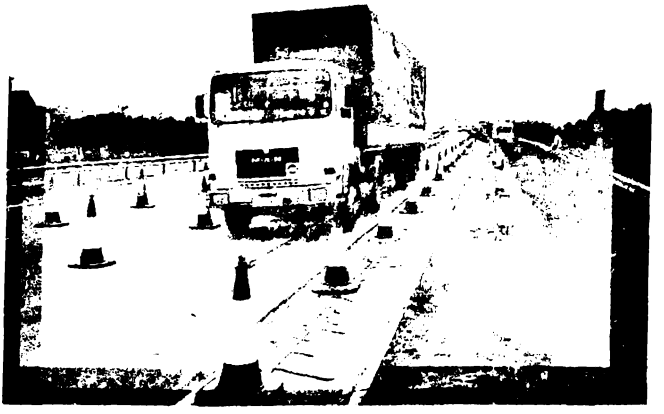


Fig. 7.6 Load-measuring mat with 144 capacitative strip sensors, installed on the A34 trunk road near Oxford in the UK.

7.4 PRINCIPAL FEATURES OF DYNAMIC TYRE FORCES

This section summarises some of the main research findings concerning the characteristics of dynamic tyre forces.

7.4.1 Probability Distribution

For *continuous* flexible or rigid pavements, the dynamic tyre forces generated by vehicles are generally observed to be broad-band, and close to Gaussian (normal probability distribution) [155, 214, 405, 443]. This is consistent with the roughness of typical asphalt road surfaces, which can normally be considered to be homogeneous, Gaussian and random. It is not expected to be the case for rigid pavements with periodic joints between slabs, but no experimental observations of this point been found in the literature.

7.4.2 Magnitudes

The magnitude of dynamic tyre forces depends on the road surface roughness and speed of the vehicle, its configuration, geometry and mass distribution, as well as the properties of the suspensions and tyres.

Under normal operating conditions, Dynamic Load Coefficients (DLC) of 0.1 – 0.3 are typical [172, 214, 244, 313, 337, 442, 443, 505] however, Sweatman [443] and Woodrooffe *et al* [505] measured values up to 0.4 for particularly poor tandem suspensions. At this level of dynamic loading, the axles spend a significant proportion of time out of contact with the road surface and peak loads are approximately twice the static loads. According to Hahn [214], measured peak dynamic loads usually exceed the RMS levels by a factor of about 3. This is consistent with a Gaussian probability distribution.

7.4.3 Frequencies

The vibration of heavy vehicles, and hence the dynamic wheel forces, fall into two distinct frequency ranges:

1.5-4 Hz: Sprung mass bounce, pitch and roll vibration modes,

8-15 Hz: Unsprung mass bounce and roll modes, 'load-sharing' suspension pitch modes.

At 100 km/h, these modes of vibration are excited by roughness irregularities with wavelengths of 6.9 m–18.5 m and 1.9 m–3.5 m respectively. Various experimental and theoretical studies [40, 91, 115, 172, 229, 232, 244, 337, 491, 505] have shown that the lower frequency sprung mass modes usually dominate the dynamic tyre forces on highways, except for vehicles which have axle group suspensions with poorly damped bogie pitching modes. This is illustrated in figure 7.7, from Ervin *et al* [172] which shows measured spectral densities of the dynamic tyre forces generated by three North American articulated vehicles, at speeds of 70 km/h (45 mph) and 90 km/h (55 mph). (This figure can be compared qualitatively with figures 5.3, 6.18 and 6.19). The only suspension displaying significant high frequency force content is the walking beam. This occurs because the pitching mode of vibration of the walking beam suspension has negligible damping, as observed for the simple model discussed in Chapter 5.

It is important to note that these suspensions are only found on a small proportion of heavy goods vehicles: approximately 15% of new tractors, and less than 2% of trailers in the USA [347]. Mitchell and Gyenes [337] noted, that the wheel-hop modes of some air suspensions are lightly damped and that this motion governs the peak transient load over an isolated irregularity, such as a pothole. This is corroborated by data presented by Görge [200].

7.4.4 Effects of Nonlinearities

The natural frequencies of heavy vehicles can be dependent on the amplitude of vibration and hence on the roughness of the road surface. This is particularly important for leaf–spring suspensions which are nonlinear because of interleaf friction [89, 175]. In general the frequencies decrease for rougher roads [405]. See Sayers and Gillespie [405] for a detailed discussion of this effect.

For high friction levels and smooth roads, interleaf friction can effectively 'lock' the suspension, so that the vehicle vibrates on its tyres with no relative suspension deflection [3, 405]. This can lead to lightly damped motion at frequencies of 3–4 Hz with little energy dissipated by the suspension, and consequently high dynamic tyre forces.

7.4.5 Wheelbase Filtering

The dominant frequencies of dynamic tyre forces can change significantly with vehicle speed due to the phenomenon known as 'wheel–base filtering' [118, 190, 229, 406]. This phenomenon can be explained as follows:

(i) All frequency (wavelength) components are present in the road surface roughness that excites vehicle vibration. However, geometric effects can result in relative attenuation of some frequency components and relative amplification of other components. (See Gillespie [190] for a detailed discussion.) These geometric effects depend on the spacings between axles and the speed of the vehicle. The dominant frequencies of excitation therefore change with vehicle speed.

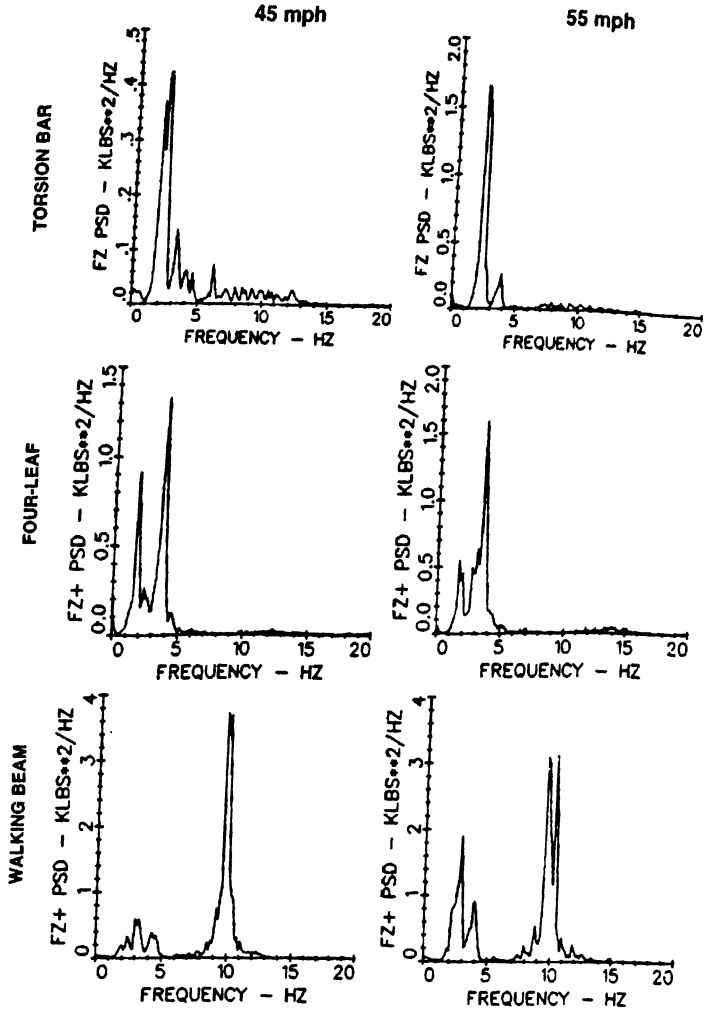


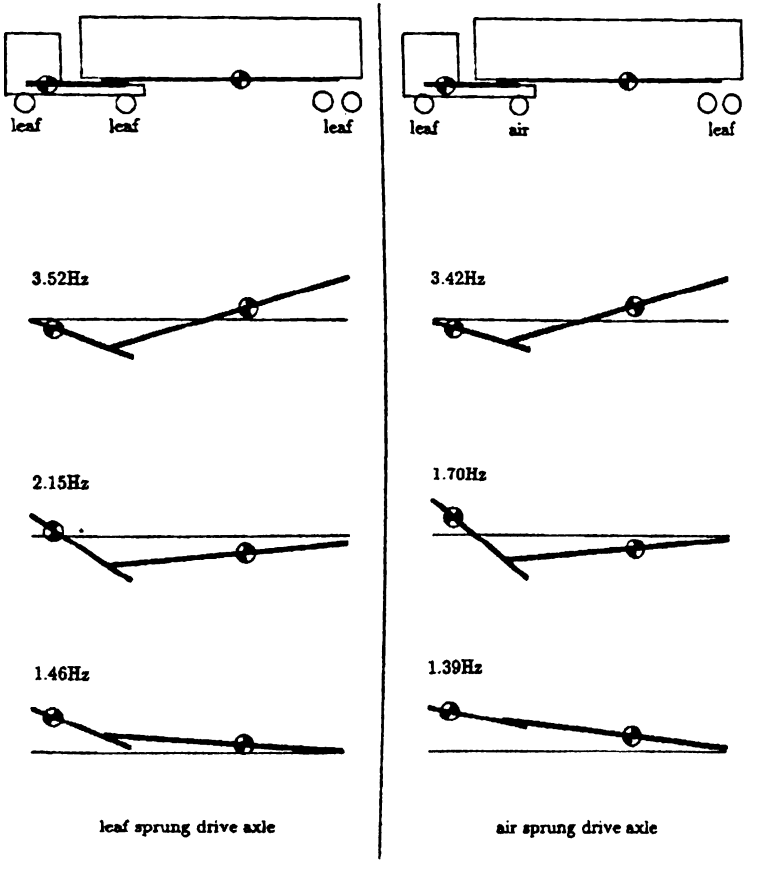
Fig. 7.7 Tyre force spectral densities generated by three tandem suspensions on an aged Portland Cement Concrete roadway. After Ervin *et al* [172].

(ii) Articulated vehicles have at least three important low frequency (sprung mass) modes of vibration; each of which involves some pitching and some bouncing motion of both the tractor and trailer [118, 244]; and each of which is significant in the generation of dynamic tyre forces. These modes generally occur at distinct frequencies in the 1.5Hz–4Hz range, and are shown for two mathematical articulated vehicle models in figure 7.8. These vehicle models are identical, except for the drive axle suspension. The one in figure 7.8a has a leaf spring suspension, while the one in figure 7.8b has an air suspension. Both vehicles have a gross mass of 32.5 tonnes, which is the current maximum for this vehicle configuration in

the UK. The eigenvalues and vectors were calculated using the procedure described in Chapter 5.4.3.

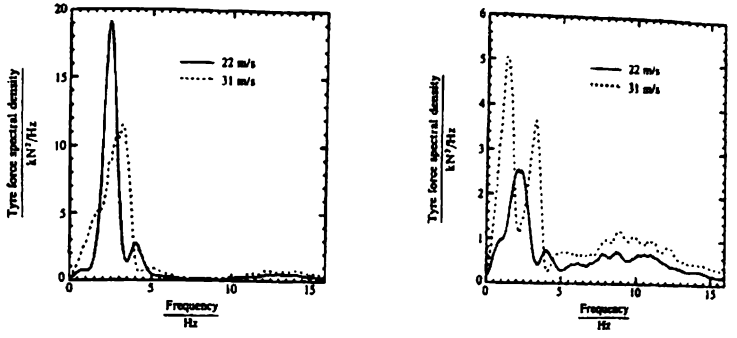
(iii) As a consequence of (i) and (ii), the natural mode (and hence resonant frequency) which is excited most by the road input, changes with speed. Therefore the dominant frequencies of the dynamic tyre forces change with speed (see figure 7.9)

(iv) A similar effect occurs for linked tandem suspensions with lightly damped pitching modes. In this case, the effect of wheelbase filtering is to amplify bogie pitching motion (and hence high frequency dynamic loads) at some speeds, and attenuate them at others.



(a) Leaf sprung drive axle, (b) Air sprung drive axle.

Fig. 7.8 Sprung mass natural frequencies and mode shapes of two articulated vehicles. From [118].



(a) Leaf sprung drive axle. (b) Air sprung drive axle.

Fig. 7.9 Simulated drive axle tyre force spectral densities for the vehicles shown in figure 36. From [118]. (a) Leaf sprung drive axle, (b) Air sprung drive axle.

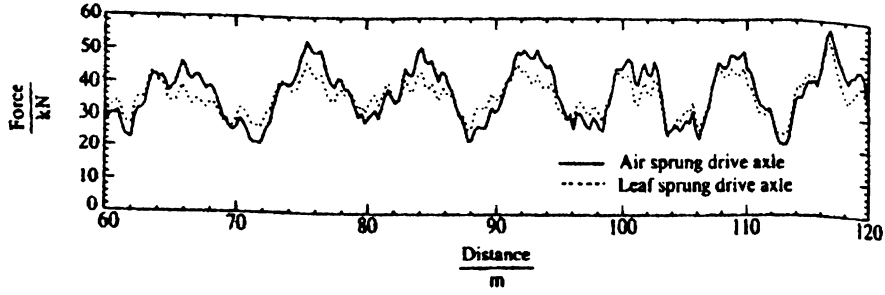
Figure 7.9a from [118] shows the simulated drive axle tyre force spectrum of the four-axle, leaf-sprung articulated vehicle, shown in figure 7.8a. When driven on a 'good' road at 22 m/s (80 km/h), it has a dominant resonant frequency of 2.4Hz. When the speed is increased to 31m/s (110 km/h), the main resonant frequency *increases* to 3.1Hz, and a smaller resonant peak appears in the tyre force spectrum at 1.6Hz. A similar effect can be seen in figure 7.9b for the vehicle model of figure 7.8b, (the same vehicle as figure 7.8a, but with the leaf-spring drive axle suspension replaced by an air suspension). In this case, at 22 m/s (80 km/h) there is one dominant peak in the tyre force spectrum at 2.1 Hz, and at 31 m/s (110 km/h) there are two peaks, one at 1.2 Hz and one at 3.2 Hz.

It is apparent, therefore, that there is no real concept of *the natural frequency* of the suspension of an articulated vehicle, despite the fact that one is often quoted.

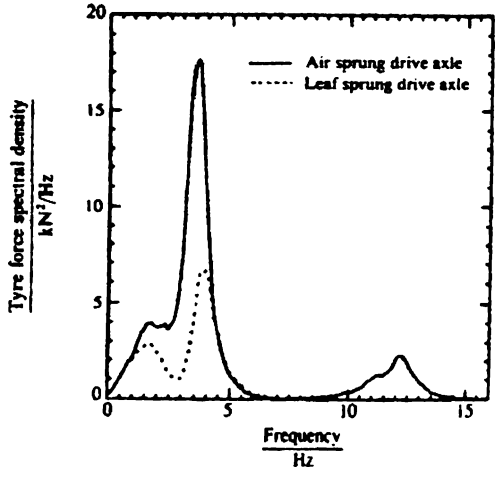
7.4.6 Cross-Coupling Between Suspensions

An important feature of the ride dynamics of articulated vehicles is that *all* of the suspensions and tyres are involved in the sprung mass modes of vibration [90, 118, 232, 244].

Figure 7.10a shows simulated tyre force histories generated by the rear *trailer* axle of the two different four-axle vehicle models shown in figure 7.8, travelling at 31m/s, from [118]. Figure 7.10b shows the corresponding spectral densities. The only difference between the two vehicle models is that one has a leaf spring suspension on the *tractor* drive axle (as per figure 7.8a), whereas the other has an air suspension (as per figure 7.8b). The graphs indicate that, for these particular operating conditions, fitment of the air suspension to the *tractor* drive axle increases the dynamic tyre forces generated by the *trailer* suspension. (The tyre forces generated by the leading axle of the trailer tandem are similarly affected.)



(a) Rear trailer tyre force history



(b) Rear trailer tyre force spectral density.

Fig. 7.10 Simulated trailer axle tyre forces at 31 m/s (110 km/h). From [118].

This important result shows that the tyre forces generated by an axle depend on the design of the whole vehicle, not solely on the suspension of that axle. The simulation illustrates that it is possible to fit a 'good' suspension to one axle and thereby increase the dynamic tyre forces at other axles. The consequences of this cross–coupling on the *road damage* done by the whole vehicle are discussed further in Chapter 28.

By implication, 'quarter–car' models of articulated vehicles are not accurate for prediction of the road damage done by a suspension. Furthermore it is necessary to account for the influence of each suspension system on the tyre forces generated by each other axle group. It is otherwise questionable whether an analysis of the tyre forces generated by a particular suspension gives a full picture of the influence of that suspension on the *road damage* done by the vehicle.

7.4.7 Influence of Payload Distribution

The important low frequency bouncing and pitching modes of vibration, described in the previous sections, depend on the moments of inertia of the tractor and trailer and therefore on the *distribution* of payload.

7.4.8 Effects of Structural Vibration

From the limited evidence available, it appears that structural vibration of the frames of heavy vehicles does not contribute significantly to dynamic tyre forces [87, 121]. Although articulated vehicles can be subject to considerable frame-bending vibration, the suspension systems are located near to the nodes of the first bending vibration mode [190, 243, 332, 386, 429]. As a result, motion imposed on the axles by frame bending is small relative to motion caused by major sprung and unsprung mass rigid body resonances. (See Section 6.4).

7.4.9 Influence of Roll Motion

Under normal highway operating conditions of roughness and speed, roll-plane excitation of heavy vehicles is small relative to pitch-plane excitation for frequencies below about 5 Hz [121, 157, 190]. Thus, sprung mass roll resonances, which typically occur below 3 Hz [87, 190] are not excited significantly and hence do not contribute to the dynamic tyre forces. (See Gillespie [190] and Cole *et al* [121] for a detailed discussion.) At higher frequencies, around 8–15 Hz, unsprung mass roll and frame torsional resonances can be excited by the road roughness, but for most vehicles these vibration modes only make a small contribution to the dynamic wheel loads [87, 113, 191]. (See case study 2 in Chapter 6.)

7.4.10 Tyre Non-uniformities

Non-uniformities in truck wheels, such as radial run-out, circumferential stiffness variations and mass out-of-balance can sometimes lead to measurable dynamic tyre force variation at the wheel rotation frequency (6-8 Hz) and higher harmonics [172, 191, 362, 406, 491], as shown in figure 7.11 from [192]. Wheel forces caused by non-uniformities are usually only significant for relatively smooth roads, when they can be of comparable magnitudes to the forces due to road roughness excitation.

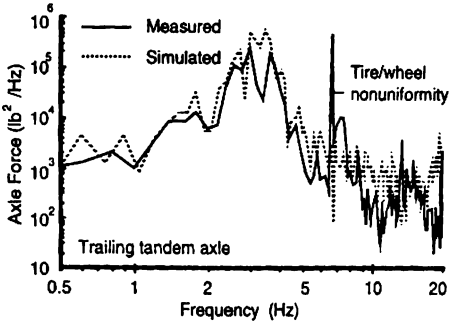


Fig. 7.11 Measured and simulated tyre force spectral densities, showing the effect of tyre/wheel nonuniformity. Testing speed = 82 km/h, high speed test track. From [192].

7.4.11 Spatial Repeatability

There is a significant body of evidence which shows that for any given testing speed, the wheel load time histories generated by a particular heavy vehicle are repeated closely on successive runs over a given stretch of road [3, 200, 208, 213, 214, 365, 506]. This may be expected since the vehicle encounters the same road profile, and hence excitation, on each test run. This phenomenon has been termed 'spatial repeatability'. Figure 7.12, from [3], shows an early observation of the effect. It shows the wheel loads measured on the axles of a tandem leaf-spring suspension, when driven over

the same section of test track three times. The loads are plotted as a function of distance and it can be seen that the same locations along the road incur the maximum loads on each run.

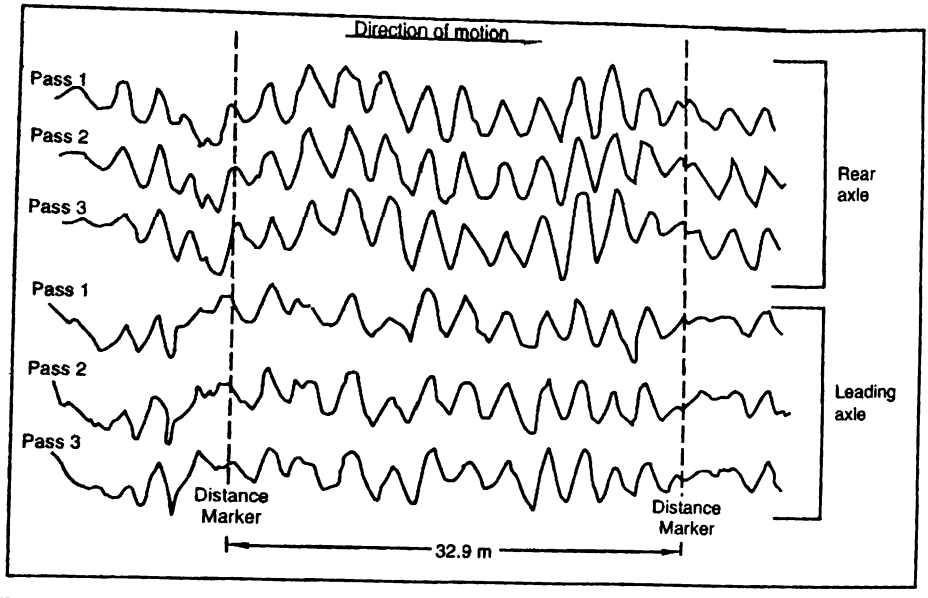


Fig. 7.12 Measured dynamic wheel loads on each axle of a leaf–sprung tandem, plotted as a function of distance, for three separate runs at 32 km/h. From [3].

7.5 INFLUENCE OF TYRES AND SUSPENSIONS ON DYNAMIC TYRE FORCES

In 1984, Magnusson *et al* [313] presented a review of literature concerned with dynamic axle loads. Largely on the basis of the theoretical publications, they concluded that soft suspension springs and tyres of low vertical stiffness are desirable for minimising dynamic loads.[1] Furthermore, they concluded that an optimal level of viscous damping usually exists, depending on the conditions, and that *any* dry (Coulomb) friction in the suspension usually increases dynamic tyre forces. Aurell [40] presented the results of experimental and theoretical parametric studies on suspension systems which agreed with Magnusson's results. Heath [232] performed a parametric study of dynamic wheel loads for 4 linearised vehicle models travelling on random road surfaces. He corroborated the view that soft suspensions and tyres are desirable, but noted that for very low tyre stiffnesses it is possible for the low frequency force components due to sprung mass motion, and hence the RMS force levels, to increase. Heath's results also indicated the existence of optimal suspension damping levels and he noted that it is usually better to have too much rather than too little suspension damping.

There have been a number of major experimental studies of dynamic forces over the years. For example: Whittemore *et al* [491] and Ervin *et al* [172] in the USA; Leonard *et al* [302], Addis *et al* [3], Mitchell, Gyenes and Simmons [337, 425], and Cole, Cebon *et al* [129, 144] in the UK;

Sweatman [442, 443] in Australia; Woodrooffe *et al* [505] in Canada; and a West German study reported by Görge [200] and Hahn [214].

Typical results showing the effects of speed and roughness on the dynamic load coefficients generated by various suspensions are shown in figure 7.13, after Sweatman [443]. (The suspensions are shown in figure 2.1.)

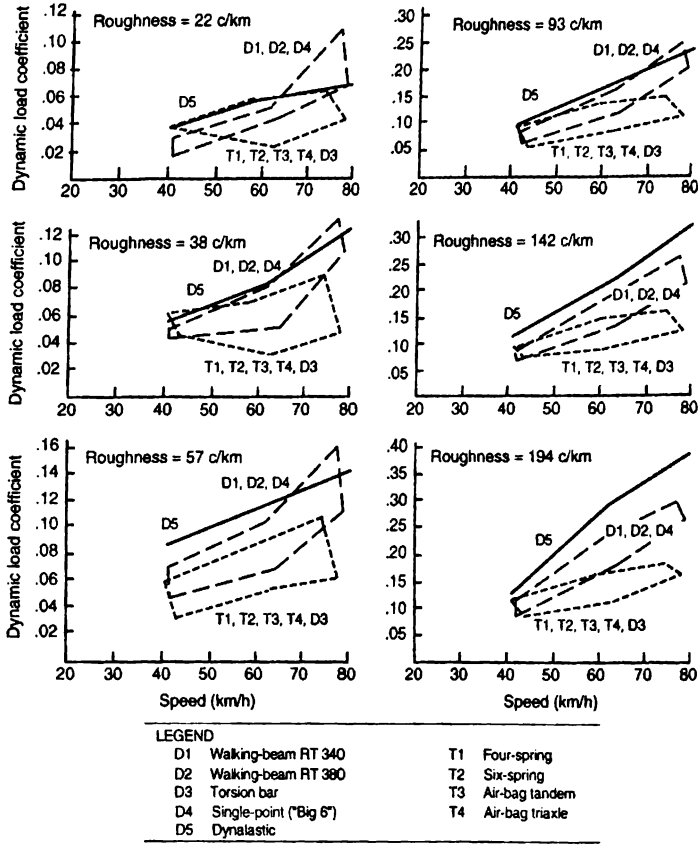


Fig. 7.13 Effects of speed and roughness (in units of 'counts per kilometre') on the dynamic load coefficients generated by various suspensions. After Sweatman [443].

In general, the researchers have drawn broadly similar conclusions about the effects of suspension and tyre types on dynamic tyre forces, and these conclusions corroborate the trends predicted in the theoretical studies described above.

(i) All studies found dynamic tyre forces to increase with speed (although not necessarily monotonically) and road roughness.

(ii) Sweatman [443] noted that reducing suspension stiffness generally reduces tyre forces.

(iii) Centrally-pivoted tandem axle suspensions such as 'walking beams' and 'single-point' suspensions were always found to generate the highest dynamic loads because of their lightly

damped pitching modes at around 8-10 Hz. Hahn [214] noted however, that these suspensions can be improved considerably by suitable use of hydraulic dampers.

(iv) 'Four-spring' tandem suspensions were generally found to generate smaller dynamic loads than walking beams. Torsion-bar and air suspensions generated the lowest loads.

(v) Hahn [214] noted that modern single-spring parabolic suspensions with good hydraulic damping were *"not significantly worse"* than stiff air suspensions. Conversely, Aurell [40] reported that air suspensions without hydraulic dampers could generate significantly higher dynamic loads than leaf spring suspensions.

(vi) Triaxle suspensions were found to generate smaller dynamic loads than tandem suspensions in several studies [214, 443, 505].

(vii) Woodrooffe *et al* [505] found that varying the axle spacing of an *air spring* tandem suspension had negligible effect on the dynamic loads, whereas the Dynamic Load Coefficient (DLC) generated by a *four-spring* tandem suspension varied considerably with axle spacing, depending on the speed and road roughness.

(viii) Mitchell and Gyenes [337] found that their test suspensions ranked in approximately the same order of DLC's, regardless of road roughness and speed. Other researchers, however, have not found this to be the case [214, 443, 504].

(ix) On smooth road surfaces, friction was found effectively to lock some leaf spring suspensions [3, 214]. This can lead to relatively large and lightly damped vibration of the vehicle mass on the tyre 'spring' stiffnesses.

(x) Most research has indicated that lower tyre pressures usually result in reduced wheel loads [155, 172, 491]. Sweatman [442, 443], however, reported that for some suspensions the opposite was true. According to Ervin *et al* [172] this anomaly could be because Sweatman did not correct his measured wheel forces for accelerations of the outboard mass, or due to "tuning" of one of the test vehicle's vibration modes to the particular road profile. A third possible explanation is the increase in the sprung mass contribution (to the wheel forces) simulated by Heath [232] and described above.

(xi) Wide-based 'super single' tyres were found by Hahn [214] to generate slightly lower dynamic forces than dual tyres and Addis *et al* [3] noted that radial ply tyres are slightly preferable to bias-ply tyres. Both of these conclusions are consistent with the observed reduction of wheel loads with lower stiffness tyres.[1]

---

[1] Note, however, that the net road contact area of wide single tires is significantly smaller than dual tires for the same load, and the contact pressures are consequently higher. As a result the overall road damaging potential of wide-single tires is thought to be considerably higher than dual pairs (see Section 17.3.4), despite the smaller dynamic tire force fluctuations.

8
INTRODUCTION TO WEIGH-IN-MOTION

8.1 SUMMARY

The errors generated by Weigh-in-Motion (WIM) systems are characterised, and their sources are identified. Calibration procedures for maximising the accuracy of WIM systems are discussed.

A theory is developed for the design of Multiple-Sensor Weigh-in-Motion (MS-WIM) systems to minimise the errors caused by the dynamic axle loads of heavy vehicles moving at highway speeds. The theory is verified using measurements from a wheel load measuring mat of total length 38 m, incorporating 96 capacitative strip WIM sensors. The mat was installed on the Navistar test track in the USA. A total of 460 test runs was performed on six different articulated heavy vehicles, for a range of speeds between 8 km/h and 80 km/h.

The experimental results agree closely with theoretical predictions of multiple-sensor WIM performance and it is found to be possible, using a 3-sensor array, to measure *static* axle loads of most suspensions with approximately 6% RMS error, or less, for typical highway conditions of speed and road surface roughness. It is concluded that a good design for multiple-sensor WIM systems is to use 3 sensors, spaced evenly along the road. The sensors should be spaced according to a simple formula which depends only on the average traffic speed and the number of sensors.

Automatic enforcement of axle-load regulations would require WIM systems with very high accuracy and reliability. The theory of MS–WIM is extended to the design of such systems. The number of sensors, their spacing, and signal analysis methods are discussed.

Much of this chapter is based on work previously published in [95, 101] and [438].

8.2 INTRODUCTION

This chapter on Weigh-in-Motion (WIM) is in the Part of the book on Vehicle Dynamics, because WIM is essentially a problem of measuring and processing *dynamic* tyre forces.

The function of most high speed WIM systems is to measure the *static* axle weights and/or gross vehicle weights of heavy vehicles at highway speeds. In order to do this, the sensors must accurately measure the wheel forces applied by passing vehicles. Section 8.3 discusses the most important performance requirements of WIM sensors, as well as calibration procedures, for maximising load estimation accuracy.

A single WIM sensor measures the instantaneous dynamic force generated by each measured axle. This force can be significantly different to the static axle load which would be measured on a conventional static weighbridge. One of the main reasons for the difference is the dynamic variation of the tyre forces due to vibration of the vehicle, as it is excited by road surface roughness: the dynamic tyre forces described in Chapter 7. The accuracy of a WIM system with one sensor is therefore limited fundamentally by the dynamics of the vehicles being measured. Typical RMS errors of single-sensor WIM systems are 12 to 29 % [195].

The advent of low cost WIM sensors provides the possibility of using two or more sensors along the road in order to compensate for the effects of dynamic forces in the determination of static axle loads. Section 8.4 describes the theory underpinning a procedure for designing multiple-sensor WIM arrays, and Section 8.5 describes experimental programme that was performed to validate the theory.

8.3 ERRORS AND CALIBRATION

8.3.1 The Objective of WIM

The aim of Weigh-in-Motion is to measure the *static* axle loads (or gross vehicle weights) of heavy vehicles travelling at highway speeds. The *static* axle load means the weight of an axle, as measured by an accurate static weigh-station, with the vehicle stationary and horizontal. *Static* axle loads are used by enforcement personnel to check trucks for overloading, and by highway authorities in calculating traffic loading data for highway design and transport statistics.

It is occasionally said that "it is really *dynamic* loads that damage roads – so it is the *dynamic* loads, as measured by WIM sensors, that are really of interest". This is not correct. At least two quantities are needed to characterise the dynamic loads generated by an axle: the *mean* and *standard deviation* of the probability distribution. Measuring these quantities for a given axle, with reasonable statistical accuracy, requires tens or even hundreds of sampled values of the dynamic wheel force, taken as the vehicle travels along the road (see Section 27.4). One load sample, taken on a single WIM sensor only provides a measure of the instantaneous wheel force at *that particular location* along the road. It gives no useful information about the statistics of dynamic load variation, and hence is of no benefit in assessing road damage due to dynamic loads.

8.3.2 Terminology

Consider a 'conceptual' WIM system with many sensors located along the road, as shown in the top of figure 8.1. For the purposes of the following discussion, it is assumed that each sensor measures the tyre force on one side of the vehicle only, *ie* half of the total axle load. (This is not a significant restriction, but simplifies the terminology.) As a vehicle travels over the array of sensors, at steady speed, it bounces due to excitation by road roughness. One of its tyres, say on the steering axle, generates total tyre force $p(t)$, (shown as the solid line on the graph in bottom of figure 8.1) which is the sum of the static tyre force P_0, and the dynamic tyre force $P(t)$.

The total force $p(t)$ is therefore given by:

$$p(t) = P_0 + P(t). \tag{8.1}$$

If the WIM sensors are perfectly accurate, as shown for the sensors in the left half of the lower figure, then the output S_i of sensor 'i' (in units of force) equals the instantaneous total tyre force applied to the sensor:

$$S_i = p(t_i), \tag{8.2}$$

where t_i is the time at which the axle passed over sensor i.

Suppose, that the sensors are not perfectly accurate (no *real* WIM sensor is), as per sensor 'j' in figure 8.1. If the sensor generates a *dynamic sensor error* e_j, and the sensor output is S_j, then:

$$S_j = p(t_j) + e_j = P_0 + P(t_j) + e_j. \tag{8.3}$$

Thus if S_j is to be considered as an estimate of P_0, there are two sources of error: the dynamic tyre force $P(t_j)$ and the sensor errors e_j.

Now the expected (mean) value of S_j, which is denoted as $E[S_j]$, is given by

$$\begin{aligned} E[S_j] &= E[P_0] + E[P(t_j)] + E[e_j] \\ &= P_0 + m_{P_j} + m_{e_j}, \end{aligned} \tag{8.4}$$

where m_{P_j} and m_{e_j} are the mean values of $P(t_j)$ and e_j respectively.

So S_j is an *unbiased* estimate of P_0, with

$$E[S_j] = P_0, \text{ if both } m_{P_j} = 0 \text{ and } m_{e_j} = 0. \tag{8.5}$$

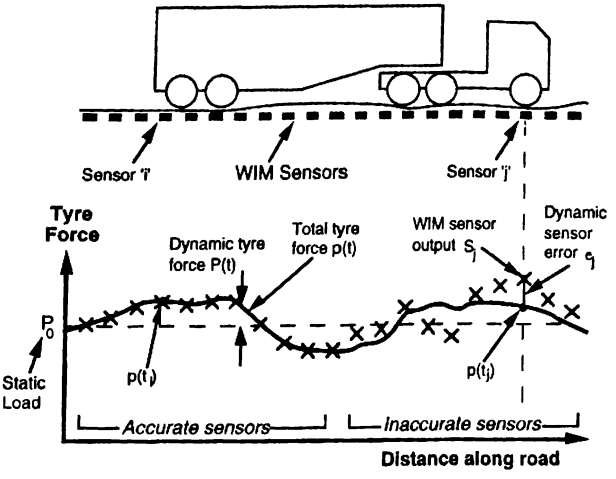


Fig. 8.1 WIM system terminology

The dynamic tyre force measured at sensor j, $P(t_j)$, has zero mean value, ($m_{P_j} = 0$) if:

(i) The *mean* value of the tyre force is equal to the static value, when averaged over a sufficiently long period of time, *ie* $E[p(t)] = P_0$, or $E[P(t)] = 0$. This requires that there is no 'static' load transfer on the vehicle - due to traction/braking forces, or inclination of the road surface from horizontal, or due to poor load equalisation in an axle-group suspension (see Section 17.3.3).

(ii) There is no 'spatial repeatability' (see Section 7.4.11). The effect of spatial repeatability is shown schematically in figure 8.2 (see also figure 7.12). Successive runs of similar vehicles, at similar speeds, generate similar 'patterns' of wheel forces along the road. This means that the tyre forces applied to *a particular location* along the road by many runs of a particular axle (*eg* a calibration axle) generally have an average value which is not the same as the time average of the force generated by that axle, *ie*

$$E\left[p(t_j)\right]\Big|_{\substack{\text{for many runs}\\ \text{of one axle at}\\ \text{sensor j}}} \neq E\left[p(t)\right]\Big|_{\substack{\text{for one axle}\\ \text{over all time}}}$$

Since spatial repeatability is inevitable (see Section 7.4.11 and Chapter 18), the output of a single WIM sensor is *always* a biased estimate of the static axle load.

The dynamic sensor error has zero mean value ($m_{e_j} = 0$) if

(i) The sensor errors are 'random' due to (say) electrical noise and are not correlated with the dynamic tyre forces. (The dynamic tyre forces are themselves biased due to spatial repeatability.)

(iii) The errors do not have systematic components caused by (say) inaccurate calibration, or sensitivity to vehicle speed or temperature.

The sources of sensor errors are discussed in Section 8.3.5.

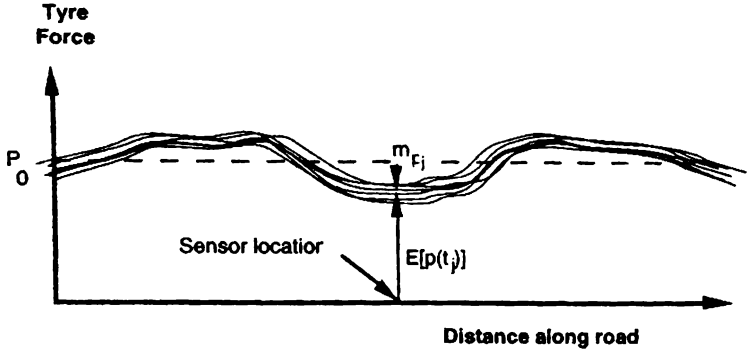


Fig. 8.2 Sketch of 'spatially repeatable' dynamic tyre forces, on successive runs of similar axles over a single WIM sensor.

8.3.3 Two Approaches to WIM

There are two different approaches to WIM:

(i) The most common approach in practice is to use *one* sensor measurement (or 'sample'), (*eg* S_j), as an estimate of P_0. This is clearly not very accurate, because of the two types of errors described above. Often, practitioners attempt to minimise the dynamic tyre force component $P(t_j)$, by making the road as smooth as possible for some distance in the lead-up to the WIM system, (*eg* [258]).

(ii) The Multiple-Sensor approach (MS-WIM) uses the outputs of several sensors, located at carefully chosen positions along the road, to estimate the static load level. For example, a MS-WIM system might use a simple averaging algorithm of the form:

$$\bar{P} = \frac{1}{n}\sum_{j=1}^{n} S_j, \tag{8.6}$$

where $\bar{P}$ is an estimate of P_0, and n is the number of sensors in the array. It could alternatively use a more sophisticated statistical analysis procedure. MS-WIM is the subject of Sections 8.3 and 8.4 of this chapter.

8.3.4 Calibration

Multiple-Sensor WIM Systems

In the case of MS-WIM, *calibration* of the sensors has the straightforward objective of minimising the dynamic sensor error e_j, so that each sensor measures the applied total tyre force $p(t_j)$ as accurately, and with as little bias, as possible. The MS-WIM algorithm (*eg* equation 8.6) then processes the individual total tyre force samples to calculate an estimate of the static load, *ie*

compensate for the dynamic component of the tyre force, P(t). This approach has the added benefit that any *random* components in the errors e_j are normally reduced by the MS-WIM algorithm.

Field calibration of WIM sensors can be achieved in three different ways. In each case, the objective is to obtain an *unbiased* calibration factor (*ie* $m_{e_j} = 0$) and to minimise the effects of dynamic tyre forces:

(i) If the sensors are capable of measuring the static loads of a stationary vehicle, (*eg* bending plate-type sensors which operate down to zero frequency) and their accuracy is not influenced by speed, then the simplest approach is a conventional static calibration - using known static loads applied by stationary weights.

(ii) If the sensors can measure slowly moving but not stationary loads, and their output is not dependent on the vehicle speed, (for example, the capacitance strip sensors described in Section 7.3.2), then a slowly moving vehicle with known static axle loads can be used. The calibration factor should be chosen so as to minimise the (mean square) error between the sensor output S_j and the known static axle load P_0. (See [102, 375]). In this case, it is important to ensure that the tyre force contains the smallest possible dynamic component ($P(t_j) \approx 0$). This can be achieved by using a vehicle with soft, well damped suspensions (*eg* air suspensions), and by using a dynamically 'quiet' axle for calibration - such as the steering axle of an articulated vehicle.

(iii) If calibration is to be done at highway speed, then it is possible to use an instrumented vehicle. The procedure requires development of an instrumentation system on the vehicle which is capable of accurately measuring dynamic tyre forces (see Section 7.3.1). It also requires a system by which the vehicle's instrumentation can be 'synchronised' with the WIM system.[1]

The instrumented vehicle is driven over the sensor array many times. The calibration factor is chosen to minimise the error e_j between the WIM sensor outputs S_j and the measured tyre forces $p(t_j)$, at the instant t_j that the instrumented axle passes over the sensor (*eg* see [102, 374]).

Single-sensor WIM

In the case of single-sensor WIM, the objective of calibration is generally to minimise the error between the sensor output S_j, and the static loads P_0 of many different vehicles. This process is problematical, because of the single-sensor bias problem, caused by spatial repeatability of dynamic tyre forces (see Section 8.3.2). This problem can best be illustrated by example.

Suppose that the sensors themselves are 'perfectly accurate' and unbiased, so that the dynamic measurement error e_j is zero. Furthermore, suppose that the static load P_{01} of a particular axle (*eg* the steering axle) of the calibration vehicle, travelling at a specified speed, is used to generate a calibration factor. Multiple calibration vehicle passes are normally used, as shown in figure 8.2; and on each pass, the dynamic tyre force histories follow a similar spatial pattern.

Assume that the total tyre force generated by the calibration axle is, on average, 10% lower than the static value (*ie* $m_j = 0.9\ P_{01}$), each time the calibration axle crosses the sensor.[2] The calibration factor of the sensor will therefore be set in error by a factor of 1/0.9 *ie* 11% high. This factor would then bias the WIM measurements of all other axles.

---

[1] This can be achieved by mounting a detector on the vehicle which generates a signal on the vehicle's instrumentation system when the instrumented axle crosses the WIM sensor eg [102, 352, 374]. Alternatively, a telemetry system could be used to transmit the output of the WIM system to the vehicle's data logger in real time (or vice versa).

[2] Typical dynamic tyre forces can have standard deviations which are 10% to 30% of the static values (DLCs of 0.1 to 0.3) - see Section 7.4.2. So an instantaneous deviation of 10% from static is quite small for any suspension system.

It is possible to smear-out this effect, and hence reduce the bias, by using several different axles (or the gross weights) of several different vehicles, and several different speeds for the calibration. But there is no scientific way to eliminate the bias error. Users of single-sensor WIM systems should therefore avoid using a specific axle of a particular class of vehicles for calibration, since most vehicles in the class will generate a similar pattern of wheel forces, and this will cause similar calibration errors to those described above (see the discussion of spatial repeatability of a vehicle fleet in Chapter 18).

The best approach for a single sensor is undoubtedly to generate an *unbiased* calibration factor which minimises the dynamic sensor error e_j. It is important to recognise that dynamic loads can be large, and they may well generate apparently systematic errors due to spatial repeatability: for example a particular axle on a particular class of vehicles may consistently measure heavy or light. Methods for determining unbiased calibration factors for single sensor systems are the same as those described in the previous section on calibration of MS-WIM.

8.3.5 Sources of WIM Error;

The probability density function (PDF) of the dynamic load error e is shown schematically in figure 8.3. There are many sources of dynamic sensor errors: some, like electrical noise, cause increased random error (*ie* they spread the PDF), without bias (shift in the mean level of the PDF). Others, like temperature dependence, cause bias (shift), without additional random components (spread). Some errors are due to the sensors, while others are due to the mounting arrangements. Some of the possible sources of error are summarised briefly in the next two sub-sections.

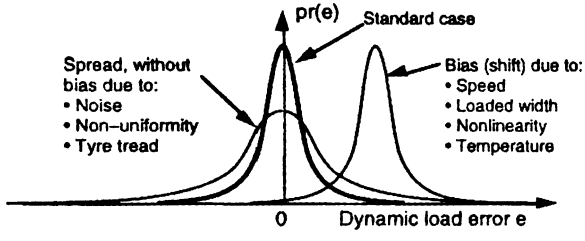


Fig. 8.3 Schematic diagram of the effects of various sensor errors on the probability density function pr(e).

Sensor Errors

The main sources of sensor error are:

(i) *Electrical noise:* appears as a *random* error.

(ii) *Non–uniformity of output*: Some sensors have varying sensitivity depending on the position of the load - for example, they may be less sensitive near the ends. Therefore the output depends on the position of the tyre across the traffic lane. This appears as a *random* error. (Clearly large errors will also result if the tyre partially misses the sensor.)

(iii) *Sensitivity to loaded area:* If the sensitivity depends on the loaded width or the length of the contact patch (*ie* the amount of tyre in contact with the sensor), then the measurement will depend on tyre/wheel type. For example dual tyres may generate a different sensor output to single or wide-single tyres, carrying the same load. This is a systematic *bias* error.

(iv) *Non–linearity:* If the sensor does not produce an output which is linear with the applied load, then the calibration factor will vary with load. This is a systematic *bias* error, which can be eliminated by applying a non-linear, load-dependent calibration factor.

(v) *Temperature sensitivity:* Sensor calibration and offset can vary significantly with temperature. This is a systematic *bias* error, which can be eliminated by applying a temperature dependent signal processing procedure.

(vi) *Sensitivity to duration and rate of loading:* If the sensor has an inadequate frequency response (≤ 100Hz), or the output is otherwise dependent on the duration of contact, it will display a systematic *bias* error, which is a function of vehicle speed. This can, in principle, be eliminated by applying a speed dependent calibration factor. However if the frequency response is very poor (≤ 20Hz), then dynamic tyre force variations will cause additional *random* errors which cannot be corrected.

(vii) *Tyre tread pattern:* Strip sensors, such as capacitance strips or piezoelectric cables are generally significantly narrower than length of a tyre contact patch. They are therefore sensitive to any variation in contact pressure along the contact patch (in the direction of vehicle motion). This is a particularly important problem for tyres with off-road tread patterns (see Section 8.5.3). The errors can be large and appear to be *random*.

Errors due to Mounting

Depending on the mounting details, aspects of the sensor mounting can affect the sensitivity, and cause errors.

(i) *Errors caused by mounting adhesive.* If the mounting adhesive (or potting compound) forms part of the load transmission path between the tyre contact area and the sensor, significant errors can occur:

  (a) if the stiffness of the adhesive changes with temperature, the sensor output will become temperature-dependent (*bias*);

  (b) if the adhesive is nonuniform in thickness or stiffness along the sensor, the sensor can become sensitive to the position of the load (*random*);

  (c) if the adhesive has a stiffness which is non-linear with load, a linear sensor can display non-linearity (*bias*).

  (d) if the adhesive or potting compound is viscoelastic, so that its response depends on the duration of contact, the system may display speed sensitivity (bias).

(ii) *Errors caused by flexibility of road/mounting:* Significant errors can occur if the road structure forms part of the load transmission path between the tyre and the sensor. This is particularly important for piezoelectric cable sensors, which can generate an output in response to axial stretching or longitudinal strain in the road (in the direction perpendicular to vehicle motion):

  (a) if the stiffness of the road structure changes with temperature (which can be a very large effect in flexible pavements [222]), the sensor output will become temperature-dependent (*bias*);

  (b) if the stiffness of the road structure changes with moisture level, the sensor output will vary with seasonal rainfall (bias). This can be a significant effect in light 'chip seal' road constructions used in Australia and New Zealand [368].

  (c) if the road structure is non–uniform in stiffness along the sensor, the system may become sensitive to the position of the load (*random*);

  (d) if the road structure has a stiffness which is non-linear with load, a linear sensor will display non-linearity (*bias*);

  (e) if the road is asphalt and therefore viscoelastic, its response will depend on the duration of contact, and the system will display speed sensitivity (*bias*).

(iii) *Flushness of mounting:* It is essential that the top of the sensor is mounted flush with the road surface. If it is (say) proud of the road surface by even a very small amount, then the tyre will have to deflect as it passes over the sensor. This will generate an additional contact pressure which will be the product of the stiffness of the tyre and its deflection (the height that the sensor is proud of the road surface). It will therefore depend on tyre construction and inflation pressure, and the deflection, which may vary across the road (*eg* due to surface rutting). These errors may appear to be *random* although there can also be some bias.

8.4 THEORY OF MULTIPLE-SENSOR WEIGH-IN-MOTION (MS-WIM)

On the assumption that the sensor errors can be reduced to satisfactory levels during the manufacture, installation and calibration of the WIM system, the most effective way to improve the accuracy is to eliminate errors caused by dynamic tyre forces, using the multiple-sensor approach. This is the subject of the remainder of this chapter.

The outputs of a several sensors in a Multiple-Sensor Weigh-in-Motion (MS-WIM) array might be processed in a variety of different ways to yield an estimate of the static loads. Some possibilities are described by Glover [194] who performed numerical simulations of the outputs of WIM arrays with 1, 2, 9, 19 and 81 sensors with a variety of spacing arrangements, including uniform, linear, geometric and logarithmic. Glover achieved good results for a 9-sensor, evenly spaced array, using a least squares procedure to correct the simulated forces for the dominant Fourier component.

In this chapter, *evenly spaced* WIM arrays are examined. It is assumed that the outputs of the individual sensors are simply averaged to yield an estimate of the static loads. The simple averaging method requires very few sensors and little computation to give comparable accuracy to more sophisticated 'curve fitting' methods [194, 195].

8.4.1 Sinusoidal Input

It is useful to begin the analysis by calculating the output of a multiple-sensor WIM array to a sinusoidal force p(t) defined by

$$p(t) = P_0 + P\sin(\omega t + \phi), \tag{8.7}$$

where P_0 is the static tyre force, P is the dynamic tyre force amplitude, ω is the angular frequency, ϕ is an arbitrary phase angle and t is time.

The force is considered to move at constant speed V over an array of n sensors which are evenly spaced, distance Δ apart as shown in figure 8.4. The sensors are assumed to be noiseless and perfectly accurate so that the output of each sensor is the instantaneous force applied to the sensor by p(t). The output of the array is taken to be the arithmetic mean of the individual sensor outputs, and is denoted $\bar{P}$. Assuming t = 0 when p(t) passes over the first sensor, the array output (average) is

$$\bar{P} = P_0 + \frac{P}{n}\sum_{j=0}^{n-1}\sin\left(\frac{j\omega\Delta}{V} + \phi\right). \tag{8.8}$$

It is convenient to define the non-dimensional WIM error ε by

$$\varepsilon = (\bar{P}-P_0)/P \tag{8.9}$$

and the non-dimensional sensor spacing δ by

$$\delta = \omega\Delta/2\pi V = \Delta/(V/f), \tag{8.10}$$

where f = cyclic frequency corresponding to ω. Then (8.8) becomes

$$\varepsilon(n,\delta,\phi) = \frac{1}{n}\sum_{j=0}^{n-1} \sin(j2\pi\delta + \phi). \tag{8.11}$$

Assuming that ϕ is a random variable with a uniform probability density function $g(\phi)$, defined by

$$g(\phi) = \begin{cases} \dfrac{1}{2\pi} & -\pi < \phi < \pi \\ 0 & \text{elsewhere,} \end{cases} \tag{8.12}$$

the expected mean square error can be found from (8.11) and (8.12) using standard expectation equations (see, for example, [355]) as follows :

$$E\left[\varepsilon(n,\delta)^2\right] = \int_{-\infty}^{\infty} \varepsilon(n,\delta,\phi)^2 g(\phi)d\phi = \int_{-\pi}^{\pi}\left[\frac{1}{n}\sum_{j=0}^{n-1}\sin(j2\pi\delta+\phi)\right]^2 \frac{1}{2\pi}d\phi, \tag{8.13}$$

where E[ ] is the expectation operator.

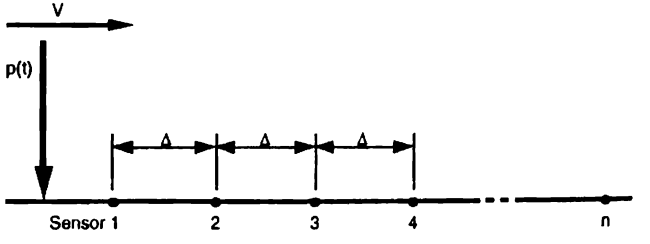


Fig. 8.4 Cross-section of an n-sensor WIM array, traversed by force p(t) at speed V. From [101].

With a little manipulation this can be shown to have the solution

$$E\left[\varepsilon(n,\delta)^2\right] = \frac{1}{2n} + \frac{1}{n^2}\sum_{k=1}^{n}(n-k)\cos(2\pi k\delta). \tag{8.14}$$

The Root Mean Square (RMS) error is then given by

$$\varepsilon_{RMS} = \sqrt{E\left[\varepsilon(n,\delta)^2\right]}.$$

It is useful to define the peak or 'envelope' error $\hat{\varepsilon}$ from the RMS error as follows:

$$\hat{\varepsilon}(n,\delta) = \pm\sqrt{2}\varepsilon_{RMS} = \pm\left[\frac{1}{n} + \frac{2}{n^2}\sum_{k=1}^{n}(n-k)\cos(2\pi k\delta)\right]^{1/2}. \tag{8.15}$$

Figure 8.5 shows a plot of equation 8.11 for n = 7, with 5 different phase angles $\phi = 2\pi/5, 4\pi/5, \ldots 2\pi$, plotted as dashed lines. Superimposed on the plot is the envelope error $\hat{\varepsilon}$ as per equation 8.15, plotted as the solid lines. It can be seen that the solid lines surround all of the dashed lines, and that $\hat{\varepsilon}$ is the largest error that can occur for any given value of δ. Thus an alternative interpretation of $\hat{\varepsilon}$ is the error corresponding to the 'worst-case' phase angle ϕ for an array with n sensors and non-dimensional spacing δ.

Figures 8.6 a-d show $\hat{\varepsilon}(n,\delta)$ for n = 2 to 5. Three observations are made:

(i) The error $\hat{\varepsilon}$ is unity for integer values of δ, which correspond to the sample points (sensors) being spaced an integer number of dynamic force cycles apart.

(ii) On each graph in figure 8.6, there are (n-1) zeros at values of $\delta = \delta_k$ corresponding to

$$\delta_k = k/n, \qquad k = 1, 2, 3...(n-1). \tag{8.16}$$

Thus the range of δ between the first and last zeros on each graph increases with n: $\delta_1 = 1/n$ to $\delta_{n-1} = (n-1)/n$. This is the region in which $\hat{\varepsilon}$ is consistently small.

(iii) The curves for $0 \le \delta < 1$ repeat for each integer value of δ and are symmetric about $\delta = 0.5, 1.5, 2.5$, *etc.* This can be verified by plotting equation 8.15 for $\delta > 1$ (see [102]). The repetition is a form of aliasing with a Nyquist spacing of $\delta = 0.5$. There is no apparent benefit in using $\delta > 1$ in a WIM array.

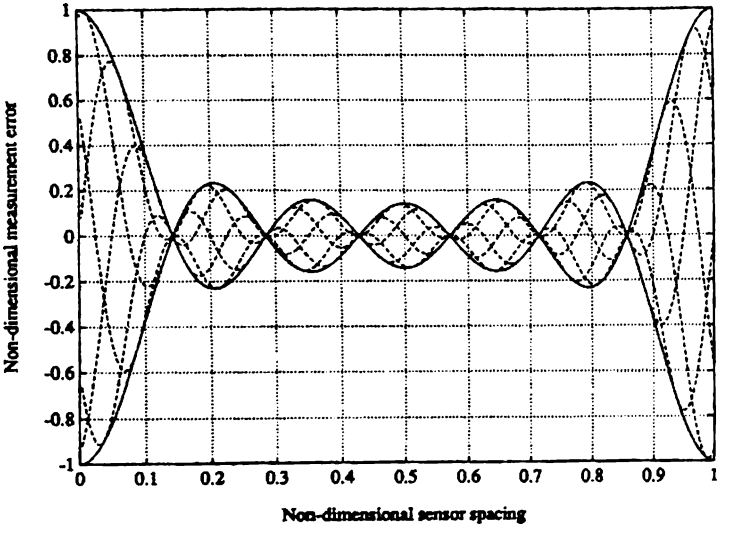


Fig. 8.5 Plot of equation 8.11 for n=7 with 5 different phase angles, $\phi = 2\pi/5, 4\pi/5, \ldots 2\pi$, (dashed lines) as well as the envelope error $\hat{\varepsilon}$ from equation 8.15, (solid lines). From [95].

8.4.2 Random Input

For particular values of n, V and Δ, equation 8.15 can be considered to be the transfer function of a linear filter which yields the worst-case error for dynamic force components of frequency ω. Using the standard input/output relationship for a linear system subject to ergodic random excitation [355], the mean square direct spectral density of the measurement error $S_{ee}(\omega)$ due to the 'two-sided' input tyre force spectral density $S_{pp}(\omega)$ is given by

$$S_{ee}(\omega) = \hat{\varepsilon}(n, \omega\Delta/2\pi V)^2 \; S_{pp}(\omega), \qquad -\infty < \omega < \infty. \tag{8.17}$$

For a linearised vehicle model, $S_{pp}(\omega)$ can be found from the road profile input displacement spectral matrix $[S_u(\omega)]$ and a vehicle transfer function matrix $[H(\omega)]$, as described in Section 5.4.2. Equation 8.17 can then be integrated with respect to frequency to obtain the worst case RMS array error $\sigma(n)$ for an n-sensor system, traversed by a linearised vehicle model:

$$\sigma(n) = \left[\int_0^\infty \hat{\varepsilon}\left(n, \frac{\omega\Delta}{2\pi V}\right)^2 [H(\omega)]^* [S_u(\omega)] [H(\omega)]^T d\omega \right]^{1/2}, \tag{8.18}$$

where '*' denotes the complex conjugate and 'T' denotes the matrix transpose. $[H(\omega)]$ can be determined easily from the equations of motion of a vehicle model (*eg* Section 5.4.2).

Equation 8.18 yields the RMS error for one stationary random tyre force passing over an 'ensemble' of n-sensor WIM arrays. It can also be considered to be the expected standard deviation of the static load estimation error for many different axles, with similar dynamic characteristics, passing over a single WIM site. This assumes that the wheel forces are sampled from an ergodic random process, which is reasonable under most circumstances [393]. It also assumes that the surface of the WIM array is not abnormally rough.

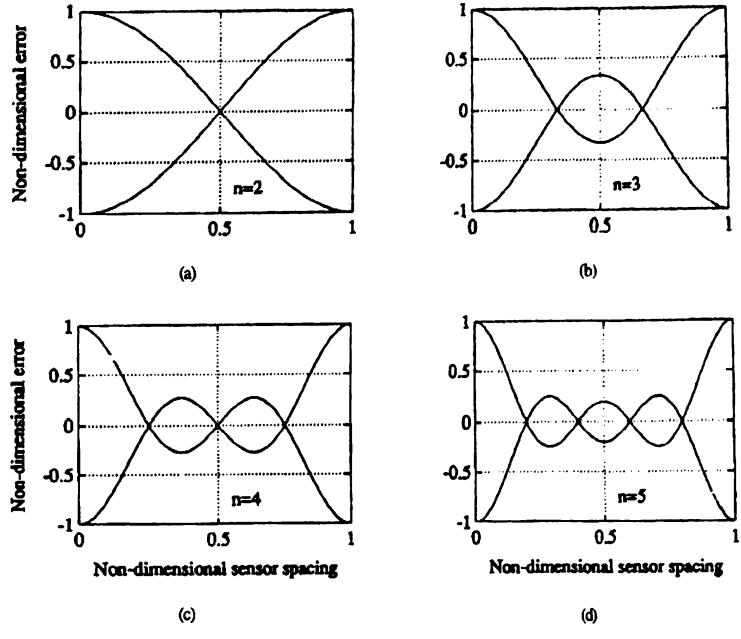


Fig. 8.6 Plots of the envelope error $\hat{\varepsilon}$ from equation 8.15. (a) n=2, (b) n=3, (c) n=4, (d) n=5. From [101].

8.4.3 Measure of WIM System Performance

It is useful to define a non-dimensional measure of WIM system performance. The 'Error Coefficient of Variation' (ECOV) $\rho(n)$, for an n-sensor system is defined by

$$\rho(n) = \sigma(n)/P_0, \tag{8.19}$$

where P_0 is the static axle load.

A perfect WIM system would have an ECOV of $\rho = 0$.

It is easily shown that the ECOV for a single-sensor array, $\rho(1)$, is equal to the Dynamic Load Coefficient (DLC) which is the ratio of the RMS dynamic load to the static load (see [102] for details). For highway conditions of road roughness and speed, DLC's in the range 0.1 - 0.3 are typical (*ie* 10% to 30% RMS single-sensor WIM error), but DLC's up to 0.4 have been measured for particularly poorly damped tandem suspensions (Section 7.4.2).

8.4.4 Simulation Model

The simple generic 'quarter-car' vehicle model shown in figure 5.1a was chosen for this study, to represent the majority of truck suspensions which generate a large low frequency wheel force

spectral peak due to sprung mass motion. It has a 'sprung mass' natural frequency of approximately 1.9 Hz. The equations of motion and formation of the transfer function matrix $[H(\omega)]$ and input spectral matrix $[S_u(\omega)]$ are discussed in Chapter 5.

MS-WIM results are presented in [102] for a walking-beam model as per figure 5.1b, which generates large dynamic wheel loads due to bogie pitching motion. (See Sections 5.4 and 7.4.3.)

The road profile displacement spectral density $S_u(\kappa)$, at wavenumber κ, used to generate $[S_u(\omega)]$ in the simulation study was the two-index function described by equation 3.1, with parameters corresponding to a 'good' road surface classification. This profile may be likened to the surface of an 'A-road' in the UK.

8.4.5 Simulation Results

Figure 8.7 shows the wheel force spectral density $S_{pp}(\omega)$ and the error spectral density $S_{ee}(\omega)$ (as calculated by equation 8.17) for the vehicle model travelling at 100 km/h over a 3-sensor WIM array with a sensor spacing of $\Delta = 4$ m. The same data is plotted on both linear and logarithmic scales. On the linear graph, the area under the solid line is proportional to the DLC^2 and the area under the dashed lines is proportional to $\rho(\hat{3})^2$. The logarithmic graph is provided to show more clearly the attenuation of $S_{pp}(\omega)$ caused by $\hat{\varepsilon}(n, \omega\Delta/2\pi V)^2$. Because the maximum value of $\hat{\varepsilon}(n,\delta)$ is unity, (figure 8.6), $S_{ee}(\omega)$ can never exceed $S_{pp}(\omega)$, hence the dashed line can never cross the solid line. This means that for 'perfectly accurate' sensors, $\rho(n)$ can never exceed the Dynamic Load Coefficient (DLC).

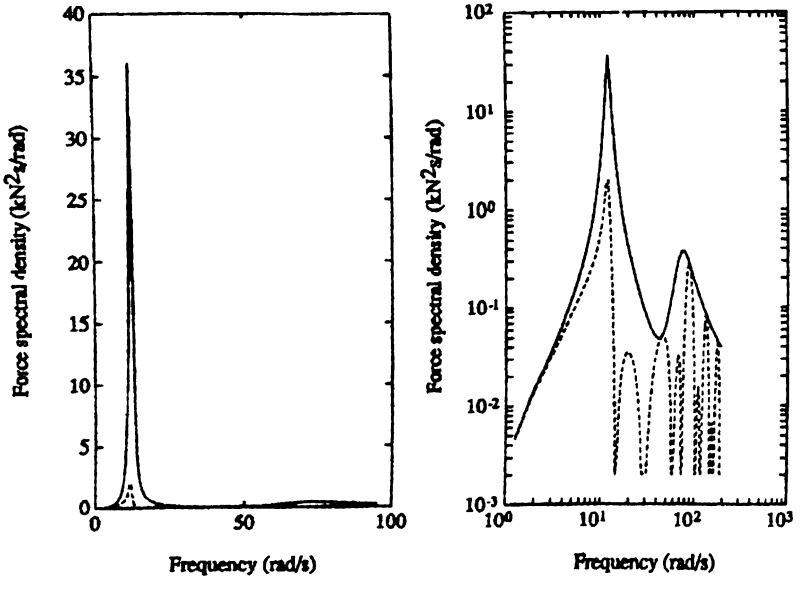


Fig. 8.7 Tyre force spectral density $S_{pp}(\omega)$ and the WIM array error spectral density $S_{ee}(\omega)$ for the vehicle model travelling at 100 km/h over a WIM array with n=3 and $\Delta = 4$ m. From [101].
———— = $S_{pp}(\omega)$, - - - - - - = $S_{ee}(\omega)$.

Performance data corresponding to this simulation were: DLC = 0.142, and $\rho = 0.051$. Thus in this case, the 3-sensor array reduces the error coefficient of variation from 14.2% to 5.1%, which corresponds to a 64.5% improvement in performance over a single sensor WIM system. This averaging scheme clearly improves the accuracy of static wheel load prediction substantially.

Figure 8.8 illustrate the influence of the sensor spacing Δ on the Error Coefficient of Variation ρ for $n = 3$ with the vehicle model travelling at speeds of 60 km/h and 100 km/h. It is apparent that for each speed, there is a range of spacings for which the WIM error (ECOV) is low, *ie* the system performs relatively accurately.

The shape of the ECOV curves is closely related to the magnitude of the error envelope curve $|\hat{\varepsilon}(n=3,\delta)|$ (shown in figure 8.6b), however because the system is subjected to an approximately narrow band random input (centred on the sprung mass natural frequency of the vehicle) instead of a single sine wave, the ECOV curve is a 'smoothed' version of $|\hat{\varepsilon}|$.

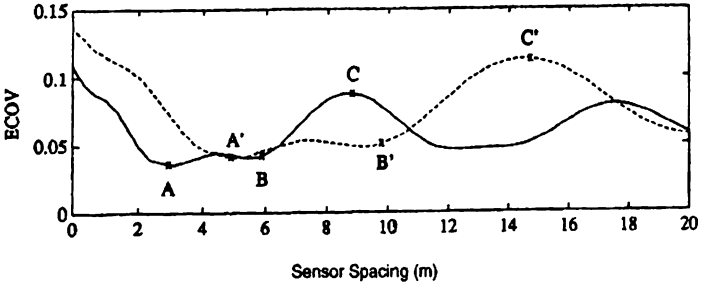


Fig. 8.8 Variation of theoretical WIM Error Coefficient of Variation (ECOV) with sensor spacing Δ. From [101]. Points A, B, C *etc.* were calculated according to the theory for sinusoidal inputs. ——— = 60 km/h, ---------- = 100 km/h.

The properties of the $\hat{\varepsilon}$ curves, described earlier can be used to interpret key features of the ECOV curves. From equation 8.16, the first two zeros in $\hat{\varepsilon}(3,\delta)$ occur when $\delta_k = \delta_1 = 1/3$ and $\delta_2 = 2/3$. These points correspond to approximately to minima in the ECOV curves. Using the definition of δ from equation 8.10, with $V = 16.7$ m/s (60 km/h) and $f = \omega/2\pi = 1.9$ Hz (the dominant resonant frequency in $S_{pp}(\omega)$), the minima are expected to occur approximately at $\Delta = V / 3f \approx 2.9$m and $\Delta = 2V / 3f \approx 5.9$m These points are labelled A and B on figure 8.8. The corresponding points for $V = 27.8$ m/s (100 km/h) are labelled A' and B'. Conversely, the worst errors are expected to occur when $|\hat{\varepsilon}(3,\delta)| = 1$. This happens when the dominant (resonant) frequency component in $S_{pp}(\omega)$ is sampled once every cycle (or once every two cycles), *ie* for integer values of δ. The points labelled C and C' on figure 8.8 correspond to $\delta_3 = 1$. Note that the labelled points on figure 8.8 are all slightly to the right of the maxima and minima of the ECOV curves at which they might be expected to occur. This is probably because $S_{pp}(\omega)$ is not symmetric about the main peak, (figure 8.7).

8.4.6 WIM Array Design

It is important that the WIM array is designed to be accurate for the widest possible range of vehicles (frequencies) and speeds. For given values of Δ and f, it is possible to estimate the range of vehicle speeds V over which the system will operate in the 'plateau region' of the ECOV curve, where the accuracy is consistently good.

From equation 8.16, the zeros in $\hat{\varepsilon}(n,\delta)$ occur when $\delta_k = k/n$, $k = 1, 2, 3, \ldots (n-1)$. Values of $k > n$ are ignored, since these represent large (often impractical) sensor spacings at which the wheel forces are sampled at frequencies well below the Nyquist frequency: *ie* less than 2 sample points per cycle. Using eqs. 8.10 and 8.16, and assuming fixed Δ and f, the zeros occur at speeds V_k where

$$V_k = \frac{\bar{f} n \Delta}{k}, \quad (m/s), \qquad k = 1,2,3\ldots(n-1) \tag{8.20}$$

and $\bar{f}$ is the frequency, in Hz, of the dominant spectral component in $S_{pp}(\omega)$.

The 'plateau region' of the ECOV curve will be governed by the first and last zeros in $\hat{\varepsilon}$: k=1 and k = n-1. Thus the maximum and minimum speeds for which the WIM system will be reasonably accurate (operate in the 'plateau region') are given by

$$V_{max} = V_1 = \bar{f}n\Delta \quad \text{and} \quad V_{min} = V_{n-1} = \bar{f}n\Delta/(n-1) \quad \text{(m/s)}, \quad n > 1. \tag{8.21}$$

A good design procedure would be to select Δ such that the average traffic speed $\bar{V}$, in m/s, corresponds to the average of V_{min} and V_{max}. Thus from equation 8.21:

$$\Delta_{d_1} = \frac{2(n-1)\bar{V}}{\bar{f}n^2}, \quad n > 1. \tag{8.22}$$

There is considerable variation in the dominant frequencies $\bar{f}$ in the dynamic wheel force spectra of common heavy vehicles. They are usually in the range 1.5 to 4.5 Hz (Section 7.4.3) and a suitable average value of $\bar{f}$ is 2.5 Hz. It is possible that a slightly higher average frequency (say $\bar{f}$ = 3.0 Hz) may be more suitable for countries where lorry suspensions are relatively stiffer, and conversely, a lower value may be more suitable for vehicles containing predominantly air suspensions.

Figure 8.9 is design chart for multiple-sensor WIM arrays using equation 8.22 with $\bar{f}$ = 2.5 Hz and speeds of 20, 40, 60, 80, 100 km/h. It yields values of Δ_{d_1} for arrays with n = 2 to 10 sensors.

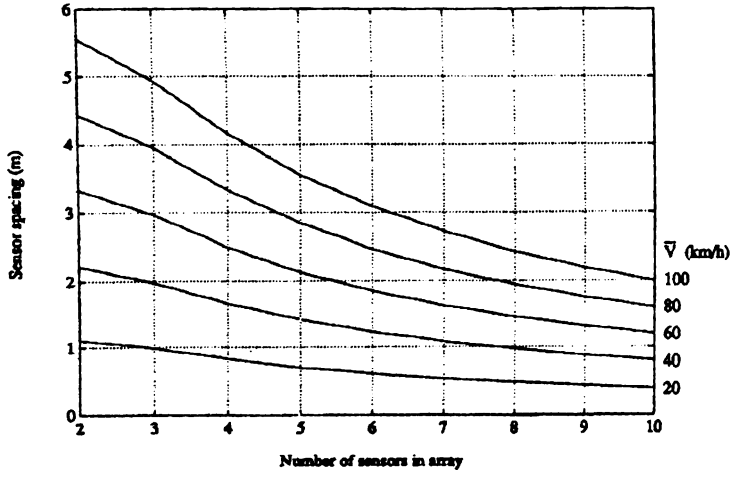


Fig. 8.9 Design chart for multiple sensor WIM systems using equation 8.22 with $\bar{f}$ = 2.5 Hz. From [101].

8.4.7 Sensitivity to Frequency and Speed

Substituting the design spacing Δ_{d_1} (from equation 8.22) into equation 8.21 gives

$$V_{max} = 2(n-1)\bar{V}/n \quad \text{and} \quad V_{min} = 2\bar{V}/n, \quad n > 1. \tag{8.23}$$

If n=2, $V_{min} = V_{max} = \bar{V}$. Thus a 2-sensor WIM system can only be designed to be accurate at one speed. If n=3, however, $V_{min} = \frac{2}{3}\bar{V}$ and $V_{max} = \frac{4}{3}\bar{V}$ and a system with sensor spacing chosen according to equation 8.22 will be accurate for speeds of $\frac{2}{3}\bar{V} \le V \le \frac{4}{3}\bar{V}$. For example if $\bar{V}$ = 80 km/h, this would yield $53 \le V \le 107$ km/h. Similarly if n=4, the range of accurate performance is given by $\frac{1}{2}\bar{V} \le V \le \frac{1}{2}\bar{V}$.

Figure 8.10 shows the ECOV ρ for 2-, 3- and 4-sensor WIM systems when traversed by the quarter-car vehicle model. The arrays were designed for an average speed of 80 km/h,

($\bar{V}$ = 22.2 m/s) according to equation 8.22 with $\bar{f}$ = 1.9 Hz. Also shown in figure 8.10 is $\rho(1)$ (the DLC) for comparison.

The following observations are made:

(i) The WIM array with only two sensors provides a significant improvement in accuracy, over the single-sensor system (DLC), in the vicinity of the design speed of 80 km/h.

(ii) The 2-sensor system loses accuracy quite quickly for speeds away from 80 km/h, whereas the 3-sensor system has an accurate 'plateau region' for $50 \le V \le 100$ km/h as expected. The 4-sensor system is accurate over an even wider speed range.

(iii) In the vicinity of 80 km/h, an increase in the number of sensors yields only a modest increase in accuracy.

(iv) For speeds less than about 30 km/h, the ECOV (ρ) curves fluctuate rapidly due to aliasing.

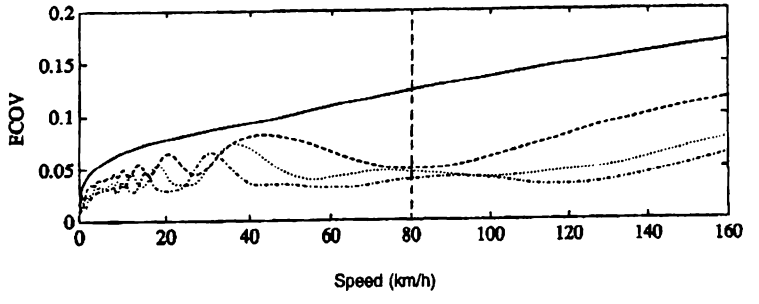


Fig. 8.10 Influence of speed on the theoretical Error Coefficient of Variation ρ of 2-, 3- and 4-sensor WIM systems, designed for an average traffic speed of 80 km/h. From [101].
——— n=1 (DLC), ---------- n=2, ····· n=3, ·····-····· n=4.

From figure 8.10 it appears that 3 sensors is a good choice, because the system is reasonably accurate and has a relatively wide operating speed range. The 4-sensor system yields a larger speed range with only a small accuracy improvement over the 3-sensor system. The extra cost of the 4th sensor may not be worthwhile in practice.

The range of frequencies over which the WIM array will be accurate for a given vehicle speed $\bar{V}$ can be found using eqs. 8.10 and 8.16 and replacing Δ by Δ_{d_1} from equation 8.22:

$$f_{min} = n\bar{f}/2(n-1) \quad \text{and} \quad f_{max} = n\bar{f}/2, \quad n > 1. \tag{8.24}$$

Thus if n=2, $f_{min} = f_{max} = \bar{f}$, that is the system can only be tuned to perform well at one input frequency. If n=3, the operating frequency range (for a fixed speed) is approximately $\frac{1}{4}\bar{f} \le f \le \frac{1}{2}\bar{f}$. For $\bar{f}$ = 2.5 Hz this gives $1.9 \le f \le 3.8$ Hz. Similarly if n=4, the operating frequency range is $\frac{2}{3}\bar{f} \le f \le 2\bar{f}$ which, for $\bar{f}$ = 2.5 Hz, yields $1.7 \le f \le 5$ Hz. Thus n=3 is a reasonable choice, although errors may occur when the frequency and speed take extreme values simultaneously. The worst error is likely to occur when $V \approx V_{max}$ and $f \approx f_{min}$ although the other extreme condition ($V \approx V_{min}$ and $f \approx f_{max}$), may also yield significant errors.

8.5 VALIDATION OF MS-WIM THEORY

8.5.1 The Experiment

Wheel Load Measuring Mat

The 'load measuring mat' used in this validation exercise was described in Section 7.3.2. Thirty two tiles, containing a total of 96 sensors were used. The tiles were mounted end-to-end along one wheel track, to provide an instrumented test section of length 38.4 m.

The mat installation utilised 6 Golden River 'Marksman 600' data loggers. Each sensor was attached to a data logger by a 5 m long cable and each data logger processed the outputs of 16 sensors, and stored the results. The data loggers were connected into a network in a 'daisy-chain' configuration by RS232 serial data cables. A micro computer was connected to the network and used to upload the raw axle load information from the data loggers after each vehicle test run.

Test Site and Vehicles

The field tests were performed on the Navistar test track in Fort Wayne, Indiana. The oval track has 2 lanes and is 1.9 km long. The polyurethane mat tiles were attached to the test track with a sheet of double-sided adhesive tape and 12 masonry anchors per tile, screwed into the asphalt road surface. Timber sheets of total length 19.5 m, width 1.2 m and thickness 13 mm were screwed to the test track at each end of the mat installation. This ensured that the test vehicles were nominally horizontal when passing over the mat sensors, and that transient vibration due to the 13 mm step was reduced slightly.

Three 6x4 tractors and three tandem axle semi-trailers were provided by Navistar for testing on the mat. The vehicles were arranged into six different tractor/semi-trailer combinations (denoted S1 to S6). Two of the tractors had tandem '4-spring' suspensions and the third had a 'trailing-arm' tandem air suspension with hydraulic dampers. Two of the trailers had 4-spring tandem suspensions, while the third had a pivoted spring 'single-point' tandem suspension. The vehicle combinations were selected to be reasonably representative of the US truck fleet. Each vehicle was weighed on a whole-vehicle static weighbridge immediately prior to, or after the testing. The weighing procedure enabled an estimate of the static load of each axle to be obtained as well as the gross weight of the vehicle. (See [102] for detailed information about the vehicles and axle loads.)

Each articulated vehicle combination was driven over the mat at nominal speeds of 8, 16, 32, 48, 64 and 80 km/h in both directions. At least six repetitions were performed for each test condition, giving a total of 460 test runs during four days of testing. The surface temperature of the mat was measured prior to each vehicle test.

Sensor Performance

Detailed information concerning the performance of the sensors can be found in [102]. The important results are summarised here.

(i) *Calibration:* Three methods were used to calibrate the sensors and test their uniformity. Two utilised purpose-built hydraulic static calibrators [116], and the third used dynamic tyre forces measured in the field [102]. The average coefficient of variation of the calibration factors, measured at three points along the length of each bare sensor, was found to be 3.2%.

(ii) *Sensitivity to Temperature:* No systematic dependence of sensor calibration with temperature was measurable for mat surface temperatures of 15 to 40 ^{0}C.

(iii) *Sensitivity to Speed:* No systematic dependence of static load errors with vehicle speed could be detected and no evidence could be found of fore-aft weight transfer affecting the static loads for higher speeds. It is concluded, therefore, that the calibration of the capacitative strip transducers in the mat was not affected significantly by vehicle speed.

(iv) *Reliability:* Approximately 2.5% of all data was lost out of 460 test runs over the 96 sensors. Almost half of the lost data (1%) was due to a single sensor which failed. The remainder was due to false triggers of the data loggers.

(v) *Accuracy:* The average dynamic sensor error e_j for measured *dynamic* loads (which is the fundamental limit on the accuracy of WIM measurements) was found to be less than 4% RMS. This can be attributed to noise and small calibration errors.

(vi) *Drift with Time:* Insufficient time was available to detect any long-term drift in calibration. Glover and Newton [195] performed similar tests on an installation of WIMstrip sensors mounted in slots cut in the TRL test track in England. They did not detect any significant drift in sensitivity during the seven month testing period.

8.5.2 Results

The mat data files for the six articulated vehicles were processed to determine the Error Coefficient of Variation (ECOV = ρ) as a function of WIM array design parameters (n and Δ), for each axle of each vehicle at the six nominal testing speeds (8, 16, 32, 48, 64, 80 km/h). Figure 8.11 shows an example of the procedure, in which many 3-sensor WIM arrays (n = 3) with Δ = 1.6 m can be obtained by averaging the outputs of appropriately spaced groups of sensors. Averages of this type were calculated for sensor spacings Δ = 0, 0.4, 0.8....12 m, and n = 2 to 6 sensors, *ie* 155 different WIM array configurations in all.

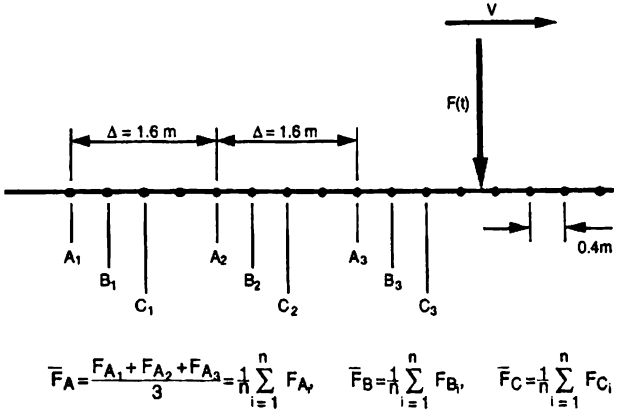
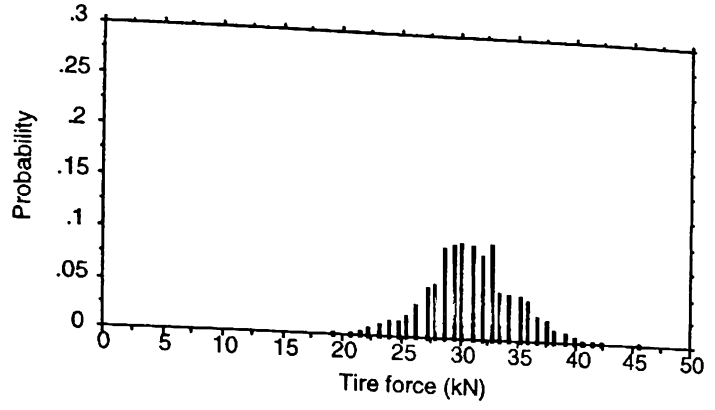


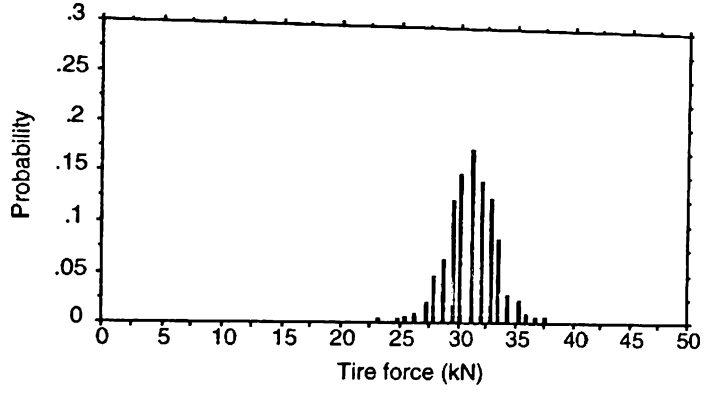
Fig. 8.11 Showing the calculation of 3-sensor WIM averages with a spacing of Δ = 4 x 0.4 = 1.6 m using data from the mat. From [101].

Due to space limitations, only a limited number of experimental results are presented here. The remaining results are presented in [102].

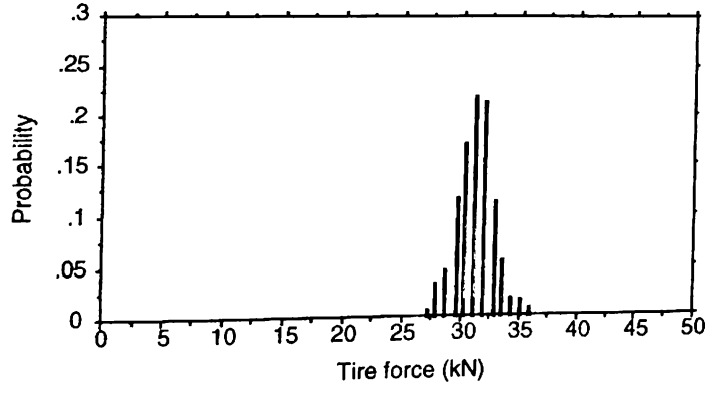
Histograms of WIM force averages are provided for vehicle S4 travelling at a speed of 85 km/h in figures 8.12a,b,c. Figure 8.12a shows the force distribution for axle 5 on the trailer, calculated by considering each transducer to be a separate WIM system (*ie* by setting Δ = 0). Figure 8.12b shows the result of analysing the same data as figure 8.12a, but with 3-sensor arrays (n = 3) and Δ = 4.0 m. (This array spacing was determined using equation 8.22 with $\bar{V}$ set to the testing speed (24 m/s) and $\bar{f}$ = 2.5 Hz.) Similarly, figure 8.12c shows the result of analysing the same data with 6-sensor averages (n = 6) and Δ = 2.4 m. It is apparent from the figures that the *spread* of the probability distribution (which is proportional to the ECOV) is reduced considerably by performing the 3-sensor averages. The ECOV ρ is reduced from 11.5% for the single-sensor system to 5.7% for the 3-sensor system and to 4.2% for the 6-sensor system.



(a) single sensor



(b) 3 sensors, $\Delta = 4.0$ m

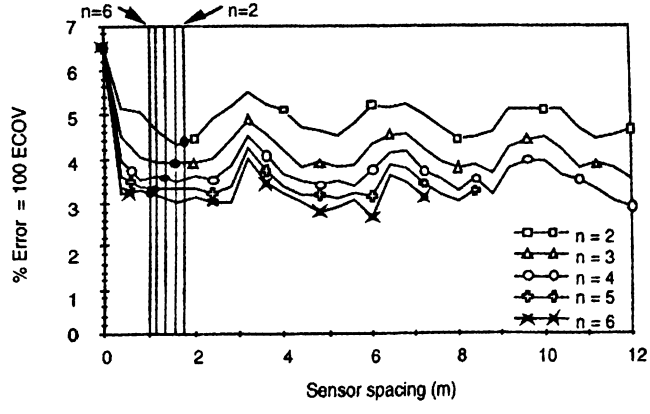


(c) 6 sensors, $\Delta = 2.4$ m.

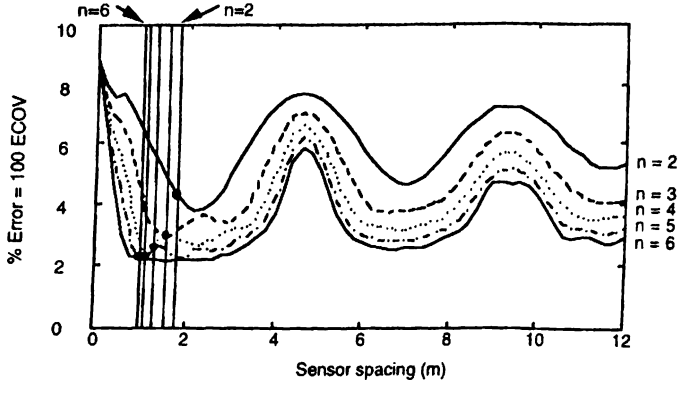
Fig. 8.12 Histograms of WIM average force, Vehicle S4, Axle 5, Speed = 85 km/h. From [101].

Comparison of Experiment and Theory

A graph of ρ vs Δ for the steering axle of vehicle S1 at 32 km/h is provided in figure 8.13a. The vertical lines on the figure labelled n = 2 to 6 correspond to the design spacing Δ_{d_1} as calculated from equation 8.22 with $\bar{V}$ = 9 m/s and $\bar{f}$ = 2.5 Hz. Figure 8.13b shows theoretical curves that were calculated using equation 8.18 for the 'l/4-car' vehicle model, travelling at 32 km/h. The vertical lines on the figure again show the design spacings, calculated using equation 8.22 with $\bar{V}$ = 9 m/s and $\bar{f}$ = 2.5 Hz.



(a) Experimental results: Vehicle S1, speed 32 km/h, steering axle.



(b) Theoretical results: 'quarter-car' model, speed = 32 km/h.

Fig. 8.13 WIM array Error Coefficient of Variation ρ vs sensor spacing Δ. From [101].
Vertical lines indicate design spacings according to equation 13 with $\bar{V}$ = 9 m/s, $\bar{f}$ = 2.5 Hz.

Several comments can be made about figures 8.13a,b: The general shapes and magnitudes of the experimental and theoretical curves are similar. This appears to verify that the quarter-car model used in the theoretical analysis is a reasonable representation of the steering axle suspension of vehicle S1.

The main differences between the theoretical and experimental curves are the spacings at which the peaks and troughs occur. This is because the natural frequencies of the test vehicle and the theoretical model are different. The theoretical model had a sprung mass natural frequency of 1.9 Hz. The natural frequency of the experimental vehicle can be deduced from figure 8.13a by considering the location of the first peak, which occurs approximately at $\Delta = 3.2$ m, corresponding to $\delta = 1$. Using equation 8.10, the natural frequency of the vehicle is given by

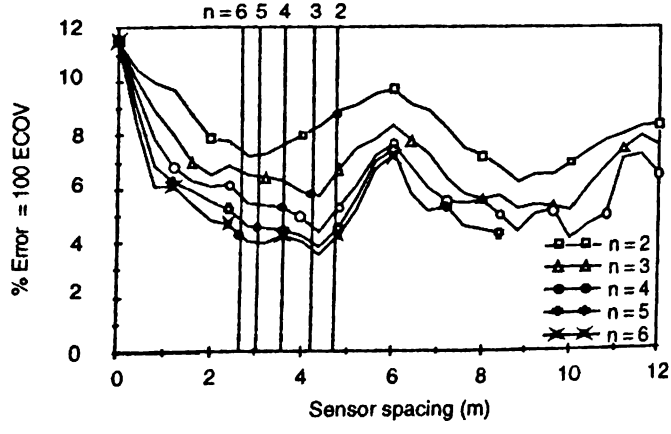
$$f = V/\Delta_1 \qquad (8.25)$$

where Δ_1 = sensor spacing corresponding to the first peak in the curve of ρ vs Δ. From figure 8.13a, $\Delta_1 = 3.2$ m, and using $V = 9$ m/s, equation 8.25 gives $f = 9/3.2 = 2.8$ Hz. The second peak in the curves is expected to occur when $\delta = 2$, *ie* $\Delta = 2V/f = 6.4$ m. This also conforms with figure 8.13a.

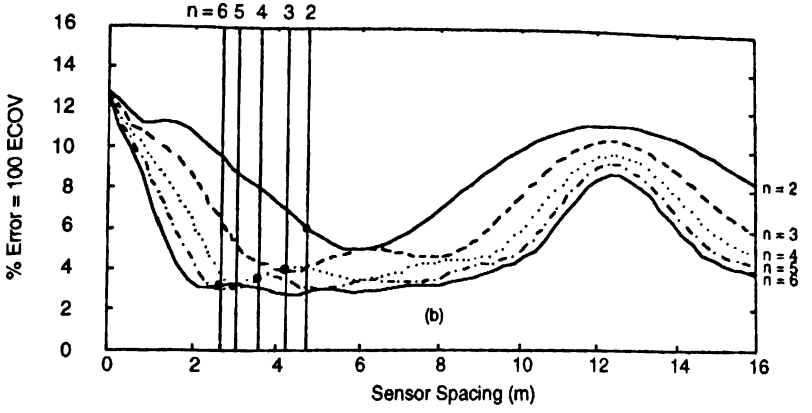
The spacings given by equation 8.22 and shown by the vertical lines in figures 8.13a,b, would be reasonable choices for the array design spacings. The vertical line corresponding to $n = 2$ falls slightly to the right of the first trough in the ρ - Δ curve in figure 8.13a, because the natural frequency of the vehicle is 2.8 Hz, which is slightly greater than the design frequency $\bar{f} = 2.5$ Hz. Conversely in figure 8.13b, the vertical line for $n = 2$ falls to the left of the first trough, since the body-bounce natural frequency of the vehicle model is 1.9 Hz.

As explained previously, arrays with 3 or more sensors are more 'robust' to frequency and speed variations because they have relatively wide, flat-bottomed 'plateau regions' (troughs). This can be seen in both the experimental and theoretical curves (figures 8.13a,b). As a result, the vertical lines for $n = 3$ to 6 in both graphs lie at spacings which are appropriate choices to minimise the ECOV ρ, despite the fact that the operating frequencies are different to the design frequency $\bar{f}$. It can also be seen that a small error in spacing of the 2-sensor system due to, say, a different vehicle speed, would cause a more rapid decrease in accuracy than for the systems with 3 or more sensors.

A second comparison between experiment and simulation is provided in figures 8.14a,b. Figure 8.14a shows a graph of ρ vs Δ for axle 5, on the 4-spring tandem trailer suspension of vehicle S4, travelling at 85 km/h. From the y-intercept, it can be seen that the DLC is approximately 11.5%, which corresponds to the ECOV value determined previously from the histogram in figure 8.12a.



(a) Experimental results: Vehicle S4, speed 85 km/h, axle 5 (on trailer).



(b) Theoretical results: 'quarter-car' model, speed = 85 km/h.

Fig. 8.14 WIM array Error Coefficient of Variation ρ vs sensor spacing Δ. From [101].
Vertical lines indicate design spacings according to equation 8.22, $\bar{V}$ = 24 m/s, $\bar{f}$ = 2.5 Hz.

The sprung mass natural frequency of the experimental vehicle can be estimated from the first peak of figure 8.14a (corresponding to δ = 1) using equation 8.25: $f \approx 23.6 / 6.0 = 3.9$ Hz. This is significantly higher than the array design frequency $\bar{f}$ = 2.5 Hz, but is within the expected range of 1.5 to 4.5 Hz discussed earlier. As a consequence, the design spacing for n = 2, at approximately 4.7 m in figure 8.14a, is far away from the optimum at approximately 3.0 m. The RMS error for n = 2 at the design spacing is approximately 8.8%.

The design spacing for n = 3 (at approximately 4.2 m) is just within the 'plateau region' of the ρ - Δ curve for n = 3. Consequently the RMS error for n = 3 at the design spacing is approximately 5.7%, a substantial improvement over 8.8%, for n = 2. This illustrates the significant benefit, in terms of operating speed and frequency ranges, which is obtained by using a WIM array with 3 or more sensors. It should be noted that [102] contains many similar results to figures 8.13a and 8.14a, with 3-sensor WIM errors ρ(3) usually in the range 3 - 7% for Δ_{d1} chosen according to equation 8.22.

Figure 8.14b shows theoretical predictions using the quarter-car model, with a speed of 85 km/h. In this figure as in figure 8.13b, the vertical line for n = 2 falls to the left of the trough in the ECOV curve for n = 2. This is because the natural frequency (1.9 Hz) is less than $\bar{f}$ = 2.5 Hz.

Influence of Tyre Tread Pattern

The contact pressure distribution under a rolling tyre depends on the tread pattern. Off-road tyres can have quite large local contact pressure variations in the vicinity of the individual tread elements. When such a tyre rolls over the mat, some of the strip transducers will be loaded by high-pressure regions of the tyre contact area and others will be loaded by low-pressure regions. The wheel force measurement involves integrating the output of each strip sensor (which is proportional to the local contact pressure) throughout the period of contact between tyre and sensor. Thus if some sensors experience a high contact pressure, they will register an abnormally high load. Conversely some sensors will register an abnormally low load. This problem is dependent on the construction of the tyre and the tread pattern. It is expected to occur for *any* type of narrow strip WIM transducers, not just capacitative strips. Thus it can be considered to be a fundamental limit on the accuracy of strip sensors. Fortunately the majority of highway vehicles use 'highway' tread tyres and these do not display a significant variation of local contact pressure due to the tread elements. Thus for most vehicles, tyre tread effects are not likely to cause serious errors with strip WIM sensors.

A graphic example of the tyre tread effect can be seen in figure 8.15 for axle 3 of vehicle S4 which was the only test suspension to have off-road tyres. Because of the air suspension, this vehicle is expected to produce relatively small dynamic loads [337, 443]. Figure 8.15, however, shows a large Error Coefficient of Variation $\rho(1)$ of approximately 16% at $\Delta = 0$, for a speed of 11 km/h. This was one of the largest ECOVs measured in all of the tests! It is interesting to note that the $\rho(1)$ value for axle 3 of vehicle S4 was found to remain approximately constant with speed, indicating that it was not influenced by the dynamics of the vehicle. For every other suspension, there was a significant increase in $\rho(1)$ with speed.

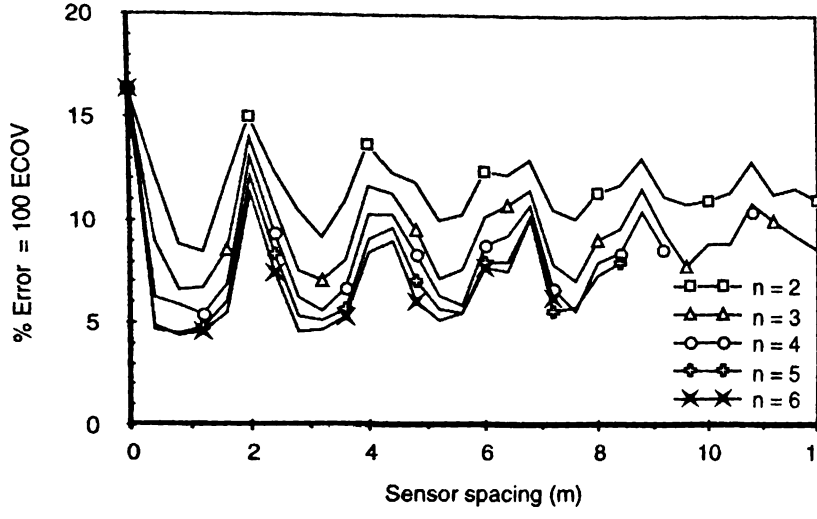


Fig. 8.15 Measured WIM array Error Coefficient of Variation ρ vs sensor spacing Δ. From [101]. Vehicle S4, Axle 3 (off-road tyres), Speed = 11 km/h.

The first peak in figure 8.15 occurs at $\Delta_1 = 2.0$ m. If this peak was caused by dynamic loads, it would shift with speed. For example, if the speed increased from 11 km/h to 85 km/h, Δ_1 would be expected to increase to $\Delta_1 = 2.0 \times 85 / 11 = 15.5$ m. This was not found to occur in the experimental result (see [102]). In fact the position of the first peak was found to stay relatively constant for speeds up to 51 km/h and then decrease slightly with higher speeds, to $\Delta_1 = 1.8$ m at 85 km/h.

The explanation of this behaviour is related to the tyre tread pattern and is described in detail in [102]. It transpires that 5 sensor spaces (2 m) corresponds to a prime number of tyre tread elements and hence the maximum contact pressure can only coincide with the location of every 5th sensor. This is an example of under-sampling or aliasing. The sensor array cannot distinguish between tyre contact pressure variation with wavelength equal to the tyre tread interval, and a force component with wavelength 2.0 m. This result is dependent only on the tread pattern and so the aliased wavelength of 2.0 m is largely independent of speed. Note that for high vehicle speeds the driving torque and hence longitudinal 'creep' or 'slip' of the driven wheels becomes significant. This causes an effective reduction in the wavelength of the contact pressure distribution along the mat and a decrease in the aliased wavelength from 2.0 m to 1.8 m.

8.6 HIGH-ACCURACY MS-WIM SYSTEMS

The 'Holy Grail' of WIM is development of systems with sufficiently high accuracy that they could be used for legal enforcement of static axle loads. Such systems would require significantly greater *accuracy* than the arrays discussed in Sections 8.4 and 8.5. They would also need to be more *reliable* – able to measure the weight of every commercial vehicle axle with similar accuracy: irrespective suspension type, vehicle speed, or other operating conditions. Such systems offer the tantalising prospect of entirely automatic operation, and hence greatly reduced costs of axle-load enforcement. This could justify more expensive capital costs.

The WIM array design formula, equation 8.22, was derived by assuming that the dynamic tyre force spectrum is dominated by low frequency components - *ie* that vehicles behave like the quarter–car model (see figures 5.1a and 5.4a). While this is true for the majority of heavy vehicles, a modest proportion of vehicles also generate large dynamic tyre forces at higher frequencies, due to wheel hop or bogie pitch. Their tyre force spectral densities look something like figure 5.4b, which was generated with a walking-beam suspension model (figure 5.1b). For these vehicles, the sensor spacing Δ_{d1} defined by equation 8.22 is too large. Consequently, their static axle loads estimated using spacings of Δ_{d1} will have substantial errors. (Examples are provided in [95] .)

In this section, an alternative MS–WIM array design procedure is developed for vehicles which generate both low frequency and high frequency dynamic tyre forces. The arrays require considerably more sensors than the designs considered so far – typically about 10 sensor lines per traffic lane. Theory is also derived for ascertaining the range of vehicle speeds and suspension frequencies for which such systems will operate reliably.

8.6.1 Design Spacing

In [438], the 'Maximum Likelihood' method is used to determine the parameters of signal models which best fit the WIM data points. Signal models with one or two sine waves are investigated:

$$p(t) = P_0 + P_1 \sin(2\pi f_1 t + \phi_1) + P_2 \sin(2\pi f_2 t + \phi_2). \qquad (8.26)$$

With two sine waves in the signal model, as in equation 8.26, there are seven unknown parameters: the mean force P_0; two amplitudes P_1 and P_2; two frequencies f_1 and f_2; and two phases ϕ_1 and ϕ_2. In order to determine unique values for these seven parameters, it is necessary to have at least seven WIM sensors. Similarly, if the signal model had just one sine wave, it would be necessary to have at least four sensors.

The theoretical minimum error that can be achieved by the Maximum Likelihood method can be found by calculating the 'Cramer-Rao Bounds' (CRBs) [438]. These bounds are shown in figure 8.16, along with the sample mean. The simulated dynamic tyre forces analysed in this example consist of a mean level plus a single sine wave, with superimposed random measurement errors (sensor noise). The amplitude of the sine wave is 20% of the mean value, and the noise is 4% of the mean. There are ten WIM sensors. Several observations can be made:

(i) For most sensor spacings, the WIM errors generated by the CRBs are less than those due to the sample mean. This implies significant scope for improving static load estimation using Maximum Likelihood methods.

(ii) The CRBs are less sensitive to sensor spacing than the sample mean - hence the flat bottom to the plateau region.

(iii) The range of sensor spacings over which the bounds are accurate is essentially the same as for the sample mean. It is determined by the first and last zeros in the envelope function (equation 8.15):

$$\frac{1}{n} < \delta < \frac{n-1}{n}. \qquad (8.27)$$

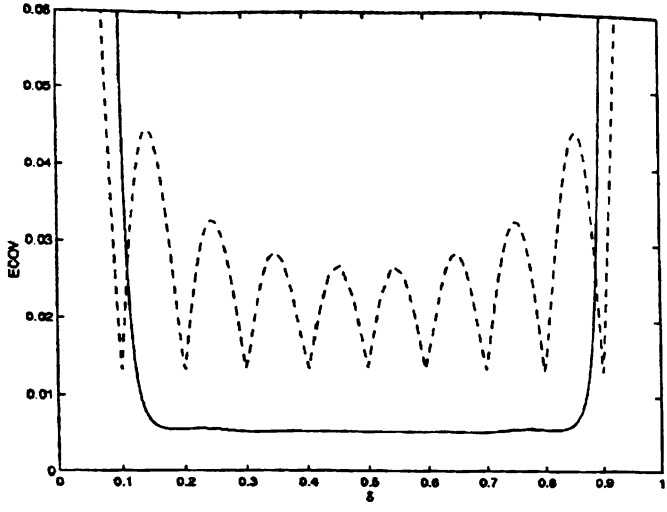


Fig. 8.16 Variation of the ECOV ρ with nondimensional spacing δ, for a 10-sensor WIM array subject to a tyre force signal consisting of a sine wave with superimposed random sensor noise. From [438].
———— = Cramer–Rao Bound; - - - - - - - - = Sample Mean.

It is known [438] that the CRBs for two sufficiently separated tones (sine waves) approach the corresponding single-tone CRBs. In this case, the suitable spacings can be derived from the requirement of sampling *both* frequency components correctly (*ie* within the plateau region of the ECOV curve). The range of applicable spacings depends exclusively on the extreme values of the ratio V/f.

Inserting $\delta = \Delta f / V$ in equation 8.27 gives suitable lower and upper values of Δ, which depend on the low frequency f_1 and high frequency f_2 tyre force components respectively.

$$\Delta > \frac{1}{n}\frac{\overline{V}}{f_1} = \Delta_1$$

and (8.28)

$$\Delta < \frac{n-1}{n}\frac{\overline{V}}{f_2} = \Delta_2.$$

Figure 8.17 shows typical CRBs as a function of spacing for two separate sine wave components of 2.5 Hz and 10 Hz. The shaded area highlights the range of spacings that could be used to sample both sine waves correctly. A good array design strategy would be to set the design spacing Δ_{d_2} to be the average of Δ_1 and Δ_2.

$$\Delta_{d_2} = \frac{\overline{V}}{2n}\left(\frac{1}{f_1} + \frac{n-1}{f_2}\right) \tag{8.29}$$

The estimation algorithm will fail if there is no overlap between the 'plateau' regions for the two frequency components. Therefore it must always be that $\Delta_2 \geq \Delta_1$. By setting $\Delta_1 = \Delta_2$, equation 8.28 can be used to determine an expression for the minimum possible number of sensors:

$$n \geq \frac{f_2}{f_1} + 1. \tag{8.30}$$

It is clear that the ratio of f_2/f_1 is very important. A system designed for low f_2/f_1 will need less sensors than a system designed for higher ratios. In practice, this ratio will be set by the types of vehicles using the road. In particular, their suspensions and tyre types and the masses of their axles and bodies.

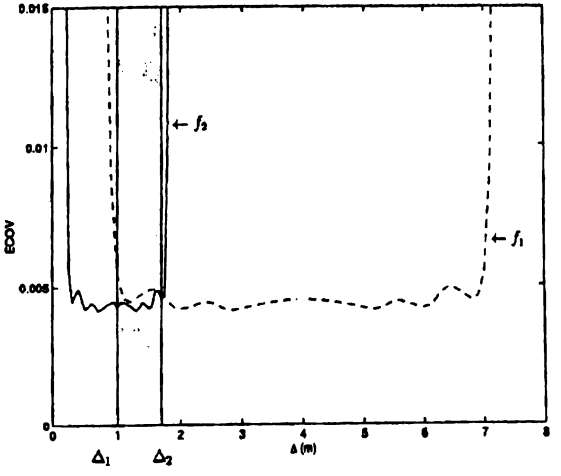


Fig. 8.17 Variation of the ECOV, (calculated from the Cramer–Rao Bounds), with sensor spacing, for a 10–sensor array, with 4% sensor noise. The two input frequencies are $f_1 = 2.5$ Hz and $f_2 = 10$ Hz, with dynamic force amplitudes of 20% of the mean value. From [438].
——— = high frequency f_2; - - - - - - - - - = low frequency f_1; shaded area = operating region.

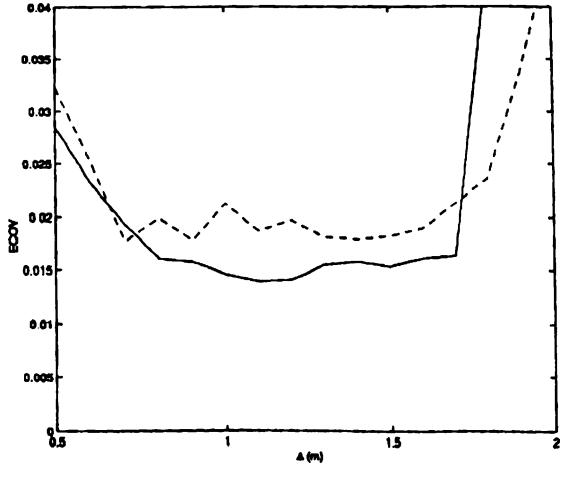


Fig. 8.18 WIM errors for the walking model at 20m/s, using a 10-sensor array with noise-free sensors.
——— = Sample mean, - - - - - - - - - = Maximum Likelihood method. From [438].

A simulation was performed using a walking-beam model similar to that shown in figure 5.1b, for a 'very good' random road, as specified by equation 3.1. The ECOV was calculated from 500 Monte Carlo simulation runs using two estimation algorithms - the Sample Mean and Maximum Likelihood method. Figure 8.18 shows the ECOV plotted as a function of sensor spacing for noise-free sensors. The design spacing $\Delta_{d_2} = 1.3\text{m}$, calculated from equation 8.29 is a good choice. The Maximum Likelihood method gives a smooth plateau region for a wide range of spacings. It gives modestly improved accuracy over the Sample Mean. (Note that it was found in [438] that the accuracy benefits of the Maximum Likelihood method become less as the sensor noise increases.)

8.6.2 Success Rate of the Weight Estimation Algorithm

Reliable operation of MS–WIM systems depends on choosing the number and spacing of sensors which give low errors for *both* frequency components in the tyre force spectrum. These frequencies vary randomly among vehicles, as do operating speeds. Reliable sensor array design therefore depends on being able to ensure a high probability of operating in the shaded region of figure 8.17. This 'probability of success' $\text{Prob}_s(n,\Delta)$, is given by:

$$\text{Prob}_s(n,\Delta) = \text{Prob}\left\{\left(\frac{V}{f_1} < n\Delta\right) \wedge \left(\frac{V}{f_2} > \frac{n}{n-1}\Delta\right)\right\}, \tag{8.31}$$

where $\Delta = \Delta_{d_2}$, is the spacing given by equation 8.29 and $\wedge$ denotes the logical 'and' function. Alternatively, this probability can be expressed as the complement of the probability of failure $\text{Prob}_f(n,\Delta)$, *ie* the probability that a measurement lies outside the operating region of the algorithm:

$$\text{Prob}_s(n,\Delta) = 1 - \text{Prob}_f(n,\Delta). \tag{8.32}$$

Assuming the worst–case scenario, with independent frequency distributions,

$$\begin{aligned}\text{Prob}_f(n,\Delta) &= \text{Prob}\left\{\left(\frac{V}{f_1} > n\Delta\right) \vee \left(\frac{V}{f_2} < \frac{n}{n-1}\Delta\right)\right\} \\ &= \text{Prob}\left\{\frac{V}{f_1} > n\Delta\right\} + \text{Prob}\left\{\frac{V}{f_2} < \frac{n}{n-1}\Delta\right\}\end{aligned} \tag{8.33}$$

where $\vee$ denotes the logical 'or'.

To determine the probability of failure in equation 8.33 it is necessary to assume that the velocity and suspension frequency are independent Gaussian variables, and to calculate the probability that the ratio V/f is less than a given threshold value Λ.

Let the corresponding probability density functions (PDF) be

$$\text{pr}(f) = \frac{1}{\sqrt{2\pi}\sigma_f}\exp\left[-\frac{(f-\bar{f})^2}{2\sigma_f^2}\right] \tag{8.34}$$

and

$$\text{pr}(V) = \frac{1}{\sqrt{2\pi}\sigma_V}\exp\left[-\frac{(V-\bar{V})^2}{2\sigma_V^2}\right] \tag{8.35}$$

Since the PDFs are independent, the joint probability density function will be

$$\text{pr}(f,V) = \frac{1}{2\pi\sigma_f\sigma_V}\exp\left[-\frac{(f-\bar{f})^2}{2\sigma_f^2} - \frac{(V-\bar{V})^2}{2\sigma_V^2}\right] \tag{8.36}$$

This is shown in figure 8.19, where the two PDFs $pr(f_1,V)$ and $pr(f_2,V)$ are displayed on the same contour map. The parameters are $\bar{f}_1 = 2.5\text{Hz}$, $\bar{f}_2 = 10\text{Hz}$, $\sigma_{f_1} = 0.4\text{Hz}$, $\sigma_{f_2} = 1\text{Hz}$. and $\bar{V} = 20\text{m/s}$, $\sigma_V = 2\text{m/s}$.

The probability that $V/f < \Lambda$ can be found by integrating the appropriate volume under the PDF $pr(f \mid V < \Lambda f)$. The domain of integration is effectively a 'wedge' defined by the frequency axis and the line $V = \Lambda f$. The overall calculation of failure involves performing two such (independent) integrations, which are illustrated by the two shaded wedges in the figure.

The volume under the lower wedge $Q_1(\Lambda)$ is given by:

$$\begin{aligned} Q_1(\Lambda) &= \iint_R pr(f,V)\,df\,dV \\ &= \int_0^\infty df \int_0^{\Lambda f} \frac{1}{2\pi\sigma_f\sigma_V} \exp\left[-\frac{(f-\bar{f})^2}{2\sigma_f^2} - \frac{(V-\bar{V})^2}{2\sigma_V^2}\right] dV \end{aligned} \tag{8.37}$$

A similar expression can be found for the volume under the upper wedge, $Q_2(\Lambda)$. These integrals can be simplified significantly (using Error Functions), but they do not have completely analytical solutions (see details in [438]). It is therefore necessary to perform small parts of the calculations numerically.

The probability of success is then given by

$$Prob_s(n,\Delta) = 1 - Q_2(n\Delta) + Q_1\left(\frac{n}{n-1}\Delta\right). \tag{8.38}$$

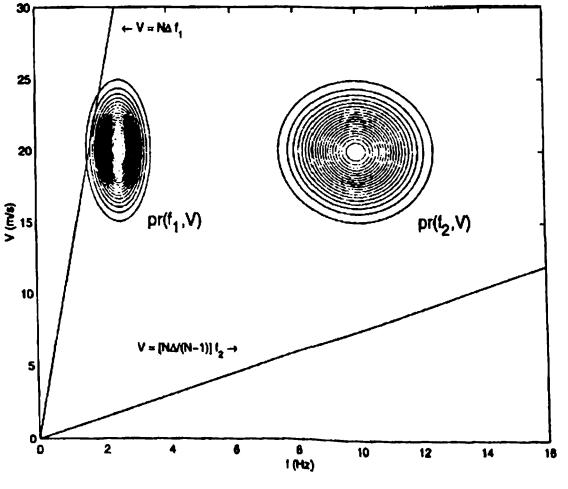


Fig. 8.19 Calculation of the probability of failure. From [438].

Figure 8.20 shows the success rate $Prob_s\left(n, \Delta_{d_2}\right)$ as a function of the number of sensors n for different spreads of the velocity distribution σ_V. For each case, the spacing was set to Δ_{d_2} as calculated from equation 8.29. It can be seen that the success rate approaches zero for arrays with less than five sensors, since, from equation 8.30, $n \geq f_2/f_1 + 1 = 5$. (Numerical errors prevent the curves from reaching the exact limit.)

It is apparent that the spread of velocities has a significant effect on the number of sensors for a specified success rate. This corresponds to the increasing size of 'plateau region' with number of sensors (*eg* figure 8.14). By performing simulations with various values of the mean velocity $\bar{V}$, it was found that the success rate graphs are almost identical for a broad range of speeds [438].

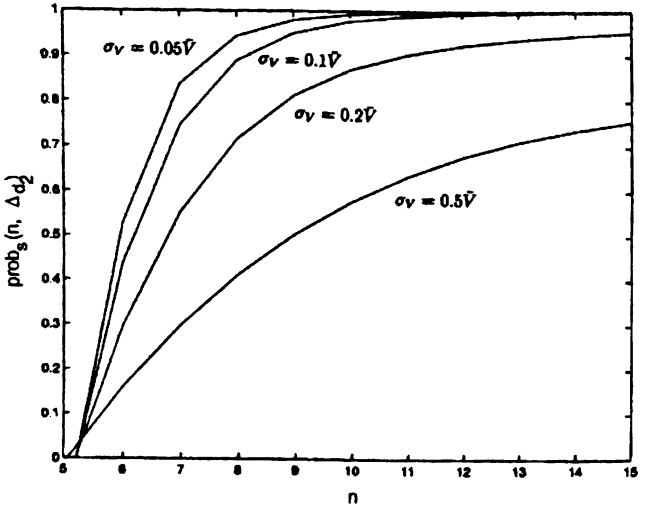


Fig. 8.20 The success rate $Prob_s\left(n, \Delta_{d_2}\right)$ vs the number of sensors, for various values of σ_V, using the same parameters as in figure 8.19. From [438].

8.6.3 Design Procedure

Making use of the results in the previous two sections, a new design procedure for high reliability MS–WIM systems can be defined.

1. Specify the minimum acceptable probability of successful weighing.
2. Define prior information:
   - Distribution of vehicle speeds $\bar{V}$ and σ_V
   - Distribution of low dynamic loading frequencies $\bar{f}_1$ and σ_{f_1}
   - Distribution of high dynamic loading frequencies $\bar{f}_2$ and σ_{f_2}.

   Note that reasonable values of $\bar{f}_1$ and $\bar{f}_2$ can be obtained from the literature (Section 7.4.3).
3. Plot the graph of $Prob_s\left(n, \Delta_{d_2}\right)$ vs number of sensors, (equation 8.38 and figure 8.20).
4. Determine the number of sensors required to achieve the desired success rate from the graph.
5. Calculate the design spacing using equation 8.29.

8.7 CONCLUSIONS

(i) Various sources of random and systematic errors in WIM arrays have been identified and characterised. The output of a single-sensor WIM system is always a biased estimate of the static load.

(ii) A simple equation defining a good design spacing for the sensors in a multiple-sensor WIM system was derived from theoretical considerations and verified by experiments with a load measuring mat.

(iii) Arrays with 3 or more evenly-spaced sensors will be more robust to speed and frequency variations than 2-sensor systems.

(iv) A good design choice for low-cost MS–WIM systems is to use 3-sensor arrays. These are likely to give RMS errors of 1/3 to 1/2 of the errors for single-sensor systems. With this arrangement it should be possible to measure routinely the static axle loads of vehicles travelling at highway speeds with RMS errors of approximately 5-8% (compared with 12 to 29% for existing systems).

(v) The calibration of the capacitative strip sensors in the load measuring mat was found to be independent of: (a) vehicle speed in the range 8-80 km/h, (b) mat surface temperature in the range 15-40 °C, (c) long term drift. The average sensor baseline error due to noise was found to be less than 4% RMS.

(vi) The strip sensors were found to be inaccurate for tyres with an off-road tread pattern. This effect is a fundamental limitation of strip WIM sensor technology and is expected for any tyre of strip transducer.

(vii) High reliability WIM arrays can be designed using a new theory which accounts for both high and low frequency dynamic tyre force components. The number of sensors can be chosen to ensure any desired level of 'success' by the weight estimation algorithm. The higher the specified success rate, the more sensors are required. Typical arrays might have 10 or more equally–spaced sensors. They are expected to achieve measurement errors of around 2–3% RMS for vehicles which generate large amplitude, high frequency wheel forces.

PART 3 - GUIDEWAY RESPONSE

9

BACKGROUND TO GUIDEWAY RESPONSE

9.1 SUMMARY

Some of the literature concerning the response of road and bridge surfaces to moving dynamic loads is reviewed. The principal characteristics of the response of road surfaces to vehicle loads are discussed, and mathematical models of static and dynamic road and bridge responses are reviewed.

9.2 PRINCIPAL FEATURES OF ROAD SURFACE RESPONSE

Since the AASHO road test [8] the *fourth power law* has been used widely by highway engineers to predict the expected life of pavements, for the optimisation of pavement designs, for comparing the amount of damage caused by different vehicles, and for establishing legislative and taxation systems.

A consequence of a high power in the damage law is that road damage calculations are very sensitive to the magnitude of the primary response of the pavement (stresses, strains and displacements). Therefore, in order to understand the importance of dynamic tyre forces on pavement damage and to assess the 'road–friendliness' of vehicles, it is necessary to predict accurately the primary responses of roads caused by fluctuating, moving axle loads. These responses are known to depend on the speed of the vehicle as well as the magnitude and frequency content of the loads, because of the rate–dependent properties of asphalts and soils, and inertia effects in the road structure.

This section reviews important features of the response of road surfaces to vehicle loads.

9.2.1 Linearity

Although granular pavement materials are essentially nonlinear [72, 78, 458], deflections in flexible and rigid pavements are usually sufficiently small under vehicle loading for the assumption of static linearity to be valid [8, 109, 166, 447]. Hardy and Cebon [220] showed that an instrumented pavement section used in their experiments was linear over a wide frequency range for impulsive loading. (See next chapter).

9.2.2 Dynamic Coupling

The responses of road surfaces and the dynamics of vehicles are essentially uncoupled. This is because: (i) the displacement of road surfaces is considerably smaller than the deflections of truck tyres and suspensions, and (ii) the speed of propagation of elastic waves in road surfaces is in the range 100-600 m/s (225-1350 mph) [266, 345], which is significantly greater than vehicle speeds. As a result of the weak coupling between the two systems it is reasonable to assume that the road surface is rigid when simulating the response of a vehicle to road roughness, and to treat the vehicle as a set of moving dynamic loads when calculating the response of the road surface.

9.2.3 *Effect of Speed and Frequency*

Road materials and structural responses are sensitive to vehicle speed [6, 8, 46, 109, 220, 226] and to the frequency content of the applied loads [220, 344, 358, 433]. Figure 9.1, which is reproduced from Harr [226], shows the effect of speed on pavement deflection, as measured in the AASHO road test [8]. As the speed increases, the peak strain under a constant moving load diminishes in amplitude and occurs behind the point of application of the load (see also [180, 220, 490]). This 'speed effect' is important when considering the road damage caused by dynamic tyre forces, because fatigue damage incurred by road materials is very sensitive to strain amplitude which in turn changes with speed. (This is discussed in Chapter 17.)

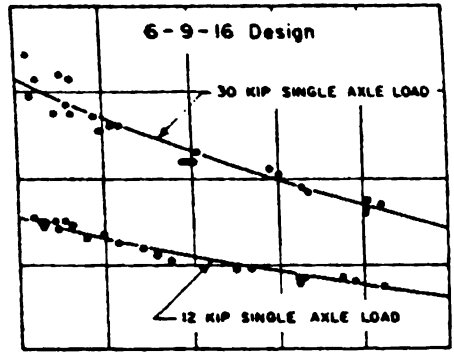


Fig. 9.1 The effect of vehicle speed on peak road surface deflection in the AASHO road test. From [226].

According to limited data presented by Görge [200] (also Hahn [213]) and by Christison and Woodrooffe [110], a linear correlation has been observed between dynamic wheel loads and peak dynamic pavement response (normalised to account for the effects of speed). One such result, reproduced from [110] is shown in figure 9.2. Although there is clearly some correlation between the dynamic load (impact factor) and the normalised pavement deflection, there is also considerable scatter on the measurements. Christison's conclusion of a linear relationship is misleading, because the apparent scatter is mostly caused by the frequency dependence of the pavement response, in addition to random experimental errors. This issue is discussed in detail in the next chapter.

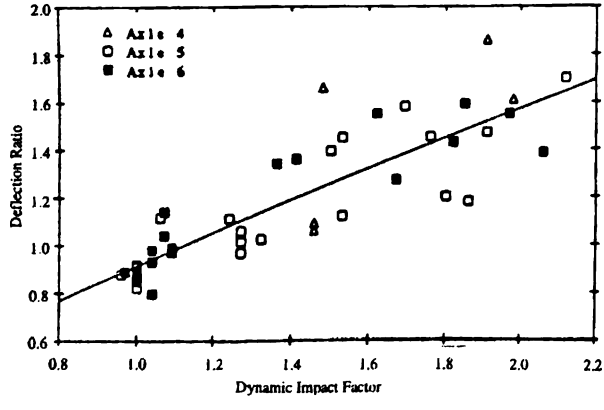


Fig. 9.2 Relationship between measured dynamic wheel load (impact factor) and measured flexible pavement deflection, normalised to account for the effect of speed, for a range of vehicle speeds. From [110].

9.2.4 Variability

Pavements are essentially variable in nature with properties that change significantly due to layer thickness and material property fluctuations [19, 262, 294]. An example of this variability is given in [19] which provides extensive data on the variation in properties of a special purpose test track: layer thicknesses – typically ± 20%; moduli – typically ± 30%; and deflection under a standard load – typically ± 25%. In a study performed by the TRRL in the UK [179], a radar technique was used to measure the thickness of a number of in-service motorways at 1m intervals. The measured coefficients of variation of the asphalt layer thicknesses were found to range from 3.7% to 6.7% (*ie* ± 11% to ± 20%, for 3 standard deviations) for asphalt layers with mean thicknesses of 240 to 430 mm. In a similar study in the USA, Maser *et al* [325] reported that one asphalt pavement of nominal thickness 200 mm varied from 178 to 241 mm, *ie* -12% to +15%. McLellan and Still [331], noted that thickness variations in five measured test sections were generally within the specification of the construction contract and that the variation in thickness of Portland Cement Concrete road surfaces was generally greater than for asphalt pavements.

9.2.5 Isotropy

The structural isotropy of a road is dependent on the local variation of its construction and materials. However, despite the variability described above, measurements by Hardy and Cebon [220] indicated that the dynamic primary response of an experimental test pavement was reasonably isotropic over short distances, up to 2 m. (See also next chapter.)

9.2.6 Effect of the Environment on Properties

Road construction materials, and road surface responses, are extremely sensitive to environmental factors, particularly moisture [8, 26, 72, 259, 306, 368], temperature [8, 19, 109, 166, 220, 259, 306], and freezing [8, 248, 259]. For example, Hardy and Cebon [222] found that the response of an instrumented test pavement was very sensitive to temperature, with approximately a factor of four variation in soil strain response for a surface temperature range of 13 to 42 °C (55 to 108 °F). Jackson [20] quoted similar stiffness variation with temperature.

9.3 MODELLING PAVEMENT RESPONSE

9.3.1 Static Road Response Models

Civil engineers have traditionally considered the structures of road surfaces to behave as continua, and have used the methods of continuum mechanics. The first such analysis was performed in 1926 by Westergaard who modelled a rigid pavement as an elastic plate supported by a Winkler foundation [489]. In the 1940's the theory of elastic layered systems was published by Burmister [82]. This theory enabled the analysis of pavement systems with 2 or 3 layers of infinite extent and accounted for the effects of the interface conditions between layers.

There has been a proliferation of computerised pavement analysis systems which use elastic layer theory for flexible pavement design and life prediction (see, for example, [66, 78, 344, 455, 473]). Tyre loading is usually modelled as a circular area with uniform contact pressure. The finite element method has also been used extensively (*eg* [1, 352, 384, 389, 458]) and is particularly useful for analysis of jointed rigid pavements which can be prone to thermal warping (curling) as well as being subject to vehicle loads [1, 45, 344]. Almost all of the models assume linear material properties. Some models include viscoelastic effects, (see, for example [46, 257, 294, 458, 490]). Many of the elastic layer calculations incorporate the effects of speed on flexible pavement response, by increasing the equivalent layer moduli with increasing vehicle speed (see for example, [294, 367, 454]), or with increasing frequency [344].

A review of computer packages for calculating static pavement response and predicting distress (damage) was presented by Rauhut, Roberts and Kennedy in 1979 [384]. See also [16, 367, 454] for further information on this subject.

9.3.2 Dynamic Road Response Models

The importance of road dynamics in calculating the stresses and strains induced by a moving vehicle has also been investigated (see [219] for a review). Methods for predicting the response of continuous pavements (flexible or un–jointed rigid) have, however, been limited by the complexity of a full analytical solution.

The most common approaches have been to use either an analogous mechanistic model with discrete masses, viscous dampers and springs [6, 226, 280] or to modify a layered elastic response model by introducing material properties that depend on vehicle speed [277, 344, 469] or the effective frequency of dynamic loads [344]. Such methods are, at best, a qualitative representation of dynamic response and few can accommodate dynamic loads.

There have been efforts to develop realistic dynamic road response models. In order to simulate the effects of moving vehicles, some authors have considered linear systems subjected to a constant moving force. Examples of such models are a beam [185, 359] or plate [185] supported by a (damped) Winkler foundation [280] or half–space [185]. [46], simulated a pavement consisting of two viscoelastic layers with a sinusoidally varying surface load.

The calculations vary in complexity according to the nature of the layers (elastic, damped elastic, viscoelastic) and the surface loading (moving, constant, sinusoidal). Few layered models include the effects of time varying moving loads and damping or viscoelasticity, because no closed-form solutions exist [416]. Kausel *et al* [273] overcame this problem by deriving the Green's functions[1] of a damped, elastic, layered structure built on a rigid base, assuming linear displacement variation through the thickness of each layer.

To calculate the response of a pavement using Kausel's formulation and ensure numerical convergence, it is necessary to model the structure with many thin layers. This method was used by Sebaaly and Mamlouk [416] to calculate the harmonic response of a road surface to a circular applied load of radius a. They then determined the response to a pulse of duration $2a/V$, (V is the speed), using Fourier transform techniques. Peak theoretical vertical pavement deflections were compared with 'speed effect' data from the AASHO road test [8] (similar to that presented in figure 9.1). Correlations were found to be good and the reduction of pavement deflection with speed was shown clearly by their results.[2]

This method only approximates the physics of dynamic vehicle/road interaction, however, because each axle influences the road surface near a particular point for considerably longer than the time taken to travel one tyre contact length, and the vehicle speed has an additional 'Doppler shift' effect on the effective frequency of the applied loads [219]. Sebaaly and Mamlouk [416] really simulated the response of the road to a 'hammer blow' rather than a moving wheel.

Govind and Walton [202] used the theory derived by Kausel *et al* [273] to calculated the response of a road surface to a set of constant moving loads, using a Fourier transform technique. They did not present any experimental validation of their approach, or justification of their choice of model parameters. Like other dynamic calculations, it appears that Govind and Walton's calculation procedure is expensive in terms of storage requirements and calculation time: *"Because of the*

---

[1] Green's functions are displacements due to a unit load.

[2] In 1962, Harr [226] presented an idealised model of the dynamic response of a pavement consisting of a heavily damped single degree-of-freedom oscillator (mass, spring, damper) subjected to a rectangular pulse of duration $6/V$ secs (ie he assumed a 6m long load). By suitable selection of model parameters, he was also able to achieve close correlation with the same AASHO road test results.

program's large memory requirements, it can be executed on only mainframe computers with one or more Gigabytes of memory. The typical execution time on the CRAY-XMP is about 1,000 sec for a 5-axle vehicle driven over 100ft with 40 discrete frequencies sampled every 0.1 sec" [202].

No papers were found in the literature which analysed the dynamic response of a realistic layered road model to moving steady or random forces. However, there are two solutions for the dynamic response of a continuous system to moving random loads:

(i) Fryba calculated the covariance of the response of a beam on a Winkler foundation which had statistically varying stiffness to a statistically stationary 'ergodic' force moving along it at constant velocity [185]. He did not extend the model to two or three dimensional systems.

(ii) Cebon [88, 92] calculated the dynamic response of linear isotropic road surfaces to moving dynamic ('random') loads by numerically convolving the applied dynamic loads with a field of road surface impulse response functions. The method is sufficiently general to predict the effects of vehicle speed, frequency of loading and combinations of these factors on pavement response, for any number of moving axles. This method is described in Chapter 10.

9.3.3 Experimental Validation

Static Models

Relatively few of the primary response models have been validated by comparison with field measurements. Valkering [474] was able to show reasonable qualitative agreement between measured and computed strains in a layered elastic system subjected to vertical and longitudinal static surface loads. Ullidtz and Busch [468] achieved partial agreement with measurements of vertical stress and strain in a flexible road and attributed the errors to spatial variations in the subgrade modulus. Battiato *et al* [46] described a two layer mathematical model of a steel bridge deck consisting of a rigid base with a single viscoelastic asphalt surface layer. They achieved good agreement between measured and predicted strains for a wheel load moving at 5 km/h. Large viscoelastic effects were observed in their results. Barenburg [45] discussed a validation study in which the strains determined by a finite element model of a jointed concrete pavement agreed moderately well with strains due to static wheel loads and thermal expansion effects.

There are probably other examples of 'primary response' validation of static road response models in the highway engineering literature. However, considering the widespread use of such models for pavement design and analysis, there appear to be surprisingly few papers which address this subject.

In general, the agreement between experiment and theory has been qualitative and for low speeds only. There are two main reasons for this. Firstly, there are significant difficulties in measuring the primary response of roads accurately. This is highlighted in an OECD report [19] which shows large discrepancies (up to a factor of two) between the outputs of various types of buried strain gauges, for 'identical' measurement conditions. Secondly, vehicles travelling at highway speeds generate substantial dynamic tyre forces even for the smoothest road surfaces. These forces appear as random errors in the pavement simulation, unless they are measured and taken into account.

Dynamic Models

A model validation study for a dynamic model of flexible pavements, by Hardy and Cebon [222], is described in Chapter 10. A similar study, for a jointed rigid (PCC) pavement, by Nasim *et al* [352] is described in Chapter 11.

9.4 MODELLING BRIDGES

Over the last 150 years, many researchers have studied bridge dynamics. The first recorded research into bridge vibration appears to be a report published in 1849 by Willis [495], which discussed the causes of the collapse of the Chester Railway Bridge. Over the next century, investigations into bridge dynamics were mainly concerned with developing analytical solutions for simple cases of moving forces. Digital computers introduced a new level of detail in bridge vibration research because the complexities of bridge and vehicle systems could be modelled in detail.

9.4.1 Bridge Model Validation Studies

Early studies of bridge-vehicle system dynamics concentrated on simply-supported bridges traversed by simple vehicle models (see for example, Biggs *et al* [58]). Investigations arising out of the AASHO road test extended these analyses to 3-span continuous and cantilever bridges with more complicated vehicle models [480]. More recently, orthotropic plate theory has been applied to the dynamic analysis of bridges in an attempt to account for two-dimensional behaviour [291, 357]. Most of these studies have used simplistic vehicle models and the equations of motion have been solved by numerical integration. Such time domain calculations can be computationally expensive. Very few of the bridge simulations have been verified experimentally.

The study by Biggs *et al* [58] contained one of the first validations of a bridge-vehicle system. The models were simple. Only simply-supported bridges were considered, and the vehicle models were restricted to one degree of freedom. Both laboratory and field experiments were included in the validation. They concluded that most of the errors were caused by improper modelling of the vehicle and of the bridge surface roughness. The validation was successful, but the simplicity of the models restricts their applicability to modern vehicles and bridges.

Validations with more complicated models were conducted in Australia. Swannell and Miller [441] considered a two-axle, four degree of freedom vehicle including non-linear suspension stiffness. They used a lumped mass model for the bridge. Viscous damping was assumed throughout. The surface profile of the bridge was measured, and bridge responses from the passage of a test vehicle were recorded. The recorded responses were compared with the computer simulations. Reasonable agreement between theory and experiment was obtained, but significant discrepancies were noted. Mulcahy *et al* [348] used similar models, but were more successful in their validation.

This brief summary of vehicle-bridge model validations indicates a need for validated models of bridges and vehicles representative of those currently in use. Such a validation study, for a dynamic bridge model, is described in Chapter 12. The model is then used in Chapter 22 to investigate the influence of leaf spring and air spring suspensions on bridge responses.

9.4.2 Dynamic Interaction Between Vehicles and Bridges

Figure 9.3 is a schematic diagram of bridge-vehicle interaction. The roughness input to the *vehicle* is the sum of the initial surface profile of the *bridge* and the dynamic deflection of the *bridge*. This input excites vertical vibration of the *vehicle* and results in dynamic tyre forces. These forces are in turn applied to the *bridge* and cause larger dynamic displacements of the *bridge*. This feedback mechanism of interaction forces couples the dynamic response of the bridge to that of the vehicle.

The largest bridge vibrations are known to occur when the natural frequencies of the bridge and vehicle are close together [60]. It is not clear, however, under what circumstances large bridge responses are mainly due to excitation of the vehicle by the initial roughness profile, or due to excitation substantially by dynamic deflection of the bridge. The former case can be considered as the feedback loop in figure 9.3 being cut at point 'A'. There has been little systematic study about when dynamic interaction is important, and when the two systems can be considered to be essentially uncoupled (as in the case of pavement response to vehicle loads).

Walker and Veletsos [484] considered the response of a simply-supported bridge to a moving constant force and to a moving sprung mass. They compared the two responses by computing the maximum *dynamic increments* for each case.

They defined the maximum dynamic increment as:

$$DI = \frac{y_{max} - y_{st}}{y_{st}}, \tag{9.1}$$

where DI is the maximum dynamic response increment,
y_{st} is the maximum bridge response to the static wheel loads,
and y_{max} is the maximum dynamic response of the bridge.

They related the importance of interaction to the frequency ratio, γ, defined as

$$\gamma = \frac{\omega_v}{\omega_b}, \tag{9.2}$$

where ω_v is the natural frequency of the vehicle and ω_b is the first natural frequency of bending of the bridge. Bridge-vehicle interaction was deemed unimportant when γ was less than 0.3 or greater than about 1.0 [484]. This criterion seems reasonable, but Walker and Veletsos did not quantify the errors incurred by neglecting bridge-vehicle interaction.

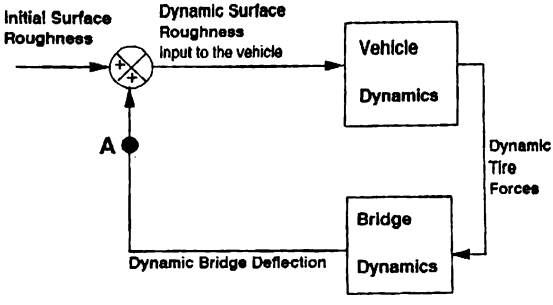


Fig 9.3 Schematic block diagram of dynamic bridge-vehicle interaction. From [206]

Chiu, Smith, and Wormley [106] conducted a parametric study similar to that of Walker and Veletsos for an elevated guideway traversed by a high-speed vehicle. They found that dynamic interaction was unimportant when the ratio of the vehicle mass to the mass of the guideway span was below 1/8, or when the frequency ratio γ was low. Most of their results were calculated for relative speeds far in excess of those usual on highway bridges. Their criteria are consistent with those of Walker and Veletsos, but do not provide enough detail for low speeds.

Ting and Genin [463] outlined interaction criteria based on the quantity $2\varepsilon\ddot{Z}$ where ε is the vehicle/bridge mass ratio, and $\ddot{Z}$ is the second time derivative of the vehicle displacement normalised by the maximum static deflection of the bridge. They concluded that interaction can be ignored if $2\varepsilon\ddot{Z} << 1$. Although this may be valid, it is based on vehicle 'acceleration' which is unknown for highway bridges.

Green and Cebon [206] performed a systematic interaction study. They used the response calculation method described in Chapter 12, with a simple, single degree-of-freedom vehicle model. A number of non-dimensional parameters of the bridge-vehicle system were varied to assess the amount of dynamic interaction between the vehicle and the bridge.

The parameters included the frequency ratio γ described by equation 9.2, a speed parameter α, defined by

$$\alpha = \frac{\pi V}{\omega_b L}, \tag{9.3}$$

(L is the length of the span); a mass parameter, κ, the ratio of the modal mass of the vehicle to that of the bridge:

$$\kappa = \frac{2m_v}{mL}, \tag{9.4}$$

and the damping ratios of the bridge ζ_b and vehicle ζ_v.

The main results of [206] are that within the normal range of parameters on highway bridges, the most important parameters are speed, frequency, and initial vehicle excitation. Large mass ratios result in a significant interaction at high speeds. Bridge and vehicle damping are important when the frequency ratio is near unity. Furthermore the coupling of the bridge and vehicle systems generally tends to *reduce* the dynamics of the bridge compared to the case when the interaction is ignored.

Green and Cebon [206] concluded that dynamic interaction between the vehicle and bridge can be ignored if:

(i) $\gamma < 0.5$, or

(ii) $\alpha < 0.1$ and $\kappa < 0.3$ for smooth bridge profiles.

In general, short-span highway bridges do not satisfy these conditions, and it is therefore concluded that the interaction effects need to be considered in most simulations of vehicle-bridge systems.

10

RESPONSE OF CONTINUOUS PAVEMENTS

10.1 SUMMARY

A linear theory of the primary response of continuous pavements to moving dynamic loads is presented. The theory is derived from the well-known convolution integral. Its practical implementation is explained and validation experiments, involving an instrumented vehicle driving over an instrumented test track, are described. The results demonstrate that the theory can be used to predict accurately the strains generated in a road as a vehicle drives over, including the effects of vehicle speed and dynamic tyre forces.

The influence of vehicle speed and loading frequency are examined. The dynamic calculation procedure is then simplified to provide a 'quasi-dynamic' calculation which accounts for vehicle speed, but not for the dependence of road response on loading frequency. The simplification decreases the necessary computer resources significantly. The validity of the simplification is tested by comparing primary road responses and fatigue damage predicted by the two methods, for theoretical wheel loads generated by two representative mathematical vehicle models. It is found that differences in response are observable, but in practical situations they are likely to be small. It is concluded that the simplified 'quasi-dynamic' calculation approach is preferable.

This chapter is based on work previously published in [92, 222, 223]

10.2 INTRODUCTION

10.2.1 Motivation

Accurate and efficient calculation of primary road responses is the main motivation for the research described in this chapter. To study the road-damaging effects of dynamic tyre forces, it is important that pavement response models accurately account for the effects of vehicle speed and the frequency content of dynamic loads. However, there is no consensus in the literature as to whether comprehensive dynamic road response models are needed in order to include the effects of frequency, speed and structural dynamics rigorously; or whether approximate calculations, which neglect one or more of these factors, can be sufficiently accurate.

10.2.2 Speed and Frequency

The effect of vehicle speed on pavement response has been the focus of several studies, but authors have drawn contradictory conclusions: some have concluded that induced stresses increase with speed [105, 342, 344, 415, 421] whilst others have concluded that strains or displacements decrease [6, 9, 46, 186, 226, 353, 415, 447, 458] or that pavement stiffness increases [367, 436].

Theoretical work by Chen *et al* [105, 432] showed that theoretical stresses in pavements under moving loads increased by only 7% (from 0 to 27m/s). They therefore suggested that it was not necessary to include speed in pavement response calculations. Conversely, measurements of surface

deflection during the AASHO road test [9] were observed to more than halve over this speed range and decrease by up to 40% between 0 and 18m/s [226]. Nazarian *et al.* [353] measured a 10% reduction in surface deflection between just 1.6 and 3.3m/s.

Cebon performed a theoretical study [93] in which he showed that under some conditions, the increase in dynamic loads with speed can increase theoretical road damage significantly. However, at high speeds, road damage may decrease somewhat because of the reduction in road response with speed. This also indicates the importance of accounting for vehicle speed correctly in road damage calculations.

Sousa *et al.* [432] used a road model that included frequency–dependent material properties in order to examine the 'road–friendliness' of several suspensions. They identified the 'predominant frequency' in the dynamic tyre forces of three different suspensions (2Hz for a torsion–bar suspension, 4Hz for a four–leaf suspension and 8Hz for a walking–beam) and then added an extra 5Hz to each identified frequency in order to make some allowance for the speed of the vehicle. The static load was superimposed with an equivalent frequency of 5Hz. (Clearly the dynamic wheel loads contain a spectrum of frequencies (see Chapter 7), even if one frequency component does appear to dominate, so this approximate correction can never yield a theoretically correct response.)

There are several reasons for the confusion over this issue:

(i) Theoretical calculations of dynamic road responses can yield different conclusions depending on the details of the road model, especially the representation of the frequency dependence of material properties, and the response component investigated: stresses, strains or displacements.

(ii) Dynamic tyre forces generated by heavy vehicles have relatively complicated frequency spectra, which are functions of the vehicle design, the vehicle speed and the roughness of the road surface. It is important to use tyre forces with realistic frequency contents, if the correct conclusions are to be drawn about the importance of loading frequency on road response.

(iii) Road material damage, particularly fatigue, is very sensitive to stress and strain level. Laboratory fatigue lives of asphalt specimens typically decrease with the fourth or fifth power of the strain level [183]. Relatively small errors in primary response predictions due to dynamics can therefore be amplified into large errors in predicted road service lives.

The only way to include the effects of pavement dynamics, speed and frequency rigorously in road response calculations is to use a validated dynamic road response model.

The analysis described and validated in this chapter is an extension of the numerical convolution theory [93] and provides a method for calculating the primary responses of continuous pavements to moving dynamic surface loads. It is sufficiently general to predict the effects of vehicle speed, frequency of loading and combinations of these effects on pavement response. The method lends itself to experimental validation, because it accounts for the influence of dynamic loads, and implicitly removes the effects of systematic strain measurement errors. The theory is used to examine the relative importance of vehicle speed, frequency and of structural dynamics in calculations of road response and damage due to dynamic vehicle loads.

The calculation method is equally valid for full depth asphalt ('flexible') pavements, and continuous (non-jointed) composite and rigid Portland Cement Concrete (PCC) pavements. Note that continuous PCC pavements, are likely to behave in an essentially elastic way, so that the effects of speed and frequency on primary pavement responses will be considerably smaller than for the flexible pavement investigated here.

It is shown that it is generally *not* necessary to use dynamic road response models: sufficiently accurate predictions of road damage can be made with efficient 'quasi–dynamic' calculations, which include the effects of vehicle speed, but do not include the frequency dependence of pavement response.

10.3 THEORETICAL RESPONSE OF A ROAD SURFACE TO MOVING DYNAMIC LOADS

10.3.1 Response in the Time Domain

The response of a linear system to a time-varying input is given by the convolution integral [355]:

$$y(t) = \int_{-\infty}^{t} h(t-\tau) f(\tau) d\tau \qquad (10.1)$$

where $y(t)$ is the response at time t,
$f(\tau)$ is the input force at time τ, and
$h(t)$ is the response at time t to a unit impulse at time t = 0.

If the input is moving with respect to the system so that its position is given by the vector $\mathbf{r}_f(t)$ at time t, and the response is measured at a point with position vector $\mathbf{r}_y$ (see figure 10.1), the impulse response function becomes dependent on three variables, and is given by $h(\mathbf{r}_y, \mathbf{r}_f, t)$. The convolution integral in equation 10.1 then becomes:

$$y(\mathbf{r}_y, t) = \int_{-\infty}^{t} h(\mathbf{r}_y, \mathbf{r}_f(\tau), t-\tau) f(\tau) d\tau \qquad (10.2)$$

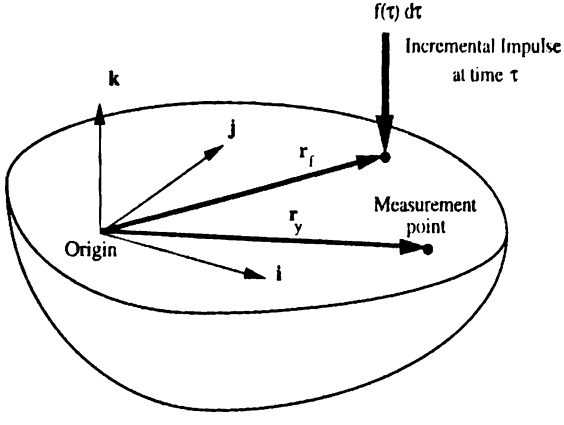


Fig. 10.1 Linear system with a moving load.

If the system has N_f inputs: f_m, m=1,2,... N_f, with positions $\mathbf{r}_{fm}$, then the total response can be calculated by summing the responses to each individual input:

$$y(\mathbf{r}_y, t) = \sum_{m=1}^{N_f} \int_{-\infty}^{t} h(\mathbf{r}_y, \mathbf{r}_{fm}(\tau), t-\tau) f_m(\tau) d\tau \qquad (10.3)$$

This is a general expression for the response of a linear system to a set of moving inputs. A number of simplifying assumptions can be made when it is used to calculate the response of a road due to a passing vehicle:

(i) If the road is isotropic, the response is not a function of the output position but only of the separation of the input and output. In this case

$$h(r_y, r_{fm}(\tau), t - \tau) = h(r_y - r_{fm}(\tau), t - \tau). \tag{10.4}$$

(ii) If the input is the force applied by the tyre of a vehicle that is moving at constant velocity then

$$r_{fm}(t) = r_{fm}(0) + Vt \tag{10.5}$$

where $r_{fm}(0)$ is the position of the force at time $t = 0$
and V is the velocity vector of the vehicle.

(iii) If all the inputs act along the same line and the response is also required on that line (*ie* each wheel follows the same path as the one in front of it and the road response is required on this wheel-path) then axes may be chosen so that all position vectors are co–linear and parallel with the velocity vector. In this case the problem is confined to one space dimension (x say) and position vectors may be reduced to ordinates along the x–axis:

$$\begin{aligned} y(r_y, t) &= y(x, t) \\ h(r_y - r_{fm}(\tau), t - \tau) &= h(x - (d_m + v\tau), t - \tau) \end{aligned} \tag{10.6}$$

where $y(x, t)$ is the response at position x at time t,
d_m is the position of tyre m at time zero: $d_m = r_{fm}(0)$,
v is the vehicle speed,
$h(x, t)$ is the response at position x and time t to a unit impulse at the origin at time $t = 0$.

Under these conditions equation 10.3 becomes

$$y(x, t) = \sum_{m=1}^{N_f} \int_{-\infty}^{t} h(x - (d_m + v\tau), t - \tau) f_m(\tau) \, d\tau. \tag{10.7}$$

This equation is similar to that derived by [93], where it was used to find the response of a continuously supported beam to arbitrary, moving excitation.

10.3.2 Response in a Moving Frame of Reference

Equation 10.7 gives the response at a position x fixed on the road. It is sometimes more convenient to calculate the response at a point moving with the load, for example the response under a tyre.

The position of a point moving with the lorry is defined by $\hat{x} = x - vt$. Substituting this into equation 10.7 gives an alternative equation for the response of the road at a point moving with the vehicle:

$$y(\hat{x}, t) = \sum_{m=1}^{N_f} \int_{-\infty}^{t} h(\hat{x} - d_m + v(t - \tau), t - \tau) f_m(\tau) \, d\tau. \tag{10.8}$$

10.3.3 Frequency Domain Solution of the Moving Convolution Integral

The simple convolution integral, equation 10.1, is often solved in the frequency domain using the Fourier transform, because the transform of the integral reduces to a simple multiplication [355]. The same technique can be used to simplify the moving convolution integral (equation 10.7) but it is necessary to take Fourier transforms with respect to both time and space variables as follows:

$$Y(\xi, \omega) = \left(\frac{1}{2\pi}\right)^2 \int\int_{-\infty}^{\infty} y(x, t)\, e^{-i\omega t}\, e^{-i\xi x}\, dt\, dx$$

$$= \left(\frac{1}{2\pi}\right)^2 \sum_{m=1}^{N_f} \iiint_{-\infty}^{\infty} h(x - (d_m + v\tau), t - \tau)\, f_m(\tau)\, e^{-i\omega t}\, e^{-i\xi x}\, d\tau\, dt\, dx \qquad (10.9)$$

$$= 2\pi \sum_{m=1}^{N_f} H(\xi, \omega)\, F_m(\omega + v\xi)\, e^{-i\xi d_m}$$

where ω is the angular frequency of loading, corresponding to the time t,
ξ is the wave number, corresponding to the distance x,
$H(\xi, \omega)$ is the two–dimensional Fourier transform of $h(x, t)$,
$F_m(\omega)$ is the Fourier transform of $f_m(t)$.

It is apparent that the term $v\xi$ is an effective frequency or 'Doppler shift'. A similar derivation from equation 10.8, for the convolution in the moving frame of reference, yields a similar solution in the frequency/wave-number domain:

$$\hat{Y}(\xi, \omega) = 2\pi \sum_{m=1}^{N_f} H(\xi, \omega - v\xi)\, F_m(\omega)\, e^{-i\xi d_m} \qquad (10.10)$$

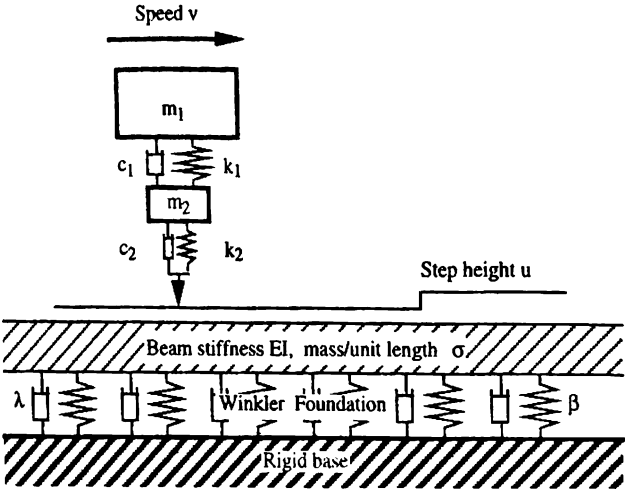
where $\hat{Y}(\xi, \omega)$ is the Fourier transform of $y(\hat{x}, t)$.

If the set of loads and impulse response function are described by analytical expressions, the response may be evaluated by direct integration of equation 10.7 or 10.8, or by using (discrete) Fourier transforms and evaluating equation 10.9 or 10.10. In order to calculate the Fourier transforms in equations 10.9 and 10.10, the wheel loads must be either periodic or transient (die away in a finite time[1]). The Fourier transforms do not exist for statistically 'stationary' random loads [355].

10.3.4 Example: Frequency Domain Calculation of Road Response to Transient Loads

The following is a sample calculation of the response of a road to transient dynamic wheel loads, using the frequency domain calculation described in the previous section. In order to illustrate the method, the simplest possible road and vehicle response models are used. The road model is an Euler beam supported by a damped elastic (Winkler) foundation [93]. The vehicle is a linear 'quarter–car' model, with parameter values typical of one wheel–station of a heavy commercial vehicle. The vehicle is excited by a step–up of height $u = 10mm$ in the road surface profile. The models and parameter values are shown in figure 10.2.

[1] The wheel loads may have a steady (DC) offset because this can be considered as 'periodic' with zero frequency.



$m_1 = 4450$ kg	$k_1 = 1\,000$ kN/m	$c_1 = 15$ kNs/m	EI = 1.38 MNm^2	$\beta = 170$ MN/m^2
$m_2 = 550$ kg	$k_2 = 1\,750$ kN/m	$c_2 = 2$ kNs/m	$\sigma = 353$ Mg/m	$\lambda = 1$ MNs/m^2

Fig. 10.2 Model and parameter values for transient road response calculation. From [222].

The equation of motion of the beam is:

$$EI\frac{\partial^4 y}{\partial x^4} + \sigma\frac{\partial^2 y}{\partial t^2} + \lambda\frac{\partial y}{\partial t} + \beta y = f(x,t) \tag{10.11}$$

where y(x, t) is the vertical displacement of the beam and f(x, t) is the applied tyre force.

In order to evaluate equation 10.10, it is necessary to determine $F(\omega)$ (the one dimensional Fourier transform of the dynamic tyre force time history), and $H(\xi, \omega)$ (the two dimensional Fourier transform of road surface impulse response function). $H(\xi, \omega)$ is essentially the harmonic response function[1] and is given by:

$$H(\xi,\omega) = \frac{1}{2\pi(EI\xi^4 - \omega^2\sigma + i\omega\lambda + \beta)}. \tag{10.12}$$

$F(\omega)$ is the product of the Fourier transform of the step input and the vehicle response transfer function relating tyre forces to road surface displacements. For the simple 'quarter–car' vehicle model, this gives:

$$F(\omega) = \frac{\frac{u}{2\pi}k_2\left[-i\omega^3 m_1 m_2 - \omega^2 c_1(m_1+m_2) + i\omega k_1(m_1+m_2)\right]}{\left[\begin{array}{l}\omega^4 m_1 m_2 - i\omega^3(m_1c_1 + m_2c_1 + m_1c_2)\\ -\omega^2(m_1k_1 + m_2k_1 + m_1k_2 + c_1c_2)\\ +i\omega(c_1k_2 + c_2k_1) + k_1k_2\end{array}\right]} + (m_1+m_2)g\,\delta(\omega). \tag{10.13}$$

[1] The harmonic response function differs from the Fourier transform of the impulse response function by a factor of $(1/2\pi)$ [355].

The last term, containing the Dirac delta function $\delta(\omega)$, is the Fourier transform of the static wheel load, $(m_1 + m_2)\,g$, where g is the acceleration due to gravity. Combining $H(\xi, \omega)$ and $F(\omega)$ according to equation 10.10 gives the Fourier transform of the beam displacement response, in a frame of reference moving with the load at speed v.

The inverse Fourier transform, required to determine $y(\hat{x},t)$ from $\hat{Y}(\xi,\omega)$ in equation 10.10 can be evaluated using a two–dimensional fast Fourier transform (FFT) algorithm. In order to generate *real* responses, the function $H(\xi, \omega-v\xi)F(\omega)$ must be sampled at a grid of points and formed into a symmetric 'Hermitian' array, before transformation (see [355] for details).

This procedure was carried out for the vehicle and beam with parameters shown in figure 10.2. The displacement of the beam immediately under (and moving with) the load was found at various speeds and the responses of the beam for speeds of 10, 20 and 30 m/s are shown in figure 10.3.

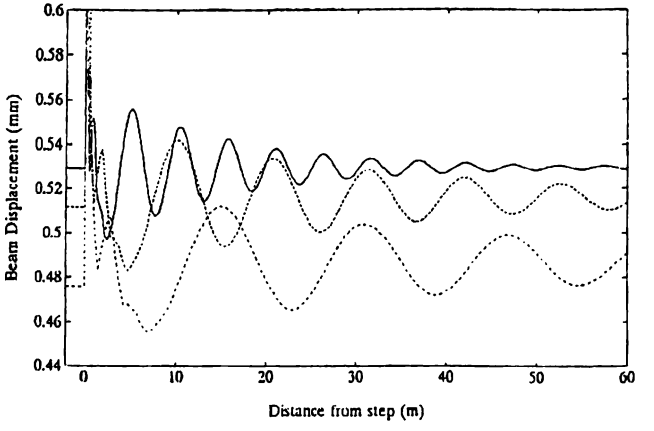


Fig. 10.3 Road surface displacement response due to the quarter–car vehicle model mounting a 10mm step at speeds of: ———— = 10m/s, - - - - - - - - - - = 20m/s, – · – · – · – = 30m/s. From [222].

The road responses can be seen to display high frequency oscillations just downstream of the step due to dynamic tyre forces at the 'wheel hop' frequency of the vehicle. Lightly damped, lower frequency oscillations also occur due to sprung mass bouncing motion, for up to 100m downstream. The wavelength of these oscillations along the road is proportional to the vehicle speed, as expected. The mean road surface deflection under the load decreases with increasing vehicle speed, in accordance with the 'speed effect' [6, 93, 226].

Increasing the vehicle speed has no effect on the dynamic loads for the assumed instantaneous step input. However, it can be observed that the amplitude of road surface motion is smaller for the higher speeds, due to the dynamics of the road surface model. The same conclusion is also true for the peak displacement, just behind the load (not shown in the figure). The decrease in the amplitude of oscillations is, however, almost completely masked by the overall change in response magnitude due to the effect of speed. The response is not simply the static response of the road, scaled according to the applied loads - the effect of speed is significant. It may, however, be approximated by the response to a unit load moving at the appropriate velocity, scaled according to the instantaneously applied load [219].

It is interesting to investigate the foundation stress under the same set of applied forces. In this case, $H(\xi, \omega)$ is replaced by $H(\xi, \omega) \times (\beta + i\omega\lambda)$, which will, on completion of the inverse Fourier transform, produce the foundation reaction force per unit length. The results for the same three

speeds are shown in figure 10.4. It is clear that the mean foundation reaction increases with increasing speed. This is again consistent with the observations of dynamic amplification [432].

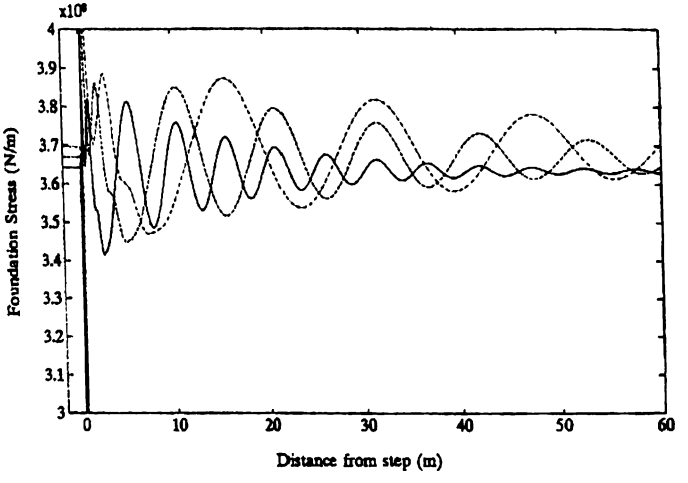


Fig. 10.4 Foundation stress response due to the quarter-car vehicle model mounting a 10mm step at speeds of: ——— = 10m/s, - - - - - - - - - -20m/s, - · - · - · - · - = 30m/s.. From [222].

10.3.5 Implementation of Theory for Measured Wheel Loads and Impulse Responses

If the impulse response function or the forces are derived from experimental measurements then the integrals (10.7) and (10.8) can in general only be solved numerically, see [219].

In order to evaluate the integral of equation 10.7 it must be replaced by a summation by substituting θ as $\theta = t - \tau$ then discretising so that $\theta = j\,\Delta\theta$.

$$y(x,t) \approx \sum_{m=1}^{N_f} \sum_{j=0}^{N_h-1} h\left(x - (d_m + vt) + vj\Delta\theta, j\Delta\theta\right) f_m(t - j\Delta\theta)\ \Delta\theta. \qquad (10.14)$$

The summation is terminated at a time $\theta = (N_h-1)\,\Delta\theta$, after which the impulse response function is considered to have effectively died away to nothing.

If the impulse response functions are measured at distances Δg along the road and with time interval $\Delta\Theta$, then a discretised version of the impulse response is: $h(k\,\Delta g, j\,\Delta\Theta) = h_{k,j}$. Similarly if the force is measured at time intervals $\Delta\tau$ and the response is required at space intervals of Δx and time intervals of Δt then the response and the input force as well as the impulse response function can be discretised as follows:

$$\begin{aligned} y(k\,\Delta x, l\,\Delta t) &= y_{k,l} \\ h(k\Delta g, j\,\Delta\Theta) &= h_{k,j} \\ f_m(l\,\Delta\tau) &= f_{m,l}. \end{aligned} \qquad (10.15)$$

Substituting these into equation 10.14 gives

$$y_{k,l} = \Delta\theta \sum_{m=1}^{N_f} \sum_{j=0}^{N_h-1} h_{\alpha(k-r_m)-\gamma l+\beta j,\ \eta j}\ f_{m,\ \nu l-\mu j} \qquad (10.16)$$

where

$$\alpha = \frac{\Delta x}{\Delta g},\quad \beta = \frac{\Delta\theta}{\Delta g},\quad \gamma = \frac{v\Delta t}{\Delta g},\quad r_m = \frac{d_m}{\Delta x},\quad \eta = \frac{\Delta\theta}{\Delta\Theta},\quad \nu = \frac{\Delta t}{\Delta\tau},\quad \mu = \frac{\Delta\theta}{\Delta\tau}.$$

If the integral is to be evaluated in a frame of reference moving with the vehicle then the same procedure can be followed starting from equation 10.8 with the result:

$$y_{k,l} = \Delta\theta \sum_{m=1}^{N_f} \sum_{j=0}^{N_h-1} h_{\alpha(k-r_m)-\gamma l+\beta j,\ \eta j}\ f_{m,\ \nu l-\mu j}. \qquad (10.17)$$

Each of these equations, (10.16) and (10.17), requires $N_h N_f+1$ multiplications for each value of y. If the response y is required at N_y positions in space and N_t times then a total of $N_y N_t (N_h N_f+1)$ real multiplications is required. Interpolation will also be required because neither the arguments of the impulse response function, nor the argument of the forcing function, are likely to fall exactly on measured data points.

10.4 EXPERIMENTAL INVESTIGATION

10.4.1 Test Sections

A programme of experiments was carried out on an instrumented section of test track at the Transport Research Laboratory (TRL) in the UK in order to verify the theory described in the previous section. The instrumented road had two test sections: Section A had 50mm of Hot Rolled Asphalt (HRA) wearing course, a 150mm roadbase of Dense Bituminous Macadam (DBM), 300mm of *Type 1*[1] crushed granite subbase, and a 1m bed of clay (CBR ≈ 2%) laid on the existing subgrade of hoggin, which had a CBR of approximately 3% (see figure 10.5). Section B, consisted of a 50mm HRA wearing course, 200mm DBM roadbase, and a 225mm crushed rock subbase laid directly on the hoggin. Both sections gave qualitatively similar test results. Unless otherwise stated, the results presented here are for Section A.

[1] *Type 1* specifies the grading (distribution of particle sizes) of the aggregate. *Type 1* material is the usual standard for subbases in the UK.

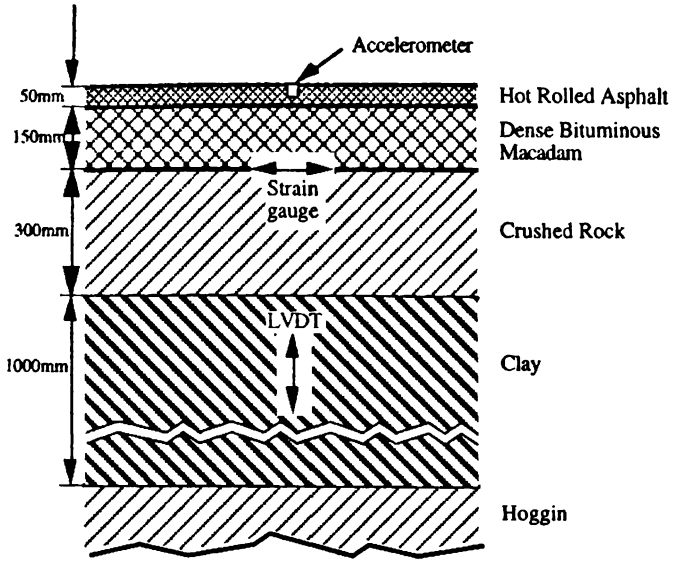


Fig. 10.5 Cross-section of the experimental test track. From [222].

10.4.2 Impulse Hammer and Instrumentation

Each test section contained two banks of instruments. Each bank consisted of a surface accelerometer, a *soil strain gauge* and a *base strain gauge*, mounted directly one above the other. The banks were nominally 3m apart and in the nearside wheel–path. The soil strain gauges were Linear Variable Differential Transformers (LVDTs) mounted vertically with their centres 650mm below the surface of the road. The undisturbed length of both LVDTs prior to installation was 79mm. The base strain gauges were of a conventional metal foil type and were mounted to measure strains transverse to the wheel–path at the bottom of the asphaltic layers.

The locations of the soil strain gauges were established as accurately as possible using the impulse hammer described next. The base strain gauges were assumed to be directly above the soil gauges and the accelerometers were installed at the surface on the same vertical line.

The instrumented hammer used to measure the impulse responses, was a modified version of the one described by Hunt [250]. The head of the hammer had a mass of 18.2kg and was faced with layers of latex so that it would not damage the road surface. The hammer arm was 2m long, giving an impact velocity of 6.3m/s when dropped from full height. The peak force during the impulse was approximately 40kN and the impulse duration was approximately 10msec.

The impulse and road responses were recorded by a digital data logger. Details of signal conditioning equipment and data processing can be found elsewhere [219].

In addition to the equipment directly involved in the measurement of impulse responses, temperature probes were mounted in the road surface. The road surface temperature was recorded with every impulse response and the temperature profile through the road was monitored at regular intervals throughout the testing period.

10.4.3 Linearity tests

The theory of Section 10.3 relies on use of the convolution integral, which is based on the principle of superposition. This requires the road to behave linearly, *ie* the magnitude of the response to be proportional to the magnitude of the input, at any excitation frequency.

The linearity of the test road was investigated by applying impulses of different magnitudes. The size of the applied impulse is proportional to the square-root of the height from which the hammer is dropped:

$$I = m_h(1 + e)\sqrt{2gh} \tag{10.18}$$

where I is the impulse,
m_h is the effective mass of the hammer head,
e is the coefficient of restitution,
g is the acceleration due to gravity, and
h is the height from which the hammer-head is released.

For each test, the hammer was dropped from three different heights: 2m, 1m and 0.5m. For every hammer drop the impulse response function was obtained by dividing the Fourier transform of the output response by the Fourier transform of the input force and then inverse Fourier transforming the result. This had the effect of normalising the response at each frequency by the magnitude of the input at that frequency.

The normalised responses from the accelerometer in one instrument bank are shown in figure 10.6. The three curves are hardly distinguishable, indicating that the response measured by this accelerometer was from a system showing a high degree of linearity. The base strain response was observed to be similarly linear. The soil strain response, illustrated in figure 10.7 however, showed distinctly nonlinear behaviour. The largest response (solid line) was to the largest impulse indicating a system with a characteristic like a *softening* spring.

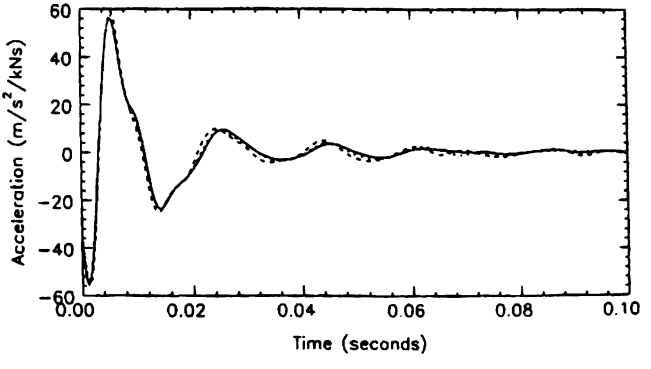


Fig. 10.6 Accelerometer linearity test on Test Section A. From [222].
Hammer height: 2m ———, 1m . . . . . , 0.5m – – – – –.

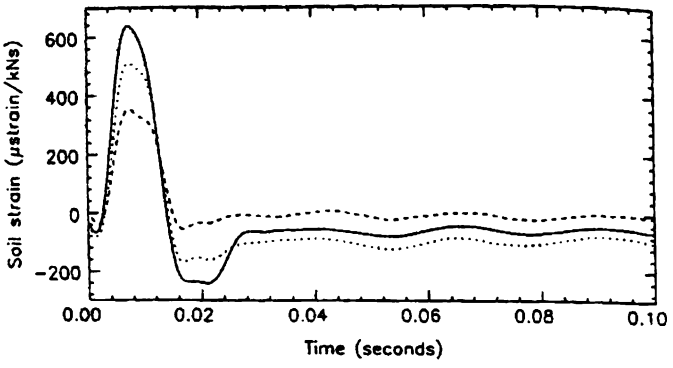


Fig. 10.7 Soil strain gauge linearity test on Test Section A. From [222].
Hammer height: ———— = 2m; ..... = 1m, – – – – – = 0.5m.

Soils have been observed to exhibit this type of behaviour under large strains [39] but conversely, [177] reported *stiffening* characteristics of a silty clay. If the soil exhibited significantly nonlinear behaviour then it would be expected to influence the response of the whole structure. This is not the case, because the responses measured by the accelerometer and base strain gauges were linear. Therefore, the nonlinearity in the soil strain response was probably introduced by the soil strain measurement system.

Figure 10.7 shows that the soil strain gauge output did not return to zero after the impulse response reached a steady state. This offset was observed to be stable and permanent. It was probably caused by sticking of the LVDT or inelasticity in the soil supporting it. If friction was present in the LVDT then it would be expected to behave with the *softening spring* characteristic as observed.

It is concluded that, under the conditions of testing, the test section behaved in an essentially linear manner but that some nonlinearities may have been introduced by the soil strain measuring system. The effect of these nonlinearities on the convolution calculation were minimised by using a hammer that applied a force of magnitude similar to typical wheel loads [51].

10.4.4 Isotropy tests

To investigate how road responses varied with absolute position on the road, impulse responses were measured for hammer drops at four positions (at 90° intervals) around each gauge. Each impulse position was 2m away from the gauge. Ten impulse response functions were measured and averaged for each position.

Figure 10.8 shows the impulse response functions measured by the accelerometer in instrument bank 1. The four responses are similar both in overall shape and magnitude and the differences are primarily in the *ringing* after the initial peaks. The largest response (solid line) was to the hammer blows that were outside the nearside wheel–path (*ie* towards the middle of the road). Similar results were observed for the accelerometer in bank 2. The differences between the responses appear to be due to anisotropy in the road construction. The road surface temperature only varied between 27.7 and 30.1°C during these measurements and is not thought to be the source of the differences.

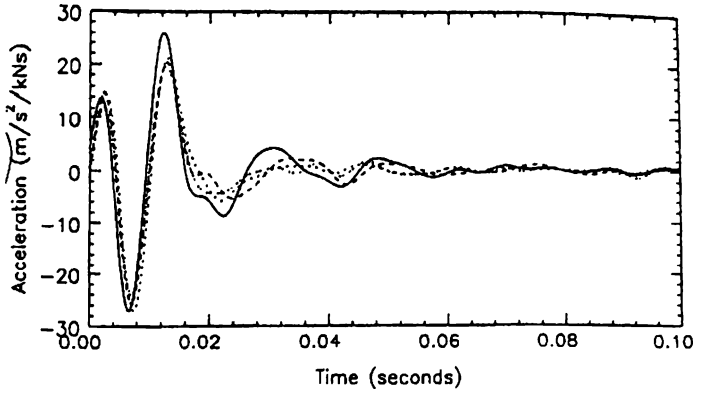


Fig. 10.8 Accelerometer isotropy test (bank 1, Test Section A). From [222].

The base strain gauge responses for bank 1 (figure 10.9) show two distinctly different characteristics. The larger responses are to hammer blows at positions off the nearside wheel-path (with the solid lines representing the responses to inputs outside it). These are longitudinal (radial) strain impulse responses. The smaller response curves are transverse (circumferential) strain impulse responses. As with the accelerometers the responses show reasonable isotropy until they start to decay.

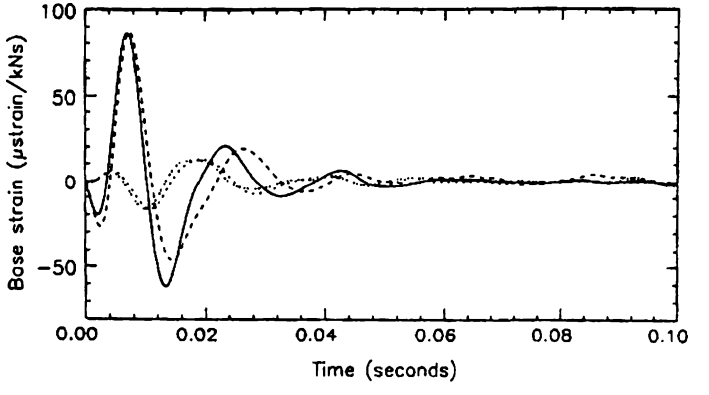


Fig. 10.9 Base strain gauge isotropy test (bank 1). From [222].

Figure 10.10 shows the responses of the two soil strain gauges to the isotropy test. The gauge in bank 1 again shows good isotropy with the solid line representing the response to hammer blows outside the wheel-path. The responses of the gauge in bank 2, were somewhat less isotropic.

The two most likely reasons why the responses from the LVDT in bank 2 did not indicate as isotropic a response as the LVDT in bank 1 are:

(i) The exact position of each LVDT gauge was not known and was difficult to determine.

(ii) The use of heavy rollers on the subgrade during construction may have rotated the soil strain gauges away from the vertical. This would give rise to a directional response.

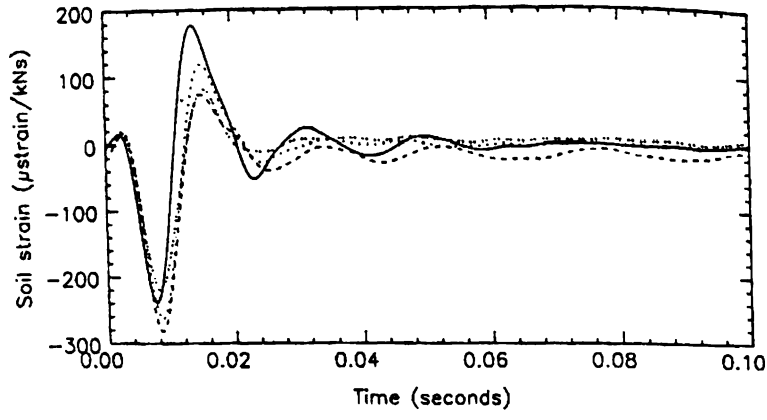


Fig. 10.10 Soil strain gauge isotropy test (bank 1). From [222].

If a road is significantly anisotropic it is not practical to use a different response model at every point, unless statistical methods are used, *eg* [277]. Otherwise it is necessary to calculate a *representative* response for the road, which is the assumption made by most mechanistic flexible pavement design procedures.

While the results of the isotropy tests have not shown ideal behaviour, it was decided that the test sections could be considered to be *locally* isotropic [469] for the purpose of further study and theoretical development.

10.4.5 Temperature effects

Road responses were observed to vary significantly as the temperature in the road varied. In order to monitor this to some degree, the road surface temperature was recorded with every impulse response. Figure 10.11 shows the peaks of the normalised impulse responses plotted against the surface temperature for all hammer drops that were directly over gauges. For base strain measurements the peaks are negative whereas they are positive for the soil strain gauges. This corresponds to peaks in compression in the soil and peaks in tension at the bottom of the asphaltic bound layers.

There is clearly a correlation between the peak impulse response and surface temperature. It should be noted, however, that the surface temperature is not always indicative of the mean effective temperature of the road structure and so a high correlation is not expected. The response of the pavement can be seen to be very sensitive to temperature, with approximately a factor of four variation in soil strain response for a surface temperature range of 13 to 42 °C.

Because of the temperature sensitivity of the road response, the impulse responses used in the convolution calculation were measured under conditions that were as close as possible to those during the vehicle tests. From an examination of the daily temperature variation it was decided to carry out these tests very early in the morning when temperatures were at their most stable and the effects of solar heating minimised.

10.4.6 Description of Vehicle Tests

An instrumented four-axle articulated vehicle was provided by TRL. Each axle was fitted with two strain gauge bridges and two accelerometers, so that all tyre forces could be measured and logged by an on-board analogue tape-recorder. Details of the instrumentation and calibration can be found in [115]. (See also Section 7.3.1.)

The static weights of the axles were measured to be 29.1kN on each wheel of the steering axle, 40.4kN on each wheel of the drive axle and 37.9kN on each wheel on the trailer's tandem axle group. The three heavily loaded axles all had dual tyres.

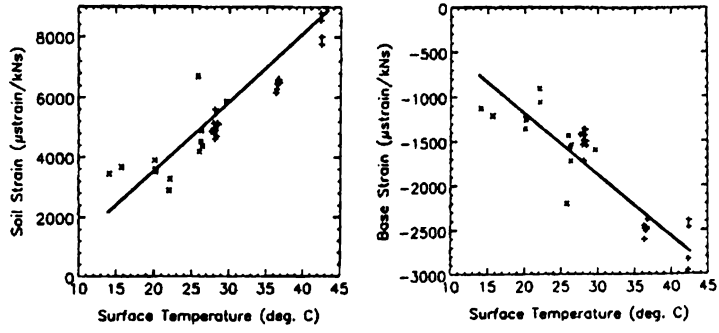


Fig. 10.11 Impulse response peaks plotted against road surface temperature. From [222].

The vehicle was driven over the test section at two nominal speeds: 50 and 80km/h. In each test the lorry was driven over the measuring points with each outside tyre of the three sets of dual-tyres passing as accurately as possible over the nominal position of the gauges. The single tyre of the steering axle was slightly in-board of the outside tyre of the dual-tyres. The longitudinal position of the vehicle along the test section was monitored at three points by infra-red beams which placed pulses on one track of the analogue tape recorder. Simultaneously, pulses were recorded by the roadside digital data-logger which also measured the pavement strains.

The lateral position of the vehicle was not monitored but observations of the tyre position as the vehicle passed showed that the tyres followed a line within 200mm of the nominal gauge position at high speeds and were more accurate at lower speeds.[1]

A set of impulse responses was measured on one side of one bank of buried strain gauges immediately before the vehicle was driven over the test section. The impulse responses were measured at twenty-one points at 150mm intervals along the wheel path. At each position the hammer was dropped five times and the normalised impulse responses were averaged.

10.4.7 Model Validation Results

The discrete convolution calculation in a stationary frame of reference (equation 10.14) was used to combine the measured wheel forces with the measured field of impulse responses. Impulse responses were taken at relatively widely spaced points along the road and it was found necessary to interpolate between these responses. No distinction was made for single or dual wheels and no correction was made for the small differences in wheel-path. The effects of the offside tyre forces on the nearside road response were assumed to be negligible.

Figure 10.12 shows a typical base strain gauge response to a lorry pass at 50 km/h. Peaks are clearly visible when each axle passes over the gauges, with the first peak in response due to the steering axle. The magnitudes of the calculated peaks are quite similar to the measured values and the main discrepancy is the rate at which the response decays after each wheel has passed. The

[1] In separate tests, using the same driver, the lateral position of a vehicle was monitored by a video recorder mounted underneath. The recorded picture showed that the steering axle strayed from its line by less than 100mm at 50 km/h

calculated rate is a little fast, giving an exaggerated trough between the wheels of the tandem axle trailer suspension. This is thought to be due to a slightly nonlinear viscoelastic response of the road surface which is more pronounced at the slower loading rates associated with the passing vehicle than at the rapid loading rates used to make the impulse response measurements.

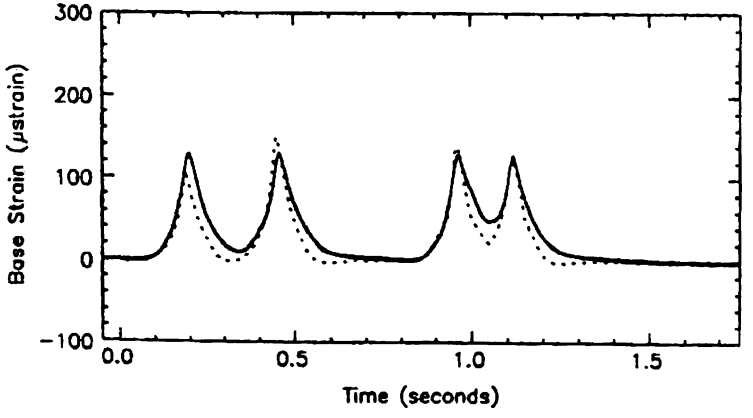


Fig. 10.12 Base strain gauge response to a 50km/h test. From [222].
——— Measured, ····· Calculated.

Figure 10.13 shows a typical base strain response for an 80km/h lorry pass. A similar pattern was shown by all other results. The calculated peak responses correlate well for all axles. Comparison with the 50km/h runs show that the peaks in the measured responses are generally lower in magnitude, as expected from the speed effect. The simulation still does not quite follow the decay of the measured response as it falls away from the peaks although it is somewhat more accurate than at 50 km/h.

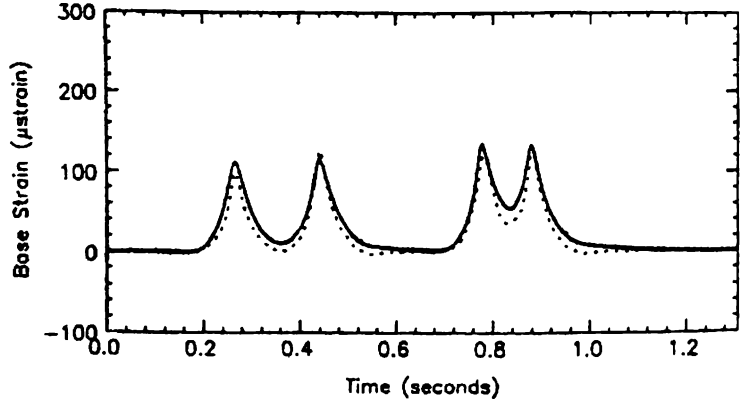


Fig. 10.13 Base strain gauge response to an 80km/h test. From [222].
——— Measured, ····· Calculated.

Typical responses of the soil strain gauges to 50km/h and 80km/h tests are shown in figures 10.14 and 10.15. At 80km/h, the peak strains under the tandem axles change significantly between the two banks of gauges for both measurement and simulation. This indicates that *dynamic* tyre forces on the tandem suspension affect the road response between the banks of gauges. The calculated responses to the 50km/h tests under–predict the measured response by approximately 15% on all of the runs. For the 80km/h tests the overall error is reduced slightly.

The calculated responses give the peaks and troughs in the correct places and also follow the dynamic component of the tyre forces. The calculated and measured responses all vary in overall magnitude with speed and the general trends are the same. The main source of error in the magnitude of the soil strain predictions is thought to be due to the nonlinearity of the soil strain gauges.

Other sources of error for both sets of gauges are thought to be:

(i) lateral off-tracking of the tyres from the strain gauge positions;

(ii) inaccuracy in the exact location of the strain gauges;

(iii) road surface temperature variations during the period between the measurement of the impulse response functions and the lorry tests;

(iv) the effects of single and dual tyres on the pavement response which was not included in the calculations;

(v) dynamic contact area variations.

10.5 RESPONSES TO IDEALISED LOADS

10.5.1 Effect of Frequency on Pavement Response

To analyse the effects of the frequency of dynamic loads on road response, an idealised load was convolved with measured impulse response functions from the test road, using the theory described and validated above. The idealised load consisted of a sinusoidal component, with a magnitude of 5kN, superimposed on a static load of 10kN so that the total was represented by

$$P(t) = 10 + 5 \sin (2\pi ft) \quad \text{(kN)}. \tag{10.19}$$

This load was not moving along the road.

The sinusoidal force component causes the road response to vary with time. For comparison purposes the soil and base strain responses have been plotted as a function of distance in figure 10.16 at the instant in the cycle when the strain directly under the load reaches its maximum value. This is not necessarily at the same moment as the load reaches its maximum because energy radiation and material damping cause the road response to lag in time behind the applied force.

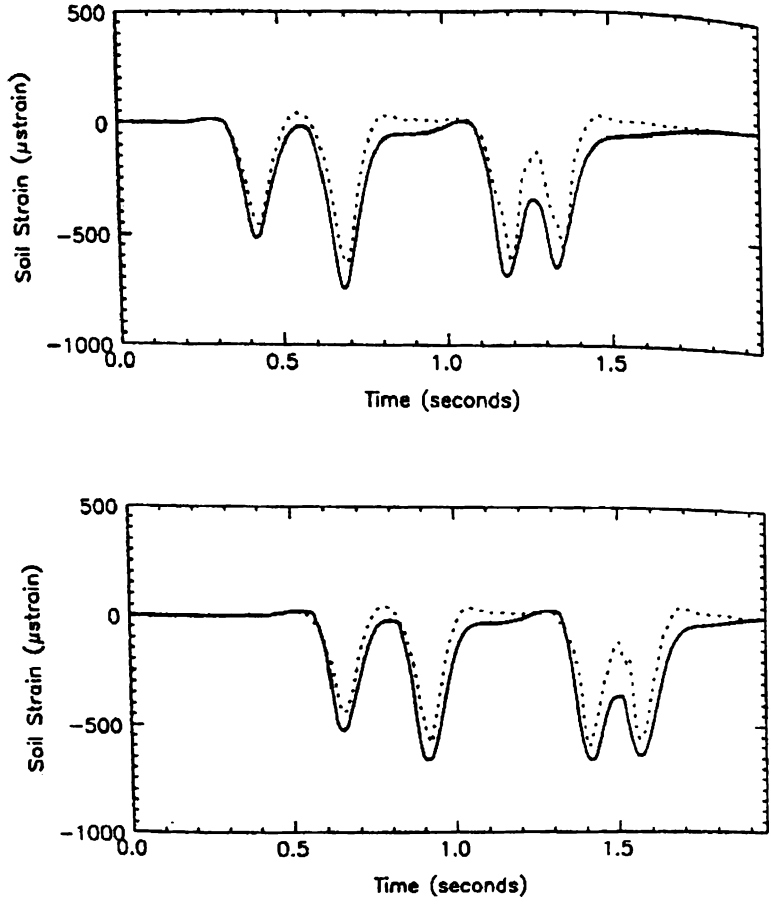


Fig. 10.14 Soil strain gauge responses to a 50km/h test. From [222].
——— Measured, ····· Calculated.

The base strains are positive, indicating tension, and the vertical soil strains show the expected (negative) compression. The base strain is observed to decrease as the frequency increases from 3.5 to 10Hz but then it remains approximately constant as the frequency is increased to 20Hz. The magnitude of the soil strain response, however, decreases when the frequency is increased to 10Hz but increases again, almost back to the 3.5Hz level, when the frequency is increased to 20Hz.

Similar behaviour has been observed in the harmonic responses of theoretical layered dynamic pavement models for road models. Hardy [219] and Sebaaly [414] identified various resonances that caused the predicted harmonic responses to rise and fall with increasing frequency of loading. Note that material damping in the structure removes any large resonant peaks from the response.

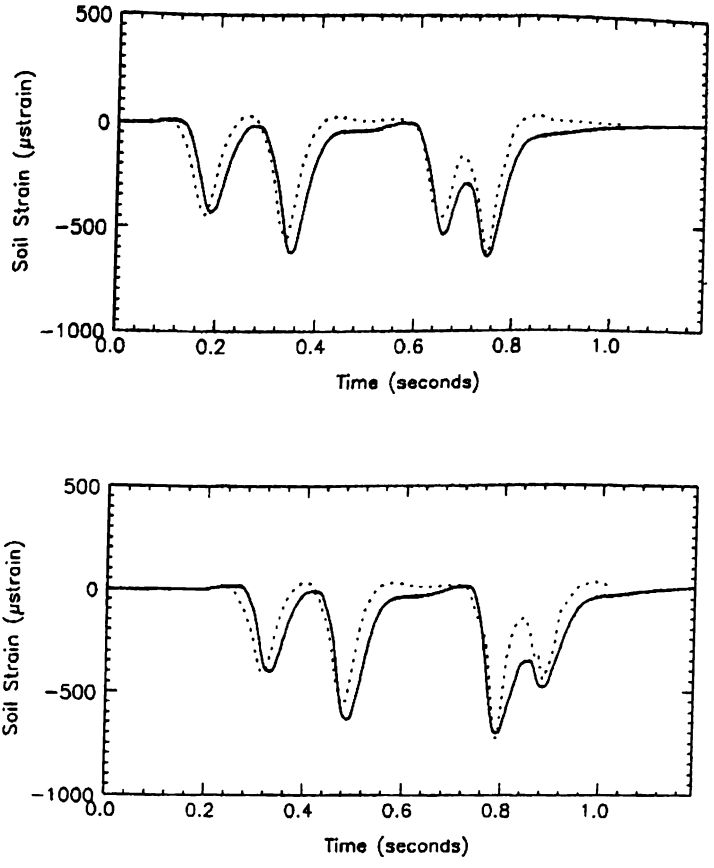


Fig. 10.15 Soil strain gauge responses to a 80km/h test. From [222].
——————— Measured, ····· Calculated.

10.5.2 Effect of Speed on Pavement Response

The effect of vehicle speed can be examined using the dynamic model by convolving a moving constant load with the measured impulse responses. Figure 10.17 shows the calculated soil and base strains due to a constant 10kN load moving at 5, 20 and 40 m/s. The responses were calculated in a frame of reference moving with the vehicle so that the horizontal axis represents distance ahead of the moving contact point at an instant in time.

Both the base and soil strains decrease in magnitude with increasing speed. The peak in base strain decreases from approximately 40 microstrain at 5m/s to approximately 30 microstrain at 40 m/s, a decrease of 25%. Note that the main reduction in response occurs between 5 m/s and 20 m/s. A smaller decrease in magnitude, can be observed in the soil strain response: just 12.5% from 160 to 140 microstrain. The response peaks move further behind the load and the responses decay more slowly with distance as the speed increases.

Such behaviour, which is consistent with theoretical calculations of a beam on an elastic foundation [92, 326, 327], cannot be simulated using a static, or stationary harmonic, road model. The observations are qualitatively consistent with previous studies, discussed in Section 10.2.4.

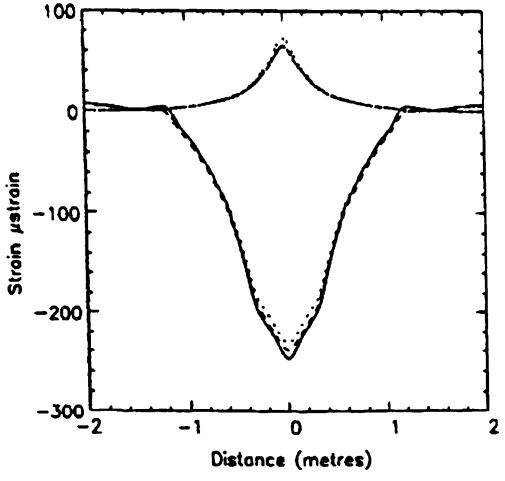


Fig. 10.16 The effect of loading frequency on pavement response. From [223].
Base Strain: _____ = 3.5Hz, ... = 10Hz, - - - - - - = 20Hz,
Soil Strain: .. .. = 3.5Hz, ... = 10Hz, ———— = 20Hz

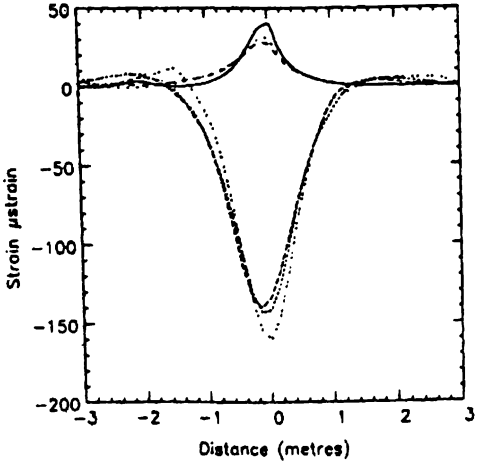


Fig. 10.17 The effect of speed on pavement response to a constant moving load. From [223].
Base Strain: _____ = 5m/s, ... = 20m/s, - - - - - - = 40m/s,
Soil Strain: .. .. = 5m/s, ... = 20m/s, ———— = 40m/s.

10.5.3 The Combined Effects of Speed and Frequency

Having examined the effects of speed and frequency independently it is important to investigate their combination. Figure 10.18 shows the theoretical base strain response to dynamic loads moving at 20m/s. The dynamic loads are described by equation 10.19, with frequencies of 3.5, 10 and 20Hz. The response to a steady 15kN load moving at 20 m/s is also shown. All the responses are calculated at the points on the road surface that suffer the *maximum* strain under the oscillating force (not necessarily the same point at which the force reaches its maximum value).

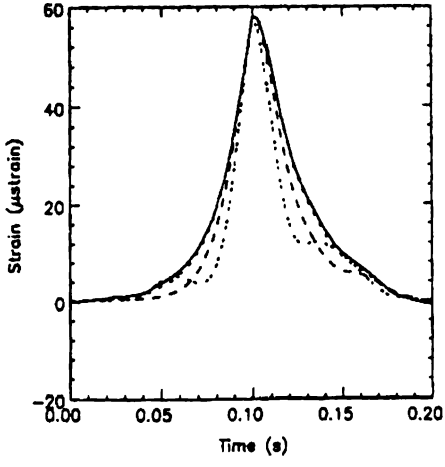


Fig. 10.18 Base strain responses to dynamic loads moving at 20m/s. From [223].
——————— = 0Hz, ... = 3.5Hz,
– – – – – – = 10Hz, ... = 20Hz.

It is clear that the loading frequency has a relatively small effect on the maximum strain suffered, although it does affect the rate at which this level is reached. The 20Hz response shows an additional oscillation which illustrates that, under some circumstances, the cycles of loading can be detected in road response. (The additional cycle may have an influence on fatigue damage calculations, in which the number and magnitude of loading cycles are considered). The static (0Hz), 15kN load forms an envelope around the other response curves, reaching a slightly higher maximum than the dynamic responses.

Figure 10.19 shows the soil strain responses of Test Section A to the same set of loads. Similar conclusions may be drawn from these curves but it is interesting to note that the 10Hz load produces a slightly greater peak than the 15kN static load. This dynamic amplification of strains is an unexpected result that could not be predicted by a static road model. Figure 10.20 shows a summary of the speed and frequency response results for both Test Sections (A and B). It is clear that the effect of loading frequency is relatively small for both test sections if the load is moving at a speed greater than 5 m/s. Furthermore, although speed has a large effect on the 0Hz response, it has relatively little effect on pavement response to the higher frequency load components.

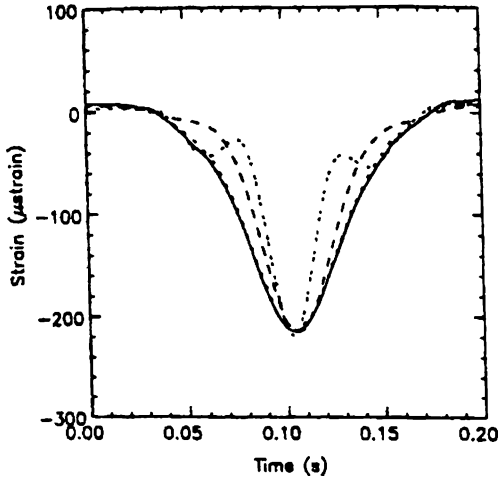
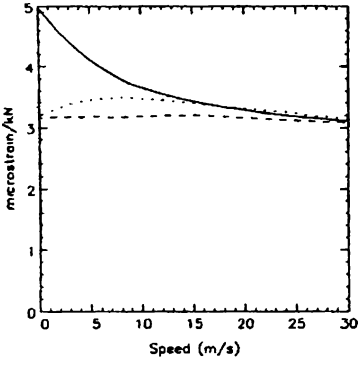
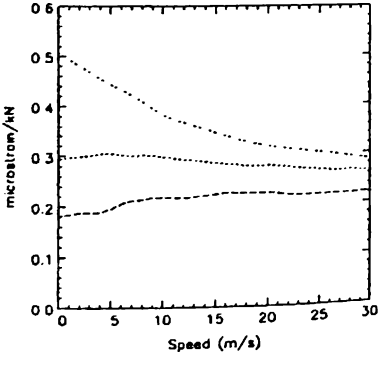


Fig. 10.19 Soil strain responses to dynamic loads moving at 20m/s. From [223].
——————— = 0Hz , ... = 3.5Hz ,
– – – – – – = 10Hz ,.. .. .. = 20Hz.



Section A



Section B

Fig. 10.20 Frequency and speed effects on both road sections: From [223].
Section A ——————— = 0 Hz; . . . . . = 10 Hz ; – – – – – – = 20 Hz;
Section B .. .. = 0 Hz; . . . . . = 10 Hz; – – – – – – = 20 Hz.

10.6 THE INFLUENCE FUNCTION APPROACH

10.6.1 Influence Function Calculation in a Fixed Frame of Reference

It is clear from the foregoing study that the effects of loading frequency on pavement strains are relatively minor compared with the effects of speed. It is possible to simplify the convolution theory, which requires considerable computer resources, to yield a 'quasi-dynamic' calculation. This simplification neglects the effect of loading *frequency* whilst maintaining correct allowance for vehicle speed, and the magnitude of the dynamic wheel loads.

Substituting $\tau' = t - \tau$ into equation 10.7 gives

$$y(x, t) = \sum_{m=1}^{N_f} \int_0^{\infty} h(x - d_m - v(t - \tau),\ \tau')\, f_m(t - \tau')\, d\tau'. \qquad (10.20)$$

The impulse response function $h(x, t)$ will eventually decay to zero so that in practice the integral does not need to be taken to infinity.

If the force changes slowly compared to the rate at which the impulse response function decays, then it may be considered to be constant over the integral, with a value of $f_m(t)$. In this case, equation 10.20 reduces to

$$y(x, t) = \sum_{m=1}^{N_f} f_m(t)\ \ I(v,\ x - d_m - vt)$$
$$\text{where } I(v, x) = \int_0^{\infty} h(x + v\tau,\ \tau)\, d\tau \qquad (10.21)$$

Here $I(v, x)$ is the 'influence function' for speed v and distance x from the point of application of the load.

This simplification reduces the total number of multiplications for each value of $y(x, t)$ from $N_f N_i$ to $N_f + N_i$, where N_i is the number of multiplications required to evaluate the integral of equation 10.21 (typically 30 to 50).

10.6.2 Influence Function in a Moving Frame of Reference

A similar transformation (to that just performed on equation 10.7) can be performed on equation 10.8, giving the response in a moving frame of reference:

$$y(\hat{x}, t) = \sum_{m=1}^{N_f} f_m(t)\ I(v, \hat{x} - d_m). \qquad (10.22)$$

10.6.3 Comparison of Influence Function and Convolution Calculations

Figure 10.21 shows a base strain response predicted by the two different calculation procedures (equations 10.7 and 10.21). The load is defined by equation 10.19 with a frequency of 10Hz and a low speed of 5m/s. There are clearly significant differences between the responses, but the applied loading is not typical of vehicle loads: vehicles travelling so slowly are unlikely to produce such large dynamic forces even on the roughest roads.

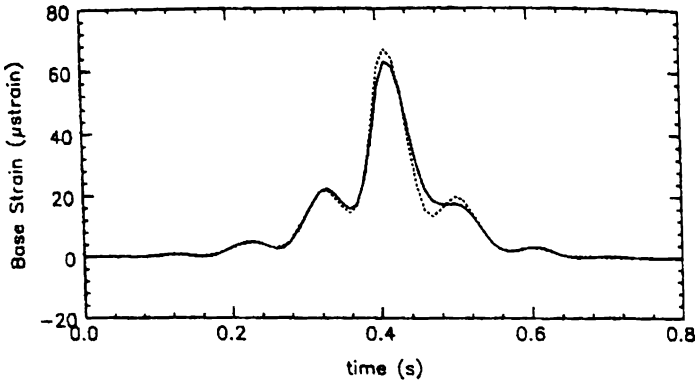


Fig. 10.21 Base strain responses predicted by the two calculation procedures. From [223].
Speed = 20m/s, loading frequency = 10Hz
——— = Convolution , ... = Influence function.

To establish the validity of the 'quasi–dynamic' assumption implied by the influence function calculation, for idealised loads, the relative error δ is defined by:

$$\delta(v, f) = \frac{\varepsilon(v, f) - \varepsilon(v, 0)}{\varepsilon(v, f)} \times 100 \qquad (\%) \tag{10.23}$$

for a dynamic pavement load defined by

$$P(t) = \cos(2\pi f t). \tag{10.24}$$

where δ is the percentage error introduced by the influence function calculation,
v is the speed,
f is the frequency of the applied load, and
$\varepsilon(v, f)$ is the peak strain due to a unit load with frequency f travelling at speed v.

The relative errors for base and soil strains are shown in figures 10.22 and 10.23. The base strain responses are modelled quite accurately by the influence function calculation, for speeds above 20m/s, but the method is less accurate for the soil strains (figure 10.23), with errors around 5%.

The relative error δ is the error in predicting the dynamic component of the road response with no static component (equation 10.24) and would be biased by the static load. The response to the static component of the load is not affected by the calculation procedure, and therefore the error in predicting the response to typical dynamic tyre forces is less than δ. For a load described by

$$P(t) = P_0\left[1 + \alpha \cos(2\pi f t)\right] \tag{10.25}$$

the true response, $E(v, f, \alpha)$, would be

$$E(v, f, \alpha) = P_0\left[\varepsilon(v, 0) + \alpha\, \varepsilon(v, f)\right] \tag{10.26}$$

and the influence function calculation would give quasi–dynamic response

$$E(v, 0, \alpha) = P_0\, \varepsilon(v, 0)\,(1 + \alpha). \tag{10.27}$$

The percentage error introduced by the influence function calculation is therefore given by:

$$\Delta(v, f, \alpha) = \frac{E(v, f, \alpha) - E(v, 0, \alpha)}{E(v, f, \alpha)} \times 100 \quad (\%)$$
$$\approx \frac{\alpha}{1 + \alpha} \times \delta(v, f). \tag{10.28}$$

For normal dynamic loads, $\alpha \leq 1.0$ (typically, $\alpha \approx 0.2 - 0.5$, see Chapter 7), so $\Delta \leq 1/2\ \delta(v, f)$. From figures 10.22 and 10.23, this is a relatively small error (typically $\leq 5\%$).

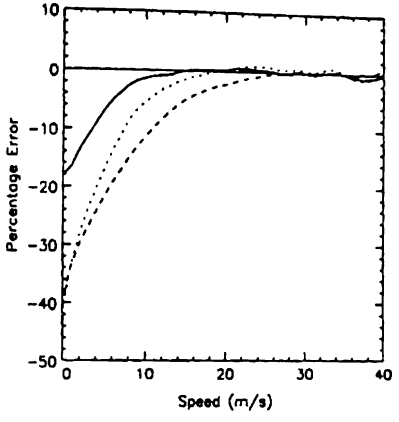


Fig. 10.22 Relative errors for computed base strains. From [223].
——— = 3.5Hz, ... = 10Hz, – – – – – = 20Hz.

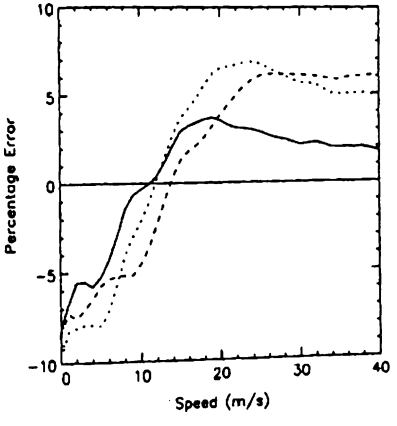


Fig. 10.23 Relative errors for computed soil strains. From [223].
——— = 3.5Hz, ... = 10Hz, – – – – – = 20Hz.

10.7 COMPARISON OF CONVOLUTION AND INFLUENCE FUNCTION CALCULATIONS

10.7.1 Modelling Dynamic Wheel Loads

To compare the calculation procedures for realistic operating conditions, a set of theoretical tyre forces was generated using the vehicle simulation methods described in Chapter 5. The two simple linear vehicle models shown in figure 5.1 were used, with similar parameter values. The 'quarter car' vehicle model generated tyre forces with the main dynamic component at 1.9Hz [95], being representative of a soft steel or air suspension. The 'walking-beam' model produced dynamic wheel loads with dominant frequencies of 2.8 and 9Hz. It represents the minority of suspensions which generate large dynamic wheel loads due to unsprung mass motion (lightly damped pitching of the walking-beam in this case).

A 'poor' random road profile, as defined by equation 3.1, was used as input to the vehicle simulations. This profile is representative of a minor country road. It was used so as to excite large dynamic loads that would yield 'worst case' differences between the convolution and influence function (dynamic and quasi-dynamic) road response calculations.

10.7.2 Pavement Strains

The tyre forces generated by the quarter-car vehicle model were used as input to the two road response calculations (convolution and influence function). Figure 10.24 shows the peak responses experienced as a function of distance along the road due to this vehicle travelling at 30m/s. The differences between the dynamic convolution calculation and the 'quasi-dynamic' influence function calculation can be seen to be relatively small, and significantly less pronounced than in figure 10.21.

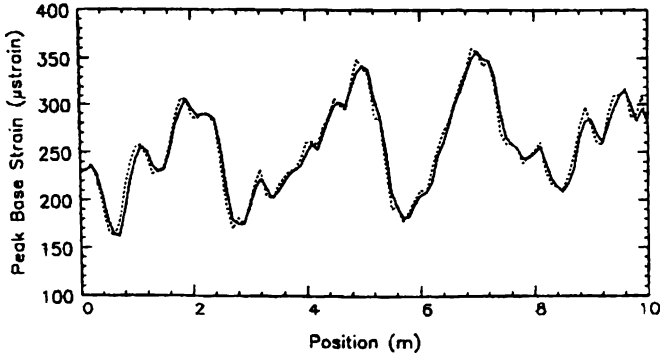


Fig. 10.24 Peak base strains predicted by the two calculation procedures (quarter-car model). From [223].
——— = Convolution, ... = Influence function.

The peak responses occur a short time after the wheel has passed. This is illustrated by figure 10.25 which shows the force applied to each point on the road plotted against the maximum base strain experienced in the structure directly at (under) that point. The hysteresis loops that can be seen are expected for a system with significant damping or viscous properties. The two curves are for speeds of 30m/s and 5m/s. They show that the road appears to be stiffer for faster vehicles.

If the hysteresis loops in figure 10.25 were sampled at discrete points, the data would appear to scatter in a fashion similar to the experimental measurements by Christison, shown in the previous chapter (figure 9.2).

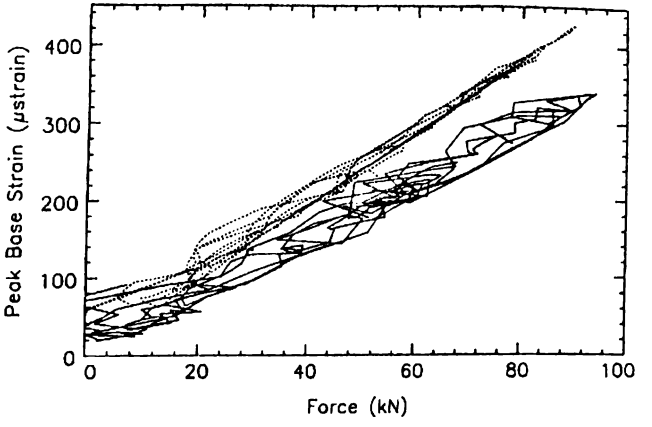


Fig. 10.25 Peak base strain plotted against the applied force, quarter car model. From [223].
——— = 30m/s, ... = 5m/s.

To establish the regimes over which the influence function calculation is sufficiently accurate, the error coefficient of variation is defined as

$$\gamma = \frac{\varepsilon_{RMS}}{m_{conv}} \tag{10.29}$$

where ε_{RMS} is the RMS difference in the peak strains evaluated at each position along the road by the two calculation procedures, and

m_{conv} is the mean of the peak strains evaluated by the convolution method.

This coefficient was evaluated for both soil and base strains over a range of speeds and is shown in figure 10.26. For each speed and calculation method the response was simulated for a period of 10 seconds. This short loading time gives rise to the observed scatter due to statistical errors. It is clear that the error coefficient of variation is generally very low ($\gamma < 0.002$, *ie* 0.2%). The increase in dynamic wheel forces with speed is reflected in the shape of the curves.

It is apparent that the influence function calculation will generally give quite accurate strains for vehicles which generate predominantly low frequency loads.

To assess the accuracy of the influence function calculation for higher frequency wheel loads, the walking–beam model was simulated over the same section of road. The peak base strains along the road are shown in figure 10.27. It is clear from this and figure 10.24 that the influence function approximation is less accurate for this suspension model than for the lower frequency loads generated by the quarter–car model.

10.7.3 Fatigue Damage

One of the main reason for predicting road strains is to evaluate the road damage inflicted by vehicles. It is important to know the magnitude of the errors in theoretical damage associated with the quasi–dynamic, influence function calculation.

Strains in the road were calculated using both the full convolution theory and the influence function calculation and these strains were then used to predict the damage incurred at equally–spaced points along the road, due to the passing of a single vehicle.

10.7 COMPARISON OF CONVOLUTION AND INFLUENCE FUNCTION CALCULATIONS

10.7.1 Modelling Dynamic Wheel Loads

To compare the calculation procedures for realistic operating conditions, a set of theoretical tyre forces was generated using the vehicle simulation methods described in Chapter 5. The two simple linear vehicle models shown in figure 5.1 were used, with similar parameter values. The 'quarter car' vehicle model generated tyre forces with the main dynamic component at 1.9Hz [95], being representative of a soft steel or air suspension. The 'walking-beam' model produced dynamic wheel loads with dominant frequencies of 2.8 and 9Hz. It represents the minority of suspensions which generate large dynamic wheel loads due to unsprung mass motion (lightly damped pitching of the walking-beam in this case).

A 'poor' random road profile, as defined by equation 3.1, was used as input to the vehicle simulations. This profile is representative of a minor country road. It was used so as to excite large dynamic loads that would yield 'worst case' differences between the convolution and influence function (dynamic and quasi-dynamic) road response calculations.

10.7.2 Pavement Strains

The tyre forces generated by the quarter-car vehicle model were used as input to the two road response calculations (convolution and influence function). Figure 10.24 shows the peak responses experienced as a function of distance along the road due to this vehicle travelling at 30m/s. The differences between the dynamic convolution calculation and the 'quasi-dynamic' influence function calculation can be seen to be relatively small, and significantly less pronounced than in figure 10.21.

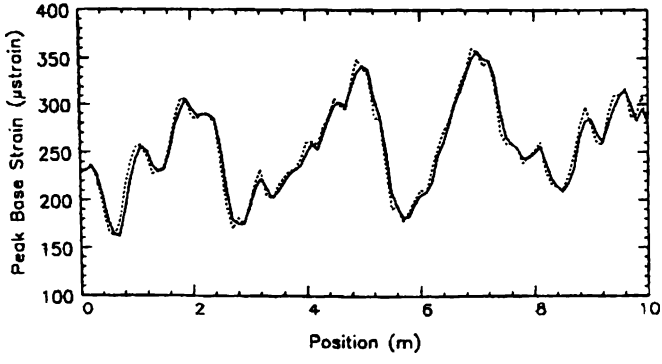


Fig. 10.24 Peak base strains predicted by the two calculation procedures (quarter-car model). From [223].
——— = Convolution, ... = Influence function.

The peak responses occur a short time after the wheel has passed. This is illustrated by figure 10.25 which shows the force applied to each point on the road plotted against the maximum base strain experienced in the structure directly at (under) that point. The hysteresis loops that can be seen are expected for a system with significant damping or viscous properties. The two curves are for speeds of 30m/s and 5m/s. They show that the road appears to be stiffer for faster vehicles.

If the hysteresis loops in figure 10.25 were sampled at discrete points, the data would appear to scatter in a fashion similar to the experimental measurements by Christison, shown in the previous chapter (figure 9.2).

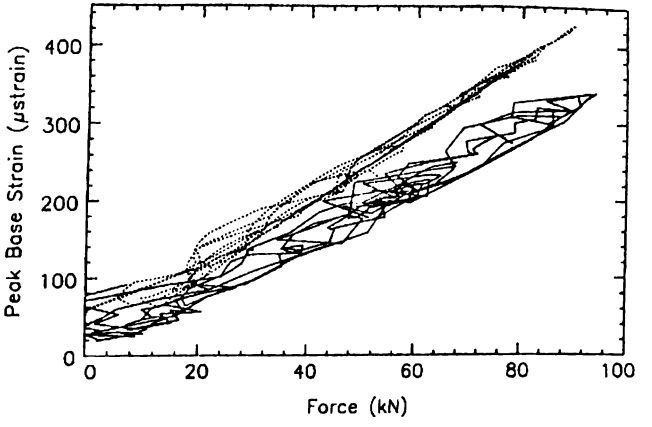


Fig. 10.25 Peak base strain plotted against the applied force, quarter car model. From [223].
——— = 30m/s, ... = 5m/s.

To establish the regimes over which the influence function calculation is sufficiently accurate, the error coefficient of variation is defined as

$$\gamma = \frac{\varepsilon_{RMS}}{m_{conv}} \tag{10.29}$$

where ε_{RMS} is the RMS difference in the peak strains evaluated at each position along the road by the two calculation procedures, and

m_{conv} is the mean of the peak strains evaluated by the convolution method.

This coefficient was evaluated for both soil and base strains over a range of speeds and is shown in figure 10.26. For each speed and calculation method the response was simulated for a period of 10 seconds. This short loading time gives rise to the observed scatter due to statistical errors. It is clear that the error coefficient of variation is generally very low ($\gamma < 0.002$, *ie* 0.2%). The increase in dynamic wheel forces with speed is reflected in the shape of the curves.

It is apparent that the influence function calculation will generally give quite accurate strains for vehicles which generate predominantly low frequency loads.

To assess the accuracy of the influence function calculation for higher frequency wheel loads, the walking–beam model was simulated over the same section of road. The peak base strains along the road are shown in figure 10.27. It is clear from this and figure 10.24 that the influence function approximation is less accurate for this suspension model than for the lower frequency loads generated by the quarter–car model.

10.7.3 Fatigue Damage

One of the main reason for predicting road strains is to evaluate the road damage inflicted by vehicles. It is important to know the magnitude of the errors in theoretical damage associated with the quasi–dynamic, influence function calculation.

Strains in the road were calculated using both the full convolution theory and the influence function calculation and these strains were then used to predict the damage incurred at equally–spaced points along the road, due to the passing of a single vehicle.

A 'good' random road profile, as defined by equation 3.1, was used as input to the vehicle simulations. This profile is representative of a major trunk road. It was used so as to excite typical dynamic loads that would yield differences between the convolution and influence function (dynamic and quasi-dynamic) road response calculations, that may be expected in practice.

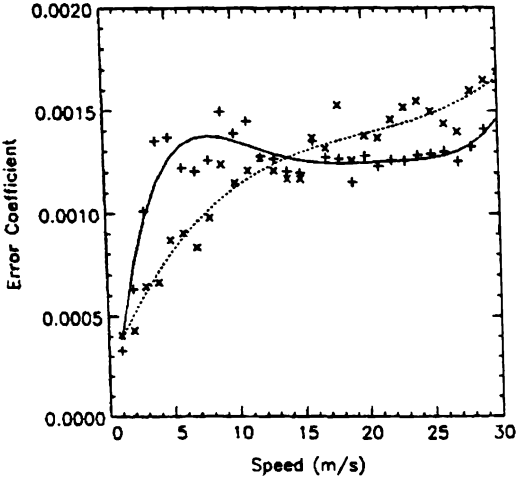


Fig. 10.26 Error coefficient of variation plotted as a function of vehicle speed for the quarter-car model. From [223].
_____ = Base strain, ... = Soil strain.

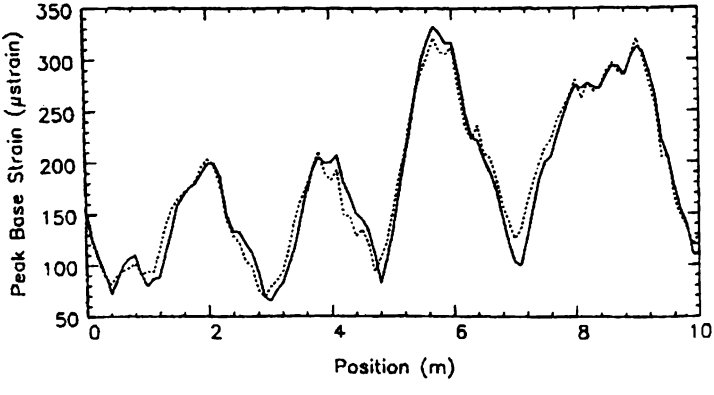


Fig. 10.27 Peak base strains predicted by the two calculation procedures (walking–beam). From [223].
_____ = Convolution, ... = Influence function.

The proportion of the total fatigue life of the pavement used by a single pass of the vehicle[1], was calculated from the predicted base strains, using Miner's hypothesis to relate damage to numbers of strain cycles [93] and fatigue properties of a typical asphalt mix:

$$d = \sum_{i=1}^{n} \frac{1}{N_i}$$

$$N_i = k_1 \varepsilon_i^{-k_2} \qquad (10.30)$$

where d is the damage due to n strain cycles with magnitudes ε_i, i=1,2,...,n,
N_i is the number of strain cycles to failure at strain level ε_i
k_1, k_2 are material constants, with values of $k_1 = 10^{14}$ and $k_2 = 5$ (from [72])

The number and magnitude of strain cycles was found from the strain time histories using the 'rainflow' counting method [430]. Figure 10.28 shows examples of the variation of damage with distance calculated in this way. The differences between the two calculation procedures (convolution and influence function) are evident in the predicted damage.

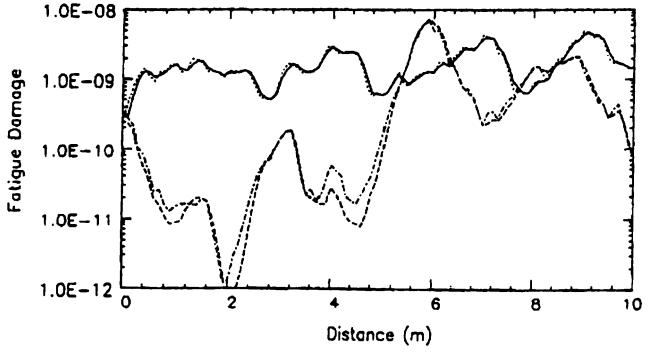


Fig. 10.28 Road damage predicted by the two calculation procedures. From [223].
Quarter-car: ———— = Convolution, ... = Influence function,
Walking-beam: – – – – – = Convolution, – – – – – = Influence function.

The road damage histories were processed to determine the *95th percentile* damage value [93]. This statistic takes into account the fact that the damage may be concentrated at certain areas along the road and that (in the worst case) the road will ultimately fail due to excessive wear at these locations [94]. Five percent of the road surface in the wheel track incurs damage greater than the *95th percentile damage* level.

The variation of the *95th percentile damage* with speed for both vehicle models and both calculation methods is shown in figures 10.29 and 10.30. In each case, the graphs are normalised by the damage incurred at 'creep speed'. Figure 10.29 was generated using impulse response measured on pavement Section A, whereas figure 10.30 was generated using impulse responses from Section B. The figures were produced by simulating 180s of vehicle and road response for each speed, the long simulation time being required to reduce statistical errors. The predicted damage increases smoothly with speed for the quarter-car model, but oscillates for the walking beam model, due to 'wheelbase filtering' [93].

[1] This type of 'single-pass' road damage calculation is described in more detail in Chapter 17.

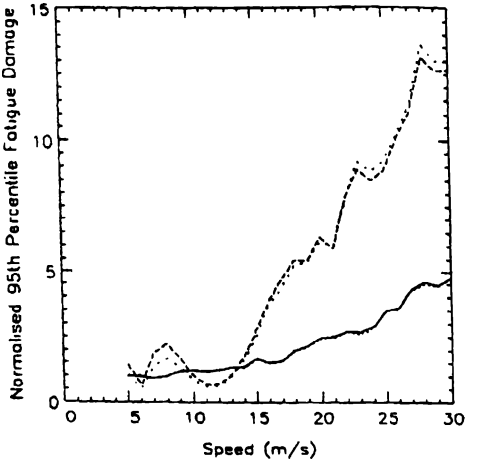


Fig. 10.29 Normalised 95th percentile road damage as a function of vehicle speed, Section A. From [223].
Quarter-car: ——————— = Convolution, ... = Influence function,
Walking-beam: — — — — — — — = Convolution, — — — — — — — = Influence function.

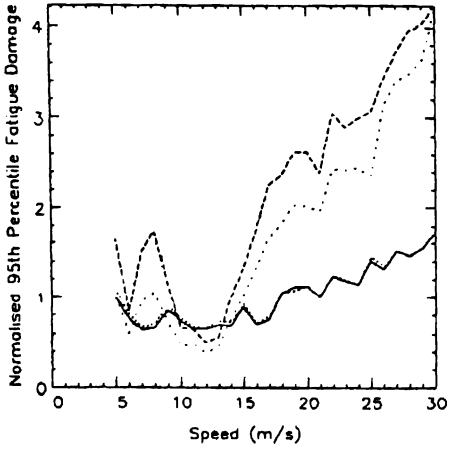


Fig. 10.30 Normalised 95th percentile road damage as a function of vehicle speed, Section B. From [223].
Quarter-car: ——————— = Convolution, ... = Influence function,
Walking-beam: — — — — — — — = Convolution, — — — — — — — = Influence function.

It is apparent that the damage predicted by the two road response calculations is virtually identical for the quarter-car model (which generated low frequency wheel loads) and only slightly different for the walking-beam (which generated both high and low frequency wheel loads). The errors are larger for Section B. The agreement between the curves for both vehicles, and the *insensitivity* of the predicted damage to road dynamics, shows that the 'quasi-dynamic' simplifying assumption is accurate, even for extreme dynamic loads.

The very large damage levels for the walking–beam suspension would not occur in practice, because: (i) heavy vehicles would not be driven along such rough roads at high speeds; (ii) the tyres would loose contact with the road surface for these conditions, thereby limiting the maximum dynamic loads. This did not occur for the linearised vehicle models and the dynamic wheel loads were therefore a worst–case.

The calculations that were performed to generate figures 10.29 and 10.30 required 30 times more CPU time for each point on the 'convolution' curve than for the influence function curve.

10.8 CONCLUSIONS

(i) The theory required to calculate the dynamic response of a continuous, linear system to moving transient, periodic and random loads has been presented.

(ii) The assumptions of linearity and isotropy that are required by the theory were tested on an instrumented section of test track. They were found to be satisfied sufficiently well to justify the use of linear theory to predict the primary response of the road to passing vehicles.

(iii) The response of the test road was found to be very sensitive to temperature, with approximately a factor of four change of response to a standard load, over a temperature range of 13 °C to 42 °C.

(iv) The theoretical dynamic response of the test road was found to agree closely with the measured response. The calculation method was found to simulate the effects of speed and dynamic wheel loads correctly.

(v) The measured and predicted strains in the test road and in a simple model were observed to decrease significantly as the load speed increased. The stresses in the simple road model were, conversely, observed to increase with increasing speed.

(vi) The predicted dynamic strains (derived from experimental data) were found to be relatively insensitive to the frequency of applied dynamic loads.

(vii) The convolution theory, for calculating the dynamic response of continuous pavements to dynamic tyre forces, was simplified, with a consequent significant reduction in computing time. The 'quasi–dynamic' simplification disregards the effect of loading frequency but accounts correctly for the speed of the loads over the road surface. It was found that the simplification had little effect on predicted base strains in the test road, and a relatively small effect on the amount of theoretical fatigue damage.

(viii) The quasi–dynamic simplification has only been checked for one test road and for one response component (the transverse base strain). The dynamic loads used in the calculation were, however, larger than normally observed on typical trunk roads, and because of the insensitivity of predicted damage to road dynamics, it is thought that the results presented here are relatively general.

(ix) From the limited experimental evidence available, it is concluded that it is *not* necessary to use dynamic models for predicting damage to flexible pavements caused by heavy vehicles. The simplified quasi–dynamic calculation method can be used successfully to estimate the road–friendliness of vehicles, as long as suitable road damage relationships are used.

11
RESPONSE OF JOINTED RIGID PAVEMENTS

11.1 SUMMARY

Computer programs for calculating strain histories in rigid pavements under heavy truck traffic are described. A finite-element structural model, ILLI-SLAB, was modified to generate influence functions which are combined with the dynamic loads under the wheels of a truck to predict the strain time histories at points of interest in the pavement. Using experimental measurements of pavement response it is demonstrated that these programs are capable of predicting strains in a jointed rigid pavement when the dynamic loads generated by the truck and pavement properties are known. Variations in truck speed cause some variations in strain not replicated by the pavement model, which has no speed-dependent effects. Behaviour in the vicinity of a pavement crack is difficult to predict because of the unknown load transfer properties of the crack, the inconsistent load transfer performance from test to test, and an apparent but unexplained sensitivity of load transfer performance to the truck travel speed.

This chapter is based on work previously published in [352]. It was performed as part of NCHRP project 1-25(1) [192].

11.2 INTRODUCTION

Rigid pavement structures are traditionally analysed by examining the stress and strain responses in the vicinity of a static load imposed on the surface of a plate supported by an elastic foundation [246, 256, 488]. The analyses have been extended by consideration of non-linear foundation models [255], and to a limited extent, inclusion of dynamic axle loads [319]. Very few rigid pavement models have been validated by comparison with field experiments. While static analysis provides a systematic method for quantifying the load bearing properties of a pavement structure, it does not lend itself to analysis of the cyclic stresses and strains caused by the moving, dynamic loads of a passing truck. At best, the static analysis methods only allow static responses from the analytical computations to be compared with experimental measurements. In the absence of a developed methodology for computing localised response to a passing truck, the analyst is hindered in studying the mechanics of the truck loading/pavement response process.

This chapter describes a methodology developed to calculate the response of jointed, rigid pavements to moving dynamic loads and shows the agreement that can be obtained between the simulation and experimental measurements of primary pavement responses.

11.3 THE RIGID PAVEMENT MODEL

The most commonly accepted method of modelling rigid pavement structures is with a finite element representation of the slab supported by an elastic base. Numerous models have been developed for

this purpose [107, 245, 256, 448, 459], most being functionally similar to the program 'ILLI-SLAB' developed by the University of Illinois [448], which was used in this study.

ILLI-SLAB is a static model capable of calculating pavement response at any location as a consequence of a single-point load, defined by a pressure applied to a rectangular contact area. The input to ILLI-SLAB is a parameter list describing the pavement design, the finite element mesh to be used, and the load and its application point. The pavement design parameters are thickness of slab and sub-base (if any), elastic modulus of the slab and sub-base, modulus of subgrade reaction, and joint information such as load transfer devices and width of the joints. Dowels are described in terms of material properties and dimensional information. Special attention is given to joints allowing them to be handled in four ways: doweled joints, joints with aggregate interlock, joints with dowels and aggregate interlock, and free joints. In the case of doweled joints, torsion, moment, and shear effects of the dowel bars can be selectively included.

The finite element mesh is described by the coordinates of a rectangular grid of nodes. In the longitudinal direction up to 10 slabs can be modelled, requiring considerable computer memory. It is usually necessary to model at least three slabs, with two joints, in order to properly represent end effects on the middle slab. The program calculates the stresses and deflections at each node of the finite element mesh and generates output responses at points selected by the user.

In order to calculate the pavement response to a load moving along the surface, an approach utilising influence functions was developed. Because the load from a truck wheel moves along a wheel path, it is sufficient to know how the stress or strain response at a point of interest is influenced by a load applied anywhere on the wheel path. This relationship between applied load and the response at a point of interest is called an 'influence function', which is defined as:

$$I_{ij} = \frac{y_j}{f_i}, \tag{11.1}$$

where:

I_{ij} is the influence function for point j due to a load at point i,
y_j is the primary response (stress, strain or deflection) at point j,
f_i is the force at point i.

Since the pavement models are linear, the influence function is not load dependent, and the response to loading from the multiple wheels of a truck can be determined by superposition of the responses to individual wheels.

The ILLI-SLAB model was modified to calculate influence functions by adding a subroutine which runs the model sequentially with a unit load applied at each point along a defined wheel path. In the modified form, the program saves the response at every node in a file, with separate files for each load position. Names are automatically assigned to each file using a common prefix and sequential numbering. At the completion of the run the files are reprocessed to obtain the influence function for all selected node positions. This is accomplished by extracting the response for the point of interest from the file for each load position and saving it in an influence function file for that point. In addition, the program performs certain housekeeping functions, such as maintaining a record of file identifications and the load and response positions.

The modified version of ILLI-SLAB, can be run in desktop computer environments. The computation time, depends directly on the finite element mesh size and the number of load positions along the road. Although computation time may be lengthy, once the influence functions have been calculated for a given pavement design, they can be stored and the FE calculations need not be repeated. The influence functions can then be used to determine the response to any arbitrary set of moving dynamic wheel loads.

A typical influence function for strain in the longitudinal direction at a point on the bottom of a 12m x 3.7m x 240mm slab near its midpoint is shown in figure 11.1.

The pavement response to a moving load is readily seen in the influence function. As a tyre approaches, compressive stress begins to build, these change sharply to much larger tensile stresses when the tyre is directly above the point. The reverse pattern is observed as the tyre departs from the point of interest. The influence functions for all regions in the interior of the slab are similar to that shown in figure 11.1.

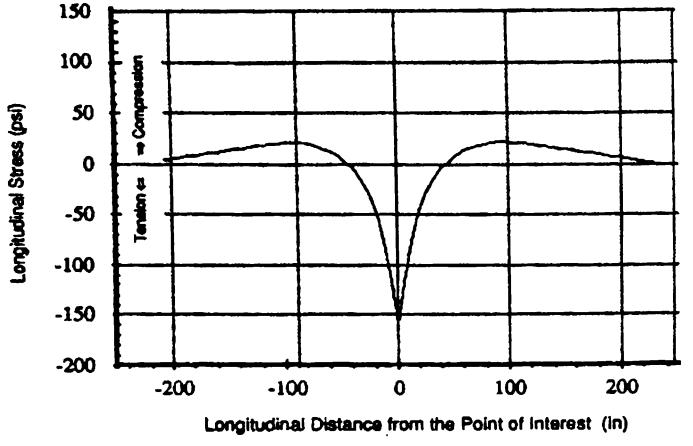


Fig. 11.1 A typical theoretical influence function for longitudinal strain at the bottom surface in the mid-region of a slab. From [352].

The influence functions of points near joints, cracks or free ends can have much different characteristics. A typical influence function for a point near a crack or joint is shown in figure 11.2. Influence functions of these forms can be used in analysing pavement response due to moving dynamic vehicle loads.

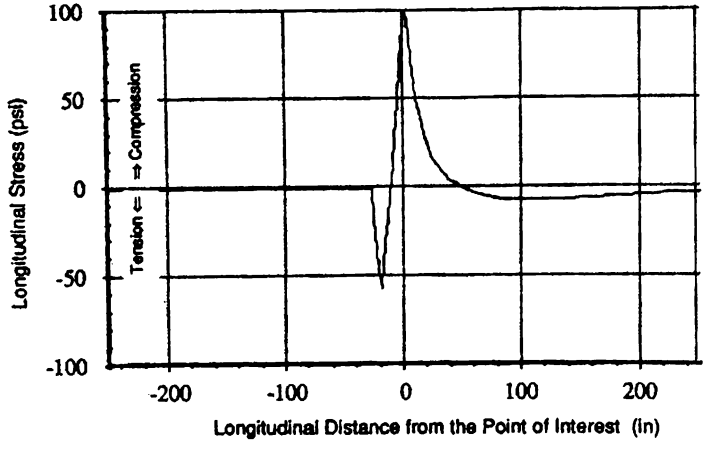


Fig. 11.2 Theoretical influence function for the response at the bottom of the slab near a crack. From [352].

11.4 COMBINATION OF LOADS WITH INFLUENCE FUNCTIONS

Once the influence functions have been obtained, they are combined with records of the dynamic wheel forces generated by the truck, to produce a time history of the pavement response at any point of interest in the slab. The process is one in which the influence function is combined with dynamic load histories for all wheels of the truck. For every time step the position of each wheel on the road surface is determined along with its instantaneous load. The response in the pavement is then computed for the loads from all the wheels at their respective positions according to the equation:

$$y_j(t) = \sum_{i=1}^{N_f} I_{ij}\, f_i(t), \tag{11.2}$$

where:

$y_j(t)$ is the response at point j at time t,
$f_i(t)$ is the load generated by tyre i at time t,
N_f is the number of wheels on the truck.

Equation 11.2 is simply a discrete version of equation 10.21, however the influence function at each point can be different. (In equation 10.21, the influence function at every point was assumed to be the same.)

Repeating the process in equation 11.2 for every time step, as the truck passes in the vicinity of the point of interest, produces the stress or strain time history for that point. Note that calculating the response in this manner is only valid when the pavement response is proportional to the applied load, and it neglects any dependency on inertia or damping of the pavement.

A program was written to perform the combination process for rigid pavements. It is configured to accept dynamic wheel loads from any source providing they are in a standard format. Thus, it can be used to predict pavement response either from records of wheel loads measured on a truck, or calculated from an analytical model of vehicle dynamics, such as those described in Chapters 5 and 6.

The combination is performed by selecting a starting point for the truck where the leading tyre is sufficiently distant from the point of interest that the influence function is zero.

The truck is moved along the pavement in a series of discrete time steps, and for each step the response is computed at the point of interest from the combined influence of all the tyres. The procedure is as follows:

(i) find the position of each tyre relative to the point of interest;

(ii) look up the value of the influence function for a unit load at the position of each tyre;

(iii) look up the dynamic load that each tyre is exerting on the road at this instant;

(iv) multiply the influence function for each tyre by the dynamic load to get the component of pavement response caused by that tyre at the point of interest; and

(v) sum up the responses due to all the tyres.

This sum is the response at the point of interest to all wheels of the truck for the particular time step. To get a complete time history of the response, the computation is repeated for a series of time steps selected to be small enough to reflect the variations in dynamic wheel loads and/or the changing position of the wheels on the slab. Generally, time steps corresponding to about 75mm of truck movement along the slab are necessary. It should be noted that once the influence functions and dynamic loads have been determined, calculation of road response using the method described above, can be carried out for the whole slab on a desktop computer very quickly.

The output of the combination program is a time record of pavement response due to dynamic wheel loads. An example of a calculated response derived from measured dynamic wheel loads is shown in figure 11.3. It presents the strain response in the longitudinal direction at a point on the bottom surface of a 12m x 3.7m x 240mm slab, at a location 8.8m (29 feet) from the upstream end, on the nearside edge, when traversed by a 3-axle rigid truck. The first tensile peak is the response when the steering axle passes over the point of interest and other two peaks correspond to the two rear axles.

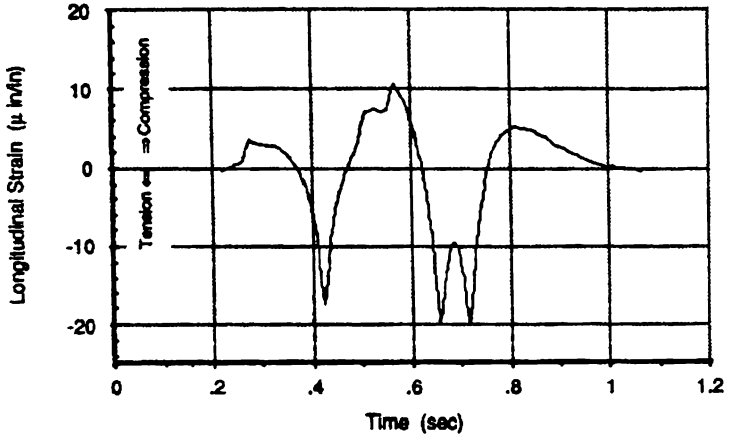


Fig. 11.3 Calculated response on the bottom surface of a 12m x 3.7m x 240mm (40 ft x 12 ft x 9.5 in) slab at a location 8.8m (29 ft) from the upstream end, on the nearside edge. From [352].

11.5 FIELD EXPERIMENTS

Experiments were conducted on instrumented rigid pavement sections near Carlyle, Illinois on route US 50 using an instrumented truck to acquire data for validating both vehicle and pavement models [99]. The pavement construction was reinforced Portland Cement Concrete slabs, 12m (40 feet) in length, laid on a stabilised sub-base. The test section was a 240mm (9.5 inch) thick slab with a 100mm (4-inch) sub-base of econocrete. The joints were doweled. The pavement was instrumented by the University of Illinois and the Illinois Department of Transportation at the time of construction [44]. Strain gauges were installed 12mm (0.5 inch) from the top and bottom surfaces of the slab according to the layout shown in figure 11.4. Odd numbers correspond to gauges on the top surface and even numbers to gauges on the bottom of the slab.

A 3-axle rigid truck was provided by the Paccar Technical Center. The axles were instrumented with strain gauges and accelerometers for measuring the dynamic forces [99] (see Chapter 7). Static tests, and dynamic tests, were conducted on various instrumented test sections, for speeds up to 27 m/s. A typical example of measured dynamic wheel forces is shown in figure 11.5.

The University of Illinois provided instrumentation for measuring and recording pavement strains. The combined instrumentation systems were configured to record dynamic loads under each of the truck wheels simultaneously with the pavement strains, using a common time marker signal to synchronise the records and to provide precise measurements of the longitudinal position of the vehicle as it passed over the test site. The lateral location of the moving wheels relative to the gauges is very important, affecting both the magnitude and shape of the strain histories. Therefore, means

were provided in the testing to record the lateral position of the truck wheels. An example of the measured strain response of gauge 4 is shown in figure 11.6 for a test speed of 22 m/s. As the truck front wheel approaches the gauge, a low-level compressive strain builds and then rapidly changes to a much larger tensile spike as the wheel moves over the top of the gauge. When the front wheel leaves the gauge, the strain returns to compression. The approach of the leading tandem axle adds to the compression until the axle arrives at the gauge and again creates a tensile peak. The gap between the leading and trailing tandem axles is large enough that the strain can diminish between the axles but not revert to compression. The third tensile spike occurs as the trailing axle passes over the gauge. As the trailing tandem axle leaves the gauge, the strain reverts to low-level compression, diminishing to zero as the truck departs.

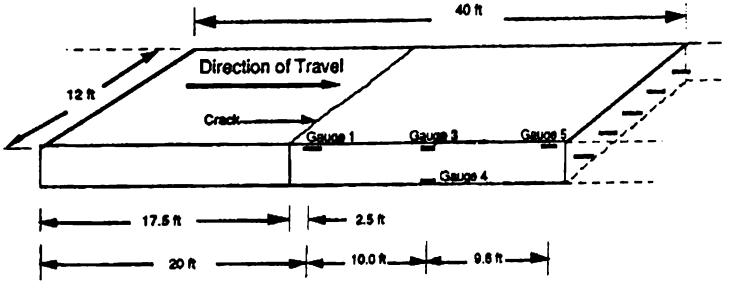


Fig. 11.4 Layout of strain gauges on the PCC test section near Carlyle, Illinois. From [352].

11.6 MODEL VALIDATION

The dynamic wheel loads generated by the truck were measured concurrently with the pavement responses. The response of the road to these measured loads was calculated using the influence function method described above. The strains predicted by the pavement model were compared with those measured by a number of gauges in the test pavement.

Figure 11.7 compares simulated and measured strains for gauge 4, for one of the tests. As evidenced by this graph, very good agreement is possible, particularly in prediction of the shape and magnitudes of the tensile strains. To achieve this level of agreement, it is essential to know the various pavement parameters (thickness, base stiffness, *etc*) quite accurately. The main disparities in figure 11.7 occur in prediction of the compressive strains, but because they are generally of low level and are not damaging to the slab, the agreement here is less critical.

It is important to note that gauge 4 is located in an area of the slab that is distant from any joints or cracks. Near a joint or crack the behaviour of pavement may be markedly different, depending on the load transfer across the discontinuity. If the load transfer characteristics are very good the response in that region will be similar to that of a continuous pavement. If the load transfer is poor, then strain reversals can occur. The test slab had a full-depth transverse crack 750 mm (2.5 ft) ahead of gauge 1, due to shrinkage early in the life of the pavement. To model the crack an additional weak joint was introduced in the finite element model at that location in the slab. (The geometry of the slab, crack and gauges is shown in figure 11.4.) The measured and calculated response of gauge 1 for a vehicle travelling at 2 m/s (5 mph) is shown in figure 11.8.

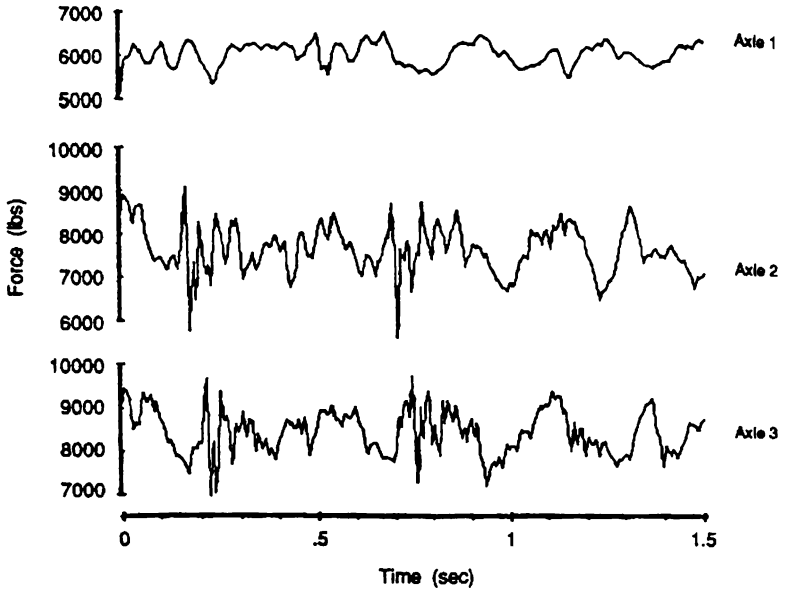


Fig. 11.5 Measured dynamic wheel forces on the nearside wheels of the three-axle test vehicle, speed = 22 m/s (50 mph). From [352].

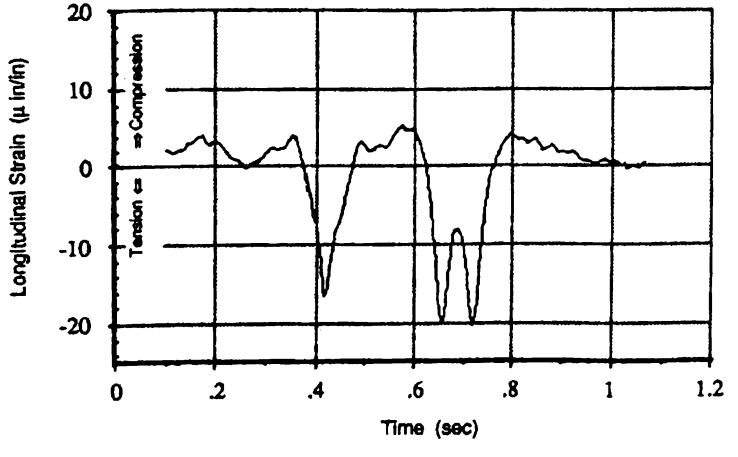


Fig. 11.6 Measured response of strain gauge 4, speed = 22 m/s (50 mph). From [352].

Prior to the front wheel of the truck crossing the crack, gauge 1 experiences only a low level of tensile strain due to the poor load transfer across the crack (presumably caused by aggregate interlock

and/or some continuity in the reinforcing mat). As the axle advances across the crack the gauge immediately experiences a large tensile strain, which changes to compression as the wheel reaches the gauge. On its departure the strain relaxes again to approximately zero.

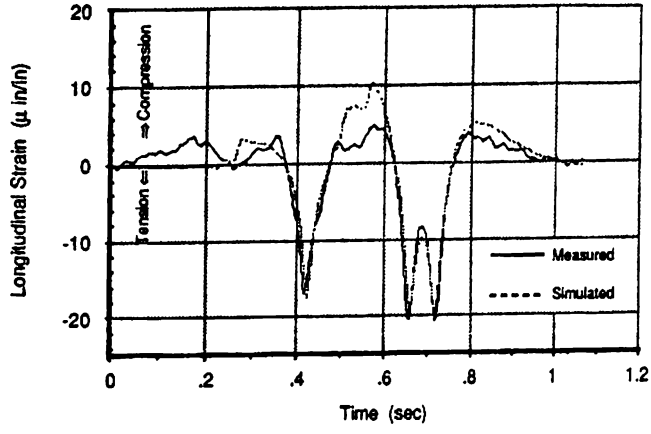


Fig. 11.7 Comparison between measured and calculated responses of gauge 4, speed = 22 m/s. From [352].

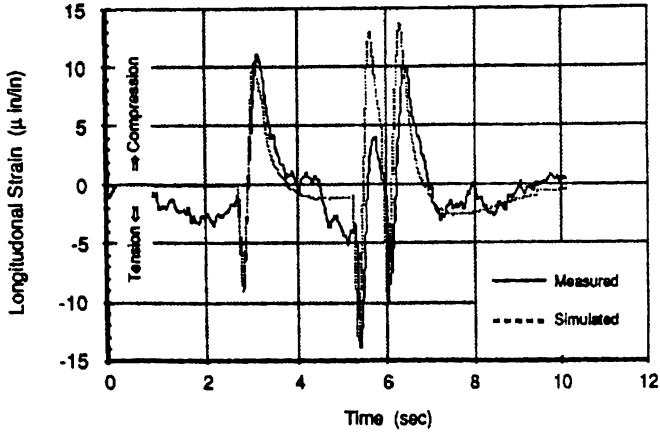


Fig. 11.8 Comparison between measured and calculated responses of gauge 1 (near crack), speed = 2 m/s (5 mph). From [352].

This pattern is repeated approximately 3 seconds later when the leading tandem axle crosses the crack. Initially, the gauge goes into tension, which changes quickly to compression as the axle passes across the gauge. The reduction of the compressive strain as the axle leaves the gauge is accelerated by the approaching load of the trailing tandem axle, 1.2m (50 inches) behind the leading axle. When the trailing axle crosses the crack its response is superimposed on that of the previous

axles. The prediction of the compressive strain as the leading tandem axle crosses the gauge is not very accurate, the error most probably being due to the uncertainty about load transfer properties of the crack. The prediction of strain under the influence of the trailing axle is more accurate for this portion of the cycle because there is no longer any load on the upstream side of the crack, and therefore no significant load transfer effect to be taken into account. After all axles have passed the gauge the strain returns to compression and then relaxes to zero in a fairly predictable fashion.

The effectiveness of the load transfer across a crack has a strong influence on the strain cycles produced in the slab in the vicinity of the crack. Figure 11.9 shows how the predicted strain history at the gauge 1 position varies with the effectiveness of the load transfer. With full load transfer (no crack) the top surface experiences a low-level tension broken by compressive strain peaks as the wheels pass over the point of interest. In the case of no load transfer, large tensile strains are experienced as each wheel traverses the crack. For intermediate levels of load transfer, an intermediate response is obtained.

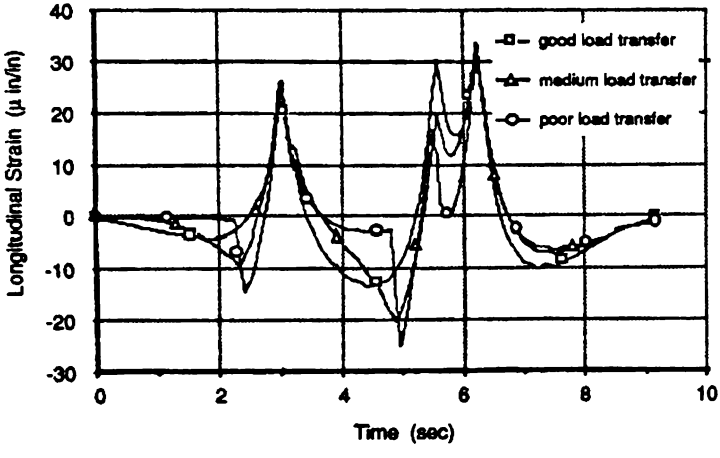


Fig. 11.9 Effect of load transfer at a crack on theoretical strain cycles at the top surface. From [352].

The measured response shown in figure 11.8 presents one example of how the test pavement behaved at gauge 1 under loading from the truck, but by and large, the load transfer obtained at the crack was not consistent from test to test. Figure 11.10 presents the results from gauge 1 for three repeat tests at a nominal speed of 2 m/s (5 mph) on the site. The major features in the strain cycles are repeatable. However, the strains in the region A of figure 11.10 (when the leading tandem axle approached the crack) are quite variable. Comparing the measured response to the predictions in figure 11.9, it would appear that the effectiveness of the load transfer varied significantly between tests – in one case behaving similar to the full load transfer case, and in another approaching the no-load transfer case. Examination of the dynamic wheel load records indicated that this marked variation from test to test was not due to variations in the dynamic loads on the axles of the truck, which were quite repeatable. The fact that the strain varied considerably in this region in the course of individual tests, leads to the conclusion that the load transfer mechanism is not consistent. Such behaviour may be expected from a nonlinearity which is heavily dependent on friction and/or the loading history.

Testing at different speeds revealed an additional phenomenon in the pavement. As the test speed increased, ever greater levels of tensile strain were observed with the approach of the leading tandem

axle. Figure 11.11 contains example strain records from gauge 1 at five speeds for this test section. The most remarkable observation is the very high level of tensile strain experienced as the leading tandem approached the crack at high speed. The tensile strain of 15 (μ in/in) seen at 2 m/s (5 mph) is indicative of the strain from the weight of the leading tandem axle as it mounts the cantilevered end of the slab. At 22 m/s (60 mph), the tensile cycle reaches more than twice that amplitude. Examination of the axle load records for the truck showed only moderate dynamic variations: not nearly large enough to account for doubling of the strain. Therefore, this effect must be attributed to a phenomenon in the pavement.

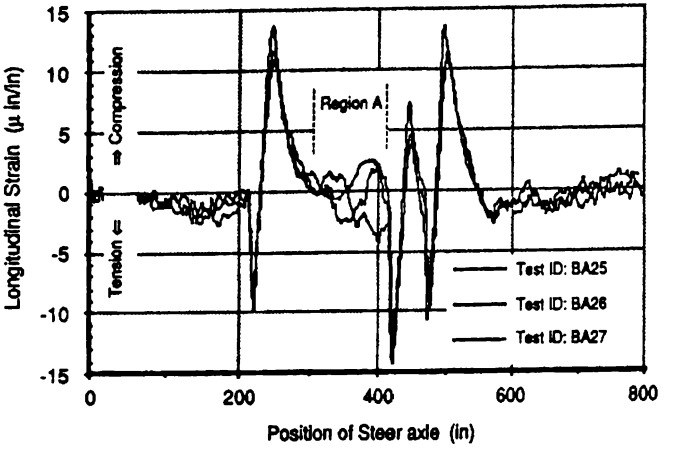


Fig. 11.10 Variations in strain histories in repeat tests, gauge 1, 2 m/s (5 mph). From [352].

Comparison of the maximum tensile strains at the bottom of the slab (as shown in figure 11.6) and tensile strain at the top of the slab near the crack (as shown in figure 11.11) reveals that the top surface strains can be 70% higher. Simulations with the pavement model indicate that even larger tensile strains can occur on the top of the slab at a distance of 1.2m (5 feet) from the crack. Although traditional analyses assume that the primary failure mode for rigid pavements arises from cracks starting at the bottom of the slab due to the tension of flexural loading, the observations made here indicate that larger tensile strains can occur on the top surface if a shrinkage crack forms. These same mechanisms would be at work when a joint loses its strength. In either case, a secondary crack is likely to initiate on the top surface some distance from the discontinuity.

In general the experimental data does not show the pavement response to increase with travel speed of the truck in regions distant from the crack. Figure 11.12 compares the strain measured on gauge 4 at 2 m/s and 22 m/s (5 and 60 mph). The reduction in the magnitude of the strain peaks under the first and last axles is not explained by changes in dynamic axle loads or by lateral tracking errors. This was established by computing the pavement response for the measured wheel loads and comparing them to the measured response at each speed, using only tests in which the wheel tracks passed within 50 mm of the strain gauge location. Figure 11.13 shows the ratio of measured to predicted strain at gauge 4 as a function of speed. While there is scatter in the data, a significant trend with speed is apparent. The response appears to increase slightly at low speeds and to decrease at higher speeds. Speed dependence has been observed in other experimental studies, particularly for flexible pavements [94], although the initial increase with speed observed here is unusual. In figure 11.13, the speed dependence is thought to be caused by dynamic motion of the slab due to its

significant mass (which is the same order of magnitude as the truck) and damping in the foundation. These characteristics were not included in the finite element model.

While this data is not conclusive, it is included here to show the contrast with pavement behaviour near a crack, and to illustrate that under some conditions rigid pavement response in interior regions of the slab can diminish with increased truck travel speed.

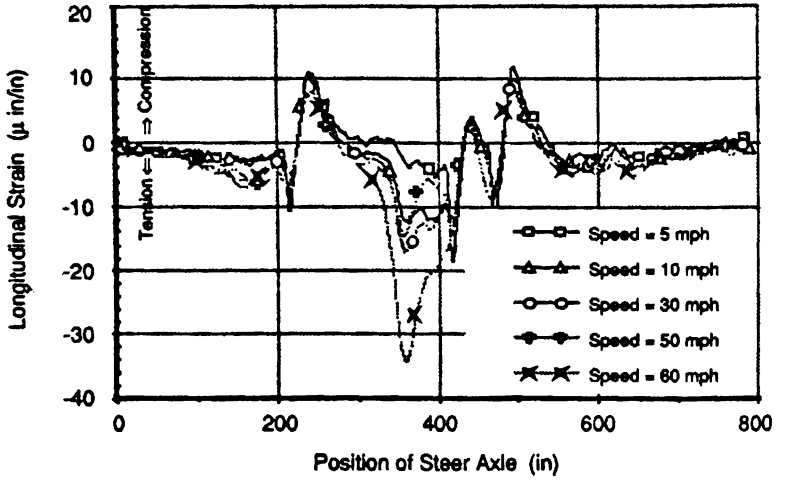


Fig. 11.11 Variation in strain histories as a function of vehicle speed in repeat tests at gauge 1. From [352].

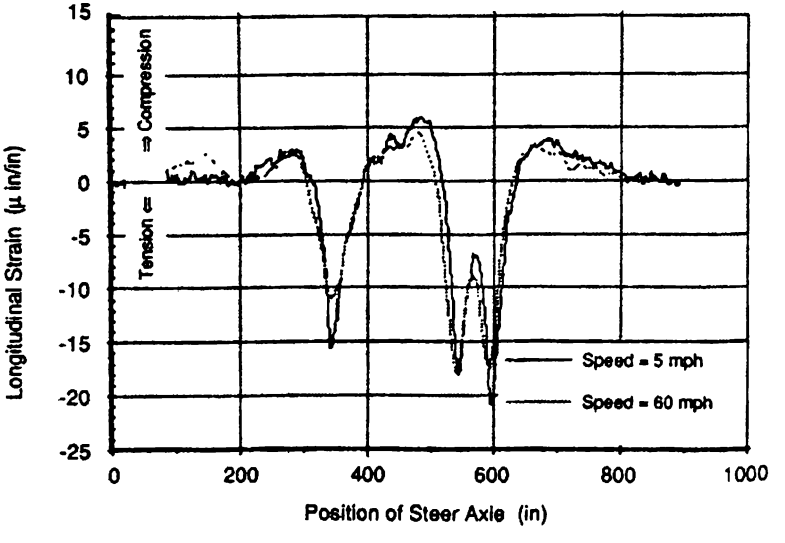


Fig. 11.12 Comparison of measured response at 5 and 60 mph, gauge 4. From [352].

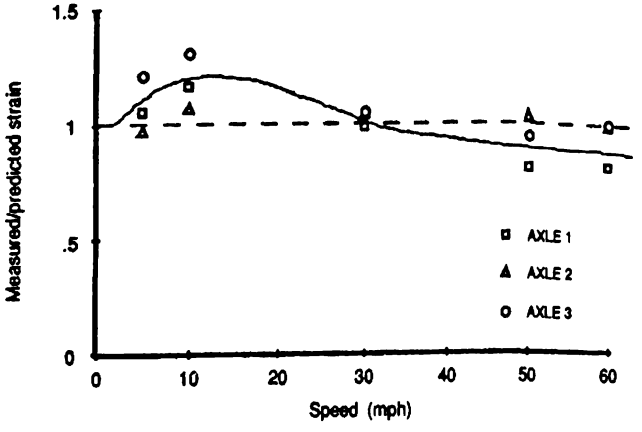


Fig. 11.13 The effect of speed on normalised pavement response. From [352].

11.7 CONCLUSIONS

(i) A method has been developed for calculating the time history of the response of a rigid pavement to moving dynamic loads of trucks. The method was validated with a program of experimental measurements and has provided new insights into rigid pavement behaviour.

(ii) It has been shown that typical finite element models of rigid pavements, such as ILLI-SLAB, are capable of predicting responses to static loads when pavement properties are known. Coupling these models with programs that allow computation of strain time histories at a point in the pavement provides a new and powerful tool for investigating truck/pavement interaction.

(iii) Experimental measurements of strains induced by truck wheel loading show large tensile strains on the top surface of the slab associated with the wheels traversing a crack. This mechanism would encourage development of secondary cracks in the top surface a short distance from the location of a shrinkage crack. The theoretical pavement models can predict the qualitative behaviour of response in the vicinity of a crack, but are limited by the uncertainty and variability of the load transfer properties of the crack.

(iv) The experimental data gives some evidence that strains in the interior region of a slab may diminish with increasing speed of travel, but may increase with speed in the vicinity of the crack. The existing pavement structural models are not able to predict this speed dependent behaviour. It is thought that dynamic models may be needed to achieve such detailed level of agreement.

12
DYNAMIC RESPONSE OF BRIDGES

12.1 SUMMARY

A calculation procedure is developed for predicting the dynamic response of a bridge to a given set of vehicle wheel loads. The method involves convolution of the vehicle loads with modal responses of the bridge. The convolution integral is solved by transformation to the frequency domain using the fast Fourier transform. The method is then extended by an iterative procedure to include dynamic interaction between the bridge and an arbitrary mathematical model of a vehicle. Examples are presented to illustrate the effectiveness of the convolution method, and to demonstrate the convergence of the iterative procedure.

Experimental measurements on a highway bridge are presented and used to validate the calculation method. The modal properties of the bridge were measured by impulse tests with an instrumented hammer and compared with simple mathematical models. Single vehicle tests, in which the dynamic wheel loads and dynamic response of the bridge were measured simultaneously, are discussed. The measured dynamic wheel loads were convolved with the measured modal properties of the bridge and the predicted responses are compared with the measured responses. Good agreement is found.

This chapter is based on work previously published in [205].

12.2 INTRODUCTION

Highway bridges serve a vital role in transportation systems. In a typical journey, a heavy goods vehicle crosses dozens of bridges. During each bridge crossing, it applies dynamic wheel loads which cause the bridge to vibrate. The repeated application of these loads can lead to deterioration and a resulting reduction in the service life of the bridge.

In recent years, heavy vehicles have become larger and have increased in number. At the same time, new materials and improved design methods have resulted in lighter and more flexible bridges. Therefore, highway bridges are increasingly susceptible to vibration. Short-span highway bridges typically have natural frequencies in the same range as those of heavy vehicles. Excitation of one system by the other is significant. Bridge damping is low (approximately 2 percent of critical in the first bending mode [387, 462]) and does not significantly reduce the vibrations caused by the bridge-vehicle interaction.

Notwithstanding the importance of vehicle-induced bridge dynamics, major bridge failures are not normally caused by dynamic wheel loads [33]. The wheel loads cause more subtle problems and contribute to fatigue, surface wear, and cracking of concrete which leads to corrosion. Thus dynamic loads continually degrade bridges, and increase the necessity of regular maintenance.

Maintenance costs for highway bridges are high. In the UK for instance, £20 million is spent each year keeping the network of concrete bridges serviceable [300]. It is not known what portion of bridge damage is caused by heavy vehicle loads because the dynamic response of bridges to heavy vehicle loads is not adequately understood. Nevertheless, even if only a small percentage of the damage arises from bridge vibrations, then this accounts for significant expenditure.

A better understanding of the dynamics of the bridge-vehicle system is necessary in order to build bridges to resist vibrations, to design better vehicles to reduce bridge damage, and/or to regulate vehicle loads and suspensions.

This chapter presents a frequency domain calculation procedure (using the fast Fourier transform) to compute the dynamic response of a bridge to arbitrary wheel loads. The method is based on a convolution formulation of the equation of motion. The convolution integral is expressed in terms of the modal responses of the bridge, and therefore can be used with any bridge as long as the modal properties are known. A significant advantage of the method is that it can be validated experimentally provided the dynamic loads applied by the test vehicle are measured. A full-scale validation study is presented.

12.3 CALCULATING BRIDGE RESPONSE TO VEHICLE LOADS

12.3.1 Equation of Motion and Modal Decoupling

A relatively general formulation of the equation of motion for vehicle–induced bridge vibration will be considered here. Assuming viscous damping, linear elasticity, small deflections, and neglecting the effects of shear deformation and rotary inertia, the equation of motion for a typical bridge can be written in the following form [354]

$$m(\mathbf{x})\frac{\partial^2 y}{\partial t^2}(\mathbf{x},t) + \mathbf{C}\left\{\frac{\partial y}{\partial t}(\mathbf{x},t)\right\} + \mathbf{L}\{y(\mathbf{x},t)\} = f(\mathbf{x},t) \tag{12.1}$$

where

- $\mathbf{L}$ is a self-adjoint linear differential operator with respect to the spatial variables,
- $\mathbf{x}$ is a two dimensional position vector,
- t is time,
- $m(\mathbf{x})$ is the mass per unit surface area,
- $y(\mathbf{x},t)$ is the vertical deflection of the bridge,
- $\mathbf{C}$ is a viscous damping operator with respect to the spatial variables,

and $f(\mathbf{x},t)$ is the force exerted by the vehicle on the bridge.

It can be shown [354] that the response of a system governed by equation 12.1, to an input, $f(\mathbf{x}_f,t)$, applied at a specified position on the bridge $\mathbf{x}_f$ is given by the convolution integral

$$y(\mathbf{x},t) = \int_{-\infty}^{\infty} h(\mathbf{x},\mathbf{x}_f,t-\tau)f(\mathbf{x}_f,\tau)d\tau, \tag{12.2}$$

where $h(\mathbf{x}, \mathbf{x}_f, t)$ is the impulse response function at position $\mathbf{x}$ for an impulse applied at $\mathbf{x}_f$.

Equation 12.1 may therefore be solved using equation 12.2, by determining the appropriate impulse response function. The impulse response function can be related to the modal responses by expressing the deflection, $y(\mathbf{x}, t)$, in terms of normal mode functions, $\phi^{(n)}(\mathbf{x})$, as follows

$$y(\mathbf{x},t) = \sum_{n=1}^{\infty}\phi^{(n)}(\mathbf{x})q_n(t) \tag{12.3}$$

where

- n is the mode number,
- $\phi^{(n)}(\mathbf{x})$ are the mass normalised mode shapes corresponding to the undamped case,

and $q_n(t)$ is the response of the n^{th} normal coordinate.

If the damping operator, $\mathbf{C}$, satisfies certain orthogonality conditions (see the Appendix to [205]) then the modes can be uncoupled. Substituting the modal expansion (equation 12.3) into equation

12.1, multiplying by $\phi^{(n)}(x)$, integrating over the surface of the bridge, and applying the orthogonality conditions gives the normal coordinate equation

$$\frac{d^2q_n}{dt^2}(t) + 2\zeta^{(n)}\omega^{(n)}\frac{dq_n}{dt}(t) + \omega^{(n)^2}q_n(t) = Q_n(t), \quad n = 1,2,3,...,\infty \tag{12.4}$$

where

$\omega^{(n)}$ is the n^{th} undamped natural frequency,

$\zeta^{(n)}$ is the n^{th} modal damping ratio,

and $Q_n(t)$ is the generalised force given by

$$Q_n(t) = \int_R \phi^{(n)}(x)f(x,t)dx \tag{12.5}$$

where R is the surface area of the bridge.

Equation 12.4 describes the response of the system in mode n. For each mode, the *modal impulse response function*, $h_n(t)$, can be determined by setting $Q_n(t) = \delta(t)$ where $\delta(t)$ is the Dirac delta function. Solving the differential equation results in a special case of $q_n(t)$, namely $h_n(t)$, which is expressed as follows

$$h_n(t) = \frac{e^{-\zeta^{(n)}\omega^{(n)}t}\sin(\omega_d^{(n)}t)}{\omega_d^{(n)}}, \quad t \geq 0 \tag{12.6}$$

where $\omega_d^{(n)}$ is the n^{th} damped natural frequency such that

$$\omega_d^{(n)} = \omega^{(n)}\sqrt{1-\zeta^{(n)2}} \tag{12.7}$$

and $\zeta^{(n)} < 1$.

The impulse response function for the bridge can be shown to be a combination of mode shapes with the normal coordinate impulse response functions $h_n(t)$ (see [204] for details):

$$h(x,x_f,t) = \sum_{n=1}^{\infty}\phi^{(n)}(x)\,\phi^{(n)}(x_f)\,h_n(t). \tag{12.8}$$

Up to this point it has been assumed that loads are applied to the bridge at only one position. This is obviously not the case for a moving vehicle, but the formulation can be extended to moving loads. The forcing function for a vehicle with N_t tyres can be described in terms of the dynamic wheel loads, $P_l(t)$,

$$f(x_f,t) = -\sum_{l=1}^{N_t}\delta(x_f - x_l(t))\,P_l(t) \tag{12.9}$$

where $x_l(t)$ is the position of the l^{th} force (see figure 12.1). If x_f is allowed to vary over the surface of the bridge to include all possible locations of wheel loads, then the forcing function will be zero except at the positions of the wheels (*ie* when $x_f = x_l(t)$) where it is equal to the instantaneous value of the wheel loads, $P_l(t)$. The negative sign is included in equation 12.9 because displacements and forces are assumed to be positive upwards for both the bridge and vehicle systems.

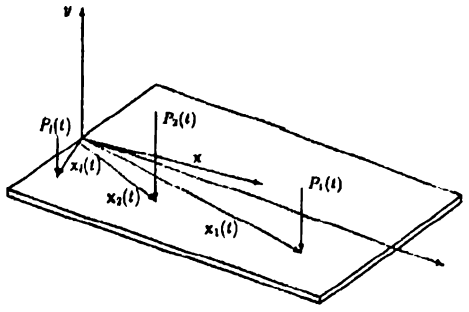


Fig. 12.1 Loads moving across a bridge. From [205].

Substituting equations 12.8 and 12.9 into the convolution integral (equation 12.2), and replacing x_i with x_l for $l = 1,2,...,N_l$ gives:

$$y(x,t) = -\sum_{l=1}^{N_l} \sum_{n=1}^{\infty} \phi^{(n)}(x) \int_{-\infty}^{\infty} h_n(t-\tau) g^{(n,l)}(\tau) d\tau, \tag{12.10}$$

where

$$g^{(n,l)}(\tau) = \phi^{(n)}(x_l(\tau))\, P_l(\tau).$$

With the general equations of motion in this convolution format, the bridge vibration problem (equation 12.1) can be solved by evaluating the convolution integral in either the time or frequency domains. For this study, a frequency domain method was chosen and the solution procedure is outlined in the next section.

12.3.2 Solution in the Frequency Domain

The Fourier transform of the bridge response, $Y(x,\omega)$ at frequency ω, is defined as [354, 355]:

$$Y(x,\omega) = \frac{1}{2\pi} \int_{-\infty} y(x,t) e^{-i\omega t} dt. \tag{12.11}$$

Substituting the convolution (equation 12.10) into the Fourier integral (equation 12.11) gives

$$Y(x,\omega) = -\sum_{l=1}^{N_l} \sum_{n=1}^{\infty} \phi^{(n)}(x) \frac{1}{2\pi} \int_{-\infty}^{\infty} \int_{-\infty}^{\infty} h_n(t-\tau) g^{(n,l)}(\tau) e^{-i\omega t} d\tau dt. \tag{12.12}$$

Putting $t = \beta + \tau$ and rearranging gives:

$$Y(x,\omega) = -\sum_{l=1}^{N_l} \sum_{n=1}^{\infty} \phi^{(n)}(x) \frac{1}{2\pi} \int_{-\infty}^{\infty} \int_{-\infty}^{\infty} h_n(\beta)\, g^{(n,l)}(\tau)\, e^{-i\omega(\beta+\tau)} d\tau d\beta$$

$$= -\sum_{l=1}^{N_l} \sum_{n=1}^{\infty} \phi^{(n)}(x) \left[\int_{-\infty}^{\infty} h_n(\beta)\, e^{-i\omega\beta} d\beta \right] \left[\frac{1}{2\pi} \int_{-\infty}^{\infty} g^{(n,l)}(\tau)\, e^{-i\omega\tau} d\tau \right],$$

or

$$Y(x,\omega) = \sum_{l=1}^{N_l} \sum_{n=1}^{\infty} \phi^{(n)}(x)\, H_n(\omega)\, G^{(n,l)}(\omega) \tag{12.13}$$

where $H_n(\omega)$ is the n^{th} modal frequency response function, which can be shown to be:

$$H_n(\omega) = \frac{1}{\omega^{(n)^2} - \omega^2 + 2i\zeta^{(n)}\omega^{(n)}\omega} \tag{12.14}$$

and $G^{(n,l)}(\omega)$ is the Fourier transform of $g^{(n,l)}(t)$. This calculation of $Y(x,\omega)$ simply requires multiplication of the appropriate terms of $\phi^{(n)}(x)$, $H_n(\omega)$, and $G^{(n,l)}(\omega)$.

Once $Y(x,\omega)$ is computed in the frequency domain, the inverse Fourier transform can be used to recover the time domain solution. The inverse Fourier transform is defined as follows [354, 355]:

$$y(x,t) = \int_{-\infty}^{\infty} Y(x,\omega)e^{i\omega t}dt. \tag{12.15}$$

12.3.3 Computer Implementation

To solve these equations by computer, the discrete Fourier transform can be used to approximate the continuous Fourier transform. The first step is to compute the transform of $g^{(n,l)}(t)$. The function is sampled to obtain N equally spaced values, $g_r^{(n,l)}$, where

$$g_r^{(n,l)} = g^{(n,l)}(r\Delta) \qquad r = 0,1,2,...,N-1 \tag{12.16}$$

and Δ is the sampling time step. The discrete Fourier transform is then applied to the g_r array as follows [354, 355]:

$$G_k^{(n,l)} = \frac{1}{N}\sum_{r=0}^{N-1} g_r^{(n,l)} e^{-i\left(\frac{2\pi kr}{N}\right)} \qquad k = 0,1,2,...,N-1 \tag{12.17}$$

A discrete version of $Y(x,\omega)$ at a particular location x is then given by

$$Y_k(x) = -\sum_{l=1}^{N_l}\sum_{n=1}^{\infty}\phi^{(n)}(x)\,H_n(k\bar{\omega})\,G_k^{(n,l)}, \qquad k = 0,1,2,....,N-1 \tag{12.18}$$

where $\bar{\omega}$ is the frequency resolution. Finally, the solution is recovered with the inverse discrete Fourier transform given by [354, 355]

$$y_r(x) = \sum_{r=0}^{N-1} Y_k(x)e^{i\left(\frac{2\pi kr}{N}\right)} \qquad r = 0,1,2,....,N-1 \tag{12.19}$$

where $y_r(x) = y(x, r\Delta)$.

In order to implement the discrete transforms in the convolution calculation, the time record must be long enough to obtain the required frequency resolution, $\bar{\omega}$, where [355]

$$\bar{\omega} = \frac{2\pi}{T} \tag{12.20}$$

and T is the length of the time record such that $T = N\Delta$.

In addition, Δ must be small enough to avoid aliasing of high frequency components into the low frequency range of the transform [355]. Aliasing is prevented by ensuring that the maximum frequency present in the signal is smaller than the Nyquist frequency:

$$\text{Nyquist frequency} = \frac{1}{2\Delta}\ \text{Hz}. \tag{12.21}$$

Finally, allowance must be made for the fact that the convolution defined by the discrete Fourier transform is 'circular' [355]. The circularity of the discrete transform means that all the time records in the convolution repeat themselves with period T (when they are, in fact, not periodic). It can be

shown [440] that the differences between circular and linear convolutions can be eliminated by choosing T such that

$$T \geq T_h + T_{vp} \tag{12.22}$$

where T_h and T_{vp} are the lengths of the non-zero portions of the time records of the impulse response function and the vehicle force input, respectively.

To satisfy all these criteria, the time record must be significantly longer than the vehicle crossing time, T_{vp}.

12.3.4 Treatment of Dynamic Bridge-Vehicle Interaction

The convolution method presented in the preceding sections includes no specific reference to the interaction between vehicles and bridges, as shown in figure 9.3. This section describes a procedure for combining mathematical vehicle models with bridge dynamics.

For the purposes of this study, the bridge-vehicle interaction was incorporated iteratively. The procedure was as follows:

(i) An initial set of vehicle wheel loads was obtained by calculating the vehicle response to a specified bridge surface profile. These loads were used as input to the bridge calculation program.

(ii) The displacement response of the bridge was calculated under each tyre of the vehicle in a coordinate frame moving with the vehicle (*ie* $y(x_l(t),t)$). Note that the displacement response in the moving reference frame is essentially only a function of time.

(iii) The bridge displacement response was added to the surface profile and their sum was used as the new input to the vehicle model. New wheel loads were then predicted.

(iv) The displacement response $y(x_l(t),t)$ from the loads in (iii) was computed by the procedure of (ii). In order to facilitate convergence, successive displacement responses were averaged

$$y_j(t) = \frac{y(x_l(t),t) + y_{j-1}(t)}{2} \tag{12.23}$$

where y_j is the j^{th} estimate of the bridge displacement in the moving reference frame.

(v) Steps (iii) and (iv) were repeated until convergence was obtained. Convergence was deemed to have occurred when the following criterion was satisfied:

$$\max\left(\frac{|y(x_l(t),t) - y_{j-1}(t)|}{|y(x_l(t),t)|}\right) \leq \text{Tolerance}, \quad \text{for} \quad 0 \leq t \leq T_{vp}. \tag{12.24}$$

where T_{vp} is the time for the vehicle to pass completely over the bridge.

Similar iterative methods have been used by other authors. In fact, Hawk and Ghali [228] outlined an almost identical convergence procedure which they termed the 'iterative dynamic sub-structuring method (IDSM)'. They compared their method with solutions obtained by Runge-Kutta Nystrom numerical integration and found good agreement. Nevertheless, the method is not guaranteed to converge. Convergence was not found to be a problem, except for vehicles with large wheel forces at frequencies greater than about 10Hz. Since a large proportion of all vehicles generate dynamic wheel loads with energy concentrated in the 1.5-4.5 Hz frequency range (Chapter 7) this limitation was not considered to be serious.

12.4 EXAMPLES

In order to demonstrate the effectiveness of the convolution method, some example calculations will be presented here and compared with known analytical solutions for simple cases.

12.4.1 Bridge Model

The bridge is idealised as a simply supported beam. The equation of motion for free vibrations of a Bernoulli-Euler beam with light viscous damping is

$$m\frac{\partial^2 y}{\partial t^2}(x,t) + C\left\{\frac{\partial y}{\partial t}(x,t)\right\} + EI\frac{\partial^4 y}{\partial x^4}(x,t) = 0 \tag{12.25}$$

where

- m is the mass per unit length of the beam,
- C is the damping operator,
- x is the position along the length of the beam,
- E is the Young's modulus of the material,

and I is the second moment of area of the cross-section.

Following the method described in Section 12.3, the solution to equation 12.25 can be written as a modal expansion (equation 12.3). The undamped mode shapes, as required for equation 12.3, are obtained by ignoring the (small) damping term in equation 12.25. Substituting the modal expansion into equation 12.25 and separating variables results in the following modal differential equation:

$$\frac{d^4\phi^{(n)}}{dx^4}(x) - k_n^4\phi^{(n)}(x) = 0 \tag{12.26}$$

which has well known solutions of the form

$$\phi^{(n)}(x) = C_1^{(n)}\cos(k_n x) + C_2^{(n)}\cosh(k_n x) + C_3^{(n)}\sin(k_n x) + C_4^{(n)}\sinh(k_n x) \tag{12.27}$$

where $C_1^{(n)}$, $C_2^{(n)}$, $C_3^{(n)}$, $C_4^{(n)}$, and k_n are constants dependent upon the boundary conditions. Once these constants are determined, the natural frequencies can be calculated from

$$\omega^{(n)} = k_n^2\sqrt{\frac{EI}{m}}. \tag{12.28}$$

For simply-supported boundary conditions, the mode shapes are given by:

$$\phi^{(n)}(x) = \sqrt{\frac{2}{mL}}\sin\left(\frac{n\pi x}{L}\right) \tag{12.29}$$

where L is the length of the beam. The natural frequencies can easily be shown to be

$$\omega^{(n)} = \left(\frac{n\pi}{L}\right)^2\sqrt{\frac{EI}{m}}. \tag{12.30}$$

The parameters describing the bridge were based on measurements of the Pirton Lane highway bridge in Gloucester by Eyre *et al* [174], Leonard [301], and Wills [496]. They reported the bridge to be simply-supported with a length of 40 metres, and a first natural frequency of 3.2Hz with a modal damping ratio of 0.02. The mass per unit length was estimated from drawings in the papers as 12000 kg/m. Three modes were used in the analysis, and the natural frequencies of the second and third modes were calculated from equation 12.30. The modal damping ratio was assumed to be 0.02 for the first two modes. For the third mode it was chosen to satisfy the orthogonality conditions (see Appendix of [205]). The modal information is summarised in Table 12.1.

Mode Number	Natural Frequency $\omega^{(n)}$ (rad/s)	Damping Ratio, $\zeta^{(n)}$
1	20.0	0.02
2	80.0	0.02
3	180.0	0.04

Table 12.1 Modal information for Pirton Lane bridge

12.4.2 Computational Considerations

To illustrate the computational considerations associated with the convolution calculation, suppose that the bridge is traversed by a vehicle of length 10m at 25m/s, giving $T_{vp} = 2.0$ seconds. If Δ is chosen to be 0.01 seconds, then the Nyquist frequency is 50Hz (314rad/s). With this Nyquist frequency, the first three bridge modes can be included because the third natural frequency is at 27Hz (180rad/s). Vehicle vibration is usually below 20Hz, so the 50Hz Nyquist frequency is quite adequate.

Using $\omega^{(1)}$ and $\zeta^{(1)}$ from Table 12.1, the impulse response for the first mode has the form:

$$h_1(t) = \frac{e^{-0.377t}}{18.8}\sin(18.8t). \tag{12.31}$$

The impulse response never completely dies away, but for computational purposes it can be ignored when the amplitude is below 0.1% of the initial amplitude. With this definition, T_h is equal to 18.3 seconds, while T_{vp} is 2.0 seconds. Therefore the time record should be chosen to be greater than 20.3 seconds. With $\Delta = 0.01$ seconds, at least 2030 points are required. For efficiency in computing the discrete Fourier transform, the number of points should be a power of 2 and so 2048 is selected. Finally, the frequency resolution is computed from equation 12.20 as 0.05Hz. This is more than adequate to resolve the frequencies of interest.

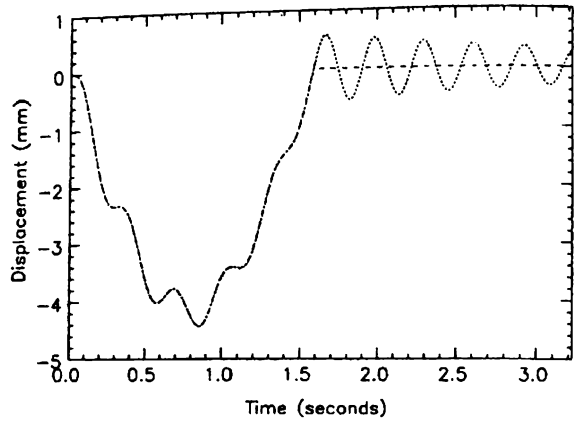
To compare the efficiency of frequency and time domain methods, suppose that for the preceding example a time history of total length 4 seconds (400 points) was required. To evaluate the convolution integral in the time domain requires 160000 (400^2) multiplications. On the other hand, the fast Fourier transform algorithm requires $N \log_2(N)$ multiplications [355] to compute each transform. The frequency domain method includes two transform calculations and one N point multiplication giving a total of $N + N \log_2(N)$ multiplications. For 2048 points, only 24576 multiplications are required making the frequency domain method about 7 times faster than a time domain convolution. Further time savings can be achieved if T_{vp} is about the same length as T_h.

12.4.3 Results for Specified Moving Forces

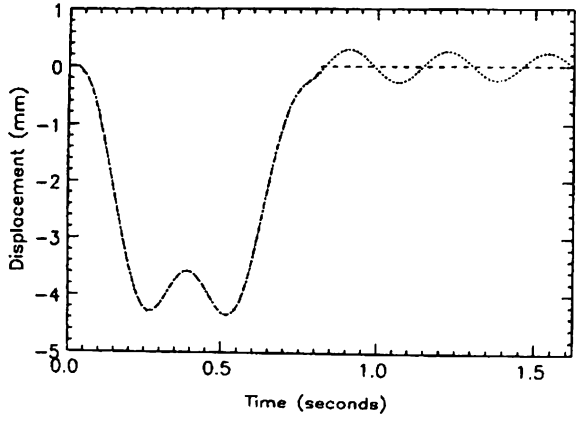
Three different types of moving point loads are considered in the following: a constant force, a sinusoidally varying force, and a linearly increasing force. On each of figures 12.2 to 12.4, two curves are drawn. One is for the solution obtained by the method described in this chapter and designated as the 'calculated' solution. The second curve is produced by using closed-form solutions for these special cases, as derived by Fryba [185].

Figure 12.2 shows the effect of speed on the midspan deflection of the bridge due to a constant force. The closed-form solutions are only defined for the time the force is on the bridge, and are set to zero otherwise. The dynamic deflection increases as the speed of the force increases. Calculated and closed-form curves agree closely.

The response of the beam to a moving sinusoidally varying force at three frequencies (Ω = 10, 20, 30 rad/s) is presented in figure 12.3, while figure 12.4 contains the response of the beam to a linearly increasing force. In both cases, deflection is plotted at midspan and the velocity is 25m/s. Once again, the calculated solutions compare well with the closed-form solutions.



(a) Speed = 25 m/s



(b) Speed = 50 m/s.

Fig. 12.2 Midspan bridge deflection for two speeds. Single constant force, P = 392 kN. From [205]. ····· = Calculated, - - - - - = Closed-form solution [185]

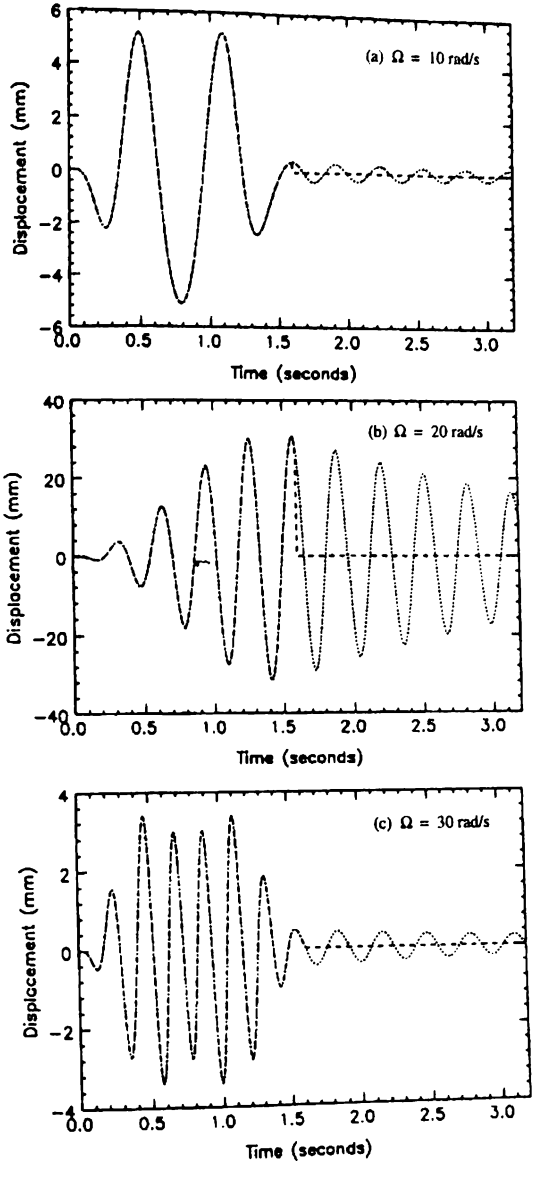


Fig. 12.3 Midspan bridge deflection (Speed = 25 m/s). Single sinusoidal force, P = 392 sin(Ωt) kN From [205]
..... = Calculated, ----- = Closed-form solution [185]

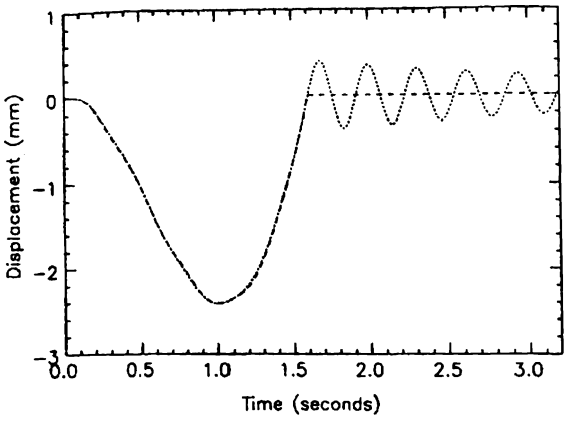


Fig. 12.4 Midspan bridge deflection (Speed = 25 m/s). Linearly increasing force, P = 392Vt/L kN, From [205]. ····· = Calculated, - - - - - = Closed-form solution [185].

12.4.4 Vehicle Models

Two different vehicle models were selected to test the convergence of the iterative procedure. The first was a '1/4 car' model with two degrees of freedom as shown in figure 5.1a. The parameters used were for a highly idealised 40 tonne vehicle (m_u = 4000 kg, m_s = 36000kg, k_t = 72MNm^{-1}, k_s = 18 MNm^{-1}; c_t = 1.4 MNsm^{-1}, c_s = 1.4 MNsm^{-1}). The natural motion (eigenvalues and eigenvectors) of the vehicle model are shown in Table 12.2.

Frequency	Damping	Mode shape
$\omega_v^{(1)}$ = 20 rad/s	$\zeta_v^{(1)}$ = 0.07	bouncing of sprung mass
$\omega_v^{(2)}$ = 150 rad/s	$\zeta_v^{(2)}$ = 0.24	axle hop

Table 12.2 Modal analysis of the 1/4-car 2-DOF vehicle model.
$\omega_v^{(j)}$ is the j^{th} natural frequency of the vehicle, and $\zeta_v^{(j)}$ is the j^{th} modal damping ratio of the vehicle.

For the second convergence test a two–axle vehicle model was used. Figure 12.5 is a schematic diagram of the model. It had four degrees of freedom: two tyre displacements, sprung mass displacement, and sprung mass pitch rotation. The corresponding natural frequencies and damping ratios are shown in Table 12.3.

Frequency	Damping	Mode shape
$\omega_v^{(1)}$ = 10 rad/s	$\zeta_v^{(1)}$ = 0.03	pitching of sprung mass
$\omega_v^{(2)}$ = 20 rad/s	$\zeta_v^{(2)}$ = 0.07	bouncing of sprung mass
$\omega_v^{(3)}$ = 150 rad/s	$\zeta_v^{(3)}$ = 0.24	axle hop
$\omega_v^{(4)}$ = 150 rad/s	$\zeta_v^{(4)}$ = 0.24	axle hop

Table 12.3 Modal analysis of the 2-axle, 4-DOF, '1/2-car' vehicle model.

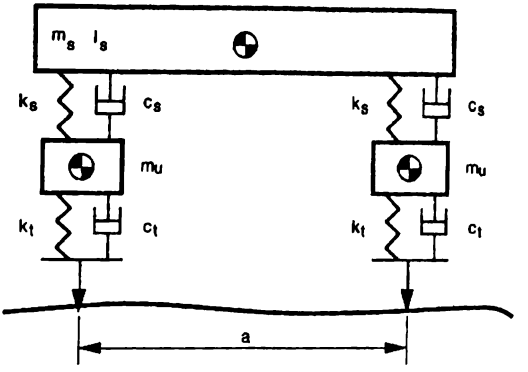


Fig. 12.5 Two-axle (4 degree of freedom, '1/2 car') vehicle model. (m_t = 2000 kg; m_s = 36000 kg; $I_s = 144x10^3$ kgm^2; a = 1.0 m; k_t = 36MNm^{-1}, k_s = 9MNm^{-1}, $c_t = c_s$ = 0.7MNsm^{-1}) From [205].

12.4.5 Dynamic Bridge-Vehicle Interaction

The results of the iterative calculation are shown in figures 12.6 to 12.8. Figure 12.6 shows the final three iterations and illustrates the convergence of the method. Two curves are shown on each plot of figures 12.7 and 12.8. The first curve is the predicted bridge response from equivalent static loads moving over the bridge. The other curve is the result when the bridge and vehicle models are combined at the specified speeds. In figure 12.7, results are shown for speeds of 25m/s and 50m/s while in figure 12.8 only curves corresponding to 50m/s are shown (50m/s is an unrealistically high speed for a heavy vehicle, but was chosen as an extreme condition to test convergence of the method). The tolerance on convergence in all cases was 1% and the number of iterations required to achieve this tolerance is shown in Table 12.4. It is evident that the iterative method works well and does not require excessive computation time.

Vehicle Model	Speed (m/s)	Iterations
1/4 car	25	5
1/4 car	50	4
1/2 car	50	4

Table 12.4 Number of iterations

12.5 INSTRUMENTATION AND EXPERIMENTAL PROCEDURE

In addition to theoretical examples, the calculation method was verified with experiments on full-scale bridges. The validation procedure consisted of four main steps. The first step was measurement of the transfer functions and mode shapes of the bridge. Step two consisted of single vehicle tests in which dynamic wheel forces and bridge responses were measured simultaneously. In step three, the measured dynamic wheel forces were combined with the modal properties of the bridge to predict bridge responses. Finally, in step 4, these predicted responses were compared with the measured bridge responses to validate the model.

Two complete model validations were performed, on two different short-span highway bridges in the UK. The tests are described in detail in reference [204]. Results for one of the bridges only will be presented here.

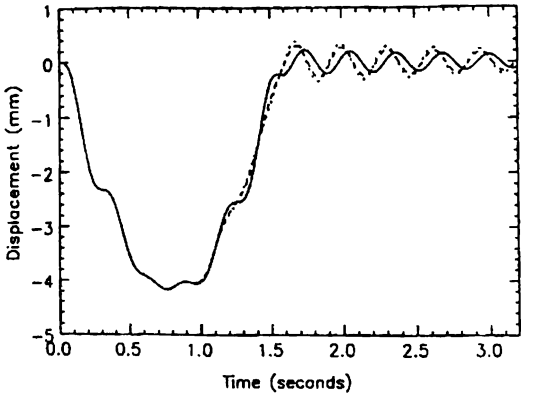


Fig. 12.6 Midspan bridge deflection, '1/4 car' (Speed = 25 m/s) From [205].
——— = Iteration 3, ····· = Iteration 4, - - - - - - = Iteration 5

12.5.1 Lower Earley Bridge

A two lane highway bridge over the River Lodden at Lower Earley in Berkshire, England was selected for testing. The Lower Earley bridge (see figure 12.9) consists of a concrete slab supported by inverted T-beams. The beams are simply supported, but the slab and reinforced concrete diaphragms provide continuity over all three spans.

12.5.2 Instrumentation

Four accelerometers were attached to the underside of the bridge at the positions indicated in figure 12.10 and Table 12.5. A digital data logger was used to record data at a sampling rate of 500Hz. Anti-aliasing filters were set to a cut-off frequency of 150Hz.

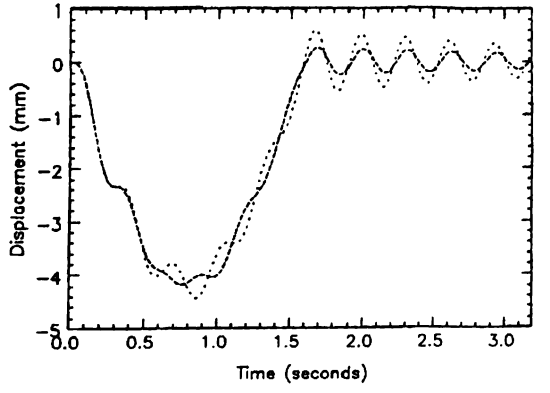
Position Number	Location
1	midspan, centre-line
2	1/3 point of span, centre-line
3	1/4 point of span, centre-line
4	midspan, offset

Table 12.5 Accelerometer positions on the Lower Earley bridge.

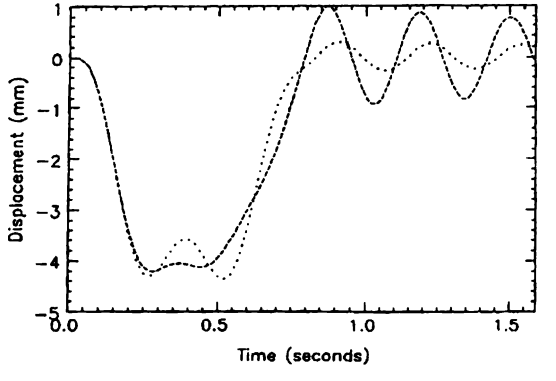
For the modal tests, excitation was applied with an instrumented hammer consisting of a 20kg mass with a slender 2m long arm of mass 3kg. A force transducer on the hammer face measured the force applied to the bridge. An accelerometer on the back of the hammer was used to correct the measured force for the inertia of the hammer components located between the plane of force transducer measurement and the bridge surface.

An instrumented, four-axle, 32.5 tonne, articulated vehicle was provided by the Transportation Research Laboratory (TRL). This vehicle was very similar to the one described in Chapter 6.4. The instrumentation consisted of strain gauges and accelerometers mounted on each axle to measure dynamic wheel loads. The test vehicle had a two-axle tractor with leaf springs on the steering axle and air springs on the drive axle; and a two-axle semi-trailer with tandem 'four spring' leaf spring

suspension. The vehicle data was logged by a data logger carried on the vehicle. Details of this measurement system can be found in references [113, 337].



(a) Speed = 25 m/s



(b) Speed = 50 m/s

Fig. 12.7 Midspan bridge deflection versus time. From [205].
····· = Single constant force, - - - - - - = '1/4 car' vehicle model

12.5.3 Experimental Procedure

In order to determine the mode shapes of the bridge, a series of impulse tests was conducted. Two parallel lines, along the wheel tracks of the test vehicles, were marked on the bridge. The hammer was dropped five times at each of 54 different hammer positions as shown in figure 12.10. Fifteen impulse positions were chosen along each wheel path of the northern span and tests were also performed on the other two spans.

Linearity of the dynamic responses of the bridge was checked by dropping the hammer from three different heights. The bridge exhibited linear behaviour over this testing range [204]. Repeatability was confirmed by dropping the hammer several times at one position.

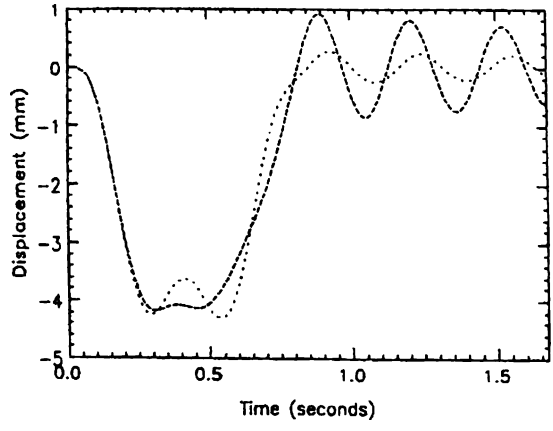
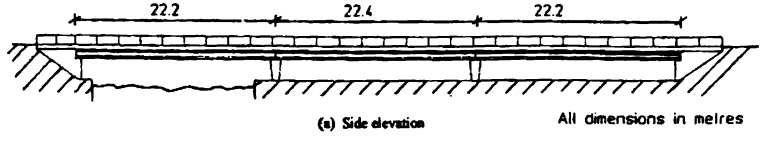


Fig. 12.8 Midspan bridge deflection (Speed = 50m/s) From [205].
····· = Two constant forces, - - - - - - = '1/2 car' vehicle model



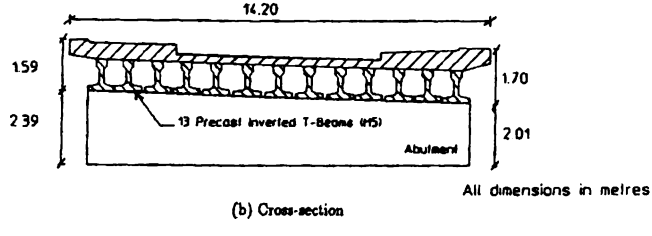


Fig. 12.9 Details of the Lower Earley bridge From [205].

The second phase of the experiments involved measuring the dynamic response of the bridge to the passage of the instrumented vehicle. The bridge instrumentation was set up in the modal testing configuration. In addition, a reflector and light beam set was erected at each end of the bridge. When the vehicle passed the light beam, a reflector on the vehicle caused a pulse to be sent to the

roadside data logger. At the same time, a light beam from the vehicle hit the roadside reflector sending a signal to the vehicle instrumentation. This enabled synchronisation of the data logger on the vehicle with that by the roadside.

The test vehicle was driven over the bridge in both directions at speeds of 15, 30, 50, 55, and 65km/h. Two runs were made at each speed in each direction. The maximum speed was limited to 65km/h by the length of the approach to the bridge.

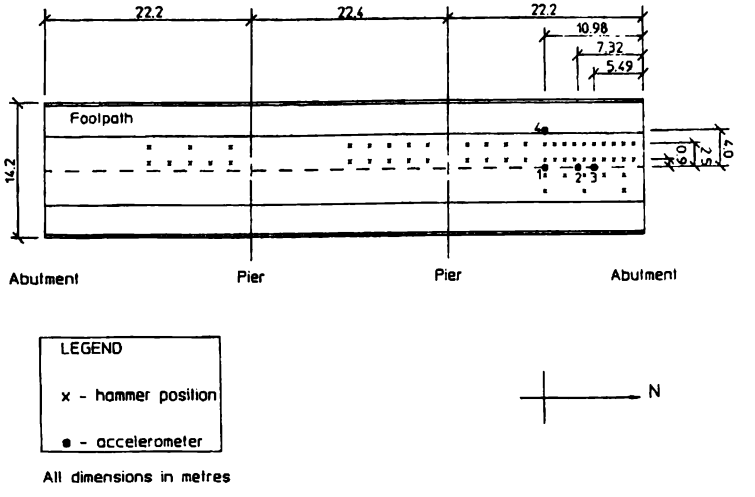


Fig. 12.10 Plan of Lower Earley bridge From [205].

12.6 MODAL ANALYSIS: EXPERIMENT AND THEORY

12.6.1 Transfer Functions

The first stage in the extraction of the modal parameters from the impulse tests was the calculation of transfer functions (frequency response functions). The tests at each hammer position generated four averaged transfer functions: one for each accelerometer position. The procedure for calculating transfer functions involved dividing the discrete Fourier transform (DFT) of the accelerometer outputs by the DFT of the hammer force, and averaging the results over five hammer drops. The details of the procedure are provided in [204].

Figure 12.11 shows the magnitude and phase of the transfer functions calculated from an impulse applied at the middle of the instrumented span. In the region below 20Hz, there are 4 obvious peaks in the responses along the centre-line of the bridge at 5.7 Hz, 9.7 Hz, 11.3 Hz, and 18.0 Hz (figure 12.11a,b,c). Examination of the transfer function corresponding to the off-centre accelerometer (figure 12.11d) indicates peaks at 6.9 Hz, 7.4 Hz, and 13.3 Hz which are not evident in the other accelerometer traces.

12.6.2 Extraction of Modal Parameters

In order to extract the modal parameters from the transfer functions, the circle fitting modal analysis technique described by Ewins [173] was employed. The circle fit is performed by plotting the real and imaginary parts of the mobility transfer function (velocity frequency response) against each other in the Argand plane. According to theory, the data will trace a circular arc near resonance, so a circle is fitted to these points. The location of the natural frequency, f_m, is determined by finding the position at which the 'sweep rate' of the circle is maximum. Damping estimates are then obtained by considering the spacing of the data points. The complex modal constant, $A_{jk}^{(n)}$, is defined as follows

$$A_{jk}^{(n)} = \phi^{(n)}(x_j)\,\phi^{(n)}(x_k) \tag{12.32}$$

where $\phi^{(n)}(x_j)$ is the mode shape value at the position of the impulse, x_j, and $\phi^{(n)}(x_k)$ is the mode shape value at the measurement position, x_k. The magnitude of the modal constant, $\left|A_{jk}^{(n)}\right|$, is determined from the diameter of the modal circle. The inclination of the radial line passing through the natural frequency position defines the phase angle, $\angle A_{jk}^{(n)}$. For mobility plots, a horizontal natural frequency radial line indicates zero phase. If the phase of the modal constants is zero for all impulse locations, then the mode is real. More details regarding the modal analysis can be found in [173, 204].

Figure 12.12 shows an example of the circle fitting procedure for mode number 4 (f_m = 9.7Hz). The circle corresponds to measurements made with the hammer at midspan and the response measured at the midspan accelerometer (number 1). For this circle and most other cases, the radial line representing the natural frequency was almost horizontal. Therefore, all of the modes were assumed to be real.

A total of eight modes was identified from the modal analysis; six of them were present on all of the transfer functions but two (modes 3 and 6 - see Table 12.6) were only identified on the transfer functions measured by the off-centre accelerometer. The second and third columns of Table 12.6 contain averaged values of measured natural frequencies and damping ratios for all eight modes.

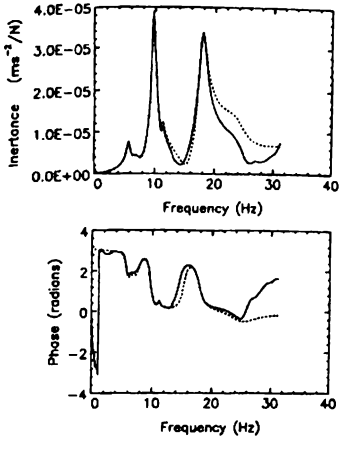
To check the accuracy of the modal analysis, the extracted modal parameters can be used to regenerate a transfer function which can be compared with the original measurement [173, 204]. Figure 12.11 also illustrates the transfer functions regenerated from the modal parameters measured at midspan. Below 20Hz, the fit is very good except for the region between 12 and 17Hz. The errors are slightly larger in this region, but should not be significant for predicting vehicle-induced bridge response which is mostly below 10Hz.

12.6.3 Bridge Models

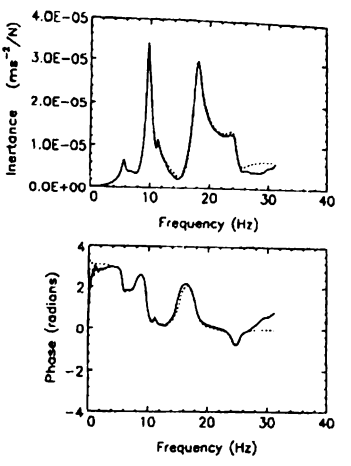
In order to compare the measured modal properties with theory, two simple models for the bridge were developed. In the first model, the bridge was approximated by a beam on rigid supports while in the second a finite element approximation was used.

The mass and stiffness properties were obtained from the construction drawings, supplied by the Berkshire County Council. The bridge was constructed of prestressed concrete, which was assumed to be uncracked. Therefore, the calculated stiffness properties relate to the gross cross-section instead of an equivalent cracked section. Full composite action between the slab and girders was assumed. The Young's modulus of concrete was estimated from values suggested in British Standard BS 5400 [15]. Table 12.7 contains the estimates of the inertia and stiffness parameters.

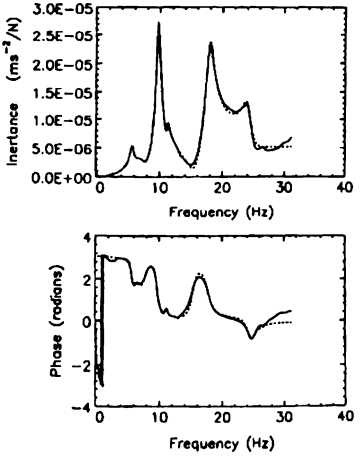
The Lower Earley bridge was initially modelled as a three span continuous beam on simple supports (see figure 12.13). Because of symmetry, it was analysed by dividing the bridge at the middle of the centre span. The anti-symmetric modes were obtained by considering a simple support at the free end of the beam (Case 1), while a vertical roller support at the free end simulated the symmetric modes (Case 2). The mode shapes and natural frequencies of the beam models were computed using the method described in Section 12.4.1.



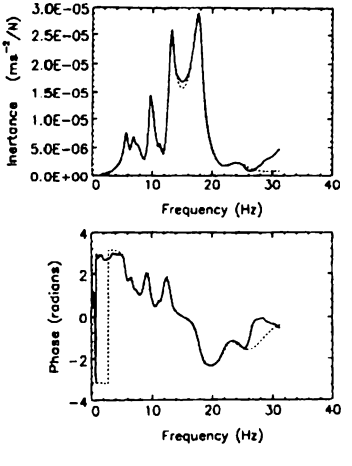
(a) Measurement position 1 (midspan)



(b) Measurement position 2 (1/3 span)



(c) Measurement position 3 (1/4 span)



(d) Measurement position 4 (midspan, offset)

Fig. 12.11 Typical transfer functions. Hammer at middle of instrumented span. From [205].
——— = Measured, ····· = Modal fit

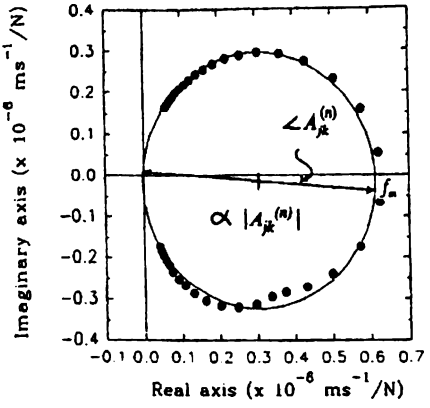


Fig. 12.12 Typical circle fit of mobility data. Mode 4, f_n = 9.7Hz. The radial line indicates the position of the natural frequency. From [205].

Mode	Measured frequency f_m (Hz)	$\zeta^{(n)}$	Beam model frequency f_b, (Hz)	Finite element model frequency f_{fe}, (Hz)
1	5.7	0.045	5.5	5.8
2	6.9	0.088	7.1	7.1
3	7.4	0.086	-	7.3
4	9.7	0.026	-	9.2
5	11.3	0.014	10.3	10.0
6	13.3	0.026	-	12.2
7	18.0	0.038	-	17.4
8	24.4	0.019	22.1	22.3

Table 12.6 Lower Earley bridge - modal parameters.

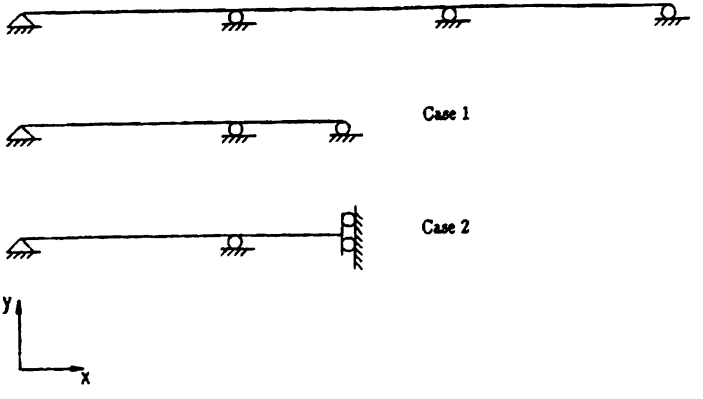


Fig. 12.13. Lower Earley bridge - Beam approximations. From [205].

The four lowest natural frequencies were computed from the beam idealisation and the results were compared with measurements (Table 12.6). Figure 12.14 compares the results of the mode shape predictions with measurements. The agreement is quite good for the four predicted modes.

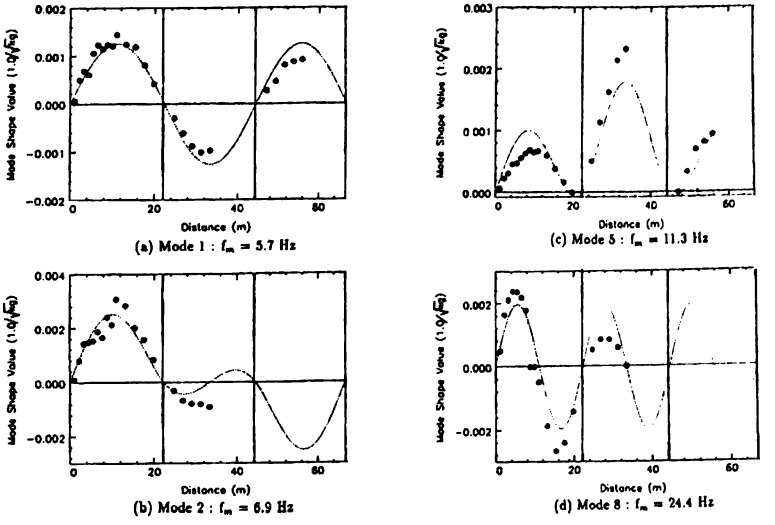


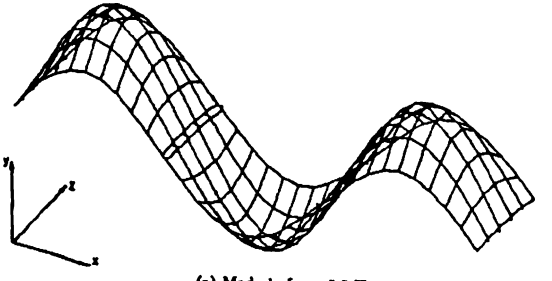
Fig. 12.14 First four beam modes; vertical lines indicate the positions of the supports; From [205].
● = Measured, ····· = Beam model.

The beam theory did not predict all the measured modes so a finite element analysis was performed. The bridge was modelled as an orthotropic plate on flexible supports at the piers using a 10x5 mesh of four-noded quadrilateral plate elements in each span. Figure 12.15 shows the coordinate axis system with the x-axis parallel to the centre-line of the bridge, the y-axis vertical, and the z-axis transverse to direction of vehicle motion. Referring to figure 12.9 it can be seen that there is a significant horizontal clearance between the bases of the inverted T-beams, it is therefore apparent that the bridge had quite different bending stiffnesses in the x and z directions. In the orthotropic plate model, the bending stiffness about the z-axis was determined by considering both the slab and the beams, whereas the stiffness about the x-axis was determined from the slab alone. The x-y shear modulus and hence the torsional rigidity of the plate elements was corrected to match that of the bridge cross-section [515].

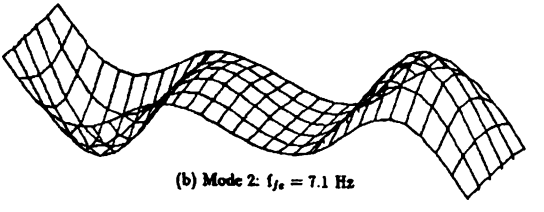
Typical results from the plate analysis are presented in Table 12.6, and figure 12.15 shows the first two predicted modes of vibration. From an examination of the plate mode shapes (see figure 12.15), it was evident that along any line in the x-axis direction the mode shapes had forms similar to those predicted by the beam model (see figure 12.14). The finite element model also indicated that the bridge displayed significant 'two-dimensional' behaviour in all modes.

E	Young's modulus of elasticity	34.0 GPa
I	Moment of Inertia	1.82 m^4
m	Mass per unit length	20.4 tonne/m
G	Shear modulus	14.2 GPa
J	Torsional constant	0.05 m^4
k_b	Bearing stiffness	25.0 kN/mm

Table 12.7 Bridge model properties.



(a) Mode 1: f_e = 5.8 Hz



(b) Mode 2: f_e = 7.1 Hz

Fig. 12.15 First two modes from the two-dimensional finite element bridge model. From [205].

12.7 VALIDATION OF THEORY

In order to validate the bridge response calculation, the measured modal parameters were combined with the measured dynamic wheel loads using the calculation method described in Section 12.3. Bridge responses for each passage of the test vehicle were predicted and compared with the measured responses.

12.7.1 Wheel Loads

The dynamic wheel loads were determined for each vehicle test run. For the purposes of illustration, one vehicle run has been selected for presentation in this chapter.

A set of wheel loads for a south to north run over the Lower Earley bridge is presented in figure 12.16. The vehicle speed is 50km/h and the front axle enters the bridge at time zero. The trailing axle leaves the bridge 5.6 seconds later. This vehicle has leaf springs on the steering axle, air springs on the tractor drive axle and leaf springs on the two trailer axles. The two tractor axles

generate lower dynamic wheel loads, but relatively more high frequency (wheel-hop) motion is present than for the leaf-spring suspensions. This behaviour is typical of air suspensions [337].

The frequency content of the wheel loads was analysed by calculating the 'Fourier Spectra' [50] of the wheel load time histories. The Fourier spectrum is defined as the magnitude of the discrete Fourier transform and is a more appropriate statistic for the analysis of transient signals than the mean square spectral density [50]. Figure 12.17 shows Fourier spectra for wheel loads measured on the Lower Earley bridge. From this figure, it is evident that the wheel loads are concentrated in the 1-4Hz range, although wheel-hop causes a second peak between 10 and 15Hz.

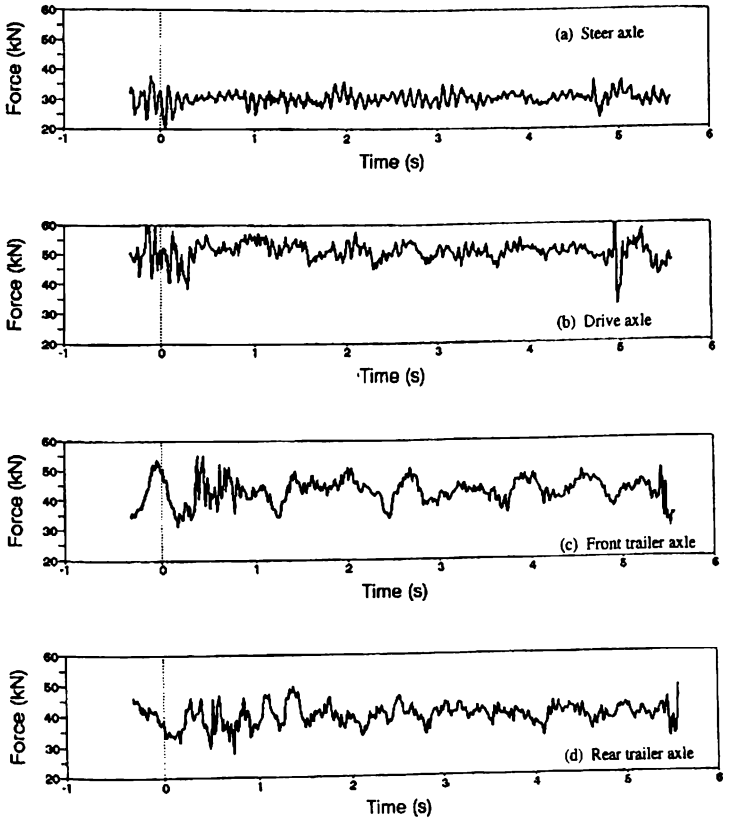


Fig. 12.16 Tyre forces (curb–side wheels), 50km/h, South to North. Vehicle enters bridge at t = 0. From [205].

12.7.2 Mode Shapes

The convolution method requires estimates of the mode shape values at many points along the bridge. To reduce experimental error, it was decided to fit smooth curves to the measured mode shape values. On the basis of the finite element analysis, it was thought reasonable to assume that all of the first eight modes of the bridge had one of the four simple beam mode shapes in the

longitudinal direction. For each measured mode, it was fairly easy to choose a beam mode shape. The relative magnitudes along the centre-line and curb-side tracks were calculated by least–squares fits with the measured magnitudes along these tracks. Figure 12.18 shows the fitted mode shape curves for all eight modes compared with the measurements.

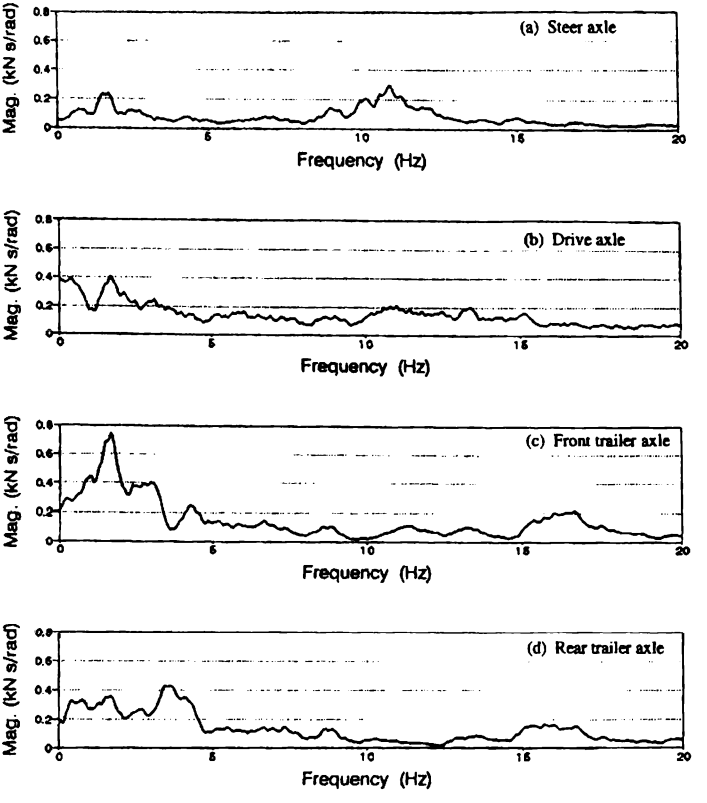


Fig. 12.17 Fourier spectra of tyre forces (curb-side wheel). (a) steer axle (b) drive axle (c) front trailer axle (d) rear trailer axle. From [205].

For measured mode number 4, it was not clear which beam mode best fitted the data. For the instrumented span, a smooth sinusoidal curve was fitted through the points. The measurements for mode 4 on the other two spans were unreliable because of measurement difficulties and were therefore neglected. The fit to mode number 4 does not correctly model the mode shape (figure 12.18d), but it will be shown to be a good engineering approximation for predicting the response of the bridge to heavy vehicle loads.

12.7.3 Validation Results

One difficulty in the comparison of measurement and theory was that it was not possible to measure the displacement response of the bridge at low frequencies (*ie* quasi-static). Since the predicted response includes the quasi-static component, it was necessary to remove this effect before an

effective comparison could be made. This was accomplished with the application of a high-pass digital filter with a cut-off frequency of 1.0Hz. The filter had attenuation properties similar to those of an eighth-order Butterworth filter [197], and was designed in accordance with the recommendations of Stockham [440].

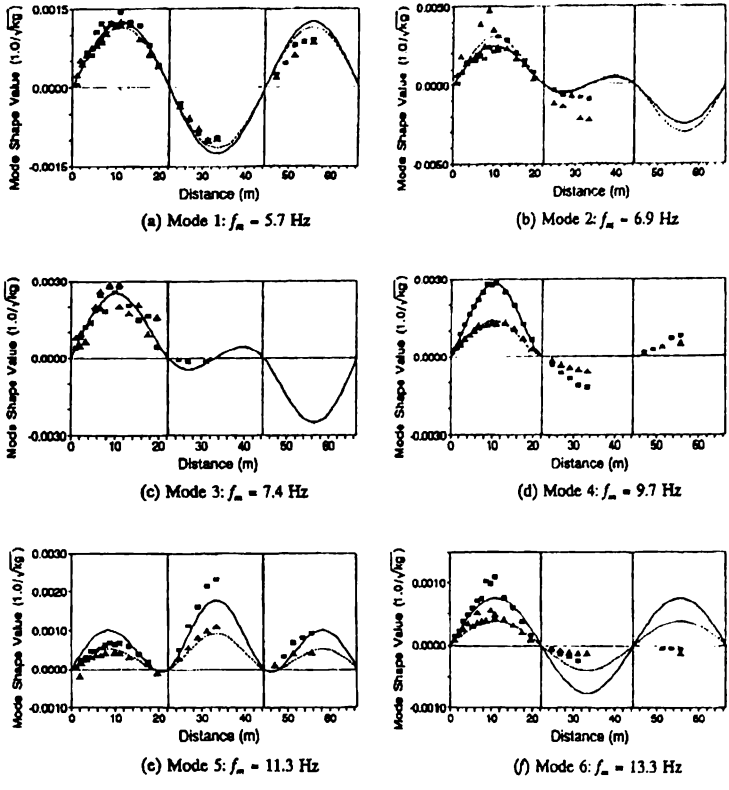


Fig. 12.18 Mode shapes for convolution calculation, vertical lines indicate the positions of supports. From [205].
Measured: ■ = Centre-line track, ▲ = Curb-side track
Fit: ——— = Centre-line track; - - - - - = Curb-side track

Figure 12.19 shows a typical validation result with the vehicle travelling south to north at 50km/h. Bridge responses are shown for accelerometer positions 1, 3, and 4 (see figure 12.10). The agreement between prediction and measurement is generally very good. The curves do not match well in the first two seconds, but during this time interval the vehicle is on the first span. Because the vehicle has not reached the instrumented span the signal to noise ratio is poor. After the first two seconds, the predicted response exceeds the measured response at a few points, but otherwise the curves are very close for all three measurement positions. The largest discrepancies occur on the offset accelerometer (number 4) in the initial two seconds. This indicates that the modes exhibiting torsional behaviour do not cancel each other correctly. Additional mode shapes are necessary to

model the response at this measurement position more accurately. This would require modal response tests on the bridge, with extra off-centre accelerometers.

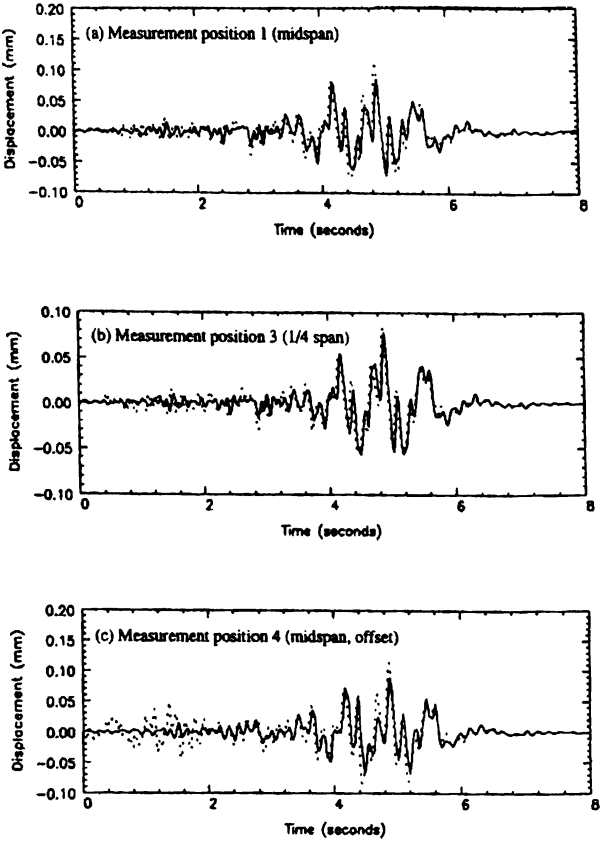


Fig. 12.19 Validation results, 50km/h, south to north. From [205]. ——— = Measured; ····· = Predicted

Figure 12.20 presents a typical result with the vehicle travelling in the other direction (north to south). The speed is 65km/h and the response is shown at the middle of the instrumented span. The agreement is excellent.

Fourier spectra of the predicted and measured responses of figure 12.19 are shown in figure 12.21. Most of the important features of the measured curves are present in the predicted curves.

Figure 12.21 shows that the response of the Lower Earley bridge is dominated by a few distinct frequencies. The body bounce modes of the vehicle induce a large response at about 1.5Hz, while the bridge modes at 5.7Hz and near 10Hz are also important. The good correlation between measurement and prediction near 10Hz indicates that the assumed mode shape for mode 4 is an adequate approximation for predicting the response of the bridge to heavy vehicle loads.

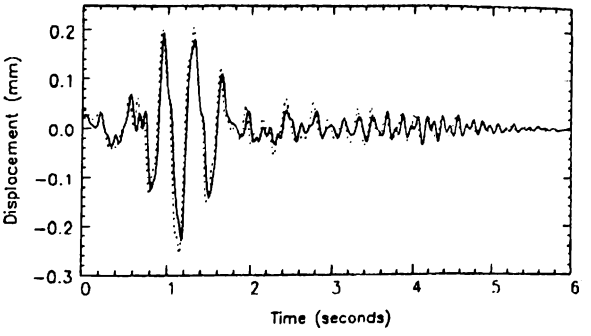


Fig. 12.20 Validation results, 65km/h, north to south, measurement position 1 (midspan). From[205].
——— = Measured; ····· = Predicted.

12.8 CONCLUSIONS

(i) A convolution formulation for calculating vehicle-induced bridge response was developed, and a new technique was described for evaluating the convolution integral in the frequency domain by using the discrete Fourier transform. This method has several advantages including:

   (a) the calculations are much faster than equivalent time domain methods, especially if the wheel loads are known (*eg* measured);

   (b) the method uses bridge vibration mode shapes which can come from many sources (*eg* measurements, simple theories, finite element predictions);

   (c) the method can be extended to calculate the response of a dynamically coupled bridge-vehicle system using any suitable vehicle model.

(ii) The convolution method was compared with closed form solutions for simple cases and good agreement was shown.

(iii) Example calculations for two simple vehicle models traversing a simply supported bridge were presented and the iterative method was shown to converge.

(iv) The calculation method was validated by extensive experiments on a typical highway bridge. Modal tests showed that simple beam and plate models of bridge dynamics gave reasonable predictions of the measured vibration mode shapes and natural frequencies of the bridge. The results from the vehicle tests indicate that the calculation method is accurate for predicting the dynamic response of short-span highway bridges to heavy vehicle loads.

Chapter 22 investigates the effects of vehicle suspension type on the response of three different highway bridges, using the methods described in this chapter.

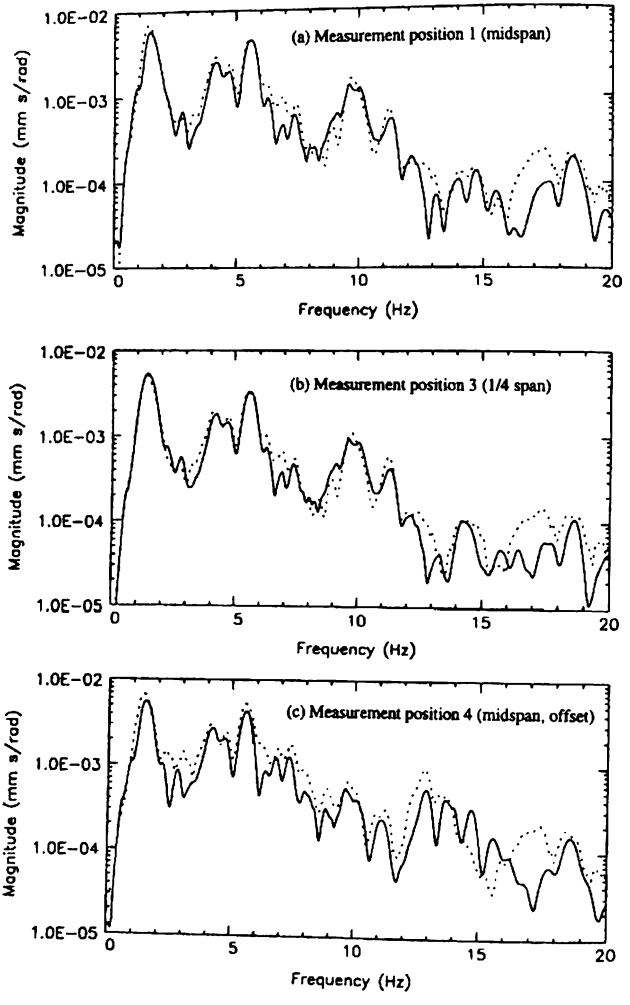


Fig. 12.21 Validation results (frequency domain), 50km/h, south to north. From [205].
——— = Measured; ····· = Predicted.

PART 4 - DAMAGE MECHANISMS:

FLEXIBLE PAVEMENTS

13

BACKGROUND TO ROAD DAMAGE PREDICTION

13.1 METHODOLOGY

Road design in many countries is largely empirical, for example as described in the 'AASHTO guide for design of pavement structures' in the USA [20]; and Road Note 29 [10], supplemented by TRRL Laboratory Report 1132 [378] in the UK.

Analytical or 'mechanistic' road design procedures have been advocated for some time and are used in some countries (*eg* in Australia [162]). These procedures provide suitable background for analysing the road damaging potential of heavy vehicles.

Current mechanistic pavement design practice is to optimise resistance to fatigue cracking and rutting [162, 367]. Analytical models are used to determine the 'primary responses' (stresses, strains and displacements) in a layered road structure due to a static, standard wheel load, often 40kN - *ie* half of an 80kN standard axle load (see figure 13.1). The 'fourth power law' (equation 1.1) is usually used to aggregate the estimated traffic during the service life into the number of equivalent standard axle loads (ESALs). Experimental fatigue and permanent deformation characteristics of the road materials are combined with the calculated primary responses to estimate the service life. Pavement layer thicknesses and material property specifications are then determined by iteration [367].

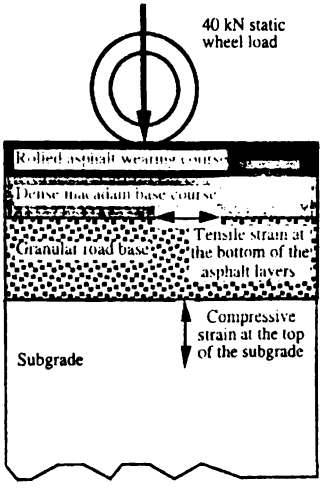


Fig. 13.1 Strain components used in mechanistic design of a typical flexible pavement

It is worth noting that the idea of *aggregating the traffic* into a number of ESALs has its historical roots in the period when pavement design was done by hand using design charts, or (later) using low-powered computers (see Chapter 1). In those days it was vital to simplify the pavement design problem in order to make it tractable, and ESALs were a very convenient way to do this.

Although it is not currently used widely, an alternative is to *aggregate the damage*. In this approach, pavement damage (rutting, fatigue cracking, *etc*) is calculated for a sample pavement section for each main vehicle condition (eg vehicle class, speed, pavement temperature, *etc*). The total damage is then aggregated for a specified time period - a week or month or season. This is continued until the end of the service life. Although this approach is more computationally expensive, it is more realistic and potentially much more accurate. Importantly, it eliminates the need to use ESALs, which have been discredited (see Section 1.3).

13.2 PRIMARY RESPONSE COMPONENTS

For the analysis of fatigue damage, the most commonly used primary responses are the horizontal tensile stress or strain at the bottom of the asphalt or PCC surface layer on the axis of the load, (see figure 13.1). Analytical models generally predict that maximum tensile stresses and strains occur at this location. Pavement designers consequently infer the upwards propagation of fatigue cracks from the layer interface.

The hypothesis of cracking 'from the bottom up' has not been confirmed experimentally: Thrower [457] noted that this failure mechanism is not well supported by observations of core samples taken from roads in Britain, where cracks almost invariably originate at the top surface and extend downward. Cores taken from Japanese roads [328] and British roads [508] also showed cracks confined to the surface, with no evidence of damage to the road base. Wu [508] noted a close association between surface cracking and a poor bond at the interface between surface and road base. He also suggested that ageing of the surface layers is likely to be a contributing factor. Matsuno *et al* [328] hypothesised that longitudinal surface cracks occur at high pavement temperatures due to transverse tensile strains at the surface close to the edge of the tyre. Jacobs *et al* [260] showed that large tensile stresses can be generated in the road surface due to transverse shear tractions in the tyre contact area. These issues are discussed in Chapter 15.

Rutting damage in flexible pavements is the result of permanent deformation in each of the pavement layers. In the AASHO road test [8] approximately 68% of the permanent deformation occurred in the granular foundation layers, while 32% occurred in the asphalt surface. Compressive strain in the subgrade was found to correlate well with rutting damage [464]. In tests performed by the Transport and Road Research Laboratory (TRRL) in the UK [305] these proportions were approximately 46% and 54% respectively. Pavement designers often attempt to minimise deformation of the granular layers by limiting the compressive stress or strain at the top of the subgrade (see figure 13.1). In other design procedures, the elastic vertical deflection of the surface, or the sum of the theoretical permanent deformations of each layer are used as design criteria.

The lack of consensus on which primary response component(s) should be used is evidence of the general lack of understanding of the mechanisms of road damage.

13.3 MATERIAL DAMAGE RELATIONSHIPS

The fatigue damage characteristics of *asphalts* are very sensitive to stress and strain amplitudes. Fatigue models developed from laboratory experiments are typically power-law relationships:

$$N_f = k_1 \varepsilon^{-k_2} \tag{13.1}$$

where

N_f is the number of cycles to failure at strain level ε,
k_1 is a constant that usually depends on the stiffness of the material, and
k_2 is a constant.

The value of k_2 depends on the material and the mode of distress.

The parameters k_1 and k_2 are typically determined from simple laboratory fatigue tests on specimens of asphaltic material (see, for example [67, 184, 349]). Experimental studies have shown that the major factors affecting the constants k_1 and k_2 are: (i) asphalt mixture stiffness, (ii) bituminous binder content, (iii) bituminous binder viscosity, (iv) gradation and characteristics of the aggregate, (v) air void content and (vi) pavement temperature [145, 184, 383].

It can be seen from equation 13.1 that the fatigue life of asphalt is extremely sensitive to the exponent k_2. Values of k_2 reported in the literature range from 1 to 8, and is often taken to be approximately 4 (see, for example, [72, 183, 184, 316, 329]). One of the major problems with this type of model is the simplified loading conditions under which the fatigue constants k_1 and k_2 are determined.

Some fatigue cracking models for *Portland cement concrete* pavements are power-laws like equation 13.1, but most are semi-log relationships of the form

$$\text{Log } N_f = k_3 - k_4 \frac{\sigma}{M_R}, \tag{13.2}$$

where N_f is the number of cycles to failure at stress level σ, k_3 and k_4 are experimentally measured constants, and M_R is the modulus of rupture (fracture strength in bending) of the concrete [192].

When vertical subgrade strain is used to estimate *rut formation*, power-law equations like (13.1) are often used to calculate the number of stress cycles required to generate a particular critical rut depth. In these models k_2 usually takes values in the range 1.85 to 7.14 [219].

If the road is assumed to be linear viscoelastic, then the average increase in rut depth is proportional to F/V, where F is the static load, and V is the speed (see [142, 192] for details). This relationship is approximately comparable to a power-law (like equation 13.1) with an exponent of 1.

13.4 SUCCESS OF THE MECHANISTIC APPROACH

Although considerable research effort has been concentrated on predicting pavement failure, agreement between theory and experiment is often unsatisfactory [457]. There are numerous complicating factors including: (i) 'healing' of bituminous materials in rest periods between load pulses [183, 457, 469]; (ii) the distribution of wheel paths across the road [344, 367, 457, 458, 469]; (iii) extreme sensitivity of material properties to climatic conditions, particularly temperature [109, 367, 457, 469, 516]; (iv) inaccuracy of the 'fourth power law' [4, 457]; (v) variations in tyre types [16, 248, 516]; (vi) inadequacies of pavement response and damage models [457]; and (vii) the variable nature of the applied loads. It is not uncommon for such analyses to underestimate pavement fatigue lives by a factor of 100 [367, 457, 469].

Some researchers have tuned or 'internally calibrated' their pavement models by making large adjustments to the input parameters on the basis of field tests of pavement deterioration (typically the AASHO road test). In these cases, the agreement between model predictions and the corresponding experiments is found to improve considerably. See, for example, [66, 277, 454].

One notable exception was presented by Thrower *et al* [458], who obtained surprisingly good agreement between predictions of rutting in controlled laboratory tests and full-scale tests, using a detailed nonlinear description of material permanent deformation characteristics.

Criteria for evaluating the road damaging effects of vehicle loads must inevitably be based on the current understanding of road surface failure. As illustrated above, this is an area of considerable uncertainty.

The rest of this part of the book describes mathematical models of the permanent deformation and cracking of asphalt roads. These models are suitable for use in the analysis of road-damaging effects of vehicles, and they are used for this purpose in Part 5.



14

PERMANENT DEFORMATION OF FLEXIBLE PAVEMENTS

14.1 SUMMARY

In this chapter, permanent deformation (rutting) in bituminous pavements is treated as a viscoelastic flow phenomenon. The *correspondence principle* is used to deduce the permanent deformation of a linear viscoelastic pavement system using a linear elastic pavement model supplied with suitable viscous parameters and vehicle loads. A simple method is introduced for determining the viscosity of asphalt mixtures from routine test data, for a wide range of environmental conditions. Rut depth predictions are compared with experimental data from a full-scale accelerated loading test in France. Agreement is generally good indicating the applicability of this linear rutting model.

This chapter is based on work previously published in [143].

14.2 INTRODUCTION

In the UK the most common form of road failure in flexible pavements, is rutting, where material from under the wheel path of a truck flows and compacts to form a groove or rut [457]. The two major mechanisms within the pavement materials contributing to rutting are densification (compaction) and shear plastic deformation. These two mechanisms contribute in varying degrees to permanent deformation in all the pavement layers. Researchers have found that if a pavement has been well compacted during construction, further densification rutting is unlikely, and permanent deformation is only due to shear flow [167].

Pavement engineers have traditionally tried to eliminate rutting by limiting the vertical stress or strain at the top of the subgrade [367]. Such methods assume that there is a unique relationship between the vertical compressive strain at the formation level and the number of wheel loads to cause failure by excessive rutting.

The 'layer strain' approach to rutting was developed in the 1970s (eg [73]). This type of model accounts for the permanent deformation in all the pavement layers by assuming either a linear or nonlinear relationship between the elastic stress field and the vertical permanent deformation in each layer. The relationships between elastic stress and the permanent deformation characteristics of the materials were usually determined from triaxial tests. Although the layer strain approach could account for permanent deformation in each pavement layer, it could not model the characteristic ridge formed adjacent to the wheel path. This type of model also assumes that permanent deformation is only dependent on the elastic stresses in the pavement.

The third major type of predictive rutting model is based on the viscoelastic behaviour of bituminous materials [360, 456]. These models generally use a combination of linear springs and dashpots to model the time-dependent rheological behaviour of asphalts. This type of model assumes that ruts form by the shear flow of pavement materials and can account for the characteristic ridge formed adjacent to the wheel path. Unlike the layer strain approach, permanent deformation is assumed to be independent of the elastic properties of the pavement materials. Rowe [395] developed a viscoelastic

rutting model, in which the asphaltic material was modelled using a Burger's model. The parameters required for the Burger's model were determined from repeated load axial tests and used in conjunction with a finite element (FE) program to predict surface rutting. For a more comprehensive review of pavement rutting models, refer to [211].

In the United States, the Strategic Highway Research Program (SHRP) project entitled 'Performance related testing and measuring of asphalt-aggregate interactions and mixtures' was set up to investigate the relationship between properties of the bituminous binder and pavement performance (see for example, [340, 341]). As part of this program a number of test methods (eg uniaxial, triaxial and simple shear tests conducted in creep, repeated, and dynamic loading modes) were investigated to assess the rutting potential of various asphalt mixtures. Results indicated that the most suitable accelerated test is a shear test in which combinations of shear and normal stresses are applied to the specimen, either continuously (creep loading) or repeatedly, with short loading durations.

The permanent deformation model presented in this chapter uses the theory of linear viscoelasticity to model steady-state rutting in flexible pavements. A new approach is developed for predicting the viscous properties of un-aged asphalt mixes from routine test data, and the model is verified by comparison with measured rut-depth data from tests in France. Ageing has not been included because data from accelerated tests was used to validate the model. For the prediction of long-term rutting, a suitable ageing law could be used to modify the properties of the bitumen with time. (See, for example, [481]).

14.3 THEORETICAL RUTTING MODEL FORMULATION

14.3.1 Linear System Theory

The response z(t) of a linear system to a time-varying input f(t) is given by the convolution integral [355]:

$$z(t) = \int_{-\infty}^{\infty} h(t-\tau)f(\tau)d\tau \tag{14.1}$$

where

- z(t) is the response at time t,
- f(τ) is the input force at time τ, and
- h(t) is the response at time t to a unit impulse at time t = 0.

Assuming that f(t) is transient, starting at time t=0, it may be defined as:

$$f(t) = \begin{cases} 0 & t < 0 \\ F(t) & 0 \le t \le T_f \\ 0 & T_f < t. \end{cases} \tag{14.2}$$

Substituting into equation 14.1 gives

$$z(t) = \int_{0}^{T_f} h(t-\tau)F(\tau)d\tau. \tag{14.3}$$

If the impulse response has a permanent offset $h(t) = h_\infty$ for large times, $t > T_h$, as shown in figure 14.1, equation 14.3 can be rewritten as:

$$z(t) = h_\infty \int_0^{T_f} F(\tau)d\tau \qquad \text{for all} \quad t > T_h + T_f . \tag{14.4}$$

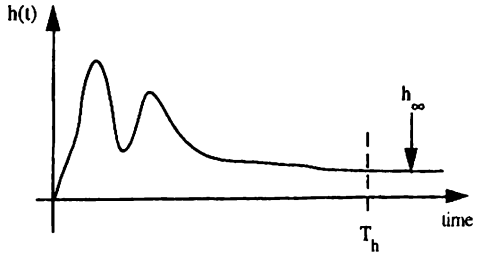


Fig. 14.1 Impulse response showing permanent offset for $t > T_h$.

Therefore, the residual deformation of the system is proportional to the product of the applied impulse (integral of the input force over time) and the final value of the impulse response, h_∞.

14.3.2 Application to Pavement Rutting

The response of a road to a single moving dynamic tyre force can be written using a form of the convolution integral (see equation 10.7):

$$z(x,t) = \int_{-\infty}^{\infty} h(x - v\tau, t - \tau) f(\tau)d\tau = \int_{-\infty}^{\infty} h\left(v\theta, \theta + t - \frac{x}{v}\right) f\left(\frac{x}{v} - \theta\right) d\theta \tag{14.5}$$

where

$$\theta = \frac{x}{v} - \tau,$$

$z(x, t)$	is the response at position x and time t,
v	is the vehicle speed,
$h(x, t)$	is the time response at position x to a unit impulse at the origin at time t=0,
$f(\tau)$	is the instantaneous value of the tyre force at time τ.

Assuming that the impulse response is negligible for distances greater than x_0 from the point of application of the impulse (*ie* $h(x, t) = 0$ for $|x| > x_0$), equation 14.5 may be rewritten as:

$$z(x,t) = \int_{-x_0/v}^{x_0/v} h\left(v\theta, \theta + t - \frac{x}{v}\right) f\left(\frac{x}{v} - \theta\right) d\theta. \tag{14.6}$$

Following a similar approach to that above, and denoting the steady state offset of the impulse response function by:

$$h(x, t) = h_\infty(x), \quad \text{as } t \to \infty,$$

it is apparent that the permanent deformation at longitudinal position x for one axle becomes:

$$z(x,\infty) = \int_{-x_0/v}^{x_0/v} h_\infty(v\theta) f\left(\frac{x}{v} - \theta\right) d\theta. \tag{14.7}$$

This result can be generalised easily using the linear superposition principle to accommodate multiple axles. $h_\infty(x)$ is an influence function giving the rate of permanent vertical displacement at a distance x from the point of load application.

If the force f(t) is constant with respect to time, equation 14.7 can be simplified to:

$$z(\infty) = \frac{F}{V} \int_{-x_0}^{x_0} h_\infty(y)dy. \tag{14.8}$$

This is simply the area under the influence function $h_\infty(y)$. Permanent deformation calculated from (14.8) will be proportional to the static load F, and inversely proportional to vehicle speed v.

14.3.3 Calculating the Influence Function:

According to the elastic/viscoelastic correspondence principle [182], the rate of permanent vertical surface displacement or strain can be obtained for a linear viscoelastic material, by supplying a linear elastic pavement model with equivalent viscous parameters [456]. It is necessary to replace the Young's modulus of each layer with a suitable extensional viscosity, and to choose an appropriate value of Poisson's ratio (normally 0.5). Then the permanent deformation influence function $h_\infty(x)$ can be calculated simply by applying a unit force to the surface of the pavement model and calculating the surface 'deflection' profile along the line of travel. More details can be found in [142].

14.3.4 Notes

This approach to calculating pavement rutting has three important features:

(i) The distribution of permanent deformation through the layers is accounted for exactly, assuming that all the layers behave as linear viscoelastic materials.

(ii) The effects of vehicle speed (loading time) and dynamic loads, are accounted for exactly in the integration stage, and require only one $h_\infty(x)$ influence function for each tyre type.

(iii) The effect of pavement temperature on rut generation can be included in the analysis by using temperature sensitive viscosities, particularly for the layers near the surface, where the temperatures can be higher.

14.4 ASPHALT MIXTURE VISCOSITY

The success of the linear viscoelastic approach relies on the ability to determine pavement layer viscosities for the range of environmental conditions experienced during the life of a pavement. No general theoretical method for doing this has been found in the literature. Researchers using viscoelastic rutting models tend to choose arbitrary viscosity values to give realistic results [456, 458], or fit simplified rheological models to limited sections of data [257, 360]. Hopman *et al.* [241] fitted a linear viscoelastic Burger's model to results from transient pulse loading tests to determine asphalt mixture properties (*ie* viscosity, initial elasticity *etc*).

The following section examines the assumption of linear viscoelasticity, and introduces a simple method for estimating asphalt mix viscosity from routine test data - the viscosity of the bituminous binder and the mix composition.

14.4.1 Rheological Properties of Pure Bitumen

Stiffness

The 'stiffness' of a bitumen specimen subjected to a constant uni-axial stress can be defined as the ratio of applied stress to cumulative or total strain, and in general will depend on: (i) loading

procedure, (ii) loading time or frequency, and (iii) temperature [236]. In the early 1950's Van der Poel carried out comprehensive uni-axial creep and dynamic tests on a large number of bitumens over a wide range of temperatures and loading times in order to determine their mechanical properties. His work resulted in the universally used 'Van der Poel nomograph' [476].

In order to determine bitumen stiffness from the nomograph, the loading time or frequency is required as well as the following properties: (i) Ring and Ball softening point temperature ($T_{R\&B}$), (ii) Penetration Index (PI) and (iii) bitumen temperature (TB). Figure 14.2 shows bitumen stiffness at three different temperatures as a function of loading time predicted from a computer implementation of the nomograph [28]. A *standard* grade of bitumen ($T_{R\&B}$ = 58°C and PI = -0.5) was used for figure 14.2 and throughout this chapter. At short loading times the curves are horizontal indicating purely elastic behaviour, whereas at long loading times the curves become straight with a slope (on log scales) of minus one, indicating purely viscous behaviour. Intermediate loading times produce viscoelastic behaviour with significant strains from both elastic and viscous deformations.

The similarity in shape of the curves is striking, and if each curve were shifted in the horizontal direction (time) they would all become coincident. This behaviour, whereby the response at a given temperature and loading period is the same as the response at a reference temperature but over a compressed or extended time scale, is known as the 'time-temperature superposition principle'. It indicates that within this range of conditions, pure bitumens are 'thermo-rheologically simple' [338, 351, 426, 494].

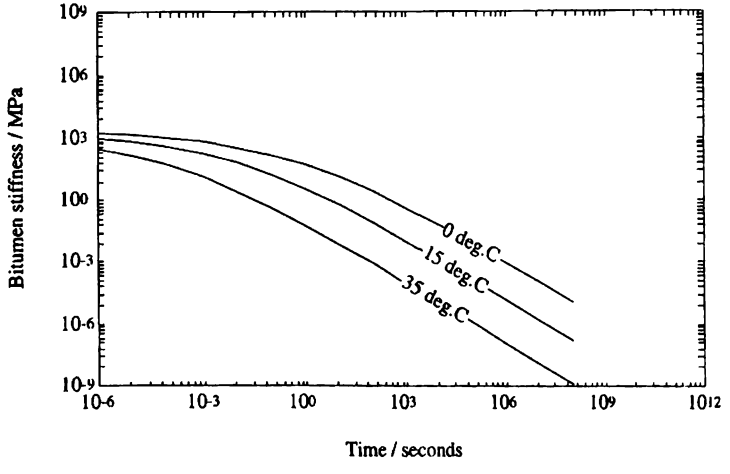


Fig. 14.2 Bitumen 'stiffness' at three temperatures as a function of loading time. From [143].

Rheological Model

A linear viscoelastic rheological model can reproduce the creep behaviour of bitumen at different temperatures with reasonable accuracy. Researchers have shown that Burger's rheological model (figure 14.3) simulates the behaviour of bitumens quite well, although it is limited to regimes of Newtonian flow [70, 241, 318, 343, 363, 366, 399, 412]. Consequently, an extended three element Burger's model with two retardation times was used to simulate the creep behaviour of bitumen, in order to determine its viscosity at a given temperature.

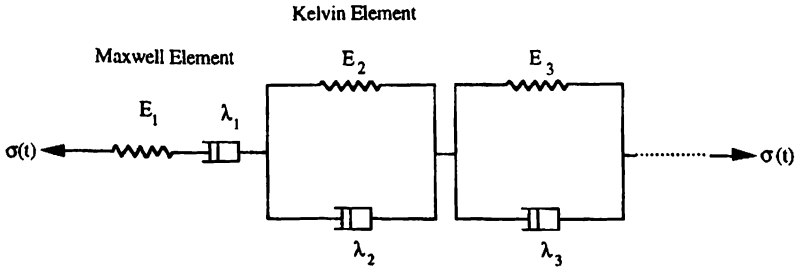


Fig. 14.3 Schematic representation of a general viscoelastic material.

Bitumen Viscosity

The creep compliances (reciprocal of the 'stiffness') generated by the Burger's model were fitted to data deduced from the Van der Poel nomograph for a number of temperatures (see figure 14.4). Long loading times were considered so as to obtain sufficient strain contribution from viscous deformation. This is particularly important at low temperatures where bitumen displays an increased resistance to viscous flow. A good fit was obtained over a range of temperatures typical of pavement wearing courses in the UK [221].

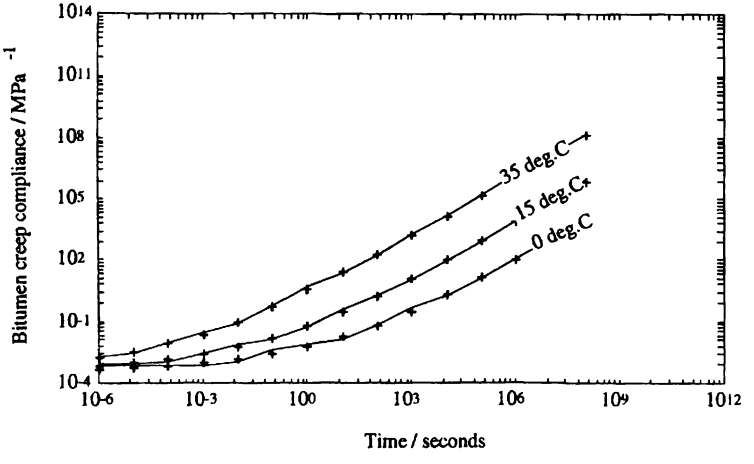


Fig. 14.4 Fitted creep compliances of a bitumen for three temperatures. From [143].

The required viscosity of the bitumen at each temperature is the value of the series viscous damper (λ_1 in figure 14.3), obtained from the parameters of the Burger's model which best fits the response. This is the only component of the Burger's model that contributes to irrecoverable (permanent) deformation.

14.4.2 Rheological Properties of Asphalt Mixtures

Asphalt Mix Stiffness

At high values of bitumen stiffness ($S_b \geq 1$ MPa), the stiffness of an asphalt mix can be estimated from the stiffness of the bituminous binder and the mix composition, using the Bonnaire nomograph; [24], or the empirical equation [34]:

$$(S_m)_H = S_b\left[1+\frac{257.5-2.5\,VMA}{n(VMA-3)}\right]^n \tag{14.9}$$

where

$(S_m)_H$ is the asphalt mix stiffness for $S_b \geq 1$ MPa,
S_b is the bitumen stiffness (MPa),

$$n = 0.83\log_{10}\left(\frac{4\times10^4}{S_b}\right), \text{ and} \tag{14.10}$$

VMA = % Voids in Mixed Aggregate = % vol. air voids + % vol. bitumen.

Equation 14.9 is only applicable for conditions in the range $12\% \leq VMA \leq 30\%$, $S_b \geq 1$ MPa and an air void content of > 3% [34].

The mix VMA may be calculated from the following equation [34]:

$$VMA = (100-V_v)\left[\frac{M_b/\gamma_b}{M_b/\gamma_b + M_a/\gamma_a}\right] + V_v \tag{14.11}$$

where V_v is the percentage of air voids in the mix by volume,
M_b is the percentage of bituminous binder in the mix by mass,
M_a is the percentage of aggregate in the mix by mass,
γ_b is the specific gravity of the bituminous binder, and
γ_a is the specific gravity of the aggregate.

Hills [236] concluded from creep tests on asphalt mixtures that the relationship between the stiffness of bitumen (S_b) and the stiffness of asphalt $(S_m)_L$ at low bitumen stiffness ($S_b < 1$ MPa) depends on the following factors in addition to mix composition and bituminous binder stiffness: (i) quality of aggregate grading; (ii) aggregate shape (*eg* crushed or rounded); (iii) state of material compaction; and (iv) confining conditions. He showed from compressive creep tests on various asphalt mixtures that at low values of bitumen stiffness there is a tendency for the strain rate in the asphalt mix to diminish, and in some cases tend towards zero, thus limiting the permanent deformation at long loading times.

To model this behaviour Hills hypothesised that the internal structure of a mix continually changes during a creep test, and he developed various theoretical models reflecting these changes (see [236] for detailed discussions of the various models). The overall result was a single equation yielding a family of low-stiffness curves of the form:

$$(S_m)_L = \frac{C_1}{\left[(1+C_2/S_b)^{2^{-q}}-1\right]} \tag{14.12}$$

where $(S_m)_L$ is the asphalt mix stiffness for $S_b < 1$MPa,
S_b is the bitumen stiffness (MPa), and
C_1, C_2 and q are experimentally determined constants.

According to Hills, the three constants C_1, C_2 and q reflect the internal structure of the mix at the time of the test, and if equation 14.12 is plotted on log scales, C_1 and C_2 shift the stiffness curve vertically and horizontally respectively, while q determines the shape of the curve for low stiffnesses.

The value of the constant q effectively represents different models for the internal structure of the mix.

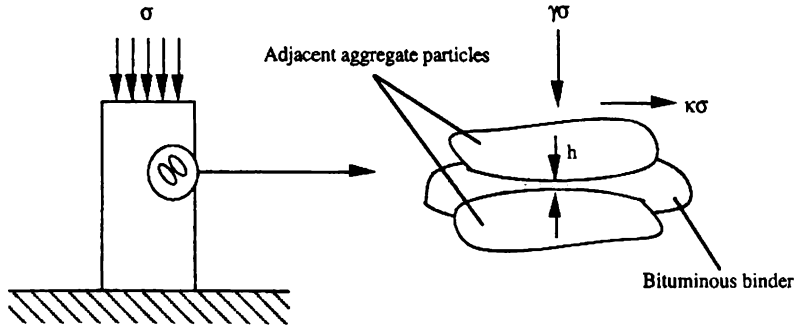


Fig. 14.5 Particle-pair separated by a thin bituminous binder film. From [143].

Consider a pair of adjacent aggregate particles of arbitrary orientation separated by a thin bitumen film of thickness h as shown in figure 14.5. The system is subjected to local normal and tangential stresses ($\gamma\sigma$ and $\kappa\sigma$), determined by resolving the applied compressive stress into directions perpendicular and parallel to the particle-pair orientation respectively. The behaviour of this system can be classified as follows [236]:

(i) $q = 0$. Deformation is due to shear displacement of the particles only with no thinning of the binder film.

(ii) $q = 1$. The binder film is allowed to thin under normal stresses by being squeezed into nearby air voids at a rate given by Stephan's equation [59].

(iii) $q = 2$ to 9. To account for the gradation of the aggregate, the binder film between adjacent aggregate particles is considered to be a model (ii) material ($q = 1$). The resulting material is considered to be the binder between two larger adjacent aggregate particles. This sub-structure is repeated q times in a recursive fashion for progressively larger particle pairs.

(iv) $q \geq 10$. The binder film between adjacent particles is assumed to be sufficiently thin to permit local frictional contact during creep deformation. It is assumed that the creep deformation rate is inversely proportional to the total nominal area of contact per unit volume, which increases with time. Under these conditions the stiffness of the mix will tend towards the stiffness of the aggregate matrix, limiting further creep deformation.

If a pavement has been well compacted during construction, further densification during rutting is unlikely, and permanent deformation is due to shear flow only [9, 167, 211, 465]. Consequently, it is reasonable to assume that deformation due to frictional contact between adjacent aggregate particles ($q \geq 10$) will not occur under typical pavement operating conditions (loading times and temperatures). However, in order to obtain a reasonable estimate of asphalt mix viscosity, longer loading times, and thus lower effective stiffnesses must be considered. This allows sufficient strain contribution from viscous deformation. It was therefore decided to use equation 14.9 to describe the behaviour of the mix for high bitumen stiffnesses ($S_b \geq 1$ MPa), and equation 14.12 with a suitable value of q to describe the behaviour of the mix for low bitumen stiffnesses ($S_b < 1$ MPa).

Figure 14.6 shows a plot of equation 14.12 with q values of 0, 1 and 5 ($Sb < 1$ MPa) as well as a plot of equation 14.9 ($Sb \geq 1$ MPa), for the same *standard* composition of asphalt mix (VMA=18%, $T_{R\&B}$=58°C and PI=-0.5).

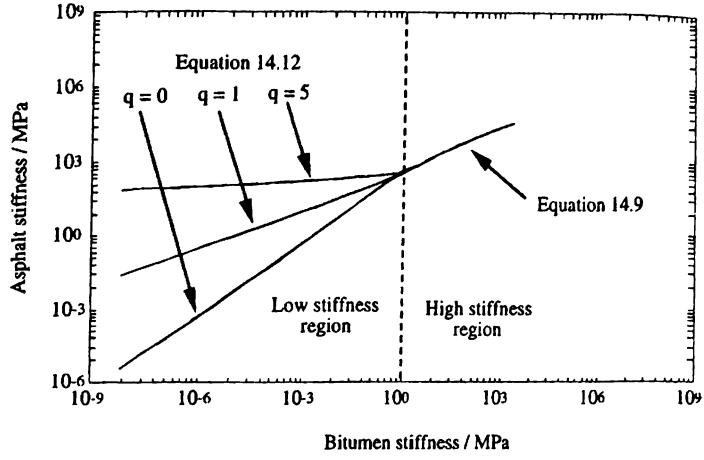


Fig. 14.6 Relationship between asphalt mix stiffness and bitumen stiffness. From [143].

In order to ensure a smooth transition between the two stiffness equations (equations 14.9 and 14.12) the following compatibility conditions were used to determine the constants C_1 and C_2 in equation 14.12:

$$\left[\frac{\partial(S_m)_H}{\partial(S_b)}\right]_{S_b=1\,MPa} = \left[\frac{\partial(S_m)_L}{\partial(S_b)}\right]_{S_b=1\,MPa} \qquad (14.13)$$

and

$$\left[(S_m)_H\right]_{S_b=1\,MPa} = \left[(S_m)_L\right]_{S_b=1\,MPa}$$

Asphalt Mix Viscosity

A linear viscoelastic model can be fitted to the creep compliance of the asphalt mix at various temperatures provided q is known. Since creep of well compacted asphalt mixes is assumed to be a shear flow phenomenon governed by the bituminous binder, it is reasonable to assume the same general rheological behaviour for the asphalt mix as for pure bitumen [241]. Consequently, it is assumed here that a three element Burger's model can be used to model the creep behaviour of asphalt mixtures. The viscosity obtained from the fitted Burger's model is an estimate of the viscosity of an asphalt pavement wearing course material for typical loading times and temperatures.

14.4.3 Determination of q from Experimental Data

The value of q determines the shape of the asphalt mix stiffness curve for low bitumen stiffnesses, and therefore the shape of the asphalt mix creep compliance curves as $t \to \infty$. q is strongly dependent on the viscosity of the mix, and can be determined by simulating measured permanent deformation in asphalt mixtures. It is important to use results of deformation tests that were conducted under pavement loading times and temperatures that are representative of in-service rutting conditions. The results of creep tests cannot be used for this purpose since they involve long loading times and/or high temperatures, and the mix continually changes its structure throughout the test. However, results from repeated load creep tests (such as those proposed by the SHRP study [340, 341]) could be used with sufficiently short loading times to simulate traffic loading.

Hills *et al* [238] compared the asphalt mix stiffness obtained from compressive creep tests with that obtained from wheel tracking tests (see [238] for a discussion of the method used to determine asphalt mix stiffness from wheel tracking tests). At high values of bitumen stiffness they found good agreement. However, at low values of bitumen stiffness they found that creep tests gave higher asphalt mix stiffnesses than wheel tracking tests. These discrepancies at low values of bitumen stiffness will result in a considerable over-estimation of asphalt mix viscosity for viscoelastic rutting models with parameters based on creep test results. Therefore, it was decided to use results of published wheel tracking test results to determine a value for q.

Wheel Tracking Tests

Hills *et al* reported wheel tracking tests performed on a number of asphalt slabs, 100mm thick, laid over a granular base in a laboratory test track [238]. The test sections were loaded by a single wheel that ran in a circular path at constant speed, giving a linear velocity of 2.78 m/s. The static load applied through the single tyre was 7kN and the asphalt temperature was kept constant at 30°C throughout the test. The measured reduction in asphalt layer thickness directly under the load for three of these mixes was considered in order to determine a value for q. Details of mixes are given in Table 14.1.

Mix No.	Mix description	Bitumen content %wt	Bitumen grade	$T_{R\&B}$	PI	Air voids % vol	VMA % vol
A7	Sandsheet with rounded sand (aged by static compaction)	7	40/50	58	0	3.5	18.4
A8	Sandsheet with rounded sand (un-aged)	7	40/50	58	0	3.5	18.4
A10	Sandsheet with rounded sand, rich	9	40/50	58	+0.2	5	23

Table 14.1 Asphalt mix compositions from [238].

The asphalt layer viscosities for each mix at the test temperature were determined from the fitting procedure described above for a given value of q. The viscosity assigned to the granular base layer was high (0.69×10^6 GPa.s), thereby restricting all the permanent deformation in the model to the asphalt layer.

The VESYS computer program [274] was used to generate the deformation-rate influence functions (h_∞) required by equation 14.7. VESYS models a pavement as a semi-infinite linear elastic layered structure supported on an elastic half-space. The tyre-road contact was assumed to be a circle of radius 66 mm. In order to calculate the deformation-rate influence function, VESYS was supplied with the viscous equivalents of Young's modulus (E_v), and Poisson's ratio (ν_v). These are given by the expressions:

$$E_v = \frac{9\chi\eta}{3\chi+\eta} \quad \text{and} \quad \nu_v = \frac{3\chi-2\eta}{2(3\chi+\eta)} \qquad (14.14a,b)$$

where χ is the bulk viscosity (analogous to bulk modulus for an elastic solid),
and η is the shear viscosity (analogous to shear modulus for an elastic solid).

The bulk viscosity χ was taken as infinity thus restricting permanent deformation to shear flow with no changes in volume. This was necessary since Van der Poel used the relationship $E = 3G$ to determine extensional stiffness from shear tests for his nomograph [476]. Consequently, equations 14.14 become:

$$E_v = 3\eta = \lambda \quad \text{and} \quad \nu_v = \frac{1}{2} \tag{14.15a,b}$$

where η is the shear viscosity, and
λ is the extensional viscosity.

The reduction in asphalt layer thickness was calculated from equation 14.8 using deformation-rate influence functions directly under the single tyre contact patch. The viscosity of the asphalt was determined from the Burger's model fit to the asphalt mix compliance at the temperature of the wheel tracking test (30°C). By adjusting the value of q it was possible to reproduce the reduction in asphalt layer thickness measured for the three test mixes. A value of q=0.47 was found to fit measured deformation well for all three mixes.

Figures 14.7a and 14.7b show the computed and measured reductions in asphalt layer thickness for the three test sections as a function of cumulative load passes. It can clearly be seen that for all three mixes after an initial compaction period the permanent deformation increases linearly with load applications, and the predicted permanent deformation reproduces measured deformation well. Mixes A7 and A8 give the same rate of viscous permanent deformation after different levels of initial compaction. This difference in initial compaction (approx 1mm) would appear to be due to the ageing of mix A7 since this was the only difference in the two mix specifications. Mix A10 has a higher bitumen content and a higher air void content than the other two mixes and hence a significantly higher rate of permanent deformation.

A value of q=0.47 represents a mix internal structure where a pair of adjacent aggregate particles are separated by a thin binder film which thins at a rate that is less than the unrestricted rate (q=1). The value of q=0.47 fitted two quite different mixes; so it might be hypothesised that this is a relatively general result which could be applied to other asphalt mixes. Clearly more experimental evidence is needed to test this hypothesis.

14.4.4 Asphalt Mix Viscosity Equation

Equations 14.9 and 14.12 (with q=0.47) were used to calculate asphalt mix stiffness for the *standard* mix (VMA=18%, $T_{R\&B}$=58°C and PI=-0.5), at different temperatures. The three element Burger's model was then fitted to the corresponding creep compliances and the results of the fit for three different temperatures are plotted in figure 14.8.

It is now possible to plot bitumen viscosity against asphalt mix viscosity (both determined from fitted Burger's models) for corresponding temperatures and different mix compositions. The result is independent of temperature and the properties of the bituminous binder ($T_{R\&B}$ and PI), and depends only on mix composition. For the range of VMA investigated (representative of most realistic asphalt mixes), the relationship between bitumen viscosity, asphalt mix viscosity and mix composition (VMA) was found to be of the form:

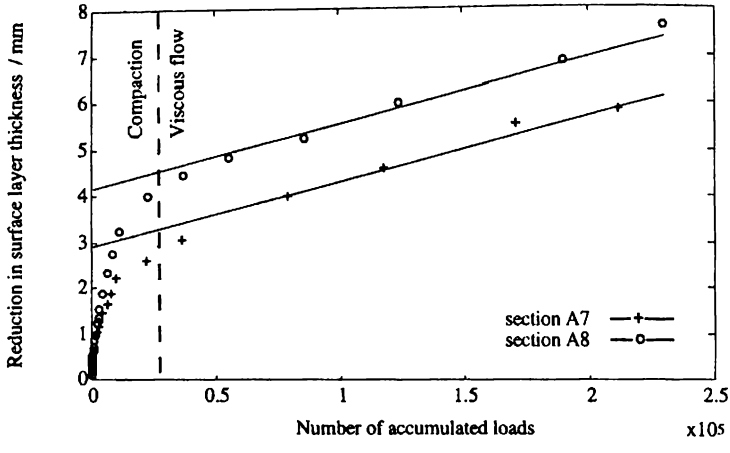
$$\log_{10}(\lambda_a) = \Phi_1(\text{VMA}) + \Phi_2(\text{VMA}) \log_{10}(\lambda_b) \tag{14.16}$$

where λ_a is the extensional viscosity of the asphalt mix (MPa.s)
λ_b is the extensional viscosity of the bitumen at the temperature of the mixture,

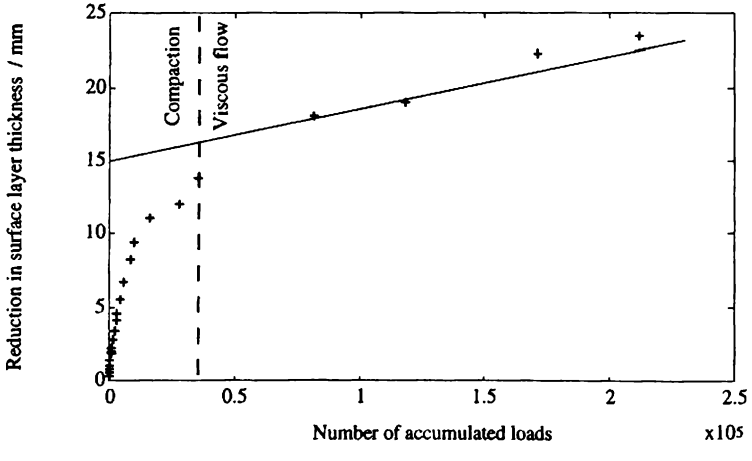
$$\Phi_1(\text{VMA}) = 1.86\times10^{-3}\,\text{VMA}^2 - 1.65\times10^{-1}\,\text{VMA} + 6.98,$$

$$\Phi_2(\text{VMA}) = -2.2\times10^{-4}\,\text{VMA} + 7.5\times10^{-1}.$$

Figure 14.9 shows equation 14.16 plotted for a number of different asphalt mix compositions. Decreasing the VMA of the mix shifts the curve vertically giving higher values of asphalt mix viscosity for a given value of bitumen viscosity and vice-versa. This is because the volume of bituminous binder in the mix affects the thickness and hence strain rate in the separating layer between adjacent aggregate particles.



(a)



(b)

Fig. 14.7 Predicted and measured reduction in surface layer thickness for: (a) Sections A7 and A8; and (b) Section A10. From [143].

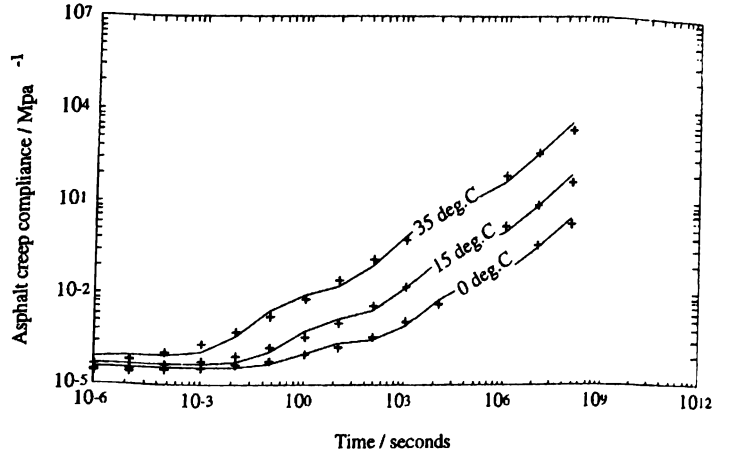


Fig. 14.8 Fitted asphalt mix creep compliances for three temperatures. From [143].

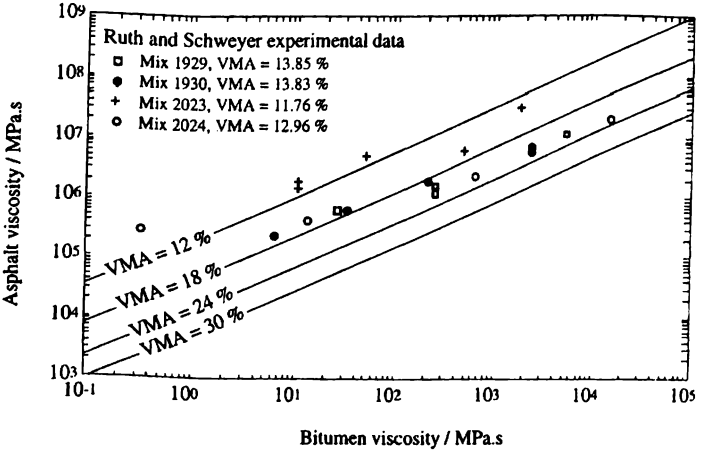


Fig. 14.9 Relationship between asphalt mix viscosity and bitumen viscosity. From [143].

Ruth and Schweyer [399] used a 'Schweyer Constant Stress Rheometer' to calculate values of 'constant power' viscosity for different types of bitumens and asphalt mixes at different strain rates (see [394, 399] for details). They found that their test data showed a general trend linking asphalt mix viscosity and bitumen viscosity but did not give a highly reliable relationship. Figure 14.9 also shows results for four of the asphalt mixes tested by Ruth and Schweyer. Although they did not use wheel tracking tests to determine asphalt mix properties their results confirm that equation 14.16 yields realistic values of asphalt mix viscosity.

14.5 VISCOSITY OF SOILS AND UNBOUND GRANULAR MATERIALS

Soils have been observed to have a similar structure to asphalts, where the water contained in the pore spaces acts as the binder [458]. Consequently, as a first approximation, it can be assumed that soils behave in a linear viscoelastic manner. This is reasonable provided the bituminous layers are thick and the effects of soil deformation are consequently small [360].

Creep tests on unbound granular materials suggest that an equilibrium level of sub-failure strain develops after a relatively small number of cycles [72, 458]. Accordingly, it can be assumed that unbound granular materials exhibit a very high effective viscosity after the initial compaction stage.

14.6 EXPERIMENTAL VALIDATION

The linear viscoelastic rutting model described above was validated by simulating permanent deformation from full scale-tests conducted during the OECD full-scale accelerated wheel-tracking tests in France [31]. The test section used for validation was Section 02 which was a bituminous structure. The pavement layer was modelled as a three-layer structure comprising a 139 mm asphalt layer, a 280 mm granular layer and a semi-infinite subgrade layer.

14.6.1 Loading

The test section was loaded by an arm of length 19m that rotated at 10 revolutions/min giving a wheel speed of 20 m/s. The arm applied a load of 56 kN to the test sections through a dual-tyre half axle arrangement, with tyre pressures of 710 kPa. The history of load applications through the test is shown in figure 14.10. Although the tests ran for over a year, most of the loads were applied between weeks 34 and 52. Successive passes of the load were distributed transversely to represent realistic traffic loading conditions and avoid canalisation. This lateral distribution was modelled in the simulation by generating laterally offset influence functions $h_m(x)$. The loads applied to the pavement sections were assumed to have no dynamic component. This is a reasonable assumption since the linear viscoelastic rutting model is largely insensitive to dynamic tyre forces.

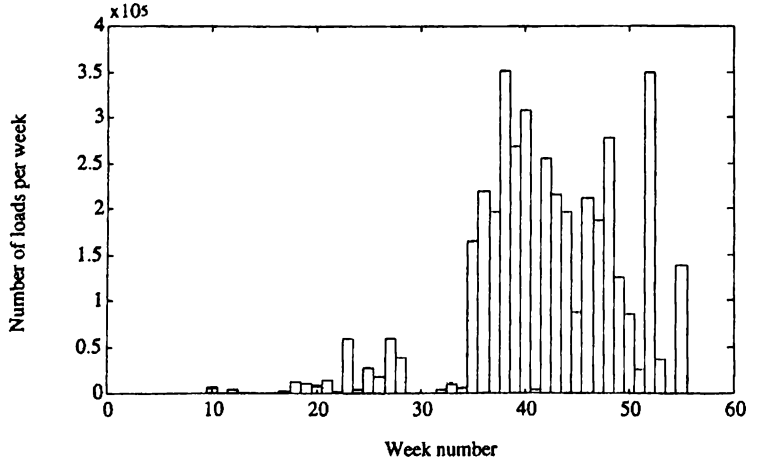


Fig. 14.10 Load applications during the OECD test [31].

14.6.2 Temperature Effects

Changes in air temperature were assumed to only affect the viscosity of the asphalt surface layer. The effective weekly temperature of the asphalt layer was estimated from the measured mean air temperature and the following empirical equation [189]:

$$T_p = T_a\left(1 + \frac{76.2}{h_1 + 304.8}\right) - \frac{84.7}{h_1 + 304.8} + 3.3 \qquad (14.17)$$

where T_p is the effective surface layer temperature (°C),
T_a is the measured mean air temperature (°C), and
h_1 is the thickness of the surface layer (mm).

Most of the loads were applied to the test sections during the summer months when the air temperature, and hence the asphalt temperature, was highest.

14.6.3 Asphalt Layer Viscosity

The bitumen viscosity was obtained from the viscoelastic fitting procedure described above for each week of the test using the mean weekly asphalt temperature. The asphalt layer viscosity was then estimated each week from the bitumen viscosity and the VMA of the asphalt mix, using equation 14.16 (assuming q=0.47). Figure 14.11 shows the effective weekly asphalt viscosity over the duration of the test plotted on a logarithmic scale. Because of the strongly non-linear relationship between temperature and viscosity, the weekly asphalt viscosity varies by over two orders of magnitude.

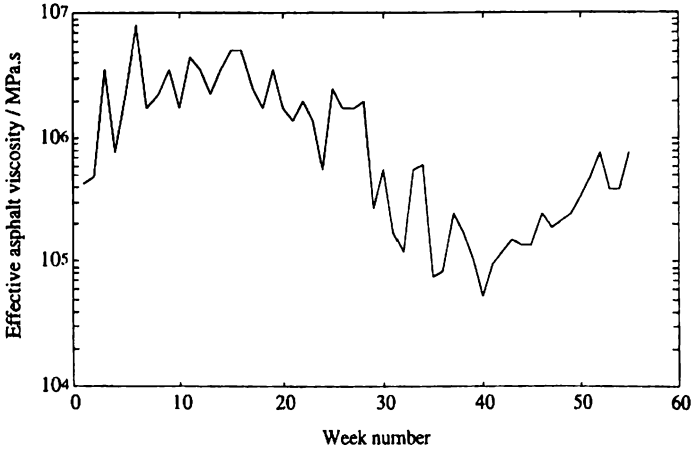


Fig. 14.11 Mean effective weekly asphalt layer viscosity. From [143].

To determine the asphalt viscosity and the mix VMA from equations 14.16 and 14.11 respectively, the properties of the bitumen and asphalt are required. The Ring and Ball softening temperature ($T_{R\&B}$) was estimated from the following empirical equation for French bitumens [470]:

$$T_{R\&B} = 95.81 - 24.84 \log_{10}(pen_{25}) \qquad (14.18)$$

where $T_{R\&B}$ is the Ring and Ball softening temperature (°C), and
pen_{25} is the standard penetration at 25°C.

The average standard penetration at 25°C obtained from the recovered binder for the 60/70 grade of bitumen used in the OECD test was 37.5. Therefore, the Ring and Ball softening temperature from equation 14.18 is: $T_{R\&B} = 56.7\ ^{o}C$

The Penetration Index (PI) can be estimated from the following empirical equation [470]:

$$PI = \frac{20T_{R\&B} + 500\log_{10}(pen_{25}) - 1{,}951.55}{T_{R\&B} - 50\log_{10}(pen_{25}) + 120.15} \qquad (14.19)$$

This gives a Penetration Index of: PI = –0.3

The average recovered binder content for the mix used in the OECD test was 6.0% (by weight) of the mix and the average void content for Section 02 was 3.45% vol of the mix. In order to estimate a VMA value for the mix the specific gravity of the 60/70 penetration grade bitumen and aggregate were taken as 1.03 and 2.60 respectively. These values give a mix VMA of 16.85%.

14.6.4 Granular and Subgrade Layer Viscosities

Examination of specimens cut from trenches on the rutted sections of the OECD test showed that most of the deformation was restricted to the top two layers with little contribution from the subgrade [31]. Consequently, viscosity values assigned to the granular and subgrade layers were high (0.69×10^{6} GPa.s), restricting almost all of the rutting in the model to the surface layer only. The viscosity assigned to the granular layer (1.38×10^{6} MPa.s) was chosen so that approximately 50% of the rutting occurred in the surface layer and 50% occurred in the granular layer, for an average asphalt viscosity determined from figure 14.11.

14.6.5 Influence Function Calculation

Contact conditions between each of the dual tyres and the road were assumed circular, with a uniform pressure distribution. The contact radius of each dual tyre was 138 mm and the spacing between the tyre centres was 360 mm. The deformation-rate influence functions $h_{\infty}(x)$ produced by VESYS for each of the pavement layer interfaces are shown in figure 14.12 for week 10 of the test. These were calculated directly below one of the contact patches. The area under each influence function is related to the permanent deformation as per equation 14.8. It can clearly be seen that almost all of the deformation occurs in the surface layer with material flowing upwards about 0.25m away from the load. This will result in the small ridge on either side of the rut often observed during wheel tracking tests [167].

14.6.6 Rut Depth Calculation

Rut depth δ was calculated by adding the height of material deposited on either side of the overall rut D_2 to the depth of the rut directly under one of the dual tyres D_1 (see figure 14.13).

14.6.7 Results

Figure 14.14 shows rut depth computed on a weekly basis compared with measured rut depth for Section 02. After 0.25×10^{6} load passes, rut depth predictions reproduce measurements well. The two circled points seem to indicate that the rut got shallower rather than deeper for short periods during the test. This behaviour is possible in a viscoelastic material if the load is offset by a certain amount from the measurement point (see figure 14.12), for the appropriate number of axle passes. However, in the absence of any documented evidence that this was indeed the case, it seems more likely that these points are due to measurement errors and therefore should be discounted.

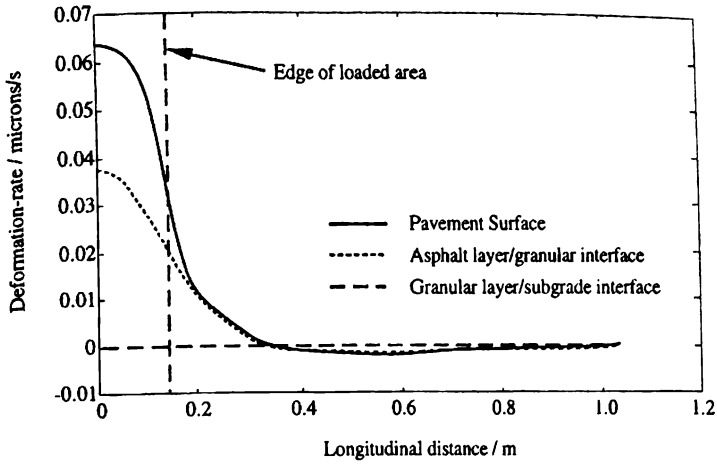


Fig. 14.12 VESYS influence functions at different depths calculated directly under a dual tyre. From [143].

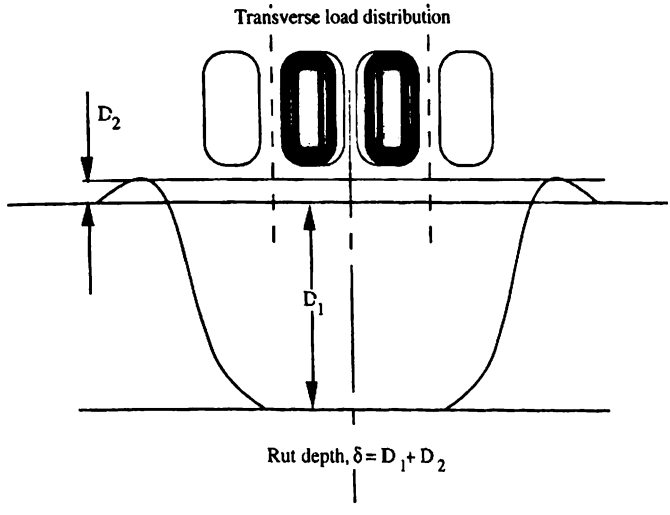


Fig. 14.13 Method for calculating rut depth.

Before 0.25×10^6 load passes the theoretical model does not fit measured permanent deformation. From figures 14.10 and 14.11 it can be concluded that this initial deformation occurred when the asphalt viscosity was at its highest (weeks 1 to 28) and the number of passes per week was lowest. It is apparent that this behaviour is not linear viscoelastic since a high asphalt viscosity and a low number of load passes would result in low permanent deformation. This initial behaviour can probably be attributed to densification in the asphalt and granular pavement layers where material is compacted to an equilibrium density under the action of the initial loads [48]. This behaviour cannot be modelled by a linear viscoelastic model.

Figure 14.15 shows the cross section of the predicted rut calculated for week 10 of the test where the number of load applications was 5784. This was calculated by using influence functions offset from the central load axis, and distributing the resulting canalised rut profile according to a normal distribution fitted to the lateral distribution of axle loads. The predicted rut profile matches typical experimental results well [167].

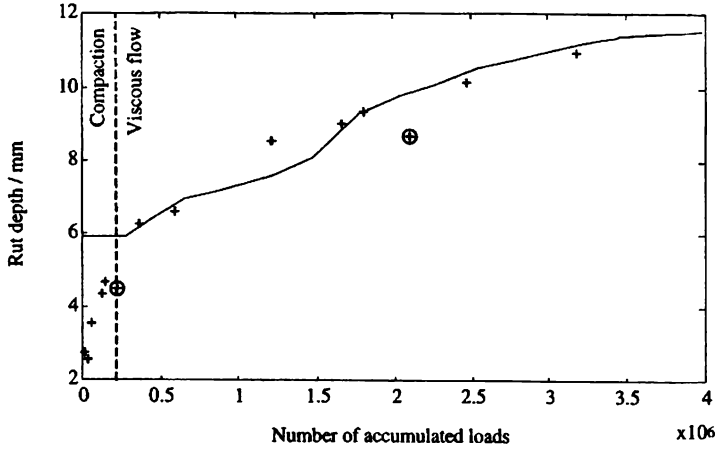


Fig. 14.14 Predicted and measured rutting in Section 02. From [143].

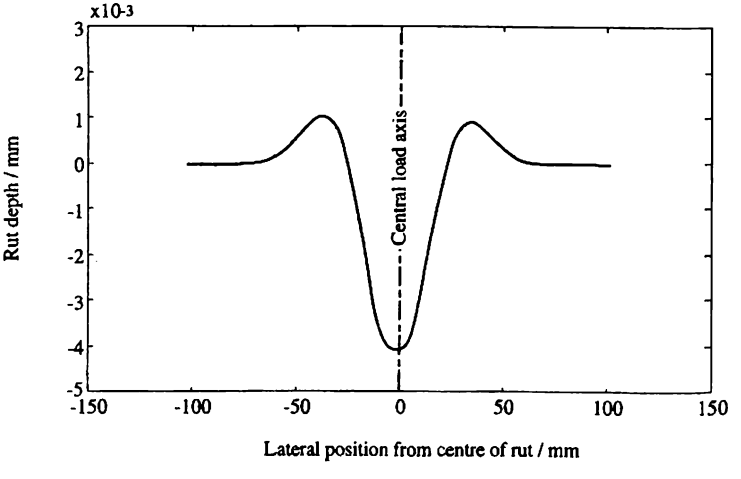


Fig. 14.15 Cross section of predicted rut profile for week 10. From [143].

14.7 CONCLUSIONS

(i) A simple methodology for calculating rutting behaviour of flexible pavements has been described. The calculation uses existing linear elastic layer models of a pavement supplied with viscous rather than elastic material properties.

(ii) The predicted residual permanent deformation field is realistic and independent of material elasticity. Permanent deformation is automatically accounted for in each layer, and the effects of temperature are included correctly.

(iii) After an initial compaction period the model predicts that the permanent deformation per wheel pass in thick asphalt pavements is proportional to the static axle load and inversely proportional to vehicle speed.

(iv) A new method has been developed for predicting asphalt mix viscosity from routine test data. Only one parameter 'q' needs to be fitted to experimental data.

(v) The parameter q needs to be measured under representative conditions for a linear viscoelastic rutting model. For the mixes tested by Hills, q=0.47 was found to be a suitable value. Additional measurements are needed to establish the range of applicability of this result.

(vi) The rutting model (with q=0.47) was successfully validated using the results of a full-scale accelerated–loading test in France.

A significant disadvantage of this method for calculating road deformation due to vehicles is that the creep of some asphalts is found to be non-linear, especially for large strain rates [72, 154, 211]. Further validation is therefore required for the wide range of asphalt wearing course materials commonly used, before the model can be applied accurately in pavement design. Nevertheless, the method is very useful for evaluating important trends and investigating the road-damaging potential of heavy vehicles.

15
FATIGUE CRACKING OF FLEXIBLE PAVEMENTS

15.1 SUMMARY

This chapter examines theoretically the possible mechanisms of fatigue cracking in asphalt pavements using linear elastic fracture mechanics (LEFM). The effects of a non-uniform transverse contact traction between the tyre and pavement on longitudinal surface fatigue cracking are examined theoretically using a finite element (FE) pavement model. Fatigue cracking due to thermal loading is also examined using a simplified linear viscoelastic pavement model. Results indicate that longitudinal surface fatigue cracking is unlikely to occur due to the non-uniform transverse contact traction. However, for short longitudinal cracks in the pavement surface, the combined vehicle and thermal load cycles may produce conditions that are favourable for fast fracture. Fatigue cracking (both longitudinal and transverse) at the base of the asphalt layer is found to be mainly dependent on the pavement geometry and the magnitude of the normal load.

This chapter is based on work previously published in [140].



15.2 INTRODUCTION

Almost all mechanistic flexible pavement design procedures calculate the fatigue life of pavements by considering the tensile stress or strain at the bottom of the bound asphaltic layers (see, for example [77, 192, 364]). These design procedures assume that fatigue cracks originate at the bottom of the bound layers and propagate vertically upwards towards the surface of the pavement, under the influence of the stress field produced by the contact between the tyre and pavement. Assuming a uniform normal contact traction, the maximum horizontal tensile stress in a continuous pavement structure occurs at the bottom of the bound layers, and the maximum horizontal compressive stress occurs at the surface of the pavement [72, 94]. However, core samples taken from cracked flexible pavements in the UK [457] and recent observations of cracked flexible pavements in Japan [328] have shown that cracks can often originate at the top surface and propagate down towards the bottom of the bound layers. The phenomenon of surface cracking cannot be explained using only the tensile stress at the bottom of the bound layers because the horizontal stresses and strains generated in the upper half of the asphalt layer are always compressive [72, 96].

More recently, researchers have hypothesised that the surface cracking phenomenon may be related to the non-uniform three dimensional contact traction distribution between the tyre and pavement, which induces large horizontal tensile stresses in the top layer of the pavement [260, 261]. Measurements performed on free-rolling car and truck tyres have shown that, in addition to the normal contact traction, there can be large transverse and longitudinal shear tractions acting in the contact area (see, for example [112, 303, 461]). Jacobs and Moraal [261] calculated primary pavement responses to a complex three dimensional contact traction distribution using the linear elastic pavement analysis program BISAR. Each component of the contact traction distribution was simplified into a number of circular areas where the traction was assumed constant (123 areas in total). The stress at each point on the surface of the pavement was then calculated by superimposing

the stress due to each of the constant traction regions. They calculated that the theoretical fatigue damage at the surface of the pavement, due to the transverse component of the contact traction distribution, was up to 70 times the fatigue damage at the base of the asphalt layer due to the vertical load. However, they did not account for the variation of horizontal stress with depth through the asphalt layer. Matsuno *et al.* [328] also hypothesised that longitudinal surface cracks occur at high pavement temperatures due to the large transverse tensile stress close to the edge of the tyre.

Both surface and base cracking in asphalt pavements has also been related to horizontal tensile stresses induced in the asphalt layers by daily temperature cycles (see, for example [150, 399]). Lytton and Shanmugham [311] developed a mechanistic surface fatigue model using an FE program to calculate the horizontal tensile stresses induced in the pavement due to thermal loading cycles. They validated damage predictions from their model with experimental data from cracked pavements in the USA. However, they found that their model required large amounts of computer time and they obtained a poor correlation between predicted and measured fatigue cracking damage.

Fast fracture of the asphalt material due to rapid falls in temperature is also thought to be a possible cause of surface cracking [237, 271]. Hills [237] developed a nomograph for predicting the critical fracture temperature for a wide range of bitumen types. He found that the critical temperature was independent of the rate of cooling in the temperature range of interest, and only dependent on the properties of the bituminous binder.

The main objectives of this chapter are to examine theoretically the possible mechanisms of fatigue cracking in flexible pavements operating under a wide range of traffic and thermal loading conditions using linear elastic fracture mechanics (LEFM). Longitudinal cracks originating at the surface and both longitudinal and transverse cracks originating at the base of the asphalt layer are considered. This chapter is divided into three main sections. The first and second sections examine theoretically the horizontal stresses and strains throughout the asphalt layer due to non-uniform contact tractions and thermal load cycles respectively. The third section uses the stresses calculated in the first two sections and examines theoretically the likely surface and base cracking rates due to both types of loading.

15.3 PRIMARY RESPONSES DUE TO A NON-UNIFORM CONTACT TRACTION DISTRIBUTION

This section describes the pavement structural model and loading conditions used to investigate the stress system generated in the asphalt layer of a pavement due to a non-uniform contact traction.

15.3.1 Loading Conditions

Jacobs and Moraal concluded from their research that the transverse component of the non-uniform contact traction contributed most significantly to the high surface stresses observed at the edge of the tyre-pavement contact area [260, 261]. Consequently, in this study, the effects of the transverse surface tractions were investigated by assuming that the normal and transverse tractions acting in the contact area are rotationally symmetric about the vertical axis through the centre of the tyre. The normal contact traction was assumed to be uniformly distributed over the contact area, while the transverse contact traction was assumed to be zero at the centre of the tyre, increasing linearly towards a maximum value at the tyre edge. This is a reasonable approximation for pneumatic tyres [112]. The magnitude of the uniform normal contact traction p_0 and the magnitude of the maximum value of the shear contact traction q_0 were both 1MPa and the radius of the contact area a was 0.125m (see figure 15.1). These loading conditions are used throughout this chapter.

The stress system set up in the pavement can be described in terms of the following Cartesian components σ_{xx}, σ_{yy}, and τ_{xy} (figure 15.1). For longitudinal surface cracking, the stress component of primary interest is the transverse direct stress σ_{xx} along the line $y = 0$. The

corresponding stress components for longitudinal and transverse cracking from the base of the asphalt layer are σ_{xx} along the line $y = 0$ and σ_{yy} along the line $x = 0$ respectively. For a single load, these components are equal $(\sigma_{xx} = \sigma_{yy})$. The stress component σ_{xx} along the line $y = 0$ will be referred to as the transverse stress σ_{xx} throughout this chapter.

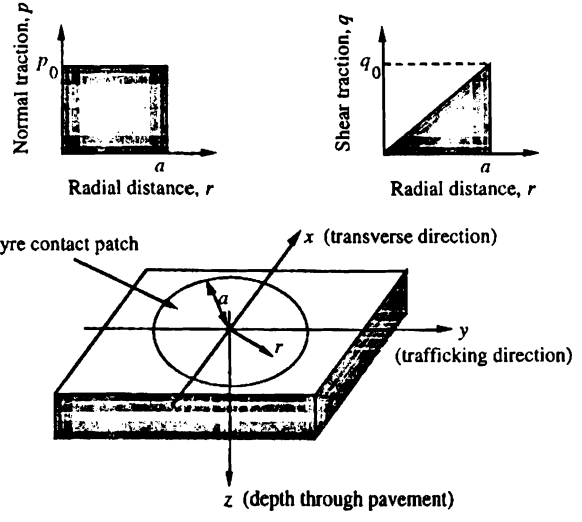


Fig. 15.1 Idealised axi-symmetric contact traction distribution between tyre and pavement. From [140].

15.3.2 Simplified Analysis: Plane Strain Elastic Half Space Model

Before a realistic model is presented, it is helpful to examine the theoretical transverse stress in a simplified system. Consider a general point (x, z) in a plane strain elastic half space. The transverse stress σ_{xx} due to a normal contact traction $p(x)$ and a transverse contact traction $q(x)$ acting over a strip $-a \le x \le a$, is given by Johnson [264] as:

$$\sigma_{xx}(x,z) = -\frac{2z}{\pi}\int_{-a}^{a}\frac{p(\xi)(x-\xi)^2}{\left[(x-\xi)^2+z^2\right]^2}\,d\xi - \frac{2}{\pi}\int_{-a}^{a}\frac{q(\xi)(x-\xi)^3}{\left[(x-\xi)^2+z^2\right]^2}\,d\xi, \qquad (15.1)$$

where x is the horizontal distance from the centre of the loaded strip,
z is the vertical distance below the surface of the half space and
ξ is a dummy variable in the x direction.

If the normal contact traction is assumed uniform $p(x) = p_0$, and the transverse contact traction is assumed to be zero at the centre of the loaded strip rising to a maximum value q_0 at $x = -a$ and a minimum value $-q_0$ at $x = +a$, equation 15.1 can be integrated in closed form, giving the transverse stress at either edge of the loaded strip $x = \pm a$:

$$\sigma_{xx}(\pm a,z) = \frac{q_0}{\pi}\left\{\ln\left(\frac{z^2+4a^2}{z^2}\right) - \frac{2\left(3z^2+10a^2\right)}{z^2+4a^2} + \frac{3z}{a}\tan^{-1}\left(\frac{2a}{z}\right)\right\} + \qquad (15.2)$$

$$\frac{p_0}{\pi}\left\{\frac{2az}{z^2+4a^2} - \tan^{-1}\left(\frac{2a}{z}\right)\right\}.$$

In the limit at the surface of the half space equation 15.2 gives:

$$\lim_{z\to 0}(\sigma_{xx}(\pm a, z)) = C_1 \ln(z) + C_2, \tag{15.3}$$

where $C_1 = -\frac{2q_o}{\pi}$ and

$$C_2 = \frac{q_o}{\pi}\left\{\ln\left(4a^2\right) - 5\right\} - \frac{p_o}{2}.$$

From equation 15.3 it can be seen that as z tends to zero, the stress becomes logarithmically singular with an infinite stress at the surface ($z = 0$). This singularity at either end of the contact strip is due to the discontinuity in transverse contact traction at this point. Figure 15.2 shows equation 15.2 plotted on semi-logarithmic scales as a function of depth through the pavement. Also shown in figure 15.2 are two corresponding curves for different triangular distributions of transverse contact traction (also shown in figure 15.2) with no discontinuity at the edges of the loaded strip, representing more realistic traction distributions [461]. The transverse stress was calculated by numerically integrating equation 15.1 with the appropriate loading conditions. For both the triangular distributions of contact traction, the stress is no longer singular at the surface. The maximum value depends on the position of the maximum transverse contact traction in relation to the edge of the loaded strip.

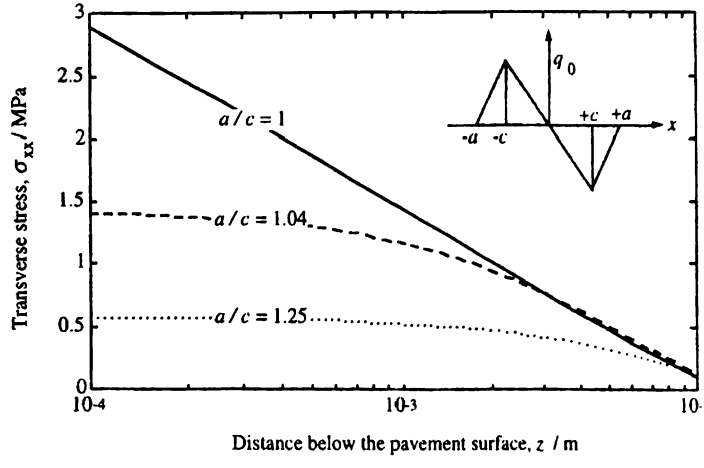


Fig. 15.2 Transverse stress at the edge of the load ($x = a$) as a function of distance below the pavement surface for different transverse contact traction distributions. From [140].

It can also be seen from figure 15.2 that the different loading geometries only affect the transverse stress very near to the pavement surface ($z \leq 10$mm). Consequently, if the stress at the surface is used to estimate a reduction in fatigue life, the exact functional form of the loading conditions are critical: the discontinuous loading assumed in [261] gives an unrealistic infinite stress concentration. If a fracture mechanics approach is used to estimate the likely surface cracking rates, the details of the transverse stress at surface are less critical since the calculation procedure is based on the transverse stress distribution throughout the asphalt layer (see later).

15.3.3 Finite Element Analysis

Pavement Structural Model

Finite Element Analysis (FEA) was used to investigate the stresses in a more realistic pavement system. The pavement was modelled as an axi-symmetric linear elastic structure, consisting of three layers; an asphalt surface layer, a granular base layer and a semi-infinite subgrade or soil layer. The loading conditions are described in Section 15.3.1. The stresses were calculated using the ABAQUS finite element code [235]. The mesh used in the analysis was finest at the edge of the contact patch where large stress gradients were expected. Axi-symmetric 8-node quadrilateral elements were used.

Pavement structures of three different thickness were considered. They were designed to correspond to a lightly trafficked pavement (case A), a moderately trafficked pavement (case B) and a heavily trafficked pavement (case C). The thickness of the asphalt layer for each case was obtained from the thickness design curves developed by the Transport Research Laboratory (TRL) for typical pavement operating conditions in the UK [10].

For each of the three cases, the elastic modulus of the asphalt layer E_1 was varied, while the modulus of the base E_2 was fixed, so that $E_1/E_2 = 10$, 50 and 100,. This enabled investigation of the effects of variation in elastic modulus ratio on the stresses generated in the asphalt layer. The value of the subgrade elastic modulus E_3 and Poisson's ratio for all three layers υ_1, υ_2 and υ_3 were held constant during the analysis. Table 15.1 gives full details of the three pavement structures used, and all the material properties for each case.

Structure	*Asphalt Surface Layer*	*Granular Base Layer*	*Subgrade Layer*
A	Thickness: 125 mm Modulus: 1.50, 7.50, 15.0 GPa Poisson's Ratio: 0.35	Thickness: 250 mm Modulus: 150 MPa Poisson's Ratio: 0.35	Thickness: ∞ Modulus: 50 MPa Poisson's Ratio: 0.35
B	Thickness: 250 mm Modulus: 1.50, 7.50, 15.0 GPa Poisson's Ratio: 0.35	Thickness: 250 mm Modulus: 150 MPa Poisson's Ratio: 0.35	Thickness: ∞ Modulus: 50 MPa Poisson's Ratio: 0.35
C	Thickness: 350 mm Modulus: 1.50, 7.50, 15.0 GPa Poisson's Ratio: 0.35	Thickness: 250 mm Modulus: 150 MPa Poisson's Ratio: 0.35	Thickness: ∞ Modulus: 50 MPa Poisson's Ratio: 0.35

Table 15.1 Details of the pavement structures and material properties used in the FE analysis.

Effects of Elastic Modulus Ratio

Figure 15.3 shows the calculated transverse stress at the surface as a function of radial distance from the centre of the contact patch for pavement B, with modulus ratios $E_1/E_2 = 10$, 50 and 100 calculated by ABAQUS. The numerical FE results do not reproduce the stress singularity at the edge of the tyre (as attempted in [261]) due to the discontinuity in transverse contact traction at this point. Instead the stress rises to a finite value dependent on the fineness of the FE mesh and the exact details of the transverse contact traction distribution. For the mesh used here, the FE results are accurate to within approximately 2 elements of the edge of the contact patch. It can also be seen from figure 15.3 that the surface of the pavement is in tension over a relatively small region centred around the edge of the loaded area. Increasing the modulus ratio tends to reduce the transverse tensile stress at the surface of the pavement.

Figure 15.4 shows the transverse stress at the edge of the tyre as a function of depth through the pavement for structure B, again with modulus ratios $E_1/E_2 = 10$, 50 and 100. The transverse stress is tensile at the surface, but it changes rapidly and becomes compressive by about 10mm below the surface. It then remains compressive until the lower half of the asphalt layer where it changes again

to become tensile due to bending. Increasing the modulus ratio tends to decrease the transverse tensile stress near the surface and increase the transverse tensile stress in the bottom half of the asphalt layer. In order to explain these effects it is helpful to consider the stresses produced by the normal and transverse contact tractions acting separately.

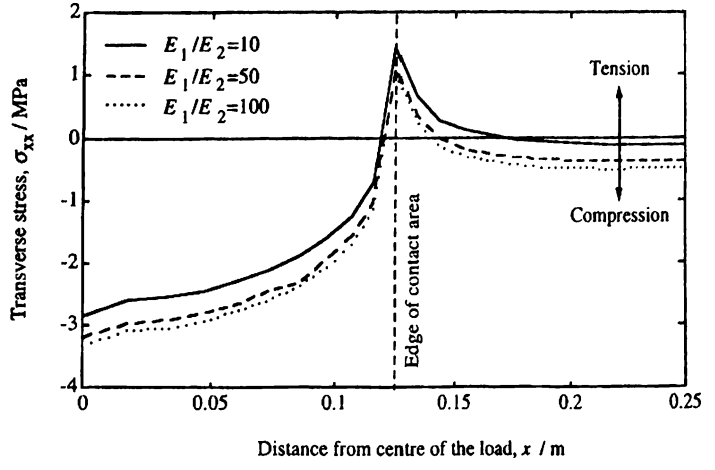


Fig. 15.3 Transverse surface stress $(z = 0)$ as a function of distance from the centre of the load for different modulus ratios and pavement structure B. From [140].

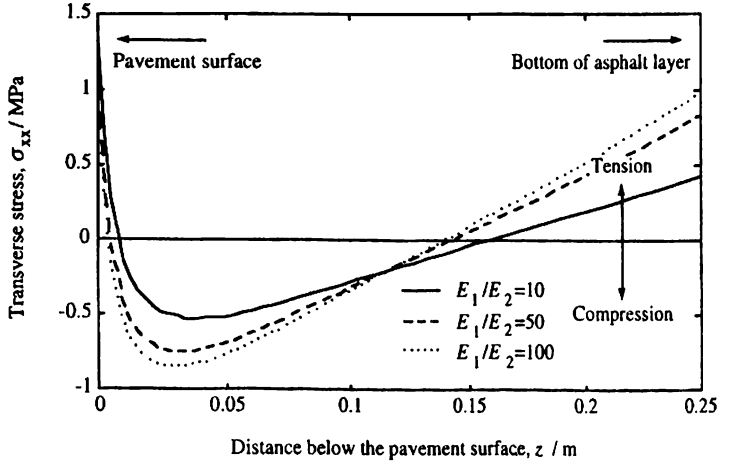


Fig. 15.4 Transverse stress at the load edge $(x = a)$ as a function of distance below the pavement surface for different modulus ratios and pavement structure B. From [140].

The transverse contact traction produces a theoretically singular, transverse stress at the tyre edge on the pavement surface. This stress is narrow, centred around the tyre edge, and is most sensitive to the magnitude and dimensions of the shear contact traction. Consequently, changing the elastic

modulus ratio and/or the thickness of the asphalt layer will not greatly affect the stress field produced by the transverse contact traction.

Superimposed on this stress field are the stresses due to the normal load. This produces transverse bending stresses that are compressive in the top half and tensile in the bottom half of the asphalt layer.

To explain the effects of a variable modulus ratio and asphalt layer thickness on these bending stresses it is convenient to consider the simpler system of an infinite Euler beam of elastic modulus E_1 and thickness h on an elastic (Winkler) foundation of stiffness E_2 subjected to a concentrated unit load. This is a reasonable assumption, provided the modulus ratio between the asphalt layer and the granular layer is large. It can be shown that for a given beam width, the compressive bending stress at the surface of the beam and tensile bending stress at the base of the beam directly under the load vary in proportion to $\left(E_1 / E_2 h^5\right)^{1/4}$ [219]. Consequently, increasing the ratio of beam modulus to foundation modulus E_1/E_2 for a given beam thickness h, increases both the tensile stress at the surface and the compressive stress at the base of the beam by $\left(E_1/E_2\right)^{1/4}$.

Therefore, for the combined traction system, increasing the modulus ratio tends to decrease the transverse tensile stress at the tyre edge near the pavement surface and increase the transverse tensile stresses in the bottom half of the asphalt layer. The overall result is that for higher modulus ratios, the surface area and depth of material in transverse tension decreases.

The variation of transverse bending stress directly under the centre of the loaded area (traditionally used in pavement fatigue calculations) is shown in figure 15.5 as a function of depth through the pavement, for the same pavement structure, with various modulus ratios. The transverse stress is compressive at the surface, increasing monotonically with depth, and becoming tensile in the bottom half of the asphalt layer. This stress distribution is dominated by the uniform normal traction, with no contribution from the addition of the transverse contact traction in the contact area. This is because the value of the axi-symmetric transverse contact traction is zero at the centre of the tyre $(x = 0)$. Consequently, as before, increasing the modulus of the asphalt layer, increases both the compressive transverse stress at the surface and the tensile transverse stress at the bottom of the asphalt layer by approximately $\left(E_1/E_2\right)^{1/4}$.



Effects of Asphalt Layer Thickness

Figure 15.6 shows the transverse surface stress as a function of radial distance from the centre of the contact area for pavement structures A, B and C, all with a modulus ratio of $E_1/E_2 = 100$. The stress distribution for the thinner pavement (A) is effectively shifted downwards compared to that for the thicker pavement (C). The calculations show that no material is in tension for the thinner pavement (C). (The height of the stress at the edge of the tyre depends on the mesh used in the FE model. A finer mesh would show a small area in tension associated with the theoretical singularity.)

This behaviour can again be explained by considering the simplified Euler beam on a Winkler foundation system. For this system, decreasing the thickness of the beam h for a given ratio of beam modulus to foundation modulus E_1/E_2, increases the compressive bending stress at the top and tensile stress at the bottom of the beam by $(1/h)^{5/4}$. This increase in compressive stress due to the normal load p exceeds the tensile stress due to the shear traction q.

It can also be seen from the beam model that the bending stresses are more sensitive to changes in beam thickness $\sigma \propto (1/h)^{5/4}$ than changes in the ratio of beam modulus to foundation modulus $\sigma \propto \left(E_1 / E_2\right)^{1/4}$. For the FE model this can be observed from figures 15.3 and 15.6.

Effects of Tyre Configuration

Dual tyres can significantly influence the horizontal stress at the base of the asphalt layer (the stress component traditionally used in fatigue calculations). The superposition of the two overlapping stress influence functions, either increases or decreases the magnitude of the effective fatigue stress

cycles depending on the pavement structure and so is an important consideration in damage calculations.

By contrast, the surface area in transverse tension at the edge of the contact area (figure 15.3) is not significantly influenced by the second tyre due to the very small region in transverse tension.

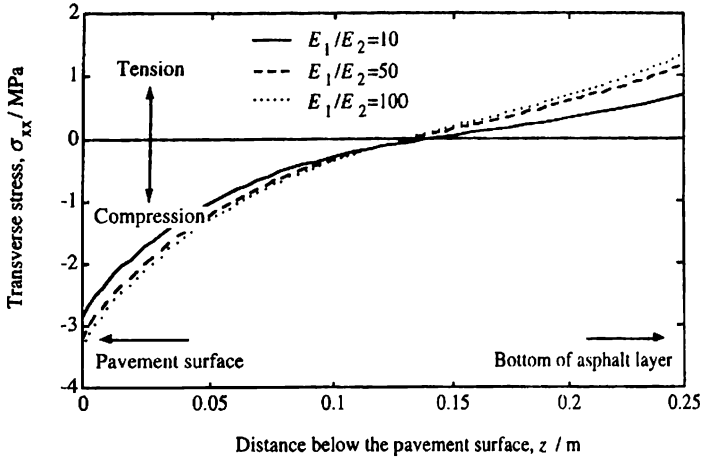


Fig. 15.5 Transverse stress at the centre of the load $(x = 0)$ as a function of distance below the pavement surface for different modulus ratios and pavement structure B. From [140].

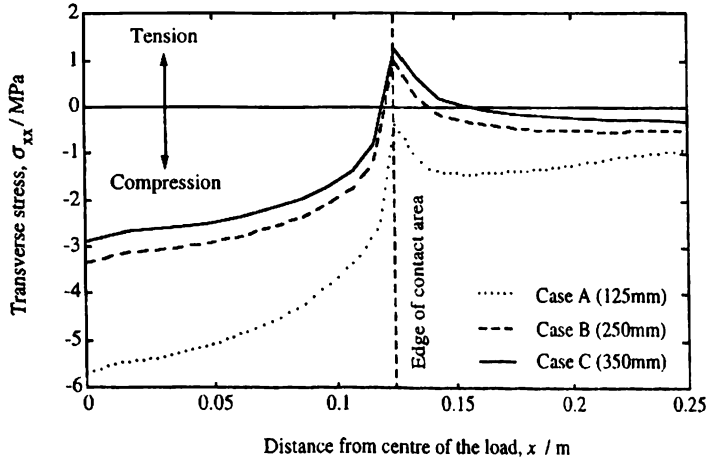


Fig. 15.6 Transverse surface stress $(z = 0)$ as a function of distance from the centre of the load for different asphalt layer thicknesses and a modulus ratio of 100. From [140].

15.4 PRIMARY RESPONSES DUE TO PERIODIC THERMAL LOADING

In order to calculate the transverse thermal stresses generated in a typical asphalt surface layer due to cyclic thermal loading it was assumed that the bottom of the asphalt layer was attached to a fixed rigid boundary (see figure 15.7). In a previous study it was shown that this assumption gives an upper bound solution to the transverse thermal stresses in the asphalt layer away from the pavement edges (see [137] for further details). A plane strain formulation was used, and the asphalt was modelled as a linear viscoelastic material with constant material properties.

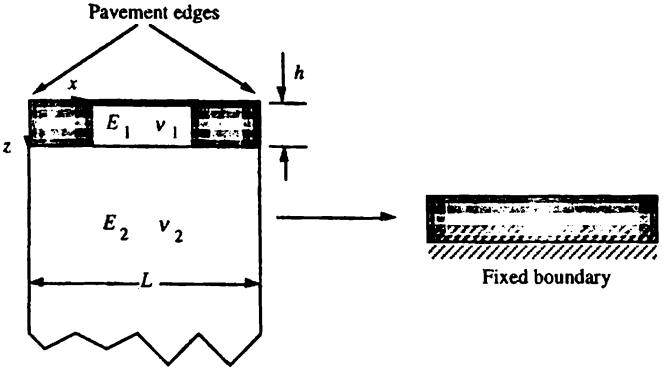


Fig. 15.7 Schematic view of the pavement cross-section showing the limiting case. From [140].

The following section briefly summarises the solution to the viscoelastic problem. Results from the linear viscoelastic model with constant material properties are compared to results from the full non-linear viscoelastic model with temperature dependent material properties. The full non-linear solution is detailed in reference [137]. Both models are based on the linear elastic solution, which is presented first.

15.4.1 Asphalt Layer Temperature Distribution

To calculate transverse stresses due to thermal loading, the temperature distribution through the asphalt layer $T(z,t)$ is required as a function of time. Assuming a general surface temperature variation, it can be shown that the solution to the one-dimensional heat conduction equation for a semi-infinite solid reduces to [137]:

$$T(z,t) = T_m + \sum_{i=1}^{N_\omega} \bar{T}_s^{(i)} e^{-z\sqrt{\omega_i/2\lambda}} \sin\left(\omega_i t - \psi_i - z\sqrt{\omega_i/2\lambda}\right). \tag{15.4}$$

where $T(z,t)$ is the pavement temperature at depth z and time t,
T_m is the mean surface temperature,
$\bar{T}_s^{(i)}$ is the surface temperature amplitude at angular frequency ω_i,
ψ_i is the surface temperature phase lag at angular frequency ω_i,
N_ω is the number of frequency components in the summation and
λ is the *thermal diffusivity* of the asphalt (conductivity/density x specific heat).

For a sinusoidal surface temperature variation with a single frequency corresponding to a loading period of 24 hours (ω_0), equation 15.4 simplifies to:

$$T(z,t) = T_m + \bar{T}_s^{(0)} e^{-z\sqrt{\omega_0/2\lambda}} \sin\left(\omega_0 t - \psi_0 - z\sqrt{\omega_0/2\lambda}\right). \tag{15.5}$$

15.4.2 Transverse Linear Elastic Stress

Assuming that the asphalt layer is fully restrained vertically (see figure 15.7), the transverse linear elastic stress σ_{xx}^{E} is a function of depth and time only, and can be shown to be given by the following expression [63]:

$$\sigma_{xx}^{E}(z,t) = -T(z,t)\frac{18GK\alpha}{3K+4G}. \tag{15.6}$$

where G is the elastic shear modulus of the material,
K is the elastic bulk modulus of the material,
α is the coefficient of thermal expansion.

15.4.3 Transverse Viscoelastic Stress

The transverse viscoelastic stress solution σ_{xx}^{V} can be obtained from the elastic solution (equation 15.6) using the elastic viscoelastic correspondence principle [182]. Assuming that the deviatoric behaviour of the asphalt can be modelled as a temperature dependent Maxwell material and the asphalt is incompressible ($K = \infty$), the transverse viscoelastic stress σ_{xx}^{V} is the solution to the following non-linear (initial value) differential equation (see [137] for further details):

$$\dot{\sigma}_{xx}^{V}(z,t) + \left\{\frac{2G(t)}{\eta(t)} - \frac{\dot{G}(t)}{G(t)}\right\}\sigma_{xx}^{V}(z,t) = -6G(t)\alpha\dot{T}(z,t) \tag{15.7}$$

where $\dot{\sigma} = d\sigma/dt$ *etc*,
$2G(t)$ is the temperature dependent elastic component of the Maxwell model,
$\eta(t)$ is the temperature dependent viscous component of the Maxwell model, and
t is time.

Note that the Maxwell material properties will vary as a function of temperature. However, since the temperature is a function of time, the Maxwell material properties may be thought of as time varying.

If the deviatoric material properties are assumed to be constant (not dependent on temperature), the problem becomes linear and it can be shown that the complex amplitude of the transverse viscoelastic stress may be expressed in terms of the complex amplitude of the transverse elastic stress (equation 15.6) and the frequency of temperature variation (see [137] for further details):

$$\bar{\sigma}_{xx}^{V}(z,i\omega) = \left(\frac{i}{i+\kappa}\right)\bar{\sigma}_{xx}^{E}(z,i\omega), \tag{15.8}$$

where $\kappa = \dfrac{2G}{\eta\omega}$, $i = \sqrt{-1}$,
$\bar{\sigma}_{xx}^{V}$ and $\bar{\sigma}_{xx}^{E}$ are complex quantities,
$2G$ is the constant elastic component of the Maxwell model and
η is the constant viscous component of the Maxwell model.

The effect of changes in temperature gradient on transverse stresses can also be examined using equation 15.8. For a sinusoidal variation in surface temperature described by equation 15.5, the magnitude of the maximum temperature gradient $\left|\partial T/\partial t\right|_{\max}$ is given by:

$$\left|\frac{\partial T(0,t)}{\partial t}\right|_{\max} = \omega_0 \bar{T}_s^{(0)}. \tag{15.9}$$

Substituting equation 15.9 into the expression for κ in equation 15.8 gives:

$$\kappa = \frac{2G\bar{T}_s^{(0)}}{\eta\left|\dfrac{\partial T(0,t)}{\partial t}\right|_{\max}}. \tag{15.10}$$

Figure 15.8a shows a plot of the magnitude of the normalised viscoelastic stress (calculated from equation 15.8) over a wide range of values for κ. The dependence of the viscoelastic stress on both the viscosity and the thermal gradient is evident using equation 15.10. The viscoelastic stress $\overline{\sigma}_{xx}^{V}$ tends to the elastic stress $\overline{\sigma}_{xx}^{E}$ as $\kappa \to 0$, *ie* the material viscosity or the cooling gradient become large $\left(\eta \to \infty, \text{ or } |\partial T/\partial t|_{max} \to \infty\right)$. At the other extreme $\kappa \to \infty$, where either the material viscosity or the cooling gradient tend to zero $\left(\eta \to 0, \text{ or } |\partial T/\partial t|_{max} \to 0\right)$, the magnitude of the viscoelastic stress tends to zero. This is because the viscoelastic stresses generated in the system can relax at a faster rate than they accumulate due to thermal expansion.

Figure 15.8b shows the phase lag between the viscoelastic and elastic stresses as a function of κ calculated from equation 15.8. For $\kappa \to 0$, *ie* large values of material viscosity or large cooling gradients $\left(\eta \to \infty, \text{ or } |\partial T/\partial t|_{max} \to \infty\right)$ where the viscoelastic solution tends to the elastic solution, the phase lag tends to zero as expected. The phase lag between the viscoelastic stress and the elastic stress increases as $\kappa \to \infty$, tending towards a constant value of $\pi/2$ (90°).



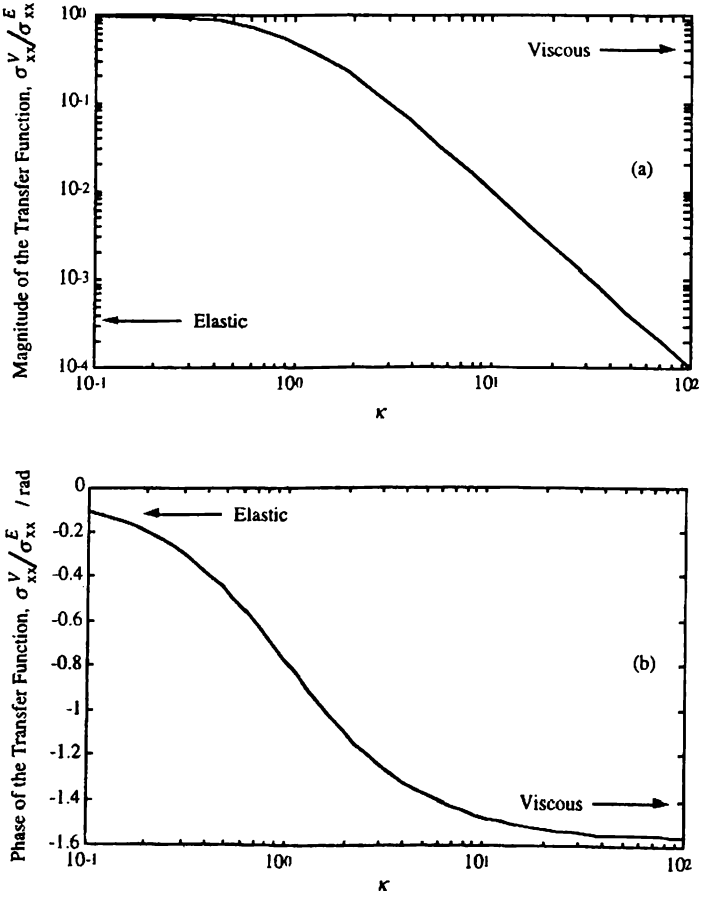


Fig. 15.8 Normalised harmonic viscoelastic stress transfer function, (a) magnitude, and (b) phase. From [140].

15.4.4 Estimation of Asphalt Material Properties

To determine the viscoelastic stresses from equations 15.7 and 15.8, the asphalt material properties are required. The following sub-sections describe the methods used to obtain these properties for a typical asphalt mix.

Thermal diffusivity λ

The thermal diffusivity of a typical asphalt surface layer was estimated by fitting equation 15.4 to experimental temperature data, previously measured over a seven day period on a section of the TRL test track [221]. The procedure involved calculating the Fourier Transforms of the temperature time histories at three depths, and least-squares fitting the thermal diffusivity to the five largest frequency components. Full details of this procedure can be found in reference [137]. The value of thermal diffusivity determined from this data was $\lambda = 5.3 \times 10^{-6}\,\mathrm{m}^2/\mathrm{s}$. This value is used throughout this chapter.

Determination of Maxwell Model Material Parameters $2G$ and η

To calculate the viscoelastic stress from equation 15.7 the temperature dependent shear elasticity ($2G$) and the shear viscosity (η) of the Maxwell model are required. These properties are not constant since they depend on the temperature of the asphalt layer which varies with time. To estimate these temperature dependent values, the creep response of a Maxwell model was fitted to shear creep compliances of an asphalt mix over a wide range of temperatures. The asphalt mix used for determination of the Maxwell model material parameters had the following specification; Ring and Ball Softening Temperature $T_{R\&B} = 50°\mathrm{C}$, Penetration Index $PI = -0.5$, and percentage Voids in Mixed Aggregate $VMA = 21\%$. This asphalt mix specification was used throughout this chapter.

The shear creep compliances of the asphalt mix were obtained from the shear creep compliances of pure bitumen using equation 14.16. The shear creep compliances of the pure bitumen were obtained from the Van der Poel Nomograph [476] using $G = E/3$.

The constant values of the shear elasticity ($2G$) and the shear viscosity (η) required by equation 15.8 were chosen to be their mean values over the duration of the simulation at the appropriate depth.

15.4.5 Transverse Stress Results

Figure 15.9 shows the transverse surface stress as a function of time predicted from equations 15.7 and 15.8 for an asphalt layer thickness of 250mm. The mean temperature T_m and half temperature range $\bar{T}_s^{(0)}$ in equation 15.5 were taken as 0°C and 5°C respectively. The most striking feature of the two solutions shown in figure 15.9 is the difference in shape of the curves. The curve corresponding to equation 15.8 is sinusoidal (as expected for a linear system) compared with the non-sinusoidal curve predicted by equation 15.7. There is also a difference in phase of approximately 2.5 hours between the maximum stress predicted by the two models. This is due to non-linearities introduced into equation 15.7 by the temperature dependent material properties. However, due to the use of the mean values of material properties in the linear solution (equation 15.8), the difference in the magnitude of the peak stress predicted by the two models is small.

Figure 15.10 shows the maximum stress as a function of distance through the pavement for both solutions under the same thermal loading conditions as above. Although the two solutions show time dependency at each depth (see figure 15.9), the variations in peak stress with depth are similar.

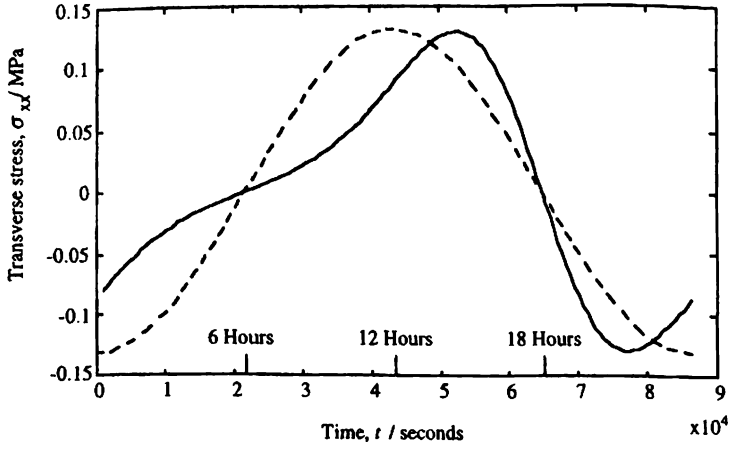


Fig. 15.9 Transverse surface stress as a function of time. From [140].
——— = Non-linear solution (equation 15.7); - - - - - - - = Harmonic solution (equation 15.8).



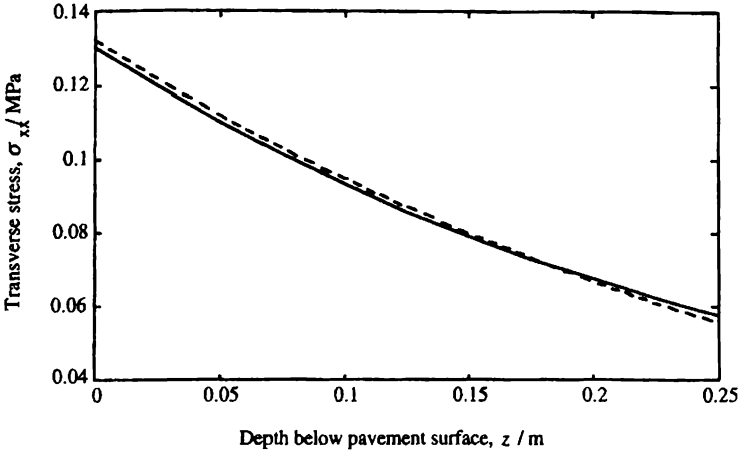


Fig. 15.10 Peak transverse stress as a function of distance below the pavement surface . From [140].
——— = Non-linear solution (equation 15.7); - - - - - - - = Harmonic solution (equation 15.8).

15.5 CRACKING DAMAGE

In the following section the fracture mechanics of asphalt pavements is considered along with the likely longitudinal cracking rates, from both the surface and base of a pavement, due to the transverse stresses induced by traffic and thermal loading calculated in previous sections.

15.5.1 Theory of Fracture Mechanics Applied to Cracking in Flexible Pavements

Cracking in asphalt pavements can be modelled as a fatigue phenomenon using linear elastic fracture mechanics (LEFM). It is assumed that fatigue cracks start from macroscopic pre-cracks (flaws) existing in either the surface or base of the asphalt layer. It will be assumed that the cracks propagate normal to the direction of maximum tensile stress (*ie* mode I crack growth). This assumption, which is commonly made in fracture mechanics, is supported by experimental evidence for fracture in metals [233]. At low temperatures the asphalt behaves in a brittle manner and cracks might propagate by fast fracture, whereas at higher temperatures cracks are more likely to propagate by progressive micro-plastic straining at the crack tip. It will further be assumed that asphalt behaves as a homogeneous linear elastic material and crack growth is not hindered by individual aggregate particles.

Stresses in the Vicinity of a Crack

Figure 15.11 shows a mode I edge crack of length c in a semi-infinite plate of thickness h in a state of plane strain. The plate is subjected to some remote loading normal to the plane of the crack. An element in the plate $dxdz$ a distance ρ and angle θ from the crack tip experiences stresses of the following general form (*eg* [68]):

$$\sigma_{ij} = \frac{K_I}{\sqrt{2\pi\rho}} f_{ij}(\theta), \tag{15.11}$$

where f_{ij} accounts for the orientation of the element in relation to the plane of the crack.

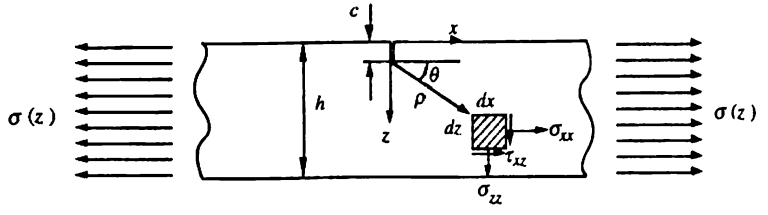


Fig. 15.11 Crack in a plane-strain plate subjected to a general remote stress. From [140].

The factor K_I is known as the mode I stress intensity factor which describes the stress field in the vicinity of the crack tip. K_I depends on the form of remote loading. For example, a uniform tensile stress $\sigma(z) = \sigma^{\infty}$ gives $K_I = \sigma^{\infty}\sqrt{\pi c}\, g(c/h)$, where the function g describes the dependence on plate geometry. When the stress intensity factor K_I reaches a critical value K_{IC}, a crack in the material will propagate by fast fracture. K_{IC} is the mode I critical stress intensity factor (or fracture toughness) and is a material constant. Typical values of K_{IC} for asphaltic materials obtained from the literature are given in Table 15.2. It can be seen from equation 15.11 that at the crack tip ($\rho = 0$) the stresses are singular. However, in reality the material around the crack tip deforms plastically or viscoelastically to keep these stresses finite. This plastic process zone is assumed to be small compared to the crack length and specimen dimensions and the material outside the process zone is assumed to be linear elastic.

Reference	K_{IC} / *MN* /$m^{3/2}$
Ramsamooj [381]	0.428 (sand asphalt) 0.604 (asphalt concrete)
Bahgat and Herrin [41]	0.55–0.77
Salam and Monismith [401]	0.6–1.2
Dongre [163]	0.67–1.03
Majidzadeh [317]	0.33 (fatigue) 0.04 (static fracture)

Table 15.2 Typical values of fracture toughness of asphalts.

Assuming a Von Mises criterion describes the yield condition of the material σ_y [68], the size of the process zone ahead of the crack tip ($\theta = 0$) (for a plane strain crack) may be estimated from $r_p = \left[K_I^2(1-2\upsilon)^2\right]/2\pi\sigma_y^2$. Taking Poisson's ratio as $\upsilon = 0.35$, the yield stress as $\sigma_y = 5.3$ MPa from [381], and assuming the specimen is at the point of fast fracture $(K_I = K_{IC})$, typical values of r_p for asphaltic materials range from 55μm to 733 μm for asphaltic materials exhibiting elastic behaviour (*ie* low temperatures or high strain rates). Consequently, the plastic zone can be considered small compared to the crack length and plate dimensions.

Due to the variation in far field stress, the mode I stress intensity factor varies with a range $\Delta K_I = K_I^{max} - K_I^{min}$ during one loading cycle. If K_I^{min} is negative, signifying that the crack closes for part of the loading cycle, ΔK_I is usually taken as K_I^{max} for fatigue calculations [233].

Empirical Relations Describing Crack Growth

The most commonly–assumed relationship between rate of crack growth and stress intensity factor range is the Paris law [449]:

$$\frac{dc}{dN} = A\,(\Delta K_I)^n, \tag{15.12}$$

where c is the crack length,
N is the number of applied loads,
ΔK_I is the mode I stress intensity factor range for one load cycle and
A and n are a material constants.

Failure of the asphalt layer may occur under two conditions:

(i) Fast fracture will occur for a critical crack length that satisfies the condition $K_I^{max} = K_{IC}$.

(ii) Fatigue failure will occur when a fatigue crack extends all the way through the asphalt layer. The number of cycles (N_f) required to extend a crack through an asphalt layer of thickness h may be calculated by integrating equation 15.12:

$$N_f = \int_{c_o}^{h} \frac{1}{A(\Delta K_I)^n}\,dc, \tag{15.13}$$

where c_o is the initial crack length in the pavement.

Experimental studies using slabs of asphalt have shown that reasonable values for c_o are between 4mm and 10mm [382].

An important shortcoming of the LEFM approach to cyclic fatigue of asphalt pavements is the assumption that the material is linear elastic and homogeneous outside the crack tip process zone. This is a reasonable approximation for asphaltic materials at low temperatures and/or high strain rates, but not at higher temperatures where there is significant creep deformation.

Determination of the Stress Intensity Factor, K_I

Assuming that the elastic modulus of the asphalt layer is at least an order of magnitude greater than the elastic modulus of the granular base layer, the pavement can be modelled as a plate in plane strain with a crack propagating from one edge towards the other (see figure 15.11). It can be shown [449] that for a non-uniform stress distribution normal to the crack plane, the mode I stress intensity factor is given by the convolution integral:

$$K_I = \int_0^c \zeta(z,c,h)\,\sigma_{xx}(z)\,dz, \tag{15.14}$$

where σ_{xx} is the normal stress across the location of the crack due to the applied loads, in the absence of a crack and

ζ is the 'weight function', is the stress intensity factor at the tip of a crack of length c for a unit point load at position z.

The weight function $\zeta(z,c,h)$ for a crack in a plane strain plate is given by Tada as [449]:

$$\zeta(z,c,h) = \frac{2\,W(z/c,c/h)}{\sqrt{\pi c}\,(1-c/h)^{3/2}\sqrt{1-(z/c)^2}}. \tag{15.15}$$

A numerical approximation to the function $W(z/c,c/h)$ is given in reference [449].

In order to determine the stress intensity factor from equation 15.14, the transverse stress, σ_{xx}, due to the applied loads in the absence of a crack needs to be calculated as a function of depth z. FEA was used to calculate this stress for surface and base cracks due to vehicle loading, and equation 15.8 was used for surface and base cracks due to thermal loading.

To account correctly for the singular stress at the edge of the tyre-pavement contact area for cracks originating at the surface, the FEA results were modified by adding the theoretical logarithmic singularity to the solution as $z \to 0$. The gradient of the logarithmic singularity (with respect to depth z) was determined from the slope of the solution for a linear elastic plane strain half space, for small values of z (constant C_1 in equation 15.3). Theoretically, the axi-symmetric layered solution and the plane strain half space solution converge as $z \to 0$ since for small values of z, the radius of the load becomes very large compared with the distance below the surface, and the circular load can be replaced by a line load (*ie* a plane strain solution). The transition point where the two solutions were blended together was determined so that the stress gradient $\partial\sigma/\partial z$ on logarithmic scales for the combined solution was continuous.

Figure 15.12 shows the transverse stress as a function of distance through the pavement for a modulus ratio $E_1/E_2 = 10$, and an asphalt layer thickness of 250mm (pavement case B). The circles show the numerical values from the FE model and the dashed line shows the plane strain solution predicted from equation 15.2. For small z, the two solutions converge until approximately 1mm below the surface where the stress predicted by the FE model tends to a constant finite value of 1.9 MPa at the pavement surface. This is due to the inability of FE solutions to accommodate singular stresses and step functions in loading. The combined stress (the original FE results modified at small z as described above) used to calculate the stress intensity factor is shown in figure 15.12 by the solid line.

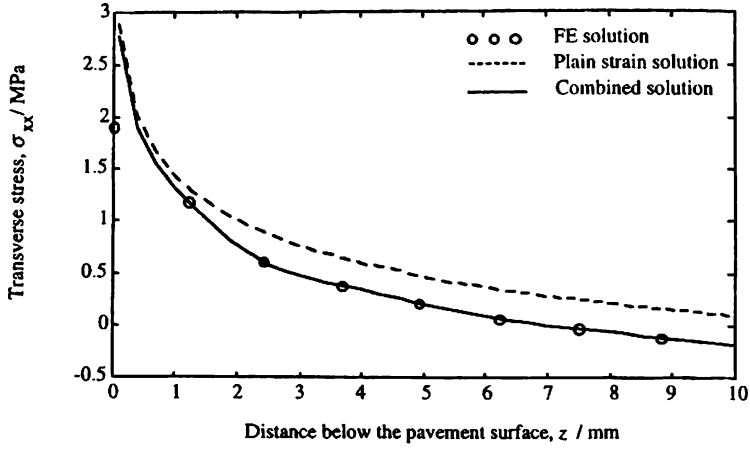


Fig. 15.12 Transverse stress at the edge of the load $(x = a)$ as a function of distance below the pavement surface for a modulus ratio of 10 and pavement structure B. From [140].

The addition of the logarithmic stress singularity does not affect the ability to evaluate equation 15.14 numerically. This can be seen by expressing equation 15.14 as:

$$K_I = \int_0^{\delta} \zeta(z,c,h)\sigma_{xx}(z)dz + \int_{\delta}^{c} \zeta(z,c,h)\sigma_{xx}(z)dz, \tag{15.16}$$

where $\delta << c$.

Substituting the plane strain solution for $\sigma_{xx}(z)$ as $z \to 0$ (equation 15.3) into the first integral of equation 15.16 gives:

$$K_I = \int_0^{\delta} \Lambda\left(C_1 \ln(z) + C_2\right)dz + \int_{\delta}^{c} \zeta(z,c,h)\sigma_{xx}(z)dz, \tag{15.17}$$

where Λ is the asymptotic value of the weight function $\zeta(z,c,h)$ as $z \to 0$.

Evaluating the first integral in equation 15.17 yields:

$$K_I = \Lambda\delta\left[C_1\left(\ln(\delta) - 1\right) + C_2\right] + \int_{\delta}^{c} \zeta(z,c,h)\sigma_{xx}(z)dz. \tag{15.18}$$

In the limit at the surface $(\delta \to 0)$ equation 15.18 gives:

$$K_I = \int_{\delta}^{c} \zeta(z,c,h)\sigma_{xx}(z)dz, \tag{15.19}$$

Consequently, although the stress $\sigma_{xx}(z)$ is logarithmically singular at the surface of the pavement $(z = 0)$, the convolution integral for the stress intensity factor (equation 15.19) is not singular and can be calculated using a numerical integration technique.

Determination of Fatigue Parameters *A* and *n*

Fatigue parameters A and n are required to determine the rate of cracking from the Paris Law (equation 15.12). Majidzadeh *et al.* [315] found from fatigue tests on asphaltic beam specimens that

values of n ranged from 0 to 4 depending on the amount creep deformation present. They concluded that $n = 4$ is appropriate for analysis of pavement systems where the effects of creep are negligible (*ie* low temperatures/high strain rates). Salam and Monismith also found that at low temperatures, a fatigue exponent of $n = 3.8$ fitted their crack propagation experiments [401]. Other values found in the literature range from 1.97 to 6.57 depending on the properties of the asphalt and the ageing of the mix [69, 311]. For the rest of this chapter, the constant value of $n = 4$ has been used.

Brooker *et al.* [69] measured the fatigue parameter A for a range of asphalt mix variables. They concluded that A was dependent on both the stiffness of the bituminous binder and the composition of the asphalt mix. A constant value of $A = 5.5 \times 10^{-30}\ \left(\mathrm{m}^7/\mathrm{N}^4\mathrm{cycle}\right)$ from [69] was chosen for typical asphalt mix operating conditions.

By using the same values of A and n for fatigue cracking from both the surface and base of the asphalt layer it is possible to examine the relative importance of surface cracking and base cracking for a wide range of pavement operating conditions, assuming linear elastic fracture mechanics. Note, however, that variation of A and n with temperature is not included in the following analysis.

15.5.2 Stress Intensity Factor Results

Surface Stress Intensity Factors

Figure 15.13 shows the maximum stress intensity factor as a function of crack length for a crack originating at the surface of the pavement due to *vehicle loading* for pavement structures A, B and C with elastic modulus ratios $E_1/E_2 = 10, 50$ and 100. It can be seen that as the crack propagates vertically downwards, the stress intensity factor first increases and then changes sign and becomes negative a short distance (about 10–20mm) below the surface of the pavement. This is in agreement with results presented by Bower and Fleck [65] who calculated the stress intensity factor for a surface breaking micro-crack perpendicular to the free surface of a brittle half space loaded by a Hertzian contact (see [264] for a detailed discussion on Hertzian contact conditions). A negative stress intensity factor indicates that the crack is closing up at the tip and will not propagate. Increasing the modulus ratio, for a given pavement thickness, tends to decrease both the magnitude of the stress intensity factor and the distance below the surface where it changes sign from positive to negative (see also figure 15.4). Conversely, increasing the thickness of the asphalt layer tends to increase both the magnitude of the stress intensity factor and the distance below the surface where it changes sign. These effects are both due to the compressive horizontal stresses induced in the top half of the asphalt layer by the normal contact traction discussed previously. The maximum value of the stress intensity factor occurs very near the surface, indicating that short cracks of less than 5mm will grow most rapidly but will stop growing when they reach a depth of approximately 10–20mm.

Figure 15.14 shows the maximum stress intensity factor as a function of crack length due to *thermal loading* cycles for temperature amplitudes $\bar{T}_s^{(0)} = 5^{\circ}\mathrm{C}, 10^{\circ}\mathrm{C}$ and $15^{\circ}\mathrm{C}$ in equation 15.5. The thermal stresses were calculated using equation 15.8. The mean temperature $\bar{T}_m$ was taken as $0^{\circ}\mathrm{C}$ and the thickness of the asphalt layer was 250mm. For all the temperature amplitudes, the stress intensity factor remains positive and increases monotonically with crack length indicating that cracks will always grow. Increasing the temperature amplitude tends to increase the stress intensity factor because the transverse tensile stress induced in the asphalt layer is increased.

Base Stress Intensity Factors

Figure 15.15 shows the maximum stress intensity factor as a function of crack length for a crack originating at the *base* of the surface layer due to vehicle loading for pavement structures A, B and C with modulus ratios $E_1/E_2 = 10, 50$ and 100. The stress intensity factor again increases monotonically with crack length for all the cases. Increasing the modulus ratio for a given asphalt layer thickness tends to increase the tensile stresses in the lower half of the asphalt layer and hence the stress intensity factor. Conversely, increasing the asphalt layer thickness tends to decrease the tensile stresses in the lower half of the asphalt layer and hence the stress intensity factor.

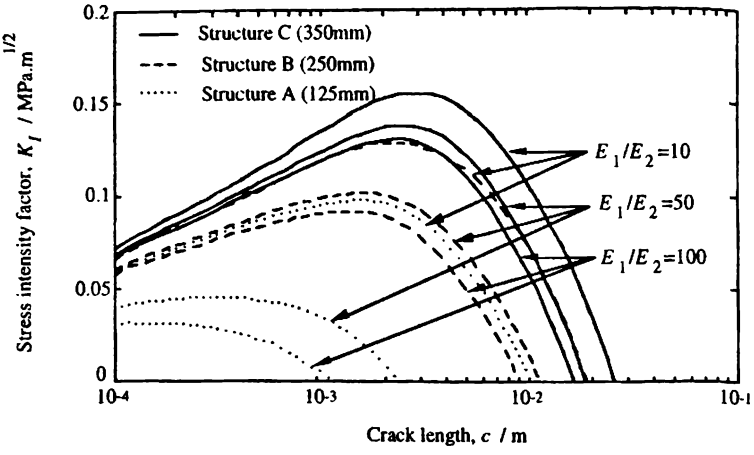


Fig. 15.13 Stress intensity factor as a function of crack length for a *surface crack* due to *vehicle loading* for pavement structures A, B and C with different modulus ratios. From [140].

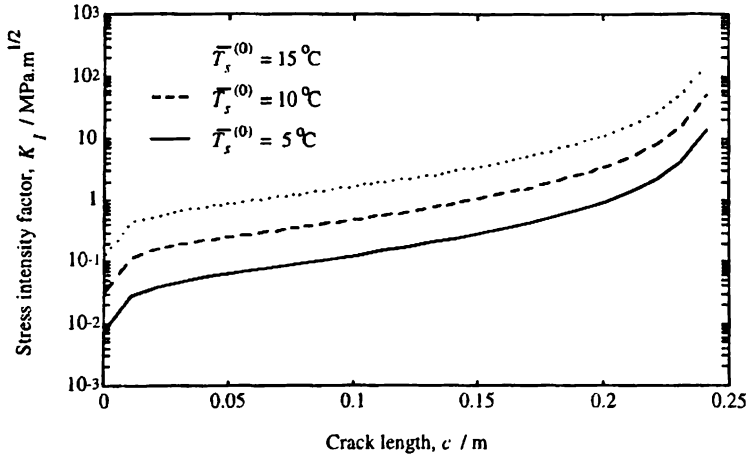


Fig. 15.14 Stress intensity factor as a function of crack length a *surface crack* due to *thermal loading* for an asphalt layer 250mm thick, with different temperature amplitudes and a mean temperature of 0°C. From [140].

Results for the maximum stress intensity factor as a function of crack length for a crack originating at the base of the surface layer due to thermal loading cycles are very similar to those for surface cracking shown in figure 15.14. The only difference is the smaller stress intensity factors for the base cracks due to the reduction in temperature through the asphalt layer.

Surface and Base Crack Evolution

Figure 15.16 shows the evolution of surface and base cracks in pavement structure B (calculated by integrating equation 15.12), with modulus ratios E_1/E_2 = 10, 50 and 100, due to traffic loading only. The most striking thing about figure 15.16 is that the surface cracks initially grow quickly, but

growth arrests at lengths of less than 10mm. This is because the stress intensity factor changes sign and becomes negative for a surface crack (see figure 15.13). Decreasing the modulus ratio tends to increase the steady state length of the surface cracks. Due to the changing temperature and hence modulus ratio of the pavement, these longitudinal surface cracks can be expected to grow to between 10mm and 20mm before they stop propagating. Conversely, the base cracks begin to grow slowly and then accelerate until they extend through the asphalt layer.

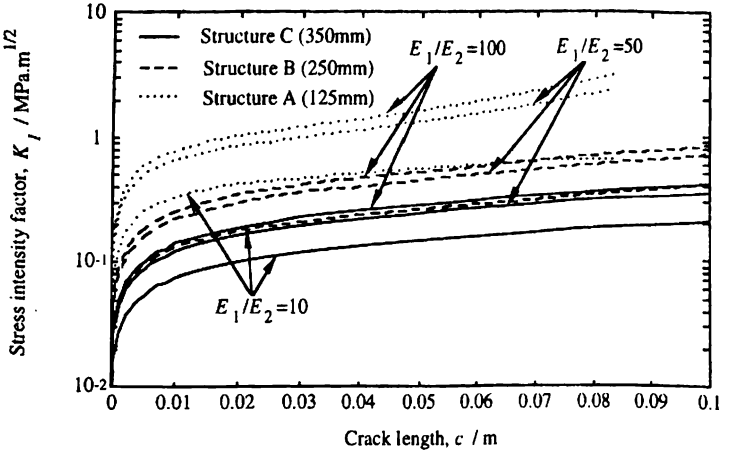


Fig. 15.15 Stress intensity factor as a function of crack length for a base crack due to vehicle loading for pavement structures A, B and C with different modulus ratios. From [140].

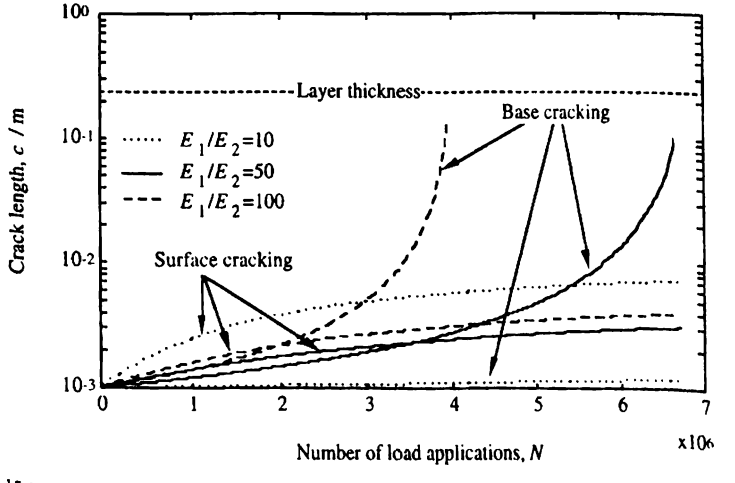


Fig. 15.16 Surface and base crack evolution for pavement structure B with different modulus ratios. From [140].

15.5.3 Parameter Study

In order to investigate the rates of crack propagation from both the surface and base of flexible pavements under typical operating conditions, a number of different pavement structures, operating under various thermal cycles and traffic loading rates, were examined.

Even though the stress intensity factors produced by thermal and traffic loading are comparable, the rate of cycling due to traffic loading is usually at least three orders of magnitude higher than the rate of thermal loading. Therefore, for fatigue cracking from the base of the asphalt layer, thermal loading cycles can be neglected compared to vehicle induced stress cycles.

However, for fatigue cracking from the surface, the vehicle induced cracks stop propagating close to the surface and only the thermal loading cycles can continue to propagate the cracks. It is therefore reasonable to model surface fatigue cracking as a thermally driven process with the starter crack produced by the initial vehicle loading, and base fatigue as being driven entirely by vehicle loading.

The rates of cracking from the surface and base of an asphalt pavement are given by the following expressions:

$$\dot{c}_s = \left(\frac{dc}{dN}\right)_s \dot{N}_s, \qquad \dot{c}_b = \left(\frac{dc}{dN}\right)_b \dot{N}_b, \tag{15.20}$$

where subscripts s and b refer to cracking at the surface and base respectively,

$\dot{N}_s$ is the rate of thermal loading at the surface and

$\dot{N}_b$ is the rate of traffic loading.



Substituting equation 15.12 into equation 15.20 gives:

$$\dot{c}_s = \left[A\left(\Delta K_I^s\right)^n\right]_s \dot{N}_s, \qquad \dot{c}_b = \left[A\left(\Delta K_I^b\right)^n\right]_b \dot{N}_b. \tag{15.21}$$

The rate of cracking from the base $(\dot{c}_b)$ can now be normalised by the total rate of cracking $(\dot{c}_s + \dot{c}_b)$ assuming $\dot{N}_s = 1$ thermal cycle per day and $\dot{N}_b$ is expressed in terms of cycles (vehicle loads) per day:

$$P_b = \frac{\dot{c}_b}{\dot{c}_b + \dot{c}_s} \times 100\% = \frac{\dot{N}_b}{\dot{N}_b + \left(\Delta K_I^s / \Delta K_I^b\right)^n} \times 100\%. \tag{15.22}$$

A value of 100% corresponds to cracking only from the base, and a value of 0% corresponds to cracking only from the surface.

Equation 15.22 is independent of fatigue parameter A and only depends on the power n in the Paris equation. A parametric study was performed for a range of traffic and environmental conditions (see Table 15.3). The transverse stresses and strains at the bottom of the asphalt layer directly under the tyre due to vehicle loading (where the transverse contact traction is not important), were calculated using VESYS IIIA [277] instead of the FEA analysis described earlier. Both VESYS and the FE model assume the pavement to be a linear elastic layered structure. However, VESYS is based on a closed form solution and, since the added complexity of the shear contact traction was not required for calculating base stresses, VESYS gives the same results in a fraction of the time required to run the FE program. The values of the elastic modulus of the asphalt layer were chosen to be the average of the modulus variation over the temperature range for each cell in Table 15.3. The elastic modulus of the asphalt mix as a function of temperature was obtained from an equation relating pure bitumen stiffness to asphalt mix stiffness [72]. The stiffness of pure bitumen was obtained, as a function of temperature, from a computer simulation of the Van der Poel nomograph assuming a loading time of 0.0125s corresponding to a vehicle speed of approximately 80 km/h.

Table 15.3 shows the normalised percentage base cracking P_b for initial crack lengths of 10mm at the top and bottom of the asphalt layer. The table is divided into cells with each cell representing a pavement operating under different thermal and traffic loading conditions. The major factors

affecting base fatigue cracking are: (i) asphalt layer thickness and (ii) traffic loading rate. The major factors affecting surface fatigue cracking are: (i) mean daily temperature and (ii) daily temperature amplitude. Thermal loading cycles also have an effect on base cracking because the elastic modulus of the asphalt is temperature dependent.

Mean Surface Temp / deg.C		0			10			20		
Surface Temp Amplitude / deg.C		5	10	15	5	10	15	5	10	15
Traffic Rate / cycles/day	Pavement Thickness / mm									
125	L	100	100	99.7	100	100	100	100	100	100
	M	100	100	100	100	100	100	100	100	100
	H	100	100	100	100	100	100	100	100	100
250	L	100	99.9	87.3	100	100	100	100	100	100
	M	100	100	98.6	100	100	100	100	100	100
	H	100	100	99.9	100	100	100	100	100	100
350	L	100	99.3	43.6	100	100	99.9	100	100	100
	M	100	98.9	88.5	100	100	100	100	100	100
	H	100	100	98.7	100	100	100	100	100	100

Key: L = 100 cycles / day
M = 1,000 cycles / day
H = 10,000 cycles / day

Table 15.3 Normalised base cracking rates, P_b.

It can clearly be seen from the values of P_b that the only cells for which significant surface cracking is likely are where the mean temperature is low, the temperature range is high, the pavement is relatively thick and the vehicle loading rates are low. This is an uncommon set of conditions.

A similar picture would be obtained using any initial crack length because both the surface stress intensity factor due to thermal load cycles and the base stress intensity factor due to vehicle loading increase monotonically with crack length.

Ageing of the asphalt can cause it to become more brittle. This may affect the material at the tips of surface cracks, resulting in faster crack propagation and hence lower values of P_b. This hypothesis needs further investigation.

Fast Fracture

If at any stage during the life of the pavement the sum of the stress intensity factor induced by vehicle loading and the stress intensity factor induced by thermal loading exceed the fracture toughness $\left(K_I^{\text{thermal}} + K_I^{\text{vehicle}} \geq K_{IC}\right)$ fast fracture of the asphalt will occur. It can be seen from figures 15.13 and 15.14 that for new pavements this is more likely to happen at the surface due to the high stress intensity factors induced by the transverse tyre contact traction, rather than at the base. This may explain longitudinal cracks occurring on pavements in warm climates where thermal cooling

grndients are high (*eg* [328]). The stress intensity factor produced by the vehicle loading will be high because of the low modulus ratio between the asphalt layer and the granular layer, and if there are large thermal cooling gradients the thermally induced stress intensity factor may also be fairly high.

15.6 CONCLUSIONS

(i) The transverse contact traction between the pavement and tyre produces a high local stress around the edge of the contact patch. This local stress does not lead to significant pavement fatigue, but may produce short cracks (10mm) that could act as starter cracks for thermal fatigue.

(ii) Cracking from the base of an asphalt pavement is mainly due to axle loads, and is not strongly influenced by thermal loading cycles.

(iii) The stresses induced in the asphalt layer due to cyclic thermal loading are strongly dependent on the viscosity of the asphalt material.

(iv) The majority of pavements will tend to fatigue from the base of the asphalt layer, except under extreme thermal cycles and low trafficking rates.

(v) Premature surface cracking may be due to fast fracture early in the life of a pavement caused by addition of the stress intensity factors due to vehicle and thermal loading.

(vi) Predicted rates of cracking using fracture mechanics are strongly dependent on the material fatigue properties A and n. More detailed information is required on how these parameters vary with temperature.



16

STIFFNESS LOSS IN FLEXIBLE PAVEMENTS DUE TO CUMULATIVE LOADING

16.1 SUMMARY

A model of the degradation of the stiffness of asphalt road surfaces with cumulative loading is described. It predicts the reduction in effective elastic modulus of the asphaltic material in a flexible pavement due to cumulative fatigue damage. The model is suitable for use with flexible pavement analysis procedures.

Measured surface deflection bowls from a number of test pavements are used with a pavement parameter back-calculation procedure, to determine the reduction in stiffness of the asphaltic material throughout the life of the pavement. Results show a semi-logarithmic relationship between the reduction in asphalt layer stiffness and cumulative fatigue damage. This type of relationship does not agree with a previous theoretical continuum damage mechanics model, where the relationship between the reduction in asphalt layer stiffness and cumulative fatigue damage was predicted to be linear.

This chapter is based on work previously published in [136].

16.2 INTRODUCTION

Pavement surface deflections have been used widely for pavement condition monitoring and evaluation for many years [278, 487]. Several studies of experimental and in-service pavements have shown that there is significant correlation between long-term pavement performance and changes in the transient deflection of the pavement surface (see, for example [149, 466, 487]). In a model of long-term pavement performance Ullidtz characterised this relationship as a reduction in the effective elastic modulus of the asphalt layer with progressive fatigue damage [466]. This modulus degradation mechanism is likely to play an important role in pavement damage due to vehicle loads, since it will be most influential at locations which suffer increased loading due to dynamic tyre forces.

The effects of cumulative fatigue damage on the stiffness of asphaltic material may be examined directly in the laboratory or indirectly using surface deflection data from Non-Destructive Testing (NDT) of in-service pavements. Each of these methods is discussed briefly in the following sections.

16.2.1 Laboratory Testing

Rowe [396] examined the reduction in stiffness of a number of trapezoidal asphalt specimens subjected to repetitive sinusoidal loading with controlled stress and controlled strain. He found that the reduction in modulus of the specimen obtained under controlled stress conditions was a different

shape to the corresponding curve obtained under controlled strain conditions (see figure 16.1). Similar results have been reported by Tayebali *et. al.* [452].

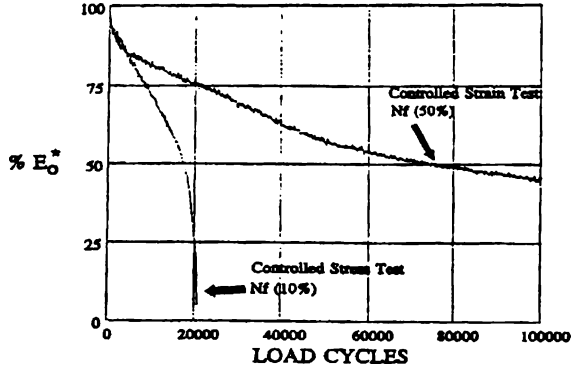


Fig. 16.1 Laboratory measured asphalt modulus reduction laws for controlled stress and controlled strain tests. From Rowe [396].

Monismith and Deacon [339] investigated theoretically the mode of loading of in-service pavements, using a number of representative pavement structures. They concluded that under normal circumstances the mode of loading tends towards controlled strain when the thickness of the asphaltic layers is less than approximately 50mm (except when the asphalt is extremely stiff or the support is very weak). The mode of loading tends towards controlled stress when the thickness of the asphaltic layers is greater than approximately 150mm (except when the asphalt is extremely weak or the support is very stiff).

With the increased popularity of thicker pavement design in the UK, controlled stress type tests are likely to better approximate in-situ stress conditions particularly during the early stages of the pavement's life. However, it should also be noted that as a thick asphalt pavement becomes progressively damaged by fatigue cracking and the effective thickness of asphaltic material is reduced, the mode of loading is likely to tend towards controlled strain.

16.2.2 Non-Destructive Pavement Testing

A different approach to determining the reduction in stiffness due to cumulative fatigue damage is to use NDT data collected from in-service pavements. Typically, the pavement surface deflection bowl is measured and used in conjunction with a mechanistic pavement model to back-calculate a set of layer properties that give a theoretical deflection bowl that best matches the measured data [263]. The following section briefly reviews the various methods for measuring the pavement surface deflection bowl, reviews back calculation models, and introduces the back calculation model 'VESYSBACK' used in this chapter.

16.3 METHODS OF SURFACE DEFLECTION MEASUREMENT

There are essentially three methods used to load pavements, so as to measure the surface deflection bowl; (i) static or slow moving loads (*eg* [242]), (ii) steady state vibratory loads [487] and (iii)

transient impulsive loads [424]. Each of these methods is discussed briefly in the following sub-sections.

16.3.1 Static or Slow Moving Loads

This method usually involves applying the load to the pavement surface through the tyres of a test vehicle travelling at creep speed (*eg* deflection beam, Benkelman Beam (BB)). Such a test does not excite the dynamic response of the pavement and the test speed (creep speed) is much slower than the loading at normal highway speeds. Consequently, the loading time is much longer and the resulting modulus is not representative of the modulus determined under typical highway operating conditions [411]. This is due to the viscoelastic (or time dependent) response of asphaltic material. Another problem with this type of test is measuring the surface deflection bowl accurately, particularly at large distances from the applied load [466].

16.3.2 Steady State Vibratory Loads

This method involves applying to the pavement surface, a steady state vibratory load superimposed on a static pre-load, and measuring the dynamic response of the pavement surface (*eg* using the *Road Rater* [487]). The main disadvantage of this method is that the stress levels induced in the pavement are significantly lower than those induced by traffic loads, so that the effects of non-linearities in the response may not be measured accurately [466].

16.3.3 Transient Impulsive Loads

The third and currently most popular method involves applying a transient load to the pavement by dropping a mass from a specified height and measuring the dynamic response of the pavement surface (*eg* Falling Weight Deflectometer (FWD) [242, 417, 424]). The FWD applies a load of similar magnitude to a typical heavy vehicle tyre and the duration of the load pulse corresponds to a wheel velocity of 60–80 km/h for the upper pavement layer. However, Sebaaly *et al.* [417] noted that although the FWD is the best NDT device available, it does not fully represent the loading conditions generated by a moving truck load. For example, the frequency content of the FWD signal is from 2–200Hz whereas the frequency content of the load history from a truck travelling at typical highway speed is from 1–20Hz.

16.4 REVIEW OF BACK CALCULATION MODELS

The subject of back calculation of elastic pavement parameters from measured surface deflection bowls has recently received much attention in the literature due to the increased popularity of the pavement surface deflection test as a method of structural evaluation. There has been a proliferation of back calculation models (see, for example [225, 312]), which can broadly be classified into two groups. Most models involve numerous calls to a linear elastic pavement analysis program [225], or non-linear elastic pavement analysis program [80]. The rest involve matching measured deflection bowls to a database of deflection bowls computed previously [225].

Typically, most back calculation procedures use a static pavement response model to reproduce the deflection bowl generated from either static or dynamic surface deflection tests. For this to be valid, the dynamic component of the response of the pavement is assumed to be unimportant and the resulting deflection bowl is assumed primarily due to the quasi-static response. This simplification was examined by Tam and Brown [450] who compared the surface deflection bowls calculated using static and dynamic pavement models. They concluded that the inertial effects of the pavement are insignificant and a static model "could be used for back-analysis with confidence". This conclusion is consistent with research by Hardy [219], who found that increasing the density of the layers in a dynamic layered elastic analysis had virtually no effect on the horizontal strain response at the base of the asphalt layer at 10Hz. However, he also found that the same strain response was relatively more

sensitive to damping in the asphaltic material. For example, he found that if the damping of the asphalt layer increased by a factor of 10, the strain at the base of the asphalt layer was decreased by approximately 60%. It therefore seems likely that material damping is a more important parameter than the inertia of the pavement.

The back calculation discussed in this chapter used data from both FWD and BB tests to determine an asphalt modulus degradation law.

16.5 VESYSBACK - BACK CALCULATION MODEL

The back-calculation model (VESYSBACK) was used to determine the combination of elastic layer moduli that give a theoretical surface deflection bowl that best matches an input measured surface deflection bowl. VESYSBACK is based on the VESYS IIIA computer program [274], which models the pavement as a layered linear elastic system, supported by a semi-infinite linear elastic subgrade. (Note that although the pavement model is essentially elastic, the viscoelastic nature of the asphaltic material can be taken into account by providing the model with an equivalent elastic stiffness determined from the asphalt creep compliance curve.) Contact between the tyre and pavement is assumed to be through a circular contact area with a uniform normal contact pressure. Dual tyres can be accommodated in the model using the principle of linear superposition. VESYS IIIA was used as the pavement model primarily because a previous study had shown that it can reproduce measured primary response influence functions accurately (see [133] for further details). The computer algorithm used to determine the best fit moduli was based on a standard optimisation routine by 'Numerical Recipes' which is detailed in [379]. The optimisation procedure is described in [134].

16.6 ACCELERATED LOADING FACILITY (ALF) TRIALS

The surface deflection data used in the back calculation procedure was obtained from the ALF Mulgrave trial [265] and the ALF Callington trial [267], performed by the Australian Road Research Board (ARRB).

16.6.1 Mulgrave Tests

Both FWD and BB surface deflection data measured during the Mulgrave tests from 5 different locations (chainages 2, 3, 4, 7 and 9) along the same test section (experiment 15) were investigated [265]. For the test sections considered, the asphaltic layers were constructed on 800mm of imported subgrade, nominally to a depth of 100mm (40mm wearing course and 60mm base course). The thickness of the asphalt layer for each of the chainages was determined by trenching after the tests were completed. Three different load levels were applied to the pavement by the FWD, through a circular plate of 300mm diameter. The force was measured during each test. For the BB tests, the load was applied to the pavement through the dual tyres of the ALF [265].

In VESYSBACK this pavement structure was idealised as a three layer system with the natural subgrade layer of infinite extent. For modelling the BB tests, contact conditions between the ALF and the pavement were idealised as two 277mm diameter circular areas of uniform constant pressure, the total wheel load was taken to be 83kN. (These values were obtained from a private communication with N.E. Vertessy of ARRB.) To simplify the back calculation procedure only the Young's moduli of each pavement layer were allowed to vary. The thickness of each layer was fixed. Poisson's ratio for each layer was also fixed at a value typical of that material. This is a reasonable approach since Poisson's ratio of the pavement layers does not significantly affect calculated surface deflections [312]. Table 16.1 gives full details of the parameters used for each pavement chainage.

	Mulgrave Trials (experiment 15)				
	C2	C3	C4	C7	C9
Asphalt layer modulus	Variable	Variable	Variable	Variable	Variable
Asphalt layer thickness	131mm	134mm	136mm	123mm	113mm
Poisson's ratio	0.4	0.4	0.4	0.4	0.4
2nd layer modulus	Variable	Variable	Variable	Variable	Variable
2nd layer thickness	800mm	800mm	800mm	800mm	800mm
Poisson's ratio	0.4	0.4	0.4	0.4	0.4
3rd layer modulus	Variable	Variable	Variable	Variable	Variable
3rd layer thickness	Infinite	Infinite	Infinite	Infinite	Infinite
Poisson's ratio	0.4	0.4	0.4	0.4	0.4

Table 16.1 Input pavement geometry to the VESYSBACK back calculation model for the Mulgrave sections (ALF data from [265]). (Note that no layer thickness measurement was made for chainage 7. The mean value of the measurements, 123mm, was used.)

16.6.2 Callington Tests

In the Callington trials, most of the test sections consisted of either thin overlay treatments or asphalt reinstatements. BB surface deflection data from three chainages (chainages 6, 7 and 8) of one reinstated test section (experiment 3) were used in VESYSBACK. The test section consisted of 100mm reinstated asphaltic material on the original pavement foundation (85mm base course, 230mm sub-base course, 175mm fill and 370mm rock fill). As before, this pavement structure was idealised as a three layer system with the natural subgrade layer of infinite extent (see Table 16.2 for details). The loading conditions for the BB were taken to be the same as in the Mulgrave trial. The exact depth of asphaltic layer for each chainage was not reported for these tests. Consequently, the nominal asphalt layer thickness of 100mm was used for all the chainages. As with the Mulgrave data, only the modulus of each layer was allowed to vary. Table 16.2 gives full details of the parameters used for the chainages.

	Callington Trials (experiment 3)		
	C6	C7	C8
Asphalt layer modulus	Variable	Variable	Variable
Asphalt layer thickness	100mm	100mm	100mm
Poisson's ratio	0.35	0.35	0.35
2nd layer modulus	Variable	Variable	Variable
2nd layer thickness	315mm	315mm	315mm
Poisson's ratio	0.4	0.4	0.4
3rd layer modulus	Variable	Variable	Variable
3rd layer thickness	Infinite	Infinite	Infinite
Poisson's ratio	0.45	0.45	0.45

Table 16.2 Input pavement geometry to the VESYSBACK back calculation model for the Callington sections (ALF data from [267]).

Figure 16.2 shows typical measured and back calculated deflection bowls (from BB deflection data) for a section from the Mulgrave trial. It can be seen from this figure that there is good agreement.

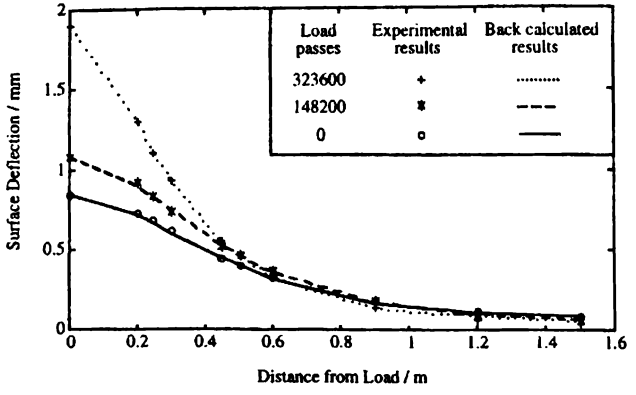


Fig. 16.2 Typical measured and back calculated surface deflection bowls. From [136].

16.7 ASPHALT MODULUS DEGRADATION MODEL

16.7.1 Modulus Reduction – Load Pass Results

Temperature Correction

Differences in temperature between the back calculated moduli were accounted for by calculating the moduli values at a single reference temperature (20°C). The temperature correction equation used in the calculations was obtained from published modulus-temperature data in [263]. This data was obtained from a back calculation procedure using measured deflections of a number of the Mulgrave test sections prior to trafficking. The result was a regression equation describing the variation of asphalt layer modulus with asphalt temperature (see [263] for further details). The form of this equation used for the temperature correction to a reference temperature of 20°C was:

$$E(20^{\circ}\mathrm{C}) = \phi(T)E(T), \tag{16.1}$$

$$\log_{10}\{\phi(T)\} = 7.226\times10^{-4}T^2 + 6.143\times10^{-3}T - 0.412.$$

where $E(20^{\circ}\mathrm{C})$ is the value of the asphalt modulus at a temperature of 20°C,
$E(T)$ is the value of the asphalt modulus at temperature T.

The surface temperature at the time of the deflection tests was assumed to be representative of the 'average' effective temperature of the asphalt layer. This may not be the case if there were large temperature gradients in the asphalt layer, which may be more pronounced in thicker pavements. The standard AASHTO method [20] for temperature correcting moduli obtained from surface deflection measurements involves determining an average asphalt layer temperature by combining: (i) the pavement surface temperature at the time of the test and (ii) the mean air temperature for 5 previous days before the test. For the ALF tests used in this study the air temperature over the 5 days previous to each deflection test was not reported and so the standard AASHTO method could not be used. The following results have all been corrected to a reference temperature of 20°C using the procedure described above.

Figure 16.3 shows the back calculated asphalt layer modulus as a function of cumulative ALF load passes obtained from the BB deflections from the Mulgrave trial, plotted on semi-logarithmic scales. It can be seen that the modulus of each section decreases with time, indicating an accumulation of damage. Figures 16.4 and 16.5 show similar results to those shown in figure 16.3 but obtained

from FWD deflections for the Mulgrave trial and BB deflections from the Callington trial. These results again show that the modulus of the asphalt layer significantly decreased as the pavement became progressively trafficked (damaged). By comparing figures 16.3 and 16.4 it can be seen that there is considerably more scatter on the moduli determined from BB deflections than those determined from FWD deflections for the same test sections. This is probably due to the difficulty in obtaining reliable BB deflection measurements (see [466]). The moduli determined from the BB deflections also tend to be lower than the corresponding moduli determined from the FWD deflections. This is probably due to the differences in loading times between the two tests. The loading time in the BB test is significantly longer than the loading time in the FWD test. Consequently, because of the viscoelastic nature of the asphaltic material, the asphalt layer moduli determined from the BB tests are expected to be lower than those obtained from FWD tests.

It can also be seen from figures 16.3–16.5 that, although the traffic loads applied to each of the chainages was nominally the same, the sections show different rates of moduli reductions with loading. For example, chainage 7 from the Mulgrave trial (figures 16.3 and 16.4) shows a larger modulus reduction than the other chainages after the same number of load cycles. These differences are probably due to differences in the amount of fatigue damage between chainages caused by variations in thickness of the asphalt layer (113mm–136mm).

While the Mulgrave tests were being conducted, the amount of surface cracking per square metre section of pavement was recorded for each chainage. This area was defined as the metre long interval centred on each chainage point (extending half a metre each side). The amount of cracking per square metre at the end of the Mulgrave tests (323600 cycles) was found to vary from 3.46m/m^2 to 6.86m/m^2 for chainages 2, 3, 4 and 9 with chainage 7 showing severe cracking (> 15m/m^2). This severe cracking resulted in a larger modulus reduction for chainage 7 compared to other chainages for the same number of load cycles (figures 16.3 and 16.4).

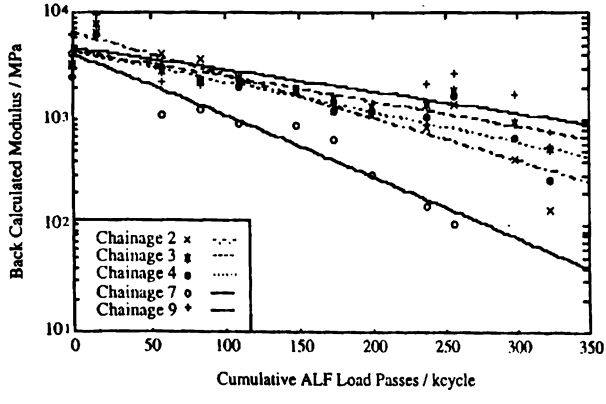


Fig. 16.3 Back calculated asphalt layer moduli reductions from BB tests for the various chainages from the ALF Mulgrave trials. From [136].

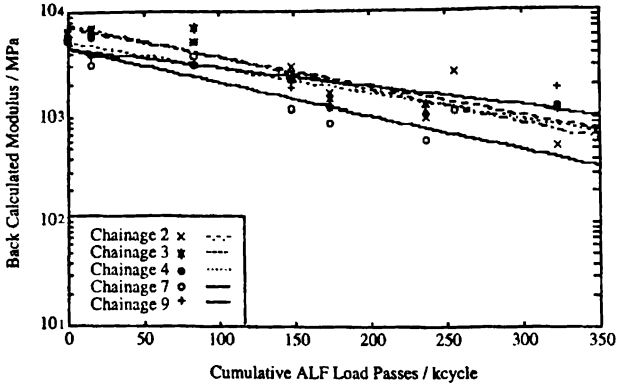


Fig. 16.4 Back calculated asphalt layer moduli reductions from FWD tests for the various chainages from the ALF Mulgrave trials. From [136].

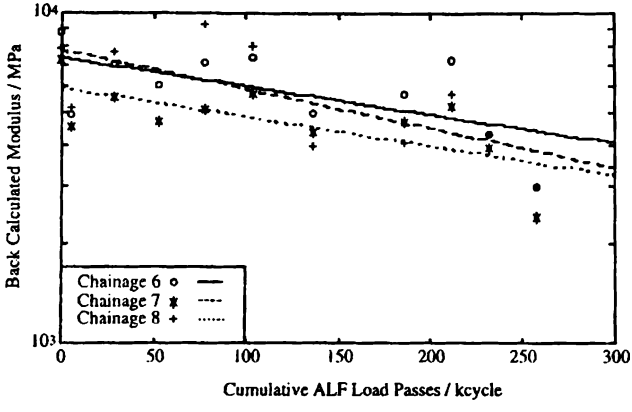


Fig. 16.5 Back calculated asphalt layer moduli reductions from BB tests for the various chainages from the ALF Callington trials. From [136].

16.7.2 Modulus Reduction – Cumulative Fatigue Damage Results

To obtain a single relationship from the data presented in figures 16.3–16.5 and account for the different layer thicknesses, the x-axis needs to be transformed from the number of load passes into cumulative fatigue damage.

Firstly it was assumed that the reduction in modulus as a function of load passes for each chainage can be described by a straight line on semi-logarithmic scales. An examination of figures 16.3–16.5 shows this to be a reasonable assumption. Consequently, a least squares fit was performed for each chainage (also shown in figures 16.3–16.5). Each fitted line was then normalised by the modulus value at zero load cycles so that the initial normalised modulus for each fitted line was 1. This gave a semi-logarithmic relationship (for each chainage) of the following form:

$$\log_{10}\left(\frac{E}{E_0}\right) = -C_1 N, \tag{16.2}$$

where E/E_0 is the elastic modulus normalised by the initial elastic modulus,
N is the cumulative number of ALF load passes and
C_1 is a constant giving the slope of equation 16.2 on semi logarithmic scales.

Equation 16.2 may also be expressed in the form:

$$\left(\frac{E}{E_0}\right) = \exp^{-C_2 N}, \tag{16.3}$$

where $C_2 = C_1 \log_e(10)$.

Secondly, a fatigue model was assumed of the general form:

$$N_f^{(i)} = k_1 \varepsilon_i^{-k_2}, \tag{16.4}$$

where $N_f^{(i)}$ is the number of cycles to failure at strain level ε_i (micro strain),
k_1 and k_2 are fatigue constants describing the fatigue behaviour of the material.

Miner's hypothesis of linear damage accumulation [72] was also assumed to apply, the non-dimensional damage D was defined as:

$$D = \sum_{i=1}^{j} \frac{N^{(i)}}{N_f^{(i)}} \tag{16.5}$$

where $N^{(i)}$ is the number of cycles of strain level ε_i,
$N_f^{(i)}$ is the number of cycles to failure of strain level ε_i and
j is the number of different strain levels.

It can be seen from equations 16.4 and 16.5 that the damage D is proportional to the number of load applications N, (*ie* $D \propto N$) for repeated tests with the same load. Consequently, each of the curves in figures 16.3–16.5 may be shifted horizontally to give a single relationship (for all the chainages) of the following general form:

$$\left(\frac{E}{E_0}\right) = \exp^{kD}, \tag{16.6}$$

where k is a new constant.

To determine the constant k the position on each of the curves where the elastic modulus is reduced to a critical level $(E/E_0)_c$ needs to be located. At this point, the damage D (from equation 16.5) can be considered equal to 1 and the pavement to have reached the end of its useful life. For controlled stress loading conditions, Rowe [396] defined this point to be $(E/E_0)_c = 0.1$. However for typical asphalt layer thickness of the order of 100mm (the nominal thickness of the ALF sections), Monismith [339] noted that the mode of loading is likely to be mixed and not well approximated by controlled stress. Consequently, a larger value of $(E/E_0)_c = 0.2$ was used. When the reduction in elastic modulus reached this critical level, the asphalt was assumed to have failed. Thereafter the modulus was considered to be constant at a value of $E = 0.2E_0$. Applying the boundary condition $E/E_0 = (E/E_0)_c$ when $D = 1$ to equation 16.6 gives $k = -\log_e(E/E_0)_c$. Consequently, equation 16.6 becomes:

$$\begin{aligned} E/E_0 &= e^{-kD} \qquad D < 1 \\ E/E_0 &= (E/E_0)_c \qquad D \geq 1. \end{aligned} \tag{16.7}$$

Differentiating equation 16.7a with respect to damage D, gives a rate of damage accumulation that is proportional to the current modulus of the asphalt layer (for $E/E_0 > (E/E_0)_c$), *ie*

$$\frac{d(E/E_0)}{dD} = k\frac{E}{E_0}. \tag{16.8}$$

Figures 16.6–16.8 show equation 16.7 plotted against D on linear scales for $(E/E_0)_c = 0.2$, together with the experimental data from the two ALF trials. It can be seen that the moduli obtained from both BB and FWD deflection testing conform reasonably well to the modulus degradation law (equation 16.7).

It should be noted that data from only a small number of sections of similar construction was used in the analysis. More data from a wider variety of pavements is required to validate this model further.

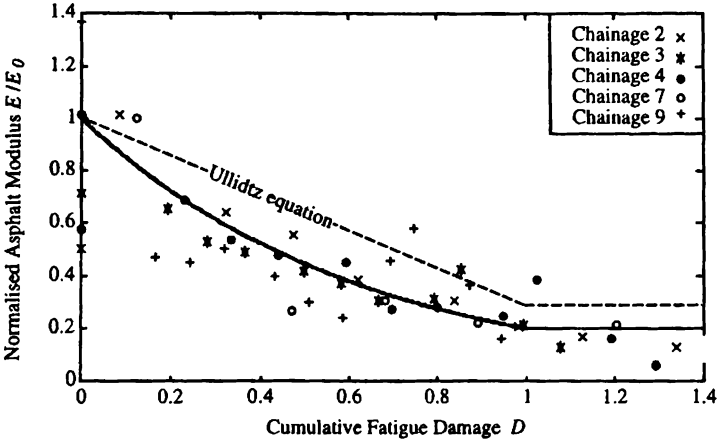


Fig. 16.6 Asphalt layer modulus reduction as a function of cumulative fatigue damage D (calculated from BB data from the Mulgrave trial). From [136].

16.8 CONTINUUM DAMAGE MECHANICS MODEL

Using the principles of continuum damage mechanics, and a fatigue law of the form of equation 16.4, Ullidtz [466] derived a simple expression relating the reduction of elastic modulus of an asphalt layer to the strain in the layer. He assumed that the asphalt was in a state of uni-axial tension.

$$\begin{aligned} \frac{E_0 - E}{E_0} &= \frac{N^{(i)}}{N_f^{(i)}}\left(\frac{E}{E_0}\right)_c \qquad && D < 1, \\ \frac{E}{E_0} &= \left(\frac{E}{E_0}\right)_c && D \geq 1, \end{aligned} \tag{16.9}$$

where $(E/E_0)_c = 0.3$.

Using Miner's hypothesis for accumulation of damage due to different strain levels (equation 16.5) equation 16.9 may be re-written in the form:

$$\begin{aligned} E/E_0 &= 1 - D(1 - E/E_0)_c \qquad && D < 1, \\ E/E_0 &= (E/E_0)_c && D \geq 1. \end{aligned} \tag{16.10}$$

Equation 16.10 is also shown in figures 16.6–16.8, plotted with the dashed line. It can be seen by comparing equations 16.10 and 16.7 that the asphalt modulus degradation law predicted from the damage mechanics model is linear with damage D whereas the modulus degradation law back-calculated from measured surface deflection bowls is better approximated by an exponential relationship.

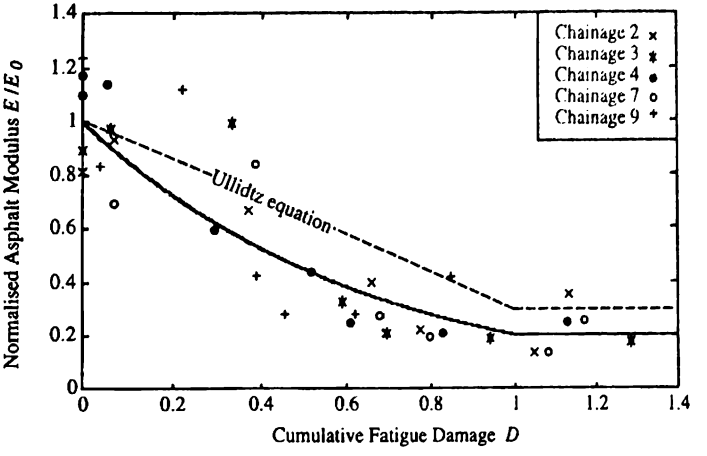


Fig. 16.7 Asphalt layer modulus reduction as a function of cumulative fatigue damage D (calculated from FWD data from the Mulgrave trial). From [136].

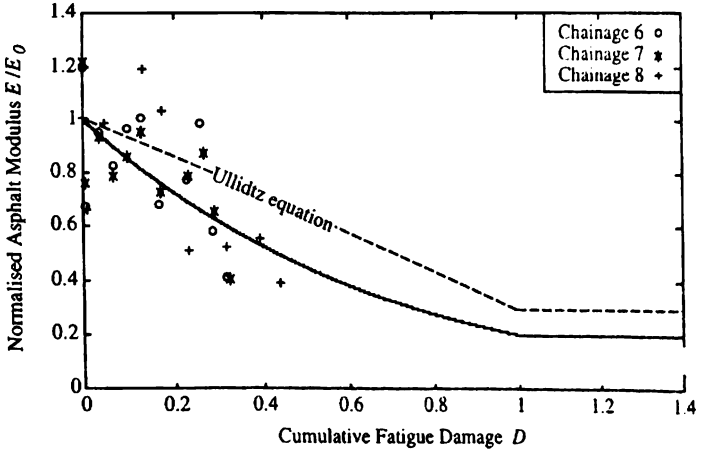


Fig. 16.8 Asphalt layer modulus reduction as a function of cumulative fatigue damage D (calculated from BB data from the Callington trial). From [136].

16.9 CONCLUSIONS

(i) A back-calculation model was developed based on the VESYS IIIA primary response computer model and a standard Numerical Recipes optimisation algorithm.

(ii) The back calculation procedure was used with measured surface deflection bowls to examine the degradation of asphalt modulus with trafficking an the experimental test sites.

(iii) The form of the relationship between the reduction in asphalt layer modulus and cumulative fatigue damage was found to be exponential, such that the rate of modulus degradation is proportional to the current value of modulus.

(iv) A modulus degradation model was developed and found to be capable of predicting the reduction in stiffness of the asphalt layer of the three test sections with reasonable accuracy.

(v) The exponential model was found to fit the experimental results more accurately than a previous theoretical model based on simple continuum damage mechanics.



PART 5 - VEHICLE-GUIDEWAY INTERACTION





17

BACKGROUND TO VEHICLE-ROAD INTERACTION

17.1 SUMMARY

Literature concerned with the road-damaging characteristics of various vehicle features is reviewed. It is concluded that there are widely differing opinions about the importance of dynamic tyre forces compared with 'static' features, such as the number of axles, static load sharing between axles and the tyre contact conditions. A key piece of information that is needed before definitive conclusions can be drawn is found to be the level of 'spatial repeatability' of the dynamic tyre forces generated by the 'fleet' of highway vehicles.

17.2 INTRODUCTION

It is convenient to separate the features of heavy vehicles that contribute to road damage into those which, to a first approximation, can be considered to have a 'static' influence, and so can be analysed without considering the motion of the vehicle; and those which depend on vehicle dynamics.

The 'static' features include: the gross vehicle weight; the axle configuration (number, static load and location); the static load sharing between axles; and the tyre contact conditions. Previous research into these four issues will be examined in the following section.

Dynamic tyre forces applied to road surfaces by heavy vehicles are believed to be an important cause of premature road failure, although the failure mechanisms are not well understood. As described in Chapter 7, they depend on the speed and dynamic characteristics of the vehicle, and the roughness of the road. Section 17.4 describes some previous research into the effects of dynamic tyre forces on road damage. Section 17.5 attempts to draw conclusions about the relative importance of the static and dynamic factors.

17.3 STATIC LOADING CONSIDERATIONS

17.3.1 Gross Vehicle Weight

An extensive theoretical study of vehicle–road interaction was performed recently by Gillespie et al [192]. The study investigated the road–damaging characteristics of 29 different US vehicles, from 15 main classes, on flexible and rigid pavements. Figures 17.1 - 17.3 are reproduced from [192]. They illustrate the importance of vehicle configuration and static loads on permanent deformation of flexible pavements, and fatigue damage of flexible and rigid pavements. In each of these charts, the damage is normalised by a single 80 kN (18 kip) axle traversing the pavement of interest. This masks the fact that the *absolute* damage levels are considerably higher on the weaker pavements than the stronger pavements.

Several important conclusions can be deduced from these figures.

(i) *In fatigue damage, the individual static axle loads are much more important than gross vehicle weight* (figures 17.1 and 17.2), because of the strong sensitivity of fatigue damage to stress or strain level (equations 13.1 and 13.2). As a result, the refuse hauler, which has a gross weight of 64 kips with three heavily loaded axles, causes nearly 3.5 times more fatigue damage to rigid pavements than the 9-axle 'Turner' truck, with a gross weight of 114 kips and a large number of relatively lightly loaded axles (figure 17.1).

(ii) *Gross vehicle weight is the dominant factor in rutting damage*, and individual static axle loads are not important at all (figure 17.3). This is because the analysis in [192] assumed a linear viscoelastic rutting model (see Chapter 14). It is important to note that for the larger combination vehicles, payload is a higher percentage of gross weight, so the rutting damage per tonne of cargo is less.

(iii) Conclusions (i) and (ii) are dependent on the damage laws (like equation 13.1) used in the analysis. *Damage laws with high exponents increase the importance of individual axle loads* and diminish the importance of gross vehicle weight.

(iv) *The ranking of vehicles for each type of road damage is essentially independent of the strength of the road.*

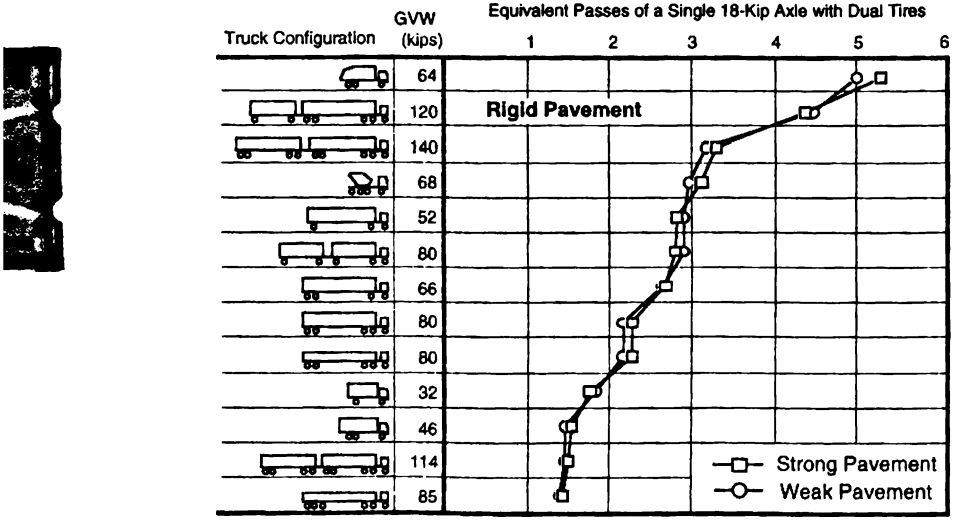


Fig. 17.1 Relative theoretical fatigue damage to *rigid* pavements caused by a single pass of the static loads of a variety of US trucks, for a 300 mm (12in.) thick slab, 'strong' pavement and a 200 mm (8in.) thick slab 'weak' pavement. From [192].

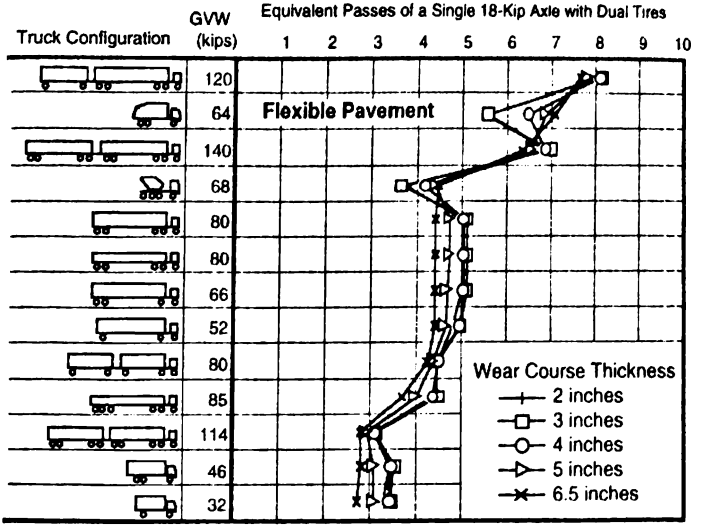


Fig. 17.2 Relative theoretical fatigue damage to *flexible* pavements caused by a single pass of the static loads of a variety of US trucks, for a range of pavement strengths. From [192].

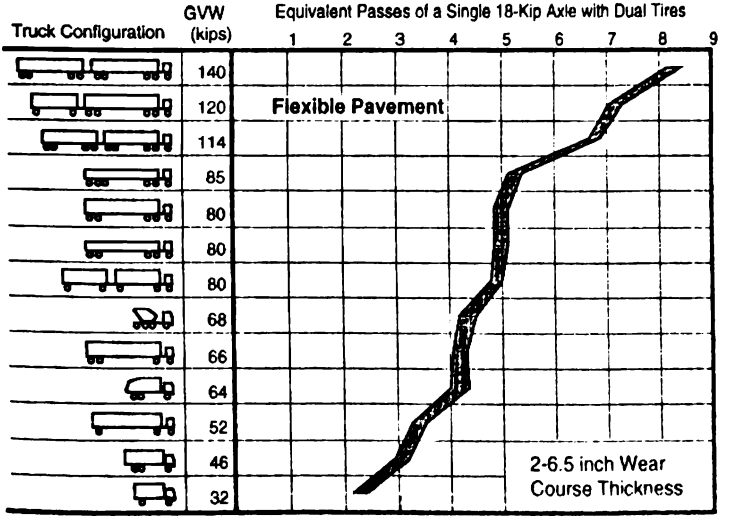


Fig. 17.3 Relative theoretical rutting damage to flexible pavements caused by a single pass of the static loads of a variety of US trucks, for pavement wearing courses with thicknesses in the range 2 to 6.5 inches. From [192].

17.3.2 Axle Configuration

There is considerable pavement engineering literature concerned with the relative road damaging effects of various axle group arrangements single/tandem/triaxle (see the comprehensive review by Morris [347]). Most studies either simulated [1, 192, 314, 361, 434, 464] or measured [2, 26, 108, 109, 247, 451] the primary response of the pavement (stress, strain, deflection) to a variety of axle configurations. Empirical road damage relationships (rutting and fatigue) were used to estimate relative pavement damage. One typical result by Southgate and Deen [434] is shown in figure 17.4.

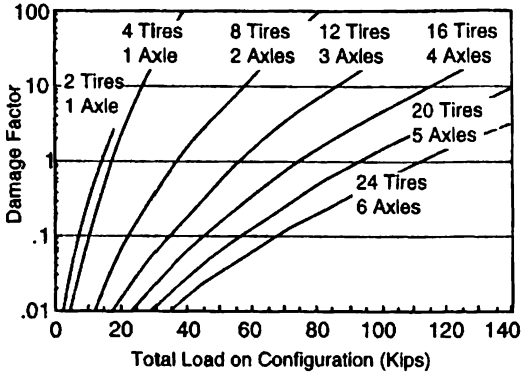


Fig. 17.4 Effect of total axle group static load on relative pavement fatigue damage. From [434].

It is generally concluded that for equal damage to flexible and rigid pavements, tandem and triaxle groups can carry more weight than the same number of widely spaced single axles, because the primary response fields of nearby axles overlap.

This effect can be understood by considering figure 17.5 from [192], which shows an influence function for longitudinal stress in a rigid pavement due to a static wheel load. For two or more closely spaced axles, the influence functions due to each axle can be superposed. If the spacing between the axles is between 3.25 ft and 15 ft, the peak tensile stress under one axle benefits from the compressive stress due to the other.

An optimum axle spacing usually exists, depending on the road structure, assumed mode of failure and damage criterion [347]. This fact is reflected by current axle load/geometry regulations in a number of countries (see, for example [26, 409]). An example is provided in figure 17.6, from [192], where it can be seen that a spacing of 7 ft (2.1 m) would reduce fatigue damage to rigid pavements by a factor of around two, compared with widely spaced axles.

17.3.3 Static Load Sharing

Uneven Tyre Forces

Most tandem and triaxle truck suspension systems are designed to equalise the static loads carried by the axles in a group. In practice, the effectiveness of load equalisation on moving vehicles varies significantly among suspensions.

Figure 17.7, after Mitchell [336], shows the result of a slow-speed axle weight survey of 259 vehicles performed by the TRRL in the UK in 1985. The range of axle weights for each suspension group is shown. For triaxle groups with leaf spring suspensions, the lightest axle is typically 60-70% of the heaviest and sometimes only 30-40%. It can be seen that air suspensions equalise much

better, the lightest axle typically being 90% of the heaviest. Tandem suspensions generally equalise better than triaxles.

Sweatman [443] introduced the 'Load Sharing Coefficient' (LSC) which he defined (for dynamic tests on instrumented vehicles) as:

$$\text{LSC} = \frac{\text{Mean measured wheel load}}{\text{Nominal static load}} \tag{17.1}$$

where

$$\text{Nominal static load} = \frac{\text{Total static load of group}}{\text{Number of wheels in group}}$$

The LSC is theoretically 1.0 for perfect load sharing, but Sweatman's road tests, for a variety of speeds, yielded values in the range 0.791–0.983 for tandem suspensions, *ie* 21%–17% equalisation error respectively.[1]

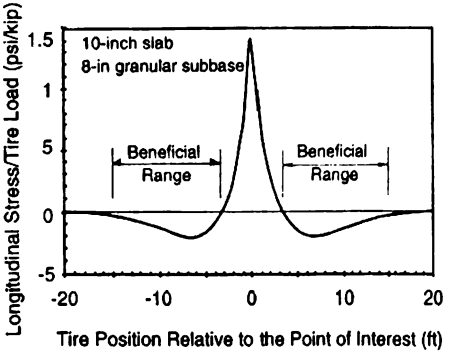


Fig. 17.5 Influence function for a 250 mm (10 in) thick rigid pavement from [192].

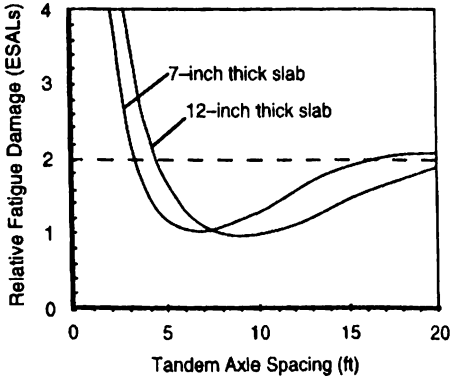
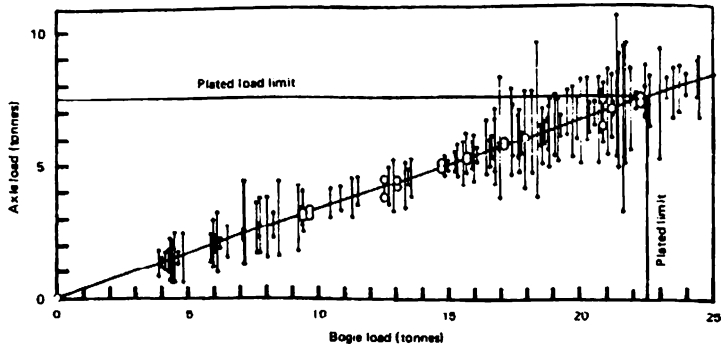
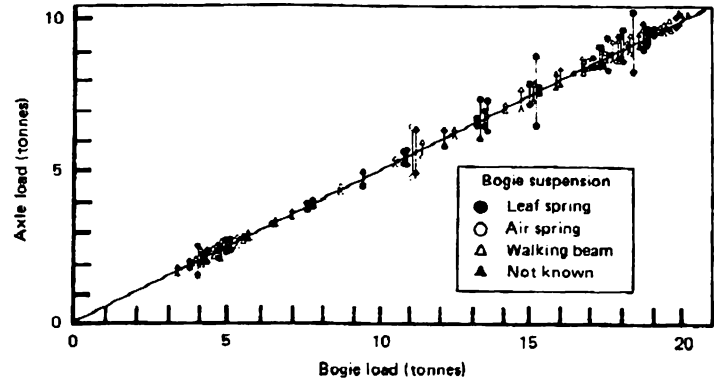


Fig. 17.6 Effect of tandem axle group spacing on theoretical fatigue damage in a rigid pavement. From [192]

[1] For a tandem suspension with LSC=0.79, the lighter axle will generate an average load which is 65% of the heavier one (0.79/(1+0.21) = 0.65), (assuming no difference between left and right wheel tracks) This can be compared with the TRRL results shown in figure 17.7.



(a) 145 3-axle semi-trailer bogies



(b) 114 2-axle rear bogies on rigid vehicles

Fig. 17.7 Static axle loads measured in a roadside survey on the M6 at Stafford, UK, in 1985, showing the range of static loads in each axle group. After Mitchell [336].

Sweatman observed some interesting anomalies, in particular that the worst tandem suspension was of the 'walking beam' type (which is designed for good static load sharing) and the best was a 'four-spring' tandem, which Mitchell reported to be poor [336] . The air spring tandem fell between these two. Sweatman attributed the poor performance of the particular walking beam suspension to bad installation practice and incorrect torque rod location. He also noted that road roughness had little effect on the relative performance of the different suspensions, but that approximately 2% variation occurred due to speed, and up to 4% variation could be attributed to road camber and cross-fall (transverse slope), which resulted in lateral load shifting.

Woodrooffe et al [505] performed quasi-static pitch tests on a trailer and concluded that their tandem walking beam suspension performed best, followed by the air spring tandem and then the four-spring suspension.

Simmons and Mitchell [336, 425] performed an extensive study of load sharing on tandem and triaxle, air and leaf spring suspensions. The work included pitch tests (see figure 6.16) and road

tests on a number of arched bridges, with vehicles that were instrumented to record dynamic wheel loads as well as the forces in the suspension components (torque rods, springs, *etc*). They drew the following main conclusions:

(i) *Poor load sharing in leaf spring suspensions is largely a quasi-static phenomenon* which is independent of speed, depends mainly on the pitch angle of the vehicle, but is also strongly dependent on the geometry of the suspension components.

(ii) On arched bridges the load on the leading axle of a 6-spring triaxle trailer suspension was 1.47–1.82 times the nominal load (LSC = 1.47–1.82). For these conditions, most of the load normally carried by the third (trailing) axle of the group was transferred to the first (leading) axle, while the centre axle load remained relatively constant. Under the same conditions, the triaxle air suspension yielded LSC = 1.16–1.31.

(iii) *Poor load sharing in four-spring and six-spring suspensions is mainly due to friction at the 'slipper' ends of the springs.* It can be improved considerably by introducing a low friction material in the sliding contact, or by utilising shackles instead of slipper connections.

Road Damaging Effects of Uneven Load Sharing

Uneven static load sharing increases fatigue damage because the power–law damage relationships (equations 13.1 and 13.2) accentuate the effects of more heavily loaded axles.

Gordon [199] analysed unevenly loaded tandem suspensions using an elastic layer pavement model and determined that for permanent deformation failure, a suspension with LSC = 0.8 (as per Sweatman's measurements) is twice as damaging as a suspension with perfect load sharing. Southgate and Deen [435, 437] performed a similar analysis for fatigue damage. They concluded that LSC = 0.8 corresponds to a factor of 2.9 increase in predicted damage. O'Connell et al [361] predicted 23% increase in cracking damage and 43% increase in rutting for LSC = 0.8.

Gillespie et al [192] calculated the effects of uneven static load sharing on flexible and rigid pavements. They noted that fatigue damage is hardly affected if the LSC is kept between 0.95 and 1.05. However, when the LSC reaches 1.2, fatigue damage increases by 40–50%, depending on the axle spacing and the type and strength of pavement. Sample results from [192] are shown in figure 17.8.

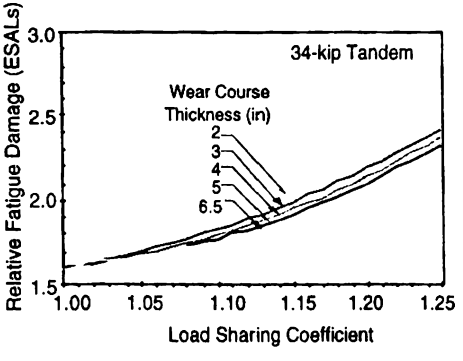


Fig. 17.8 Influence of load sharing coefficient and wear course thickness on flexible pavement fatigue damage. From [192].

Southgate and Deen [435, 437] also analysed the *measured* static wheel loads of 670 tandem suspensions and 1,951 triaxle suspensions and used this data to simulate the influence of uneven load sharing on road damage. They predicted that fatigue damage due to the tandem suspensions

was 1.4 times worse than if they had perfect load-sharing suspensions, and damage for the triaxle suspensions was 2.3 times worse.

17.3.4 Tyre Effects

During the period since the AASHO road test, cross-ply tyres have largely been replaced by radial-ply tyres on heavy trucks [104, 511], and average inflation pressures have increased from 550 kPa (80 psi) to 690-760 kPa (100-110 psi) [104, 347, 390, 435]. Wide-base single tyres ('super singles') are replacing dual tyres in Europe, particularly on triaxle trailer group suspensions, but they are not widely used in the USA, except on heavily loaded steering axles [347, 435].

There is concern in the pavement engineering community that these changes in operating patterns may increase pavement damage, particularly rutting [104, 211, 248, 347, 390, 391].

Contact Pressure Distribution

Most pavement analysts have assumed that the normal component of the contact pressure between tyre and road surface is uniform, acts over a circular area and is nominally equal to the inflation pressure (see, for example [66, 78, 112, 211, 277, 384, 435]). Considerable experimental evidence exists to suggest that this is not the case. Pressures are observed to increase around the edges of the contact area: in the 'shoulder' areas at either side, due to the stiffness of the side walls and at the front and rear due to bending of the tread band [104, 112, 248, 322, 391, 420, 511].

Under normal inflation and loading conditions, the maximum shoulder pressure is typically observed to be twice the inflation pressure [104, 322, 391, 460, 511], although the contact pressure distribution is found to be more uniform for higher inflation pressures and/or lower vertical loads [104, 322, 460, 511]. The contact area is also found to decrease with increased inflation pressure and to increase with total load. Marshek et al [322] reported typical results for truck tyres: 8-20% decrease in area for 50% increase in inflation pressure; 30-35% increase in area for 50% increase in load.



It is important to note that even in straight–line, steady–speed motion the contact pressure distribution between tyres and road surfaces contains significant lateral and longitudinal shear tractions as well as the vertical pressure [112, 261, 420]. These are caused by differences in the stiffness of the side-walls, tread band and tread.

Effects of Tyre Contact Conditions on Pavements

A number of authors have calculated [166, 211, 389, 390, 391, 435], or measured [2, 109, 166, 248, 516], the influence of tyre contact conditions on stresses and strains in the road surface.

The general consensus is clear: the details of the contact conditions, such as the exact area, pressure and pressure distribution, affect stresses and strains near to the surface of the pavement, whereas the response in the lower layers depends mainly on the overall load [104, 166, 211, 391]. For example, Haas and Papagiannakis [211] showed that increasing tyre inflation (contact) pressure from 415 kPa to 830 kPa at constant load increased the theoretical vertical compressive strain near to the surface of a 200 mm thick asphalt layer by up to a factor of eight, but hardly affected the strain at the bottom of the layer. Conversely, doubling the axle load at constant pressure increased subgrade compressive strain by a factor of two, but made little difference to compressive strain in the asphalt layer. These trends were corroborated by Marshek et al [321].

Roberts et al [390, 391] and Marshek et al [321] applied relatively realistic (axisymmetric) contact pressure distributions to elastic layer pavement models. Both studies established that assumptions about contact conditions can alter predicted horizontal strains at the bottom of thin surface layers (less than 50 mm) substantially, particularly for under-inflated tyres which have large shoulder contact pressures. The effects of non-uniform loading are much less significant for vertical compressive subgrade strains and for thicker pavements.

Research into pavement *damage* confirms the localised influence of contact conditions [104, 347]. Theoretical studies by Southgate and Deen [435] indicated that fatigue damage due to tensile strain at the bottom of thin asphalt pavements is likely to increase rapidly with average contact pressure. This was confirmed by Marshek et al [321] and O'Connell et al [361]. Both of these studies, however, reported that inflation pressure has little effect on subgrade rutting. Roberts et al [390, 391] and Haas and Papagiannakis [211] estimated rut formation by summing theoretical permanent deformations of the pavement layers and both ascertained that rutting damage is sensitive to contact pressure. In view of the localised influence of contact pressure on compressive strain observed in [211] (see above), this was presumably due to near-surface effects.

On the basis of asphalt pavement strain measurements, Addis reported that a 40% increase in tyre pressure would increase fatigue damage by 26%. Laboratory measurements by Eisenmann et al [166] on a 225 mm thick asphalt road surface model showed that rut depth development was approximately linearly related to the average contact pressure, (independent of load).[1]

Gillespie et al [192] simulated the effects on 'high' type pavements, of increasing the contact pressures of a super-single tyre and a pair of dual tyres, at constant total load. They found that: *"Elevated tyre inflation pressure greatly increases the fatigue damage of flexible pavements. Over inflation of conventional dual tyres by 170 kPa (25 psi) nearly doubles flexible pavement fatigue. Similarly over-inflation of wide-base single tyres is especially critical, increasing fatigue (damage) by a factor of four."* They also found that tyre inflation has a moderate influence on fatigue of rigid pavements and a relatively small effect on rutting of linear visco-elastic flexible pavements. See also Section 15.3 for a discussion of the effects of non-uniform surface tractions on pavement response.

Tyre contact conditions (pressure and area) vary dynamically with dynamic tyre forces. No analysis of road damage which accounts for this effect has been found in the literature. On the basis of the static analyses and measurements presented above, it seems reasonable to speculate that these dynamic effects will make some difference to stresses and strains in the upper pavement layers, and probably have negligible influence in the lower layers, where the overall dynamic force level will be the most important factor.

Effect of Tyre Configuration on Pavements

Several authors have considered the influence of the number and type of tyres on an axle.

In 1963, Zube and Forsyth [516] performed an experimental comparison of the vertical deflections and transverse strains of a flexible pavement surface, to wide-base single tyres and dual wheels (see figure 17.9). Their results indicated that pavement deflection was equivalent for 27 kN (6 kips) carried on a single tyre or 40 kN (9 kips) carried on a dual pair.

Experimental measurements of asphalt layer interface strains and surface deflections by Christison et al [109] for a variety of axle and tyre configurations gave very similar results. Christison's analysis of the measured strains in terms of pavement damage indicated that a single tyre is theoretically 7-10 times worse than a dual tyre pair for equal load. This was confirmed theoretically by Treybig [464]. Eisenmann et al [166] and Addis [2] both reported that the measured strains under wide single tyres were 50% greater than those under dual tyres carrying the same total load. Addis reported that this would increase pavement fatigue damage by as much as a factor of 2.5.

---

[1] This study also indicated that rut development was largely due to flow of the material at constant volume rather than compaction, and was proportional to the square root of the number of load applications. The latter conclusion is likely to be correct only for the early stages of rutting, when compaction is the main mode of deformation [142], therefore Eisenmann's two conclusions appear to be inconsistent.

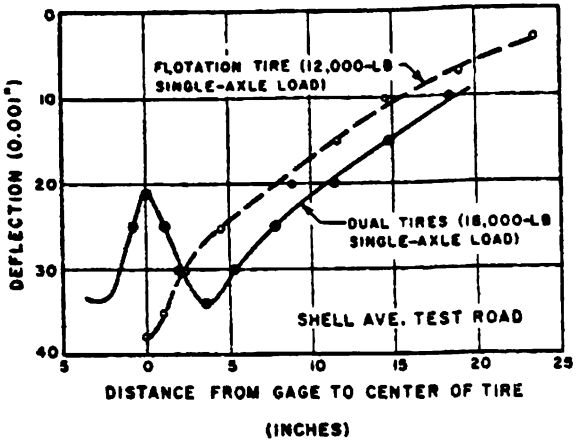


Fig. 17.9 Comparison of vertical surface deflections measured under wide single and dual tyres, by Zube and Forsyth in 1963 [516].

An OECD (Organisation of Economic Cooperation and Development) report [16] recommended that relative to dual tyres, wide-base single tyres should be considered to be 2.1 times more damaging and conventional single tyres to be 2.9 times more damaging.

On the basis of asphalt strain measurements, Huhtala [248] reported that wide-base single tyres are likely to cause 3.5 to 7 times more damage than dual tyres, and that the worst conditions are for thinner asphalt layers. He also noted that the contact pressures under each tyre in a pair can be quite different due to a number of factors, including differential inflation pressures or temperatures, tread wear, axle bending or transverse road roughness. He reported that a wide-base single tyre is only 1.5 times more damaging than an unevenly inflated dual pair with 500 kPa in one tyre and 1000 kPa in the other.

Gillespie et al [192] reported that heavily-loaded conventional tyres on a steering axle carrying 53 kN (12 kips) can be more damaging to flexible pavements than conventional dual tyres carrying 89 kN (20 kips). Theoretical strains and load equivalence factors, *normalised to account for payload*, are shown in Table 17.1 for tyres of various sizes on flexible pavements (from [192]). It can be seen, for example, that on a 6.5 in thick flexible pavement, a 15R22.5 single tyre generates 29% more strain per unit load than a pair of 11R22.5 dual tyres (fourth column of the table). This corresponds to 70% more fatigue damage per unit load than the dual pair (column 8).

It is important to note that the large pavement damage factors in the studies cited above were derived from a two-stage process. First, strains in the road were measured (or calculated) under dual and wide single tyres. These strains were typically 1.5 to 2 times greater for the wide single tyres than the duals for the same total load. Second, relative pavement damage was estimated using a power-law damage relationship like equation 13.1, typically with a fourth power, to weight the strains. This raises the important question of whether a fourth power is appropriate, or whether it may bias the results excessively. (See Chapter 1 for a discussion of the 'Fourth Power Law'.)

Wear Course Thickness (inches)	Strain Range of Tires / Strain Range of 11R22.5 Duals (Per pound of load)				Equivalence Factors[1] for Tyres at Rated Load (ESAL)			
	LP duals	11R22.5 single	15R22.5 single	18R22.5 single	LP duals[2]	11R22.5 single[3]	15R22.5 single[4]	18R22.5 single[5]
2.0	1.25	1.74	1.07	0.76	1.95	1.81	0.81	0.51
3.0	1.19	1.74	1.19	0.89	1.61	1.81	1.23	0.95
4.0	1.13	1.70	1.25	0.98	1.29	1.67	1.52	1.43
5.0	1.10	1.64	1.28	1.05	1.17	1.44	1.67	1.86
6.5	1.07	1.55	1.29	1.11	1.04	1.13	1.70	2.28

1. EFs are defined in these columns as the number of passes of an 11R22.5 dual-tyre axle loaded to 18 kips required to consume the same amount of pavement fatigue life as an axle with subject tyres at rated load.
2. Based on rated load of 17,000 lb per axle.
3. Based on rated load of 12,000 lb per axle.
4. Based on rated load of 16,000 lb per axle.
5. Based on rated load of 20,000 lb per axle.

Table 17.1 Load equivalence factors for flexible pavement fatigue damage, for tyres of various sizes, from [192].

Most evidence suggests that when fatigue cracking is the dominant mode of failure, a fourth power is a reasonable average value for the exponent k_2 in equation 13.1. Therefore, for fatigue cracking of *thin* pavements, the high power in the damage law, and hence high relative damage factors cited above (up to 10) for wide single tyres, appear to be reasonable. For thicker pavements, sub-surface tensile strains are less affected by the tyre contact conditions and more strongly influenced by the total load, so it is likely that the relative fatigue damage factors for wide single tyres will be less than cited above.

The situation is less clear in the case of permanent deformation, particularly for thicker asphalt pavements. There is considerable evidence to suggest that permanent deformation in asphalts is directly proportional to the wheel load, rather than some high power of it [64, 167, 211, 316, 367, 475]. This would be exactly true if asphalt could be regarded as a linear viscoelastic material [196, 456] (see equation 14.8). If this is the case, then use of the fourth power law to weight stress levels cannot be justified, and the relative increase in rutting damage for wide single tyres is likely to be a factor of 1.5 or 2, as shown in [192].[1]

Tests performed by the Federal Highway Administration (FHWA) with an accelerated pavement loading facility (ALF) confirmed these general conclusions. According to Bonaquist [64], wide single tyres generated pavement strains approximately twice those of dual tyres (for the same total load). They generated *twice the rutting damage*, and *four times the fatigue damage*. Sample results from these tests are shown in figure 17.10.

The use of radial ply tyres in preference to bias ply tyres is thought to be an exacerbating factor in rut formation. The way that a tyre responds to cross-slope, such as the side of a rut in a wheelpath, is governed by its *camber stiffness*. Tyres with high camber stiffness will tend to climb out of a rut, whereas tyres with a low camber stiffness will tend to track in a rut. Figure 17.11 from [192] shows that radial ply tyres generally have low camber stiffnesses and are more likely to track in ruts than bias ply tyres.

[1] If rut formation is proportional to the stress or strain level, and hence approximately proportional to the applied load, then dynamic load variations would be expected to be relatively unimportant, compared with the static loads. The depth of ruts would therefore be expected to be relatively constant along a road, as is generally observed on the highway. Conversely, fatigue damage (governed by equation 13.1) would be expected to be much more sensitive to the magnitude of the applied loads and hence fatigue cracking would be expected to occur in localised areas where the dynamic loads are consistently high [113, 118, 213].

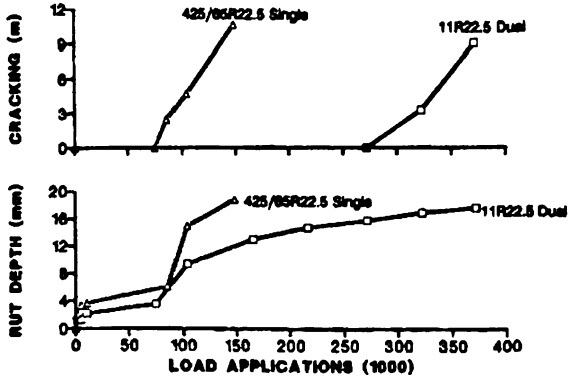


Fig. 17.10 Measured fatigue cracking and rutting damage to 178 mm (7 in.) thick asphalt test sections loaded by a wide single tyre and by a pair of dual tyres. After Bonaquist [64].

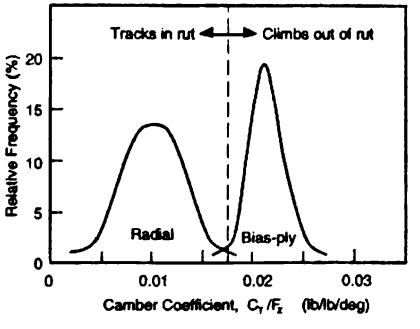


Fig. 17.11 Probability distributions of the camber coefficients of cross ply and radial ply tyres of passenger cars, showing that the radial tyres are more likely to track in a rut. From [192].

Collecting the above evidence together, the following tentative conclusions may be drawn about the influence of wide single tyres on road damage:

(i) For relatively thin asphalt pavements that fail by fatigue cracking, wide single tyres are likely to cause up to 7 times more damage than dual tyres carrying the same total load.

(ii) For thicker pavements, where permanent deformation is the main mode of failure, wide single tyres are likely to cause 1.5 to 2 times more damage than dual tyres.

(iii) For rigid pavements, wide single tyres are likely to cause a relatively small increase in fatigue damage [192].

17.4 DYNAMIC LOADING CONSIDERATIONS

17.4.1 Road Damage Criteria

Road Stress Factor

In 1975, Eisenmann [164] derived a quantity known as the 'road stress factor', Φ, using the assumption that road damage depends on the fourth power of the instantaneous (dynamic) wheel force at a point on the road (see Chapter 1 for a discussion of the 'Fourth Power Law'). Assuming that dynamic wheel forces are Gaussian (follow a normal distribution), Eisenmann showed that the expected value of the fourth power of the instantaneous wheel force is given by:

$$\Phi = E\left[P(t)^4\right] = \left(1 + 6\,\bar{s}^2 + 3\,\bar{s}^4\right) P_{stat}^4 \qquad (17.2)$$

where

$P(t)$ = Instantaneous tyre force at time t
P_{stat} = E[P(t)] = Static (average) tyre force
$\bar{s}$ = Coefficient of variation of dynamic tyre force (essentially the DLC from equation 5.6, see Sweatman [443])
E[ ] = Expectation operator (average value).

Sweatman [443] generalised equation 17.2 to account for departure of the wheel force probability distribution from Gaussian, but showed that the effects of skewness and kurtosis on Φ were negligible for his measured tyre force data.

In 1978, Eisenmann [165] proposed a modified version of equation 17.2 which accounted for the effects of wheel configuration and tyre pressures:

$$\Phi' = \nu\,(\eta_I\,\eta_{II}\,P_{stat})^4 \qquad (17.3)$$

where

$$\nu = 1 + 6\,\bar{s}^2 + 3\,\bar{s}^4 \qquad (17.4)$$

ν is the 'dynamic road stress factor' (Sweatman [443]),
η_I accounts for tyre configuration (single or dual tyres),
η_{II} accounts for tyre contact pressures.

Equation 17.3 is sometimes written: $\Phi' = (\eta_I\,\eta_{II}\,\eta_{III}\,P_{stat})^4$ where $\eta_{III} = \nu^{1/4}$ [16, 486]. An additional factor is also sometimes included to account for the type of axle group (single/tandem/triaxle) [16, 486].

Equation 17.3 underpinned a substantial body of research in West Germany during the 1980's by the 'Road Stress Committee' [16, 47, 166, 200, 486]. The equation has the desirable (although not necessarily justifiable) effect of decoupling the road damage problem into three sub-problems, which can be studied separately: dynamic loads, tyre configurations and contact pressures.

Considerable research effort has gone into quantifying η_I, η_{II} and ν for a variety of suspensions and tyre contact conditions. Values for η_I and η_{II} can be found in several papers [47, 166, 200, 486].

It is interesting to note that η_I and η_{II} are considered to be 'penalty' factors or 'bonus' factors depending on the author. For example, the OECD report: 'Impacts of heavy freight vehicles' [16] recommended $\eta_I = 1.0$ for twin tyres and 1.3 for single tyres, *ie* a 30% 'penalty' for single tyres, whereas Eisenmann et al [166] recommended $\eta_I = 1.0$ for single tyres and 0.9 for twin tyres, *ie* a 10% 'bonus' for twin tyres.

For typical highway conditions of roughness and speed, Sweatman [443] measured the dynamic road stress factor v in the range 1.11 to 1.46 depending on the suspension system. Other researchers have published similar results [172, 200, 337]. It is expected that suspensions should *rank* in the same order whether the wheel loads are compared in terms of road stress factor or DLC.

Mitchell and Gyenes [337] used the road stress factor to analyse their measured wheel forces and those presented by Hahn [214]. They estimated that widespread replacement of steel and rubber suspensions with air suspensions in the UK would reduce overall damage due to drive axles by 8% and damage due to semi-trailer axle groups by 10–20%. Their analyses of the UK and West German wheel force data yielded qualitatively similar conclusions.

The road stress factor approach was used to analyse West German research results for buses [213]. This provided the information for West German legislation, introduced in 1984, which allowed two-axle buses to carry 11 tonnes rather than 10 tonnes on air-suspended rear axles with dual wheels, providing the sprung mass 'natural frequency' is less than 1.5 Hz, and the 'damping ratio' greater than 0.25 [483]. A similar regulation was subsequently implemented by the European Community for single drive axles of articulated vehicles [32] (see Chapter 27).

It is worth noting that the West German Road Stress Committee developed a nomograph for determining Φ' graphically, depending on the road roughness, speed, static axle load and vehicle characteristics. It assumes a quarter–car representation of the vehicle [47]. The Committee used this method to compare a number of different vehicle configurations, and recommended several 42 tonne articulated combinations which might be expected to do less damage than existing 38 tonne combinations [47].

Magnusson et al [313] criticised use of the road stress factor. They noted that the fourth power law arose from measurements of the overall loss of serviceability of the AASHO road test sections due to vehicles that applied wheel loads which included a dynamic component. As a result, the fourth power law implicitly accounts for dynamic wheel loads. *"Eisenmann's supplementing of the formula (fourth power law) consequently appears somewhat dubious"* [313].

Ullidtz [467, 471] developed a model of pavement performance due to dynamic tyre forces and concluded that the effects of dynamic loads may be quite different on different types of pavement damage and pavement structures. He noted that accounting for dynamic loads using a number of equivalent standard axles calculated using a fourth power law (as per the Road Stress Factor), would result in *"completely erroneous"* results.

The Road Stress Factor approach incorporates all of the uncertainties inherent in the fourth power law, which has itself been the subject of considerable criticism [4, 281, 457] (see Chapter 1). It has three other highly questionable features:

(i) It assumes that strain in the road surface is directly proportional to the instantaneous wheel force and neglects the sensitivity of road surface response to the speed and frequency of the applied loads and to the structural response characteristics of the road (Chapter 10).

(ii) In using the *mean* value of the damage criterion, it implicitly assumes that road damage is spread randomly over the surface and does not account for any concentration of damage which may occur in the vicinity of particular roughness features. (See discussion of *spatial repeatability* in Section 7.4.11 and Chapter 18.)

(iii) It assumes that each suspension system on a vehicle is dynamically independent and does not influence the tyre forces, and hence road damage, generated by other axles (see Section 7.4.6 and Chapter 28). Thus suspensions are compared through analysis of the wheel loads generated by individual axles or axle groups, rather than through analysis of road damage done by the whole vehicle.

According to Morris [347], the road stress factor is *"a plausible rule of thumb that can serve as a bench-mark for comparison with more analytical approaches."*

Aggregate Tyre Forces

Since the spatial distribution of tyre forces is important, road damage criteria that relate to specific points along the road surface are needed for assessing road damage [88]. The simplest approach involves summing the dynamic forces, raised to a power n, applied to each location along the road by each tyre. This type of damage criterion is known as a 'weighted aggregate force model' [88, 93] The aggregate nth power force A_k^n, measured at location k along the road is given by:

$$A_k^n = \sum_{j=1}^{N_a} P_{jk}^n , \qquad k = 1, 2, 3, \ldots N_s \qquad (17.5)$$

where P_{jk} is the force applied by tyre j to location k on the road,
N_a is the number of axles on vehicle, and
N_s is the number of points along the road.

The power n is chosen to represent the type of road damage being considered. For flexible pavements, a value of $n = 4$ is suitable for fatigue damage [281], whereas $n = 1$ is more suitable for permanent deformation (rutting) [143, 192] (See Chapters 13-15).

Equation 17.5 can be used to *compare* the road-damaging potential of vehicles, provided all tyres are assumed to have the same contact area. The calculation can be enhanced somewhat, by dividing each wheel force by an appropriate nominal tyre contact area, so as to base the damage prediction on the nominal contact *stress* [88, 93]. The resulting 'damage' D_k is then given by:

$$D_k^n = \sum_{j=1}^{N_a} \left(\frac{P_{jk}}{a_j} \right)^n , \qquad k = 1, 2, 3, \ldots N_s \qquad (17.6)$$

where a_j is the nominal contact area of tyre j .

Equation 17.6 does not account for dynamic variations of contact area with oscillating tyre forces. however this is thought to be a second order effect. By including an appropriate material constant outside the summation in equation 17.6, D_k can be considered to be a measure of fatigue damage (proportion of the fatigue life used) [93].

The importance of the exponent n is shown in figure 17.12, which examines the dynamic tyre forces generated by a single-wheel 'quarter-car' vehicle model (as per figure 5.1a), travelling on a 'good' road (Section 3.3) at 100km/h. Figure 17.12(a) shows the tyre force P(t), normalised by the static tyre force P_{stat}, for a 100 m long section of road. Note that the dynamic fluctuation is typical: about 20%-30% either side of the mean, with components at the body bounce and wheel hop frequencies (Section 7.4). It can be seen that the mean tyre force and static tyre force coincide at $P/P_{stat}=1$.

Figure 17.12b shows the same tyre force history, this time with every data point raised to a fourth power and then normalised by P_{stat}^4. Raising the force to this high power has two important effects. Firstly, it shifts the mean value above the static value. It is this mean ('expected') value that is calculated by the road stress factor Φ in equation 17.2. Secondly, it skews the wheel forces so that the dynamic fluctuations are amplified. This has the effect of increasing the theoretical 'damage' at some points along the road by a large amount. For example, at 35m and 55m along the road, the *damage* P^4 is nearly three times greater than that generated by the static tyre forces P_{stat}^4
ie $P(t)^4 / P_{stat}^4 \approx 3$.

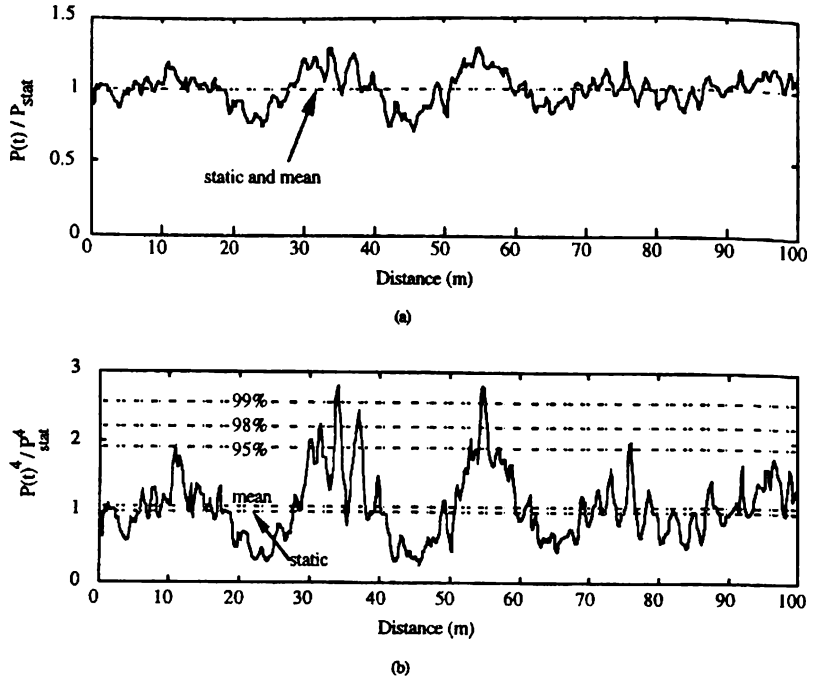


Fig. 17.12 Dynamic tyre forces generated by a quarter-car model on a 'good' road at 100km/h
(a) Normalised dynamic tyre forces
(b) Normalised dynamic tyre forces, raised to the fourth power.

If the relevant value of n is 1 (as for permanent deformation of asphalt - see Section 13.3 and Chapter 14), then it can be seen from figure 17.12a, that the first order effect is that of the static loads *ie* the dynamic fluctuations have a relatively small influence. Conversely, if $n = 4$ (as may be expected for fatigue damage of asphalt - Section 13.3 and Chapter 15), then it can be seen in figure 17.1b, that the dynamic fluctuations become very important at some locations along the road.

These locations (sometimes called 'hot spots') might be expected to be the first places to show signs of pavement failure (*eg* formation of a pot-hole), if four conditions apply:

(i) the road is prone to fail by fatigue and does not fail first due to permanent deformation, or some environmental cause;

(ii) all trucks apply their peak loads in the vicinity of these same locations (this is known as 'spatial repeatability', and is the subject of Chapter 18);

(iii) there are no large surface profile changes which cause the hot spots to move to different locations along the road;

(iv) the structural properties of the road are relatively constant - *ie* there are no locations which are much weaker or more flexible than others, where premature failure might occur.

Under these particular conditions, the life of the road would be governed by the damage at a few hot spots - say 1-5% of the surface area of the road. The damage incurred at this small proportion of points during the passage of a particular vehicle can be determined from the cumulative probability

density function of the road damage criterion. Thus 5% of the area of the road in the wheel path incurs damage exceeding the 95th percentile level, and 2% incurs damage exceeding the 98th percentile level. These 'upper percentile' levels are shown on figure 17.12b.

Example - Aggregate Tyre Forces due to a Tandem-Axle Vehicle Model

The six degree-of-freedom vehicle model shown schematically in figure 17.13 was used to simulate the dynamic tyre forces generated by a 'four-spring' trailer suspension (figure 2.1e). The suspension has two leaf springs, modelled by two rigid beams and four nonlinear leaf spring elements (using equation 4.2). The springs are joined by a short 'load-leveller' beam. The axles are free to bounce vertically and the leaf spring beams are free to pitch. The tyres are free to bounce clear of the road surface. The model was simulated traversing a 'good' random road at 30m/s [93]. The suspension of this vehicle has a lightly damped oscillation at 9.8Hz, in which the two axles bounce in anti-phase, and the central levelling beam pitches. The road damage criteria in equations 17.5 and 17.6 were evaluated at equally spaced intervals along the road. These intervals were sufficiently short as to enable resolution of peak forces at the highest frequency of interest.

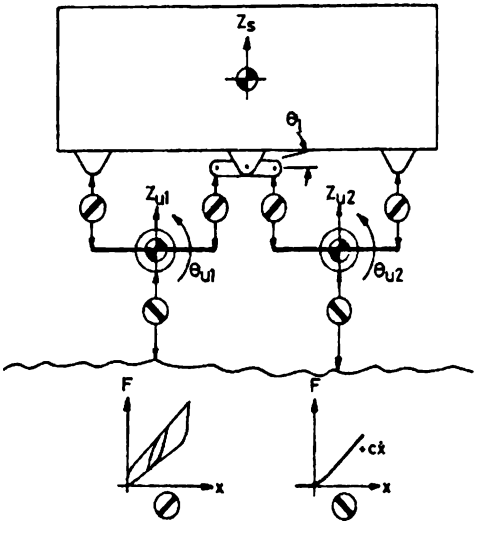
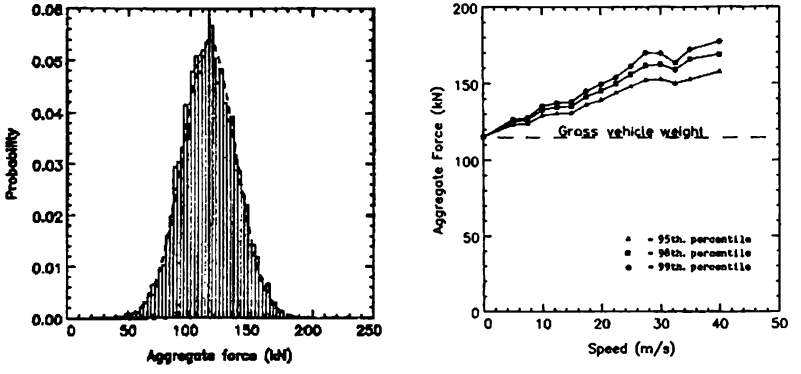


Fig. 17.13 Tandem-axle vehicle model representing a four-spring suspension. From [93]

Figure 17.14 shows the probability distribution of the aggregate tyre forces A_k^1 (*ie* calculated from equation 17.5 with n = 1). It can be seen that the distribution is Gaussian, as might be expected. The mean value of the distribution is the gross vehicle weight. Figure 17.14b shows the 95th, 98th and 99th percentile aggregate force levels as a function of vehicle speed. When the vehicle is stationary and there are no dynamic loads these upper percentile values converge on the gross vehicle weight. At higher speeds they diverge as the dynamic tyre forces increase. Small peaks in each curve can be seen at speeds of 9m/s and 27m/s. At these speeds, both unsprung masses reach maximum force levels in their 9.8Hz anti-phase bounce oscillation at the same locations on the road surface. This can be explained as follows.

Let the suspension's anti-phase bounce frequency be f and the vehicle speed be V. In a lightly damped, narrow-band, random oscillation, the trailing axle is expected to reach its maximum force

levels 1/2 and 3/2 cycles after the leading axle, corresponding to times of 1/2f and 3/2f. In these times the vehicle travels distances of V/2f and 3V/2f. If either of these distances is equal to the axle spacing L then the peak forces of each axle will occur at the same locations on the road surface. This leads to 'critical' speeds of $V_{cr} = 2fL$ and $2fL/3$. For this vehicle model, f = 9.8Hz, and L = 1.4m, so V_{cr} = 27 and 9 m/s. In reference [91] it is shown that sprung mass modes of articulated vehicles can also lead to such critical speeds.



(a) Probability distribution at 30m/s
---------- = Gaussian distribution

(b) Upper percentile aggregate forces as a function of speed.

Fig. 17.14 Aggregate tyre forces generated by the vehicle model travelling on a 'good' road. From [93].

Figure 17.15a shows a probability distribution of the damage criterion D_k^5, (*ie* calculated from equation 17.6 with n = 5). Unlike figure 17.14a, the distribution is no longer Gaussian. The high power in the damage equation skews it towards the higher damage values. The upper percentile values of this distribution (normalised by the static values) are plotted as a function of speed in figure 17.5b, for a 'good' random road, and a 'very good' random road (see Section 3.3). Also shown on this plot are the peak values, for a 12mm step up, on an otherwise smooth road surface profile.

The following observations can be made:

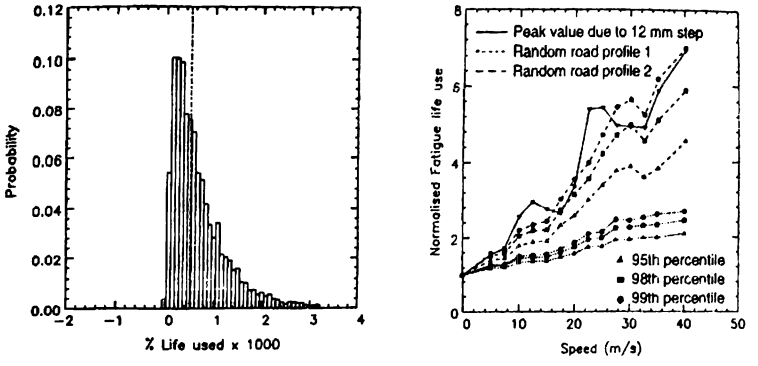
(i) Depending on the percentage of the road surface area considered in the analysis (the percentile level), the ratio of 'dynamic' to 'non-dynamic' fatigue damage may be in the range 2-7 for normal highway conditions of speed and roughness.

(ii) The 'critical speeds' at 9m/s and 30m/s are present in figure 17.15b, for the reasons described above for figure 17.14b.

17.4.2 Single-Vehicle Pass Road Response Calculations

A number of theoretical studies of the interaction between vehicles and road surfaces have been performed in recent years (see summary in [96]). These studies can be divided into two distinct classes known as 'single-vehicle-pass' calculations and 'whole-life models'.

'Single vehicle pass' calculations [88, 91, 93, 129, 192, 344, 361, 374, 375] determine the incremental road damage due to one passage of a vehicle over a particular road. They are useful for comparing the effects of vehicle features on road damage.



(a) Probability distribution at 30m/s.
·-·-·-·-· = damage due to static load

(b) Normalised fatigue damage for three different road profiles as a function of speed.

Fig. 17.15 Theoretical road damage generated by the vehicle model travelling on a 'good' road, using equation 17.5 or 17.6 with n = 5. From [93].

The procedure generally involves simulating (or measuring) the dynamic tyre forces generated by a vehicle travelling over a specified road profile. These forces are used as input to a pavement model (flexible or rigid) and primary pavement responses, *ie* stresses or strains, are calculated at many points along the road. Finally material damage models like equations 13.1 and 13.2 are used with damage accumulation calculations to determine theoretical road damage D_k at location k. For example, Miner's rule may be used to accumulate fatigue damage (equation 17.7), perhaps using the 'rainflow' method [187] to count fatigue cycles (*eg* [192, 374]).

$$D_k = \sum_{j=1}^{N_\varepsilon} \frac{1}{N_{jk}}, \qquad k = 1, 2, 3 \ldots N_s \tag{17.7}$$

Here

N_{jk} is the number of cycles to failure at location k due to strain cycle j, calculated using equation 13.1 or 13.2;

N_ε is the number of strain cycles incurred at each point on the road;

and N_s is the number of calculation points along the road.

The concept is shown schematically in figure 17.16.

Example - Fatigue Damage due to a Tandem-Axle Vehicle Model

The calculation procedure shown in figure 17.16 was used to calculate the theoretical fatigue damage generated in the surface of a flexible pavement, due to the tandem-axle vehicle model shown in figure 17.13 [88, 93]. The road response model consisted of an Euler Beam, supported by a damped 'Winkler' foundation, similar to that shown in figure 10.2. The analysis was performed for the same road profiles as in the previous example (Section 17.4.1). Maximum longitudinal tensile strains in the road model were calculated at stations spaced 150 mm apart along the road, using the dynamic road response calculation method described in Chapter 10. Strain time histories were calculated at each station. These are shown in figure 17.17, where the variation in strain due to dynamic loads can be seen clearly. Equation 13.1, with $k_2 = 5$, along with equation 17.7 were used to calculate the fatigue damage D_k accumulated at each station.

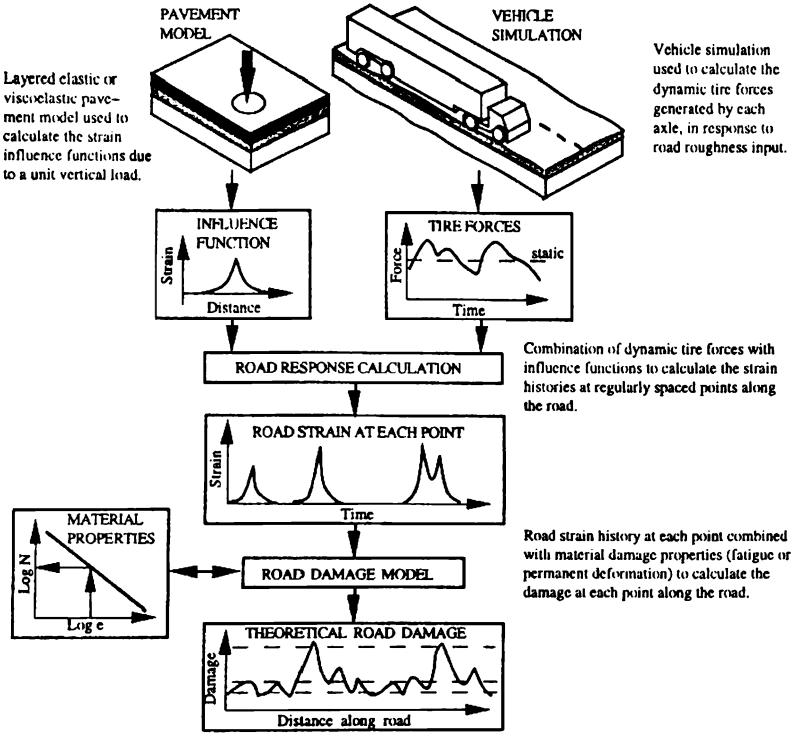


Fig. 17.16 Schematic diagram of 'single pass' road damage calculation. From [96].

The probability distribution of this quantity was 'skewed', and similar to that for the weighted aggregate forces shown in figure 17.15a. The upper percentile values of the fatigue damage were calculated for the random profile tests. These were normalised by the 'non-dynamic' fatigue damage (*ie* calculated using the static wheel loads) and the results are shown in figure 17.18. The largest peak values for the step tests are also shown.

Figure 17.18 is similar to figure 17.15b, except that the accumulated damage levels *decrease* for speeds above 25 m/s for the random profile tests. This is a result of two conflicting factors:

(i) The dynamic force levels increase with speed in this frequency range (see figure 17.14b).

(ii) The deflections of the road surface (and hence longitudinal strains) decrease with increasing speed of the vehicle (see figure 17.19), due to energy dissipation in the road structure (*ie* the 'speed effect', described in Sections 9.2.3 and 10.5.2).

In this example, factor (ii) outweighs factor (i), and the net road damage accumulation decreases slightly with vehicle speeds above 25 m/s. This is not the case for the step input, where the increase in the maximum dynamic forces with speed outweighs the effect of the road model response.

The ratio of dynamic to non-dynamic fatigue damage varies between 2 and 7 for typical conditions of highway roughness and speed in figure 17.18. Furthermore, the two 'critical' speeds (described in the example in Section 17.4.1) are apparent in the fatigue damage plot, just as in the aggregate force plots (figures 17.14b and 17.15b).

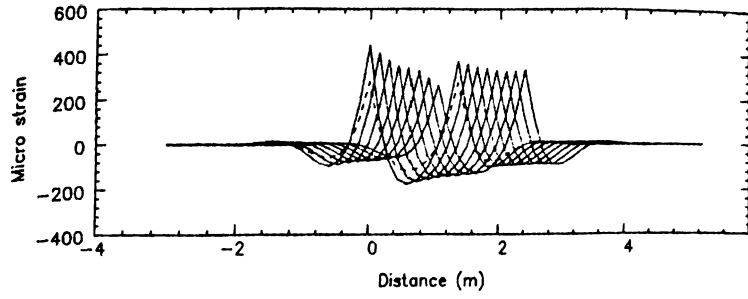


Fig. 17.17 Extreme fibre strains in the roadway model at 5ms time intervals as it is traversed by the vehicle model at 30 m/s. Tension is plotted positive. Variations in the peak strain levels is caused by dynamic fluctuation of the wheel forces. From [88].

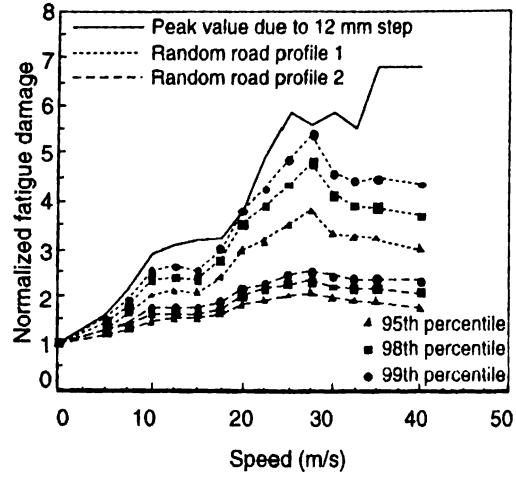


Fig. 17.18 Variation of normalised theoretical fatigue damage with speed, due to one pass of a tandem axle vehicle model with a 'four-spring' tandem suspension system in figure 17.13. From [88].

Previous studies – Flexible Pavements

O'Connell et al [361], Monismith et al [344] and Gillespie et al [192] used *static* models of flexible pavement response based on elastic layer theory. Monismith et al recognised the importance of the frequency dependence of road response and modified the elastic modulus of the asphalt according to the 'predominant' loading frequency (wheel load resonant frequency + 5Hz to account for the speed of 90 km/h). The model used by Gillespie et al included a viscoelastic correction for vehicle speed

Monismith et al and O'Connell et al assumed that dynamic wheel loads are randomly distributed over the road surface so that "any single point in the wheel path is likely to sustain the same level of loading as any other point ... (and hence) ... may be subjected to the full spectrum of loads that a given truck might apply" [344]. Thus they calculated the average value of the particular road damage criterion by assuming that each axle or axle group damages the road independently. O'Connell et al achieved this by calculating a modified Road Stress Factor (similar to equation 17.2) based on

theoretical pavement strains instead of the dynamic wheel loads. Monismith et al analysed the wheel loads generated by one axle only of a tandem group.

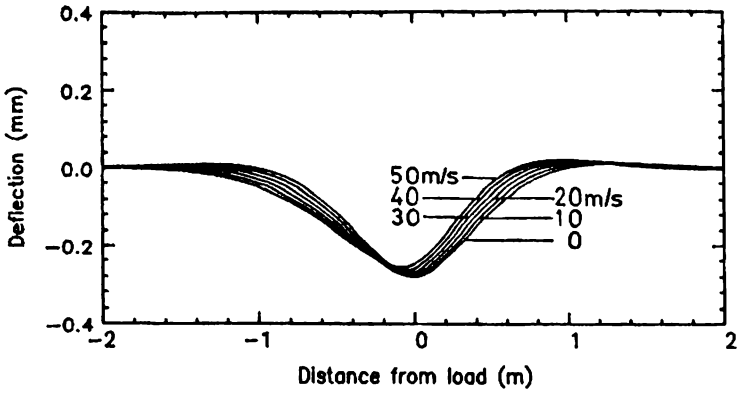


Fig. 17.19 The effect of speed on beam deflections in a moving coordinate frame, for a steady 40kN load, located at x = 0, moving from left to right. As the speed of the load increases, the peak deflections can be seen to decrease, and to occur increasingly aft of the point of application of the load.

Monismith et al [344] concluded that for their particular conditions, the theoretical increase in damage done by dynamic wheel loads of three tandem suspensions compared with damage due to static wheel loads alone was: 19% for a torsion bar suspension; 22% for a four-spring suspension; and 37% for a walking-beam suspension.

O'Connell et al [361] performed a parametric study of vehicle and pavement variables. They concluded that dynamic tyre forces can cause up to 25% increase in theoretical pavement damage, depending on the conditions, but that this can be improved by suspension design. Air suspensions were found to be the least damaging and walking beam suspensions, the most damaging. Although dynamic loads and theoretical cracking damage were found to increase slightly with tandem axle spacing, rutting damage was found to decrease dramatically because of reduced compressive strains in the subgrade.

Cebon [93] (see examples above), Gillespie et al [192] and Cole et al [129, 374, 375] based their damage predictions on the hypothesis that road deterioration is likely to be governed by damage at the worst locations rather than the average value over the road surface. (This hypothesis is consistent with the assumption of 'spatial repeatability' (see Chapter 18), because it assumes that particular locations will be damaged significantly more than others by all vehicles in the 'fleet'.) They calculated the accumulated damage at particular points along the road due to all of the axles of a vehicle, and then performed an upper percentile analysis as described in the previous sections.

In the extensive parametric study of the effects of dynamic tyre forces on damage to flexible and rigid pavements by Gillespie et al, [192], it was found that road damage increases with road roughness, but at different rates, depending on the suspension type. Walking-beam suspensions were found to generate their maximum fatigue damage at approximately 100 km/h, for reasons similar to those for the 'critical speeds' described in the previous section. They also found that rutting damage decreases rapidly with speed, because of the viscoelastic nature of flexible pavements (equation 14.8), and that dynamic loads have only a small influence.

From these upper percentile analyses, the researchers concluded that dynamic wheel loads are likely to have a much greater influence on pavement fatigue damage than predicted by the uniformly

distributed damage hypothesis (typically up to four times greater - *eg* figure 17.18). Note, however, that theoretical rutting damage in the Cebon's analysis [93], and later in Gillespie's study [192] was found to be much less sensitive to dynamic loads. This was because the exponent k_2 in their respective damage equations (*eg* equation 13.1) was effectively 1.

Previous Studies – Rigid Pavements

The analysis of jointed rigid (PCC) pavements by Abbo et al [1, 319] was essentially a 'single vehicle pass' calculation but it included a model of joint fault degradation with time. This study concluded the following:

(i) Under static vehicle loads, the ends of concrete slabs are more prone to fatigue damage than the mid-slab region, due to the discontinuity in bending strength at the joints. Under dynamic loading, however, excitation of the sprung mass modes of the vehicle by joint faults can increase significantly the fatigue damage predicted for the mid-slab regions.

(ii) Suspensions ranked in order of increasing damage:

$$\underset{\text{axle}}{\text{single}} < \underset{\text{tandem}}{\text{four-spring}} < \underset{\text{tandem}}{\text{walking beam}}$$

Reducing the spacing of the four-spring tandem *increased* the predicted pavement strains and damage slightly. Reducing the walking beam spacing *decreased* dynamic loads substantially at highway speeds (depending on the speed, because of wheelbase filtering effects) and hence decreased predicted damage.

(iii) Suspension spring characteristics (stiffness and hysteresis) were found to be important, but tyre pressure was not.

Gillespie et al [192] also examined the effects of dynamic loads on rigid pavements and observed a similar suspension ranking to Abbo et al (above). Figure 17.20 is a typical result showing the influence of roughness level and suspension type on rigid pavement fatigue.

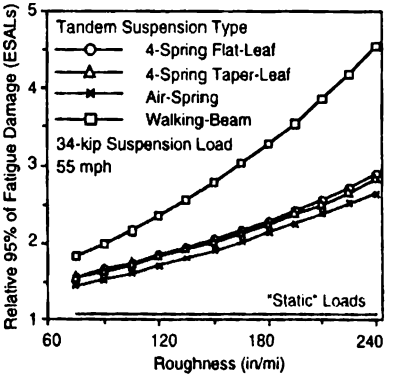


Fig. 17.20 Influence of tandem suspension type and roughness level on rigid pavement fatigue. From [192]

17.4.3 Whole-life Models of Flexible Pavements

'Whole-life' models of vehicle–pavement interaction [66, 365, 469] attempt to predict the deterioration of a pavement's structural integrity and surface profile with time, due to the applied dynamic wheel loads. This requires an empirical relationship between the wheel forces and degradation of the road surface profile, which is an area of uncertainty. It also requires some assumptions to be made about the level of repeatability of wheel loads generated by the vehicle fleet.

Some of the previous calculations also attempted to include the affects of environmental/seasonal factors (temperature, freezing, *etc*) on road strength, and the statistical variation of structural properties along the road.

Previous whole-life flexible pavement analyses [66, 365, 469] were all validated using data from the AASHO road test [8]. Predictions of rutting and cracking by Ullidtz et al [469] and Papagiannakis et al [365] reproduced the AASHO test results well. Papagiannakis et al found that the dynamic analysis improved the accuracy of their damage predictions considerably. Brademeyer et al [66] also achieved relatively convincing agreement of rutting and serviceability predictions with AASHO test data. In this case, however, the improvement in accuracy was relatively small over the results presented by Kenis et al [277] who performed a similar analysis of the AASHO road test (using the same VESYS analysis program) without including dynamic loads. Fatigue cracking predictions in [66] were inaccurate.

Neither [66] nor [469] drew any conclusions about the influence of vehicle design on road damage because the main emphasis of these studies was prediction of pavement degradation with time. Papagiannakis et al [365] deduced that rubber walking beam suspensions cause 17-22% additional theoretical damage due to dynamics (over that caused by the static loads alone), and air suspensions cause an additional 6-8%.

There are numerous difficulties and uncertainties in developing realistic whole–life models. Nevertheless, the whole-life modelling approach offers the best prospects for understanding the complex interactions that occur in the vehicle-road-environment system. Recent research in this area is the subject of Chapters 20 and 21.

17.5 CONCLUSIONS: COMPARISON OF VEHICLE FEATURES

The conclusions of this chapter regarding the importance of various vehicle features on relative road damage are collected together in figure 17.21. The vertical axis indicates road damage (plotted on a logarithmic scale) relative to that caused by a 'baseline' condition of tandem axles, dual tyres, perfect static load sharing, and no dynamic tyre forces. Each dark bar in the chart represents the results published in one or more papers.

Some conclusions that can be drawn from the chart are:

(i) Applying a tandem suspension load to a single axle can be expected to increase road damage by a factor of up to 25 (first bar of chart)[1].

(ii) Replacing dual tyres with wide–base single tyres may increase road damage by a factor of up to 10 (second bar of chart).

(iii) Unequal static load sharing between axles in a tandem suspension may increase road damage by a factor of up to 3 (third bar of chart).

(iv) The fourth bar summarises the literature on the road–damaging effects of dynamic tyre forces. The *average* increase in damage caused by dynamic forces, compared to static forces alone is approximately 10% – 40% ('mean damage' on the fourth bar of the chart, as calculated by the road stress factor and/or by neglecting spatial repeatability). This is small compared with the effects of tyre type and unequal static load sharing shown in the second and third bars.

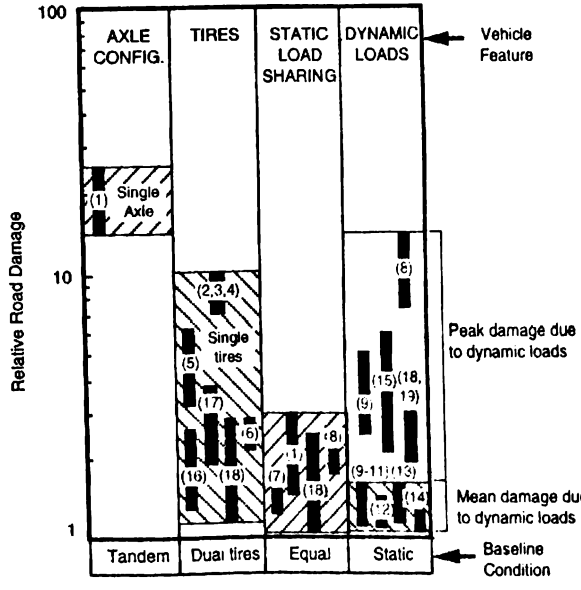
Assuming a high degree of 'spatial repeatability', the relative increase in *peak* road damage caused by dynamic forces is in the range 2 – 14 ('peak' damage in the fourth bar of the chart), which is comparable with the effects of tyres and unequal static load sharing. It

[1] This is not a particularly realistic scenario, but is included for comparison purposes.

should be noted that the higher value of 14 is for 'walking-beam' and 'pivoted-spring' tandem suspensions [199].

If the assumption of *uniformly distributed (average) damage* is correct, then dynamic loading is a relatively unimportant factor in road damage, compared with the effects of uneven static load sharing and wide single tyres. Conversely, if the assumption of *spatial repeatability* is found to be correct, then dynamic loads are an important factor in road damage and suspension design has a strong influence.

Spatial repeatability is the subject of the next chapter. The remaining chapters in this part of the book discuss the analysis of road-damaging potential of measured dynamic tyre forces and whole life road response models.



References

1 Southgate and Deen, USA, (1983,1984), [434, 437]
2 Zube and Forsyth, USA, (1965), [516]
3 Christison et al, Canada, (1978), [109]
4 Treybig, USA, (1983), [464]
5 Huhtala, Finland, (1988), [248]
6 Anon (OECD) (1982), [16]
7 O'Connell et al, USA, (1986), [361]
8 Gordon, Australia, (1987), [199]
9 Sweatman, Australia (1983), [443]
10 Eisenmann, Germany, (1975), [164]
11 Görge, Germany, (1984), [200]
12 Mitchell and Gyenes, UK (1989), [337]
13 Monismith et al, USA, (1988), [342]
14 Papagiannakis et al, Canada, (1989), [365]
15 Cebon, UK, (1985), [91, 93]
16 Addis, UK, (1991), [2]
17 Bonaquist, USA, (1992), [64]
18 Gillespie et al USA (1992) [192]
19 Cole et al, UK, (1992) [129]

Fig. 17.21 Summary of literature on the effects of various vehicle features on road damage.

18
SPATIAL REPEATABILITY

18.1 SUMMARY

This chapter examines the extent to which lorries in normal traffic flow apply peak forces to the same locations along the road.

A validated vehicle simulation is used to generate a fleet of thirty-seven different hypothetical leaf-sprung articulated vehicles. The spatial distribution of tyre forces generated by each vehicle is compared with the distribution generated by a reference vehicle, and the conditions for which repeated heavy loading occurs at specific points along the road are established. It is estimated that two-thirds of four-axle leaf-sprung articulated vehicles (a large proportion of all heavy vehicles) may contribute to a repeated pattern of road loading.



An experimental study is described in which dynamic tyre forces were measured with a load measuring mat, 56m long, with 141 capacitative strip sensors, spaced at 0.4m intervals. Two sets of experiments are described. In the Phase I experiments the dynamic tyre forces generated by fourteen articulated vehicle combinations (3 tractors and 5 trailers) on a test track were measured. These forces are used to confirm the theoretical predictions of repeatability. In the Phase II experiments, the dynamic tyre forces generated by 540 heavy goods vehicles on a UK trunk road were measured. These results are used to estimate the degree of repeatability exhibited by a typical highway fleet of heavy goods vehicles. The experimental results are found to be largely in agreement with the theoretical predictions, and approximately half the vehicles tested are found to contribute to a spatially repeatable pattern of road loading.

This chapter is based on work previously published in [120, 130]

18.2 INTRODUCTION

Various researchers have suggested that the peak forces applied by the heavy vehicle fleet are concentrated at specific locations along the pavement [88, 172, 213]. This effect has been termed 'spatial repeatability', and was initially based on evidence like that shown in figure 7.12. Under these circumstances, some locations along the pavement may be expected to incur significantly more damage than the average [88]. The life of the pavement is then expected to be governed by the damage at these heavily loaded areas.

The first observation of spatial repeatability under highway conditions appears to have been made in 1913 by Crompton [146] who noted that *"commercial vehicles now consist of large fleets of wagons which are practically identical in all their harmonic features, and as these run over roads as regular as a train service on a railway they have a severe harmonic effect on the surface"*.

In 1983, Ervin et al [172], noted that three vehicles with different suspensions were all excited by the same roughness feature and consequently applied peak wheel forces to the same localised area in the vicinity of that feature. In 1985, the author [88] proposed that this load concentration would cause local road failure in the vicinity of the roughness feature. He therefore calculated the influence of

dynamic tyre forces on road damage using this hypothesis. Hahn [213] suggested that because a large proportion of heavy vehicles tend to have similar geometry and dynamic characteristics, and tend to travel at similar speeds, spatial repeatability of pavement loading may be expected in normal traffic flow.

Vehicles in a particular weight class tend to have similar geometry because of the nature of vehicle size and weight regulations. There is greater variation in suspension characteristics, although at the time of this study leaf spring suspensions were fitted to a large proportion of heavy articulated vehicles. In the UK in 1986, 85-90% of trailers were fitted with leaf springs [336]. In 1987, Morris [347] estimated that of new vehicles in the USA, up to 70% of tractors and over 80% of trailers had leaf spring suspensions. Morris also quoted the results of surveys in Canada [171] and Australia [443] which show that leaf spring trailer suspensions and walking beam drive axle suspensions were the most popular. In the intervening period, air suspensions have become considerably more popular, however this does not affect the basic outcome of the theoretical analysis described here.

Spatial repeatability is a central issue in the interaction between vehicles and roads. The level of repeatability might be expected to vary around the world, depending on road surface roughness standards, the local size and weight regulations and homogeneity of the vehicle fleet. This chapter describes theoretical and experimental research that has been performed to quantify the level of spatial repeatability on UK highways under typical operating conditions.

18.3 THEORETICAL STUDY

18.3.1 Simulation of a Vehicle Fleet

The two-dimensional articulated vehicle model described in Chapter 6 was used to create a 'fleet' of geometrically similar articulated vehicles, by varying eight parameters of the 'reference' model:

Tractor	*Trailer*
Tyre stiffness	Tyre stiffness
Drive axle spring stiffness	Spring stiffness
Drive axle spring friction force	Spring friction force
	Sprung mass
	Sprung mass pitch inertia

These parameters were chosen because they can vary widely between vehicles and have a significant influence on dynamic tyre forces. Dimensional parameters were kept constant because most four-axle articulated vehicles in the UK have very similar geometry [22, 472].

Ten vehicle models, numbered 1 to 10, were created by randomly increasing by 15% (multiplying by 1.15) or decreasing (dividing by 1.15) or keeping constant, each of the eight parameters. The parameter variations of two further models were chosen to maximise and minimise the resonant frequencies, for models 11 and 12 respectively. This set of twelve models will be referred to as set (a). Two additional sets of twelve models, sets (b) and (c), were created by increasing the variations of the same parameters to 40% and 100%. In total there were 36 vehicle models, plus the reference model. Table 18.1 summarises the parameters of the reference model and nine other models. The parameters of the other models may be found in [113]. Tyre force histories were calculated for each vehicle model travelling over 220m of the measured test section profile used in the vehicle model validation study, described in Chapter 6.

The aggregate tyre force history (equation 17.5, with n = 1) was calculated so that the accumulated effect of all the axles of the vehicle could be assessed at various points along the road. Figure 18.1 shows aggregate force histories of the reference model and models 8a-c, for a speed of 22 m/s.

A disadvantage of using aggregate force with n = 1 is that no distinction is made between peaks and troughs in the force history. In the analysis of road damage it is the accumulation of peak forces that is of most concern. The peak forces can be weighted by calculating the aggregate fourth power tyre force history, using equation 17.5 with n = 4.

		Vehicle									
Parameters	Units	Ref	4a 15%	4b 40%	4c 100%	5a 15%	5b 40%	5c 100%	8a 15%	8b 40%	8c 100%
Tractor											
Tyre stiffness (single tyre)	MN/m	0.9	0.78	0.64	0.45	1.04	1.26	1.8	1.04	1.26	1.8
Drive axle spring stiffness	MN/m	1	0.87	0.71	0.5	1.15	1.4	2	1.15	1.4	2
Drive axle spring friction force	kN	7.5	6.52	5.36	3.75	7.5	7.5	7.5	6.52	5.36	3.75
Trailer											
Tyre stiffness (single tyre)	MN/m	0.9	1.04	1.26	1.8	1.04	1.26	1.8	0.9	0.9	0.9
Spring stiffness	MN/m	1.5	1.3	1.07	0.75	1.73	2.1	3	1.5	1.5	1.5
Spring friction force	kN	7.5	8.63	10.5	15	7.5	7.5	7.5	6.52	5.36	3.75
Sprung mass	Mg	20	23	28	40	17.4	14.3	10	23	28	40
Sprung mass pitch inertia	Mgm^2	250	250	250	250	250	250	250	288	350	500

Table 18.1 Vehicle model parameter variations.

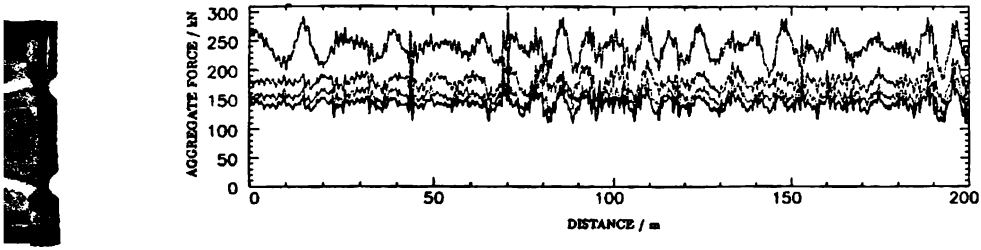


Fig. 18.1 Aggregate force histories of the reference vehicle and vehicles 8a-c, speed 22m/s. The corresponding correlation coefficients are 1.0, 0.959, 0.843, 0.626. From [120]
·-·-·-·-·- vehicle 8c; - - - - - - - vehicle 8b; · · · · · · · vehicle 8a; ——— reference vehicle

18.3.2 Measures of Repeatability

Correlation Coefficient

The approach taken to quantify spatial repeatability was to compare the aggregate tyre force histories generated by each vehicle with those generated by the reference vehicle. A suitable measure of spatial repeatability should indicate high repeatability when the peaks of the two force histories occur close together along the road. Low repeatability should be indicated when the peaks of one history occur near the troughs of the second history.

A statistic which has this property is the correlation coefficient ρ [355], defined by

$$\rho = \frac{E\left[\left(x(t) - m_x\right)\left(y(t) - m_y\right)\right]}{\sigma_x \sigma_y}, \tag{18.1}$$

where m_x, m_y and σ_x, σ_y are the means and standard deviations of two signals x(t) and y(t). The value of ρ can be between +1 and -1. The properties of ρ may be examined using two sine waves of frequency ω and phase difference ϕ:

$$x(t) = \sin(\omega t) \qquad y(t) = \sin(\omega t + \phi) \tag{18.2}$$

In this case equations (18.1) and (18.2) give

$$\rho = \cos \phi. \tag{18.3}$$

When $\phi = 0°$, $\rho = +1$ the two waves are in phase and the peaks (and troughs) of each wave are at the same locations.

When $\phi = 180°$, $\rho = -1$ the two waves are in anti-phase and the peaks of one wave are at the troughs of the other wave.

The correlation coefficient was used to assess spatial repeatability of tyre force histories (compared to a reference tyre force history) by calculating the correlation coefficient in the spatial domain rather than the temporal domain. Figure 18.2 shows how the correlation coefficient relates to the phase difference in terms of distance along the road, for frequencies of 3Hz and 15Hz and a vehicle speed of 22m/s. A reasonable threshold of repeatability is one eighth of a cycle phase difference, or 45°, corresponding to a correlation coefficient of 0.707. For a frequency of 15Hz this threshold corresponds to 0.18m phase distance, about the length of a tyre contact patch or a small pothole. For a frequency of 3Hz the threshold phase distance is 0.92m.

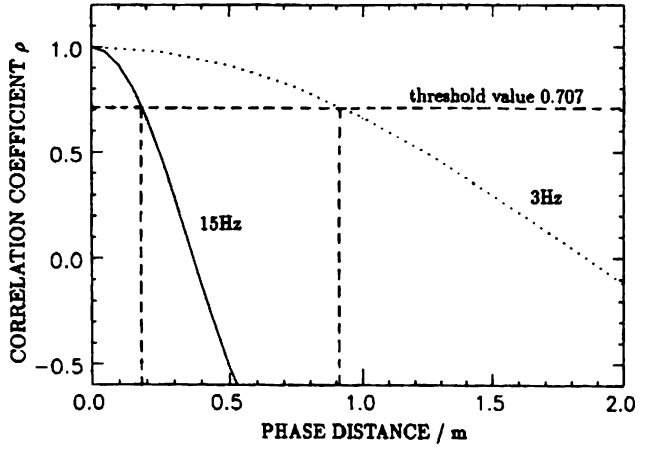


Fig. 18.2 Correlation coefficient against phase distance, for frequencies of 3Hz and 15Hz and a speed of 22m/s. From [120].

Accumulated Damage

A simple indication of spatial repeatability may be obtained simply by adding together all the aggregate tyre force histories of all the models. A high degree of spatial repeatability would be indicated by an accumulated force history with as much variation as the reference force history. A low degree of repeatability would be indicated by a uniform distribution of accumulated force.

Separation of Peaks

In [120], the *mean separation of peaks* in the aggregate tyre forces was also used as a measure of spatial repeatability. A high degree of spatial repeatability would be indicated by a small mean separation. The general form of the results was found to be similar to the correlation coefficient. However the results were generally found to be unsatisfactory because this measure does not

distinguish between low and high frequency force components, and because the calculation of the distance between peaks can be unreliable. It will not be pursued further in this book.

18.3.3 Results

Correlation Coefficient

Tyre force histories were calculated for the reference vehicle and the 36 vehicle 'fleet' travelling at a 'reference' speed of 22m/s. The correlation coefficients between the aggregate tyre force history of the reference vehicle and the histories of each other vehicle in the fleet were calculated, and are shown in figure 18.3. The graph shows that about one third of the vehicles have correlation coefficients *below* the threshold value of 0.707. However, examination of the parameters of these vehicles (for example, vehicle 8c) reveals that they are unlikely to exist in reality.

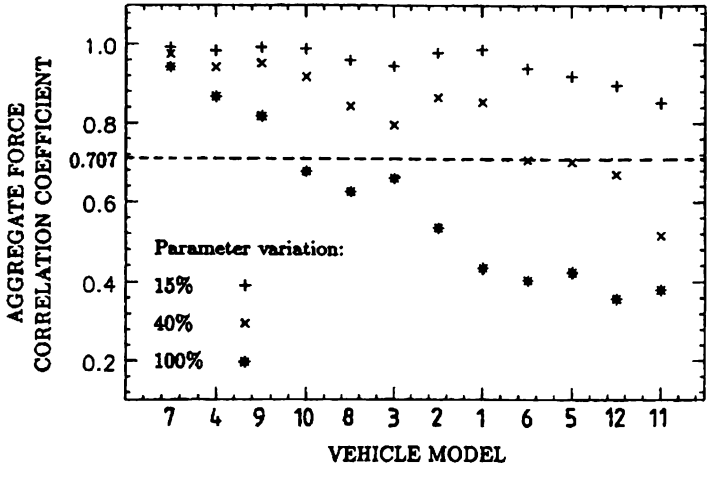


Fig. 18.3 Aggregate force correlation coefficients of the vehicle model fleet, speed 22m/s. From [120].

The aggregate force histories of vehicles 8a-c shown on figure 18.2 have correlation coefficients from 0.959 to 0.626. This graph shows that there is a high degree of spatial repeatability even when the correlation coefficient has reduced to 0.626.

These results suggest that leaf-sprung articulated vehicles travelling at one speed are likely to load a road with a high degree of spatial repeatability. However, vehicle speed may have a significant influence, and this is investigated next.

Aggregate tyre force histories were calculated for the reference vehicle travelling at speeds greater and less than the reference speed (22m/s ±5%, ±10%, ±20%, ±40%). The correlation coefficients between each of these histories and the reference aggregate tyre force history were calculated. Figure 18.4 shows that the coefficient decreases as the vehicle speed moves away from the reference speed. The coefficient is greater than 0.707 for a speed range equal to about half of the reference speed.

The effect of speed variation on correlation coefficient for vehicle 5b is also shown in figure 18.4. The value of correlation coefficient at 22m/s, 0.702, is the same as shown on figure 18.3, but becomes closer to unity as the speed increases. The maximum value is 0.925 at 27m/s. This result indicates that the dominant modes of vibration of vehicle 5 have higher frequencies than those of the

reference vehicle, so that peak correlation in the spatial domain occurs at a speed higher than the reference speed.

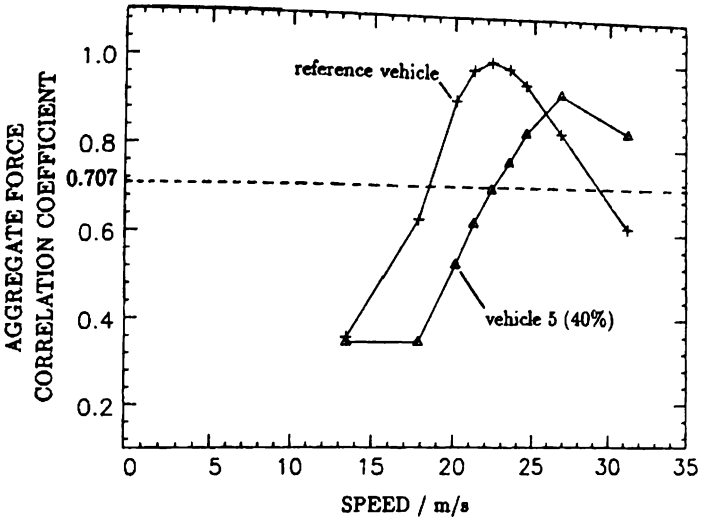


Fig. 18.4 Aggregate force correlation coefficient against vehicle speed, for the reference vehicle and vehicle 5b. From [120].

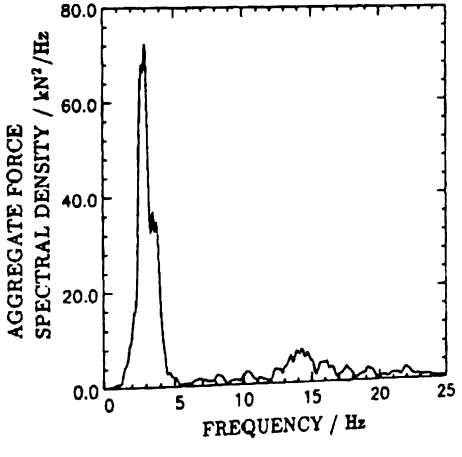


Fig. 18.5 Spectral density of aggregate tyre force for the reference vehicle at 22m/s. From [120]

Examination of the spectral density of *aggregate tyre force* for the reference vehicle at the reference speed (figure 18.5) shows that sprung mass modes dominate in a narrow band at about 3Hz. It is likely therefore that spatial repeatability is related to the wavelength along the road corresponding to the dominant frequency in the aggregate tyre force spectral density. This was examined by plotting correlation coefficient against 'average sprung mass mode wavelength', which was calculated by dividing the vehicle speed by the 'average' frequency in the aggregate tyre force spectral density. For most of the vehicle models in the fleet, the sprung mass mode frequencies are in a narrow band, and therefore the aggregate tyre force histories resemble a 'narrow band' vibration. An average frequency can be determined by calculating the mean-level crossing frequency ν_0^+ [355], defined by

$$\nu_0^+ = \frac{1}{2\pi}\frac{\sigma_x}{\sigma_{\dot{x}}} \tag{18.4}$$

where σ_x is the standard deviation of aggregate tyre force and $\sigma_{\dot{x}}$ is the standard deviation of the first time derivative of aggregate tyre force. These values were calculated from the aggregate tyre force spectral density over the frequency range 0–7Hz, to eliminate the effect of wheel hop modes from the calculation.

The correlation coefficients and average sprung mass mode wavelengths were calculated for the aggregate tyre force histories of nine vehicles (vehicles 4a-c,5a-c, 8a-c,) at nine speeds (22m/s, ±5%, ±10%, ±20%, ±40%). The values are plotted in figure 18.6, with the nine points belonging to each vehicle joined by lines. The peak value of correlation coefficient obtained from each vehicle corresponds closely to the sprung mass mode wavelength (7.0m) of the reference vehicle travelling at the reference speed.

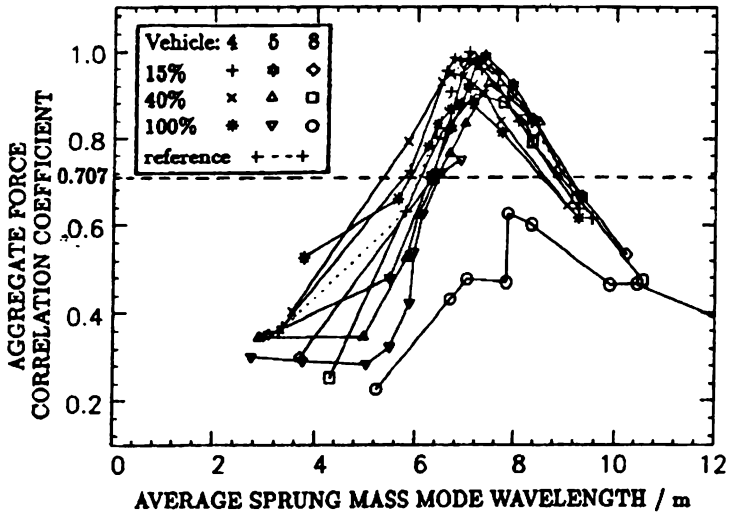


Fig. 18.6 Aggregate force correlation coefficient against average sprung mass mode wavelength for the reference vehicle and vehicles 4a-c, 5a-c, 8a-c. From [120].

This result confirms the importance of average sprung mass mode wavelength on the spatial repeatability of tyre forces. All but one of the vehicles have peak correlation coefficients well above 0.707. Vehicle 8c does not exceed 0.64, because it has two distinct sprung mass frequencies, at 1.5Hz and 3Hz. This vehicle would be unlikely to exist as an entirely leaf-sprung vehicle because

leaf spring suspensions are not usually soft enough to give a 1.5Hz frequency. However, these frequencies might be obtained, for example, from a vehicle comprising a leaf-sprung tractor and an air-sprung trailer.

The general shape of figure 18.6 may be regarded as a characteristic of four-axle leaf-sprung articulated vehicles. It relates sprung mass mode wavelength to spatial repeatability of tyre force.

Figure 18.7 shows the correlation coefficients calculated from the *aggregate fourth power force* histories (equation 17.5, with n = 4) plotted against average sprung mass mode wavelength, in the same manner as figure 18.6. The two graphs are very similar. This indicates that when the correlation coefficient is used as a measure of repeatability, the choice between aggregate force and aggregate fourth power force does not have a strong influence on the result.

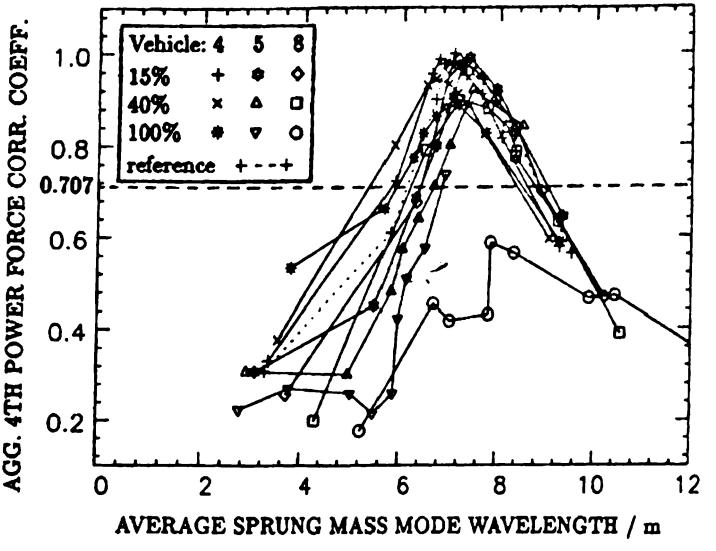


Fig. 18.7 Aggregate fourth power force correlation coefficient against average sprung mass mode wavelength for the reference vehicle and vehicles 4a-c, 5a-c, 8a-c. From [120].

Accumulated Damage

The aggregate tyre force history of the reference vehicle at 22m/s is shown in figure 18.8a. The coefficient of variation is 0.072. Figure 18.8b shows the accumulation of the 108 different aggregate tyre force histories calculated during this study. The coefficient of variation is 0.060. Summing a large number of different force histories has not resulted in a significant decrease in the coefficient of variation, despite the inclusion of vehicles with extreme parameter variations.

Figure 18.8c shows the accumulated fourth power tyre force histories. The data have been normalised so that a value of one corresponds to static forces alone. If this graph is considered to be an indication of road damage distribution, then it can be seen that some areas of the road receive nearly four times the damage caused by static forces alone.

The road profile is shown in figure 18.8d. It is possible to see that peaks in the accumulated force correspond to particular features of the road profile.

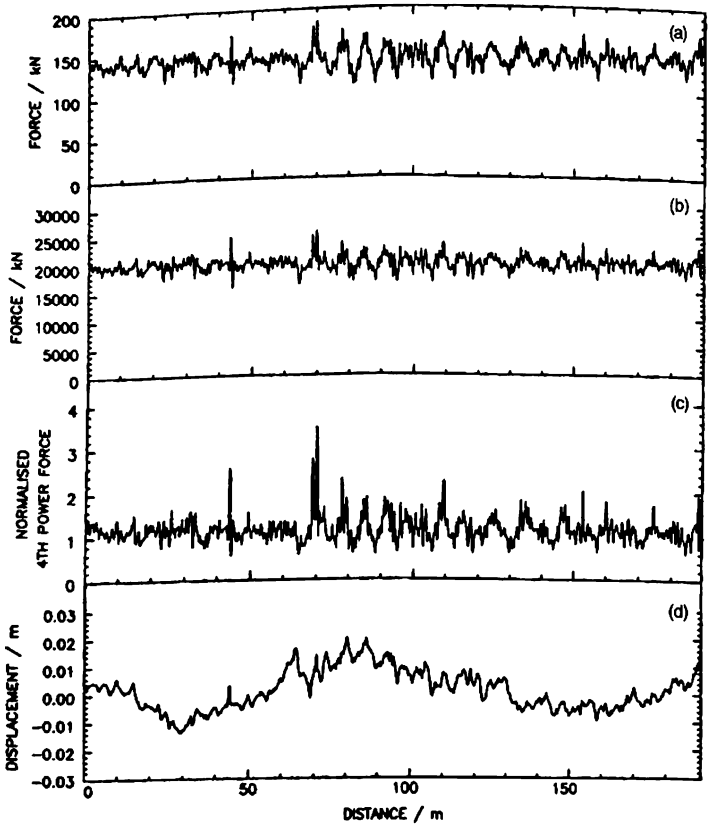


Fig. 18.8 (a) Aggregate force history of the reference vehicle at 22m/s. Coefficient of variation 0.072
(b) Accumulated forces from 108 vehicle passes. Coefficient of variation 0.060.
(c) Accumulated fourth power forces from 108 vehicle passes, normalised by static forces.
(d) Road profile. All from [120].

Summary of Results

The correlation coefficient is preferred over the mean separation of peaks as a criterion for spatial repeatability of tyre forces. The choice between aggregate tyre force and aggregate fourth power tyre force is not critical. The aggregate tyre force is used in the rest of this chapter.

18.3.4 Analysis of Fleet Operating Conditions

The previous section showed that for four-axle leaf-sprung articulated vehicles, the *average sprung mass mode wavelength* is significant in determining the spatial distribution of tyre force. In this section the distribution of average sprung mass mode wavelength in normal traffic flow is estimated, and using the characteristic in figure 18.6, the proportion of four-axle leaf-sprung articulated vehicles that contribute to a repeated pattern of road loading is estimated.

The calculation procedure is:

1. Estimate the distribution of vehicle speed v.
2. Estimate the distribution of sprung mass mode period T.
3. Calculate the distribution of sprung mass mode wavelength λ, where $\lambda=vT$.
4. Calculate the proportion of vehicles that have sprung mass mode wavelengths within the limits set by the characteristic in figure 18.6.

Distribution of Vehicle Speed

Results from the 1987 National Speed Survey [27] were used to determine the mean and standard deviation of the speeds of heavy articulated vehicles. The survey measured the speeds of vehicles in unimpeded traffic flow on 26 single-carriageway A-roads, 23 dual-carriageway A-roads, and 5 motorways. For each of these three classes of road, the survey presented speed distributions for several classes of vehicle, including heavy articulated vehicles. The results from the motorway sites were used for this study, to minimise the speed variation that might exist between sites. The speed distribution for heavy articulated vehicles in the survey was found to be approximately Gaussian (see [120]). The mean speed m_v was found to be 24.2m/s and the standard deviation σ_v was 3.6m/s (14.8% of the mean).

Distribution of Sprung Mass Mode Period

Published test data of leaf-sprung articulated heavy vehicles (see [113] for details) were used to estimate the probability distribution of the sprung mass mode period. A reasonable estimate is that 95% of leaf-sprung articulated vehicles have periods between 0.25s and 0.5s (corresponding to frequencies of 4Hz and 2Hz). Assuming that the distribution is Gaussian, the mean period m_T is 0.375s (2.7Hz) and the standard deviation σ_T is 0.0625s (16.7% of the mean).

Distribution of Sprung Mass Mode Wavelength

The sprung mass mode wavelength λ is related to speed v and sprung mass mode period T by

$$\lambda=vT \tag{18.5}$$

An expression for calculating the mean and standard deviation of the product of two non-zero mean Gaussian variables is needed. From equation (3.132) of [50],

$$E[y_1y_2y_3y_4]=E[y_1y_2]E[y_3y_4]+E[y_2y_3]E[y_1y_4]+E[y_1y_3]E[y_2y_4]-2m_{y_1}m_{y_2}m_{y_3}m_{y_4} \tag{18.6}$$

where $y_{1\text{-}4}$ are Gaussian random variables and $m_{y_{1\text{-}4}}$ are their mean values. Substituting $y_1=y_2=v$, $y_3=y_4=T$, and $vT=\lambda$ gives

$$E[\lambda^2]=E[v^2T^2]=E[v^2]E[T^2]+2E[\lambda]^2-2m_v^2m_T^2 \tag{18.7}$$

where

$$E[\lambda^2]=m_\lambda^2+\sigma_\lambda^2$$

$$E[v^2]=m_v^2+\sigma_v^2$$

$$E[T^2]=m_T^2+\sigma_T^2$$

$$E[\lambda]^2=m_\lambda^2$$

Thus

$$m_\lambda^2+\sigma_\lambda^2=m_v^2m_T^2+\sigma_v^2m_T^2+\sigma_T^2m_v^2+\sigma_v^2\sigma_T^2+2m_\lambda^2-2m_v^2m_T^2 \tag{18.8}$$

If v and T are independent, which is a reasonable assumption in this case, then

$$m_\lambda = m_v m_T \tag{18.9}$$

and, from (18.8),

$$\sigma_\lambda = \sqrt{\sigma_v^2\sigma_T^2 + \sigma_v^2 m_T^2 + \sigma_T^2 m_v^2}. \tag{18.10}$$

Substituting the numerical values for m_v, σ_v, m_T, σ_T gives

$$m_\lambda = 9.1\text{m} \qquad \sigma_\lambda = 2.0\text{m}. \tag{18.11}$$

This result is an estimate of the mean and standard deviation of sprung mass mode wavelength for four-axle leaf-sprung articulated vehicles in normal motorway traffic flow.

Proportion of Vehicles

The general characteristics in figure 18.6 can be scaled to account for the ratio of $m_\lambda = 9.1$m, estimated for highway conditions, to $m_\lambda = 7.0$m calculated above for the theoretical vehicle fleet. The threshold wavelengths of 5.8 m and 9.0 m (in figure 18.6) then become 7.5m and 11.7m. The proportion of vehicles having sprung mass mode wavelengths between these two limits can be estimated using the Gaussian probability integral, tabulated in [355], and is found to be 68%. It is therefore likely that the peak forces generated by approximately two-thirds of heavy articulated vehicles are concentrated at specific locations along the road.

The main consequences of this result are: (a) road life is likely to be governed by damage at these locations, (b) the effects of dynamic tyre forces are likely to be significant compared with other vehicle features, such as tyre configuration, (c) any measure of vehicle dynamic loading such as may be used in a suspension assessment test should consider peak dynamic forces rather than average or RMS dynamic forces.

18.4 EXPERIMENTAL STUDY

Most experimental work on dynamic tyre forces has been performed using instrumented vehicles [96]. This approach has the advantage of relative simplicity and low cost when testing a small number of vehicles. However, when the dynamic tyre forces of many vehicles are to be assessed quickly, either on the test track or on the public highway, instrumenting each vehicle is not practical. For this reason, the measurements described in this chapter were performed using the 'load measuring mat', described in Chapters 7 and 8 to measure the dynamic tyre forces generated by a heavy commercial vehicles. Two sets of tests are described. The Phase I tests were performed on a section of the Transport Research Laboratory (TRL) test track in the UK, using 14 different vehicle combinations. The Phase II tests were performed on a section of a highway in normal traffic.

18.4.1 Experimental Measures of Spatial Repeatability

Definition of *SRI*

The correlation coefficient between two *measured* aggregate force histories, the 'subject' history u and a carefully selected 'reference' history v is known as the 'Spatial Repeatability Index' (*SRI*) [144]. Using equation 18.1, the *SRI* can be shown to be:

$$\text{SRI} = \frac{\sigma_{uv} - \mu_u\mu_v}{\sqrt{\left[\sigma_u^2 - \mu_u^2\right]\left[\sigma_v^2 - \mu_v^2\right]}}, \tag{18.12}$$

where σ_{uv} is the co-variance between u and v,
σ_u^2 and σ_v^2 are the variances of u and v, and
μ_u and μ_v are the mean values of u and v.

Representing the two aggregate tyre force histories u and v by their Fourier expansions, it can be shown that equation 18.12 becomes (see [376] for further details):

$$SRI = \frac{\sum_{i=1}^{\infty} F_i^u F_i^v \cos\phi_i}{\left(\sum_{i=1}^{\infty}\left(F_i^u\right)^2 \sum_{i=1}^{\infty}\left(F_i^v\right)^2\right)^{1/2}} = \frac{\sum_{i=1}^{\infty} F_i^u F_i^v \cos\phi_i}{2\sigma_u\sigma_v}. \qquad (18.13)$$

where F_i^u and F_i^v are the amplitudes of the i^{th} wavenumber components of u and v, and ϕ_i is the phase shift of the i'th wavenumber component between F_i^u and F_i^v.

It can be seen from equation 18.13 that the *SRI* contains magnitude and phase information from all wavenumbers present in the aggregate force histories.

Effects of Measurement Noise

The reduction in *SRI* due to measurement noise may be investigated by considering the correlation between the same two aggregate force histories u and v but with added noise terms present. Assuming that the added noise on the aggregate force histories are uncorrelated functions of distance (but with the same statistics) it can be shown that equation 18.13 becomes:

$$SRI = \frac{\sum_{i=1}^{\infty} F_i^u F_i^v \cos\phi_i}{2\left[\left(\sigma_u^2 + \sigma_{\varepsilon_u}^2\right)\left(\sigma_v^2 + \sigma_{\varepsilon_v}^2\right)\right]^{1/2}}. \qquad (18.14)$$

where $\sigma_{\varepsilon_u}^2$ and $\sigma_{\varepsilon_v}^2$ are the variances of the measurement noise on aggregate force histories u and v.

Referring to equation 18.13, equation 18.14 can be rewritten as:

$$\frac{SRI}{SRI|_{\varepsilon=0}} = \frac{1}{\left[\left\{1+\left(\sigma_{\varepsilon_u}/\sigma_{f_u}\right)^2\right\}\left\{1+\left(\sigma_{\varepsilon_v}/\sigma_{f_v}\right)^2\right\}\right]^{1/2}}. \qquad (18.15)$$

where $SRI|_{\varepsilon=0}$ is the *SRI* for the aggregate force histories with no measurement noise.

Now consider the value of *SRI* for two tests of the same vehicle, at speeds near to the reference speed. Assuming the standard deviations of the dynamic loads on the two aggregate force histories are equal ($\sigma_u = \sigma_v = \sigma_f$) and that the standard deviations of the noise on the two aggregate force histories are equal ($\sigma_{\varepsilon_u} = \sigma_{\varepsilon_v} = \sigma_\varepsilon$). Then equation 18.15 can be simplified to:

$$\frac{SRI}{SRI|_{\varepsilon=0}} = \frac{1}{\left[1+\left(\sigma_\varepsilon/\sigma_f\right)^2\right]}. \qquad (18.16)$$

It can be seen from equation 18.16 that increasing the noise to signal ratio $\sigma_\varepsilon/\sigma_f$ decreases the maximum possible *SRI* between the two aggregate force histories. If there is no noise $(\sigma_\varepsilon/\sigma_f = 0)$, then the maximum possible *SRI* is 1.0. However, if the standard deviation of the noise is equal to the standard deviation of the dynamic tyre force $(\sigma_\varepsilon/\sigma_f = 1)$, the maximum possible *SRI* between the two aggregate force histories is 0.5.

Determination of Noise to Signal Ratio for an Aggregate Force History

To calculate the *SRI* from equation 18.16 the noise to signal ratios $\left(\sigma_{\varepsilon_u}/\sigma_u, \sigma_{\varepsilon_v}/\sigma_v\right)$ for both of the aggregate force histories is required. It can be shown that the noise to signal ratio for a typical aggregate force history u may be calculated from the noise on the individual tyre force histories using the following equation (see [376] for further details):

$$\frac{\sigma_{\varepsilon_u}}{\sigma_u} = \frac{1}{\left[\left(\sigma^2_{u+\varepsilon} \Big/ \sum_{j=1}^{N_a} \sigma^2_{\varepsilon_j}\right) - 1\right]^{1/2}}. \tag{18.17}$$

where $\sigma^2_{u+\varepsilon}$ is the variance of the noisy aggregate force history u,
$\sigma^2_{\varepsilon_j}$ is the variance of the noise on an individual axle and
N_a is the number of axles on the vehicle.

This can be calculated easily if the RMS measurement errors σ_{ε_j} are known.

Accuracy of the *SRI* Calculation

The accuracy of a correlation coefficient estimate, on which the *SRI* is based, was examined by Bendat and Piersol [50]. Following their method, the $(1-\alpha)\times 100\%$ confidence interval may be estimated using the equation (see [50] for further details):

$$\tanh\left(\tanh^{-1}(\mathrm{SRI}) - \frac{z_{\alpha/2}}{\sqrt{N-3}}\right) < \mathrm{SRI}_T \le \tanh\left(\tanh^{-1}(\mathrm{SRI}) + \frac{z_{\alpha/2}}{\sqrt{N-3}}\right), \tag{18.18}$$

where SRI_T is the true value of the sample estimate *SRI*,
N is the number of pairs of observations and
z_α is the 100α percentage point of the standardised normal distribution.

Figure 18.9 shows equation 18.8 for $\alpha = 0.05$ (*ie* 95% confidence limits) for different numbers of pairs of observations N. It can be seen that as the number of pairs of observations decreases, the confidence in the *SRI* estimate decreases rapidly. For all the curves the confidence interval increases to a maximum as the *SRI* estimate tends to zero and decreases to zero as the *SRI* estimate tends to ± 1. For example, if the number of pairs of observations was $N = 1000$ and the *SRI* estimate was zero, there is a 95% probability that the true *SRI* falls within $-0.062 < \mathrm{SRI}_T \le 0.062$. However, if the number of pairs of observations was limited to $N = 10$, the corresponding 95% confidence interval would be $-0.63 < \mathrm{SRI}_T \le 0.63$ indicating a low degree of confidence in the *SRI* estimate.

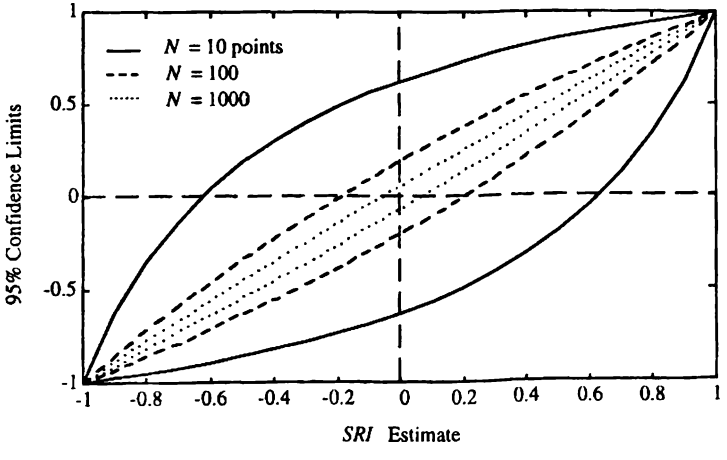


Fig. 18.9 95th percentile confidence limits for the *SRI* estimate. From [130].

18.4.2 Phase I tests

Mat Installation

The first phase of the tests described in this chapter were performed on the Transport Research Laboratory (TRL) test track during the winter months of 1991/92. The load measuring mat (described in Chapter 8) was installed on a long straight section of the track. Each mat tile was attached to the relatively smooth brushed concrete surface by an adhesive sheet and six screws. There were 47 tiles in total, containing 141 sensors, giving an overall instrumented length of 56.4m. Sheets of plywood were used to provide a ramp up to the mat, and a run-off section, both 15m long.

The outputs of the sensors were logged and processed by nine Golden River 'Marksman M600' data-loggers. The data stored by each logger was transferred to a personal computer by a serial communications line.

Vehicle Tests

The accuracy of the mat for measuring dynamic tyre forces was investigated using a vehicle instrumented to measure dynamic tyre forces. The test vehicle was a two axle rigid truck, with single tyres on the steering axle and dual tyres on the drive axle. Steel spring suspensions were fitted to both axles, and the gross mass was 17 tonnes. The instrumentation fitted to the end of each axle consisted of strain gauges to measure axle bending and an accelerometer to correct for the inertia (linear and angular) of the mass outboard of the gauges [337]. The data was logged by a digital data-logger on–board the vehicle. Three measured force components (axle strain gauge, bounce correction and roll correction) were added together to produce the total dynamic tyre force (see Section 7.3 for details).

Synchronisation of the on–board measurements with the mat sensor measurements was achieved by means of an infra-red transmitter and detector mounted on the vehicle. The detector sensed reflective markers placed alongside the mat. Five markers were used along the length of the mat. The instrumented vehicle was driven over the mat 35 times at speeds varying from 2 to 27 m/s.

Following the instrumented vehicle tests, fourteen un-instrumented articulated vehicles were tested on the mat. All the vehicles belonged to TRL and each comprised one of three tractor units, and one of five trailers. Each vehicle was fully laden, and driven over the mat about fifty times at speeds between 2m/s and 27m/s. Table 18.2 describes the tractors (designated by numbers 1–3) and trailers (designated by letters A–E). The combination vehicles are designated by a number and a letter throughout the remainder of this chapter (*eg* vehicle 2C refers to tractor 2 with trailer C).

Calibration

The steering axles of articulated vehicles usually have relatively low dynamic force variation, and at low speeds the forces applied to the pavement surface are close to the static weights. Therefore, the mat sensors were initially calibrated by using the measured static weights of the steering axles of three of the test vehicles. The static axle weights were measured by portable weigh-pads.

Using this initial set of calibration factors, all of the low speed axle force time histories measured with the mat were examined to determine which axles showed the least dynamic force variation. Five axles (two steer, one drive, and two trailer axles) were observed to have low dynamic loads. The results from a total of 23 low speed tests for these axles were then used to determine a final set of calibration factors for the sensors in the mat.

Figure 18.10a shows a histogram of the errors in the measurements by sensor 9, where the 'Static Error' is defined by:

$$\text{Static Error} = \left(\frac{\text{Static force} - \text{Mat force}}{\text{Mat force}} \right) \times 100\%. \qquad (18.19)$$

The un-shaded bars show the sensor errors for all the low speed runs of all the vehicles; the RMS error (standard deviation) is 5.5%. The shaded bars show the sensor errors for the twenty three calibration runs only; the RMS error is 2.6%.

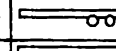
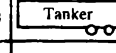
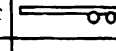
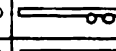
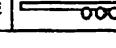
		No. Axles	Suspensions	Tyres*
Tractor 1		2	Front: Multileaf springs + dampers Rear: Multileaf springs + dampers	S, D
Tractor 2		2	Front: Multileaf springs + dampers Rear: Air springs + dampers	S, D
Tractor 3		3	Front: Multileaf springs + dampers Rear: Multileaf '4-spring' tandem	S, D, D
Trailer A		2	Wide-spread steel '4-spring' tandem (monoleaf)	D, D
Trailer B		2	Wide-spread steel '4-spring' tandem (monoleaf)	D, D
Trailer C		2	Rubber 'walking-beam' tandem + dampers	D, D
Trailer D		2	Air tandem + dampers	D, D
Trailer E		3	Steel '6-spring' triaxle (multileaf)	W, W, W

Table 18.2 Descriptions of vehicles tested using the load measuring mat on the TRL test track.
* Tyre types: S = Single, D = Dual, W = Wide single

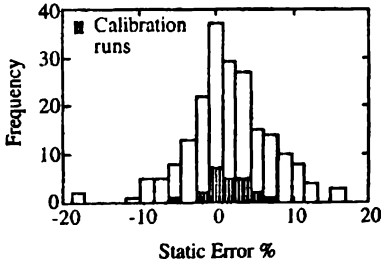


Fig. 18.10a Error between measured and static force, sensor number 9. From [130].

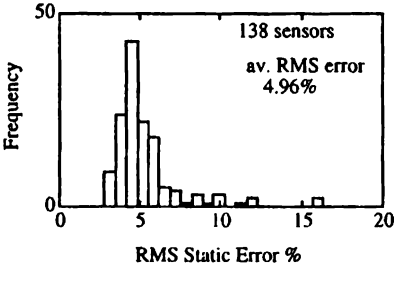


Fig. 18.10b RMS static error for 23 calibration runs. From [130].

Of the 141 sensors in the mat, three were found not to work, and seven were found to be noisy (most likely due to damage in transit). The seven noisy sensors were included in the following accuracy calculations, but were ignored for subsequent analyses of the wheel forces.

Figure 18.10b shows the distribution of the RMS error for all of the sensors in the mat (including the seven noisy ones) for the final calibration runs. The average RMS error of all the sensors was 5%. This value can be considered to be the 'baseline' accuracy of the system, and compares closely to the 4% observed previously for a similar mat by Cebon and Winkler [102] (see Section 8.5). The main difference is due to the seven noisy sensors. It is also apparent that there is a spread of sensor performance, with individual sensors showing errors as low as 2.5% RMS.

When all the low speed mat runs are combined, the average RMS error increases to 7.8%. The difference between these two average error levels is due to dynamic force variation.

Figures 8.11a,b show comparisons of the steering and drive axle tyre forces measured by the mat and measured by the sensors on the instrumented vehicle, for a speed of 25m/s. It is apparent from these figures that the sensor measurements closely follow the on-board measurements. Note that there is considerable discrepancy in the last 5m of the drive axle trace. This was caused by the vehicle moving off the correct path, so that the whole of the tyre width was not over the mat.

Further information about the accuracy of the mat during these tests can be found in [374].

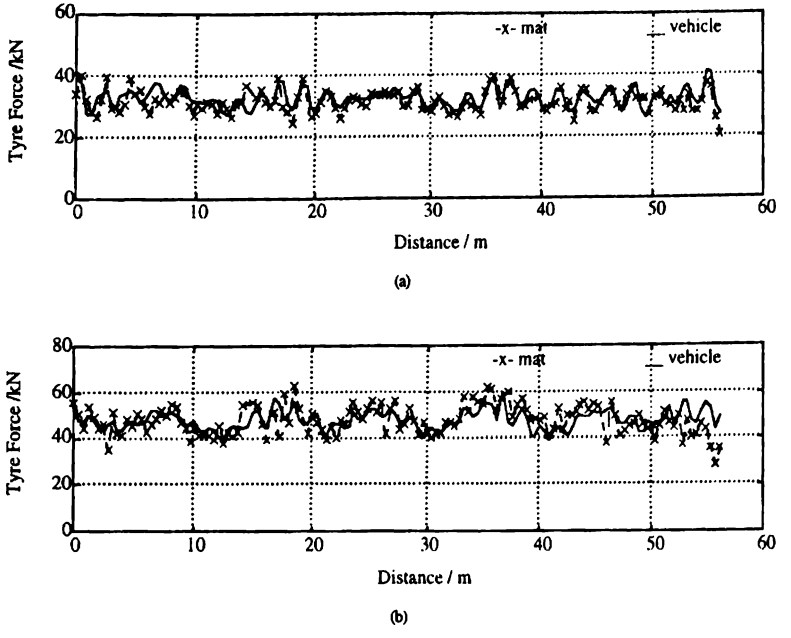


Fig. 18.11 Comparison of wheel forces measured by the mat and the instrumented vehicle travelling at 25 m/s. (a) Steer axle, (b) Drive axle. From [374].

Correction for Measurement Errors

To minimise the effects of the 5% average RMS sensor error, tyre force measurements from repeat runs at the same speed were averaged together before the aggregate force was calculated. There were nominally three repeat runs for each vehicle test speed.

The individual *SRI* points may be corrected for measurement errors by calculating the reduction in peak *SRI* using equation 18.15 with the noise to signal ratios calculated from equation 18.17. For three averaged tyre force measurements, the standard deviation of the sensor error is $\sigma_{\epsilon_j} = 5/\sqrt{3} = 2.9\%$. The noise-corrected *SRI* curve was therefore obtained by dividing each un-corrected *SRI* point by the corresponding reduction calculated from equation 18.15.

Effect of Speed

The effect of vehicle speed on spatial repeatability was investigated initially by calculating the *SRI* between the aggregate force history of a reference vehicle (vehicle number 1A) travelling at a reference speed of 22m/s, and aggregate force histories for the same vehicle (1A) travelling at speeds greater and less than the reference speed. The results (un-corrected for measurement errors) are

presented in figure 18.12, which shows that the *SRI* is 1.0 when the speed is the same as the reference speed (as expected), and less than 1.0 when the speed is different from the reference speed (22 m/s). Also shown in figure 18.12 (dotted line) is the noise corrected *SRI* curve and the 95th percentile confidence limits for a typical measurement point calculated from equation 18.18 (plotted as an error bar).

Figure 18.12 also shows the results of a simulation of the aggregate force *SRI* for a similar vehicle, from the theoretical study described in Section 18.3. The two results agree well throughout the speed range, although the theoretical results tend to over predict the *SRI* at higher test speeds and under predict the *SRI* at lower test speeds. This is probably due to differences between the vehicle model and the test vehicle.

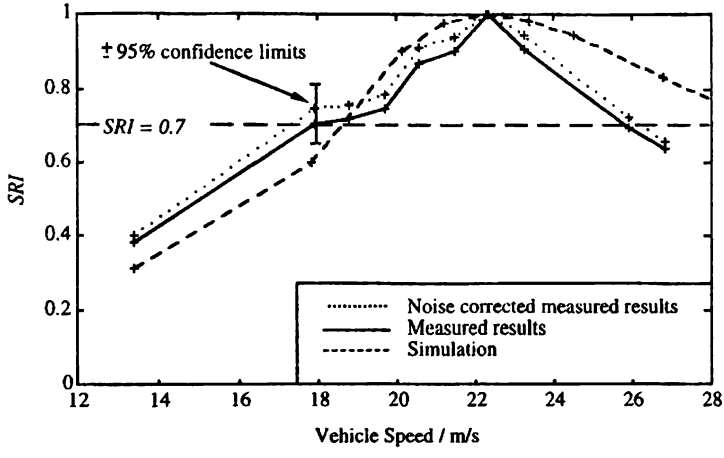


Fig. 18.12 Measured and predicted *SRI* values for vehicle 1A. From [130].

Effects of Vehicle Configuration

Figure 18.13 shows results (corrected for measurement errors) for vehicles 1A, 1B, 1C, 1D and 1E at various speeds, correlated with the reference vehicle (1A) travelling at the reference speed of 22 m/s. These vehicles all have the same tractor, with six different trailers (see Table 18.2). All the vehicles show a peak in corrected *SRI* near to the reference speed. The maximum *SRI* values range from 0.91 for vehicle 1C, to 0.63 for vehicle 1D. The threshold level of repeatability is shown in figure 18.13 by the horizontal dashed line at 0.7.

The theoretical study above showed that the dominant wavelength of the aggregate force history is the main factor in determining the correlation between vehicles. Vehicle 1D comprises a steel-sprung tractor and an air-sprung trailer. It is likely that the aggregate force history of this vehicle is not dominated by a single wavelength (see [120]), and therefore the correlation with the reference vehicle is low. All the other vehicles (steel-sprung trailers and a rubber-sprung trailer) are likely to have similar wavelengths to the reference vehicle and therefore have higher maximum SRIs.

Figure 18.14 shows the corresponding graph for vehicles 2A – 2E, using vehicle 2A at 22m/s as the reference (see Table 18.2). The corrected SRIs vary less with speed than for vehicles 1A–E (figure 18.13). The reason for this may be due to the combination of dissimilar suspensions on the tractor and trailer leading to the absence of a single dominant wavelength in the aggregate forces.

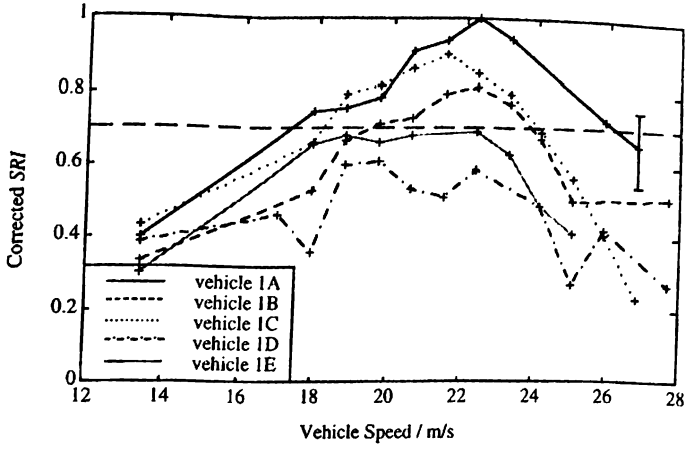


Fig. 18.13 *SRI* for vehicles 1A, 1B, 1C, 1D and 1E. Vehicle 1A is the reference vehicle. From [130].

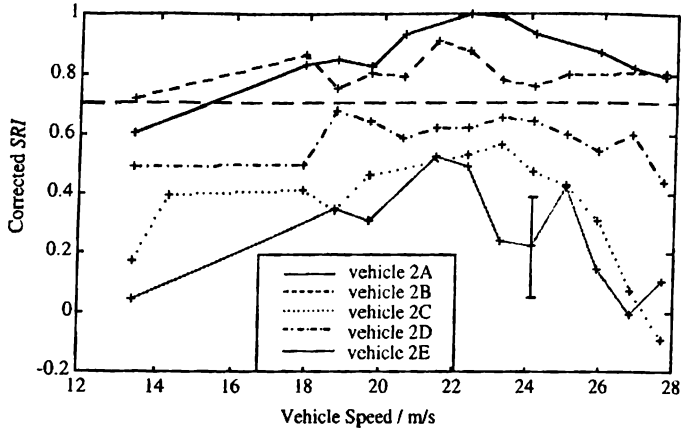


Fig. 18.14 *SRI* for vehicles 2A, 2B, 2C, 2D and 2E. Vehicle 2A is the reference vehicle. From [130].

Figure 18.15 shows the results for vehicles 3A, 3B, 3D, and 3E, using vehicle 3A at 22m/s as the reference (see Table 18.2). All the vehicle combinations shown in figure 18.15 (apart from the reference) display low repeatability. The tractor used in all these vehicle combinations (tractor 3) had a stiff tandem drive axle suspension with lightly damped axle pitch and body bounce modes of vibration. Possible causes of the low repeatability are: (i) poor correlation due to the high frequency tandem pitching mode and (ii) an increase in sensitivity to changes in the trailer suspension group, caused by the stiff tractor suspension.

Figure 18.16 shows corrected SRIs for the fourteen vehicles travelling at 19 m/s correlated with vehicle 1A also travelling at 19 m/s. The vehicles are ordered along the horizontal axis in descending order of correlation at this speed. The graph also shows the corresponding results for the speeds of 22 m/s and 26 m/s. In these cases, the reference vehicle is also 1A, travelling at 22 m/s and 26 m/s respectively.

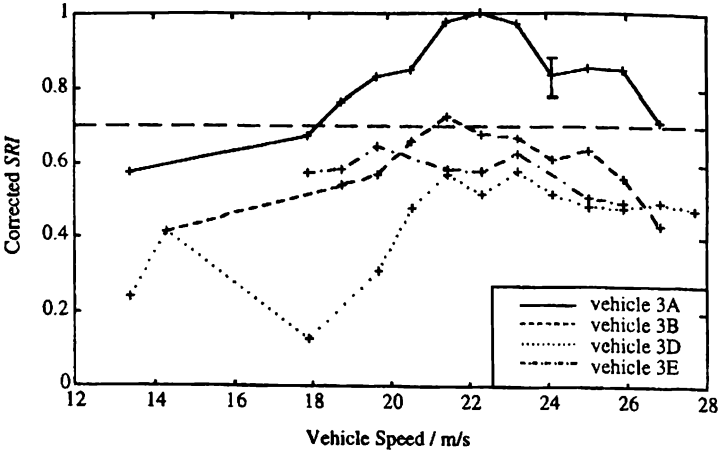


Fig. 18.15 *SRI* for vehicle 3A, 3B, 3D and 3E. Vehicle 3A is the reference vehicle. From [130].

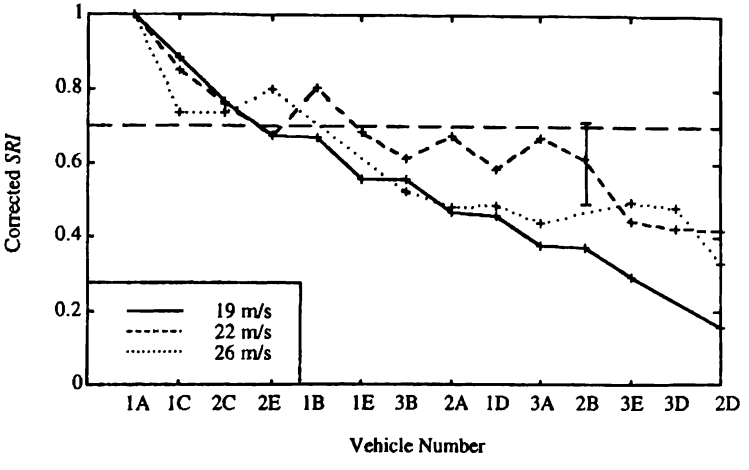


Fig. 18.16 Ordered *SRI* for all vehicles correlated with vehicle 1A travelling at different reference speeds. From [130].

For all three speeds the corrected *SRI* decreases as the vehicle becomes less similar to the reference vehicle. Most of the vehicles with the reference tractor (number 1) have relatively high corrected SRIs, and the vehicles most different to the reference vehicle tend to have low corrected SRIs. This is particularly evident for tractor 3, with its stiff tandem leaf spring suspension, and trailer D which has an air suspension.

Aggregate Fourth Power Force

Figure 18.17 shows the accumulated pavement damage caused by 140 aggregate 4th power force histories (equation 17.5, with n = 4) for the 14 different vehicles. Interpolation was used to estimate sensor forces where no reading was available. The results have been normalised by the

damage due to the static tyre forces alone (*ie* a value of one corresponds to the damage caused by the static axle loads of the 140 vehicle passes). Despite the wide range of vehicles and speeds used in this study, there is a dominant wavelength of approximately 8m in the aggregate fourth power force history. This wavelength is probably associated with the sprung mass modes of vibration of the vehicles. It agrees reasonably well with the 7m predicted in Section 18.3.3. The peak pavement damage is approximately 1.8 times that caused by the static loads alone.

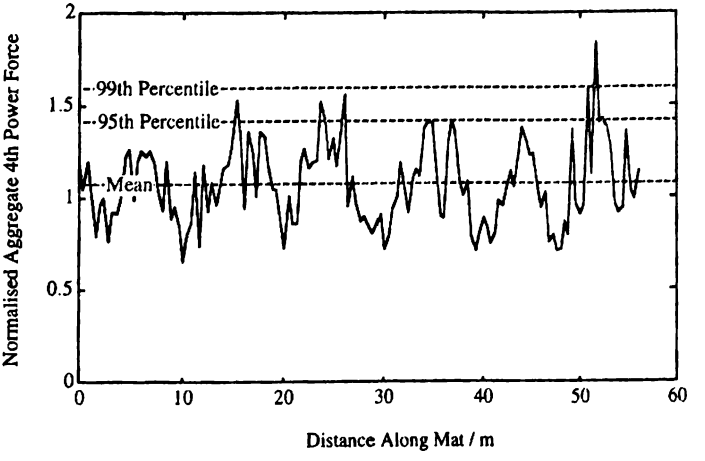


Fig. 18.17 Normalised aggregate 4th power forces for 140 vehicle runs. From [130].

The horizontal lines on figure 18.17 show upper percentile levels of A_k^4. The 95th percentile level of damage is 1.4 times the 'static damage' (due to the static loads alone). If it was assumed that there was no spatial repeatability (dynamic forces randomly distributed along the pavement), the damage would be uniformly distributed along the pavement at the mean level, which is 1.05 times the static damage. Spatial repeatability therefore caused a significant increase in the theoretical damage at some locations along the pavement surface by dynamic loads, even for the relatively smooth surface of the TRL test track and the diverse set of vehicles tested on the mat.

18.4.3 Phase II Tests

Results from the Phase I tests verified that theoretical predictions of spatial repeatability for individual vehicles agreed relatively well with experimental results. However, the fleet of vehicles used during the Phase I tests may not have been typical of the distribution of vehicles in mixed traffic and so the results did not provide information about spatial repeatability on the highway. Consequently, a second set of tests were conducted on a section of highway in the normal flow of traffic. The following section describes the installation, calibration and operation of the Phase II tests and investigates the spatial repeatability of the measured tyre forces.

Installation

The Phase II tests were performed in June 1992 on the south-bound carriageway of the A34 trunk road near Oxford, just north of the A44 junction. The mat was installed in a 'lay-by' situated along a straight section of jointed-concrete pavement. The installation procedure was similar to that used for the Phase I tests with the addition of one extra mat tile giving a total of 144 sensors, and an overall instrumented length of 57.6m. The installation used 12 screws per tile. A tapered strip of rubber was also laid along the offside edge of the mat to reduce the danger to motorcyclists from the 12mm

thick longitudinal step along the mat. The surface of the lay-by was relatively smooth, and as a result, the vehicles passing over the mat were expected to generate small dynamic tyre forces. Installing the mat and all instrumentation took seven workers approximately 30 hours, and was completed within three days.

As before, data logged by the Golden River Marksman M600 data-loggers was transferred by serial communications lines to a personal computer. Separate files were produced for each minute or so of traffic (between one to ten vehicles, depending on the concentration of traffic). In the subsequent data reduction, individual vehicles were extracted from these files. Figure 7.6 shows the completed mat installation. The data-loggers can be seen on the footpath, and the caravan containing the personal computer can be seen in the distance, at the upstream end of the mat.

In order to classify the vehicles, a video record of the tests was compiled. Three video cameras were installed, two for vehicle identification purposes, and one which acted as a 'black box' recorder of the entire site, in case of an accident. One vehicle identification camera was positioned next to the mat at the beginning of the sensor array, 1m above ground level, pointing towards oncoming traffic in order to record vehicle licence plates. The other was sited directly along the line of the mat beside the caravan in order to assess the accuracy with which the tyres tracked along the mat. Two researchers recorded vehicle suspension types as vehicles passed over the mat, for use in later analysis. After the tests, a database of the vehicles passing over the mat was compiled, containing the test time, configuration, suspension type *etc*, in order to provide a link-up with the data recorded by the load measuring mat.

To restrict traffic flow as little as possible, both lanes were kept open. An elaborate arrangement of traffic cones and signs was devised to ensure that trucks used the inside lane containing the mat, and all other vehicles used the outside lane. The traffic cones were also used to restrict the lane width over the site to ensure that all truck tyres tracked along the centreline of the mat. The vehicle speed limit was set to 18m/s (40mph) over the test site for safety reasons. To avoid congestion (the A34 is the main route from Oxford to Birmingham), testing only took place on Tuesday to Thursday from 10.00am–4.00pm.



Calibration

In the Phase II tests, the mat was tested for only three days on a public highway, so there was less opportunity to gather calibration data than in the Phase I tests. The sensors in the mat were calibrated using the measured static loads from a two-axle rigid vehicle provided by TRL. The TRL vehicle had steel springs fitted to both axles and the static loads were measured using on-board instrumentation. The TRL vehicle was driven over the mat eight times at speeds varying from 2m/s to 6m/s. The number of calibration runs was restricted by the traffic on the highway. Between calibration runs the instrumented vehicle had to travel around two junctions of the A34 (each circuit took approximately 20 minutes). The sensors were calibrated using the static loads from the four least dynamic steering axle passes, and two of the least dynamic drive axle passes. This gave an average RMS sensor error of 7.5%. This can be compared to an average RMS error of 5% found during the Phase I tests. It is reasonable to assume that if more calibration runs had been possible, the RMS error would have been reduced to the previously measured level of accuracy (5%).

A typical force history measured with the mat during the A34 tests is shown in figure 18.18. The axle load shown is for the last axle of a three axle articulated vehicle fitted with steel suspensions, travelling over the mat at a speed of 15m/s. The effects of vehicle dynamics are clearly visible.

Of the 144 sensors in the mat, 13 were unplugged during operation, as they were either not operating, or noisy. (This problem was thought to be caused by damage during transit.) During three days of testing, approximately 20 Megabytes of data were collected.

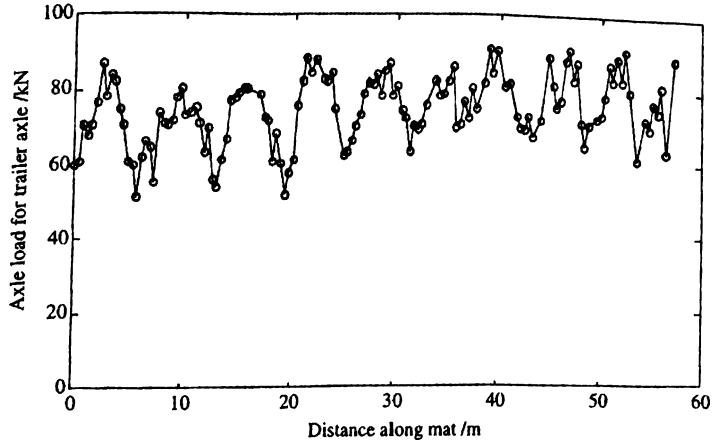


Fig. 18.18 Force history of the trailer axle of a three axle articulated vehicle. From [375].

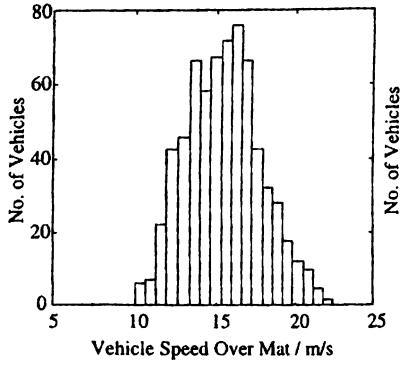


Fig. 18.19 Vehicle speeds tested over mat, [130].

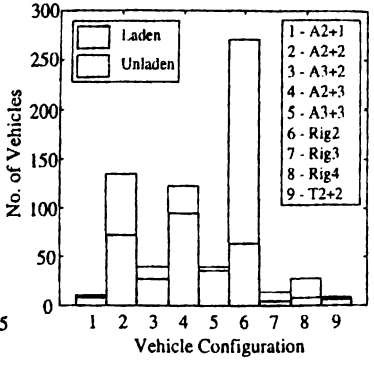


Fig. 18.20 Measured vehicles by type, [130].

Operation

Figure 18.19 shows the distribution of measured speeds of the vehicles passing over the mat (ignoring vehicles travelling at crawling speed). The average speed was around 15m/s. This is significantly lower than the 18m/s limit because of the narrow spacing between the rows of cones forming the traffic lanes.

During the three days of testing, approximately 1500 vehicles passed over the mat. About half of these vehicles travelled over the mat at crawling speed owing to congestion that the mat inevitably caused. However, about 700 vehicles were recorded at speeds over 10m/s. A detailed breakdown of these vehicles by vehicle class is shown in figure 18.20. This figure also divides the vehicle categories into laden and unladen. In order to classify vehicles as laden or unladen, the unladen weight of each vehicle was estimated. This was compared with the maximum legal limit for the vehicle class, to enable the transportable load to be estimated. A vehicle was classified as unladen if it was carrying less than half its legal transportable load. Over half the vehicles recorded were articulated ('A' in the key), the largest categories being two axle tractors with tandem axle trailers

(A2+2) and two axle tractors with tri-axle trailers (A2+3). Most of the remaining vehicles were two-axle rigids (Rig2) with the remainder consisting of three and four axle rigids (Rig3 and Rig4) and truck-full-trailer configurations (T2+2).

Figure 18.21 shows the gross vehicle weight distribution for all the articulated lorries. It can be seen from this figure that gross vehicle weights for the A2+3 vehicles are grouped around two distinct bands, one at 150kN, and the other at 360kN (corresponding to unladen and laden conditions respectively) whereas the corresponding curve from the A2+2 vehicles shows only one distinct peak at 120kN, which tapers off at higher weights. This is thought to be due to differences in the type of cargo carried by the two vehicle types. The 5-axle articulated vehicles are likely to be used to carry mass-limited cargo whereas the 4-axle articulated vehicles are more likely to be used to carry bulk-limited cargoes. Further information about the static loads of vehicles measured in these tests can be found in [375].

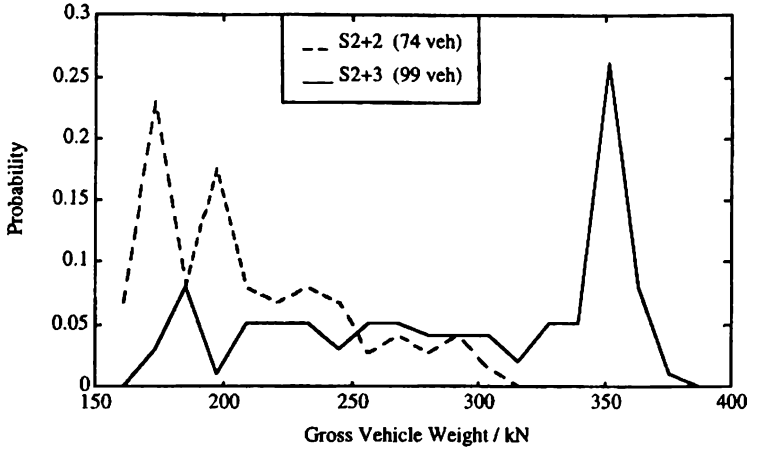


Fig. 18.21 Gross vehicle weight distribution for all articulated vehicles. From [130].

Determination of the Reference Vehicle

To determine the reference vehicle from a number of aggregate force histories measured using the load measuring mat, a matrix of SRIs was determined using each vehicle in turn as the reference vehicle, for example considering n vehicles:

$$SRI_{ij} = \begin{bmatrix} SRI_{1,1} & SRI_{1,2} & \cdots & SRI_{1,n} \\ SRI_{2,1} & SRI_{2,2} & & \vdots \\ \vdots & & \ddots & \vdots \\ SRI_{n,1} & & \cdots & SRI_{n,n} \end{bmatrix} \quad (18.20)$$

Note that all the SRIs on the leading diagonal are 1, and the matrix is symmetric $\left(\text{ie } SRI_{ij} = SRI_{ji}\right)$. The number of vehicles in each row (or column) with SRIs greater than the threshold repeatability level of 0.7 was then calculated. The reference vehicle was then chosen to be the vehicle corresponding to the row (or column) with the greatest number of repeatable vehicles.

Comparison with Theoretical Predictions

Figure 18.22 shows the SRIs for the 4-axle semi-trailers with steel suspensions on both the tractor and trailer, measured using the mat. As before, the SRIs were corrected for measurement errors by

dividing the un-corrected SRIs by the corresponding reductions in peak *SRI* calculated using equations 18.16 and 18.17. The reference vehicle was determined using the method described above. However, it was found that when the average sensor error of 7.5% RMS was used, the corrected SRIs were too high, with some vehicles having values greater than 1. Consequently, an average sensor noise level of 5% RMS (calculated from the Phase I tests) was used to correct the *SRI* values in figure 18.22 and the other Phase II test results. This is likely to give a conservative estimate of the proportion of vehicles showing repeatability.

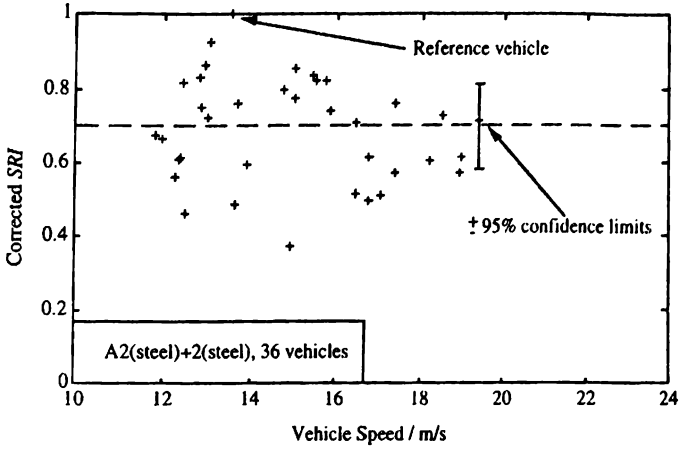


Fig. 18.22 Repeatability for 4-axle articulated vehicles with steel tractor and trailer suspensions. From [130].

It can be seen from figure 18.22 that the proportion of vehicles above the threshold repeatability level is 53% which may be compared to the 67% estimated for similar vehicles in the theoretical study (Section 18.3). The difference between the measured and predicted repeatability is most likely due to differences between the simulated and measured fleet of vehicles.

Repeatability within Vehicle Classes

Figures 18.23-18.25 show the corrected SRIs for the 3 major classes of vehicles measured using the mat; 4-axle semi-trailers (A2+2), 5-axle semi-trailers (A2+3) and 2-axle rigid vehicles (Rig2). The vehicles within each major class have also been sub-divided according to the type of suspension on the trailer unit (*eg* A2+2(air) refers to air suspension on the trailer). The reference vehicle for each sub-class was chosen using the procedure detailed above .

The proportion of vehicles having corrected SRIs above the threshold level determined from figures 18.22-18.24 was: 49% A2+2(steel), 49% A2+2(air), 35% A2+3(steel), 38% A2+3(air) and 37% Rig2. The proportion of repeatable vehicles in each group is generally high because there is a single dominant wavelength component in all the aggregate force histories due to the sprung mass modes of vibration of the vehicle. However, the characteristic shape of the corrected *SRI*-speed curve seen in figure 18.12 for a single vehicle is not evident from figures 18.23-18.25. This is because the effects of vehicle differences within a given class (*eg* axle spacing, suspension characteristics, gross vehicle weight *etc*) are much greater than the variations produced by speed differences alone.

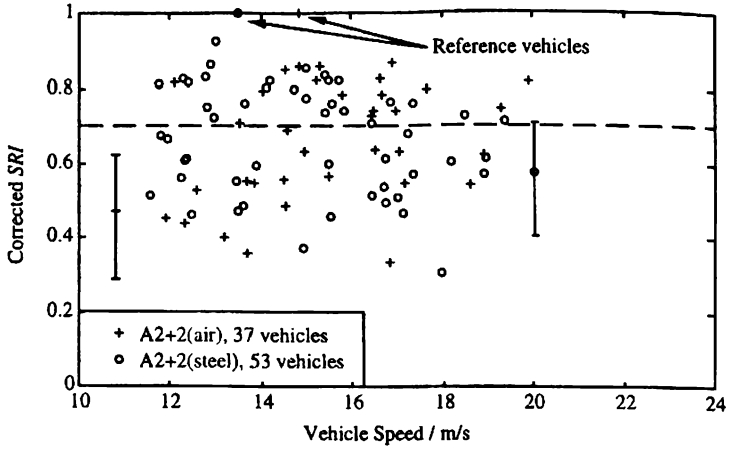


Fig. 18.23 Repeatability for 4-axle articulated vehicles. From [130].

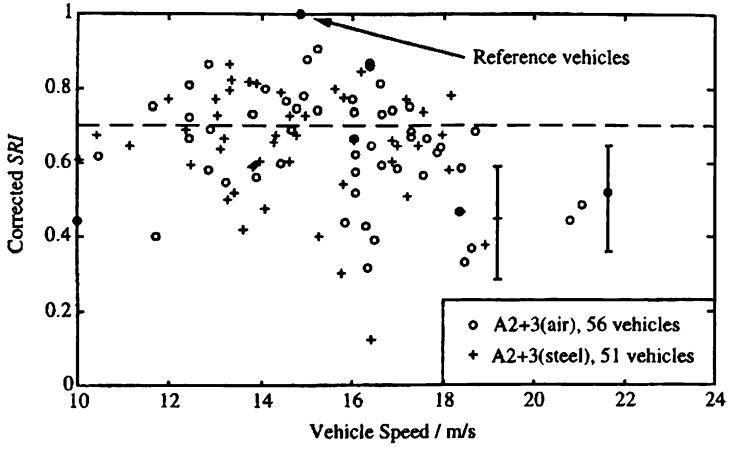


Fig. 18.24 Repeatability for 5-axle articulated. From [130].

It can also be seen from these figures that the proportion of repeatable vehicles is lower for the 5-axle (A2+3) articulated vehicles than for the 4-axle (A2+2) articulated vehicles. This is probably due to the differences between the gross vehicle weight distributions for the two classes of vehicle (shown in figure 18.21).

Repeatability for all Vehicles

Figure 18.26 shows the corrected SRIs for all the vehicles measured with the mat (including 2-axle rigid vehicles). The reference vehicle was a 2-axle rigid vehicle travelling at 16.5m/s (chosen using the procedure detailed above). This vehicle was correlated with all other vehicles, both articulated and rigid. From this figure, it can be established that 42% of all vehicles showed corrected SRIs above the threshold level.

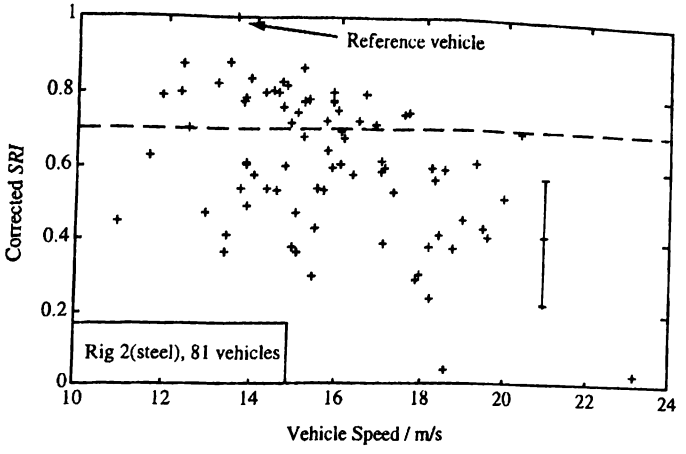


Fig. 18.25 Repeatability for 2-axle rigid vehicles. From [130].

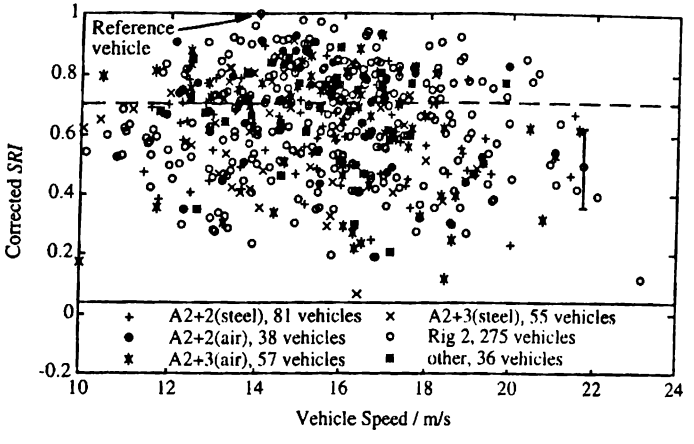


Fig. 18.26 Repeatability for all vehicles including 2-axle rigid vehicles. From [130].

Aggregate Fourth Power Force

Figure 18.27 shows the accumulated pavement damage caused by the 542 aggregate fourth power force histories for the same vehicles shown in figure 18.26. Interpolation has again been used where no sensor reading was available and the results have been normalised by the damage due to the static tyre forces alone. The dominant wavelength of 8m found from the Phase I data (figure 18.17) is not as strongly present in this data. This is probably due to the diversity of the vehicles included in figure 18.27 and additional sensor noise in the Phase II tests. The peak damage is approximately 2 times that caused by the static loads alone. Also shown in figure 18.27 are the 95th, 99th percentile and mean damage levels. If it was assumed that there was no spatial repeatability, the damage would be uniformly distributed along the pavement at the mean level, which is 1.1 times the static damage.

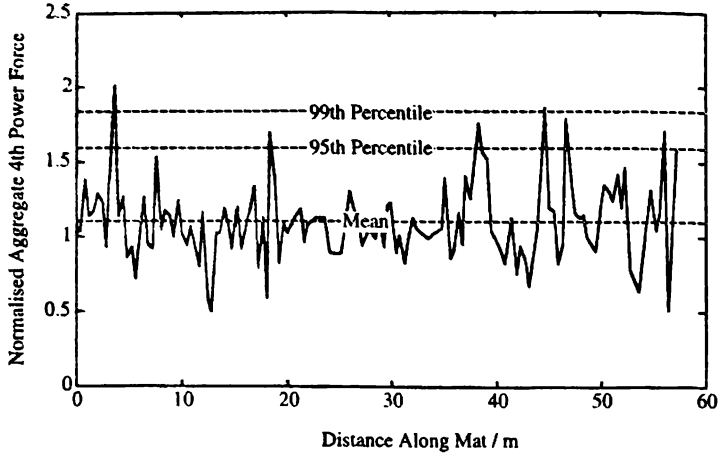


Fig. 18.27 Normalised aggregate 4th power forces for all vehicles including 2-axle rigid vehicles. From [130].

However, the upper percentile levels of the aggregate fourth power force are strongly influenced by the accuracy of the few sensor readings in the most heavily loaded areas. Consequently, the reliability of these upper percentile levels is likely to be lower than the reliability of the *SRI* which relies equally on all the sensor readings (see equation 18.12).

18.5 CONCLUSIONS

(i) A fleet of leaf-sprung articulated vehicle models was created from a validated simulation. Calculated tyre force histories were used to investigate spatial repeatability of tyre forces.

(ii) The correlation coefficient between aggregate tyre force histories (otherwise known as the Spatial Repeatability Index - *SRI*) is a convenient measure of repeatability, a suitable threshold value being 0.707.

(iii) The average sprung mass mode frequency and vehicle speed are significant in determining the spatial distribution of aggregate tyre force for leaf-sprung articulated vehicles.

(iv) From the theory it was estimated that approximately two-thirds of *four-axle leaf-sprung heavy articulated vehicles* may contribute to a repeated pattern of road loading.

(v) The results of the Phase I experiments largely confirmed the theoretical predictions of the influence of speed on spatial repeatability of aggregate tyre forces.

(vi) The Phase II tests indicated that approximately half of *all* vehicles tested on the A34 in the normal flow of traffic were found to contribute to a spatially repeatable pattern of loading.

(vii) The implication of conclusion (vi) is that fatigue failure of pavements is likely to be governed by peak dynamic forces at specific locations along the road. Any measure of dynamic loading performance should consider these peak forces rather than average dynamic forces.

19

ROAD-DAMAGING POTENTIAL OF MEASURED DYNAMIC TYRE FORCES

19.1 SUMMARY

The measured dynamic wheel loads generated by fourteen articulated vehicle configurations (3 tractors with 5 trailers) are assessed in terms of a variety of road damage criteria. The results are used to investigate the effects of vehicle configuration, vehicle dynamics, speed, road strength, and road damage criteria on the relative theoretical road damage caused by the vehicles. Conclusions are drawn about tests for measuring and assessing the road-damaging potential of heavy lorries.

The dynamic tyre forces generated by approximately 700 heavy goods vehicles (HGVs) *on a highway* were analysed to investigate the relative road damaging potential of the various classes of vehicles. Air suspensions were found to be more effective at static load equalisation than steel suspensions. Two criteria were used to rank *axle-groups* in terms of road damage: the average dynamic load coefficient, and the 95th percentile aggregate fourth power force. These criteria were found to rank *axle-groups* in different orders, due to spatial correlation between tyre forces. On average, *air suspended* vehicles were found to generate smaller dynamic loads and hence less road damage than *steel suspended* vehicles. However, some air suspensions with inadequate suspension damping were found to generate high dynamic loads and consequently high levels of road damage.

This chapter is based on work previously published in [93, 374, 375]

19.2 INTRODUCTION

One way to reduce road damage due to heavy vehicles is to introduce regulations which encourage the use of 'road-friendly' suspensions, which generate lower dynamic tyre forces [118, 210]. Although such regulations do exist in limited form, current assessment and testing procedures have serious deficiencies, because they are based on various vehicle response criteria which are not directly related to *road damage*. (Vehicle assessment is discussed in Part 7).

It is important that a vehicle assessment procedure should account for all of the important vehicle and road factors [96]. To achieve this, it is necessary to devise a testing procedure which ranks vehicles in terms of their road-damaging potential. It is not possible to measure road damage directly, but it is possible to measure dynamic tyre forces, then to use some of the approaches described in Chapter 17 to estimate road-damage - at least for the purposes of *ranking* vehicles. This is thought to be one practical way to assess the road-damaging performance of vehicles [96, 118].

Before such a vehicle performance test can be introduced, several important, detailed questions must to be resolved:

(i) Does the ranking of vehicles in terms of road damage depend on the strength of the road?

(ii) Is it necessary to process dynamic tyre forces with a theoretical road response/damage model, or can vehicles be ranked correctly using simplified criteria based directly on measured dynamic tyre forces?

(iii) Does every tractor/trailer combination have to be tested as a coupled unit, or is it possible to rank suspension performance by testing all tractors using a standard trailer, and all trailers using a standard tractor?

(iv) Can the road-damaging qualities of a suspension be assessed by measuring the loads generated by individual axle groups, or is it necessary to examine the road damage done by the whole vehicle?

The main aim of the research described in the *first* part of this chapter was to answer these questions, using experimental measurements of the dynamic tyre forces generated by a representative sample of UK articulated vehicles.

Previous experimental studies of dynamic tyre forces were performed under controlled conditions using specially prepared heavy vehicles, with instrumented axles (see [96]). Most of these instrumented vehicles were tested on test tracks [214, 302, 337, 505], although some were tested on public roads [443]. This approach has the advantage of relative simplicity and low cost when testing a small number of vehicles. The researchers generally concluded that soft, hydraulically damped suspensions (air or torsion bar) generate lower levels of dynamic forces than stiff suspensions with friction (steel leaf springs). Consequently, they inferred that air and torsion bar suspensions are more *road friendly*.

There are two main deficiencies of the previous research:

(i) The studies investigated a limited number of well maintained (or new) suspensions, under artificial conditions. The results cannot necessarily be extrapolated to the operation of typical vehicles on the highway.

(ii) Because of the difficulty and expense of the instrumentation systems, many of the previous studies only examined the dynamic forces generated by one instrumented axle. They therefore ignored the dynamic interaction between axles.

The research described in the *second* part of this chapter examined the dynamic tyre forces generated by many heavy vehicles, under highway conditions, in order to assess the influence of suspension design. It was considered to be important to record the tyre forces generated by *all* axles of the vehicles, and to use realistic road damage criteria.

The experimental data analysed in this chapter was collected during the 'Phase I' and 'Phase II' experiments described in the previous chapter (Sections 18.4.2 and 18.4.3).

19.3 PHASE I TESTS

19.3.1 Methodology

The Phase I tests involved controlled measurements on 14 different articulated vehicle combinations, using the load measuring mat on the TRL test track (see Sections 18.4.2). Two different approaches were used to compare the road-damaging effects of different vehicles: (i) analysis of aggregate force as per equation 17.5; and (ii) 'single-vehicle-pass' road damage calculations as described in Section 17.4.2. Damage was assessed for each tractor unit alone, for each trailer unit alone, and for each vehicle combination.

19.3.2 Details of the Single-Vehicle-Pass Model

Road Structure Models

The road response calculation used the 'influence function' formulation, equation 10.21. This includes the effects of vehicle speed and variation of load magnitude, but not the effects of the frequency of the applied dynamic loads on dynamic pavement response. All primary response

influence functions were generated using a modified version of the VESYS IIIA pavement model [277].

Fatigue Damage Model

The general form of the asphalt fatigue damage model was based on a power law relationship like equation 13.1, with the value of k_1 and k_2 taken from the literature [72]: $k_1 = 10^{-12}$ cycles, $k_2 = 4$. The same power was used in one of the aggregate force calculations.

The 'rainflow' method [187] was used to convert the strain time history at each point along the road into N_ε equivalent single strain cycles. Accumulation of fatigue damage due to passage of the vehicle was then calculated using Miner's hypothesis for accumulation of fatigue damage (equation 17.7).

Permanent Deformation Model

The rutting calculation (vertical permanent deformation), was based on a linear viscoelastic model, using the elastic–viscoelastic correspondence principle as described by equation 14.7.

Influence functions for the rates of permanent vertical surface displacement were calculated using an elastic layer calculation (VESYS IIIA), with the elastic modulus E for each road layer replaced by its viscous equivalent λ. Permanent deformation was restricted to shear flow in the surface layer only, by assuming Poisson's ratio to be 0.5, and the equivalent viscosities of the lower layers to be infinite. The equivalent asphalt mix viscosities λ were obtained using the procedure described in Section 14.4.

Road Model Parameters

Four different road models were used in the study – two for the fatigue analysis and two for rutting. The parameters were chosen to represent weak and strong roads. Each model had three layers: asphalt surface, subgrade and base. The layer moduli were the same for each model, but the layer thicknesses were different. The model parameters are listed in Table 19.1.

	Fatigue model		Rutting model		Layer thickness	
Pavement Layer	Young's Modulus E (MPa)	Poisson's Ratio v	Uniaxial Viscosity λ (MPa s)	Poisson's Ratio v	'Weak' road (mm)	'Strong' road (mm)
Surface	Variable*	0.4	60	0.5	110	320
Base	125	0.3	5620	0.5	150	300
Subgrade	50	0.4	5620	0.5	∞	∞

Table 19.1 Parameters of the road surface primary response models.

* The surface layer elastic modulus varied from 11,000 to 15,000 MPa depending on vehicle speed.

Damage Statistics

The results of the investigations of 'spatial repeatability' described in Chapter 18 indicated that approximately half of the vehicles recorded on the mat in the Phase II (highway) tests contributed to a spatially repeatable pattern of loading. This means that some locations along the road surface are likely to incur much higher levels of damage than the average. Assuming that dynamic wheel loads are repeatable in space, it is logical to assess vehicle performance by considering the damage incurred at these most heavily damaged locations along the road. Thus the 95th percentile level of the road damage criterion of interest (aggregate forces, fatigue or permanent deformation) was used in this study as a measure of road damage.

19.3.3 Effect of Static Loads and Speed on the Road Damage Models

Figure 19.1 shows rutting damage due to the *static* axle loads of each vehicle plotted against speed, and figure 19.2 shows a similar graph for fatigue damage. For both models, the road damage decreases with speed due to reductions in primary pavement responses, caused by viscoelastic effects. This is typical for asphalt pavements (see Chapters 14 and 17). Over the speed range of interest, rutting damage decreases at a faster rate than fatigue.

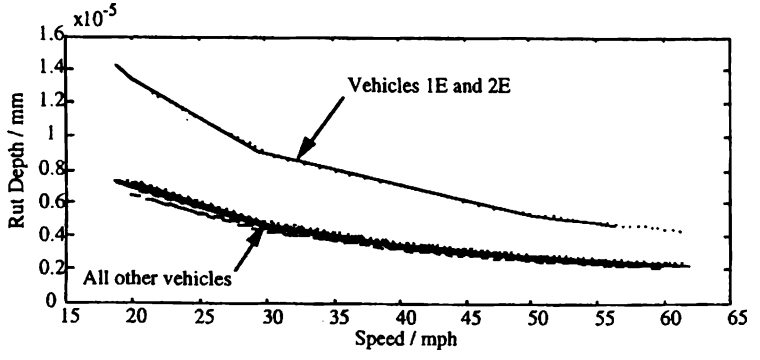


Fig. 19.1 Theoretical rutting damage to the strong road, due to the static loads of the test vehicles, as a function of speed. From [374].

For the viscoelastic permanent deformation model (Chapter 14), rutting damage is governed by the gross vehicle weight. This is shown by the close grouping of most of the curves in figure 19.1. These vehicles were all loaded to the same nominal weights, and all had the same axle and tyre configurations. Vehicles 1E and 2E cause significantly greater damage than the rest because the triaxle trailer (E): (i) carried a higher total load, and (ii) was equipped with wide single tyres, which are known to be more damaging than dual tyres carrying the same static load (see Chapter 17).

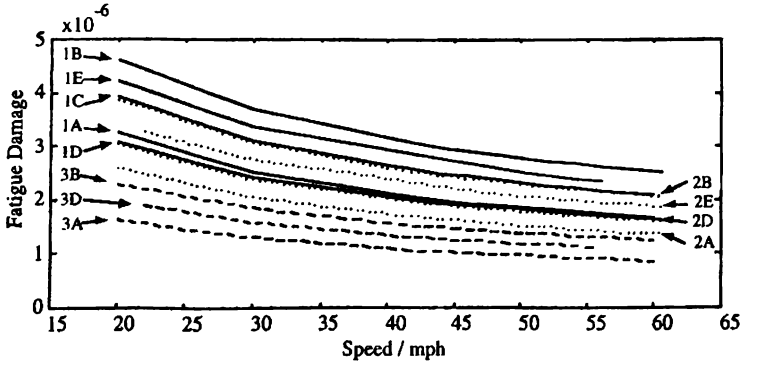


Fig. 19.2 Theoretical fatigue damage to the strong road, due to the static loads of the test vehicles, as a function of speed. From [374].

Fatigue damage is governed by individual axle loads, rather than gross vehicle weight [96, 192]. The wide variation between the individual damage curves in figure 19.2 is due to differences in the

static axle loads of the test vehicles. The damaging effects of the wide single tyres on trailer (E) are not as obvious as for rutting (figure 19.1), because the three axles in the triaxle group carry lower static loads than the two axles in the tandem groups on the other trailers. This accounts for the two vehicles 1E and 2E causing relatively less fatigue damage than rutting damage.

19.3.4 Effects of Damage Criteria and Speed

Rutting and Aggregate First Power Forces

Plotting the theoretical 95th percentile rut depths for the *dynamic* wheel loads of vehicles 1A–1E yields a graph which is hardly distinguishable from figure 19.1, for the *static* wheel loads (see [374]). The dominant factors are the sensitivity of the road response model to speed, and to a lesser extent the tyre type, as well as the gross vehicle weight, just as for the case of the static loads. Dynamic loads have very little effect on rutting damage. Consequently it is difficult to distinguish between vehicles, and there is no significant change in the ranking of various vehicles with speed.

Figures 19.3 shows the 95th percentile level of the aggregate first power forces A_k^1 plotted against speed, for tractor 1 with all trailers (combinations 1A–1E). Similar graphs for tractors 2 and 3 can be found in [374].

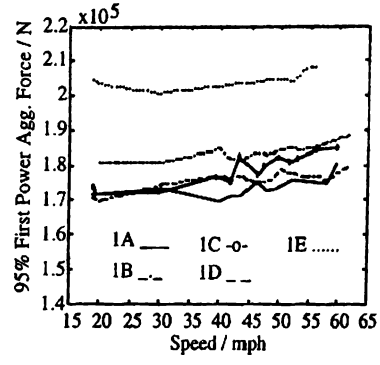


Fig. 19.3 95th percentile aggregate first power forces for vehicles 1A, 1B, 1C, 1D and 1E as a function of vehicle speed. From [374].

The aggregate first power force damage criterion does not account for road response effects, or tyre types. In the absence of vehicle dynamics, the aggregate damage would remain constant at a value equal to half of the gross vehicle weight (the mat measured the forces generated by the wheels along one side of the vehicle only), independent of speed. The shallow slope of the curves indicates a small increase of vehicle dynamics with speed. The curves would be steeper if the road surface was rougher [93].

Vehicle 1E generates the highest aggregate forces because it has the highest gross weight. The vehicles generally rank in the same order for each speed, however, vehicle 1C can be seen to cause more damage relative to other vehicles at higher speeds. This is because the rubber 'walking-beam' suspension on the trailer generates large dynamic loads, and is the most sensitive to speed.

Comparing figures 19.1 and 19.3 illustrates the importance of road response on the damage criterion. Although both the rutting and aggregate first power forces are proportional to the applied loads, rutting damage can be seen to decrease with speed due to decreasing road response, whereas aggregate first power forces increase with speed due to increasing dynamic loads.

Fatigue and Aggregate Fourth Power Forces

Theoretical 95th percentile fatigue damage due to dynamic loads, is plotted as a function of speed for the 'strong' road in figure 19.4. The effect of speed on the road response model is again the dominant factor controlling variation of road damage, although dynamic loads have a significant effect, especially for vehicles incorporating tractor unit 3 (not shown - see [374]). The general trend is towards road damage decreasing with speed, because the decreasing primary road response overcomes the increasing magnitude of dynamic tyre forces with speed. It should be recognised, however, that this result is strongly dependent on the amplitude of the dynamic loads and the assumptions incorporated in the pavement response model. For rougher roads the increase in dynamic loads with speed may outstrip the decrease in pavement response, so that fatigue damage will increases with speed [93, 192] (see Figure 17.18).

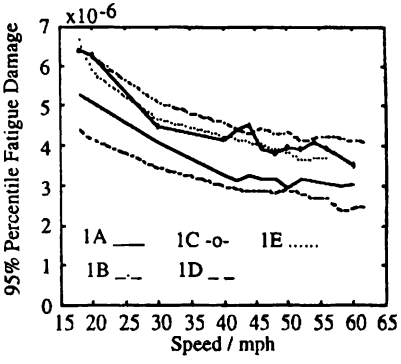


Fig. 19.4 95th percentile theoretical fatigue damage to the strong road for vehicles 1A–E as a function of vehicle speed. From [374].

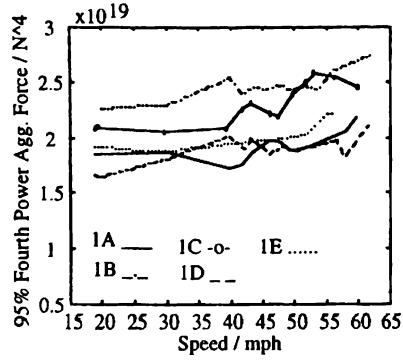


Fig. 19.5 95th percentile aggregate fourth power forces for vehicles 1A–E as a function of vehicle speed. From [374].

Figures 19.5 shows the 95th percentile aggregate fourth power force A_k^4 plotted as a function of speed for the same vehicles as figure 19.4. This graphs is similar to the first power plots (figure 19.3), although the steeper slopes indicate that the fourth power criterion is more sensitive to dynamic load level and hence vehicle speed.

For most speeds, the vehicles rank in similar orders for both the fatigue criterion (figure 19.4) and the aggregate fourth power forces (figure 19.5). One exception is vehicle 1E, which has the triaxle trailer with wide single tyres. This trailer causes relatively more damage according to the fatigue criterion than the aggregate fourth power criterion, because of the higher tyre contact pressures.

The main difference between the two damage criteria is caused by the effect of road response: fatigue damage tends to decrease with speed, but aggregate fourth power force damage increases with speed.

In summary:

(i) If vehicle assessment requires absolute values of road damage and/or its dependence on speed, tyre types and axles spacings; then it is necessary to assess vehicle loads with road damage criteria that incorporate road response calculations.

(ii) The dominant factors in rutting damage (and the aggregate first power forces) are vehicle speed and gross vehicle weight: dynamic tyre forces do not have a significant influence. Dynamic forces are much more important in fatigue damage.

As a consequence of (ii), rutting damage and aggregate first power forces will not be considered further in this chapter.

19.3.5 Effect of Road Strength

In [374], fatigue damage calculations are performed for the 'weak' road as well as the 'strong' road It is shown that although the absolute road damage is several orders of magnitude more for the weak road than the strong road, the variation with speed is similar and there is very little difference in the ranking of the vehicles at each speed. Similar results were obtained for all vehicle combinations and for rutting damage. This agrees with previous results by Gillespie et al [192].

Note, however, that in the long term, the mode of failure of 'weak' and 'strong' roads may be different. It is likely that 'weak' (thin) asphalt roads will fail by fatigue and strong (thick) asphalt roads will fail by permanent deformation, with very little fatigue damage (see Chapter 20). In this scenario, the correct ranking for vehicles on the 'strong' road should probably be that for permanent deformation, which will be different to the ranking for 'weak' roads - which would be for fatigue.

19.3.6 Normalised Results

In figures 19.6 to 19.9, the road damage level plotted is normalised *by damage due to the static axle loads of the vehicle at the corresponding speed.* This isolates the effects of vehicle dynamics, and removes the influences of: (i) primary pavement response variation with speed and (ii) static load levels. This normalisation allows direct comparison of rutting damage with the aggregate first power force criterion; and fatigue damage with the aggregate fourth power force criterion. Damage data on the plots are grouped into average results for three speed bands: 35–45mph, 45–55mph and 55–65mph.

Results for Tractor Units

Figures 19.6 and 19.7 show the fatigue damage and the aggregate fourth power forces calculated from the forces generated by *tractor axles alone.* The levels of normalised 95th percentile damage are similar for both criteria, and approximately 1.5 to 2 times the static values.

An important feature of figures 19.6 and 19.7 is that the damage done by each tractor is almost the same, whichever trailer is attached. Thus tractor 3 can be seen to generate the largest normalised road damage for all of the trailers, when assessed by any of the four damage criteria. Similarly tractor 2, which has an air suspension on the drive axle, can be seen to generate slightly lower damage than tractor 1 (steel drive axle suspension) for all trailers.

There are some small differences between the response of the tractors with the various trailers, however the trailers affect the tractor results in essentially the same way (*ie* the tractors rank in the same order) for both the fatigue and aggregate fourth power force criteria, in each of the speed ranges. An exception is vehicle 3E, which shows relatively higher aggregate fourth power forces than fatigue damage. This is thought to be caused by the effects on pavement strain response of the closely spaced tandem drive axles of tractor 3, combined with a relatively lower static load on the tractor drive axle group when triaxle trailer E is attached, than for the other (tandem axle) trailers.

Note also that the air suspended trailer D causes *all tractors to generate slightly higher damage,* for both criteria. This is thought to be due to a trailer pitch vibration mode which causes high dynamic loads to be applied to the tractor fifth wheel coupling.

In summary:

(i) The normalised fatigue damage of vehicles *with similar arrangements of axles and tyres,* can be assessed using the simple aggregate fourth power force criterion

(ii) To an acceptable level of accuracy, the suspensions of tractor units can be assessed with any trailer attached. In order to minimise the small variations in theoretical road damage with trailer type, apparent in figures 19.6 and 19.7, it would be advisable to use a standard trailer for testing all tractors.

Results for Trailer Units

Figure 19.8 shows the fatigue damage plotted for the trailer units alone, with various tractors attached. The aggregate fourth power forces were found to be similar to the fatigue damage and are not shown (see [374]). The normalised fatigue damage takes values in the range 1.5–2.5.

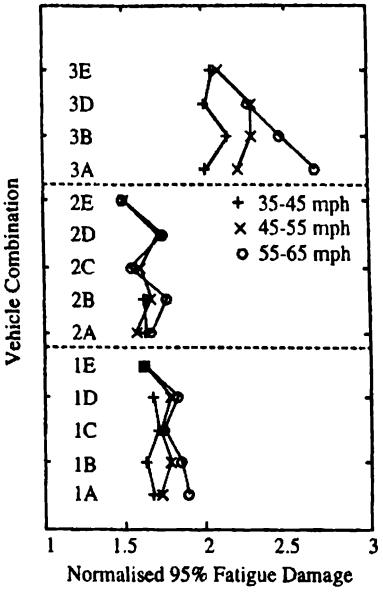


Fig. 19.6 Normalised 95th percentile fatigue damage to the strong road for tractors alone. From [374].

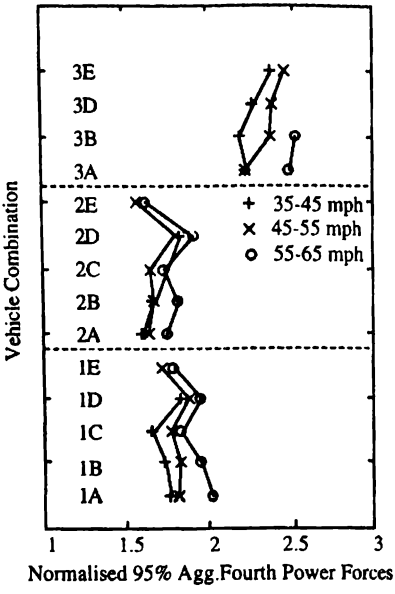


Fig. 19.7 Normalised 95th percentile aggregate fourth power forces for tractors alone. From [374].

The rubber walking-beam suspension on trailer C generates significantly higher dynamic loads and higher road damage than the other trailers, especially in the highest speed band. This results in normalised 95th percentile fatigue damage approximately 2.5 times the value for static loads. Conversely, the air suspended trailer (D) generates relatively low damage for all tractors.

These plots show a strong influence of *tractor* dynamics on the road damage done by the *trailer* axles. Tractor 3 causes all trailers to generate the highest road damage at the higher speeds, for all criteria. Similarly, the trailers with the air suspended 'road-friendly' tractor 2 almost always generate higher damage than the trailers with steel suspended tractor 1. This type of tractor/trailer discussed in Section 7.4.6, in Chapter 28 and in [127].

In summary: from the limited set of vehicles tested here, it appears that trailer suspensions cannot be assessed using a standard tractor, because the tractor significantly affects the response of the trailer.

Results for the Whole Vehicles

The damage generated by the whole vehicle is more complex, because it involves many conflicting factors. Nevertheless, it is presented in figure 19.9 for completeness. Vehicle combinations 3A and 3E are particularly damaging. This is because the suspension of tractor 3 is lightly damped for low frequency body pitch and bounce modes, and when it is combined with trailers A and E, tuning of the two vehicle units causes high dynamic loads to be applied at some locations along the road.

In general the normalised damage level for the whole vehicle is affected more by the trailer unit, than by the tractor unit. This is may be expected since all the vehicles tested were loaded to the legal limit and the largest proportion of this load was in all cases carried by the trailer axle group. As a consequence of this, the ranking of the trailers alone can generally be used to predict the ranking of the whole vehicles. For example, vehicle 3E is worse that vehicle 2E both in figure 19.8 (trailer only results), and in figure 19.9 (whole vehicle results). Conversely, the ranking of tractor suspensions cannot be used to predict the ranking of the whole vehicles. For example vehicle 1C is *better* than vehicle 1B in figure 19.6 (tractor only results), but vehicle 1C is *worse* than vehicle 1B in figure 19.9 (whole vehicle results).

In summary: for the vehicles tested in this study, it is possible to estimate the influence of trailer suspensions on damage done by the whole vehicle by measuring the dynamic loads generated by the trailer alone. However, it is only possible to assess the effects of the tractor suspensions on damage done by the whole vehicle by measuring the dynamic forces generated by all axles simultaneously.

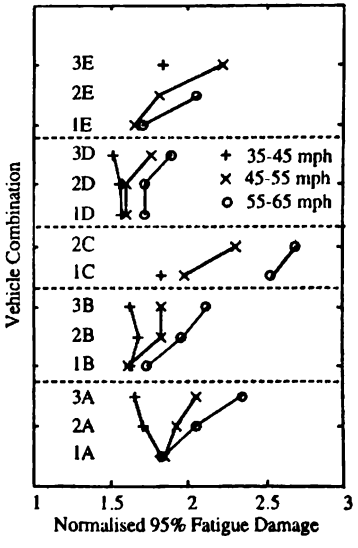


Fig. 19.8 Normalised 95th percentile fatigue damage to the strong road for trailers alone. From [374].

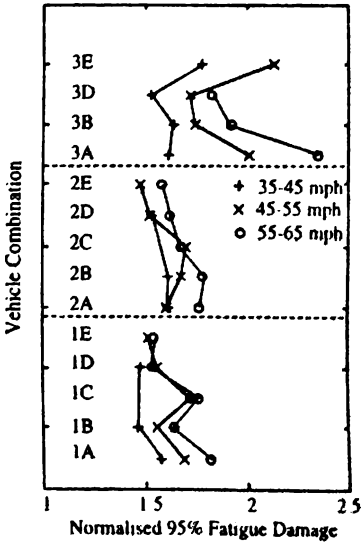


Fig. 19.9 Normalised 95th percentile fatigue damage to the strong road for whole vehicles. From [374]

19.4 PHASE II TESTS

The Phase II tests involved measurements using the load measuring mat on the A34 trunk road (see Section 18.4.3). In this section, the tyre forces of approximately 700 vehicles, both rigid and articulated, measured during the Phase II tests, are analysed to assess their road-damaging potential

19.4.1 Load Sharing Coefficient

The effectiveness of static load sharing of multiple-axle suspensions can be quantified using the Load Sharing Coefficient (*LSC*) introduced in Chapter 17 (equation 17.1). In this study, it was assumed

that the load on each axle was equally distributed over the tyres on both sides of the vehicle. Ideal performance corresponds to all tyres in the group carrying equal static loads during operation, which corresponds to the *LSC*=1.0.

Figure 19.10 shows the distribution of *LSC*s for all the trailer tandem groups where a suspension type could be identified. (The suspension type was recorded when the vehicles were travelling across the mat, so it was not possible to identify the suspension type more accurately than simply *air* or *steel*.) The spread of *LSC* values for the air suspensions is considerably less than for the steel suspensions. This indicates that the air suspensions have better load equalisation performance. This agrees with the conclusions of previous researchers (see Section 17.3.3 and [337, 443]).

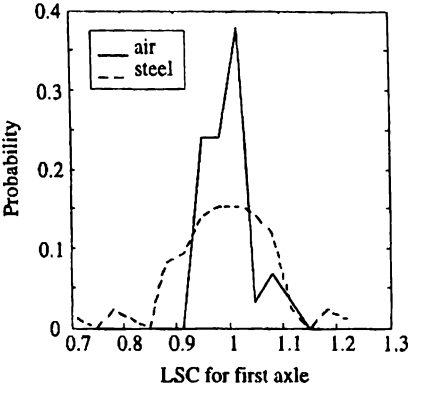


Fig. 19.10 Load Sharing Coefficient for trailer tandem groups. From [375]

Figure 19.11 shows the distribution of *LSC*s for all the tri-axle trailer groups. Two separate probability distributions have been drawn, corresponding to equation 17.1 evaluated for the first and second axles in the groups. (The probability distribution for the third axle in the groups is very similar to that of the first axle.) For all three axles the mean value of *LSC* is very close to unity. For the middle axle in the group (figure 19.11b), the distribution of *LSC* about the mean value is very similar for steel and air suspensions. When the first axle is considered however (figure 19.11a), there is a large difference, with the steel suspensions showing a much wider spread of *LSC*s (with over twice the standard deviation of the air suspension *LSC*s). This indicates that for the steel suspension units, there is, on average, relatively poor load sharing between the first and third axles, whereas for air suspensions, there is good load sharing.

19.4.2 Dynamic Load Coefficient

The Dynamic Load Coefficient (*DLC*) was introduced in Chapter 5 (equation 5.6). It has previously been found to be strongly dependent on speed, suspension design, vehicle configuration and road roughness. In this study, an average *DLC* for each axle-group was calculated. This was the mean value of *DLC* for all axles in the group. The purpose of generating an average *DLC* was to enable a comparison between different suspension groups more easily.

In figures 19.12 and 19.13, the *DLC* is used to compare the average road damaging potential of various laden vehicles. Vehicle axle-groups are split into the following classes: tandem axle air and steel suspensions (2a and 2s), tri-axle air and steel suspensions (3a and 3s) and single axle air and steel suspensions (1a and 1s). The error bars show the standard deviation of *DLC* for the vehicles within each category. This will arise from variations in vehicle configuration and suspension design between vehicles.

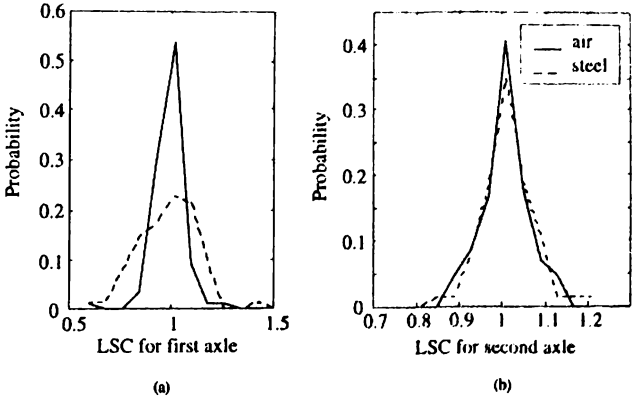


Fig. 19.11 Load Sharing Coefficient for trailer tri-axle groups. From [375]

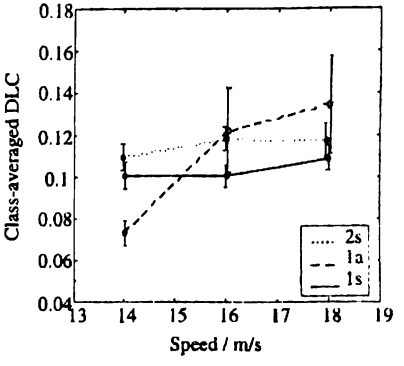


Fig. 19.12 Class-averaged *DLC* vs speed for drive axle-groups (error bars show the standard deviation). From [375].

Figure 19.12 shows the *DLC* averaged over all suspensions in each class (*class averaged DLC*), plotted against speed for tractor drive axle groups, over speed ranges of ±2m/s. There is an increase in *DLC* with speed, which is expected. The results also show that in the lowest speed range, the air suspended tractor axles have, on average, a lower *DLC* than steel suspensions, but in the high speed range, this is reversed. This is contrary to previous results measured on instrumented vehicles [337] which have shown that single axle air suspensions generate lower *DLC*s for all speeds. The poor performance of air suspensions on the highway is probably due to insufficient vibration damping caused by inadequate or poorly maintained hydraulic dampers.

Figure 19.13 shows the class averaged *DLC* plotted against speed, for trailer axle-groups. Again, the *DLC* increases with speed. There is also a clear ranking between suspensions, with the steel suspensions being more dynamic on average than the air suspensions. There is little difference between tandem and tri-axle suspensions of the same type. This is thought to be because the main dynamic force peaks occur at low frequencies due to vehicle sprung mass motion which is not affected strongly by the number of trailer axles in the group.

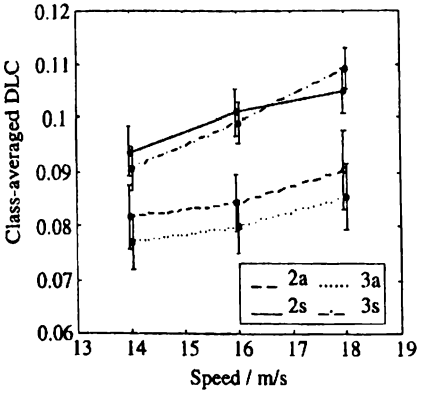


Fig. 19.13 Class-averaged *DLC* vs speed for trailer axle-groups (error bars show the standard deviation). From [375].

19.4.3 Aggregate Force Damage Criterion

It was not possible to carry out a detailed fatigue damage analysis using road response models, because the tyre types of the vehicles were not recorded (they could not be identified from the video recordings). However, for the Phase I tests (above) it was shown that the aggregate fourth power force criterion (equation 17.5) is useful for comparing the relative fatigue damage of vehicles with similar tyre and axle configurations.

In the following analysis, the aggregate fourth power forces are normalised by the static weight of the vehicle (or axle-group) to allow the test vehicles to be compared directly. Axle-groups are identified in the same way as the previous section, and error bars again show the standard deviation of aggregate force for vehicles within each category.

Aggregate Forces for Axle Groups

Figure 19.14 shows the class-averaged 95th percentile aggregate fourth power force for all tractor drive axle groups for which the suspension type was identified. The average normalised damage level is approximately 2.2. The highest levels of damage are caused by air-sprung drive-axles (1a). Comparing figures 19.12 and 19.14, it can be seen that the two damage criteria rank the *single axle* suspensions in the same order (as expected).

Figure 19.15 shows the class-averaged 95th percentile aggregate fourth power force for all trailer axle-groups for which the suspension type was identified. The average normalised damage level is roughly 1.9, which is less than for the drive axle-groups. Comparing mean values, it can be seen that the tri-axle trailer suspensions on average generate lower aggregate forces than tandem trailer axle groups for the same class of suspension, and that air suspensions generate higher aggregate forces than steel axle groups with the same number of axles.

When the class-averaged *DLC* is compared with the 95th percentile aggregate fourth power force criterion (by comparing figures 19.12 and 19.13 with figures 19.14 and 19.15), it is apparent that the two criteria rank the suspension classes in different orders. For the trailer axle-groups, the average *DLC* of the air suspensions is less than the *DLC* of the steel suspensions (figure 19.13), whereas the 95th percentile aggregate fourth power tyre force is higher for air suspensions than for steel suspensions with the same number of axles (figure 19.15). This is due to spatial correlation between the tyre forces in an axle group which is explained in the next section.

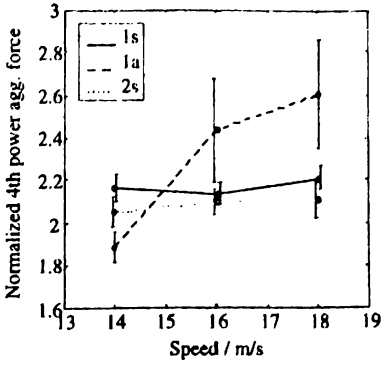


Fig. 19.14 95% fourth power aggregate force vs speed for drive axle-groups (error bars show the std. dev.), [375].

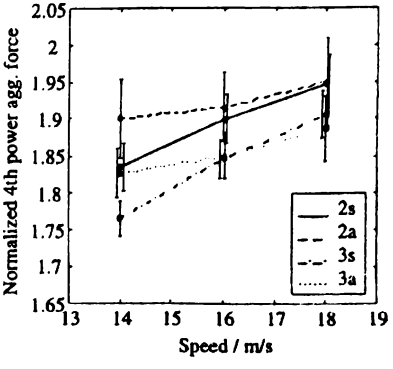


Fig. 19.15 95% fourth power aggregate force vs speed for trailer axle-groups (error bars show the std. dev.), [375].

Correlation Between Tyre Forces Within Axle Groups

The correlation coefficient can be used to investigate the *spatial* correlation between two tyre force histories. It is defined as [51]:

$$\rho = \frac{E\left[(p_1(x) - m_1)(p_2(x) - m_2)\right]}{\sigma_1 \sigma_2}. \tag{19.1}$$

The spatial correlation coefficient lies in the range $-1 \le \rho_{12} \le 1$. $\rho_{12}=1$ indicates that the two tyre force histories are perfectly correlated in space, and $\rho_{12}=0$ shows that $p_1(x)$ and $p_2(x)$ are uncorrelated. The theory of spectral analysis gives the following relations [355]:

$$E\left[p_1(x).p_2(x)\right] = \int_{-\infty}^{\infty} S_{p_1 p_2}(\omega) d\omega \tag{19.2a}$$

$$\sigma_1^2 = E\left[p_1(x).p_1(x)\right] = \int_{-\infty}^{\infty} S_{p_1 p_1}(\omega) d\omega \tag{19.2b}$$

$$\sigma_2^2 = E\left[p_2(x).p_2(x)\right] = \int_{-\infty}^{\infty} S_{p_2 p_2}(\omega) d\omega. \tag{19.2c}$$

For zero mean signals, using equations 19.1 and 19.2a-c, the spatial correlation coefficient can be rewritten as:

$$\rho_{12} = \frac{\int_{-\infty}^{\infty} S_{p_1 p_2}(\omega) d\omega}{\left[\int_{-\infty}^{\infty} S_{p_1 p_1}(\omega) d\omega \int_{-\infty}^{\infty} S_{p_2 p_2}(\omega) d\omega\right]^{1/2}}. \tag{19.3}$$

The spatial correlation coefficient can be calculated for tyre forces in specified frequency ranges, by changing the limits of the integration in equation 19.3.

Figure 19.16 shows the measured spatial correlation coefficients for the air and steel trailer tandem axle groups. The air suspended axle groups show a significantly higher correlation between tyre forces than the steel suspended groups. A similar result was found for the tri-axle trailer groups [376], although the graphs are not presented here. If the tyre forces on the tandem axle group are highly correlated, the 95th percentile aggregate force will be larger than if the same tyre forces are uncorrelated. This accounts for the different ranking of the air and steel suspended bogies for the two road damage criteria shown in figures 19.13 and 19.15.

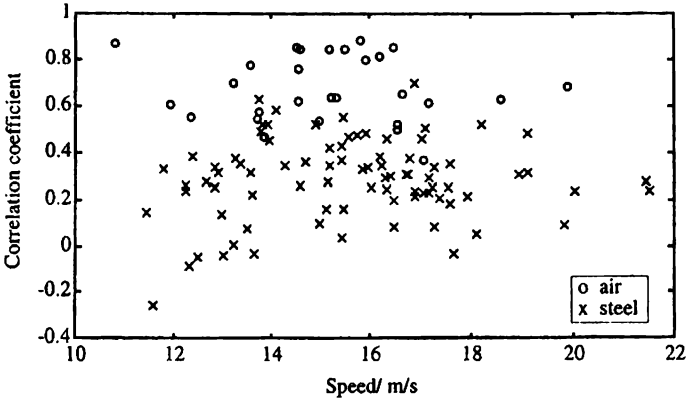


Fig. 19.16 Spatial correlation coefficient between front and rear tyre forces of tandem axle trailer groups for air and steel suspensions. From [375].

In order to investigate the reasons for the higher correlation in the air suspended tandem axle groups, a simulation study was performed using the linear tandem bogie model shown in figure 17.13. The four suspension spring elements in the model were replaced by linear springs and viscous dampers; and a torsional spring-damper combination was added at the levelling beam pivot. The suspension and levelling beam stiffnesses were adjusted to examine four cases: load levelling hard (steel) suspensions, independent hard (steel) suspensions, load levelling soft (air) suspensions, and independent soft (air) suspensions. The parameter values were based on the validated simulation discussed in Chapter 6.4 and are given in [375].

The input to the model was a single sided spectrum of road displacement, defined by equation 3.2, with $n = 2.5$ and $S_0 = 10 \times 10^{-8}$ $m^{0.5}cycles^{1.5}$. This simulates a relatively smooth 'motorway'.

Figures 19.17-19.19 show the results of the simulation. Figure 19.17 shows the correlation of the low frequency components of the tyre force (<5Hz). This frequency band contains the sprung mass bounce mode. The correlation coefficients increase with speed, and are greater for the soft suspensions than the hard suspensions. Furthermore, load levelling has little influence on the results in this frequency range.

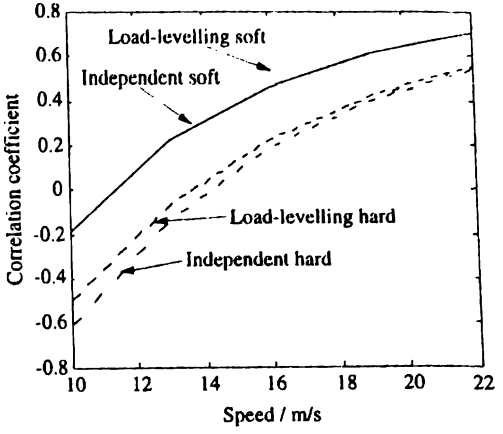


Fig. 19.17 Correlation coefficients for bogie models (Low frequencies <5Hz). From [375].

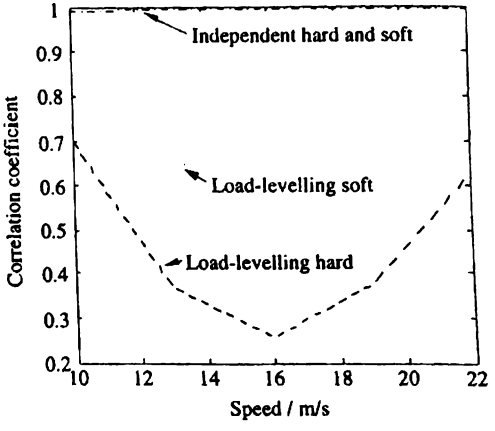


Fig. 19.18 Correlation coefficients for bogie models (High frequencies >5Hz). From [375].

These results can be explained as follows. At low frequencies, the dynamic tyre forces generated by two closely spaced axles $p_1(t)$ and $p_2(t)$ are dominated by sprung mass motion over a narrow frequency band, and are essentially in phase. Assume that

$$p_1(t) = P_1 \sin(\omega t) \quad \text{and} \quad p_2(t) = P_2 \sin(\omega t) \tag{19.4}$$

If the speed of the vehicle is V, and axle 2 is a distance ℓ behind axle 1, then equation 19.5 can be written as a function of distance x along the road

$$p_1(x) = P_1 \sin\left(\frac{\omega x}{V}\right) \quad \text{and} \quad p_2(x) = P_2 \sin\left(\frac{\omega(x+\ell)}{V}\right) \tag{19.5}$$

If equation 19.5 is substituted into equation 19.1, it is straightforward to show [120] that

$$\rho_{12} = \cos\left(\frac{\omega \ell}{V}\right) \tag{19.6}$$

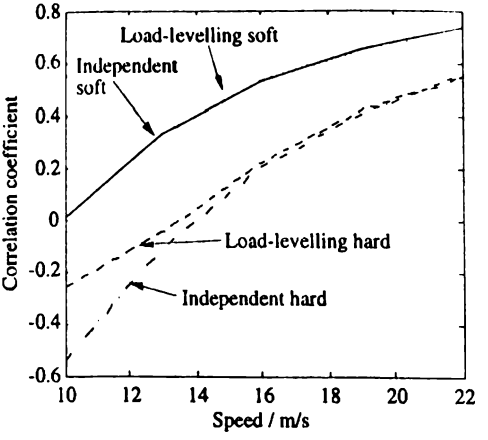


Fig. 19.19 Correlation coefficients for bogie models (All frequencies). From [375].

As the vehicle speed V increases, the time taken between each axle passing the same point ℓ / V is reduced. This increases the spatial correlation coefficient given by equation 19.6. Furthermore, the softer suspensions have a lower sprung mass natural frequency ω which lowers the ratio $\omega\ell / V$ and hence increases ρ_{12}.

Figure 19.18 shows the correlation of the high frequency (>5Hz) component of tyre forces. This range contains the unsprung mass bounce and pitch modes. The independent suspensions are highly correlated, because there is little interaction between the axles, and both tyres are subjected to the same road input. The load-levelling suspensions show a lower degree of correlation because the load levelling beam transmits high frequency forces between axles. The troughs in the load levelling suspension curves are due to wheel-base filtering effects.

Figure 19.19 shows the correlation coefficients for all frequencies. The graph is similar to figure 19.17 indicating that for this vehicle model, the low frequency tyre force components dominate the dynamic tyre forces. This is typical for current vehicle designs [101]. Overall, the simulation predicts the patterns in the measured correlation coefficient (figure 19.16) reasonably well.

Aggregate Forces for Whole Vehicles

Figures 19.20 and 19.21 show the normalised 95th percentile aggregate fourth power forces for all of the 2+2 and 2+3 axle semi-trailer combinations for which both drive axle and trailer suspension types were identified. Each vehicle is plotted as a point, with shaded areas linking all vehicles of the same class. The standard deviations given in the captions of these figures are based on the 7.5% RMS random sensor error found during mat calibration. They were quantified using a computer simulation of a two degree of freedom vehicle model passing over an artificial road profile [376].

The measured normalised 95th percentile aggregate forces lie in the range 1.5-2.5 for the majority of vehicles. This level of aggregate force is governed by the vehicle speed and road roughness. Normally on the A34, vehicles would be travelling at a considerably higher speed, which would increase the level of 95th percentile aggregate forces. In figure 19.21, the worst vehicle has steel suspensions (2s+3s), but the vehicles generating the lowest aggregate forces are also found to have these suspensions. When vehicles with air suspended drive axles are compared, those with air suspended trailers (x) cause noticeably higher normalised aggregate forces than those with steel suspended trailers (o). The wide distribution of aggregate forces caused by 2a+3a combinations indicates that the vehicles also have widely varying dynamic characteristics. These results, and those

of figure 19.12, indicate that some air suspensions are likely to have poorly maintained or incorrectly fitted shock absorbers, and so generate high dynamic loads.

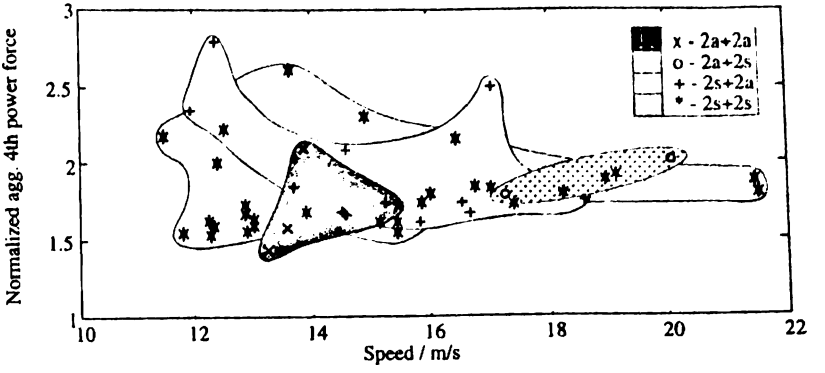


Fig. 19.20 95% Aggregate Fourth Power force - 4-axle vehicles (the standard deviations of individual points are ±0.08). From [375].

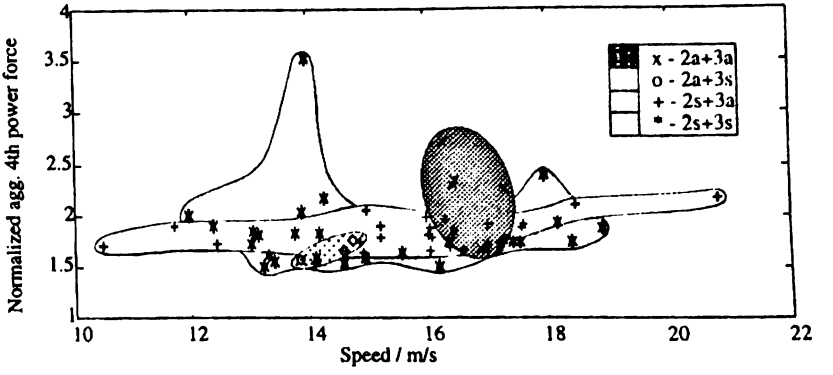


Fig. 19.21 95% Aggregate Fourth Power force - 5-axle vehicles (the standard deviations of individual points are ±0.07). From [375].

19.5 CONCLUSIONS

19.5.1 Phase I Tests - on the Test Track

(i) Calculation of *absolute* values of road damage to flexible pavements requires use of damage criteria which incorporate road response models. Such models are also needed if the influence of axle and tyre configurations are to be included in vehicle assessment.

(ii) Vehicle suspensions rank in essentially the same order, irrespective of road strength. This assumes the same mode of failure for strong and weak roads, which is not necessarily true.

(iii) Dynamic forces are not important in rutting damage, where gross vehicle weight is the dominant factor. Conversely, dynamic forces are important in fatigue damage, and relatively

low levels of dynamic loads investigated in this study can lead to theoretical damage up to 2.5 times the value for static axle loads.

(iv) For vehicles *with similar arrangements of axles and tyres*, the aggregate fourth power force can be used to compare dynamic loads in terms of normalised pavement fatigue.

(v) In the Phase I tests (a) The rubber 'walking–beam' trailer suspension was found to generate the highest road damage for the trailer alone, and often the highest damage for the whole vehicle. (b) The trailer air suspension was found to generate the lowest damage for the trailer alone, but it caused all tractors to generate slightly higher road damage than the other trailers. (c) The air suspended 'road friendly' tractor caused all trailers to generate higher road damage than a similar steel suspended tractor, and often caused a higher level of road damage to be generated by the whole vehicle.

(vi) It appears to be possible to measure the dynamic loading performance of tractor suspensions using a standard trailer. However, it may not be possible to assess trailer suspensions accurately using a standard tractor, because the tractor significantly influences the trailer.

(vii) For the class of vehicles examined in the Phase I tests, the influence of trailer suspensions on road damage done by the whole vehicle can be estimated by measuring the dynamic loads generated by the trailer alone. Conversely, it is only possible to assess the effects of the tractor suspensions on damage done by the whole vehicle, by measuring the dynamic forces generated by all axles.

19.5.2 Phase II Tests - on the Highway

(i) For all the vehicles tested in the Phase II tests, the fatigue damage (calculated using the aggregate fourth power force) incurred by 5% of the pavement surface was found to be at least 1.5 times the fatigue damage due to the static loads alone. This value would be expected to increase significantly for rougher pavements and higher vehicle speeds.

(ii) Air suspended axle-groups were found to be better at static load sharing than steel suspended axle-groups. Within these classes, tandem axle-groups performed better than tri-axles.

(iii) In these tests, air suspended drive axles were found to generate higher *DLC*s than those with leaf springs. Conversely, air suspended trailer axle-groups generated lower *DLCs* than the steel suspended trailer units. There was little difference between the *DLC*s for tandem and tri-axle groups within these categories.

(iv) The air suspended axle-groups were found to generate higher normalised 95th percentile aggregate forces than the steel suspended units. For the trailer units, the tandem axle-groups caused higher 95th percentile aggregate forces than the tri-axle groups.

(v) Tandem axle bogies fitted with soft (air) suspensions show a higher degree of correlation between low frequency (sprung mass) tyre forces. Similarly, tandem axle bogies with independent suspensions show a higher level of correlation between high frequency (unsprung mass) tyre forces. The differences can be explained using simple vehicle models.

(vi) The ranking of axle-group suspensions depends on the pavement damage criterion used. This is due to the degree of spatial correlation between tyre forces. The *DLC* is unable to distinguish correctly between the road-damaging abilities of different axle group suspensions, and therefore it should not be used for suspension assessment purposes. The aggregate force approach is considered to be a more realistic, yet straightforward assessment criterion.

(vii) For the vehicles tested, a higher level of relative pavement damage was generated by drive axle-groups than by trailer axle-groups.

(viii) Some trailer and drive axle-group air suspensions cause relatively high pavement damage on the highway, probably due to lack of suspension damping.

20

MODELLING WHOLE-LIFE FLEXIBLE PAVEMENT PERFORMANCE

20.1 SUMMARY

A new 'whole-life' pavement performance model (WLPPM) has been developed. It is capable of making deterministic pavement damage predictions due to realistic traffic and environmental loading. A vehicle simulation is used to generate dynamic tyre forces that are a function of distance along the road. These dynamic tyre forces are then combined with the appropriate pavement primary response influence functions (stress, strain and displacement) to give primary response histories at regularly spaced points along the pavement. The primary response histories are then transformed into increments of pavement damage (fatigue and permanent deformation) using an appropriate damage model. The result is the theoretical damage at each point along the pavement due to a single vehicle pass. The pavement surface profile is then updated to reflect permanent deformation damage, and the layer material parameters are changed to reflect fatigue damage. The procedure is then repeated for the next vehicle pass. Particular attention is given to modelling strength variations in the pavement and dynamic tyre forces.

The model is used to investigate the relationship between 'hot spots' (due to peak dynamic loads), 'weak spots' (due to initial pavement stiffness variations) and long-term pavement wear. The performance of two classes of pavement, operating under typical UK climatic conditions, are then examined. It is concluded that both dynamic tyre forces and asphalt layer stiffness variations can significantly influence long-term flexible pavement performance.

This chapter is based on work previously published in [138, 139]

20.2 INTRODUCTION

This chapter describes a 'Whole-Life Pavement Performance Model' (WLPPM), developed to investigate the relationship between dynamic vehicle loads, pavement stiffness variations, environmental factors and pavement wear. This section reviews previous whole-life pavement models that have included dynamic vehicle effects. The next section describes the new WLPPM and the calculation procedure. The WLPPM is then used to investigate four simplified case studies, and finally to evaluate the relative importance of dynamic loads and asphalt layer stiffness variations in three typical UK pavement constructions.

20.2.1 Review of Previous Whole-Life Pavement Performance Models

The literature contains reference to only a few previous whole-life models. The following section briefly reviews these. For a more detailed discussion, refer to reference [134].

Brademeyer *et al.* [66] used a modified version of the VESYS IIIA pavement analysis program to simulate measured damage from 23 sections of the AASHO pavement test. They assumed that, for flexible pavements, vehicle loading was randomly distributed and not correlated with specific points along the pavement. A non-linear two-dimensional vehicle model (described in [361]) traversing a

pavement surface displacement profile was used to generate the required dynamic tyre force histories. These force histories were combined with pavement primary response influence functions for each pavement response variable, and the statistics (mean and variance) of each response were then used to calculate the expected level of pavement damage (rutting, cracking, slope variance and Present Serviceability Index). Brademeyer *et al.* obtained reasonable agreement with measured data from the 23 AASHO test sections, although Cebon [94] noted that a static (un-modified) version of the VESYS IIIA model showed very similar performance predictions in other research.

Papagiannakis *et al.* [365] also used a modified version of VESYS IIIA to model the performance of 10 AASHO test sections; six that developed severe roughness, and four that remained fairly smooth throughout the AASHO test. Material parameters were characterised by a spatial mean and coefficient of variation which they varied over five seasons. The five smooth AASHO test sections were used to calibrate the VESYS simulation with respect to the unknown material properties. They found that by assuming the loads applied to the smooth section were constant (*ie* static), VESYS IIIA provided reasonably accurate predictions of flexible pavement wear. To model the damage on the six rougher pavement sections, the dynamic loads applied by the vehicle in the AASHO test were assumed to be 'spatially repeatable' (*ie* peak loads always applied to the same locations along the road) and the analysis was concentrated on a pavement length over which one axle under-goes a complete load cycle. The increase in pavement roughness (slope variance) with time was calculated from the amount of fatigue cracking. Papagiannakis *et al.* found that their inclusion of dynamic loads in VESYS IIIA improved performance predictions for 4 out of 6 of the rough AASHO test sections analysed. This model was then used to compare the damaging effects of two different suspensions (rubber and air) assuming no spatial repeatability. They concluded that, with respect to the static loads, the rubber suspension caused an additional 17–22% damage, and the air suspension caused an additional 6–8% damage.

In 1983 Ullidtz and Larsen [469] published a model which predicted the performance of flexible pavements, in terms of roughness, rutting and fatigue cracking, as a function of climatic conditions and traffic loading. This model was based on the performance of a pavement discretised into 0.3m sub-sections. Each sub-section was assigned different layer thicknesses and material properties and was loaded using a linear 'quarter car' vehicle model. The variations in the layer thicknesses and material properties between sub-sections were described by two autocorrelation coefficients for each variable. The model calculated permanent deformation and fatigue cracking weekly. The stresses and strains were calculated using a simplified method that reduced the layered elastic system to an elastic half space. Permanent deformation was calculated in each pavement layer and summed to give surface rutting for each sub-section. The permanent deformation in the asphaltic layers was assumed to be purely viscous whereas the permanent deformation in the granular layers was determined from the elastic stress field. To model the reduction of elastic modulus of the asphalt layer with progressive fatigue damage, the asphalt layer for each sub-section was divided into 100 sub-layers. The proportion of the fatigue life used was then calculated for each sub-layer and the elastic modulus of the sub-layers where the fatigue limit had been exceeded (at the bottom of the undamaged asphalt) was reduced to the elastic modulus of the pavement sub-base layer. Consequently, the effective thickness of the asphalt layer was reduced as the cumulative fatigue damage increased. This process was then repeated with an updated pavement profile (determined from rutting between sub-sections) and updated asphalt layer moduli for the sub-sections. The model was used to simulate damage from 180 sections of the AASHO test. They found that agreement with the measured performance of the sections was good.

In later versions of this model Ullidtz [467, 471] changed the asphalt fatigue and elastic modulus degradation models. These were combined into a single model that gave the reduction in asphalt modulus directly as a function of the strain at the base of the bound asphaltic layers, using a damage mechanics approach. Ageing was also included in the asphalt surface layer. The new whole-life model was re-validated by simulating the measured monthly performance of two sections from the AASHO test. The AASHO traffic, for the same sections, was then extended over 20 years and the effects on pavement wear of; (i) varying the quarter car suspension parameters (spring and damping

constants), (ii) different wheel configurations and (iii) changing to mixed traffic, were investigated. Ullidtz modelled mixed traffic using a linear quarter car model with different suspension (spring and damper) parameters, but did not draw any conclusions about the effects of the repeatability of the dynamic tyre forces on subsequent pavement damage. He concluded that the effects of dynamic loads may be quite different on different types of pavement damage and pavement structures.

20.2.2 Research Needs

None of the whole-life models reviewed above investigated the relationship between damage propagation due to 'weak spots' in the pavement structure (produced by asphalt layer thickness variations *etc*) and 'hot spots' on the pavement surface produced by peak dynamic loading. Consequently, there is some doubt as to which damage propagation mechanism is more important. This information is central to understanding the influence of dynamic loads on long-term flexible pavement wear.

The size and magnitude of the 'hot spots' on the pavement surface is likely to be influenced significantly by the spatial repeatability of the dynamic tyre forces generated by a fleet of articulated vehicles. This was not included in any of the whole-life models reviewed above. Most of the previous models [66, 365, 466, 467, 469, 471] were used to simulate results from the AASHO test where the loading conditions consisted of one vehicle travelling at a constant speed in each test lane.

The model described in this chapter attempts to include the important mechanisms of pavement surface degradation using a deterministic (rather than statistical) approach and to account realistically for the distribution of dynamic loads and construction variations along the road.

The model draws heavily on many of the elements described in previous chapters. These include: (i) vehicle simulation, using the tools of Part 2; (ii) primary pavement response calculations, using the techniques of Part 3; (iii) material damage mechanisms from Part 4; as well as (iv) element from the initial chapters of Part 5.

20.3 DESCRIPTION OF THE WHOLE-LIFE PAVEMENT PERFORMANCE MODEL (WLPPM)

Figure 20.1 shows a schematic view of the calculation procedure used in the WLPPM. It follows a similar pattern to the models developed by Ullidtz [466, 467, 469, 471] but differs in the detail. The overall calculation procedure is summarised in the following few paragraphs and then described in detail.

The initial inputs to the WLPPM are: (i) the specification of the pavement being simulated (*ie* layer thicknesses, mix specifications *etc*); (ii) the time increment to be used in the simulation; (iii) the rate of traffic loading; and (iv) the climatic conditions under which the pavement will operate. From this initial specification, a length of pavement surface profile is generated and divided into smaller sub-sections. Each sub-section has three layers. It is assigned a random value for the thickness of the bound asphaltic layer, with the overall variation between sub-sections being representative of *measured* thickness variations. The thickness of the granular layer is assumed to be constant, and the subgrade is modelled as semi-infinite.

A time domain vehicle simulation is used to generate dynamic tyre forces for one or more vehicles as a function of distance along the pavement. The vehicle model parameters and initial road surface roughness are chosen to best represent the traffic conditions for the type of pavement being simulated.

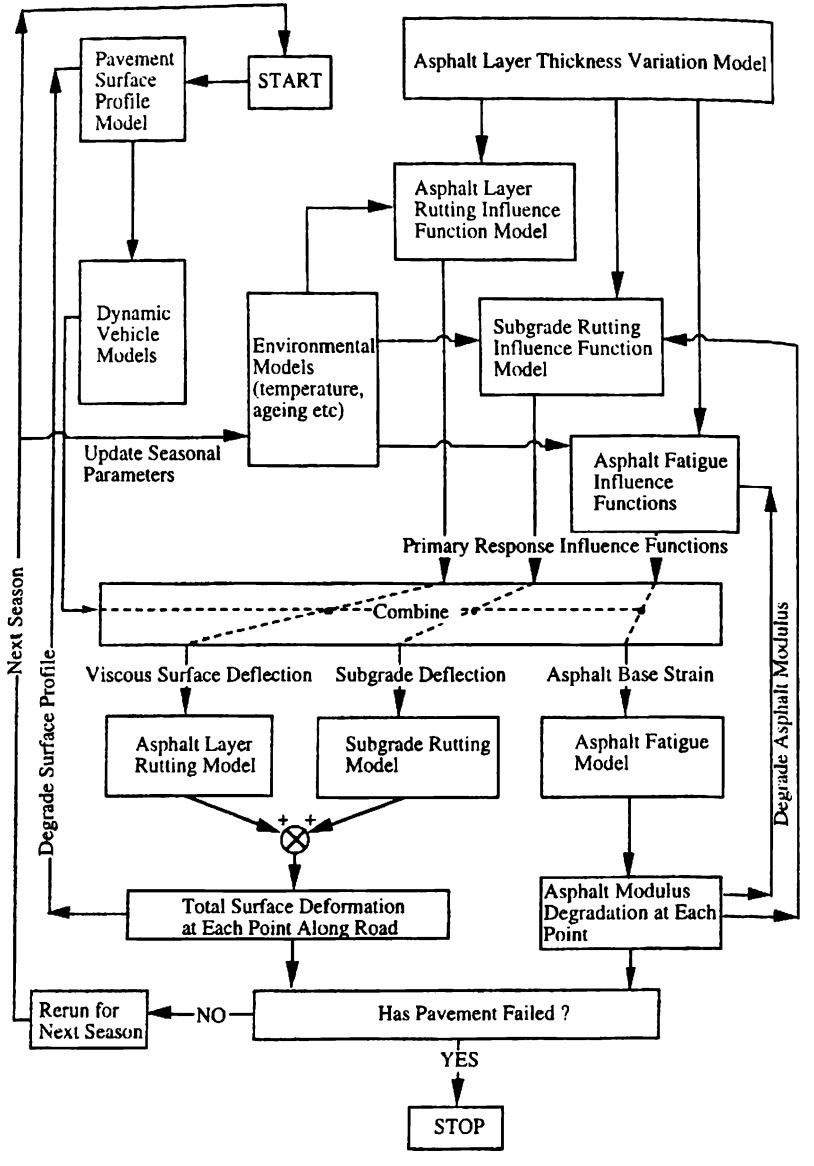


Fig. 20.1 Whole-life pavement performance model methodology. From [138].

A set of primary response influence functions, for each sub-section and each mode of damage, is generated (*ie* horizontal asphalt base strain for fatigue, subgrade strain and permanent vertical surface velocity for rutting). These primary response influence functions are combined with the previously calculated dynamic tyre forces to give primary pavement response time histories at a large number of equally spaced points along the pavement.

The primary responses are processed with the appropriate pavement damage models (rutting and fatigue) and the number of load applications, to give damage as a function of distance along the pavement for the current time increment.

An updated surface profile is then generated by subtracting the calculated rutting in the wheel path from the initial profile used for that time increment. This mechanism accounts for the effects of changing surface roughness on the dynamic tyre forces. The resulting fatigue damage is used to reduce the elastic modulus of the asphaltic material for each sub-section. This mechanism reflects the effects of cumulative fatigue damage on the primary responses and hence subsequent pavement damage.

The above process is then repeated for the next time increment, with an updated climate, and so on, until the pavement has reached the end of its serviceable life. The following section describes the models used in each area of the WLPPM in more detail.

20.3.1 Climatic Factors

Many climatic and environmental factors influence the performance of a pavement. The environmental effects that are currently included in the WLPPM are temperature and ageing of the asphalt layer. However, due to the modular structure of the program, it is relatively straightforward to include other environmental effects such as the effects of frost and moisture on unbound materials, (*eg* [290, 427]) provided these effects can be easily quantified.

Temperature of the Asphalt Layer

Changes in the temperature of the asphalt layer affect the elastic and viscous properties of the bitumen. The variation in the monthly mean air temperature T_{air} (^{o}C) was assumed to be sinusoidal of the form:

$$T_{air} = \left[\frac{\left(T_{air}^{max} + T_{air}^{min}\right)}{2}\right] + \left[\frac{\left(T_{air}^{max} - T_{air}^{min}\right)}{2}\right] \cos\left[\frac{(U - U_0)\pi}{6}\right], \qquad (20.1)$$

where T_{air}^{max} is the maximum monthly air temperature throughout the year (°C)
T_{air}^{min} is the minimum monthly air temperature throughout the year (°C),
U is the month number (January is 1) and
U_0 is the month number corresponding to the maximum monthly temperature.

Ullidtz [466] noted that, in many cases, equation 20.1 gives a good approximation to measured mean monthly temperatures. If more detailed temperature data is available, it can easily be incorporated in the WLPPM. For simulation time increments of longer than 1 month, the air temperature was determined by averaging the appropriate monthly temperatures together (determined from equation 20.1).

Predicting the temperature profile of the asphaltic material T_{asp} from the air temperature T_{air} is complicated, and requires detailed information about the thermal properties of the asphalt and the ambient conditions (see, for example [43]). Consequently, a simplified approach was used, where the effective monthly temperature of the asphalt layer was estimated from the air temperature using the following empirical equation (see [189] for further details):

$$T_{asp} = T_{air}\left(1 + \frac{76.2}{h_{asp} + 304.8}\right) - \frac{84.7}{h_{asp} + 304.8} + 3.3, \qquad (20.2)$$

where T_{asp} is the effective surface layer temperature (°C),
T_{air} is the measured mean air temperature (°C), and
h_{asp} is the thickness of the surface layer (mm).

20.3.2 Pavement Surface Profile Model

The pavement surface roughness profiles were generated using equation 3.2 with the values of S_0 being the geometric mean of the ranges in Table 3.2: $S_0 = 12.2$ for a motorway; $S_0 = 49.0$ for a principal road; $S_0 = 387.3$ for a minor road.

A one-dimensional surface profile was generated from equation 3.2 by applying a set of random phase angles, uniformly distributed between 0 and 2π, to a series of coefficients derived from the desired spectral density (see Chapter 3 for further details). Typically, the resulting surface displacement profiles were generated with data points every 0.1m giving a lower wavelength limit (corresponding to the Nyquist frequency) of 0.2m. The upper wavelength limit was several hundred metres.

In order to quantify pavement surface roughness using a single statistic in this chapter the International Roughness Index (IRI) was used [408]. The IRI is the ratio of the accumulated suspension motion divided by the total distance travelled, calculated from the response of a linear 'quarter car' vehicle model travelling at 80km/h over the pavement profile of interest. On the IRI scale, a perfectly smooth pavement is rated as 0, an asphalt pavement in good condition is rated at approximately 2mm/m and a severely damaged pavement may be rated as high 10mm/m. A detailed description of the method used to calculate the IRI for a given profile is given in reference [408].

Hardy [224] found that the constant S_0 in equation 3.2 was correlated with the IRI and could be estimated from:

$$S_0 = 1.69 \times 10^{-8} (IRI)^2 \qquad \left(m^{1/2} cycle^{3/2}\right). \tag{20.3}$$

20.3.3 Vehicle Simulation

A simple linear 'quarter car' vehicle model was used in the case studies described in this chapter (see figure 5.1a). The WLPPM can incorporate more realistic (validated) articulated vehicle models without difficulty, but at the expense of significantly increased computation time. The vehicle parameter values used were representative of a fully laden vehicle with a typical single-axle steel suspension. They were essentially half of those shown in figure 5.1 (*ie* for one wheel only), but with zero tyre damping. The tyre also had a facility to bounce clear of the road surface if the surface was sufficiently rough (see [138] for further details).

The dynamic tyre forces generated by the vehicle model were obtained by numerically integrating the equations of motion using the pavement surface profile displacement as the input to the tyre (see Chapter 5).

20.3.4 Pavement Primary Response Model

A modified version of the VESYS IIIA quasi-static pavement model [277] (modifications by Cebon for NCHRP project 1-25, see [192]) was used to generate the required primary pavement response influence functions. (See Chapter 10 for a discussion of the Influence function method for calculating primary pavement responses.) Typical contact radii for single and super single tyres were taken to be 108mm and 135mm respectively [512]. Dual tyres were modelled as two separate circular contact areas of radius 108mm.

All the pavement structures investigated were modelled as three layer systems comprising; (i) an asphaltic layer (wearing course plus base course), (ii) a granular sub-base layer, and (iii) a subgrade or soil layer. The primary response model required the elastic properties (Young's modulus and Poisson's ratio) and the thickness of each layer (except the subgrade which is of infinite thickness). The methods used to obtain these parameters are described in the following sub-sections.

Asphalt Surface Layer Elastic Properties

Typically, a full-depth asphaltic pavement consists of three separate layers of bituminous material; a wearing course, a road base and a base course. The properties of the road base and base course are usually similar, whereas the wearing course has different mix proportions and hence properties. However, according to Brown [75], typical UK wearing courses have a relatively small influence on the structural performance of the pavement and, for the purposes of structural analysis, the wearing course may be combined with the other two layers. Consequently, a single asphaltic layer of typical road base (or base course) material was used to represent the asphaltic layers of a full-depth flexible pavement.

The elastic modulus of the bituminous binder E_b(MPa) was calculated using the following equation derived from the Van der Poel nomograph [34]:

$$E_b = 1.157\times10^{-7} t_l^{-0.368} 2.718^{-PI^{(R)}} \left(T_{RB}^{(R)} - T_{asp}\right)^5, \tag{20.4}$$

where $T_{RB}^{(R)}$ is the recovered bitumen 'Ring and Ball softening temperature' (°C),
T_{asp} is the temperature of the asphalt layer (°C),
$PI^{(R)}$ is the recovered bitumen 'Penetration Index' and
t_l is the loading time (secs).

Equation 20.4 is only applicable when:

$$0.01\text{sec} < t_l < 0.1\text{sec},$$

$$-1.0 < PI^{(R)} < 1.0,$$

$$20°\text{C} < \left(T_{RB}^{(R)} - T_{asp}\right) < 60°\text{C}.$$

The bitumen properties recovered after the asphalt has been mixed and laid $\left(T_{RB}^{(R)}\right.$ and $\left.PI^{(R)}\right)$ may be estimated from the initial penetration of the bitumen $P^{(I)}$ using the following empirical equations [75]:

$$P^{(R)} = 0.65P^{(I)}, \tag{20.5a}$$

$$T_{RB}^{(R)} = 98.4 - 26.35\log_{10}\left(P^{(R)}\right), \tag{20.5b}$$

$$PI^{(R)} = \frac{27\log_{10} P^{(I)} - 21.65}{76.35\log_{10} P^{(I)} - 232.82}, \tag{20.5c}$$

where $P^{(I)}$ is the initial penetration of the bitumen.

The effective loading time t_l was estimated from [34, 72]:

$$\log_{10}(t_l) = 5\times10^{-4} h_{asp} - 0.2 - 0.94\log_{10}(V), \tag{20.6}$$

where h_{asp} is the thickness of the asphalt layer (mm) and
V is the vehicle speed (km/hr).

The elastic modulus (stiffness) of the asphalt mixture $E_m = (S_m)_H$ (MPa) was calculated using equations 14.9 and 14.10, with $S_b = E_b$ from (20.4).

The thickness of the asphalt layer was determined from the standard UK design procedure for the type of pavement being simulated (see [378] for further details).

Poisson's ratio for asphaltic material has been shown to be highly dependent on temperature with values ranging from 0.15 (low temperatures) to 0.45 (high temperatures) [20]. A typical value was taken to be $\upsilon_{asp} = 0.4$ [75].

Ageing of the Asphalt Surface Ageing

Ageing of bituminous materials has been shown to occur in two stages: (i) short term and (ii) long term [49, 392, 481]. Short term ageing occurs during manufacture and laying, and is mainly due to the loss of volatile components and oxidation while the mix is hot. Long term ageing is mainly due to progressive oxidation of the mixture while it is in service.

Short term ageing was included in the model by using typical bitumen properties *recovered* after mixing and laying ($T_{RB}^{(R)}$, $PI^{(R)}$, *etc*).

Long term ageing of the bitumen was accounted for by increasing the *recovered* 'Ring and Ball' softening point temperature $T_{RB}^{(R)}$, with the age of the pavement, according to a one-dimensional kinetic diffusion model developed by Verhasselt and Choquet [481]:

$$T_{RB}^{(R)}\Big|_{t=t_1} = T_{RB}^{(R)}\Big|_{t=0} + \sqrt{\Lambda t}, \tag{20.7}$$

where $T_{RB}^{(R)}\Big|_{t=t_1}$ is the recovered 'Ring and Ball' temperature (°C) at time $t = t_1$,

$T_{RB}^{(R)}\Big|_{t=0}$ is the initial Ring and Ball temperature (°C) at time $t = 0$,

Λ is the reaction constant (°C^2 / hour) and

t is the time (hours).

Verhasselt and Choquet [481] determined the value of the reaction constant Λ from accelerated laboratory ageing tests on different types of bitumen. They found that it depended strongly on the temperature of the bitumen. Consequently, to apply equation 20.7 to an in-service pavement where the temperature of the asphalt layer is constantly changing, they related the mean annual air temperature to the effective temperature at which the reaction constant should be determined (see [481] for further details). For typical climatic conditions in Belgium, the average reaction constant Λ was found to vary between 1.2×10^{-3} to 2.1×10^{-3} °C^2 / hour depending on the type of bitumen being considered. Verhasselt and Choquet used these values of the reaction constant to predict ageing of the whole asphalt layer for typical pavements in Belgium. They obtained a reasonable agreement with the measured ageing of the material. A value of $\Lambda = 1.65\times10^{-3}$ °C^2 / hour together with equation 20.7 was therefore used to model ageing of the whole asphalt layer in a typical UK pavement in this study.

An ageing model of this type will affect both the elastic and viscous properties of the asphaltic material since they both depend on the properties of the bituminous binder.

Subgrade Layer Elastic Properties

The elastic modulus of the subgrade E_{sub}(MPa) was estimated from the empirical equation [75]:

$$E_{sub} = 10CBR, \tag{20.8}$$

where CBR is the 'California Bearing Ratio' of the subgrade.

For details of the CBR test refer to [403]. Poisson's ratio for soil has been shown to depend on the degree of soil cohesion and ranges from 0.3 (cohesive-less soils) to 0.5 (very plastic clays, cohesive soils) [20]. A typical value was taken to be $\upsilon_{sub} = 0.4$ [75].

Granular Sub-base Layer Elastic Properties

The elastic modulus of the granular base layer E_{gra} was taken to be a constant 100MPa, corresponding to a good quality granular base [75]. The thickness of the granular base was taken to be a standard 200mm from [75].

Poisson's ratio for the granular material depends on the degree of crushing of the material and ranges from 0.3 (crushed material) to 0.4 (unprocessed gravels/sands) [20]. A typical value was taken to be $\upsilon_{gra} = 0.3$ [75].

20.3.5 Fatigue Cracking Model

From the analysis in Chapter 15, it was concluded that under almost all circumstances, traffic-generated fatigue damage initiates at the base of the bound asphaltic layers and propagate towards the surface. Thermal load cycles have little effect. Consequently, the fatigue model chosen for the WLPPM was a traditional fatigue model which assumes that cracks originate at the bottom of the asphaltic layers, where the tensile strain is greatest, and propagate vertically upwards towards the pavement surface.

Simplified laboratory test on asphaltic specimens have led to a relationship between fatigue life and strain of the form of equation 13.1:

$$N_f^{(i)} = k_1 \varepsilon_i^{-k_2}, \tag{13.1}$$

where $N_f^{(i)}$ is the number of cycles to failure at strain level ε_i (micro strain),
k_1 and k_2 are fatigue constants describing the fatigue behaviour of the material.

Cooper and Pell [145] examined the effect of various asphalt mix variables and temperature on the fatigue life of over 2000 specimens of a wide variety of both base course and wearing course asphaltic mixes. They concluded that fatigue performance, on the basis of applied tensile strain, was primarily influenced by the type and amount of bituminous binder. The effects of temperature and loading time were assumed to be accounted for by their effect on elastic stiffness. However, it was found that the resulting fatigue law gave conservative results when compared with experimental field data and thus required 'calibrating' [76]. This calibration was performed for average UK conditions giving fatigue constants k_1 and k_2 as a function of the properties of the asphalt mix [76]:

$$\begin{aligned} \log_{10}(k_1) &= 14.39\log_{10}(V_B) + 24.2\log_{10}\left(T_{RB}^{(I)}\right) - 46.06, \\ k_2 &= 5.13\log_{10}(V_B) + 8.63\log_{10}\left(T_{RB}^{(I)}\right) - 15.8, \end{aligned} \tag{20.9}$$

where V_B is the percentage volume of bituminous binder and
$T_{RB}^{(I)}$ is the initial 'Ring and Ball' softening temperature of the bitumen (°C).

The initial 'Ring and Ball' softening temperature of the bitumen $T_{RB}^{(I)}$ may be obtained from equation 20.5b by replacing the recovered penetration $P^{(R)}$ with the initial penetration $P^{(I)}$. The fatigue properties defined by equation 20.9 include a factor of 440 to allow for differences between laboratory test conditions and those in the pavement [76]. This 'correction' comprises a factor of 20 for rest periods between load applications, a factor of 20 for the time taken for the crack to propagate through the bituminous layer, and a factor of 1.1 for the lateral distribution of wheel loads on the pavement surface [76].

The accumulation of fatigue damage D at each point along the road due to the passage of a vehicle was estimated using Miner's hypothesis of linear damage accumulation equation 17.7 [72].

Gillespie *et al.* [192] investigated two different methods for reducing a complex strain time history to a number of equivalent strain cycles, 'rainflow' counting and 'peak' counting. The 'rainflow' counting method involves determining the overall strain range (largest peak to lowest valley) and removing this from the history. This is taken as the first strain cycle and the process is repeated until all strain reversals have been considered. This method is commonly used for metal fatigue due to complex time histories and corresponds to counting complete hysteresis loops in the stress-strain curve for the material (see [192] for further details). The 'peak' counting method considers just the peak tensile strain to be the equivalent strain cycle. This type of approach cannot account for compressive strains between tensile peaks or strain levels that do not recover to zero between multiple axles. Gillespie *et al.* [192] concluded that the ranking of the vehicles in their study was not greatly affected by the method of cycle counting. Consequently, the simpler 'peak' counting method was used with the WLPPM.

20.3.6 Permanent Deformation Model

Asphalt Surface

The rutting model used in the WLPPM comprised two parts. The first part is the linear visco-elastic rutting model presented in Chapter 14, which was used to model the asphaltic layers of the pavement where permanent deformation is primarily due to viscous flow. This linear visco-elastic calculation requires the viscosity of the bituminous binder, and the mix specification. The viscosity of the bituminous binder λ_b (MPa.s) was obtained using the following approximate expression [466]:

$$\lambda_b = 3\times10^{-6}\left\{1.3\times10^{\left[3+\left(T_{RB}^{(R)}-T_{asp}\right)/10\right]}\right\}. \qquad (20.10)$$

The viscosity of the asphalt mix was then obtained from equations 14.16.

Subgrade

A simple relationship between vertical subgrade strain and permanent deformation was used to include rutting in the subgrade and granular layer. This relationship is of the same general form as the model used to relate vertical subgrade strain to permanent surface deflection (see, for example [10, 74, 281]). The incremental permanent deformation in the subgrade and granular layer due to a single axle load may be expressed as:

$$\delta_i = L_1\varepsilon_i^{L_2}, \qquad (20.11)$$

where δ_i is the incremental vertical permanent deformation in the subgrade and granular layer due to vertical subgrade compressive strain ε_i,

and L_1 , L_2 are material constants.

This model will be referred to as the subgrade rutting model. As with the fatigue model, Miner's cumulative damage law (equation 17.7) and peak cycle counting were used to calculate subgrade rutting due to strain cycles of different magnitudes.

In the literature reviewed by Hardy [219], the value of the exponent L_2 in the damage law relating vertical subgrade strain to permanent surface deformation was found to vary considerably from 1.85 to 7.14 depending on the pavement design and the test conditions. Brown [74] investigated the relationship between the maximum allowable elastic subgrade strain and the number of load repetitions concluding that a value of $L_2 = 3.57$ was suitable for typical UK pavements. However, no models capable of predicting these constants from the subgrade specification and operating conditions were found in the literature. The parameter L_2 was therefore considered to be an unknown input variable to the WLPPM and its importance was investigated in a parametric study.

The multiplicative subgrade rutting constant L_1 in equation 20.11 directly affects the proportions of surface rutting to subgrade and granular layer rutting. These proportions have been shown to vary from pavement to pavement. In a typical UK pavement, approximately half the rutting was found to occur in the surfacing and road base and half in the sub-base and subgrade [74, 367]. Consequently, the subgrade rutting multiplicative constant L_1 in equation 20.11 was chosen such that, for a relatively thick asphalt pavement (250mm), at a mean yearly air temperature of 10°C (typical of a UK climate [76]), approximately half the rutting occurred in the asphaltic layers and half in the subgrade and granular layers.

A summary of the input pavement data to the WLPPM and the functional relationships used to determine the rest of the required parameters is shown in figure 20.2.

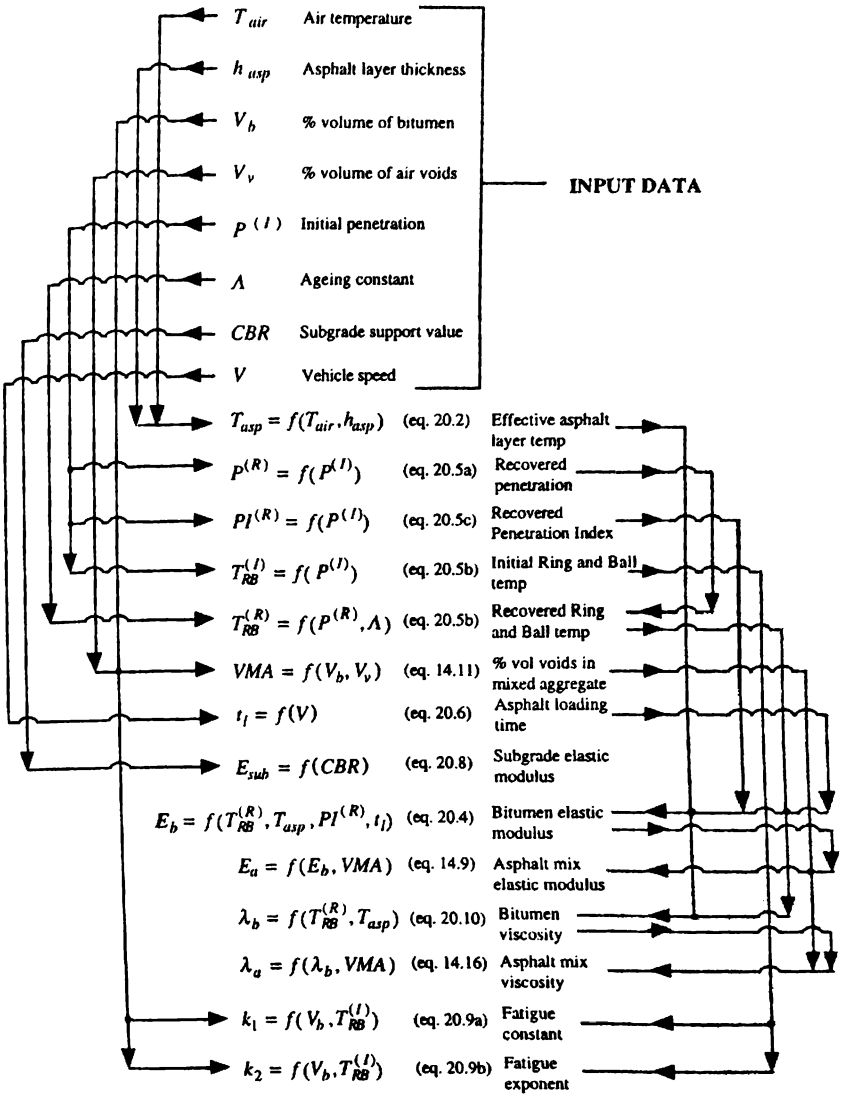


Fig. 20.2 Functional relationships for WLPPM pavement data. From [138].

20.3.7 Asphalt Modulus Degradation Model

The asphalt modulus was assumed to degrade according to the stiffness degradation model which is described in detail in Chapter 16 (see figures 16.6 to 16.8). The equations are summarised as follows:

$$E/E_0 = \exp^{KD} \qquad \left(E/E_0 > (E/E_0)_c\right),$$
$$E/E_0 = (E/E_0)_c \qquad \left(E/E_0 \le (E/E_0)_c\right), \tag{20.12}$$
$$K = \log_e (E/E_0)_c.$$

where E/E_0 is the reduction in elastic modulus of the asphaltic material,
D is the cumulative fatigue damage (see equation 17.7) and
$(E/E_0)_c$ is a constant that determines the level of modulus reduction corresponding to the end of the fatigue life of the asphalt (*ie* $D = 1$).

20.3.8 Pavement Stiffness Variations

One of the major causes of stiffness variations along the length of the pavement is variations in the thickness of the asphalt layer. The method used to quantify this variation is explained in this section.

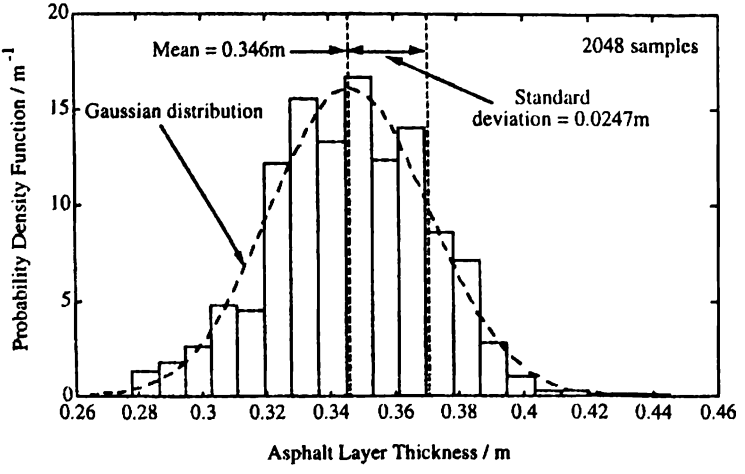


Fig. 20.3 Measured asphalt layer thickness probability distribution from the A500T. From [134].

Measured asphalt layer thickness data from a section of the A500T trunk road in the UK was measured by GB Geotechnics using ground penetrating radar techniques (*eg* [307, 324]). Figure 20.3 shows the probability density function of this data. Spectral analysis was used to determine the thickness spectrum S_h from the same data. The thickness spectrum is plotted in figure 20.4, together with a fitted equation of the form:

$$S_h(\kappa) = \frac{F}{1 + (\kappa / \kappa_0)^H}. \tag{20.13}$$

The fitted constants were found to be; $F = 6.3 \times 10^{-2}$ m^3/cycle, $\kappa_0 = 3.13 \times 10^3$ *m / cycle* and $H = 2.25$. It can be seen by comparing equation 20.18 with equation 20.3 (the equation for the spectral density of the pavement profile surface displacement) that the value of the exponent is similar (2.25 in equation 20.13, compared with 2.5 in equation 3.2). Consequently, the amplitude of the thickness spectrum and the amplitude of the surface displacement spectrum decrease at approximately the same rate with increasing wavenumber (decreasing wavelength).

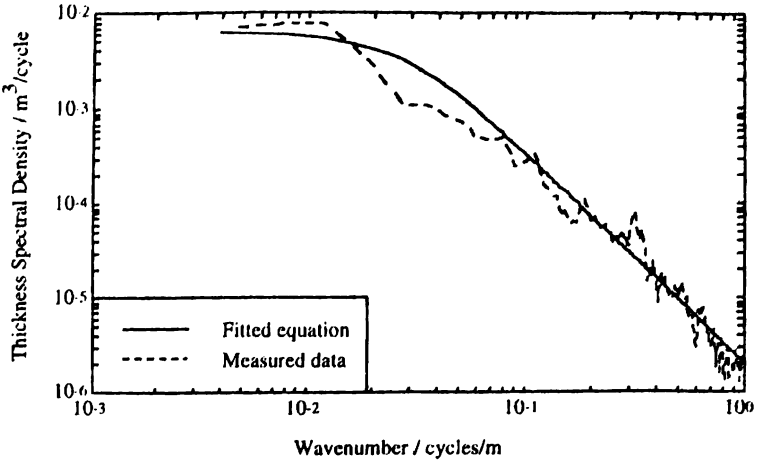


Fig. 20.4 Measured asphalt layer thickness spectral densities (for the data shown in figure 20.4) from the A500T. From [138].

A random asphalt layer thickness displacement history can be obtained from equation 20.13 using the same method used to obtain the pavement surface profile. Note that this method gives a Gaussian amplitude distribution, which agrees well with the measurements (figure 20.3). The phase relationship between the various roughness components in the surface profile and the thickness profile is not known. This would require information about the cross-spectrum between the surface roughness and the thickness. Such information could only be obtained from simultaneous measurements of the surface profile and thickness, and data of this type could not be found. Consequently, in the absence of suitable cross-spectral information, the thickness profile was assumed to be uncorrelated with the surface profile. This was implemented using random phase angles to generate the thickness profile that were uncorrelated with the random phase angles used to generate the surface profile. Any other degree of correlation could be included in the model, if suitable cross-spectral information was available, using the method described in Section 3.4.2.

To determine thickness profiles for pavements with a different mean asphalt layer thickness to the A500T (different mean asphalt layer thickness), the thickness spectrum (equation 20.13) was scaled such that ratio of the standard deviation to the mean thickness was the same for pavements with different mean asphalt layer thicknesses.

Once a thickness profile was generated, it was divided into a number of equally spaced, discrete sub-sections where the thickness was assumed constant. This simplified thickness variation was then used in the WLPPM.

To avoid step changes in the primary responses at a boundary between sub-sections with different asphalt layer thicknesses and/or different asphalt layer moduli, linear interpolation was used between the two adjoining influence functions (see [134] for further details).

20.4 SIMPLIFIED CASE STUDIES

To illustrate the various features of the WLPPM described above, four simplified case studies are examined in this section, and a parametric study of various vehicle and road features is performed in Section 20.5 For all of the case studies the vehicle loading was applied using the linear 'quarter car' vehicle model travelling at a constant speed of 22.5m/s (80km/h) over a 100m length of surface

profile. The loads generated by the vehicle model were applied to the pavement through a 'super-single' tyre with a contact patch radius of 0.135m.

A typical 50 pen modified hot rolled asphalt was used, and to simplify the simulations, all the material properties that are functions of temperature (*eg* asphalt modulus, viscosity *etc*) were fixed at a temperature of 10°C. Full details of the mix specification and input parameters are given in Table 20.1. For each of the case studies, the nominal thickness of the asphalt layer was 250mm and ageing of the asphaltic material was assumed not to occur. The subgrade was assumed to have a *CBR* of 4%. Where a random surface profile was required, an initial profile with IRI = 2 was used. This corresponds to the typical roughness of a new principal road.

Pavement Property	*Simplified case studies Section 20.4*	*Motorway Section 20.5*	*Principal Road Section 20.5*	*Minor Road Section 20.5*
Maximum air temp. T_{air}^{max} /° C	10	18	18	18
Minimum air temperature T_{air}^{min} /° C	10	4	4	4
Asphalt layer thickness h_{asp} / mm	250	250	200	125
Percentage volume of bitumen V_b	12	12	12	12
Percentage volume of air voids V_v	4	4	4	4
Initial bitumen penetration $P^{(I)}$	50	50	50	50
Ageing constant A /° C^2 / hour	1.65×10^{-3}	1.65×10^{-3}	1.65×10^{-3}	1.65×10^{-3}
Subgrade CBR percentage	4	4	4	4

Table 20.1 Pavement model input parameters used in the simulations.

To include asphalt layer thickness variations in the model the pavement was divided into 0.5m sub-sections, each of constant thickness. To limit the number of computations required, the random thickness variation was discretised into 6 levels and the modulus of the asphalt layer was degraded in 10% steps (9 increments altogether). The pavement surface profiles were updated 80 times (approximately every 260,000 load passes). It was found that, using the above parameters, a satisfactory trade off was achieved between computation speed and convergence of the results (see [134] for further details).

For all of the case studies in this chapter, the rutting due to the static vehicle loads at the end of the loading period was approximately 20mm.

To investigate the importance of the subgrade rutting law, the rutting exponent L_2 in equation 20.11 was taken to be either 1 or 4. The corresponding values of the multiplicative rutting constant L_1, were chosen such that approximately half the rutting occurred in the surface and half in the lower layers: $L_1 = 2.47\times10^{-3}$mm and $L_1 = 3.31\times10^{8}$mm respectively. The importance of the modulus degradation law feedback loop on the primary response model was also investigated.

Each of the four case studies is explained in the following sub-sections.

20.4.1 Damage Propagation due to a 'Hot Spot'

The first case study examines damage propagation due to a 'hot spot' on an otherwise flat pavement surface. The 'hot spot' was modelled as half a sine wave of amplitude 15mm and length 4m. The asphalt layer had a uniform thickness. The vehicle speed was the same on all the runs.

Figure 20.5 shows the initial pavement surface profile together with surface profiles after 10.11 million and 20.75 million load passes, using $L_2 = 1$ in the subgrade rutting law (equation 20.11). It can be seen from this figure that the mean surface level drops as the number of load passes increases. This corresponds to the formation of a rut in the wheel path. With no modulus degradation (solid line), the surface irregularity excites the modes of vibration of the vehicle model with the result that the downstream surface profile fluctuates about the mean rut depth. The wavelength of these fluctuations corresponds to the frequency of sprung mass vibration of the vehicle model (approximately 2.5Hz). The unsprung mass motion of the vehicle model (approximately 10Hz) decays away more rapidly and only affects the shape of the profile in the vicinity of the hot spot.

Also shown in this figure (dashed line) are the results of the same case, but including degradation of the elastic modulus of the asphalt layer as the pavement becomes progressively damaged by fatigue. It can be seen that in this case, including the modulus degradation feedback loop has virtually no effect on the surface profile. This is because, even at the most heavily loaded areas, only a small proportion of the fatigue life has been used up by the time the permanent deformation becomes excessive. This is shown in figure 20.6 where the reduction in asphalt layer modulus is shown at the corresponding loading stages. It can be seen from this figure that the modulus reduction due to the static loads alone (*ie* the section before the bump where the vehicle loads are essentially static) is approximately 3% and the modulus reduction around the hot spot (where the dynamic loads are expected to be high) is approximately 8%. It can also be seen from this figure that, after the bump, the modulus reduction profile is essentially in phase with the pavement surface profile.

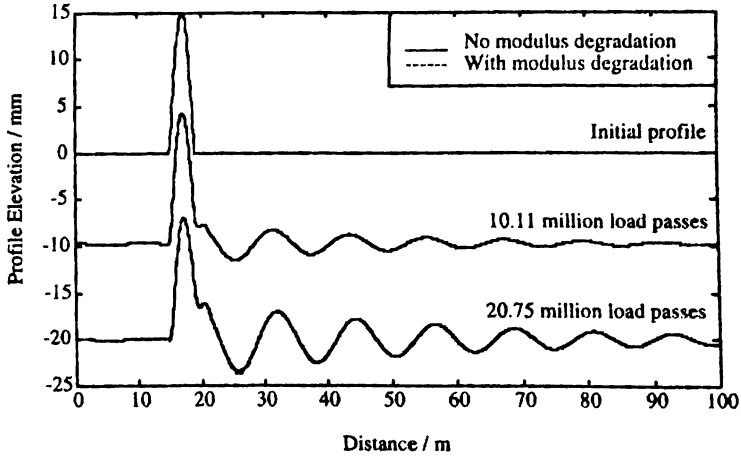


Fig. 20.5 Pavement surface displacement profiles near a 'hot spot' at various loading stages, using a subgrade rutting exponent of L_2=1. From [138].

Figure 20.7 shows the corresponding situation using $L_2 = 4$ in the subgrade rutting law (equation 20.11). For no modulus degradation (solid line) the amplitude of surface damage fluctuations downstream of the surface irregularity is greater, and the waveform is less symmetrical, than the corresponding situation shown in figure 20.5. This is due to the larger exponent in the subgrade rutting model weighting the peaks of the dynamic loads more than the troughs. The dashed line in figure 20.7 show the same test case but including degradation of the asphalt layer modulus (equation 20.12). It can be seen that including this feedback loop increases the amount of permanent surface deformation, particularly at the most heavily loaded areas (troughs). This is because the cumulative fatigue damage of the asphalt, and hence modulus reduction, is greatest at these areas of greatest load concentration and this effect becomes more important when the subgrade is more sensitive ($L_2 = 4$).

Consequently, the vertical subgrade strain is increased at these locations, resulting in an increased rate of subgrade deformation (rutting).

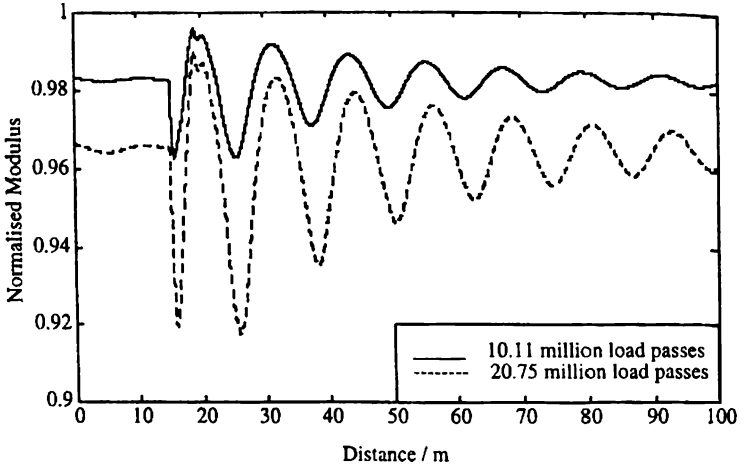


Fig. 20.6 Reduction in normalised asphalt layer modulus (E/E_0) near a 'hot spot' at various loading stages, using a subgrade rutting exponent of L_2=1. From [138].

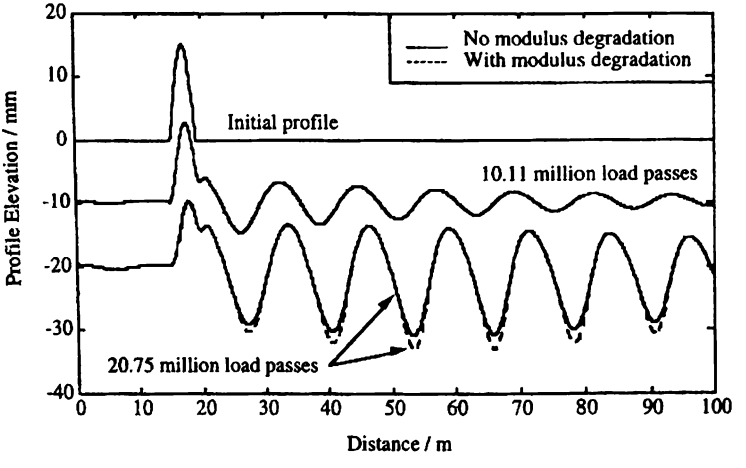


Fig. 20.7 Pavement surface displacement profiles near a 'hot spot' at various loading stages, using a subgrade rutting exponent of $L_2 = 4$. From [138].

20.4.2 Damage Propagation due to a 'Weak Spot'

The second case study examines damage propagation due to a 'weak spot' on an otherwise flat surface. The 'weak spot' was modelled as a 4m section of pavement with an asphalt layer 50mm thinner than the rest of the pavement (200mm instead of 250mm nominal).

Figure 20.8 shows the initial pavement surface profile together with surface profiles after 10.11 million and 20.75 million load passes using $L_2 = 1$ in the subgrade rutting law (equation 20.11). It

can be seen from this figure that, without modulus degradation (solid line), a surface depression forms where the asphalt layer is thinnest and the rest of the pavement profile essentially degrades at uniform rate (due to the static loads) with little additional downstream damage due to dynamic loads. This is because the level of dynamic loading produced by the surface depression at the weak spot, combined with the low power in the subgrade rutting law, is not sufficient to influence the downstream surface profile greatly. Also shown in this figure (dashed line) are the same results but including degradation of the elastic modulus of the asphalt layer as the pavement becomes progressively fatigue damaged. Including this feedback loop increases the depth of the surface depression significantly, but has little effect on the level of downstream damage. The reason for this is shown in figure 20.9 where the modulus reduction profile at the corresponding loading stages is shown. It can be seen from this figure that the modulus of the asphaltic material at the weak spot has been reduced to 70% of its initial value, whereas the rest of the asphalt layer modulus is at 96% of its initial value. This modulus reduction is larger than the reduction produced by dynamic loads in the previous case study, because of the sensitivity of the asphalt base strain (used in fatigue calculations) to the thickness of the asphalt layer.

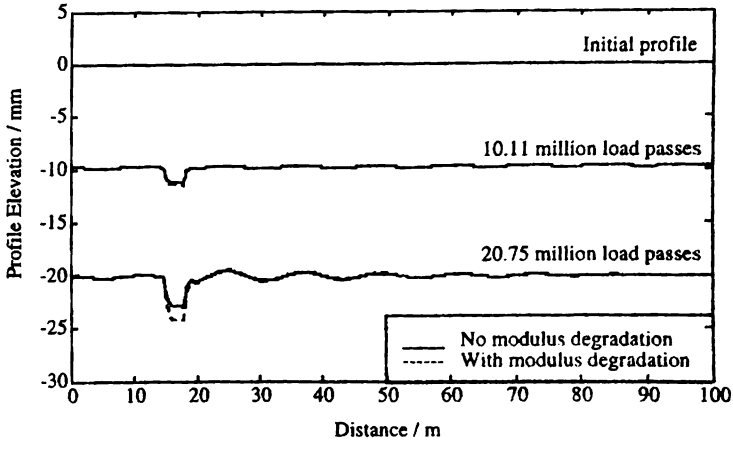


Fig. 20.8 Pavement surface displacement profiles near a 'weak spot' at various loading stages, using a subgrade rutting exponent of $L_2 = 1$. From [138].

The weak spot simulation, using $L_2 = 4$ in the subgrade rutting law (equation 20.11), is shown in figure 20.10. By comparing figures 20.8 and 20.10 it can be seen that, for the larger subgrade rutting exponent, the depression formed at the weak spot is approximately 25mm deeper than the depression formed using the lower exponent. Consequently, the level of dynamic loading produced by the vehicle model is higher, resulting in more downstream damage. As before, including the asphalt modulus degradation law (dashed line) increases the rate of rutting at the most heavily loaded areas (troughs).

20.4.3 Random Thickness Variation and a Flat Profile

The third case study examines damage propagation on a pavement with a random asphalt layer thickness variation and an initially flat surface profile. The random thickness variation was created using the procedure detailed in Section 20.3.8. Figure 20.11 shows the random asphalt layer thickness distribution (dashed line) together with the distribution averaged over 0.5m intervals and discretised into 6 levels (dashed line). This discretised distribution was used in the WLPPM.

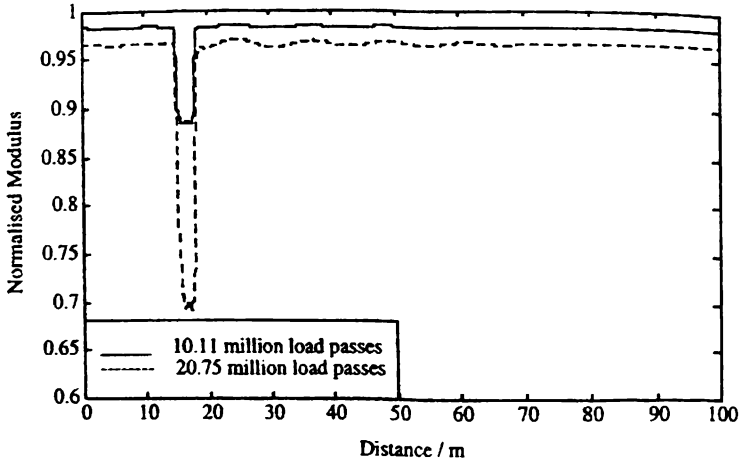


Fig. 20.9 Reduction in normalised asphalt layer modulus (E/E_0) near a 'weak spot' at various loading stages, using a subgrade rutting exponent of L_2=1. From [134].

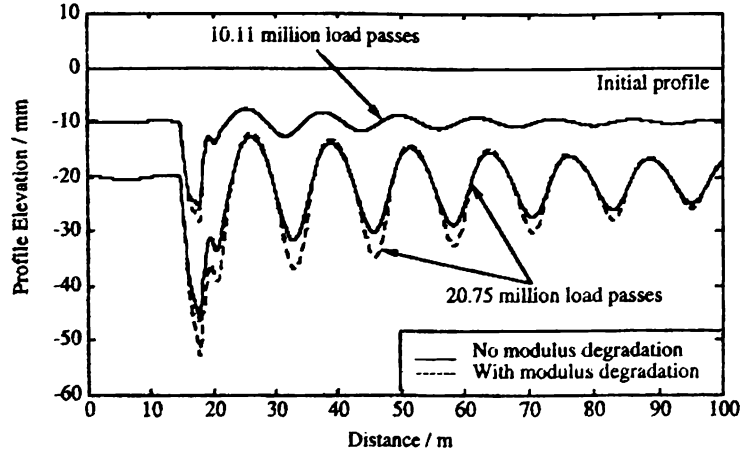


Fig. 20.10 Pavement surface displacement profiles near a 'weak spot' at various loading stages, using a subgrade rutting exponent of $L_2 = 4$. From [138].

Figure 20.12 shows the initial pavement surface profile together with profiles after 10.11 million and 20.75 million load passes using $L_2 = 1$ in the subgrade rutting law (equation 20.11). It can be seen from this figure that, for no modulus degradation (solid line), the pavement surface profile degrades at an approximately uniform rate due to the static vehicle loads, with only a small effect from dynamic loading induced by the surface roughness. As before, including degradation of the asphalt layer elastic modulus (dashed line) slightly increases the amount of rutting particularly at the most heavily loaded areas (troughs).

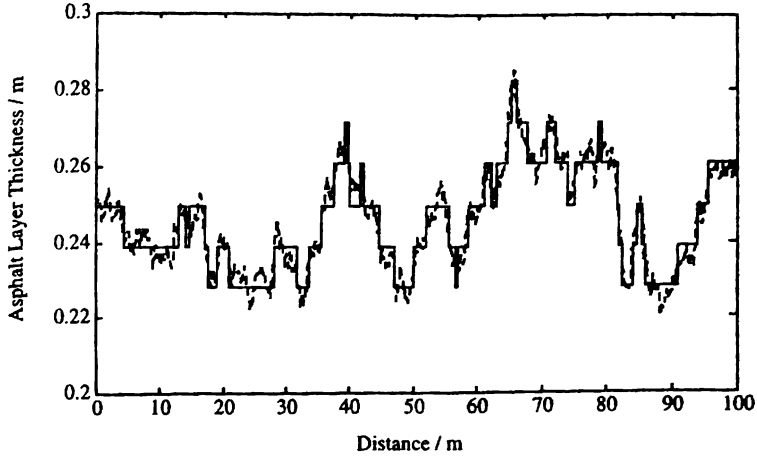


Fig. 20.11 Discretised random thickness variation. From [138].

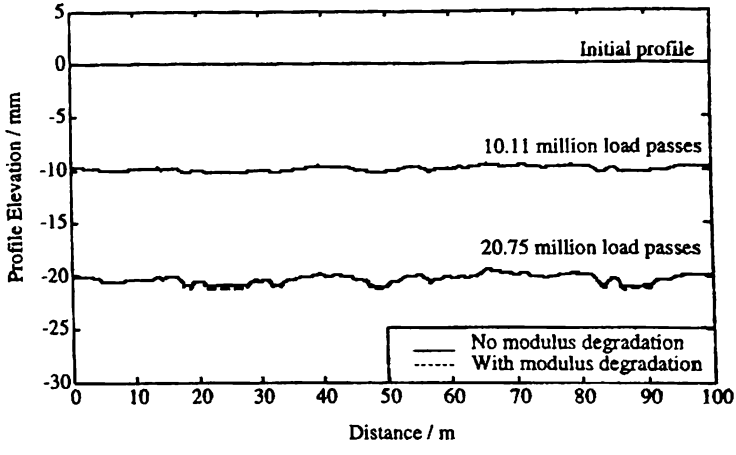


Fig. 20.12 Pavement surface displacement profiles at various loading stages for a pavement with random thickness, using a subgrade rutting exponent of $L_2 = 1$. From [138].

Figure 20.13 shows the random thickness simulation using $L_2 = 4$ in the subgrade rutting law (equation 20.11). It can be seen from this figure that, with no modulus degradation, the magnitude of the damage is significantly increased and dynamic loads induced by the initial asphalt layer thickness profile have a more prominent effect. For example, it can be seen that although the rutting due to the static loads after 20.75 million load passes is 20mm, the profile at 90m along the pavement shows a depression approximately 4m long and 40mm deep (20mm below the 'static' rut depth). It can also be seen by comparing this figure with the input thickness profile (figure 20.11) that the depression has formed where the asphalt layer is at its thinnest. Including degradation of the asphalt layer modulus (dashed line) increases the rut depth at these heavily loaded areas still further. This is due to the reduction of stiffness of the asphalt layer at these points.

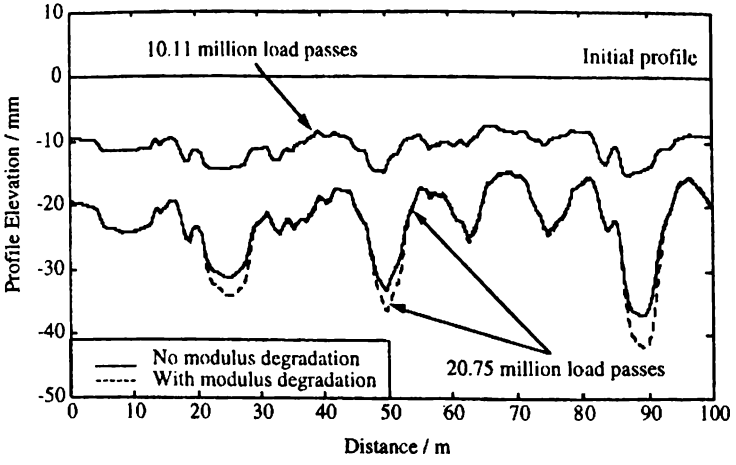


Fig. 20.13 Pavement surface displacement profiles at various loading stages for a pavement with random thickness, using a subgrade rutting exponent of $L_2 = 4$. From [138].

Figure 20.14 summarises the profile roughness data shown in figures 20.12 and 20.13 and shows the change in IRI roughness as a function of cumulative load passes. The IRI starts at zero. It can be seen from this figure that, as expected, the rate of increase in roughness and the effects of modulus degradation are much greater for the larger subgrade rutting exponent. It should be noted that the effects of modulus degradation are likely to be significantly greater for pavements with thinner asphaltic layers where the fatigue damage is higher.

Figures 20.15 and 20.16 show the 95th percentile levels of rutting and fatigue damage as a function of the number of cumulative load passes for the same simulation as shown in figures 20.12 and 20.13. The 95th percentile level can be interpreted as the damage incurred at the worst 5% of locations along the pavement. It can be seen from these figures that, for no asphalt modulus degradation (solid lines) and $L_2 = 1$ in the subgrade rutting law (equation 20.11), both the 95th percentile rutting and fatigue damage increase approximately linearly with the number of load passes. Including degradation of the asphalt layer modulus has a greater effect on fatigue damage than rutting. This is due to the greater sensitivity of the strain at the base of the asphalt layer (used in fatigue damage calculations) to the elastic modulus of the asphaltic material. For $L_2 = 4$ in the subgrade rutting law (equation 20.11), the rate of rutting and is greatly increased. For example, using the lower subgrade rutting power, 5% of the pavement has reached failure conditions (20mm rut depth) after 20 million load passes whereas for the larger subgrade rutting power this is reduced to approximately 14 million load passes. The rate of fatigue damage also increases, but not in the same proportion. This is because increasing the subgrade rutting power only influences the fatigue damage indirectly, by increasing the surface roughness and hence level of dynamic loading.

It can be seen by comparing figure 20.14 with figures 20.15 and 20.16, that there is a larger difference between the IRI curves (figure 20.14) for the different subgrade rutting powers than between the corresponding 95th percentile rutting and fatigue curves (figures 20.15 and 20.16 respectively). This is because the IRI calculation is insensitive to the mean (DC) level of the profile whereas the 95th percentile fatigue and rutting include a mean level of damage due to the static vehicle loads.

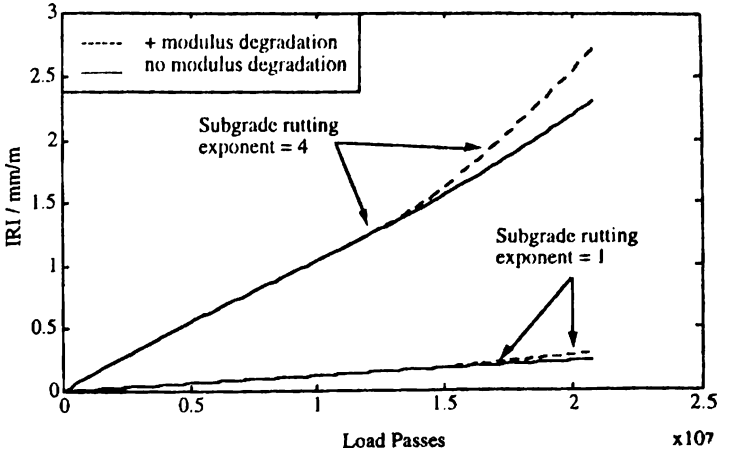


Fig. 20.14 IRI roughness curves for damage accumulation on an initially smooth pavement with a random thickness variation. From [138].

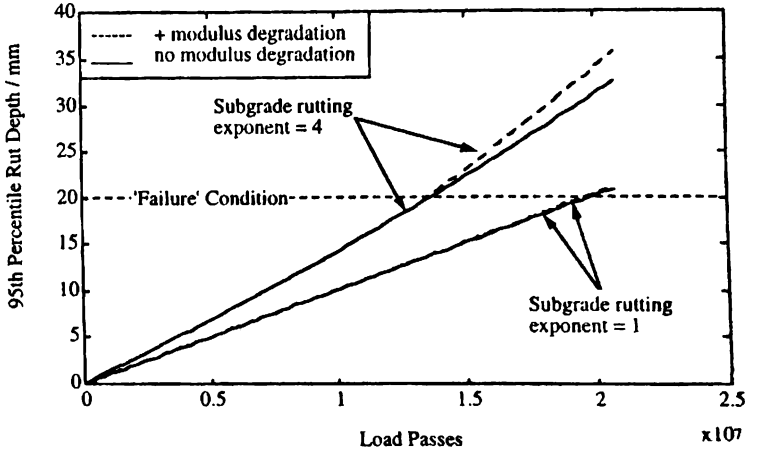


Fig. 20.15 Accumulation of 95th percentile rutting on an initially smooth pavement with a random thickness variation. From [138].

20.4.4 Uniform Asphalt Layer Thickness with a Random Surface Profile

The final case study in this section examines damage propagation on a pavement with a random surface profile and a uniform asphalt layer thickness profile. The initial surface profile was generated from equation 3.2 with a roughness corresponding to an IRI value of 2.

Figure 20.17 shows the initial pavement surface profile together with profiles after 10.11 million and 20.75 million load passes using $L_2 = 1$ in the subgrade rutting law (equation 20.11). It can be seen

from this figure that the profile essentially degrades at a uniform rate due to the static vehicle loads, although the short wavelength irregularities tend to get smoothed out by the dynamic tyre forces.

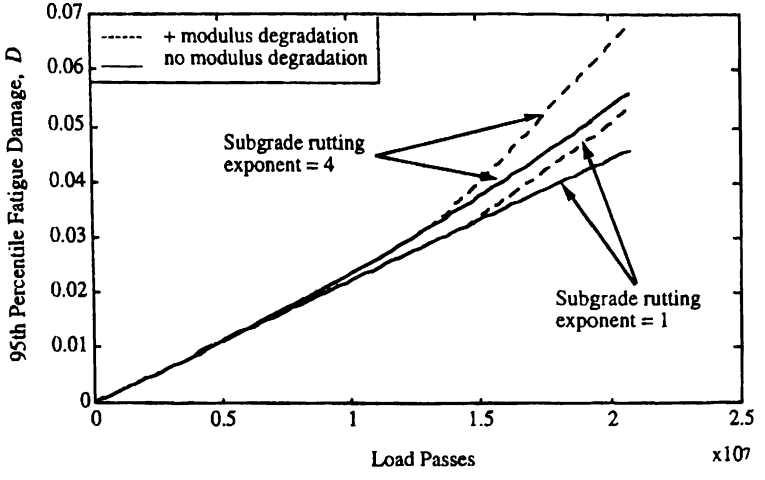


Fig. 20.16 Accumulation of 95th percentile fatigue damage on an initially smooth pavement with a random thickness variation. From [138].

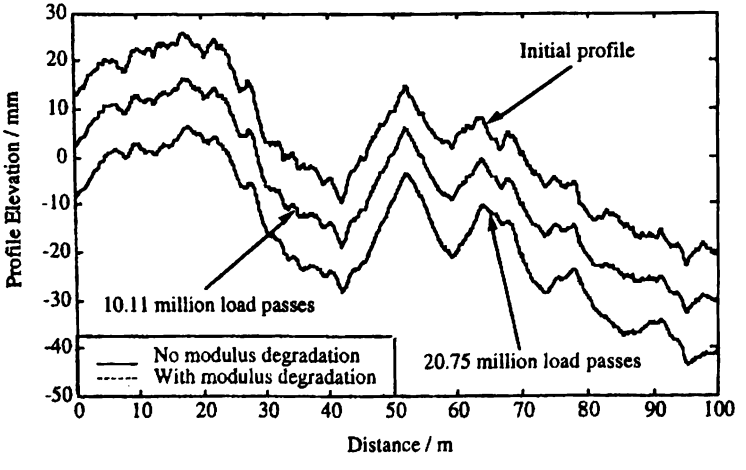


Fig. 20.17 Surface displacement profiles of a pavement with random initial roughness at various loading stages, using a subgrade rutting exponent of $L_2 = 1$. From [138].

This smoothing effect is mainly due to the phase relationship between the various frequency (wavenumber) components present in the tyre force and surface displacement profile histories. At low wavenumbers (long wavelengths) the tyre force tends to be 180° out of phase with the surface profile. This corresponds to the peak loads being applied to the troughs in the pavement profile history and the minimum loads being applied on the peaks in the pavement profile history. Consequently the amplitude of the pavement profile increases in this wavenumber range.

Conversely, at high wavenumbers (short wavelengths) the tyre force is in phase with the surface profile. This corresponds to the peak loads being applied to the peaks in the pavement profile history and the minimum loads being applied to the troughs in the pavement profile history. Consequently the amplitude of the pavement profile decreases in this wavenumber range (see [134]).

The smoothing effect is also exaggerated by the averaging that occurs in the asphalt and subgrade rutting models. For a typical point along the pavement the asphalt rutting calculation procedure involves integrating over the length of the permanent surface displacement influence function weighted by the variation in tyre force over the same length. Consequently, although the linear visco-elastic rutting model is essentially proportional to the instantaneous dynamic load (see Chapter 14), the wavelength components shorter than the length of the influence function will tend to become smoother. For the subgrade rutting model, the influence function is much longer and flatter, and when it has been weighted with the dynamic tyre forces the peak strain does not always occur directly over the point where the subgrade rutting is being calculated. This also has the effect of smoothing the higher wavenumber components.

Figure 20.18 shows the corresponding situation using $L_2 = 4$ in the subgrade rutting law (equation 20.11). It can be seen from this figure that, for no modulus degradation, the vehicle tends to 'tune' into the pavement surface with the result that the body bounce wavelength (approx. 10m) is imposed on the profile. As expected, including degradation of the asphalt layer modulus (dashed line) tends to increase the rate of damage, particularly at the areas of largest load concentration (troughs).

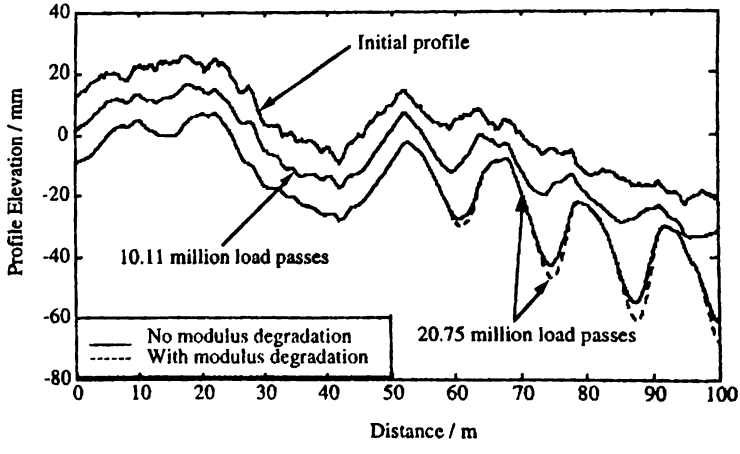


Fig. 20.18 Surface displacement profiles of a pavement with random initial roughness at various loading stages, using a subgrade rutting exponent of $L_2 = 4$. From [138].

Figure 20.19 shows the IRI roughness as a function of cumulative load passes for the data shown in figures 20.17 and 20.18. Note that the IRI has an initial value nearer 2. It can be seen from this figure that changing the rutting exponent has a more dramatic effect on the roughness than including degradation of the asphalt layer modulus. For the lower power in the subgrade rutting law, the IRI tends to decrease slightly, indicating that the pavement is becoming smoother. This is due to the smoothing of high wavenumber components. However, the situation is different for the larger power in the subgrade rutting law. After an initial period when the IRI decreases, the pavement tends to become rougher quickly. This is because the lower frequency vibrations of the vehicle model are imposed on the pavement profile, resulting in increased surface roughness.

In accelerated pavement tests with realistic dynamic tyre forces, performed as part of the 'DIVINE' project [275], the test pavement was also observed to become smoother initially, before becoming rougher as damage progressed. To some extent, this evidence verifies the trends in figure 20.19.

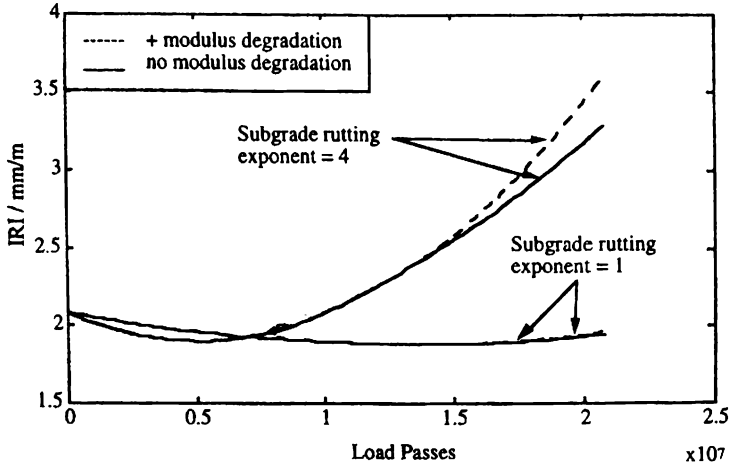


Fig. 20.19 IRI roughness curves for damage accumulation on a pavement with a random surface roughness. From [138].

Figures 20.20 and 20.21 show the accumulation of 95th percentile rutting and fatigue damage as a function of the number of load passes. As with the previous case study, increasing the power in the subgrade rutting law from 1 to 4 reduces the number of loads to failure (20mm rut) significantly, in this case by approximately 35%.

20.5 PARAMETRIC STUDY OF FACTORS AFFECTING FLEXIBLE PAVEMENT PERFORMANCE

This section investigates the importance of typical levels of dynamic loads and pavement variability on long-term pavement performance. The models are more realistic than the simplified case studies described in the previous section.

20.5.1 WLPPM Input Parameters

The following sections investigate the long-term performance of three different strengths of flexible pavement operating under typical UK climatic conditions. The pavements correspond to a typical motorway, a principal road and a minor road. The only difference between the different pavements is the average thickness of the asphalt layer. This was taken to be 250mm for the motorway, 200mm for the principal road, and 125mm for the minor road. The length of each simulated pavement section was 100m. A typical 50 pen modified hot rolled asphalt was used for the bituminous binder and the subgrade was assumed to have a *CBR* of 4%, as in the simplified cases in the previous section. Full details of the mix specification and input parameters are given in Table 20.1. For the motorway, an initial IRI roughness of 2 was used and for the minor road an initial IRI roughness of 3 was used. The variation in monthly air temperature for each pavement type was sinusoidal, with a mean temperature of 11°C and a temperature amplitude of 7°C. These are typical of UK conditions [74]. The surface profile was updated every three months of the simulation.

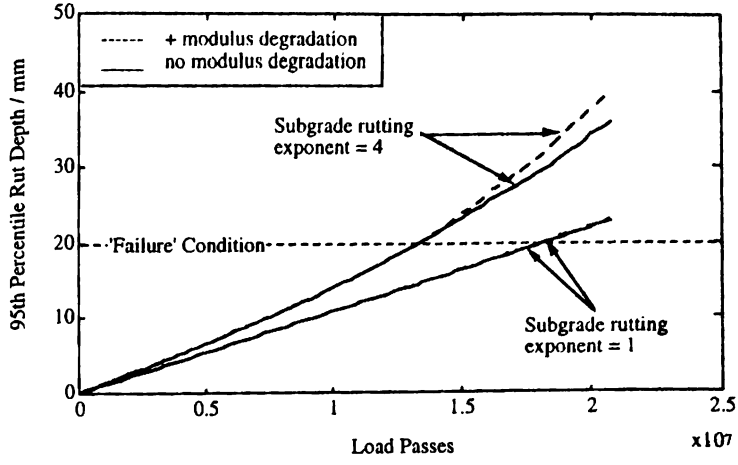


Fig. 20.20 Accumulation of 95th percentile rutting on a pavement with a random surface roughness. From [138].

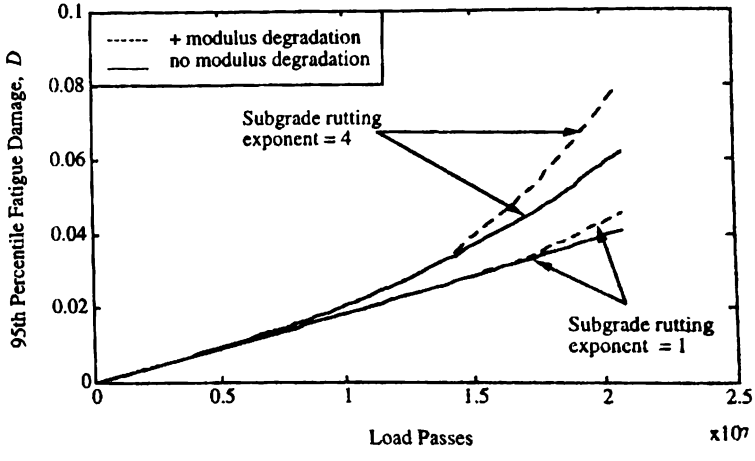


Fig. 20.21 Accumulation of 95th percentile fatigue damage on a pavement with a random surface roughness. [138].

Two different assumptions were again considered for the exponent chosen in the subgrade rutting model (equation 20.11). In the first, a value of $L_2 = 3.5$ was used. This corresponds to the value proposed by Brown [74] for use with pavement design procedures in the UK. The value of the subgrade multiplicative constant was taken to be $L_1 = 4.63 \times 10^6$ mm, giving approximately half the rutting in the asphaltic material and half the rutting in the lower layers for a thick pavement with an air temperature of 10°C. For the second assumption a value of $L_2 = 1$ was used. This can be considered to be a pessimistic estimate of subgrade damage and gives lower layer rutting that is proportional to the instantaneous value of the vertical subgrade strain. The value of the subgrade multiplicative constant was taken to be $L_1 = 2.47 \times 10^{-3}$ mm giving approximately half the rutting in the asphaltic material and half the rutting in the lower layers for a thick pavement with an air temperature of 10°C.

For each of the 3 pavement types, 4 cases were considered, as shown in Table 20.2.

Case	Initial Profile	Asphalt Thickness	Vehicle Loads
0	Smooth	Uniform	Static
1	Random	Uniform	Dynamic
2	Smooth	Random	Static
3	Random	Random	Dynamic

Table 20.2 Operating cases in the parametric study.

For cases 2 and 3 the required asphalt layer thickness profile was generated using the procedure described in Section 20.3.8. The main assumption in this procedure is that the ratio of the standard deviation to the mean asphalt layer thickness is constant for pavements with different mean asphalt layer thicknesses. Consequently, the standard deviation of the asphalt layer thickness profile changes in proportion to the mean asphalt layer thickness.

Note that graphical results are only presented her for two of the pavement strengths (motorway and minor road). Further details can be found in [134].

20.5.2 Spatial Repeatability

It is important that the dynamic loads used in the WLPPM are representative of the distribution of loads applied to the pavement by a typical vehicle fleet. In particular, the levels of spatial repeatability of dynamic loads should be included accurately.

For each pavement type, four quarter car simulations were used to represent measured vehicle fleet speed variations (taken from the National Speed Survey [27]). Previously measured levels of spatial repeatability (see Chapter 18) were modelled by adjusting the value of the suspension stiffness for each of the four simulations. Full details of this process are given in reference [134]. Table 20.3 gives details of the suspension stiffnesses used in the quarter-car model for each pavement and each speed range used in the WLPPM.

Speed Range, V / m/s	*Suspension Stiffness / MN/m*		
	Minor Road	Principal Road	Motorway
$V \leq 13.4$ (30mph)	0.396	—	—
13.4 (30mph) $< V \leq$ 17.9 (40mph)	0.817	0.541	0.546
17.9 (40mph) $< V \leq$ 22.4 (50mph)	1.616	0.784	0.763
22.4 (50mph) $< V \leq$ 26.8 (60mph)	1.017	1.214	1.169
26.8 (60mph) $< V \leq$ 31.3 (70mph)	—	0.417	0.427
31.3 (70mph) $< V$	—	—	—

Table 20.3 Suspension stiffness required to obtain desired average repeatability for each speed range.

20.5.3 Evaluation Criteria

To compare results from the 4 cases shown in Table 20.2, two criteria were used. The first is denoted the 'Pavement Life Reduction Factor' (PLRF). For case *i*, this is defined as:

$$\text{PLRF}^{(i)} = \frac{N^{(0)} - N^{(i)}}{N^{(0)}} \times 100\%, \qquad (i = 1,2,3), \tag{20.14}$$

where $N^{(i)}$ is the number of load passes in case *i* required to produce 'critical' conditions,

and $N^{(0)}$ is the number of load passes in case 0 required to produce 'critical' conditions.

'Critical' conditions are defined to be the first point where the 95th percentile rut depth reached 10mm (often defined as the point where overlaying is required [378]) or the 95th percentile fatigue damage reached 0.5. The PLRF is a measure of the *importance of dynamic loads or asphalt layer thickness variations on pavement life.*

The second criterion is the 'Conventional Simulation Error' (CSE). For case *i*, this is defined as:

$$CSE^{(i)} = \frac{F^{(3)} - F^{(i)}}{F^{(3)}} \times 100\%, \qquad (i = 0, 1, 2) \tag{20.15}$$

where $F^{(i)}$ is the case *i* 'failure' condition when the case 3 'failure' condition $F^{(3)}$ is reached.

'Failure' conditions are defined to be the point where the 95th percentile rut depth reaches 20mm or the 95th percentile fatigue damage reaches 1.0. The CSE is a measure of *the error in predicted pavement damage* if dynamic loads and/or asphalt layer thickness variations are neglected.

'Failure' conditions were not used in the PLRF calculation because they were not reached in some of the cases and thus extrapolation would be required to calculate the PLRF.

20.5.4 Parametric Study Results

Motorway (Subgrade Rutting Exponent = 3.5)

Figures 20.22-20.24 show the pavement surface profiles at various loading stages for case 1 (random roughness, constant thickness), case 2 (constant roughness, random thickness) and case 3 (random roughness, random thickness) respectively. It can be seen from these figures that more rutting occurs in the first 10 years (before 22.8 million load passes) than the last 10 years (between 22.8 million load passes and 45.6 million load passes). This is due to ageing of the bituminous material decreasing the rutting susceptibility of the asphalt mix by increasing its elastic modulus and viscosity. It can also be seen from the cases that include random surface roughness (cases 1 and 3) that the shorter wavelength surface profile components tend to get smoothed, whereas the amplitude of the longer wavelength components increase as the profile degrades (figures 20.22 and 20.24). This is similar to the simplified case studies shown above (figures 20.17-20.19) . Results from case 2 (figure 20.23) show that, as expected, the profile degradation is closely related to the input asphalt layer thickness profile (shown in figure 20.25).

It is interesting to compare figure 20.25 (which shows the asphalt layer thickness variations along the pavement) and figure 20.24 (case 3 results). It can be seen that a depression begins to form in the surface profile at 40m (figure 20.24) which clearly results from the weak pavement at this location (see figure 20.25). A similar effect occurs at 69m. On the other hand, the depressions that form at 55m and 83m (where the pavement is relatively strong) are due to the surface roughness features just upstream of these locations (figure 20.24). It is particularly interesting to note that a weak pavement from 77m–80m does not cause a surface depression. This is because the surface profile rises at this point and the resultant dynamic loads are relatively small: the vehicles 'jump–over' this point.

Figures 20.26–20.28 show the increases in IRI roughness, 95th percentile rutting and 95th percentile fatigue damage as a function of cumulative load passes for cases 0, 1, 2 and 3 using $L_2 = 3.5$ in the subgrade rutting model (equation 20.11). The small oscillation superimposed on the curves (particularly figure 20.27) is due to the effects of seasonal variation in temperatures on pavement

strength and stiffness. The pavement ruts faster in the summer than in the winter. It can be seen from these figures that, for case 3 (random roughness, random thickness), the pavement fails by excessive rutting after approximately 25 million load passes (figure 20.27). However, for case 0, the pavement would take approximately 70 million load passes to failure (this is off the graph). Case 0 corresponds to a conventional pavement engineering calculation assuming constant loads and uniform properties. At failure (2.5×10^7 load passes), the 95th percentile fatigue damage for case 3 is approximately 3.5% (figure 20.28).

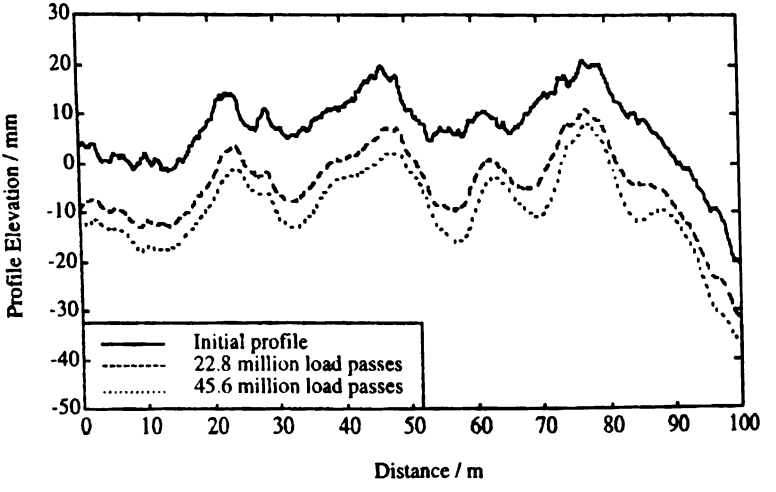


Fig. 20.22 Case 1 motorway surface displacement profiles at various loading stages, using a subgrade rutting exponent of $L_2 = 3.5$.

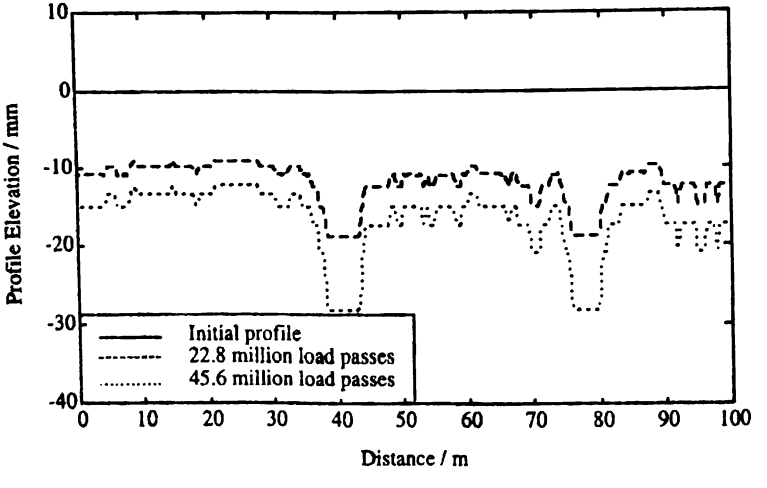


Fig. 20.23 Case 2 motorway surface displacement profiles at various loading stages, using a subgrade rutting exponent of $L_2 = 3.5$. From [139].

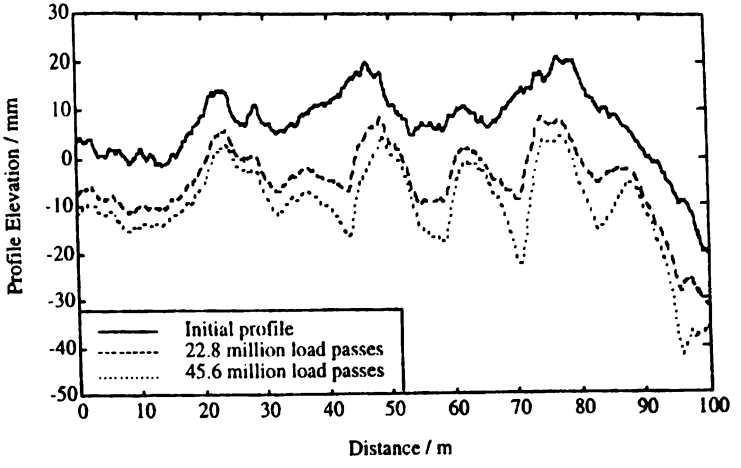


Fig. 20.24 Case 3 motorway surface displacement profiles at various loading stages, using a subgrade rutting exponent of $L_2 = 3.5$. From [139].

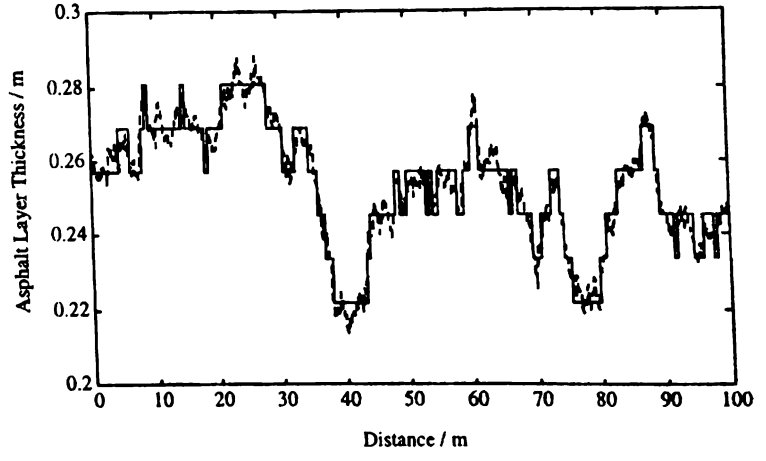


Fig. 20.25 Discretised random thickness variation for a typical motorway. From [139].

From the IRI roughness curves (figure 20.26) it can be seen that, for case 1 (random roughness, uniform thickness), the pavement becomes smoother initially with a subsequent gradual increase in roughness with progressive trafficking. This is due to the smoothing at high wavenumbers that is shown in figures 20.22 and 20.24. The subsequent increase in roughness is because the body bounce wavelengths of the vehicle models are imposed on the surface profile. Asphalt layer modulus reductions caused by progressive fatigue damage do not greatly effect the rate of surface profile deterioration because the proportion of the fatigue life used at failure, for case 3 is small (3.5%).

The corresponding IRI roughness curve for case 3 (random roughness, random thickness) shows a similar trend although the final rate of increasing roughness is greater than for case 1. This is

because the rate of profile degradation is dependent on the interaction between surface roughness induced dynamic loads and thickness variations within the asphalt layer (included in case 3 but not case 1). As a result of this interaction, the surface profile degrades unevenly thus producing larger levels of dynamic vehicle loading and an increased rate of pavement wear.

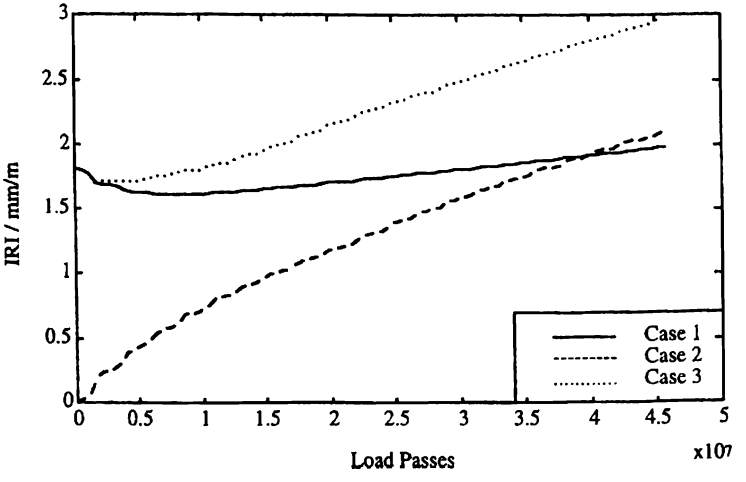


Fig. 20.26 IRI roughness curve for damage accumulation on a motorway, using a subgrade rutting exponent of $L_2 = 3.5$. From [139].

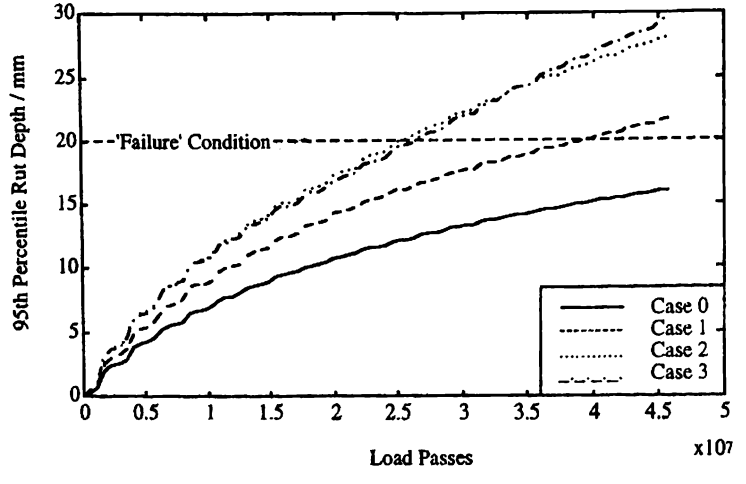


Fig. 20.27 Accumulation of 95th percentile rutting on a motorway, using a subgrade rutting exponent of $L_2 = 3.5$. From [139].

Tabulated values of the PLRF and CSE are given in Tables 20.4 and 20.5 respectively. It can be seen from Table 20.4 that the inclusion of surface roughness induced dynamic loads (case 1) and asphalt layer thickness variations (case 2) produce PLRFs of 34.4% and 50% respectively.

Including both these effects (case 3) also produces a PLRF of 50%. The pavement life is therefore reduced by 50% as a result of dynamic loads and asphalt layer thickness variations. The CSE values from Table 20.5 are 36.9% (case 0), 16.4% (case 1) and -4.4% (case 2). (Note that, for case 2, the predicted rut depth is greater than 20mm, hence the negative CSE value.) Thus a conventional pavement life simulation which neglected both dynamic loads and asphalt layer thickness variations would over estimate pavement life by 36.9%.

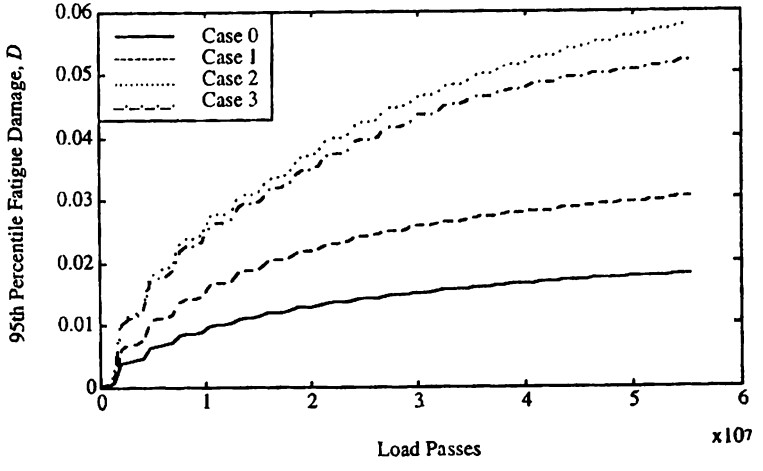


Fig. 20.28 Accumulation of 95th percentile fatigue damage on a motorway, using a subgrade rutting exponent of $L_2 = 3.5$. From [139].

It can be seen from this data that, for thick asphalt pavements (using $L_2 = 3.5$), variations in the thickness of the asphalt layer (case 2) give a greater rate of rutting than surface roughness induced dynamic loads (case 1). This is because it was assumed that the ratio of the standard deviation of the asphalt layer thickness profile to the mean asphalt layer thickness was constant for different classes of pavements. Consequently, for a thick pavement, the standard deviation of the thickness distribution is largest, thus dominating the surface profile degradation process.

Road	*Failure Mode*	*PLRF %*	*PLRF %*	*PLRF %*
		Case 1, $L_2 = 3.5$	*Case 2*, $L_2 = 3.5$	*Case 2*, $L_2 = 3.5$
Motorway (250mm)	Rutting	34.4	50.0	50.0
Principal Road (200mm)	Rutting	60.0	68.8	75.0
Minor Road (125mm)	Rutting	48.0	58.7	66.7
		Case 1, $L_2 = 1$	*Case 2*, $L_2 = 1$	*Case 3*, $L_2 = 1$
Motorway (250mm)	Rutting	9.5	9.5	14.3
Principal Road (200mm)	Rutting	18.2	18.2	27.3
Minor Road (125mm)	Fatigue	N/A	N/A	N/A

Table 20.4 Pavement Life Reduction Factors (PLRF) for typical UK pavements.

Road	Failure Mode	CSE %	CSE %	CSE %
		Case 0, $L_2 = 3.5$	Case 1, $L_2 = 3.5$	Case 2, $L_2 = 3.5$
Motorway (250mm)	Rutting	36.9	16.4	-4.4
Principal Road (200mm)	Rutting	58.8	25.3	12.5
Minor Road (125mm)	Rutting	63.1	28.2	16.5
		Case 0, $L_2 = 1$	Case 1, $L_2 = 1$	Case 2, $L_2 = 1$
Motorway (250mm)	Rutting	12.6	3.1	0.7
Principal Road (200mm)	Rutting	27.3	14.0	10.7
Minor Road (125mm)	Fatigue	90.6	69.4	70.9

Table 20.5 Conventional Simulation Errors (CSE) for typical UK pavements.

Motorway (Subgrade Rutting Exponent = 1)

Figure 20.29 shows the increases in 95th percentile rutting as a function of cumulative load passes for cases 0, 1, 2 and 3 using $L_2 = 1$ in the subgrade rutting model (equation 20.11). It can be seen from this figure that there is less difference between the cases compared to the corresponding results using the larger subgrade rutting exponent (figure 20.28). The number of load passes to failure for case 3, has increased to approximately 28 million. This is because the lower power in the subgrade rutting model reduces the weighting applied to the peaks of the dynamic loads and hence lowers the amplitude of the dynamic rutting damage. Consequently, more load passes are required to produce a 95th percentile rut depth of 20mm and the rate of change in IRI is lower. The increased life also results in a slightly greater amount of fatigue damage at failure compared to the results using the larger subgrade rutting power.

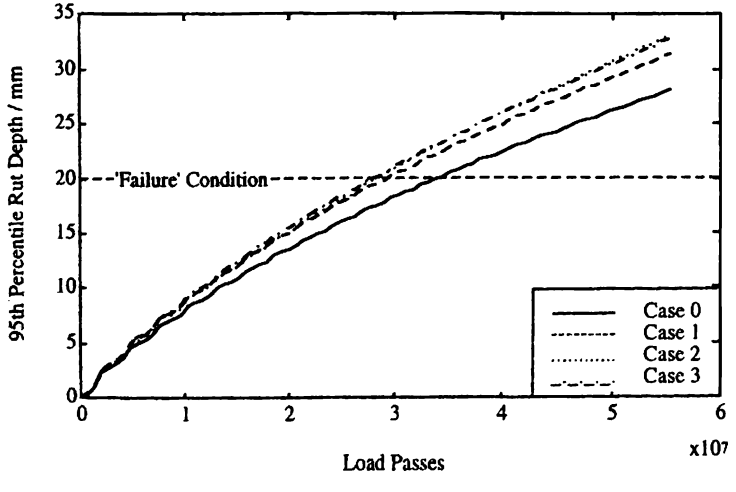


Fig. 20.29 Accumulation of 95th percentile rutting on a motorway, using a subgrade rutting exponent of $L_2 = 1$. From [139].

It can be seen from the PLRF values in Table 20.4 that the inclusion of surface roughness induced dynamic loads (case 1) and asphalt layer thickness variations (case 2) both reduce pavement life by 9.5%. Including both these effects (case 3) reduces pavement life by 14.3%. The CSE values from Table 20.5 are 12.6% (case 0), 3.1% (case 1) and 0.7% (case 2). By comparing this data with the

corresponding results using $L_2 = 3.5$ in the subgrade rutting model, it can be seen that the importance of both dynamic loads and asphalt layer thickness variations on surface damage are much greater when the subgrade is more susceptible to rutting.

Minor road (Subgrade Rutting Exponent = 3.5)

Figure 20.30 shows the increase in 95th percentile rutting as a function of cumulative load passes for cases 0, 1, 2 and 3 using $L_2 = 3.5$ in the subgrade rutting model. It can be seen from this figure that, for case 3, the pavement fails by excessive rutting after approximately 0.48 million vehicle passes. It can be seen by comparing this figure with the corresponding results for the motorway (figure 20.28) that, after the nominal failure condition has been passed, there is an increased rate of rutting. This is due to the non-linear relationship that exists between subgrade rutting and the thickness of the asphalt layer. The rate of subgrade rutting is greater for the minor road which has a thinner asphalt layer. From Table 20.4 it can be seen that the inclusion of surface roughness induced dynamic loads (case 1) and asphalt layer thickness variations (case 2) produce pavement life reductions of 48% and 58.7% respectively. Including both these effects (case 3) produce a PLRF of 66.7%. The CSE values from Table 20.5 are 63.1% (case 0), 28.2% (case 1) and 16.5% (case 2). It can be seen from this data that there is an increase in the simulation error (CSE) for all 3 cases is greater compared to the corresponding principal road data.

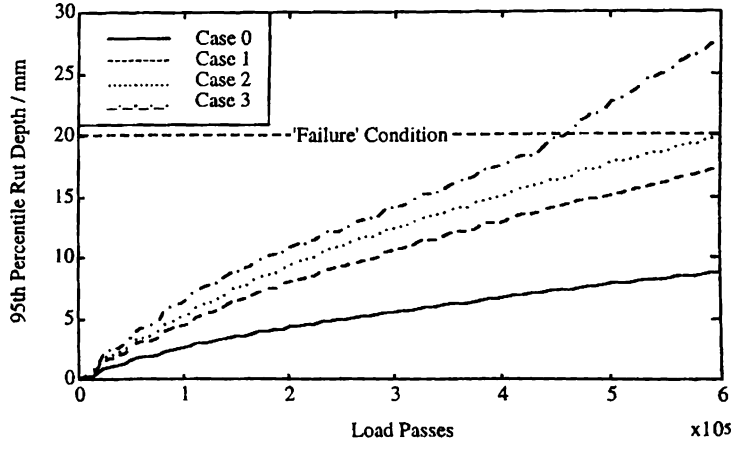


Fig. 20.30 Accumulation of 95th percentile rutting on a minor road, using a subgrade rutting exponent of $L_2 = 3.5$. From [139].

Minor road (Subgrade Rutting Exponent = 1)

Figures 20.31 and 20.32 show the increases in 95th percentile rutting and 95th percentile fatigue damage as a function of cumulative load passes for cases 0, 1, 2 and 3 using $L_2 = 1$ in the subgrade rutting model. It can be seen from these figures that, for case 3, instead of failing by rutting, the pavement lasts longer and fails by fatigue damage after approximately 0.55 million load passes. At failure, for case 3, the 95th percentile rut depth is only 1.5mm. This change in the mode of failure is due to the lower power in the subgrade rutting model reducing the weighting applied to the peaks of the dynamic loads and hence lowering the amplitude of the dynamic rutting damage in the subgrade. Tabulated CSE values are given in Table 20.5. PLRF values have not been presented for this case in Table 20.4 because the 95th percentile fatigue damage for case 0 does not reach 1. It can be seen from this data that neglecting dynamic loads and asphalt layer thickness variations results in a 90.6% under-prediction of the fatigue damage at failure.

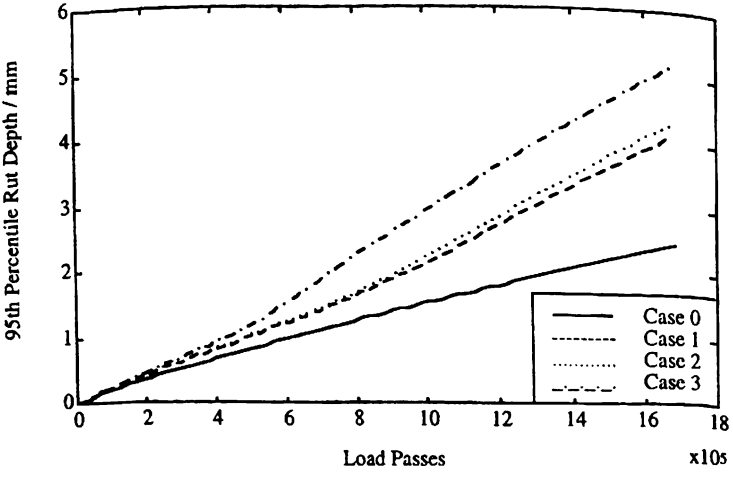


Fig. 20.31 Accumulation of 95th percentile rutting on a minor road, using a subgrade rutting exponent of $L_2 = 1$. From [139].

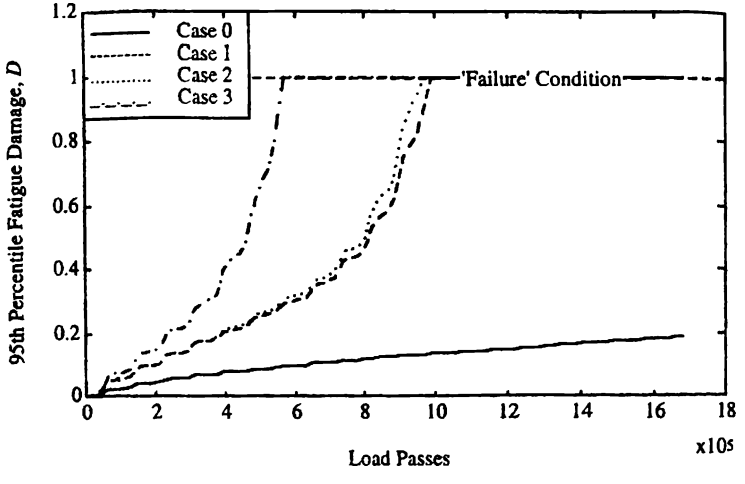


Fig. 20.32 Accumulation of 95th percentile fatigue damage on a minor road, using a subgrade rutting exponent of $L_2 = 1$. From [139].

Notes on Assumptions

There are several unvalidated assumptions that affect the results of the above parameter study. The most important of these are:

(i) The ratio of the standard deviation to the mean asphalt layer thickness is constant for different class pavements.

(ii) The asphalt layer thickness profile is uncorrelated with the pavement surface profile.

(iii) The values of the parameters L_1 and L_2 in the subgrade rutting model (equation 20.11).

To validate these assumptions WLPPM predictions need to be compared with measured performance data from a large number of flexible pavements. However, the un-validated model yields realistic pavement performance predictions, qualitatively in line with experimental results presented in [275].

20.6 CONCLUSIONS

(i) A whole-life pavement performance model that is capable of making deterministic predictions of fatigue, rutting and surface roughness throughout the life of a pavement has been developed. The model includes the following features: (i) dynamic tyre forces; (ii) environmental effects; (iii) realistic pavement stiffness variations; (v) a realistic asphalt modulus degradation law due to fatigue damage; and (v) surface and subgrade rutting.

(ii) Results from preliminary case studies indicated the considerable importance of the sensitivity in the subgrade rutting model on all aspects of flexible pavement wear (fatigue, rutting, roughness).

(iii) Asphalt modulus degradation has been shown to have a significant effect on pavement wear, particularly when combined a large subgrade rutting exponent.

(iv) The simulation indicates that dynamic tyre forces and pavement stiffness variations can have a significant effect of pavement degradation, particularly surface roughness, when the subgrade rutting characteristics are sensitive to stress level.

(v) The simulation predicts that short wavelength roughness components are smoothed out and long wavelength components increase in amplitude. This agrees with the limited experimental evidence available.

(vi) For thinner pavements (125mm), the failure mode is dependent on the exponent in the subgrade rutting model. For a low power ($L_2 = 1$) the mode of failure is predicted to be fatigue, whereas for a high power ($L_2 = 3.5$) the mode of failure is predicted to be rutting.

(vii) Asphalt layer thickness variations tend to dominate the profile degradation process for thick pavements (250mm of asphalt) whereas surface roughness induced dynamic loads become more important for thinner pavements (125mm of asphalt).

(viii) Typical reductions in pavement life due to asphalt layer thickness variations are predicted to be between 50% and 70% using a subgrade rutting power of $L_2 = 3.5$. The corresponding reductions in life using a subgrade rutting power of $L_2 = 1$ are between 9% and 20%.

(ix) Typical reductions in pavement life including initial surface roughness and the consequent dynamic tyre forces are predicted to be between 30% and 60% using a subgrade rutting power of $L_2 = 3.5$. The corresponding reductions in life using a subgrade rutting power of $L_2 = 1$ are between 9% and 20%.

(x) Typical reductions in pavement life due to both initial surface roughness and asphalt layer thickness variations are predicted to be between 50% and 75% using a subgrade rutting power of $L_2 = 3.5$. The corresponding reductions in life using a subgrade rutting power of $L_2 = 1$ are between 14% and 30%.

(xi) For thin pavements (125mm) where the mode of failure is fatigue, neglecting surface roughness induced dynamic loads and asphalt layer thickness variations may result in a 90% under-prediction of the fatigue damage at failure.

21

EFFECTS OF SPATIAL REPEATABILITY AND SUSPENSION TYPE

21.1 SUMMARY

The effects of spatial repeatability of dynamic tyre forces on the long-term performance of three typical UK pavement constructions are investigated. Long-term pavement performance is calculated using the 'Whole-Life Pavement Performance Model' (WLPPM) described in Chapter 20. Particular attention is given to modelling dynamic tyre forces and patterns of loading applied to the pavement by a typical fleet of heavy vehicles. A method is described for simulating vehicle fleets with varying degrees of spatial repeatability using a small number of dynamic tyre force histories. Results indicate that thinner pavements are most sensitive to the level of spatial repeatability exhibited by the vehicle fleet. Pavement damage predictions made without assuming an appropriate level of spatial repeatability can be in error by 20–150%, the higher values being for thinner pavements that fail by fatigue damage.

The effects of 'road friendly' heavy goods vehicle suspensions on long-term flexible pavement performance are then examined. The traffic is modelled either as a fleet of steel sprung heavy goods vehicles or as a fleet of 'road friendly' air suspended vehicles. The pavement life predictions are compared for the two cases and with results from a simple road damage analysis based on the 'fourth power law'. It is concluded that changing to a fleet of 'road friendly' vehicles would not significantly affect the life or maintenance costs of thicker asphalt pavements (motorways and trunk roads) where the mode of failure is permanent deformation (rutting). However, the life of thinner pavements (minor roads) that fail by fatigue damage and localised failure would be increased significantly if the vehicle fleet changed to road friendly suspensions. Predictions from the simplified fourth power law approach tend to significantly overestimate the benefits of road-friendly suspensions for motorway conditions compared to the WLPPM predictions. It is concluded that the potential economic benefits in England and Wales of converting to air suspensions, may be only 30% of those predicted by the authors of the European 'road friendly suspensions' regulations.

This chapter is based on work first published in [141] and [132].

21.2 INTRODUCTION

This chapter contains two case studies on the influence of dynamic tyre forces on whole-life pavement performance.

The importance of spatial repeatability on road damage has been discussed throughout this part of the book. The only way that the influence of spatial repeatability can be assessed with confidence is to use a WLPPM, since this can model the pavement degradation process with various different assumptions about spatial repeatability. Fortunately, all of the tools are now in place. Spatial repeatability has been characterised, simulated and measured (Chapter 18); and a relatively realistic WLPPM has been developed and tested (Chapter 20). In the first case study of this chapter (Section 21.4), the two are combined. The WLPPM is used to evaluate the relative importance of spatial

repeatability on long-term pavement damage, for three typical UK constructions: motorway, principal road and minor road.

Legislation has been in place for many years limiting Gross Vehicle Weight (GVW) and the static loads on individual axles, but only in the last few years have regulations controlling dynamic tyre forces been introduced [52]. Recent European legislation has encouraged the use of 'road-friendly' suspensions on heavy goods vehicles [32]. A payload advantage is given to air suspensions or 'equivalent', for the drive axles of certain vehicles. ('Equivalent' suspensions are defined on the basis of a parametric test, where a step input is applied to the axle. The measured 'natural frequency' and 'damping ratio' must lie within certain limits [32]. This test is discussed in detail in Chapter 27.)

The effect that this legislation is expected to have on pavement life was estimated by the European Commission using a load equivalence law of a similar form to equation 1.1 [52]:

$$\frac{N_i}{N_j} = \alpha\left(\frac{P_i}{P_j}\right)^n, \tag{21.1}$$

where N_i is the number of loads (static) of magnitude P_i to cause failure,
N_j is the number of 'standard' loads (static) of magnitude P_j to cause failure,
n is a constant, depending on the type of pavement construction (typically 4 for flexible pavements), and
α is a coefficient relating the life of the pavement surface under a dynamically varying load to that under a rolling static load.

The parameter α can be seen to be equivalent to the dynamic road stress factor in equation 17.3. For smooth pavement surfaces and a vehicle speed of 80km/hr, typical values of α are given in [52]. They range from 1.01 for an air suspension to 1.25 for a steel leaf semi-trailer suspension. On rougher pavements these values increase to 1.08 for an air suspension and 1.54 for a steel semi-trailer suspension. Using these factors, and assuming a design life of 20 years with no change in static axle loads, the additional dynamic loading produced by air suspensions and steel suspensions would reduce the life of a smooth pavement (motorway) to 19.8 years and 16 years respectively. The corresponding values for a rougher pavement (minor road) are 18.5 years (air suspension) and 13 years (steel suspension). Consequently, according to equation 21.1, changing from a steel sprung vehicle to an air sprung vehicle would increase the life of a smooth pavement (motorway) by approximately 24% and increase the life of a rough pavement (minor road) by approximately 42%. As mentioned in Chapter 17 there have been a number of criticisms of the road stress factor approach.

The second case study in this chapter (Section 21.5) examines the effects on long-term flexible pavement performance and road maintenance costs, of changing from a fleet of vehicles with steel suspensions to a fleet of vehicles with 'road friendly' air suspensions. Long-term pavement performance due to environmental and traffic loading is calculated using the WLPPM. Results are compared to predictions using the dynamic road stress factor approach.

21.3 MODELLING ASSUMPTIONS

Most modelling assumptions used in the simulations described in this chapter were the same as in Chapter 20. These include: the climatic factors; the primary response models; and the asphalt fatigue damage and permanent deformation models. Full details of the mix specification and input parameters are given in Chapter 20 (Table 20.1).

The modelling assumptions that were different for the analyses in this chapter are as follows:

(i) To simplify the calculations, asphalt layer thickness variations were not included in either of the case studies.

(ii) Ageing of the asphalt was not considered in the analysis of spatial repeatability (Section 21.4), but it was considered in the analysis of suspension types (Section 21.5).

(iii) In Section 21.4, three different pavement structures are analysed. The only geometrical differences between the structures is the thickness of the asphalt layer. This was taken to be 250mm for the motorway, 200mm for the principal road and 125mm for the minor road.

(iv) In Section 21.5, the thickness of the asphalt layer is taken to be 350mm for the motorway and 125mm for the minor road.

(v) In both sections, the 'motorway', is assumed to have an initial *IRI* roughness of 2mm/m, whereas the 'principal' and 'minor roads', are assumed to have an initial *IRI* roughness of 3mm/m.

(vi) A linear quarter car vehicle model was used to generate a tyre force histories, as in Chapter 20. The speed of the vehicle is taken to be the average speed for traffic on the class of pavement being simulated. This is 24.1m/s (54mph) for a motorway, 23.7m/s (53mph) for a principal road, and 17.9m/s (40mph) for a minor road [27].

(vii) The suspension stiffness is set to a value of: 0.7MN/m - corresponding to an average suspension [125] for the study of spatial repeatability in Section 21.4; and values of 1.0MN/m and 0.4MN/m, corresponding to typical steel and air suspensions [125], in Sections 21.5. The vehicle model parameters are provided in Table 21.1.

Vehicle parameter	*Generic suspension (Section 21.4)*	*Air suspension (Section 21.5)*	*Steel suspension (Section 21.5)*
Sprung mass m_s	4500 kg	4500 kg	4500 kg
Unsprung mass m_u	500 kg	500 kg	500 kg
Suspension stiffness k_s	0.7 MN/m	0.4 MN/m	1.0 MN/m
Tyres stiffness k_t	2 MN/m	2 MN/m	2 MN/m
Suspension damping c_s	20 kNs/m	20 kNs/m	20 kNs/m

Table 21.1 Vehicle model parameters (see Figure 5.1a).

21.4 EFFECTS OF SPATIAL REPEATABILITY

21.4.1 Characterising Spatial Repeatability

The assumptions about spatial repeatability used in this chapter are based on the measurements taken on the A34 trunk road in the UK, which are described in Section 18.4.3.

The probability distribution of the Spatial Repeatability Index (*SRI*) for the data shown in figure 18.26 was calculated by dividing the difference between the minimum *SRI* and maximum *SRI* values into 50 equal segments of width ΔSRI=0.016. The number of vehicles in each segment was calculated and scaled to give the probability distribution curve shown in figure 21.1. It can be seen from this figure that the probability curve increases as the *SRI* increases until $SRI \approx 0.7$, where it decreases rapidly. Theoretically this probability distribution should peak at an *SRI* value of one. The sudden decrease is due to noise on the individual tyre force measurements caused by the sensors in the load measuring mat. It was shown theoretically in equation 18.16 that random noise on the tyre force measurements would result in an under–prediction of the *SRI*, and hence a roll-off similar to that in figure 21.1 (see [134] for further details).

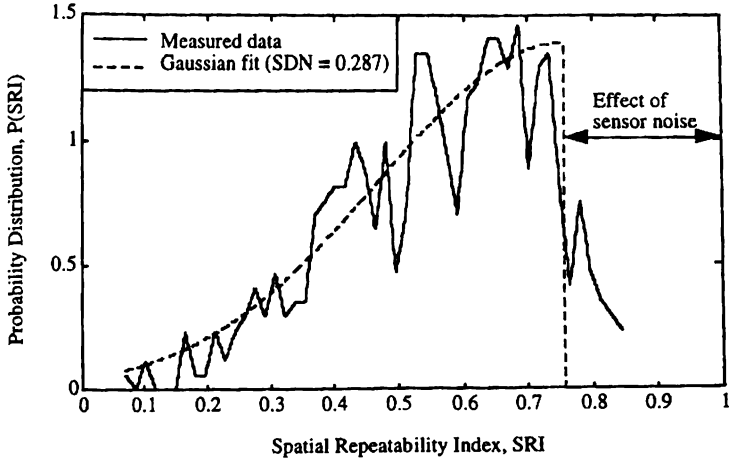


Fig. 21.1 Measured *SRI* probability distribution. From [132].

To correct for the effects of noise, a Gaussian (normal) probability distribution was fitted to the data in figure 21.1. The fitted curve is shown by the dashed line. This curve was then shifted horizontally such that the peak occurred at $SRI = 1$. This shift of 0.25 can be interpreted as the reduction in *SRI* due to the average amount of noise on the individual tyre force measurements. The standard deviation of the fitted probability distribution was *0.287*. This parameter can be considered to characterise the degree of spatial repeatability exhibited by the vehicle fleet and is known as the 'Spatial Distribution Number' *(SDN)*.

By adjusting the value of *SDN* it is possible to simulate vehicle fleets with different levels of repeatability. For example, $SDN = 0$ would correspond to perfect repeatability where all the vehicles apply their peak loads at exactly the same points on the pavement surface. Conversely, $SDN = \infty$ would correspond to the situation where the loads applied by the vehicle fleet are random in space with each point receiving statistically similar levels of loading. Both of these extreme assumptions have been used in pavement performance models used to predict long-term pavement damage [66, 365, 471].

To compare the results for different levels of repeatability, a 'Simulation Error' *(SE)* was used. For a repeatability level *SDN*, the *SE* is defined as:

$$SE(SDN) = \frac{\Psi(SDN) - \Psi(\infty)}{\Psi(\infty)} \times 100\%, \qquad (21.2)$$

where $\Psi(SDN)$ is the calculated road damage for spatial repeatability *SDN* when the 'failure' damage level is reached for perfect repeatability ($SDN = 0$), and

$\Psi(\infty)$ is the calculated road damage level for no spatial repeatability ($SDN = \infty$) when the 'failure' damage level is reached for perfect repeatability($SDN = 0$).

'Failure' damage levels are defined to be the point where the 95th percentile rut depth reaches 20mm or the 95th percentile fatigue damage reaches 1.0. The *SE* is a measure of the error in predicted pavement damage relative to the damage caused by a vehicle fleet exhibiting no repeatability (*ie* $SDN = \infty$ as per the 'Road Stress Factor' approach). For example, a repeatability level with an *SE* of 100% indicates that there is a 100% difference in predicted pavement damage compared to a vehicle fleet exhibiting no repeatability (*ie* $SDN = \infty$). A repeatability level with an *SE* of 0% indicates that there is no difference in predicted pavement damage compared to a vehicle fleet exhibiting no repeatability (*ie* $SDN = \infty$).

21.4.2 Modelling Spatial Repeatability

The method used to model vehicle fleets exhibiting differing levels of repeatability, using a finite number of aggregate tyre force histories is explained in this section.

If all the wavenumber components in an aggregate force history u are phase shifted by a constant amount (*ie* $\phi_i = \phi$), and the phase–shifted history v is compared to the original, then equation 18.13 simplifies to:

$$SRI = \cos(\phi). \tag{21.3}$$

Thus the spatial repeatability index is simply related to the phase angle (see also Section 18.3.2). Consequently, using equation 21.3 it is possible to re–plot the Gaussian probability distribution shown in figure 21.1 (corrected for noise) as a function of phase angle ϕ. This is shown in figure 21.2. Note that negative phase angles have to be included in this step. This distribution can be discretised into a number of regions of equal width and constant phase angle. An example of this is also shown in figure 21.2 where the distribution has been discretised into three equal width regions. The constant phase angles are the average values in each region (*ie* –0.96, 0, +0.96 radians).

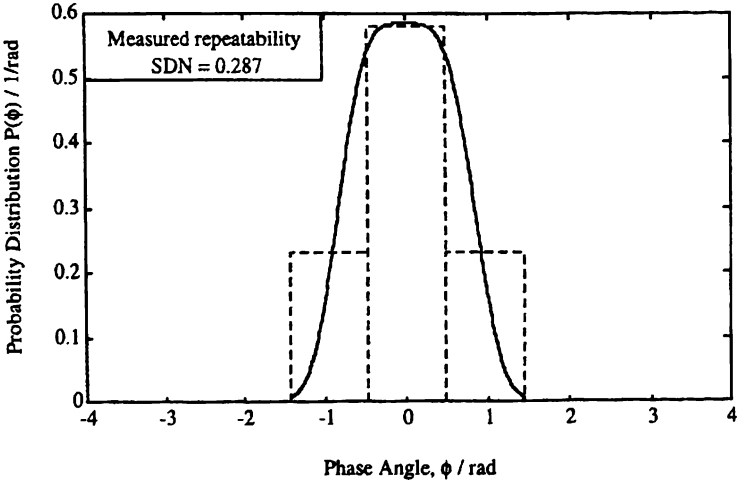


Fig. 21.2 Phase angle probability distribution. From [132].

For the example shown in figure 21.2, this repeatability level can be modelled approximately using a reference aggregate force history, calculated with a vehicle simulation, and two other aggregate force histories derived from the reference aggregate history, by phase shifting all the wavenumber components by ±0.96 radians respectively. This is easily achieved by calculating the Discrete Fourier Transform (DFT) of the reference aggregate force history, adding or subtracting a constant phase angle to all the components, and then calculating the inverse DFT to regain the phase-shifted aggregate force history. (This procedure is similar to that for generating a correlated random road surface profile, as discussed in Section 3.4.1.)

An illustrative example of this is shown in figure 21.3. The reference history is shown by the solid line, and the dashed and dotted lines are for phase shifts of $+\pi/4$ and $+\pi$ respectively. The corresponding SRIs for these curves are $SRI = 0.71$ for a phase shift of $+\pi/4$, and $SRI = -1.0$ for a phase shift of $+\pi$ (calculated using equation 21.3). It can be seen from this figure that the peak loads from the $+\pi/4$ force history (dashed line) occur at similar positions to the peak loads from the reference force history (solid line). Consequently, for this illustrative example, the repeatability level

is high[1]. Conversely, the peak loads from the $+\pi$ force history (dotted line) occur at the same positions as the troughs from the reference force history (solid line) and the repeatability is low. By altering the *SDN* it is possible to simulate varying levels of spatial repeatability. The number of discrete values of ϕ used to ensure convergence of the WLPPM results is discussed in the following section.

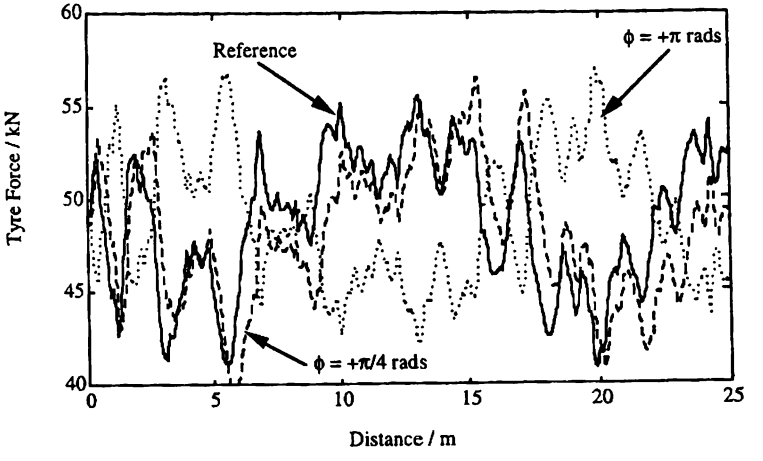


Fig. 21.3 Phase shifted dynamic tyre force histories. From [132].

21.4.3 Convergence Study

A 100m section of the 'minor road' pavement was selected to examine the dependence of WLPPM predictions on the number of force histories needed to model different repeatability levels, *ie* the number of discrete levels chosen in the probability distribution of *SRI* in figure 21.2. Each time traffic load histories were needed by the WLPPM, the quarter-car model was used to calculate a 'reference' dynamic tyre force history, and the phase-shifting method was used to generate additional histories with appropriate levels of repeatability. The results are briefly summarised in the following section.

Figure 21.4 shows the 95th percentile rut depth on a minor road as a function of load passes using 3, 5 and 7 'vehicle models', (*ie* 2, 4 and 6 phase-shifted time histories), in addition to the reference model). The *SDN* was taken to be the measured value, $SDN = 0.287$, and a subgrade rutting constant of $L_2 = 3.5$ was used. Figures 21.5 and 21.6 show the 95th percentile fatigue damage and *IRI* roughness for the same pavement. It can be seen from these figures that the increase in each mode of damage is not smooth. This is due to the annual cyclic variation in air temperature affecting the rate of damage accumulation. It can also be seen from these figures, that the pavement fails by rutting after approximately 0.18 million load passes and, at failure, approximately 40% of the fatigue life has been used up over 5% of the pavement (*ie* the 95th percentile level). It is apparent from these figures that there is no appreciable difference between the curves for 5 and 7 vehicle models. The curve for 3 vehicle models slightly under-predicts each mode of damage.

From the *IRI* curves (figure 21.6) it can be seen that the pavement becomes smoother initially with a subsequent increase in roughness with progressive trafficking. (See explanation in Chapter 20.)

[1] In fact a value of 0.71 is the threshold proposed in Section 18.3.2.

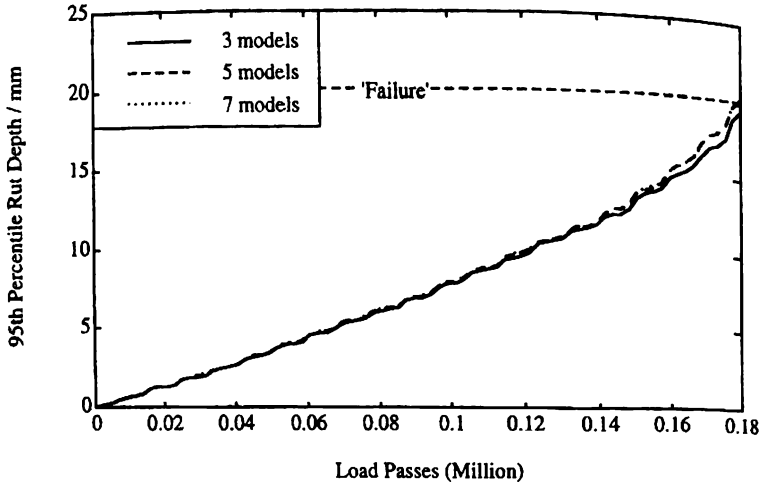


Fig. 21.4 95th percentile rut depth in a thin pavement calculated using 3, 5 and 7 vehicle models and $L_2 = 3.5$ in the subgrade rutting model assuming measured repeatability ($SDN = 0.287$). From [132].

To determine if these findings apply to other levels of repeatability, a value of $SDN = 10$ (low repeatability) for the same pavement was also investigated. This corresponds to the situation where the loads applied by the vehicle fleet are approximately evenly distributed, with each point on the pavement surface receiving statistically similar loading to each other point. For brevity the results are not shown here but, as before, it was found that there was little difference between the curves for 5 and 7 vehicle models and that the curve for 3 vehicle models slightly under–predicted each mode of damage. Consequently it was decided to use 3 tyre force histories for modelling different levels of spatial repeatability. This results in a slight under-prediction in each mode of damage, but at a significantly reduced computation time compared with the same simulation using 5 vehicle models.

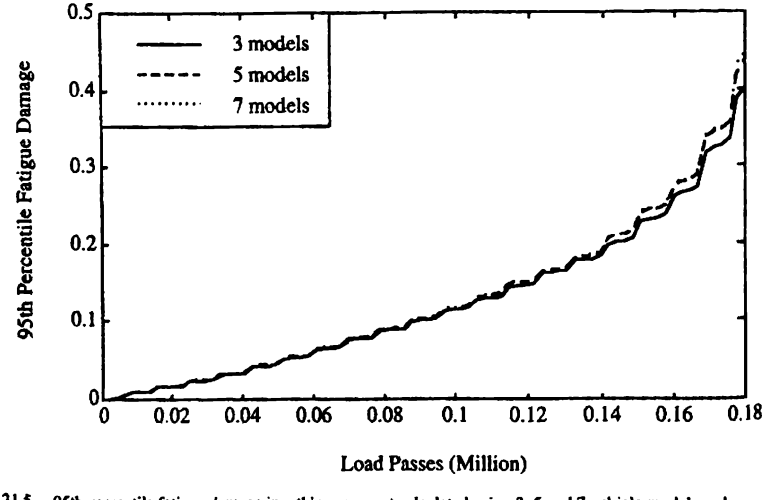


Fig. 21.5 95th percentile fatigue damage in a thin pavement calculated using 3, 5 and 7 vehicle models and $L_2 = 3.5$ in the subgrade rutting model assuming measured repeatability ($SDN = 0.287$). From [132].

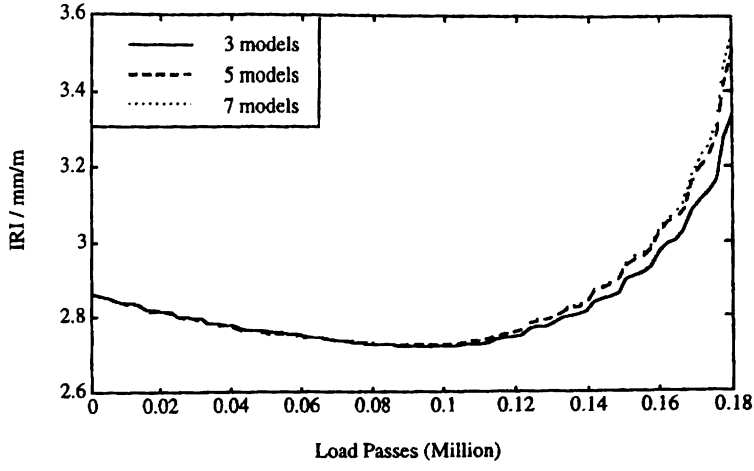


Fig. 21.6 IRI roughness in a thin pavement calculated using 3, 5 and 7 vehicle models and $L_2 = 3.5$ in the subgrade rutting model assuming measured repeatability ($SDN = 0.287$). From [132].

21.4.4 Minor Road (Subgrade Rutting Exponent = 3.5)

Results from a parameter study for three typical UK pavement constructions are presented in the following sections. For brevity, only the results for the minor road are given in detail. Results for the other two pavement types (motorway and principal road) are given in summary form.

Figures 21.7-21.9 show the 95th percentile rut depth, 95th percentile fatigue damage and *IRI* roughness as a function of cumulative load passes, for a range of repeatability levels, using $L_2 = 3.5$ in the subgrade rutting model (equation 20.11). It can be seen that assuming perfect repeatability ($SDN = 0$) the pavement fails by excessive rutting after approximately 0.17 million load passes (figure 21.7). It can also be seen from figure 21.7 that as the *SDN* increases (*ie* repeatability decreases), the rate of accumulation of 95th percentile rutting decreases. This is because the peak loads are distributed over the pavement surface and are not concentrated at the same locations. At failure, the 95th percentile fatigue damage (figure 21.8) for perfect repeatability ($SDN = 0$) is approximately 50%.

From the *IRI* curves (figure 21.9) it can be seen that for lower SDN*s* (higher repeatability), the pavement becomes smoother initially with a subsequent increase in roughness with progressive trafficking. As the *SDN* increases (repeatability decreases) the curves become flatter with a more gradual increase with progressive trafficking. This is because the peak loads become distributed randomly along the pavement and are not concentrated at the worst locations. Consequently, the roughness does not increase so rapidly.

21.4.5 Minor Road (Subgrade Rutting Exponent = 1)

Figures 21.10-21.12 show the 95th percentile rutting, 95th percentile fatigue damage and *IRI* roughness as a function of cumulative load passes for various repeatability levels using $L_2 = 1$ in the subgrade rutting model (equation 20.11). It can be seen from these figures that for perfect repeatability ($SDN = 0$), instead of failing by rutting, the pavement lasts longer and fails by fatigue after approximately 0.22 million load passes (rather than 0.17 million load passes in the previous case, figure 21.7). At failure, the 95th percentile rut depth for perfect repeatability ($SDN = 0$) is only approximately 0.7mm. This change in the mode of failure is due to the lower power in the subgrade rutting model which reduces the weighting applied to the peaks of the dynamic loads and hence

lowers the amplitude of the dynamic rutting in the subgrade. This gives sufficient extra pavement life for fatigue damage to become significant and ultimately to cause failure.

It can also be seen by comparing the change in *IRI* roughness (figure 21.12) with the corresponding case using the larger power in the subgrade rutting model (figure 21.9) that there is no increase in roughness as the pavement is progressively trafficked. This is because the magnitude of surface deformation at failure is low, for all repeatability levels.

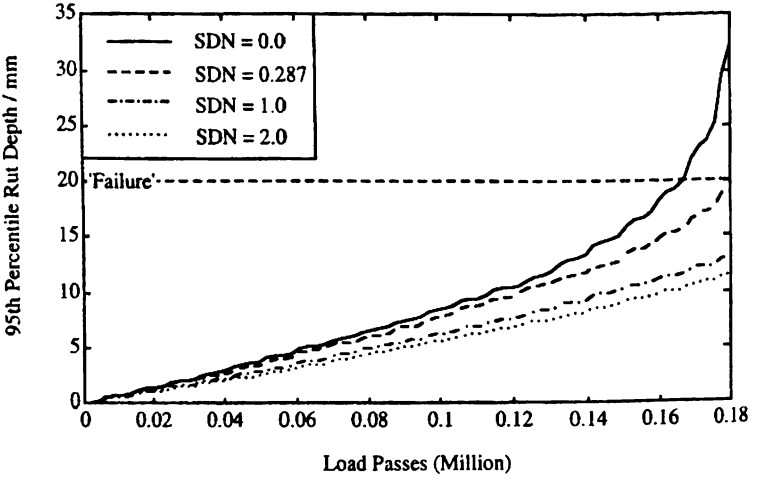


Fig. 21.7 95th percentile rut depth in a thin pavement for various repeatability levels using $L_2 = 3.5$ in the subgrade rutting model. From [132].

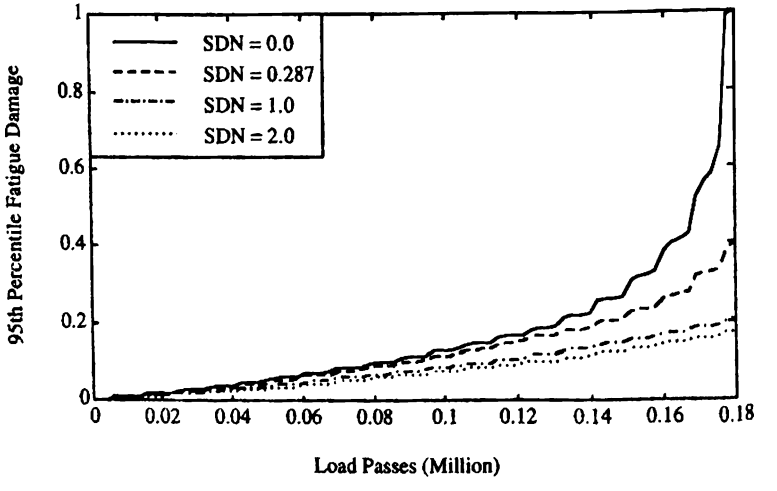


Fig. 21.8 95th percentile cumulative fatigue damage in a thin pavement for various repeatability levels using $L_2 = 3.5$ in the subgrade rutting model. From [132].

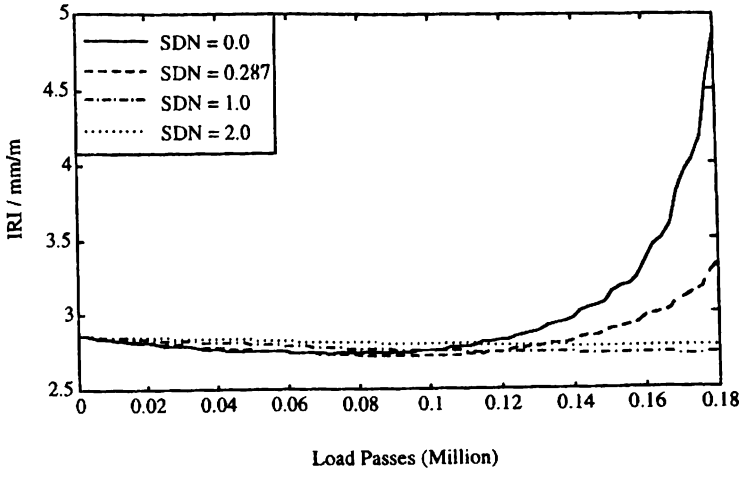


Fig. 21.9 IRI roughness in a thin pavement for various repeatability levels using $L_2 = 3.5$ in the subgrade rutting model. From [132].

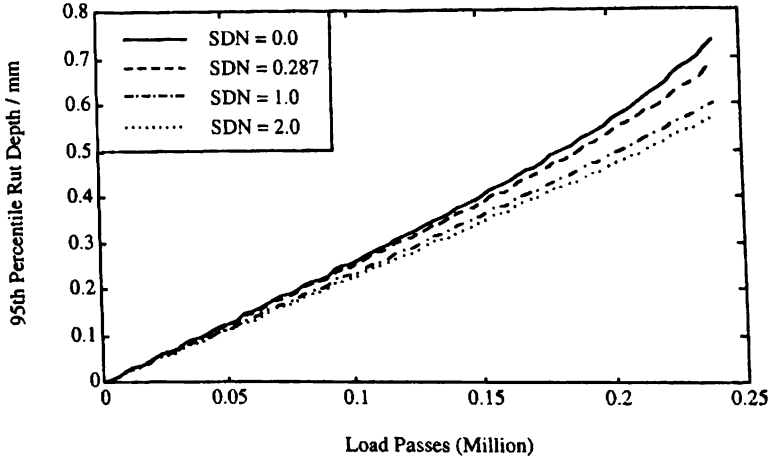


Fig. 21.10 95th percentile rut depth in a thin pavement for various repeatability levels using $L_2 = 1$ in the subgrade rutting model. From [132].

21.4.6 Summary Data

The data presented in figures 21.7-21.12 can be presented in summary form by calculating the *SE* using equation 21.2. The results for subgrade rutting powers of 3.5 and 1 are shown in figures 21.13 and 21.14 respectively. Also shown in these figures are the summary results for the motorway and principal road. It can be seen from both of these figures that all the curves show a characteristic shape. As the *SDN* increases there is a large drop in *SE* and the curves tend to level out to a constant value of $SE = 0$. This behaviour can be explained by considering the limiting case of

no repeatability ($SDN = \infty$) which is the datum for calculating the *SE* from equation 21.2. This limit corresponds to the situation where the vehicle loads are evenly applied to the pavement surface and the pavement degrades due to the average level of dynamic loading. Consequently, as the *SDN* increases (repeatability decreases), the *SE* curves should level out to this limit.

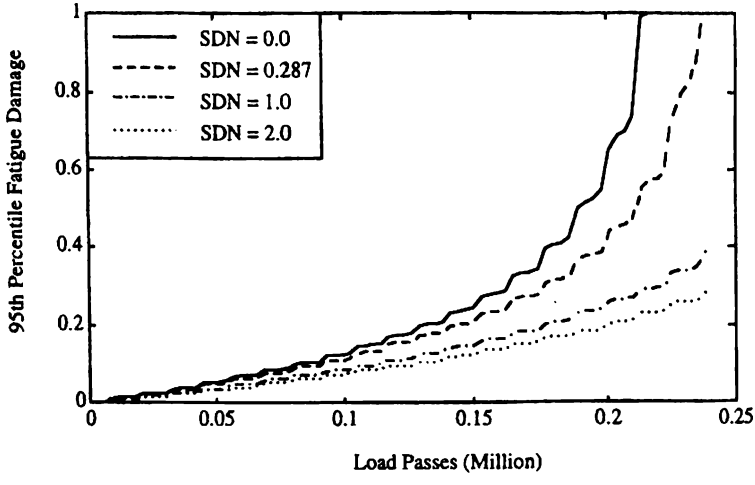


Fig. 21.11 95th percentile cumulative fatigue damage in a thin pavement for various repeatability levels using $L_2 = 1$ in the subgrade rutting model. From [132].

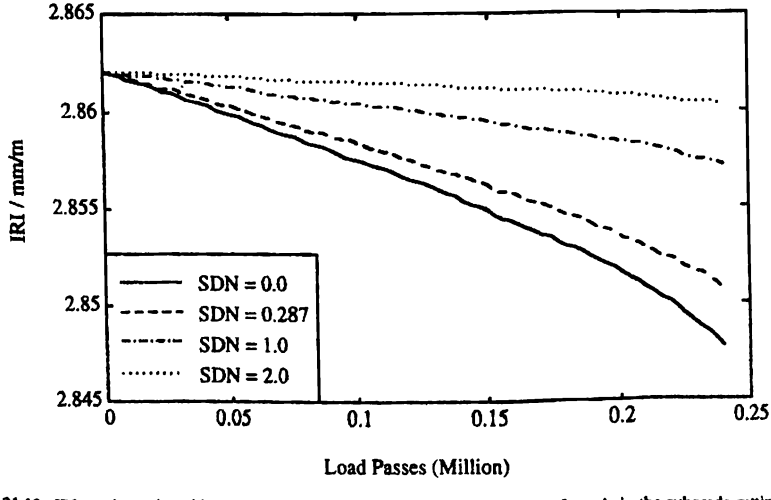


Fig. 21.12 IRI roughness in a thin pavement for various repeatability levels using $L_2 = 1$ in the subgrade rutting model. From [132].

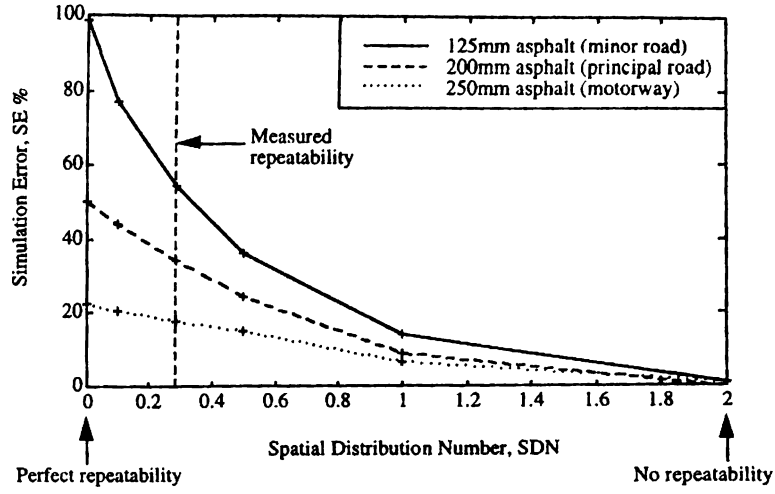


Fig. 21.13 Simulation Error (SE) as a function of repeatability level using $L_2 = 3.5$ in the subgrade rutting model. From [132].

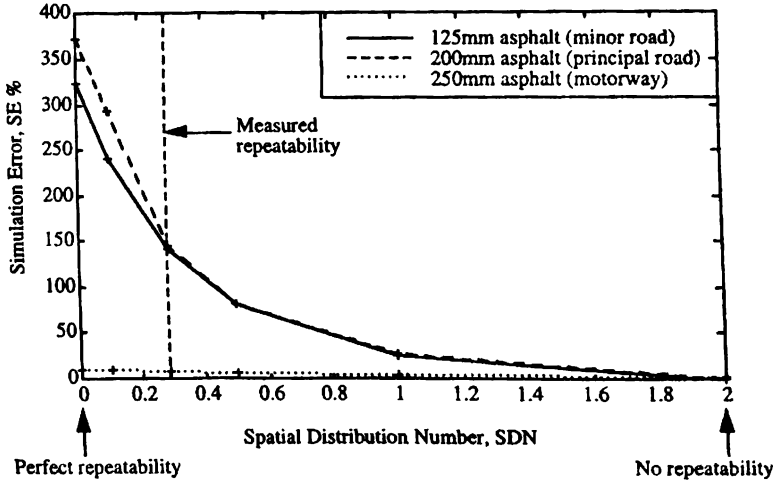


Fig. 21.14 Simulation Error (SE) as a function of repeatability level using $L_2 = 1$ in the subgrade rutting model. From [132].

For a subgrade rutting exponent of 3.5 (figure 21.13) the failure mode for all three types of pavement is rutting. The *SE* curve for the minor road is greater than the *SE* for the principal road which is greater than the *SE* for the motorway. This is because for thinner asphalt layers there is proportionately more rutting occurring in the lower pavement layers where the material is more sensitive to the dynamic level of loading. It can be seen from this figure that the *SEs* for the measured vehicle fleet ($SDN = 0.287$) are between 20% (motorway) and 55% (minor road). It can

also be seen from this figure that if the vehicle fleet is assumed to be perfectly repeatable ($SDN = 0$), the *SEs* increase to between 22% (motorway) and 100% (minor road). It can be concluded from this figure that, for a high power in the subgrade rutting model and failure by rutting, thinner pavements are more sensitive to different levels of spatial repeatability than thicker pavements.

For a subgrade rutting exponent of 1 (figure 21.14) the failure mode for the motorway is rutting whereas the failure mode for the principal road and minor road is fatigue. Consequently, since the exponent in the fatigue model is larger than the exponent in the subgrade rutting model, the *SEs* for the principal road and minor road are greater than the *SE* for the motorway. For the motorway, rut depth accumulation is essentially due to the static vehicle loads with dynamic forces having only a small effect. It can be seen from this figure that the *SEs* for the measured vehicle fleet ($SDN = 0.287$) for the pavements that failed by fatigue damage are approximately 150% whereas the *SE* for the pavement that has failed by rutting is only 8%. It can also be seen from this figure that if the vehicle fleet is assumed to be perfectly repeatable ($SDN = 0$), the *SEs* for the pavements that failed by fatigue damage increase to approximately 350%. It can be concluded from this figure that, for a low power in the subgrade rutting model, thinner pavements that fail by fatigue damage are extremely sensitive to different levels of spatial repeatability.

By comparing figures 21.13 and 21.14 it can be concluded that the pavements most sensitive to the level of spatial repeatability are thinner pavements that fail by fatigue damage. However, even for thicker pavements that fail by rutting, neglecting to model the distribution of dynamic loads applied to the pavement surface can result in relatively significant errors in the levels of predicted damage.

21.5 EFFECTS OF SUSPENSION TYPE

21.5.1 Characterising Suspension Differences

The effects of suspension type on pavement performance will be considered in this section. The level of spatial repeatability measured during the field tests on the A34 road (is $SDN = 0.287$) is used in all the simulations. Two pavements are modelled, a minor road and motorway, as described in Section 21.3.

For both pavement types, damage was calculated due to a fleet of steel sprung vehicles and compared with the damage caused by a fleet of 'road friendly' air suspended vehicles. The results are compared using a 'Pavement Life Reduction Factor' (PLRF), defined as:

$$\text{PLRF} = \frac{N^{air} - N^{steel}}{N^{steel}} \times 100\%, \tag{21.4}$$

where N^{air} is the number of load passes of air suspended vehicles required to produce 'critical' conditions, and

N^{steel} is the number of load passes of steel sprung vehicles required to produce 'critical' conditions.

'Critical' conditions were defined to be the first point where the *average* rut depth along the road reached 15mm, or the 95th percentile fatigue damage reached 0.5. The 95th percentile level was chosen for fatigue damage (rather than the average) because fatigue damage is likely to be localised at the most heavily loaded points on the pavement due to the high power in the fatigue damage model. Consequently, pavement failure due to fatigue is likely to be governed by excessive damage at these locations rather than the average level. This type of upper percentile approach is consistent with the method commonly used to evaluate deflectograph surface deflection measurements (see [36] for further details). The *average* value of the rut depth was used because this is normally the statistic which is used to trigger surface maintenance intervention.

The PLRF is a measure of the increase in pavement life caused by changing from a fleet of steel sprung vehicles to a fleet of air sprung vehicles. For example, a PLRF of 100% would indicate that

the pavement life would be increased by a factor of two if trafficked by a fleet of 'road friendly' vehicles compared to a fleet of steel sprung vehicles.

21.5.2 Motorway (Subgrade Rutting Exponent = 3.5)

Figure 21.15 shows the surface profile at various stages in the life of the motorway, trafficked by a fleet of steel sprung vehicles, using $L_2 = 3.5$ in the subgrade rutting model (equation 20.11). It can be seen from this figure that as the pavement is progressively trafficked, the average surface profile elevation decreases due to the accumulation of rutting deformation in the wheel path. It can also be seen from this figure that the rate of damage accumulation is not constant but tends to decrease with time. This is due to ageing of the asphaltic material (as per equation 20.7) slowing down the rutting process (see [138] for further details).

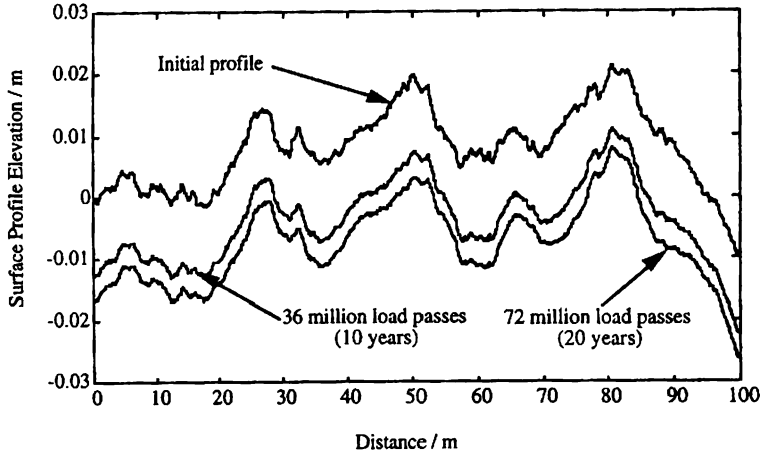


Fig. 21.15 Surface profile evolution due to a fleet of steel sprung vehicles on the motorway using $L_2 = 3.5$ in the subgrade rutting model. From [141].

Figure 21.16 shows the increase in average rut depth as a function of load passes (time) for fleets of air and leaf sprung vehicles, travelling over the simulated road section. The 'ripple' on the curves is again caused by seasonal temperature variations changing the rate of damage accumulation. It can be seen from this figure that, for the fleet of steel sprung vehicles (solid line), the pavement reaches critical conditions (15mm average rut depth) after approximately 65 million heavy vehicle passes. At 10 000 lorries per day (a moderately heavily trafficked road lane) this would correspond to approximately 18 years. It can also be seen from this curve that the fleet of air sprung vehicles causes very slightly less damage, with the result that the pavement life is increased by approximately 2.8% (as characterised by the PLRF).

Figure 21.17 shows the corresponding 95th percentile fatigue damage as a function of load passes for both fleets of vehicles. It can be seen from this figure that, at the critical conditions (15mm average rut depth), the 95th percentile fatigue damage for the fleet of steel sprung vehicles is approximately 0.003, *ie* 0.3% of the fatigue life. The corresponding value for the fleet of air sprung vehicles is 0.23%. These values would be expected to increase significantly for thinner pavements that are more susceptible to fatigue damage. It can be seen by comparing figures 21.16 and 21.17 that there is a significantly greater difference between the 95th percentile fatigue damage curves (figure 21.17) than the average rut depth curves (figure 21.16). This is because fatigue damage at the bottom of the asphalt layer is much more sensitive to the level of dynamic loading than rutting in

the asphaltic surface material. However, the small amount of fatigue damage incurred by the pavement in each of the cases has little effect on its life.

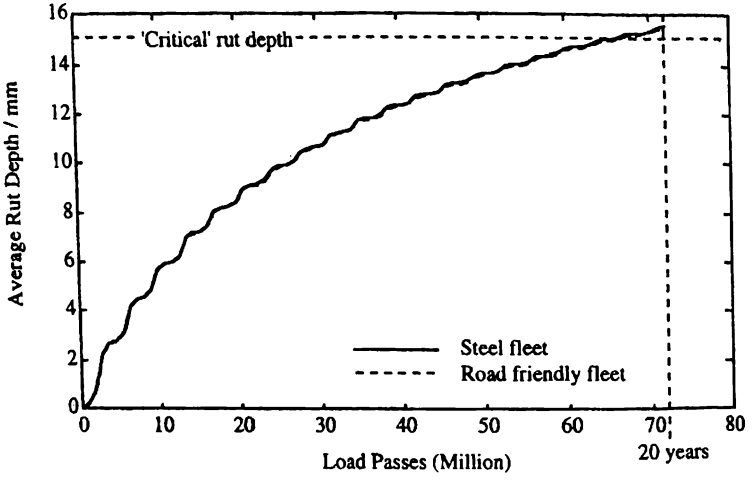


Fig. 21.16 Accumulation of average rut depth on the motorway using $L_2 = 3.5$ in the subgrade rutting model. From [141].

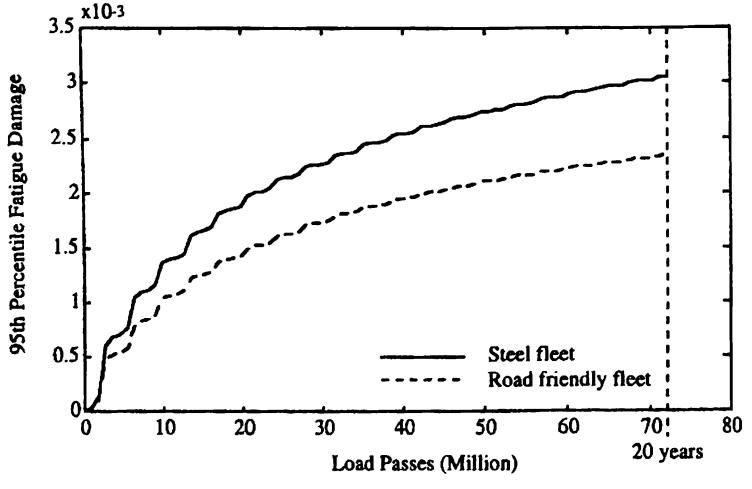


Fig. 21.17 Accumulation of 95th percentile fatigue damage on the motorway using $L_2 = 3.5$ in the subgrade rutting model. From [141].

Figure 21.18 shows the change in IRI (surface roughness) with load passes for both fleets of vehicles. It can be seen from this figure that, for both fleets of vehicles, the pavement initially becomes smoother. This is because during the early part of the pavement's life, the short wavelength surface roughness features are smoothed out by the dynamic tyre forces. This is due to the phase relationship between the dynamic tyre force histories and the pavement surface profile history (see

Section 20.4.4 for further details). It can also be seen from figure 21.18 that the curve for the fleet of steel sprung vehicles (solid line) shows a gradual increase in roughness after about 15 million load passes. This is because the longer wavelength surface roughness components start to become amplified by the dynamic loading. The corresponding curve for the fleet of air sprung vehicles (dashed line) does not show this increase in roughness, because the level of dynamic loading, and corresponding surface deformation, is not sufficient to magnify the longer wavelength roughness components in the pavement surface profile. If the simulation were continued, the level of dynamic loading would gradually increase and the IRI roughness curve would eventually start to rise.

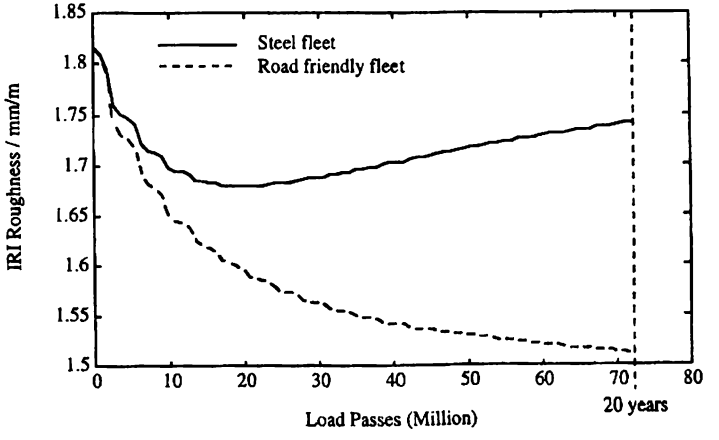


Fig. 21.18 Surface roughness evolution on the motorway using $L_2 = 3.5$ in the subgrade rutting model. From [141].

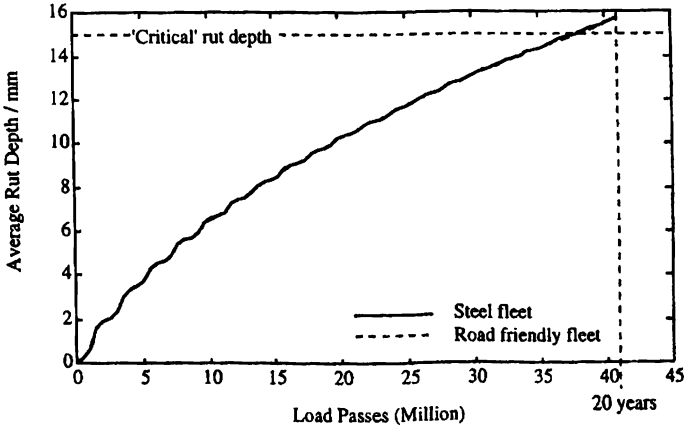


Fig. 21.19 Accumulation of average rut depth on the motorway using $L_2 = 1$ in the subgrade rutting model. From [141].

21.5.3 Motorway (Subgrade Rutting Exponent = 1)

Figure 21.19 shows the increases in average rut depth for both fleets of vehicles trafficking a thick pavement construction (350mm asphalt layer thickness), using $L_2 = 1$ in the subgrade rutting model. It can be seen from this figure that, for the fleet of steel sprung vehicles, the pavement reaches critical conditions (15mm rut depth) after approximately 38 million load passes. It can also be seen that there is essentially no difference between the curves for the steel sprung vehicle fleet (solid line) and the air-suspended vehicle fleet (dashed line) and there is negligible increase in life associated with the road friendly fleet of vehicles (PLRF≈0). This is lower than the corresponding value of PLRF = 2.8% calculated from figure 21.16 ($L_2 = 3.5$), because the subgrade is less sensitive to the level of dynamic loading and hence permanent deformation is reduced.

At critical conditions (15mm average rut depth), the 95th percentile fatigue damage for the fleet of steel sprung vehicles (not shown) is approximately 0.0017 (*ie* 0.17% of the fatigue life). The corresponding value for the fleet of air sprung vehicles is 0.13%. The IRI curves (also not shown) showed a similar pattern to the curves in figure 21.18. (See Collop [141] for details.)

Since permanent deformation of the pavement occurs mainly in the surface layer for either subgrade deformation model ($L_2 = 1$, or $L_2 = 3.5$), the service life is governed by the deformation characteristics of the asphalt. The dominant factor in permanent deformation of a linear viscoelastic asphalt surface is the static vehicle load, and dynamic load fluctuations have only a small effect (see Chapter 14 and figure 17.12a). Consequently the surface deformation is essentially uniform along the road (as illustrated by figure 21.16). This result is consistent with field observations of heavily rutted motorways, where the ruts are usually of relatively uniform depth, with little localised variation in depth that could be attributed to dynamic load fluctuations. It can therefore be concluded that *suspension type has little effect on the service life of this type of road.*

21.5.4 Minor road (Subgrade Rutting Exponent = 3.5)

Figures 21.20–121.22 show the variation in average rut depth, 95th percentile fatigue damage and IRI roughness for both fleets of vehicles trafficking the 'minor road', using $L_2 = 3.5$ in the subgrade rutting model. It can be seen from figure 21.20 that the pavement trafficked by the steel sprung vehicles reaches critical conditions (15mm average rut depth) after approximately 0.61 million heavy load passes compared with approximately 0.86 million heavy load passes for the air suspended fleet. The increase in pavement life (characterised by the PLRF) for the fleet of air suspended vehicles is approximately 38.6% (compared with 2.8% for the thicker pavement). This larger influence of suspension type is due to the higher proportion of permanent deformation occurring in the lower pavement layers which are more sensitive to the level of dynamic loading (see [138] for a detailed discussion). Consequently, the differences in dynamic loading produced by the two vehicle fleets becomes more important.

It can be seen by comparing figures 21.21 and 21.17 that the fatigue damage at the 'critical conditions' for the minor road trafficked by the steel sprung vehicles is 30.6% compared to 0.3% for the motorway. This increase in fatigue damage is due to the 'positive feedback' that occurs in the damage process. As the pavement becomes rougher, the dynamic loads increase, and the damage per vehicle pass at critical locations increases. The roughness therefore increases, as do subsequent dynamic loads. Consequently, the fatigue damage increases rapidly towards the end of the life.

Figure 21.22 shows the increase in IRI roughness for a thin pavement trafficked by both fleets of vehicles. It can be seen from this figure that, for the fleet of steel sprung vehicles (solid line), there is a gradual initial reduction in IRI roughness. After approximately 0.65 million load passes there is a dramatic increase in the level of IRI roughness. It can be seen by comparing figure 21.22 with figure 21.20 that this increase happens just after the pavement has reached the critical rut depth, and occurs simultaneously with the rapid rise in surface fatigue damage (figure 21.21). The corresponding curve for the road friendly vehicle fleet (dashed line) shows that this dramatic increase in roughness does not occur. This is due to the lower dynamic loading for the road friendly vehicles.

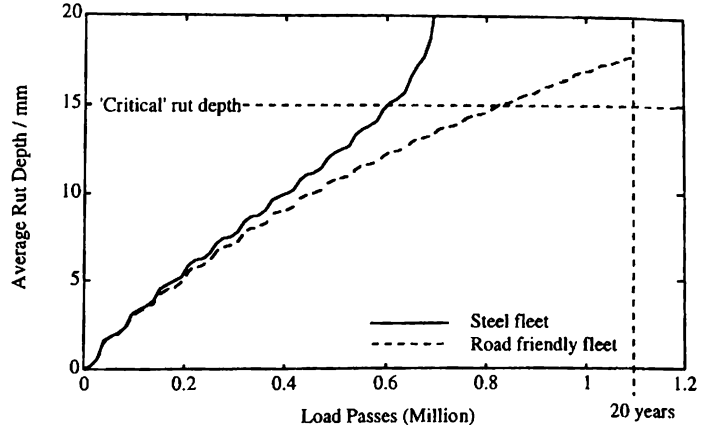


Fig. 21.20 Accumulation of average rut depth on the minor road using $L_2 = 3.5$ in the subgrade rutting model. From [141].

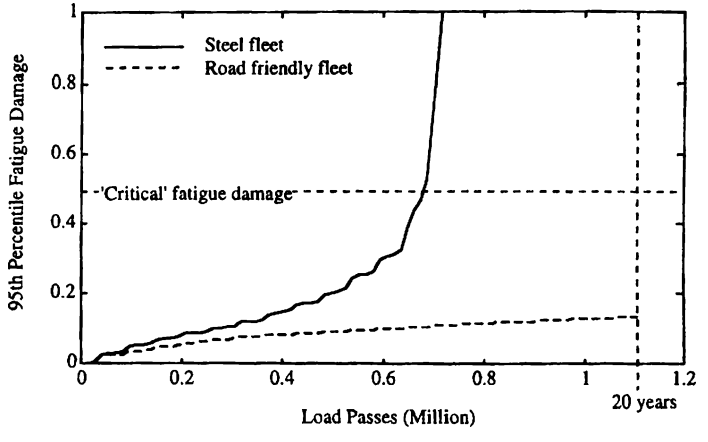


Fig. 21.21 Accumulation of 95th percentile fatigue damage the minor road using $L_2 = 3.5$ in the subgrade rutting model. From [141].

The surface profile evolution for the fleet of steel suspensions is shown in figure 21.23, where it can be seen that late in the service life, large pot-holes begin to form at locations where the dynamic loads are high. These are the points that suffer high fatigue damage, and hence where the asphalt surface becomes the most flexible. This allows excessive subgrade deformation and hence formation of pot holes at these locations. The corresponding surface profile evolution for the air suspended fleet, at the same time increments, is shown in figure 21.24. Here it can be seen that the deformation is essentially uniform with no significant localised damage due to dynamic loading.

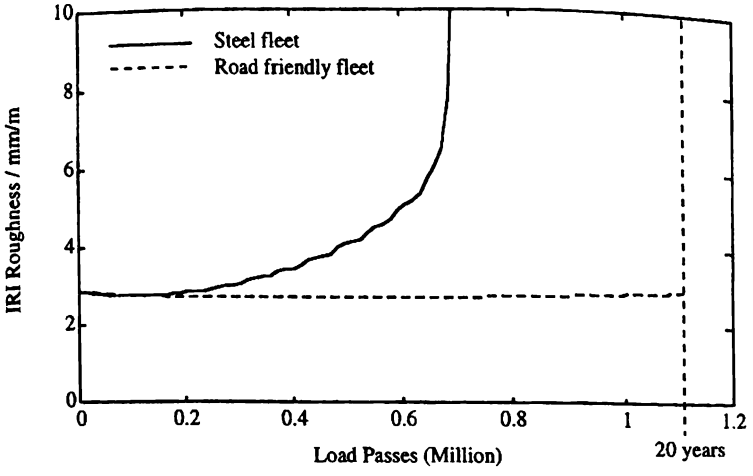


Fig. 21.22 Surface roughness evolution on the minor road using $L_2 = 3.5$ in the subgrade rutting model, [141].

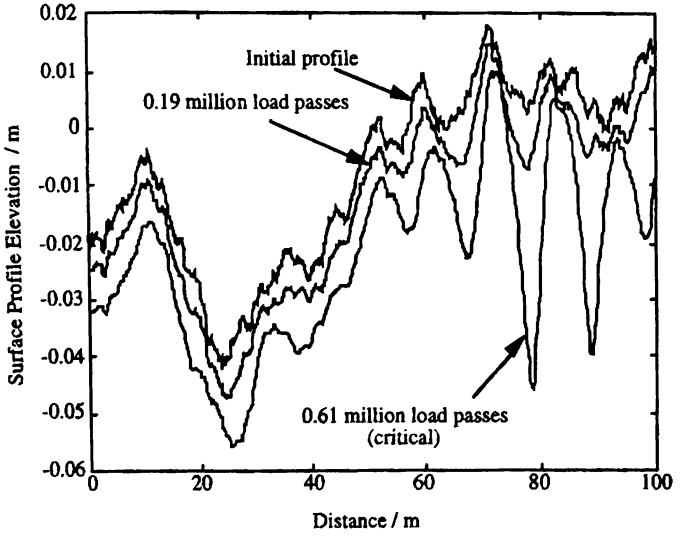


Fig. 21.23 Surface profile evolution due to a fleet of steel sprung vehicles on the minor road using $L_2 = 3.5$ in the subgrade rutting model. From [141].

21.5.5 Minor road (Subgrade Rutting Exponent = 1)

Figures 21.25 and 21.26 show the variation in average rut depth and 95th percentile fatigue damage for both fleets of vehicles trafficking the minor road, using $L_2 = 1$ in the subgrade rutting model. It can be seen from these figures that for the fleet of steel sprung vehicles (solid line), the 95th percentile fatigue damage reaches critical conditions (0.5) after approximately 0.87 million load passes when the average rut depth is only 1.45mm. Thus the change in parameter L_2 has caused the pavement to last about 40% longer (than the 0.61 million load cycles to failure for L_2=1, in

figure 21.20) and has caused the mode of failure to change from rutting to fatigue. It can also be seen from this figure that the pavement trafficked by the fleet of road friendly vehicles lasts approximately twice as long and reaches critical conditions after approximately 1.68 million load passes. This corresponds to a PLRF value of 89.7%.

Photographs of typical deterioration of a motorway and a minor road are shown in figures 21.27 and 21.28. These figures illustrate deterioration which is representative of that type shown in figures 21.15 (rutting) and 21.23 (potholing) respectively. They confirm that the modes of road damage predicted by the whole-life model are realistic.

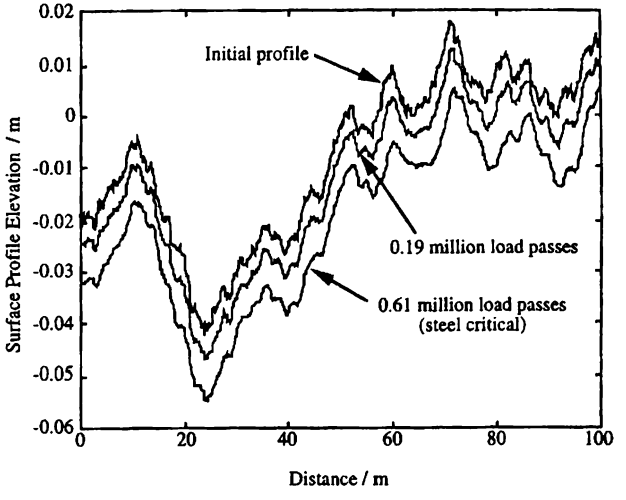


Fig. 21.24 Surface profile evolution due to a fleet of air sprung vehicles on the minor road using $L_2 = 3.5$ in the subgrade rutting model. From [141].

21.5.6 Economic Evaluation

Table 21.2 shows the estimated annual expenditure[1] on structural maintenance of roads in England and Wales in 1995/96, according to road class and geographical region, based on survey returns from 394 local authorities, extracted from [37]. The estimated total expenditure on motorways and trunk roads[2] was £694m; the expenditure on 'principal roads'[3] was £113m; while that for 'other roads'[4] was £775m; giving a total of £1581m.

Structural damage to motorways, trunk roads and principal roads can largely be attributed to heavy vehicle traffic. In the following approximate analysis, it is assumed that motorways and trunk roads are of 'motorway' construction, and principal roads are of 'minor road' construction.

---

[1] Data in [37] shows that historically, the annual *estimates* are accurate to within about 10% of the '*actual*' data collected in subsequent years.

[2] Roads maintained by various local authorities for the Department of Transport.

[3] Roads maintained by local authorities using local finance.

[4] Suburban streets and country lanes - both surfaced and unsurfaced.

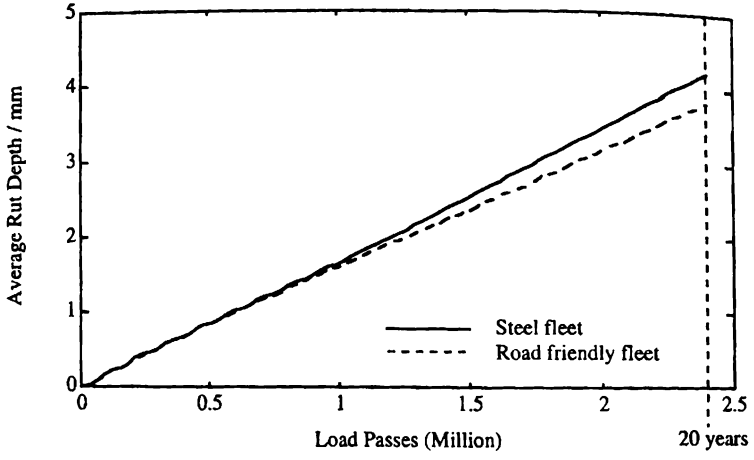


Fig. 21.25 Average rut depth accumulation on the minor road using $L_2 = 1$ in the subgrade rutting model, [141].

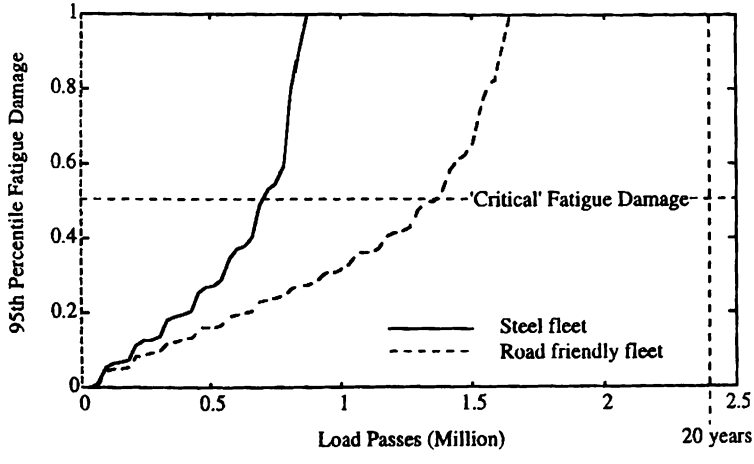


Fig. 21.26 Accumulation of 95th percentile fatigue damage on the minor road pavement using $L_2 = 1$ in the subgrade rutting model. From [141]

'Other' roads (suburban streets and country lanes) generally encounter very little heavy vehicle traffic. For these roads, most structural damage is likely to be caused by environmental influences, ground subsidence, inadequate drainage, *etc*, rather than infrequent heavy vehicles. Consequently, the cost of heavy-vehicle-related maintenance on 'other roads' will be small compared with the equivalent costs for motorways, trunk roads and principal roads. Therefore, in the following approximate analysis of economic benefits, the total cost of road maintenance *attributed to the effects of heavy vehicles* in England and Wales is assumed to be £694m + £113m = £807m.

By comparing the WLPPM simulation results with results from the dynamic road stress factor approach used in the European regulations [52] (see Section 21.2), it can be seen that there is a considerable difference in the predicted benefits of changing from a fleet of steel sprung vehicles to a fleet of 'road friendly' air sprung vehicles. These results are summarised in Table 21.3. The road stress factor approach tends to substantially *overestimate* the effects of dynamic loads on thicker,

smoother pavements (motorways), for which the WLPPM has shown that dynamic loads have little effect on the rate of damage accumulation (24% for the road stress factor, compared with 2.8%, for the WLPPM with L_2=3.5 and 0% for L_2=1.0). Conversely, for thinner pavements that can fail by fatigue, the simplified road stress factor approach tends to *underestimate* the effects of dynamic loads on pavement damage (42%, compared with 38.6%, for L_2=3.5 and 89.7% for L_2=1.0). This is because the Road Stress Factor is based on the average damage level along the road. As can be seen from the results (*eg* figure 21.23), fatigue damage occurs in a localised manner, causing potholes. The damage at these highly loaded locations dominate the life and is related to the peak, rather than the average dynamic loads.



Fig. 21.27 Ruts in the surface of a motorway (Courtesy of SF Brown).

	Motorways, Trunk roads	*Principal Roads*	*Other Roads*	*Total*
English Counties	300	39	299	638
London Boroughs	21	10	41	72
Metropolitan Districts	12	11	74	96
Welsh Counties	30	7	30	68
Shire Counties, *etc*	331	46	330	707
Total	694	113	775	£1581m

Table 21.2 Estimated cost of structural maintenance of roads in England and Wales, in 1995/96, from [37]. Units are millions of pounds sterling (£m).

The eventual average annual reduction in structural maintenance costs (in 'net present value' terms[1]), available through converting the entire vehicle fleet to road friendly suspensions, can be estimated by

[1] The average level of cost reduction would theoretically not be reached until all roads had been reconstructed and were *only* trafficked by road-friendly suspensions, throughout their service lives. In practice, the benefits would build up to this level over a period of about 20–30 years. By this time, inflation will have increased the cost of structural maintenance by the same amount as the indexing required to convert it into 'net present value' terms. These two factors will therefore cancel out.

multiplying the reduction in road damage by the cost of structural maintenance. The last column of Table 21.3 shows the estimated benefits for the three different calculations of road damage. Since most of the £807m road maintenance attributed to lorries in England and Wales is spent on motorways (motorways and trunk routes) which are not very susceptible to dynamic loads, it can be seen from the last column of Table 21.3, that 'road friendly' suspensions are likely to be much less beneficial than previously assumed by the authors of the European regulations. For L_2=3.5, the available benefit is estimated to be £63m. This corresponds to a saving of approximately 4% of the annual expenditure on structural maintenance in England and Wales, compared to 14% savings predicted by the road stress factor calculation. Almost all of this expenditure would be on the maintenance of principal roads, with virtually no financial benefit for motorways and trunk roads. At this level of financial benefit it seems doubtful whether the cost of enforcing the regulations justifies the marginal benefits of reduced pavement maintenance expenditure.



Fig. 21.28 Potholes on a heavily-trafficked minor road.

21.6 CONCLUSIONS

(i) The 'Spatial Distribution Number' *(SDN)*, defined as the standard deviation of the *SRI* probability distribution, was identified as a suitable parameter for characterising the statistics of spatial repeatability exhibited by a vehicle fleet. Analysis of data from a previous study showed that a typical heavy vehicle fleet was found to have an *SDN* of 0.287.

(ii) A method was developed for modelling the patterns of loading exhibited by vehicle fleets with differing repeatability levels using a finite number of aggregate tyre force histories. A convergence study indicated that at least three aggregate force histories are required.

(iii) A number of simulations were performed to investigate the effects of spatial repeatability on long-term flexible pavement performance. For thinner pavements, the failure mode was found to be dependent on the exponent in the subgrade rutting model. For a low power $(L_2 = 1)$ the mode of failure was predicted to be fatigue, whereas for a high power $(L_2 = 3.5)$ the mode of failure was predicted to be rutting.

(iv) Spatial repeatability was found to be more important for thinner pavements that fail by fatigue. There was found to be approximately a 350% difference between the predicted damage calculated assuming no repeatability ($SDN = \infty$) and perfect repeatability ($SDN = 0$). For the measured vehicle fleet ($SDN = 0.287$) the predicted damage was approximately 150% higher than that calculated assuming no repeatability ($SDN = 0$).

(v) For pavements that fail by rutting, the difference between the predicted damage calculated assuming no repeatability ($SDN = \infty$) and perfect repeatability ($SDN = 0$) was between 20% (motorway) and 100% (minor road). For the measured vehicle fleet ($SDN = 0.287$) the predicted damage was between 20% (motorway) and 60% (minor road) higher than that calculated assuming no repeatability ($SDN = 0$).

(vi) Changing from a fleet of steel sprung vehicles to a fleet of air sprung vehicles is estimated to increase the life of thick asphaltic constructions, that fail by rutting, by less than 3%. The same change is estimated to increase the life of minor roads by between 40% and 90%, depending on the sensitivity of the deformation of the lower pavement layers to strain level.

(vii) The dynamic road stress factor approach used in European regulations considerably overestimates the potential benefits of 'road friendly' suspensions on thick constructions (motorways) and underestimates the potential benefits on thin constructions (minor roads) that fail by fatigue.

(viii) The reduction in road maintenance costs in England and Wales, due to introduction of road-friendly suspensions, is estimated to be between £63m and £101m per year (in 1995/96). This compares to £215m calculated with the method used to develop the European 'road-friendly suspension' regulations.

Although the whole life pavement performance model used in this study is based on the best available material degradation models in the civil engineering literature, the overall model has not yet been validated. (This work is currently in progress.) Nevertheless, the general trends exhibited by the model agree well with qualitative field observations of road failure modes in the UK and other temperate climates. The simulation results presented in this study are not strongly sensitive to any unvalidated assumptions made in the analysis.

Road damage analysis	*Motorway (Motorways, Trunk roads)* £694m	*Minor road (Principal roads)* £113m	*Estimated annual maintenance cost saving, England and Wales*
Assumed by European regulations [52]	24% £167m	42% £47.5m	£215m
WLPPM ($L_2 = 3.5$)	2.8% £19.4m	38.6% £43.6m	£63m
WLPPM ($L_2 = 1$)	0% £0m	89.7% £101m	£101m

Table 21.3 Summary of the estimated potential benefits of 'road friendly' suspensions on road maintenance costs in England and Wales in 1995/96.



22

EFFECTS OF VEHICLE SUSPENSIONS ON THE RESPONSE OF HIGHWAY BRIDGES

22.1 SUMMARY

The effects of heavy vehicles with leaf-spring and air-spring suspensions on the dynamic response of short-span highway bridges are considered. The vehicle models consist of a leaf-sprung, four-axle articulated vehicle, and a similar vehicle fitted with air suspensions and hydraulic dampers. These two vehicle models are combined with three different bridge models to predict dynamic bridge responses, using the method described in Chapter 12. Two surface roughness profiles are used on each bridge: a step-up at the entrance, and a pseudo random profile. Dynamic response increments are used to compare the effects of the two vehicles on the bridges. The air suspended vehicle is found to cause significantly lower dynamic bridge responses than the leaf-spring suspended vehicle.

This chapter is based on work previously published in [207].

22.2 INTRODUCTION

The importance of vehicle-induced bridge vibrations has long been recognised by engineers. For nearly 60 years, bridges have been designed to account for dynamic loads by increasing the design live loads by an empirical 'impact factor' or 'dynamic load allowance' [14]. However, the influence of heavy vehicle design on the dynamic response of bridges has largely been overlooked.

Three factors are repeatedly cited in the literature as the main vehicle influences on bridge vibrations:

(i) vehicle speed,

(ii) matching of bridge and vehicle natural frequencies,

(iii) roughness of the bridge surface and approaches which excites the vehicle and causes large dynamic loads to be applied to the bridge.

A good example is the report on the OECD DIVINE Bridge project by Cantieni and Heywood [85]. The authors measured the effects of road vehicles with air and steel suspensions on short to medium span bridges in Switzerland and Australia. They found that the suspension which excited the most vibration of a bridge was generally the one which had a vehicle body bounce frequency closest to the first bending mode of the bridge. A steel suspension caused greatest vibration of a Swiss bridge with a natural frequency of 3.0Hz; whereas an air suspension caused greatest vibration of a different Swiss bridge with a frequency of 1.6Hz. Their research in Australia showed that when the wheel-hop modes of an air-suspended vehicle were excited by the bridge surface profile, large dynamic responses could be generated in short-span bridges.

Ideally, vehicles would be designed so that their natural frequencies do not coincide with bridge natural frequencies. In practice, most heavy vehicles apply their largest dynamic loads in the 1.5-4.5Hz frequency range (see Chapter 7), while the first natural frequencies of bridges generally vary from 1 Hz to as high as 15 Hz [61, 83]. Since vehicle frequencies normally occupy a relatively

narrow frequency band, one possible design solution is to build bridges that avoid the 1-5 Hz frequency range. Bridge design based on this concept has been implemented in the Ontario Highway Bridge Design Code (OHBDC) [17] as well as the Swiss design code [84]. In both design codes, the static design loads are increased by a 'dynamic load allowance' that varies with the first natural frequency of the bridge (see Figure 22.1).

The dynamic load allowance (DLA) is defined implicitly as follows:

$$\textit{Dynamic design load} = (1 + \text{DLA}) \times \textit{Static design load} \tag{22.1}$$

and is largest for bridge frequencies between 2 and 5Hz. Therefore, a penalty is imposed on designers if the natural frequency of their bridge coincides with the range of heavy vehicle frequencies.

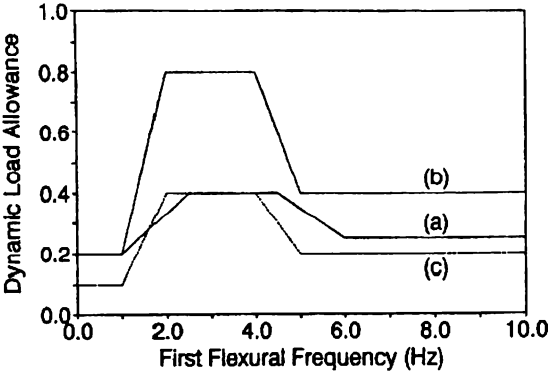


Fig. 22.1 Dynamic Load Allowances: (a) OHBDC 1983 [17], (b) Swiss 1987 - Single vehicle load, [84] (c) Swiss 1987 - Lane load. From [207].

The most obvious way to reduce bridge response is to moderate the effects of surface roughness. Good maintenance of bridge approaches and surface helps to avoid excessively large dynamic wheel loads. A second possibility is to encourage the use of soft, well damped suspensions which apply smaller dynamic wheel loads regardless of the surface roughness. Tests on bridges in the UK showed that vehicles with air suspensions apply smaller dynamic loads to bridges than do similar vehicles with leaf-spring suspensions [210].

This chapter investigates the dynamic effects of vehicle suspension design parameters and surface roughness on the response of bridges. Specifically, leaf-spring and air-spring suspensions are compared by calculating the dynamic displacements of three bridges, using the methods described in Chapter 12.

22.3 PARAMETRIC STUDY OF DYNAMIC BRIDGE DISPLACEMENTS

22.3.1 Vehicle Models

In order to assess the effects of vehicle suspension design on bridge vibrations, the articulated vehicle model described in Chapter 6.4 was modified to represent a typical vehicle with air suspensions. The leaf-spring elements on the drive axle and the two trailer axles were replaced by models of air springs with parallel viscous dampers. The suspension on the steer axle was the same

for both vehicle models. The air suspensions were assumed to be the popular trailing-arm type (figure 2.1g) and were modelled with the following adiabatic deflection equation:

$$F_{air} = F_{stat}\left[1 - \frac{Ax}{V_0}\right]^{-\gamma} \tag{22.2}$$

where

F_{air} is the force in the spring,
F_{stat} is the static suspension force,
A is the cross-sectional area of the spring (0.045 m^2),
V_0 is the static volume of the spring (0.020 m^3),
γ is the ratio of specific heats (1.38 for air),
and x is the deflection of the spring.

The suspension trailing arm lever ratio was 0.4 and the air-springs in the tandem trailer suspension were assumed to be dynamically independent. Each vehicle model was two-dimensional, and did not simulate roll motions. This is a reasonable approximation for predicting wheel loads for typical highway conditions (see Chapter 7.4 and [113, 121]). Table 22.1 presents the natural frequencies and damping ratios of the low frequency modes of linearised versions of the vehicle models.

Vehicle Configuration	*Frequency [Hz]*	*Damping Ratio [-]*	*Description of Mode Shape*
Leaf Spring suspension	2.3	0.06	tractor bounce
	2.9	0.08	tractor pitch
	3.2	0.04	trailer pitch
Air Spring suspension	1.5	0.15	tractor + trailer bounce
	1.7	0.16	trailer pitch
	2.4	0.10	tractor pitch

Table 22.1 Natural frequencies and damping ratios of the linearised vehicle models (low frequency modes).

The vehicle model was validated with a programme of experimental measurements performed with an instrumented vehicle on the TRL test track. The simulated and measured tyre force spectral densities for the tractor drive axle and leading trailer axle can be found in [207]. Good agreement was obtained up to 20Hz.

22.3.2 Bridge Models

To make the analysis as general as possible, the parametric study considered three real bridges which cover a range of frequencies representative of many short-span bridges. The first bridge was the Lower Earley bridge which was described in Chapter 12 (figure 12.9).

The second was a pre-stressed concrete box girder bridge over the M4 motorway located on Drift Road in Berkshire, UK. The 4-span superstructure is continuous over three supporting columns and symmetric about its middle column. The two central spans are 22m long, and the two outer spans are 12.5m long. The bridge is relatively stiff, with its first bending frequency at 6.8 Hz. A bridge model validation study (similar to that described in Chapter 12) was undertaken - see [204] for details. The model was found accurately to predict dynamic bridge response to the measured vehicle loads.

The third bridge was the simply-supported 'Pirton Lane' bridge tested by the TRRL in the 1970s [174, 301, 496]. They reported the bridge length as 40 metres, and the first natural frequency as 3.2Hz with a modal damping ratio of 0.02. The mass per unit length was estimated from drawings in their papers as 12000 kg/m. The three lowest vibration modes were used in the analysis.

The vehicle and bridge models were combined using the convolution method described in Chapter 12. The vehicles were assumed to apply dynamic loads along the centre-line of the bridges. Dynamic displacement responses were calculated at the mid-span and quarter span of each bridge. Only the flexural modes (no torsion) were included in the computations for the Drift Road bridge [204], and only the mode shapes along the centre-line wheel path were included in the Lower Earley bridge model [204]. Table 22.2 shows the modal parameters for all three bridge models.

Bridge	*Mode*	*Natural Frequency [Hz]*	*Damping Ratio [-]*
Pirton Lane	1	3.2	0.020
	2	12.7	0.020
	3	28.6	0.020
Lower Earley	1	5.7	0.045
	2	6.9	0.088
	4	9.7	0.026
	5	11.3	0.014
	7	18.0	0.038
	8	24.4	0.019
Drift Road	1	6.8	0.019
	2	8.6	0.021
	3	18.0	0.034

Table 22.2 Modal parameters of the three bridges.

22.3.3 Bridge Surface Profiles

Two different bridge surface profiles were considered. For most of the results in this study, the surface profile was assumed to be smooth except for a 20mm step up at the entrance to each bridge. This step modelled differential settling of the abutments, or poorly maintained expansion joints. (Honda and Kobori [240] measured the surface profiles of the expansion joints of approximately 400 bridges in Japan, and found that three quarters of the bridges had a maximum abutment differential between 10 and 25mm.)

For some trials in this study, a pseudo-random surface profile was used. Honda, Kajikawa, and Kobori [239, 240] measured the roughness of several hundred bridges in Japan and calculated spectral densities. They found that most bridges had medium to good surface profiles that could be classified by the same general standards as used for roads. As a consequence, the roughness spectrum used in this study was a 'good' road surface according to the two index spectral description proposed for the draft ISO standard [12], see figure 3.1. The pseudo-random profile was generated from the roughness spectrum using the inverse DFT method described in Chapter 3. The maximum roughness amplitude in the resulting profile was approximately 10mm.

22.3.4 Speed

Six different vehicle speeds were chosen for this study: 10, 15, 20, 25, 30, and 40m/s. Speeds of 20 to 30m/s are typical of motorways. Although 40m/s is faster than the legal maximum in most countries, it provides information on the dynamic effects at higher speeds.

22.3.5 Bridge Responses

Bridge responses were calculated for most combinations of the parameters outlined above. All three bridge models were combined with both vehicles at all six speeds for the 20mm step, while for the pseudo random roughness profile, only speeds of 15m/s and 40m/s were considered.

Figure 22.2 to Figure 22.5 show some typical bridge responses. The horizontal axis on all the plots is the position of the steer axle of the vehicle, with the entrance to the bridge defined as position zero. The solid curves show the response of the bridge to the leaf-sprung vehicle while the dashed curves show the response to the air suspended vehicle.

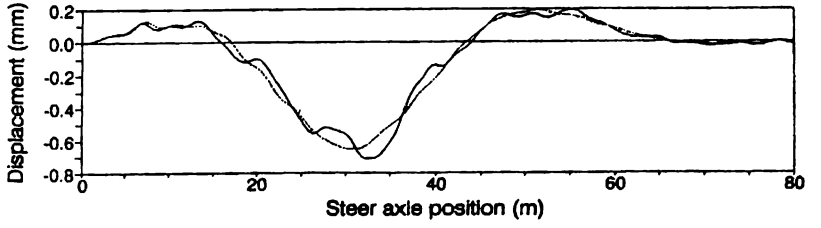


Fig. 22.2 Drift Road bridge - Mid-span displacements. Speed = 30 m/s. 20mm step at bridge entrance. From [207]. ——— = Leaf-sprung vehicle; - - - - - - = Air-sprung vehicle

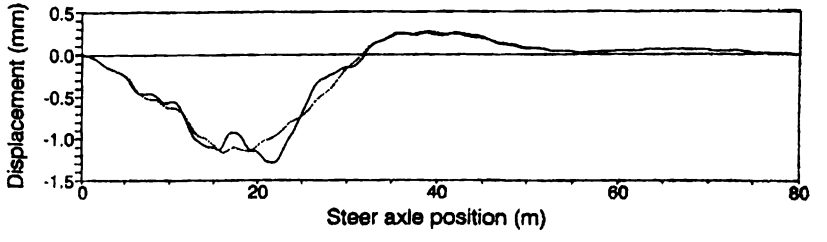


Fig. 22.3 Lower Earley bridge - Mid-span displacements. Speed = 30 m/s. 20mm step at bridge entrance. From [207]. ——— = Leaf-sprung vehicle; - - - - - - = Air-sprung vehicle

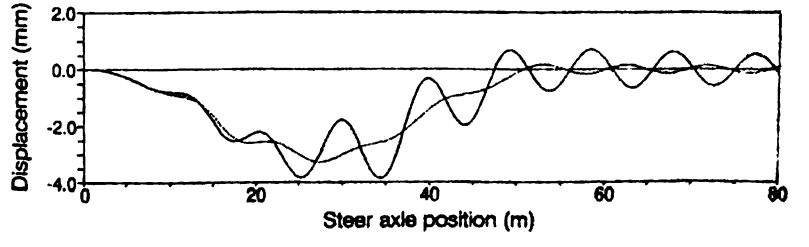


Fig. 22.4 Pirton Lane bridge - Mid-span displacements. Speed = 30 m/s. 20mm step at bridge entrance. From [207]. ——— = Leaf-sprung vehicle; - - - - - - = Air-sprung vehicle

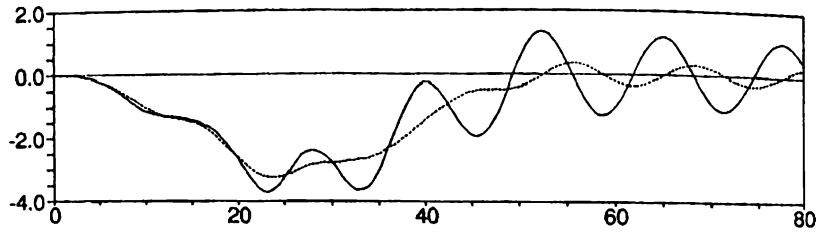


Fig. 22.5 Pirton Lane bridge - Mid-span displacements. Speed = 40 m/s. Pseudo random surface profile. From [207]. ——— = Leaf-sprung vehicle; - - - - - - = Air-sprung vehicle

For the Drift Road bridge (figure 22.2) and the Lower Earley bridge (figure 22.3) the dynamic responses are relatively small whereas for the Pirton Lane bridge (figure 22.4 and 22.5) the response is quite large for the leaf-sprung vehicle. Larger responses are expected on the Pirton Lane bridge because its first natural frequency (3.2 Hz) is closest to the natural frequencies of the leaf-sprung vehicle [61, 84]. Smaller responses are expected on the Drift Road bridge because its first natural frequency is significantly higher than the bounce frequencies of the vehicles, and the highest dynamic wheel loads due to the step input are applied to the first (short) span and not to either of the longer central spans.

The accuracy of these theoretical results may be confirmed by comparing the amplitude of the dynamic responses in figures 12.20 and 22.3. Although the vehicles are slightly different, the amplitude of the dynamic response is approximately equal to 0.2 mm for both cases. It may be concluded that the theoretical dynamic bridge responses in figure 22.3 are of reasonable magnitude.

All of the figures show that the air-sprung vehicle causes the least dynamic bridge response. The reasons for this are threefold. Firstly, the air-sprung vehicle has lower natural frequencies than the leaf-sprung vehicle (see Table 22.1). Therefore, the air-sprung vehicle does not excite the Pirton Lane bridge as much because the bridge and vehicle frequencies do not coincide (Table 22.2). Secondly, the air-sprung vehicle applies smaller dynamic loads to the bridge. This is typical of air suspensions (Chapter 7) . Thirdly, the air suspensions were better damped than the leaf-spring suspensions and the vehicle dampers absorbed energy from the bridge vibration.

Figure 22.5 shows a typical response of the Pirton Lane bridge calculated with the pseudo random roughness surface profile. In general, the main effect of this different surface profile is to distribute more evenly the dynamic response throughout the passage of the vehicle, thus causing slightly larger dynamic bridge responses than observed for the step profile. This effect was particularly evident on the Drift Road bridge [204]. In all the cases examined with the pseudo random profile, the dynamic responses of the bridges were lower for the air-sprung vehicle than for the leaf-sprung vehicle [204].

22.3.6 Dynamic Response Increments

To quantify the comparison between the two different suspensions, maximum dynamic response increments were calculated according to equation 9.1.

$$DI = \frac{y_{max} - y_{st}}{y_{st}}, \tag{9.1}$$

where D is the maximum dynamic response increment,
y_{st} is the maximum bridge response to the static wheel loads,
and y_{max} is the maximum dynamic response of the bridge.

The maximum bridge displacement response increment for each parameter combination with the step surface profile was computed and the results are shown in Figure 22.6 . Two major features should be noticed:

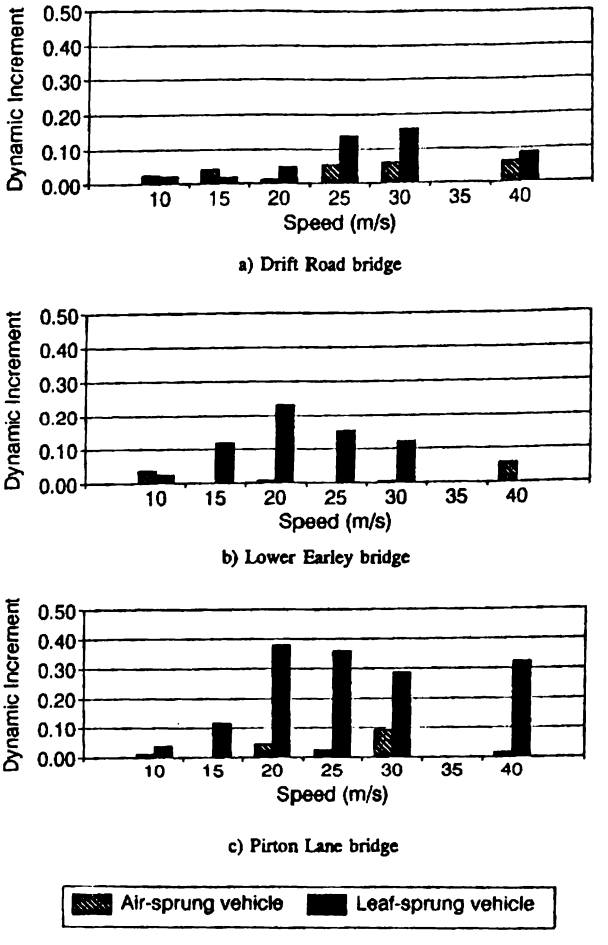


Fig. 22.6 Maximum dynamic displacement increments. 20mm step at bridge entrance. From [207].

Suspensions

The simulated bridge responses to the air suspended vehicle are significantly less than for the steel suspensions in all cases. The maximum dynamic response increments for the air suspension are less than 10% while those for the steel suspension are as high as 40%. This effect is the result of two factors: (i) the air suspension applies lower dynamic wheel loads to the bridges, and (ii) it also has more viscous damping.

Speed

The relationship between maximum dynamic response increment and speed is unclear. For the leaf-sprung vehicle, the critical speed appears to be 30 m/s for the Drift Road bridge, but closer to

20 m/s for the other two bridges. The responses to the air suspended vehicle show a less pronounced dependence on speed.

22.4 DISCUSSION

22.4.1 Numerical Accuracy

The mathematical modelling techniques used for this parametric study have been shown to be accurate when compared to measurements. For example, figure 12.20 shows discrepancies of the order of 0.02 mm between measured and predicted displacement response of the Lower Earley bridge. Similar agreement was obtained for the model of the Drift Road bridge [204]. Furthermore, the tolerance used in equation 12.24 (to ensure mathematical convergence of the bridge displacements) was 2% of the maximum responses. For the Lower Earley bridge with y_{st} = 1.2 mm, this tolerance is equivalent to ±0.02 mm. By contrast, the air suspended vehicle causes a reduction in the dynamic response of the Lower Earley bridge of up to 0.20 mm. This reduction is approximately ten times larger than the expected error of the calculation method presented in Chapter 12. Therefore, the differences between the results for the two different suspensions types cannot be explained by errors in modelling.

22.4.2 Limitations

The results presented in this chapter apply to bridges with first natural frequencies in the 3 to 10 Hz range. For bridges with natural frequencies lower than 3 Hz, it is expected that the beneficial aspects of air suspensions will be reduced because of matching between the natural frequency of these bridges and the bounce mode of vibration of the vehicle. Nevertheless, the dynamic response should still be lower than for a leaf-sprung vehicle because of the softer, more heavily damped suspension. Another area of concern is the dynamic interaction between air suspensions and bridges with relatively high natural frequencies (*eg* 10-15 Hz) because air suspensions apply larger dynamic wheel loads in the wheel-hop mode (typically 10-15 Hz). However, bridges with these higher natural frequencies tend to be quite short and relatively few in number, and thus are of minor importance when compared to the majority of highway bridges.

22.5 CONCLUSIONS

(i) The air-sprung vehicle generated significantly smaller theoretical dynamic responses than the leaf-sprung vehicle on all three bridges. The largest dynamic responses were observed for the bridge with a 3.2 Hz natural frequency.

(ii) Air-sprung vehicles cause lower dynamic responses of bridges because they:

  (a) have lower natural frequencies than most short-span highway bridges;

  (b) apply smaller dynamic loads to the bridges;

  (c) and are often more heavily damped than leaf-sprung vehicles.

(iii) Based on the theoretical analysis performed here, there is tentative evidence to suggest that air-sprung vehicles could be allowed to carry larger loads than vehicles with leaf-spring suspensions. Nevertheless, more theoretical and experimental work is required before this conclusion can be extended to apply to all bridges and heavy vehicles in general.

PART 6 - SUSPENSION DESIGN TO MINIMISE ROAD DAMAGE



23
BACKGROUND TO SUSPENSION DESIGN

23.1 INTRODUCTION

This part of the book investigates the potential for reducing road damage by optimising the design of heavy vehicle suspensions, without compromising other aspects of performance: safety, ride and attitude control.

23.1.1 Design Trade-offs

There are a number of important trade-offs in the design of conventional truck suspensions. The most important suspension attribute concerned with safety is the static roll stiffness, which provides resistance to roll-over. The need for a high roll stiffness conflicts directly with 'road-friendliness'. The best way to reduce dynamic tyre forces is to decrease vertical suspension stiffness [103], but this generally has the effect of degrading roll stiffness and hence reducing static roll-over performance. It also increases static suspension deflection, and therefore increases the sensitivity of ride height to static load, which is undesirable in a truck.

Large increases in roll-over stability can be obtained by using anti-roll bars. However, these add mass, and can degrade roll vibration performance and the response to a single-wheel input if they are very stiff. Use of independent suspensions de–couples the vertical and roll dynamics of the axle which can be used to reduce dynamic tyre forces moderately, without necessarily degrading roll-over performance. Using wide-single tyres, instead of dual pairs, offers the potential for wider spacing between spring centres, and enhanced roll stability. However, wide single tyres generate higher contact stresses and have been implicated in increased road damage (Chapter 17).

Computer-controlled active and semi-active suspensions offer opportunities to de–couple ride and roll performance, and hence to eliminate some of the suspension design trade-offs. They can also be designed to provide 'optimal' performance, and to tune themselves to the operating conditions.

23.1.2 Design Criteria

Time-averaged statistics, such as RMS body acceleration; RMS suspension deflection; and RMS dynamic tyre force are often used in automobile suspension design: as criteria for ride comfort, suspension stroke and road holding [103]. However in road damage analysis, aggregate tyre forces, or single-pass road damage calculations are the operative performance criteria (see Chapters 17 and 19). Thus the vehicle motion (dynamic tyre forces) must be viewed in the stationary frame of reference of the road, rather than the moving frame of reference of the vehicle.

23.1.3 Options for Improvement

There are various ways in which suspensions may be improved. These range from improving the performance of passive leaf spring suspensions; to optimising the stiffness and damping of air spring suspensions; to use of computer-controlled active and semi-active suspension elements.

23.2 PASSIVE SUSPENSIONS

A large proportion of semi-trailer suspensions in the UK are fitted with steel spring suspensions [336]. Such suspensions have been observed to have poor static load equalisation between axles [336, 443] and to generate higher dynamic tyre forces than air suspensions [337, 443]. Both of these factors are thought to increase the road damaging potential of steel suspended vehicles significantly, for particular conditions, as explained in previous chapters.

The first part of Chapter 24 is concerned with improving the performance of a conventional four-spring tandem trailer suspension, using low cost 'bolt-on' modifications. The second part of Chapter 24 investigates the advantages and disadvantages of using wide-single tyres on trucks. Simple mathematical models are used throughout, in order to reveal the most important factors.

The main objective of the work described in Chapter 25 is to establish guide-lines for the design of passive suspensions that cause minimum road damage. A procedure for calculating road-damage criteria efficiently is developed, and used to optimise the suspension parameters of a typical air-suspended vehicle.

23.3 ADVANCED SUSPENSIONS

There are three possible types of advanced suspensions that could be used on heavy goods vehicles [422]:

(i) active suspensions, in which the suspension spring and damper is replaced by a high performance hydraulic actuator with an associated hydraulic power supply;

(ii) slow active suspensions, in which a low bandwidth hydraulic actuator is used in series with a soft suspension spring;

(iii) semi–active suspensions, in which controllable dampers (which can only dissipate energy) are used instead of (or alongside) conventional hydraulic suspension dampers.

Of these, only semi–active suspensions are likely to be economically viable in the foreseeable future, and some research has been undertaken to examine their potential for reducing dynamic tyre forces and road damage [40, 53, 54, 283, 285, 286, 514].

In Chapter 26, the benefits of using relatively straightforward control strategies for semi-active dampers are investigated. This would builds on the research into force control of a semi-active damper, described in Chapter 4. More sophisticated control strategies, involving the feed-back of information from one axle station to another (*eg* 'preview' control) are also discussed briefly. Additional performance gains are found to be possible over the simpler strategies.

24
LEAF SPRINGS AND TYRES

24.1 SUMMARY

A test rig for measuring the quasi-static performance of tandem suspensions in the laboratory is described. Measurements on a standard tandem leaf-spring suspension show it to have high effective stiffness in bounce and poor static load equalisation. A method for eliminating the spring-end friction is investigated, and found to improve the performance significantly.

A two-dimensional articulated vehicle simulation is validated with measurements from a test vehicle. The simulation is then used to study the effect on dynamic tyre forces of three modifications to the trailer suspension: (i) softer springs; (ii) elimination of spring-end friction; and (iii) hydraulic dampers. The RMS dynamic loads generated by the trailer axles are predicted to decrease by approximately 31%, and the theoretical road damage to decrease by about 13%. The trailer suspension of the test vehicle is adapted to incorporate the three modifications, and the measured reductions in dynamic tyre forces are found to be about half those predicted by the simulation.

A theoretical study is then performed to assess the effects of tyre configuration on the dynamic tyre forces generated by heavy vehicles with wide single tyres or dual tyres. The rollover performance of vehicles with these tyres is also assessed and the trade-off between dynamic tyre forces and roll-over stability is investigated. Conclusions are drawn about the road-damaging and roll-over performance of wide single tyres compared with dual tyre configurations.

This chapter is based on work previously published in [123] and [126].

24.2 INTRODUCTION

This chapter is concerned with reducing the road-damaging potential of conventional heavy goods vehicles, while maintaining safety. It examines two important issues: (i) improving the performance of conventional leaf-spring suspensions; and (ii) the choice of dual tyres or wide single tyres. In both cases, the analysis concentrates on the performance of the suspensions and tyres of a typical UK tractor–semi–trailer unit.

The work described in the first part of this chapter has the objective of investigating means for reducing the road damaging potential of typical steel sprung articulated vehicles. If suitable suspension modifications were available, it would be possible for vehicle operators to take advantage of future legislation that might be introduced concerning the 'road-friendliness' of existing trailer suspensions. In order to be attractive to vehicle operators the suspension modifications would need to be cheap to fit and maintain, and low in weight.

Under straight–line, steady running conditions, (*ie* in the absences of turning, accelerating or braking forces), road damage caused by a heavy commercial vehicle can be attributed to two tyre factors: (i) the vertical forces applied to the road surface by each of the tyres (static and dynamic); and (ii) the contact conditions: contact area, pressure and pressure distribution, by which the vertical forces are transmitted to the road [96] (see Chapter 17).

The main *tyre* parameter influencing dynamic tyre forces is the overall vertical stiffness. Tyre damping is generally small and can be ignored in predictions of vehicle response to road roughness. Wide single tyres have lower vertical stiffness than dual tyres, which generally results in lower dynamic tyre forces (see Section 7.5). However, they also generate considerably higher contact pressures than dual tyres, and this has been implicated in increased road damage (see Chapter 17).

Tyre and suspension characteristics influence various aspects of heavy vehicle safety: braking handling (understeer, oversteer, jack-knifing, trailer swing); and roll-over [25]. Of primary concern in this chapter is roll-over stability. This is influenced by the stiffness and lateral spacing of the tyres; the stiffness and the spacing of the suspension springs; and any auxiliary roll stiffness (*e.g.* provided by an anti-roll bar). Wide single tyres have lower vertical stiffness, but a wider track. Overall this tends to increase the roll stiffness of the suspension, compared with dual tyres, and to improve roll-over performance. These issues are discussed in the second part of this chapter.

Section 24.3 describes the vehicle used for the leaf-spring-improvement study, and summarises the validation of a nonlinear computer simulation of the vehicle. Section 24.4 describes a test rig for measuring the performance of tandem axle suspensions. The reasons for the poor performance of the standard suspension are identified, and modifications to improve its performance are investigated. In Section 24.5, the validated vehicle simulation is used to predict the reductions in dynamic tyre forces and theoretical road damage achievable by modifying the trailer suspension. The modifications considered are: (i) half stiffness springs; (ii) low friction spring-ends; and (iii) hydraulic dampers. Finally, modification and testing of the vehicle are described, and the performances of the modified vehicle and standard vehicle are compared in Section 24.6. Section 24.7 compares the influence of dual tyres and wide single tyres on dynamic tyre forces, and Section 24.8 investigates the trade-off between dynamic tyre forces and roll-over stability.

24.3 TEST VEHICLE AND SIMULATION VALIDATION



24.3.1 Vehicle Tests

The test vehicle was provided by the Transport Research Laboratory (TRL). It was an articulated tanker vehicle with four axles and laden to the maximum allowable gross mass (for this class of vehicle) of 32.5 tonnes. It was similar to that used in the study to validate an articulated vehicle simulation, (described in Section 6.4), but the semi-trailer had a tank body rather than flat-bed style. The suspensions of the flat-bed trailer and the tanker were of identical design.

The tractor had two axles, both fitted with multi-leaf springs, hydraulic dampers and anti-roll bars. The trailer was fitted with a wide-spread 'four-spring' tandem axle group with mono-leaf springs and a load equalising mechanism. Dual radial-ply tyres were fitted to all axles except the steering axle which had single tyres. The vehicle was instrumented by TRL to measure dynamic tyre forces, by means of strain gauges bonded to each axle, and accelerometers to compensate for inertia effects.

The vehicle was tested on a straight section of the TRL test track at five speeds: 9, 13, 18, 22, 27m/s (20, 30, 40, 50, 60mph). The roughness profiles of the nearside and offside wheel tracks were measured by TRL using their high-speed profilometer. The test section corresponds approximately to the 'good' classification proposed by the ISO [12], which can be likened to a poor motorway or average principal road. See figure 3.1 and Section 6.4.1 for further details of the profiles.

24.3.2 Vehicle Simulation

The vehicle simulation model was very similar to that described in the second case study in Chapter 6, with changes to the parameters of the trailer sprung mass so that they represented the tanker instead of the flat-bed trailer, and some small modifications to the trailer leaf spring parameters. The parameter values can be found in [123].

The simulated tyre forces were calculated in the time domain using the measured profile of the test section as the input. Figure 24.1 shows the measured and simulated spectral densities of the offside tyre forces on the tractor drive axle and first trailer axle at a speed of 22m/s. Comparisons at other speeds and other axles show similar agreement. The agreement is similar to that seen in Chapter 6.

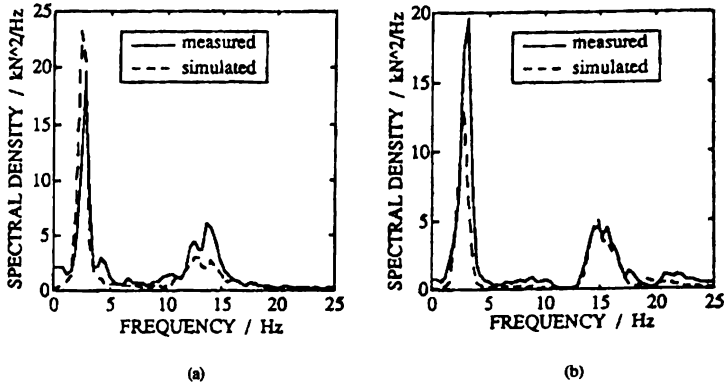


Fig. 24.1 Spectral densities of measured and simulated offside tyre forces, vehicle speed 22m/s. (a) tractor drive axle; (b) first trailer axle

24.4 TANDEM SUSPENSION MEASUREMENTS

24.4.1 Test Rig

A hydraulic test facility for testing tandem suspensions at low velocities was built for this study; a schematic view is shown in figure 24.2. A tandem suspension assembly was provided by TRL, consisting of two leaf springs, radius rods, an equalising beam, and all the correct mounting brackets. Two hydraulic cylinders were used to apply forces to 'dummy' axles. The applied forces were measured by strain gauged force transducers, and the axle displacements were measured by linear resistive displacement transducers. The radius rods of the suspension were strain gauged to measure axial force. The maximum actuator velocity was 0.05m/s, which is low compared to typical suspension working velocities (up to 1m/s). However, previous work has shown that for leaf spring suspensions, the main factors influencing the performance are stiffness and dry friction, which are not strongly dependent on velocity amplitude (see Chapter 4).

24.4.2 Standard Suspension

In-Phase Displacement

Figure 24.3a shows the forces generated at each axle as the displacements of the axles are varied sinusoidally in phase. Both force-deflection curves show hysteresis, resulting from friction at the slipper ends of the springs. This hysteresis characteristic is typical of many leaf spring suspensions (see Chapter 4). For large deflections the effective stiffness of the suspension is equal to the slope of the upper and lower parts of the loop BC and DA, approximately 2MN/m. For small spring deflections the effective stiffness approaches the slope of the sides of the loop AB and CD, approximately 12MN/m.

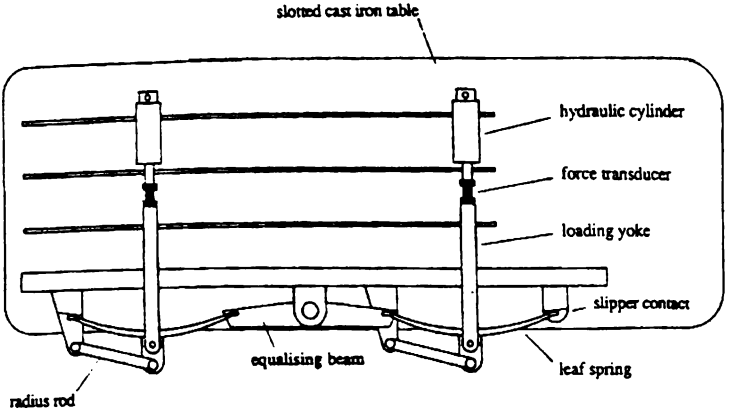


Fig. 24.2 Test rig for measuring the quasi-static performance of tandem leaf-spring suspensions. From [123].

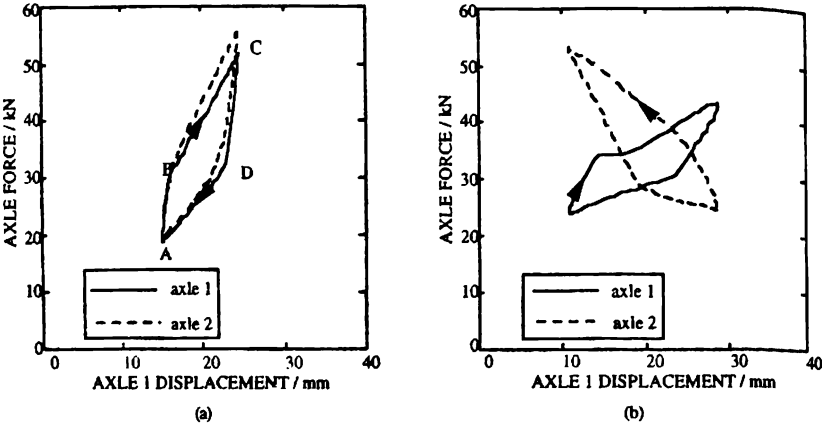


Fig. 24.3 Force against axle 1 displacement, measured on the standard suspension. From [123].
(a) Displacements in phase. (b) Displacements antiphase.

The measurements from the test vehicle (Section 24.3) indicated that the dominant frequency o dynamic tyre forces was about 3Hz. This frequency is in the range of the sprung mass vibratio modes, when the displacements of the tandem trailer axles relative to the body will be of simila amplitude and in phase with each other. The spring deflection was not measured during the vehicl tests, but the validated vehicle simulation predicted that at a speed of 22m/s on the test lane th standard deviation of the spring deflection was approximately 3mm. This level of deflection mean that the springs are operating largely on the steep parts of the hysteresis curves, and therefore th effective stiffnesses are considerably higher than the large deflection stiffnesses. This high effectiv stiffness is a major factor in the generation of high dynamic tyre forces by the trailer axles.

Antiphase Displacement

Figure 24.3b shows the forces resulting from the two axles being displaced in antiphase (180° out-of-phase). Despite the presence of the equalising beam, the axle forces vary considerably throughout the cycle. The force amplitude at axle 2 is greater than at axle 1. This arises because of the forces generated in the radius rods. When the axles are displaced in antiphase, the kinematic constraint provided by the radius rods causes significant sliding at the slipper ends of the springs. The friction forces generated at these sliding contacts are reacted by the radius rods. As axle 1 is displaced upwards (A1 B1 C1), radius rod 1 goes into tension. The vertical component of this force acts to decrease the net vertical force at axle 1. As axle 2 is displaced upwards (C2 D2 A2), radius rod 2 goes into compression. The vertical component of this force acts to increase the vertical force at axle 2. See also Section 6.4.2.

24.4.3 Modified Suspension

From the results presented above, it can be seen that friction between the spring-ends and the chassis is the cause of two undesirable characteristics of the suspension: (i) high vertical stiffness for small displacements (figure 24.3a), and (ii) poor load equalisation (figure 24.3b).

The use of PTFE inserts in the spring contacts to improve these characteristics was investigated by TRL [425]. PTFE inserts were also tried on the test rig, but although they improved the characteristics of the suspension significantly, they were not thought to be suitable for long-term use. After only a few cycles of testing, the PTFE showed signs of excessive wear and permanent deformation.

An alternative modification was investigated. Rectangular rubber blocks (120mm x 50mm x 30mm thick), bonded to steel plates, were fitted between the spring-ends and the chassis. The rubber blocks accommodate spring-end movement by shearing elastically. The advantage of using rubber instead of PTFE to reduce forces at the spring-ends is that there is no sliding contact and therefore no wear.

Figure 24.4 shows test rig results for the standard suspension fitted with rubber blocks between the spring-ends and the chassis. Figure 24.4a shows that the hysteresis for in-phase displacement is nearly eliminated. The compressive flexibility of the blocks means that the static deflection of the suspension is 30mm, compared to 20mm for the standard suspension, for the same static load. Once loaded to the static force the small deflection stiffness of the suspension is 1.9MN/m. Figure 24.4b shows the axle force response to antiphase axle displacements. The axle force amplitudes are about one third of those for the standard suspension (figure 24.3b). Equalisation is still not perfect because of the stiffness of the rubber blocks and of the rubber bush in the equalising beam pivot.

24.5 SUSPENSION PARAMETER STUDY

24.5.1 Suspension Modifications

A simple two degree-of-freedom (DOF) quarter car model, shown in figure 24.5, was used to investigate the influence of suspension stiffness and damping on dynamic tyre forces. The parameter values represented one wheel station of the laden trailer. The model neglects several important features of the trailer suspension: (i) nonlinearity, particularly due to friction; (ii) interaction between the trailer axles; (iii) roll and pitch motions of the axles and sprung masses.

The dynamic load coefficient, DLC, (equation 5.6) was calculated for a white noise velocity input at the road surface, with spectral density of $13.8 \times 10^{-6} m^2/s$. This input represents a vehicle speed of 22m/s over a road of roughness similar to the test lane. The upper graph in figure 24.5 shows contours of DLC for a wide range of suspension damping and stiffness values. The lower graph shows an expanded view of the upper graph. The minimum DLC is 0.051, at point D,

corresponding to a spring stiffness of 200kN/m and damping of 25kNs/m. The position of the optimum depends on the slope of the road displacement spectrum: a steeper slope results in a lower value of optimum stiffness.

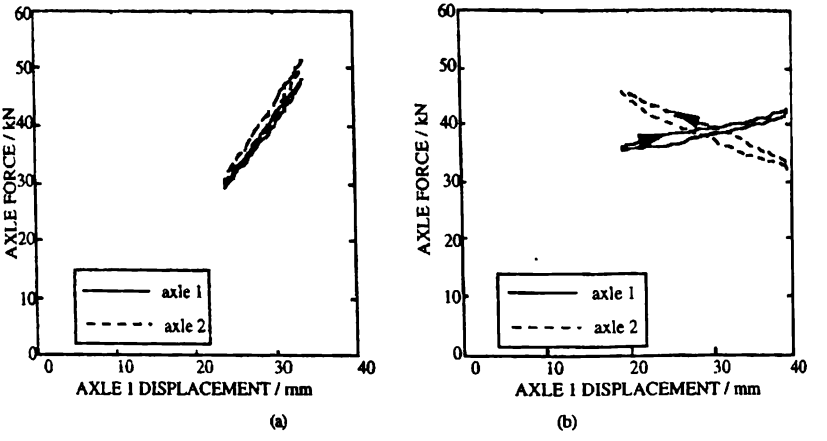


Fig. 24.4 Force against axle 1 displacement, measured on the suspension modified with rubber blocks. From [123]. (a) Displacements in phase; (b) Displacements antiphase.

Three modifications to the tandem suspension were investigated. These involved altering the stiffness and damping of the suspension. They are discussed in detail in the following sections.

Rubber Blocks

The measurements described in Section 24.4 showed that rubber blocks in the slipper ends of the springs almost eliminate the hysteresis caused by friction. This has the effect of reducing the small deflection stiffness of the spring from a maximum value of 12MN/m to approximately 2MN/m, the large deflection stiffness. Figure 24.5 indicates that the minimum DLC at a spring stiffness of 12MN/m is 0.27 (point A), when the damping is 600kNs/m. The minimum DLC reduces to 0.11 when the stiffness is 2MN/m (point B), with damping of 90kNs/m .

Half Stiffness Spring

According to the quarter car model, a further reduction in DLC is possible if the large-deflection spring stiffness is reduced towards the optimum value indicated on figure 24.5 (point D). Halving the spring stiffness to 1MN/m was thought to be a reasonable aim, which reduces the minimum DLC to 0.077 (point C). However, significantly reducing the large-deflection stiffness of the trailer springs is likely to introduce two problems: (i) excessive static deflection, and (ii) inadequate roll-over threshold.

Static Deflection: The static displacement of the body mass due to a vertical force of 30kN (a typical change in payload weight per wheel) is 30mm for the standard spring stiffness of 2MN/m. Halving the stiffness to 1MN/m results in a static displacement of 45mm. This is thought not to be an excessive increase.

Roll-Over Threshold: A simple vehicle roll model was used to predict the influence of spring stiffness on roll-over threshold [25]. The model is shown in figure 24.6. It represents only the trailer suspension; the influence of the tractor on the roll-over threshold of the whole vehicle is neglected.

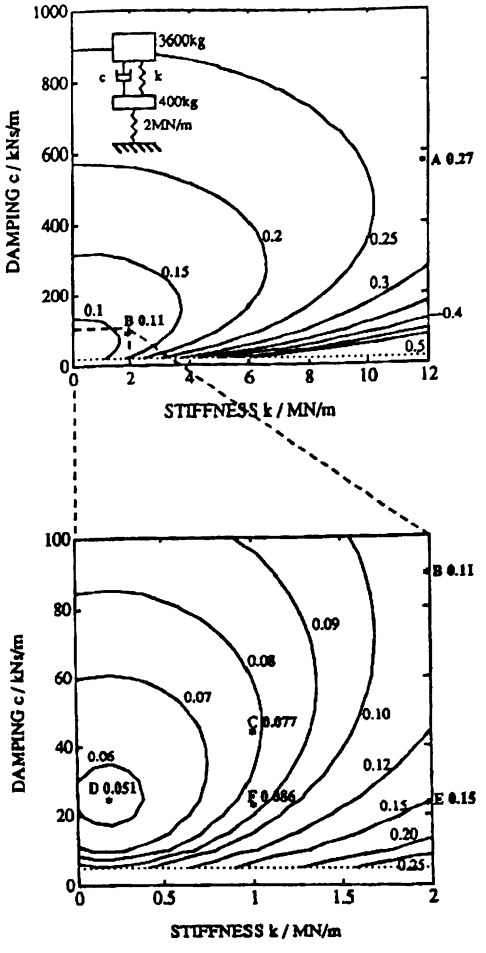


Fig. 24.5 Contours of dynamic load coefficient (DLC) as a function of suspension stiffness and damping, [123].

The roll-over threshold is defined as the lateral acceleration needed to reduce the vertical force on one of the tyres to zero. Figure 24.7 shows the dependence of roll-over threshold on spring stiffness, sprung mass CG height, and spring 'lash'. (Spring lash is the clearance between the underside of the spring-end and the chassis mount, which becomes free-play as the spring force changes from compression to tension). For a typical CG height of 2.0m, reducing the spring stiffness from 2MN/m to 1MN/m reduces the roll-over threshold from $4.2m/s^2$ to $3.9m/s^2$. However, if the spring lash is reduced from 40mm to zero the threshold is restored to $4.2m/s^2$.

These simple models indicate that the large deflection spring stiffness can be reduced by half without significant detrimental effect on static roll-over threshold or static deflection, providing the spring lash is removed. However, detailed simulation and testing would be necessary to ensure safety under the full range of operating conditions.

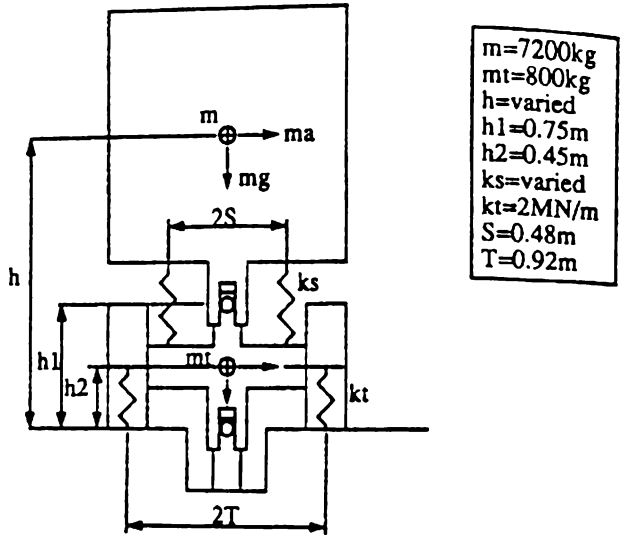


Fig. 24.6 Static roll model of the trailer. From [123].

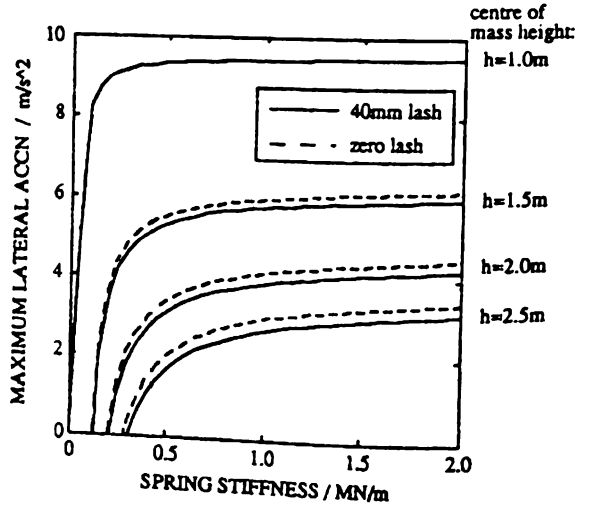


Fig. 24.7 Static roll-over threshold (maximum lateral acceleration) as a function of suspension stiffness, centre of mass height, and spring lash. From [123].

Hydraulic Dampers

The standard trailer suspension is not fitted with hydraulic dampers, but relies instead on friction at the spring ends to provide the damping action. Eliminating the friction by the use of rubber blocks means that an alternative source of damping must be provided. The use of hydraulic dampers can give the required damping without increasing the effective stiffness of the suspension.

Figure 24.5 indicates that for the standard spring stiffness, 2MN/m, a minimum DLC of 0.11 can be achieved when the damper coefficient is about 90kNs/m (point B). The corresponding damping coefficient for half spring stiffness is 45kNs/m (point C), where the DLC is 0.077.

The linearised damping coefficient of a typical truck suspension damper is approximately 12kNs/m. Therefore, to achieve the damping coefficient of 45kNs/m, required for minimum DLC, with rubber blocks and half-stiffness springs, approximately four dampers would be required on each end of the axle. In practice, it was thought that two dampers on the end of each axle would be a practical maximum, giving a damping coefficient of 24kNs/m, points E and F. The corresponding DLCs of the model are 0.15 for standard stiffness springs and 0.086 for half stiffness springs.

24.5.2 Road Damage Criterion

The validated two-dimensional simulation described in Section 24.3 was used to investigate the effect of the three modifications to the trailer suspension. In addition to calculating the dynamic load coefficients of each axle, the 95th percentile aggregate fourth power force (equation 17.5) was also calculated. This criterion is referred to as the 'road damage' throughout the rest of this chapter, and is calculated for the four axles of the whole vehicle and for the two trailer axles alone. Use of this criterion is based on the results presented in Chapter 19, which showed that: for comparing vehicles with similar arrangements of axles and tyres, the simple aggregate fourth power force calculation gives similar results to more realistic criteria, based on road response calculations.

24.5.3 Simulation Results

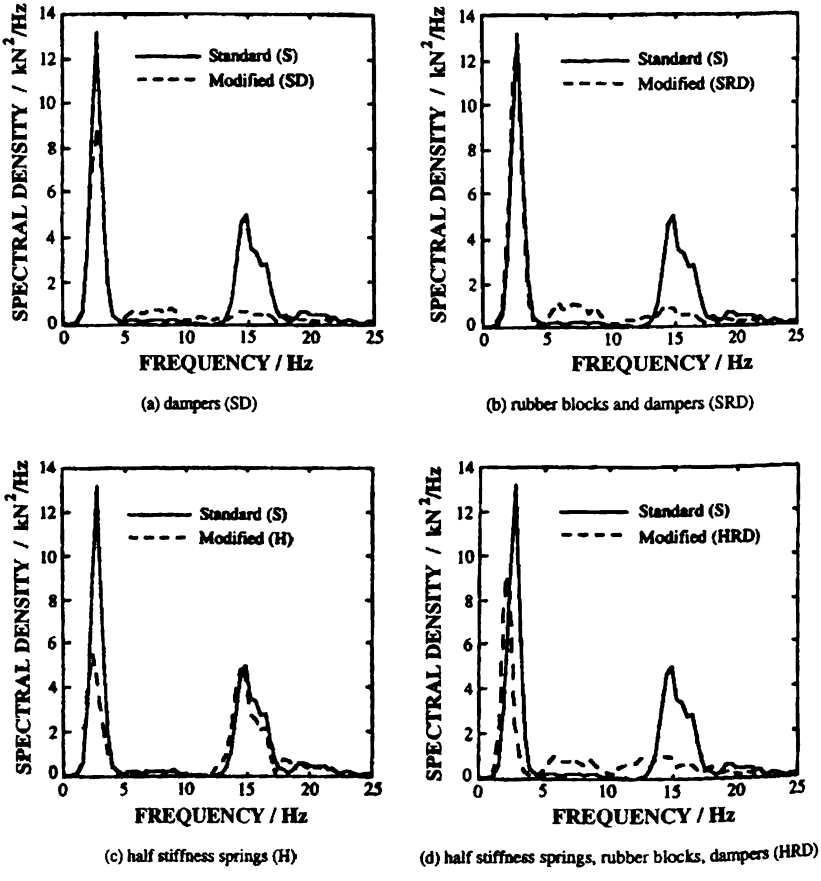
The three modifications (rubber blocks (R), half stiffness springs (H), and hydraulic dampers (D)) were applied to the trailer suspension of the validated simulation and evaluated in eight combinations, defined in Table 24.1. Tyre force histories were calculated for the same road profile input and vehicle speeds used in the validation study (Section 24.3). The vehicle was modelled in the fully laden condition only.

Vehicle Model	*Spring stiffness*	*Rubber blocks*	*Dampers*
S	standard		
SR	standard	fitted	
SD	standard		fitted
SRD	standard	fitted	fitted
H	half		
HR	half	fitted	
HD	half		fitted
HRD	half	fitted	fitted

Table 24.1 Definition of vehicle models.

The effect of fitting rubber blocks without additional dampers (models SR and HR) is to increase the vibration response of the sprung mass modes significantly: this modification was therefore not investigated.

Figure 24.8 shows tyre force spectral densities for the first trailer axle for four of the other combinations. The effect of adding dampers to the standard suspension is shown in figure 24.8a (model SD). The response of the unsprung mass mode at about 15Hz is eliminated, and the response of the sprung mass modes (3Hz) is slightly reduced. The combined effect of rubber blocks and dampers (model SRD) is shown in figure 24.8b. The unsprung mass mode response remains low, but the sprung mass mode response is unchanged from the standard vehicle: this is because the viscous damping only just compensates for the loss of dry friction damping. Figure 24.8c shows the effect of half-stiffness springs (model H). The frequency and response of the sprung mass modes are reduced, but the unsprung mass mode is unchanged. The addition of dampers and rubber blocks to the half-stiffness springs (model HRD, figure 24.8d) causes the sprung mass mode response to increase slightly and the unsprung mass mode response to decrease. Models H and HRD give similar reductions in DLCs and road damage, but modification HRD is preferable because static-load sharing performance is better, and the viscous damping is not amplitude dependent.



(a) dampers (SD)

(b) rubber blocks and dampers (SRD)

(c) half stiffness springs (H)

(d) half stiffness springs, rubber blocks, dampers (HRD)

Fig. 24.8 Simulated spectral densities of the first trailer axle tyre forces of four vehicle models, vehicle speed 22m/s. From [123].

The effect of the HRD modification on the DLCs of each axle, and on the road damage of the trailer only, and of the whole vehicle are summarised in figure 24.9. The theoretical road damage values were averaged over the five speeds, and then the percentage changes from the corresponding values for the standard vehicle were calculated. The chart shows that the DLCs of the tractor axle are little affected by the modifications. The trailer axle DLCs are reduced on average by 31%, and the reduction in road damage by the trailer axles is 13%. The DLCs are calculated from only the dynamic force components, whereas the road damage calculation also includes the static force components, which are not changed by the suspension modifications. The percentage reduction in DLC is therefore greater than the percentage reduction in road damage The predicted reduction in road damage by the whole vehicle is 6.7%.

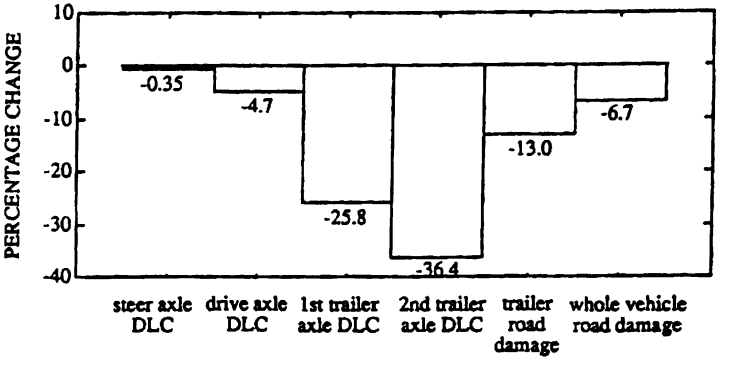


Fig. 24.9 Simulated change in tyre force criteria (averaged over five speeds), modified vehicle (HRD) compared to the standard vehicle (S). From [123].

24.6 TESTS ON THE MODIFIED VEHICLE

24.6.1 Suspension Modifications

The vehicle was modified to incorporate half stiffness springs, rubber blocks and dampers. A constraint on the modifications, imposed by TRL, was that their vehicle had to be returned to its original condition. Consequently the modifications were designed to be bolted onto the trailer without welding or drilling the chassis or suspension components.

Half Stiffness Springs

Parabolic steel springs with approximately half the large-deflection stiffness of the standard springs were supplied by Tinsley Bridge Ltd. The reduced stiffness was accomplished by reducing the thickness of the spring and using stronger material and improved production techniques to accommodate the increased stresses.

Rubber Blocks

The rubber blocks were chosen from the Dunlop Metalastik range of rectangular mountings. The particular mounting chosen was the largest that would fit into the available space. The height of the mounting was sufficient to eliminate the lash between the spring end and chassis.

The rubber blocks were supplied with two 5mm thick steel rectangular mounting plates bonded to the rubber. One of these plates was bolted to the end of the spring by three bolts, through holes drilled into each end of the spring. The second mounting plate did not have sufficient bending strength to support the point load at the contact with the chassis mounting. This mounting plate was replaced with a steel U section, bonded to the rubber with appropriate adhesive.

Hydraulic Dampers

Two dampers were fitted to each end of the trailer axles. The dampers were a standard Ford-Iveco part, and to the same specification as those described in Section 4.4. They were chosen because they had a relatively high damping coefficient (linearised value 12kNs/m), and had been shown to perform satisfactorily at 15Hz, the frequency range of the wheel hop modes.

The assembly of dampers and mounting brackets for one axle is shown in figure 24.10. The top mountings of the dampers were attached to the chassis via a cross-beam clamped between the chassis rails. The bottom mountings of the dampers were attached to the axle via longitudinal beams clamped to the underside of the axle tube by U-bolts. A necessary precaution was to provide some damping of axle pitch motion, which might be excited during vehicle braking. The two dampers on each side of the axle were therefore inclined towards each other in side view.



Fig. 24.10 Arrangement of dampers and mounting beams for one axle. From [123].

24.6.2 Vehicle Tests

The modified vehicle was tested under the same conditions as the standard vehicle. During the course of the testing the vehicle was subjected to moderate braking and cornering manoeuvres. The suspension modifications were thought not to have affected the stability and safety of the vehicle under these conditions. However, thorough testing would need to be performed to confirm this conclusion. At the end of the short test period inspection of the vehicle revealed no signs of failure of the new components. Long-term testing would be needed to confirm the durability of the modifications.

24.6.3 Analysis of Test Results

The DLCs calculated from the measured tyre forces are shown in figure 24.11. Figures 24.11a-b show that the DLCs of the tractor axle were little changed by the modifications to the trailer suspension, which is in agreement with the simulation (figure 24.9).

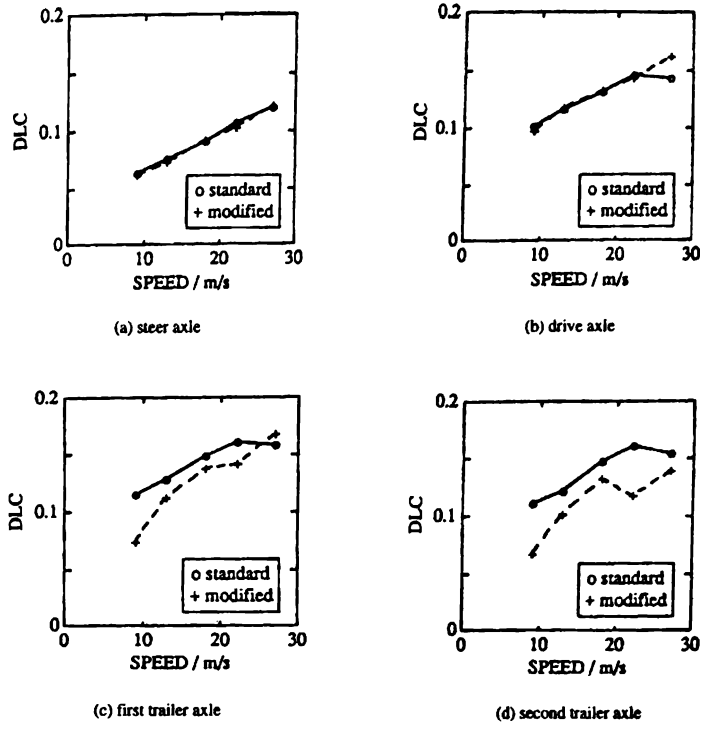


Fig. 24.11 Measured DLCs for the standard and modified vehicles. From [123].

Figures 24.11c-d show that, except at the highest speed, the trailer axle DLCs are reduced throughout the speed range. Figure 24.12 compares measured tyre force spectral densities of the standard and modified vehicles. The graph shows that the reduction in trailer tyre force occurs in the range of the sprung mass modes. The change in the sprung mass mode response agrees quite well with the prediction shown in figure 24.8d. However, figure 24.8d also predicts a significant reduction in the unsprung mass mode response, which is not apparent in the measured response. The reason for this is not fully understood, but may be due to inadequate modelling of the high frequency behaviour of the dampers (Section 4.4).

Figure 24.13a shows the theoretical road damage by the trailer axles alone; and figure 24.13b shows the damage done by the whole vehicle. The modifications to the trailer suspension, despite significantly reducing the trailer axle DLCs, resulted in little overall reduction in damage by the whole vehicle.

Figure 24.14 summarises the measured effect of the modifications, and may be compared with figure 24.9 which shows the predicted changes. The measured reductions in trailer axle DLCs (15.5%) and road damage by the trailer (5.2%) are about half the predicted reductions. This is mainly because the simulation predicted a significant reduction in the trailer axle tyre forces at the wheel hop frequency which did not occur in practice.

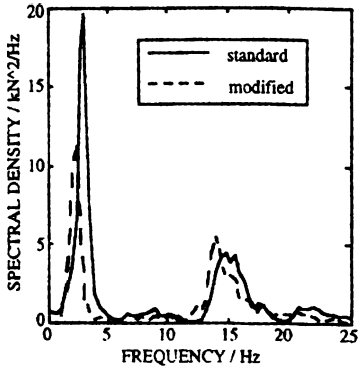
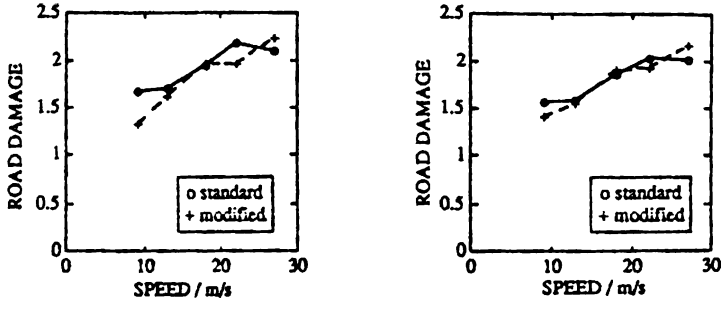


Fig. 24.12 Measured spectral density of first trailer axle offside tyre force, speed 22m/s. From [123].



(a) trailer axles only (b) whole vehicle

Fig. 24.13 Normalised road damage calculated from the measured tyre forces of the standard and modified vehicles. From [123].

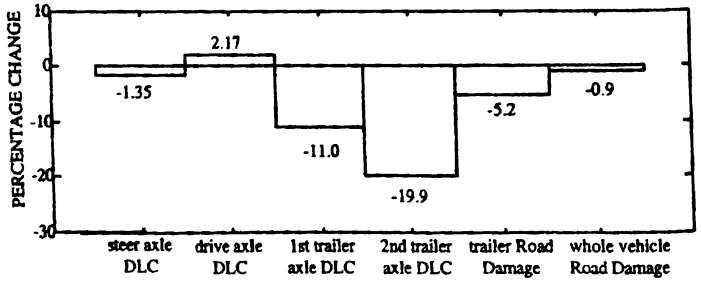


Fig. 24.14 Measured change in tyre force criteria (averaged over five speeds), modified vehicle compared to the standard vehicle. From [123].

24.7 DYNAMIC TYRE FORCES DUE TO SINGLE AND DUAL TYRES

24.7.1 Model description

In this section, the quarter-truck model described in Section 24.5 (and shown in figure 24.15) is used to quantify the difference in dynamic tyre forces that can be expected due to use of wide single tyres instead of dual tyres.

The input to the model was a single-sided spectrum of road displacement defined by equation 3.2, with parameter values corresponding to an average motorway or good principal road ($n = 2.5$, $S_0 = 50 \times 10^{-8}$).

The tyre force spectrum was calculated over the frequency range 0.2 to 30Hz at intervals of 0.2Hz, for a vehicle speed of 22m/s (80km/hour). The RMS dynamic tyre force was calculated by integrating the spectral density over this frequency range and taking the square root. This in turn gave a value for the Dynamic Load Coefficient $\bar{s}$ (equation 5.6).

The main criterion used for assessing road damage was the 95th percentile, fourth-power weighted dynamic force J. Assuming that the dynamic tyre forces can be considered to have a Gaussian probability density function, Sweatman [443] noted that the 95th percentile fourth power force can be calculated from the DLC using:

$$J = (1 + 1.65\bar{s})^4, \tag{24.1}$$

Assuming further, that the magnitude of the dynamic force component is small compared to the static load, and using the binomial expansion J is approximately given by:

$$J \approx 1 + 6.6\bar{s} \tag{24.2}$$

This can be calculated efficiently in the frequency domain.

24.7.2 Optimum Stiffness and Damping

Figure 24.15 shows a contour map of road damage J as a function of suspension stiffness k and damping c for the vehicle model with *dual tyres* and operating conditions described in the previous section. The minimum road damage is 1.73 times the static road damage, and occurs when the suspension stiffness k=74kN/m, and the damping c=20kNs/m. The optimum value of stiffness is very low compared to the values used in practice: a typical air spring provides a stiffness of 400kN/m, and the large deflection stiffness of a monoleaf steel spring is typically 2MN/m. Conversely the optimum value of damping is higher than that usually provided on trucks. A typical mean damping coefficient provided by a truck damper is 10 kNs/m.

Figure 24.16 shows the corresponding graph for wide-single tyres. The tyre stiffness is 1.3MN/m and the unsprung mass is 350kg (compared to 2MN/m and 400kg for dual-tyres). The total mass remains fixed at 4000kg. The contour plot shows that the minimum damage is 12% lower than for the dual-tyre case, at 1.53 times the static damage. The corresponding suspension stiffness is 38kN/m and the damping is 15kNs/m. For stiffness and damping typical of an air suspension, wide single tyres reduce the damage criterion by 6%, from 2.10 to 1.96.

The damping rate needed to achieve minimum damage is about 25% lower for wide single tyres than for dual tyres. This is largely due to the lower unsprung mass. This lower damping requirement is a significant fringe benefit of wide single tyres. It can result in smaller, lighter dampers, and improves the ability of suspension designers to provide near optimum performance with practical suspension components.

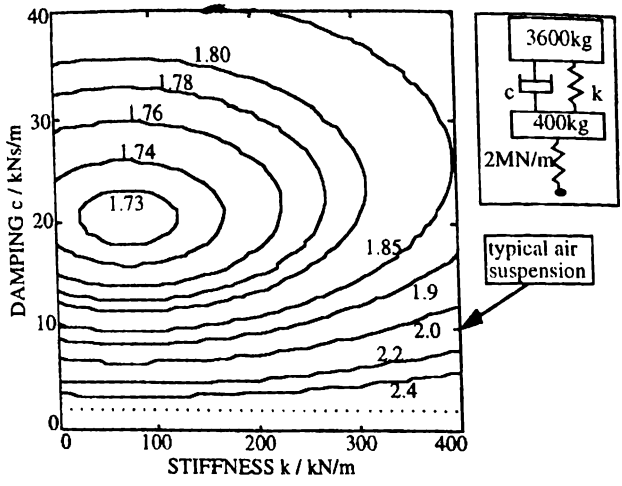


Fig. 24.15 Road damage J as a function of suspension damping and stiffness of the bounce model with dual tyres, vehicle speed 22m/s. From [126].

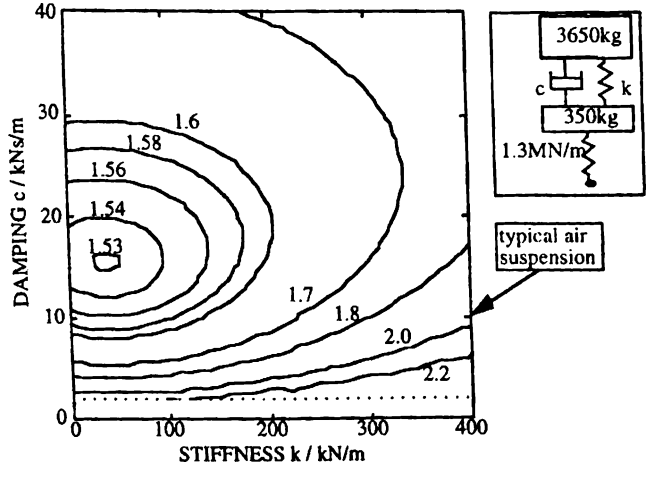


Fig. 24.16 Road damage J as a function of suspension damping and stiffness of the bounce model with wide-single tyres, vehicle speed 22m/s. From [126].

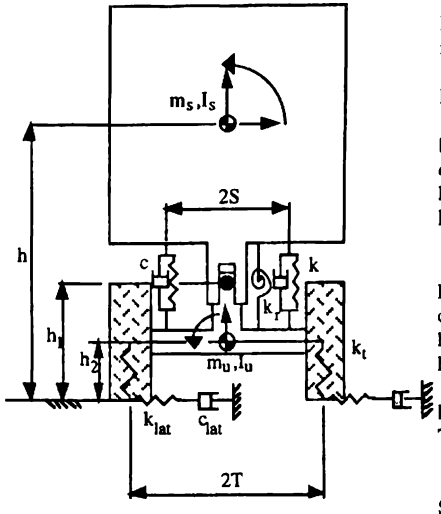
24.8 INFLUENCE OF TYRES ON ROLL-PLANE PERFORMANCE

24.8.1 Model description

The relationships between road damage and roll-over performance for vehicles with dual and wide-single tyres were investigated using the roll-plane model shown in figure 24.17. The model has six degrees of freedom, with parameter values chosen to represent one axle station of a typical laden truck. It is similar to the static roll-over model in figure 24.6, but contains additional parameters

which are relevant to the bounce and roll dynamics. As with the bounce model, the roll-plane model must neglect some important effects. In particular, the pitch coupling between axle stations by the sprung mass and inter-axle load transfer mechanisms is ignored.

The sprung mass has three degrees of freedom: vertical, lateral, and roll. The unsprung mass has two degrees of freedom: vertical and roll. The sprung mass rolls relative to the unsprung mass at roll centre height h_1, and the roll centre of the axle is at ground level. The suspension consists of a parallel spring and damper on each side of the axle, separated by distance 2S. Auxiliary roll stiffness k_r is provided by a torsional spring (anti-roll bar). An independent suspension is simulated by setting the distance between the line of action of the suspension units to be equal to the tyre spacing (S=T), and setting the sprung mass roll centre height h_1 to 0.1m [501]. A rigid axle suspension is simulated by setting the distance between the line of action of the suspension units to 1.0m or 1.2m, depending on tyre configuration, and the sprung mass roll centre height h_1 to 0.6m [501].



m_s =7200kg (dual-tyres)
7300kg (wide-single tyres)
I_s =m_s*0.781 kgm^2
m_u =800kg (dual-tyres)
700kg (wide-single tyres)
I_u =$m_u T^2$ (independent suspension)
m (T-0.1)^2 (rigid axle)
k =varied
c =varied
k_r =varied
k_t =2MN/m (dual-tyres)
1.5MN/m (under-inflated dual-tyres)
1.3MN/m (wide-single tyres)
k_{lat}=676kN/m
c_{lat} =(338/v)kNs/m (v=speed in m/s)
h =2.0m
h_1 =0.1m (independent suspension)
0.6m (rigid axle)
h_2 =0.5m
T =0.910m (dual-tyres)
0.970m (under-inflated dual-tyres)
1.023m (wide-single tyres)
S =T (independent suspension)
0.5m (dual-tyres, rigid axle)
0.6m (wide-single tyres, rigid axle)

Fig. 24.17 Roll-plane model with six degrees of freedom. From [126].

The lateral force generating properties of the tyre are an important part of the model, because they react the lateral inertia forces on the vehicle. Loeb *et al* [309] show that the properties can be described using a first order equation with time constant τ_{lat}. This characteristic is therefore represented by a spring and damper in series (k_{lat} and c_{lat}), as shown in figure 24.17.

The time constant τ_{lat} is given in [309] as:

$$\tau_{lat} = \frac{C_\alpha F}{v k_{lat}}, \tag{24.3}$$

where: C_α is the tyre cornering stiffness (typically 8.6N per unit normal force per radian of slip angle [176]),
F is the normal force,
v is the vehicle speed,
k_{lat} is the lateral stiffness of tyre.

The time constant of the series spring and damper is

$$\tau_{lat} = \frac{c_{lat}}{k_{lat}}. \tag{24.4}$$

Equating expressions (24.3) and (24.4) gives an expression for c_{lat}:

$$c_{lat} = \frac{C_\alpha F}{v}. \tag{24.5}$$

Substituting for c_{lat} from (24.5) into (24.4) gives an expression for k_{lat}:

$$k_{lat} = \frac{C_\alpha F}{v \tau_{lat}}. \tag{24.6}$$

$\tau_{lat} v$ is known as the relaxation length L of the tyre, (approximately equal to the contact length of the tyre, 0.3m), hence

$$k_{lat} = \frac{C_\alpha F}{L}. \tag{24.7}$$

Three tyre configurations were considered. Dual-tyres were simulated with a stiffness k_t=2MN/m and track T=0.910m. Wide-single tyres had a lower stiffness, k_t=1.3MN/m, but because they are narrower than dual tyres, the track was wider, at T=1.023m. A major concern over the use of dual-tyres is the possibility that the inner tyre of the pair may run under-inflated (the pressure of the inner tyre is often difficult to check). Therefore the third configuration considered was dual-tyres with the inner tyre half-inflated. By assuming that the stiffness of the inner tyre is halved, the overall stiffness is calculated as k_t=1.5MN/m and the effective track as T=0.970m.

In order to calculate the tyre force response, the coherence of the road displacements in the two wheel paths must be specified. A suitable method is to treat the road surface as an isotropic random surface, as described in Chapter 3. The coherence function was calculated using the method devised by Heath [230].

Roll-over threshold was defined as the steady lateral acceleration needed to reduce the vertical force on one of the tyres to zero. Dynamic effects on roll-over stability were also not considered.

24.8.2 Roll-Over Stability

Figure 24.18 shows the conflict between road damage and roll-over threshold for a rigid axle suspension with three different tyre configurations.

There are six lines on the graph. The three solid lines correspond to the roll-over threshold being increased by stiffening the suspension springs (there is no anti-roll bar, $k_r = 0$). The three dashed lines correspond to suspensions with stiffnesses set to the optimum values (as per figures 24.15 and 24.16), and with roll-over thresholds being increased by means of anti-roll bars of stiffness k_r. At every point the damping was chosen to minimise the road damage (the damping has no effect on the static roll-over threshold).

The maximum possible roll-over threshold for dual-tyres is 4.7 m/s^2, whereas, the maximum for wide-single tyres is 5.1 m/s^2, an increase of 9%. This is because the track is the narrowest of the three configurations. The higher stiffness of the dual-tyres is not enough to compensate for the narrower track. The roll-over performance of the under-inflated dual-tyres lies between that of wide-single tyres and equally inflated dual-tyres. (The recommended minimum acceptable limit in Canada is 4 m/s^2 [503], and a requirement for 3.5 m/s^2 has been proposed for the USA [499].)

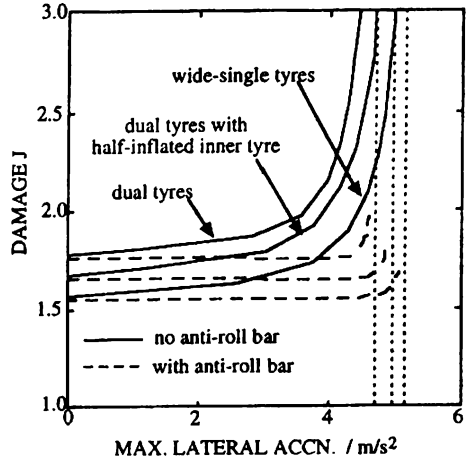


Fig. 24.18 Minimum road damage J as a function of roll-over threshold, for a rigid axle suspension with three tyre types, with and without anti-roll bars. Vehicle speed is 22m/s. From [126].

24.8.3 Road Damage

Figure 24.18 shows that without anti-roll bars, the suspensions generate high road damage at any acceptable levels of roll-over threshold. The models with anti-roll bars (dashed lines) cause significantly less road damage, and it appears that there need be little compromise between roll-over threshold and road damage if a stiff anti-roll bar is employed.

In terms of both the road damage criterion and roll-over threshold, under-inflation of the inner tyre is not a concern. However, under-inflation may cause the load on the outer tyre to exceed the rated load, and cause excessive contact stress and rutting. In all cases, the vehicle with wide single tyres has the highest roll-over threshold, and its dynamic tyre forces cause lowest road damage.

24.9 CONCLUSIONS

(i) A test rig for measuring the quasi-static performance of tandem suspensions in the laboratory was built, and measurements on a standard tandem steel suspension showed it to have high effective stiffness in bounce and poor load equalisation. Introducing rubber blocks into the sliding contacts significantly reduced the hysteresis in bounce and improved the load equalisation performance. Simple models of the trailer indicated that the spring stiffnesses could be halved without significant detrimental effect on static roll-over threshold or static deflection.

(ii) A validated two-dimensional articulated vehicle simulation was used to study the effect on dynamic tyre forces of the rubber block modification, and the effect of softer springs and additional hydraulic dampers on the trailer suspension. When rubber blocks were used to eliminate friction at the spring ends, additional viscous damping was found to be necessary to compensate for the loss of friction damping. However, it was estimated that the damping needed to minimise the DLCs would require an impractically large number of dampers if standard or half stiffness springs were used.

(iii) The effect of fitting rubber blocks, half-stiffness springs and two hydraulic dampers per axle side was predicted by the simulation. The trailer axle DLCs were predicted to reduce by approximately 31%, and the road damage by the trailer axles to reduce by 13%.

(iv) The trailer suspension was successfully modified to incorporate these modifications. The modifications were entirely 'bolt-on' and could be fitted to vehicles in service. Averaged over the five test speeds, the measured trailer axle DLCs were reduced by 15.5%, and the measured road damage by the trailer axles was reduced by 5.2%.

(v) Use of wide-single tyres, as opposed to dual tyres, leads to lower dynamic tyre forces and lower associated road damage (neglecting the effects of changes in content area and pressure). For an optimum suspension design, the reduction in road damage available is approximately 12%. For a typical air suspension, the reduction available is about 6%.

(vi) Approximately 25% less damping is needed to achieve minimum dynamic tyre forces for wide single tyres than for dual tyres.

(vii) Use of wide single tyres can be expected to increase the roll-over threshold of the vehicle by approximately 9%.

It is generally concluded that wide single tyres are likely to be beneficial in terms of roll-over performance, and fatigue damage to minor roads, caused by dynamic loads. Conversely, they are likely to be detrimental to rutting damage of principal roads. However, there is still some uncertainty about the relative importance of contact conditions, compared with dynamic tyre forces on road surface failure mechanisms.

25
OPTIMISING PASSIVE SUSPENSIONS

25.1 SUMMARY

An efficient procedure for calculating a realistic measure of road damage in the frequency domain is derived. Simple models of truck vibration are then used to examine the influence of suspension parameters on this road damage criterion and to select optimal values.

It is found that to minimise road damage a suspension should have stiffness about one fifth of current air suspensions and damping up to twice that typically provided. The use of an anti-roll bar allows a high roll-over threshold without increasing road damage. It is thought that optimisation in the pitch-plane should exclude correlation between the axles, to ensure that the optimised suspension parameters are robust to payload and speed changes.

A three-dimensional 'whole-vehicle' model of an air suspended articulated vehicle is validated against measured tyre force histories. Optimising the suspension stiffness and damping results in a 5.8% reduction in road damage by the whole vehicle (averaged over three speeds). This compares with a 40% reduction if the dynamic components of the tyre forces are eliminated completely.

This chapter is based on work previously published in [125].

25.2 INTRODUCTION

The main objective of the work described in this chapter is to establish guidelines for the design of passive suspensions that cause minimum road damage.

Section 25.3 derives an efficient procedure for calculating the 95th percentile aggregate fourth power force for linearised vehicle models in the frequency domain. Sections 25.4-25.6 use three simple models of truck vibration to examine the influence of suspension parameters on road damage. Section 25.7 validates a three-dimensional 'whole-vehicle' model of an air suspended articulated vehicle and optimises the suspension parameters using the design guidelines from the simple models.

The criteria used for assessing dynamic tyre forces are the DLC, (eq. 5.6) and the 95th percentile aggregate fourth power force (eq. 17.5). The latter is called 'road damage' throughout.

25.3 CALCULATION OF TYRE FORCES AND ROAD DAMAGE

In this section a procedure for calculating the road damage is outlined. All the calculations are performed in the frequency domain, which is very efficient for linear vehicle models.

25.3.1 Tyre Forces

The input to the models was a single-sided spectrum of road displacement $S_u(\kappa)$ defined by equation 3.2. The frequency–domain vehicle simulation methods described in Section 5.4.2 were used to calculate tyre force spectral densities.

25.3.2 Road Damage Criterion

The author [90] derived an equation for the spectral density of the aggregate (first power) dynamic tyre force. The following analysis extends this derivation to include (approximately) the weighting caused by using a fourth power (n = 4) in equation (17.5).

The spectral density of the aggregate fourth power force can be calculated from the direct and cross spectral densities of the individual tyre forces as follows. The aggregate fourth power force, defined in equation (17.5), can be written as a continuous function of time t:

$$A^4(t) = F_1(t)^4 + F_2(t + T_{12})^4 + \ldots + F_n(t + T_{1n})^4, \tag{25.1}$$

where $F_n(t)$ is the force history of axle n and T_{1n} is the time delay between the first and n'th axles following the same wheel path. The tyre force history can be defined as a static component $\bar{F}_n$ plus a dynamic component with zero mean $f_n(t)$:

$$F_n(t) = \bar{F}_n + f_n(t) = \bar{F}_n(1 + \delta_n(t)), \tag{25.2}$$

where $$\delta_n(t) = \frac{f_n(t)}{\bar{F}_n}.$$

The expression for the aggregate fourth power force history (25.1) then becomes

$$A^4(t) = \bar{F}_1^4(1 + \delta_1(t))^4 + \bar{F}_2^4(1 + \delta_2(t + T_{12}))^4 + \ldots + \bar{F}_n^4(1 + \delta_n(t + T_{1n}))^4. \tag{25.3}$$

Assuming that $\delta_n(t)$ is relatively small (*ie* the dynamic fluctuation is small relative to the static force), the binomial expansion can be used to linearise equation 25.3 by neglecting second and higher order terms of δ:

$$A^4(t) = \bar{F}_1^4(1 + 4\delta_1(t)) + \bar{F}_2^4(1 + 4\delta_2(t + T_{12})) + \ldots + \bar{F}_n^4(1 + 4\delta_n(t + T_{1n})). \tag{25.4}$$

In order to derive an expression for the spectral density of the aggregate fourth power force, the autocorrelation function of $A^4(t)$ will first be calculated:

$$R_{A^4}(\tau) = E\left[A^4(t)A^4(t + \tau)\right] \tag{25.5}$$

where E[ ] is the expectation operator. Substituting the linearised expression for the aggregate force equation 25.4 into equation 25.5 gives

$$R_{A^4}(\tau) = E\Big[\left(\bar{F}_1^4(1 + 4\delta_1(t)) + \bar{F}_2^4(1 + 4\delta_2(t + T_{12})) + \ldots + \bar{F}_n^4(1 + 4\delta_n(t + T_{1n}))\right)\ldots.$$

$$\ldots.\left(\bar{F}_1^4(1 + 4\delta_1(t + \tau)) + \bar{F}_2^4(1 + 4\delta_2(t + T_{12} + \tau)) + \ldots + \bar{F}_n^4(1 + 4\delta_n(t + T_{12} + \tau))\right)\Big] \tag{25.6}$$

Simplifying this expression, noting that $E[\delta(t)]=0$, and separating the static force components gives

$$R_{A^4}(\tau) = \sum_{j=1}^{n}\sum_{k=1}^{n} 16E\left[\bar{F}_j^4\delta_j(t + T_{1j}).\bar{F}_k^4\delta_k(t + T_{1k} + \tau)\right] + \left(\sum_{j=1}^{n}\bar{F}_j^4\right)^2 \tag{25.7}$$

Now $E\left[\bar{F}_j\delta_j(t + T_{1j}).\bar{F}_k\delta_k(t + T_{1k} + \tau)\right] = R_{jk}(T_{jk} + \tau)$ is a time-shifted cross correlation function for the dynamic tyre forces of axles j and k (f_j and f_k), so equation 25.7 may be simplified further to

$$R_{A^4}(\tau) = \sum_{j=1}^{n}\sum_{k=1}^{n} 16\bar{F}_j^3\bar{F}_k^3R_{jk}(T_{jk} + \tau) + \left(\sum_{j=1}^{n}\bar{F}_j^4\right)^2. \tag{25.8}$$

The spectral density of the aggregate fourth power force $S_{A^4}(\omega)$ can be obtained from the autocorrelation function $R_{A^4}(\tau)$ by using the Fourier transform [355]:

$$S_{A^4}(\omega) = \sum_{j=1}^{n}\sum_{k=1}^{n} \frac{16}{2\pi} \bar{F}_j^3 \bar{F}_k^3 \int_{-\infty}^{\infty} R_{jk}\left(T_{jk}+\tau\right) e^{-i\omega\tau} d\tau + \frac{1}{2\pi}\int_{-\infty}^{\infty}\left(\sum_{j=1}^{n}\bar{F}_j^4\right)^2 e^{-i\omega\tau} d\tau \qquad (25.9)$$

Introducing the dummy variable $\rho=T_{jk}+\tau$, and dividing through by a factor $e^{i\omega T_{jk}}$, the spectral density becomes [355]:

$$S_{A^4}(\omega)\big|_{\omega>0} = \sum_{j=1}^{n}\sum_{k=1}^{n} 16\bar{F}_j^3\bar{F}_k^3 e^{i\omega T_{jk}} S_{F_jF_k}(\omega) \qquad (25.10a)$$

$$\text{and} \quad S_{A^4}(\omega)\big|_{\omega=0} = \left(\sum_{j=1}^{n}\bar{F}_j^4\right)^2 \delta(\omega), \qquad (25.10b)$$

where $S_{FjFk}(\omega)$ are the cross spectral densities of the tyre forces, which can be obtained from equation 5.8, and $\delta(\omega)$ is the Dirac Delta function.

The standard deviation of the aggregate fourth power force is the square root of the area under the spectral density above zero frequency:

$$\sigma_{A^4} = \sqrt{\int_{\omega=0^+}^{\infty} S_{A^4}(\omega)\big|_{\omega>0} d\omega}, \qquad (25.11)$$

and the 'static' aggregate force is given by

$$m_{A^4} = \sqrt{\int_{\omega=0^-}^{0^+} S_{A^4}(\omega)\big|_{\omega=0} d\omega} = \sum_{j=1}^{n}\bar{F}_j^4. \qquad (25.12)$$

The dynamic tyre forces can be considered to have a Gaussian probability density function [443] so, assuming that $\delta_n(t)$ is relatively small, the 95th percentile aggregate fourth power force, normalised by the static component, can be approximated by:

$$J \approx \frac{1.65\sigma_{A^4}}{m_{A^4}} + 1 \qquad (25.13)$$

In the remainder of this chapter, the quantity J will be referred to as the 'road damage'. For the case of a single axle, it can be shown that the 95th percentile fourth power force is given by:

$$J \approx \frac{1.65*4\sigma_F}{\bar{F}} + 1 \qquad (25.14)$$

where σ_F is the standard deviation of the tyre force. Note that this follows directly from the discarding of higher order terms in equation 25.4, so it is an approximate result.

25.4 BOUNCE MODEL

25.4.1 Model Description

Figure 25.1 shows a quarter-car model with two degrees of freedom (DOF) to represent the bounce (vertical) motions of a typical laden tractor suspension. The tyre stiffness corresponds to dual tyres.

The input to the model was a single sided spectrum of road displacement defined by (3.2), with a spectrum slope n=2.5 and roughness $S_0=50\times10^{-8}$, corresponding to an average motorway or good principal road standard [270]. A vehicle speed of 22m/s (80km/hour) was used, and the tyre force spectrum was calculated over the frequency range 0.2 to 30Hz in intervals of 0.2Hz. The mean

square dynamic tyre force was calculated by integrating the spectral density over this frequency range. The theoretical road damage J was then calculated using equation 25.14.

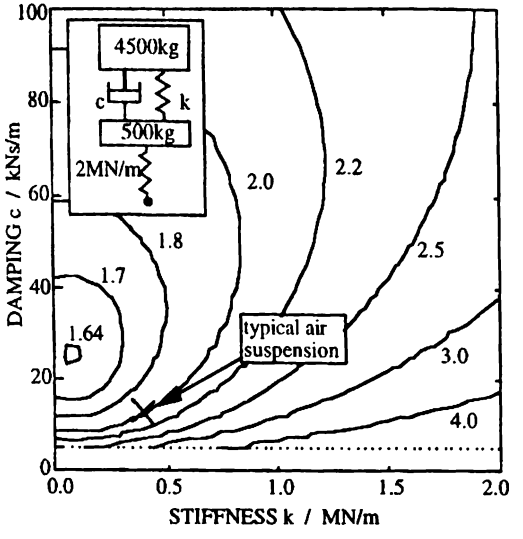


Fig. 25.1 Road damage J as a function of suspension damping and stiffness of the bounce model, vehicle speed 22m/s. From [125].

25.4.2 Optimum Stiffness and Damping

Figure 25.1 shows a contour map of road damage J as a function of suspension stiffness k and damping c for the operating conditions described in the previous section. The minimum road damage is 1.63 times the static road damage, and occurs when the suspension stiffness k=0.074MN/m, and the damping c=23kNs/m. The optimum value of stiffness is very low compared to the values used in practice: a typical air spring provides a stiffness of 0.4MN/m, and the large deflection stiffness of a monoleaf steel spring is typically 2MN/m. Conversely the optimum value of damping is higher than that often provided on trucks. A typical mean damping coefficient provided by a truck damper is 10kNs/m.

Two vibration modes contribute to the tyre force: the sprung mass mode (0-3Hz) and the wheel hop mode (10-15Hz). Examination of the tyre force spectral density curves (not shown) reveals that the effect of increasing the suspension stiffness is to increase the response of the sprung mass mode and decrease the response of the wheel hop mode. To quantify the contribution of the sprung mass mode to the total dynamic tyre force, the mean square tyre force over the frequency range 0.2Hz to 7.0Hz was calculated and then divided by the total mean square tyre force (0.2Hz to 30Hz). Figure 25.2 shows this ratio as a function of the suspension stiffness and damping. The graph shows that the mean square tyre force is caused mainly by the sprung mass mode, except at low values of stiffness and damping. At the minimum level of road damage (figure 25.1) the ratio is about 0.5, that is, the two modes contribute about equally to the mean square tyre force.

25.4.3 Effect of Road Spectrum Slope

The optimum values of stiffness and damping depend on the slope of the road displacement spectrum (n in equation 3.2). Figure 25.3 shows the optimum pairs of values of stiffness and damping calculated for values of n between 1 and 4. The graph shows that the optimum value of k

decreases as the spectrum slope steepens. The optimum stiffness is zero for n f greater than about 3. As the spectrum slope is steepened the excitation of the sprung mass mode is increased in relation to that of the wheel hop mode. A decreased value of suspension stiffness is therefore needed to reduce the response of the sprung mass mode and thereby achieve minimum dynamic tyre force. For typical road surfaces, values for n range between 2 and 3 [158, 270].

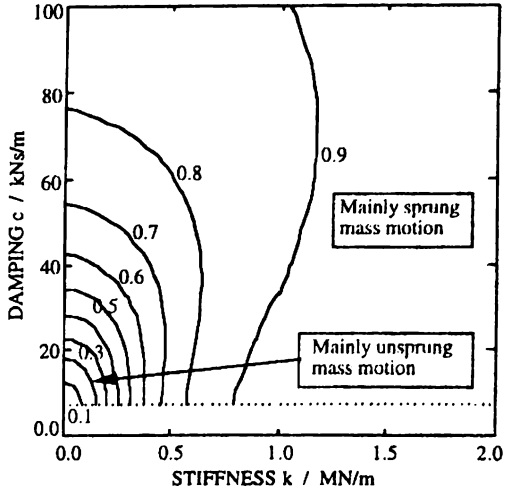


Fig. 25.2 Ratio of mean square tyre force between 0.2 and 7Hz to the mean square tyre force between 0.2 and 30Hz, as a function of the suspension damping and stiffness of the bounce model. From [125].

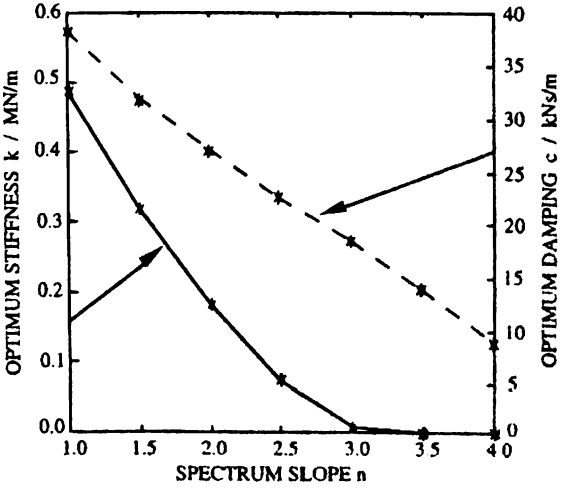


Fig. 25.3 Optimum values of suspension stiffness and damping as a function of the slope of the road displacement spectrum. From [125].

25.4.4 Effect of Reduced Sprung Mass

It is of interest to calculate the road damage for lower values of the sprung mass, in order to predict the effect of the vehicle operating partly laden. Figure 25.4 shows the road damage calculated for the vehicle with sprung mass between 500kg (unladen) and 4500kg (fully laden). The two solid lines show the road damage normalised by the static road damage of the corresponding partly laden vehicle, and the two dashed lines show the same road damage normalised by the static road damage of the fully laden vehicle. The upper line of each pair corresponds to the vehicle with the stiffness and damping fixed to the optimum values for the fully laden vehicle (k=0.074MN/m, c=23kNs/m). The lower line in each pair corresponds to the stiffness and damping optimised to minimise the road damage for each particular sprung mass.

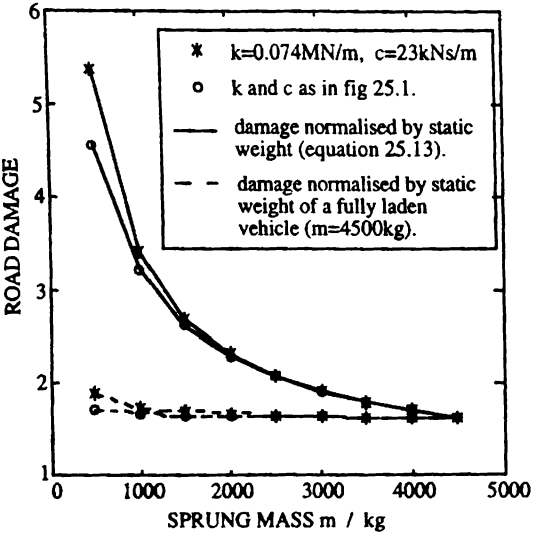


Fig. 25.4 Road damage as a function of sprung mass. From [125].

The solid lines on figure 25.4 show that as the sprung mass is reduced, the road damage due t dynamic forces increases compared to the road damage due to the static forces. The dashed line show that the absolute road damage by the partly laden vehicle remains fairly constant compared t the static road damage of the fully laden vehicle as the sprung mass is reduced, increasing slightly a very low sprung masses. The reduction in road damage due to the lower static weight of the partl laden vehicle is therefore offset by the increase in road damage due to the increased dynamic force The spacing of the lines in each pair indicates the benefit that might be gained by implementing a adaptive suspension, in which the passive stiffness and damping values are altered according to th payload of the vehicle.

Figure 25.5 shows the optimum suspension parameters corresponding to figure 25.4. It can be see that the variation in optimum stiffness with sprung mass is greater than the variation in optimur damping.

In interpreting the preceding results it must be realised that for certain road roughnesses and speed and particularly for low values of sprung mass, the peaks in the dynamic force are likely to exce the static force, leading to wheel lift-off. This non-linear behaviour is not included in the model, an would significantly affect the predicted forces and road damage. The road damage calculation itse also becomes inaccurate for dynamic forces large compared to the static force, because of th linearisation of equation (25.3).

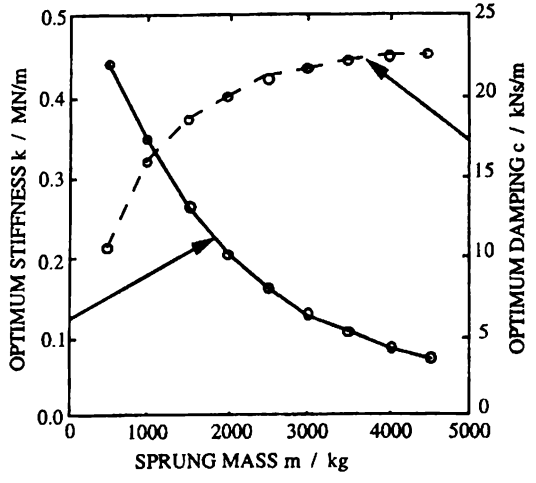


Fig. 25.5 Optimum stiffness and damping as a function of sprung mass. From [125].

25.4.5 Summary

A stiffness of 0.074MN/m and damping of 23kNs/m are needed to minimise the road damage of the bounce model for the input conditions described in Section 25.4.1. This stiffness is considerably less than current air suspensions and the damping is approximately double conventional levels. The optimum values vary considerably with the 'slope' of the road displacement spectrum. As the sprung mass is reduced, the absolute level of road damage stays nearly constant. There is a small benefit in adapting the damping, and particularly the stiffness, to suit changes in the sprung mass. It may also be beneficial to adapt these parameters to suit the slope of the road displacement spectrum.

25.5 ROLL-PLANE MODEL

25.5.1 Model Description

The roll–plane model shown in figure 24.17 was used in this study. The parameter values are shown in Table 25.1. They chosen to represent one axle station of a typical laden tractor.

The road surface was assumed to be isotropic [158, 270] (see Section 3.4.2). The spectral density was calculated from equation 3.2, and the coherence function was calculated using the method of Heath [230].

25.5.2 Roll-Over Stability

The potential problem of inadequate roll stability associated with low values of suspension stiffness was investigated by calculating the static roll-over threshold of the model shown in figure 24.6 [25]. As noted in Section 25.8.1, the model represents only one axle station; the influence of other axles on the roll-over threshold of the whole vehicle is neglected. Dynamic effects on roll-over stability are also not considered. Roll-over threshold is defined as the steady lateral acceleration needed to reduce the vertical force on one of the tyres to zero.

Figure 25.6 shows the compromise between road damage and roll-over threshold for a sprung mass CG height h of 2m. The effect of an anti-roll bar is also shown. The upper two lines correspond to a rigid axle suspension and the lower two lines correspond to an independent suspension. The solid line in each case corresponds to the roll-over threshold being increased by stiffening the suspension springs (there is no anti-roll bar, k_r=0). The dashed lines correspond to the roll-over threshold being increased by stiffening the suspension springs until they reach a stiffness of 100kN/m (approximately the optimum value shown in figure 25.1). The roll-over threshold is then increased by means of an anti-roll bar of stiffness k_r. At every point the damping is chosen to minimise the road damage (the damping has no effect on the static roll-over threshold).

Parameter	*Value*	*Parameter*	*Value*
m_s	9000 kg	c_{lat}	422/v kNs/m (v=speed in m/s)
I_s	m_s*T^2	h	2.0 m
m_u	1000 kg	h_1	0.1 m (independent suspension)
I_u	m_u*T^2	h_1	0.6 m (rigid axle)
k	varied	h_2	0.5 m
c	varied	T	0.925 m
k_r	varied	S	T (independent suspension)
k_t	2 MN/m	S	T/2 (rigid axle)
k_{lat}	843 kN/m		

Table. 25.1 Roll-plane model parameters, used in the model shown in figure 24.17.

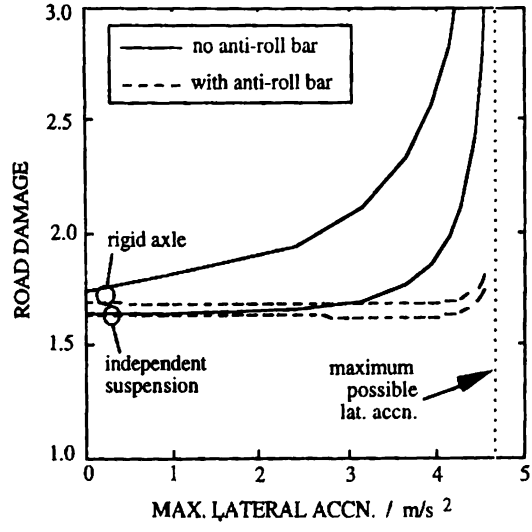


Fig. 25.6 Minimum road damage as a function of rollover threshold, for independent and rigid axle suspensions, with and without anti-roll bars. v=22m/s. From [125].

The maximum possible roll-over threshold is 4.7m/s^2, corresponding to infinite spring stiffness. Figure 25.6 shows that without anti-roll bars, the rigid axle and independent suspension models (solid lines) both cause very high road damage at acceptable levels of roll-over threshold. The models with anti-roll bars (dashed lines) cause significantly less road damage, and it appears that

there need be little compromise between roll-over threshold and road damage if an anti-roll bar is employed.

For the models without anti-roll bars the increase in suspension spring stiffness causes an increase in road damage primarily due to the bounce modes (according to the bounce model, Section 25.4.2). (The corresponding increase in suspension roll stiffness does not lead to a significant increase in road damage by the lateral/roll modes).

For the models with anti-roll bars, the bounce stiffness of the suspension is always near the level required to minimise the road damage by the bounce modes. The high anti-roll bar stiffness necessary to provide an acceptable roll-over threshold does not result in a significant increase in road damage because:

(i) the lateral tyre 'damping' c_{lat} introduces an adequate level of damping into the sprung mass lateral/roll modes, and

(ii) for the axle roll mode the increase in suspension roll stiffness leads to an increase in resonant frequency and decrease in damping ratio. This does not result in increased road damage because the reduced road displacement excitation at the higher frequency of the axle roll mode more than compensates for the reduced damping of this mode.

The rigid axle suspension causes more road damage than the equivalent independent suspension. This is because the narrower spacing of the dampers in the rigid axle suspension prevents adequate damping of the axle roll mode.

In practice it might be unwise to fit a very stiff anti-roll bar to bring the roll-over threshold close to the maximum. The resulting low damping ratio of the axle roll mode might be problematical in the case of a large amplitude and high frequency roll (or single-wheel) input, such as might be caused by a pot-hole. There is therefore some limit to the amount by which the anti-roll bar stiffness should be increased (perhaps to give a roll over threshold equal to 90% or 95% of the maximum), but even below this limit, there is significant benefit in using an anti-roll bar to provide the necessary roll stiffness.

The shape of the curves in figure 25.6 is not greatly changed if the suspension damper coefficient is fixed at 23kNs/m, and therefore similar conclusions can be drawn in this case of non-optimal damping. It should also be remembered that all the results given above correspond to a vehicle speed of 22m/s. The value of lateral tyre damping varies inversely with speed. However, simulation results at other typical operating speeds suggest that the conclusions are not greatly affected.

25.5.3 Summary

For a given roll-over threshold and for the parameters given in figure 25.6, (i) the use of an anti-roll bar with soft springs causes less road damage than stiff springs alone, and (ii) an independent suspension causes less road damage than a rigid axle suspension. The use of a very stiff anti-roll bar to achieve close to the maximum roll-over threshold may lead to an undesirably lightly damped axle roll mode.

25.6 PITCH PLANE MODEL

25.6.1 Model Description

Figure 25.7 shows a pitch-plane vehicle model with four degrees of freedom; the longitudinal degrees of freedom are not included. The centre of gravity of the sprung mass is located equally between the axles, and the pitch inertia corresponds to the mass uniformly distributed between the axles (r=0.58). (If the mass is concentrated at each axle (r=1.0), the front and rear of the vehicle are uncoupled, and each behaves like the bounce model). The parameter values represent the trailer

dynamics of an articulated vehicle consisting of a tractor unit with tandem drive axles and a semi-trailer with tandem axles. The sprung mass of the model represents one quarter of the trailer sprung mass, and each unsprung mass of the model represents one quarter of the tandem axle group mass (one half of a single axle). The model therefore treats the two axles in each tandem group as one unsprung mass. As with the bounce model and roll-plane model, this model neglects some important effects such as the tractor dynamics and tandem axle bogie pitch modes.

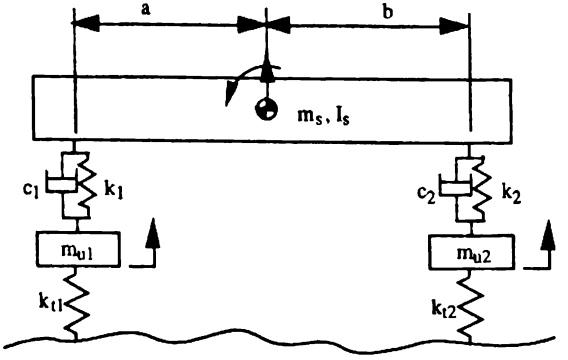


Fig. 25.7 Pitch-plane model with four degrees of freedom. From [125].
m_s=9000kg, $I_s=m_s abr^2$, r=1.0 or 0.58, a=b=4.0m, $m_{u1}=m_{u2}$=500kg, $k_{t1}=k_{t2}$=2MN/m.

The response of the model was calculated for the same road roughness input used in Section 25.4. In calculating the response of the pitch-plane model to road displacement input it is necessary to account for the correlation between the inputs to the axles. The road displacement input to the second axle was considered to be a delayed version of the input to the first axle. This was included in the calculations using equation 5.10.

When calculating the aggregate force history along the road, it is also necessary to account for the correlation between the axles. The aggregate force history consists of the first axle tyre force time history plus the second axle tyre force history delayed by the time between the axles. This was included in the calculations using the matrix terms $e^{i\omega T_{jk}}$ in the calculation of the aggregate fourth power force spectral density $S_{A^4}(\omega)$, equation 25.10a.

25.6.2 Correlation and Wheelbase Filtering

In this section the effect of correlation between the axles for both displacement inputs (equation 25.4) and force outputs (equation 25.10a) is investigated.

The upper solid line in figure 25.8 shows the road damage done by the whole vehicle as a function of vehicle speed. The spring stiffnesses k_1 and k_2 are 0.4MN/m, typical of an air suspension, and the damper coefficients c_1 and c_2 are 10kNs/m (less than the optimum value for the bounce model, 23kNs/m). The graph shows that the vehicle has a set of critical speeds at which the road damage is locally a maximum. The critical speeds are caused by the input displacement correlation and the output force correlation (see Section 17.4.1).

The influence of input correlation and output correlation can investigated separately by excluding them from the road damage calculation individually. The lower solid line in figure 25.8 shows the whole vehicle road damage calculated without both correlation effects ($e^{i\omega T_{jk}}=1.0$ in both equations 5.10 and 25.10a). The dotted line shows the road damage calculated when either the input correlation or the output correlation is excluded ($e^{i\omega T_{jk}}=1.0$ in either equation 5.10 or equation 25.10a); the result is the same in each case. The graph shows that both correlations contribute equally to the formation of critical speeds. The term 'wheelbase filtering' is often used to describe

the effect on vehicle response of correlation between the input road displacements [406], but figure 25.8 shows that it can equally be used to describe the effect of correlation between the output tyre forces on whole vehicle road damage.

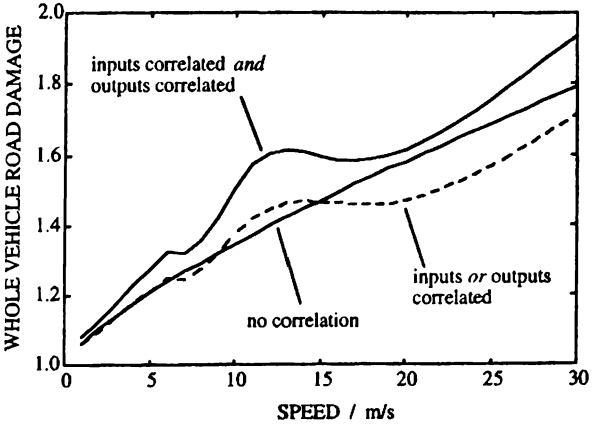


Fig. 25.8 Whole vehicle road damage as a function of speed. From [125]. r=0.58, k_1=k_2=0.4MN/m, c_1=c_2=10kNs/m.

25.6.3 Optimisation of the Pitch-Plane Model

The wheelbase filtering effect provides an extra freedom for minimising the road damage caused by a vehicle. At any particular speed it may be possible to minimise road damage by choosing stiffness and damping to give modes that are not excited strongly because of wheelbase filtering. This is demonstrated in figure 25.9, which shows road damage as a function of speed for three different suspension configurations.

The solid line of figure 25.9 corresponds to the suspension optimised with correlation excluded from the calculation, by setting $e^{i\omega T_{ik}} = 1.0$ in both equations 5.10 and 25.10a. In this case the optimisation is independent of the vehicle speed and the optimum stiffness is 0.13MN/m and the optimum damping is 21kNs/m.

The dashed line corresponds to the suspension optimised with correlation included in the damage calculation. Since the optimisation now depends on vehicle speed, the optimum values of suspension stiffness and damping vary with speed, as shown in figure 25.10. Figure 25.9 shows that optimising at each speed with correlation included results in a significant damage reduction compared to optimisation without correlation, particularly at speeds above 15m/s. However, if the suspension parameters optimised at one particular speed (for example 22m/s) are used at other speeds, there is a significant increase in damage, as shown by the dash-dot line.

A compromise might be to optimise over a range of speeds. Figure 25.11 shows the result of optimising the suspension to minimise the average of the road damage calculated at three speeds (13, 18, 22m/s). The optimum stiffness is 0.26MN/m and the optimum damping is 19.8kNs/m. In this speed range, the damage is slightly less than when optimised without correlation, but slightly greater at lower speeds.

Figure 25.12 shows the effect of changing the payload distribution from uniformly distributed (r = 0.58) to concentrated at each end (r = 1.0). In all cases the suspension parameters are the same as calculated previously, for r = 0.58 (figure 25.11). The solid line shows that the damage by the vehicle optimised without correlation is little affected by the change in payload distribution

(compare with the solid line in figures 25.9 and 25.11). The damage by the vehicle optimised for speed range 13, 18, 22m/s and r=0.58 (dotted line) is slightly increased by the payload cha (compare with dotted line in figure 25.11). The payload change to r = 1.0 has a large effect on suspensions optimised for r = 0.58 at each speed (dashed line). The damage is very m increased, particularly at high speeds (compare with the dashed lines in figures 25.9 and 25.11).

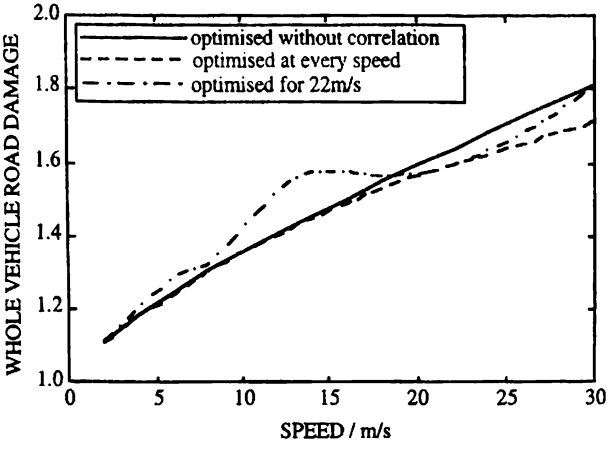


Fig. 25.9 Whole vehicle road damage as a function of speed, for three different suspension settings, r=0.58, [12

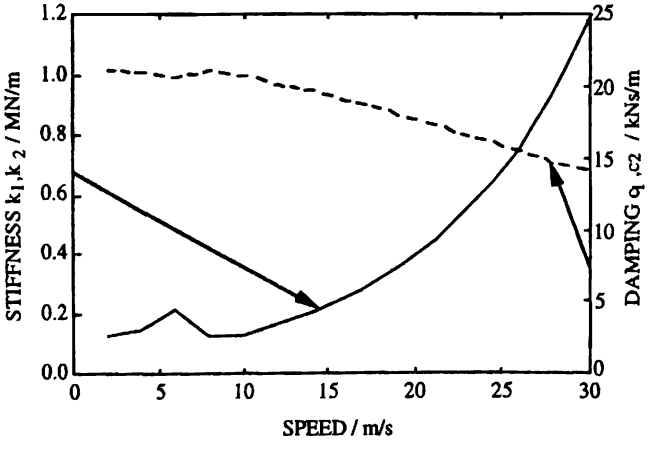


Fig. 25.10 Optimum suspension stiffness and damping as a function of speed. From [125].

25.6.4 Summary

The results given in figures 25.9 and 25.11 show that a vehicle suspension optimised for a partic speed is not robust to payload or speed variations. In practice it is thought that optimisation sh be performed with correlation excluded from the calculation, to provide optimum suspen parameters that are robust to speed and payload changes. Optimising for particular speeds may valid optimisation strategy if an advanced suspension is available in which the stiffness and dam parameters can be adapted to suit the speed and payload.

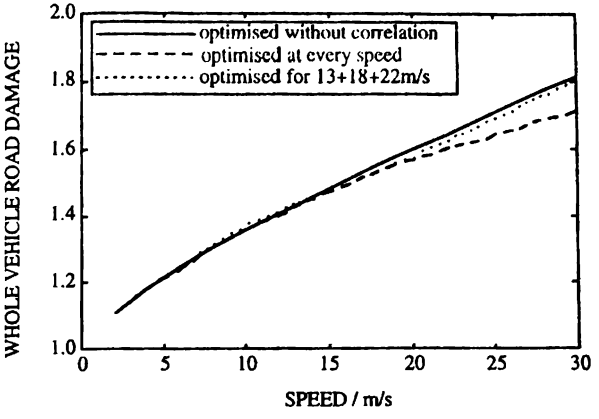


Fig. 25.11 Whole vehicle road damage as a function of speed, for three different suspension settings, r=0.58, [125].

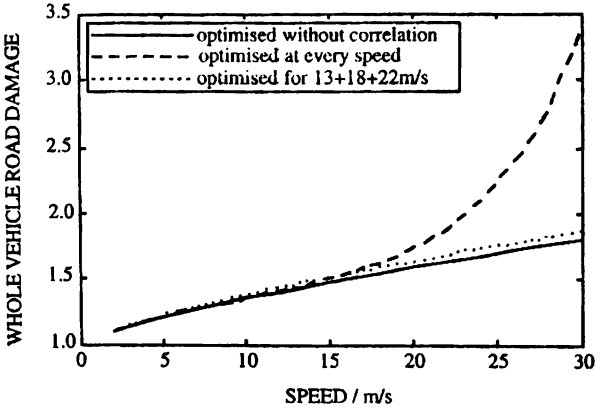


Fig. 25.12 Whole vehicle road damage as a function of speed, for three different suspension settings, r=1.0, [125].

25.7 OPTIMISATION OF AN AIR SUSPENDED ARTICULATED VEHICLE

In this section, tyre force histories measured from an air suspended articulated vehicle are used to validate a nonlinear three-dimensional mathematical model of the vehicle. The suspension parameters of the model are then optimised using the techniques described in the earlier sections. The objective is to predict the reduction in road damage that can be achieved by improving the design of a suspension that performs well in standard form. Further details of this study are given in [122].

25.7.1 Validation of the Whole-Vehicle Model

Dynamic tyre force histories measured on an articulated vehicle were provided for this study by the Transport Research Laboratory. The vehicle was a typical UK articulated lorry, with five axles and a maximum allowable gross mass of 38 tonnes. The tractor had two axles, both fitted with hydraulic

dampers and anti-roll bars. The steering axle was fitted with multi-leaf springs and single tyres, the drive axle was fitted with air springs and dual radial-ply tyres. The flat-bed semi-trailer had th rigid axles, fitted with air springs, hydraulic dampers and single wide radial-ply tyres. The t trailing arms on each axle provided additional suspension roll stiffness. The vehicle was tested in fully laden condition at speeds of 13, 18, and 22m/s (30, 40, 50mph) on a 150m straight sectior the TRL test track.

The non-linear vehicle vibration simulation program described in Chapters 5 and 6 was used to cre a three-dimensional model with 19 degrees of freedom, shown in figure 25.13. The hyster characteristic of the steer axle leaf springs were modelled according to the equation 4.2. The spr masses of the tractor and trailer were assumed to be rigid.

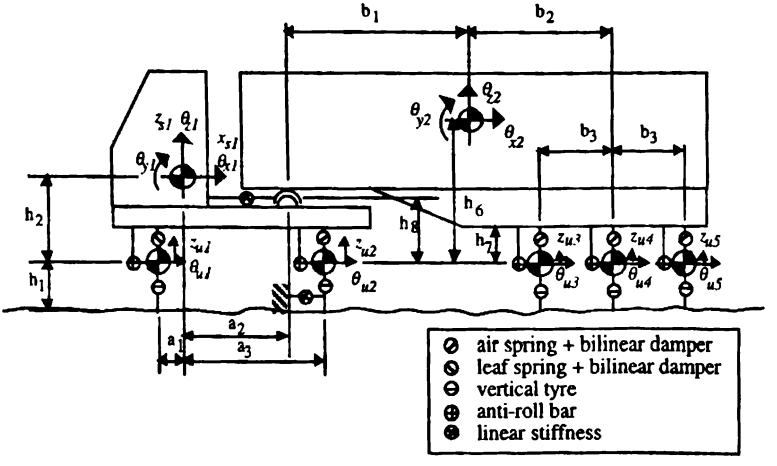


Fig. 25.13 Three-dimensional model of the test vehicle, with 19 degrees of freedom. From [125].

Simulated tyre force histories were generated in the time domain using the measured test track pro as the input. Figure 25.14 shows good agreement between measured and simulated DLCs at three test speeds. Examination of the tyre force spectral densities showed good agreem throughout the frequency range.

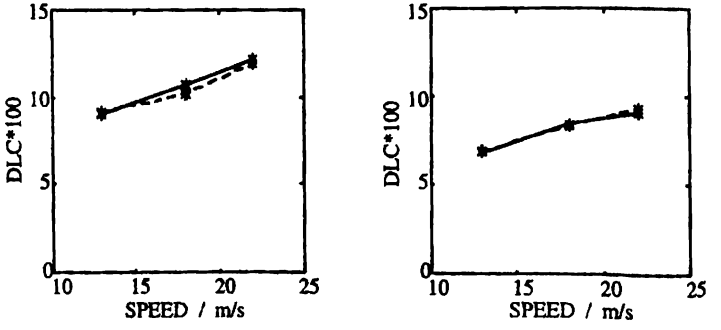


Fig. 25.14 Measured and simulated DLCs of the nearside tyre forces. From [125].
——— measured - - - - - - - - - simulated

25.7.2 Optimisation of the Whole-Vehicle Model

Section 25.6 considered a simple pitch-plane model, with equal mass distribution front to rear. However, the symmetric model considered was not representative of the test vehicle, which has a single tractor drive axle and a tri-axle group on the trailer. A more realistic linear pitch-plane model was therefore created, consisting of a tractor sprung mass, trailer sprung mass, and five unsprung masses. The model has eight degrees of freedom. The model is two-dimensional and therefore ignores the roll motions of axles and sprung masses. For full details see [122].

To account for the effect of tyre configuration on the primary responses of the road (stress, strain), a tyre equivalency factor b_j was incorporated into the calculation of the aggregate fourth power force (equation 25.1) as follows:

$$A^4(t) = b_1^4 F_1(t)^4 + b_2^4 F_2(t+T_{12})^4 + \ldots + b_n^4 F_n(t+T_{1n})^4 \tag{25.15}$$

The corresponding expressions for spectral density of aggregate fourth power force are

$$S_{A^4}(\omega)\big|_{\omega>0} = \sum_{j=1}^{n}\sum_{k=1}^{n} 16 b_j^4 b_k^4 \overline{F}_j^3 \overline{F}_k^3 e^{i\omega T_{jk}} S_{F_jF_k}(\omega) \tag{25.16a}$$

$$S_{A^4}(\omega)\big|_{\omega=0} = \left(\sum_{j=1}^{n} b_j^4 \overline{F}_j^4\right)^2 \delta(\omega), \tag{25.16b}$$

Calculation of the 'road damage' from these spectral densities followed the procedure given in equations 25.11 to 25.13. Values of tyre equivalency factor b_j were taken from [192] and are given in Table 25.2. The values chosen account for the influence of tyre type on the fatigue damage of a flexible pavement with a wearing course thickness of 125mm.[1]

Axle	Tyre Configuration	Equivalence Factor, b_j
Tractor steer axle (j=1)	Single	1.64
Tractor drive axle (j=2)	Duals	1.00
Trailer axles (j=3,4,5)	Wide single	1.28

Table 25.2 Tyre equivalency factors.

Optimisation was performed with no correlation between the axles ($e^{i\omega T_{jk}} = 1.0$ in equations 5.10 and 25.10a). The optimum stiffness values were typically one quarter of the standard values. The optimum damping values for the drive axle were about four times standard, but the standard trailer dampers were found to be close to optimum.

The optimised suspension parameters were applied to the nonlinear whole-vehicle model described in Section 25.7.1. The anti-roll bar stiffnesses were set to give total roll stiffness at each axle the same as the standard vehicle. The friction parameters of the steer axle leaf springs were set to zero; a practical means of achieving this (for some springs) is to use rubber blocks in the sliding contacts of the spring, as described in Chapter 24. Tyre force histories were calculated for three speeds: 13m/s, 18m/s and 22m/s. The input to the simulation was an artificially generated pair of profiles 4km long, with roughness representative of a poor motorway or average principal road. The calculated nearside tyre force histories were used to calculate the tyre force criteria, and a tyre equivalency factor was incorporated into the calculation of the aggregate fourth power force (25.16a).

---

[1] Note that use of the equivalency factors has a very similar effect to basing the damage calculation on the nominal contact stress as in equation 17.6.

25.7.3 Results

Figure 25.15 shows the change in tyre force criteria (averaged over the three speeds) resulting fr the optimisation of the standard vehicle model. The DLCs of the tractor axles are reduced on avera by 26%. The reductions in the trailer axle DLCs are not so marked, typically 11%, although the 3 trailer axle DLC is reduced by 16.8%.

The road damage calculated for the tractor unit is reduced by nearly 11%, but the reduction for t trailer axles is only 0.8%. The reduction in road damage by the whole vehicle is 5.8%. Tl compares with a 40% reduction if the dynamic components of the tyre forces are eliminat completely.

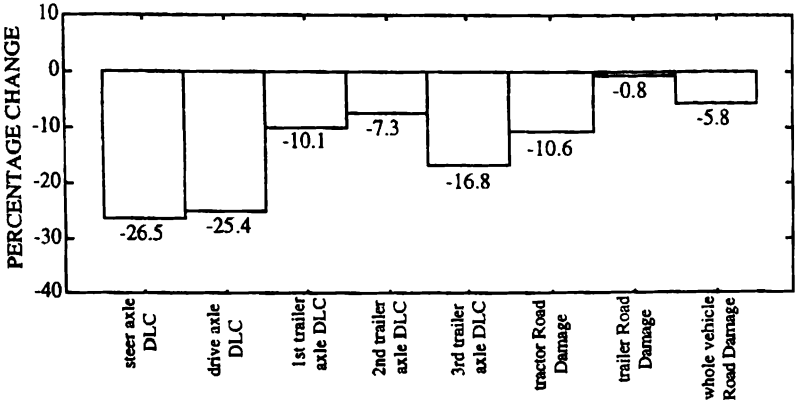


Fig. 25.15 Predicted change in tyre force criteria (averaged over three speeds), modified vehicle compared to standar vehicle. From [125].

25.8 CONCLUSIONS

(i) A method has been developed for calculating the 95th percentile aggregate fourth power fo from the direct and cross spectral densities of tyre forces. The influence of tyre type can included.

(ii) A model with two degrees of freedom (DOF) was used to represent the bounce (vertic motions of a vehicle. A suspension with about one fifth the stiffness and twice the dampi of a typical air suspension is needed to minimise the road damage of the model, for typi input conditions. As the sprung mass is reduced, the absolute level of road damage st nearly constant. There is a small benefit in adapting the damping, and particularly stiffness, to suit changes in sprung mass. It may also be beneficial to adapt these paramet to suit the slope of the road displacement spectrum.

(iii) A model with six DOF was used to represent the motions of a vehicle in the roll-plane. Fo given roll-over threshold and optimum damping, and for the typical parameters chos (a) the use of an anti-roll bar with soft springs results in less road damage than stiff spri alone; and (b) an independent suspension causes less road damage than a rigid a suspension. The use of a very stiff anti-roll bar to achieve close to the maximum roll-o threshold can lead to an undesirable lightly damped axle roll mode. These conclusions a apply to case when the damper coefficient is set to the optimum value for the bounce mode

(iv) A model with four DOF was used to represent the motions of a trailer in the pitch-plane. At any particular speed it may be possible to minimise road damage by choosing stiffness and damping to give modes that are not excited strongly because of wheelbase filtering. In practice, it is thought that taking advantage of wheelbase filtering to minimise road damage is not advisable and that it is better to optimise suspension parameters for uncorrelated inputs.

(v) A three-dimensional 19 DOF nonlinear model of an air suspended articulated vehicle was created and validated against spectral densities of measured tyre forces. Agreement was generally good throughout the frequency range. The measured and simulated DLCs agreed closely.

(vi) A linear eight DOF two-dimensional pitch-plane model was used to calculate optimum suspension stiffness and damping values for the validated nonlinear whole-vehicle model. The optimisation resulted in a road damage reduction of 5.8%, averaged over three speeds. Eliminating the dynamic component of tyre force completely would lead to a road damage reduction of 40%.

26
SEMI-ACTIVE SUSPENSIONS

26.1 SUMMARY

The optimum level of passive damping for minimising the RMS dynamic tyre force and RMS bc acceleration of a heavy vehicle is determined by testing a damper in a 'hardware-in-the-loop' (H test rig. Two different control strategies, ('modified skyhook damping' (MSD), and linear optir control with full state feedback (FSF)), are investigated theoretically using linear models, a suspension force control laws are derived. These control laws, along with simple 'on–off' contı are then tested experimentally using a prototype semi-active damper which is controlled so as follow the demanded force, except when power input is required. The achievable performai improvements are compared, and differences between the linear theory, computer simulations a experimental performance are discussed. It is found that using FSF control, RMS body accelerat and RMS tyre force can be reduced simultaneously by 28% and 21% of their values for optir passive damping.

A four-degree-of-freedom (4-DOF), two-axle, pitch-plane HiL simulation is presented, in which experimental semi-active lorry damper is used on the drive axle. It is found that use of 'Previ control, (in which states from the leading axle are used in the control algorithm for the rear axle) provide significant improvements in response, compared with the single-axle MSD approach. T time delay inherent in the response of the damper is found to degrade the potential benefits of system significantly, however this can be overcome using a 'Phase Lag Compensation' (Pl strategy, which predicts the demanded damper force 20-30*ms* ahead of the time it is required. T PLC approach is shown to improve the performance of the HiL system significantly.

This chapter is based on work previously published in [97], [56] and [283].

26.2 INTRODUCTION



The aim of this chapter is to establish the potential improvements in the vertical vibration dynan (dynamic tyre forces and ride quality) of heavy goods vehicles that can be achieved through the of semi-active dampers.

A detailed summary of the development of active control in vehicle suspension systems up to ab 1983 may be found in Goodall and Kortüm [198]. Sharp and Crolla [422] publishe comprehensive study of more recent developments in road vehicle suspension design in 1987. further extensive study of recent literature on advanced suspensions can be found in [282]. Li work has been published on the use of semi-active dampers for heavy goods vehicles.

Ahmadian and Marjoram [5] simulated the responses of a two–degree–of–freedom vehicle mc with mass and stiffness parameters representative of a lorry, and investigated 'skyhook' damp with different extension and compression damping rates. They showed that most of the benefi semi–active damping was in reducing the sprung mass vibration at low frequencies. On the basi a theoretical study, Aurell [40] reported that 'on–off' dampers are not likely to provide a signific reduction in dynamic tyre force levels, but that continuously variable semi-active dampers are lil

to reduce RMS dynamic tyre forces by up to 17% and reduce RMS sprung mass vertical acceleration by up to 25%. Aurell also concluded that little benefit can be achieved from semi–active dampers unless the suspension springs are relatively soft. Gillespie et al [192] performed a theoretical analysis and concluded that a fully active suspension could reduce road damage due to dynamic tyre forces by 20% compared with a well maintained air suspension. Wilkinson [493] presented the results of an articulated vehicle simulation study incorporating various advanced suspension systems. He concluded that for a laden vehicle travelling on a motorway surface, semi–active suspensions could reduce RMS body accelerations by 23% and RMS dynamic tyre forces by 13% compared with passive air suspensions. Fully active systems were found to give little further benefit.

Yi and Hedrick [513] analysed a five axle tractor/semi-trailer pitch–plane truck model with leaf spring suspensions. The force demand for the semi–active damper was generated using tyre force feedback. In this study 15%–20% reductions in RMS tyre force were predicted, however, this could only be achieved at the expense of increasing body acceleration. It was also found that reductions achieved using continuously variable and *on-off* dampers were similar. In the same investigation the pavement damage generated by the truck was estimated and it was concluded that semi–active suspensions can increase the pavement life by 11.5% compared to optimal passive suspensions. In an associated laboratory study, Yi *et al* [514] found that peak dynamic tyre forces could be reduced significantly through the use of semi-active dampers.

More recently, Kortüm and Valasek [288] began a study to optimise semi-active lorry suspensions for road-friendliness. They investigated a number of control strategies, including: LQR, Neural networks, Fuzzy Control, Sliding Mode Control and a new concept which they named 'Extended Ground–Hook' (EGH) Control. In the EGH approach, the demand signal for the damper is proportional to the tyre deflection rate. The authors achieved a 5-10% reduction in the Road Stress Factor (equation 17.2), for a quarter car simulation model, compared with a 'road-friendly' air suspension. No experimental results were available at the time of writing, although tests on a 6 x 2 rigid vehicle with four experimental dampers on the middle axle are planned.

Most theoretical studies of semi–active suspension systems have assumed that controlled dampers can track a prescribed force demand perfectly (when they dissipate energy). This assumption is not accurate for many *real* controllable dampers, because of time delays, valve dynamics, friction, and limits on the range of possible damping coefficients. In order to quantify the errors caused by implementing semi–active control strategies in hardware, and to establish the realisable performance improvements of semi–active compared with optimised passive systems it is necessary to perform laboratory tests on a semi-active damper

Theoretical studies investigating the use of 'Preview' control [249, 310, 369, 431] have predicted significant potential benefits. However, only a limited number of experimental studies have implemented preview control.

In 1990, Langlois *et al* [296] used look-ahead preview on an off-road military vehicle with an active suspension, fitted with ultrasonic surface height sensors. The initial approach used the techniques derived from optimal control theory given by Thompson [453]. However, the non-linearity of the application (actuator delays *etc*) resulted in an ad-hoc algorithm being implemented. Testing of the vehicle over a $50mm$ high rounded hump showed that preview control provided a 15% reduction in the RMS body acceleration relative to a conventional passive suspension and a 4% improvement over an active system without preview.

In 1992, Nagiri *et al* [350] used a look-ahead sensor on an automobile with a hydro-pneumatic active suspension, which was regulated by a 'skyhook' controller. The road profile $0.9m$ ahead of the front axle of the vehicle was measured using a non-contact optical sensor mounted underneath the front bumper. A theoretical vehicle model running ahead of the prototype vehicle was used to predict the demanded actuator force so as to compensate for delays in the hydro-pneumatic system (these delays originated mainly from the dynamics of the servo-valves and $6ms$ of digital processing time).

A compensation time[1] of $48ms$ was found to minimise the RMS body acceleration. Experimental measurements on a rough random road showed that the spectral density of the body accelerations was decreased by between 30% to 45% in the frequency range $1Hz$ to $8Hz$ due to the additional information acquired through the look-ahead sensor.

Morita *et al* [346] reported on a study in which a look-ahead sensor was implemented on a test vehicle fitted with a skyhook-controlled semi-active suspension. The look-ahead preview was realised using bilateral ultrasonic sensors, which provided a preview distance of between $0.7m$ to $1.3m$ in front of the vehicle. Significant time delays of approximately $30ms$ had been measured between the demanded and achieved damping force with the semi-active dampers. The additional information gained through the look-ahead sensor was used to overcome this problem. Unfortunately, quantitative figures for the measurements were limited, however, it was stated that a compensation time of $70ms$ was used in the experimental study.

In Sections 26.3 to 26.5, research on a prototype continuously variable semi-active damper, provided by a European manufacturer, is presented. (This damper was described in Chapter 4.) The damper was designed for use in passenger cars, however, the forces were scaled appropriately in the 'hardware-in-the-loop' experiments so that approximate conclusions could be drawn about lorry suspensions. Three strategies for controlling the semi-active damper are discussed in the chapter:

(i) *Modified Skyhook Damping* requires a continuously variable damper with good dynamic response and appropriate range of damping performance. A control system is also needed to enable the damper to track a demanded force signal. Two possible force tracking systems, 'open loop' and 'force feedback', are discussed in Section 4.5. The feedback signal for MSD control is obtained from a vertical accelerometer or velocity transducer attached to the body of the vehicle. It is therefore relatively straightforward to implement.

(ii) *On–Off Control* can be used instead of MSD if a two–state, switchable damper is available. The feedback signal also requires measurement of the vertical velocity of the vehicle body. It is a lower cost solution than MSD control, but it will be shown in this chapter that the performance is considerably worse, particularly for vehicle body acceleration (ride).

(iii) *Full State Feedback* requires a continuously variable damper and a force control system, as for MSD control. Generating the damper force demand signal requires measurements of all states of the vehicle, or alternatively, a state estimator to calculate the values of un-measured states from limited measurements. It is shown that this additional sophistication does not provide much performance benefit, and that FSF control is only slightly superior to MSD control.

In Section 26.6, research on more sophisticated control strategies, using 'Preview' control with a 4-DOF HiL model are discussed. This work used a semi-active truck damper that was developed specifically for the purpose [284].

26.3 EXPERIMENTAL DETAILS

The semi-active damper used in the first set of experiments was described in Section 4.5. The Hardware-in-the-loop (HiL) rig described in Section 4.4.1, with vehicle Model 2 (Table 4.1) and the road roughness inputs described in Table 4.2, were used in the damper tests. The computer driving the HiL apparatus was also used to control the semi-active damper.

The root mean square (RMS) dynamic tyre force and RMS body acceleration responses are used throughout the chapter to characterise vehicle performance. Dynamic tyre forces are directly relevant

[1] This is the time between the prediction model running ahead of the vehicle (used to control the actuator) and the real vehicle.

to road damage and vehicle handling performance, and body acceleration is a measure of driver ride comfort and cargo vibration. All RMS values were calculated by integrating the measured or simulated mean square spectral densities in the frequency range between 0 Hz and 20 Hz.

26.4 PASSIVE DAMPING

26.4.1 Damper Model

Sinusoidal tests on the experimental damper, described in Section 4.5.2 and figure 4.23, indicated that during 'passive' operation, its characteristics could be represented as a simple linear viscous dashpot. In order to assess the accuracy of the HiL apparatus and the simple linear damper model, the semi-active damper was tested in 'passive' mode with the damping set to maximum level. The measured damper force feedback signal (see diagram of apparatus in figure 4.10) was multiplied by a scale factor of 4 (corresponding to four automobile dampers in the HiL lorry model), giving a maximum passive damping rate of approximately 30kNs/m.

The accuracy of the linear damping approximation was assessed by comparing the HiL measurements with an entirely digital simulation, using a linear viscous damper model, and an identical road input time history.

The body acceleration (BA) and tyre force (TF) time histories obtained from HiL measurement and digital simulation are compared in figures 26.1a,b for a 'principal road' input. Measurement and simulation agree quite closely. The corresponding spectra are shown in figures 26.1c,d. At the wheel hop frequency, the tyre force spectral density for the HiL measurement is slightly lower than the power spectral density obtained from the digital simulation. This suggests that the real damper has slightly higher damping than the simulated damper at higher velocities, which agrees with the slightly curved force-velocity-characteristics of figure 4.23. RMS values of various vehicle responses are summarised in Table 26.1 for each of the road inputs. The RMS values for measurement and simulation generally agree to within a few percent, giving reasonable confidence in the HiL apparatus and the linear damper model.

26.4.2 Optimum Passive Damping

In order to determine the optimum level of passive damping, the passive damping rate in the HiL system was varied by multiplying the measured damping force by appropriate scale factors before feeding it back into the HiL computer model (figure 4.10). For these measurements the semi-active damper was set to its maximum damping coefficient. Damping force multipliers between 3 and 6.5 were used. The HiL measurement method became unstable for higher damping force multipliers because of the extra open loop gain.

The trade-off between tyre force and body acceleration is shown as a function of the damping coefficient in the 'conflict diagram' in figure 26.2, for the principal road input. The figure shows the results of the HiL tests and the corresponding results of a digital simulation with linear viscous damping. The numbers shown on the experimental (HiL) curve are the damping force multipliers, and the numbers on the curve for the digital simulation are the equivalent linear damping rates (in units of kNs/m). The discrepancies between RMS body accelerations for the two curves on the figure are mainly due to noise introduced by the hydraulic actuator and the instrumentation. (The damping force acts directly on the body mass of the vehicle, thus any noise due to the fluid flow developing within the damper or switching will increase body acceleration. The dynamic tyre force is less affected by noise because the damping force is 'filtered' by the dynamics of the wheel mass.)

The optimum level of passive damping corresponds to the points on the curves closest to the origin in figure 26.2, where both the RMS tyre force and RMS body acceleration are minimised simultaneously. For the principal road input, the optimum level of passive damping can be seen to

be 30 kNs/m, corresponding to four of the test dampers, each set to maximum damping. The same amount of damping was also found to be optimal for the other road inputs. In the remainder of this chapter, the performance of the vehicle using various semi-active damper control strategies is compared with this 'optimal passive' point.

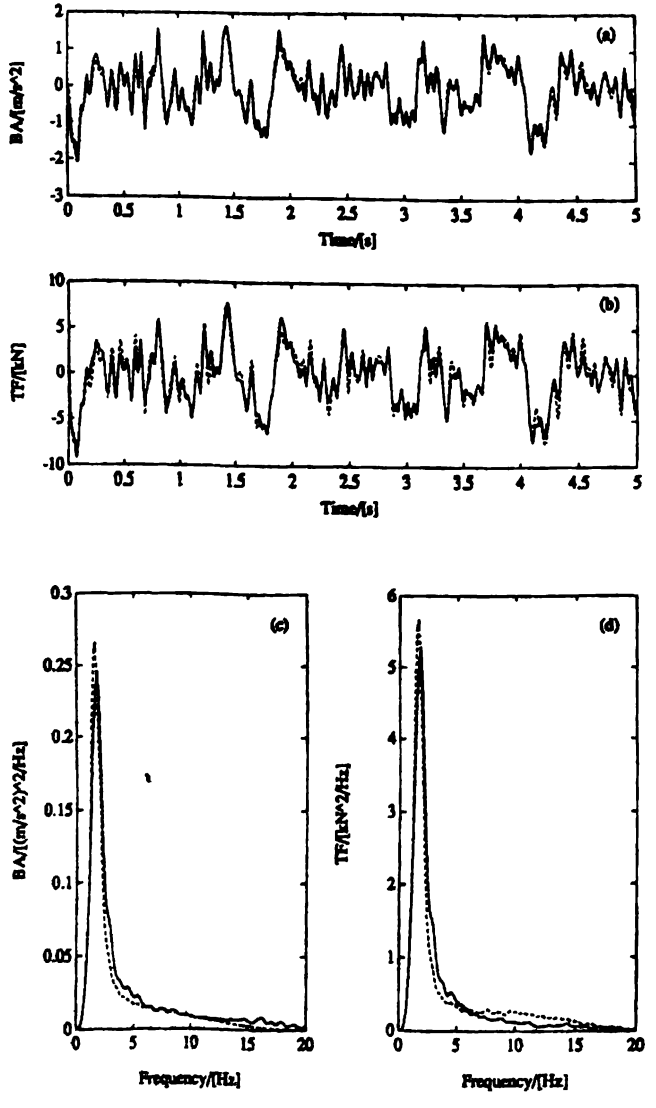


Fig. 26.1 Responses of the vehicle model with passive damping for the principal road input. From [97]
(a) body acceleration time history, (b) tyre force time history,

(c) body acceleration spectral density, (d) tyre force spectral density.
———— HiL measurement, - - - - digital simulation with linear viscous damping.

	Road input	*Body Acceleration (m/s^2)*	*Tyre Force (kN)*	*Suspension Deflection (mm)*	*Damper Force (kN)*
HiL experiment	Motorway	0.62	2.70	3.4	1.88
	Principal road	0.71	3.11	3.9	2.24
	Minor road	0.87	3.76	4.9	2.67
Computer simulation	Motorway	0.57	2.71	3.7	1.74
	Principal road	0.67	3.14	4.3	2.03
	Minor road	0.81	3.86	5.1	2.58

Table 26.1 Comparison of RMS values of HiL measurements and digital simulations using the linear vehicle model, with the semi-active damper in passive mode. The passive suspension damping of 30kNs/m is near the optimal passive value.

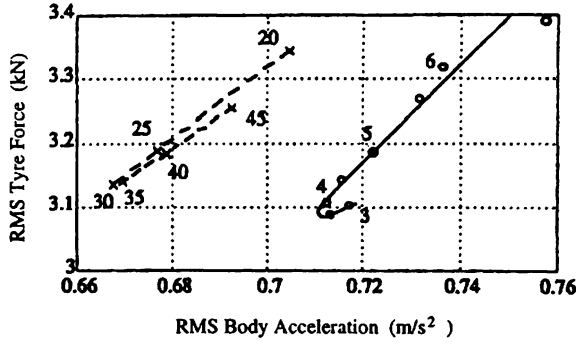


Fig. 26.2 Conflict diagram, showing the trade-off between RMS tyre force and RMS body acceleration as a function of the level of passive damping, 'principal road' input. From [97]
x - damping rate (kNs/m), theory, o - damping force scale factor, HiL tests.

26.5 SEMI-ACTIVE DAMPING

All semi-active damper control strategies investigated in the project utilised two nested controllers.:

(i) The inner controller adjusted the damper valve so as to track the desired force. Two alternative control strategies for the inner loop were investigated in the project: 'open loop' and 'force feedback' control. These strategies were described in detail in Section 4.5.

(ii) The outer controller (outer control loop) set the desired damping force level in accordance with the measured states of the vehicle. Three different strategies for the outer control loop are discussed in the following sections.

26.5.1 Modified 'Skyhook' Damping (MSD)

Control strategy

'Skyhook damping' commonly refers to a control strategy in which the force demand signal for a controllable suspension element is proportional to the absolute vertical velocity of the sprung mass. The suspension element, which is mounted between body and axle, then emulates a passive damper attached between the sprung mass and an inertial frame.

The effects of passive damping and skyhook damping on the body acceleration and tyre forces generated by a two degree-of-freedom automobile model were discussed by Redfield and Karnopp [385]. They modelled the skyhook damper as a 'perfect' actuator, capable of supplying and dissipating energy. It was assumed to produce a force F_s given by:

$$F_s = C_s v_s \tag{26.1}$$

where C_s is the 'skyhook' damping rate and v_s is the absolute vertical velocity of the sprung mass.

Trade-offs in performance improvements were found to occur at various frequencies [385]. Increasing conventional passive damping was found initially to decrease dynamic tyre forces at both the body bounce and wheel hop frequencies (1.5 Hz and 12 Hz), but for high damping, the sprung and unsprung masses were found to 'lock' together, causing increased dynamic loads in the intermediate frequency range. Conversely, increasing skyhook damping was found to attenuate the body acceleration and dynamic tyre forces at low frequencies, with a relatively small increase in tyre force at high frequencies.

An alternative control strategy is to generate the suspension damping force F_s using a combination of passive damping and skyhook damping. This is denoted as 'Modified Skyhook Damping' (MSD) and is given by [53]:

$$F_s = C_p v_{rel} + C_s v_s \tag{26.2}$$

where C_p and C_s are the passive and skyhook damping rates;
v_s and v_{rel} are the absolute velocity of the sprung mass and the relative velocity between sprung and unsprung masses.

The maximum damping rate C_{max} is a physical limit on the performance of a particular damper:

$$C_p + C_s = C_{max}. \tag{26.3}$$

Depending on C_{max}, different levels of passive and skyhook damping are required to reduce simultaneously the RMS body acceleration and RMS tyre force. The ratio of passive to maximum damping α can be substituted into equation 26.2, and this gives a control law for Modified Skyhook Damping:

$$F_s = C_{max} \{\alpha v_{rel} + (1-\alpha)v_s\} \tag{26.4}$$

where $\alpha = C_p/C_{max}$.

When $\alpha = 1$, $F_s = C_{max} v_{rel}$, *ie* the suspension element provides conventional passive damping. When $\alpha = 0$, $F_s = C_{max} v_s$, *ie* pure 'skyhook' damping (assuming the suspension element is a perfect actuator).

Theoretical RMS Performance – 'Perfect' Actuator

Figure 26.3 shows a 'conflict diagram' for RMS body acceleration and RMS dynamic tyre force, using theoretical modified skyhook damping, and quarter car vehicle Model 2 (Table 4.1). The suspension damper was assumed to be a 'perfect' actuator which could supply or dissipate energy. The RMS responses were normalised by the RMS values for a passive suspension with an 'optimal'

passive damping rate[1] of 30 kNs/m (see [53] for details). The solid lines are contours of constant maximum damping rate C_{max}, while the dashed lines are lines of constant α.

Assuming a maximum damping coefficient of C_{max} = 40 kNs/m, the perfect actuator theory predicts a maximum reduction in RMS dynamic tyre force of 20% compared to the optimal passive RMS levels, for α = 0.4 (point A on figure 26.3). The corresponding reduction in body acceleration is 28%. The maximum achievable reduction in RMS body acceleration is 37% (at α = 0.125 – point B on figure 26.3) for which the RMS tyre force is slightly more than for the optimal passive system.

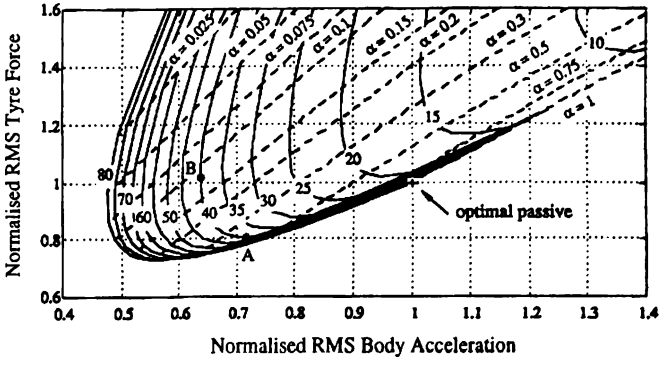


Fig. 26.3 Conflict diagram showing the variation of RMS body acceleration and RMS dynamic tyre force with MSD control parameter α and the maximum damping coefficient C_{max}, for a fully active suspension. From [97] ——— Contours of constant C_{max} (kNs/m), - - - - - - - Contours of constant α.

For low maximum damping rates (C_{max} < 20 kNs/m), 50% passive damping (α = 0.5) provides essentially minimum body acceleration and tyre force (*ie* the 'knee' of the curves, nearest to the origin). For maximum damping rates larger than 30 kNs/m, the optimum *tyre force* response occurs at varying values of α, corresponding to approximately constant passive damping of $C_p = \alpha\, C_{max}$ = 16 kNs/m. Increasing the maximum damping rate above 50 kNs/m, yields diminishing improvements, particularly for tyre forces.

Semi-Active Modified Skyhook Damping (SAMSD)

In this section the semi-active damper is modelled as a variable linear viscous damper, capable of dissipating energy over a finite range of damping rates: C_{min} to C_{max}. Unlike the 'perfect actuator', it is unable to supply energy.

The theoretical semi-active damper force is known as Semi-Active Modified Skyhook Damping (SAMSD) and is given by [53]

$$F_s = \begin{cases} C_{max}\{\alpha v_{rel} + (1-\alpha)v_s\}, & \text{when } F_s v_{rel} > 0, \\ C_{min} v_{rel}, & \text{when } F_s v_{rel} \le 0. \end{cases} \qquad (26.5)$$

In order to *model* the performance of a heavy goods vehicle equipped with semi-active damping, the force generated by the automobile damper discussed in the previous sections was 'scaled-up' by a factor of 6 (*ie* one truck damper was assumed to be equivalent to 6 car dampers). Using the

[1] The 'optimal passive' damping rate simultaneously generates the minimum RMS dynamic tyre forces and the minimum RMS body accelerations, as shown in figure 26.2.

measured damping characteristics shown in figure 4.23, the maximum damping rate was assumed to be C_{max} = 6 x 6.7 kNs/m = 40 kNs/m, and the minimum damping rate was assumed to be C_{off} = 6 x 0.5 kNs/m = 3 kNs/m.

The results of a digital simulation of the theoretical semi-active damper, using the modified skyhook damping (MSD) control strategy, for a 'motorway' input are shown as crosses (x) on figure 26.4. In this case, the scales are not normalised. Again $\alpha = 1$ corresponds to optimal passive damping. For $\alpha = 0.35$, the theoretical RMS tyre force is minimised (reduced by 18% from the optimal passive level), while at the same time the body acceleration is reduced by 24%. The maximum reduction that can be achieved in RMS body acceleration is 27% (for $\alpha = 0.1$), and this is accompanied by a 13% reduction in the RMS tyre force.

The reductions in dynamic tyre force for the theoretical semi-active damper (figure 26.4) and the perfect actuator (figure 26.3) are similar. However, the achievable percentage reductions in body acceleration with theoretical semi-active damping are significantly less than for the perfect actuator.

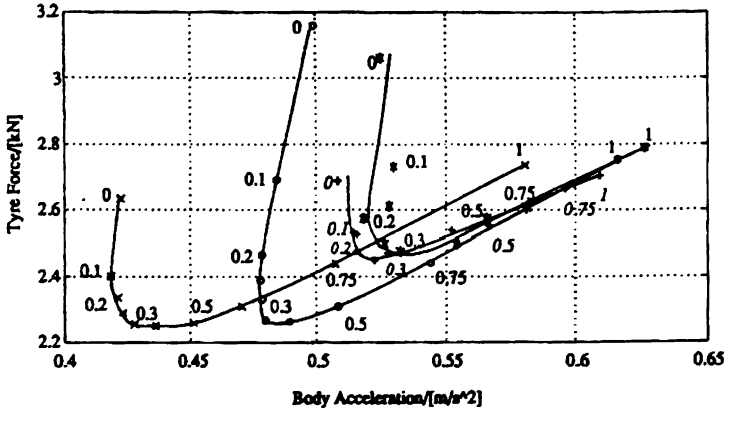


Fig. 26.4 Conflict diagram showing the variation of RMS body acceleration and RMS dynamic tyre force with modified skyhook damping control parameter α for the quarter car, 'motorway' input. From [56].
x – theoretical semi-active damping (simulation)
o – Open loop control (HiL measurements)
+ – Force feedback (velocity) control (HiL measurements)
* – Force feedback (force) control (HiL measurements)

Experimental RMS Performance - HiL Measurements

For HiL tests, the measured force generated by the experimental automobile damper in the HiL rig was also scaled up by a factor of 6. This factor emulated the behaviour of a reasonably realistic truck damper[1], while ensuring stable operation of the HiL system. The scaled damper had a maximum damping rate (C_{max}) of approximately 40 kNs/m.

All three force tracking strategies in Section 4.5 were investigated:

[1] Note that an important difference is that a truck damper will contain a larger volume of hydraulic fluid than the car damper. As a consequence of the compressibility of the fluid, it will have a somewhat longer time delay than the car damper. This will degrade its force tracking performance. HiL experiments with a prototype semi-active truck damper are described in the next section.

(i) Open loop control (equation 4.12)
(ii) Force feedback (velocity) (equation 4.14a)
(iii) Force feedback (force) (equation 4.14b).

The force was sampled at 600Hz, and for the force feedback controllers, the PID gains in equation 4.17 were $K_P = 10$ mV/N, $K_I\tau = 5$ mV/N and $K_D/\tau = 0$ mV/N.

In addition to the simulation results for the theoretical semi-active damper, figure 26.4 shows the HiL measurements for all three control strategies. There is reasonable agreement between the simulated tyre forces and the measurements for open loop damper control. The measured RMS body acceleration is larger than the simulation for all three sets of measurements. This is due to noise in the measured acceleration signal, which increases the RMS accelerations and shifts the experimental graphs to the right uniformly (as shown in figure 26.2).

For open loop control with $\alpha < 0.2$, the agreement between simulated and measured RMS tyre force deteriorates because the switching dynamics of the damper, which are not included in the simulation, reduce the overall level of damping. The force feedback results also show more variability for low proportions of passive damping ($\alpha < 0.2$). This is caused by noise in the measured damping force.

The body acceleration and tyre force levels achieved using force feedback are significantly larger than the responses obtained using open loop control. This is caused by the inferior phase performance of the force feedback strategy noted in Section 4.5. Both force feedback control strategies give similar RMS responses, the force feedback (velocity) control strategy performing slightly better than the force feedback (force) strategy.

Experimental Performance – Frequency Response

Figures 26.5 and 26.6 show the measured and simulated mean square spectral densities of body acceleration and tyre force, obtained from the vehicle model with motorway input, for two different values of α. The measured performance for open loop damper control is shown as a solid line, force feedback (force) damper control is a dashed line, and theoretical semi-active damping is a dotted line.

The spectral densities for purely skyhook damping control ($\alpha = 0$) are shown in figure 26.5. The body accelerations (figure 26.5a) show low damping at the body bounce frequency. The tyre force responses (figure 26.5b) show low damping at both the body bounce and wheel hop frequencies. There is reasonable agreement between the body acceleration spectral densities for simulated theoretical semi-active damping and force feedback control, although, the measured responses at both resonance peaks are larger than the simulation predicts. This is caused by a reduced overall level of damping for HiL measurements, due to the damper switching dynamics (see previous section). The tyre force spectral densities (figure 26.5b) have resonance peaks of approximately the same heights for open loop damper control and theoretical semi-active damping. The reduced height of the wheel hop resonance for force feedback control indicates a higher level of passive damping.

Mean square spectral densities for MSD damper control with half passive damping ($\alpha = 0.5$) are shown in figure 26.6. The main effect of changing α is almost complete elimination of the wheel hop resonance from the tyre force spectral densities. For force feedback damper control, the responses at the sprung mass natural frequency (approx 1.8 Hz) are significantly greater for $\alpha = 0.5$ (figure 26.6) than the corresponding values for $\alpha = 0$ (figure 26.5). For open loop damper control and theoretical semi-active damping, the responses at the sprung mass frequency are less for $\alpha = 0.5$ than for $\alpha = 0$.

Experimental Performance – Force Tracking

The tracking performance of the HiL measurements, and the damping forces and control voltages for the open loop and the force feedback damper control strategies are compared in figure 26.7 for $\alpha = 0.35$. The measured damping forces in figure 26.7b (solid and dashed lines) track the demanded force (dotted line) quite well, with the measured damping forces lagging 20ms–40ms behind the

demanded force. This is a somewhat larger lag than measured in the damping force transients (figure 4.25), but the damping force transient tests were conducted with a constant velocity input, whereas in this case, the velocity usually starts to rise from almost zero at the same time as the damper force. This can cause a delay until the flow of damping fluid is fully established. The phase lag is larger for the force feedback controller than for the open loop controller.

From the control voltage time history in figure 26.7a it can be seen that the force feedback controller operates mainly by *integrating* the force error. The response during each switching transient is initially very steep, levelling off with higher control voltages. If the demanded force changes after a short time, (*eg* at 1.17s in figure 26.7a) the velocity and demanded force often change signs and the control voltage is reset to −10V before maximum force is reached. If demanded force and velocity have the same sign for long enough (*eg* at 1.25s), the force tracking operates well.

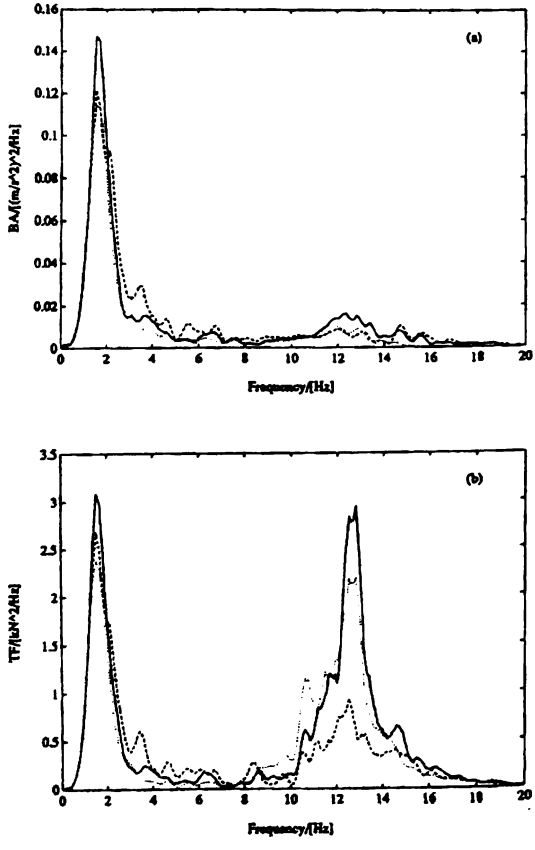


Fig. 26.5 Mean square spectral densities of vehicle response for pure skyhook damping with $\alpha = 0$.
(a) body acceleration (b) dynamic tyre force. From [56].
· · · · · · · Theoretical semi-active damping (simulation)
——— Open loop control (HiL measurements)
- - - - - - Force feedback (force) control (HiL measurements)

The loop gain and bandwidth of the damper controller were reduced to prevent occasional transient force overshoots from exceeding the maximum allowable damper force. This lower gain results in greater phase lag. To reduce the phase lag, the force feedback controller needs to be tuned for a faster response, and it is then necessary to remove the high frequency content of the damping force by filtering. This was not possible in the HiL tests, because the low-pass filtering caused additional phase delays and instability of the HiL test rig. Increasing the gains will also increase overshoot. The choice of gains is therefore a compromise between speed of response, stability and overshoot.

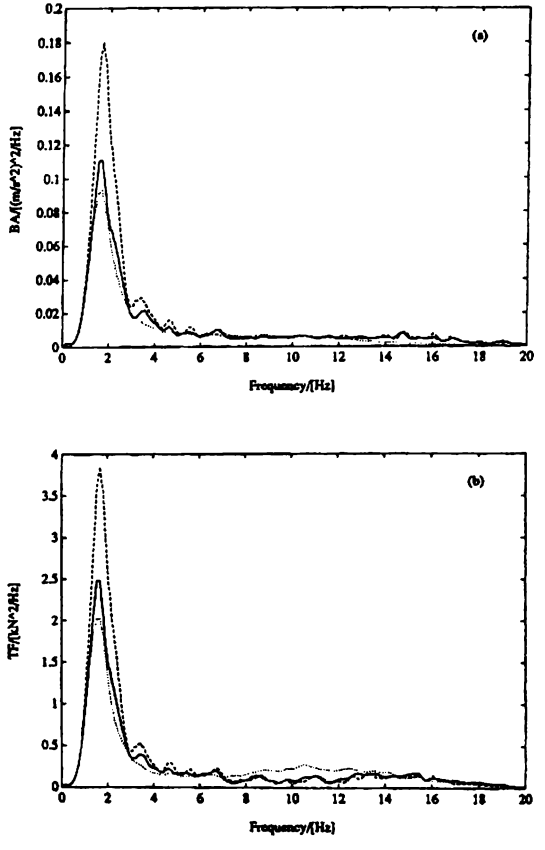


Fig. 26.6 Mean square spectral densities of vehicle response for modified skyhook damping with $\alpha = 0.5$.
(a) body acceleration (b) dynamic tyre force. From [56].
. . . . . Theoretical semi-active damping (simulation)
——— Open loop control (HiL measurements)
- - - - - - Force feedback (force) control (HiL measurements)

Figure 26.8 shows a section of the damping force and control voltage between 1s and 2s and compares the time histories of the force feedback (force) and force feedback (velocity) strategies and the control voltage. The demand and response control voltage time histories agree very well

(figure 26.8a). The damping force time histories are shown in figure 26.8b. The solid line is the measured damping force of the force feedback (force) strategy, the dashed line is the force feedback (velocity) strategy and the dotted line is the demanded force.

Both force feedback strategies track the demanded force with similar accuracy. However the force feedback (force) strategy sometimes causes large spikes in the damping force (*eg* 1.88s). Noise in the damping force can cause increased switching in the control voltage as seen at 1.49s and 1.95s of the voltage time history. Both force feedback control strategies produce similar values of RMS body acceleration and tyre force. This demonstrates that force feedback control can be implemented successfully using the measured force signal to determine the damper switching time (as per equation 4.14b), without the need to measure suspension velocity as well.

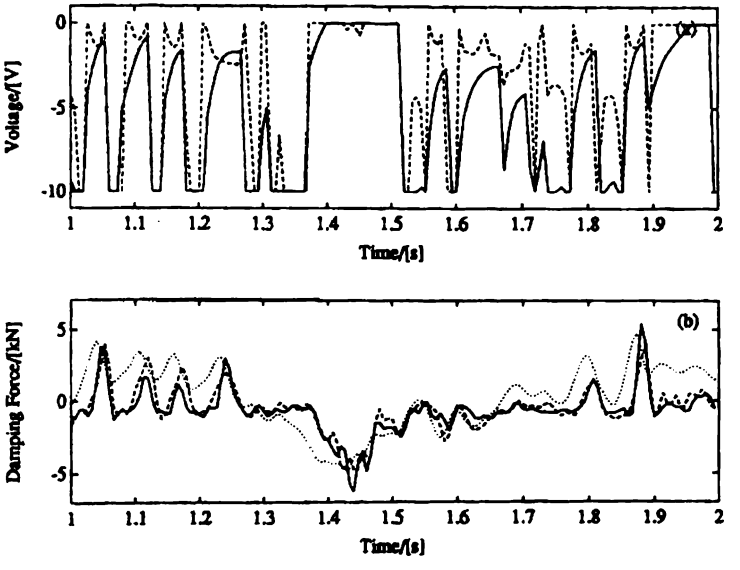


Fig. 26.7 Comparison of the force tracking performance of the open loop damper controller and the force feedback (velocity) controller. From [56].

(a) Control voltage
——— Force feedback (velocity) controller
- - - - - - Demanded voltage

(b) Damping force
- - - - - - Open loop controller
——— Force feedback (velocity) controller
. . . . . Demanded force (force feedback)

The damper force and tyre force responses from the HiL measurements were also found to agree closely with the simulation, although these results are not shown (see [53] for details).

Overall, open loop damper control has higher speed response because is not affected by the transport delay associated with measuring and processing the damping force. This improves the dynamic performance of the vehicle. The force tracking performance is, however, influenced by temperature and/or by damper wear. A velocity transducer, a reasonably good 'look-up table', (*eg* the damping-voltage model, equation 4.10), and perhaps a temperature sensor are necessary to implement the open loop control method. This is simpler than the force feedback control, which requires a force transducer, and it was found to provide superior performance to force feedback damper control for

almost all tests performed. The advantage of feedback control is that the tracking performance of the damper is not affected by temperature changes, or by damper wear.

It was found that the tracking performance of the semi-active damper could be improved by increasing C_{max} in equation 26.5, and hence demanding a larger force than the nominal level. This change in control law caused the damping force to increase more rapidly and thereby increased the speed of response, compensating for time delays inherent in the hardware. The increased damper forces were found to reduce the dynamic tyre forces, particularly at the body bounce frequency, and did not affect the body acceleration. This gave better agreement between theory and experiment for the spectral densities (figures 26.5 and 26.6). C_{max} = 55 kNs/m was found to be 'optimal' [53] .

Throughout the remainder of this chapter, 'open-loop' control is used for the inner control loop, since this was generally found to provides superior vehicle performance.

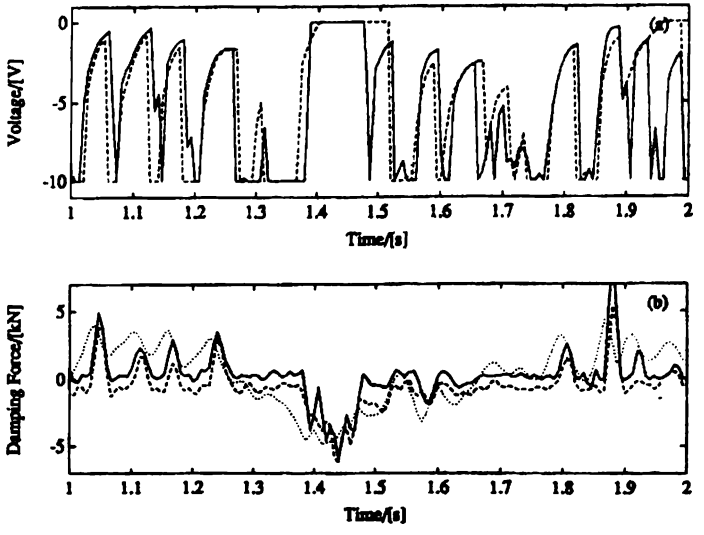


Fig. 26.8 Comparison of the force tracking performance of the force feedback (force) controller and the force feedback (velocity) controller. From [56].

(a) Control voltage
——— Demanded voltage
- - - - - - Force feedback (force) controller

(b) Damping force
——— Force feedback (force)
- - - - - - Force feedback (velocity)
Demanded force

26.5.2 On-Off Control

Less sophisticated controllable dampers than the one used in the tests may have only two states 'on' and 'off', instead of continuously variable damping characteristics. This section therefore compares the performance of 'on-off' control with continuously variable SAMSD control. The damper control strategy was designed to approximate the continuous SAMSD control defined by equation 26.5, using a control voltage U as follows:

$$U = \begin{cases} 0\,V & \text{(on)} \quad \text{when } F_d v_{rel} > 0, \\ -10\,V & \text{(off)} \quad \text{when } F_d v_{rel} \le 0, \end{cases} \qquad (26.6)$$

$$\text{with} \quad F_d = C_m\left\{\alpha v_{rel} + (1-\alpha)v_{body}\right\}.$$

The on and off settings of the damper corresponded to passive damping values of: $C_{min} \approx 3$ kNs/m (off), and $C_{max} \approx 40$ kNs/m (on). The controller parameter C_m was set to 55 kNs/m. The tests were performed with the 'principal' road input (Table 4.2).

The trade-off between measured RMS body acceleration (BA) and RMS tyre force (TF) for MSD and *on-off* control is shown in figure 26.9 for varying α. Dynamic tyre forces and body accelerations are minimised at $\alpha = 0.15$ for *on-off* control, compared with $\alpha = 0.25$ for continuous SAMSD control. *On-off* control achieves a similar minimum RMS tyre force to SAMSD control, but the minimum RMS body acceleration level is about 7% larger than the minimum for SAMSD.

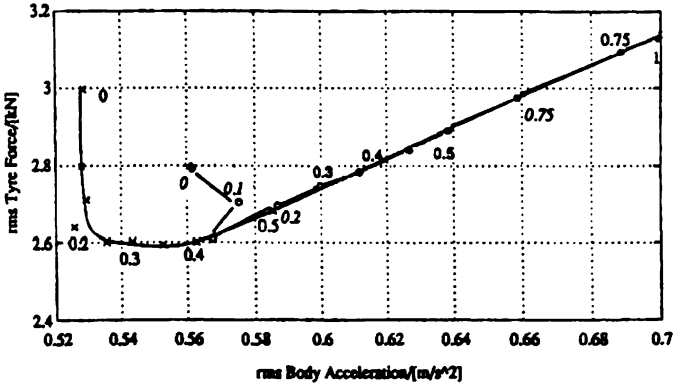


Fig. 26.9 Conflict diagram for measured body acceleration and tyre force, with α varying from 0 to 1 in equation 26.6, principal road. From [97] x - SAMSD control, o = on-off control.

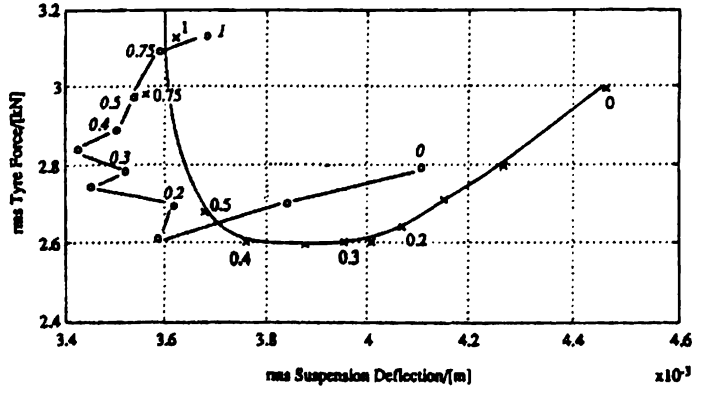


Fig. 26.10 Conflict diagram for measured RMS tyre force and RMS suspension deflection, with varying from 0 to 1 in equation 26.6, principal road. From [97] x - SAMSD control, o = on-off control.

The RMS tyre force and RMS suspension deflection responses of the two damper control laws are shown in figure 26.10. As the proportion of passive damping demanded, α, is increased, RMS suspension deflection is reduced. Large scatter of the RMS suspension deflection measurements can be seen for *on-off* control. This is caused by the noisy damping force due to repeated switching. For minimum RMS tyre force, *on-off* control uses approximately 10% less suspension working space than continuous damper control. More information about *on-off* control can be found in [53].

26.5.3 Full State Feedback (FSF) Control

Linear Optimal Control Theory

Linear optimal control theory has been used to investigate potential performance benefits of active suspensions. See [81] for a comprehensive treatment of the theory.

The equation of motion of a linear vehicle model with active suspension can be written:

$$\dot{\mathbf{x}} = \mathbf{A}\,\mathbf{x} + \mathbf{B}\,\mathbf{u} + \mathbf{L}\,v_f \tag{26.7}$$

$$\mathbf{y} = \mathbf{C}\,\mathbf{x} + \mathbf{D}\,\mathbf{u}. \tag{26.8}$$

$\mathbf{x}$ is a vector of state variables, given by:

$$\boldsymbol{x} = \left[x_r \quad x_2 \quad x_1 \quad \dot{x}_2 \quad \dot{x}_1\right]^T, \tag{26.9}$$

where x_1 is the absolute vertical displacement of the sprung mass, x_2 is the absolute vertical displacement of the unsprung mass, and x_r is the absolute vertical displacement of the road surface input. Vector $\mathbf{u}$ is the control input, v_f is a white noise disturbance input and $\mathbf{y}$ is a vector of system output variables.

The road surface is assumed to have a displacement spectral density function $S(\kappa)$ given by [497]:

$$S(\kappa) = \frac{S_0}{\gamma^2 + \kappa^2} \tag{26.10}$$

where S_0 is a road roughness constant, κ the wavenumber and $\gamma = 0.005$ is a filter constant.

The matrices $\mathbf{A}, \mathbf{B}, \mathbf{C}, \mathbf{D}$ and $\mathbf{L}$ are defined as follows:

The various combined system matrices for the road and vehicle model are as follows:

$$\mathbf{A} = \begin{bmatrix} -2\pi\gamma & 0 & 0 & 0 & 0 \\ 0 & 0 & 0 & 1 & 0 \\ 0 & 0 & 0 & 0 & 1 \\ \frac{K_t}{m} & \frac{K_s + K_t}{m} & \frac{K_s}{m} & \frac{C_s}{m} & \frac{C_s}{m} \\ 0 & \frac{K_s}{M} & \frac{K_s}{M} & \frac{C_s}{M} & \frac{C_s}{M} \end{bmatrix} \qquad \mathbf{B} = \begin{bmatrix} 0 \\ 0 \\ 0 \\ \frac{1}{m} \\ \frac{1}{M} \end{bmatrix} \tag{26.11}$$

$$\mathbf{C} = \begin{bmatrix} 0 & \frac{K_s}{M} & \frac{K_s}{M} & \frac{C_s}{M} & \frac{C_s}{M} \\ 0 & -1 & 1 & 0 & 0 \\ -K_t & K_t & 0 & 0 & 0 \end{bmatrix} \qquad \mathbf{D} = \begin{bmatrix} \frac{1}{M} \\ 0 \\ 0 \end{bmatrix}$$

$$\mathbf{L} = \left[2\pi\sqrt{S_0\kappa} \quad 0 \quad 0 \quad 0 \quad 0\right]^T$$

where the values of K_t, K_s, C_s, M and m are provided in Table 4.1.

Assuming that all of the states of the vehicle system can be measured and fed-back, the control signal for Full State Feedback, $\mathbf{u}(t)$ (t is time) is the product of the state vector $\mathbf{x}$ and a gain matrix $\mathbf{G}$:

$$\mathbf{u}(t) = -\mathbf{G}\,\mathbf{x}(t). \tag{26.12}$$

The steady-state linear stochastic regulator problem consists of determining the controller gains (elements of $\mathbf{G}$) which minimise a cost function J given by:

$$J = \int_0^{\infty} \left(\mathbf{x}^T\mathbf{Q}\mathbf{x} + 2\mathbf{x}^T\mathbf{N}\mathbf{u} + \mathbf{u}^T\mathbf{R}\mathbf{u}\right) dt, \tag{26.13}$$

where $\mathbf{Q}$, $\mathbf{R}$ and $\mathbf{N}$ are positive, symmetric, definite weighting matrices which are derived later. Solving this problem involves finding the solution, $\mathbf{P}$, to the algebraic Riccati equation:

$$\mathbf{A}^T\mathbf{P} + \mathbf{P}\mathbf{A} + \mathbf{Q} - (\mathbf{P}\mathbf{B} + \mathbf{N})\mathbf{R}^{-1}(\mathbf{B}^T\mathbf{P} + \mathbf{N}^T) = \mathbf{0}\,. \tag{26.14}$$

The optimal control gains $\mathbf{G}$ are then calculated using:

$$\mathbf{G} = \mathbf{R}^{-1}(\mathbf{N}^T + \mathbf{B}^T\mathbf{P}). \tag{26.15}$$

Suppose we define:

$$\mathbf{Y}_{max} = \begin{bmatrix} \beta_1 a_{max}^{-1} & 0 & 0 \\ 0 & x_{max}^{-1} & 0 \\ 0 & 0 & F_{tyre}^{-1} \end{bmatrix} \quad \text{and} \quad \mathbf{U}_{max} = [\beta_2\, F_{cntrl}^{-1}], \tag{26.16}$$

where a_{max}, x_{max}, F_{tyre} and F_{cntrl} are arbitrary values assigning costs associated with body acceleration, suspension deflection, tyre force and control force; and β_1 and β_2 are weights used to shape the controller design.

Then the weighting matrices $\mathbf{Q}$, $\mathbf{R}$ and $\mathbf{N}$ can be calculated as follows:

$$\mathbf{Q} = \mathbf{C}^T\mathbf{Y}_{max}^T\mathbf{Y}_{max}\mathbf{C} \tag{26.17}$$

$$\mathbf{R} = \mathbf{U}_{max}^T\mathbf{U}_{max} + \mathbf{D}^T\mathbf{Y}_{max}^T\mathbf{Y}_{max}\mathbf{D} \tag{26.18}$$

$$\mathbf{N} = \mathbf{C}^T\mathbf{Y}_{max}^T\mathbf{Y}_{max}\mathbf{D}. \tag{26.19}$$

FSF Controller Design Procedure

The controller design procedure for Full State Feedback (FSF) described in the following assumes that the controllable suspension element is a 'perfect' linear actuator capable of supplying and dissipating energy. The validity of this assumption is investigated later using tests on the real semi-active damper in the HiL rig.

1. The controller can be designed to minimise RMS body acceleration or RMS tyre force by specifying the parameter β_1, which is used to determine the elements of the weighting matrices $\mathbf{Q}$, $\mathbf{R}$ and $\mathbf{N}$. Small values of β_1 produce a controller which minimises dynamic tyre forces while large values of β_1 result in a controller which minimises body acceleration. Intermediate values ($\beta_1 \approx 1$) reduce both responses simultaneously.

2. The second weighting parameter β_2 is used to adjust the RMS control force. The maximum demanded RMS control force is assumed to be F_{Cmax}. Having specified F_{Cmax} and β_1 it is necessary to select a starting value for β_2 and some arbitrary reference values for body acceleration a_{max}, suspension deflection x_{max}, tyre force F_{tyre} and control force F_{cntrl}. The optimal controller gain $\mathbf{G}$ can then be calculated using equation 26.15.

3. The RMS control force F_C is obtained from the product of the road input spectral density and the square of the transfer function relating the input to the control force. This force is then compared to the maximum allowed control force F_{Cmax}.

4. Finally parameter β_2 is adjusted, and steps 2 and 3 are repeated, until:

$$F_{Cmax} - F_C \approx 0 \tag{26.20}$$

This procedure ensures that the control algorithm demands suspension forces that are achievable by the test damper. See Besinger [53] for a table of the controller gains for various values of the shaping weights β_1 and β_2, and the case when $F_{Cmax} = 2.03$ kN, (*ie* the 'optimal passive' value for the Principal road surface, F_{Cpass}, listed in Table 26.1).

Theoretical FSF Responses

The theoretical RMS responses of the vehicle model on the principal road, with passive damping of 30kNs/m (see Table 26.1) were used for the reference values a_{max}, F_{tyre} and F_{cntrl}. (Passive damping of 30 kNs/m is near to the optimal value, see figure 26.4). Suspension working space was not considered to be an important constraint, which may be reasonable for lorry suspensions. The factor x_{max} was therefore set to a very large value so that the penalty factor associated with it became negligible.

Figure 26.11 shows simulated values of RMS tyre force and RMS body acceleration using FSF control. The values were obtained for values of the normalised RMS control force F_{Cmax} between 0.6 to 1.4 times the 'optimal passive' value of $F_{pass} = 2.03$ kN in Table 26.1. β_1 was varied between 0.01 and 100. In this figure the RMS body acceleration and RMS tyre force were normalised by the RMS responses with optimal passive damping (*ie* values in Table 26.1).

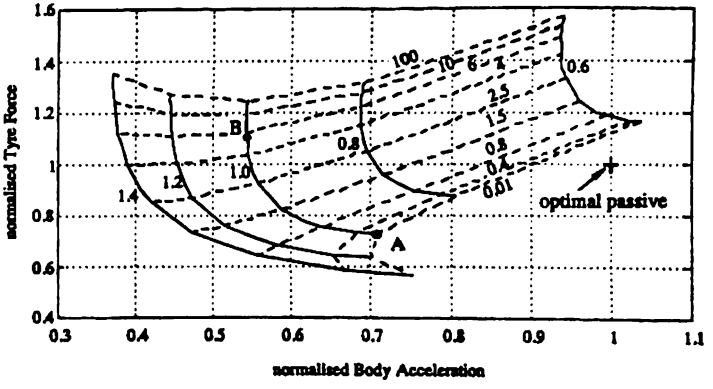


Fig. 26.11 Theoretical conflict diagram for body acceleration and tyre force on a principal road, using Full State Feedback. Tyre Force and Body Acceleration normalised by the values for 'optimal passive' damping (Table 26.1). From [97]

——— Contours of normalised RMS control force, F_{Cmax}/F_{pass}

- - - - - - Contours of constant β_1.

Consider the contour for $F_{Cmax}/F_{pass} = 1$. If the controller is designed for minimum dynamic tyre force, *ie* setting $\beta_1 = 0.01$ (point A on figure 26.11), the RMS tyre force and RMS body acceleration are reduced simultaneously by 26% and 29% of the optimal passive RMS responses. If the controller is designed to minimise body acceleration, ($\beta_1 = 100$, Point B), the RMS body acceleration is reduced by 46%, but only at the expense of tyre force, which is increased by 10% of the optimal passive RMS value.

Semi-Active Full State Feedback (SAFSF)

Semi-Active Full State Feedback (SAFSF) control is defined as:

$$F_s = \begin{cases} u, & \text{when } F_s v_{rel} > 0, \\ C_{min} v_{rel}, & \text{when } F_s v_{rel} \le 0, \end{cases} \tag{26.21}$$

where u is the control input specified by equation 26.12. (Compare with SAMSD, equation 26.5).

RMS body acceleration and RMS tyre force responses were obtained for SAFSF control using HiL measurements. The damper force was controlled using SAFSF as per equation 26.21. Figure 26.12 compares RMS tyre forces and RMS body accelerations for various controller designs, for the principal road input. The figure includes measured and theoretical responses for a SAFSF controller designed with a RMS control force of $F_{Cmax}/F_{pass} = 1.0$ and measured responses using a SAFSF controller designed for a larger RMS control force of $F_{Cmax}/F_{pass} = 1.2$. Finally, measured responses are presented for a SAFSF controller designed with $F_{Cmax}/F_{pass} = 1.0$, but with an extra gain of 1.5 in the damping force demand signal. This extra gain was found to improve body acceleration performance significantly.

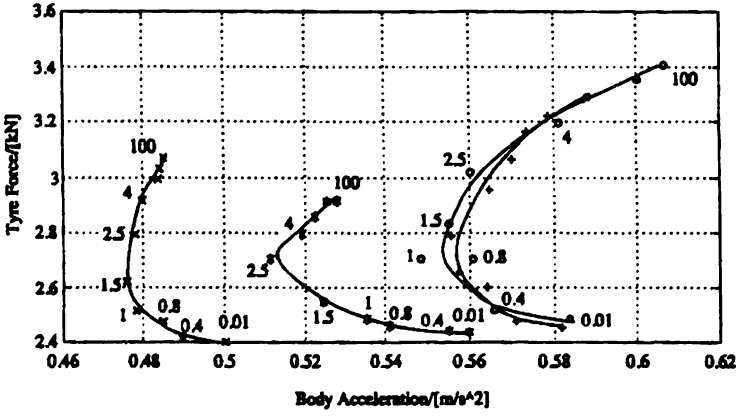


Fig. 26.12 Conflict diagram for body acceleration vs tyre force as a function of β_1, with SAFSF. From [97]
x = Theoretical SAFSF for $F_{Cmax}/F_{pass} = 1.0$
o = HiL measurements for $F_{Cmax}/F_{pass} = 1.0$
+ = HiL measurements for $F_{Cmax}/F_{pass} = 1.2$
* = HiL measurements for $F_{Cmax}/F_{pass} = 1.0$, with extra force gain of 1.5.

The results show reasonable similarity with the theoretical FSF curves in figure 26.11, except that for high values of β_1, there is an increase in the measured body acceleration which is not consistent with the linear optimal control theory. For theoretical SAFSF (figure 26.12), minimum body acceleration occurs at $\beta_1 = 1.5$, not at the largest value of β_1 as would be expected for theoretical FSF (figure 26.11). This indicates that control laws designed to minimise body acceleration produce damping force demands which cannot be realised with a semi-active damper, because they require power input. Conversely, control laws designed to minimise body acceleration and tyre force simultaneously generate force demands that are better suited to semi-active dampers. Thus for a real damper, the established view that 'theoretical' SAFSF control gives the best possible semi-active control law [212] is not necessarily correct.

The various controller designs in figure 26.12 achieved similar reductions in tyre forces, however large differences can be seen in the RMS body acceleration responses. In general the reductions in body accelerations achievable using SAFSF are smaller than those predicted using FSF. The experimental conflict curve for the SAFSF controller designed for $F_{Cmax}/F_{pass} = 1.0$ (o) shows significantly larger RMS body acceleration levels than predicted by the simulation (×). This is probably caused by measurement noise due to damper switching and may also be a function of the imperfect dynamic response of the damper. The measured responses for the controller designed with $F_{Cmax}/F_{pass} = 1.2$ (+) show little significant improvement in body acceleration response over the case for $F_{Cmax}/F_{pass} = 1.0$ (o). Similar results were obtained for the other two road input conditions.

Figure 26.13 shows measured and simulated RMS damper forces for various SAFSF controllers. It can be seen that the RMS damper force increases with F_{Cmax}/F_{pass} (as expected). The RMS damper force decreases with larger β_1 (*ie*, as the controller design becomes biased towards minimising body acceleration). This is not expected, because for each value of F_{Cmax}/F_{pass}, the FSF controllers are designed to have equal RMS damping force demands, irrespective of the value of β_1. The reduction in RMS damper force occurs because the FSF control law requires the damper to input power into the system more often for higher β_1. As a consequence, the damper is switched 'off' for longer periods, and so the RMS force level decreases.

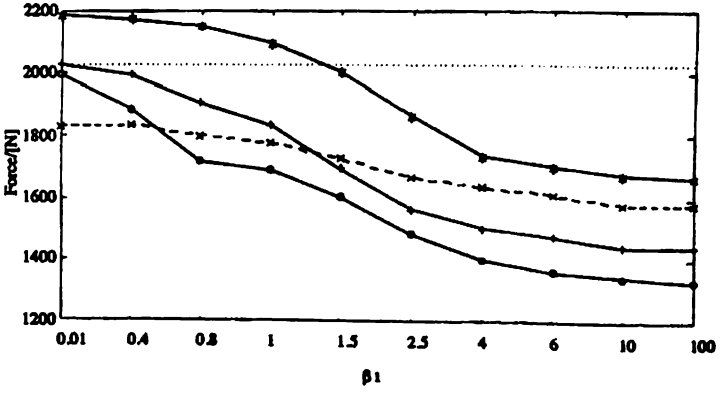


Fig. 26.13 RMS damping forces for full state feedback control, principal road input. From [97]
..... Theoretical FSF for $F_{Cmax}/F_{pass} = 1.0$
× = Theoretical SAFSF for $F_{Cmax}/F_{pass} = 1.0$
o = HiL measurements for $F_{Cmax}/F_{pass} = 1.0$
+ = HiL measurements for $F_{Cmax}/F_{pass} = 1.2$
* = HiL measurements for $F_{Cmax}/F_{pass} = 1.0$, with extra force gain of 1.5.

Mean square spectral densities for FSF controllers designed to minimise tyre force (β_1=0.01), are shown in figures 26.14a,b; and spectral densities for FSF controllers designed to minimise body acceleration (β_1=100) are shown in figures 26.15a,b. Each graph shows three cases: (i) theoretical FSF, (ii) theoretical SAFSF, and (iii) measured SAFSF (HiL rig). All controllers are designed for the case when $F_{Cmax}/F_{pass} = 1$.

Comparing the theoretical FSF responses on each graph (·····), it can be seen that the theoretical RMS *tyre force* (area under the spectral density curve) is smaller for β_1=0.01 (figure 26.14b) than for β_1=100 (figure 26.15b). Conversely, the RMS *acceleration* for FSF control is smaller for

β_1=100 (figure 26.15a) than for β_1=0.01 (figure 26.14a). These results follow directly from the FSF design procedure.

Comparison Between FSF and SAFSF Responses

Comparing FSF (·····) and theoretical SAFSF (- - - -) on figures 26.14 and 26.15 shows the consequences of using a semi-active damper instead of an ideal actuator. The differences between these two responses are a consequence of the damper not being able to track the desired control force when power input is required, and not having zero minimum damping (equation 26.21).

Significant differences in the FSF and theoretical SAFSF body acceleration responses occur at the body bounce frequency for both values of β_1 (figure 26.14a, 26.15a), whereas these two responses are very similar at the wheel hop frequency.

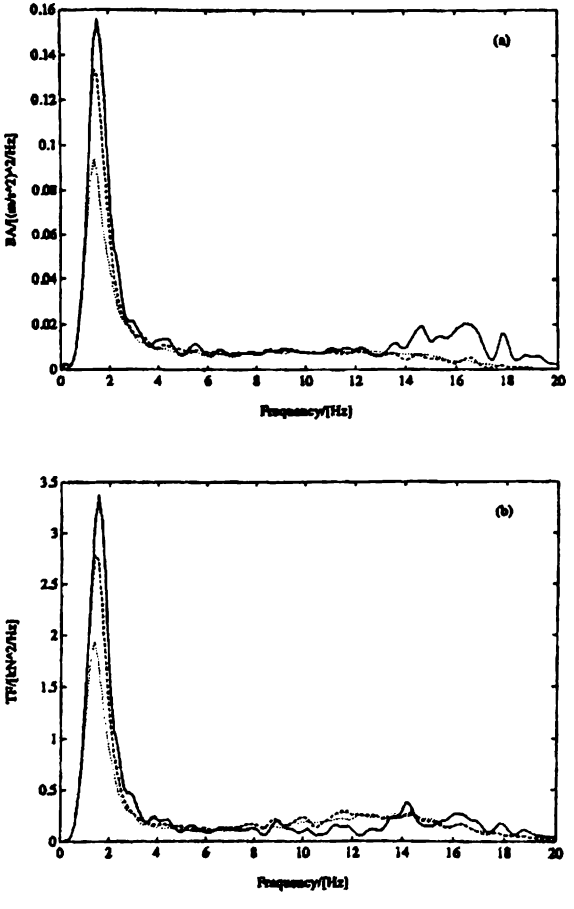


Fig. 26.14 Mean square spectral densities for FSF control designed for minimum tyre force (β_1=0.01). (a) Body Acceleration, (b) Tyre Force. From [97]
..... Theoretical FSF; - - - - - - Theoretical SAFSF; ———— Measured SAFSF (HiL)

The FSF and theoretical SAFSF tyre forces show similar effects at the body bounce frequency (figures 26.14b and 26.15b), however, there is a dramatic difference between these responses at the wheel hop frequency for β_1=100 (figure 26.15b). It is apparent that the control strategy for minimising body acceleration (β_1=100) requires large amplitude tyre forces at the wheel hop frequency. The theoretical semi-active damper is not able to generate the required forces, and consequently, the tyre forces for theoretical SAFSF are much less than for FSF. It is interesting to note from the body acceleration responses in figure 26.15b, that the theoretical semi-active response (SAFSF) is almost the same as the theoretical active response (FSF) in the range of wheel hop frequencies, despite the large discrepancies in the tyre forces.

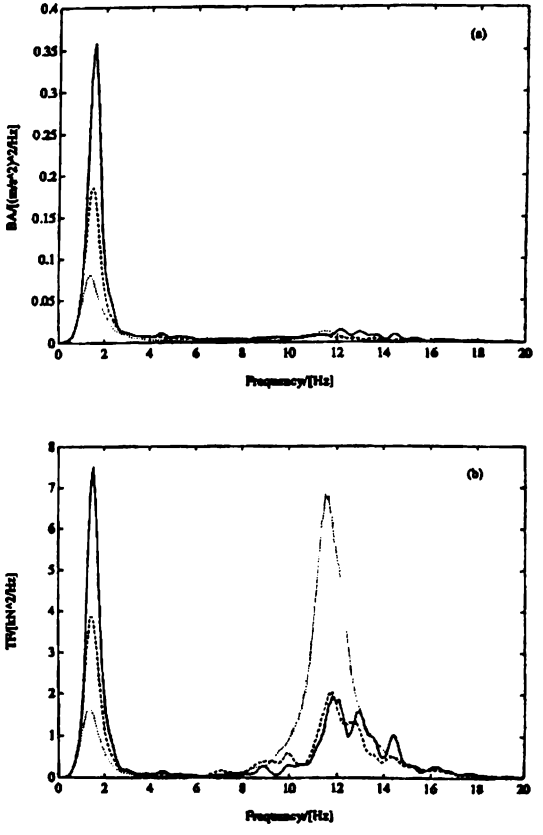


Fig. 26.15 Mean square spectral densities for FSF control designed for minimum body acceleration (β_1=100).
(a) Body Acceleration, (b) Tyre Force. From [97]
..... Theoretical FSF
- - - - - - Theoretical SAFSF
———— Measured SAFSF (HiL)

Comparison Between Theoretical and Experimental SAFSF Responses

Comparing theoretical and experimental SAFSF on figure 26.14 and 26.15 shows the consequence of using a real semi-active damper instead of an 'ideal' (theoretical) semi-active damper. The differences are mainly due to the dynamic response of the damping valve, the delay in generating the demanded force; and noise present in the measurements, which particularly affects the body acceleration responses.

The main effects of the damper imperfections occur at the body bounce frequency, particularly for β_1=100 (figures 26.15a,b). A similar effect can be observed on the body acceleration response at the wheel hop frequency for β_1=0.01 (figure 26.14a). In each case the measured response is higher than the theoretical response, indicating that the real semi-active damper generates a lower effective level of damping than the theoretical damper.

In practice it was found that increasing the force feedback gain in the HiL rig by a factor of 1.5 (as shown in figure 26.12) partially compensated for the non-ideal response of the real damper. This significantly decreased the differences between measured and theoretical SAFSF spectral densities at the body bounce frequency and the wheel hop frequency, for both body acceleration and tyre forces responses. (See [53] for results and discussion).

HiL measurements were also performed for the other road inputs described in Table 4.1 ('motorway' and 'minor road'). In general the results were similar to those for the 'principal road' input described above. One noticeable difference was that the measured responses improved on the rougher 'minor' road input relative to theoretical SAFSF responses. This was because of the nonlinear 'stiffening' force-velocity characteristics (see figure 4.23) which gave higher damping for the higher velocities experienced on the rougher road.

26.5.4 Modified Skyhook Damping vs Full State Feedback

RMS suspension deflection, RMS body acceleration and RMS tyre force for SAMSD and SAFSF control are compared in figures 26.16a,b for the principal road input. In each case, the control law has an optimised feedback gain. For SAMSD, this was achieved by setting C_{max}=55kNs/m in equation 26.5 (instead of the nominal 40kNs/m), and in the SAFSF case, it was achieved by multiplying the force feedback signal by 1.5.

It can be seen that full state feedback control (SAFSF) generally uses more suspension working space for equal levels of RMS tyre force and RMS body acceleration, except at very low values of α, where SAMSD uses more suspension working space. Designing the full state feedback controller for minimising body acceleration (high values of β_1) always results in increased suspension deflections.

For β_1=0.01 in the SAFSF controller (figure 26.16b), the RMS tyre force is lower than for the SAMSD controller for any value of α. However, the body acceleration generated by the SAFSF controller is relatively high at this value of β_1 (figure 26.16a). Similarly, for β_1=2.5, (corresponding to a suspension deflection of 4.6mm), the body acceleration generated by the SAFSF controller is less than at any point on the curve for the SAMSD controller. Thus if the suspension controller is designed to minimise *either* body acceleration *or* dynamic tyre force, full state feedback control is the better strategy. However, if it is desired to minimise *both* body acceleration and tyre force simultaneously, then SAMSD provides better overall performance, when α = 0.25. The same result was found for the other two road input conditions.

26.5.5 Theoretical Road Damage

Assuming that the dynamic tyre forces have a Gaussian probability density function and are randomly distributed along the road, the road damaging potential of a vehicle can be estimated from its dynamic tyre forces using the 'road stress factor' Φ defined in equation 17.12.

In practice it is found that peak dynamic tyre forces generated by heavy vehicles often occur repeatedly at specific locations along the road surface (see [130]). Hence road life is likely to be governed by damage at these locations, and the influence of dynamic tyre forces may be substantially greater than estimated by equation 26.22. For a single axle vehicle model, the effects of these peak loads can be quantified using the 95th percentile level of the dynamic road stress factor J which is given by equation 24.1.

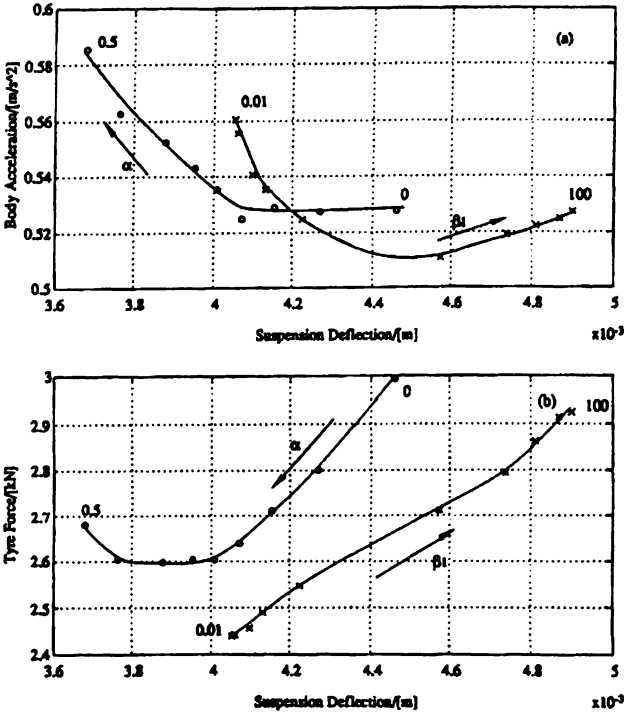


Fig. 26.16 Comparing HiL measurements of SAMSD and SAFSF control for a principal road. From [97]
(a) Conflict diagram for suspension deflection and body acceleration.
(b) Conflict diagram for suspension deflection and tyre force.
x = SAFSF with F_{Cmax}/F_{pass} = 1.0, and feedback gain scaled by 1.5
o = SAMSD with C_m = 55 kNs/m

In order to evaluate the reduction in road damage, the dynamic loading coefficient ($\bar{s}$) and 'road damage' J (95th percentile fourth power force, from equation 24.1) were calculated from the results of the HiL measurements for the three road input conditions. To provide a realistic basis of comparison, the dynamic load coefficients were scaled to a common vehicle speed of 80km/h for all three road surfaces. (This was necessary because it was not possible to run the HiL apparatus at 80km/h for the 'minor' road. The scaling procedure is described in detail in [53].) The road damage criteria were then compared with the results for the same conditions with optimal passive damping.

The results are shown in Table 26.2. It can be seen that semi-active damping is most effective for reducing road damage on rough (minor) roads. For a vehicle travelling on a minor road and fitted

with semi-active suspensions, using the SAFSF control strategy, the damage J would be reduced by 19.1%. For smooth motorways at 80km/h, the benefits of semi-active suspensions are considerably less.

Suspension System	Road Input	DLC ($\bar{s}$) at 80km/h	% reduction DLC ($\bar{s}$)	% reduction J
Optimal Passive	Motorway	0.044		
	Principal road	0.109		
	Minor road	0.188		
SAMSD (Modified Skyhook Damping)	Motorway	0.038	13.4%	3.6%
	Principal road	0.093	14.2%	8.3%
	Minor road	0.159	15.7%	14.0%
SAFSF (Full State Feedback)	Motorway	0.035	21.2%	5.7%
	Principal road	0.086	21.0%	12.2%
	Minor road	0.147	21.8%	19.1%

Table 26.2 Reduction in dynamic load coefficient $\bar{s}$ and the road damage J, for semi-active damping compared with optimal passive damping. Data from HiL measurements.

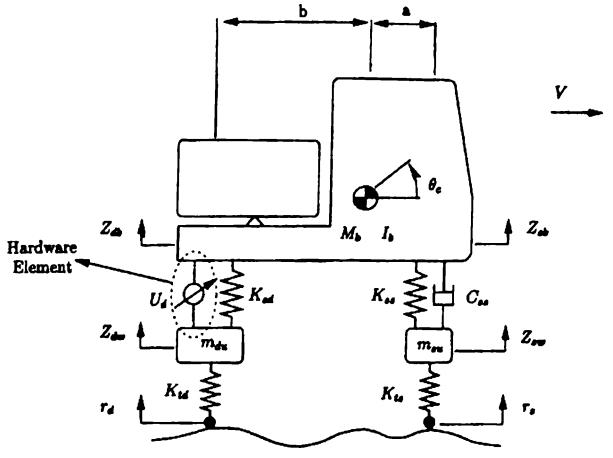
26.6 MORE SOPHISTICATED CONTROL STRATEGIES

Considerably more sophistication can be incorporated in the control strategies, particularly if vehicle models with more than one axle are considered. Kitching *et al* [285] investigated various control strategies for optimising the response of a two-axle (4-DOF) 'pitch-plane' rigid truck model as shown in figure 26.17. They concentrated on benefits that could be obtained by feeding-forward information from the leading axle to the controller of the trailing axle suspension (this has been termed 'Preview' control). Kitching *et al* tested a semi-active hydraulic damper that was developed specifically for heavy vehicle applications [284] and used the hardware-in-the-loop method to measure the performance of the control strategies [283].

They found that the 20*ms* to 30*ms* time delay that was measured in the transient response of their test damper (largely due to compressibility of the hydraulic oil) caused a significant degradation in the performance of the Preview control strategies. They therefore developed a Phase-Lag Compensation 'PLC' strategy, which involved predicting the demand force required from the damper a short time before the force is required. This was achieved by using a prediction model with a wheelbase that was shorter than the HiL model by a distance $t_c V$, where t_c is the compensation time and V is the speed (figure 26.18). Vehicle parameter values were chosen appropriately (see [283]). The PLC model incorporated a simple ideal model of the semi-active damper. Kitching measured the best phase lead time t_c, to be approximately the same as the lag time of the damper, *ie* 20-30*ms*.

A summary of the improvements obtained with the prototype damper relative to an optimised passive suspension, for the four-DOF HiL simulations, is presented in figure 26.19. Figures 26.19a-c show the results for three random road profiles, while figure 26.19d shows the results for a smoothed step ('ramp') input. Each figure shows the benefits of using SAMSD control, Optimal Preview Control, and Preview + PLC - using $t_c = 20ms$.

The benefits available through PLC for reducing the RMS body acceleration of the HiL vehicle are encouraging for both random and transient road profiles. The improvements achieved in terms of RMS tyre force and working stroke were disappointing. However, using more sophisticated models of the prototype semi-active damper in the PLC model could be expected to improve these aspects of PLC. The benefits of PLC can be seen to be greater in the case of a transient input (figure 26.19d).



$$\mathbf{x} = [\,(Z_{sw} - r_s)\,,\,(Z_{sb} - r_s)\,,\,(Z_{dw} - r_d)\,,\,(Z_{db} - r_d)\,,\,\dot{Z}_{sw}\,,\,\dot{Z}_{sb}\,,\,\dot{Z}_{dw}\,,\,\dot{Z}_{db}\,]^T$$

Fig. 26.17 The four-DOF HiL heavy vehicle tractor unit model, used by Kitching *et al* [283] to test suspension control strategies.

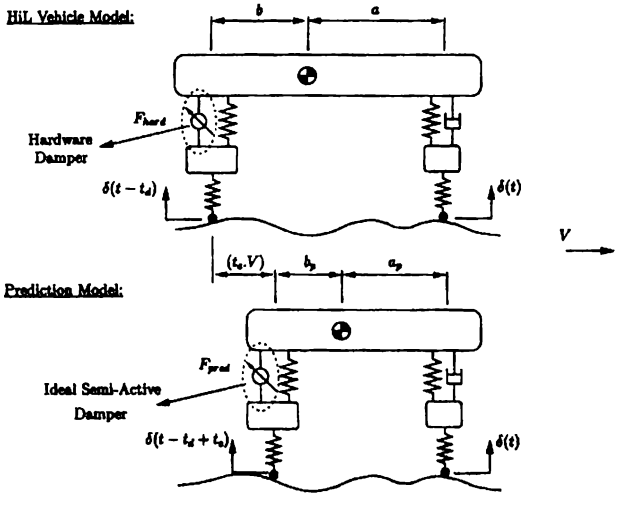


Fig. 26.18 Structure of the four-DOF HiL simulations with the four DOF 'Phase-Lag-Compensation' (PLC) vehicle model, after Kitching *et al* [283].

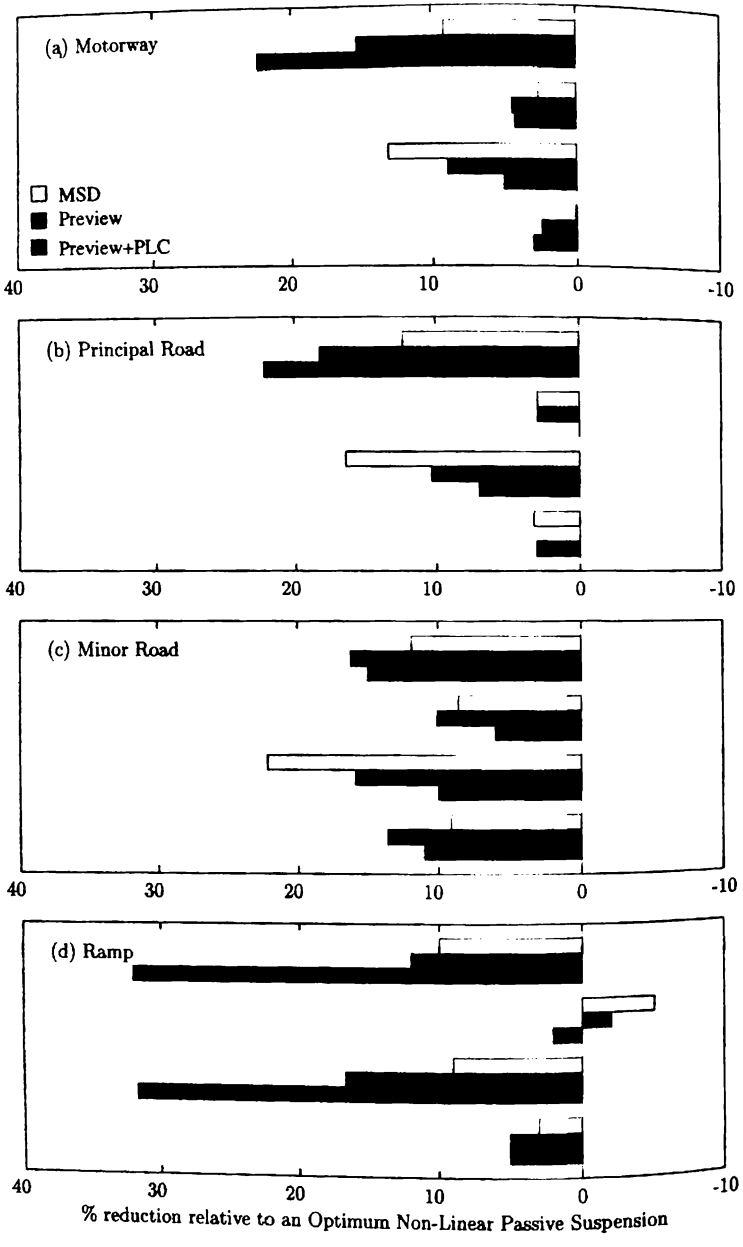


Fig. 26.19 Summary of the measurements with the prototype semi-active damper using a four DOF HiL test rig. All criteria with the exception of road damage relate to the measurements at the drive axle only. From [283]. (a) Motorway; (b) Principal road; (c) Minor road; (d) Filtered step (ramp).

26.7 CONCLUSIONS

The key findings of Besinger's study [97], [56] are summarised as follows:

(i) The semi-active damper was found to track the demanded force well, using an 'open loop' force control strategy. The tracking was improved by demanding a larger force than the nominal level, thereby increasing the speed of response, and the overshoot.

(ii) For the conditions investigated in this study, using Semi-Active Modified Skyhook Damping (SAMSD) control, RMS tyre force and RMS body acceleration could be reduced simultaneously by at least 13% and 22% of the responses for optimal passive damping.

(iii) *On-off* damping control was found to achieve reductions in RMS tyre force comparable to continuous SAMSD damper control with less working space usage; however, the body acceleration levels produced were larger.

(iv) Minimum RMS tyre forces are achieved for SAFSF controllers weighted to minimise dynamic tyre forces. However, minimum body acceleration is *not* achieved for a SAFSF controller weighted to minimise body acceleration, because the control law requires frequent power input which the semi-active damper cannot provide. The minimum body acceleration occurs for controller designs with an intermediate weighting. This questions the established view that SAFSF control gives the best possible semi-active performance.

(v) Using SAFSF control it was found that RMS body acceleration and RMS tyre force could be reduced simultaneously by 28% and 21% of the values for optimal passive damping.

(vi) If either dynamic tyre forces or body acceleration is to be minimised individually, SAFSF control gives better performance than SAMSD control. However, if tyre force and body acceleration are to be minimised simultaneously, SAMSD control is a good choice.

(vii) Semi-active dampers are more effective in reducing dynamic tyre forces (and the resulting road damage) on rough roads than smooth ones. In this study it was predicted that at the worst 5% of locations along the minor road, road damage could be reduced by 14% - 19%.

The key findings of Kitching's study [283] are summarised as follows:

(i) The theoretical benefits of Preview control for semi-active suspensions were partially achieved experimentally. Relative to an optimised non-linear passive suspension, Preview control improved the RMS body acceleration at the drive axle by 15.4%, 18.2% and 16.2% for the HiL simulations over the motorway, principal and minor roads respectively.

(ii) It was found that the demanded phase–lead–compensated damping force for the semi-active damper could be predicted with reasonable success, using a shortened-wheelbase model. The best performance was measured with a compensation time of approximately 20ms, which agreed with the known time delay of the damper.

(iii) For the motorway and principal road simulations PLC reduced the RMS body acceleration at the drive axle by 7% and 4% respectively, relative to the optimal measurements without PLC. A deterioration of 2% was measured for the minor road. For a filtered step input, the peak and RMS body accelerations at the drive axle were reduced by 25% and 20% respectively compared to the measurements without PLC.

(iv) It was found that there was little to be gained through PLC with respect to reducing the RMS dynamic tyre force and suspension working stroke. Increasing the accuracy of the prediction model is expected to improve this aspect of PLC.

Some sort of phase lag compensation approach is necessary in order to achieve the full potential benefits of semi-active dampers on heavy vehicles. From a practical viewpoint, if PLC can be shown to work successfully on real vehicles then it may become possible to reduce the complexity of the damper hardware without degrading the performance of the system significantly.



PART 7 - ASSESSING ROAD–DAMAGING POTENTIAL

27

BACKGROUND TO SUSPENSION ASSESSMENT

27.1 SUMMARY

This chapter is concerned with assessing the road–damaging potential of dynamic tyre forces generated by articulated heavy goods vehicles. The European suspension assessment test is reviewed. Various testing factors are discussed, including: (i) general testing methodologies; (ii) road damage issues such as 'spatial repeatability' of dynamic tyre forces and road damage criteria; (iii) vehicle response issues, such as test duration and data sampling details, road roughness, testing speed and wheelbase filtering. Various conclusions are drawn about the requirements for objective suspension assessment.

This chapter makes use of work published previously in [118] and [372].

27.2 INTRODUCTION

This part of the book is concerned with assessing heavy vehicles for 'road–friendliness'. This is an important topic, for the highway agencies which are involved in setting and enforcing vehicle regulations, and for the vehicle industry which has to satisfy these regulations. This part comes near to the end of the book because it requires knowledge of both vehicle and pavement effects.

Legislation has been in place for many years limiting the static weight of whole vehicles and individual axles. During the last decade regulations controlling dynamic tyre forces been introduced [52, 444, 446]. A particular problem with regulating dynamic tyre forces is devising suitable vehicle testing procedures which reflect the *road-damaging* potential of the vehicles. An assessment procedure should be objective, and not design restrictive.

There are three main scenarios for 'road–friendliness' assessment testing:

(i) A small number of representative vehicles can be tested by research agencies and the results used by government to develop regulations which encourage the use of particular generic suspension types. An example is the regulation in favour of air suspensions in the European Community [32].

(ii) A 'type approval' test can be used to assess the main vehicle (or suspension) models or variants produced by each manufacturer, when they are first introduced. The costs of performing such tests would usually be carried by the manufacturers.

(iii) An annual inspection can be used to assess every heavy vehicle. This type of testing can be coupled with spot checks by the roadside. The costs of performing annual inspections are usually be carried by the operators.

Scenario (i) inevitably leads to design–restrictive regulations which prevent the operation of a free-market for suspensions. It is, however, cheap to implement because only a few vehicles need to be tested. Scenario (ii) is not design restrictive, but can lead to vehicles which pass the test when new

and well maintained, but have poor performance after a period of operation. The testing is of moderate cost. Scenario (iii) is good from a technical viewpoint, because it ensures that vehicles are always well maintained (*eg* the dampers work). Depending on the details of the test, it can be very expensive - because of the large infrastructure needed to test many vehicles.

This chapter reviews some of the main technical issues concerned with assessing the road damage caused by dynamic tyre forces of heavy vehicles.

27.2.1 Requirements for Suspension Assessment

Whatever assessment procedure is chosen, the test itself should be objective, and not design-restrictive. As a consequence of the basic characteristics of dynamic tyre forces, (see Section 7.4); and other information about vehicle-road interaction, (See Chapters 18 and 19), it is possible to state a set of requirements which should be satisfied by an assessment procedure, if it is to be objective. These are listed in Table 27.1.

1	Account for the effects of tyre and axle arrangements and static load sharing *as well* as dynamic loading performance.
2	Account for the nonlinearity of suspension components.
3	Be conducted for representative conditions of speed and road roughness.
4	Account correctly for the sprung-mass distribution, sprung mass geometry, and wheel-base filtering effects.
5	Account for the effects of all axles of the vehicle on the pavement.
6	Account for the effects of spatial repeatability of dynamic pavement loads.
7	Account for the dynamic interaction between the suspensions of tractors and trailers.
8	Resolve/sample correctly both high and low frequency dynamic tyre forces.
9	Utilise statistically significant samples of tyre force time histories.
10	Be based on assessment criteria which reflect the potential of the vehicle to inflict fatigue and rutting damage to representative pavement structures.

Table 27.1 Criteria for an objective assessment test for 'road-friendliness'.

The 'ideal' way to assess the road-damaging potential of a heavy vehicle (following all of the ten requirements in Table 27.1) would be to measure the distribution of damage (permanent deformation and fatigue cracking) due to its passage over a standard test road at various speeds. Appropriate statistics of the measured damage (eg peak values) would be used to rate the vehicle. Such a test is not practical, because the incremental damage done in a single pass over a road surface is too small. There are, however three related quantities which could, in principle, be measured during a vehicle test: (i) the primary response of a test pavement (stresses, strains, displacements); (ii) dynamic tyre forces; and (iii) vehicle suspension parameters.

27.2.2 Measurement of Primary Pavement Responses

If primary pavement responses were measured and used to infer road damage, then it would be necessary to build a standard test road with sufficient buried instruments (*eg* asphalt strain gauges) to provide a statistically reliable measurement of the influence of the vehicle. The number and spacing of instruments would be governed by the speed of the vehicle and the frequency content of the dynamic tyre forces. This would dictate an arrangement of sensors somewhat like the arrangement of wheel force transducers in the 'load measuring mat', described in Section 7.3.2. The test would therefore require many buried strain gauges, at approximately 0.4 m (16 in.) intervals along the road.

The primary responses measured at each of the strain gauges would be converted into theoretical road damage using known road material fatigue and permanent deformation properties. The resulting theoretical damage distribution would be analysed statistically, to assess the effects of various vehicle parameters and to compare vehicles.

Unfortunately this approach would have a number of experimental difficulties, the most serious of which is the sensitivity of pavement response to construction details and environmental factors such as temperature and moisture. The test would produce very different results depending on the test pavement, the environmental conditions, and wheel path tracking. It would not be a reliable way of comparing vehicle suspensions, particularly if the test had to be standardised and performed in several different locations. Thus an objective assessment procedure needs to be based on measurement of dynamic tyre forces or vehicle suspension parameters.

27.2.3 Testing Methodologies

Table 27.2 gives an overview of various methods available for assessing the relative road damaging potential of heavy vehicle suspensions, based on dynamic tyre forces or suspension parameters. The columns are divided into tests of *single axles* (such as the drive axle), and tests of *whole vehicles*. The most realistic test will include all axles of a vehicle, because all axles interact, and contribute to road damage to some extent [96].

	Single axles	*Whole vehicle*
Direct methods	Single axle shaker rig [151, 152, 502] Instrumented axle [214, 406, 443, 491, 505]	Primary road response [108, 213, 276] Instrumented vehicle [117, 335] Road simulator [209, 244] Load measuring mat [374, 375]
Indirect methods	Parametric test [32] Design-based criterion [444, 483, 492]	Linear mathematical model [57, 371, 373] Non-linear mathematical model [371, 373]

Table 27.2 Methods of assessing 'road-friendliness'.

The rows of Table 27.2 are divided into 'direct' and 'indirect' test methods. *Direct* test methods are those where a tyre force or road response history is recorded directly for the vehicle subject to a realistic road roughness. *Indirect* test methods involve a simple test to characterise the vehicle/axle dynamics in some way, and from this test, road damaging potential is predicted. Table 27.2 shows currently used and possible future test methods, and previous research into each method. Cost, complexity and accuracy generally increase from the bottom left to top right of the table.

Tests on Single Axles using Indirect Methods

Current legislation falls into the category of *indirect tests*, measuring *single axles* (bottom left of Table 27.2). Two test methods are noted: 'parametric' tests and 'design-based' criteria (or 'type approval' tests). Design-based criteria have been in existence for a number of years, and are the simplest form of assessment. Certain types of suspension group are either banned (as in Australia [444]), or given a reduced weight limit (as in Germany [483] and the UK [492]).

Parametric tests measure vehicle parameters such as *natural frequency* and *damping ratio*. This type of test was introduced in European [32]. A suspension is considered to be 'road friendly' if its 'natural frequency' is less than 2Hz and its 'damping ratio' is 0.2 or more, with at least half of the

damping generated by hydraulic shock absorbers. The testing procedure can provide some information about suspension performance, but there is no clear relationship between the measured parameters and *road damage* [118].

The European test is discussed in detail later in this chapter, where it is concluded that it is not a reliable way to assess suspensions for 'road-friendliness'. The same conclusion is likely to apply to most other single axle parametric tests, because they do not satisfy objectivity requirements 1–5, 7 and 10, listed in Table 27.1.

Tests on Single Axles using Direct Methods

Direct tests on *whole vehicles* can most easily meet the criteria specified in Table 27.2, as the testing conditions most nearly represent those on the highway. However, they are also the most expensive. Direct tests on single axles, and indirect tests on whole vehicles provide compromise solutions.

One method of carrying out direct tests on single axles is to instrument the axles, using strain gauges and accelerometers, or special wheel hubs to measure the dynamic tyre forces [96]. Various experimental studies of this type have been performed under controlled conditions using specially prepared heavy vehicles. Most of these instrumented vehicles were tested on test tracks [214, 302, 337, 505], although some were tested on public roads [443]. This approach to vehicle assessment has the advantage of relative simplicity and low cost when testing a small number of vehicles. The researchers generally concluded that soft, hydraulically damped suspensions (air or torsion bar) generate lower levels of dynamic forces than stiff suspensions with friction (steel leaf springs). Consequently, they inferred that air and torsion bar suspensions are more 'road friendly' (see Chapter 7 for details).

An alternative test method investigated by de Pont [152] is to use a hydraulic actuator to excite one axle of a heavy vehicle in an attempt to recreate the dynamic tyre forces measured for that axle on a typical road. However, this method has a number of experimental difficulties, mainly due to the fact that it is not possible to excite all of the important modes of vibration of the vehicle correctly, using just one input actuator.

It was shown in Chapter 19 that direct tests on single axles can give erroneous conclusions about the ranking of suspensions in terms of 'road-friendliness'. They also fail to satisfy objectivity requirements 1, 4, 5, 7 listed above.

Tests on Whole Vehicles using Direct Methods

To overcome the experimental difficulties with pavement-based instrumentation, but still assess the vehicles in terms of *road damage*, it would be possible to *simulate* the primary responses of an instrumented test road, using a procedure rather like the 'single pass' road damage calculation shown in figure 17.16. A set of *measured* dynamic tyre forces could be used as input to a computer model of the primary response of the road, or simpler road-damage-related performance criteria (*eg* weighted aggregate forces). The computer model would calculate stress or strain time histories at particular locations along the road and these would be converted into theoretical road damage as described in Section 17.4.2. This approach has the advantage of comparing vehicles in terms of theoretical road damage using the response of a standard test road, but does not have the experimental problems associated with measuring primary pavement responses directly. Such a test could be designed to meet most of the objectivity criteria in Table 27.1.



It would be necessary to measure the tyre forces generated by *all* of the axles along one side of the test vehicle as it drove along a test road. Many vehicles would probably have to be tested. Such measurements could be performed in three ways:

(i) Using vehicle mounted instrumentation [117, 335]. This is impractical for testing many vehicles, as it requires three or four channels of instrumentation for every axle [96].

(ii) Using a 'road simulator' (hydraulic testing machine) to test the vehicle in the laboratory. This has the advantage of providing a variety of repeatable, standard testing conditions, and does

not require any on-vehicle instrumentation, so many vehicles can be tested relatively easily. The main disadvantage is that road simulators with sufficient actuators to excite all wheels on an articulated vehicle simultaneously (10 or 12) are expensive to purchase and run. Setting up the road simulator for each vehicle can be time consuming.

(iii) Using wheel force sensors attached to (or buried in) the road surface. This has the major advantage that tyre forces generated by all axles of the vehicles can be recorded, and many different vehicles can be tested rapidly, without having to instrument each one, or mount each one on a road simulator. One such system is the 'wheel load measuring mat' described in Chapters 7 and 8.

A number of important conclusions about using single-pass road damage calculations for suspension assessment can be found in Chapter 19.

Indirect Testing of Whole Vehicles

The final category of test in Table 27.2 is indirect testing of whole vehicles. The concept is to perform a simple laboratory test on each axle of the vehicle, to measure its dynamic characteristics. This information is then used to generate a numerical model of the response of the whole vehicle to typical road roughness inputs. In principle, this method has the advantage of requiring relatively simple and low cost laboratory testing equipment, and yet can provide sufficient information to assess the road-damaging potential of the whole vehicle, and satisfy all of the objectivity criteria in Table 27.1. Various methods, both linear and nonlinear, have been proposed for achieving this. They are described in Chapter 29.

27.3 THE EUROPEAN SUSPENSION TEST

The measurement of suspension parameters, such as 'natural frequency' and 'damping ratio' can provide some information about suspension performance, but there is no clear relationship between these parameters and road damage. For some suspensions, however, the body bounce frequency (measured from the wheel force spectrum) can be correlated with the Dynamic Load Coefficient, see figure 27.1, from Gyenes *et al* [210].

Measurement of 'natural frequency' and 'damping ratio' is difficult, because: (i) the vehicle response is inherently non–linear and the measured frequency and damping depend on the magnitude of the input (Section 7.4.4); (ii) many different natural modes of vibration contribute to the dynamic tyre forces, depending on the speed of the vehicle: there are several important 'natural frequencies' (Section 7.4.5); (iii) there is no reason to believe that a particular transient input will excite the natural mode(s) that dominate the generation of dynamic tyre forces for a given highway speed.

Nevertheless, parameter measurement is the approach that was introduced by the Commission of the European Community (EC) for determining whether a suspension is 'equivalent' to an air suspension. (Air suspensions on the single drive axles of tractors are allowed to carry an extra tonne of load.) The test is described in *Council Directive 92/7/EEC* [32]. The author of this directive [52] noted that this approach was considered to be a first step towards assessing vehicles for 'road friendliness.' The procedure is *not* based on measuring road damage, nor on measuring dynamic tyre forces under realistic conditions.

The European test involves deducing a single resonant frequency and damping ratio from the measured suspension deflection of a tractor drive axle, during a transient event. The transient motion can be excited in one of three ways [52]:

(i) Drive the vehicle slowly off an 80 mm step;
(ii) Pull the chassis down to increase the drive axle tyre force by 50%, then suddenly release;
(iii) Lift the chassis to increase the spacing between the drive axle and chassis by 80mm, then suddenly release.

The 'resonant frequency' is deduced from the time separation of the first two compression peaks of the transient response time history. The 'damping ratio' is calculated from the ratio of amplitudes of the same peaks. The Directive does not state how the payload should be applied to the tractor.

To be 'equivalent' to an air suspension, a leaf spring suspension must have a resonant frequency less than 2.0 Hz and a damping ratio greater than 0.2, with at least half of the damping being generated by hydraulic shock absorbers.

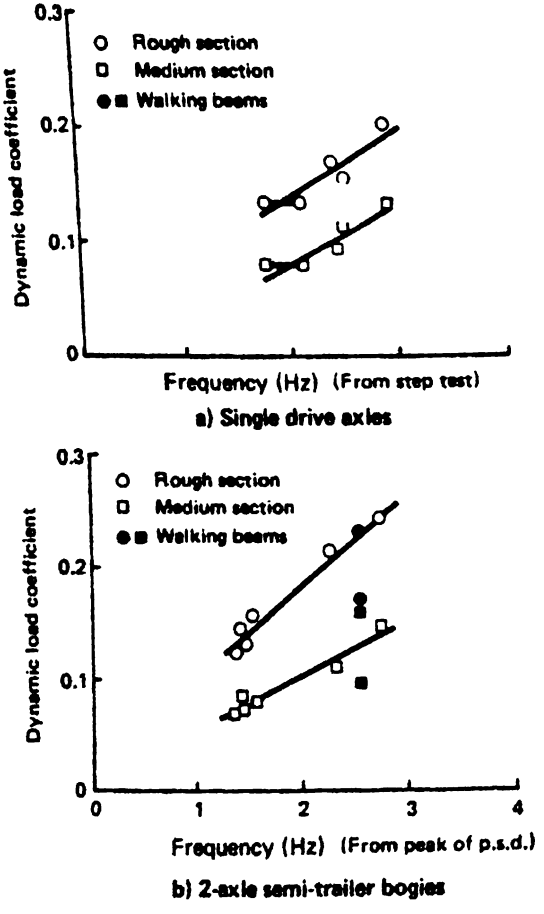
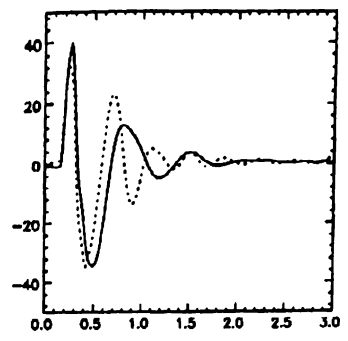
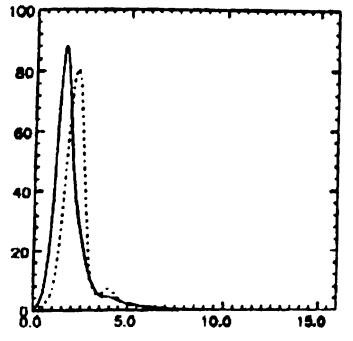


Fig. 27.1 Relationship between body bounce frequency and dynamic load coefficient measured at 80 km/h (50mph). From [210].

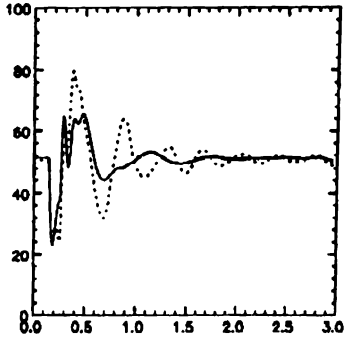
The European test was simulated, using the validated non-linear articulated vehicle model described in Section 6.4, and using a modified version of this vehicle with an air suspension on the tractor drive axle (see also [118]). (Other relevant results for this same simulation study can be found in figures 7.8 to 7.10.) Figure 27.2 shows the results of the 80 mm step test on each vehicle. The drive axle *suspension deflection* histories are shown in figure 27.2a, and the corresponding spectral densities are shown in figure 27.2b. Figures 27.2c and 27.2d show the drive axle *tyre force* histories and spectral densities.



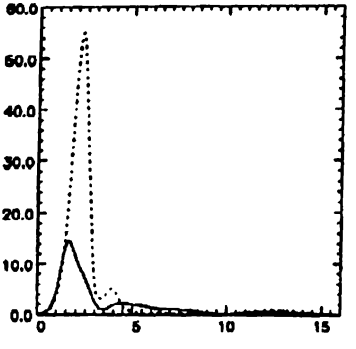
(a) Drive axle suspension deflection history



(b) Drive axle suspension deflection spectral density



(c) Drive axle tyre force history



(d) Drive axle tyre force spectral density

Fig. 27.2 Results of simulated European step tests (step height 80mm, vehicle speed 1.4m/s = 5mph), from [118].

For both vehicles, one frequency appears to dominate the suspension deflection spectral density: 1.5 Hz for the air suspended tractor and 2.2 Hz for the leaf sprung tractor. In practice, the vehicles have at least three important vibration modes. (These are shown in figure 7.8 for the same two vehicle models.) The three modes 'smear' together in the simple step test, depending strongly on the initial conditions or excitation. The test therefore yields some sort of average of the three main natural frequencies, and in general it is not possible to determine the frequency of any one mode from the measurements. Under normal operating conditions 'wheelbase filtering' effects will cause various modes of the vehicle vibration to be dominant, depending on the speed (see figure 7.9).

The tyre force histories of both vehicles show high frequency variations (due to wheel hop) which are not present in the suspension deflection histories. The suspension deflection cannot therefore be used to infer the dynamic tyre force response. The tyre force *spectral densities* show little evidence of the wheel hop modes because they do not make a large contribution to the overall mean-square response, despite affecting the peak forces significantly. Under normal operating conditions, the wheel hop mode can make a significant contribution to dynamic tyre forces, see figure 6.18. The step test clearly does not provide excitation in any way representative of a typical road profile.

To determine the influence of payload configuration on the frequency determined from the European test, an additional vehicle model was created from the leaf sprung vehicle (of figure 6.13). This model consisted of the leaf sprung tractor with a lumped mass attached to the fifth wheel coupling, instead of the laden semi-trailer. The lumped mass was chosen so that both vehicle models had the same static loads on the tractor axles.

Figure 27.3 shows four drive axle suspension deflection histories. Two of the curves correspond to the original tractor + semitrailer model subjected to an 80 mm step test and a 20 mm step test. The other two curves correspond to the same tests on the tractor + lumped mass model. An average frequency was 'measured' from each deflection history from the time separation of the first two compression peaks, as prescribed by the European Directive. The frequencies are shown in Table 27.3.

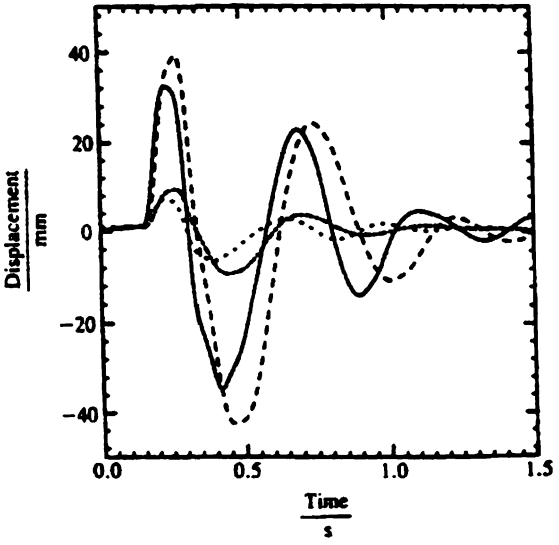


Fig. 27.3 Effect of step height and payload configuration on drive axle suspension deflection history.

———— tractor + semi-trailer, 80mm step (2.1Hz)
– – – – – – tractor + lumped mass, 80mm step (1.9Hz)
- - - - - - tractor + semi-trailer, 20mm step (2.4Hz)
– – – – – – tractor + lumped mass, 20mm step (2.1Hz)

The average frequency deduced from the step test was found to depend on the configuration of the payload on the tractor. By removing the laden semi-trailer and replacing it with a lumped mass, the frequency was found to *decrease* from 2.1Hz to 1.9Hz. The suspension would therefore pass a 2.0Hz assessment criterion if tested with a lumped mass, but would fail if fitted with a laden semi-trailer. This effect occurs because the natural vibration modes that are excited in the step test involve pitching of the semi-trailer (see figure 7.8). Therefore the measured frequency depends on the moment of inertia of the semi-trailer as well as the static load applied to the fifth wheel coupling. The European Directive does not prescribe the loading conditions for the tractor.

The frequency deduced from the step test was also found to depend on the step height. In reducing the step height from 80 mm to 20 mm, the frequency of the tractor + lumped mass model was found to *increase* from 1.9 Hz to 2.1 Hz. The suspension would therefore pass a 2.0 Hz assessment criterion if tested (with a lumped mass) on an 80 mm step, but would fail if tested on a 20 mm step.

This dependence of frequency on excitation amplitude is caused by the non-linear, hysteretic characteristics which are typical of leaf spring suspensions (see Section 4.3).

Step height	*Tractor+ Semi-trailer*	*Tractor+ Lumped mass*
80mm	2.1Hz	1.9Hz
20mm	2.4Hz	2.1Hz

Table 27.3 Frequencies determined from simulated European step tests on leaf-sprung vehicles (see figure 27.3).

It can be concluded that the European parametric test is not a reliable way to assess suspensions for 'road-friendliness'. When this fact is combined with uncertainties concerning the economic importance of dynamic loads on road damage in Europe (Chapter 21), it seems doubtful that the new European legislation should every have been introduced.

27.4 VEHICLE RESPONSE ISSUES

A number of experimental issues need to be resolved for any assessment test that utilises *direct* measurements of dynamic tyre forces under field conditions. These issues are examined in more detail in the following sections. The emphasis is on tests utilising pavement-based instrumentation, (*eg* the load measuring mat described in Section 7.3.2). However, the issues are relevant to any 'direct' assessment test.

27.4.1 Sampling Frequency

For heavy vehicles, the highest frequency of interest in the dynamic tyre forces is due to wheel-hop vibration. This frequency f_{high}, is normally in the range of 10 Hz to 18 Hz. For vehicle-mounted instrumentation, dynamic tyre force signals should be sampled at a frequency at least twice the maximum frequency of interest, *ie* at least 36 Hz. This presents no problem to conventional data logging systems. However, for sensors mounted in the road surface (*eg* in a load measuring mat), the spacing between sensors must be small enough to record this frequency. If the vehicle speed over the sensor array is V for dynamic tyre forces at f_{high} to be resolved correctly, the sensor spacing Δ must be $\Delta \leq V / 2f_{high}$. The *maximum* acceptable spacing is therefore limited by the *minimum* speed at which vehicles are to be tested. For a minimum speed of 50 km/h (14 m/s) this gives a spacing Δ of approximately 0.4m.

27.4.2 Test Duration and Test Track Length

A highway can be considered to be a random road surface of infinite length. A finite length test site with the same nominal roughness statistics will not give the same average assessment results as the infinite length road, due to the limitation of the finite length process [50]. This will lead to variability of results between test sites which will increase for shorter test section lengths. This aspect of test section length is important for ensuring the repeatability of tests between different test sites, and for accurately relating the results of a test to highway conditions.

It is possible that a limited number of specific test surfaces of precisely known profile could be employed for vehicle assessment. However, using a short deterministic road profile may influence the ranking of vehicles in an unpredictable way. The following conclusions on required test track length are based on the assumption that the test track will be a sample from a stationary Gaussian random process [157].

Provided that a long enough signal is considered, a dynamic tyre force history $f(t)$ can be regarded as a stationary random process [214, 405, 443]. Assuming a Gaussian probability distribution (Section 7.4.1), the 95th percentile level of tyre force $f_{95\%}(t)$ is given by

$$f_{95\%}(t) = m_f(t) + 1.645\sigma_f(t), \tag{27.1}$$

where $\sigma_f(t)$ is the standard deviation of the tyre force, measured for time t, and
$m_f(t)$ is the mean value of the tyre force measured for time t.

This quantity is important because it is often hypothesised that road damage done by peak dynamic tyre forces (rather than average values) causes the road to fail (see Section 17.4).

The variance of $m_f(t)$ has been shown to be smaller than the variance of $\sigma_f(t)$ [370], and it can be ignored as a first approximation, if the number of data points in the sample being analysed is large. Taking the static load to be f_{static}, and the mean square value of the *dynamic* component of the tyre force to be $\psi_F(t)$ gives

$$f_{95\%}(t) = f_{static} + 1.645\sqrt{\psi_F(t)}. \tag{27.2}$$

$\psi_F(t)$ has a χ^2 probability distribution, which will approximate a Gaussian distribution for a large number of data points [216]. The range within which 95% of data points lie is therefore given by

$$f_{95\%}(t) = f_{static} + 1.645\sqrt{\overline{\psi}_F \pm 1.98\sqrt{Var[\psi_F(t)]}}, \tag{27.3}$$

where $\overline{\psi}_F$ is the true mean square dynamic tyre force, and
$Var[\psi_F(t)]$ is the variance of the mean square dynamic tyre force.

Equation 27.3 was tested using simulated runs of a quarter car vehicle model travelling at 22m/s over a medium roughness road [370]. Figure 27.4 shows the results of 50 simulation runs in which the model travelled over different pseudo-random road profiles with the same spectral density. The solid lines show the simulation results, and the dotted lines show the 95th percentile ranges for the data using the theory described above. Equation 27.3 predicts the bounding 'envelope' accurately at larger track lengths, but is a less accurate predictor at distances below 150 m. This is due to the small number of data points for short distances. The errors also depend on the number of low frequency cycles recorded in the sample. The quarter car model had body bounce natural frequency of 1.8 Hz. This gives a low frequency wavelength of approximately 12 m for a speed of 22 m/s. To include (say) ten complete cycles, a recording distance of 120 m would be necessary. This is similar to the distance at which equation 27.3 starts to become inaccurate (see figure 27.4).

The range in which 95% of values lie for $f_{95\%}(t)$ can be calculated as a percentage of the expected value:

$$Err_{f95\%}(t) = \frac{1.645\left(\sqrt{\overline{\psi}_F + 1.98\sqrt{Var[\psi_F(t)]}} - \sqrt{\overline{\psi}_F - 1.98\sqrt{Var[\psi_F(t)]}}\right)}{f_{static} + 1.645\sqrt{\overline{\psi}_F}} \times 100 \quad (\%). \tag{27.4}$$

Figure 27.5 shows the test track length required for 2%, 5%, 10%, and 20% error ranges of $f_{95\%}(t)$ plotted as a function of speed, for a medium roughness road. This graph provides a means of comparing results for a short length of track with results for an infinite track length. At low speeds, the dynamic component of the tyre forces is low, so the error range will also be small. As vehicle speed increases, the error range increases, so a longer track length is required for the same error. Typical highway speeds are between 18-27m/s. Consequently for a medium roughness road and typical speeds, the 95th percentile tyre force will be within 5% of the level for an infinite length of road if the track length is greater than 250 m. The rate of decay of this error is exponential. In order to reduce it to 2.5%, a track length of at least 700 m is required. The difference between the 95th percentile tyre force for a track length of 60 m (as used in the load measuring mat in the tests described previously) and for an infinite length of track, for vehicles travelling at highway speeds is 10% or more.

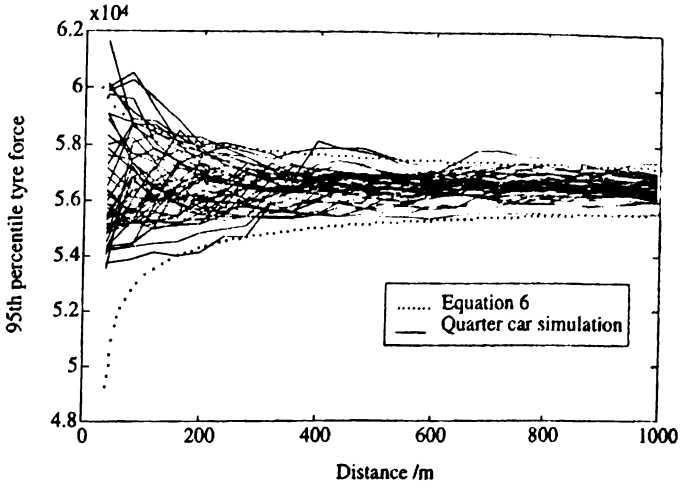


Fig. 27.4 95th percentile tyre force vs. track length. From [372].

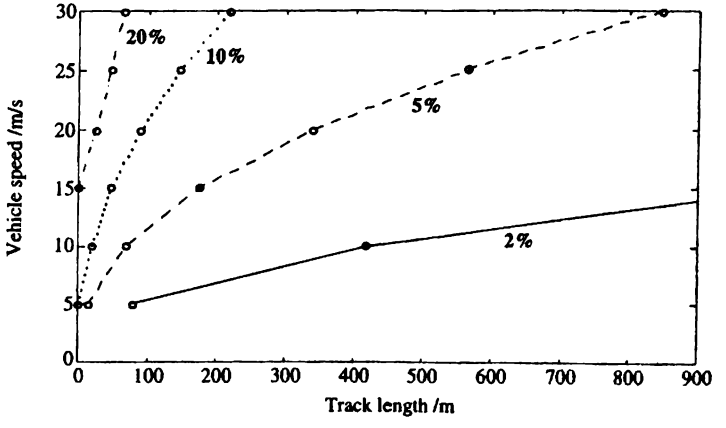


Fig. 27.5 Error contours for 95th percentile tyre force for various combinations of track length and vehicle speed. A test performed on an 'infinite' length test section would have zero error. From [372].

Equation 27.2 is valid for aggregate tyre forces as well as for individual tyre forces, since the aggregate tyre forces will also have a Gaussian probability distribution [88]. If the vehicle model contains significant non-linearities, the theoretical 95% range for the 95th percentile tyre force will only be approximate, due to the 'transfer function' varying with input conditions (speed and road roughness). However, the method described above will give a reasonable approximation to the track length required for a vehicle assessment test.

It can be concluded that for a statistical accuracy of 5%, and tests on a road of medium roughness at typical speeds, a test using pavement-based instrumentation would need at least 250m of accurate sensors, spaced at approximately 0.4m intervals, *ie* 600 sensors in all. Although this is possible with current technology [116], it would probably be too expensive for practical implementation.

27.4.3 Road Roughness

There have been a number of studies over the last 25 years investigating dynamic pavement loading. Some of these investigations have quantified the effects of speed and road roughness on dynamic loads. Major studies include [172, 210, 214, 302, 335, 337, 443, 491, 504]. See review in Section 7.5.

It has generally been concluded that: at highway speeds the parameter which causes the greatest variation in dynamic tyre forces, and the largest changes in ranking of suspensions is the road roughness level. If an assessment procedure is required to rank suspensions over all conditions of roads in common usage by heavy vehicles, a series of tests at different roughness levels is necessary. If tests were to be performed at several different testing stations, it would be necessary for each test site to have road profiles with similar roughness *statistics*, if not identical profiles.

27.4.4 Testing Speed and Wheelbase Filtering

Constructing long road surface test sections, with typical highway roughness characteristics, to sufficient accuracy, is technically demanding. This section investigates the possibility of testing vehicles at low speeds on shorter lengths of artificially–rough profiles, which would be easier to construct and replicate. It would be desirable to design such profiles to excite dynamic tyre forces that would be statistically similar to those for normal highway conditions.

All wheels on one side of a vehicle are subject to the same road profile input with different time delays. This results in 'wheelbase filtering' which significantly affects the dynamic tyre forces (Section 7.4.5). Cole and Cebon [125] examined the effect of wheelbase filtering using a four degree of freedom model with different suspension stiffnesses. They found that the *ranking* of different suspensions in terms of whole vehicle road damage varied with vehicle speed. This was due to wheelbase filtering.

The two degree of freedom model in figure 27.6 was used to investigate the effects of vehicle testing speed on pitch and bounce vibration. The model parameters were representative of a two axle rigid truck. The bounce frequency of this model is 2.5 Hz and the pitch frequency is 4.4 Hz.

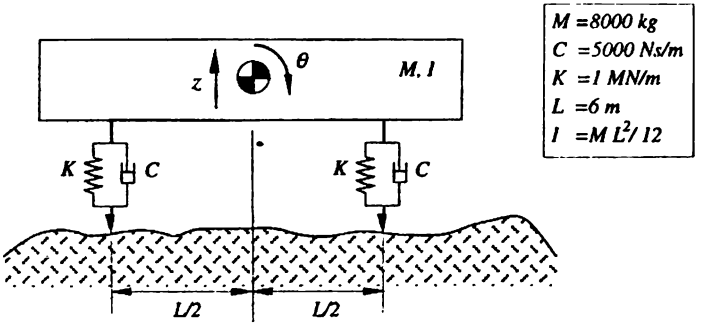


Fig. 27.6 Two degree of freedom linear vehicle model used to investigate wheelbase filtering. From [372].

Figure 27.7 shows the tyre force spectral densities of the vehicle model travelling at various speeds over a medium roughness road. Since the magnitude of the input road profile spectral density at any frequency is proportional to the vehicle speed V, the spectral densities in this figure have been scaled by $V/22$ to remove the effect of changing input amplitude from the magnitude of response. The spectral densities in figure 27.7 show peaks and troughs at different frequencies, depending on the speed. This is caused by 'wheelbase filtering' [406].

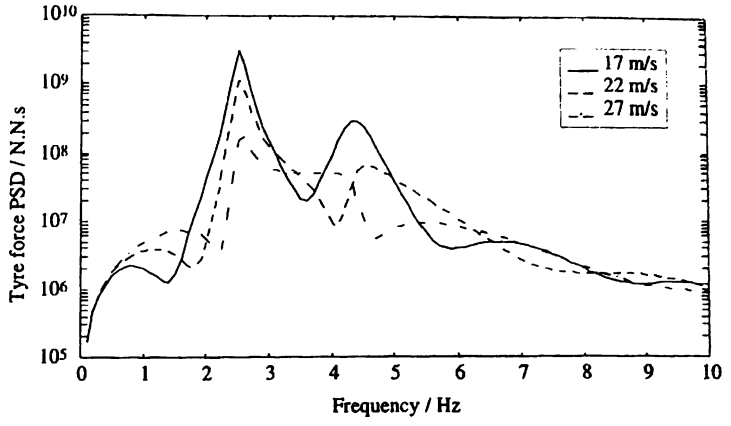


Fig. 27.7 Comparison of front tyre force PSDs for vehicle model travelling at three typical highway speeds. From [372].

For a two axle vehicle traversing a sinusoidal road profile, the two axles are excited in anti-phase by road profile 'waves' of length twice the wheelbase. This results in a pure *pitch* input to the vehicle, and zero *bounce*. Conversely, when the wavelength of the road profile equals the wheelbase, the axles are excited in phase with each other, and pure bouncing results [406]. This effect also occurs for road wavelengths shorter than the wheelbase. In general, the *i*th *pitch excitation* frequency occurs when the road profile wavelength is

$$\lambda_p(i) = \frac{2L}{(2i-1)} \qquad i=1,\ 2,\ 3,\ \ldots \tag{27.5}$$

where L is the wheelbase. The corresponding wavelength for the *i*th *bounce excitation* frequency is

$$\lambda_b(i) = \frac{L}{i} \qquad i=1,\ 2,\ 3,\ \ldots \tag{27.6}$$

The speed range over which the effects of bounce excitation become important depend on the bandwidth of the peak in the vehicle bounce mode transfer function. This in turn, depends on the damping of the bounce mode ζ_b. The speed range, $V_b(i)$, over which the ith bounce excitation frequency is important was shown by Potter [370] to be:

$$\frac{Lf_b}{i}(1-\zeta_b) < V_b(i) < \frac{Lf_b}{i}(1+\zeta_b) \qquad i=1,\ 2,\ 3,\ \ldots \tag{27.7}$$

where f_b is the bounce mode natural frequency and ζ_b is the corresponding damping ratio.

A similar procedure can be followed for *pitch* mode excitation, resulting in

$$\frac{2Lf_p}{(2i-1)}(1-\zeta_p) < V_p(i) < \frac{2Lf_p}{(2i-1)}(1+\zeta_p) \qquad i=1,\ 2,\ 3,\ \ldots \tag{27.8}$$

where $V_p(i)$ is the speed range at which the effects of pitch excitation frequency *i* become important,

f_p is the pitch mode natural frequency, and

ζ_p is the pitch mode damping ratio.

A damping ratio of 0.1 is a reasonable value to use for the sprung mass pitch and bounce modes for the majority of heavy vehicles. Using equations 27.7 and 27.8 with this damping ratio, the chart in figure 27.8 can be constructed. This chart shows vehicle speed plotted against the product of vehicle wheelbase and natural frequency. The chart highlights the speeds at which the pitch and bounce natural modes of the vehicle model are strongly excited by the road profile. For the vehicle model in figure 27.6, the product of bounce natural frequency (2.5 Hz) and wheelbase (6 m) is Lf_b = 15 m/s, and the product of pitch natural frequency (4.4 Hz) and wheelbase is Lf_p = 26.4 m/s.

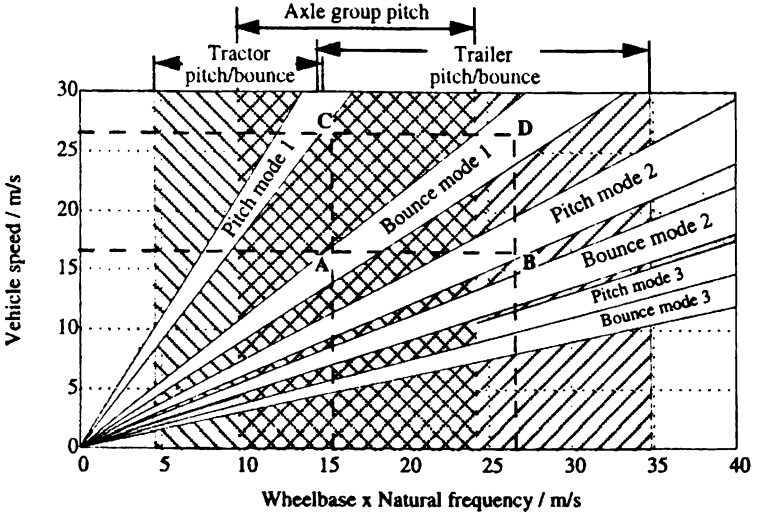


Fig. 27.8 Pitch and bounce excitation modes for heavy vehicles. The non-shaded radial bands indicate areas in which the pitch or bounce modes are strongly excited. The damping ratios of the pitch and bounce modes are assumed to be 0.1. From [372].

The general shapes of the spectral curves in figure 27.7 can be explained using figure 27.8. At a vehicle speed of 17 m/s , the bounce mode (Lf_b = 15 m/s) is excited by inputs at bounce excitation frequency 1 (point 'A' on figure 27.8), so the response at the bounce natural frequency of 2.5 Hz increases. Similarly, the pitch mode (Lf_p = 26.4 m/s) is excited by inputs at pitch excitation frequency 2 (point B), increasing the response at 4.4 Hz. At 27 m/s however, the bounce natural frequency is near to pitch excitation frequency 1 (point C), so the bounce response at 2.5 Hz decreases. The pitch natural frequency coincides with bounce excitation frequency 1 (point D), so the pitch response at 4.4 Hz also decreases.

Figure 27.8 can be used to investigate the effect of wheelbase filtering on HGVs travelling at different speeds. The vibration modes of HGVs that are affected by wheelbase filtering can be classified into three groups. The range of the product of wheelbase and natural frequency (Lf) for each group is superimposed in figure 27.8 as vertical shaded bands. These groups are tractor sprung mass pitch and bounce (4.5 m/s < Lf < 14 m/s); trailer sprung mass pitch and bounce (13.5 m/s < Lf < 35 m/s), and tandem axle group pitch (9.6 m/s < Lf < 24 m/s). (See Potter [370] for details.)

Consider a typical articulated vehicle travelling at highway speeds (17-27 m/s). The first pitch excitation frequency will be near to the pitch natural frequency of the tractor unit, and the first bounce excitation frequency will be near to the bounce natural frequency of the trailer, so these two resonant frequencies will typically be excited. If the speed is reduced to an artificially low value for testing, it

is clear that different pitch and bounce excitation frequencies will be close to the vehicle natural frequencies, thus causing different resonant frequencies to be excited and a completely different response spectral density.

Although it is possible to find highway speeds at which wheelbase filtering for an individual vehicle unit is small, it is not possible to replicate these conditions for artificially low testing speeds, where wheelbase filtering is always important. This means that it is *not possible* to decrease vehicle speed and artificially increase road roughness, and still generate similar vehicle response statistics as under highway conditions. Consequently, in order to account correctly for wheelbase filtering behaviour, tests to characterise vehicle response on public roads need to be carried out over a range of representative highway speeds.

27.4.5 Tractor - Trailer Interaction

An important feature of dynamic loading is that all the suspensions and tyres on a vehicle are involved in the sprung mass modes of vibration [96, 244]. For example, Cole and Cebon [118] showed by simulation, that improving the 'road friendliness' of the tractor axle on an articulated vehicle model can cause the dynamic tyre forces generated by the trailer axles to increase (figure 7.10). As a result, it is likely that the whole vehicle must be considered when examining road damage, rather than individual suspension groups. The issues involved in this interaction are examined in detail in the next chapter.

27.4.6 Tests on Whole Vehicles using Indirect Methods

The results described so far lead to the conclusion that it is necessary to devise a performance test which is able to measure or predict the dynamic tyre forces generated by all axles, for highway conditions. The measurement methods available for achieving this were reviewed in Section 27.2.3 and the test duration requirements were considered in Section 27.4.2. None of the available direct measurement methods are particularly attractive from a practical point of view, because of their high cost of implementation.

Chapter 29 investigates the possibility of performing simple 'indirect' laboratory tests on each vehicle combination, and using the measured responses to simulate the performance of the vehicle under highway conditions. This type of combined measurement and calculation approach may be the only practical way to assess the road-damaging potential of heavy vehicles reliably.

27.5 CONCLUSIONS

(i) (From Chapter 19) For vehicles with similar arrangements of axles and tyres, a simple fourth power aggregate force calculation can be used to compare dynamic loads in terms of normalised pavement fatigue damage.

(ii) (From Chapter 19) The ranking of axle group suspensions depends on the pavement damage criterion used. The *DLC* is unable to distinguish correctly between the road damaging abilities of different axle group suspensions, because it does not take into account the spatial correlation between tyre forces.

(iii) (From Chapter 19) Some air suspended axles on the highway cause high relative road damage, probably due to inadequate suspension damping. Regulations which encourage the use of air suspensions should include a provision for regular damper performance monitoring.

(iv) *Direct* and *indirect* tests on *single axles* (including the European suspension assessment test) cannot be used in an objective assessment procedure, because they do not satisfy several of the basic requirements for objectivity.

(v) It appears to be impractical to base an assessment procedure on *direct* tests using *whole vehicle*. Such a test should satisfy the following requirements:

(a) For a typical road and a vehicle speed of 27 m/s, a test length of at least 250 m is required to measure the 95th percentile tyre force accurately (to within ±5% error). A load measuring mat with sensors placed at 0.4m intervals would require approximately 600 sensors.

(b) A series of tests is needed at different road roughness conditions.

(c) Vehicles must be tested at a range of highway speeds to account for wheelbase filtering effects.

(d) The problem of tractor–trailer interaction must be solved somehow. One way may be to use a standard tractor to test all trailers and vice versa. This possibility is examined in the next chapter.

28
TRACTOR-TRAILER INTERACTION

28.1 SUMMARY

The influence of dynamic interaction between tractor and trailer on the assessment of the road damaging performance of heavy goods vehicles is investigated using simple mathematical models. Tractor and Trailer Damage Indices are used to quantify the 'in-service' road damaging performance of a fleet of vehicles with parametric variations typical of UK highway traffic.

Assessment tests requiring measurements on individual tractor-trailer combinations are simulated and the results are correlated with the performance of the vehicle fleet. The main aim is to establish the characteristics of a 'standard' semi-trailer to be used in the assessment of tractors, and a 'standard' tractor for testing semi-trailers. It is found that measurement of suspension 'frequency' gives the worst correlation with the damage indices, whilst the 'Dynamic Aggregate Force Coefficient' gives the best. Correlation achieved when assessing trailers is higher than when assessing tractors. Optimum specifications for standard tractors and trailers to maximise test accuracy are determined.

This chapter is based on work previously published in [128].

28.2 INTRODUCTION

The simulation study described in Sections 7.4.5 and 7.4.6 showed that articulated vehicles have many natural modes of vibration, and that the dynamic forces generated by an axle cannot be characterised by a single resonance frequency and damping ratio. The study also showed that there is significant interaction between suspensions, that is, the stiffness and damping properties of each suspension affect the dynamic forces generated by each other suspension. In particular, the tractor drive axle suspension was found to have a strong influence over the dynamic tyre forces generated by the semi-trailer axles. This chapter attempts to characterise this interaction for a wide range of tractor-trailer combinations, in order to develop specifications for standard vehicle units that could be used in an assessment test.

28.2.1 Tyre Force Criteria

The Dynamic Load Coefficient (DLC), which is defined by equation 5.6, is commonly used to characterise the level of dynamic tyre force variation. The DLC generated by axle k is denoted D_k. Typical values of DLC are 0.05 to 0.3, a low value generally being considered desirable. As discussed earlier in this book, the DLC is not a good indicator of road damage.

The Aggregate Force criterion considers the sum of all forces applied to particular points along the road by all the axles of the vehicle. The aggregate force history $A(x)$, where x is distance along the road, can be calculated by equation 17.5. The dynamic variation of the aggregate force can be characterised using the Dynamic Aggregate Force Coefficient (DAFC) given by:

$$f = \frac{\text{std}\{A(x)\}}{\text{mean}\{A(x)\}} \tag{28.1}$$

The DAFC is a measure of road damage caused by dynamic forces, normalised by the damage due to the static forces. In this chapter it is the criterion against which other damage criteria will be judged. The road damage analysis can be extended to take account of the sensitivity of road material properties to load level, tyre contact areas, and can also include detailed road response models. However, in Chapter 19 it was shown that the added sophistication of these road damage criteria are not necessary as long as it is only desired to rank the vehicles (rather than calculate absolute road damaging potential) and all the vehicles have the same arrangement of tyres.

In this chapter, D_L and f are calculated for a simple three degree of freedom (DOF) tractor semi-trailer model in the frequency domain, using the method described in Section 25.3.2 (see [125] for details). It is also possible to calculate the DAFC for the tractor axles alone or the trailer axles alone.

To account for the spatial concentration of loading applied by a fleet of heavy vehicles, it is sometimes useful to consider the damage (DAFC) incurred at the worst 5% of locations along the road. This is given by the normalised 95th percentile aggregate force J, which can be calculated using equation 25.13.

28.2.2 Tractor-Trailer Interaction

Potter *et al* [374] used a tyre force measuring mat to collect dynamic tyre force data from a representative sample of British articulated vehicles. This work was described in Chapter 19 and is summarised briefly here. Fourteen articulated vehicle combinations were tested, each comprising one of three tractors (denoted 1-3) and one of five trailers (denoted A-E). The tractors and trailers had a variety of suspension types. Figure 28.1 shows normalised 95th percentile aggregate forces J for the tractors and trailers.

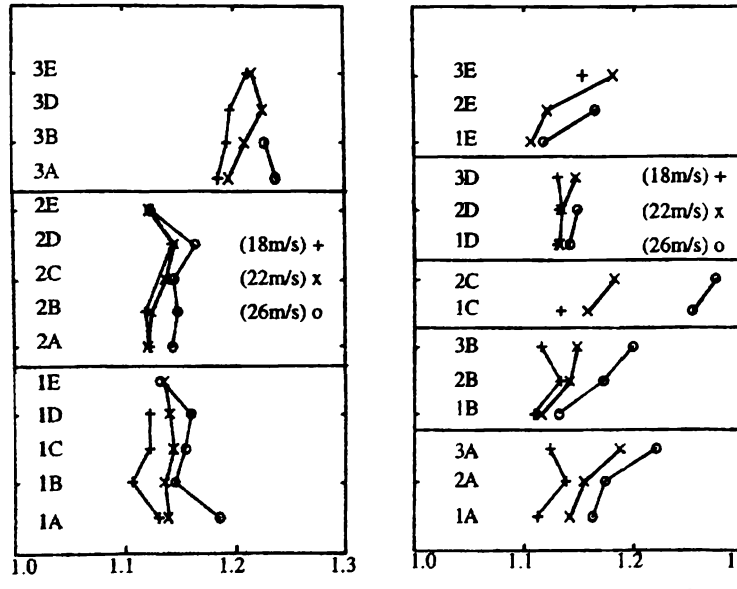


Fig. 28.1 Measured normalised 95th percentile aggregate forces for tractors alone and trailers alone. The number and letter denote the tractor-trailer combination. From [128].

The measured data shown in figure 28.1 confirmed the existence of strong interaction between the tractor and trailer. For example, it was found that the trailer fitted with air suspension (D) consistently generated low road damage for the trailer alone (figure 28.1(b)), but tended to cause the tractors to generate slightly higher road damage than when they were attached to the other trailers (figure 28.1(a)). The air suspended 'road-friendly' tractor (2) caused all trailers to generate higher road damage than when connected to a similar steel-suspended tractor (1), figure 28.1(b), and often caused a higher level of road damage to be generated by the whole vehicle (not shown).

Potter *et al* concluded that trailer suspensions cannot be assessed using a standard tractor because the tractor significantly affects the response of the trailer. However, they considered that it is possible to measure the dynamic loading performance of tractor suspensions using a standard trailer because the trailer does not affect the tractor so strongly.

Cole and Cebon [124] examined tractor-trailer interaction behaviour using two and three degree of freedom (DOF) sprung mass models. The models satisfactorily predicted the measured interaction behaviour, which was explained in terms of wheelbase filtering, natural modes of vibration, and phase relationships between modal responses. It was concluded that the conditions for strong interaction from tractor to trailer exist in a large proportion of articulated vehicles.

28.2.3 Assessment of Road Damage Potential

The review of vehicle assessment in the last chapter concluded that direct tests of whole vehicles are the most accurate ways to assess road-damaging potential. Indirect tests of individual axles, such as the frequency measurement approach of the European test, are considered to be the least accurate. Another possibility is indirect testing of whole vehicle performance, which is discussed in the next chapter.

Whichever assessment test is used, the influence of tractor-trailer interaction must be considered. In service, a trailer will often be used with a wide variety of tractors. Because there is strong interaction between the tractor and trailer, a trailer that performs well in an assessment test with one tractor may perform badly when used in service with a different tractor. The same situation may occur when assessing a tractor which may be used with many different trailers. It is not practical to measure the damaging potential of every possible tractor and trailer combination. A practical test is therefore likely to need a standard tractor for testing every trailer, and a standard trailer for testing tractors.

This chapter addresses three questions: (i) how accurately can a practical test measure the in-service damaging potential of a tractor or trailer, (ii) what is the best vehicle performance parameter to measure, and (iii) what should be the specifications of the standard test tractor, standard test trailer and its payload distribution?

The next section describes the mathematical model employed in the study. Possible test procedures are investigated in Section 28.4. The results of the study are discussed in Section 28.5, and conclusions are given in Section 28.6.

28.3 MATHEMATICAL MODEL

28.3.1 Vehicle Model

The vehicle model is shown in figure 28.2. The two masses represent the tractor and semi-trailer sprung masses. Motion is confined to bounce and pitch so that there are three degrees of freedom. Tandem and triaxle suspensions are each modelled with one parallel spring-damper combination with appropriate parameter values. The unsprung masses are not included since the sprung mass modes of vibration usually dominate the dynamic tyre forces (Section 7.4.3) and are the source of all the tractor-trailer interaction (Section 7.4.6). Subscript 1 denotes the tractor front (steering) axle, 2 denotes the tractor drive axle group and 3 denotes the trailer axle group.

All response calculations were performed in the frequency domain. An input road displacement spectrum was specified to represent the roughness of an average principal road or poor motorway (equation 3.2). Direct and cross-spectral densities of the dynamic tyre forces were calculated over the frequency range 0.1 to 20Hz at intervals of 0.1Hz. See Section 5.4.2 and [125] for details.

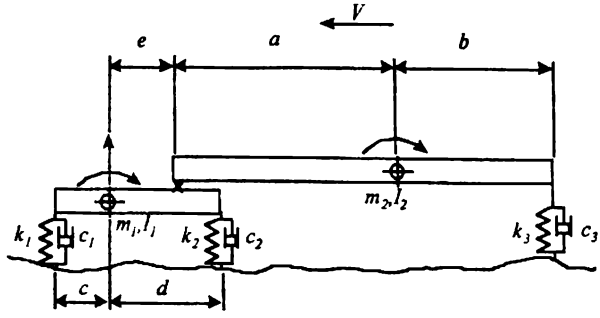


Fig. 28.2 Three DOF tractor and semi-trailer model. From [128].

28.3.2 Validation

The interaction calculation was validated with measurements from the mat tests described in Section 19.3. Nine of the fourteen vehicle combinations were simulated. The parameter values can be found in [124]. The normalised 95th percentile aggregate force J was calculated for the tractor and trailer of each vehicle combination using the frequency domain method described in Section 25.3.2. The road profile spectrum and vehicle speeds were specified to match the test conditions closely.

The results are plotted in figure 28.3, in a format that allows comparison with the experimental results given in figure 28.1. Although there is not exact agreement between figures 28.1 and 28.3, the simulated results clearly show similar trends in interaction between the tractor and trailer. It is concluded that a model which represents only the pitch and bounce motions of the tractor and trailer sprung masses is sufficient to demonstrate the measured interaction behaviour.

28.3.3 Simulation of Vehicle Fleet

A fleet of articulated vehicles was generated by varying the parameters of the three DOF model. Each vehicle consisted of a tractor with two or three axles and a semi-trailer with two or three axles. The vehicle dimensions and axle group weights were chosen to reflect current UK regulations on weights and dimensions. The suspension stiffnesses and damping coefficients were chosen to represent the range typically found in the UK vehicle fleet. The parameter values of each vehicle model were derived as follows.

The following parameters were fixed:

tractor sprung mass	m_1 = 3200kg
tractor pitch inertia	I_1 = 6200kgm^2
tractor geometry	c = 1.4m, d = 2.1m, e = 1.6m
driver axle to trailer axle distance	$a+b$ = 8.5m
steer axle spring stiffness	k_1 = 300kN/m
steer axle damping rate	c_1 = 10kNs/m.

The trailer sprung mass (m_2) and CG position (a/b) were chosen to give axle group masses of:

single tractor drive axle	M_2 = 5250kg
tandem tractor drive axle group	M_2 = 8000kg
tandem trailer axle group	M_3 = 9000kg
triaxle trailer axle group	M_3 = 11250kg.

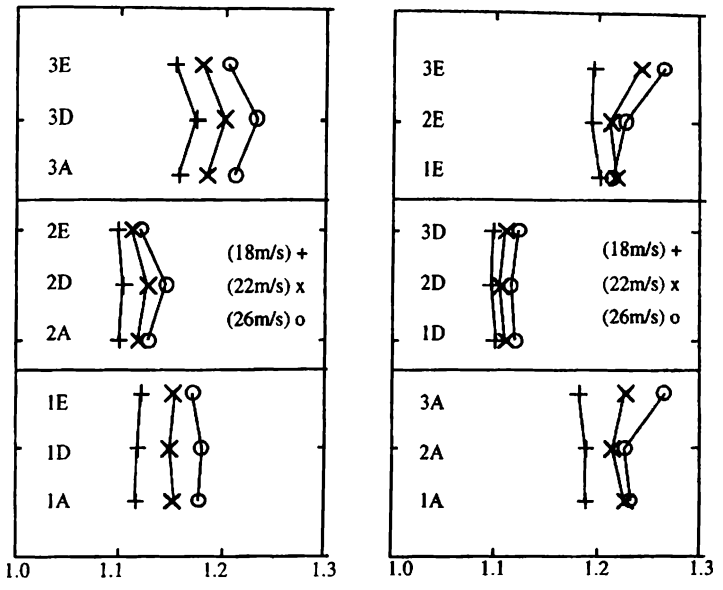


Fig. 28.3 Simulated normalised 95th percentile aggregate forces for tractors alone and trailers alone. The number and letter denote the tractor-trailer combination. From [128].

The trailer pitch inertia (I_2) was varied to account for different payload distributions. The pitch inertia can be written in terms of a normalised radius of gyration r, as

$$I_2 = m_2 abr^2 \tag{28.2}$$

A value of $r = 1$ corresponds to the trailer and payload mass concentrated at each end of the trailer. A value of about 0.85 corresponds to a uniform distribution of payload along the length of the trailer. Smaller values correspond to the mass being concentrated near the centre of the trailer. Values of normalised radius of gyration were set to $r = 0.7$, 0.8, 0.9, or 1.0.

The spring stiffnesses (k_k) of the tractor drive axle and the trailer axle groups were derived from the required natural frequency (p_k = 1.5, 2.0, 2.5, 3.0, or 3.5Hz) of an equivalent single mass/spring/damper system, according to:

$$k_k = M_k(2\pi p_k)^2. \tag{28.3}$$

The damping rates (c_k) of the tractor drive axle and the trailer axle groups were derived from the required damping ratio (ζ_k = 0.10, 0.15, or 0.20) according to:

$$c_k = 2\zeta_k\sqrt{k_k M_k}. \tag{28.4}$$

The frequencies and damping ratios were chosen to reflect the range of values found in the UK vehicle fleet [337].

The four axle combinations, five frequencies and three damping ratios provided thirty unique tractor units and thirty unique trailer units, giving 900 unique tractor and trailer combinations. When

combined with four trailer inertias (that is, four payload distributions) there were 3600 different vehicles in the simulated fleet.

28.4 CORRELATION ANALYSIS

28.4.1 Vehicle Assessment

For the purposes of this study, the in-service road-damaging potential of a tractor number i is quantified as follows. The tractor is connected to each of the trailers in the fleet in turn ($j = 1$ to 30). The DAFC of the whole vehicle is calculated for three speeds ($V_v = 18$, 22, 26m/s) and four trailer pitch inertias r. The average of the resulting 360 DAFC values is denoted $F_{tractor\,i}$:

$$F_{tractor\,i} = \frac{1}{360}\sum_{j}^{30}\sum_{r}^{3}\sum_{v}^{4} f_{i,j,r,v} \tag{28.5}$$

This value quantifies the average in-service road damage potential of the tractor, and will be termed the 'Tractor Damage Index'. The 'Trailer Damage Index' $F_{trailer\,j}$ is calculated in a similar way:

$$F_{trailer.j} = \frac{1}{360}\sum_{i}^{30}\sum_{r}^{3}\sum_{v}^{4} f_{i,j,r,v} \tag{28.6}$$

Figure 28.4 shows the values of tractor damage index for the thirty tractors and values of trailer damage index for the thirty trailers in the simulated vehicle fleet, arranged in ascending order. The figure shows that the tractor damage index varies from 0.12 to 0.18, whereas the trailer damage index varies over a larger range, 0.10 to 0.24. This is a result of the strong interaction from tractor to trailer.

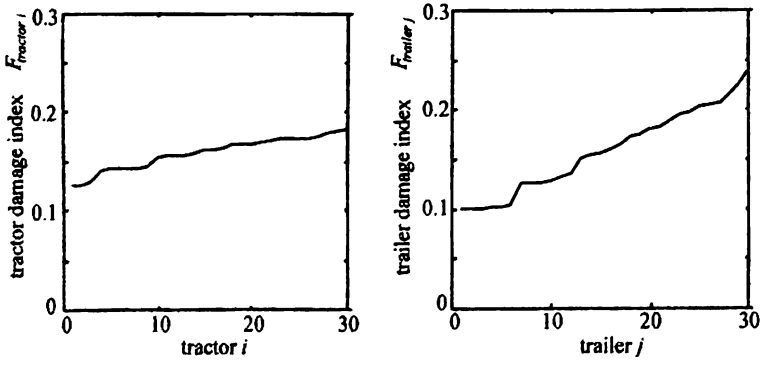


Fig. 28.4 Tractor and trailer damage indices for the simulated fleet, in ascending order. From [128].

28.4.2 Correlation Coefficient

It would be impractical to assess a tractor by averaging the measured damage indices generated by it with many different trailers in the manner described above. An acceptable test might consist of testing a tractor with one standard trailer and payload distribution, perhaps for a range of speeds. The measured vehicle performance parameter and the standard trailer and payload distribution would be specified to maximise the correlation with the Tractor Damage Index defined in equation 28.5. Similarly for assessing trailers, a standard tractor and payload distribution would be specified.

Three vehicle performance parameters for use in an assessment test were investigated: suspension frequencies (p_2 and p_3), DLCs (D_2 and D_3) and DAFC (f). The 'correlation coefficient' ρ_{xy} was used to determine the suitability of each form of assessment test. The correlation coefficient for two variables x and y is defined by equation 18.1. The correlation coefficient takes values in the range −1 to 1. A value of 1 indicates perfect correlation (x proportional to y), and a value of 0 indicates no correlation between x and y. A value of −1 indicates perfect negative correlation (x proportional to $-y$). In the next section the three vehicle performance parameters are investigated in turn, using their correlation with the damage indices to assess their suitability.

28.4.3 Measures of Road Damaging Potential

Suspension Frequency

To determine the suitability of suspension frequency as a measure of tractor road damage potential (as specified in the European test [32]), the Tractor Damage Index $F_{tractor}$ was plotted against the suspension frequency p_2 of the tractor drive axle group for all tractors, shown in figure 28.5a. The correlation coefficient of 0.903 indicates the suitability (or otherwise) of the drive axle suspension frequency p_2 as an assessment parameter for tractors. Ideally the correlation coefficient would be 1.0, with all the points on a straight line with positive slope.

The suspension frequency p_3 of the trailer axle group was correlated with the Trailer Damage Index $F_{trailer}$ for all trailers, shown in figure 28.5b, giving a correlation coefficient of 0.975. This value is much closer to 1.0 than the value of 0.903 obtained for tractors. The reasons for this are discussed in Section 28.5.

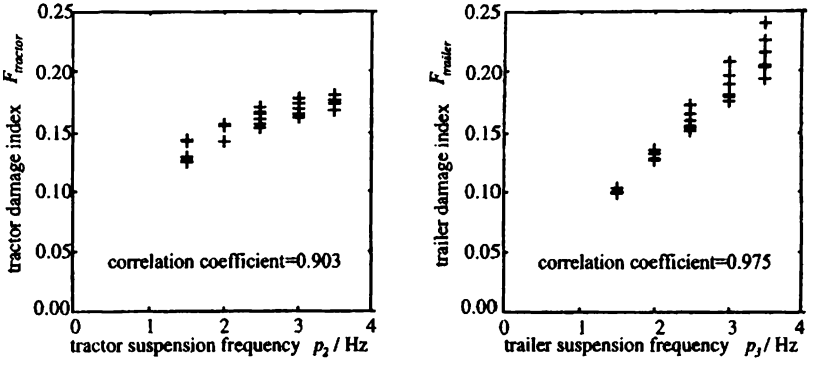


Fig. 28.5 (a) Tractor Damage Index $F_{tractor}$ vs suspension frequency p_2 of the tractor drive axle group.
(b) Trailer Damage Index $F_{trailer}$ vs suspension frequency p_3 of the trailer axle group. From [128].

Dynamic Load Coefficient

Tractors can be assessed by measuring the DLC of the drive axle group D_2. The vertical axis on figure 28.6 shows the Tractor Damage Index $F_{tractor}$ calculated for the thirty tractors of the simulated fleet. On the horizontal axis are the tractor drive axle DLCs D_2 of the same tractors connected to just one of the trailers (2 axles, $p_3 = 1.5$Hz, $\zeta_3 = 0.2$, $r = 1.0$). The correlation coefficient of 0.924 indicates the level of correlation between the drive axle DLC and the Tractor Damage Index for this particular trailer. This gives an indication of the suitability of the parameter D_2 and this particular trailer as an assessment test for tractors. For assessing tractors the objective is to find a trailer specification and payload distribution that maximise the correlation coefficient.

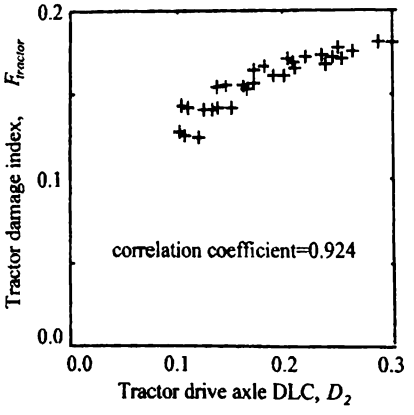


Fig. 28.6. Tractor damage index against tractor drive axle DLC determined with one trailer (2 axles, $p_3 = 1.5$Hz, $\zeta_3 = 0.2$, $r = 1.0$). From [128].

Figure 28.7a shows the correlation coefficient between D_2 and $F_{tractor}$ as functions of the test trailer suspension frequency p_3 and inertia parameter r. The graph contains 120 points, corresponding to the number of trailer suspension and pitch inertia combinations. The graph shows that high values of trailer suspension frequency (p_3 = 3.0Hz or 3.5Hz) and a low value of trailer pitch inertia (r = 0.7) provide the highest correlation coefficients, between 0.950 and 0.963. The number of axles and the damping ratio do not have a strong influence on the correlation.

Trailers can be assessed by measuring the DLC of the trailer axle group D_3. Figure 28.7b shows the correlation coefficient between D_3 and $F_{trailer}$ as functions of the test tractor suspension frequency p_2 and the trailer inertia parameter. The number of axles and the damping ratio do not have a strong influence on the correlation. A tractor suspension frequency at the low end of the range (1.5Hz or 2.0Hz) and a low value of trailer pitch inertia ($r = 0.7$) give the highest coefficients, between 0.995 and 0.998.

The result that a low value of trailer pitch inertia ($r = 0.7$) gives the highest correlation coefficients is surprising and not fully understood. It might be expected that a value of $r = 1$ would give best results, since this value eliminates dynamic interaction between the tractor and trailer. However, the tractor and trailer damage indices ($F_{tractor}$ and $F_{trailer}$) are evaluated on the basis of the whole-vehicle performance. It is thought that some dynamic coupling between the tractor and trailer in the assessment test is necessary to ensure that the tractor or trailer under test is operating in conditions representative of those in the fleet.

Dynamic Aggregate Force Coefficient

Tractors can be assessed by measuring the dynamic aggregate force coefficient (DAFC) f of the whole vehicle. Figure 28.8a shows the correlation coefficient between DAFC and $F_{tractor}$ as functions of the test trailer suspension frequency p_3 and inertia parameter r. The figure shows that a trailer suspension frequency p_3 of 2.0Hz to 3.0Hz and a low trailer pitch inertia ($r = 0.7$) provide correlation coefficients between 0.976 and 0.996.

Trailers can also be assessed by measuring the DAFC of the whole vehicle. The data in figure 28.8b show that correlation coefficients between 0.993 to 0.999 can be obtained if the test tractor suspension frequency p_2 is 2.5Hz or 3.0Hz and the trailer inertia parameter r is 0.8 or 0.9. The number of axles and the damping ratio of the test tractor and test trailer do not have a strong influence on the correlation.

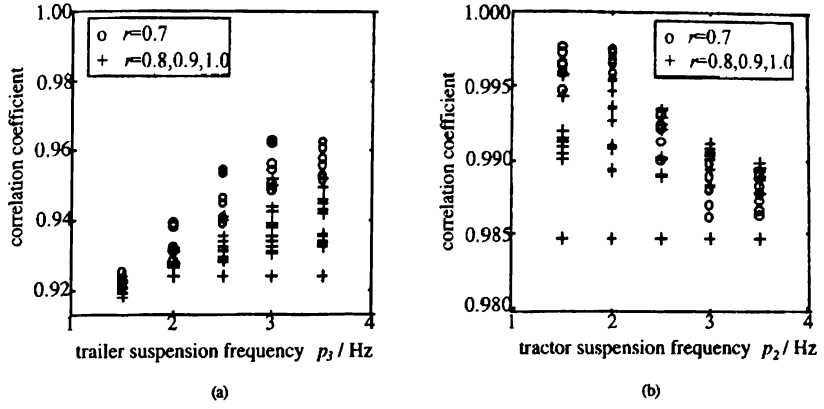


Fig. 28.7 Assessing tractors and trailers: correlation coefficient between D_2 or D_3 and $F_{tractor}$ or $F_{trailer}$ plotted as a function of suspension frequency (p_3 or p_2) and trailer inertia parameter r.
(a) Assessing Tractors, (b) Assessing Trailers. From [128].

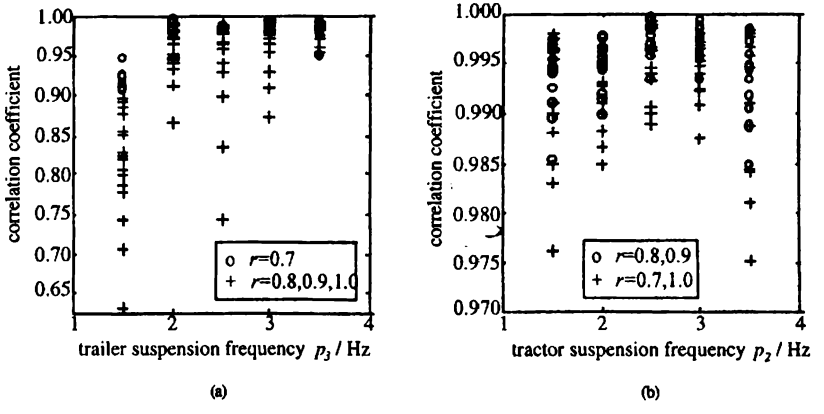


Fig. 28.8 Assessing tractors and trailers: correlation coefficient between DAFC and $F_{tractor}$ or $F_{trailer}$ plotted as a function of suspension frequency (p_2 or p_3) and trailer inertia parameter r. (a) Assessing Tractors, (b) Assessing Trailers. From [128].

Figure 28.9 shows the correlation achievable between Trailer Damage Index and DAFC when the test tractor has one drive axle, with suspension frequency $p_2 = 2.5$Hz, and damping $\zeta_1 = 0.15$. The trailer inertia parameter $r = 0.8$. It can be seen that the points lie very close to a straight line, with correlation coefficient 0.998. This may be contrasted with the scatter of points shown in figure 28.5 corresponding to a correlation coefficient of 0.924.

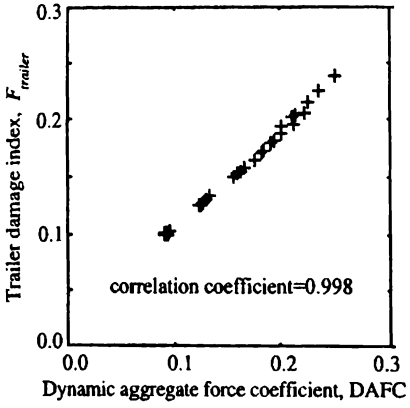


Fig. 28.9 Trailer damage index $F_{trailer}$ against DAFC determined with one tractor (1 drive axle, $p_2 = 2.5$Hz, $\zeta_2 = 0.15$, $r = 0.8$). From [128].

28.5 DISCUSSION OF RESULTS

The results of the correlation analysis are summarised in Table 28.1. It shows the highest correlation coefficients achieved in the simulations, and the corresponding parameter conditions.

	ASSESSING TRACTORS	ASSESSING TRAILERS
Measured Parameter	Correlation Coefficient (Conditions)	Correlation Coefficient (Conditions)
Suspension Frequency	0.903	0.975
Dynamic Load Coefficient	0.950 to 0.963 (p_3 = 3.0Hz to 3.5Hz, r = 0.7)	0.995 to 0.998 (p_2 = 1.5Hz to 2.0Hz, r = 0.7)
Dynamic Aggregate Force Coefficient	0.976 to 0.996 (p_3 = 2.0Hz to 3.0Hz, r = 0.7)	0.993 to 0.999 (p_2 = 2.5Hz to 3.0Hz, r = 0.8 to 0.9)

Table 28.1. Summary of correlation analysis.

In the introduction it was noted that indirect measures of road damage on individual axles, such as suspension frequency, are considered to be less accurate than direct measures on individual axles or whole vehicles (such as the DLC or DAFC). The results in Table 28.1 confirm this: the correlation coefficients calculated between suspension frequency and the tractor and trailer damage indices are the lowest.

It is also clear that the correlation coefficients achieved when assessing tractors are lower than those obtained when assessing trailers. This appears to contradict the findings of Chapter 19, where it was concluded that it was possible to assess tractors with a standard test trailer, whereas trailers could not be assessed using a standard test tractor.

In this study, tractors were assessed in terms of the Tractor Damage Index which is determined from the damage caused by the whole vehicle, not the damage caused by the tractor alone. Because a tractor strongly influences its trailer, measures of tractor damage determined with only one trailer correlate poorly with the Tractor Damage Index determined using a fleet of trailers. This also

explains why the DAFC gives higher correlation coefficients than the tractor drive axle DLC: the DLC does not account for the strong influence of the tractor on the trailer.

A trailer does not influence the tractor so strongly, and so measures of trailer damage made with only one tractor correlate closely with the Trailer Damage Index determined using a fleet of tractors. The DAFC and trailer axle DLC give similarly high levels of correlation because little more information about the performance of the trailer is obtained by considering the tractor axles.

For assessing tractors, the DAFC parameter gives the highest correlation coefficients of the three considered. To achieve best accuracy, the test trailer should have a suspension frequency of 2.0Hz to 3.0Hz and low pitch inertia ($r = 0.7$).

For assessing trailers, the DLC and DAFC parameters both give high correlation coefficients. For the DLC to give best accuracy the tractor suspension should have low frequency (1.5 to 2.0Hz) and the trailer should have a payload distribution that gives low pitch inertia ($r = 0.7$). For the DAFC to give best accuracy, the tractor suspension should have frequency of 2.5Hz to 3.0Hz and the trailer pitch inertia parameter should be 0.8 or 0.9.

This study is a preliminary investigation of the influence of tractor-trailer interaction on the assessment of road damage potential. The vehicle models and damage criteria are very simple, and although the simulated fleet covers most practical vehicles, there has been no attempt to reflect the proportion of vehicle types in service when calculating the tractor and trailer damage indices. It is thought that the conclusions regarding the relative merits of the road damage measures are not strongly affected by these simplifications. However, it is likely that the conclusions regarding the specifications of standard test tractor, trailer and payload will depend strongly on the make-up of the vehicle fleet. A large scale experimental program would be needed to verify the results of this chapter before the preliminary conclusions could be implemented.

28.6 CONCLUSIONS

(i) The existence of dynamic interaction between the tractor and trailer makes accurate assessment of road damaging potential difficult in practice.

(ii) Tractor and Trailer Damage Indices have been defined which quantify the in-service road damaging performance of the vehicles.

(iii) Assessment tests requiring measurements on only one tractor-trailer combination have been simulated. Measurement of suspension frequency gave the poorest correlation with the in-service damage indices. The Dynamic Aggregate Force Coefficient gave the best correlation, and it is thought that this parameter would provide acceptable accuracy for an assessment test.

(iv) Correlation achieved when assessing trailers was higher than when assessing tractors.

(v) Optimum specifications for standard test tractors and trailers were calculated, but these results are likely to depend strongly on the make-up of the vehicle fleet.

29
INDIRECT VEHICLE TESTING

29.1 SUMMARY

Two methods for assessing the road damaging potential of heavy vehicles are described in this chapter. The methods use a simple laboratory test to characterise vehicle dynamics. This information is then used to predict the dynamic tyre forces generated by the vehicle for typical highway conditions. A 'quarter car' laboratory test rig fitted with a leaf spring suspension is used to investigate these methods. Step inputs are used to excite the rig, and various sensors measure the response. A linear technique using the convolution algorithm is investigated initially. A non-linear method using parameter estimation is then examined. The accuracy of both systems is determined by comparing tyre force data measured on the test rig with predicted tyre forces.

This chapter is based on work previously published in [372].

29.2 INTRODUCTION

As discussed in Chapter 27, the most accurate way to assess the *road–damaging potential* of a heavy vehicle is to measure dynamic tyre forces generated by *all* of its axles as it traverses a typical road profile at a typical highway speed. Three such whole vehicle direct test methods have been used previously: (i) the axles of a vehicle have been instrumented with strain gauges [117, 335], (ii) a road simulator (hydraulic vehicle shaker) has been used to excite the vehicle [244], and (iii) a load measuring mat has been installed on a suitable section of road [57, 375]. The main disadvantage of direct tests on whole vehicles is the high cost of the instrumentation.

A less expensive testing option for assessing whole vehicle performance is *indirect* testing. Best [57] investigated a linear indirect technique for estimating dynamic tyre forces in the frequency domain from tests performed on a single axle. The method he proposed was also suitable for multi-axle vehicles. This chapter investigates two additional methods using time domain calculations (needed for road damage predictions as discussed in Chapter 17): the *convolution* method, and the *parameter estimation* method. In Section 29.3, a simple two degree of freedom test rig representing one wheel station of a heavy vehicle is described. The rig is used to investigated the two methods.

Section 29.4 describes the convolution method; this is a *linear* indirect testing method which can be adapted to test a whole vehicle. A measured impulsive response is convolved with a typical road profile input to obtain a predicted tyre force history for one wheel travelling along the road. The road profile may be measured or artificially generated.

The parameter estimation method described in Section 29.5, is a *non-linear* testing method. It uses a step test, from which the parameters of a non-linear vehicle model of the appropriate generic vehicle type are estimated. The model is then used to simulate tyre force histories for the vehicle on a typical road profile.

Both methods can be used with realistic road–damage criteria like those described in Section 17.4 to calculate theoretical road damage for an individual axle, a suspension group, or a whole vehicle.

29.3 TEST RIG

29.3.1 Description

Figure 29.1 shows a diagram of the rig used to investigate the indirect testing methods. Physical constraints on the available testing facilities prevented the testing of full scale truck components, so the design of the rig was based around one wheel station of a leaf-sprung four-wheel drive 'recreational' vehicle (all suspension components were Land Rover parts). Although the rig did not contain the complexities of sprung mass motion that are typical of articulated vehicles, the dynamic tyre forces had a representative frequency content, and the non-linearities are typical. The main structure of the rig was constructed from channel section steel beams. The main beam (sprung mass) pivoted about a pin that passed through holes in the supporting uprights. The axle beam (unsprung mass) pivoted about a ball-joint attached to the underside of the main beam. Extra weights were added to the main beam and axle so that the test rig had realistic natural frequencies for vertical motion.

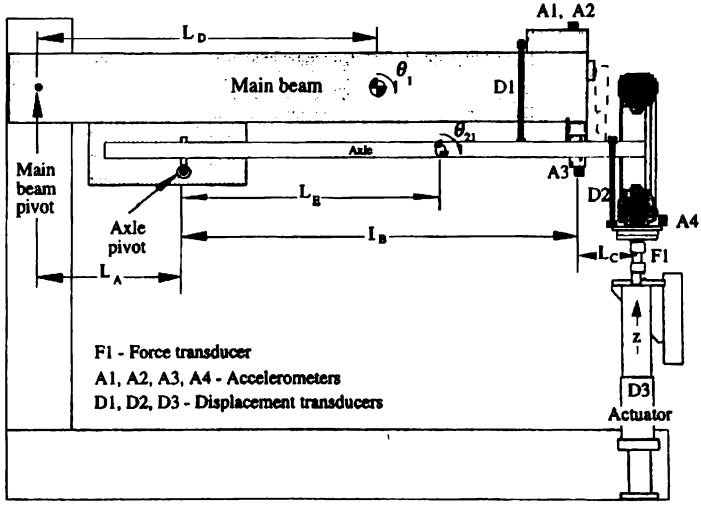


Fig. 29.1 Diagram of test rig. From [372].

A facility for attaching a Land Rover shock absorber in parallel with the leaf spring was also provided. The dashed outline of the shock absorber position can be seen in figure 29.1 at the end of the main beam.

Figure 29.1 also shows the positions of the sensors attached to the rig. Accelerometers (A1-A3) measured motion of the sprung and unsprung masses, and displacement transducers (D1-D2) measured the relative displacements. A load cell attached to the actuator measured the vertical tyre force. The vertical accelerometer attached to the tyre table (A4) enabled the tyre force measurement to be corrected for the inertia of the tyre table. The hydraulic actuator contained an integral displacement transducer (D3), allowing direct measurement of the tyre table displacement (road profile input).

After fabrication, the rig was tested extensively for any unwanted structural vibrations that would interfere with measurements. The main beam had a torsional vibration mode at 27 Hz. Other structural vibration modes were found, but none were below 30 Hz. These vibration modes were at

sufficiently high frequencies to be removed by filtering, without significantly affecting the wheel-hop vibration response at 13-18 Hz.

29.3.2 Mathematical Model of Test Rig

A mathematical model was developed to simulate the test rig. Figure 29.1 shows the geometry of the model, and the co-ordinate system used. Measurements from the rig were translated into this co-ordinate system. The equations of motion for this two degree of freedom model are:

$$\begin{bmatrix} I_P & I_{2Q}+m_2L_AL_E \\ I_{2Q}+m_2L_AL_E & I_{2Q} \end{bmatrix}\begin{Bmatrix} \ddot{\theta}_1(t) \\ \ddot{\theta}_{21}(t) \end{Bmatrix}+\begin{bmatrix} L_A+L_B+L_C & 0 \\ L_B+L_C & -L_B \end{bmatrix}\begin{Bmatrix} f_t(t) \\ f_s(t) \end{Bmatrix}=0, \qquad (29.1)$$

where L_A to L_E are defined in figure 29.1; $\ddot{\theta}_1, \ddot{\theta}_{21}$ are the angular accelerations of the body and of the axle relative to the body; f_s, f_t are the suspension and tyre forces; m_2 is the mass of the axle; I_P is the combined inertia of the body and axle about the main pivot; and I_{2Q} is the moment of inertia of the axle about the axle pivot.

Geometric relationships are required between the tyre and suspension deflections (δ_t, δ_s) and the angular displacements of the rig (θ_1, θ_{21}). These relationships are given by:

$$\begin{Bmatrix} \delta_t(t) \\ \delta_s(t) \end{Bmatrix}=\begin{bmatrix} L_A+L_B+L_C & L_B+L_C \\ 0 & -L_B \end{bmatrix}\begin{Bmatrix} \theta_1(t) \\ \theta_{21}(t) \end{Bmatrix}-\begin{Bmatrix} z(t) \\ 0 \end{Bmatrix}. \qquad (29.2)$$

The tyre model contained a spring element in parallel with a dry friction element. The friction element modelled the friction force between the tyre and tyre table due to distortion of the contact patch. This friction force would not be present if the tyre was rotating. The mathematical description of the tyre model is:

$$f_t(t)=k_t\delta_t(t)+N_t\zeta_t(t) \qquad (29.3)$$

where
$$\zeta_t(t)=\begin{cases} +1 & \text{if } \left(\delta_t(t)-\delta_t(t-\Delta t)\right)>\delta_{thr} \\ \left(\delta_t(t)-\delta_t(t-\Delta t)\right)/\delta_{thr} & \text{if } \left|\delta_t(t)-\delta_t(t-\Delta t)\right|\le\delta_{thr} \\ -1 & \text{if } \left(\delta_t(t-\Delta t)-\delta_t(t)\right)>\delta_{thr} \end{cases},$$

and δ_{thr} is a small (constant) deflection used to smooth the force signal.

The suspension model is a simplified version of Fancher's leaf spring model (equation 4.2). The force generated by the leaf spring (f_l) is a function of the spring displacement (δ_s), given by:

$$f_s(t)=f_l(t)=f_{env}(t)+\left(f_s(t-\Delta t)-f_{env}(t-\Delta t)\right)e^{-\left|\delta_s(t)-\delta_s(t-\Delta t)\right|/\beta}, \qquad (29.4)$$

where
$$f_{env}(t)=\begin{cases} k_s\delta_s(t)+N_s & \text{if } \delta_s(t)>\delta_s(t-\Delta t) \\ k_s\delta_s(t)-N_s & \text{if } \delta_s(t)\le\delta_s(t-\Delta t) \end{cases}$$

N_s is the suspension friction, β is an exponential suspension parameter, and k_s is the leaf spring 'envelope' stiffness. Typical measured leaf spring force deflection curves are shown in figure 29.2.

To use this two degree of freedom model, values were required for three leaf spring parameters, β, k_s and N_s, two tyre parameters, k_t and N_t and two mass parameters, I_P and m_2 (I_{2Q} is a function of m_2). An initial series of tests was performed to measure these parameters directly in order to generate a baseline model for comparison with the parameter estimation method (see later).

Figure 29.3 shows the variation in spring 'envelope' stiffness k_s with amplitude of suspension deflection. These values were obtained by fitting equation 29.4 to the measured suspension force, using a least squares minimisation [370]. These results are for a 1 Hz sinusoidal input. A 5 Hz sinusoidal input was used as well, and the results were found to be independent of frequency as expected [175]. The best fit envelope stiffness k_s was found to increase slightly with static load.

However, from the figure, the deflection amplitude clearly has a much greater effect. For suspension deflections between 2 - 16 mm, k_s varied between 0.1 MN/m and 0.3 MN/m. These results are qualitatively similar to those presented in [89] for similar springs.

Tests were also carried out with a conventional hydraulic shock absorber fitted between the body and the axle. Typical damper force - velocity characteristics are shown in figure 29.4. The suspension force in equation 29.3 was modified to include a shock absorber model consisting of a bi-linear damper in series with a linear spring representing the compliance of the bushes. This three parameter model had the minimum complexity required to give an acceptable fit with experimental data (see Section 4.4).

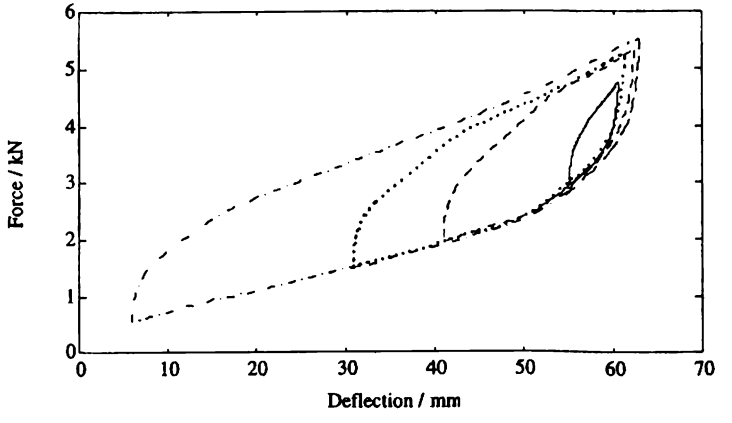


Fig. 29.2 Measured large scale leaf spring force-deflection characteristic. From [372].

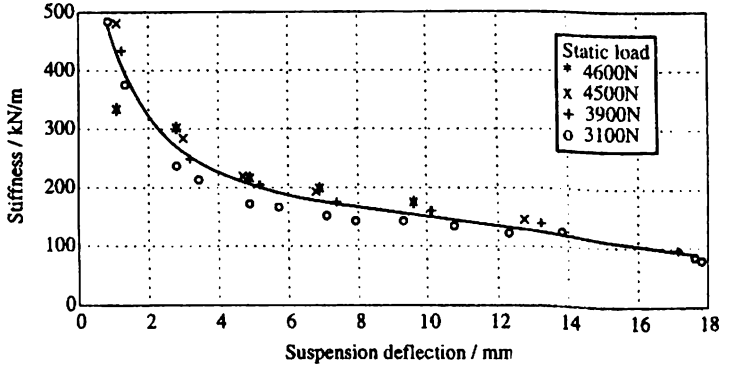


Fig. 29.3 Variation in suspension stiffness k_s with suspension deflection. From [372].

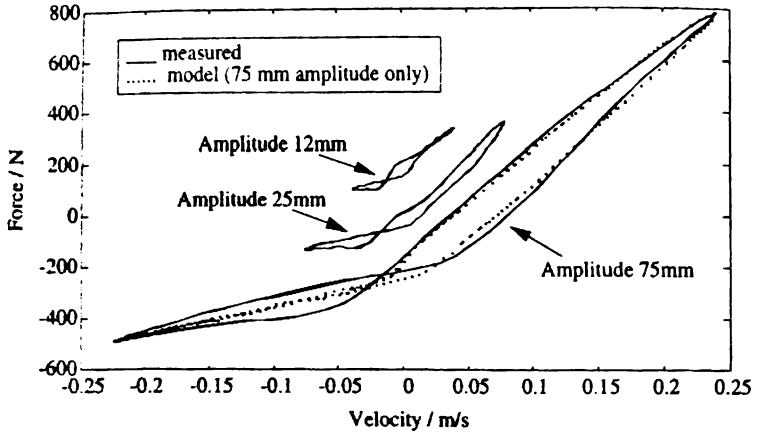


Fig. 29.4 Damper force-velocity characteristic (responses have been shifted by ±200 N for clarity). From [372].

Since the shock absorber was modelled by two elements in series, the displacement and velocity at the point connecting the two elements was required in order to characterise the system. Equating the forces in the shock absorber bush spring and damper elements gives:

$$(v_m - v_b) \times c(v_m - v_b) = k_b \times u_b \tag{29.5}$$

where $c(v)$ is the damper coefficient, given by $\begin{cases} c_b & \text{when} \quad v < 0 \\ c_r & \text{when} \quad v > 0 \end{cases}$

v_m is the velocity across the damper and bush elements, v_b is the velocity across the bush, k_b is the stiffness of the bush, and u_b is the deflection of the bush.

Sensors on the rig or on a vehicle can be used to measure v_m, but v_b and d_b are difficult to measure directly. However, since $v_m >> v_b$, the measured velocity applied to the shock absorber v_m can be used instead of $v_m - v_b$ to evaluate the damping coefficient in equation 29.5 approximately. Therefore, replacing $c(v_m - v_b)$ with $c(v_m)$ in equation 29.5, and putting $v_b = [u_b(t) - u_b(t - \Delta t)]/\Delta t$ gives:

$$u_b(t) = \frac{u_b(t - \Delta t) + v_m(t)\Delta t}{\left(1 + k_b \Delta t_j c(v_m(t))\right)}. \tag{29.6}$$

The force transmitted through the damper, $f_d(t)$ is then given by:

$$f_d(t) = k_b u_b(t), \tag{29.7}$$

and the total suspension force $f_s(t)$ can be found from:

$$f_s(t) = f_l(t) + f_d(t). \tag{29.8}$$

The model parameters found from the initial component tests are given in the second column of Table 29.1.

29.3.3 Model Validation

A random road profile with a spectral density corresponding to a 'good' road traversed at a vehicle speed of 20 m/s (equation 3.1) was used as an input to the rig, and the responses were recorded. Figure 29.5 shows the measured and simulated dynamic tyre forces. The figure shows that the simulated force agrees relatively well with the measured tyre force.

Rig parameter	*Measured values*	*Estimated values*
β	0.88 mm	0.70 mm
k_s	162 kN/m	140 kN/m
N_s	±674 N	±600 N
k_t	297 kN/m	370 kN/m
N_t	±126 N	±130 N
I_P	2970 kgm^2	2950 kgm^2
$I_{2Q} + m_2 L_A L_E$	436 kgm^2	470 kgm^2
c_b	1.10 kNs/m	3.20 kNs/m
c_r	4.40 kNs/m	6.50 kNs/m
k_b	0.40 MN/m	1.20 MN/m

Table 29.1 Model parameters for test rig.

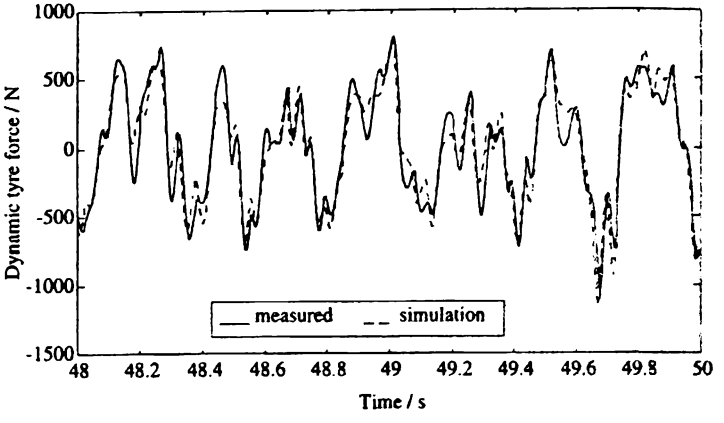


Fig. 29.5 Measured and simulated response to road input excitation for the case with damper fitted. From [372].

29.4 THE CONVOLUTION METHOD

29.4.1 Theory

For a linear system, the convolution integral (equation 10.1) can be used to combine the impulse response function with an arbitrary input. For a digital calculation, it is necessary to convert the integral into a summation using discrete values of the input and the impulse response function.

Consider a vehicle, with a road displacement d_n as the input, and tyre force f_n as the output. If the vehicle system is assumed to be linear, the convolution integral can be used to obtain the response f_n at time $n\Delta t$ by adding together the separate responses to all the small impulses which make up the input time history d_n over the preceding N time steps, according to:

$$f_n = \sum_{r=1}^{N} d_{n-N+r} h_r \Delta t, \tag{29.9}$$

where h_r is the impulse response function, $N = T_{max}/\Delta t$ and T_{max} is the duration of $h(t)$.

Equation 29.9 can be used to determine the tyre force history for any road profile, assuming the system is linear. The dynamics of typical heavy vehicles are non-linear however, which will limit the accuracy of the convolution integral. One purpose of this investigation is to examine the effects of the non-linearities on the accuracy of the method.

In order to obtain the dynamic tyre force impulse response, the axle was excited by a 'non-perfect' step input. For such a discrete input, the transfer function $H(\omega_k)$ between the tyre force f_n and the road displacement input d_n is given by the ratio of their discrete Fourier transforms (DFTs):

$$H(\omega_k) = \frac{F_k}{D_k}, \tag{29.10}$$

where

$$\omega_k = \frac{2\pi k}{N\Delta t} \qquad 0 \le k \le N/2$$

$$F_k = \frac{1}{N}\sum_{r=0}^{N-1} f_r e^{-i(2\pi kr/N)} \qquad k = 0,1,2,....,(N-1)$$

and

$$D_k = \frac{1}{N}\sum_{r=0}^{N-1} d_r e^{-i(2\pi kr/N)} \qquad k = 0,1,2,....,(N-1).$$

The impulse response function h_r was obtained from the transfer function $H(\omega_k)$ using the inverse DFT:

$$h_r = \sum_{k=0}^{N-1} H(\omega_k) e^{i(2\pi kr/N)} \qquad r = 0,1,2,....,(N-1) \tag{29.11}$$

which can be calculated using the FFT algorithm.

The convolution method can easily be extended to vehicles with P axles with the same input on each side (*ie* pitch-plane calculation). In this case equation 29.9 becomes:

$$\begin{bmatrix} f_{1,n} \\ \vdots \\ f_{j,n} \\ \vdots \\ f_{P,n} \end{bmatrix} = \sum_{r=1}^{N} \begin{bmatrix} h_{11,r} & \cdots & h_{P1,r} \\ \vdots & h_{jk,r} & \vdots \\ h_{1P,r} & \cdots & h_{PP,r} \end{bmatrix} \begin{bmatrix} d_{n-N+r} \\ \vdots \\ d_{n-N+r-a_{r1}/V} \\ \vdots \\ d_{n-N+r-a_{P1}/V} \end{bmatrix} \Delta t. \tag{29.12}$$

The method can easily be extended to three–dimensional models if left–hand and right–hand wheel path profiles are known.

The accuracy of the convolution method can be quantified by comparing its output with experimental results. The RMS difference e between two dynamic force histories $f_{t1}(t)$ and $f_{t2}(t)$ is first calculated. The 'Normalised RMS Error' (*NRE*) is defined as:

$$NRE = \frac{e}{\sqrt{\overline{f_{t1}^2(t)}}}, \tag{29.13}$$

where $e = \sqrt{\overline{(f_{t1}(t) - f_{t2}(t))^2}}$, and $\overline{f_{t1}(t)}$ is the time averaged value of $f_{t1}(t)$.

In order to interpret the magnitude of the *NRE* for errors between measured and estimated maximum tyre forces, the RMS dynamic tyre force error, e can be normalised by the static tyre force f_{stat}. The normalised error with respect to the static tyre force (the Error Coefficient of Variation or '*ECOV*') is therefore e/f_{stat}. The Dynamic Load Coefficient (*DLC*) is the ratio of the RMS dynamic tyre force to the static tyre force, so:

$$ECOV = DLC \times NRE. \tag{29.14}$$

A typical value of *DLC* for heavy vehicles travelling at highway speeds over a poor quality road is 0.25 (Section 7.4.2) Using this value, an *NRE* of 40% will give an *ECOV* of 10%. Assuming a narrow band (sinusoidal) dynamic tyre force, there will be a 10% error between the estimated maximum tyre force and the measured maximum tyre force. An *NRE* of 40% is therefore considered to be an acceptable (threshold) level of error. See [370] for further details.

29.4.2 Experimental Investigation

Results obtained from tests using the rig described in Section 29.3 were used in an experimental investigation of the convolution method. A smoothed step input was used to excite the rig, and displacement input and tyre force response signals were recorded. Equation 29.10 was then used to generate transfer functions for data from different amplitude inputs.

Figure 29.6 shows three experimentally determined transfer functions for different step heights. The results show clearly the effect of non-linearities on $H(\omega_k)$. If the experimental vehicle was linear, the transfer functions would be independent of the input amplitude – *ie* all three curves would be the same. As the step height increases: the amplitude of the low frequency bounce vibration decreases; the amplitude of high frequency wheel-hop vibration increases; and the two resonance frequencies decrease. It is interesting to note that although the frequency of the wheel-hop resonance decreases with step height, the 20 mm response shows an additional peak at the same frequency as the 4 mm response. There is also an anti-resonance at around 5 Hz, which is thought to be an artefact of the actuator or the test rig.

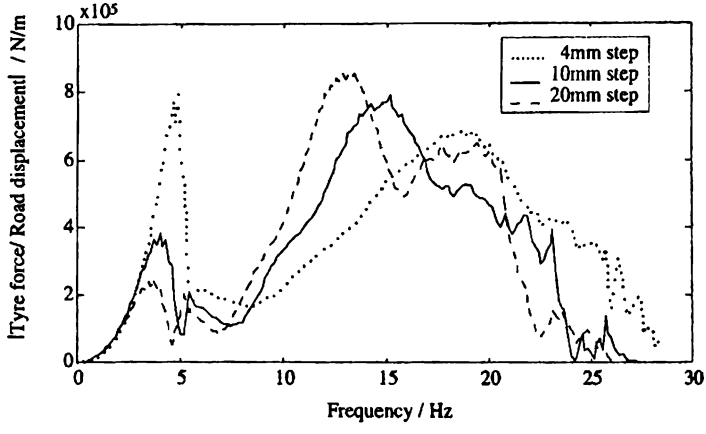


Fig. 29.6 Experimentally determined transfer functions. From [372].

Impulse response functions were calculated from the transfer functions in figure 29.6, using equation 29.11, and these are shown in figure 29.7. The frequencies and amplitudes of the various vibrational components can be seen to vary with the input amplitude.

The rig was also used to generate tyre force histories from random road profile inputs. Nine road profiles (three roughness levels) were used in conjunction with 21 impulse responses (seven different input amplitudes) to generate a series of convolved tyre force histories. These estimated tyre forces were compared with the measured tyre force histories using the *NRE*. An example is given in figure 29.8 for an impulse response generated from a step test of amplitude 10 mm, convolved with a smooth road profile. For this data, the *NRE* was 150%.

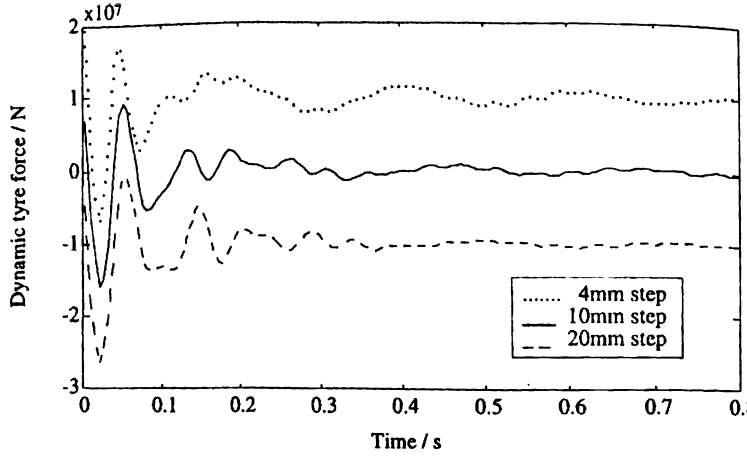


Fig. 29.7 Unit impulse responses calculated from the transfer functions in figure 29.6. Responses shifted by ±10 MN for clarity. From [372].

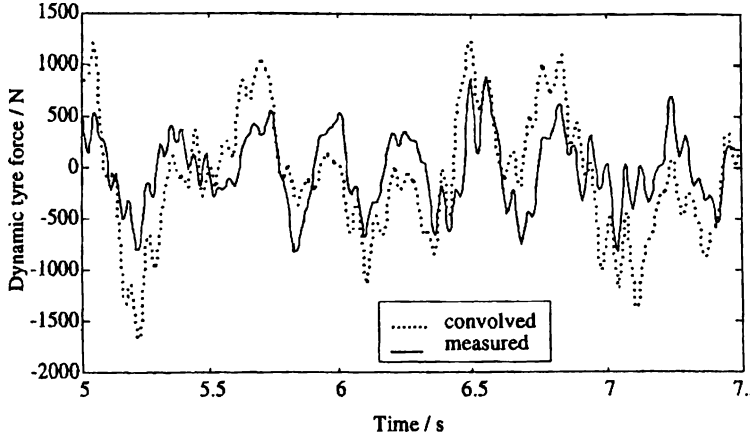


Fig. 29.8 Tyre force histories for a smooth road. The convolution calculation used the impulse response from a 10 mm step test. From [372].

Figure 29.9 shows the *NRE* plotted against the amplitude of the step input used to generate the estimated tyre force. The graph shows that the optimum step height for minimum *NRE* increases with increasing road roughness, as expected. One other feature is that the *NRE* increases with road roughness. The magnitudes of errors seen in the experimental results essentially rule-out the convolution method (or any other *linear* method) for assessing the tyre forces generated by leaf spring suspensions.

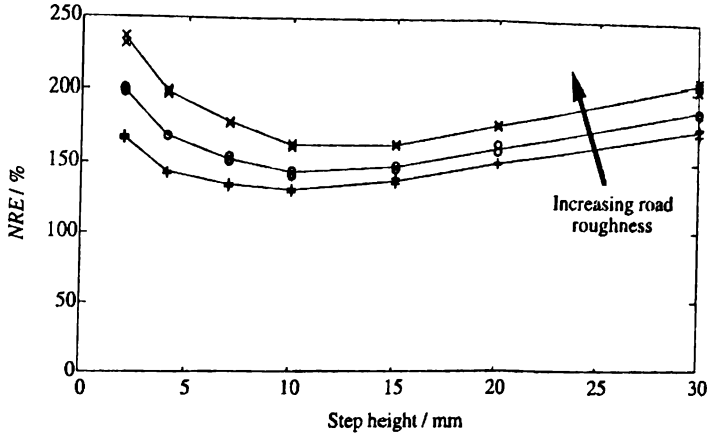


Fig. 29.9 *NRE* vs. step height for convolution method (smooth roads). From [372].

29.5 PARAMETER ESTIMATION METHOD

The *parameter estimation* method involves developing a mathematical model of the dynamics of the vehicle and suspension system, by determining experimentally, a set of parameters for a generic nonlinear vehicle model.

There are a number of issues that need to be resolved in order to use the parameter estimation method in practice:

(i) A generic vehicle model is required. In this study, the simple two degree of freedom model described in Section 29.3 is used. However, the method could be extended to include multiple axles and sprung mass pitching motions.

(ii) The parameter estimation procedure must be developed. The field of parameter estimation is large (see review by Kallenbach [268]). The method developed in this chapter is effective for the system investigated.

(iii) In order to estimate vehicle parameters, instrumentation is required to measure response quantities in the indirect test. For the tests described in this section, accelerometers and displacement transducers were attached to the experimental rig. A force transducer was used to record tyre loads, but this was not physically attached to the rig (vehicle). This system of transducers was found satisfactory for characterising the dynamics of the rig, and was relatively straightforward to set up, compared to other instrumentation such as strain gauges. Similar instrumentation could easily be attached to a test vehicle in a 'commercial' implementation of the test.

(iv) A simple repeatable road profile input is required to excited the dynamics of the vehicle. A smoothed step input was chosen for this series of tests. This input allowed the tyre and tyre table to remain in contact throughout the transient motion of the rig, at the same time as exciting the natural frequencies of the vehicle that are important for road damage (body bounce and wheel-hop). Such an input could be implemented cheaply in a real vehicle test.

29.5.1 Parameter Estimation

The set of equations used for parameter estimation consisted of the vehicle model equations 29.1 - 29.8. The parameters were estimated in four groups: (i) inertia parameters; (ii) tyre parameters; (iii) leaf-spring parameters; and (iv) damper parameters. For each group of parameters, a set of algebraic equations was obtained for each time step of the simulation:

$$M_t - E_t(p_1, p_2, p_3, ...) = \varepsilon_t. \tag{29.15}$$

where M_t and E_t are the measured and estimated variable at time t, p_i is the set of parameters being estimated, and ε_t is the error.

The parameter values were optimised to minimise the sum of the squared error over all time steps. A numerically efficient solution technique was used to solve these least squares problems [203]. The algorithm found the minimum of a constrained multi-variable function. This allowed constraints to be placed on the parameters, to improve the efficiency of the method. Approximate parameter values were assumed to be known, and constraints were set one order of magnitude above and below these values (it is reasonable to make this assumption for the current problem). See [203] for further details.

A series of tests was performed using step inputs of different heights to investigate the effect of system non-linearities on the parameter estimation. For each step input, the body and axle accelerations, the body and axle displacements and the tyre force responses were recorded. Tests were carried out for two configurations of the rig: with and without the hydraulic damper fitted. The parameter values determined by this method are given in the third column of Table 29.1 for a step height of 20 mm.

Table 29.2 provides a summary of the fitting strategy. Mass parameters were estimated using the body and axle acceleration, and the tyre force response, as indicated in the first row of Table 29.2. The sum of squared error between the estimated tyre force (the product of accelerations and mass parameters), and the measured tyre force was minimised. A very good fit was obtained with the RMS error between the two tyre force histories typically 15 N for all step heights. There was less than 5% variation in estimated inertia with step height. For both the sprung and unsprung inertias, the estimates found using equation 29.1 agreed well with the values given in the second column of Table 29.1.

Tyre parameters were estimated using the tyre force and tyre deflection responses, as shown in the second row of Table 29.2. The sum of squared error between the estimated tyre force (the RHS of equation 29.3, and the measured tyre force was minimised. Figure 29.10 shows the fitted (estimated) and measured dynamic tyre forces for a 15 mm step up. In general there is reasonable agreement between the two force histories, although the estimated data shows a greater high frequency content than the measured data. The RMS error between the measured and estimated tyre forces varied between 50 N for small steps (4 mm) and 100 N for large steps (30 mm).

The suspension force and deflection can be measured (indirectly and directly respectively) on the rig. The velocity across the suspension can be found by differentiating the deflection. With this information, it is theoretically possible to calculate both the three leaf spring and the three damper parameters required to characterise the suspension system using equations 29.3 - 29.8. In practice however, the parameter estimation procedure was not able to identify the six damper and leaf spring parameters simultaneously, because several of the model parameters have similar effects on the vehicle dynamics, and these conflict during the optimisation process. To overcome this problem, the leaf spring parameters were found first, by testing the vehicle model with the damper disconnected. The damper was then reconnected and a second series of tests was performed in order to estimate damper parameters.

In practice, it would be straightforward to disconnect the dampers from the vehicle and perform a first test to estimate leaf spring parameters, and then reconnect the dampers and carry out a second

test. (Alternatively, a quasi-static test could be used to estimate leaf spring parameters [114] without the need to disconnect the damper.)

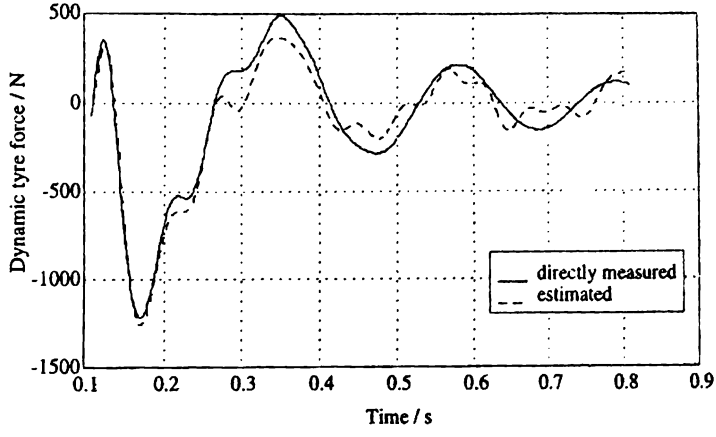


Fig. 29.10 Dynamic tyre force response to 15 mm step up. From [372].

Order	*Estimated parameters*	*Quantities used in error calculation*	*Equations used for estimates*	*Signals used for estimates*
1	Inertia parameters $(I_P,\ I_{2O}+m_2L_AL_E)$	Tyre force (measured)	29.1	$\ddot{\theta}_1(t),\ \ddot{\theta}_{21}(t)$
2	Tyre parameters $(k_t,\ N_t)$	Tyre force (measured)	29.3	$\delta_t(t)$
3	Leaf spring parameters $(k_s\ N_s,\ \beta)$	Spring force (estimated from eq. 29.1)	29.4	$\delta_s(t)$
4	Damper parameters $(c_b,\ k_b,\ c_r)$	Suspension force (estimated from eq. 29.1)	29.8	$\delta_s(t), \dot{\delta}_s(t)$

Table 29.2 Summary of parameter fitting strategy.

29.5.2 Results for the Suspension With No Damper Fitted

Leaf spring parameters were estimated using the measured suspension deflection, and the suspension force, as indicated in the third row of Table 29.2. This force was not measured directly, but was determined using equation 29.1. The sum of squared errors between the estimated spring force (RHS of equation 29.4) and the 'measured' spring force (from equation 29.1) was minimised. Figure 29.11 shows variation of the estimated leaf spring stiffness envelope (k_r) with input step height. These suspension parameter estimates are similar to values determined from sinusoidal tests documented in Section 29.3 (figure 29.3).

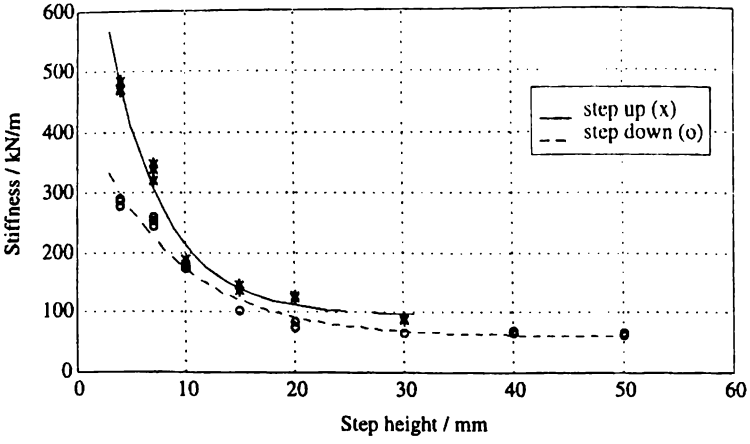


Fig. 29.11 Suspension stiffness estimate for rig with no damper fitted. From [372].

The estimated leaf spring stiffness changes rapidly for step inputs in the range 0-15 mm. For step heights above 15 mm, the parameter estimates do not change much. This indicates that step heights above 15 mm are likely to give the best parameter estimates.

These parameter estimates indicate that the largest errors in the model of the rig arose from the leaf spring model. However, the RMS force errors were less than 10% of the static load, which is probably acceptable, given the simplicity of the generic leaf spring model.

The parameter estimates were used in a non-linear vehicle simulation. A random profile was used to excite the rig, and the same (measured) road displacement was used as an input to the simulation. The simulated dynamic tyre force response was then compared with the measured tyre force history.

A typical tyre force history is given in figure 29.12 for a smooth road profile (corresponding to a 'good' primary road). The parameters used for the non-linear model in the simulation were determined from a 15 mm step *down* test. There is good similarity between the estimated and measured tyre forces. Figure 29.13 shows the spectral densities of the same data. This shows the discrepancies between estimated and measured tyre forces more clearly. The estimated tyre force has a bigger wheel-hop response (15 - 20 Hz), and a smaller body bounce response (2 - 5 Hz).

Figure 29.14 summarises the results from simulations using models with parameters estimated from the full range of step heights over which tests were performed. *NRE*s were calculated for a range of relatively smooth road roughnesses. The speed of the vehicle model was 20 m/s, which resulted in measured *DLC*s of 0.07 - 0.12. Tests were carried out for step inputs up to 50 mm. For steps larger than this, the tyre table reached the end of its travel during the transient motion. Large errors between estimated and measured tyre forces were generated using parameter estimates from step heights of less than 15 mm. For small steps, there is not sufficient excitation to identify the parameters of the leaf spring model correctly. This can be seen in figure 29.11 where the stiffness estimate changes rapidly for small step heights.

As the step height increases above 20 mm, the *NRE* increases slightly. This is because the measured large scale force - deflection envelope in figure 29.2 is curved for large deflections, and not straight, as assumed in the model. This is also the reason why the *NRE* increases with road roughness.

For step heights between 15 and 30 mm, the *NRE* is at or below 40%. This is considered to be a reasonable threshold accuracy (equation 29.14) which indicates that for this type of suspension, the parameter estimation method probably gives sufficient accuracy to estimate the dynamic tyre forces for use in an assessment test.

The non-linear method is much more accurate than the convolution method described in the previous section (figure 29.9), which showed a minimum experimentally determined *NRE* of over 130%.

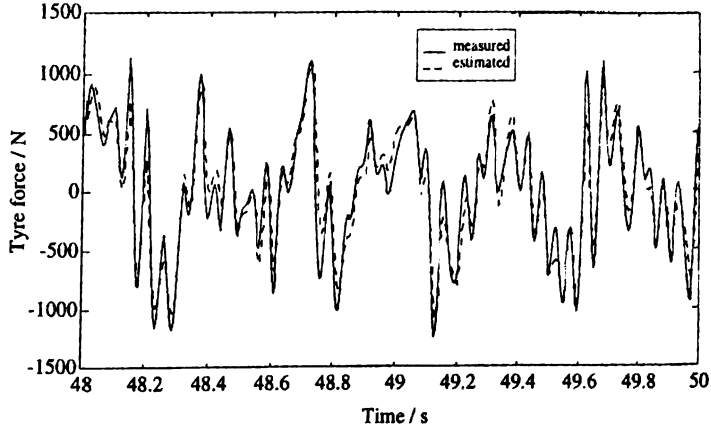


Fig. 29.12 Tyre force history for rig with no damper, smooth road (model parameters from 15 mm step down test). From [372].

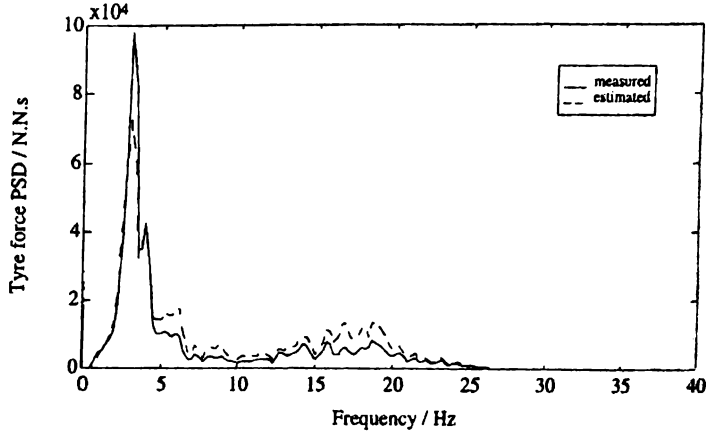


Fig. 29.13 Tyre force spectral densities for data in figure 29.12. From [372].

29.5.3 Results for the Suspension With Damper Fitted

Damper parameters were determined from the suspension force (equations 29.8 and 29.1). The damper parameters were first estimated using the responses to separate step up and step down tests. These two tests were found to yield very different parameter values. This is not surprising, since the damper has different rates for extension and compression, and the initial damper force for steps up and down will be compressive and tensile respectively. Damper parameters were therefore estimated from an input signal comprising both a step up *and* a step down.

The leaf spring parameters used in this section were those found in Section 29.5.2 (*eg* figure 29.11). The estimated mass and tyre parameters were very similar to results for Section 29.5.2. The main difference was a slight increase in the unsprung mass estimate, as the damper was attached to the axle, adding to its effective mass.

Using the parameters estimated from a 15 mm combined step-up and step-down test, the vehicle model was simulated over a random road profile, and results compared to experimental measurements. Figure 29.15 shows part of the time history for a smooth road and a vehicle speed of 20 m/s. The responses show reasonably good agreement.

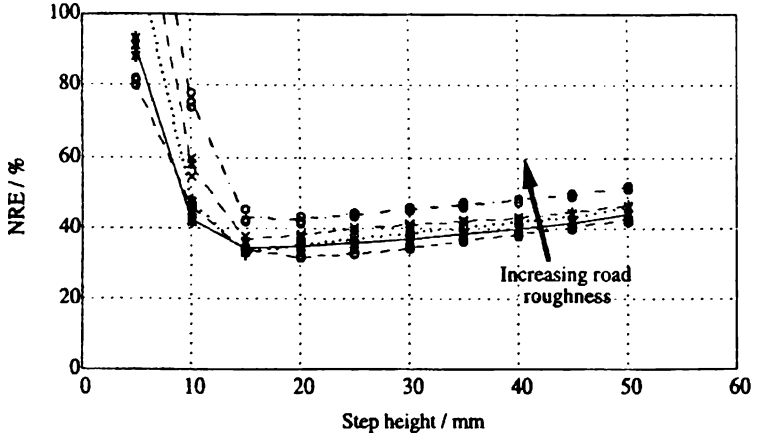


Fig. 29.14 *NRE* vs. step height for simulation using parameters obtained from step down tests (rig with no damper fitted). From [372].

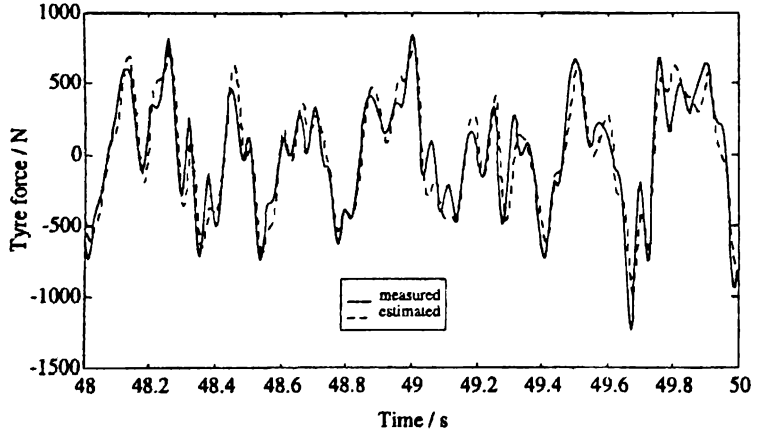


Fig. 29.15 Tyre forces for rig with damper fitted, smooth road (model parameters from 15 mm step tests).

Figure 29.16 shows results for a range of step heights in the parameter measurement (smooth road and speed of 20 m/s). For all step heights above 10 mm, the *NRE* is below the threshold level of

40%, indicating that this method would probably provide acceptable accuracy for an assessment test. The graph is similar to results for the test rig with no damper fitted (figure 29.14).

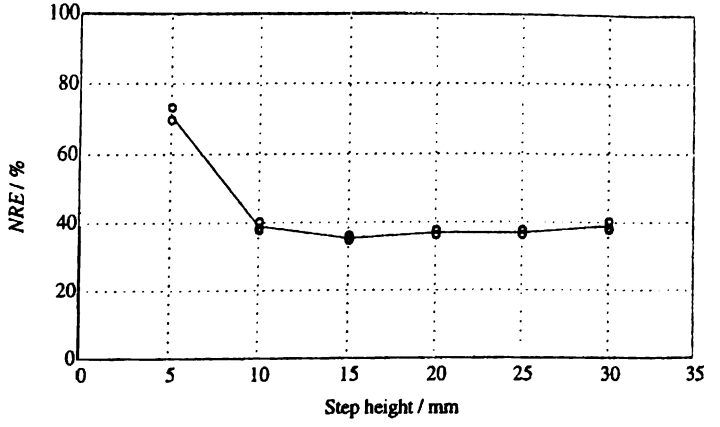


Fig. 29.16 *NRE* vs. step height for simulation for rig with damper fitted. From [372].

29.6 CONCLUSIONS

(i) An experimental investigation of the convolution method over a limited range of road roughnesses (smooth roads only) showed unacceptably large errors with a minimum *NRE* of 130%.

(ii) The experimental results show that the optimum step height for the convolution method increases with increasing road roughness, and also that the *NRE* increases with increasing road roughness. The optimum level of step input varies from about 10mm to 15mm. It is a function of the non-linearities in the suspension, and the combination of road roughness and vehicle speed for which the tyre forces are to be predicted.

(iii) Parameters for a leaf spring and a bilinear damper were successfully estimated using step input tests with step heights above 15 mm. A step-up *and* a step-down test are required to obtain accurate parameters for the hydraulic damper.

(iv) The best method for estimating all six spring and damper parameters is to perform two series of step tests on the vehicle, one with the damper removed, and one with the hydraulic damper fitted.

(v) It was possible to estimate the parameters of a leaf spring vehicle, with and without a hydraulic damper, with a *NRE* less than the threshold level of 40% for a wide range of speed and roughness input levels. The parameter estimation method for assessing the dynamic tyre forces of vehicles is therefore viable.

It remains a topic of future research to implement the parameter estimation method for a full-scale vehicle.

30
IMPLEMENTATION ISSUES AND RECOMMENDATIONS

30.1 SUMMARY

The discussion of Part 7 of the book on suspension assessment are reviewed. It is concluded that the most practical method of assessment testing would be to use a 'type approval' test on new vehicle models, combined with annual inspections of every vehicle to ensure adequate performance in-service. Various testing methods are discussed.

30.2 IMPLEMENTATION ISSUES

30.2.1 The Move to Air Suspensions

Whether or not it is technically correct from a 'road-friendliness' perspective (see Chapters 19, 22, 27), the overwhelming weight of technical opinion is currently pushing heavy vehicle suspension regulations towards soft, hydraulically-damped systems. This almost inevitably means *air* suspensions, even though there are feasible alternatives, such as torsion-bar suspensions. Air suspensions have the additional advantages of good ride performance, and a constant ride height, independent of the static load and stiffness. These factors are driving their wide-spread adoption, world-wide.

Current European regulations encourage the use of air suspensions (or "equivalent"), by providing a one tonne payload incentive [32][1]. These regulations control the adoption of new suspensions, but have no provision for controlling the performance of the suspensions in-service. From the limited results shown in Chapter 19, it appears that some air suspensions can generate very high dynamic loads - probably because they have inadequate damping. It is thought that this is due to hydraulic dampers being fitted incorrectly, or poorly maintained[2]. This has the effect of increasing the road damage done by these vehicles. The only way to alleviate this problem is to have a requirement for adequate in–service damping for all suspensions.

30.2.2 Type Approval or Annual Test?

In the UK, heavy vehicles have to pass 'type approval' tests in order to use the road network. These currently assess brakes, emissions, structural integrity *etc.* They are performed *once* for each make and model of vehicle. Tractors and trailers are tested separately. A re-test is only necessary if the

---

[1] The regulations consider *any* air suspension to be 'road-friendly', but only those steel leaf spring suspensions having appropriate natural frequency and damping characteristics. Air suspensions are not required to have adequate damping levels, when new or in-service.

[2] Previous studies investigating dynamic tyre forces (eg those described in Chapter 7) have used well maintained vehicles, with good damping. The poor in-service performance of some air suspensions has not previously been identified.

specification of the vehicle changes. The *vehicle manufacturer* is responsible for ensuring that the vehicle unit passes the tests. Once a vehicle is in use, its *operators* are responsible for ensuring that it passes an annual inspection test which certifies the truck to be road-worthy. This includes, for example, dynamometer testing of brake performance. A test to assess road damage could, in principal, fit into either category of testing procedure: type approval or annual inspection.

It is important to note that the objectives of a type-approval test and an annual inspection may be quite different. While the former may need to test for 'road-friendliness', the latter may only need to check that the suspension is adequately maintained – *ie* has working dampers, and low dry friction levels. If different tests are used in each case, then it is important to consider how the two are related. (A good approach may be for the annual inspection to use *one component* of the overall type-approval testing procedure.)

A *type-approval* test would be relatively inexpensive to run, since only one test is needed per vehicle make and model. It could be performed at a central national test site if desired. However, if this test was the only component in the suspension regulation system (as it is currently in Europe), it would inevitably lead to vehicles which passed the test when new and well maintained, but had poor performance after a period of operation, particularly due to worn dampers.

An *annual* test of 'road-friendliness' would probably not be a viable option, because of the large infrastructure needed to test the whole vehicle fleet (see below). However an annual inspection of damper performance would appear to be feasible.

Thus a *combination of type approval and annual inspection tests* would seem to provide the best balance between the cost of regulation and road-damage generated by the vehicle fleet.

30.2.3 Type-Approval Tests

The Technically Rigorous Solution

Chapters 27 to 29 discussed the issues involved in 'technically rigorous' assessment of road-friendliness. Because the vehicle and road systems are complex, there is no 'quick fix' testing system. The only way to assess road-friendliness (satisfying all of the requirements of Table 27.1) is to predict theoretical road damage for a given vehicle. This requires information about the dynamic tyre forces generated by *all* axles of the vehicle, for a range of typical operating conditions. *Measuring* or *predicting* these forces requires elaborate methods.

Measurement (Direct Tests)

Road simulators or load measuring mats are viable options for measuring the dynamic tyre forces generated by all axles of many vehicles. Alternatively, each vehicle could conceivably be fitted with force measuring hubs on all wheels.

It would be necessary to have 'standard' tractor and trailer units available at each testing site. These units would need to be specified using a methodology similar to that described in Chapter 28. A range of testing speeds and road excitations would be required. If road tests were to be used (as for a load-measuring mat or instrumented hubs), great care would need to be taken over the design/specification of the road surface profile, and to ensure that it remained the same shape over time.

Any of these direct testing systems would be expensive to build and operate, and could only be implemented at a few national test sites.

Predicting Dynamic Tyre Forces (Indirect Tests)

Indirect tests would be a much cheaper and more efficient solution than direct tests on whole vehicles[1]. The testing procedure would probably require a hydraulic actuator (with force and displacement transducers) which would apply a controlled displacement input to each axle of the vehicle in-turn. Simple removable instrumentation (accelerometers and LVDTs) mounted on the vehicle would be used to measure relevant responses. Tests would be required with and without the hydraulic dampers fitted to the suspensions.

The measured responses would be used to *estimate* the parameters of a generic non-linear vehicle model, so as to generate an accurate mathematical model of the test vehicle unit. Mathematical models of 'standard' tractor and trailer units could be developed using the same process (this would only need to be done once). These could be coupled mathematically to the model of the test vehicle. The whole (articulated) vehicle model could then be exercised in a computer, to calculate its responses to various input conditions. Road-friendliness could be assessed, using realistic road-damage criteria.

It would even be possible to simulate a 'fleet' of vehicles incorporating the tractor or trailer of interest, with a wide range of different attached vehicle units, and so calculate the average road damage done by that vehicle unit in-service. (This might resemble the simulation approach used in Chapter 28). The experimental identification of vehicle characteristics would only need to be performed once for the tractor units or the trailer units in isolation.

A Pragmatic Approach

Soft, hydraulically-damped suspensions generate smaller RMS dynamic tyre forces than other suspensions. Unfortunately, this does not guarantee that they are more 'road-friendly' for the reasons discussed in Chapter 27. Nevertheless, a widely held pragmatic view is to encourage their use, in the hope that, on average, this will reduce road damage.

In this case, the parameters which should be measured and controlled are the overall vertical stiffness and damping of the suspension (alternatively the 'bounce' natural frequency and damping ratio), and the damping of any unsprung-mass bounce or bogie pitch modes.

If suspension frequency and damping are to be assessed, then there are two key pitfalls. These prevent the European test [32], from satisfying requirements 2 to 4 in Table 27.1. They can easily be avoided, so as to make the testing process more objective.

Accounting for Sprung-Mass Characteristics

The aim of the test should be to measure the performance of *the suspension* – not the characteristics of a *vehicle and suspension combination*. There are two problems with testing a suspension while it is mounted on a vehicle:

(i) the results are strongly influenced by the sprung mass and the moments of inertia of the vehicle body (for example, see Table 27.3);

(ii) each vehicle unit has several natural modes of vibration, so it is possible to get different results for *the* natural frequency and damping depending on which modes are excited by the test input.

Therefore, in order to obtain consistent results in a *suspension + vehicle* test it is necessary to test every suspension for a particular duty using the *same standardised vehicle*, and to excite the same mode of vehicle vibration on every test.

---

[1] The parameter estimation method described in Chapter 29 would need to be developed further to include whole vehicle responses - but this is not thought to be too difficult.

A much better approach would be to build a test rig, containing a representative rigid sprung mass which was constrained to move vertically, and to test every suspension using this rig. The test would therefore measure characteristics of the suspension under standard conditions, and not the characteristics of the vehicle to which it is mounted. Such a rig could be excited by transient inputs (*eg* a drop test) or steady–state sinusoidal inputs.

Accounting for Non–Linearities

It is necessary to assess the performance of each suspension for a range of input excitation amplitudes and frequencies, so as to ensure that it behaves well on all typical road surfaces. By contrast, the European test only ensures adequate performance for very large amplitude transient inputs (see Table 27.3).

30.2.4 Annual Inspection

It would clearly be prohibitively expensive to assess 'road-friendliness' rigorously in an annual inspection test. The objective of an annual inspection test should therefore be to check that the suspension remains within a reasonable specification throughout its operating life. The main challenge would be to assess the integrity of hydraulic shock absorbers.

It is possible to gauge whether a car shock absorber is functioning by applying a transient force to one corner of the vehicle body. This is not possible with heavy vehicles, which have axle-group suspensions with two, or even four dampers per axle.

Damper function could be assessed in at least three ways:

(i) Remove each damper from the vehicle and measure its force–deflection performance in a simple test rig.

(ii) Attach a device such as that described in [218] to the body of each damper and drive the vehicle over a known bump.

(iii) Apply dynamic (sinusoidal) inputs to each axle in turn and measure the damping of the axle bounce and roll modes. These modes are essentially independent of the sprung-mass payload distribution, and of the suspensions on other axles in a group. So they are just a function of the axle inertia, the suspension springs and dampers. The excitation frequency would need to be somewhere between 8Hz and 20Hz. (Special testing methods may be needed for bogie suspensions.)

The three approaches to damper assessment above are all technically feasible and all suffer from a similar difficulty: In order to test the performance of the damper in the annual inspection, it is necessary to have some additional information which is specific to the damper or axle under test:

(i) In the first and second approaches, the damper's in-service behaviour must be compared with its expected 'as-new' performance. The 'as-new' characteristics would either need to be supplied to the testing authority by the damper manufacturer (perhaps engraved on the side of the damper), or measured as part of the initial type-approval test and carried in the vehicle's documentation.

(ii) In the third testing approach it would be necessary to have information about the mass and moment of inertia of the axle. This could be estimated, or provided by the vehicle manufacturer as part of the initial type-approval process.

30.3 RECOMMENDATIONS

On considering the work reviewed in this Part of the book, it is recommended that a performance testing system for road-damaging potential should consist of both an initial type approval test as well as an annual inspection. The tests should have the features described in the following sections.

30.3.1 Type Approval Test

Technically Rigorous Test

A 'technically-rigorous' type-approval test would be based on the parameter estimation method and would consist of the following basic elements:

(i) Simple single-axle measurements on each vehicle unit, using a hydraulic actuator to excite vibration of the vehicle; removable instrumentation to measure the motion; and an automated software system to estimate the parameters of a generic nonlinear vehicle model. The characteristics of the dampers would be recorded for use in the annual inspection.

(ii) A time-domain vehicle simulation program, to calculate the response of the vehicle unit of interest, when connected to a simulation model of a standard trailer or tractor unit. These standard units should be specified using the approach of Chapter 28.

(iii) Simulation of the vehicle combination's performance when subjected to a variety of typical highway test conditions (speeds and roughnesses).

(iv) Assessment of the wheel forces generated by the simulation program using the 95th percentile aggregate fourth power force criterion. The effects of tyre configuration on pavement stress should be taken into account in the calculations.

(v) The road damage results for various highway test conditions should be averaged to determine an 'in-service' vehicle damage index with which to rate the vehicle.

Pragmatic Tests

A pragmatic approach to type-approval would consist of a 'drop-test' on the suspension using a standardised test rig. It would contain the following elements:

(i) A test rig consisting of a rigid sprung mass, constrained to move vertically, and an unsprung mass (axle) with wheels and tyres. The suspension would be mounted between the sprung and unsprung masses.

(ii) A drop-test conducted from various heights (5mm to 80mm), in which the natural frequency and damping ratio of the system are measured. Tests should be performed with and without the suspension dampers fitted.

(iii) An assessment criterion based on the natural frequency and damping ratio of the suspension with the proviso that a significant proportion of the energy dissipation should arise from the hydraulic dampers, as per the European test. The characteristics of the dampers would be estimated from the tests and recorded for use in the annual inspection.

30.3.2 Annual Inspection

An annual test should be performed to ensure that all hydraulic dampers on the vehicle perform within satisfactory limits. The simplest approach would be to build a standardised testing machine and compare the measured damper performance with the values recorded in the type approval tests.

PART 8 - MAIN CONCLUSIONS AND RECOMMENDATIONS



31
SUMMARY OF MAIN CONCLUSIONS

31.1 VEHICLE DYNAMICS

(i) Methods for characterising the roughness of road surfaces are well established. Techniques are available for artificially generating one, two or more correlated tracks across a random surface with specified statistical properties.

(ii) Straightforward and relatively accurate mathematical models exist for most common suspension elements used in heavy road vehicles including: leaf springs, air springs, hydraulic dampers, and computer-controlled dampers. Models of various suspension assemblies have been developed and validated: tandem and triaxle leaf spring and air spring suspensions; pivoted spring and walking beam suspensions, and so on.

(iii) Techniques for simulating the response of heavy vehicles to road roughness are well developed and validated.

(iv) Dynamic tyre forces of heavy vehicles can be considered to be Gaussian with typical RMS amplitudes approximately 10-30% of the static load. They increase with speed and road roughness. Most vehicles generate their dynamic tyre forces because of sprung mass motion in the 1.5-4 Hz frequency range, but some poorly damped axle group suspensions also generate large components at 8-15 Hz, due to unsprung mass vibration. All suspensions contribute to the dynamic loads generated by each axle of an articulated vehicle but the effects of structural vibration, roll-plane motion and tyre non-uniformities are small. Wheelbase filtering effects alter the frequencies at which dominant tyre forces are generated, depending on vehicle speed.

(v) Viscous damping and soft spring and tyre stiffnesses are desirable for minimising dynamic loads. Dry (Coulomb) friction is undesirable.

(vi) Multiple-axle suspension systems generally rank in the following order of increasing dynamic loads:

$$\begin{matrix}\text{Semi-active} \\ \text{(air spring)}\end{matrix} < \begin{matrix}\text{Air spring} \\ \text{Torsion bar}\end{matrix} < \begin{matrix}\text{4-spring} \\ \text{6-spring}\end{matrix} < \begin{matrix}\text{walking beam} \\ \text{pivoted-spring}\end{matrix}$$

This order depends to a certain extent on the particular suspension system and test conditions.

(vii) The stiffness and damping properties of each suspension affect the dynamic tyre forces generated by each other suspension. It is possible to fit a 'good' suspension to one axle but thereby increase the dynamic tyre forces generated by other axles.

31.2 GUIDEWAY RESPONSE

(i) The principal features of the response of road surfaces to vehicle loads are relatively well understood. The primary responses of roads are essentially linear for vehicle loads, isotropic

over short distances, dependent on the speed and frequency of the applied loads, and highly sensitive to environmental influences.

(ii) Mathematical models of the primary response of flexible pavements to dynamic wheel loads have been developed and validated. It is probably not necessary to use dynamic road response models for predicting road damage. Sufficient accuracy can be attained using simplified quasi–dynamic calculations, which account for the effects of vehicle speed but not loading frequency.

(iii) Typical elastic finite element models of jointed rigid pavements are capable of predicting their response to static loads when the pavement properties are known. The same models can be used to predict pavement response to dynamic tyre forces with reasonable accuracy.

(iv) The dynamic response of short-span highway bridges to moving dynamic tyre forces can be predicted with good accuracy, providing the modal responses of the bridge are known from measurements or mathematical models. When calculating the response of a bridge model to a passing truck, it is normally necessary to account for dynamic interaction effects.

31.3 ROAD DAMAGE MECHANISMS

(i) A simple linear viscoelastic rutting model can be used to predict the rate of permanent deformation in a pavement subjected to repetitions of a single load. The viscosity of an asphalt mixture can be estimated from routine test data, for a wide range of environmental conditions.

(ii) Linear elastic fracture mechanics predicts that roads should crack upwards from the base of the asphalt layer, except under conditions of extreme thermal cycles and low trafficking rates. This conflicts with field observations of 'top-down' cracks originating at the surface of some pavements.

(iii) A simple relationship was found between the elastic modulus of the asphalt layer and cumulative fatigue damage in an accelerated test pavement. This type of stiffness reduction would be consistent with the formation of distributed micro-cracks at the base of the asphalt layer. Such cracks would not necessarily coalesce to form a single through-thickness crack during the service life. Therefore, significant fatigue damage could occur in the pavement without any cracks appearing at the surface.

(iv) Top-down cracks in asphalt pavements remain a mystery. However it should be noted that thick asphalt roads in Europe do not often crack - rather they fail by excessive permanent deformation. This would appear to indicate either that fatigue cracking is insignificant, or that where it occurs, it is invisible: below the surface. It may only be detectable from a change in surface deflection or other non-destructive *in-situ* measurement on the pavement.

31.4 VEHICLE–GUIDEWAY INTERACTION

(i) Individual static axle loads are much more important than gross vehicle weight in fatigue damage, whereas the opposite is true for rutting.

(ii) Static analyses have shown that optimum spacings exist for axles in tandem and triaxle groups. These minimise road damage for given static loading conditions.

(iii) The physics of uneven load sharing in some axle group suspensions is relatively well understood. Depending on the assumptions, theoretical road damage may be increased by a factor of 1.2 to 2.9 for tandem suspensions with (typical) load sharing error of 20% (LSC = 0.8).

(iv) Variations in tyre contact conditions, including the number and type of tyres on an axle, contact area, pressure and pressure distribution, mainly influence primary pavement responses just below the surface of flexible pavements, particularly for thin wearing courses. Subgrade rutting and fatigue damage in thicker pavements are largely governed by the total wheel load.

(v) Various experimental and theoretical studies have indicated that single and 'super-single' tyres can inflict up to 10 times more fatigue damage to thin asphalt pavements than dual tyres carrying the same static load. Tyre contact conditions are less important for rutting of thicker flexible pavements for which wide single tyres are only 1.5 to 2 times more damaging than dual tyres. Tyre type has little influence on fatigue damage of rigid pavements.

(vi) Theoretical road fatigue damage increases with road roughness and vehicle speed. For flexible pavements, it may decrease at higher speeds due to decreasing primary dynamic response of the road structure. Depending on the method of analysis, assumptions, and mode of failure, dynamic wheel loads increase *average* theoretical road damage by 10–40 %, and *peak* theoretical damage by a factor of 2 to 4 over the damage due to static loads, for typical vehicles and operating conditions.

(vii) The dynamic loads generated for given test conditions are repeatable in space on subsequent tests. Approximately half the vehicles in a typical traffic stream contribute to a pattern of repeated loading on the pavement. The implication of this conclusion is that fatigue failure of pavements is likely to be governed by peak dynamic forces at specific locations along the road.

(viii) Calculation of *absolute* values of road damage to flexible pavements requires use of damage criteria which incorporate road response models. Such models are also needed if the influence of axle and tyre configurations are to be included in vehicle assessment.

(ix) Vehicle suspensions rank in essentially the same order for fatigue and rutting damage, irrespective of road strength.

(x) The ranking of axle-group suspensions depends on the pavement damage criterion used. This is due to the degree of spatial correlation between tyre forces. The *DLC* is unable to distinguish correctly between the road-damaging abilities of different axle group suspensions, and therefore it should not be used for suspension assessment purposes. The aggregate force approach is considered to be a more realistic, yet comparatively straightforward assessment criterion.

(xi) Dynamic forces are not important in rutting damage, where gross vehicle weight is the dominant factor. Conversely, dynamic forces are important in fatigue damage, and relatively low levels of dynamic loads can lead to theoretical damage up to 2.5 times the value for static axle loads.

(xii) Some trailer and drive axle-group air suspensions on the highway cause relatively high pavement damage, probably due to lack of suspension damping.

(xiii) A whole-life pavement performance model that is capable of making deterministic predictions of fatigue, rutting and surface roughness throughout the life of a pavement has been developed. The model includes the following features: (a) dynamic tyre forces; (b) environmental effects; (c) realistic pavement stiffness variations and surface roughness; (d) a realistic asphalt modulus degradation law due to fatigue damage; and (e) surface and subgrade rutting.

(xiv) For thin flexible pavements (125mm) where the mode of failure is fatigue, neglecting surface roughness induced dynamic loads and asphalt layer thickness variations may result in a 90% under-prediction of the fatigue damage at failure. For thicker flexible pavements, where the

mode of failure is likely to be permanent deformation, asphalt thickness variations and dynamic tyre loads play little part in road surface life.

(xv) Changing from a fleet of steel sprung vehicles to a fleet of air sprung vehicles is estimated to increase the life of thick asphalt roads (motorways), that fail by rutting, by less than 3%. Conversely, the life of minor roads may increase by between 40% and 90%, depending on the sensitivity of the deformation of the lower pavement layers to strain level.

(xvi) The dynamic road stress factor approach used in EC regulations considerably overestimates the potential benefits of 'road friendly' suspensions on thick constructions (motorways) and underestimates the potential benefits on thin constructions (minor roads) that fail by fatigue damage.

(xvii) Air-sprung vehicles cause lower dynamic responses of short–span highway bridges because they have lower natural frequencies than most of these bridges; apply smaller dynamic loads to the surface; and are often more heavily damped than leaf-sprung vehicles.

31.5 SUSPENSION DESIGN

(i) A suspension with about one-fifth the stiffness and twice the damping of a typical tractor drive axle air suspension is needed to minimise road damage. There is little compromise between theoretical Road Damage and roll-over threshold if an anti-roll bar is employed.

(ii) Simple modifications were made to the steel spring suspension of a tandem axle trailer (addition of rubber blocks and additional dampers). It was found experimentally that RMS dynamic tyre forces could be reduced by 15% and theoretical road damage by 5.2% (see figure 31.1, bar 1).

(iii) A mathematical model of an air-sprung articulated vehicle was validated, and its suspension was optimised according to the simple models. This vehicle was predicted to generate 9% less damage than the leaf-sprung vehicle in the unmodified state and it was predicted that, for the operating conditions examined, the road damage caused by the whole vehicle could be reduced by a further 5.4% (figure 31.1, bar 2).

(iv) It was shown experimentally that computer-controlled semi-active dampers have the potential to reduce road damage by typically 5-6%, compared to a soft air suspension with optimum passive damping (figure 31.1, bar 3).

(v) Reductions in Road Damage by the whole vehicle are not simply related to reductions in the RMS dynamic tyre forces generated by individual axles... All axles are involved, and must be improved.

(vi) A key requirement of controllers of semi-active dampers is to compensate for the time delays caused by compressibility of the hydraulic fluid and flexibility of the damper.

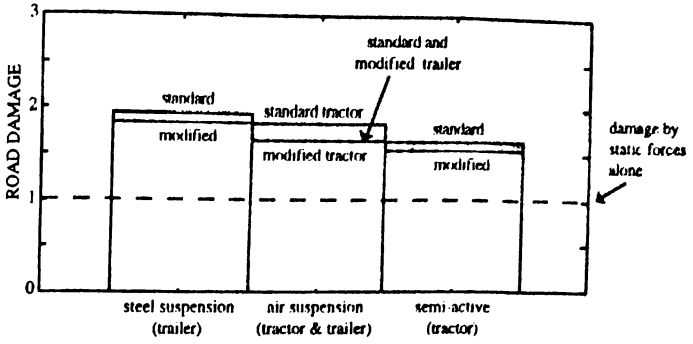


Fig. 31.1. Comparison of three suspensions for a principal road.

31.6 SUSPENSION ASSESSMENT

(i) Assessment of vehicles for 'road–friendliness' should be based on criteria that measure road damaging potential. However, it appears to be impractical to base an assessment procedure on *direct* tests of *whole vehicles.*

(ii) The road–damaging potential of an axle or vehicle cannot be determined from the parametric measurement prescribed by the EC step test because: (a) it does not use assessment criteria that are based on road–damaging potential; (b) it does not provide excitation comparable to normal highway operating conditions; (c) the dynamic forces generated by an axle cannot be characterised by a single natural frequency and damping ratio; (d) the frequency which dominates dynamic tyre forces changes with vehicle speed and the amplitude of input excitation.

(iii) The existence of dynamic interaction between the tractor and trailer makes accurate assessment of road damaging potential difficult in practice. Nevertheless, it appears to be possible to specify a standard tractor, with which to test all trailers; and a standard trailer, with which to test all tractors. The optimum specification of these standard vehicles depends strongly on the make-up of the vehicle fleet.

(iv) It is possible to estimate the parameters of a leaf spring vehicle model, with and without a hydraulic damper, with acceptable accuracy, using measurements based on simple laboratory tests. It therefore appears that the 'parameter estimation method' is a viable method for assessing the dynamic tyre forces generated by heavy vehicles. The assessment criteria could be based on realistic measures of road-damaging potential.

(v) Two different methods were suggested for performance testing of heavy vehicle suspensions. Both involve an initial type–approval test and subsequent annual inspection to confirm that the suspension operates within reasonable performance limits throughout its life. One test measures the road–damaging potential of the suspension when fitted to a vehicle, while the other tests the spring rate and damping performance.

32
RECOMMENDATIONS AND FUTURE RESEARCH

32.1 RECOMMENDATIONS

32.1.1 Recommendations for Tyre and Suspension Design

(i) Dual tyres generate lower ground contact pressures, and therefore less road damage than wide single tyres carrying the same static load.

(ii) Suspensions should have low vertical stiffnesses while maintaining adequate roll stability.

(iii) Dry friction should be minimised. This reduces dynamic loads and generally improves static load sharing in axle group suspensions. Suspension damping should be provided by hydraulic shock absorbers.

(iv) Centrally-pivoted suspensions (*eg* walking beams) should have sufficient viscous damping to prevent lightly damped tandem pitching motion.

(v) Suspensions with optimal passive damping and soft springs can be improved by the use of semi-active suspension dampers.

32.1.2 Recommendations for Road Design and Construction

(i) Fatigue design of roads should account for large overloads at some locations, caused by dynamic tyre forces. Such overloads can cause up to a factor of four reduction in fatigue life of thin pavements, and are likely to be an important reason for discrepancies between pavement life predictions and field performance.

(ii) Road surfaces should be as smooth as possible over the range of wavelengths that affect heavy vehicle dynamics: 0.5 m to 20 m.

(iii) Roads should be constructed with the smallest possible strength and stiffness variations. Weak spots can be degraded badly by dynamic loads and should be minimised.

32.1.3 Recommendations for Vehicle Regulation

(i) Substantial reductions in road damage (approximately a factor of three) could be achieved by encouraging improved static load sharing in axle group suspensions (which can be tested by simple static load measurement) and by encouraging the use of dual tyres on heavily loaded axles.

(ii) According to the current state of knowledge, the potential reduction in road damage achievable by regulating tyre configuration and static load sharing may be significantly greater than the benefits of discouraging particular generic suspension classes.

(iii) The exceptions to (ii) are centrally-pivoted suspensions with lightly damped pitching vibration modes. These suspensions should be discouraged, or regulations introduced to ensure adequate pitch damping in service.

(iv) The EC 'drop test' is not a reliable way to assess the road-damaging potential of heavy vehicles and should not be used as the basis for future 'road-friendly' suspension regulations.

(v) A suspension assessment programme should include two components: an initial type approval test, performed on each vehicle (or suspension); and an annual inspection to confirm compliance with in-service damping requirements.

(vi) Two different approaches are available for performing the initial type approval test. These are presented in Chapter 30.

32.2 FUTURE RESEARCH

Many aspects of the interaction between heavy vehicles and roads are now well understood and can be measured/modelled/predicted accurately. These include:

(i) the dynamic characteristics of most common forms of heavy vehicle suspension elements;

(ii) the dynamic tyre forces generated by individual heavy vehicles due to road surface roughness and the influence of most common forms of suspensions and tyres;

(iii) the patterns of dynamic loading generated by fleets of vehicles (spatial repeatability);

(iv) conventional and computer controlled methods for improving the performance of heavy vehicle suspensions, so as to minimise their road-damaging effects;

(v) the dynamic response of flexible and rigid pavements to dynamic vehicle loads;

(vi) the dynamic response of short-span highway bridges to heavy goods vehicles;

(vii) the influence of suspension and tyre factors on theoretical road damage.

There remains considerable further work to be performed on the damage to roads caused by heavy vehicles:

(i) Many important issues concerned with assessing the road-damaging performance of heavy goods vehicles have been investigated and understood. A practical assessment method, which can account for the most important vehicle factors, including the main sources of nonlinearity, has been tested on a model vehicle rig in the laboratory. Considerable work still remains to try out the proposed method on full-scale heavy vehicles and convert the method into a standard vehicle testing procedure.

(ii) Methods and devices are needed to monitor the in-service performance of heavy vehicle dampers, so as to ensure that vehicles with air suspensions are indeed 'road-friendly' throughout their service lives.

(iii) Considerable development work is still needed on hardware for computer-controlled suspension elements. In particular, efficient methods are needed for compensating for time delays in controllable components.

(iv) There is a severe lack of information concerning the failure mechanisms of paving materials, particularly the deformation and fatigue characteristics of asphalts, and the rutting characteristics of granular materials. A substantial body of fundamental research is needed in this area.

(v) Mathematical models have been developed to predict the long-term performance of roads subject to heavy vehicle loads and the environment. There is a need to validate these models and keep them up to date by incorporating the latest information about the damage mechanisms of road materials.

32.3 CLOSING COMMENTS

There are significant benefits available through the introduction of more 'road–friendly' heavy goods vehicles.

Improvements in vehicles which minimise dynamic tyre forces and hence road damage are also generally good design practice. They reduce vehicle vibration levels, and improve ride comfort and road holding, which are attractive vehicle selling features. It is in the interests of manufacturers to be pro–active in this regard.

Operators can benefit from better vehicles, through reduced payload damage, reduced vehicle maintenance bills, and by improved public perceptions of the heavy vehicle industry. There is also the possibility of load or taxation allowances for vehicles with 'road–friendly' suspensions, as per the regulations introduced recently in Europe.

Governments and tax payers can benefit through reduced road maintenance bills and hence more economic transport of freight by road.

It is therefore in everyone's interests to advance the state of knowledge in this area and to minimise the costs to the world economy of freight transportation, road construction and maintenance.

APPENDICES

APPENDIX A
ABBREVIATIONS

AASHO	American Association of State Highway Officials (former name of AASHTO) (USA)
AASHTO	American Association of State Highway and Transport Officials (USA)
ALF	Accelerated Loading Facility
ARRB	Australian Road Research Board
BA	Body Acceleration
BB	Benkleman Beam
BPR	Bureau of Public Roads (USA)
CBR	California Bearing Ratio
CRB	Cramer–Rao Bound
CSE	Conventional Simulation Error
CUED	Cambridge University Engineering Department
DAFC	Dynamic Aggregate Force Coefficient
DBM	Dense Bituminous Macadam
DFT	Discrete Fourier Transform
DI	Dynamic Response Increment (Bridges)
DLA	Dynamic Load Allowance (Bridges)
DLC	Dynamic Load Coefficient
DOF	Degrees of Freedom
EC	European Community
ECOV	Error Coefficient of Variation
EGH	Extended Ground–Hook control
ESAL	Equivalent Standard Axle Load
EU	European Union
FE	Finite Element
FEA	Finite Element Analysis
FFT	Fast Fourier Transform
FHWA	Federal Highway Administration (USA)
FSF	Full State Feedback
FWD	Falling-weight Deflectometer
HiL	Hardware in the Loop testing method
HRA	Hot Rolled Asphalt
IRI	International Roughness Index
LEFM	Linear Elastic Fracture Mechanics
LSC	Load Sharing Coefficient
LVDT	Linear Variable Differential Transformer

MIRA	Motor Industry Research Association (UK)
MS-WIM	Multiple-Sensor Weigh in Motion
MSD	Modified Skyhook Damping
NDT	Non-Destructive Testing
NLGR	National League for Good Roads (USA)
NRE	Normalised RMS Error
OECD	Organisation for Economic Co-operation and Development
OHBDC	Ontario Highway Bridge Design Code
OPR	Office of Public Roads (USA)
OPRI	Office of Public Road Inquiry (USA)
ORI	Office of Road Inquiry (USA)
PCC	Portland Cement Concrete
PDF	Probability Density Function
PEN	Penetration
PI	Penetration Index
PID	Proportional, Integral, Derivative (Controller)
PLC	Phase Lag Compensation
PLRF	Pavement Life Reduction Factor
PSD	Power Spectral Density
PSI	Present Serviceability Index
P–P	Peak to Peak
R&B	Ring and Ball (softening temperature)
RMS	Root mean square
SAC	Semi-Active Constraint
SAFSF	Semi-Active Full State Feedback
SAMSD	Semi-Active Modified Skyhook Damping
SD	Suspension Deflection
SDN	Spatial Distribution Number
SE	Simulation Error
SHRP	Strategic Highway Research Program
SRI	Spatial Repeatability Index
TF	Tyre force
TRL	Transport Research Laboratory (UK)
TRRL	Transport and Road Research Laboratory - former name of TRL, (UK)
VMA	Voids in Mixed Aggregate
WIM	Weigh-in-Motion
WLPPM	Whole-Life Pavement Performance Model

APPENDIX B
REFERENCES

1. Abbo E, Hedrick K, Markow M and Brademeyer B, 'Analysis of moving dynamic loads on rigid pavements.' *ARRB/FORS Symposium on Heavy Vehicle Suspension Characteristics,* Canberra, 1987.
2. Addis RR, 'The effect of wheel loads on road pavements.' *IMechE conference on road wear: The interaction between vehicle suspensions and the road,* London, 1991.
3. Addis RR, Halliday AR and Mitchell CGB, 'Dynamic loading of road pavements by heavy goods vehicles.' *Congress on Engineering Design, Seminar 4A-03,* Birmingham, Institution of Mechanical Engineers, 1986.
4. Addis RR and Whitmarsh RA, *'Relative damaging power of wheel loads in mixed traffic.'* Transport and Road Research Laboratory, Laboratory Report LR 979, 1981.
5. Ahmadian M and Marjoram RH, 'Effects of passive and semi-active suspensions on body and wheel hop control.' *SAE Trans,* 892487 ((SP-802)) pp 37-45, 1989.
6. Alpan I and Baker R, 'The speed effect in pavement deflection.' *Acta Technica,* 85 (1-2) pp 11-28, 1977.
7. Anon, *'The AASHO Road Test, Report 6, Special Studies.'* Highway Research Board, Washington D.C., Special Report 61F, 1962.
8. Anon, *'The AASHO Road Test, Report 5, Pavement Research.'* Highway Research Board, Special Report 61E, 1962.
9. Anon, *'The AASHO Road Test, Report 7, Summary Report.'* Highway Research Board, Special Report 61G, 1962.
10. Anon, *'A guide to the structural design of pavements for new roads.'* Road Research Laboratory, Road Note 29, 1970.
11. Anon, *'Manual on design and application of leaf springs.'* SAE, SAE HSJ788a, 1970.
12. Anon, *'Proposals for generalised road inputs to vehicles.'* ISO/TC 108/WGp draft No.3e, 1972.
13. Anon, *'Lifelines. How trucks and buses serve America's needs.'* Motor Vehicle Manufacturers Association, Inc., Detroit, Michigan, USA, 1977.
14. Anon, *'Standard Specifications for Highway Bridges, 12th ed.'* American Association of State Highway and Transportation Officials (AASHTO), Washington, D. C., 1977.
15. Anon, *'Steel, concrete and composite bridges.'* British Standards Institution, London, England, British Standard BS 5400, 1978.
16. Anon, *'Impacts of heavy freight vehicles.'* OECD, Paris, 1982.
17. Anon, *'Ontario Highway Bridge Design Code.'* Ontario Ministry of Transportation and Communications. Downsview, Ontario, 1983.
18. Anon, *'Pave test track topographical data.'* Motor Industry Research Association, 1983.
19. Anon, *'Strain measurement in bituminous layers.'* OECD Road Transport Research, Paris, 12, 1985.
20. Anon, *'AASHTO guide for design of pavement structures.'* American Association of State Highway and Transport Officials, Volume 1, 1986.
21. Anon, *'Motor vehicle milestones.'* Motor Vehicle Manufacturers Association, Public Relations Department, Detroit, Michigan, 1986.
22. Anon, *'Results from the M6 (Doxey) axle weight survey 1985.'* JMP Consultants Ltd, TRRL Contractors Report CR39, 50p, Crowthorne, 1986.
23. Anon, *'Department of Transport: Regulation of Heavy Lorries.'* Comptroller and Auditor General, National Audit Office, House of Commons, 1987.
24. Anon, *'Pavement design: a guide to the structural design of road pavements.'* N.A.A.S.R.A., 1987.
25. Anon, *'Course on the Mechanics of Heavy-Duty Trucks and Truck Combinations.'* University of Michigan Transportation Research Institute, 1988.
26. Anon, *'Heavy trucks, climate and pavement damage.'* OECD Road Transport Research, Paris, 175 p 1988

27. Anon, *'National speed survey 1987.'* Department of Transport, Statistics Bulletin (88)30, 1988.

28. Anon, 'Bitumen and asphalt nomographs developed by shell.' 1989.

29. Anon, *'The allocation of road track costs 1990/91 United Kingdom.'* Department of Transport, London, 1990.

30. Anon, *'Highway Statistics 1990.'* Federal Highway Administration, 1990.

31. Anon, *'OECD full-scale pavement test.'* Organisation for Economic Co-operation and Development, IRRD No. 837329, 1991.

32. Anon, *'Council Directive 92/7/EEC.'* The Council of the European Communities, 1992.

33. Anon, *'Dynamic loading of pavements.' Road Transport Research.* OECD, Paris, 1992.

34. Anon, *'Residential course on bituminous pavements: materials, design and evaluation.'* University of Nottingham, Department of Civil Engineering, 1992.

35. Anon, *'Whitaker's Almanack.'* J Whitaker and Sons Ltd, London, 1993.

36. Anon, *'Design manual for roads and bridges: Volume 7 pavement design and maintenance.'* Department of Transport, UK, 1994.

37. Anon, *'Highways and transportation statistics, 1995/96 estimates & 1993/94 actuals.'* The Chartered Institute of Public Finance and Accountancy, Statistical Information Service, 14.95, ISSN 0964-5624, 1995.

38. Anon, *'Mechanical vibration - road surface profiles - reporting of measured data.'* ISO, Standard ISO 8608: 1995; BS 7853: 1996, 1995.

39. Atkinson JH and Bransby PL, *'The Mechanics of Soils: An Introduction to Critical State Soil Mechanics.'* McGraw Hill, 1987.

40. Aurell J, 'The influence of different suspension parameters on dynamic wheel loads.' *IMechE conference on road wear: The interaction between vehicle suspensions and the road,* London, 1991.

41. Bahgat AG and Herrin M, 'Brittle fracture of asphaltic mixtures.' *A.A.P.T,* 37 pp 32-55, 1968.

42. Baladi G, 'Fatigue life and permanent deformation characteristics of asphalt concrete mixes.' *Transp. Res. Rec. TRB,* 1227 pp 75–87, 1989.

43. Barber E, 'Calculation of maximum pavement temperatures from weather reports.' *Highway Research Board,* Bulletin 168 1957.

44. Barenberg EJ and Zollinger. DG, 'Validation of Pavement Designs Using Instrumented Pavements.' *Annual TRB meeting,* Washington DC, Transportation Research Board, 1990.

45. Barenburg EJ, 'Role of instrumented pavements in establishing load equivalencies.' *FHWA Load Equivalence Workshop,* Washington D.C., 1988.

46. Battiato G, Verga C and Ronca G, 'Viscoelastic deformations in a two layered paving system predicted from laboratory creep results.' *Transp. Res. Rec. TRB,* 640 pp 34-38, 1977.

47. Baum, *'Comments on increasing total weights of commercial vehicles from the point of veiw of road stress.'* Road and Traffic Research Institute, Cologne, Report 99, Road Stress Working Committee, (Translated by TRRL as WP/V&ED/87/27), 1983.

48. Beckedahl H *et al.*, 'Effects of different pavement rehabilitations types on the development of rut depth and fatigue cracking.' *7th International Conference on Asphalt Pavements,* 4 vols. Nottingham, 1992.

49. Bell CA *et al.*, 'Aging of asphalt-aggregate mixtures.' *7th International Conference on Asphalt Pavements,* 5 vols. Nottingham, UK, 1992.

50. Bendat JS and Piersol AG, *'Random Data: Analysis and Measurement Procedures.'* John Wiley & Sons, Inc, 1971.

51. Bendat JS and Piersol AG, *'Engineering Applications of Correlation and Spectral Analysis.'* John Wiley and Sons, 1980.

52. Berry J, *'Proposal for a Council Directive, COM(90) 486.'* Commission of the European Communities, Brussels, 1990.

53. Besinger FH, *'The performance of passive and semi-active suspensions for lorries.'* PhD Thesis, Cambridge University Engineering Department, 1992.

54. Besinger FH, Cebon D and Cole DJ, 'Experimental investigation into the use of semi-active dampers on heavy lorries.' *12th IAVSD symposium on the dynamics of vehicles on roads and on railway tracks,* Lyon, Swets and Zeitlinger, 1991.

55. Besinger FH, Cebon D and Cole DJ, 'Damper models for heavy vehicle ride dynamics.' *Vehicle System Dynamics,* 24 (1) pp 35–64, 1995.

56. Besinger FH, Cebon D and Cole DJ, 'Force control of a semi-active damper.' *Vehicle System Dynamics*, 24 pp 695-723, 1995.

57. Best A and Schlesinger A, 'Predicting HGV road loads from rig tests with inputs on one axle at a time.' *Engineering Foundation conference on vehicle-road interaction*, Netherlands, 1994.

58. Biggs JM, Suer HS and Louw JM, 'Vibration of simple-span highway bridges.' *Transactions of the ASCE*, pp 291-318, 1957.

59. Bikerman JJ, *'The science of adhesive joints.'* Academic Press, New York and London, 1968.

60. Billing J and Green R, 'Design provisions for dynamic loading of highway bridges.' *TRB Second Bridge Engineering Conference, Transportation Research Record*, 950 pp 94-103, 1984.

61. Billing JR, 'Dynamic loading and testing of bridges in Ontario.' *Can. J. of Civl. Engng*, (11) pp 833-843, 1984.

62. Bird A, *'Roads and vehicles.'* Longmans, London, 1969.

63. Boley BA and Weiner JH, *'Theory of thermal stresses.'* John Wiley and Sons Inc., 1960.

64. Bonaquist R, 'An assessment of the increased damage potential of wide based single tires.' *7th Int. Conf. on Asphalt Pavements*, Ed. Brown SF and Hicks RG. 4 vols. Nottingham, UK, International Society for Asphalt Pavements, 1992.

65. Bower AF and Fleck NA, 'Brittle fracture under a sliding line contact.' *Submitted to J. Mech. Phys. Solids*, 1993.

66. Brademeyer BD, Delatte NJ and Markow MJ, 'Analysis of moving dynamic loads on highway pavements. Part II: Pavement response.' *Int. Symp. on Heavy Vehicle Weights and Dimensions*, Kelowna, British Columbia, Canada, 1986.

67. Brennan MJ and Clancy F, 'A new initiative in measuring the fatigue performance of bituminous materials.' *7th International Conference on Asphalt Pavements*, Nottingham, UK, 1992.

68. Broek D, *'Elementary engineering fracture mechanics.'* Martinus Nijhoff, 1982.

69. Brooker T, Foulkes MD and Kennedy CK, 'Influence of mix design on reflection cracking growth rates through asphalt surfacing.' 6th International Conference on the Structural Design of Asphalt Pavements, 1987.

70. Brown AB and Sparks JW, 'Viscoelastic properties of a penetration grade paving asphalt at winter temperature.' *A.A.P.T.*, 27 pp 35-51, 1958.

71. Brown SF, 'State-of-the-art report on field instrumentation for pavement experiments.' *Transp. Res. Rec.*, 640 pp 13-28, 1977.

72. Brown SF, 'Material characteristics for analytical pavement design. Ch. 2.' *Developments in highway pavement engineering. 1* Pell PS ed. Applied Science Publishers Ltd, London, 1978.

73. Brown SF and Bell CA, 'The validity of design procedures for the permanent deformation of asphalt pavements.' *4th International Conference on the Structural Design of Asphalt Pavements*, Ann Arbor, 1977.

74. Brown SF and Brunton JM, 'Improvements to pavement subgrade strain criterion.' *ASCE Journal of Transportation Engineering*, 110 (6) pp 551-567, 1984.

75. Brown SF and Brunton JM, *'An introduction to the analytical design of bituminous pavements (3rd edition).'* University of Nottingham, Department of Civil Engineering, UK, 1992.

76. Brown SF, Brunton JM and Stock AF, 'The analytical design of bituminous pavements.' *Proc. ICE*, 79 pp 1-31, 1985.

77. Brown SF and Dawson AR, 'Two-stage mechanistic approach to asphalt pavement design.' *7th International Conference on Asphalt Pavements*, Nottingham, UK, 1992.

78. Brown SF, Stock AF and Pell PS, 'The structural design of asphalt pavements by computer.' *J. Inst. Highway Eng.*, 1980.

79. Bruce AG, *'Highway design and construction.' International Texts in Civil Engineering.* O'Rourke CE ed. International Textbook Press, Scranton PA, 1941.

80. Brunton JM and De Almeida JR, 'Modeling material nonlinearity in a pavement backcalculation procedure.' *TRR*, 1377 pp 17-25, 1991.

81. Bryson AE and Yu-Chi H, *'Applied Optimal Control: optimization, estimation and control.'* Hemusphere Publishing Corporation, 1975.

82. Burmister DM, 'The theory of stresses and displacements in layered systems.' *Journal of Applied Physics*, 16 (2, 3, and 5) 1945.

83. Cantieni R. *'Dynamic load tests on highway bridges in Switzerland.'* Swiss Federal Laboratory for Materials Testing and Research (EMPA), 211, 1983.

84. Cantieni R. 'Dynamic load testing of a two-lane highway bridge.' *Int. Conf. on Traffic Effects on Struct. and the Environment,* Strbske Pleso, Czechoslovakia, 1987.

85. Cantieni R and Heywood RJ, *'Final report of OECD DIVINE project Element 6, Bridge Research.'* OECD, 1997.

86. Captain KM, Boghani AB and Wormley DN, 'Analytical tire models for dynamic vehicle simulation.' *VSD,* 8 (1) pp 1-32, 1979.

87. Cebon D, 'Heavy vehicle vibration - a case study.' *Proc. 9th IAVSD symposium on The Dynamics of Vehicles on Roads and on Tracks.,* Linkoping, Swets and Zeitlinger, 1985.

88. Cebon D, *'An investigation of the dynamic interaction between wheeled vehicles and road surfaces.'* PhD Thesis, University of Cambridge, 1985.

89. Cebon D, 'Simulation of the response of leaf springs to broad band random excitation.' *VSD,* 15 (6) pp 375-392, 1986.

90. Cebon D, 'Assessment of the dynamic wheel forces generated by heavy road vehicles.' *ARRB/FORS Symposium on Heavy Vehicle Suspension Characteristics,* Canberra, Australian Road Research Board, 1987.

91. Cebon D, 'Examination of the road damage caused by three articulated vehicles.' *Proc. 10th IAVSD Symposium on the dynamics of vehicles on roads and on tracks.,* Prague, Swets and Zeitlinger, 1987.

92. Cebon D, 'Theoretical road damage due to dynamic tyre forces of heavy vehicles. Part 1: Dynamic analysis of vehicles and road surfaces.' *Proc I.Mech.E.,* 202 (C2) pp 103-108, 1988.

93. Cebon D, 'Theoretical road damage due to dynamic tyre forces of heavy vehicles. Part 2: Simulated damage caused by a tandem-axle vehicle.' *Proc. I.Mech.E.,* 202 (C2) pp 109-117, 1988.

94. Cebon D, 'Vehicle-generated road damage: A review.' *Vehicle System Dynamics,* 18 (1-3) pp 107-150, 1989.

95. Cebon D, 'Design of multiple-sensor weigh-in-motion systems.' *J. Automobile Engineering Proc. I.Mech.E.,* 204 pp 133-144, 1990.

96. Cebon D, 'Interaction between heavy vehicles and roads.' *SAE SP–951,* 930001 1993.

97. Cebon D, Besinger FH and Cole DJ, 'Control strategies for semi–active lorry suspensions.' *J. Auto. Eng, IMech E,* 210 (D2) pp 161-178, 1996.

98. Cebon D and Bevan B, *'Foden tanker test data.'* Motor Industry Research Association, 1984.

99. Cebon D and Gillespie TD, *'Effect of Heavy Vehicle Characteristics on Pavement Response and Performance - Phase II - Model Validation Studies.'* UMTRI, Report on NCHRP project 1-25(1), 1989.

100. Cebon D and Newland DE, 'The artificial generation of road surface topography by the inverse FFT method.' *Proc. 8th IAVSD Symposium on the dynamics of vehicles on roads and on railway tracks,* Cambridge, MA, Swets & Zeitlinger, 1984, 1983.

101. Cebon D and Winkler CB, 'Multiple-sensor weigh-in-motion: Theory and experiments.' *Transportation Research Record, TRB,* 1311 pp 70–78, 1991.

102. Cebon D and Winkler CB, *'A study of road damage due to dynamic wheel loads using a load measuring mat.'* Strategic Highway Research Program, National Research Council, Report SHRP–ID/UFR–91–518, 1991.

103. Chalasani RM, 'Ride performance potential of active suspension systems. Part I: simplified analysis based on quarter–car models.' *ASME symposium on simulation of ground vehicles and transport systems,* Anaheim CA, ASME, 1986.

104. Chan GP, Kannapan SM, Marshek KM and Hudson WR, 'Laboratory measured tire-pavement contact pressures.' *FHWA Load Equivalence Workshop,* Washington D.C., FHWA, 1988.

105. Chen SS, *'The response of multilayered systems to dynamic surface loads.'* PhD Thesis, University of California at Berkeley, 1987.

106. Chiu WS, Smith RG and Wormley DN, 'Influence of vehicle and distributed guideway parameters on high speed vehicle-guideway dynamic interactions.' *J. of Dyn. Sys. Meas. and Control ASME,* March pp 25-34, 1971.

107. Chou YT, *'Structural Analysis Computer Programs for Rigid Multi-Component Structures with Discontinuities - WESLIQUID and WESLAYER.'* U. S. Army Waterways Experiment Station, Vicksburg, Miss., Technical Report GL-80, 1980.

108. Christison JT, *'Pavements response to heavy vehicle test program: Part 2 - Load equivalency factors.'* Canroad Transportation Research Corporation, Vol. 9, 1986.

109. Christison JT, Anderson KO and Shields BP, 'In situ measurements of strains and deflections in a full-depth asphaltic concrete pavement.' *Proc. Assoc. Asphalt Paving Technology*, 47 pp 398-430, 1978.

110. Christison JT and Woodrooffe JHF, *'Pavement response to bump induced axle loads.'* Canroad Transportation Research Corporation, Vol 10, 1986.

111. Chu ML and Doyle GR, 'Non-deterministic analysis of a four-wheeled model vehicle traversing a simulated random terrain.' *SAE Trans*, 780789 1978.

112. Clark SK, 'The contact between tire and roadway, Ch. 5.' *NBS Monograph 122, Mechanics of pneumatic tires.* Clark SK ed. NBS, Washington D.C., 1971.

113. Cole DJ, *'Measurement and analysis of dynamic tyre forces generated by lorries.'* PhD Thesis, Cambridge University Engineering Department, 1990.

114. Cole DJ, 'Design, analysis and testing of a slow-active car suspension.' *Proc. IMechE International Conference on Vehicle Ride and Handling*, Birmingham, England, MEP Ltd, 1993.

115. Cole DJ and Cebon D, 'Simulation and measurement of vehicle response to road roughness.' *Proc. Inst. Acoustics*, 10 (2) pp 477–484, 1988.

116. Cole DJ and Cebon D, 'A capacitative strip sensor for measuring dynamic tyre forces.' *Proc. 2nd Int. Conf. on Road Traffic Monitoring.*, London, IEE, 1989.

117. Cole DJ and Cebon D, 'Simulation and measurement of dynamic tyre forces.' *Proc. 2nd Int. Symp. on Heavy Vehicle Weights and Dimensions*, Kelowna, Canada, 1989.

118. Cole DJ and Cebon D, 'Assessing the road–damaging potential of heavy vehicles.' *Proc. I.Mech.E., Part D*, 205 pp 223–232, 1991.

119. Cole DJ and Cebon D, 'Performance and application of a capacitative strip tyre force sensor.' *Proc 6th Int. Conf. on Road Traffic Monitoring*, London, 1992.

120. Cole DJ and Cebon D, 'Spatial repeatability of dynamic tyre forces generated by heavy vehicles.' *J. Automobile Engineering Proc. I.Mech.E, Part D*, 206 pp 17–27, 1992.

121. Cole DJ and Cebon D, 'Validation of an articulated vehicle simulation.' *Vehicle System Dynamics*, 21 pp 197–223, 1992.

122. Cole DJ and Cebon D, *'Truck suspension design to minimise road damage.'* Cambridge University Engineering Department, Technical Report CUED/C-MECH/TR64, 1994.

123. Cole DJ and Cebon D, 'Modification of a heavy vehicle suspension to reduce road damage.' *Proc. IMechE, J. Automobile Engineering*, 209 (D3) pp 183-194, 1995.

124. Cole DJ and Cebon D, *'A preliminary investigation of tractor/trailer interaction in articulated vehicles.'* Cambridge University Engineering Department, Technical Report CUED/C-MECH/TR68, 1995.

125. Cole DJ and Cebon D, 'Truck suspension design to minimise road damage.' *J. Auto. Eng, IMech E*, 210 (D2) pp 95-107, 1996.

126. Cole DJ and Cebon D, 'Truck tyres, suspension design, and road damage.' *International Rubber Conference IRC'96*, Manchester, UK, Institute of Materials, 1996.

127. Cole DJ and Cebon D, 'Front-rear interaction of a pitch-plane truck model.' *Vehicle System Dynamics*, 30 pp 117-141, 1998.

128. Cole DJ and Cebon D, 'Influence of tractor-trailer interaction on assessment of road damaging performance.' *J. Auto. Eng, Proc IMechE*, 212 (D1) pp 1-10, 1998.

129. Cole DJ, Collop AC, Potter TEC and Cebon D, 'Use of a Force Measuring Mat to Compare the Road Damaging Potential of Heavy Vehicles.' *Proc. 3rd International Symposium on Heavy Vehicle Weights and Dimensions*, Ed. Cebon D and Mitchell CGB. Cambridge, Thomas Telford, 1992.

130. Cole DJ, Collop AC, Potter TEC and Cebon D, 'Spatial repeatability of measured dynamic tyre forces.' *J. Auto. Eng, IMech E*, 210 (D3) pp 185-197, 1996.

131. Collins HJ and Hart CA, *'Principles of road engineering.' The roadmaker's library.* Spielmann PE ed. Edward Arnold, London, 1936.

132. Collop A, Cebon D and Cole D, 'Effects of spatial repeatability on long-term flexible pavement performance.' *IMechE J. Mech. Eng. Sci.*, 210 (C2) pp 97-110, 1996.

133. Collop AC, *'Effects of traffic and the environment on road damage.'* CUED, Project Report 1991.

134. Collop AC, *'Effects of traffic and temperature on flexible pavement wear.'* PhD Thesis, Cambridge University Engineering Department, 1994.

135. Collop AC, Al-Hakim B, Thom NH and Lloyd WG, 'The use of WIM data in traffic assessment.' *Second European WIM conference*, Lisbon, 14-16 September, 1998.

136. Collop AC and Cebon C, 'Stiffness reductions of flexible pavements due to cumulative fatigue damage.' *ASCE J. Transp. Eng.*, 122 (2 March/April) pp 131-139, 1996.

137. Collop AC and Cebon D, *'A theoretical analysis of fatigue cracking in flexible pavements.'* Cambridge University Engineering Department, Technical Report CUED/C–MECH/TR 56, 1993.

138. Collop AC and Cebon D, 'A model of whole-life flexible pavement performance.' *Proc IMechE, J. Mech. Eng. Sci*, 209 (C6) pp 389-408, 1995.

139. Collop AC and Cebon D, 'Parametric study of factors affecting flexible pavement performance.' *ASCE J. Transp. Eng.*, 121 (6) pp 485-494, 1995.

140. Collop AC and Cebon D, 'A theoretical analysis of fatigue cracking in flexible pavements.' *Proc I Mech E, J Mech Eng Sci*, 209 (C5) pp 345-361, 1995.

141. Collop AC and Cebon D, 'Effects of road-friendly suspensions on long term flexible pavement performance.' *J. Mech. Eng. Sci, IMech E*, 211 (Part C) pp 411-424, 1997.

142. Collop AC, Cebon D and Hardy MSA, *'A visco–elastic approach to rutting in flexible pavements.'* Cambridge University Engineering Department, Technical Report CUED/C–MECH/TR 49, 1992.

143. Collop AC, Cebon D and Hardy MSA, 'A visco-elastic approach to rutting in flexible pavements.' *ASCE Journal of Transportation Engineering*, 121 (1) pp 82-93, 1995.

144. Collop AC, Potter TEC, Cebon D and Cole DJ, 'Investigation of spatial repeatability using a tire force measuring mat.' *Transportation Research Record*, 1448 pp 1-7, 1994.

145. Cooper KE and Pell PS, *'The effect of mix variables on the fatigue strength of bituminous materials.'* TRRL, Laboratory Report 633, 1974.

146. Crompton REB, 'Mechanical engineering aspects of road construction.' *Proc. I. Mech. E.*, December 1913 1913.

147. Cron FW, 'Highway design for motor vehicles – A historical review. Part 1: The beginnings of traffic measurement.' *Public Roads*, 38 (3) pp 85–95, 1974.

148. Cron FW, 'Highway design for motor vehicles – A historical review. Part 8: The evolution of highway standards.' *Public Roads*, 40 (3) pp 93–100, 1976.

149. Croney D, 'Is the measured deflection of a flexible pavement a reliable guide to life prediction and overlay design.' *Highways*, 58 (Part 1968) pp 24-26, 1990.

150. Dauzats M and Rampal A, 'Mechanism of surface cracking in wearing courses.' *6th International Conference on the Structural Design of Asphalt Pavements*, 1987.

151. de Pont J, 'Using servo-hydraulics to assess heavy vehicle suspensions for road wear.' *3rd Int. Symposium on Heavy Vehicle Weights and Dimensions*, Cambridge, 1992.

152. de Pont J, 'Experiences with simulating on-road heavy vehicle suspension behaviour using servo-hydraulics.' *Engineering Foundation Conference on Vehicle-Road and Vehicle-Bridge Interaction*, Noordwijkerhout, To be published in Int. J. Vehicle Dynamics, 1994.

153. Decker H, Schramm W and Kallenbach R, 'A Practical Approach towards Advanced Semiactive Suspension Systems.' *Proc Conference on Advanced Suspensions*, London, IMechE, 1988.

154. Deshpande VS and Cebon D, 'Models of a particle reinforced nonlinear-viscous composite.' *ASCE Journal of Engineering Mechanics (in press)*, 1997.

155. Dickerson RS and Mace DGW, *'Dynamic pavement force measurements with a two-axle heavy goods vehicle.'* TRRL, Supplementary Report SR 688, 1981.

156. Diplock BJ, *'A new system of heavy goods transport on common roads.'* Longmans, Green and Co, London, 1902.

157. Dodds CJ, 'The laboratory simulation of vehicle service stress.' *J. Eng. Ind, ASME Trans.*, May pp 391-398, 1974.

158. Dodds CJ and Robson JD, 'The description of road surface roughness.' *Journal of Sound and Vibration*, 31 (2) pp 175-183, 1973.

159. Dodds CJ and Robson JD, 'Simulation of the dynamic stresses in vehicles and components.' *Proc IUTAM Symposium on the dynamics of vehicles on road and on railway tracks*, Delft, Swets and Zeitlinger, 1975.

160. Doi S, Yasuda E and Hayashi Y, 'An Experimental Study of Optimal Vibration Adjustment Using Adaptive Control Methods.' *Proc. Conference on Advanced Suspensions*, London, IMechE, 1988.

161. Dokainish M and ElMadany M, 'Nonlinear random response of articulated vehicles.' *6th IAVSD Symposium on the dynamics of vehicles on roads and tracks*, Berlin, Swets & Zeitlinger, 1979.

162. Donald G *et al.*, *'Pavement design: A guide to the structural design of road pavements.'* NAASRA, 1987.

163. Dongre R, Sharma MG and Anderson DA, 'Development of fracture criterion for asphalt mixes at low temperature.' *Transportation Research Record*, 1228 pp 94-105, 1989.

164. Eisenmann J, 'Dynamic wheel load fluctuations - road stress.' *Strasse und Autobahn*, 4 pp 127-128, 1975.

165. Eisenmann J, 'Beuteilung der Strassenbeanspuchung.' *Strasse und Autobahn*, 3 1978.

166. Eisenmann J, Birman D and Hilmer A, 'Effects of commercial vehicle design on road stress - research results relating to the roads.' *Strasse und Autobahn, (Translated by TRRL as WP/V&ED/87/29)*, 37 (6) pp 238-244, 1987.

167. Eisenmann J and Hilmer A, 'Influence of wheel load and inflation pressure on the rutting effect at asphalt-pavements – experiments and theoretical investigations.' *Sixth international conference on the structural design of asphalt pavements*, Ann Arbor, 1987.

168. El Madany MM, 'Nonlinear ride analysis of heavy trucks.' *Computers and Structures*, Vol.25 (No.1) pp 69-82, 1987.

169. El Madany MM, Dokainish MA and Allan AB, 'Ride dynamics of articulated vehicles - a literature survey.' *VSD*, 8 (4) pp 287-316, 1979.

170. ElMadany MM, 'An analytical investigation of isolation systems for cab ride.' *Computers and Structures*, Vol.27 (No.5) pp 679-688, 1987.

171. Ervin RD, *'RTAC study on weights and dimensions – Report on task 1.'* University of Michigan Transportation Research Institute, Ann Arbor, 1984.

172. Ervin RD *et al.*, *'Influence of truck size and weight variables on the stability and control properties of heavy trucks.'* University of Michigan Transportation Research Institute, UMTRI-83-10/2, 1983.

173. Ewins DJ, *'Modal Testing: Theory and Practice.'* Research Studies Press, Letchworth, England, 1984.

174. Eyre R and Tilly GP, *'Damping measurements on steel and composite bridges.'* Transport and Road Research Laboratory, Crowthorne, England., Symposium on dynamic behaviour of bridges, TRRL Supplementary Report 275, 1977.

175. Fancher PS, Ervin RD, MacAdam CC and Winkler CB, 'Measurement and representation of the mechanical properties of truck leaf springs.' *SAE Trans.*, 800905 pp 16, 1980.

176. Fancher PS, Ervin RD, Winkler CB and Gillespie TD, *'A factbook of the mechanical properties of components for single-unit and articulated heavy trucks.'* University of Michigan Transportation Research Institute, 1986.

177. Felice CW, Gaffney ES, Brown JA and Olsen JM, 'Dynamic High Stress Experiments on Soil.' *Geotechnical Testing Journal*, 10 (4) pp 192-202, 1977.

178. Fernando EG and Lytton RL, 'A system for evaluating the impact of truck characteristics and use on flexible pavement performance and life-cycle costs.' *7th Int. Conf. on Asphalt Pavements*, Ed. Brown SF and Hicks RG. 4 vols. Nottingham, UK, International Society for Asphalt Pavements, 1992.

179. Ferne B, *Private Communication*, 1989

180. Ferrari P, 'Calculation of the deformations caused by vehicles to flexible pavements.' *3rd. Int. Conf. Structural Design of Asphalt Pavements*, University of Michigan, Ann Arbor, 1972.

181. Fisher JW and Huckins HC, 'Measuring dynamic vehicle loads.' *The AASHO road test, proceedings of a conference*, Washington D.C., Highway Research Board, 1962.

182. Flugge W, *'Viscoelasticity.'* Blaisdell Publishing Company, 1967.

183. Francken L, 'Fatigue performance of a bituminous road mix under realistic test conditions.' *Transp. Res. Rec. TRB*, 712 pp 30-37, 1979.

184. Francken L and Verstraeten J, 'Methods for predicting moduli and fatigue laws of bituminous road mixtures under repeated bending.' *Transp. Res. Rec. TRB*, 515 pp 114-123, 1974.

185. Fryba L, *'Vibration of solids and structures under moving loads.'* Noordhoff International Publishing, Groningen, Netherlands, 1972.

186. Fryba L, 'Dynamic interaction of vehicles with tracks and roads.' *Vehicle System Dynamics*, 16 pp 129–138, 1987.

187. Fuchs HO and Stephens RI, *'Metal fatigue in engineering.'* John Wiley and Sons, New York, 1980.

188. Gadala ME, ElMadany MM and Gadala MS, 'Finite element and analytical modelling of a tractor-semitrailer vehicle.' *Computers and Structures*, Vol.23 (No.6) pp 831-836, 1986.

189. George KP and Husain S, 'Thickness design for flexible pavement: A probablistic approach.' *Transportation Research Record*, 1095 pp 27-36, 1986.

190. Gillespie TD, *'Heavy Truck Ride.'* SAE, SP-607, 1985.

191. Gillespie TD, 'Modelling Truck Dynamic Loads.' *FHWA Load Equivalence Workshop,* Washington D.C., FHWA, 1988.

192. Gillespie TD *et al., 'Effects of heavy vehicle characteristics on pavement response and performance.'* Transportation Research Board, NCHRP Report 353, 1993.

193. Gillespie TD, Sayers MW and Segel L, *'Calibration of response-type road roughness measuring systems.'* TRB, NCHRP Report 228, 1980.

194. Glover MH, *'Weighing axles in motion with a multiple sensor system.'* TRRL, Working paper WP VED/88/50, 1988.

195. Glover MH and Newton WH, *'Evaluation of a multiple-sensor weigh-in-motion system.'* TRRL, Working paper WP VED/90/69, 1989.

196. Goacolou H, 'Calculation of the rutting of structures – Castor program: Method for prediction of permanent deformations in asphaltic structures.' *Sixth international conference on the structural design of asphalt pavements,* Ann Arbor, 1987.

197. Gold B and Rader C, *'Digital Processing of Signals.'* McGraw-Hill., London, 1984.

198. Goodall RM and Kortüm W, 'Active Controls in Ground Transportation - A Review of the State-of-the-Art and Future Potential.' *VSD,* 12 pp 225-257, 1983.

199. Gordon RG, 'Influence of vehicle suspensions on pavement costs and performance.' *Proc. ARRB/FORS Symposium on Heavy Vehicle Suspension Characteristics,* Canberra, Australia, 1987.

200. Gorge W, 'Evaluation of research reports concerning the influence of commercial vehicle development and design on the road fatigue.' *English translation by International Road Transport Union, Geneva,* 1984.

201. Gottenberg WG and Lo KH, 'Glass fibre reinforced epoxy leaf spring design.' *Int. J. of Vehicle Design,* 4 (3) pp 312-322, 1983.

202. Govind S and Walton CM, 'Fatigue model to assess pavement damage.' *Transp. Res. Rec. TRB,* 1227 pp 88–96, 1989.

203. Grace A, 'Optimisation toolbox for use with MATLAB.' 1994.

204. Green MF, *'The dynamic response of short-span highway bridges to heavy vehicle loads.'* PhD Thesis, Cambridge University Engineering Department, 1990.

205. Green MF and Cebon D, 'Dynamic response of highway bridges to heavy vehicle loads: Theory and experimental validation.' *J. S. Vib.,* 170 (1) pp 51-78, 1994.

206. Green MF and Cebon D, 'Dynamic interaction between heavy vehicles and highway bridges.' *Computers and Structures,* 62 (2) pp 253-264, 1997.

207. Green MF, Cebon D and Cole DJ, 'Effects of heavy vehicle suspension design on the dynamics of highway bridges.' *ASCE Journal of Structural Engineering,* 121 (2) pp 272-282, 1995.

208. Gyenes L and Mitchell CGB, 'The spatial repeatability of dynamic pavement loads caused by heavy goods vehicles.' *Third Int. Symp. on Heavy Vehicle Weights and Dimensions,* Ed. Cebon D and Mitchell CGB. Cambridge, UK, Thomas Telford, 1992.

209. Gyenes L and Mitchell CGB, 'Measuring dynamic loads for heavy vehicle suspensions using a road simulator.' *3rd Engineering Foundation conference on vehicle-road and vehicle-bridge interaction,* Noordwijkerhout, The Netherlands, 1994.

210. Gyenes L, Mitchell CGB and Phillips SD, 'Dynamic pavement loads and tests of road-friendliness for heavy vehicle suspensions.' *Third International Symposium on Heavy Vehicle Weights and Dimensions,* Ed. Cebon D and Mitchell CGB. Cambridge, UK, Thomas Telford, 1992.

211. Haas RCG and Papagiannakis AT, 'Understanding pavement rutting.' *Special workshop on rutting in asphalt pavements,* Toronto, Roads and Transport Association of Canada, 1986.

212. Hac A and Youn I, 'Optimal Semi-Active Suspension with Preview based on a Quarter Car Model.' *Proc. IEEE. American Control Conference,* Boston, USA, 1991.

213. Hahn WD, *'Effects of commercial vehicle design on road stress - vehicle research results.'* Institut fur Kruftfahrwesen, Universitat Hannover (Translated by TRRL as WP/V&ED/87/38), 1985.

214. Hahn WD, *'Effects of commercial vehicle design on road stress - quantifying the dynamic wheel loads for stage 3: single axles, stage 4: twin axles, stage 5: triple axles, as a function of the springing and shock absorption system of the vehicle.'* Institut fur Kruftfahrwesen, Universitat Hannover (Translated by TRRL as WP/V&ED/87/40), 453, 1987.

215. Hahn WD, 'Measurements of road loadings by HGV suspensions – Survey of the German research program.' *IMechE conference on road wear: The interaction between vehicle suspensions and the road,* London, 1991.

216. Hald A, '*Statistical theory with Engineering Applications.*' John Wiley &sons, New York, 1952.

217. Hall BB and Gill KF, 'Performance of a Telescopic Dual-Tube Automotive Damper and the Implications for Vehicle Ride Prediction.' *Proc. IMechE, Part D,* 200 (D2) pp 115-123, 1986.

218. Hammond RJ, '*Damper Integrity Indicator.*' MEng Thesis, Cambridge University Engineering Department, Confidential Report, 1996.

219. Hardy MSA, '*The response of flexible pavements to dynamic tyre forces.*' PhD Thesis, Cambridge University Engineering Department, 1990.

220. Hardy MSA and Cebon D, 'The response of a flexible pavement to moving dynamic loads.' *Proc. Inst. Acoustics,* 10 (2) pp 485–492, 1988.

221. Hardy MSA and Cebon D, 'Measurement and analysis of the dynamic response of flexible pavements.' *Proc. 2nd Int. Symposium on heavy vehicle weights and dimensions,* Ed. Pearson J. Kelowna, British Columbia, Canada, RTAC, 1989.

222. Hardy MSA and Cebon D, 'Response of continuous pavements to moving dynamic loads.' *ASCE J. Eng. Mechanics,* 119 (9) pp 1762-1780, 1993.

223. Hardy MSA and Cebon D, 'Importance of speed and frequency in flexible pavement response.' *ASCE J. Eng. Mechs.,* 120 (3) pp 463–482, 1994.

224. Hardy MSA and Cebon D, 'An investigation of anti-lock braking strategies for heavy goods vehicles.' *J. Auto. Eng, IMech E,* 209 (D4) pp 263–271, 1995.

225. Harichandran RS, Mahmood T, Raab AR and Baladi GY, 'A modified Newton algorithm for backcalculation of pavement layer properties.' *Presented at the Transportation Research Board 72nd Annual Meeting,* Washington, DC, 1993.

226. Harr ME, 'Influence of vehicle speed on pavement deflections.' *Proc. Highway Research Board,* 1962.

227. Hartree D, 'Evolution of truck tyres.' *SAE Australasia,* 46 (3) pp 127–131, 1986.

228. Hawk H and Ghali A, 'Dynamic response of bridges to multiple truck loading.' *Canadian Journal of Civil Engineering,* 8 pp 392-401, 1981.

229. Heath A and Good MC, 'Heavy vehicle design parameters and dynamic pavement loading.' *Australian Road Research,* 15 (4) pp 249-263, 1985.

230. Heath AN, 'Application of the isotropic road roughness assumption.' *Journal of Sound and Vibration,* 115 (1) pp 131-144, 1987.

231. Heath AN, 'Evaluation of the Isotropic Road Roughness Assumption.' *Proc. 10th IAVSD Symposium on the Dynamics of Vehicles on Roads and on Tracks,* Prague, Swets and Zeitlinger, 1987.

232. Heath AN, 'Heavy vehicle design affecting road loading.' *Proc. ARRB/FORS Symposium on Heavy Vehicle Suspension Characteristics,* Canberra, Australia, 1987.

233. Hellan K, '*Introduction to fracture mechanics.*' McGraw-Hill, 1984.

234. Hennecke D, 'Frequency Dependent Variable Suspension Damping - Theoretical Background and Practical Success.' *Proc. Conference on Advanced Suspensions,* London, IMechE, 1988.

235. Hibbit, Karlsson and Sorensin, 'ABAQUS user's manual.' 1987.

236. Hills JF, 'The creep of asphalt mixes.' *J. Inst Petroleum,* 59 (570) 1973.

237. Hills JF, 'Predicting the fracture of asphalt mixes by thermal stresses.' *Proc Institute of Petroleum,* Paper IP 74–014 1974.

238. Hills JF, Brien D and Van de Loo PJ, 'The correlation of rutting and creep tests on asphalt mixes.' *Journal of the Institute of Petroleum,* IP 74-001 1974.

239. Honda H, Kajikawa Y and Kobori T, 'Spectra of road surface roughness on bridges.' *J. of the Struct. Div., Proc. of the ASCE,* 108 (ST9) pp 1956-1966, 1982.

240. Honda H and Kobori T, 'Numerical data base on roadway roughness of highway bridges and roughness characteristics.' *Proc. of JSCE,* 398 (I-10) pp 385-394, 1986.

241. Hopman PC *et al.*, 'Application of the visco-elastic properties of asphalt concrete.' *7th International Conference on Asphalt Pavements,* 4 vols. Nottingham, 1992.

242. Hoyinck WT, Van der Loo JMM, Mulderij J and Wegmeetdienst RK, 'Comparative tests of FWD and Lacroix-deflectograph.' *7th International Conference on Asphalt Pavements,* 5 vols. Nottingham, UK, 1992.

243. Hu G, 'Simulation of heavy truck ride using a desktop computer.' *SAE Trans.,* 871557 1987.

244. Hu G, 'Use of a road simulator for measuring dynamic wheel loads.' *SAE Conference on Vehicle/Pavement Interaction, SAE 881194, SP765,* Indianapolis, SAE, 1988.

245. Huang YH and Wang ST, 'Finite Element Analysis of Concrete Slabs and Its Implications for Rigid Pavements.' *Highway Research Record 466, HRB, National Research Council Washington, D.C.,* pp 55-69, 1973.

246. Hudson WR and H. M, 'Analysis of Discontinuous Orthotropic Pavement Slabs Subjected to Combined Loads.' *Highway Research Record 13, HRB National Research Council Washington DC,* 131 pp 1-39, 1966.

247. Huhtala M, 'The effect of diferent trucks on road pavements.' *Proc. Int. Symp. on Heavy Vehicle Weights and Dimensions,* Kelowna, British Columbia, 1986.

248. Huhtala M, 'Field tests to compare tires.' *FHWA Load Equivalence Workshop,* Washington D.C., 1988.

249. Huisman RGM, *'A controller and observer for active suspensions with preview.'* Thesis, Eindhoven University of Technology, 1994.

250. Hunt HEM, *'Measurement and Modelling of Traffic-Induced Ground Vibration.'* PhD Thesis, Cambridge University Engineering Department, 1988.

251. Hveem FN, 'Devices for recording and evaluating pavement roughness.' *Highway Research Board Bulletin,* 264 pp 1–26, 1960.

252. Ilosvai L and Szucs B, 'Random vehicle vibrations as effected by dry friction in wheel suspensions.' *Vehicle System Dynamics,* 1 pp 197-209, 1972.

253. Imai HI, K., 'Nonelasticity of leaf springs.' *Bull. Japan Soc. of Prec. Engg,* 11 (2) pp 93-94, 1977.

254. Ingram A, *'Lorries, trucks and vans 1927–1973.'* Blandford Press, London, 1975.

255. Ioannides AM and Donnelly JP, 'Three-Dimensional Analysis of Slab on Stress-Dependent foundation.' *Transportation Research Record 1196, TRB, National Research Council Washington, D.C,* pp 72-84, 1988.

256. Ioannides AM, Thompson MR and Barenberg EJ, ' Finite Element Analysis of Slab-on-Grade Using a Variety of Support Models.' *Proc., 3rd International Conference on Concrete Pavements Design and Rehabilitation,* Purdue University, West Lafayette, Ind., 1985.

257. Ishihara K and Kimura T, 'The theory of viscoelastic two-layer systems and conception of its application to the pavement design.' *Proc. 2nd. Int. Conf. Structural Design of Asphalt Pavements,* University of Michigan, Ann Arbor, 1967.

258. Izadmehr B and Lee CE, 'Accuracy and tolerances of weigh-in-motion systems.' *Transp. Res. Rec. TRB,* 1123 pp 127-135, 1987.

259. Jackson NC, 'Pavement performance - a state DOT perspective.' *SAE Conference on Vehicle/ Pavement Interaction, SAE Trans. 881843, SP765,* Indianapolis, SAE, 1988.

260. Jacobs MMJ, de Bondt AH, Molenaar AAA and Hopman PC, 'Cracking in asphalt concrete pavements.' *7th Int Conf on Asphalt Pavements,* Ed. Brown SF and Hicks RG. 4 vols. Nottingham, UK, The International Society for Asphalt Pavements, 1992.

261. Jacobs MMJ and Moraal J, 'The influence of tyre characteristics on the normal stresses in asphalt concrete pavements.' *Third Int. Symp. on Heavy Vehicle Weights and Dimensions,* Ed. Cebon D and Mitchell CGB. Cambridge, UK, Thomas Telford Ltd, 1992.

262. Jain SP, 'Stochastic principles applied to flexible pavement design.' *J. Inst. Eng. (India) Civ. Eng. Div,* 59 (CI) pp 214-218, 1978.

263. Jameson GW, Sharp KG, Vertessy NJ and Yeo R, 'The fatigue performance of asphalt and cement treated crushed rock under accelerated loading.' *16th ARRB Conference,* Perth, Australia, 1992.

264. Johnson KL, *'Contact mechanics.'* Cambridge University Press, 1987.

265. Johnson-Clark JR *et al., 'Data report on testing of full depth asphalt pavements: Mulgrave ALF trial.'* Australian Road Reseach Board, Research Report ARR No. 209, 1991.

266. Jones R, Thrower EN and Gatfield EN, 'Surface wave method.' *Proc. 2nd. Int. Conf. Structural Design of Asphalt Pavements,* University of Michigan, Ann Arbor, 1967.

267. Kadar P, *'The performance of overlay treatments and modified binders under accelerated full-scale loading - The Callington ALF trial.'* Australian Road Research Board, Research Report ARR No. 198, 1991.

268. Kallenbach RG, 'Identification methods in vehicle system dynamics.' *Vehicle System Dynamics,* 16 pp 107-127, 1987.

269. Kamash KMA and Robson JD, 'Implicatlons of Isotropy in Random Surfaces.' *J.Sound Vib.,* 54 (1) pp 131-145, 1977.

270. Kamash KMA and Robson JD, 'The application of isotropy in road surface modelling.' *Journal of Sound and Vibration*, 57 (1) pp 89-100, 1978.

271. Kanerva H, 'Effects of asphalt properties on low temperature cracking of asphalt mixtures' *7th International Conference on Asphalt Pavements*, Nottingham, UK, 1992.

272. Karadayi R and Masada GY, 'A Nonlinear Shock Absorber Model.' *ASME, AMP-Vol 80, DSC-Vol 2*, pp 149-165, 1989.

273. Kausel E and Peek R, 'Dynamic Loads in the Interior of a Layered Stratum: An Explicit Solution.' *Bulletin of the Seismological Soc. of America*, 72 (5) pp 1459-1481, 1982.

274. Kenis W, *'Predictive Design Procedures, VESYS Users Manual. An Interim Design Method for Flexible Pavements Using the VESYS Structural Subsystem.'* FHWA, Final Report FHWA-RD-77-154, 1977.

275. Kenis W, *'Accelerated dynamic pavement testing - DIVINE Element 1.'* OECD, Final Report ??, 1997.

276. Kenis WJ, Kulakowski BT and Streit DA, 'Heavy vehicle pavement loading - a comprehensive testing program.' *3rd Int. Symp. on Heavy Vehicle Weights and Dimensions*, Ed. Cebon D and Mitchell CGM. Cambridge, UK, Thomas Telford, 1992.

277. Kenis WJ, Sherwood JA and McMahon TF, 'Verification and application of the VESYS structural subsystem.' *Proc. 5th Int. Conf. on the Structural Design of Asphalt Pavements*, 1 pp 333-345, 1982.

278. Kennedy CK, Fevre P and Clarke CS, *'Pavement deflection: Equipment for measurement in the United Kingdom.'* Transport and Road Research Laboratory, TRRL Laboratory Report 834, 1978.

279. Kennedy TW, Roberts FL and Rauhut JB, 'Distress and related material properties for premium pavements.' *Transp. Res. Rec. TRB*, 715 pp 15-21, 1979.

280. Kerr AD, 'Elastic and Viscoelastic Foundation Models.' *J. of Applied Mechanics*, pp 491-498, 1964.

281. Kinder DF and Lay MG, *'Review of the Fourth Power Law.'* ARRB, Internal Report AIR000-248, 1988.

282. Kitching KJ, *'Semi-active damping of heavy vehicles.'* PhD Thesis, Cambridge University, 1997.

283. Kitching KJ, Cebon D and Cole DJ, 'An experimental investigation of preview control.' *Vehicle System Dynamics (in press)*, 1998.

284. Kitching KJ, Cole DJ and Cebon D, 'Performance of a semi-active damper for heavy vehicles.' *submitted to ASME. J. Dyn Sys Meas Control*, 1998.

285. Kitching KJ, Cole DJ and Cebon D, 'Use of controllable suspensions to minimise road damage.' *IMechE J. Auto. Eng. (In press)*, 1998.

286. Kitching KJ, Cole DJ and Cebon D, 'Use of semi-active dampers to minimise road damage.' *Fifth International Symposium on Heavy Vehicle Weights and Dimensions*, Maroochydoore, Australia, Australian Road Research Board, 1998.

287. Klinkner W, 'Adaptives Dämpfungs-System "ADS".' *zur fahrbahn- und fahrzustandsabhängigen Steuerung von Dämpfern einer Fahrzeugfederung*, VDI Berichte Nr. 778 pp 323-356, 1989.

288. Kortüm W and Valasek M, 'Development of semi-active road-friendly truck suspensions.' *5th International Symposium on Heavy Vehicle Weights and Dimensions*, Queensland, Australia, Australian Road Research Board, 1998.

289. Kuipers JFJ, *'Commercial vehicles of the world.'* The Oakwood Press, Exeter, UK, 1972.

290. Kujala K, 'Frost action and the mechanical properties of an artificially frozen test plot.' *12th International Conference on Soil Mechanics and Foundation Engineering*, Rio de Janeiro, 1989.

291. Kulkarni GG and Ng SF, 'Dynamic analysis of two dimensional simply supported orthotropic bridge decks.' *Canadian Journal of Civil Engineering*, 5 pp 58-69, 1978.

292. Kunjamboo KK and O'Connor C, *'Truck suspension models.'* Department of Civil Engineering, University of Queensland, 29p Research Report No CE 21, 1981.

293. La Barre RP, Forbes RT and Andrews S, *'The measurement and analysis of road surface roughness'* Motor Industry Research Association, Report No 1970/5, 1970.

294. Lai S, 'Probabalistic solution for viscoelastic layered systems.' *Int. Conf. on Statistics and Probability in Soil and Structural Engineering*, 1979.

295. Laker IB, *'The dynamic response of a single wheel suspension to computer generated road profiles.'* TRRL, Supplementary Report SR 360, 1978.

296. Langlois RG, Anderson RJ and Hanna DM, 'Implementing Preview Control on an Off-Road Vehicle with Active Suspension.' *Proc. 12th IAVSD Symposium on the Dynamics of Vehicles*, France, Lyon, Swets and Zeitlinger, 1991.

297. Lay MG. *'History of Australian roads.'* Australian Road Research Board, SR 29, 1984.

298. Lay MG. *'Ways of the world.'* Rutgers University Press, New Brunswick, New Jersey, 1992.

299. Le Blanc PA, Woodrooffe JH and Papagiannakis AT. 'A comparison of two types of instrumentation for measuring vertical wheel load.' *Third International Symposium on Heavy Vehicle Weights and Dimensions*, Ed. Cebon D and Mitchell CGB. Cambridge, UK, Thomas Telford, 1992.

300. Lee D. 'Comparative maintenance costs of different bridge types.' *Bridge Management: Inspection, Maintenance, Assessment, and Repair.* Harding J, Parke G and Ryall M ed. London: Elsevier Applied Science, 1990. pp. 145-154.

301. Leonard D. *'Damping and frequency measurements on eight box girder bridges.'* Transport and Road Research Laboratory, Crowthorne, England, TRRL Laboratory Report 682, 1975.

302. Leonard DR, Grainger JW and Eyre R. *'Loads and vibrations caused by eight commercial vehicles with gross weights exceeding 32 tons.'* TRRL, Laboratory Report LR582, 1974.

303. Lippmann SA and Oblizajek KL. *'The distributions of stress between the tread and the road for freely rolling tires.'* Society of Automotive Engineers, SAE Report 740072, 1974.

304. Lippmann SA, Piccin WA and Baker TP. 'Enveloping characteristics of truck tires - a laboratory evaluation.' *SAE Trans.*, 650184 1965.

305. Lister NW. 'The transient and long term performance of pavements in relation to temperature.' *Proc. 3rd. Int. Conf. on structural design of asphalt pavements*, University of Michigan, Ann Arbor, 1972.

306. Lister NW and Addis RR. 'Field observations of rutting and their practical implications.' *Transp. Res. Rec. TRB*, 640 pp 27-34, 1977.

307. Livneh M and Siddiqui HM. 'Assessment of radar technology for determining the thickness of pavement layers.' *7th International Conference on Asphalt Pavements*, Nottingham, UK, 1992.

308. Lizell M. 'Semiactive damping.' *Proc. Conference on Advanced Suspensions*, London, IMechE, 1988.

309. Loeb JS, Guenther DA, Chen HHF and Ellis JR. 'Lateral stiffness, cornering stiffness and relaxation length of the pneumatic tyre.' *SAE Proceedings*, 900129 1990.

310. Louam N, Wilson DA and Sharp RS. 'Optimal Control of a Vehicle Suspension Incorporating the Time Delay between Front and Rear Wheel Inputs.' *VSD*, 17 pp 317-336, 1988.

311. Lytton RL and Shanmugham U. 'Analysis and design of pavements to resist thermal cracking using fracture mechanics.' *5th International Conference on the Structural design of asphalt pavements*, 1982.

312. Maestas JM and Mamlouk MS. 'Comparison of pavement deflection analysis methods using overlay design.' *TRR*, 1377 pp 17-25, 1991.

313. Magnusson G, Carlsson HE and Ohlsson E. *'The Influence of heavy vehicles' springing characteristics and tyre equipment on the deterioration of the road.'* VTI (Translated by TRRL as WP/V&ED/86/16, 1986), Report Number 270, 1984.

314. Majidzadeh K and Ilves GJ. 'Methods for determining primary response load equivalency factors.' *FHWA Load Equivalence Workshop*, Washington D.C., 1988.

315. Majidzadeh K, Kauffmann EM and Ramsamooj DV. 'Application of fracture mechanics in the analysis of pavement fatigue.' *Association of Asphalt Paving Technologists*, 40 pp 227-246, 1971.

316. Majidzadeh K, Kedhr S and Mojarrush M. 'Evaluation of permanent deformation in asphalt concrete pavements.' *Transp. Res. Rec. TRB*, 715 pp 21-31, 1979.

317. Majidzadeh K, Ramsamooj DV and Fletcher TA. 'Analysis of fatigue of a sand-asphalt mixture.' *A.A.P.T.*, 38 pp 495-518, 1969.

318. Majidzadeh K and Schweyer H. 'Viscoelastic response of asphalts in the vicinity of the glass transition point.' *A.A.P.T.*, 551 pp 80-105, 1967.

319. Markow MJ, Hedrick JK, Brademeyer BD and Abbo E. 'Analyzing the interactions between dynamic vehicle loads and highway pavements.' *Trans. Res. Rec. TRB*, 1196 pp 161–169, 1988.

320. Marshall P and Bishop D. *'Lorries, trucks and vans 1897–1927.'* Blandford Press, London, 1972.

321. Marshek KM, Chen HH, Connell RB and Saraf CL. 'Effect of truck tire inflation pressure and axle load on flexible and rigid pavement performance.' *Transp. Res. Rec. TRB*, 1070 pp 14-21, 1986.

322. Marshek KM *et al.*, *'Experimental investigation of truck tire inflation pressure on pavement-tire contact area and pressure distribution.'* University of Texas Center for Transportation Research Research, Report Number 386-1, 1985.

323. Martin JR and Wallace HA. *'Design and construction of asphalt pavements.'* McGraw–Hill Book Company Inc, New York, 1958.

324. Maser KR and Richter C, 'Ground penetrating radar surveys to characterize pavement layer thickness variations at GPS sites.' *Presented at Transportation Research Board 72nd Annual Meeting*, Washington, DC, 1993.

325. Maser KR, Scullion T and Briggs RC, 'Use of radar technology for pavement layer evaluation.' *7th Int Conf. on Asphalt Pavements*, Ed. Brown SF and Hicks RG. 4 vols. Nottingham, UK, International Society of Asphalt Pavements, 1992.

326. Mathews PM, 'Vibrations of a beam on elastic foundation I.' *Zeit. angew. Math. Mech.*, 38 (3/4) pp 105-115, 1958.

327. Mathews PM, 'Vibrations of a beam on elastic foundation II.' *Zeit. angew. Math. Mech.*, 39 (1/2) pp 13-19, 1959.

328. Matsuno S and Nishizawa T, 'Mechanism of longitudinal surface cracking in asphalt pavement.' *Proceedings of the 7th International Conference on Asphalt Pavements*, 5 vols. Nottingham, UK, The International Society of Asphalt Pavements, 1992.

329. Maupin GW, 'Test for predicting fatigue life of bituminous concrete.' *Transp. Res. Rec. TRB*, 659 pp 32-37, 1977.

330. McAdam JL, *'Remarks on the present system of roadmaking.'* Longman, Hurst, Rees, Orme and Brown, London, 1822.

331. McLellan JC and Still PB, 'The effect of construction practice on pavement thickness and surface evenness.' The Highway Engineer. 1983.

332. Michelberger P and Szoke D, 'Speed dependent vertical vibrations of elastic vehicle bodies.' *Int. J. Vehicle Design*, 8 (1) pp 87-95, 1985.

333. Mikaila J, 'Two-stage multileaf spring design.' *SAE Trans. 730272*, pp 14p, 1973.

334. Minami T, 'Fundamental analysis of lateral vibration of a leaf spring.' *Bulletin of the JSME*, 13 (62) pp 978-986, 1970.

335. Mitchell C, 'An experimental assessment of steel, rubber and air suspensions for heavy goods vehicles.' *IMechE seminar*, London, 1991.

336. Mitchell CGB, *'The effect of the design of goods vehicle suspensions on loads on roads and bridges.'* TRRL, Research Report 115, 1987.

337. Mitchell CGB and Gyenes L, 'Dynamic pavement loads measured for a variety of truck suspensions.' *2nd Int. Conf. on Heavy Vehicle Weights and Dimensions*, Kelowna, British Columbia, 1989.

338. Monismith CL, Alexander RL and Secor KE, 'Rheological behaviour of asphalt concrete.' *A.A.P.T.*, 556 pp 401-449, 1966.

339. Monismith CL and Deacon JA, 'Fatigue of asphalt paving mixtures.' *ASCE Journal of Transportation Engineering*, 95 (TE2) pp 317-346, 1969.

340. Monismith CL, Hicks RG and Finn FN, 'Development of performance related specifications for asphalt aggregate mixtures.' *The United States Strategic Highway Research Program*, London, UK, 1990.

341. Monismith CL, Hicks RG and Finn FN, 'Accelerated load tests for asphalt-aggregate mixtures and their role in AAMAS.' *Asphalt Paving Technology*, 60 pp 587-631, 1991.

342. Monismith CL, Lysmer J, Sousa J and Hedrick JK, 'Truck pavement interactions - requisite research.' *SAE Conference on Vehicle/Pavement Interaction, SP765, SAE Trans*, Indianapolis, SAE, 1988.

343. Monismith CL and Secor KE, 'Viscoelastic behaviour of asphalt concrete pavements.' *1st Int. Conf. on the Structural Design of Asphalt Pavements*, 1962.

344. Monismith CL, Sousa J and Lysmer J, 'Modern pavement design technology including dynamic load conditions.' *SAE Conference on Vehicle/Pavement Interaction, SP765, SAE Trans. 881845*, Indianapolis, SAE, 1988.

345. Moore WM, Hanson DI and Hall JW, *'An introduction to nondestructive structural evaluation of pavements.'* TRB, Transport Research Circular 189, 1978.

346. Morita T, Tanaka T and Kishimoto N, 'Ride comfort improvement using preview sensor.' *International symposium on Advanced Vehicle Control.*, Yokohama, Japan, 1992.

347. Morris JR, *'Effects of heavy vehicle characteristics on pavement response - phase 1.'* TRB, Prepared for NCHRP project 1-25, 1987.

348. Mulcahy NL, Pulmano VA and Traill-Nash RW, 'Vehicle properties for bridge loading studies.' *Proceedings of the International Association of Bridge and Structural Engineering*, pp 153-167, 1983.

349. Myre J, 'Fatigue of asphalt materials for Norwegian conditions.' *7th International Conference on Asphalt Pavements*, Nottingham, UK, 1992.

350. Nagiri S, Doi S, Shoh S and Hiraiwa, N., *'Improvement of ride comfort by preview vehicle suspension system.' SAE 920277*, pp 364-370, 1992.

351. Nair K, Smith WS and Chang CY, 'Applicability of a linear viscoelastic characterisation for asphalt concrete.' *3rd Int. Conf. on the Structural Design of Asphalt Pavements*, 1972.

352. Nasim MA *et al.*, The behavior of a rigid pavement under moving dynamic loads.' *Transportation Research Record, TRB*, 1307 pp 129–135, 1991.

353. Nazarian S and Alexander DR, 'Determination of surface deflection of pavements under moving loads.' *Proc. TRB Annual Meeting*, 1989.

354. Newland D, *'Mechanical vibration analysis and computation.'* Longman, Singapore, 1989.

355. Newland DE, *'An Introduction to Random vibrations and spectral analysis, 2nd Edition.'* Longman, 1985.

356. Newland DE, 'The effect of a footprint on perceived surface roughness.' *Proc. Royal Society, Series A*, 405 pp 303, 1986.

357. Ng SSF and Kaul V, 'Free vibration analysis of continuous orthotropic bridge decks.' *Journal of Sound and Vibration*, 119 (1) pp 29-38, 1987.

358. Nijboer LW and Van der Poel C, 'A study of vibration phenomena in asphaltic road constructions.' *Asphalt Paving Technology*, pp 187-237, 1953.

359. Nogemi T and Lam YC, 'Two-parameter layer model for analysis of slabs on elastic foundation.' *J. of Eng. Mechanics*, 113 (9) 1987.

360. Nunn ME, 'Prediction of permanent deformation in bituminous pavement layers.' *3rd Eurobitume Conference*, The Hague, Holland, 1985.

361. O'Connell S, Abbo E and Hedrick K, 'Analyses of moving dynamic loads on highway pavements, Part I: vehicle response.' *Proc. Int. Symp. on Heavy Vehicle Weights and Dimensions*, Kelowna, British Columbia, 1986.

362. Page J, *'A review of dynamic loading caused by vehicle suspensions.'* TRRL, Supplementary Report 82UC, 1974.

363. Pagen CA, 'Size and thermorheological relationships of asphaltic concrete.' *A.A.P.T.*, 564 pp 228-257, 1968.

364. Papagiannakis AT, Amoah N, LeBlanc P and Woodrooffe J, 'Viscoelastic pavement response under moving dynamic loads.' *72nd Annual Meeting of the Transportation Research Board*, Washington DC, 1993.

365. Papagiannakis AT, Haas RCG, Woodrooffe JHF and Leblanc PA, 'Impact of roughness-induced dynamic load on flexible pavement performance.' *First. Int. Symp. on Surface Characteristics*, Penn. State College, ASTM, 1988.

366. Papazian HS, 'The response of linear viscoelastic materials in the frequency domain with emphasis on asphalt concrete.' *1st Int. Conf. on the Structural Design of Asphalt Pavements*, 1962.

367. Peattie KR, 'Flexible pavement design. Ch. 1.' *Developments in highway pavement engineering. 1* Pell PS ed. Applied Science Publishers Ltd, London, 1978.

368. Peters RJ, 'Low cost calibration management.' *Second Eurpoean Conference on Weigh in Motion of Road Vehicles*, Ed. O'Brien EJ and Jacob B. Lisbon, Portugal, 1998.

369. Pilbeam C, *'Slow-active and passive control of automotive suspension system vibrations.'* PhD Dissertation Thesis, Cranfield University, School of Mechanical Engineering, 1995.

370. Potter TEC, *'Assessing the road damaging potential of heavy vehicles.'* PhD Thesis, Cambridge University Engineering Department, 1995.

371. Potter TEC, Cebon D and Cole DJ, 'Using parameter estimation to assess road damage.' *IAVSD 14th Symposium on the dynamics of vehicles on roads and on tracks*, Ann Arbor, MI, USA, Swets & Zeitlinger, 1995.

372. Potter TEC, Cebon D and Cole DJ, 'Assessing 'road-friendliness': a review.' *J. Auto. Eng, IMech E*, 211 (Part D) pp 455-475, 1997.

373. Potter TEC, Cebon D and Cole DJ, 'Indirect methods for asessing road friendliness of lorry suspensions.' *J. Auto. Eng, IMech E*, 211 (Part D) pp 243-256, 1997.

374. Potter TEC, Cebon D, Cole DJ and Collop AC, 'An investigation of road damage due to measured dynamic tyre forces.' *I. Mech. E. Journal of Automotive Engineering*, 209 (D1) pp 9–24, 1995.

375. Potter TEC, Cebon D, Collop AC and Cole DJ, 'Road damaging potential of measured dynamic tyre forces in mixed traffic.' *J. Automobile Engineering Proc. I.Mech.E*, 210 (D3) pp 215-225, 1996.

376. Potter TEC, Collop ACC, Cole DJC and Cebon D, *'A34 Mat tests: results and analysis.'* Cambridge University Engineering Department, Technical Report CUED/C–MECH/TR61, 1994.

377. Potts GR and Walker HS, 'Nonlinear truck ride analysis.' *J. Engineering for Industry (Trans. ASME)*, May pp 597-602, 1974.

378. Powell WD, Potter JF, Mayhew HC and Nunn ME, *'The structural design of bituminous roads.'* Transport and Road Research Laboratory, Laboratory Report LR 1132, 1984.

379. Press WH, Flannery BP, Teukolsky SA and Vetterling WT, *'Numerical recipies.'* Cambridge University Press, 1992.

380. Quinn BE and Wilson CC, 'Can dynamic tire forces be used as a criterion of pavement condition.' *Highway Research Record*, No 46 pp 88-100, 1964.

381. Ramsamooj DV, 'Fatigue cracking of asphalt pavements.' *Transportation Research Record*, 756 pp 43-48, 1980.

382. Ramsamooj DV, Majidzadeh K and Kauffmann EM, 'The analysis and design of the flexibility of pavements.' *3rd international conference on the structural design of asphalt pavements*, 1972.

383. Rauhut JB and Kennedy TW, 'Characterizing fatigue life for asphalt concrete pavements.' *Transportation Research Record*, 888 pp 47-56, 1982.

384. Rauhut JB, Roberts FL and Kennedy TW, 'Response and distress models for pavement studies.' *Transp. Res. Rec. TRB*, 715 pp 7-14, 1979.

385. Redfield RC and Karnopp DC, 'Performance Sensitivity of an Actively Damped Vehicle Suspension to Feedback Variation.' *J. Dynamic Systems, Measurement and Control*, 111 pp 51-60, 1989.

386. Ribarits JI, Aurell J and Andersers E, 'Ride comfort aspects of heavy truck design.' *SAE Trans.*, 781064 pp 4046-4069, 1978.

387. Richardson HH and Wormley DN, 'Transportation vehicle/beam-elevated guideway dynamic interactions: A state-of-the-art review.' *ASME Journal of Dynamic Systems, Measurement, and Control*, pp 169-179, 1974.

388. Rill G, 'The influence of correlated random road excitation processes on vehicle vibration.' *8th IAVSD Symposium on the dynamics of vehicles on roads and on railway tracks*, Cambridge, Mass, Swets and Zeitlinger, 1984, 1983.

389. Roberts FL, 'Flexible pavement strains caused by auto tyres.' *ASCE J. Transportation Engineering*, 113 (5) 1987.

390. Roberts FL, 'Overview: tire types pressures and models to evaluate pressure effects.' *FHWA Load Equivalence Workshop*, Washington D.C., 1988.

391. Roberts FL *et al.*, *'Effects of tire pressures on flexible pavements.'* Texas Transportation Institute Research, Report 372-IF, 1986.

392. Robertson RE *et al.*, 'Chemical properties and their relationships to pavement performance.' *Association of Asphalt Paving Technologists*, 60 pp 413-436, 1991.

393. Robson JD, 'Road surface description and vehicle response.' *Int. J. of Vehicle Design*, 1 (1) pp 25–35, 1979.

394. Roque R, Tia M and Ruth BE, 'Asphalt rheology to define the properties of asphalt concrete mixtures and the performance of pavements.' *Asphalt Rheology: Relationship to Mixture*. Briscoe OE ed. 1985. pp. 3-27.

395. Rowe GM, *'Development of a computer based pavement design method for visco-elastic materials.'* SWK Pavement Engineering, Nottingham UK, Unpublished Report 1993.

396. Rowe GM, 'Performance of asphalt mixtures in the trapezoidal fatigue test.' *Asphalt Paving Technology*, 62 1993.

397. Rowland F, 'Variable rate leaf springs - their design and characteristics.' *SAE Trans. 73027*, pp 12p, 1973.

398. Ruf G, 'The calculation of vibrations of a 4-wheeled vehicle, induced by random roughness of the left and right track.' *VSD*, 7 (1) pp 1-23, 1978.

399. Ruth B and Schweyer HE, 'Asphalt and mixture rheology as related to cracking of asphalt pavements.' *Fatigue of Asphalt Concrete Pavements*, Albuquerque, New Mexico, 1981.

400. Sakuma N, Kadono I, Dohi M and Nakai H, 'Heavy duty truck ride comfort analysis by computer simulation.' *Int. J. Veh. Des.*, pp 279–290, 1986.

401. Salam YM and Monismith CL, 'Fracture characteristics of asphalt concrete.' *A.A.P.T.* 41 pp 215-256, 1972.

402. Salter DR and Davies P, 'Development and testing of a portable microprocessor-based weigh-in-motion system.' *Transp. Res. Rec. TRB*, 997 pp 61–70, 1984.

403. Salter RJ, *'Highway design and construction.'* Macmillan Education, 1988.

404. Sayers M, 'Characteristic power spectral density functions for vertical and roll components of road roughness.' *Proc. Symposium on Simulation and Control of Ground Vehicles and Transportation Systems,* Anaheim, Calif., ASME, 1986.

405. Sayers M and Gillespie TD, 'The effect of suspension system nonlinearities on heavy truck vibration.' *Proc. 7th IAVSD Symposium on the Dynamics of Vehicles on Roads and on Tracks,* Cambridge, UK, Swets and Zeitlinger, 1981.

406. Sayers M and Gillespie TD, 'Dynamic pavement/wheel loading for trucks with tandem suspensions.' *Proc. 8th IAVSD Symposium on the Dynamics of Vehicles on Roads and on Railway Tracks,* Cambridge, MA, Swets and Zeitlinger, 1983.

407. Sayers MW, *'Dynamic terrain inputs to predict structural integrity of ground vehicles.'* University of Michigan Transportation Research Institute, UMTRI–88–16, 1988.

408. Sayers MW, Gillespie TD and Paterson WDO, *'Guidelines for conducting and calibrating road roughness measurements.'* World Bank, Technical Paper 46, 1986.

409. Schacke I and Barenholdt E, 'Heavy vehicles - some European observations.' *Proc. International Symposium on Heavy Vehicle Weights and Dimensions,* Kelowna, British Columbia, 1986.

410. Schiehlen W and Schäfer P, 'Modeling of Vehicles with Controlled Components.' *Proc. 10th IAVSD Symposium on the Dynamics of Vehicles,* Ed. Apetau M. Prague, Swets and Zeitlinger, 1987.

411. Schmidt B, *'A study of the relationship between temperature and stiffness of full depth asphalt pavements.'* Australian Road Research Board, Internal Report AIR 357-12, 1989.

412. Schweyer HE and Burns AM, 'Low temperature rheology of asphalt cements: stiffness and viscosity.' *Transportation Research Record,* 659 TRB 1977.

413. Scrivner FH and Duzan HC, *'Application of AASHO road test equations to mixed traffic.'* Proceedings of a Conference on The AASHO Road Test, St. Louis, Mo., National Academy of Sciences–National Research Council, Special Report 73, 1962.

414. Sebaaly BE, *'Dynamic Models for Pavement Analysis.'* PhD Thesis, Arizona State University, 1987.

415. Sebaaly PE and Mamlouk MS, 'Development of dynamic fatigue failure criterion.' *ASCE J. Transp. Eng,* 114 (4) pp 450-464, 1988.

416. Sebaaly PE and Mamlouk MS, 'Pavement response to dynamic loads.' *FHWA Load Equivalence Workshop,* Washington D.C., 1988.

417. Sebaaly PE, Tabatanee N and Scullion T, 'Comparison of backcalculated moduli from falling weight deflectometer and truck loading.' *TRR,* 1377 pp 17-25, 1991.

418. Seely B, *'Building the American highway system.' Technology and urban growth.* Brownell BAea ed. Temple Press, Philadelphia, 1987.

419. Segel L and Lang HH, 'The Mechanics of Automotive Hydraulic Dampers at High Stroking Frequencies.' *Vehicle System Dynamics,* 10 pp 79-83, 1981.

420. Seitz N and Hussmann AW, 'Forces and displacement in contact area of free rolling tires.' *SAE Trans.,* 710626 1971.

421. Semenov VA, 'Stress–strain state of a composite structure consisting of a stack of elastic plates on a multilayer granular base.' *Soviet Applied Mechanics,* 12 (3) pp 318–321, 1976.

422. Sharp RS and Crolla DA, 'Road vehicles suspension system design - a review.' *VSD,* 16 (3) pp 167–192, 1987.

423. Shinozuka M and Jan CM, 'Digital Simulation of Random Processes and its Applications.' *J.Sound Vib.,* 25 (1) pp 111-128, 1972.

424. Siddharthan R, Sebaaly PE and Javaregowda M, 'Influence of statistical variation in falling weight deflectometers on pavement analysis.' *TRR,* 1377 pp 57-66, 1992.

425. Simmons ICP and Mitchell CGB, 'The equalisation of truck bogie axle weights.' *2nd Int. Symp. on Heavy Vehicle Weights and Dimensions,* Kelowna, Canada, 1989.

426. Sisko AW and Brunstrum LC, 'The rheological properties of asphalts in relation to durability and pavement performance.' *A.A.P.T.,* 571 pp 448-475, 1968.

427. Slunga E and Saarelainen S, 'Determination of frost-susceptibility of soil.' *12th International Conference on Soil Mechanics and Foundation Engineering,* Rio de Janeiro, 1989.

428. Smiley RF and Horne WB, *'Mechanical properties of pneumatic tires, with special reference to modern aircraft tires.'* NACA, Tech. Note 4110, 76p, 1958.

429. Smith AR, *'Frame beaming, fifth wheel location - special body mounting and loading problems.'* SAE, Special Report SR 260, 1965.

430. Socie DF, 'Fatigue–life prediction using local stress–strain concepts.' *Experimental Mechanics*, February 1977 pp 50–56, 1977.

431. Soliman AMA and Crolla DA, 'Preview control of a semi-active suspension system.' International Journal of Vehicle Design, *17* (4) pp 384-397, 1996.

432. Sousa JB, Lysmer J, Chen SS and Monismith CL, 'Effects of dynamic loads on performance of asphalt concrete pavements.' *Transp. Res. Rec. (TRB)*, 1207 pp 145–168, 1988.

433. Sousa JB and Monismith CL, 'Dynamic response of paving materials.' *Transp. Res. Rec. TRB*, 1136 pp 57-68, 1987.

434. Southgate HF and Deen RC, *'Variations of fatigue due to unevenly loaded axles within tridem groups.'* University of Kentucky, Reserch Report UKTRP-84-11, 1984.

435. Southgate HF and Deen RC, *'Effect of load distributions and axle and tire configurations on pavement fatigue.'* University of Kentucky, Research Report UKTRP-85-13, 1985.

436. Southgate HF, Deen RC, Cain DH and Mayes JG, *'Modifications to Chevron N–Layer computer program.'* Coll. of Eng., Univ of Kentucky, Kentucky Transp. Res. Rep. UKTRP–87–28, 1987.

437. Southgate HF, Deen RC and Mayes JG, 'Strain energy analysis of pavement designs for heavy trucks.' *Transp. Res. Rec. TRB*, 949 pp 14-20, 1983.

438. Stergioulas LK, Cebon D and Macleod MD, 'Static weight estimation and system design for multiple-sensor weigh-in-motion.' *Submitted to J Mech Eng Sci, IMechE*, 1999.

439. Still PB and Jordan PG, *'Evaluation of the TRRL high-speed profilometer.'* TRRL, Crowthorne, Laboratory Report 922, 1980.

440. Stockham TJ, 'High-speed convolution and correlation with applications to digital filtering.' *Digital Processing of Signals*. Gold B and Rader C ed. McGraw-Hill, London, 1984.

441. Swannell P and Miller CW, 'Theoretical and experimental studies of a bridge-vehicle system.' *Proceedings of the Institution of Civil Engineers*, Part 2 (83) pp 613-615, 1987.

442. Sweatman PF, *'Effect of heavy vehicle suspensions on dynamic road loading.'* Australian Road Research Board, Research Report ARR 116, 1980.

443. Sweatman PF, *'A study of dynamic wheel forces in axle group suspensions of heavy vehicles.'* Australian Road Research Board, Special Report SR27, 1983.

444. Sweatman PF, 'Suspension research and its implementation.' *ARRB / FORS Symposium on Heavy Vehicle Suspension Characteristics*, Canberra, Australia, 1987.

445. Sweatman PF, 'Dynamic road loading: Instrumented vehicles.' *FHWA Load Equivalence Workshop*, Washington D.C., 1988.

446. Sweatman PF, Pearson R and Duncan W, *'Heavy vehicle suspension characteristics: The need for a design rule.'* Australian Road Research Board, Internal Report AIR 264-4, 1986.

447. Szendrei ME and Freeme CR, 'Road response to vibration tests.' *J. Soil Mech. and Founds. Div. of ASCE*, SM6 pp 2099-2123, 1970.

448. Tabatabaie A and Barenberg EJ, 'Finite Element Analysis of Jointed or Cracked Concrete Pavements.' *Transportation Research Record 671, TRB, National Research Council Washington, D.C.* pp 11-19, 1978.

449. Tada H, Paris PC and Irwin G, *'The stress analysis of cracks handbook.'* Paris Productions Inc., St Louis, MO, 1985.

450. Tam WS and Brown SF, 'Back-analyzed elastic stiffness: Comparison between different evalation procedures' *Nondestructive Testing of Pavements and Back-calculation of Moduli, ASTM STP 1026*, 1026 pp 189-200, 1989.

451. Tayabji SD, Ball CG and Okamoto P, 'Effect of frozen support and tridem axles on concrete pavement performance.' *Transp. Res. Rec. TRB*, 954 pp 38-51, 1984.

452. Tayebali AA, Rowe GM and Sousa JB, 'Fatigue response of asphalt-aggregate mixtures.' *AAPT*, pp 333-352. 1992.

453. Thompson AG, Davis BR and Pearce CEM, 'An Optimal Linear Active Suspension with Finite Road Preview.' *SAE Transaction, No 800520*, pp 2009-2020, 1980.

454. Thompson M and Barenburg EJ, *'Calibrated mechanistic structural analysis procedures for pavements.'* final report of NCHRP project 1-26 1989.

455. Thrower EN, *'Calculations of stresses, strains and displacements in a layered elastic structure, part II.'* RRL, Laboratory Report LR373, 1971.

456. Thrower EN, *'Permanent deformation in a linear viscoelastic model of a road pavement.'* TRRL, Supplementary Report SR184UC, 1975.

457. Thrower EN, *'A parametric study of a fatigue prediction model for bituminous road pavements.'* TRRL, Laboratory Report LR892, 1979.

458. Thrower EN, Mortazavi S and Dougill JW, *'Methods for predicting permanent deformation - flexible pavements.'* TRRL, Contractors Report CR38, 1986.

459. Tia M *et al.*, 'FEACONS III Computer Program for Analysis of Jointed Concrete Pavements.' *Transportation Research Record 1136, TRB, National Research Council Washington, D.C.*, pp 12-22, 1987.

460. Tielking JT, 'Finite element tire model.' *FHWA Load Equivalence Workshop*, Washington D.C., 1988.

461. Tielking JT and Roberts L, 'Tire contact pressure and its effect on pavement strain.' *A.S.C.E. Journal of Transportation Engineering*, 110, No:1 pp 56-71, 1987.

462. Tilly GP, *'Damping of highway bridges: a review.'* Transportation and Road Research Laboratory, Crowthorne, England., Symposium on dynamic behaviour of bridges, TRRL Supplementary Report 275, 1977.

463. Ting EC and Genin J, 'Dynamics of bridge structures.' *Solid Mech. Arch.*, 5 (3) pp 217-252, 1980.

464. Treybig HJ, 'Equivalency factor development for multiple axle configurations.' *Transp. Res. Rec. TRB*, 949 pp 32-44, 1983.

465. Uge P and Van de Loo PJ, 'Permanent deformation in asphalt mixes.' *Canadian Technical Asphalt Association*, 19 pp 307-341, 1974.

466. Ullidtz P, *'Pavement analysis.' Developments in Civil Engineering, 19.* Elsevier, 1987.

467. Ullidtz P, 'Mathematical model of pavement performance under moving wheel load.' *72nd Annual Meeting of the Transportation Research Board*, Washington DC, 1993.

468. Ullidtz P and Busch C, 'Laboratory testing of a full-scale pavement: the Danish road-testing machine.' *Transp. Res. Rec. TRB*, 715 pp 52-62, 1979.

469. Ullidtz P and Larsen BK, 'Mathematical model for predicting pavement performance.' *Transp. Res. Rec. TRB*, 949 pp 45-55, 1983.

470. Ullidtz P and Peattie R, 'Pavement analysis by programmable calculators.' *Transportation Engineering Journal of ASCE*, 106 No.TE5 pp 581-597, 1980.

471. Ullidtz P and Stubstad RN, 'Modelling of pavement performance.' *7th International Conference on Asphalt Pavements*, Nottingham, UK, 1992.

472. Urquhart FA and Rhodes AH, *'Characteristics of payload distribution on heavy goods vehicles: a case study.'* TRRL, Crowthorne, Research Report 80, 18p, 1986.

473. Uzan J, Kivneh M and Ishai I, 'Thickness design of flexible pavements with different layer structures.' *Australian Road Research*, 10 (1) pp 8–20, 1980.

474. Valkering CP, 'Effect of multiple wheel system and horizontal surface loads on pavement structures.' *Proc. 3rd Int. Conf. Struct. Design. Asphalt Pavements*, University of Michigan, Ann Arbor, 1972.

475. Van de Loo PJ, 'The creep test: a key tool in asphalt mix design and the prediction of pavement rutting.' *Proc. Assoc. Asphalt Paving Technology*, 47 pp 522–554, 1978.

476. Van der Poel C, 'A general system describing the visco-elastic properties of bitumen and its relation to routine test data.' *J. Appl. Chem.*, 4 pp 221-236, 1954.

477. Van Deusen BD, *'A statistical technique for the dynamic analysis of vehicles traversing rough yielding and non-yielding surfaces.'* NASA, CR-659, 43p, 1967.

478. Van Deusen DB, 'Truck suspension system optimisation.' *SAE Trans.*, 710222 1971.

479. Van Eldek Thieme HCA and Pacejka HB, 'The tire as a vehicle component, Ch. 7.' *NBS Monograph 122, Mechanics of pneumatic tires.* Clark SK ed. NBS, Washington D.C., 1971.

480. Veletsos A and Huang T, 'Analysis of dynamic response of highway bridges.' *ASCE Journal of Engineering Mechanics Division*, 96 (EM5) pp 593-620, 1970.

481. Verhasselt AF and Choquet FS, 'Comparing field and laboratory ageing of bitumens on a kinetic basis.' *Presented at the 72nd Annual Meeting of the Transportation Research Board*, Washington, DC, 1993.

482. Vinson TS, Jackson NM and Jung DH, 'Thermal cracking resistance of asphalt concrete: and experimental approach.' *7th Int. Conf. on Asphalt Pavements*, Ed. Brown SF and Hicks RG. 4 vols. Nottingham, UK, International Society for Asphalt Pavements, 1992.

483. Von Becker P, 'Commercial vehicle design - road stress: effect on transport policy decisions.' *Strasse und Autobahn (Translated by TRRL as WP/V&ED/87/28)*, 12 pp 493-498, 1985.

484. Walker W and Veletsos A, *'Response of simple-span highway bridges to moving vehicle loads.'* University of Illinois, Engineering Experiment Station, Urbana, Illinois, Bulletin 486, 1966.

485. Wallaschek J, 'Dynamics of Non-Linear Automobile Shock-Absorbers.' *Int. J. Non-Linear Mechanics*, 25 pp 299-308, 1990.

486. Walloschek HJ, 'Road loading as a function of vehicle characteristics.' *Proc. ARRB/FORS Symposium on Heavy Vehicle Suspension Characteristics*, Canberra, Australia, 1987.

487. Wang MC and Larson TD, 'Use of road rater deflections in pavement evaluation.' *Transportation Research Record*, 666 pp 129-150, 1978.

488. Westergaard HM, ' Computation of Stresses in Concrete Roads.' *Proceedings, Highway Research Board*, 5 (I) pp 90-112, 1926.

489. Westergaard HM, 'Stresses in concrete pavements computed by theoretical analysis.' *Public Roads*, 7 (2) 1926.

490. Westmann RA, 'Viscoelastic layered system subjected to moving loads.' *Proc. ASCE, J. Engineering Mechanics Div.*, EM3 (June) pp 201-218, 1967.

491. Whittemore AP, Wiley JR, Shultz PC and Pollock DE, *'Dynamic pavement loads of heavy highway vehicles.'* NCHRP, Highway Research Board, Report 105, 1970.

492. Wilding T, 'The long and short of our weighty laws.' *Roadway*, (March) pp 25-29, 1990.

493. Wilkinson PA, 'Advanced Commercial Vehicle Suspensions.' *Road wear: the interaction between vehicle suspensions and the road*, London, IMechE, 1991.

494. Williams ML, 'Structural analysis of viscoelastic materials.' *AIAA Journal*, 2 (1) pp 785-808, 1964.

495. Willis R, *'Appendix report of the commissioners appointed to inquire into the application of iron to railway structures.'* HMSO, London, 1849.

496. Wills J, *'Correlation of calculated and measured dynamic behaviour of bridges.'* Transport and Road Research Laboratory, Crowthorne, England., Symposium on dynamic behaviour of bridges. TRRL Supplementary Report 275, 1977.

497. Wilson DA, Sharp RS and Hassan SA, 'The Application of Linear Optimal Control Theory to the Design of Active Automotive Suspensions.' *VSD*, 15 pp 105-118, 1986.

498. Winkler CB, 'Measurement of inertial properties and suspension parameters of heavy highway vehicles.' *SAE Trans. 730182*, pp 720-732, 1973.

499. Winkler CB and Fancher PS, 'A rationale for regulating roll stability of combination vehicles.' *Proc. 3rd International Symposium on Heavy Vehicle Weights and Dimensions*, Ed. Cebon D and Mitchell CGB. Cambridge, Thomas Telford, 1992.

500. Winkler CB and Hagan M, 'A test facility for the measurement of heavy vehicle suspension parameters.' *SAE 800906*, pp 2754-2782, 1980.

501. Winkler CB, Karamihas SM and Bogard SE, 'Roll-stability performance of heavy-vehicle suspensions ' *SAE 922426*, 1992.

502. Woodrooffe J, 'Heavy vehicle suspensions: methods for evaluating road-friendliness.' OECD DIVINE Project, Element 3 Report, 1996.

503. Woodrooffe JH and El-Gindy M, 'Application of handling and roll stability performance measures for determining a suitable tractor wheelbase.' *Proc. 3rd International Symposium on Heavy Vehicle Weights and Dimensions*, Ed. Cebon D and Mitchell CGB. Cambridge, Thomas Telford, 1992.

504. Woodrooffe JHF and Le Blanc PA, 'Heavy vehicle suspension variations affecting road life.' *Proc ARRB/FORS Symposium on Heavy Vehicle Suspension Characteristics*, Canberra, Australia, 1987.

505. Woodrooffe JHF, LeBlanc PA and LePiane KR, *'Effects of suspension variations on the dynamic wheel loads of a heavy articulated highway vehicle.'* Canroad Transportation Research Corporation, Canada, Vehicle Weights and Dimensions Study Vol 11, 1986.

506. Woodrooffe JHF, LeBlanc PA and Papagiannakis AT, 'Suspension dynamics - experimental findings and regulatory implications.' *SAE Conference on Vehicle/Pavement Interaction, SP765, SAE Trans. 881847*, Indianapolis, 1988.

507. Wren JA, *'Motor trucks of America.'* The University of Michigan Press, Ann Arbor, USA, 1979.

508. Wu F, 'Effect of traffic loading and binder ageing on the structural deterioration of bituminous pavements.' *Third International Symposium on Heavy Vehicle Weights and Dimensions*, Ed. Cebon D and Mitchell CGB Cambridge, UK, Thomas Telford Ltd, 1992.

509. Yabuta K, Hidaka K and Fukushima N, 'Influence of suspension friction on riding comfort.' *7th IAVSD Symposium on the Dynamics of Vehicles on Roads and Tracks*, Cambridge, Swets & Zeitlinger, 1981.

510. Yang JN, 'On the Normality and Accuracy of Simulated Random Processes.' *J.Sound Vib.*, 26 (3) pp 417-428, 1973.

511. Yap P, 'A comparative study of the effects of truck tire types on road contact pressures.' *SAE Conference on Vehicle/Pavement Interaction, SAE SP765, SAE Trans. 881847*, Indianapolis, 1988.

512. Yap P, 'Truck tire types and road contact pressures.' *2nd International Symposium on Heavy Vehicle Weights and Dimensions*, Kelowna, British Columbia, 1989.

513. Yi K and Hedrick JK, 'Active and semi-active heavy truck suspension to reduce pavement damage.' *SAE Trans*, 892486 ((SP 802)) pp 29-36, 1989.

514. Yi K, Wargelin M and Hedrick JK, 'Semi-active suspensions to reduce pavement damage: theoretical design and implementation.' *Third Int. Conf. on Heavy Vehicle Weights and Dimensions*, Ed. Cebon D and Mitchell CGB. Cambridge, UK, Thomas Telford, 1992.

515. Young W, *'Roark's Formulas for Stress and Strain, 6th Edition.'* McGraw-Hill, London, 1989.

516. Zube E and Forsyth R, 'An investigation of the destructive effect of floatation tires on flexible pavement.' *Highway Res. Rec., HRB*, N71 pp 129-150, 1965.

APPENDIX C
INDEX

A

ABAQUS 264
A34 trunk road 357
A500T trunk road 379
AASHO 8, 567
AASHO road test 9, 10, 157, 162, 238, 369
AASHTO 567
AASHTO
  Pavement design guide 15
  Temperature correction 288
Abbreviations 567
Accelerated Loading Facility (see ALF)
Accelerometers 84, 92, 109, 174, 535
Accuracy of WIM sensors 114, 126
Active suspensions 438
Adaptive suspension 464
Adiabatic deflection equation 429
Advanced Suspensions 438
Ageing of asphalt 281, 371, 374
Aggregate First Power Forces 353
Aggregate force 311, 323, 353, 360, 523
Aggregate Force Damage Criterion 360
Aggregate Fourth Power Forces 354, 360, 447, 460, 473
Aggregate
  Gradation 248
  Interlock 202
Aggregate tyre force spectral density 327
Air bag 31
Air spring
  Model 429
  Stiffness 462
Air sprung drive axle 119
Air suspensions 12, 31, 124, 302, 320, 356,403, 428–434, 438, 459, 507, 511, 525, 550
  Static load sharing 358
  Equivalent 511
Air temperature 288, 371
ALF 286, 287, 307, 567
Anisotropy 178
Annual inspection 507, 550–553
Anti-roll bar 91, 97, 459, 467
ARRB 286, 567
Articulated beam suspensions 14
Asphalt Layer
  Frequency dependence of 166
  Temperature distribution 268
  Viscosity 255
Asphalt Mix
  Ageing 374
  Damping 286
  Elastic Properties 373
  Modulus Degradation 288, 377
  Properties 271
  Stiffness 247, 373
  Viscosity 244, 249, 251
Asphalt strain gauges 174, 508
Assessment of suspensions
  Convolution Method 539
  Criteria 508, 514
  Direct Methods 509, 510
  Dynamic interaction 508
  Frequencies 508
  Implementation Issues 550
  Indirect testing 509, 511, 534
  Laboratory tests 511
  Mass distribution 508
  Methods 509
  Nonlinearity 508
  Parameter Estimation Method 543
  Parameter measurement 511
  Payload configuration 514
  Pragmatic approach 552
  Proposed tests 551
  Recommendations 550, 554
  Requirements 508
  Road roughness 508, 518
  Sampling Frequency 515
  Spatial repeatability 508
  Static load sharing 508
  Step height 515
  Technically rigorous 551
  Test Duration 515
  Test rig 553
  Test track length 515
  Testing scenarios 507
  Testing speed 518
  Tests on Whole Vehicles using Indirect Methods 521
  Theoretical road damage 510
  Tractor - Trailer Interaction 521
  Vehicle Response Issues 515
  Wheelbase filtering 518
Assessment of road damage potential 525
Assumptions in WLPPM 400
Autocorrelation function 26
Auxiliary roll stiffness 90
Axle
  Configuration 300
  Spacing 73, 116, 124
  Travel 84

B

BA 567 (see Body Acceleration)
Back calculation of modulus 285
Base strain 175, 180, 191
BB (see Benkelman Beam)
Bending
  Acceleration 96
  Frequency 429
  Moment 109
  Strain 108, 109
  Vibration 121
Benkelman Beam 284–286, 567
Benz, Carl 7
Bernoulli-Euler beam 214
Bias ply tyres 307
Bicycle 5
Binder film 248, 251
BISAR 260
Bitumen 6, 17
  Viscosity 246
Blow-ups 15
Body Acceleration 48, 50, 477–479, 498
Body bounce
  Frequency 171
  Mode of vibration 75
Bogie suspension 12, 85
  Pitch 85
  Pitch damping 71
  Pitching motion 118
Bonnaire nomograph 247
Bounce
  Accelerations 94
  Components of tyre forces 94
  Excitation frequency 520
  Model 461
  Spectral density 92
Boundary conditions 214
Bridge 208
  Bending modes 227
  Deflection 213, 222
  Displacement response increment 432
  Dynamic response 162, 228
  Effects of suspension type 428
  Extraction of Modal Parameters 224
  Failures 208
  Fourier Spectra 234
  Frequencies 427, 432
  Instrumentation 219
  Instrumentation 220
  Instrumented vehicle tests 223
  Linearity 222
  Maintenance 208
  Modal analysis 221, 223, 224
  Mode Shapes 229
  Mode shapes 231
  Response to Vehicle Loads 209, 431, 433
  Surface profile 213
  Surface Profiles 427, 430
  Torsional vibration 232
  Transfer functions 223, 225
  Vehicle effects 427
  Vibration 208, 427
  Vibration modes 430
Bridge models 214, 224, 429
  Beam models 226
  Closed-form solutions 215
  Equation of Motion 209
  Finite element analysis 227, 228
  Properties. 228
  Solution in the Frequency Domain 211
  Validation 162, 228–234
Bridge simulation
  Computational sonsiderations 215
  Convergence 219
  Convergence procedure 213
Bridge-vehicle interaction 163, 213, 219, 428
  Criteria 163
Bump stops 84, 85
Burger's model 242, 246, 251
Buried strain gauges 508
Burmister 159

C

Cab vibration 102
California Bearing Ratio 9
Callington trials 287
Camber stiffness (tyres) 307, 308
Capacitative strip sensor 114, 115, 131
CBR 567
Central limit theorem 24
Centrally-pivoted suspensions 124
Centre of pressure 109
Chassis
  Bending 90
  Twisting 90
Circular correlation function 26
Climatic Factors 371
Coal tar 4
Coherence function 25, 26, 72, 73, 85, 456
Collar 8
Compaction 241
Comparison of Vehicle Features 320
Compensation time 478
Compliance 53
Computer simulations of heavy vehicles 83
Computer–controlled suspensions 437
Conclusions
  Guideway response 557
  Road Damage mechanisms 558
  Suspension assessment 561
  Suspension design 560
  Vehicle dynamics 557
  Vehicle–guideway interaction 558
Conflict diagram 479, 483
Contact pressure 159
  Distribution 145, 304
  Stress 457
Continuous pavements 165
Continuously variable damper 478

Controllable Dampers 31, 55, 66
Controlled strain 284
Controlled stress 284
Controller bandwidth 487
Conventional Simulation Error 393
Convolution integral 167, 195, 209, 243, 276, 539
Convolution method - errors 543
Coordinate transformation matrices 79
Cornering manoeuvres 450
Cornering stiffness (tyres) 456
Correlation 25
  Axles 468
  Coefficient 361, 528
  Road Profiles 25
  Tyre Forces 361
Correlation Analysis 528
  Tractor-trailer interaction 532
Correspondence principle 244
Cost
  Structural maintenance 423
  Vehicle testing 551
Crack
  Evolution 278
  Growth 274
  Initial length 280
  Tip 273
Cracking 238
Cramer-Rao Bounds (CRB) 147
Creep
  Compliances 246
  Deformation 248
  Speed 285
  Test 247
Critical speeds 316, 468
Crompton 8
Cross spectral densities 21, 25, 72
Cross-coupling of suspensions 120
Cross-spectral analysis 37
CSE 398, 567
CUED 567
Cugnot 7
Cycles to failure 291

D

d'Alembert 110
DAFC (see Dynamic Aggregate Force Coefficient)
Damage mechanics 292
Damage propagation 369, 387
Damper Force Control (Semi-Active)
  Force Feedback 60
  Open Loop 59
  Transients 57
Damper Model 43
  Look-up table 488
  Model Assumptions 49
  Parameter estimation 547
  Parameters 544, 545
Dampers 447
  Force 48, 50
  Rate 453, 527
  Wear 365, 553
Damping matrix 69
Damping ratio 310, 511, 520, 527
DBM (see Dense Bituminous Macadam)
Definition
  Asphalt 14
  Composite pavements 14
  Contact tractions 14
  Flexible pavement 14
  Frequency 12
  Mean square spectral density 12
  Power spectral density 12
  Primary response 14
  PSD 12
  Random 12
  Rigid pavements 14
  Road base 14
  Root Mean Square 12
  Spectral Density 12
  Spectrum 12
  Subbase 14
  Subgrade 14
  Tandem suspensions 12
  Triaxle suspensions 12
  Wearing course 14
Deflection bowl 285
Deflection of tyres 111
Degrees of freedom 69, 70
Dense Bituminous Macadam 14, 173, 567
Densification rutting 241
Derivative control 63
Design life of pavements 17
DFT 567 (see Discrete Fourier Transform)
Diffusion model 374
Diplock 7
Direct spectral densities 72
Direct assessment tests 551
Discrete Fourier Transform 24, 85, 212, 215, 223
Displacement spectral density 22
DIVINE project
  Accelerated pavement tests 390
  Bridge project 427
DLA 567 (see Dynamic Load Allowance)
DLC 567 (see Dynamic Load Coefficient)
DOF 567
Dominant frequencies 118
Dominant wavelength 338
Doppler shift in pavement response 169
Draft ISO classification for road roughness 22, 23
Dual tyres 130, 304, 305, 308, 372, 440, 453
Dynamic Aggregate Force Coefficient 523, 530, 567
Dynamic bridge displacements 428
Dynamic bridge model 162
Dynamic interaction
  Tractors and trailers 508
  Vehicles and bridges 162

Dynamic Load Allowance 428
Dynamic Load Coefficient 71, 75, 115, 123, 135, 309, 358, 443, 453, 511, 523, 529
Dynamic Response Increments 163, 432, 433
Dynamic road response models 160, 165, 166
Dynamic sensor error 141
Dynamic Tyre Forces vi, 67, 108
  Calibration 110
  Cross–coupling between suspensions 119
  Effect of axle spacing 124
  Effect of friction 124
  Effect of nonlinearities 116
  Effect of road roughness 124
  Effect of speed 76, 123
  Effect of structural vibration 121
  Effect of suspension stiffness 123
  Effect of tyre pressure 124
  Effect of tyre type 124
  Experimental studies 123
  Frequencies 116
  Influence of payload distribution 120
  Influence of roll motion 121
  Influence of tyres and suspensions 122
  Instrumentation 109
  Literature review 108
  Magnitudes 115
  Principal features 115
  Probability distribution 115
  Spatial repeatability 121
  Tyre non–uniformities 121
  Wheelbase filtering 116
Dynamic wheel (axle) load vi

E

EC road-friendly regulation 510
Economic evaluation
  Suspensions 403, 421
  Dynamic loads 515
ECOV 567 (see Error Coefficient of Variation)
Effect of axle spacing on road damage 300
Effect of:
  Ageing on rutting 415
  Loading frequency on pavement response 165, 184, 185
  Spatial repeatability on road damage 404
  Speed on flexible pavements 159, 165, 166, 171, 184
  Speed on rigid pavements 205
  Suspension type on road damage 414
  Temperature on road response 178
  Vehicle features on road damage 321
Effective stiffness of leaf springs 441, 442
EGH 567
Eigenvalues and Eigenvectors 76, 118
Elastic
  Half space 262
  Layer calculations 159
  Modulus 280, 281, 373
  Waves 157
Elastic layer pavement models 159, 304
Electric trucks 7
Energy dissipation in suspensions 87, 116
Energy radiation in roads 181
Engine vibration 102
Environmental conditions 280, 320
Environmental effects on pavements 371
Equation of motion
  Bridge vibration 209
  First order form 70
  Vehicle dynamics 69,77
Equivalence factors 11
Equivalent standard axle loads 9, 10, 237, 238
Error Coefficient of Variation 135, 141, 143
Error spectral density 136
ESAL 567 (see Equivalent Standard Axle Loads)
Euler beam 169, 315
European regulations 424, 515
European suspension test 510–512, 529
Excitation by road roughness 126
Excitation frequencies 116
Expansion joints 430
Experimental Measures of Spatial Repeatability 332
Experimental studies of dynamic forces 122
Extended ground–hook control 477

F

Failure mechanisms 238
Failure mode 421
Falling Weight Deflectometer 284–286,
Fancher leaf spring model 32
Fast fracture 274, 281
Fatigue cracking 14, 15, 280–284, 308, 320, 354
  Asphalt 239
  Cycle counting 315, 351, 375
  Damage 191, 238, 299, 305, 316, 318, 355, 419
  Damage accumulation 416
  Damage model 291, 351
  Model 375
  Parameters 276
  PCC 239
Faulting 15
FEA 567 (see Finite Element Analysis)
FFT 171, 567
FHWA 567
Finite Element
  Analysis of Cracking 264
  Method 159, 197
  Model 197, 201
Fixed footprint tyre model 85
Flat-bed trailer 440
Fleet Operating Conditions 330
Flexibility of road/mounting 131

Flexible pavement 16, 165
  Deflection 158
  Design 159
  Fatigue cracking 260
  Response 159
  Stiffness loss 283
Flexural vibration 90, 111
Fluid viscosity 57
Flushness of mounting 132
Force feedback 60, 63, 485, 488
Force measuring hubs 551
Force transformation matrices 79
Force-deflection
  Leaf springs 32, 85
  Tandem suspension 441
Foundation
  Reaction 172
  Stress 172
Four-spring suspension 31, 97, 313, 318, 443
Fourier spectrum 229
Fourier transform 169, 175, 211, 271
Fourth power law 9, 10, 237, 306, 309, 310, 403
Fracture Mechanics 273
Fracture toughness of asphalts 274
Frame bending 84, 90
  Flexibility 107
  Frequency 96
  Modes 97
  Torsional resonances 121
  Twisting 84
  Vibration 121
Frequencies of dynamic loads 138
Frequency Domain Calculation
  Bridge response 211
  Road response 169
  Vehicle response 72
Friction 12, 29, 98, 102
Full state feedback (FSF) 476, 478, 491, 492, 498
  Control law 495
  Controller Design 492
Future Research 563
FWD 567 (see Falling Weight Deflectometer)

G

Gaussian 21, 24, 115, 150
Generalised coordinates 69
Generalised forces 69, 78
Generic vehicle model 552
Golden River 335, 342
Goodyear 8
Granular sub-base layer properties 374
Gravitational vector 81
Gross Vehicle Weight 297
Gross vehicle weight distribution 344
Guidelines for suspension design 459
Guideway response 157

H

Hardware in the Loop Method 41
  Apparatus 41
  Measurements 494
  Rig 478
  Tests 476
Harmonic response function 170
Heat conduction 268
Hertzian contact 277
High-speed profilometer 440
HiL 567 (see Hardware in the Loop)
History of vehicle-road interaction 3
Hot Rolled Asphalt 14, 173
Hot spots 312, 369, 380
HRA 567 (see Hot Rolled Asphalt)
Hydraulic Dampers 30, 41, 65, 91, 537, 450
  Model 44
Hysteresis loops 46, 190

I

ILLI-SLAB 197
Impulse Hammer 174, 220
Impulse response 167, 178
Impulse response function 167, 175, 209, 541
Independent suspension 455, 466, 467
Indirect Tests 552
Inertia
  Correction 32, 84, 92, 109, 111
  Force 110
  Matrix 77
  Parameters 544, 545
  Properties 97
Inertial frame of reference 76
Inflation pressures 306
Influence Function 187, 190, 197, 257, 300, 301, 379
  Calculation 191, 256
  Near a crack 198
  Permanent Deformation 244
Input correlation 468
Input spectral matrix 72, 75, 136
Instrumented
  Axle 509
  Hammer 220
  Hubs 111
  Vehicle 178, 221, 342, 440, 509, 534
Integral control 63
Interface conditions 159
International Roughness Index 372, 387, 567
Inverse Fourier transform 171, 212
In-service damping 550
IRI 372 (see International Roughness Index)
Isotropic
  Pavement response 177
  Surface roughness 26, 28, 73, 456

J

Jointed rigid pavements 159, 196

K

Kinetic energy 77

L

Lagrange's equations 77
Land Rover 535
Lateral tyre force 455, 467
Layer strain approach 241
Layer thickness 266
  Artificial generation 392
  Variations 380
Leaf spring 29, 32, 65, 85, 116, 121, 313, 439, 535
  Data 97
  Drive axle suspension 119
  Elements 97
  Kinematics 98
  Model 536
  Parameters 544, 545, 548
  Stiffness 462
  Suspensions 12, 124, 428, 434
  Testing Apparatus 32
LEFM 567 (see Linear Elastic Fracture Mechanics)
Legislation 507
Linear autocorrelation function 26
Linear elastic fracture mechanics 261, 273
Linear
  Optimal control theory 491
  PID Controller 60
  System Theory 242
  Vehicle models 67, 69, 72
  Viscous Damping 53
Linearised 67
  Damper model 53
  Vehicle Model 80, 87, 134
Linearity of flexible pavement response 175
Literature review
  Asphalt fatigue 260
  Back-calculation of structural properties 285
  Bridge-vehicle interaction 162
  Dynamic road response models 165
  Dynamic tyre forces 108
  Effects of static loads on pavements 297
  Effects of tyres 304
  Effects of vehicle features on road damage 320
  Effects of vehicles on bridge response 427
  Features of dynamic tyre forces 115
  Features of road surface response 157
  Influence of vehicle features on dynamic tyre forces 122
  Measuring dynamic tyre forces 108
  Pavement response models 159
  Pavement stiffness testing 283
  Permanent deformation 241
  Road damage due to dynamic loads 309
  Road damage prediction 237
  Semi-active suspensions 476
  Spatial repeatability 322
  Static load sharing 300
  Suspension assessment 507
  Suspension components 29
  Validation of vehicle simulations 83
  Weigh-in motion 125
  Whole-life pavement performance models 368
Load cell 535
Load equalisation 127, 358, 443
Load equivalence factors 8, 307
Load levelling beam 101
Load measuring mat 114, 115, 335, 509, 515, 534, 551
  Accuracy 140, 141
  Calibration 140
  Calibration 335, 342
  Drift 141
  Highway tests 342
  Installation 335, 341
  Operation 343
  Sensitivity to speed 140
  Vehicle Tests 335
Load Sharing Coefficient 301, 357, 359
Load transfer across a crack 204
Load transfer across joints 201
Loading times 246
Longitudinal acceleration 98
Longitudinal pavement strain 198, 203
Look-ahead preview 478
Look-ahead sensor 478
Loop gain 487
Low temperature cracking 15
LSC 567 (see Load Sharing Coefficient)
LVDT 176, 177, 567

M

Mass matrix 69
Mass parameters 544
Material
  Damage models 315
  Damage relationships 239
  Damping 181, 286
  Parameters 271
Mathematical models 85
  Suspension test Rig 536
  Vehicle fleet 526
Matrix formulation of vibration equations 77
Maximum likelihood method 147, 150
Maxwell model 269, 271
McAdam 4, 5, 8

Measurement noise (effect on spatial repeatability) 333
Measures of Road Damaging Potential 529
Measuring Dynamic Tyre Forces 108
measuring the primary response of roads 161
Mechanistic
  Road damage prediction 239
  Road design 237
Miner's hypothesis 193, 291, 315, 351, 375
MIRA 568
Modal
  Analysis 76
  Circle fitting 224
  Damping ratio 214, 429
  Excitation 519
  Expansion 209
  Frequency response function 212
  Impulse response function 210
Mode shapes
  Articulated vehicle 118
  Bridge vibration 209
Modes of vibration 116
Model validation 83
  Bridges 162
  Pavement Response 159
  Quarter–car test rig 538
Modified skyhook damping 476–498
Modulus Ratio 264
Moisture level 131, 159
Monte Carlo simulations 150
Moving convolution integral 169
Moving frame of reference 183
MSD 568 (see Modified Skyhook Damping)
Mulgrave tests 286
Multiple-Sensor Weigh-In-Motion (MS-WIM) 128, 132, 568
  Aliasing 134, 146
  Design procedure 138
  Design spacing 145
  Envelope error 133
  Experimental results 143, 144
  Influence of tyre tread 145
  Nondimensional spacing 133
  Off-road tyres 145
  Random input 134
  RMS error 133, 135
  Sensitivity to frequency 138
  Sensitivity to speed 144
  Sensor spacing 132, 138, 144
  Sinusoidal input 132
  Theoretical results 143, 145
  Vehicle speeds 138
Multi-leaf springs 91

N

National Speed Survey (UK) 392
Natural frequencies 118, 310, 429, 511
Natural Motions 76
Navistar test track 114, 140
NDT 283, 568
Noise 62
Noise to signal ratio 333
Non-destructive testing, pavements 283, 284
Non-dimensional sensor spacing 132
Non-dimensional WIM error 132
Nonlinear
  Constitutive elements 76
  Gain compensation 61
  Soil strain gauges 181
  Vehicle models 86
  Vehicles 67, 508
Normalised RMS Error (NRE) 48, 540
Numerical Accuracy 434
Numerical convolution 166, 172, 539
Numerical integration 70, 79, 83
Nyquist frequency 212, 215

O

OECD 254, 256, 306, 309, 568
Off-road
  Tyres 145
  Vehicle 84
  Suspensions 68
Ontario Highway Bridge Design Code (OHBDC) 428, 568
On–Off Control 478, 489
Open loop damper control 62, 485
Optimal
  Axle spacing 300
  Control gains 492
  Damping 453, 462
  Passive damping 464, 479, 480
  Stiffness 444, 453, 462
Orthogonality conditions 209
Orthotropic plate 227
Out-of-balance 121
Outboard mass 109, 110
Output correlation 468
Overloading 126

P

Paccar Technical Center 200
Parabolic steel springs 124, 449
Parameter estimation 543, 544
  Effect of step height 549
  Fitting strategy 544
  Method 544
Parametric tests 509
Paris law 274
Passive Damping 479
Passive Suspensions 438, 459
Pavement analysis systems 159

Pavement
Cracking - parametric study 280
Dynamics 166
Failure criteria 393, 418
Inertia 286
Instrumentation 174
Instrumentation 515
Life evaluation criteria 393
Life prediction 159
Life reduction factor (PLRF) 393, 397, 568
Maintenance expenditure 424
Material nonlinearity 157
Primary response 368, 372, 508
Stiffness variations 378
Strains 190, 200
Structural model 264
Surface profile 372
Surface response 304
Temperature 131
Thickness variations 378
Paving stones 4
Payload 92
Configuration 514
Distribution 97, 107
PCC 568
PDF 568
Peak dynamic loads 423
PEN 568
Penetration 373
Penetration and layer systems 6
Penetration Index 245, 373
Permanent deformation 14, 241, 307, 418
Model 351, 352, 376
Phase lag (semi-active damper) 487
Phase Lag Compensation 476, 500,568
Phase of dynamic tyre force 407
Phase shift 406
PID 568
Controller 61
Gains 485
Piezoelectric cables 112, 131
Pitch-plane
Excitation 121, 520
Vehicle models 73, 107, 467
Pitching
Modes 118
Motion 84, 68, 75
Pivoted-spring suspensions 14, 85
Plane strain elastic half space model 262
Plant mix 6
PLC 568 (see Phase Lag Compensation)
Pneumatic tyre 5, 8
Point contact tyre model 85
Poisson's ratio 250, 373
Portland cement bound macadam 4
Portland cement concrete 14, 117, 166
Positive feedback 419
Potholes 21, 312, 419, 423
Present Serviceability Index (PSI) 9
Preview control 476, 500
Primary pavement responses 197, 238, 508, 509, 157, 261, 509
Continuous pavements 166
Influence functions 370
Model 372
Principal features
Dynamic tyre forces 108
Road surface response 157
Probability density function 130
Probability distribution 21
Profilometer 92
PSD 568
Pseudo-random profiles 21
PSI 9, 568
Punch-outs 15
P-P 568

Q

Quarter car model 42, 67, 75, 169, 310, 372

R

R&B 568
Radial ply tyres 91, 307
Radial run-out 96, 121
Radius rods 102, 443
Railways 4
Rainflow counting 193, 315, 375
Random thickness variation 388
Ranking of vehicles 298, 349, 354
Recommendations
Assessment 550
Road design and construction 562
Tyre and suspension design 562
Vehicle regulation 562
Red Flag Act 6
References 569
Reflection cracking 15
Regulations controlling dynamic tyre forces 507
Regulator problem 492
Removable instrumentation 552
Rheology
Asphalts 241, 247
Bitumen 244, 245
Rheometer 253
Riccati equation 492
Ride accelerations 97
Ride height 550
Rigid axle suspension 455, 467
Rigid pavement 6, 16, 301, 319
Design 9
Field Experiments 200
Influence functions 199
Model 196
Model Validation 201
Ring and Ball softening temperature 245, 255, 373

RMS 568
Body acceleration 43
Damper force 495
Suspension deflection 43
Tyre force 43, 72
Road construction methods 6
Road damage 447, 454, 498
Criteria 240, 309, 447, 460
Mechanisms 15
Prediction 237
Statistics 351
Road damaging potential 349, 524, 508
Road design 237
Road material properties (see Material)
Road model parameters 351
Road profile 21, 68, 92
Spectral density 25, 93, 462
Road Rater 285
Road Response
Calculations 314
Due to dynamic tyre forces 166
Models 237
Moving inputs 167
Road simulator 509, 510, 534, 551
Road Strength 355
Road Stress Committee 309
Road Stress Factor 309, 310, 317, 403, 405, 423, 498
Road structure
Models 350
Nonlinearity 131
Nonuniformity 131
Road surface
Deterioration vi
Profiles 85
Roughness 72, 84, 440
Stresses 261
Topography 21
Road Traffic Act of 1930 7
Road-friendly suspension 416, 510
Assessment 508
Road-based instrumentation 108, 112
Roll 84, 94
Acceleration 110
Angle 110
Components of tyre forces 94
Excitation 93
Moment of inertia 110
Plane excitation 121
Spectral density 92
Roll-over
Model 454
Performance 454, 437
Stability 440, 456, 465
Threshold 444
Roll-Plane
Model 73, 465
Performance 454
Roll/bounce ratio 93
Roman routes 4
Rotational acceleration 110
Rotational inertia 98
Roughness
Flexible pavements 115
Rigid pavements 115
Rubber
Blocks 443, 450, 473
Bushings 43
Walking-beam suspension 356
Rut formation 307
Rutting 14, 16, 238, 241, 308, 353, 354, 415
Calculation 256
Model 242
Proportions in each layer 391

S

SAC 568
SAFSF 494, 568
Sample Mean 150
SAMSD 568
SD 568
SDN 405, 568
SE 568
Seal-coated pavements 6, 14
Seasonal variation in temperatures 393
Semi-active damper 31, 42, 55, 438, 500, 476-481
Force tracking 61, 64, 65, 486
Phase lag 63
Switching time 488
Semi-Active Damper Control
Full State Feedback 494
Modified Skyhook Damping 483
Pre-processor 60
Sensor spacing 515
Shackles 303
Shear force 108
Shear strains 110
Shear tractions 304
Shock absorber flexibility 46
Shock absorber model 538
Short wavelength filtering 85
short-span highway bridges 164, 427, 429
SHRP 114, 242, 568
Side forces 109
Side-slip 110
Simply-supported bridge 163
Simulation, 67
Assumptions 97
Dynamic wheel loads 83
Errors 90
Methods 70
Vehicle fleet 323, 526, 533
Single and dual tyres 453
Single axles 509, 510
Air suspension 68
Single-point tandem suspension 14, 31, 124
Single-sensor WIM systems 125, 129
Single-vehicle pass calculations 314, 350
Skid resistance 15
Skyhook damper 476, 482
Sliding contact 303, 443, 473

Slipper ends 303
Slipper friction 102, 441, 443
Slow active suspensions 438
Small deflections 76, 77
Softening point temperature 374
Soil strain
  Gauge responses 182
  Measurement 176
  Response 175, 186
Solid rubber tyres 7
Sources of WIM Error 130
Spalling 15
Spatial concentration of loading 524
Spatial correlation 361
Spatial Distribution Number 405
Spatial repeatability 122, 127, 130, 312, 318, 322, 369, 392, 402, 499
  Accumulated damage 325, 329
  Aggregate fourth power force 340
  Characterising 404
  Correction for measurement errors 337
  Correlation coefficient 324, 326
  Effect of sensor noise 405
  Effect of speed 327, 337
  Effects of vehicle configuration 338
  Experimental study 332
  Index (SRI) 332, 404
  Measurement noise 333
  Measurements 338
  Measures 324
  Reference vehicle 328, 344
  Results of highway tests 347
  Separation of Peaks 325
  Simulation 323
  Summary of Results 330
  Theoretical Study 323
Spectral analysis 24
Spectral density 21, 24, 72
Spectral descriptions of road roughness 21, 22
Speed effect 158, 165, 166, 286, 316
Speed sensitivity 131
Spring
  Ends 303
  Lash 445
  Stiffnesses 527
Sprung mass 67, 464
  Bounce 84
  Mode wavelength 328
  Modes 119
  Roll 94, 121
  Roll modes 93
  Vibration 118, 442
  Vibration modes 116
SRI 332, 404, 568
Standard axle loads 9
Standard
  Tractor 525
  Trailer 525
  Vehicle units 551
Static Loading 297
Static axle load vi, 125, 171
  Enforcement 147
  Equalisation 438
  Levelling 101
  Sharing 68, 300, 301, 508
  Transfer 127
Static Deflection 443, 444
Static road response models 159
Stationary random process 516
Steam engines 7
Steam-powered trucks 7
Steel spring suspensions 7, 403, 416, 438
  Static load sharing 358
Step response 70
Stiffness
  Degradation model 377
  Loss in flexible pavements 283
  Matrix 69
Stiffness of bitumen 244, 247, 280
Stiffness of the road structure 131
Strain gauge 92, 109, 200
Strain measurement errors 166
Strain-gauged axles 108
Strategic Highway Research Program 242
Stress intensity factor 273–277
Stresses in pavements 165
Strip sensors 131
Structural isotropy 159
Subgrade layer elastic properties 374
Subgrade rutting 386
  Model 389, 410
Super-single tyres 304
Superposition 175, 197, 199, 244
Surface
  Cracking 238, 261, 281, 289
  Deflection 165
  Deflection measurement 284
  Roughness 372
  Roughness evolution 386, 417
  Stress 265
  Temperature 268
Suspension
  Assessment 332, 507
  Components 29
  Dampers 438
  Damping 432, 527
  Deflection 48, 50, 493, 498, 511
  Design criteria 437
  Design trade-offs 437
  Frequencies 527, 529
  Geometry 303
  Models 85
  Modifications 443, 444, 449, 450, 451
  Nonlinearities 68
  Options for improvement 437
  Parameter study 443
  Parameters 508
  Test rig 535, 539, 553
  Trade-off 455
  Type 402
Swiss design code 428
Synchronisation 335

T

Tandem Suspension Measurements 441
Tandem suspensions 124, 353
Tar–macadam 4
Telford 4, 5
Temperature 159
  Air 371
  Correction 288
  Dependence 45
  Distribution 268
  Effects 255
  Pavement surface 371
  Sensitivity of the road response 178
  Variation 407
Terminology 12
Test rig for tandem suspension 441, 535
Test track length 516
Testing Methodologies
  Assessment 509
  Procedures 507
Theoretical road damage 191, 457, 509
Thermal diffusivity 268, 271
Thermal Loading 268, 280
Thickness design 373
Thickness Variation 383, 395
Three dimensional vehicle models 25, 72, 85, 102
Time delays 478
Time domain simulations 70, 83
Time lag 486
Time lag between axles 73
Tinsley Bridge Ltd 449
Topographical data 84
Torsion bar suspension 13, 124, 318, 550
Torsional flexibility 94
Track width 457
Tractor
  Damage index 528
  Suspension model 97
Tractor-trailer interaction 119, 355, 523–525
Trailer
  Bending 96, 102
  Damage index 528, 531
  Pitch inertia 527, 530
  Suspension model 97
Transfer Function 72, 74, 136, 541
Tansformation matrices 78, 81
Transport and Road Research Laboratory (TRRL) 91, 101, 238, 429, 568
Transport Research Laboratory (TRL) 114, 173, 220, 332, 440, 449, 471, 568
TRL test track 23
Transport statistics 126
Transverse stress 262–264, 269, 271, 276
Tread pattern 153
Tread wear 306
Trésaguet 4, 5
Trevithick 7
Triaxle suspensions 124, 353
Twin-tube shock 42
Two-dimensional models 96
Two–dimensional Fourier transform 169
Type-Approval Tests 507, 550, 551
Tyre 439, 454
  Configuration 266, 305
  Contact Conditions 304
  Contact pressure 114, 159
  Effects 304
  Envelopment 24, 85, 97, 107
  Loading 159
  Models 85, 97
  Nonuniformities 107, 121
  Parameters 544, 545
  Position 179
  Side force 456
  Side walls 304
  Stiffness 97
  Tread pattern 131
Tyre Force 48, 50, 89, 459, 479, 498
  Criteria 523
  Spectral densities 72, 75, 88, 102, 117, 119, 121, 485
Tyre pressure 309
  Measurements 111
  Variations 111
Tyre/wheel nonuniformity 121

U

Under-inflation 457
Uneven Load Sharing 303
Uneven Tyre Forces 300
University of Illinois 200
University of Michigan 114
Unsprung mass 67
  Bounce modes 106
  Roll 106, 121
  Vibration modes 116

V

Validation
  Bridge response models 162
  Vehicle models 83
Van der Poel nomograph 245, 280
Variable contact length tyre model 85, 87
Vehicle Assessment 528
Vehicle Body Accelerations 111
Vehicle Fleet
  Sprung mass mode period 331
  Sprung mass mode wavelength 331
  Speed variation 331, 392

Vehicle
Dynamics case studies 83
Geometry 67
Instrumentation 84, 92, 108, 335
Performance test 349
Pitch 519
Regulations 507
Ride 67
Roll motions 93
Simulation 440
Test data 83
Testing 84, 91, 450
Vehicle-bridge interaction 162, 427
Vehicle models 67, 85
For bridge response calculations 428
Guide-lines 107
Parameters 526
Tractor semi-trailer 97
Validation 83
VESYS 250, 280, 286, 351, 368, 372
Vibration Equations 76
Virtual displacements 77
Virtual work 77
Viscoelastic correction 317
Viscoelastic rutting models 244
Viscosity of asphalt 244
Viscosity of Soils and Unbound Granular Materials 254
Viscous dampers 97, 209, 557
Viscous deformation 246
VMA 247, 251, 568

W

Walking beam suspension 13, 31, 71, 116, 124, 302, 318, 320, 353
Model 68, 75, 81
Wavelength 24
Wavenumber 22, 169, 388
Weak spots 369, 382
Weigh plates 112
Weigh-in-motion 112, 114, 125
Weighbridge 125
Weighting matrices 492
Westergaard 9, 159
Wheel
Configuration 309
Force measurement systems 112
Hop frequency 171, 451
Hop mode 116, 513, 541
Load measuring mat 113, 140, 511
Non-uniformities 96
Rotation frequency 96
Tracking tests 250
Wheelbase 520
Wheelbase filtering 76, 107, 116, 118, 193, 319, 364, 468, 513, 521
Whole Vehicle Simulations 88
Whole-Life Flexible Pavement Performance 319, 367, 369
Whole-Vehicle Model 471
Whole-life costs 17
Wide single tyres 304, 305, 308, 353, 372, 440, 453
Wide-spread tandem 91
WIM (Weigh-in-Motion) 568
Array design 137
Calibration 128
Errors and calibration 126
Errors due to mounting 131
Influence of tyre tread pattern 145
Measure of performance 135
Sensor errors 130
Sensor performance 140
Simulation model 135
Terminology 126
Validation 140
WIM sensor errors 132
Bias 127
Calibration 131
Electrical noise 130
Flexibility of mounting 131
Load transmission path 131
Nonlinearity 130
Nonuniformity 130
Random 128
Sensitivity to loaded area 130
Sensitivity to loading rate 131
Systematic 128
Temperature sensitivity 131
Tyre deflection 132
Tyre tread pattern 131
WIM sensors
Accuracy 126
Calibration bias 129
Calibration with instrumented vehicles 129
Frequency response 129
Requirements 113
Spacing 113
Speed dependence 129
Unbiased calibration 130
WIM systems
Calibration 129
Errors due to mounting adhesive 131
Smooth run-up 128
Sources of error 130
Winkler foundation 9, 169
WLPPM 367, 369, 568
Modelling assumptions 403
Wooden block pavements 6
Working life 17
Worsley 7

Y

Young's modulus 250

ADVANCES IN ENGINEERING

1. *Nonlinear Dynamics of Compliant Offshore Structures.*
   Patrick Bar-Avi and Haym Benaroya
   1997. ISBN 90 265 1449 9

2. *Handbook of Vehicle-Road Interaction.*
   David Cebon
   1999. ISBN 90 265 1554 5

This handbook discusses tyre-road contact forces generated by heavy vehicles, their influence on road surface and bridge response and damage, as well as ways of regulating and improving vehicles so as to minimise road damage.

The main incentive for understanding vehicle-road interaction is the possibility of reducing the road damage caused by heavy vehicles and the very high associated costs. This may be achieved by highway authorities, through improved design and construction of roads; by government agencies, through regulations intended to encourage the use of more 'road-friendly' vehicles; or by vehicle engineers, through design of improved vehicle configurations and suspensions, which minimise road damage.

The book provides a unified mechanistic approach to the entire subject, covering the main topics of: vehicle dynamics; dynamic tyre forces; weigh-in-motion; pavement and bridge response; damage mechanisms of paving materials; vehicle-guideway interaction; suspension design to minimise road damage, and assessing road-damaging potential of vehicles for regulatory purposes. It includes 25 literature reviews, covering topics from asphalt deformation to weigh-in-motion, and citing over 500 references. It discusses both the fundamental mechanics of the mechanical and civil engineering systems, as well as practical and implementation issues, and therefore provides both a first introduction to the subject and a comprehensive reference source.

This handbook is essential reading for mechanical and civil engineers, researchers and policy makers in the heavy vehicle and highway engineering industries.

ISBN 90-265-1554-5

